SECOND EDITION

Optical Fiber Communication Systems with MATLAB® and Simulink® Models

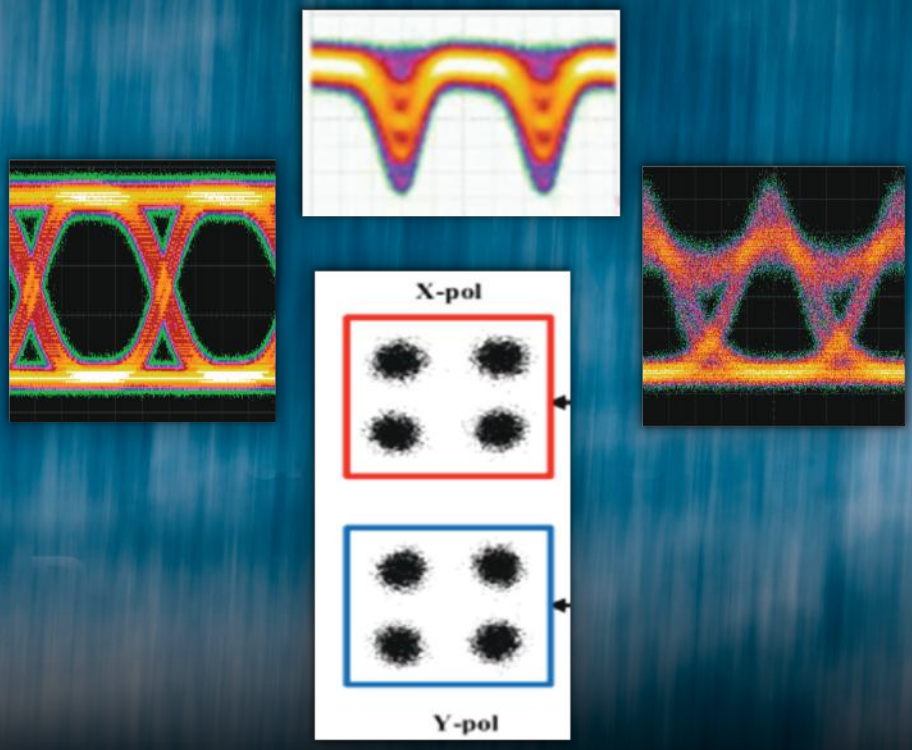

Le Nguyen Binh

CRC Press
Taylor & Francis Group

SECOND EDITION

Optical Fiber Communication Systems with MATLAB® and Simulink® Models

Optics and Photonics

Series Editor

Le Nguyen Binh

Huawei Technologies, European Research Center, Munich, Germany

1. Digital Optical Communications, *Le Nguyen Binh*
2. Optical Fiber Communications Systems: Theory and Practice with MATLAB® and Simulink® Models, *Le Nguyen Binh*
3. Ultra-Fast Fiber Lasers: Principles and Applications with MATLAB® Models, *Le Nguyen Binh and Nam Quoc Ngo*
4. Thin-Film Organic Photonics: Molecular Layer Deposition and Applications, *Tetsuzo Yoshimura*
5. Guided Wave Photonics: Fundamentals and Applications with MATLAB®, *Le Nguyen Binh*
6. Nonlinear Optical Systems: Principles, Phenomena, and Advanced Signal Processing, *Le Nguyen Binh and Dang Van Liet*
7. Wireless and Guided Wave Electromagnetics: Fundamentals and Applications, *Le Nguyen Binh*
8. Guided Wave Optics and Photonic Devices, *Shyamal Bhadra and Ajoy Ghatak*
9. Digital Processing: Optical Transmission and Coherent Receiving Techniques, *Le Nguyen Binh*
10. Photopolymers: Photoresist Materials, Processes, and Applications, *Kenichiro Nakamura*
11. Optical Fiber Communication Systems with MATLAB® and Simulink® Models, Second Edition, *Le Nguyen Binh*

SECOND EDITION

Optical Fiber Communication Systems with MATLAB® and Simulink® Models

Le Nguyen Binh

HUAWEI TECHNOLOGIES CO., LTD., EUROPEAN RESEARCH CENTER

MUENCHEN, GERMANY

CRC Press

Taylor & Francis Group

Boca Raton London New York

CRC Press is an imprint of the

Taylor & Francis Group, an **informa** business

CRC Press
Taylor & Francis Group
6000 Broken Sound Parkway NW, Suite 300
Boca Raton, FL 33487-2742

Version Date: 20141003

International Standard Book Number-13: 978-1-4822-1752-0 (eBook - PDF)

To the memory of my father

To my mother, Mrs. T. H. Nguyen

To Phuong and Lam

Contents

Preface

Written as self-contained material for the principles, practices, and modeling of optically amplified fiber communications systems using MATLAB® Simulink® platform, this book is intended for use in university and professional training courses in the specialized field of optical communications. This lecture-based book should also appeal to undergraduate students of engineering and science who have already taken courses in electromagnetic theory, signal processing, and digital communications and, as an introduction to the modeling, to optical engineers, designers, and practitioners in industry.

The contents of the first edition of this book were used as a set of lecture notes for senior students of bachelor of computer systems engineering and master of telecommunications engineering at Monash University, Melbourne, Australia, and it is not a compendium of all the multifaceted aspects of light wave optical fiber communications engineering. The tremendous advancement of reception techniques using coherent mixing of signals and a local oscillator in association with ultra-high-speed analog to digital convertors and thence digital processors has allowed the transmission of several thousands of kilometers of single-mode optical fibers without using dispersion compensating modules, hence reducing the accumulated noises contributed by optical amplifiers. This edition puts more emphasis on these DSP-based coherent reception techniques in order to prepare the readers for short- and long-term optical transmission networks in the future. Thus, this is one of the main focus of this edition.

Optical fiber communications technology has been developing at a very fast pace since the 1970s and has, in combination with the advancement of digital processing technology, revolutionized global communications, but also the manner in which the fundamentals of telecommunications and information systems and networks are presented. Currently, the transmission of 40 Gb/s per channel in dense wavelength division multiplexed optical systems of 80 wavelength channels is a "done deal" matter leading to the possibility of a transmission capacity of 3–10 Tb/s per single single-mode fiber. The emerging technological development of 100 Gb/s Ethernet under either incoherent or coherent detection with incorporation of electronic processing will stretch further the speed and capacity of optical fiber communications and networks in terrestrial and intercontinental information transport networking.

The design of the contents is very vertical. The applications of optical fibers and related optical technology are built across all optical components of the optical communication engineering. The emphasis is on concepts and interpretation, mathematical procedures, and engineering applications. In this approach, the ground works in the propagation of light waves in planar slab optical waveguides and optical fibers are presented in the first two chapters. The single-mode fibers have reached its maturity, and thus, only the principal parameters of the fibers for operations and for identification of the structures are given rather than going deeply into the design of optical fibers as some textbooks have pursued.

MATLAB software packages have now been a common computing platform for students in global university systems. It is thus sensible to make available programs and simulation models in MATLAB, so that students and instructors can be used for laboratory experiments as well as for further research developments. Therefore, in this book, we provide a detailed description of MATLAB Simulink models. We also

provide samples of the models for readers to download on the book's Web site, http://www.crcpress.com/product/isbn/9781482217513. Thus, the principles of operation of all optical components and optical systems are much more important than their detailed mathematical descriptions.

Chapter 1 gives an overview of the development of optical fiber communications technology over the last three decades of the twentieth century. Readers can skip Chapters 2 and 3 and proceed to other chapters on optical transmitters and receivers if the fundamental understanding of light waves transmission through optical fibers is not required. The transmitters and receivers are treated independently and they form the basic elements of optical communications systems.

Chapters 3 and 4 describe the optical transmitters for direct and external modulation techniques, respectively. It is no doubt that the combination of coherent detection and digital signal processing will play a major role in next-generation ultra-high-speed optical transmission systems. Therefore, the detection of optical signals under direct coherent and incoherent receptions is described in Chapters 9 and 10. They are followed by two chapters on lumped erbium-doped and distributed Raman optical amplifiers (Chapters 9 and 10) with extensive models for the amplification of signals and structuring the amplifiers on Simulink platform.

Thence, Chapter 12 discusses the optical transmission systems design and MATLAB Simulink models with dispersion and attenuation budget methodology. Chapter 13 gives an introduction to advanced modulation formats for long-haul optical fiber transmission systems with accompanied Simulink models. With the significant progresses of the advanced optical communications systems over the last decade for extremely long and extremely high bit rate transmission employing an advanced modulation format, we thus present in this chapter the techniques for the generation of modulation formats and optical transmission. These chapters will deal with the advanced aspects of optical communications engineering for long-haul optical communications systems and intercontinental networks, and emphasis will be focusing on the design and implementation of these optical communications beyond the dispersion limits and networks.

Coherent reception techniques and transmission systems in association with digital processing are introduced in Chapters 13 through 15 (processing algorithms), the three new chapters of this edition.

A number of appendices are used to supplement materials common for all the chapters. In particular, the relationship between the frequency response and its time domain sequence is presented to allow readers to identify the unknown spectral or frequency response when observing the eye pattern obtained by a sampling oscilloscope and the effects of any cable connected between the output of an electrical system and the input port of a high-speed sampling system.

Further emphasis is also placed on "wavelength division multiplexed optical fiber communications systems and networks," which will also give the most advanced aspects to date and beyond the first decade of the twenty-first century (2010) of networking of multicarrier optical multiplexed communications systems engineering. Although research and development of flexible grids with bit rates of 100G and 400G, and 1, 2, 4, and even 10 Tb/s per wavelength channel for optical networks emerges, the technology is not matured enough to be introduced into practice. I hope to introduce this technological development into the next edition of this book.

The contents of the book have been taught to undergraduate students at Monash University over the last decade. Many contributions and questions from many undergraduate and postgraduate students have enriched the writing of this set of notes. In particular,

Dr. Ngo Q. N. (now with NTU Singapore), Dr. Nguyen D. N., Dr. Lam Q. H., K.-Y. Chin, Ho S. C., and D. Lam, who undertook honors and doctoral projects in the modeling of optical fiber communications, have contributed to several software sections of the Monash Optical Communications Systems Simulator using both MATLAB and Simulink as well as an experimental platform setup. I also wish to thank many colleagues at Huawei Technologies Co. Ltd. for helping me understand the modern transmission technologies using coherent receptions and digital signal processing.

Furthermore, many challenging questions from my former undergraduate and postgraduate students studying this subject have made us think and understand deeply the field of optical communications.

Over the last decade, the course developed at Monash University has gone through a number of changes during the last few lectures on the advanced aspects of optical communications engineering, in order to give students at honors level a deeper understanding of the future development of these optical systems and networks. Several fundamental issues involving coherent optical communications were taught. However, we are now more certain in the development and deployment of optical systems and networks in the next few decades of the twenty-first century. They will be long-haul and wavelength multiplexed optical systems and distribution optical networks.

The contents of the chapters given in these lecture notes are thus focused on the practical understanding and fundamental issues that students can use for their future engineering careers. Readers, especially lecturers who are interested in some samples of the basic Simulink models described in this book, can contact the publisher.

It is no doubt that there would be mistakes in the book and we would like to receive fruitful comments from readers and scholars in order to improve the next edition.

Last but not least, I would like to sincerely thank my wife Phuong and our son Lam for their understanding while I have been busy preparing this edition. My parents always supported their son's endeavors to completion with discipline. This book is thus dearly dedicated to my parents.

Le Nguyen Binh
Muenchen, Deutschland

List of Abbreviations

AM	Amplitude modulation/modulator
ASE	Amplified spontaneous emission
ASK	Amplitude-shift keying
BDPSK	Binary differential phase-shift keying
CD	Chromatic dispersion
CPFSK	Continuous-phase frequency-shift keying
CS-RZ	Carrier-suppressed return-to-zero format
DBM	Duobinary modulation
DCF	Dispersion compensating fiber
DCM	Dispersion compensating module
DD	Direct detection
Demux	Demultiplexer
DFB	Distributed feedback (laser)
DI	Delay interferometer
DPSK	Differential phase-shift keying
DQPSK	Differential quadrature phase-shift keying
DSF	Dispersion-shifted fiber
DSP	Digital signal processing/processor
DuoB	Duobinary
EDF	Erbium-doped fibers
EDFA	Erbium-doped fiber amplifier
FMF	Few-mode fiber
FO	Frequency offset
FWM	Four-wave mixing
GVD	Group velocity dispersion
IF	Intermediate frequency
IM	Intensity modulation/modulator
IM/DD	Intensity modulation/direct detection
I-Q	In-phase and quadrature
ISI	Intersymbol interference
ITU	International Telecommunication Union
LO	Local oscillator
MADPSK	Multilevel (*M*-ary) amplitude-differential phase-shift keying
MMF	Multimode optical fibers
M-QAM	*M*-ary QAM or M-constellation points QAM (e.g., 16 QAM is 4 bits per symbol)
MSK	Minimum shift keying
Mux	Multiplexers
MZI	Mach–Zehnder interferometer
MZDI	Mach–Zehnder delay interferometer
MZIM	Mach–Zehnder interferometer modulator or Mach–Zehnder interferometric intensity modulator
NF	Noise figure
NLPN	Nonlinear phase noise

NLSE	Nonlinear Schrödinger equation
NRZ	Non–return to zero
NZDSF	Nonzero dispersion-shifted fiber (ITU-655)
OA	Optical amplifier
O-DPSK	Offset differential phase-shift keying
OFDM	Orthogonal frequency division multiplexing
OOK	On–off keying or amplitude-shift keying (ASK) with binary level
OPLL	Optical phase-locked loop
OSNR	Optical signal-to-noise ratio
Pdf	Probability density function
PLL	Phase-locked loop
PM	Phase modulator
PMD	Polarization mode dispersion
PMF	Polarization-maintaining fiber
QAM	Quadrature amplitude modulation
QPSK	Quadrature phase-shift keying
ROA	Raman optical amplifier
RZ	Return-to-zero format
RZ33	RZ pulse of width of 33% of bit period format
RZ50	RZ pulse of width of 50% of bit period format
RZ67	RZ pulse of width of 67% of bit period format (normally CS-RZ)
SBS	Stimulated Brillouin scattering
SMF	Single-mode fiber
SPM	Self-phase modulation
SSMF	Standard single-mode fiber (ITU-652)
STAR-QAM	Star quadrature amplitude modulation
TOD	Third-order dispersion
XPM	Cross-phase modulation

List of Notations

α_L	Attenuation (linear scale)
α_{dB}	Attenuation factor in dB
β	Propagation constant of fiber
β_1	First-order differentiation of the propagation with respect to the angular frequency—propagation delay
β_2	Second-order differentiation of the propagation constant—group velocity dispersion (GVD)
β_3	Third-order differentiation of the propagation constant—dispersion slope
b_0, b_1	Energy of a "1" transmitted and received at the front end of a photodetector
δ	Delta-factor—equivalent to the Q-factor
f_c	Optical carrier frequency (center)
h	Plank's constant
L	Fiber length
L_a	Fiber length of optical amplifier
η	Quantum efficiency

N	Number of fiber spans
$\Re$	Responsivity
λ	Wavelength
q	Electronic charge
B_e	Electrical bandwidth
B_o	Optical bandwidth
i_{Neq}	Total equivalent noise current at the input of an electronic amplifier
i_{Ns}	Shot noise current
i_d	Dark current noise of a photodetector
$<i_s(t)>$	Average current generated by signal power $P_s(t)$
S_N	Noise spectral density (A^2/Hz)
$[y]$	Admittance parameter matrix of the small signal model of an electronic device

1

Introduction

Optical communication systems employ lightwaves to transmit information from one place to another separated across distances that range from a few kilometers to thousands of kilometers. These systems deliver information from central exchanges to homes and vice versa or to and between major cities, respectively. Furthermore, these distances are now transoceanic distances, reaching several thousands of kilometers as shown in Figure 1.1. Figure 1.2 shows a map from KDD Submarine Cable Systems Inc. that shows the submarine cable infrastructure in the Asian region in 1996. More details of the fiber cable networks in South East Asia and Australia–Oceania region are given. The connection and the cable from Australia to America and Europe is the longest and is considered to be the most extensively laid out one of all the optical transmission systems. The lightwave frequency is in the range of nearly 200 THz for a wavelength of 1550 nm, and several wavelength channels can be multiplexed to make the total capacity reach few tens of terabytes/second over this spectral band. This band is only a very small part of the optical spectrum. Fortunately, this region is the lowest attenuation spectral window of silica fiber which is the critical guiding medium with minimum broadening effects on transmitted data pulse sequences. The electromagnetic spectrum for communications is shown in Figure 1.3. As observed, the spectrum of optical communication based on silica fiber occupies only a small fraction of the electromagnetic spectrum but extensive bandwidth and capacity will be made available in the years to come.

The bit rate for information can now reach several tens of gigabytes/second in the first decade of the twenty-first century. At present, 10 Gb/s Ethernet is standard and 100 Gb/s Ethernet will inevitably be introduced in global fiber networks. Similarly, transmission rates under synchronous digital hierarchy OC-192 and OC-768 at 10 Gb/s and 40 Gb/s, respectively, have been demonstrated over the last decade. Recently, the possibility of 1 Tb/s per wavelength channel has been proposed but is yet to be demonstrated.

The modulated lightwaves are guided through single-mode optical fibers and compensated over several spans, which are made of cascading dispersive and compensating fibers as well as optical amplifiers through which direct amplification of photons is achieved.

Over the last 10 years and, especially, since the publication of the first edition of this book, the development and deployment of optic networks with baud rates have increased to 25 GB and then to 28 or 32 GB depending on the error coding required. Using coherent reception and digital signal processing (DSP) has allowed the possibility of massive capacity transmission and networking to reach 100, 400 Gb/s, and Tb/s per wavelength channel employing advanced modulation formats and polarization multiplexing techniques. The transmission distance can reach longer than 3000 km using fiber spans without dispersion compensation (DC) and optical amplification. The additional aim of this edition of the book is to emphasize coherent reception and transmission without DC in association with DSP.

Despite the great advantages that coherent transmission offers, significant attention is still being paid to noncoherent systems because they offer a reasonable performance at relatively low cost. In the near future, we will witness explosions in the deployment of incoherent systems in access and metropolitan optical networks while coherent systems

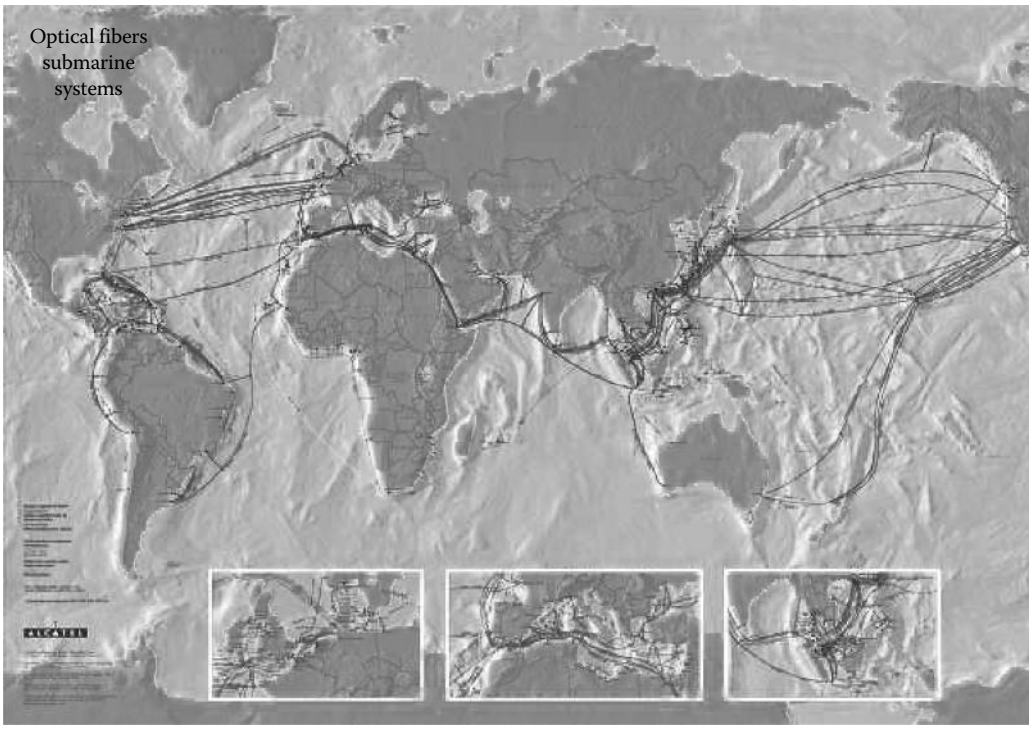

FIGURE 1.1
Alcatel map of submarine cable systems across the globe.

will be extensively deployed in core networks. This chapter treats both techniques intensively and readers should pay close attention to these two complementary techniques and identify the differences in treatment, especially in the reception subsystems and transmission systems.

1.1 Historical Perspectives

Optical fiber communications has advanced at a tremendous pace since its inception in 1966. Its technological development has progressed through three principal phases: the multimode fiber era at the initial stage when silica fiber was first fabricated and manufactured in the early 1970s. Then at the end of the 1970s, single-mode fibers and laser sources in the 1300 nm wavelength were available for research laboratories. At this wavelength, the fiber dispersion is almost zero and the transmission system is limited by the attenuation of the lightwaves.

Since then single-mode optical fibers with low loss at a wavelength of 1550 nm have been used with sources in this region. The loss is nearly half of that at a wavelength of 1300 nm. So, the repeater distance in practice was limited to 40 km. This scenario did not improve until the late 1980s when optical amplifiers were invented, in particular, the Er:doped fiber amplifier that offers significant optical gain in the 1530–1565 nm. Amplification for the

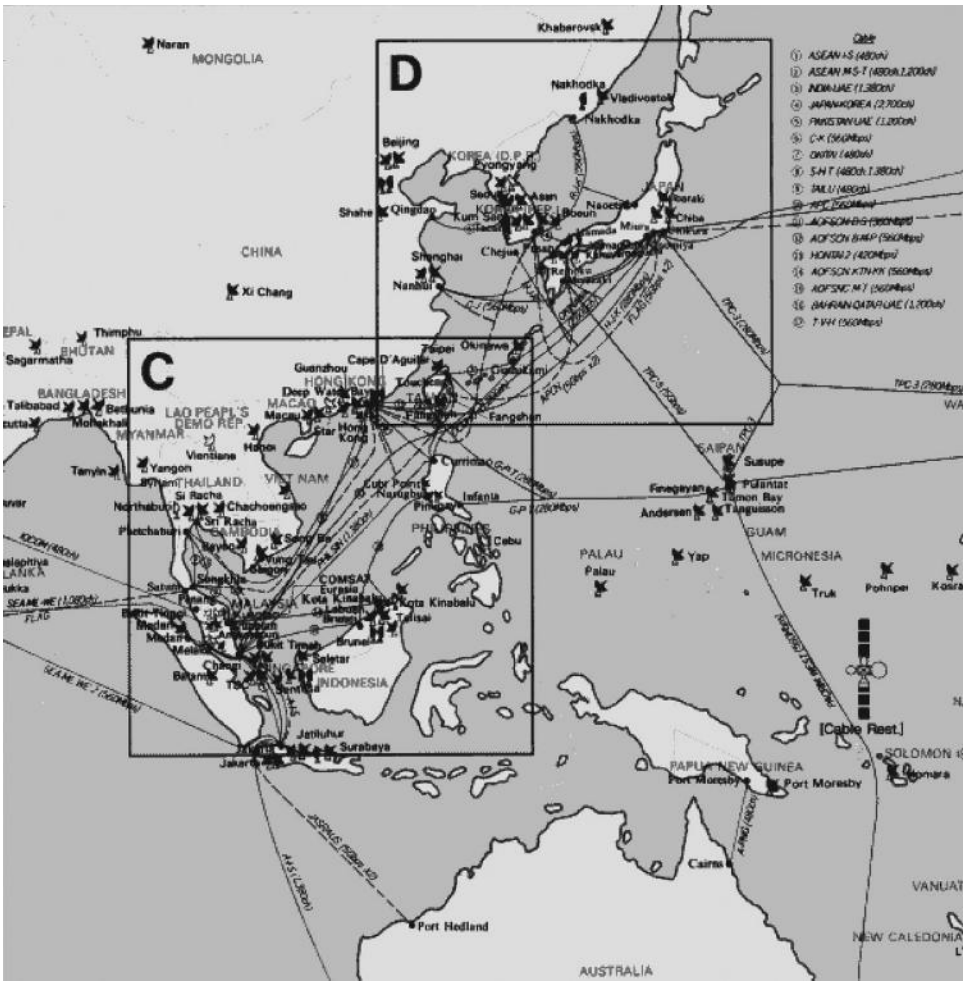

FIGURE 1.2
Optical fiber cable networks in South East Asia and the Australia Oceania region.

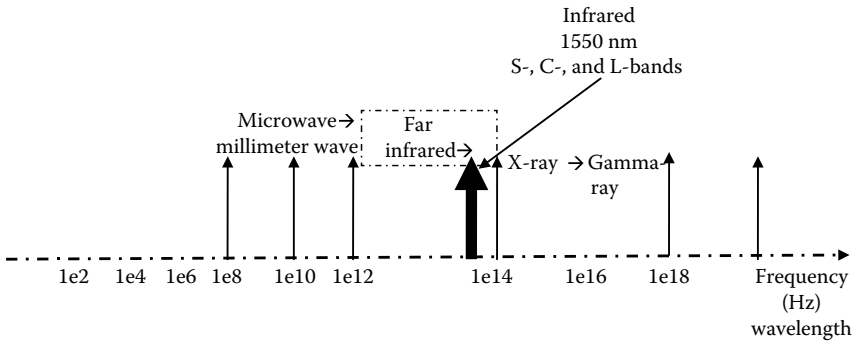

FIGURE 1.3
Electromagnetic spectrum of waves for communications and lightwave region for silica-based fiber optical communications.

L-band would also be available using different doped agents in the silica fiber. However, Raman amplification is also available and the gain is distributed along the length of propagation of the optical signals. These optical amplifiers have since revolutionized the design and implementation of optical transmission systems and networks in which the attenuation factor is no longer a major obstacle. This is why a whole chapter is dedicated to both types of optical amplifiers and their models.

The technological improvements in single-mode optical fibers of transmission, dispersion compensating devices, and single frequency source as well as wide band and low-noise optical receivers have permitted the transmission of high-quality signals over extremely long hauls (of the order of more than a few thousands) at bit rates reaching 40–100 Gb/s. Dispersion management techniques can be exploited to extend the transmission distance further.

Since the linewidth of laser sources can now be narrowed to allow us to consider them as single frequency sources, the modulation by direct manipulation of electron density in the lasing cavity is seldom employed for bit rate equal or greater than 10 Gb/s for long-haul transmission, but external cavity lasers (ECLs) can offer tunable wavelength and linewidth as narrow as 100 Hz. They allow overcoming of the phase noises and thus limit transmission distance. Furthermore, the ECL makes it possible to use coherent reception to boost the receiver sensitivity.

External modulation via the use of electro-optic effects and interference of the continuously turned on lightwaves is the technique that is commonly used currently. Thus, modulation formats have been used to achieve effective bandwidth in the optical passband and to combat the effects of nonlinearity and dispersion.

The employment of narrow linewidth ECL and wideband optical modulators has pushed the symbol rate to 32 and 56 GBaud. Furthermore, the availability of ultra-high sampling rate of 56–GSa/s over the last 3 years and now to 90 GSa/s allows for the flexibility of shaping the optical pulse sequence, for example, raising the cosine leads to a rectangle-like channel spectrum, permitting close packing of information channels.

The progress in ultra-sampling electronic application-specific integrated circuits and analog to digital converters allows the possibility of integrating the DSP. These DSP-based coherent receivers have pushed the coherent transmission systems to grow exponentially at a tremendous pace. Today, in the first two decades of the twenty-first century, 100G coherent long-haul transmission takes place over 3500 km of standard single-mode fibers without dispersion compensation without much difficulty. This bit rate has been now increased to 200G and 400G using 16 quadrature amplitude modulation (QAM) with the symbol rate of 28G or 56G for single wavelength and multiplexed polarization modes. Multiple narrow linewidth sources, generated and locked to one original ECL, the comb generator, have been employed for transmission systems at Terabits/s. by modulating the sub carriers of the comb generator. We expect that these Tb/s will be soon deployed in optical networks.

Besides the long-haul transmissions, metropolitan and access networks now demand high-capacity transmission and networking; in particular, the data centers require this to supply the bandwidth demands of Internet communities at data rates of several Tb/s with transmission distance in the range of 2–10 km. At the same time, the interconnection plane of ultra-high-speed transmission units in data centers and optical network node exchanges demands low-cost and ultra-high-speed optical links. Thus, integrated distributed feedback (DFB) lasers and electro-absorption (EA) modulators have been employed to create transmission optical assembly in association with receiving optical

assembly to achieve 4 × 28 Gb/s (4 wavelength channels at 28 GB) optical link over distances of 40–400 km and a few hundred meters to few kilometers for very low-cost access links.

In this chapter, we concentrate on models that modulate the continuous wave operation of the lasers with advanced methods of detection and transmission of information over optically amplified multi-span single-mode optical fiber systems.

1.2 Digital Modulation for Advanced Optical Transmission Systems

In this chapter, we concentrate on the digital modulation format as a way of carrying information over long distances via the use of the optical carrier. The modulation of the lightwave carrier is described in the following paragraphs.

The optical signal field that has the ideal form in the duration of a one-bit period is given by

$$E_s(t) = E_P(t)a(t)\cos\left[\omega(t)t + \theta(t)\right] \quad \text{for } 0 \le t \le T \tag{1.1}$$

where $E_s(t)$, $E_P(t)$, $a(t)$, $\omega(t)$, and $\theta(t)$ are the signal optical field, the polarized field coefficient as a function of time, the time-variant amplitude, the optical frequency change with respect to time, and the time-variant phase of the carrier under the modulation amplitude, respectively. Depending on the modulation of the carrier by amplitude, frequency, or phase, the modulation formats are as given in the following.

- For amplitude-shift keying (ASK), the amplitude $a(t)$ takes the value $a(t) > 0$ for a "ONE" symbol and the value of 0 for a "ZERO" symbol. Other values such as the angular frequency and the phase parameter remain unchanged over the one-bit period.
- For phase-shift keying (PSK), the phase angle $\theta(t)$ takes a value of π rad for a "ONE" symbol and 0 rad for the symbol "ZERO" so that the distance between these symbols on the phase plane is at a maximum and hence, minimum interference or error can be obtained. These values change if the number of phase states is increased as shown in Figure 1.6. The values of $a(t)$, $\omega(t)$, and $E_p(t)$ remain unchanged.
- For frequency-shift keying (FSK), the value of $\omega(t)$ takes the value $\omega 1$ for the "ONE" symbol and $\omega 2$ for the "ZERO" symbol. The values of $a(t)$, $\theta(t)$, and $E_p(t)$ remain unchanged. Indeed, FSK is a form of phase modulation provided the phase is continuous. Sometimes continuous phase modulation is also used as the term for FSK. In the case when the frequency spacing between $\omega 1$ and $\omega 2$ equals a quarter of the bit rate then the FSK is called minimum-shift keying (MSK).
- For polarization-shift keying (PolSK), we have $E_p(t)$ taking one direction for the "ONE" symbol and the other for the "ZERO" symbol. Sometimes continuous polarization of light wave is used to multiplex two optically modulated signal sequences to double the transmission capacity.

These four digital modulation formats form the basis of modulation formats in advanced optical fiber communication systems. Besides these formats, pulse shaping also plays an important part in these advanced systems. They include Non-Return-to-Rero (NRZ), return to-zero (RZ), and duobinary (DuoB). RZ and NRZ are binary formats taking two levels "0 and 1" while DuoB is a tri-level shaping taking the values of "–1, 0, 1". The –1 in optical waves is taken care of by an amplitude of "1" and a phase shift of π with respect to the "+1", which implies that a differential phase is used to distinguish between the +1 and –1 states. The phase of the carrier under modulation with a phase shift π of the BPSK at the edge of the pulse period is shown in Figure 1.4. Figure 1.5 depicts the constellations of various QAM schemes from PSK to QPSK, 8 PSK, 16 QQAM, and 64 QAM. Note the distance from one constellation to the other. Under the propagation of the optical channels over a single-mode optical fiber (SMF), the maximum amplitude is limited by the nonlinear threshold of the self-phase modulation, which is about 10 dBm. Whenever the degree of the constellation of the QAM is increased then the distance between the constellations is decreased and hence, the probability of error, and in turn the bit error rate (BER) is increased. Thus to obtain the same level of BER, either the noise is to be reduced or more coding is to be implemented to obtain coding gain to reduce the errors.

Another problem with the higher QAM is the transitional period between the amplitude levels, in particular, the highest level to lower levels. This demands that the rise and fall time for the electronic components should be "shorter" than normally specified for a binary signal level. One would gain a higher capacity with a higher-order QAM but there will be higher degrees of difficulty in coding, noise reduction, and higher component

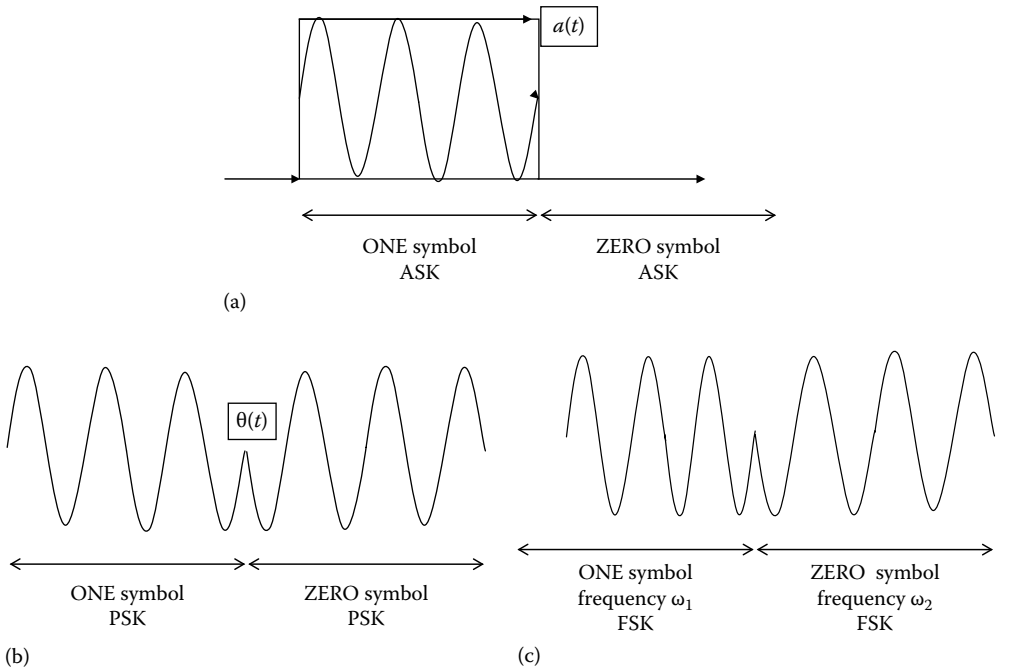

FIGURE 1.4
Illustration of ASK, PSK, and FSK with the symbol and variation of the optical carrier (a) amplitude, (b) phase, and (c) frequency.

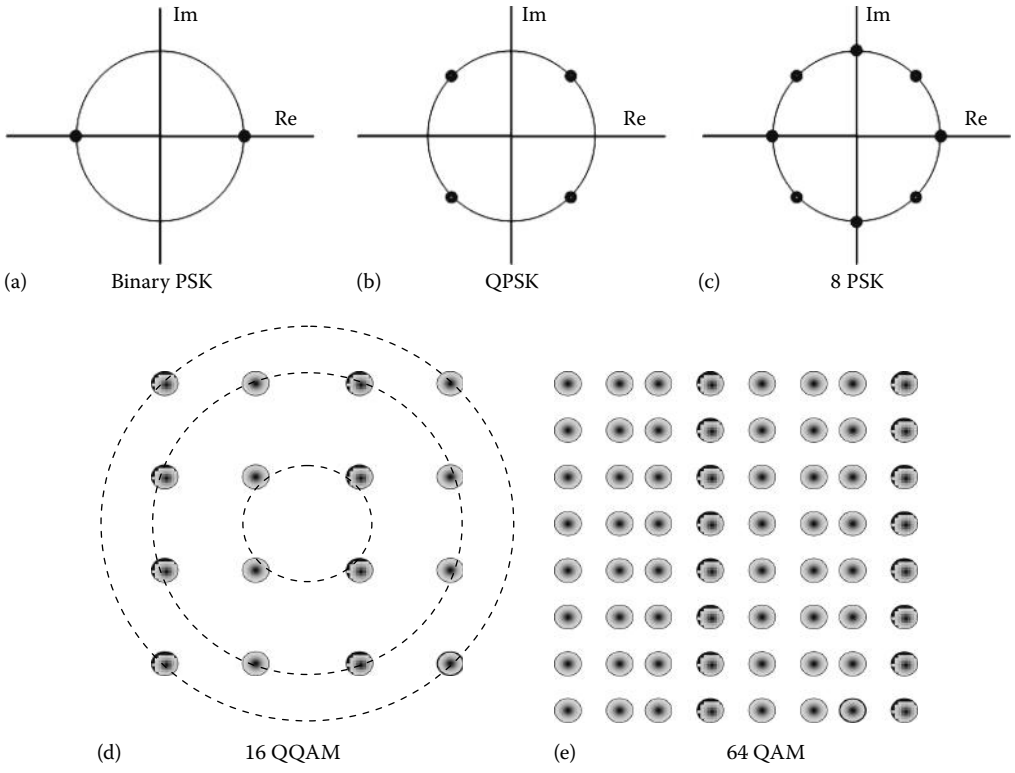

FIGURE 1.5
Constellations of various QAM schemes from (a) PSK to (b) QPSK, (c) 8 PSK, (d) 16 QQAM, and (e) 64 QAM. Note the distance from one constellation to the others.

bandwidth. Several research and development works have been attempted to reduce such difficulties. However, as of now QPSK seems to offer the best performance for long-haul transmission due to its gain of 2 in the capacity while offering the same BER as PSK. So with dual polarizations of a linearly polarized (LP) mode of SMF, two polarized channels can be multiplexed and with the use of QPSK at 25 GBaud the aggregate bit rate can reach 100 Gb/s. The optical modulation for this QPSK scheme can be implemented by using two sets of IQ modulators and polarized multiplexing in an integrated structure. The modulation of the I and Q components are done in a similar way as for binary levels with a $\pi/2$ phase shift in the optical domain. Hence, the combined lightwave channel offers the IQ-modulated lightwaves.

At the receiver, the transmitted channels can be demixed in the wavelength optical domain and the I and Q channels, which are processed in the digital domain after passing through an analog to digital conversion stage. The channels are now mixed with a local oscillator to recover the phase states and the amplitude of the signals. The local oscillator and the carrier are of the same frequency with possibly a small difference (called intradyne coherent detection) that can be recovered by the digital processor. This edition of the book places more emphasis on this coherent reception aspect and DSP. Hence, three chapters have been added to the content of this edition.

The modulated lightwaves at the output of the optical transmitter are then fed into the transmission fibers and fiber spans as shown in Figure 1.6.

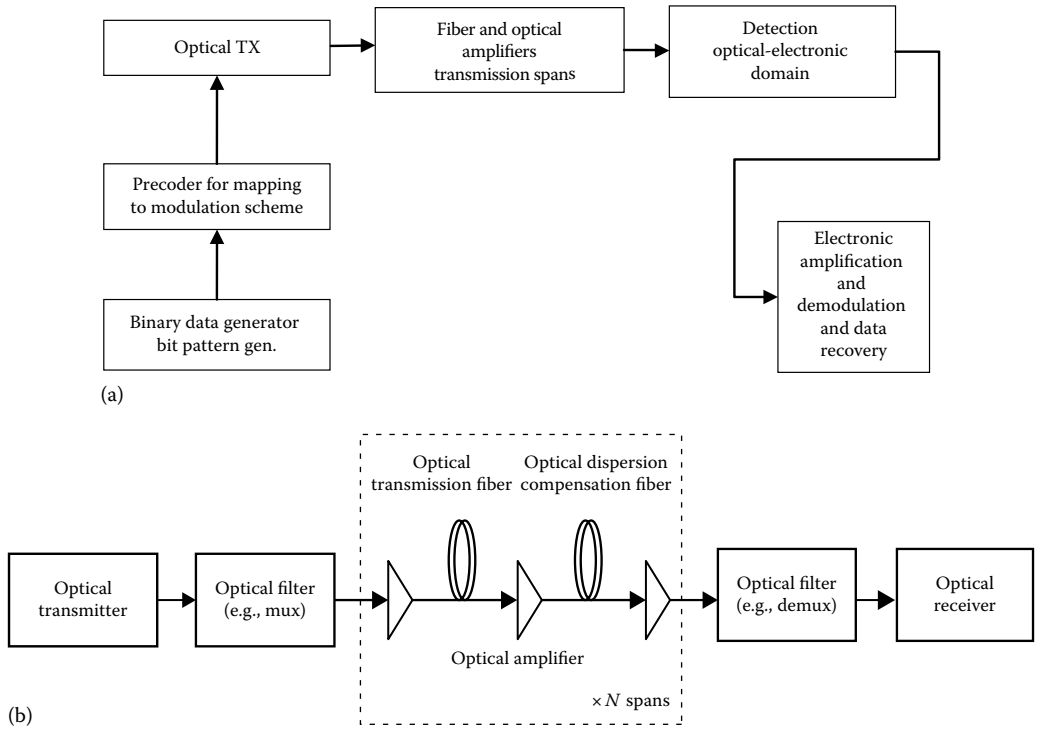

FIGURE 1.6
(a) Generalized diagram of optical transmission systems. (b) More details of the optical transmission system.

1.3 Demodulation Techniques

The output transmitted signals, which are normally distorted, are then detected by a digital optical receiver. The main function of this optical receiver is to recognize whether the current received and hence, the "bit symbol" voltage at the output of the amplifiers following the detector is ONE or ZERO. The modulation of amplitude, phase, or frequency of the optical carrier requires an optical demodulation. That is, the demodulation of the optical carrier is implemented in the optical domain. This is necessary because the extremely high frequency of the optical carrier (of the order of nearly 200 THz for 1550 nm wavelength) makes it impossible to demodulate in the electronic domain by direct detection using a single photo detector. On the other hand, it is quite straightforward to demodulate in the optical domain using optical interferometers to compare the phases of the carrier in two consecutive bits.

However, the phase and frequency of the lightwave signals can be recovered via an intermediate step by mixing the optical signals with a local oscillator, a narrow linewidth laser, to beat it to the baseband or an intermediate frequency region. This is the coherent detection technique. Figure 1.7a and b shows the schematics of optical receivers using direct detection and coherent detection, respectively.

The main difference between these detection systems and those presented in several textbooks is the electronic signal processing subsystem following the detection circuitry.

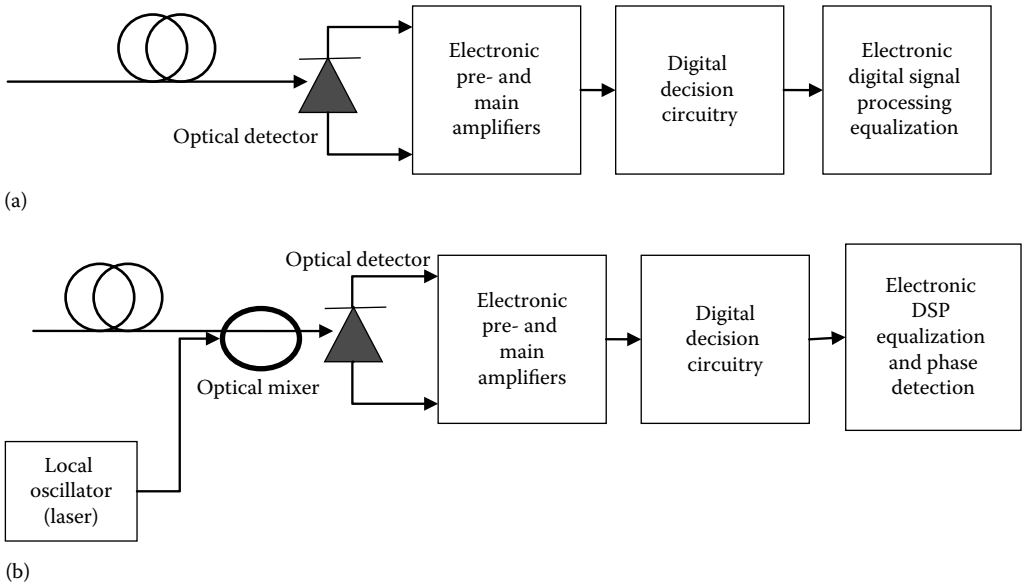

FIGURE 1.7
Schematics of optical receivers using (a) direct detection and (b) coherent detection.

In the first decade of the twenty-first century, we have witnessed tremendous progress in the speed of electronic ultra-large-scale integrated circuits where the number of samples per second can reach a few tens of Giga-samples. This has permitted consideration of applications of DSP of optical signals that are received in a distorted fashion in the electronic domain. This flexibility in the equalization of signals in transmission systems and networks is very attractive.

1.4 MATLAB® Simulink® Platform

Why is MATLAB® Simulink® selected as a modeling and simulation platform for optical fiber transmission systems? Simulink is a separate software package within MATLAB. It is based on a number of block sets, making it easy to use and shortening the learning and development time. Furthermore, MATLAB Simulink requires users to understand the principles of digital communications and does not require a strong foundation in mathematics with various communication and mathematical blocks. There are no such optical communication blocks in MATLAB Simulink, and so one of the main objectives of this chapter is to provide the operational principles of optical communication blocks as examples for users who wish to model their systems. Last but not least, MATLAB packages have now been very popular in the global university computing environment. Students of worldwide universities have been familiar with MATLAB and Simulink is only an extension of MATLAB with several blocks of functions and monitoring equipment available to observe the signals and behavior of the developed systems.

Therefore, our secondary principal objective of this chapter is to describe several optical components and transmission systems in this Simulink platform, so that senior and

research students can adapt their proposed transmission systems without resorting to expensive commercial packages such as VPI Transmission system maker, Optiwave, and so on.

1.5 Organization of the Book Chapters

The presentation of this chapter follows the integration of optical components and modulation techniques in optical communications.

Chapters 2 and 3 give the fundamentals of waveguiding in optical fibers and the essential parameters of such waveguides that would influence the transmission and propagation of optically modulated signals through the fibers. Naturally, only SMFs are treated for advanced optically amplified transmission systems. Chapter 2 gives the static parameters including the index profile distribution and the geometrical structure of the fiber. Mode spot size and mode field diameter of optical fibers are also given to aid in the estimation of the nonlinear self-phase modulation effects. Operational parameters such as group velocity, group velocity dispersion, dispersion factor, and dispersion slope of the single-mode fiber as well as the attenuation factor are described in Chapter 3. The frequency responses including impulse and step responses of optical fibers are also given so that the chirping of an optically modulated signal when propagated through an optical fiber, a quadratic phase modulation medium, can be understood from the point of view of phase evolution. The propagation equation, the nonlinear Schroedinger equation (NLSE), which represents the propagation of the complex envelope of the optical signals, is also described so that the modeling of the signal propagation can be related.

Chapter 4 gives a general outline of the modeling technique based on MATLAB Simulink in which the basic operations of all subsystems of an optically amplified fiber transmission system are outlined. Basic Simulink models are also given.

In Chapters 5 and 6, optical transmitter configurations based on principles of direct modulation (Chapter 5) and external modulation (Chapter 6) are given. They are based on the interferometric effects for generation of phase and frequency modulation, either in the CPFSK format or in the in-phase and quadrature phase (I–Q) structure of PSK format. In an optical transmitter, data modulation is implemented by using either external Electro–Optic Phase Modulators or Mach–Zehnder Intensity Modulators (MZIM). Phasor principles are extensively applied in this chapter to derive the modulation of the carrier phase and amplitude. A fast method for evaluation of the statistical properties of the distribution of the received eye diagrams is described enabling the measurement of the BER from the received eye diagram rather than resorting to the Monte Carlo Method, which would consume a considerable amount of time for computing the errors.

Chapters 7 and 8 give fundamental techniques of direct and coherent detection, respectively, for optical communication systems. Optical receivers and associated noises in such receiving systems are described. The principal aim of Chapter 8 on coherent detection is to address the emerging technological developments of photonic, optoelectronic components and digital signal processors to overcome a number of significant limitations of coherent reception faced by the first generation of coherent systems developed in the 1980s, such as frequency offset between carrier and local laser, the narrow linewidth of the carrier, etc. The limitation and obstacles due to the linewidth of the laser source are no longer a major hurdle. They are now used both as transmitters and as local oscillators at the receiver.

The high sampling speed of electronic digital processors makes possible the estimation of the phase of the signal carrier after producing the beat signals with the local oscillator. Thus, it is necessary that coherent techniques be described for their applications in modern digital optical communication systems. These high-speed digital signal processors are also employed as electrical equalization systems to compensate for disturbance or residual dispersion in the optical transmission systems. The equalization techniques in the electrical domain of digital optical communications are described in Chapter 13. In coherent receivers, the noise sources from producing the beat signals and the amplified stimulated emission (ASE) noise sources would dominate the electronic noises at the front end of the receiver. Analysis and simulation are described in this chapter.

Chapters 9 and 10 describe the optical amplification processes of lumped and distributed amplifiers based on the Erbium-doped fiber amplifier and Raman-distributed amplifiers via pumping in the transmission fibers. Associated Simulink models are given and described in detail.

Chapter 11 presents the theoretical and experimental results of studying performance characteristics of optical transmission systems employing digital modulation techniques. Optical DPSK with the focus on its robustness to tight optical filtering is described in the first section which introduces the phase discrete modulation, especially the differential phase coding. It aims to show the feasibility of implementing cost-effective hybrid optical transmission systems in which 40 Gb/s DPSK channels can be cotransmitted simultaneously with the 10 Gb/s OOK channels over the existing 10 Gb/s network infrastructure. A section describes the modulation of the phase of the carrier but continuous modulation rather than discrete as in Chapter 5. In this, the MSK is described extensively as it is the most efficient continuous phase modulation due to the orthogonal properties of the spectra of the modulated signals at the two distinct carriers. Then it gives an introduction to multilevel formats in amplitude and phase modulation. The driving conditions for a dual-drive MZIM for generation of multilevel amplitude differential PSK are derived. The models for these in MATLAB Simulink platform are also discussed. Dual-level MSK signals are also given. A 16-ADPSK and 16-Star QAM are studied as two typical case studies that would allow the reduction of the symbol rate from 100 to 25 Gb/s at which rate electronic processing would be able to assist in detection using either direct or coherent detection.

Chapter 12 gives detailed designs of optical transmission systems with an outline of the design strategy using attenuation and dispersion to ensure that there is a high probability of success in the transmission. This is then followed by simulation and details of the simulation model using Simulink. A few case studies with complete details of the Simulink models are given.

A number of Appendices of the first edition chapters have been rearranged into Annexes. Chapters 13 through 15 have been added to this second edition to address the modern development of coherent reception with DSP association at the receiver to extend the transmission over optical lines without using DC fibers. Under this scenario, the accumulated noises contributed by the additional optical amplifiers required for DCMs can be eliminated and hence better optical signal to noise ratio so that longer distances can be reached. The impairment due to dispersion and nonlinear effects are compensated by DSP algorithms. Thus, Chapter 15 gives details of DSP algorithms. Chapters 13 and 14 give more details on modeling techniques and performances of transmission systems under these modern modulation formats.

Practice problems are given wherever appropriate at the end of each chapter, whenever appropriate.

2

Optical Fibers: Geometrical and Guiding Properties

This chapter describes the fundamentals of guiding lightwaves in planar and circular optical waveguides. A brief derivation of the wave equation from the Maxwell's equations is given for symmetric planar waveguides leading to the phenomenon of guiding in optical fibers, that is, circular optical waveguides.

Only geometrical parameters of optical fibers are presented here. The attenuation and dispersion effects of modulated lightwave signals, that is, the operational parameters, are described in Chapter 3. However, a brief introduction to fiber nonlinear effects is given here so that the distortion impacts on signals can be treated in the next chapter.

2.1 Motivations and Some Historical Background

Optical fiber communication is no longer the term used in research centers or university research and teaching laboratories. It is now more than 35 years since optical fiber communications came into use and the technology has imposed a significant revolution in the information technology–oriented society of the twenty-first century. Indeed, it was a simple idea proposed in an article in the Proceedings of the Institution of Electrical Engineers by Kao and Hockham [1] in1966 that started it all. The idea was to guide optical waves in a wavelike light guide; the term dielectric waveguide was first used due to the fact that the waveguide is made of nonconducting dielectric materials, later known as silica glass. Light waves, whose frequencies are extremely high, are guided to make ultra-wideband regions available to accommodate information channels. This was believed to be the most fundamental component of optical communications technology.

The first optical fiber was produced in the early 1970s by Maurer and Keck [2,3]; it was the multimode type and excited by sources of wavelength in the visible region. Since then, multimode silica fibers were produced en masse and transmission demonstrated over few kilometers at the bit rate of 34 Mb/s employing pulse code modulations. The multimodal features create variations of the detected light intensities by mode cross-coupling and sensitivity because of bending and temperature variation. Thus, highly dynamic optical receivers were required. Furthermore, as a result of the dispersion of the modulated pulse sequence by the propagation delays of different modes or "rays," the transmission bit rate was limited to a few tens of Mb/s over only a few kilometers. The length-bandwidth product was only about 600 MHz-km or signal bandwidth was limited to 600 MHz for a transmission distance of 1 km in contrast to the several thousands of kilometers with the

capacity of tens of Tera-bits/s over the C-band of single-mode fibers (SMFs) in this first decade of the twenty-first century [4].

In the late 1970s, both theoretical and experimental demonstrations of single-mode operations in circular dielectric waveguides were realized. In the early 1980s, SMFs were extensively deployed over several terrestrial communication links. The bit rate was increased to 2.56 Gb/s in the late 1980s. The structure of SMF also reached the optimized feature with the index profile of step or graded with a core radius of about 4 μm. This structure has not changed significantly till now. Multimode fibers (MMFs) were then used only in the access network due to its low cost in coupling.

The transmission distance was significantly increased to several hundreds of kilometers without repeaters or transponders in the electrical domain due to the invention of rare-earth fiber-doped optical amplifiers in the late 1980s. The bit rate of 10 Gb/s appeared as the new standard transmission rate. During the 1980s, there was intensive research on and development of coherent reception techniques and transmission because of the single-mode nature of the light waves guided along the SMF. However, the requirement for single longitudinal modes and narrow line width of the laser source has deterred the exploitation of the advantage of coherent transmission. At present, however, the progress in digital signal processing and ultra-high sampling rate in the analog-to-digital-converter (ADC) and digital to analog converter (DAC) at 56 GSa/s [5] has allowed the coherent techniques to be extensively employed to extend the reach with the information capacity reaching several thousands of kilometers and Tera-bits/s. In addition, the advancement of narrow laser source of 100 Hz has allowed coherent mixing with a local oscillator/laser. Any frequency difference between the carrier and the oscillator can be compensated by the digital signal processors.

Further features of the single-mode and some operations of the circular fiber are described wherever appropriate in various sections of this chapter. The transmission capacity can be significantly increased by spatial multiplexing of different channels carrying 28 or 56 GBaud and 100 or 400 Gb/s, thus giving rise to the term SDM for spatial division multiplexing [6].

An optical fiber's static operation is described by its geometrical and index profile, guiding conditions, and phase velocity of the guided mode. The dynamic operations of the fibers are described by its dispersion and attenuation properties. This is followed in the next chapter. This chapter is dedicated to provide a fundamental understanding of optical waveguiding and the structures as well as the conditions under which the waveguide can be designed to guide light waves over extremely long distances. The basic components for optical fiber communication networks are the optical guiding media for transmission of optical signals in the form of light waves, called optical waveguides or optical fibers. These light wave transmission media must satisfy the conditions that first, it must be able to guide light waves over a long distance without losing significant optical energy. Second, the signal transmitting through them must not be distorted, and third, they must be structured in such a way that they can support a number of optical electromagnetic field modes.

The main objectives of this chapter are as follows: first to give an introduction to the concept of guided modes in optical waveguides in which light waves are confined to one dimension only, namely, the planar optical waveguides, second to give an introduction to the concept of optical waveguides that extend to a circular geometrical structure, the optical fibers. The properties of the step-index optical fiber which supports only one mode, the single-mode optical fiber, are described and used as the fundamental elements for studying nonstep-index fiber types that are installed throughout global networks. The noncircular or nonstep optical profile fibers can be transformed to a circular optical fiber by using an equivalent step-index profile technique which is given in a later section of this chapter.

Advanced design of optical fibers for dispersion-shifted, dispersion-flattening, and dispersion-compensated fibers are also briefly dealt with. These fibers have gained much attention lately due to their potential applications in optical solution communication systems, dispersion-equalized optical fiber systems, and so on.

We must note here that this chapter presents only the geometrical structures and index distribution of circular optical waveguides and guiding conditions as well as some optical properties of the guided modes. In Chapter 3, we describe the mechanism of distortion and attenuation of optical signals when they are transmitted over long lengths of optical fibers.

This chapter does not aim to give a complete picture of the theoretical development of optical waveguides but provides the essentials for students of physics and engineering that would allow them to use some applications such as transmission of light-wave modulated signals and/or possibly fiber sensors.

This chapter is organized as follows: Section 2.2 describes the fundamental aspects of planar optical waveguides with a derivation of the wave equation from first principles using the derivation of the Maxwell equation. Symmetric planar optical waveguides are given as a simple example of optical waveguiding so as to guide readers to the modes of both planar and circular optical waveguides. The V parameter is identical for both types of waveguides and hence it will be easy for readers to appreciate the importance of this parameter of optical waveguides.

Section 2.3 describes the optical fibers or circular optical waveguides including their geometrical structures and the conditions for supporting one and only one mode. An equivalent step-index profile method is also presented so that different index profile fibers can be designed. The Gaussian approximation of the guided single-mode optical waveguide is given so that the operation parameters of optical fibers can be derived without resorting to mathematical complexity by using the wave equation. One can find from practice when measuring the mode field distribution across a single-mode optical fiber that its radial distribution is very close to that of a Gaussian function. All one has to do is to substitute this function in the wave equation to obtain the propagation constant, and hence other guided parameters. Section 2.4 gives estimation techniques for power distribution over the fiber cross section and the approximation of the spot size of the guided mode.

Section 2.5 describes the method for transforming a nonstep-index profile into an equivalent step-index profile SMF. Section 2.6 outlines briefly the nonlinear effects of self-phase modulation (SPM, cross-phase modulation (XPM), and so on so that the concepts of distortion due to these effects can be estimated for system transmission impairments. Section 2.7 then gives a brief introduction to the manufacture of optical fibers so that readers can appreciate the technological development in optical fibers. Readers are referred to Annex 1 for detailed technical data sheets of a number of optical fibers—standard single-mode fibers (SSMF) ITU-G-652, standard (Corning SMF-28) ITU-G655, and nonzero dispersion–shifted fiber (Corning LEAF—large effective area fiber). Three sample programs written in MATLAB® are provided for readers who may be interested in the design of optical fibers.

2.2 Dielectric Slab Optical Waveguides

Dielectric slab waveguide is the simplest optical waveguiding structure that was first investigated in the early 1960s. It is from this structure that the proposal for an optical fiber was born.

The optical slab waveguide is now widely used as the basic structure for optical integrated circuits such as semiconductor lasers and optical modulators. This section gives the fundamental aspects of optical waveguides with a symmetrical structure, that is, the optical guiding layer sandwiched between two cladding regions with dielectric constants or refractive index smaller than that of the core region.

2.2.1 Structure

A dielectric slab waveguide consists of a slab of dielectric material of refractive index n_1 embedded in a material of index n_2 as shown in Figure 2.1.

Assuming that the structure extends to infinity in the y and z directions, and has a thickness of $2a$ and that the materials are isotopic and lossless, that is, the permittivity coefficients are real and scalar, this leads to a 1D wave equation in the electric field of the light waves and hence, has a simplified mathematical solution. The main reason for this approximation is

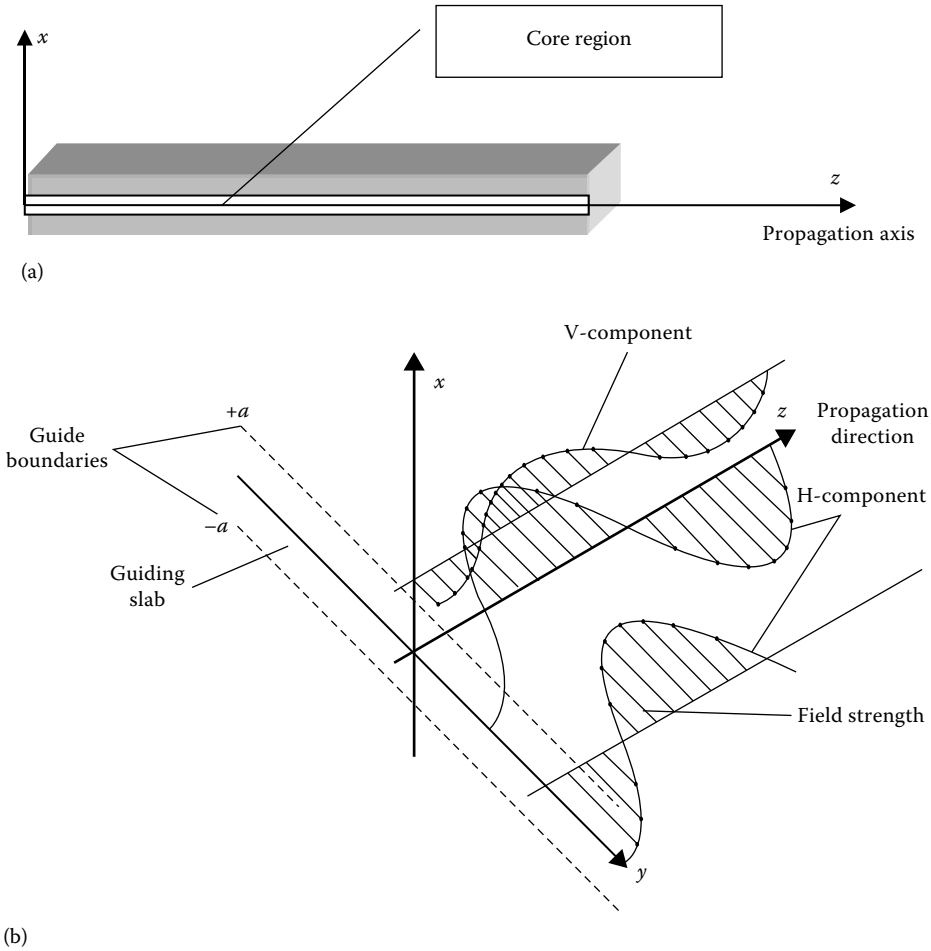

FIGURE 2.1
(a) Geometrical structure of a slab dielectric waveguide. (b) Real part of *E*-field in a slab waveguide ($t = 0$) with thickness of $2a$ and boundaries at $+a$ and $-a$. V = vertical; H = horizontal.

that a circular optical fiber can be easily analyzed by confining the optical waveguide in the y-direction into a circular structure. The wave equation for this type of structure involves cylindrical coordinates and is more complicated to visualize analytically.

2.2.2 Numerical Aperture

If we assume for the moment that the total internal reflections at the boundaries are required for guiding, what is the acceptance angle at which the light waves can be launched? The ray path entering the optical fiber core for total internal reflection is shown in Figure 2.2.

$$n_0 \sin\theta_0 \leq n_1 \cos\theta_c. \tag{2.1}$$

By applying Snell's law at the air-core and core-cladding boundaries of the dielectric waveguide, the total internal reflection can take place only if:

$$n_1 \sin\theta_c = n_2 \sin 90° = n_2 \tag{2.2}$$

where θ_c is the critical angle such that

$$NA = (\sin\theta_0)_{\max} = n_1 \cos\theta_c. \tag{2.3}$$

The numerical aperture (NA) can be defined as the maximum value of $\sin\theta_0$ as given by (2.1), then from (2.2) and (2.3) we have

$$NA = \left(n_1^2 - n_2^2\right)^{1/2} \tag{2.4}$$

When the refractive indices n_1 and n_2 are different by a small index difference then the NA is approximated by

$$NA = n_2(2\Delta)^{1/2} \tag{2.5}$$

where Δ is the relative refractive index difference between the refractive indices of the core and cladding regions. Thus, the refractive index difference determines the magnitude of the NA and hence determines the acceptance angle at which an optical fiber can be guided by incident light waves in the core region. In practice, designers want to increase the NA to maximize optical power that can be coupled to an optical fiber. However, the larger the NA the larger the V parameter and hence the optical fibers will become multimode thus suffering larger delay and more interference effects between the guided modes, resulting in distortion. So in designing a single-mode optical fiber, one has to consider several parameters that affect its performance from a communication systems point of view. We have to, therefore, resort to the wave equation to understand the behavior of light waves in a single-mode optical fiber so that its transmission characteristics can be optimized.

2.2.3 Modes of Symmetric Dielectric Slab Waveguides

The number of optically guided modes of light waves transmitted in an optical waveguide is very important because this indicates the degree of concentration of energy of the light waves in the guiding region and propagating along the guide. The confinement

of the light waves in the transverse plane is similar to the elastic waves propagating in a string or wind instrument, terminated with the two ends open or closed. To find the number of optically guided modes one has to find the conditions under which the light waves would be confined or resonating. Normally, this condition is the eigenvalue equation that is derived from the wave equation and that satisfies the boundary conditions.

Associated with each solution of the optical wave equation is the propagation wave number of each guided wave, which is derived from the eigenvalues of the equation. Thus, the propagation constants take discrete values.

2.2.3.1 The Wave Equations

Let us assume a monochromatic, single frequency or wavelength (we mean a single one and only one frequency component of light waves), wave propagates in the z-direction with its electric field component given by:

$$E(x,y,z) = E(x)e^{(\omega t-\beta z)} \tag{2.6}$$

Indicating that the field is dependent on x and uniform along the y-direction, β is the propagation constant along the propagating z-direction in a slab dielectric waveguide shown in Figure 2.1. Then in the absence of charges and currents, Maxwell's equation reduces to

$$j\beta E_y = -j\omega\mu H_x \tag{2.7a}$$

$$0 = -j\omega\mu H_y \tag{2.7b}$$

$$\frac{dE_x}{dx} = -j\omega\mu H_z \tag{2.7c}$$

$$-j\beta H_x - \frac{dH_x}{dx} = j\omega\varepsilon E_y \tag{2.7d}$$

A visualization of the E-field guided in the slab waveguide is shown in Figure 2.1b and the geometrical structure in Figure 2.1a. By substituting H_x from (2.7a) and H_z from (2.7c) in (2.7d), we get

$$\frac{d^2E_y}{dx^2} + (\beta^2 - \omega^2\mu\varepsilon)E_y = 0 \tag{2.8}$$

where μ and ε are the permeability and permittivity of medium n_1 or n_2, respectively. Similarly, a wave equation involving H_y is given by

$$\frac{d^2H_y}{dx^2} - +(\beta^2 - \omega^2\mu\varepsilon)H_y = 0. \tag{2.9}$$

Equations 2.8 and 2.9 can be rewritten using $k = \omega/c$ and $c = \sqrt{\mu_0 \varepsilon_0}$ (μ_0 and ε_0 are the permeability and permittivity of the vacuum, respectively) where c is the light velocity in vacuum and k is the wave number in vacuum, as

$$\frac{d^2E_y}{dx^2} = -\left(k^2 n_j^2 - \beta^2\right)E_y, \tag{2.10}$$

$$\frac{d^2H_y}{dx^2} = -\left(k^2 n_j^2 - \beta^2\right)H_y \tag{2.11}$$

where $n_j = n_1$ or n_2 ($j = 1, 2$) indicate the refractive index for either the core or the cladding region, respectively.

From (2.10) and (2.11), we observe that the field variation along Ox always exhibits (1) a sinusoidal behavior when $k^2 n_j^2 > \beta^2$, that is, oscillating or light waves are guided and (2) an exponential decaying behavior when $k^2 n_j^2 < \beta^2$, that is, evanescent leading to the radiation of light waves to the cladding region. In another word, the EM field oscillates in regions where the longitudinal propagation constant is smaller than that of the plane wave in this region and becomes evanescent with exponential-like behavior elsewhere.

2.2.4 Optical-Guided Modes

Optical waves are guided along the waveguide when their EM fields are oscillatory in the slab waveguide region and exponentially decaying in the cladding region, that is,

$$kn_2 < \beta < kn_2. \tag{2.12}$$

We need to define a transverse propagation constant u/a and transverse decay constant v/a as

$$\frac{u^2}{a^2} = k^2 n_1^2 - \beta^2 \tag{2.13}$$

$$\frac{v^2}{a^2} = -k^2 n_2^2 + \beta^2 \tag{2.14}$$

thus from (2.13) and (2.14), we obtain

$$\frac{u^2}{a^2} + \frac{v^2}{a^2} = k^2\left(n_1^2 - n_2^2\right) \tag{2.15}$$

or alternatively

$$V^2 = u^2 + v^2 = k^2 a^2\left(n_1^2 - n_2^2\right) \tag{2.16}$$

where the parameter V is defined as the normalized frequency which is dependent only on the core guide size and the refractive index difference between the excitation and the

excitation light frequency. The V parameter and its expression are identical for both planar and circular waveguides, which is treated in the next section. The refractive index difference term is usually much less than 1. The V parameter can be normally approximated by a simpler expression when the refractive index difference is small.

Equations 2.10 and 2.16 show that the field E_y for TE modes and H_y for TM mode form a linear combination of the oscillating functions cos(ux/a) and sin(ux/a) inside the core region, ($|x| \le a$) and they follow an exponentially decaying form outside the core $\left(|x| \le a\right)$ with $e^{-vx/a}$ for $x > a$ and $e^{+vx/a}$ for $x < a$. We therefore have two distinct cases: the even TE modes and the odd TE modes. Their solutions are given in detail in the following text.

2.2.4.1 Even TE Modes

- For $|x| \le a$: inside the core region and oscillating waves, the field solution is

$$E_y \text{ or } H_x = A\cos\frac{ux}{a} \tag{2.17}$$

$$H_z = \frac{j}{\omega\mu_o}\frac{\delta E}{\delta x} = -\frac{j}{\omega\mu_o}\frac{u}{a}A\sin\frac{ux}{a} \tag{2.18}$$

- For $|x| > a$: outside core region and exponentially decaying waves

$$E_y = Ce^{-\frac{V(x-a)}{a}} \tag{2.19}$$

Other field components like H_x and H_z can also be expressed by similar expressions. Applying the boundary condition (continuity of the E-field) at the interface between the cladding and core, that is, at $x = a^+$, and $x = a-$. Using (2.17) through (2.19), we arrive at

$$-j\frac{u}{\omega\mu}\sin u = -j\frac{v}{\omega\mu}\cos u \Rightarrow v = u\tan u. \tag{2.20}$$

This is commonly known as the eigenvalue equation of the wave equation which dictates the number of guided (discrete) modes and the values of the propagation constants of these guided even TE modes.

2.2.4.2 Odd TE Modes

Similarly, the solutions for guided TE odd modes can be found as follows:

- For $x > |a|$

$$E_y \text{ or } H_x = A\sin\frac{ux}{a} \tag{2.21a}$$

$$H_z = \frac{j}{\omega\mu_o}\frac{\delta E}{\delta x} = -\frac{j}{\omega\mu_o}\frac{u}{a}A\cos\frac{ux}{a} \tag{2.21b}$$

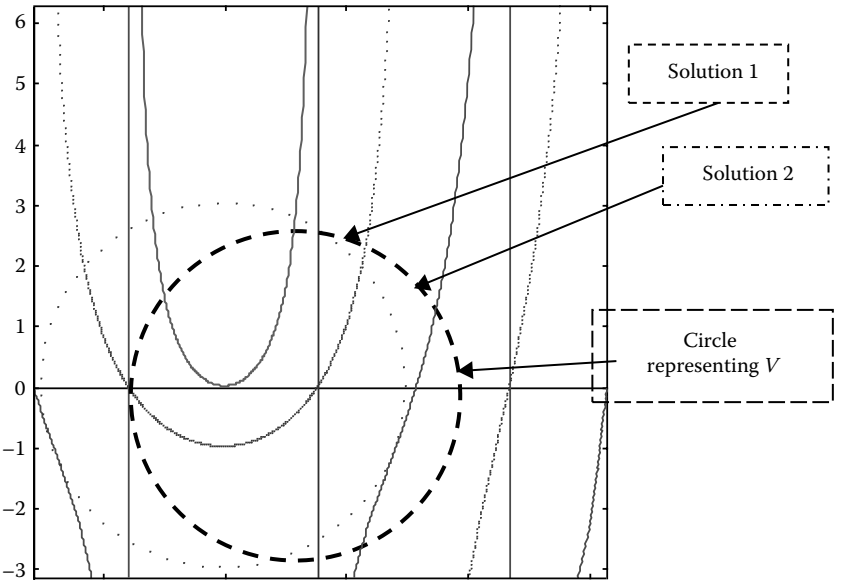

FIGURE 2.2
Graphics and solution of Equations 2.20 and 2.22. The curve indicated by _____ denotes the expression $v = u \tan u$; … denotes $v = u/\tan u$; and …_ denotes $V^2 = u^2 + u^2$.

- For $|x| \leq a$

$$E_y = Ce^{-\frac{V(x-a)}{a}} \tag{2.21c}$$

and the eigenvalue equation can be found by applying the boundary conditions:

$$v = \frac{u}{\tan u} \tag{2.22}$$

Equation 2.21 is obtained by using the continuity of the normal H field component at the boundaries. This is the eigenvalue equation for guided *odd* TE modes of a symmetric planar optical waveguide.

The eigen solutions for the confined modes of the planar waveguide can be found by the graphical technique illustrated in Figure 2.2, in which the intersection of the two curves is represented by Equations 2.20, 2.26, and 2.16. Thus, depending on the number of intersections of the "circle V" and the two curves, the odd and even modes represented can be found to be supported by the waveguide under consideration.

2.2.4.3 Graphical Solutions for Guided TE Modes (Even and Odd)

Combining Equations 2.16, 2.17, and 2.21 we observe that the waveguides can support only discrete modes and the propagation constant β related to the u and v parameters can be found by solving graphically the intersection between circles of V and curves representing Equations 2.20, 2.22, and 2.16. These solutions are illustrated in Figure 2.2. The field distribution of the even and odd TE mode can be found in Figure 2.3.

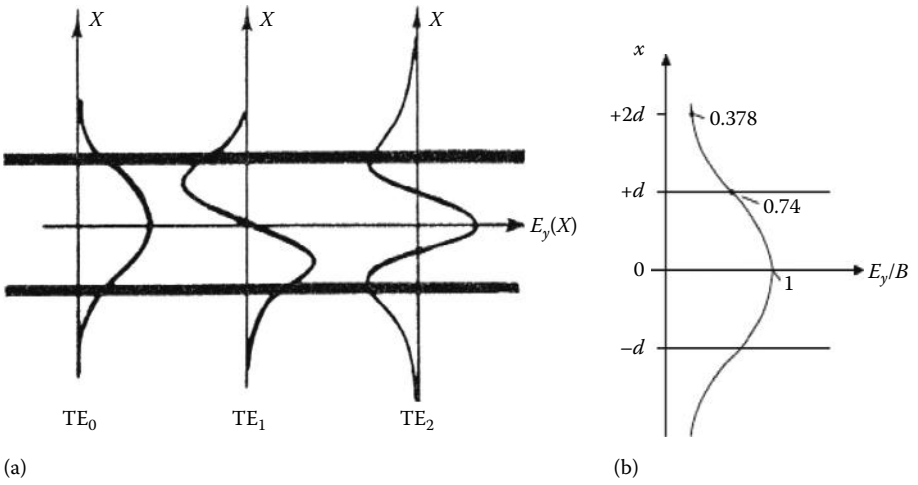

FIGURE 2.3
(a) Field distribution of TE modes of order 0, 2 (even modes) and 1 (odd mode) and (b) field distribution of the fundamental mode.

2.2.5 Cutoff Properties

From Figure 2.2, we observe that:

- $V = 0$, when we excite with light waves of zero optical frequency or when $\lambda = 0$. This is absurd.
- For $\lambda > 0$: we observe that we always have at least one guided mode, TE_0.
- $V < \pi/2$, only one guided mode is supported by the waveguide.
- $V \rightarrow \pi/2$, the odd TE_1 mode appears greater, this is the second-order mode.
- $V = \pi$: the third mode (TE_2) starts appearing and is supported by the waveguide.

That is, each time the V parameter reaches an integral multiple of $\pi/2$, a new mode reaches its cutoff corresponding to $v = 0$ and $\beta = kn_2$. We note that for TE-guided modes the optical waveguide can always support at least one. However for TM-guided modes, the waveguide can support a guide mode if its thickness or the optical wavelength and the refractive index difference, v (lower case), has a value of at least $\pi/2$. This is true for planar optical waveguides only. For circular optical waveguides, such as in the case of circular optical fibers, the cutoff condition is different. We deal with this type of optical waveguide in the next section.

It is to be noted that the theoretical waveguide (planar type) always supports an optical-guided mode. The cutoff is for cutting off the higher-order mode to ensure that the waveguide supports only one mode.

Exercise 2.1

A slab waveguide of width 10 μm has refractive indices $n_1 = 1.505$ and $n_2 = 1.495$. Find the V parameter at 1550 and 850 nm operating wavelengths and the corresponding number of guided modes and their propagation constants at these spectral regions for each case.

2.3 Optical Fiber: General Properties

2.3.1 Geometrical Structures and Index Profile

An optical fiber consists of two concentric dielectric cylinders. The inner cylinder, or core, has a refractive index of $n(r)$ and radius a. The outer cylinder, or cladding, has index n_2 with $n(r) > n_2$ and a larger outer radius. Core of about 4–9 μm and a cladding diameter of 125 μm are the typical values for silica-based single-mode optical fiber. A schematic diagram of an optical fiber is shown in Figure 2.4.

The refractive index n of an optical waveguide is usually changed with radius r from the fiber axis ($r = 0$) and is expressed by

$$n^2(r) = n_2^2 + NA^2 s\left(\frac{r}{a}\right) \tag{2.23}$$

where NA is the numerical aperture at the core axis, while $s(r/a)$ is the profile function, which characterizes any profile shape ($s = 1$ at maximum) with a scaling parameter, the core radius.

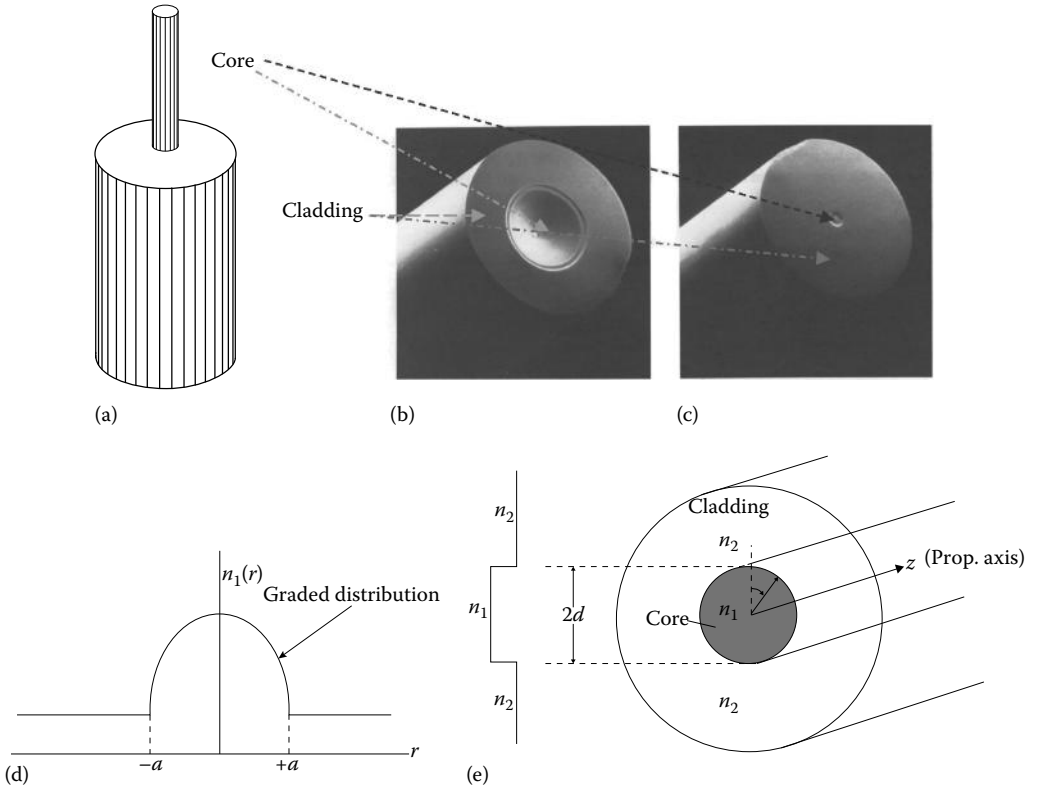

FIGURE 2.4
(a) Schematic diagram of the step-index fiber: coordinate system, structure. The refractive index of the core is uniform and slightly larger than that of the cladding. For silica glass the refractive index of the core is about 1.478 and that of the cladding about 1.47 at 1550 nm wavelength region. (b) Cross section of an etched fiber—multimode type—50 μm diameter. (c) Single-mode optical fiber etched cross section. (d) Graded-index profile. (e) Fiber cross section and step-index profile $d = a$ = radius of fiber.

2.3.1.1 Step-Index Profile

In a step-index profile, the refractive index remains constant in the core region, thus

$$s\left(\frac{r}{a}\right) = 1 \quad \text{for } r \le a, \tag{2.24}$$

$$s\left(\frac{r}{a}\right) = 0 \quad \text{for } r > a \tag{2.25}$$

so we have for a step-index profile

$$n^2(r) = n_1^2; \quad \text{for } r < a \tag{2.26}$$

and

$$n^2(r) = n_2^2; \quad \text{for } r > a \tag{2.27}$$

Exercise 2.2

Refer to the technical specification of the single-mode optical fiber Corning SMF-28. State whether the index profile of the fiber is a perfect step-index profile or graded-index profile? Is it true that the profile is a perfect step-index distribution? If not, then what is the real manufactured profile?

2.3.1.2 Graded-Index Profile

We consider here under the two most common types of graded-index profiles: power-law-index and the Gaussian profile.

2.3.1.3 Power-Law-Index Profile

The core refractive index of the optical fiber usually follows a graded profile. In this case, the refractive index rises gradually from the value n_2 of the cladding glass to value n_1 at the fiber axis. Therefore, $s(r/a)$ can be expressed as

$$s\left(\frac{r}{a}\right) = \begin{cases} 1 - \left(\frac{r}{a}\right)^{\alpha} & \text{for } r \le a \\ 0 & \text{for } r < a \end{cases} \tag{2.28}$$

with α = power exponent. Thus, the index-profile distribution $n(r)$ can be expressed in the usual way by using (2.28) and (2.24) and then substituting $NA^2 = n_1^2 - n_2^2$.

$$n^2(r) = \begin{cases} n_1^2\left[1 - 2\Delta\left(\dfrac{r}{a}\right)^{\alpha}\right] & \text{for } r \le a \\ n_2^2 & \text{for } r > a \end{cases} \tag{2.29}$$

with $\Delta = NA^2/n_1^2$ is the relative refractive difference. From the equation describing the profile shape in (2.29), it can be seen that there are three special cases:

1. α = 1: The profile function $s(r/a)$ is linear and the profile is called a triangular type.
2. α = 2: The profile is a quadratic function with respect to the radial distance and the profile is called the parabolic profile.
3. α = ∞: The profile is a step type.

2.3.1.4 Gaussian-Index Profile

In the Gaussian-index profile, the refractive index changes gradually from the core centre to a distance very far away from it and $s(r)$ can be expressed as

$$s\left(\frac{r}{a}\right) = e^{-\left(\frac{r}{a}\right)^2} \tag{2.30}$$

2.3.2 The Fundamental Mode of Weakly Guiding Fibers

The electric and magnetic fields $E(r,\phi,z)$ and $H(r,\phi,z)$ of the optical fibers in cylindrical coordinates can be found by solving Maxwell's equations. However, only lower-order modes of ideal step-index fibers are important to the present optical fiber communication systems, so that one can approximate the wave equation as a scalar equation. The well-known fact is that Δ < 1%, or the difference in the refractive index of the core and cladding regions is very small. Therefore, the optical waves are weakly guided and the field components E and H can then be approximated by the solutions of the scalar wave equation

$$\left[\frac{\partial^2}{\partial r^2} + \frac{1}{r}\frac{\partial}{\partial r} + k^2 n_j^2 - \beta^2\right]\varphi(r) = 0 \tag{2.31}$$

where $n_j = n_1$ or n_2 and $\varphi(r)$ is the spatial field distribution of the nearly transverse EM waves given as

$$\begin{aligned} E_x &= \varphi(r)e^{-i\beta z} \\ H_y &= \left(\frac{\varepsilon}{\mu}\right)^{1/2} E_x = \frac{n_2}{Z_0} E_x \end{aligned} \tag{2.32}$$

with E_y, E_z, H_x, H_z negligible, $\varepsilon = n_2^2\varepsilon_0$ and $Z_0 = \sqrt{\mu\varepsilon}$ as the vacuum impedance. That is, the waves can be seen as a plane wave traveling down along the fiber tube. These plane waves

are reflected between the dielectric interfaces, or in other words, they are trapped and guided in and along the core of the optical fiber.

2.3.2.1 Solutions of the Wave Equation for Step-Index Fiber

The field spatial function $\varphi(r)$ would take the form of Bessel functions, from (2.31) as

$$\varphi(r) = A\frac{J_0(ur/a)}{J_0(u)} \quad \text{for } 0 < r < a, \tag{2.33}$$

$$\varphi(r) = A\frac{K_0(vr/a)}{K_0(v)} \quad \text{for } r > a \tag{2.34}$$

where J_0 and K_0 are the Bessel functions of the first kind and modified second kind, respectively, and u and v are defined similarly as given in (2.13) and (2.14). Thus following Maxwell's equations, we can find that E_z can take two possible solutions that are orthogonal to each other as

$$E_z = -\frac{A}{kan_2}\begin{pmatrix}\sin\phi\\ \cos\phi\end{pmatrix}\begin{cases}\dfrac{uJ_1\left(u\dfrac{r}{a}\right)}{J_0(u)} & \text{for } 0 \le r < a\\[2ex] \dfrac{vK_1\left(\dfrac{vr}{a}\right)}{K_0(v)} & \text{for } r > a\end{cases} \tag{2.35}$$

The terms u and v must satisfy simultaneously two equations:

$$u^2 + v^2 = V^2 = ka\left(n_1^2 - n_2^2\right)^{1/2} = kan_2(2\Delta)^{1/2} \tag{2.36}$$

$$u\frac{J_1(u)}{J_0(u)} = v\frac{K_1(v)}{K_0(v)} \tag{2.37}$$

where (2.37) is obtained by applying the boundary conditions at the interface $r = a$. E_z is the tangential component and must be continuous at this dielectric interface. Equation 2.37 is commonly known as the eigenvalue equation. The solution of this equation would give the values of β, which would take discrete values and represent the propagation constants of the guided light waves.

Equation 2.37 shows that the propagation velocity of the longitudinal field is depending on the order of the transverse component. In practice, $\Delta \ll 1$, then by using (2.36), we observe that this longitudinal component can be negligible as compared to the transverse component. We thus consider the mode as transversely polarized. The fundamental mode is then usually denominated as linearly polarized mode LP_{01} (LP = Linearly Polarized) for which the field distribution is shown in Figure 2.5 and the graphical representation of the

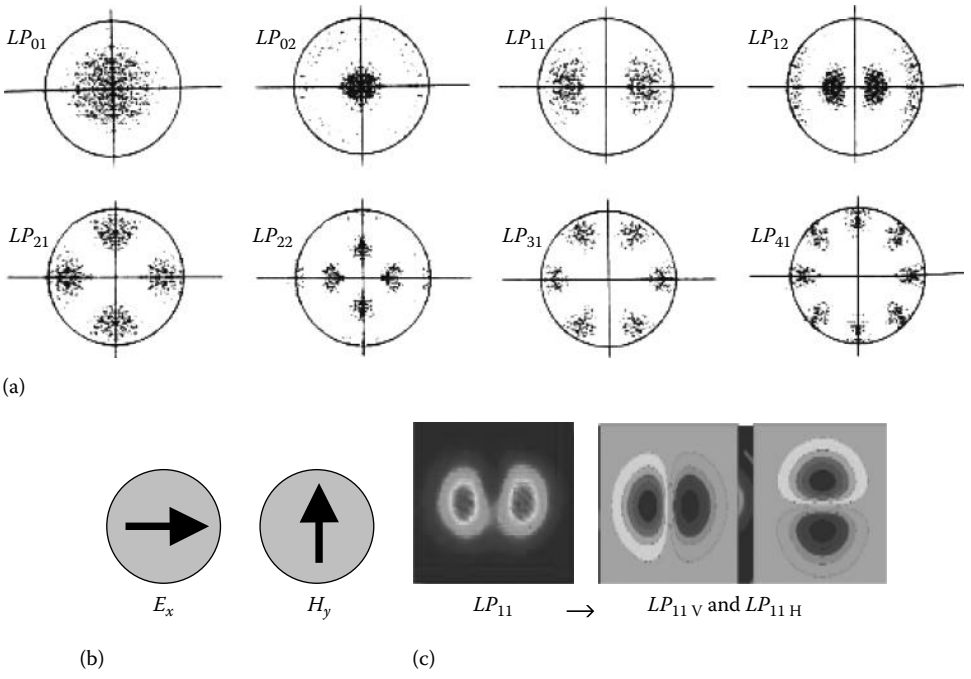

FIGURE 2.5
(a) Spectrum of guided modes in a multimode fiber and calculated intensity distribution of LP-guided modes in a step-index optical fiber with $V = 7$. (b) Electric and magnetic field distribution of an LP_{01} mode polarized along O of the fundamental mode of a single-mode fiber. (c) The observed mode LP_{11}. Both polarization modes are included—no distinction. However, distinct polarized modes for LP_{11} are shown on the right. H = horizontal, V = vertical.

eigenvalue equation (2.37) with the variation of $b = \beta/k$ defined as the normalized propagation constant and the V parameter is shown in Figure 2.6c.

2.3.2.1.1 Fundamental Mode Revisited by Gaussian Approximation

We note again that the **E** and **H** are approximate solutions of the scalar wave equation and the main properties of the fundamental mode of weakly guiding fibers are as follows:

- The propagation constant β (in the z-direction) of the fundamental mode must lie between the core and cladding wave numbers. This means the effective refractive index of the guided mode lies with the range of the cladding and core refractive indices.
- The fundamental mode must be close to that of a transverse electro-magnetic wave as described by (2.32).

$$\frac{2\pi n_2}{\lambda} < \beta < \frac{2\pi n_1}{\lambda}. \tag{2.38}$$

- The spatial dependence of $\phi(r)$ is a solution of the scalar wave equation (2.31).

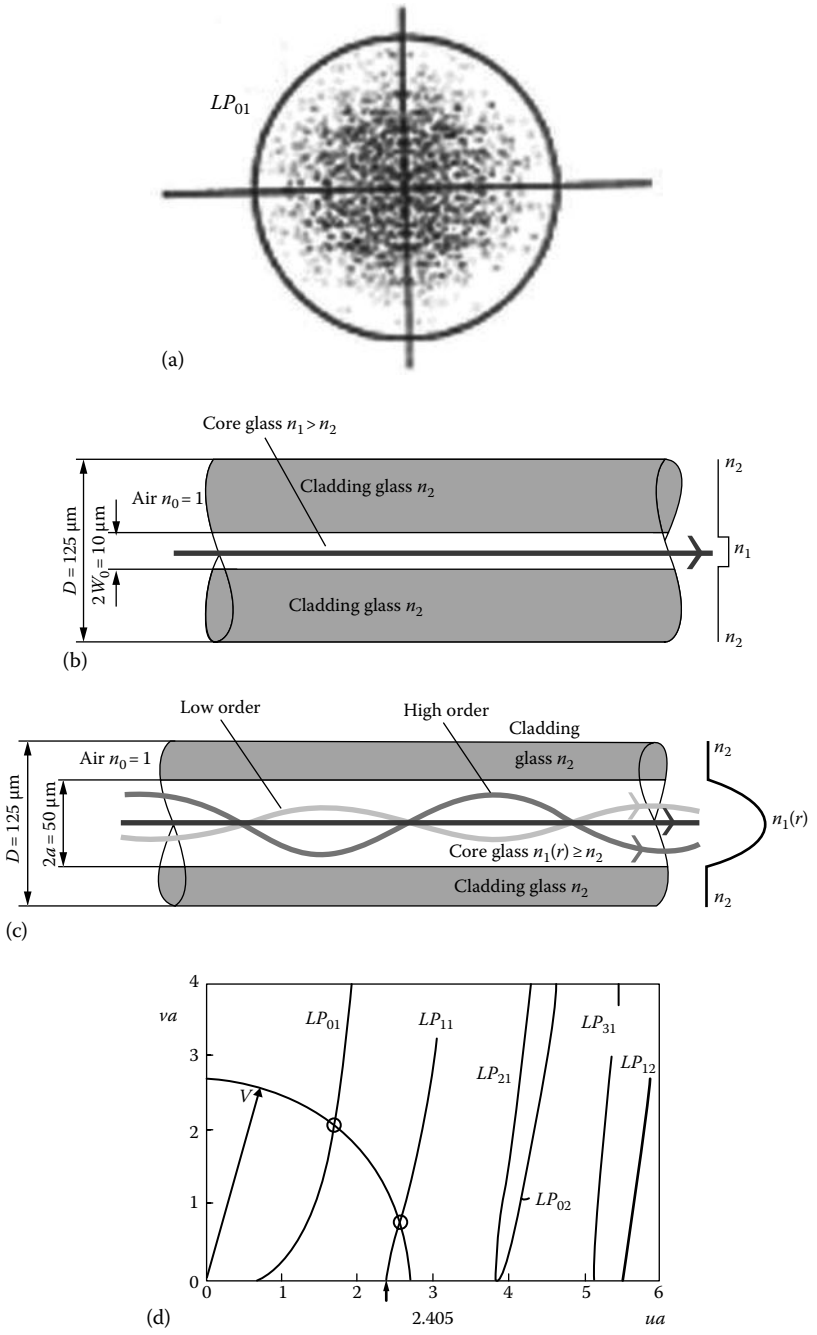

FIGURE 2.6
(a) Guided modes as seen in the transverse plane of a circular optical fiber. (b) "Ray" model of light wave propagating in single-mode fiber. (c) Ray model for multimode graded-index fiber. (d) Graphical illustration of solution for eigenvalues (propagation constant—wave number of optical fibers). (*Continued*)

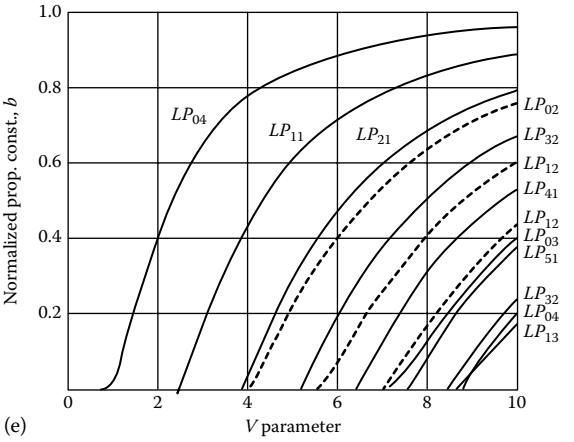

FIGURE 2.6 (*Continued*)
(e) b–V relationship for a number of guided modes in circular fibers.

The main objective is to find a good approximation for the field $\varphi(r)$ and the propagation constant β, which can be found as the eigen solution of the eigenvalue equation, which would follow the Bessels function as described in the previous section. It would be desirable to obtain a good approximation for the field to obtain simple expressions to have a clearer understanding of light transmission on single-mode optical fibers without going through graphical or numerical methods. Furthermore, experimental measurements and numerical solutions for fibers of step-index and power-law-index profiles show that $\varphi(r)$ can be approximated as a Gaussian spatial distribution. Thus, we can approximate the field of the fundamental mode as

$$\varphi(r) \cong Ae^{-\frac{1}{2}\left(\frac{r}{r_0}\right)^2} \tag{2.39}$$

where r_0 is defined as the mode spot size, that is, the radial distance at which the intensity of the mode equals to $1/e$ of its maximum value, commonly situated at the center of the fiber. Thus multiplying the wave Equation 2.31 by $r\varphi(r)$ and using the identity

$$r\varphi\frac{\delta^2\varphi}{\delta r^2} + \varphi\frac{\delta\varphi}{\delta r} = \frac{\delta}{\delta r}\left(r\varphi\frac{\delta\varphi}{\delta r}\right) - r\left(\frac{\delta\varphi}{\delta r}\right)^2 \tag{2.40}$$

and by integrating from 0 to ∞, using the identity $\left[r\varphi(r)\frac{d\varphi}{dr}\right]_0^\infty = 0$ leads to

$$\beta^2 = \frac{\int_0^\infty \left[-\left(\frac{\delta\varphi}{\delta r}\right)^2 + k^2n^2(r)\varphi^2\right] r\delta r}{\int_0^\infty r\varphi^2\delta r} \tag{2.41}$$

The procedure to find the spot size can then be followed by substituting $\varphi(r)$ given by (2.39) into (2.41), then differentiating and setting $\frac{\delta^2\beta}{\delta r}$ equal to zero at r_0, that is, the propagation constant β of the fundamental mode *must* give the largest value of r_0.

Knowing r_0 and β, the fields E_x and H_y (see (2.32)) can be fully specified.

Case 1: Step-index fiber
Substituting the step-index profile given by (2.32) and φ(*r*) in (2.39) into (2.41) leads to an expression for β in terms of r_0. The mode spot size can be evaluated by setting

$$\frac{\partial^2 \beta}{\partial r_0} = 0 \tag{2.42}$$

and r_0 is then found as

$$r_0^2 = \frac{a^2}{\ln V^2} \tag{2.43}$$

Substituting (2.43) into (2.40), we have

$$(a\beta)^2 = (akn_1)^2 - \ln V^2 - 1. \tag{2.44}$$

This expression is physically meaningful only when $V > 1$ and r_0 is positive.

Case 2: Gaussian-index profile fiber
For the case of a Gaussian-index profile, by following the procedure for step-index profile fiber we obtain

$$\left(a\beta\right)^2 = \left(an_1 k\right)^2 - \left(\frac{a}{r_0}\right)^2 + \frac{V^2}{\left(\frac{a}{r_0} + 1\right)} \tag{2.45}$$

and

$$r_0^2 = \frac{a^2}{V - 1} \text{ by using } \frac{\partial^2 \beta}{\partial r_0} = 0 \tag{2.46}$$

that is, maximizing the propagation constant of the guided waves. The propagation constant is at maximum when the "light ray" is very close to the horizontal direction. Substituting (2.46) into (2.45), we have

$$\left(a\beta\right)^2 = \left(akn_1\right)^2 - 2V + 1. \tag{2.47}$$

Equations 2.46 and 2.47 can be physically meaningful only when $V > 1 (r_0 > 0)$, that is, to satisfy

$$r_0^2 = \frac{a^2}{V - 1} \neq \infty \tag{2.48}$$

It is obvious from Equation 2.48 that the spot size of the optical fiber with a *V* parameter of 1 is extremely large. This is a very important point, namely, that one must not design the optical fiber with a near unit value for the *V* parameter. In practice, we observe that the spot size is large but finite (observable). In fact if *V* is smaller than 1.5 the spot size becomes large. In the next chapter this is investigated in detail.

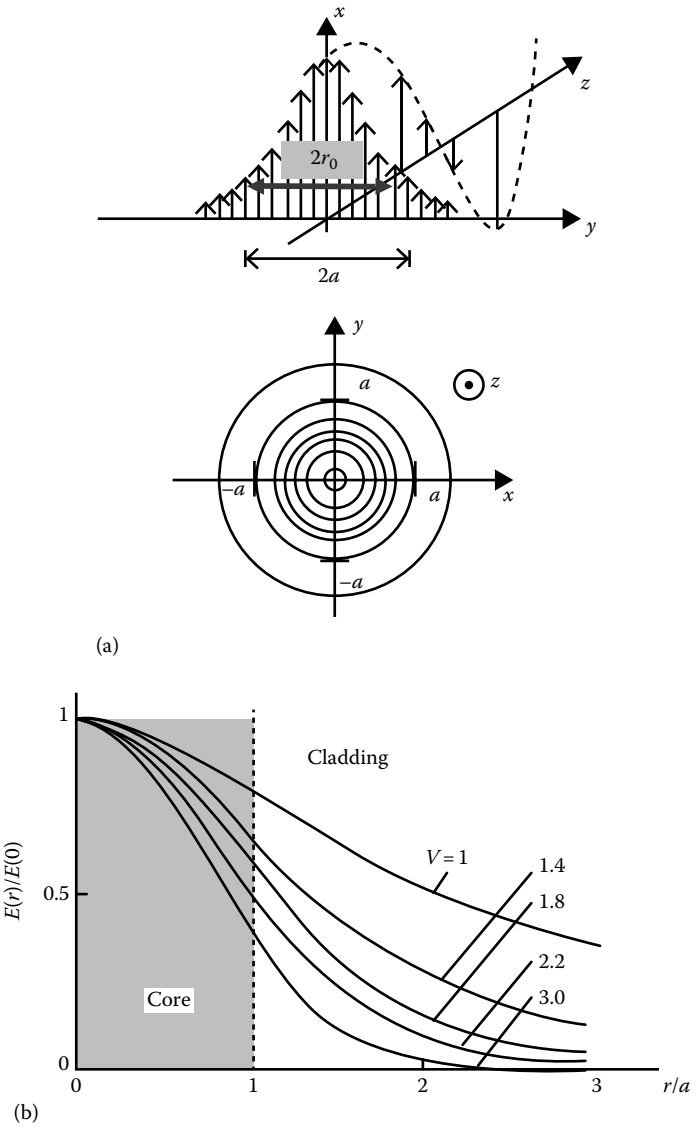

FIGURE 2.7
(a) Intensity distribution of the LP_{01} mode. (b) Variation of the spot size—field distribution with radial distance r normalized with respect to the core radius a and with V as a parameter.

2.3.3 Cutoff Properties

As in the case of planar dielectric waveguides, from Figure 2.6 we observe that when we have $V < 2.405$, only the fundamental LP_{01} exists. Note that for single-mode operation the V parameter must be less than or equal to 2.405. However, in practice, $V < 3$ is acceptable. The variation of the mode field distribution over the core and cladding area of a single mode fiber is depicted in Figure 2.7. The higher the V-parameter the more the power concentrated in the core region. However, it will be described later that for modern optical transmissions, the optimum fiber distribution would be about 70%–80% in the core with a V of about 1.8. In fact, the value 2.405 is the first zero of the Bessel function $J_o(u)$. In practice, one cannot

really distinguish between the V values lying between 2.3 and 3.0. Experimental observation shows that the optical fiber can still support only one mode. Thus, designers do usually take the value of V as 3.0 or less to design a single-mode optical fiber.

The V parameter is inversely proportional with respect to the optical wavelength. Thus, if an optical fiber is launched with light waves whose optical wavelength is smaller than the operating wavelength at which the optical fiber is in single mode then the optical fiber is supporting more than one mode. The optical fiber is then said to be operating in a multimode region.

One can define the cutoff wavelength for optical fibers as follows: the wavelength (λ_c) above which only the fundamental mode is guided in the fiber is called the cutoff wavelength λ_c. This cutoff wavelength can be found by using the V parameter as $V_c = V_{at-cut-off} = 2.405$, thus

$$\lambda_c = \frac{2\pi aNA}{V_c} \tag{2.49}$$

Exercise 2.3

An optical fiber has the following parameters: a core refractive index of 1.46, a relative refractive index difference of 0.3%, and a cladding diameter of 125 μm and a core diameter of 8.0 μm. (a) Find the fiber NA and hence the fiber acceptance angle, (b) what is the cutoff wavelength for this fiber ?, (c) What is the number of optical-guided modes that can be supported if the optical fiber is excited by light waves with a wavelength of 810 nm, (d) if the cladding diameter is reduced to 50 and 20 μm, comment on the field distribution of the guided single mode.

In practice, the fibers tend to be effectively single mode for larger values of V say $V < 3$ for the step profile, because the higher-order modes suffer radiation losses due to fiber imperfections. Thus if $V = 3$, from (2.36) we have $a < 3\lambda/2$ NA. In this case taking $\lambda = 1$ μm, for radius a to have some reasonable dimension, the NA value must be very small ($\ll 1$). Usually, Δ is about 1% or less for standard single-mode optical fibers (SSMFs) for use in optical transmission systems. The typical dimensions of an SSMF (Corning SMF-28) are given in Annex 1.

2.3.4 Single and Few Mode Conditions

How light waves can be guided in circular optical waveguides can be analytically found by solving the eigenvalue equation (2.37), which has been employed to find the number of modes supported by the waveguide and their specific propagation constants. However, if the spatial mode distribution of the fundamental mode and the Gaussian function that is commonly confirmed by experimental measurements of the mode field intensity are well known, then the solving the eigenvalue equation (2.37) is not required. The propagation constant can be obtained by substituting the Gaussian function into the wave equation. Under current extensive research interests in the spatial multiplexing in DSP-based coherent optical communication systems, a few mode fibers have attracted quite a lot of interest due to their potential to support many channels with their modes and their related field polarizations. This section is extended to consider both the fundamental mode and higher-order modes.

Equation 2.36 shows that the longitudinal field is in the order of $u/(kan_2)$ with respect to the transverse component. In practice, $\Delta \ll 1$, and by using (2.36), we observe that this longitudinal component is negligible compared to the transverse component. Thus, the guided mode is *transversely polarized*. The fundamental mode is then usually denominated as LP_{01} mode (LP = Linearly Polarized) for which the field distribution is shown in Figure 2.5a and b. The graphical representation of the eigenvalue equation (2.37) calculated

with the variation of $b = \beta/k$ as the normalized propagation constant and the V parameter is shown in Figure 2.6d. There are two possible polarized modes, the horizontal and vertical polarizations, which are orthogonal to each other. These two polarized modes can be employed for transmission of different information channels. They are currently exploited in optical transmission systems employing polarization division multiplexed (PDM) in association with QPSK (quadrature phase-shift keying) modulation formats so as to offer a transmission bit rate of 100 Gb/s and beyond. This is derived from 2 (polarizations) × (2-bits/symbol) × 25 GBaud/s to result in 100 Gb/s. Furthermore, when the number of guided modes is higher than the two polarized modes, they form a set of modes over which information channels can be simultaneously carried and spatially demultiplexed at the receiving end so as to increase the transmission capacity as illustrated in Figure 2.5a and b [7,8]. A few such mode fibers are employed in the most modern optical transmission system whose schematic is shown in Figure 2.8. The mode multiplexer aids mode spatial

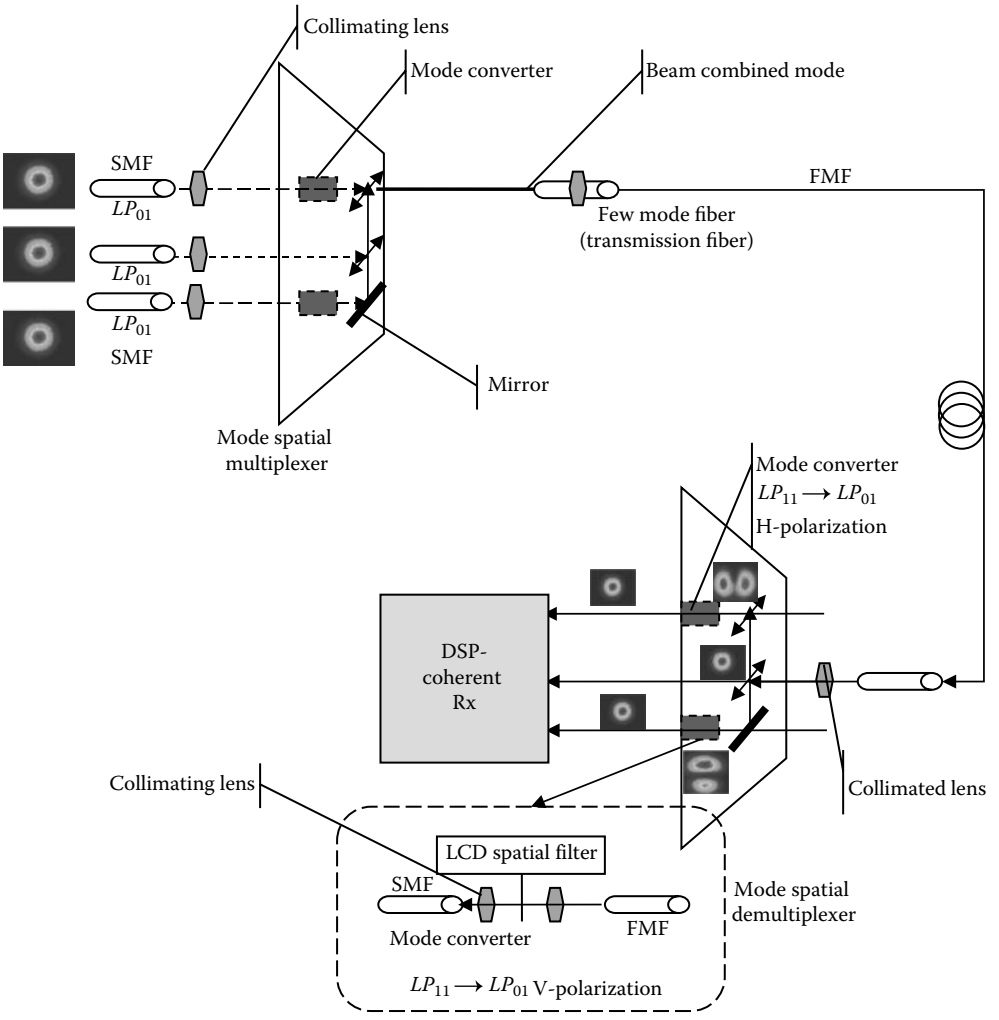

FIGURE 2.8
Few mode fiber (FMF) employed as a spatial multiplexing and demultiplexing in DSP-based coherent optical transmission systems operating at 100 Gb/s and higher bit rate.

mixing and likewise the demultiplexer splits the modes LP_{11}, LP_{01} into individual modes, converts them to the LP_{01} mode field, and injects them into the SMF to feed into the coherent receiver. Obviously, mode spatial demultiplexing should be followed by modulation and then multiplexing back into the transmission fiber for transmission. Similar structures are available at the receiver to separate and detect the channels. Note the two possible polarizations of the mode LP_{11}. Note that there are four polarized modes of the LP_{11} mode, although only two polarized modes are shown in this diagram (Figure 2.9). The delay caused by the propagation velocity because of the difference in the propagation constant is easily compensated in the DSP algorithm, similar to that caused by the polarization mode dispersion (PMD). The main problems to resolve in this spatial mode multiplexing optical transmission system are the optical amplification for all modes so that long-haul transmission, that is, the amplification in MMF structure, can be achieved.

The number of guided modes is determined by the number of intersecting points of the circle of radius V and the curves representing the eigenvalue solutions (2.37). Thus for an SMF the V parameter must be less than 2.405 and for a few mode fibers this value must be higher. For example, if $V = 2.8$ we have three intersecting points between the circle of radius V and the three curves, then the number of modes would be LP_{01}, LP_{11}, and their corresponding alternative polarized modes as shown in Figure 2.5b and c. For a single

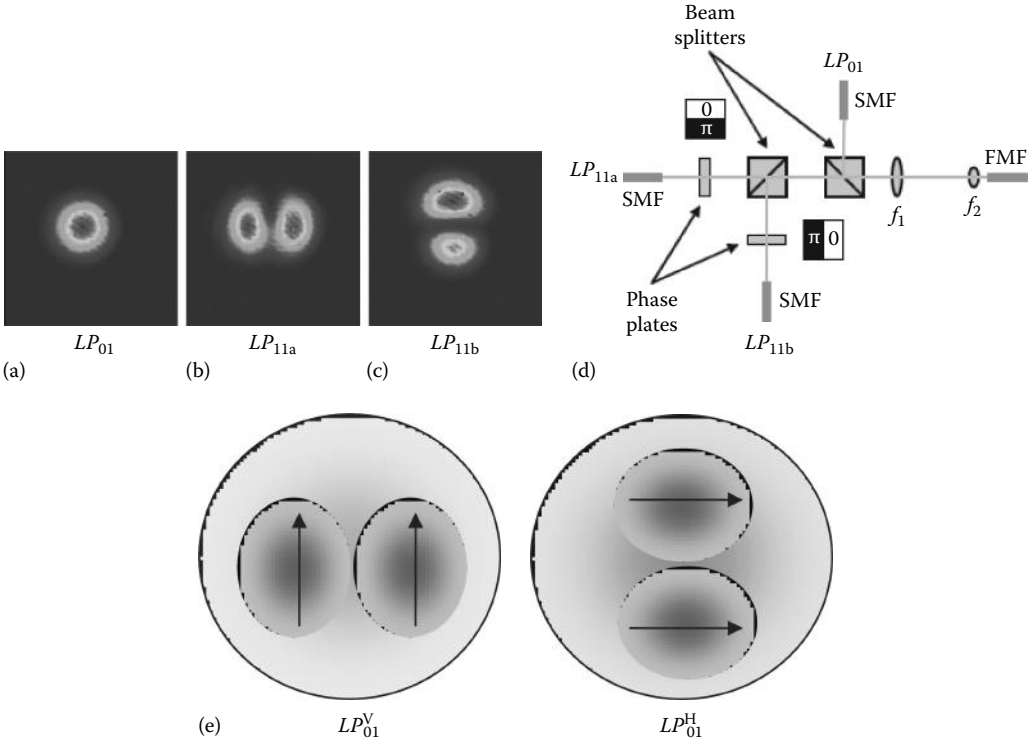

FIGURE 2.9
(a–c) Intensity profiles of the first few order modes of a few-mode optical fiber employed for 5 × 65 Gb/s optical transmission system [9] and optical system arrangement for spatially demux and mux of modal channels. (d) Optical arrangement for launching different spatial modes into the same fiber—spatial mode multiplexing. (e) Horizontal (H) and vertical (V) polarized modes $LP_{01}^{V,H}$, polarization directions indicated by arrows.

mode there are two polarized modes whose polarizations can be vertical or horizontal. An SMF is, therefore, not monomode but supports two polarized modes! The main issue is on the optical amplification gain in the transmission of modulated signals in a few such mode fibers. This remains the principal obstacle.

We observe the propagation of the fundamental mode and higher-order modes as shown in Figure 2.6a and b. The rays of these modes can be axially straight or skewed and twisted around the principal axis of the fiber. This implies that there are different propagation times between these modes. This property is used to compensate for the chromatic dispersion effect [10]. Figure 2.6 shows a spectrum of the graphical solution for the modes of optical fibers. In Figure 2.6d, the regions of single operation and that of the second-order mode as determined by the value of the V parameter are indicated.

There are also modes that propagate spirally around the fiber axis, never passing through this axis. This is a typical skew mode whose LP notation would be LP_{n1} with n indicating half the total number of null points in the field distribution around the fiber azimuthal directions such as the mode LP_{41} illustrated in Figure 2.5b. One can use this mode with spatial distributions of the optical field to launch different channels so as to increase the transmission capacity, a technique now commonly known as orbital angular momentum (OAM) multiplexing method [11,12]. The main difficulty in this type of transmission technique lies in determining how the different spatial modes have to be launched into appropriate field distribution areas of the cross section of the FMF.

The delay differences between the spatial modes can be equalized by DSP without any difficulty, using the MIMO technique, which has been well known in wireless transmission systems for several years [13,14].

2.4 Power Distribution and Approximation of Spot Size

2.4.1 Power Distribution

The axial power density or intensity profile is given by the Poynting vector $S(r)$. The z-component of the Poynting vector is given by

$$S(r) = \frac{1}{2} E_x H_y^*. \tag{2.50}$$

Using (2.2), (2.32), and (2.50), we have

$$S(r) = \frac{1}{2}\left(\frac{\varepsilon}{\mu}\right)^{1/2} e^{-\left(\frac{r}{r_0}\right)^2} \tag{2.51}$$

The total power can then be represented by

$$P = 2\pi \int_0^\infty rS(r)dr = \frac{1}{2}\left(\frac{\varepsilon}{\mu}\right)^{1/2} r_0^2 \tag{2.52}$$

TABLE 2.1

Analytical Expressions for Total Optical-Guided Power and Its Fractional Power Confined inside the Core Region for Step-Index and Gaussian-Index Profiles

Parameter/Profile	Step-Index	Gaussian
$S(r/a)$ for $V > 1$	$\frac{1}{2}\left(\frac{\varepsilon}{\mu}\right)^{1/2} e^{-\left(\frac{r}{a}\right)^2 \ln V^2}$	$\frac{1}{2}\left(\frac{\varepsilon}{\mu}\right)^{1/2} e^{-\left(\frac{r}{a}\right)(V-1)}$
Power P for $V > 1$	$\frac{1}{2}\left(\frac{\varepsilon}{\mu}\right)^{1/2} \frac{a^2}{\ln V^2}$	$\frac{1}{2}\left(\frac{\varepsilon}{\mu}\right)^{1/2} \frac{a^2}{V-1}$
$\eta(r)$ for $V > 1$	$1 - e^{-\left(\frac{r}{a}\right)^2 \ln V^2}$	$1 - e^{-\left(\frac{r}{a}\right)^2 (V-1)}$
$\eta(r)$ for $V > 1$	$= 1 - \frac{1}{V^2}$ for $r = a$	

and hence, the fraction of power $P(r)$ within the radial area covered from $0 \rightarrow r$ over the fiber cross section is given by

$$\eta(r) = \frac{\int_0^r rS(r)dr}{\int_0^\infty rS(r)dr} = 1 - e^{-\left(\frac{r^2}{r_0^2}\right)} \tag{2.53}$$

Table 2.1 gives various expressions for P and $\eta(r)$ for the step-index and Gaussian-index profile fibers. These expressions can be derived by substituting the appropriate values of r_0 given in (2.46) into (2.52) and (2.53).

As a rule of thumb optical power in the core of about 70%–80% of the total power is best for an optical fiber to support the fundamental guided mode and this has also been experimentally confirmed.

Exercise 2.4

Using Gaussian approximation for the intensity distribution of the fundamental mode of the single-mode optical fiber with $V = 2$, find the fraction of power in the core region with $a = 4$ μm.

Exercise 2.5

Find the radius a for maximum confinement of light power, that is, maximum r_0, for step-index and parabolic profile optical fibers.

2.4.2 Approximation of Spot Size r_0 of a Step-Index Fiber

As stated earlier, spot size r_0 would play a major role in determining the performance of the SMF. It is useful if we can approximate the spot size as long as the fiber is operating

in the single-mode region over a certain spectral window. When an SMF is operating above its cutoff wavelength, a good approximation with accuracy greater than 96% for r_0 is given by

$$\frac{r_0}{a} = 0.65 + 1.619V^{-3/2} + 2.879V^{-6} = 0.65 + 0.434\left(\frac{\lambda}{\lambda_c}\right)^{+3/2} + 0.0419\left(\frac{\lambda}{\lambda_c}\right)^{+6}$$

$$\text{for } 0.8 \le \frac{\lambda}{\lambda_c} \le 2.0 \text{ and valid for SMF only.} \tag{2.54}$$

Exercise 2.6

What is the equivalent range for the V parameter given in Equation 2.36? Inspect the b–V and $V^2\frac{d^2(Vb)}{dV^2}$ versus V and b (Chapter 3), if possible do a curve fitting, to obtain the approximate relationship for r/a and V (MATLAB procedure is recommended).

Exercise 2.7

Refer to the technical specification of Corning SMF-28 and LEAF

(a) State the core diameter of the fibers, the spot size, or mode field diameters of the fibers.
(b) Hence, estimate the effective areas of these fibers.
(c) What is the ratio of the effective area to the physical area of the cores of the fibers.

2.5 Equivalent Step-Index (ESI) Description

As we have seen in Section 2.2.4, there are *two possible orthogonally polarized modes* (E_x,H_y) and (E_y,H_x) which can propagate simultaneously. These modes are usually approximated by a single linearly polarized (LP) mode. These mode properties are well known and well understood for step-index optical fibers and analytical solutions are also readily available [15].

Unfortunately, practical SMFs never have perfect step-index profiles due to the variation in the dopant diffusion, and consequently in the refractive index distribution. Furthermore, when drawing the fiber over a very long length, sometimes longer than 25 km, the core of the fiber is not uniform throughout but has a variable core radius distributed in a random manner. These *non step-index* fibers can be approximated, under some special conditions, by *an equivalent step-index* (*ESI*) profile technique.

A number of index profiles of modern SMFs, for example, nonzero dispersion-shifted fibers is shown in Figure 2.10. The ESI profile is determined by approximating the spatial distribution $\phi(r)$ of the fundamental mode electric field by a Gaussian function as described in Section 2.3.1.4. The electrical field can thus be totally specified by the $1/e$ width of this function or the *mode spot size* (r_0)**.** Alternatively, the term mode field diameter (*MFD*) is also used and is equivalent to twice the mode spot size, r_0.

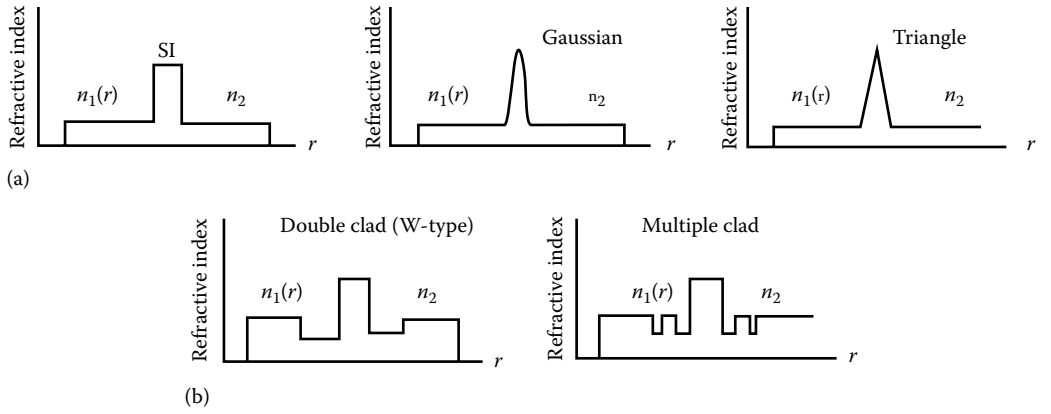

FIGURE 2.10
Index profiles of a number of modern fibers, for example, dispersion-shifted single-mode fibers. (a) SSMF having step, Gaussian, and triangular distribution. (b) Dispersion-shifted single mode having depressed cladding with double and multiple depressed cladding profiles.

2.5.1 Definitions of ESI Parameters

The ESI description can be used to design SMF with graded index, W- or segmented core profiles (under some limitations) as illustrated in Figure 2.8. These non step-index profiles can be described by ESI parameters denoted by V_e = the effective or equivalent V parameter; a_e = the ESI core radius; λ_{ec} = the ESI cutoff wavelength; Δ_e = the equivalent relative index difference.

These parameters are related to the first two moments M_0,M_1 defined as

$$M_n = \int_0^\infty \left[n^2(r) - n^2(a) \right] r^n dr. \tag{2.55}$$

For $n = 1, 2$, the effective V_e *parameter* and effective core radius r_e are given by

$$V_e^2 = 2k^2 \int_0^\infty \left[n^2(r) - n^2(a) \right] r \, dr, \tag{2.56}$$

$$V_e^2 = 2k^2 M_1, \tag{2.57}$$

and

$$a_e = 2\frac{M_1}{M_0} \tag{2.58}$$

It follows from (2.56) and (2.58), and the parameters λ_{ec} and Δ_e

$$V_e^2 = 2k^2 a_e^2 n_1^2 \Delta_e \tag{2.59}$$

and $V_e = 2.405$ (cutoff condition for step index). Therefore, the cutoff wavelength for an ESI profile fiber is:

$$\lambda_{ec} = \frac{2\pi\sqrt{2M_1}}{2.405} \tag{2.60}$$

It is noteworthy that V_e given in (2.59) is equivalent to the mode volume. Physically, the significance of V_e can be compared to the average density of a disk with a local density equal to $[n^2(r)-n^2(a)]$.

2.5.2 Accuracy and Limits

The ESI approximation is generally accurate to within 2% at least over the wavelength range $0.8 < \lambda/\lambda_c < 1.5$. For most practical purposes, this range is the operating wavelength to minimize the dispersion property of SM optical fibers.

2.5.3 Examples on ESI Techniques

2.5.3.1 Graded-Index Fibers

These index profiles of graded fibers are given by (2.29). We thus have

$$n^2(r) - n^2(a) = s(r/a) = 1 - \left(\frac{r}{a}\right)^{\alpha} \tag{2.61}$$

Substituting (2.61) into (2.56) gives

$$\frac{V_e}{V} = \left(\frac{\alpha}{\alpha+2}\right)^{1/2} \tag{2.62}$$

where $V = ka(NA)^{1/2}$ is the V parameter of a step-index fiber with the core index at the fiber axis of n_1. Hence, we have

$$\lambda_{ec} = \frac{V}{2.405}\left(\frac{\alpha}{\alpha+2}\right)^{1/2} \tag{2.63}$$

Exercise 2.8

For a single-mode optical fiber with a triangular profile index distribution whose equivalent V parameter is equal to 2 at 1550 nm wavelength. What is the V parameter value at the center of the core of the fiber? If the diameter of the core of the two fibers is kept identical then what is the ratio of the refractive indices at the core center of the fibers? Repeat for parabolic profile.

2.5.3.2 Graded-Index Fiber with a Central Dip

The fiber-index profile with central dip and gradually graded increase toward the outer cladding is shown in Figure 2.11.

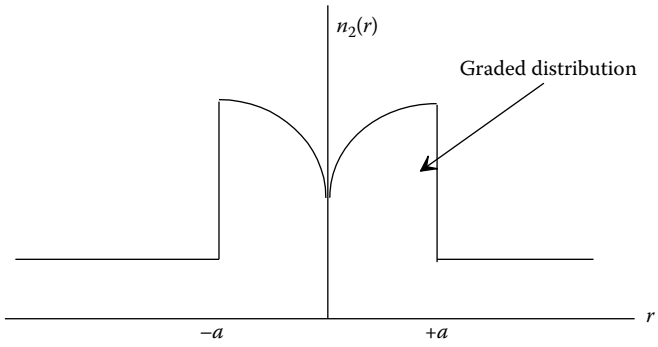

FIGURE 2.11
Refractive index profile of a graded-index fiber with a central dip. This is typical profile of manufactured fiber if a good collapsing of the preform is not achieved.

As in Equation 2.28 for graded-index fiber with maximum index at the core axis we have

$$S(r/a) = 1 - \gamma(1-x)^{\alpha} \quad \text{for } 0 < r < a \tag{2.64}$$

where γ is the depth and $0 < \gamma < 1$. When $r = 0$ we have the step-index profile and when $r = 1$ we have the central axis refractive index that is equal to the cladding index. Using (2.55) and (2.56), V_e can be easily found and is given by

$$\frac{V_e^2}{V^2} = 1 - \frac{2\gamma}{(\alpha+1)(\alpha+2)} \tag{2.65}$$

2.5.4 General Method

The general technique to find the ESI parameters for optical fibers is to use the stationary expression in (2.41) for expressing β of the actual fiber as compared to *its* equivalent propagation constant β_e by

$$\beta^2 = \beta_e^2 + k^2 \frac{\int_0^{\infty} \left[n^2(r) - n_e^2(r) \right] r\psi^2(r)dr}{\int_0^{\infty} r\psi^2(r)dr} \tag{2.66}$$

where $n_e^2(r)$ is the equivalent counterpart of $n(r)$ when the fiber is expressed in its equivalent step form. The field expression φ(*r*) is assumed (in fact to be obtained) to be similar to the actual fiber and its step equivalence. Once the field φ(*r*) can be replaced by the approximate exact field shape, we can find V_e and a_e that minimize $\beta^2 - \beta_e^2$ of (2.66). Generally, these parameters are functions of both *V* and *a*, thus it is impossible to get one ESI technique applicable to a wide range of wavelengths and it is required to apply complicated numerical calculations.

2.6 Nonlinear Optical Effects

In this section, the nonlinear effects are described. These effects play important roles in the transmission of optical pulses along single-mode optical fibers. The nonlinear effects can be classified into three types: the effects that change the refractive index of the guided medium due to the intensity of the pulse, the self-phase modulation; the scattering of the light wave to other frequency-shifted optical waves when the intensity reaches over a certain threshold, the Brillouin and Raman scattering phenomena; and the mixing of optical waves to generate a fourth wave, the degenerate four wave mixing. Besides these nonlinear effects there is also photorefractive effect, which is due to the change in the refractive index of silica due to the intensity of ultra-violet optical waves. This phenomenon is used to fabricate grating whose spacing between the dark and bright regions satisfies the Bragg diffraction condition. These are fiber Bragg gratings and would be used as optical filters and dispersion compensators when the spacing varies or is chirped.

2.6.1 Nonlinear Phase Modulation Effects

All optical transparent materials are subject to change in refractive index with the intensity of the optical waves, the optical Kerr effect. This physical phenomenon originates from the anharmonic responses of electrons in optical fields leading to the change in the material's susceptibility. The modified refractive index $n_{1,2}^K$ of the core and cladding regions of the silica-based material can be written as:

$$n_{1,2}^K = n_{1,2} + \bar{n}_2 \frac{P}{A_{eff}} \tag{2.67}$$

where

n_2 is the nonlinear index coefficient of the guided medium, the average typical value of n_2 being about 2.6×10^{-20} m^2/W
P is the average optical power of the pulse
A_{eff} is the effective area of the guided mode

The power of a light wave is the square of the RMS value of the sinusoidal behavior of the light wave carrier. Annex 2 shows the basic definition and evaluation of the RMS of the modulated envelope of the carrier. The nonlinear index changes with the doping materials at the core. Although the nonlinear index coefficient is very small, the effective area is also very small, about 50–70 μm^2, and the length of the fiber under the propagation of optical signals is very long and the accumulated phase change is quite substantial. This leads to the self-phase modulation (SPM) and cross-phase modulation (XPM) effects in the optical channels.

2.6.1.1 SPM: Self-Phase Modulation

Under a linear approximation, we can write the modified propagation constant of the guided linearly polarized mode in a single-mode optical fiber as

$$\beta^K = \beta + k_0 \bar{n}_2 \frac{P}{A_{eff}} = \beta + \gamma P \quad \text{with } \gamma = \frac{2\pi \bar{n}_2}{\lambda A_{eff}} \tag{2.68}$$

β^K is an important nonlinear parameter of the guided medium taking an effective value from 1 to 5 (km/W) depending on the effective area of the guided mode and the operating wavelength. The smaller the mode spot size or mode field diameter the larger the nonlinear self-phase modulation effect. For the dispersion compensating fiber the effective area is about 15 μm^2 while for SSMF and NZ_DSF the effective area ranges from 50 to 80 μm^2. Thus, the nonlinear threshold power of DCF is much lower than that of SSMF and NZ-DSF. We would see later that the maximum power launched into DCF would be limited at about 0 dBm or 1 mW in order to avoid nonlinear distortion effect while about 5 dBm for SSMF.

The accumulated nonlinear phase changes due to the nonlinear Kerr effect over the propagation length L is given by

$$\phi_{NL} = \int_0^L (\beta^K - \beta) dz = \int_0^L \gamma P(z) dz = \gamma P_{in} L_{eff} \quad \text{with } P(z) = P_{in} e^{-\alpha z} \tag{2.69}$$

α represents the attenuation of the optical signals along the propagation direction z. To consider the nonlinear SPM effect as small compared to the linear chromatic dispersion effect one can set $\phi_{NL} \ll 1$ or $\phi_{NL} = 0.1$ rad and the effective length of the propagating fiber is set at $L_{eff} = 1/\alpha$ with optical losses equalized by cascaded optical amplification subsystems. Then the maximum input power to be launched into the fiber can be set at

$$P_{in} < \frac{0.1\alpha}{\gamma N_A} \tag{2.70}$$

For γ = 2 (W/km) and N_A= 10, α = 0.2 dB/km (or 0.0434 × 0.2 km^{-1}), P_{in} < 2.2 mW or about 3 dBm and accordingly 1 mW for DCF. In practice, due to the randomness of the arrival "1" and "0" this nonlinear threshold input power can be set at about 10 dBm as the total average power of all wavelength multiplexed optical channels launched into the propagation fiber.

2.6.1.2 XPM: Cross-Phase Modulation

The change in the refractive index of the guided medium as a function of the intensity of the optical signals can also lead to the phase of optical channels in different spectral regions close to that of the original channel. This is the cross-phase modulation effect (XPM). This is critical in wavelength division multiplexed (WDM) transmission systems, and even more critical in dense WDM when the frequency spacing between channels is only 50 GHz or even narrower. In such systems, the nonlinear phase shift of a particular channel depends not only on its power but also on that of other channels. The phase shift of the ith channel can be written as [16]:

$$\phi_{NL}^i = \gamma L_{eff} \left(P_{in}^i + 2 \sum_{j \neq i}^{M} P_j \right) \quad \text{with } M = \text{number of multiplexed channels.} \tag{2.71}$$

The factor 2 in (2.71) is due to the bipolar effects of the susceptibility of silica materials. The XPM thus depends on the bit pattern and the randomness of the synchronous arrival of the "1". It is hard to estimate, and so, the numerical simulation is normally employed to obtain the cross-phase modulation distortion effects by numerical simulation using

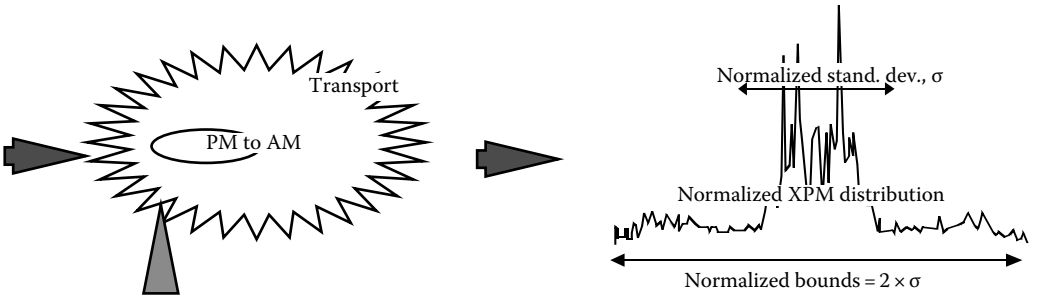

FIGURE 2.12
Illustration of XPM effects—phase modulation conversion to amplitude modulation and hence interference between adjacent channel.

the wave propagation of the signal enveloped via the nonlinear Schrodinger equation. The evolution of slow varying complex envelopes $A(z, t)$ of optical pulses along a single-mode optical fiber is governed by the nonlinear Schrodinger equation (NLSE) [22]:

$$\frac{\partial A(z,t)}{\partial z} + \frac{\alpha}{2}A(z,t) + \beta_1 \frac{\partial A(z,t)}{\partial t} + \frac{j}{2}\beta_2 \frac{\partial^2 A(z,t)}{\partial t^2} - \frac{1}{6}\beta_3 \frac{\partial^3 A(z,t)}{\partial t^3} = -j\gamma \left|A(z,t)\right|^2 A(z,t) \quad (2.72)$$

where
- z is the spatial longitudinal coordinate
- α accounts for fiber attenuation
- β_1 indicates DGD
- β_2 and β_3 represent second- and third-order factors of fiber CD
- γ is the nonlinear coefficient

This equation is described in detail in Chapter 3. The phase modulation due to nonlinear phase effects is then converted to amplitude modulation and the cross talk to other adjacent channels. This is shown in Figure 2.12.

2.6.1.3 Stimulated Scattering Effects

The scattering of light waves by impurities can occur due to the absorption and vibration of the electrons and dislocation of molecules in silica-based materials. The backscattering and absorption are commonly known as Rayleigh scattering losses in fiber propagation in whose phenomena the frequency of the optical carrier does not change. Scattering processes in which the frequency of the light wave carrier is shifted to another frequency region are commonly known as inelastic scattering or Raman scattering and Brillouin scattering. In both cases, the scattering of photons to a lower energy level photon with energy difference between these levels falling with the energy of phonons. Optical phonons result from the electronic vibration of Raman scattering while acoustic phonons or mechanical vibrations of the linkage between molecules result from Brillouin scattering. At high power, when the intensity crosses a certain threshold then the number of scattered photons increases exponentially and the phenomena become a stimulated process. Thus, the phenomena can be called

stimulated Brillouin scattering (SBS) and stimulated Raman scattering (SRS). SRS and SBS were first observed in the 1970s [17–19].

2.6.1.4 Stimulated Brillouin Scattering (SBS)

Brillouin scattering comes from the compression of the silica materials in the presence of an electric field, the electrostriction effect. Under the pumping of an oscillating electric field of frequency f_p, an acoustic wave of frequency F_a is generated. Spontaneous scattering is an energy transfer from the pump wave to the acoustic wave and then a phase matching transfer of a shifted optical wave of frequency as the sum of the optical signal waves and the acoustic wave occurs. This acoustic wave frequency shift is around 11 GHz with a bandwidth of around 50–100 MHz (due to the gain coefficient of the SBS) and a beating envelope modulates the optical signals. Thus, jittering of the received signals at the receiver occurs, resulting in the closure of the eye diagram in the time domain.

Once the acoustics wave is generated it beats with the signal waves to generate the sideband components. This beating beam acts as a source and further transfers the signal beam energy into the acoustic wave energy and amplifies this wave to generate further jittering effects. The Brillouin scattering process can be expressed by the following coupled equations [20,23]:

$$\begin{aligned} \frac{dI_p}{dz} &= -g_B I_p I_s - \alpha_p I_p, \\ -\frac{dI_s}{dz} &= +g_B I_p I_s - \alpha_s I_s \end{aligned} \tag{2.73}$$

where

I_p is the intensity of pump beam
I_p is the intensity of signal beam
g_B is the Brillouin scattering gain coefficient
α_s, α_p are the losses of signal and pump waves

The SBS gain g_B is frequency dependent with a gain bandwidth of around 50–100 MHz for a pump wavelength at around 1550 nm. For silica fiber, g_B is about 5e–11 m/W. The threshold power for the generation of SBS can be estimated (using Equation 2.73) as

$$\begin{aligned} & g_B P_{th\_SBS} \frac{L_{eff}}{A_{eff}} \approx 21 \\ & \text{with the\_effective\_length } L_{eff} = \frac{1 - e^{-\alpha L}}{\alpha} \end{aligned} \tag{2.74}$$

For SSMF, this SBS power threshold is about 1.0 mW. Once the launched power exceeds this power threshold level the beam energy is reflected back. Thus, the average launched power is usually limited to a few dBm due to this low threshold power level.

2.6.1.5 Stimulated Raman Scattering (SRS)

Stimulated Raman scattering occurs in silica-based fiber when a pump laser source is launched into the guided medium, the scattering light from the molecules and dopants in the core region shifting to a higher energy level and then jumping down to a lower energy level, thereby amplifying photons in this level. Thus, a transfer of energy from photons at different frequency and energy levels occurs. The stimulated emission occurs when the pump energy level crosses the threshold level. The pump intensity and signal beam intensity are coupled via the coupled equations:

$$\begin{aligned} \frac{dI_p}{dz} &= -g_R I_p I_s - \alpha_p I_p, \\ -\frac{dI_s}{dz} &= +g_R I_p I_s - \alpha_s I_s \end{aligned} \tag{2.75}$$

where

I_p is the intensity of pump beam
I_p is the intensity of signal beam
g_R is the Raman scattering gain coefficient
α_s, α_p are the losses of signal and pump waves

The spectrum of the Raman gain depends on the decay lifetime of the excited electronic vibration state. The decay time is in the range of 1 ns and the Raman gain bandwidth is about 1 GHz. In single-mode optical fibers, the bandwidth of the Raman gain is about 10 THz. The pump beam wavelength is usually about 100 nm below the amplification wavelength region. Thus in order to extend the gain spectra, a number of pump sources of different wavelengths are used. Polarization multiplexing of these beams is also used to reduce the effective power launched in the fiber so as to avoid damage to the fiber. The threshold for stimulated Raman gain is given by

$$\begin{aligned} & g_R P_{th\_SRS} \frac{L_{eff}}{A_{eff}} \approx 16 \\ & \text{with the\_effective\_length } L_{eff} = \frac{1 - e^{-\alpha L}}{\alpha} \text{ or } \approx 1/\alpha \text{ for long\_length} \end{aligned} \tag{2.76}$$

For SSMF with an effective area of 50 μm², g_R ~ 1e–13 m/W then the threshold power is about 570 mW near the C-band spectral region. This would require at least two pump laser sources that should be polarization multiplexed. The SRS is used frequently in modern optical communications systems, especially when no undersea optical amplification is required, the distributed amplification of SRS offers significant advantages as compared to lumped amplifiers such as EDFA. The broadband gain and low gain ripple of SRS are also another advantage for DWDM transmission.

2.6.1.6 Four-Wave Mixing

Four-wave mixing (FWM) is considered a scattering process in which three photons are mixed to generate the fourth wave. This happens when the momentum of the four waves satisfies a phase matching condition, namely, the condition of maximum power transfer. Figure 2.13

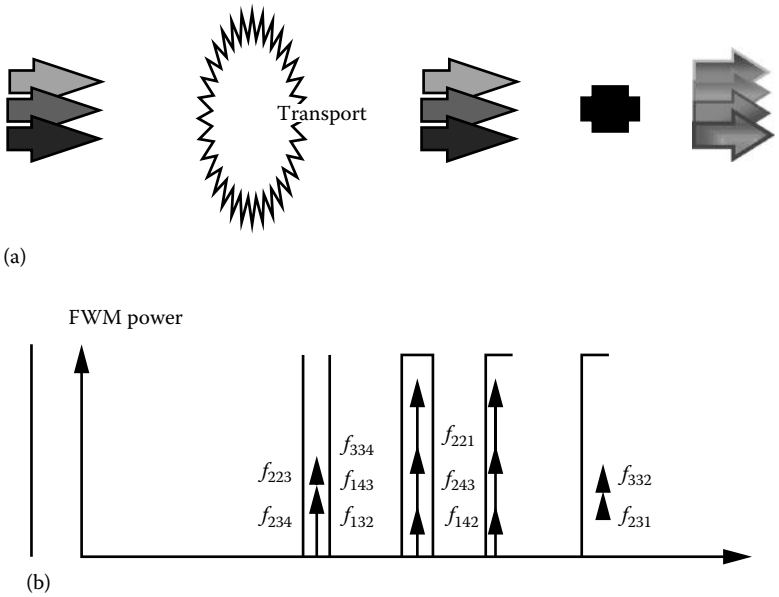

FIGURE 2.13
Illustration of four-wave mixing of optical channels (a) momentum vectors of channels (b) frequencies resulted from mixing of different channels.

illustrates the mixing of different wavelength channels to generate interchannel cross talk. The phase matching can be represented by a relationship between the propagation constant along the *z*-direction in a single-mode optical fiber as:

$$\beta(\omega_1) + \beta(\omega_2) - \beta(\omega_3) - \beta(\omega_4) = \Delta_{FWM}(\omega) \tag{2.77}$$

where
ω_1, ω_2, ω_3, and ω_4 are the frequencies of the first to fourth waves
Δ_{FWM} is the phase mismatching parameter

In the case when the channels are equally spaced with a frequency spacing of Ω as in DWDM optical transmission then we have $\omega_1 = \omega_2$; $\omega_3 = \omega_1 + \Omega$; $\omega_4 = \omega_1 - \Omega$. One can use the Taylors series expansion around the propagation constant at the center frequency of the guide carrier β_0 then we can obtain [21]:

$$\Delta(\omega) = \beta_2 \Omega^2 \tag{2.78}$$

The phase matching is thus optimized when β_2 is zero that implies that in the region where there is no dispersion FWM is maximum generating the maximum interchannel cross talk. This is the reason why dispersion-shifted fiber is not commonly used when the zero dispersion wavelength falls in the spectral region of the operating channel. In modern transmission fibers, the zero dispersion wavelength is shifted to outside the C-band, say 1510 nm, so that there is a small dispersion factor at 1550 nm and the C-band ranging from

2 to 6 ps/nm·km, for example, in the Corning LEAF or nonzero dispersion-shifted fibers (NZ-DSF). This small amount of dispersion is sufficient to avoid the FWM with a channel spacing of 100 or 50 GHz.

The XPM signal is proportional to instantaneous signal power. Its distribution is bounded by <5 channels and otherwise effectively unbounded. Thus, the Link budgets include XPM evaluated at maximum outer bounds.

2.7 Optical Fiber Manufacturing and Cabling

This section is devoted to a brief description of the manufacture of optical fibers and the cabling of several fibers for optical communication systems. The manufacturing techniques and cabling process affect the transmission and physical properties of the fibers. We focus on these aspects for a general understanding of optical transmission systems.

As we have described in the previous sections, the SSMF structure is a cylindrical core with a refractive index slightly higher than that of the cladding region. For optical communications operating in the 1300 and 1700 nm wavelength regions, silica is the base material [24,25]. A "pure" silica tube is the starting structure, and a combination of silica, Germanium Oxide GeO_2, and P_2O_5 is then deposited inside the tube. Other dopants such as B_2O_3 and fluoride can also be used to reduce the refractive index of some small regions of the core [26,27]. These form the segmented core and W-type fibers which are described in the next chapter.

Once the deposition of the impurities is done (see Figure 2.16), the tube is collapsed to produce a preform as shown in Figure 2.14. Also shown in this figure is a schematic of the fiber drawing machine and fiber drawing tower. The refractive index of the preform is also shown in Figure 2.15 as noted in its caption and in the detail area shown in Figure 2.16.

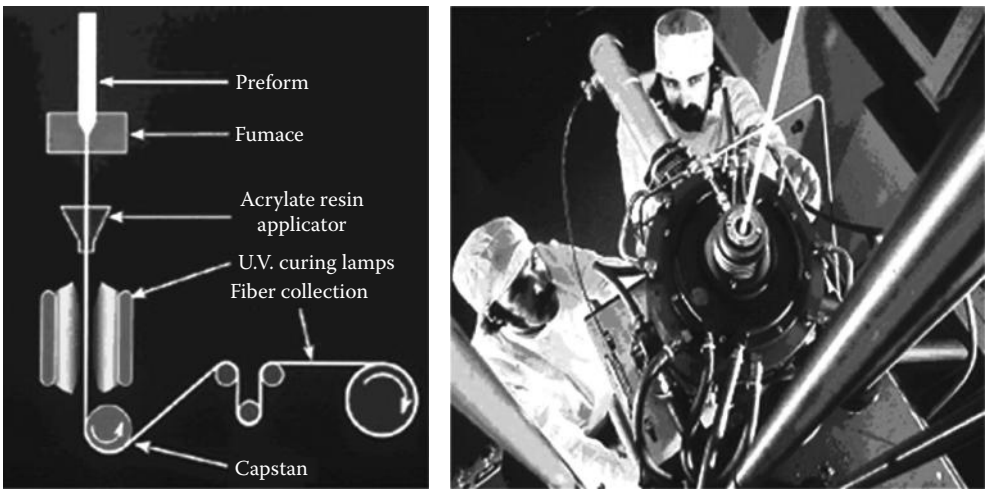

FIGURE 2.14
(a) Schematic of fiber drawing machine. (b) Picture of fiber microwave furnace and diameter monitoring and feedback control. (From Mahlkc, G. and Gossing, P., *Fiber Optic Cables*, Siemens A.G./John Wiley, Chichester, U.K., 1987. With permission.)

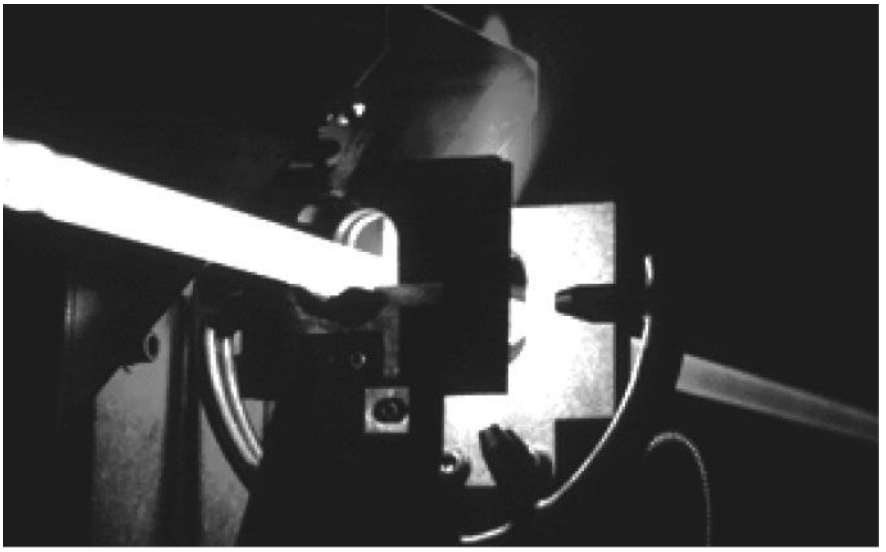

(a)

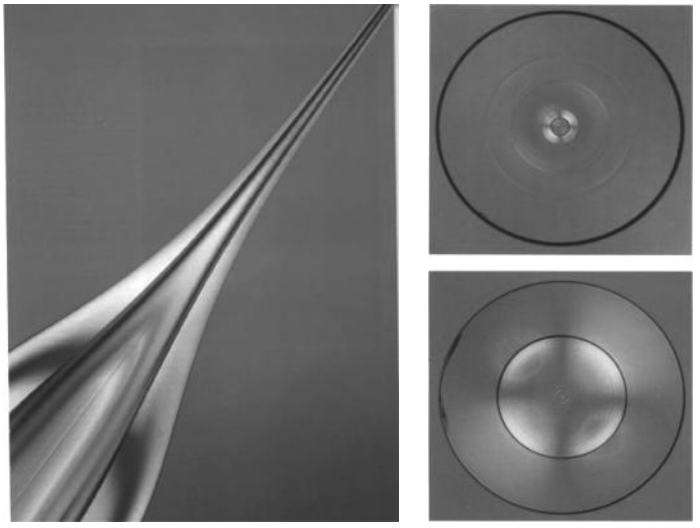

(b) (c)

FIGURE 2.15
(a) Schematic of a fiber deposition and fabrication of fiber preform, deposition of core material and collapsing. (b) Fiber preform, before drawing into fiber stands. (c) Cross section of fiber preform with refractive index profile exactly the same as the fiber-index profile of single-mode (upper) and multimode (lower) types.

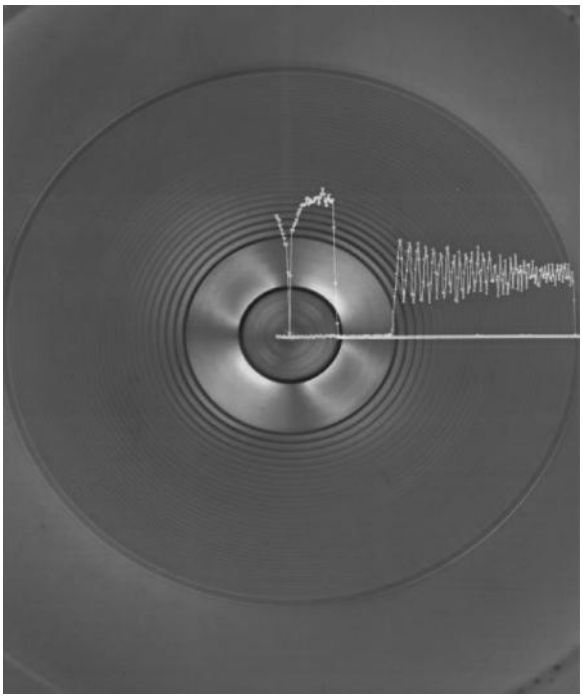

FIGURE 2.16
Real index profile across an SMF fiber preform. *Note*: Non-step-like profile—so why modeled as step-index structure?

2.8 Concluding Remarks

This chapter has introduced the fundamental concepts of optical slab waveguide and the circular optical waveguide or optical fibers. The basic properties of the fiber structures, its profile, the spot size, the cutoff wavelength, and the Gaussian approximation are described. The Gaussian approximation makes the understanding of the optical-guided mode simple. It also allows us to obtain directly the optical mode distribution and several other approximations required to obtain in the simplest form important parameters of single-mode optical fibers (Figure 2.17).

Once the basic properties of a single-mode optical fiber are found, they form the basic set of parameters so that optical fibers whose effective index profiles are nonstep can be found based on the ESI technique that converts the parameters to an equivalent step-like profile and other optical properties.

Only structural and wave properties of light wave signals traveling in optical fibers are presented here. As optical communication systems engineers, we have to understand and develop techniques for analyzing and identifying the transmission of digital and analogue signals through optical fibers, the attenuation and broadening of optical signals after transmission through the medium, namely, the attenuation and broadening via dispersion of light wave pulses. These topics are treated in the next chapter.

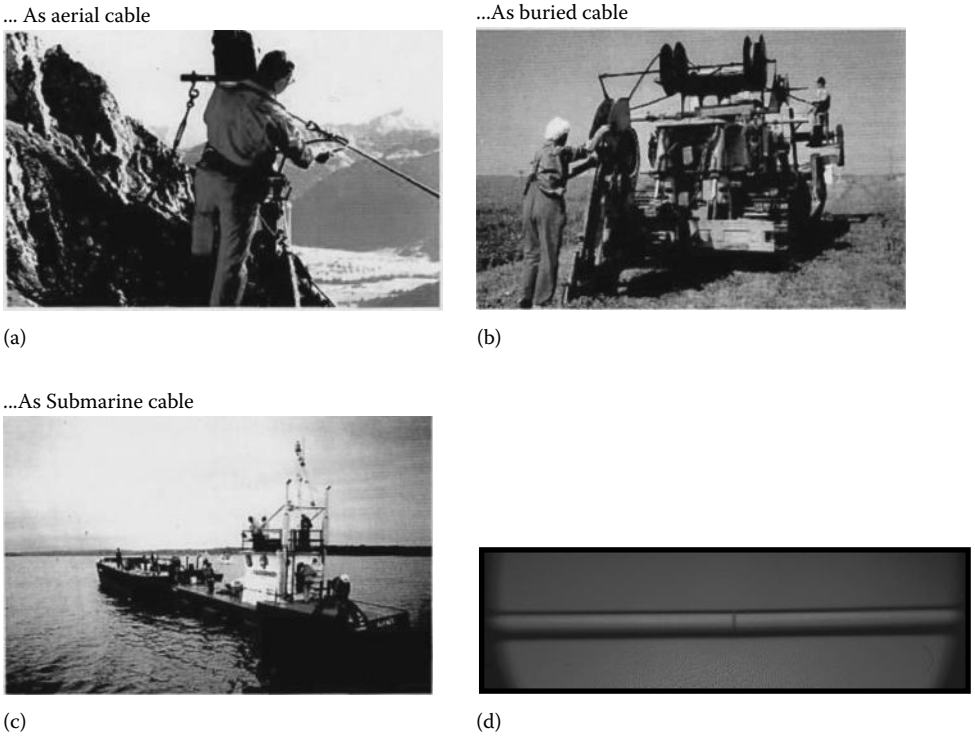

FIGURE 2.17
Installation scenarios for fiber cables. (a) Installation of fiber cables by hanging. (b) Installation of fiber cables by ploughing. (c) Installation of undersea fiber cables. (d) Splicing two optical fibers.

In addition, Chapters 13 and 14 give detailed examples of the design given in this chapter and Chapter 3 describes how to design fibers for dispersion flattening and compensating, especially when they are used for Raman optical amplification medium in distributed or lumped configurations.

Problems

2.1 An optical fiber with a step-index profile, a core diameter of 62.5 μm, and a numerical aperture of 0.2 at a wavelength of 1300 nm is used for signal distribution and transmission in a local area network.

(a) What is the V parameter of this optical fiber?

(b) How many guided modes would it support. Can you comment on this number regarding the velocities of light waves.

(c) Select a cladding diameter. Give reasons for your selection.

(d) Find the maximum acceptance angle of this fiber. Hence, estimate the coupling loss of a laser source with a uniform radiation cone of 30°.

2.2A An optical fiber has the following parameters: index profile = step-like; core diameter = 9.0 μm; numerical aperture NA = 0.11; and a cladding refractive index = 1.48.

(a) Find the normalized frequency of the fiber at 1550 nm wavelength.

(b) Is the fiber operating in the single-mode or multimode region at 1550 nm? If it is in the single-mode region, estimate its mode field diameter and its spot size. Sketch its field and intensity distribution across the fiber cross section.

(c) Find the cutoff wavelength of the fiber. If light waves of wavelength smaller than this cutoff wavelength are launched into the fiber will the fiber still operate in single-mode region?

2.2B A single-mode step-index optical fiber has the following parameters: core diameter = 8.0 μm, cladding diameter = 0.125 mm, core refractive index = 1.460, relative index difference = 0.2% at 1550 nm.

(a) Confirm that the fiber can be operating in the single-mode regime at 1550 nm wavelength.

(b) Find the fiber cutoff wavelength.

(c) What is the fiber mode field diameter if it is operating at 1550 nm wavelength.

2.3 For the optical fiber in Problem 2.2, if the refractive index profile is parabolic ($\alpha = 2$) or triangular ($\alpha = 1$) with the above numerical aperture at the central axis, repeat (a), (b), and (c).

2.4 Single-mode optical fibers produced by Corning (and Optical Waveguides Pty. Ltd. Noble Park, Victoria, Australia) have typical characteristics as per the technical data sheet attached at the end of this chapter.

(a) Using the fiber physical characteristics and technical data on its numerical aperture confirm the fiber functional characteristics such as the cutoff wavelength range.

(b) If this fiber is launched with a 850 nm laser, how many modes would it support. Sketch the mode fields for LP_{01} and LP_{11} modes.

(c) If light waves at 1300 nm travel over 10 km of this fiber, calculate the travel time of these waves.

(d) Estimate the fiber core diameter at 1300 nm wavelength.

(e) If the same spot size of (d) is required for the fiber to operate at 1550 nm, can you advise the manufacturer for any change in the fiber physical parameters.

2.5 (a) The optical fiber in Problem 2.3 is used in an optical fiber transmission system with a laser source operating at 1310 nm having an output power of 1.0 mW. The fiber length is 50 km. An optical receiver can detect an average optical power of 0.1 μW. Is it possible to detect the optical power at the end of the fiber length?

(b) Referring to the technical data of the standard optical fiber, estimate the spreading of optical pulse after transmitting through the 50 km length fiber if the source has an optical line width of 2.0 nm.

2.6 A step-index optical fiber is used for an optical communication system operating at 1310 nm and has a core radius of 25 μm and refractive indices in the core and cladding regions of 1.460 and 1.4550, respectively.

(a) What is the numerical aperture of the fiber?

(b) Estimate the number of guided modes.

2.7 (a) Show that for a graded-index fiber having a core refractive index $n^2(r) = n_2^2\left[1 + 2\Delta s\left(\frac{r}{a}\right)\right]$ with $s(r/a) = 1 - (r/a)^{\alpha}$; the acceptance angle $\alpha(r)$ is given by $\sin\alpha(r) = \left[n^2(r) - n_2^2\right]^{1/2}$.

(b) If the optical fiber has a parabolic profile shape show that $\sin\alpha(r) = NA\sqrt{1 - \left(\frac{r}{a}\right)^{1/2}}$ where $NA = n_2(2\Delta)^{1/2}(1 + \Delta)$.

(c) A parabolic graded-index silica optical fiber has a cladding refractive index of 1.460 and a relative index difference at the core axis of 1%. Find the maximum acceptance angle at the core axis of the fiber. Plot sin $\alpha(r)$ as a function of r. What is the acceptance angle of the fiber at the core and cladding interface. Comment on the launch of a laser source into this fiber.

2.8 (a) For a single-mode optical fiber having a graded-index central dip, that is, $s(r/a) = 1 - (1 - r/a)^{\alpha}$; the ESI parameters of V and radius are given by

$$\frac{V_e}{V} = \left[1 - \frac{2\gamma}{(\alpha+1)(\alpha+2)}\right]^{1/2} \quad \text{and} \quad \frac{a_e}{a} = \frac{(\alpha+1)(\alpha+2)(\alpha+3) - 6\gamma}{(\alpha+1)(\alpha+2)(\alpha+3) - 2\gamma}$$

where $V = ka(2\Delta)^{1/2}$.

(b) The fiber has a physical core radius of 8.0 μm, a maximum relative index difference of 0.3%, and a cladding refractive index of 1.460. Find its ESI parameters for the normalized frequency and radius at 1550 nm wavelength. Find also its ESI cutoff wavelength and its mode field diameter at this wavelength.

References

1. K.C. Kao and G.A. Hockham, Dielectric-fibre surface waveguides for optical frequencies, *Proceedings of the IEE*, 113(7), 1151–1158, July 1966.
2. R.D. Maurer and P.C. Schultz, Fused silica optical waveguide, U.S. Patent 3,659,915, 1972–05.
3. D.B. Keck and P.C. Schultz, Method of producing optical waveguide fibers, U.S. Patent 3,711,262, 1973–01.
4. G.P. Agrawal, *Fiber Optic Communications Systems*, 3rd ed., John Wiley, New York, 2002, Chapter 2.
5. I. Dedic, 56Gs/s ADC enabling 100GbE, *Proceedings of Optical Fiber Conference OFC 2010*, Invited Paper, Digital Transmission Systems, OFC 2010, Anaheim, CA. http://www.fujitsu.com/downloads/MICRO/fme/dataconverters/OFC-2010-56Gss-ADC-Enabling-100GbE.pdf, access date, May 18, 2014.
6. R. Ryf, S. Randel, A.H. Gnauck, C. Bolle, R.-J. Essiambre, P. Winzer, D.W. Peckham, A. McCurdy, and R. Lingle, Space-division multiplexing over 10 km of three-mode fiber using coherent 6 × 6 MIMO processing, in *Optical Fiber Communication Conference*, Los Angeles, CA, March 6–10, 2011.
7. A. Safaai-Jazi and J.C. McKeeman, Synthesis of intensity patterns in few-mode optical fibers, *IEEE Journal of Lightwave Technology*, 9(9), 1047, September 1991.

8. M. Salsi, C. Koebele, D. Sperti, P. Tran, P. Brindel, H. Mardoyan, S. Bigo et al., Transmission at 2 × 100 Gb/s, over two modes of 40 km-long prototype few-mode fiber, using LCOS based mode multiplexer and demultiplexer, in *Optical Fiber Conference, OFC 2011, and National Fiber Optic Engineers Conference (NFOEC)*, Los Angeles, CA, March 6, 2011.
9. S. Randel, R. Ryf, A. Sierra, P.J. Winzer, A.H. Gnauck, C.A. Bolle, R.-J. Essiambre, D.W. Peckham, A. McCurdy, and R. Lingle, Jr., 6 × ×56-Gb/s mode-division multiplexed transmission over 33-km few-mode fiber enabled by 6 × 6 MIMO equalization, *Optics Express*, 19(17), 16697, August 2011.
10. C.D. Poole, J.M. Wiesenfeld, D.J. DiGiovanni, and A.M. Vengsarkar, Optical fiber-based dispersion compensation using higher order modes near cutoff, *IEEE Journal of Lightwave Technology*, 12(10), 1746, October 1994.
11. L. Allen, M.W. Beijersbergen, R.J.C. Spreeuw, and J.P. Woerdman, Orbital angular momentum of light and the transformation of Laguerre–Gaussian laser modes, *Physical Review A*, 45, 8185–8189, 1992.
12. J. Wang, J.Y. Yang, I.M. Fazal, N. Ahmed, Y. Yan, H. Huang, Y. Ren et al., Terabit free-space data transmission employing orbital angular momentum multiplexing, *Nature Photonics*, 6, 488–496, 2012. doi:10.1038/nphoton.2012.138.
13. D. Tse and P. Viswanath, *Fundamentals of Wireless Communication*, Cambridge University Press, Cambridge, U.K., 2005.
14. A. Lozano and N. Jindal, Transmit diversity vs. spatial multiplexing in modern MIMO systems, *IEEE Transactions on Wireless Communications*, 9(1), 186–197, 2010.
15. L.B. Jeunhomme, *Single Mode Fiber Optics*, Marcel Dekker, New York, 1983.
16. G.P. Agrawal, *Fiber Optic Communications Systems*, 3rd ed., John Wiley, New York, 2002.
17. R.H. Stolen, E.P. Ippen, and A.R. Tynes, Raman oscillation in glass optical waveguide, *Applied Physics Letters*, 20(2), 62, 1972, http://dx.doi.org/10.1063/1.1654046.
18. E.P Ippen and R.H. Stolen, Stimulated Brillouin scattering in optical fibers, *Applied Physics Letters*, 21(11), 539, 1972, http://dx.doi.org/10.1063/1.1654249.
19. R.G. Smith, Optical power handling capacity of low loss optical fibers Raman and Brillouin scattering, *Applied Optics*, 11, 2489–2494, 1972.
20. G.P. Agrawal, *Fiber Optic Communications Systems*, 3rd ed., John Wiley, New York, p. 60, 2002.
21. G.P. Agrawal, *Fiber Optic Communications Systems*, 3rd ed., John Wiley, New York, p. 67, 2002.
22. G. Mahlkc and P. Gossing, *Fiber Optic Cables*, Siemens A.G./John Wiley, Chichester, U.K., 1987.
23. D. Jones, *Optical Fiber Communications Systems*, Holt, Rinhart Winston, New York, 1988.
24. A.W. Snyder, Understanding monomode optical fibers, *Proceedings of the IEEE*, 69(1), 6–13, January 1981.
25. D. Keck, Single mode fibers outperform multimode cables, *IEEE Spectrum*, pp. 30–37, March 1983.
26. D. Marcuse, Loss-analysis of single-mode fiber splices, *Bell System Technical Journal*, 56(5), 703–718, 1977.
27. P.S. Henry, Lightwave primer, *IEEE Journal Quantum Electronics*, QE-21(12), 1862–1879, December 1985.

3

Optical Fibers: Signal Attenuation and Dispersion

This chapter describes the mechanism and properties of light-wave modulated signals when they propagate in optical fibers, single-mode optical fibers (SMFs) only, in particular standard SMF (SSMF) and nonzero dispersion-shifted fibers (NZDSFs) and dispersion-compensating fibers. Attenuation and dispersion effects, the two principal phenomena in the design of transmission systems, are described in detail.

3.1 Introduction

In Chapter 2, the basic structure and fundamental aspects of light wave propagation in optical fibers were treated. In particular, SMFs provide the basic structure for standard communication transmission systems. This chapter deals with the transmission of optical signals over optical fibers, in particular, the loss and spreading of optical signals transmitted through optical fibers, namely, the attenuation and dispersion effects.

Attenuation and dispersion are the two most important effects that play a major part in optical fiber transmission systems. The attenuation of optical signals would limit the availability of optical power along the transmission path, and for very low attenuation, dispersion limits the repeater spacing below what would be possible from the attenuation factor.

The fiber loss was reduced from 100 dB/km (i.e., transmission is possible over only a few meters) at 1300 nm in 1970 to about 0.25 and 0.15 dB/km, which is very close to the theoretical possible transparent limit and transmission over several hundred kilometers of fibers in the 1300 and 1550 nm wavelength region, respectively, in 1980 [1–3].

The dispersion and pulse broadening of optical fibers have been also reduced due to the "smart design" of optical fiber structures. In early 1970s, we saw a remarkable development of theories for understanding light wave guiding in optical fibers of multimode types. The breakthrough in the reduction of loss in optical fibers and the ability to manufacture optical fibers with a very small core diameter led to the design of single optical fibers. The remarkable theoretical development of optical waveguiding in a "weakly guiding" (i.e., a very small difference between the core and cladding regions) fiber structure led to a planewave-like transmission of light waves. Further, the availability of narrow linewidth lasers allows system engineers to design and implement several high-speed long-distance fiber optic communication systems.

The attenuation that arises from intrinsic material properties and from waveguide properties is described and a general attenuation coefficient is derived. The chromatic dispersion for SM fiber in linear limit, which means that we assume that the optical power

launched into the fiber to be less than the threshold for nonlinear effects, is then treated. The effects of optical waveguide parameters on the dispersion factors are analyzed. The balance of the opposite signed dispersion factors between the materials and waveguides is analyzed so that a minimum dispersion factor, designed for optical fibers with dispersion-compensated or -shifted characteristic, is achieved.

In later chapters of this book, we treat optical amplifiers and techniques to compensate for the broadening of optical pulses so that an ultra-long ultra-high-speed optical fiber communication system can be designed and implemented.

3.2 Signal Attenuation in Optical Fibers

Optical loss in optical fibers is one of the two main fundamental limiting factors as it reduces the average optical power reaching the receiver. The optical loss is the sum of three major components: intrinsic loss, microbending loss, and splicing loss.

3.2.1 Intrinsic or Material Attenuation

Intrinsic loss consists mainly of absorption loss due to OH impurities and Rayleigh scattering loss. The intrinsic loss is a function of λ^{-6}. The longer the operating wavelength the lower the loss. However, it also depends on the transparency of the optical material that is used to form the optical fibers. For silica fiber, the optical material loss is low over the wavelength range 0.8–1.8 μm. Over this wavelength range, there are three optical windows that optical communication systems use. The first window has about 20.0 nm bandwidth range over the central wavelength of 810 nm. The second and third windows most commonly used in present-day optical communication systems have a range of 80 and 40 nm over the central wavelength of 1300 and 1550 nm, respectively. The intrinsic losses are about 0.3 and 0.15 dB/km at the 1550 and 1300 nm regions, respectively.

This is a few hundred thousand times improvement over the original loss of about 60 dB/km in the transmission of signal over 5.0 m. Most communication fiber systems are operating at 1300 nm as dispersion is a minimum at this range. For "power hungry" systems, optical or extra-long systems should operate at 1550 nm.

3.2.2 Absorption

The absorption loss in silica glass is composed mainly of ultraviolet (UV) and infra-red (IR) absorption tales of pure silica. The IR absorption tale of pure silica has been shown to be the result of the vibration of the basic tetrahedron and thus strong resonances occur around 8–13 μm with a loss about 10^{10} dB/km. This loss is shown in IR curve of Figure 3.1. Overtones and combinations of these vibrations lead to various absorption peaks in the low wavelength range as shown by UV curve.

Various impurities that also lead to spurious absorption effects in the wavelength range of interest (1.2–1.6 μm) are transition metal ions and water in the form of OH ions. These sources of absorptions have been practically reduced in recent years. Figure 3.1 shows the variation of the attenuation coefficients as a function of wavelength.

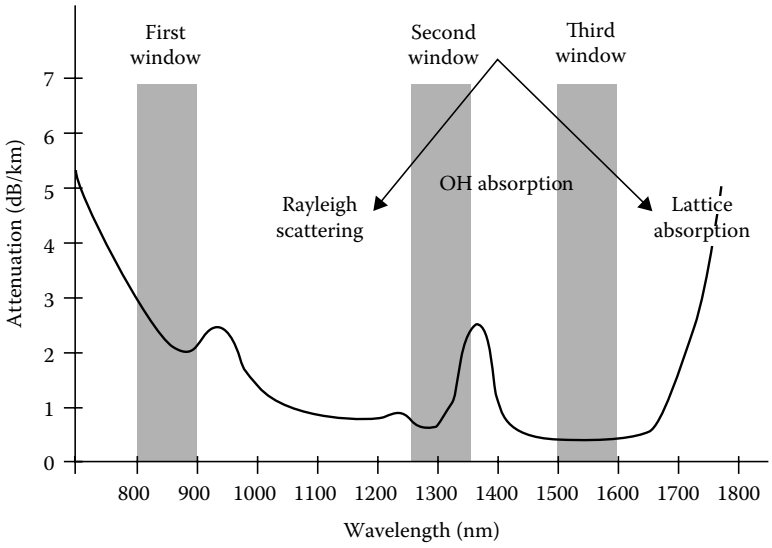

FIGURE 3.1
Attenuation of silica as a function of wavelength: attenuation windows and corresponding loss mechanism to attenuation coefficients.

3.2.3 Rayleigh Scattering

The Rayleigh scattering loss, L_R, which is due to microscopic inhomogeneities of the material, shows a λ^{-6} dependence and is given by

$$L_R = (0.75 + 4.5\Delta)\lambda^{-6} \text{ dB/km} \tag{3.1}$$

where
Δ is the relative index difference as defined in Chapter 2
λ is the wavelength in μm

Thus to minimize the loss, Δ should be made as low as possible.

3.2.4 Waveguide Loss

The losses that result from the waveguide structure arise from power leakage, bending, microbending of the fiber axis, and defects and joints between fibers. The power leakage is significant only for depressed cladding fibers.

3.2.5 Bending Loss

When a fiber is bent, the plane wave fronts associated with the guided mode are pivoted at the center of curvature and their longitudinal velocity along the fiber axis increases with the distance from the center of curvature. As the fiber is bent further over a critical curve, the phase velocity exceeds that of the plane wave in the cladding and radiation occurs.

The bend loss L_B for a radius of curvature R is given by

$$L_B = -10\text{Log}_{10}\left(1 - 890\frac{r_0^6}{\lambda^4 R^2}\right) \text{ for silica.} \tag{3.2}$$

3.2.6 Microbending Loss

Microbending loss results from power coupling from the guided fundamental mode of the fiber to radiation modes. This coupling takes place when the fiber axis is bent *randomly* in a *high* spatial frequency. Such bending can occur during packing of the fiber during the cabling process as shown in Figure 3.2.

The microbending loss of an SM fiber is a function of the fundamental mode spot size r_0. Fibers with large spot size are extremely sensitive to microbending. It is therefore desirable to design the fiber to have as small a spot size as possible to minimize bending loss. The microbending loss can be expressed by the relation

$$L_m = 2.15 \times 10^{-4} r_0^6 \lambda^{-4} L_{mm} \text{ dB/km} \tag{3.3}$$

where L_{mn} is the microbending loss of a 50 μm core multimode fiber having an NA of 0.2.

3.2.7 Joint or Splice Loss

Ultimately, the fibers will have to be spliced together to form the final transmission link. With fiber cable that averages 0.4–0.6 dB/km, splice loss in excess of 0.2 dB/splice drastically reduces the unrepeated distance that can be achieved. It is therefore extremely important that the fiber be designed so that splicing loss can be minimized.

Splice loss is mainly due to the result of axial misalignment of the fiber core as shown in Figure 3.2.

Splicing techniques, which rely on aligning the outside surface of the fibers, require extremely tight tolerances on core to outside surface concentricity. Offsets of the order of 1 μm can produce significant splice loss. This loss is given by

$$L_s = \frac{10}{\ln 10}\left(\frac{d}{r_0}\right)^2 \text{ dB} \tag{3.4}$$

where d is the *axial* misalignment of the fiber cores. It is obvious that minimizing optical loss involves making trade-offs between the different sources of loss. It is advantageous to

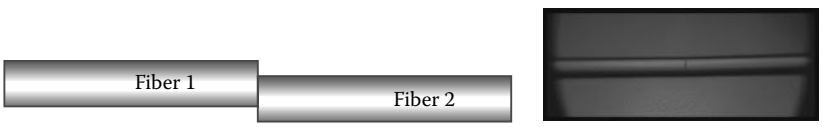

FIGURE 3.2
(a) Misalignment in splicing two optical fibers generating losses. (b) Aligned spliced fibers.

have a large spot size to minimize both Rayleigh and splicing losses whereas minimizing bending and microbending losses requires a small spot size. In addition as described in the next section, the spot size plays a significant role in the chromatic dispersion properties of single-mode fibers.

3.2.8 Attenuation Coefficient

Under general conditions of power attenuation inside an optical fiber, the attenuation coefficient of the optical power P can be expressed as

$$\frac{dP}{dz} = -\alpha P \tag{3.5}$$

where α is the attenuation coefficient. This attenuation coefficient includes all effects of power loss when signals are transmitted through the optical fibers.

If we consider optical signals with an average optical power, P_{in}, entering at the input of a fiber of length L and if P_{out} is the optical power output, then P_{in} and P_{out} are related to the attenuation coefficient α by

$$P_{out} = P_{in}\, e^{(-\alpha L)} \tag{3.6}$$

It is customary to express α in dB/km by using the relation

$$\alpha(\text{dB/km}) = -\frac{10}{L}\log_{10}\left(\frac{P_{out}}{P_{in}}\right) = 4.343\alpha \tag{3.7}$$

Standard optical fibers with a small Δ would exhibit a loss of about 0.2 dB/km indicating that the silica in them is very pure. Such purity in a bar of silica would allow us to see through a 1 km glass bar without distortion the person standing at the other end. The attenuation curve for silica glass is shown in Figure 3.1. Three spectral windows are of particular interest for telecommunication experts. The first window is in the range of 800–900 nm, this is the near IR region. This window was first employed in the 1970s because the available light sources were fabricated using GaAs band gap materials. However, at present, the availability of the vertical cavity stimulated emission laser (VCSEL) leads to the use of this window for short-distance optical interconnection (OIC) for ultra-high-speed back plane interconnection, especially in data centers and/or high-speed exchange centers.

The second and third windows are located in the 1310 and 1550 nm band, respectively. The 1310 nm band offers a higher attenuation coefficient than the 1550 nm band but no dispersion whatsoever as outlined in the next section. The third window has generated more interest over the last three decades because of lower loss and the availability of optical amplification devices, especially the Er: doped fiber amplifiers (EDFA). This window is classified into three bands, the S-band of 1510–1530 nm, the C-band of 1530–1565 nm, and the L-band of 1535–1565 nm. The 1550 nm band offers the lowest loss in addition to an excellent region for long-haul transmission.

3.3 Signal Distortion in Optical Fibers

3.3.1 Basics on Group Velocity

Consider a *monochromatic* field given by

$$E_x = A\cos(\omega t - \beta z) \tag{3.8}$$

where
A is the wave amplitude
ω is the radial frequency
β is the propagation constant along the z-direction

If we set $\omega t - \beta z$ to be a constant then the wave phase velocity is given by

$$v_p = \frac{dz}{dt} = \frac{\omega}{\beta} \tag{3.9}$$

Now we consider a propagating wave consisting of *two* monochromatic fields of frequencies $\omega + \partial\omega$ and $\omega - \partial\omega$

$$E_{x1} = A\cos[(\omega + \partial\omega)t - (\beta + \partial\beta)z)], \tag{3.10}$$

$$E_{x2} = A\cos[(\omega - \partial\omega)t - (\beta - \partial\beta)z)]. \tag{3.11}$$

The total field is then given by

$$E_x = E_{x1} + E_{x2} = 2A\cos\left(\omega t - \partial z\right)\cos\left(\partial\omega t - \partial\beta z\right). \tag{3.12}$$

If $\omega \gg \partial\omega$, then the variation in $\cos(\omega t - \beta z)$ is much faster than that in $\cos(\partial\omega t - \partial\beta z)$. Now we set $(\partial\omega t - \partial\beta z)$ to be a constant and define the *group velocity* as

$$v_g = \frac{d\omega}{d\beta} \rightarrow v_g^{-1} = \frac{d\beta}{d\omega} \tag{3.13}$$

Then the group delay t_g per unit length (setting L at 1.0 km) is then written as

$$t_g = \frac{L\,(\text{of } 1\,\text{km})}{v_g} = \frac{d\beta}{d\omega} \tag{3.14}$$

The pulse spread $\Delta\tau$ per unit length due to group delay of light sources of spectral width σ_λ (i.e., the full-width-half-mark (FWHM) of the optical spectrum of the light source) is

$$\Delta\tau = \frac{dt_g}{d\lambda}\sigma_\lambda \tag{3.15}$$

that is, the spread of the group delay due to the spreading of source wavelength is in ps/km. Thus, the linewidth of the light source makes a great difference in the distortion of optical signals transmitted through the optical fiber. The narrower the source linewidth the less dispersed the optical pulses are. The typical linewidth of Fabry–Perot semiconductor lasers is about 1–2.0 nm while the distributed feedback (DFB) laser would exhibit a linewidth of 100 MHz (how many nm is this 100 MHz optical frequency equivalent to?).

An optical signal traveling along a fiber becomes increasingly distorted. This distortion is a consequence of *intermodal* delay effects and *intramodal* dispersion. Intermodal delay effects are significant in multimode optical fibers due to each mode having a different value of group velocity at a specific frequency. This is the most dominant impairment in MMF transmission systems. Currently, few-mode fiber (FMF) can be used to increase the transmission capacity and these phase velocity delay differences can be compensated by the use of digital signal processing in the electronic domain [4]. Intermodal dispersion is pulse spreading that occurs within a single mode. It is the result of the group velocity being a function of the wavelength λ and is therefore referred to as chromatic dispersion.

The two main causes of intermodal dispersion are as follows:

1. Material dispersion arises because of the variation in the refractive index $n(\lambda)$ as a function of wavelengths. This implies that the group velocity of any given mode is dependent on the wavelength.
2. Waveguide dispersion occurs because the mode propagation constant $\beta(\lambda)$ is a function of wavelength λ, core radius a, and the difference in the refractive index.

The group velocity associated with the fundamental mode is dependent on the frequency because of chromatic dispersion. As a result, different spectral components of the light pulse travel at different group velocities, a phenomenon referred to as *the group velocity dispersion* (GVD), intra-modal dispersion, or as material dispersion and waveguide dispersion

3.3.2 Group Velocity Dispersion (GVD)

3.3.2.1 Material Dispersion

The refractive index of silica as a function of wavelength is shown in Figure 3.3. The refractive index is plotted over the wavelength region of 1.0–2.0 μm, which is the most important range for silica-based optical communication systems as the loss is lowest at 1300 and 1550 nm windows.

The propagation constant β of the fundamental mode guided in the optical fiber can be written as

$$\beta(\lambda) = \frac{2\pi n(\lambda)}{\lambda} \tag{3.16}$$

The group delay t_{gm} per unit length of (3.14) can be obtained as

$$t_{gm} = \frac{d\beta}{d\omega} \tag{3.17}$$

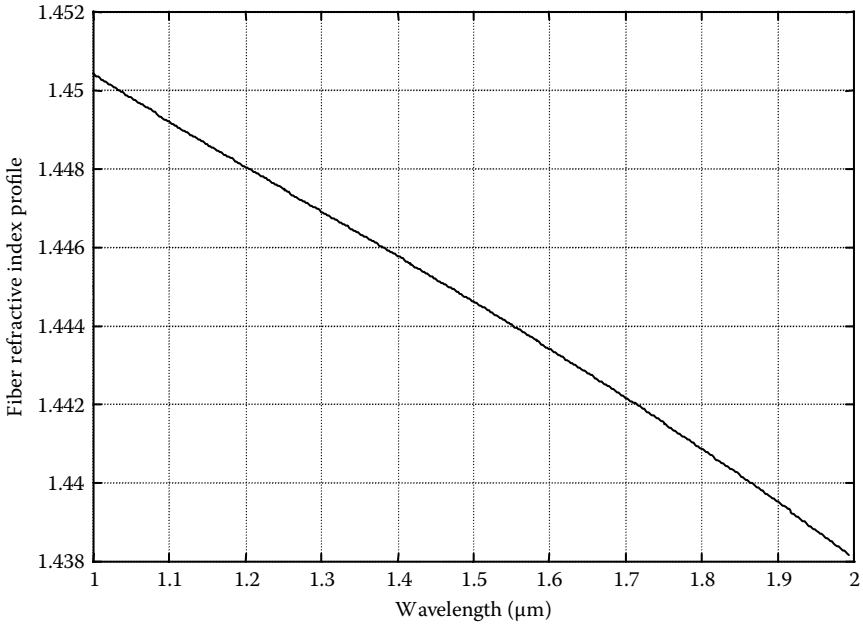

FIGURE 3.3
Variation in the refractive index as a function of optical wavelength of silica.

where we can use

$$d\omega = d\left(\frac{2\pi c}{\lambda}\right) = -\frac{2\pi c}{\lambda^2}d\lambda. \tag{3.18}$$

Thus

$$t_{gm} = -\frac{\lambda^2}{2\pi c}\frac{d\beta}{d\lambda} \tag{3.19}$$

Substituting (3.16) into (3.19), we have

$$t_{gm} = \frac{1}{c}\left[n(\lambda) - \frac{\lambda dn(\lambda)}{d\lambda}\right] \tag{3.20}$$

Thus the pulse dispersion per unit length $\Delta\tau_m/\Delta\lambda$ due to the material (using (3.20)) for a source having RMS spectral width σ_λ of

$$\Delta\tau_m = -\frac{\lambda}{c}\frac{d^2n}{d\lambda^2}\sigma_\lambda \tag{3.21}$$

The delay interference can be explained as illustrated in Figures 3.4, 3.5, and 3.6.

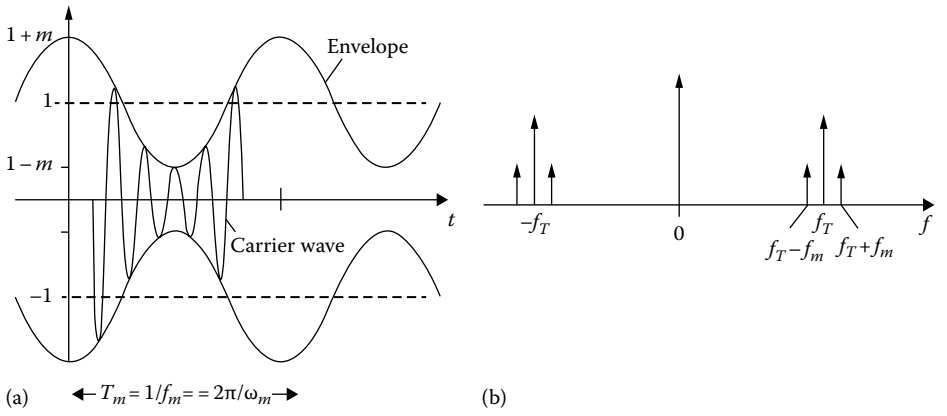

FIGURE 3.4
(a) Time signal and (b) spectrum.

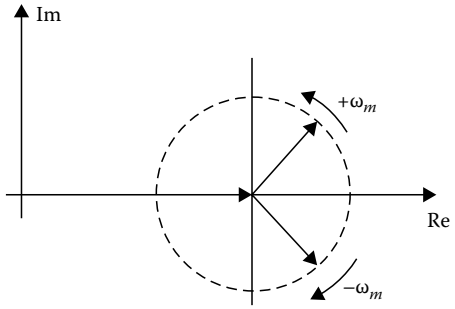

FIGURE 3.5
Vector phasor diagram of the complex envelope.

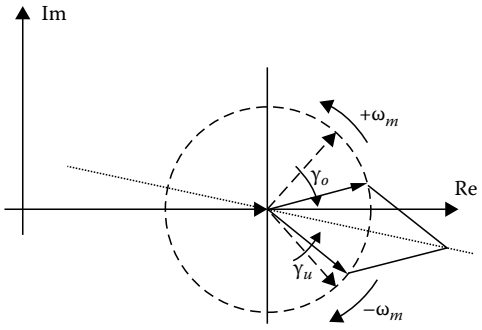

FIGURE 3.6
Magnitude of complex envelope when not sinusoidal, the envelope subject to nonlinear distortions.

If we set $\Delta\tau_m = M(\lambda)\sigma_\lambda$, thence

$$M(\lambda) = -\frac{\lambda}{c}\frac{d^2n}{d\lambda^2} \tag{3.22}$$

$M(\lambda)$ is assigned as *the material dispersion factor* or *material dispersion parameter*, its unit is commonly expressed in ps/(nm · km) (Figure 3.7).

Thus, if the refractive index can be expressed as a function of the optical wavelength then the material dispersion can be calculated. In fact, in practice, optical material engi-

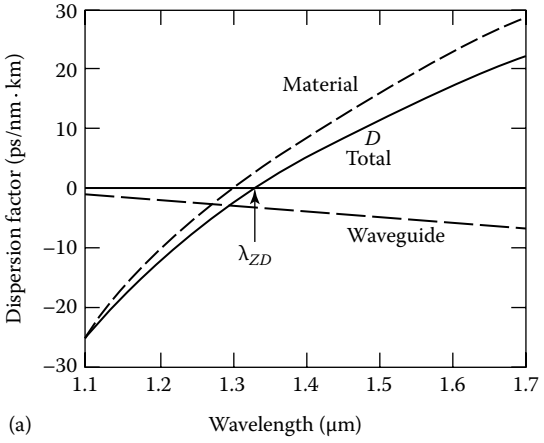

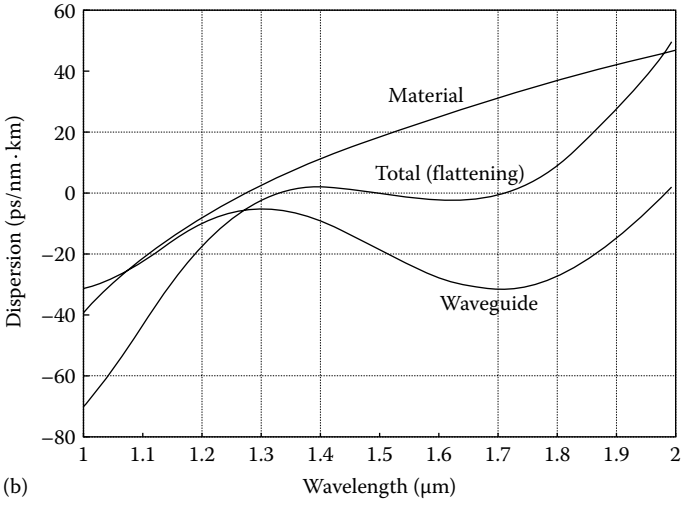

FIGURE 3.7
Chromatic dispersion factor of (a) SSMF. (b) Dispersion-flattened fiber: Plotted curves representing the material dispersion factor as a function of the optical wavelength for silica-based optical fiber (yellow curve) with a zero dispersion wavelength at 1290 nm. This curve is generated as an example. For standard single-mode optical fibers which are currently installed throughout the world the total dispersion is around +17 ps/(nm · km) at 1550 nm and almost zero at 1310 nm. Can we estimate the waveguide dispersion curve for the standard SM optical fiber at around 1300 and 1550 nm windows?

TABLE 3.1

Sellmeier's Coefficients for Several Optical Fiber Silica-Based Materials with Germanium Doped in the Core Region

	Germanium Concentration, C (mol%)			
Sellmeiere's Constants	**0 (Pure Silica)**	**3.1**	**5.8**	**7.9**
G_1	0.6961663	0.7028554	0.7088876	0.7136824
G_2	0.4079426	0.4146307	0.4206803	0.4254807
G_3	0.8974794	0.8974540	0.8956551	0.8964226
λ_1	0.0684043	0.0727723	0.0609053	0.0617167
λ_2	0.1162414	0.1143085	0.1254514	0.1270814
λ_3	9.896161	9.896161	9.896162	9.896161

Source: Kobayashi et al. 1978.

neers have to characterize all optical properties of new materials. The refractive index $n(\lambda)$ can usually be expressed in Sellmeier's dispersion formula as

$$n^2(\lambda) = 1 + \sum_k \frac{G_k \lambda^2}{(\lambda^2 - \lambda_k^2)} \tag{3.23}$$

where

G_k are Sellmeier's constants

k is an integer and normally $k = 1$, 2, and 3

In the late 1970s, several silica-based glass materials were manufactured and their properties measured. The refractive indices were usually expressed using Sellmeier's coefficients. These coefficients for several optical fiber materials are given in Table 3.1.

By using curve fitting, the refractive index of pure silica $n(\lambda)$ can be expressed as:

$$n(\lambda) = c_1 + c_2\lambda^2 + c_3\lambda^{-2} \tag{3.24}$$

where

$c_1 = 1.45084$

$c_2 = -0.00343\ \mu m^{-2}$

$c_3 = 0.00292\ \mu m^2$

Thus from Table 3.1 and (3.24), we can use (3.22) to determine the material dispersion factor for a certain wavelength range.

For the doped core of the optical fiber, the Sellmeier expression (3.23) can be approximated by using the curve-fitting technique to approximate it to the form in (3.24). The material dispersion factor $M(\lambda)$ becomes zero at wavelengths around 1350 nm and about –10 ps/(nm · km) at 1550 nm. However, the attenuation at 1350 nm is about 0.4 dB/km as compared to 0.2 dB/km at 1550 nm (Figure 3.7).

3.3.2.2 Waveguide Dispersion

The effect of waveguide dispersion can be approximated by assuming that the refractive index of the material is independent of wavelength. Let us now consider the group delay, that is, the time required for a mode to travel along the fiber of length L. This kind of

dispersion depends strongly on the Δ and V parameters. To find expressions for the fiber parameters, we define a *normalized propagation constant b* as

$$b = \frac{\frac{\beta^2}{k^2} - n_2^2}{n_1^2 - n_2^2} \tag{3.25}$$

for small Δ. We note that the β/k is in fact the *effective refractive index* of the guided optical mode propagating along the optical fiber, that is, the guided waves traveling in the axial direction of the fiber "see" it as a medium with a refractive index of an equivalent "effective" index.

In case the fiber is a weakly guided waveguide with effective refractive index taking a value significantly close to that of the core or cladding index, (3.25) can then be approximated by

$$b \cong \frac{\frac{\beta}{k} - n_2}{n_1 - n_2} \tag{3.26}$$

Solving (3.26) for β, we have

$$\beta = n_2 k(b\Delta + 1). \tag{3.27}$$

The group delay for waveguide dispersion is then given by (per unit length)

$$t_{wg} = \frac{d\beta}{d\omega} = \frac{1}{c}\frac{d\beta}{dk} \tag{3.28}$$

$$t_{wg} = \frac{1}{c}\left[n_1 + n_2\Delta\frac{d(bk)}{dk}\right] = \frac{1}{c}\left[n_1 + n_2\Delta\frac{d(bk)}{dk}\right] = \frac{1}{c}\left[n_1 + n_2\Delta\frac{d(bV)}{dV}\right] \tag{3.29}$$

Equation 3.29 can be obtained from (3.28) by using the expression of V. Thus, the pulse spreading $\Delta\tau_\omega$ due to the waveguide dispersion per unit length by a source having an optical bandwidth (or linewidth) σ_λ is given by

$$\Delta\tau_\omega = \frac{dt_{gw}}{d\lambda}\sigma_\lambda = -\frac{n_2\Delta}{c\lambda}V\frac{d^2(Vb)}{dV^2}\sigma_\lambda \tag{3.30}$$

and the *waveguide dispersion factor or waveguide dispersion parameter* (similar to the material dispersion factor) is then defined as:

$$D(\lambda) = -\frac{n_2(\lambda)\Delta}{c\lambda}V\frac{d^2(Vb)}{dV^2} \tag{3.31}$$

in units of ps/(nm·km). In the range of $0.9 < \lambda/\lambda_c < 2.6$, the factor $V\frac{d^2(Vb)}{dV^2}$ can be approximated (to <5% error) by

$$V\frac{d^2(Vb)}{dV^2} \cong 0.080 + 0.549(2.834 - V)^2 \tag{3.32}$$

or alternatively using the definition of cut off wavelength and the expression of the V parameters we obtain

$$V\frac{d^2(Vb)}{dV^2} \cong 0.080 + 3.175\left(1.178 - \frac{\lambda_c}{\lambda}\right)^2 \tag{3.33}$$

NOTE: Readers/students to prove the equivalent equation of (3.28) to (3.33). Further, the sign assignment of the material and waveguide dispersion factors must be the same. Otherwise a negative and positive of these dispersion factors would create confusion. Can you explain what would happen to the pulse if it is transmitted through an optical fiber having a total negative dispersion factor?

Thus from Equations 3.33 and 3.32, we can calculate the waveguide dispersion factor and hence the pulse dispersion factor for a particular source spectral width σ_λ. It is noted that the dispersion considered in this chapter is for step-index fiber only. For graded-index fiber, ESI parameters must be found and the chromatic dispersion can then be calculated.

Alternatively, the waveguide dispersion parameter can be expressed as a function of the propagation constant β by using $\omega = 2\pi c/\lambda$ and (3.33), then the waveguide dispersion factor can be written as (Figure 3.8):

$$D(\lambda) = -\frac{2\pi c}{\lambda^2}\beta_2 = -\frac{2\pi c}{\lambda^2}\frac{d^2\beta}{d\omega^2} \tag{3.34}$$

Thus, the waveguide dispersion factor is directly related to the second-order derivative of the propagation constant with respect to the optical radial frequency.

An example of a design of an optical fiber operating in the single-mode region is given in Figure 3.7. The cladding material is pure silica. Shown in this figure are the curves of the material dispersion, waveguide dispersion, and total dispersion for an SMF with nonuniform refractive index profile in the core.

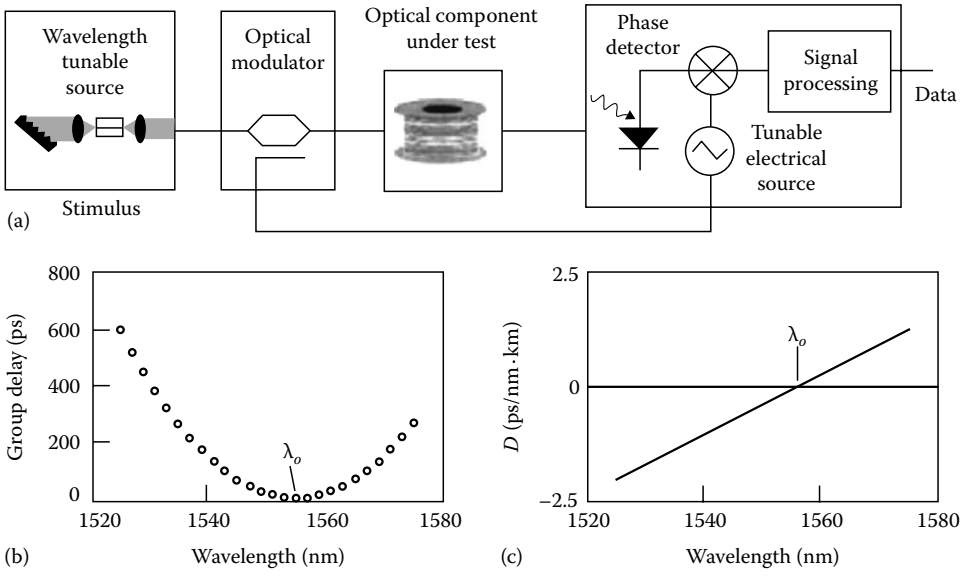

FIGURE 3.8
(a) Chromatic dispersion measurement of the two-port optical device. (b) Relative group delay versus wavelength and (c) dispersion parameter versus wavelength.

3.4 Transfer Function of Single-Mode Fibers

The linear time-variant system such as the SMF would have a transfer function of (Figures 3.9 through 3.12)

$$H(f) = |H(f)|e^{-j\alpha(f)} \tag{3.35}$$

3.4.1 Higher-Order Dispersion

We observe also from Figure 3.6 that the bandwidth–length product of the optical fiber can be extended to infinity if the system is operating at the wavelength such that the total dispersion is zero. However, the dispersive effects do not disappear completely at this zero-dispersion wavelength. Optical pulses still experience broadening because of higher-order dispersion effects. It can be easily imagined that the total dispersion factor cannot be made zero "flatten" over the optical spectrum. This is higher-order dispersion which is governed by the slope of the total dispersion curve, called the dispersion slope $S = \partial(M(\lambda) + D_w(\lambda))/\partial\lambda$; $S(\lambda)$ can thus be expressed as:

$$S(\lambda) = \left(\frac{2\pi c}{\lambda^2}\right)^2 \frac{d^3\beta}{d\lambda^3} + \left(\frac{4\pi c}{\lambda^3}\right)\frac{d^2\beta}{d\lambda^2} \tag{3.36}$$

$S(\lambda)$ is also known as the differential-dispersion parameter.

3.4.2 Transmission Bit-Rate and the Dispersion Factor

The effect of dispersion on the system bit rate B_r is obvious and can be estimated by using the criterion:

$$B_r \cdot \Delta\tau < 1 \tag{3.37}$$

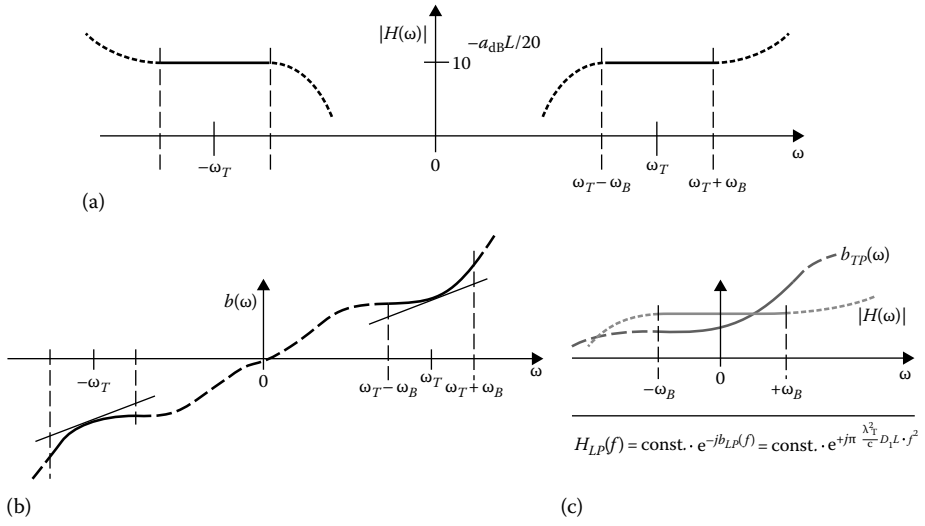

FIGURE 3.9
Frequency response of a single-mode optical fiber (a) magnitude, (b) phase response in bandpass regime, (c) baseband equivalence.

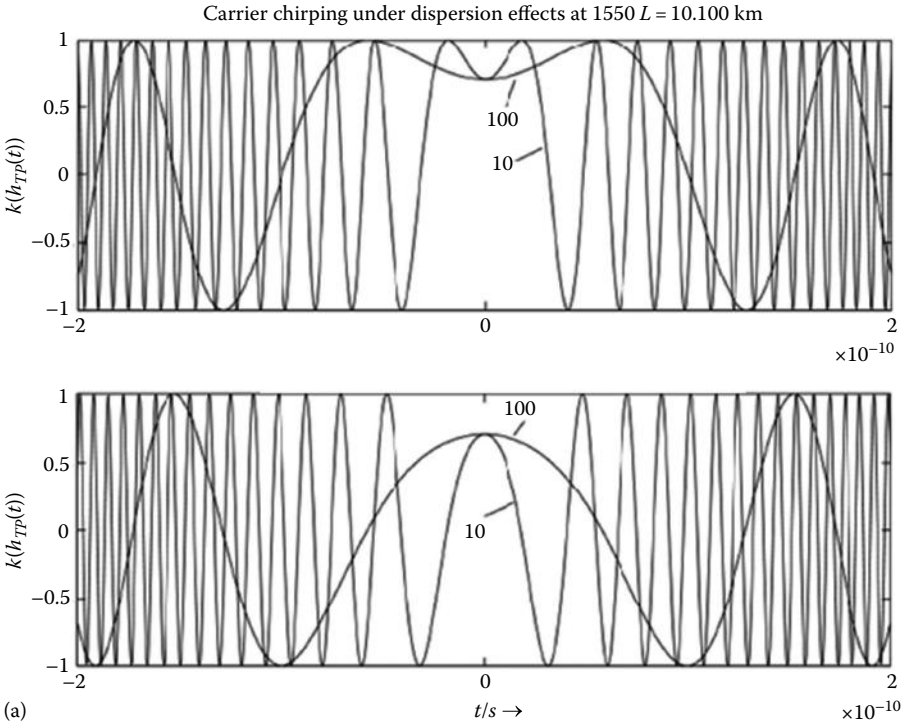

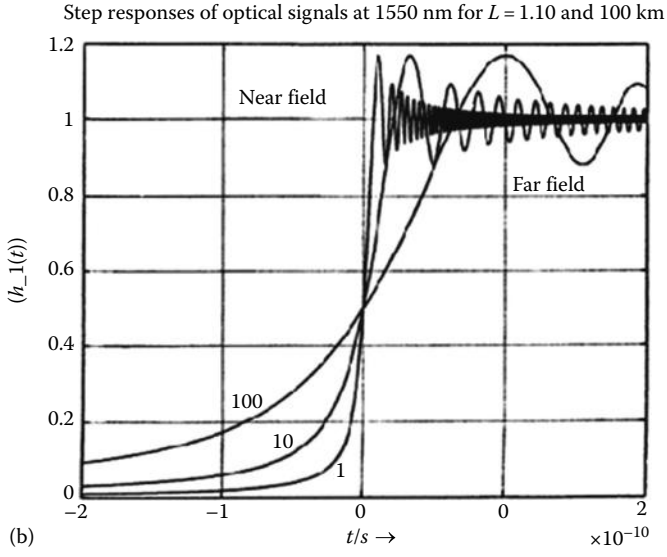

FIGURE 3.10
(a) Carrier chirping effects and (b) step response of a single-mode optical fiber of L = 1, 10, and 100 km.

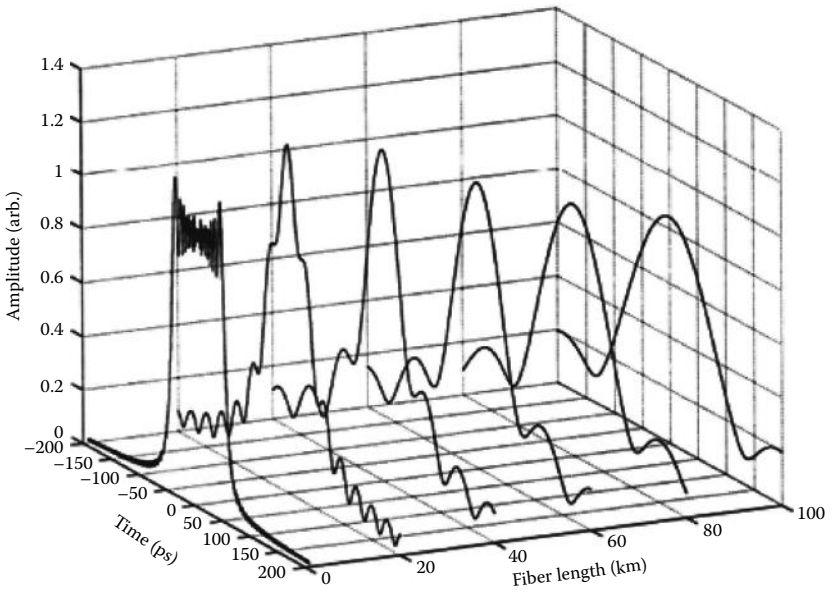

FIGURE 3.11
Pulse response from near field (~ <2 km) to far field (>80 km).

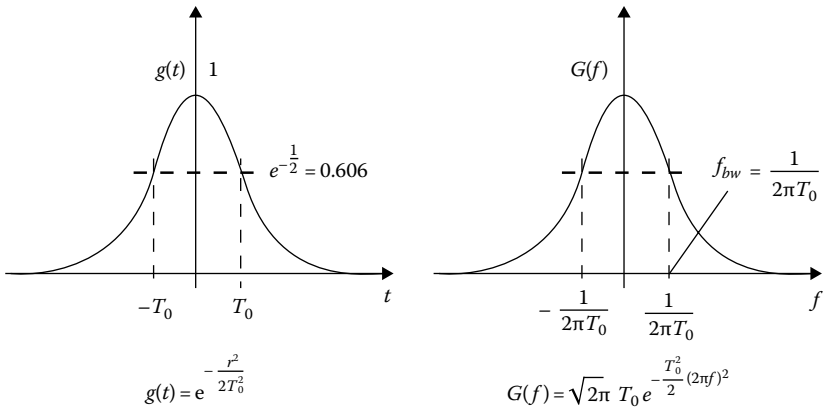

FIGURE 3.12
Fiber response to Gaussian pulse. Gaussian → Gaussian!

where $\Delta\tau$ is the total pulse broadening. Over the length L, the total dispersion $D_T(\lambda) = M(\lambda) + D_w(\lambda)$ and a source linewidth σ_λ the criterion becomes

$$B_r \cdot L \cdot |D_T| \sigma_\lambda \leq 1. \tag{3.38}$$

For a total dispersion factor of 1 ps/(nm·km) and a semiconductor laser of line width of 2–4 nm, the bit rate-length product cannot exceed 100 Gb/s·km. That is, if a 100 km transmission distance is used then the bit rate cannot be higher than 1.0 Gb/s (Figures 3.13 and 3.14).

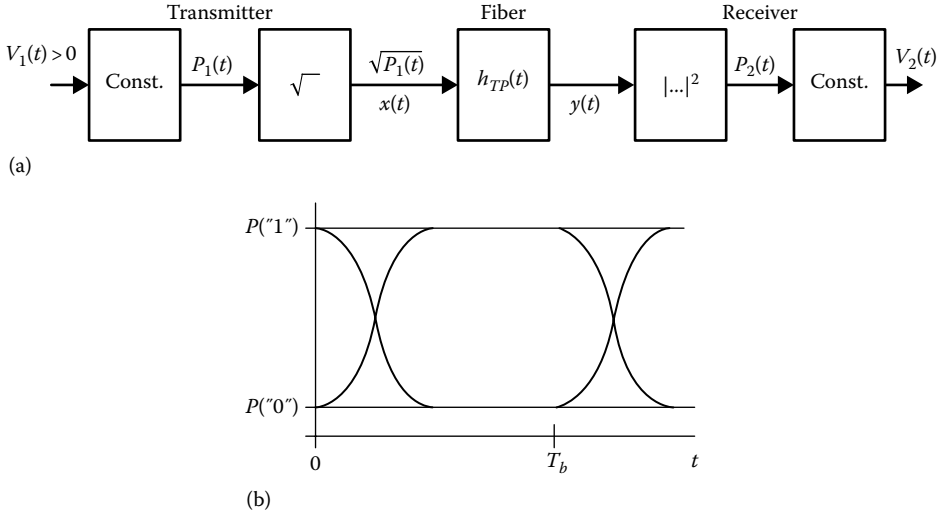

FIGURE 3.13
Schematic of an optical transmission system and its equivalent transfer functions (a) transmission system structure and (b) eye diagram.

3.4.3 Polarization Mode Dispersion

The delay between two PSPs is normally negligibly small at 10 Gb/s. However, at high bit rate and in an ultra long-haul transmission, PMD severely degrades the system performance [5–8] (Figures 3.15 and 3.16). The instantaneous value of DGD ($\Delta\tau$) varies along the fiber and follows a Maxwellian distribution [9,10] (see Figure 3.17).

The Maxwellian distribution is governed by the following expression:

$$f(\Delta\tau) = \frac{32(\Delta\tau)^2}{\pi^2\langle\Delta\tau\rangle^3}\exp\left\{-\frac{4(\Delta\tau)^2}{\pi\langle\Delta\tau\rangle^2}\right\} \quad \Delta\tau \geq 0 \tag{3.39}$$

The mean DGD value $\langle\Delta\tau\rangle$ is commonly termed "fiber PMD" and provided in the fiber specifications. The following expression gives an estimate of the maximum transmission limit $L_{\max}$ due to the PMD effect:

$$L_{\max} = \frac{0.02}{\langle\Delta\tau\rangle^2 \cdot R^2} \tag{3.40}$$

where R is the bit rate. Based on (3.40), $L_{\max}$ for both old fibers and contemporary fibers are obtained as follows:

- $\langle\Delta\tau\rangle$ = 1 ps/km (old fiber vintages): for bit rate of R = 40 Gb/s then the maximum distance $L_{\max}$ = 12.5 km; for B_R = 10 Gb/s then $L_{\max}$ = 200 km.
- $\langle\Delta\tau\rangle$ = 0.1 ps/km (contemporary fiber for modern optical systems): if the bit rate R = 40 Gb/s then the maximum transmission distance is $L_{\max}$ = 1250 km; for R = 10 Gb/s, $L_{\max}$ = 20,000 km.

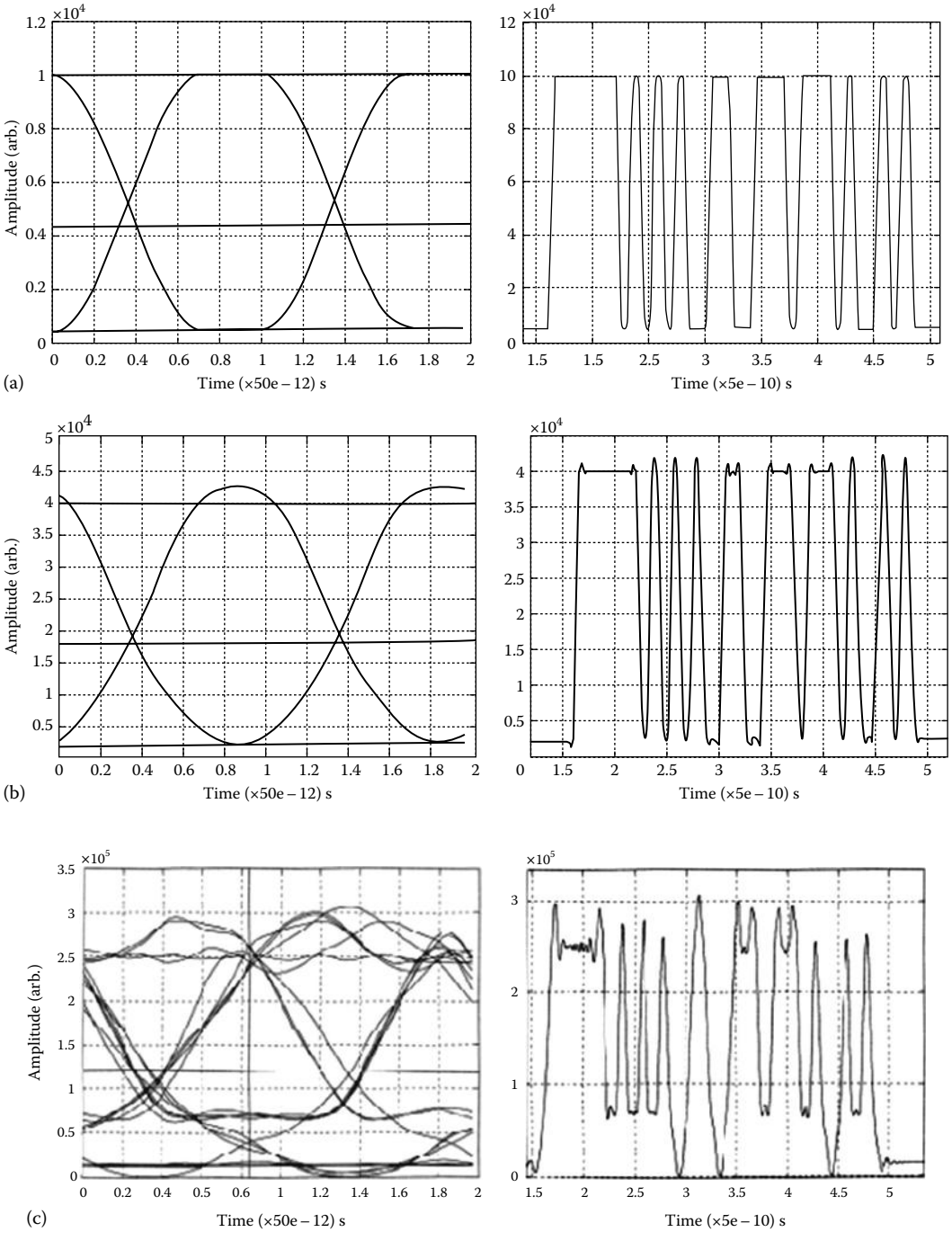

FIGURE 3.14
Eye diagram of time signals at 40 Gb/s transmission over SSMF after (a) 0 km or back-to-back, (b) 20 km, and (c) 80 km SSMF length.

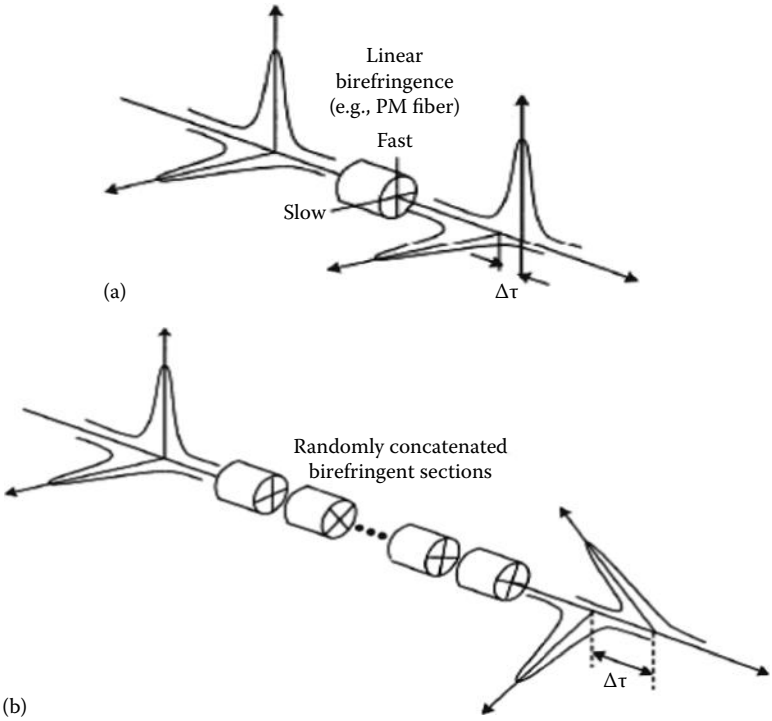

FIGURE 3.15
Conceptual model of PMD: (a) simple birefringence device and (b) randomly concatenated birefringence.

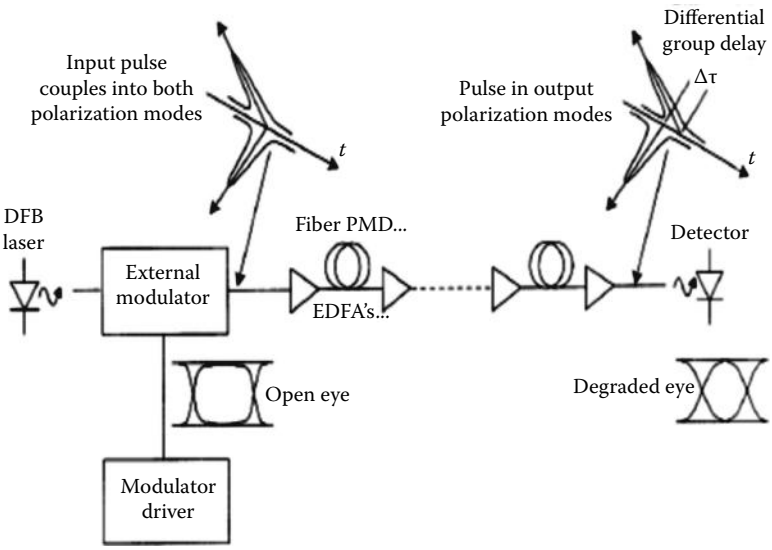

FIGURE 3.16
Effect of PMD in a digital optical communication system, degradation of the received eye diagram.

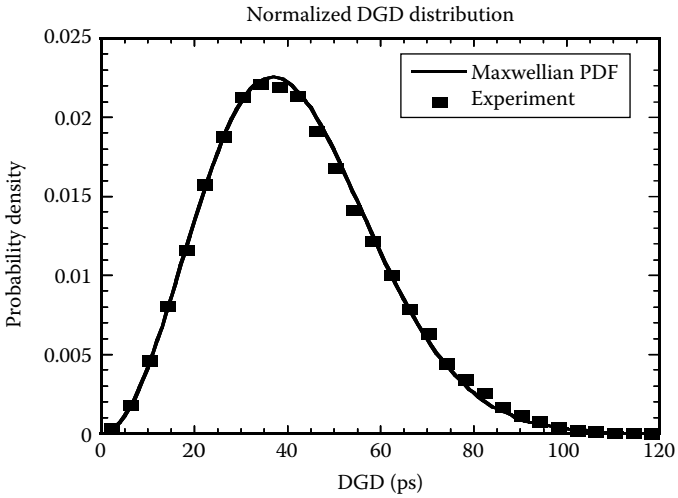

FIGURE 3.17
Maxwellian distribution of PMD random process.

Exercise 3.1

Inspect the technical specifications of Corning fibers given in Annex, extract the values of the PMD. Explain the difference between the values of the fibers. What is the standard value allowable for PMD in modern fibers?

3.4.4 Fiber Nonlinearity

Although the nonlinear effects have been described in Chapter 2, this section strengthens these effects associated with the propagation equation so that the MATLAB® simulation can be clearly identified, especially when the Raman scattering effects or gain coefficients are included. This section thus revisits these effects and their influence on the propagation of optical signals over long lengths of fibers. The nonlinear and linear effects in optical fibers can be classified as shown in Figure 3.18.

Fiber RI is dependent on both operating wavelengths and light wave intensity. This intensity-dependent phenomenon is known as the Kerr effect and is the cause of fiber nonlinear effects. The power dependence of RI is expressed as:

$$n' = n + \bar{n}_2 \left(\frac{P}{A_{eff}} \right) \tag{3.41}$$

where

P is the average optical power of the guided mode
$\bar{n}_2$ is the fiber nonlinear coefficient
A_{eff} is the effective area of the fiber

Fiber nonlinear effects include intrachannel SPM, interchannel XPM, FWM, stimulated Raman scattering (SRS) and stimulated Brillouin scattering (SBS). SRS and SBS are not the main degrading factors as their effects are only getting noticeably large with very high optical power. On the other hand, FWM degrades the performance of an optical system severely with the generation of ghost pulses only if the phases of optical signals are matched with each other. However, with high local dispersions such as in SSMF, effects of

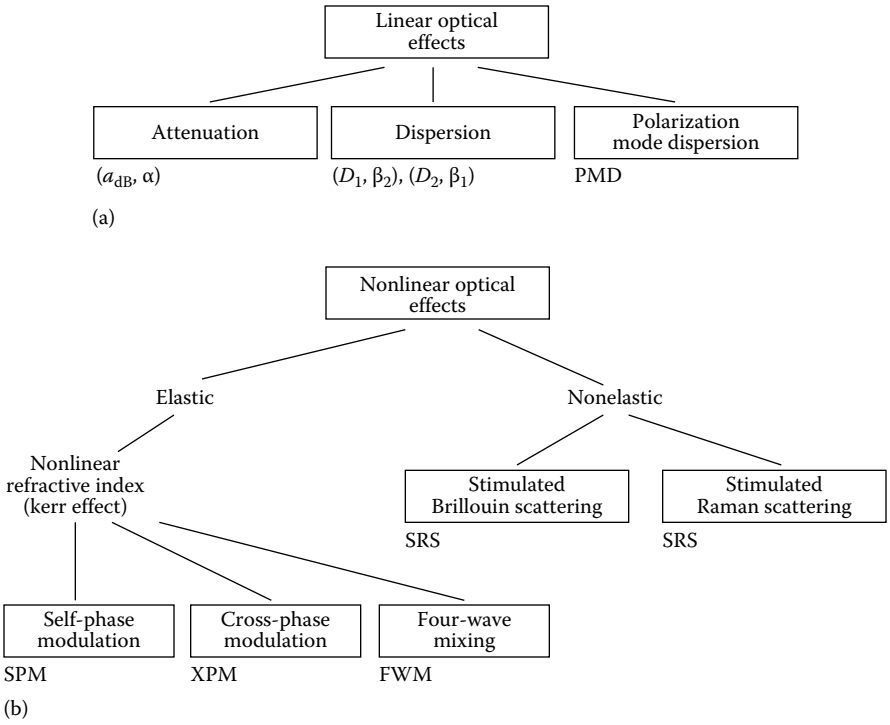

FIGURE 3.18
Linear (a) and nonlinear (b) fiber properties in single-mode optical fibers.

FWM become negligible. In terms of XPM, its effects can be considered to be negligible in a DWDM system in the following scenarios: (1) highly locally dispersive system and (2) large channel spacing. However, XPM should be taken into account for optical transmission systems deploying NZ-DSF fiber where local dispersion values are small. Thus, SPM is usually the dominant nonlinear effect for systems employing transmission fiber with high local dispersions, for example SSMF and DCF. The effect of SPM is normally coupled with the nonlinear phase shift ϕ_{NL} defined as:

$$\begin{aligned} \phi_{NL} &= \int_0^L \gamma P(z)dz = \gamma L_{eff} P \\ \gamma &= \frac{\omega_c \bar{n}_2}{A_{eff} c} \\ L_{eff} &= \frac{1 - e^{-\alpha L}}{\alpha} \end{aligned} \tag{3.42}$$

where

ω_c is the light wave carrier
L_{eff} is the effective transmission length
α is the fiber attenuation factor which normally has a value of 0.17–0.2 dB/km in the 1550 nm spectral window

The temporal variation of the nonlinear phase ϕ_{NL} results in the generation of new spectral components far apart from the light wave carrier ω_c, indicating the broadening of the signal spectrum. This spectral broadening $\delta\omega$ can be obtained from the time dependence of the nonlinear phase shift as follows:

$$\delta\omega = -\frac{\partial\phi_{NL}}{\partial T} = -\gamma\frac{\partial P}{\partial T}L_{eff} \tag{3.43}$$

Equation 3.43 indicates that $\delta\omega$ is proportional to the time derivative of the average signal power P. Additionally, the generation of new spectral components occurs mainly at the rising and falling edges of optical pulses, that is, the number of generated chirps is larger for an increased steepness of the pulse edges.

The wave propagation equation can be represented as

$$\frac{\partial A(z,t)}{\partial z} + \frac{\alpha}{2}A(z,t) + \beta_1\frac{\partial A(z,t)}{\partial t} + \frac{j}{2}\beta_2\frac{\partial^2 A(z,t)}{\partial t^2} - \frac{1}{6}\beta_3\frac{\partial^3 A(z,t)}{\partial t^3}$$
$$= -j\gamma|A(z,t)|^2 A(z,t) - \frac{1}{\omega_0}\frac{\delta}{\delta t}\left(|A|^2 A\right) - T_R A\frac{\delta\left(|A|^2\right)}{\delta t} \tag{3.44}$$

in which we ignore the pure delay factor involving β_1. The last term on the right-hand side (RHS) represents the Raman scattering effects.

Modulation instability: The mutual effect between the nonlinear dispersion effects and the nonlinear effects can lead to the modulation of the light wave pulses and

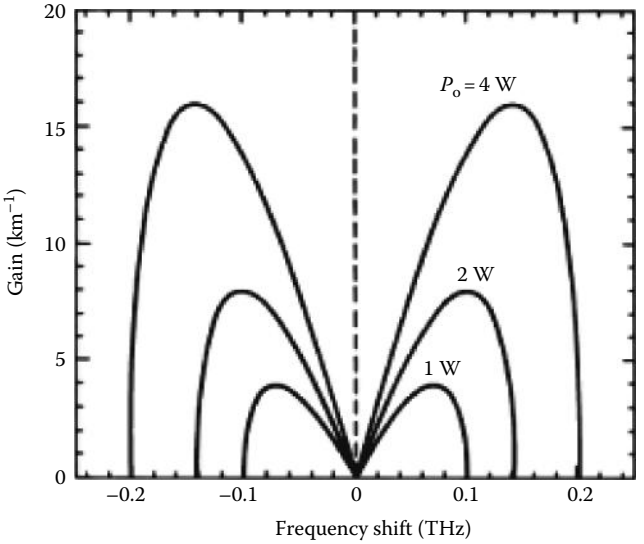

FIGURE 3.19
Spectrum of the optical gain due to modulation instability at three different average power levels in an optical fiber with β_2 = 20 ps^2/km and γ = 2 W/km.

create unstable states of the optical pulses. This phenomenon is usually called the modulation instability, normally observed in soliton lasers.

The gain spectrum of the modulation instability is shown in Figure 3.19 [11].

3.5 Advanced Optical Fibers: Dispersion-Shifted, -Flattened, and -Compensated Optical Fibers

At the beginning of the 1980s, there was great interest in reducing the total dispersion $[M(\lambda) + D(\lambda)]$ of SMFs at 1550 nm where the loss is lowest for silica fiber. There were two significant trends, one to reduce the linewidth and to stabilize the laser center wavelength and the other to reduce the dispersion at this wavelength. The fibers designed for long-haul transmission systems usually exhibit a near zero dispersion at a certain spectral window. These are dispersion-shifted fibers, that is, at this wavelength we prefer to have the total dispersion = $M(\lambda) + D_W(\lambda) \sim 0$. The material dispersion factor $M(\lambda)$ is natural and only slightly affected by variation in the doping material and concentration. However, $D_W(\lambda)$ can be designed, by using the appropriate refractive index profile, to balance/equalize the material dispersion effect. Note that the dispersion factors due to the material and waveguide take algebraic values and thus can be designed to take opposite values to cancel each other.

Advanced optical fiber design technique can offer dispersion flattened fibers where the dispersion factor is flat over the wavelength range from 1300 to 1600 nm by tailoring the refractive index profile of the core of the optical fibers in such distributions as the *W*-profile, the segmented profile, multilayer core structure, and so on.

Exercise 3.2

What is the principal phenomenon for an optical fiber so that the dispersion characteristic is flattened over the wavelength range of 1300–1550 nm?

Another type of optical fiber would be required for compensating the dispersion effect of optical signals after transmission over a length of fiber. This is the dispersion-compensated fiber whose dispersion factor is many times larger than that of the standard communication fiber and has the opposite sign. This can be designed by setting the total dispersion as equal to the required dispersion compensation, and thus, the waveguide dispersion can be found over the required operating range. Optical fiber structures can then be tailored suitably.

3.6 Effects of Mode Hopping

Up to now we have assumed that the emission wavelength from the source center is unaffected by the modulation. In fact when a short current pulse is applied to a semiconductor laser, its central emission wavelength may hop from one mode to its neighbor, a longer wavelength. In the case where a multilongitudinal mode laser is used this hopping effect is negligible; however, it is very significant for a single longitudinal laser.

3.7 Numerical Solution: Split-Step Fourier Method

3.7.1 Symmetrical Split-Step Fourier Method (SSFM)

The evolution of slow varying complex envelopes $A(z,t)$ of optical pulses along a single-mode optical fiber is governed by the nonlinear Schrödinger equation (NLSE) [12]:

$$\frac{\partial A(z,t)}{\partial z}+\frac{\alpha}{2}A(z,t)+\beta_1\frac{\partial A(z,t)}{\partial t}+\frac{j}{2}\beta_2\frac{\partial^2 A(z,t)}{\partial t^2}-\frac{1}{6}\beta_3\frac{\partial^3 A(z,t)}{\partial t^3}=-j\gamma|A(z,t)|^2A(z,t) \tag{3.45}$$

where
- z is the spatial longitudinal coordinate
- α accounts for fiber attenuation
- β_1 indicates DGD
- β_2 and β_3 represent second- and third-order dispersion factors of fiber CD
- γ is the nonlinear coefficient

In a single channel transmission, Equation 3.45 includes the following effects: fiber attenuation, fiber CD and PMD, dispersion slope and SPM nonlinearity. Fluctuation of optical intensity caused by Gordon–Mollenauer effect [13] is also included in this equation.

The NLSE and hence the modeling of pulse propagation along an SMF is solved numerically by using split-step Fourier method (SSFM) [7]. In SSFM, the fiber length is divided into a large number of small segments ∂z. In practice, fiber dispersion and nonlinearity are mutually interactive at any distance along the fiber. However, these mutual effects are small within δz and thus the effects of fiber dispersion and fiber nonlinearity over ∂z are assumed to be statistically independent of each other. As a result, SSFM can separately define two operators: (1) the linear operator that involves fiber attenuation and fiber dispersion effects and (2) the nonlinearity operator that takes into account fiber nonlinearities. These linear and nonlinear operators are formulated as follows:

$$\begin{aligned}\hat{D}&=-\frac{i\beta_2}{2}\frac{\partial^2}{\partial T^2}+\frac{\beta_3}{6}\frac{\partial^3}{\partial T^3}-\frac{\alpha}{2}\\ \hat{N}&=i\gamma\,|A|^2\end{aligned} \tag{3.46}$$

where
- A replaces $A(z, t)$ for simpler notation
- $T = t - z/v_g$ is the reference time frame moving at the group velocity

Equation 3.46 can be rewritten in a shorter form, given by

$$\frac{\partial A}{\partial z}=(\hat{D}+\hat{N})A \tag{3.47}$$

and the complex amplitudes of optical pulses propagating from z to $z + \delta z$ are calculated using the approximation shown here.

$$A(z+h,T)\approx\exp(h\hat{D})\exp(h\hat{N})A(z,T) \tag{3.48}$$

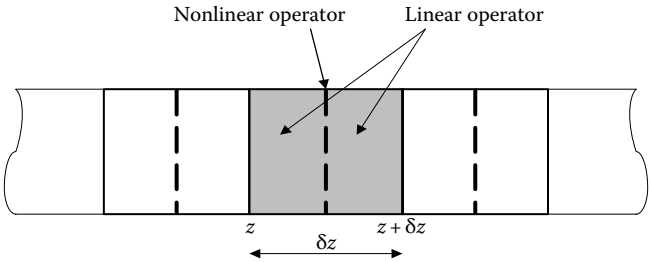

FIGURE 3.20
Schematic illustration of symmetric SSFM.

Equation 3.48 is accurate to the second order of the step size δz [3]. The accuracy of SSFM can be improved by including the effect of fiber nonlinearity in the middle of the segment rather than at the segment boundary (see Figure 3.20). This modified SSFM is known as the symmetric SSFM.

Equation 3.49 can now be modified as:

$$A(z+\partial z,T) \approx \exp\left(\frac{\partial z}{2}\hat{D}\right)\exp\left(\int_{z}^{z+\delta z}\hat{N}(z')dz'\right)\exp\left(\frac{\partial z}{2}\hat{D}\right)A(z,T) \tag{3.49}$$

This method is accurate to the third order of the step size ∂z. In symmetric SSFM, the optical pulse propagates along a fiber segment δz in two stages. First, the optical pulse propagates through the linear operator that has a step size of $\partial z/2$ in which the fiber attenuation and dispersion effects are taken into account. Then, the fiber nonlinearity is calculated in the middle of the segment. After that, the pulse propagates through the second half of the linear operator. The process continues repetitively in consecutive segments of size ∂z until the end of the fiber. It should be highlighted that the linear operator is computed in the frequency domain while the nonlinear operator is calculated in the time domain.

3.7.2 MATLAB® Program and MATLAB® Simulink® Models of the SSFM

A MATLAB® program is given in the following section. This program propagates the optical signals along the optical fiber transmission distance as shown in Figure 3.21. This program must be included in the folder storing the MATLAB Simulink® model. In this folder, an initialization program (Appendix 3.A.5) must be also included to set the data and parameters required for the Simulink model and subroutines. Furthermore, the SSMF including Raman gain amplification effects is given in Appendix 3.A.3.

3.7.2.1 MATLAB® Program

```
function output = ssprop_matlabfunction_modified(input)

nt = input(1);
u0 = input(2:nt+1);
dt = input(nt+2);
dz = input(nt+3);
nz = input(nt+4);
```

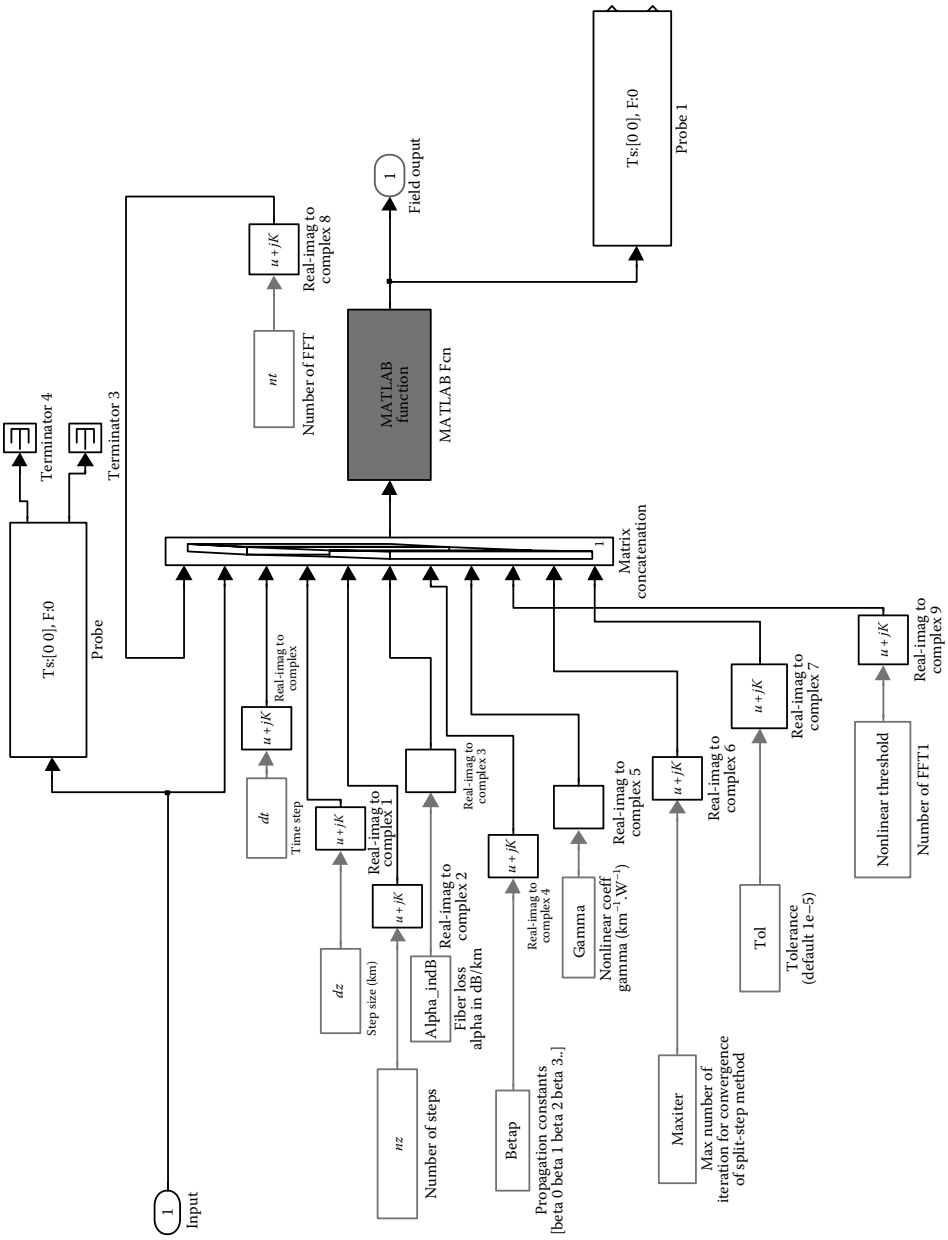

FIGURE 3.21
MATLAB® Simulink® model of the SSMF, MATLAB function includes the MATLAB program, other inputs are data to pass to the MATLAB program SSMF, usually defined in the Initialization file (given in Appendix 3.A.5).

```
alpha_indB = input(nt+5);
betap = input(nt+6:nt+9);
gamma = input(nt+10);
P_non_thres = input(nt+11)
maxiter = input(nt+12);
tol = input(nt+13);
  tic;
%tmp = cputime;
% This section solves the NLSE for pulse propagation in an optical fiber
using the SSF method
% The following effects are included: group velocity dispersion
% (GVD),higher order dispersion, loss, and self-phase modulation (gamma).
%
% USAGE
%
% u1 = ssprop(u0,dt,dz,nz,alpha,betap,gamma);
% u1 = ssprop(u0,dt,dz,nz,alpha,betap,gamma,maxiter);
% u1 = ssprop(u0,dt,dz,nz,alpha,betap,gamma,maxiter,tol);
%
% INPUT
%
% u0 - starting field amplitude (vector)
% dt - time step - [in ps]
% dz - propagation stepsize - [in km]
% nz - number of steps to take, ie, ztotal = dz*nz
% alpha - power loss coefficient [in dB/km], need to convert to linear to
% %have P=P0*exp(-alpha*z)
% betap - dispersion polynomial coefs, [beta_0 ... beta_m] [in ps^(m-1)/km]
% gamma - nonlinearity coefficient [in (km^-1.W^-1)]
% maxiter - max number of iterations (default = 4)
% tol - convergence tolerance (default = 1e-5)
%% OUTPUT
%% u1 - field at the output
%
% Convert alpha_indB to alpha in linear domain
%---------------
alpha = log(10)*alpha_indB/10;    % alpha (1/km)
%---------------

ntt = length(u0);

w = 2*π*[(0:ntt/2-1),(-ntt/2:-1)]'/(dt*nt);
%w = 2*π*[(ntt/2:ntt-1),(1:ntt/2)]'/(dt*ntt);

clear halfstep

halfstep = -alpha/2;
for ii = 0:length(betap)-1;
  halfstep = halfstep - j*betap(ii+1)*(w.^ii)/factorial(ii);
end
```

```
clear LinearOperator
% Linear Operator in Split Step method
LinearOperator = halfstep;
% pause
halfstep = exp(halfstep*dz/2);

u1 = u0;
ufft = fft(u0);

% Nonlinear operator will be added if the peak power is greater than the
% Nonlinear threshold
iz = 0;
while (iz < nz) & (max((abs(u1).^2 + abs(u0).^2)) > P_non_thres)
  iz = iz+1;

  uhalf = ifft(halfstep.*ufft);

  for ii = 1:maxiter,
    uv = uhalf .* exp(-j*gamma*(abs(u1).^2 + abs(u0).^2)*dz/2);
    ufft = halfstep.*fft(uv);
    uv = ifft(ufft);

    %fprintf('You are using SSFM\n');

    if (max(uv-u1)/max(u1) < tol)
      u1 = uv;
      break;
    else
        u1 = uv;
    end
  end
  if (ii == maxiter)
    warning(sprintf('Failed to converge to %f in %d iterations',...
      tol,maxiter));
  end

  u0 = u1;

end

if (iz < nz) & (max((abs(u1).^2 + abs(u0).^2)) < P_non_thres)

%   u1 = u1.*rectwin(ntt);
    ufft == fft(u1);
    ufft = ufft.*exp(LinearOperator*(nz-iz)*dz);
    u1 = ifft(ufft);
%fprintf('Implementing Linear Transfer Function of the Fibre
Propagation');
end

toc;
output = u1;
```

3.7.2.2 MATLAB® Simulink® Model

The MATLAB program (subroutine) is incorporated in the MALAB Simulink model for signal propagation. Under the mask of the block MATLAB Function [ssprop_matlab-function_modified(input)] the MATLAB program subroutine as shown in Figure 3.22 is included.

3.7.3 Modeling of Polarization Mode Dispersion (PMD)

First-order PMD can be implemented by modeling the optical fiber as two separate paths representing the propagation of two PSPs. The symmetrical SSFM can be implemented on each polarized transmission path and then their outputs are superimposed to form the output optical field of the propagated signals. The transfer function to represent the first-order PMD is given by

$$H(f) = H^{+}(f) + H^{-}(f) \tag{3.50}$$

where

$$H^{+}(f) = \sqrt{k}\exp\left[j2\pi f\left(-\frac{\Delta\tau}{2}\right)\right] \tag{3.51}$$

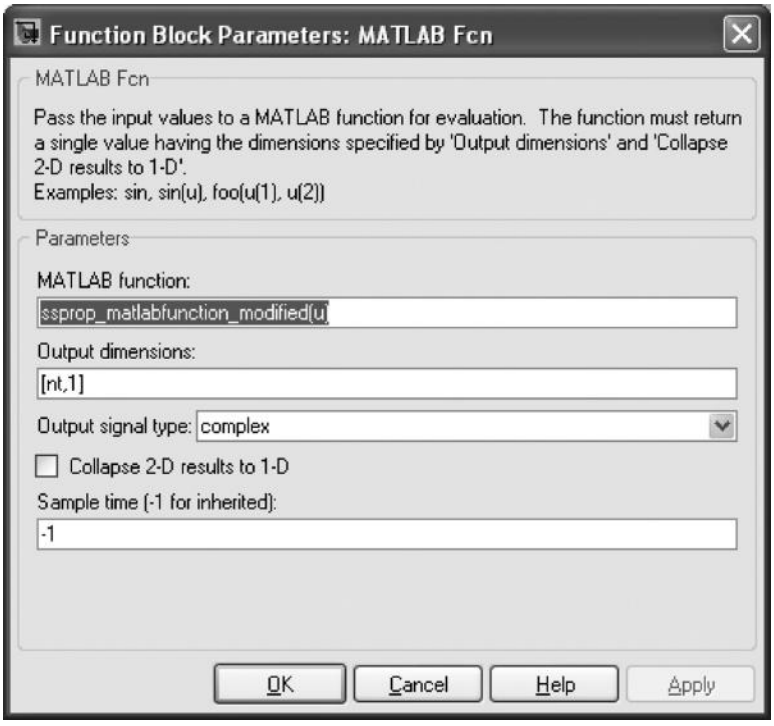

FIGURE 3.22
Screen of MATLAB® Simulink® model under mask of the MATLAB function of the SSMF algorithm.

and

$$H^{-}(f) = \sqrt{k}\exp\left[j2\pi f\left(-\frac{\Delta\tau}{2}\right)\right], \tag{3.52}$$

in which k is the power splitting ratio; $k = 1/2$ when a 3 dB or 50:50 optical coupler/splitter is used, $\Delta\tau$ is the instantaneous DGD value following a Maxwell distribution (refer to Equation 3.39) [14,15].

3.7.4 Optimization of Symmetrical SSFM

3.7.4.1 Optimization of Computational Time

A huge amount of time is spent on symmetric SSFM for FFT and IFFT operations, in particular, when fiber nonlinear effects are involved. In practice, when optical pulses propagate toward the end of a fiber span, the pulse intensity has been greatly attenuated due to the fiber attenuation. As a result, fiber nonlinear effects become negligible for the rest of that fiber span and hence, the transmission operates in a linear domain in this range. In this research, a technique to configure symmetric SSFM is proposed to reduce the computational time. If the peak power of an optical pulse is lower than the nonlinear threshold of the transmission fiber, for example, around −4 dBm, the symmetrical SSFM is switched to a linear mode operation. This linear mode involves only fiber dispersions and fiber attenuation and its low-pass equivalent transfer function for the optical fiber is:

$$H(\varpi) = \exp\left\{-j\left[(1/2)\beta_2\varpi^2 + (1/6)\beta_3\varpi^3\right]\right. \tag{3.53}$$

If β_3 is not considered in this fiber transfer function, which is normally the case due to its negligible effects on 40 Gb/s and lower bit rate transmission systems, the transfer function given earlier has a parabolic phase profile [14,15].

3.7.4.2 Mitigation of Windowing Effect and Waveform Discontinuity

In symmetric SSFM, mathematical operations of FFT and IFFT play very significant roles. However, due to a finite window length required for FFT and IFFT operations, these operations normally introduce overshooting at two boundary regions of the FFT window, commonly known as the windowing effect of FFT. In addition, since the FFT operation is a block-based process, there exists the issue of waveform discontinuity, that is, the right-most sample of the current output block does not start at the same position as the left-most sample of the previous output block. The windowing effect and the waveform discontinuity problems are resolved with the following solutions (see Figure 3.23).

The actual window length for FFT/IFFT operations consists of two blocks of samples ($2N$ sample length). The output, however, is a truncated version with the length of one block (N samples) and output samples are taken in the middle of the two input blocks. The next FFT window overlaps the previous one by one block of N samples.

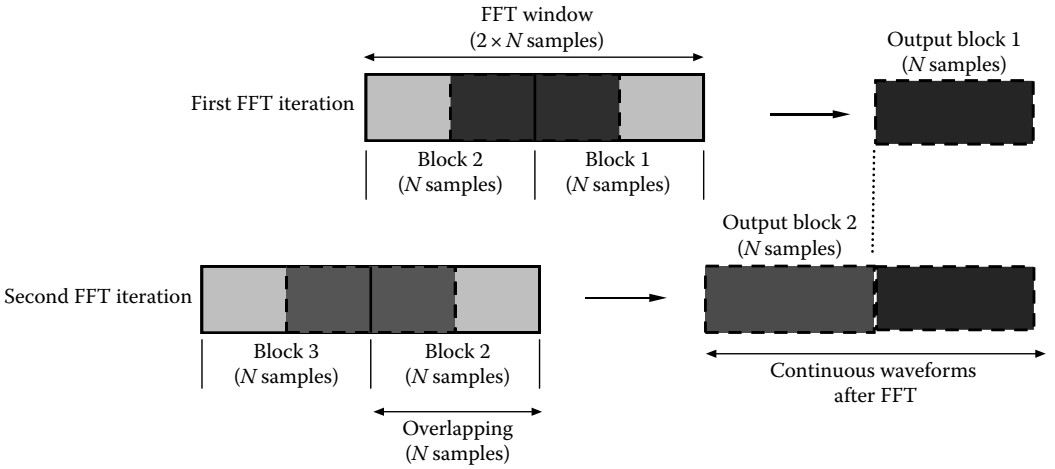

FIGURE 3.23
Proposed solution for mitigating windowing effect and waveform discontinuity caused by FFT/IFFT operations.

3.8 Concluding Remarks

The attenuation and dispersion of optical signals transmitted through silica optical fibers are described. Attenuation can be reduced by using the optical wavelength in the longer wavelength range. For example, for silica fiber the preferred wavelength is at 1.55 μm. However, natural forces are not kind to us and a dispersion factor of about 17 ps/(nm · km) generates pulse broadening for signals transmitted at this wavelength in a circular fiber.

Longer wavelength carriers can be used in the mid-infrared range of about 2.5–5 μm. At this wavelength range, different kinds of glasses must be used such as chalcogenite type or fluoride type. Another technique presently used to compensate for the dispersion effect is to reduce the linewidth of the lasers or use equalizing techniques such as spectrum inversion at the transmitter ends or at the center of the transmission length by optical filtering at the receiving end. Alternatively, the optical fiber can be tailored to achieve dispersion-shifted or -flattened characteristics.

3.A Appendix

3.A.1 Appendix: MATLAB® Program for the Design of Optical Fibers—A Solution to the Mini-Project Design

```
%------------OPTICAL COMMUNICATIONS LABORATORY 1----------------%
% Copyright CRC Press - Le Nguyen Binh
% clear after each run.
```

```
c=2.997925e8;

G1=0.711040;
G2=0.408218;
G3=0.704048;

lambda1=0.064270e-6;
lambda2=0.129408e-6;
lambda3=9.425478e-6;

a=4.1e-6;
delta=0.0025;
start=input('Enter lambda start point (nm) ---: ');
finish=input('Enter lambda end point (nm) -----: ');
resolution=input('Enter lambda resolution (nm) ----: ');
disp('');

lambda=start*1e-9;
lambdavector(1,1)=lambda;

for(i=1:(((finish-start)/resolution)+1))

    n1squared=1+((G1*power(lambda,2))/(power(lambda,2)
-power(lambda1,2)))+((G2*power(lambda,2))/(power(lambda,2)
-power(lambda2,2)))+((G3*power(lambda,2))/(power(lambda,2)
-power(lambda3,2)));
    n1=sqrt(n1squared);
    n1vector(1,i)=n1;

    n2=n1*(1+delta);
    n2vector(1,i)=n2;

    V=(2*π/lambda)*a*n1*sqrt(2*delta);
    Vvector(1,i)=V;

    dy1dx=(-2*G1*power(lambda1,2)*lambda)/(power(power(lambda,2)
-power(lambda1,2),2));
    dy2dx=(-2*G2*power(lambda2,2)*lambda)/(power(power(lambda,2)
-power(lambda2,2),2));
    dy3dx=(-2*G3*power(lambda3,2)*lambda)/(power(power(lambda,2)
-power(lambda3,2),2));

d2y1dx2=(2*G1*power(lambda1,2)*(3*power(lambda,2)+power(lambda1,2)))/
(power(power(lambda,2)-power(lambda1,2),3));

d2y2dx2=(2*G2*power(lambda2,2)*(3*power(lambda,2)+power(lambda2,2)))/
(power(power(lambda,2)-power(lambda2,2),3));

d2y3dx2=(2*G3*power(lambda3,2)*(3*power(lambda,2)+power(lambda3,2)))/
(power(power(lambda,2)-power(lambda3,2),3));

    d2ndx2=0.5*(((d2y1dx2+d2y2dx2+d2y3dx2)*power(n1,2)
-0.5*(power(dy1dx+dy2dx+dy3dx,2)))/power(n1,3));
```

```
    M=(-d2ndx2/c)*lambda;
    Mvector(1,i)=M; %row vector

    Dw=(-n2*delta)/c*(0.080+0.549*power(2.834-V,2))*(1/lambda);
    Dwvector(1,i)=Dw;

    if(i < (((finish-start)/resolution)+1))
        lambdavector(1,i+1)=lambdavector(1,i)+(resolution*1e-9);
        lambda=lambdavector(1,i+1);
    end
end

plot(lambdavector,Mvector,lambdavector,Dwvector,lambdavector,Mvector+
Dwvector);
grid;
%%%%% Copyright 2014 – Le Nguyen Binh CRC Press %%%%%%%%%%%%%%%%%%%%%
```

3.A.2 Appendix: Program Listings for the Design of Standard Single-Mode Fiber

```
% totdisp_SMF.m
%
% MatLab script for calculating of total dispersion for
% Non-Zero Dispersion Shifted Fiber. The script plots
% the material dispersion, the waveguide dispersion, and
% the total dispersion for the designed fiber.
% copyright – Le Nguyen Binh – CRC Press 2014%%%%%%%%%
% Optical Fiber Design
%

lambda = [1.1:0.01:1.700]*1e-6;

G1=0.7028554;            %Sellmeier's coefficients for germanium
G2=0.4146307;            %doped silica (concentration B in table)
G3=0.8974540;
lambda1=0.0727723e-6;    %Wavelengths for germanium doped silica
lambda2=0.1143085e-6;
lambda3=9.896161e-6;

c = 299792458;           %Speed of light
π = 3.1415926;           %Greek letter π
a = 4.1e-6;              %Core radius
delta = 0.003;           %Greek letter delta (ref. index difference
                         %between core and cladding)
% Calculating the refractive index
% -----------------------------------

npow2oflambda = 1 + (G1.*lambda.^2./(lambda.^2.-lambda1*lambda1)) ...
   + (G2.*lambda.^2./(lambda.^2.-lambda2*lambda2)) ...
   + (G3.*lambda.^2./(lambda.^2.-lambda3*lambda3));

noflambda=sqrt(npow2oflambda);

pointer=find(lambda==1.550e-6);
```

```
n1=noflambda(pointer)      %Refractive index in the core

% Calculating the material dispersion
% -----------------------------------

t1 = diff(noflambda);
t2 = diff(lambda);
t3 = t1./t2;

t4 = diff(t3);
t5 = diff(lambda);
t5 = adjmat(t5);

lambda=adjmat(lambda);
lambda=adjmat(lambda);

%Material dispersion
Matdisp = - (lambda./c) .* (t4./t5);

% Converting to ps/nm.km
Matdisp = Matdisp.*1e6;
figure(1)
clf
hold

xlabel('nm')
ylabel('ps/nm.km')
title('Standard Single Mode Fiber')
plot(lambda, Matdisp, '.-')
grid on

% Calculating waveguide dispersion
% --------------------------------

V = (2 * π * a * n1 * sqrt(2 * delta)) ./(lambda);

Dlambda1 = - (n1 * delta)./(c * lambda);
%plot(lambda,Dlambda2)

Dlambda2 = 0.080 + 0.549 * (2.834 - V).^2;
%plot(lambda,Dlambda2)

Dlambda = Dlambda1 .* Dlambda2;

% Converting to ps/nm.km
Dlambda = Dlambda.*1e6;
plot(lambda,Dlambda, '-')

% Calculating total dispersion
% --------------------------------

TotDisp = Matdisp + Dlambda;
plot(lambda, TotDisp, ':')
```

```
legend('Material Dispersion', 'Waveguide Dispersion', 'Total Dispersion', 0)

% Finding the dispersion at 1460, 1550 and 1625 nm
% -------------------------------------------------

pointer=find(lambda==1.460e-6);
Disp1460=TotDisp(pointer)
pointer=find(lambda==1.550e-6);
Disp1550=TotDisp(pointer)
pointer=find(lambda==1.6250e-6);
Disp1625=TotDisp(pointer)
% refind_SMF.m
%
% MatLab script for calculating of possible values for
% refractive index in the core, n1, and cladding, n2,
% its corresponding relative refractive index.
%
% PROJECT DESIGN: Optical Fiber Design
%
lambda = [1.1:0.01:1.700]*1e-6;

n1 = [1.0487:0.001:1.8587];             %Refractive index of the core
n2 = [1.0435:0.001:1.8535];             %Refractive index of the cladding

% Calculating the refractive index for the index profile
% ------------------------------------------------------
delta = (n1 - n2) ./ n1;
deltap = delta * 100;


plot(n1, deltap)
grid on

xlabel('n1')
ylabel('Delta - Relative Refractive Index(%)')
title('Refractive Index')

%%% Copyright Le Nguyen Binh - CRC Press 2014 %%%%%%%%%
```

3.A.3 Appendix: Program Listings for Design of Nonzero Dispersion-Shifted Fibers

```
% totdisp_NZDSF.m
%
% MatLab script for calculating of total dispersion for
% Non-Zero Dispersion Shifted Fiber. The script plots
% the material dispersion, the waveguide dispersion and
% the total dispersion of the designed fiber.
%
% PROJECT 1: Optical Fiber Design
%

lambda = [1.1:0.001:1.700]*1e-6;
```

```
G1=0.7028554;    % Sellmeier's coefficients for germanium
G2=0.4146307;    % doped silica (concentration B in table)
G3=0.8974540;

lambda1=0.0727723e-6;    %Wavelengths for germanium doped silica
lambda2=0.1143085e-6;
lambda3=9.896161e-6;

c = 299792458;   %Speed of light
π = 3.1415926;   %Greek letter π
a = 2.4e-6;      %Core radius
delta = 0.0043;  %Greek letter delta (ref. index difference
                 %between core and cladding)

% Calculating the refractive index
% ----------------------------------

npow2oflambda = 1 + (G1.*lambda.^2./(lambda.^2.-lambda1*lambda1)) ...
   + (G2.*lambda.^2./(lambda.^2.-lambda2*lambda2)) ...
   + (G3.*lambda.^2./(lambda.^2.-lambda3*lambda3));

noflambda=sqrt(npow2oflambda);

pointer=find(lambda==1.550e-6);
n1=noflambda(pointer)                    %Refractive index in the core
@1550nm

% Calculating the material dispersion
% ----------------------------------

t1 = diff(noflambda);
t2 = diff(lambda);
t3 = t1./t2;

t4 = diff(t3);
t5 = diff(lambda);
t5 = adjmat(t5);

lambda=adjmat(lambda);
lambda=adjmat(lambda);

%Material dispersion
Matdisp = - (lambda./c) .* (t4./t5);

% Converting to ps/nm.km
Matdisp = Matdisp.*1e6;
figure(1)
clf
hold

xlabel('nm')
ylabel('ps/nm.km')
title('Non-Zero Dispersion Shifted Fiber')
```

```
plot(lambda, Matdisp, '.')
grid on

% Calculating waveguide dispersion
% ---------------------------------

V = (2*π*a*n1*sqrt(2*delta))./(lambda);

pointer=find(lambda==1.550e-6);
V1550=V(pointer)

Dlambda1 = - (n1 * delta)./(c * lambda);
Dlambda2 = 0.080 + 0.549 * (2.834 - V).^2;
Dlambda = Dlambda1 .* Dlambda2;

% Converting to ps/nm.km
Dlambda = Dlambda.*1e6;
plot(lambda,Dlambda, '-')

% Calculating total dispersion
% ---------------------------------

TotDisp = Matdisp + Dlambda;
plot(lambda, TotDisp, '+')

legend('Material Dispersion', 'Waveguide Dispersion', 'Total Dispersion', 0)

% Finding the dispersion at 1460, 1550 and 1625 nm
% ------------------------------------------------

pointer=find(lambda==1.460e-6);
Disp1460=TotDisp(pointer)

pointer=find(lambda==1.550e-6);
Disp1550=TotDisp(pointer)

pointer=find(lambda==1.6250e-6);
Disp1625=TotDisp(pointer)

%%%%%%%%%%%%%%END%%%%%%%%%%%%%%%%%%%%%%%%%%%%%%%%%%%%%%%%%%%%
% Copyright: Le Nguyen Binh -CRC Press %%%%%%%%%%%%%%%%%%%%%%
% refine_NZDSF.m
%
% MatLab script for calculating of possible values for
% refractive index in the core, n1, and cladding, n2,
% its corresponding relative refractive index.
%

lambda = [1.1:0.01:1.700]*1e-6;

n1 = [1.0487:0.001:1.8587];             %Refractive index of the core
n2 = [1.0324:0.001:1.8424];             %Refractive index of the cladding
```

```
% Calculating the refractive index for the index profile
% -------------------------------------------------------

delta = (n1 - n2) ./ n1;
deltap = delta * 100;

plot(n1, deltap)
grid on

xlabel('n1')
ylabel('Delta - Relative Refractive Index(%)')
title('Refractive Index')
```

3.A.4 Appendix: Program Listings of the Split Step Fourier Method with SPM and Raman Gain Distribution

```
function output = ssprop_matlabfunction_raman(input)

nt = input(1);
u0 = input(2:nt+1);
dt = input(nt+2);
dz = input(nt+3);
nz = input(nt+4);
alpha_indB = input(nt+5);
betap = input(nt+6:nt+9);
gamma = input(nt+10);
P_non_thres = input(nt+11);
maxiter = input(nt+12);
tol = input(nt+13);
%Ld = input(nt+14);
%Aeff = input(nt+15);
%Leff = input(nt+16);

tic;
%tmp = cputime;

%-------------------------------------------------------------
%
%-------------------------------------------------------------
% This function solves the nonlinear Schrodinger equation for
% pulse propagation in an optical fiber using the split-step
% Fourier method described in:
%
% The following effects are included in the model: group velocity
% dispersion (GVD), higher order dispersion, loss, and self-phase
% modulation (gamma). Raman gain as a distributed amplification
%
% USAGE
%
% u1 = ssprop(u0,dt,dz,nz,alpha,betap,gamma);
% u1 = ssprop(u0,dt,dz,nz,alpha,betap,gamma,maxiter);
% u1 = ssprop(u0,dt,dz,nz,alpha,betap,gamma,maxiter,tol);
%
```

```
% INPUT
%
% u0 - starting field amplitude (vector)
% dt - time step - [in ps]
% dz - propagation stepsize - [in km]
% nz - number of steps to take, ie, ztotal = dz*nz
% alpha - power loss coefficient [in dB/km], need to convert to linear to
have P=P0*exp(-alpha*z)
% betap - dispersion polynomial coefs, [beta_0 ... beta_m] [in ps^(m-1)/km]
% gamma - nonlinearity coefficient [in (km^-1.W^-1)]
% maxiter - max number of iterations (default = 4)
% tol - convergence tolerance (default = 1e-5)
%
% OUTPUT
%
% u1 - field at the output
%---------------
% Convert alpha_indB to alpha in linear domain
%---------------
alpha = 1e-3*log(10)*alpha_indB/10;
% alpha (1/km) - see Agrawal p57
%---------------
%P_non_thres = 0.0000005;

ntt = length(u0);
w = 2*π*[(0:ntt/2-1),(-ntt/2:-1)]'/(dt*nt);
%t = ((1:nt)'-(nt+1)/2)*dt;

gain = numerical_gain_hybrid(dz,nz);

for array_counter = 2:nz+1
    grad_gain(1) = gain(1)/dz;
    grad_gain(array_counter) = (gain(array_counter)-gain(array_
counter-1))/dz;
end
gain_lin = log(10)*grad_gain/(10*2);

clear halfstep
 halfstep = -alpha/2;
    for ii = 0:length(betap)-1;
        halfstep = halfstep - j*betap(ii+1)*(w.^ii)/factorial(ii);
    end

       square_mat = repmat(halfstep, 1, nz+1);
       square_mat2 = repmat(gain_lin, ntt, 1);
       size(square_mat);
       size(square_mat2);
       total = square_mat + square_mat2;

clear LinearOperator
    % Linear Operator in Split Step method
    LinearOperator = halfstep;
    halfstep = exp(total*dz/2);
```

```
u1 = u0;
ufft = fft(u0);

% Nonlinear operator will be added if the peak power is greater than the
% Nonlinear threshold
iz = 0;
while (iz < nz) && (max((gamma*abs(u1).^2 + gamma*abs(u0).^2)) > P_non_
thres)
  iz = iz+1;

  uhalf = ifft(halfstep(:,iz).*ufft);

  for ii = 1:maxiter,
     uv = uhalf .* exp((-j*(gamma)*abs(u1).^2 +
     (gamma)*abs(u0).^2)*dz/2);
     ufft = halfstep(:,iz).*fft(uv);
     uv = ifft(ufft);

     if (max(uv-u1)/max(u1) < tol)
        u1 = uv;
        break;
     else
        u1 = uv;
     end

  end
% fprintf('You are using SSFM\n');
  if (ii == maxiter)

  fprintf('Failed to converge to %f in %d iterations',tol,maxiter);
  end

  u0 = u1;

end

if (iz < nz) && (max((gamma*abs(u1).^2 + gamma*abs(u0).^2)) < P_non_
thres)

% u1 = u1.*rectwin(ntt);
  ufft = fft(u1);
  ufft = ufft.*exp(LinearOperator*(nz-iz)*dz);
  u1 = ifft(ufft);

  %fprintf('Implementing Linear Transfer Function of the Fiber
propagation');
end

%toc;

output = u1;

%%% Copyright le Nguyen Binh CRC Press 2014%%%%%%%%%%%%%%
```

3.A.5 Appendix: Program Listings of Initialization File

```
% This file initialization file – declaring all parameters and data
% required for Simulink model and Split Step Fourier Method (SSFM)

clear all
close all

% CONSTANTS
c = 299792458;                          % speed of light (m/s)
% NUMERICAL PARAMETERS

numbitspersymbol = 1
P0 = 0.003;                             % peak power (W)
FWHM = 25                               % pulse width FWHM (ps)
%halfwidth = FWHM/1.6651                % for Gaussian pulse
halfwidth = FWHM                        % for square pulse

bitrate = 1/halfwidth;                  % THz
baudrate = bitrate/numbitspersymbol;
signalbandwidth = baudrate;

%%%%%%%%%%%%%%%%%%%%%%%%%%%%%%%
% for DPSK
Vπ = 5;
halfVπ = Vπ/2;
twoVπ = Vπ*2;

% nt = 2^8;                             % number of points in FFT
PRBSlength = 2^5;

% Make sure : FFT time window (=nt*dt) = PRBSlength * FWHM...
% FFTlength nt = PRBSlength/block * numbersamples/bit = PRBSlength *
(FWHM/dt)
% num_samplesperbit = FWHM/dt           should be about 8 - 16 samples/bit
num_samplesperbit = 32; % should be 2^n
dt = FWHM/num_samplesperbit ;           % sampling time(ps); % time step (ps)
nt = PRBSlength*num_samplesperbit;      % FFT length

% nt = 2^9;
% nt =num_samplesperbit;

dz = 0.2;                               % distance stepsize (km)
nz = 500;

%melbourne to gippsland
%170km two spans
nz_MelbToGipps = 500;

%undersea link
%290km
nz_Raman = 250;
```

```
nz_undersea = 950;
nz_DCF = 145;

%George Town to Hobart
nz_GtownToHobart = 500;

% number of z-steps
maxiter = 10;                          % max # of iterations
tol = 1e-5;                            % error tolerance

% OPTICAL PARAMETERS

nonlinearthreshold = 0.010; % 10mW -- % Nonlinear Threshold Peak Power

lambda = 1550;                         % wavelength (nm)
optical_carrier = c/(lambda*1e-9);
%dBperkm = 0.2;                        % loss (dB/km)
alpha_indB = 0.17;                     % loss (dB/km)
D = 18.5;                              % GVD (ps/nm.km); if anomalous
dispersion(for compensation),D is negative
beta3 = 0.06;                          % GVD slope (ps^3/km)

ng = 1.46;                             % group index
n2 = 2.6e-20;                          % nonlinear index (m^2/W)
Aeff = 76;                             % effective area (um^2)

% CALCULATED QUANTITIES

T = nt*dt;                             % FFT window size (ps) -Agrawal:
should be about 10-20 times of the pulse width
alpha_loss = log(10)*alpha_indB/10;  % alpha (1/km)
beta2 = -1000*D*lambda^2/(2*π*c);    % beta2 (ps^2/km);

%-----------------------------------------------------
% beta 3 can be calculated from the Slope Dispersion (S) as follows:]
% Slope Dispersion
% S = 0.092;                           % ps/(nm^2.km)
% beta31 = (S - (4*π*c./lambda.^3))./(2*π*c./lambda.^2)
%-----------------------------------------------------
gamma = 2e24*π*n2/(lambda*Aeff);     % nonlinearity coef (km^-1.W^-1)
t = ((1:nt)'-(nt+1)/2)*dt;           % vector of t values (ps)
t1 = [(-nt/2+1:0)]'*dt;              % vector of t values (ps)
t2 = [(1:nt/2)]'*dt;                 % vector of t values (ps)

w = 2*π*[(0:nt/2-1),(-nt/2:-1)]'/T;  % vector of w values (rad/ps)
v = 1000*[(0:nt/2-1),(-nt/2:-1)]'/T;% vector of v values (GHz)
vs = fftshift(v);                    % swap halves for plotting
v_tmp = 1000*[(-nt/2:nt/2-1)]'/T;

% STARTING FIELD

% P0 = 0.001                           % peak power (W)
% FWHM = 20                            % pulse width FWHM (ps)
```

```
%halfwidth = FWHM/1.6651            % for Gaussian pulse

%For square wave input, the FWHM = Half Width
%halfwidth = FWHM;

L = nz*dz

Lnl = 1/(P0*gamma)                  % nonlinear length (km)
Ld = halfwidth^2/abs(beta2)         % dispersion length (km)
N = sqrt(abs(Ld./Lnl))              % governing the which one is
dominating: dispersion or Non-linearities
ratio_LandLd = L/Ld                 % if L << Ld --> NO Dispersion Effect
ratio_LandLnl = L/Lnl               % if L << Lnl --> NO Nonlinear Effect

% Monitor the broadening of the pulse with relative the Dispersion Length
% Calculate the expected pulsewidth of the output pulse
% Eq 3.2.10 in Agrawal "Nonlinear Fiber Optics" 2001 pp67
FWHM_new = FWHM*sqrt(1 + (L/Ld)^2)

% N<<1 --> GVD ; N >>1 ---> SPM

Leff = (1 - exp(-alpha_loss*L))/alpha_loss
expected_normPout = exp(-alpha_loss*2*L)
NlnPhaseshiftmax = gamma*P0*Leff

betap = [0 0 beta2 beta3]';

% Constants for ASE of EDFA
% PSD of ASE: N(at carrier freq) = 2*h*fc*nsp*(G-1) with nsp = Noise
% Figure/2 (assume saturated gain)
%***************** Standdard Constant ********************************
h = 6.626068e-34;       %Plank's Constant
%*****************************************
% Copyright Le Nguyen Binh CRC Press 2014%%%%%
```

Problems

3.1 What are the wavelength ranges of infrared light, ultraviolet light, and far-infrared light? What are the approximate wavelengths of the colors in the color band of resistors? Are they corresponding to the colors of the rainbow?

3.2 A GeO_2-doped silica-based optical fiber has the following parameters: (i) step-index profile, (ii) refractive index difference at the core of 0.5%, and (iii) core diameter of 9.0 μm

(a) Calculate the refractive index of the fiber core and cladding at 1.310 and 1.55 μm wavelengths

(b) What is the estimated loss of this fiber at the wavelengths mentioned?

(c) What are the V parameters of the fiber at these wavelengths?

(d) What are the material dispersion and waveguide dispersion factors at these wavelengths? Hence, what is the total dispersion factor?

(e) This fiber is to be used in optical systems of bit rates of 2.2 Gb/s. What is the maximum fiber length that the signal can be transmitted through without suffering the allowable signal degradation?

3.3 (a) Give a brief account of the pros and cons for optical fiber communication systems operating at 810, 1300, and 1550 nm wavelength regions.

(b) Why does silica optical fiber suffer losses at 1400 nm wavelength region?

(c) What are the typical optical fiber losses at the above wavelength regions? And hence, give typical cable losses.

3.4 (a) Show that the material dispersion factor is zero at the wavelength given by

$$\lambda^4 = -\frac{3c_3}{c_2}$$

(b) The coefficients c_1, c_2, and c_3 for pure and GeO_2-doped silica fiber are:

Coefficients c's	Pure Silica	7.9% GeO_2-Doped Silica
c_1	1.45084	1.46286
c_2 in μm^{-2}	−0.00334	−0.00331
c_3 in μm^2	0.00292	0.00320

Find the zero dispersion wavelengths due to the material of these fibers.

(c) Derive an expression for the group delay per km unit length. Plot this group delay versus wavelength for part (b).

(d) Hence, find the transit time difference of light waves propagating through the fiber emitted by light sources centered at 810 and 1550 nm with a linewidth of 10 nm.

3.5A Using the approximate expression for the normalized propagation constant b as a function of V, derive the group velocity delay due to the waveguide and hence, the dispersion factor due to the waveguide as a function of V.

3.5B Using the data of the SMF manufactured by Corning, calculate

(a) The material dispersion factor

(b) The waveguide dispersion factor

at 1330 and 1550 nm.

3.6 Design a dispersion-shifted SMF at 1550 nm. Each group of 3–4 students is requested to select a particular group of doped material with different Sellmeiere's coefficients for the design.

3.7 Mini-Project: Design of Single-Mode Optical Fibers

Project Objectives

Design

The main aim is to design the geometrical and index profiles of silica optical fibers to meet certain dispersion criteria as required. Furthermore, the performance of a set of fibers with dispersion as the main factor must be investigated as a function of the fiber core radius and the relative refractive index difference.

System Applications

Your designed fiber must be incorporated with a dispersion-compensated fiber. In this case, use the SSMF, whose specifications have been given in the lectures. If the total length of the transmission is 10,000 km specify the length of your designed fiber and the SMF so that the average fiber dispersion is 0.01 ps/nm·km. It can be assumed that the spacing of optical amplifiers is 100 km.

Design Specifications

A number of types of SMFs are required to be designed for optical communication systems in long- and short-haul transmission. Table 3.2 shows the characteristics of the required fibers. Tables 3.3 and 3.4 give Sellmeier's coefficients of different materials and doping concentrations so that different refractive indices can be achieved.

TABLE 3.2

Index Distribution Profile and Requirements for Dispersion of the Fibers To Be Designed

		Material-Type Core		Other Requirements
Fib. No.	**Optical Fibers Profile**	**See Tables below for Sellmeier's Constants**	**Systems Requirement**	**Maximum Dispersion in the Wavelength Range 1510–1590 nm in ps/(nm·km)**
1	Triangular	A–J	Dispersion-shifted wavelength at 1550 nm	<1.5
2	Parabolic	A–J	Dispersion-shifted wavelength at 1520 nm	<1.5
3	Triangular	A–J	Dispersion-shifted wavelength at 1560 nm	<2
4	Parabolic	A–J	Dispersion-shifted wavelength at 1530 nm	<3
5	Triangular	A–J	Dispersion-compensated wavelength at 1550 nm	>0.5
6	Parabolic	A–J	Dispersion-compensated wavelength at 1540 nm	>1.0
9	Triple-clad	A–J	Dispersion-flattened over 1500–1590 nm	Not more than 0.2 ps/(nm·km)
10	Triangular in core and segmented in cladding	A–J	Dispersion-flattened over 1500–1590 nm	Not more than 0.2 ps/(nm·km)

TABLE 3.3

Sellmeier's Coefficients for Several Optical Fiber Silica-Based Materials with Germanium Doped in the Core Region Wavelength in μm and G_k in μm^{-2}

Sellmeier Constants	Germanium Concentration, *C* %mol			
	A	**B**	**C**	**D**
Types	**0**	**3.1%**	**5.8%**	**7.9%**
G_1	0.6961663	0.7028554	0.7088876	0.7136824
G_2	0.4079426	0.4146307	0.4206803	0.4254807
G_3	0.8974794	0.8974540	0.8956551	0.8964226
λ_1	0.6840432	0.0727723	0.0609053	0.0617167
λ_2	0.1162414	0.1143085	0.1254514	0.1270814
λ_3	9.896161	9.896161	9.896162	9.896161

Source: Kobayashi et al. 1978.

TABLE 3.4

Sellmeier's Coefficients for Several Optical Fiber Silica-Based Materials with Germanium Doped in the Core Region Wavelength in μm and G_k in μm^{-2}

Sellmeier Constants	Concentration Composition			
	E	**F**	**G**	**H**
Types	**Quenched SiO_2**	**13.5 GeO_2:86.5 SiO_2**	**9.1 P_2O_5:90.0 SiO_2**	**13.3 B_2O_3:86.7SiO_2**
G_1	0.696750	0.711040	0.695790	0.690618
G_2	0.408218	0.408218	0.452497	0.401996
G_3	0.890815	0.704048	0.712513	0.898817
λ_1	0.069066	0.064270	0.061568	0.061900
λ_2	0.115662	0.129408	0.119921	0.123662
λ_3	9.900559	9.425478	8.656641	9.098960
	I	**J**	**K**	**L**
	1.0 F:99.0 SiO_2	**16.2 Na_2O:32.5 B_2O_3: 50.6 SiO_2**		
G_1	0.691116	0.796468		
G_2	0.399166	0.497614		
G_3	0.890423	0.358924		
λ_1	0.068227	0.094359		
λ_2	0.116460	0.093386		
λ_3	9.993707	5.999652		

Source: Fleming, J.W., *Elect. Lett.*, 14, 326, 1978.

Mini-Project: Design of Optical Fibers

Practical limits for the fiber core radius and relative index difference must be taken into account. A set of curves must be obtained with the core radius or the relative index difference as a parameter. Make sure that the material dispersion factors are correctly modeled.

Software Environment

The preferred package is MATLAB or MATLAB 7.0 and above for Windows.

Assessment of Design Assignments

A major design assignment on optical fibers for communications systems is counted for 10% of the total marks allocated for the optical systems part. Twenty percent would be awarded to design groups selecting index profile types 9 or 10.

The design assignment is specified for a different group of students. The maximum number of members of each group is two. Higher number of members in a group can only be accepted in exceptional circumstances and in this case the complexity of the design assignment will be increased accordingly.

References

1. W.D. Jones, *Optical Fiber Communications Systems*, Holt, Rinhart Winston, New York, 1988.
2. A.P. Agrawal, *Fiber Optic communications Systems*, 2nd ed., Academic Press, New York, 1997.
3. J.B. Jeunhomme, *Single Mode Fiber Optics*, Marcel Dekker, New York, 1983.
4. S. Randel, R. Ryf, A. Sierra, P.J. Winzer, A.H. Gnauck, C.A. Bolle, R.-J. Essiambre, D.W. Peckham, A. McCurdy, and R. Lingle, Jr., 6 × 56-Gb/s mode-division multiplexed transmission over 33-km few-mode fiber enabled by 6 × 6 MIMO equalization, *Optics Express*, 19(17), 16697–16707, 2011.
5. J.P. Gordon and H. Kogelnik, PMD fundamentals: Polarization mode dispersion in optical fibers, *PNAS*, 97(9), 4541–4550, April 2000.
6. Corning Inc., An introduction to the fundamentals of PMD in fibers, White Paper, July 2006.
7. A. Galtarossa and L. Palmieri, Relationship between pulse broadening due to polarisation mode dispersion and differential group delay in long singlemode fiber, *Electronics Letters*, 34(5), 492, March 1998.
8. J.M. Fini and H.A. Haus, Accumulation of polarization-mode dispersion in cascades of compensated optical fibers, *IEEE Photonics Technology Letters*, 13(2), 124–126, February 2001.
9. A. Carena, V. Curri, R. Gaudino, P. Poggiolini, and S. Benedetto, A time-domain optical transmission system simulation package accounting for nonlinear and polarization-related effects in fiber, *IEEE Journal on Selected Areas in Communications*, 15(4), 751–765, 1997.
10. S.A. Jacobs, J.J. Refi, and R.E. Fangmann, Statistical estimation of PMD coefficients for system design, *Electronics Letters*, 33(7), 619–621, March 1997.
11. G.P. Agrawal, *Nonlinear Fiber Optics*, 3rd ed., Academic Press, San Diego, CA, 2001.
12. A.P. Agrawal, *Fiber Optic communications Systems*, Academic Press, 2nd ed., New York, 1997. *Note*: The first edition of this book included the detailed process of the SSFM—published in 1983.
13. J.P. Gordon and L.F. Mollenauer, Phase noise in photonic communications systems using linear amplifiers, *Optics Letters*, 15(23), 1351–1353, 1990.
14. A.F. Elrefaie and R.E. Wagner, Chromatic dispersion limitations for FSK and DPSK systems with direct detection receivers, *IEEE Photonics Technology Letters*, 3(1), 71–73, 1991.
15. A.F. Elrefaie, R.E. Wagner, D.A. Atlas, and A.D. Daut, Chromatic dispersion limitation in coherent lightwave systems, *IEEE Journal of Lightwave Technology*, 6(5), 704–710, 1988.
16. J.W. Fleming, Low-loss single-mode fibers prepared by plasma-enhanced MCVD, *Electronics Letters*, 14, 326–328, 1978.

4

Overview of Modeling Techniques for Optical Transmission Systems Using MATLAB® Simulink®

This chapter outlines general aspects for modeling techniques for optical transmission systems using two principal MATLAB® platforms: the Simulink® and m-files. MATLAB Simulink is based on subsystem modules and the parameters are passed onto the submodules via an initiation m-file, while m-file platform set ups are based on three layers and graphic units. Generic models are described from the transmitters to receivers and signal processing to evaluate the transmission performances.

4.1 Overview

A digital photonic transmission system can be divided into three main subsystems: optical transmitter, optical fiber channel, and optical receiver, as shown in Figure 4.1.

The first key subsystem is the optical transmitter. The main function of an optical transmitter is to generate light waves carrying a particular modulation format. Modulation formats are classified into three groups depending on whether the amplitude, phase, or frequency component of the light wave carrier is modulated. In modern photonic communications, the modulation process is implemented by using external optical modulators that can be categorized into phase and intensity modulators. Advantages of the external data modulation over the direct data modulation on semiconductor lasers and operational descriptions of external optical modulators are presented in the next section.

The second subsystem is the optical fiber channel. Classification of optical fibers is based on their dispersion characteristics and some notable types are standard single-mode fiber (SSMF), commonly known as ITU-G.652 type and nonzero dispersion-shifted fiber (NZDSF), ITU—G.655 type. SSMF has a chromatic dispersion (CD) factor of about ±17 ps/(nm·km) at 1550 nm wavelengh compared to small values of ±(2–6) ps/(nm·km) for NZDSF. The dispersion induced by these optical transmission fibers is compensated by the dispersion compensating fiber (DCF) that has negative CD factors. In addition, recent progress in fiber design has also introduced several new types of fibers such as dispersion-flattened fibers (DFF) and Corning Vascade fibers [1,2].

Optical fibers consist of several impairments that cause severe degradations to the system performance. These impairments are grouped into fiber dispersions and fiber nonlinearities. The fiber dispersion includes the second-order CD dispersion, the third-order dispersion slope, and polarization mode dispersion (PMD). On the other hand, fiber nonlinearities, which are power-dependent impairments, contain a number of effects including intrachannel self-phase modulation (SPM), interchannel cross-phase modulation (XPM), and four-wave mixing (FWM). Dispersion and nonlinearity impairments are embedded in

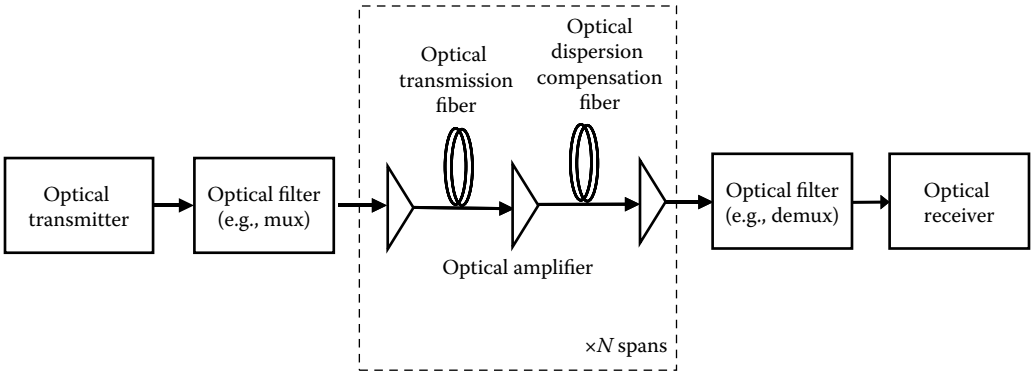

FIGURE 4.1
Generalized diagram of optical transmission systems.

the nonlinear Schrodinger equation (NLSE) that governs signal propagation along the optical fiber. The most popular method to solve NLSE numerically is the symmetric split-step Fourier method (SSFM) [3]. This method, however, encounters a number of issues such as long computation time and artificial errors caused by the windowing effect of fast Fourier transform (FFT) and inverse FFT (IFFT) operations. These operations are described in Section 4.4 using numerical methods dealing with both linear and nonlinear impairments. The symmetric SSFM can overcome some limiting factors of modeling.

Optical signals are attenuated when propagating along the optical fiber channel, thus necessitating the signal amplification. This amplification is carried out in the photonic domain by using erbium-doped fiber amplifiers (EDFA). Figure 4.1 illustrates the conventional configuration in which DCFs are normally accompanied by two EDFAs. The first EDFA compensates the attenuation of the preceding SSMF span while the other EDFA boosts optical intensity to a designated level before launching into the next transmission span. From the system point of view, there are two key parameters modeling an EDFA: amplified spontaneous emission (ASE) noise and noise figure (NF). These parameters are formulated in Section 4.3. Unless specifically stated, it is assumed in this chapter that optical amplifiers are operating at their saturation modes. Figure 4.1 also shows optical filters whose bandwidths have significant impact on the system performance. The modeling of these optical filters as well as electrical filters is presented in Section 4.5.1.

The last key subsystem is the direct detection optical receiver, which can be classified into two types: single-photodiode receivers and Mach–Zehnder delay interferometer (MZDI) balanced receivers, for incoherent detection of optical OOK and DPSK signals, respectively [4,5]. The performance of these receivers is influenced by several noise sources whose formulations are provided in Section 4.7.

Evaluation of the performance of the system is critical in fiber-optic communications for both modeling/simulation and practical experiments. The performance of optical transmission systems can be characterized by several measures. A quick measure is based on simple metrics such as eye opening (EO) and eye opening penalty (EOP) of detected signals. However, the most popular measure is bit error rate (BER) as a function of the optical signal-to-noise ratio (OSNR), average received powers, or average input powers. Moreover, power or OSNR penalties can be inferred from the obtained BER curves, at a particular BER level. Conventional methods for calculating BER to evaluate the system performance are presented in Section 4.8, while Section 4.9 provides thorough descriptions of statistical

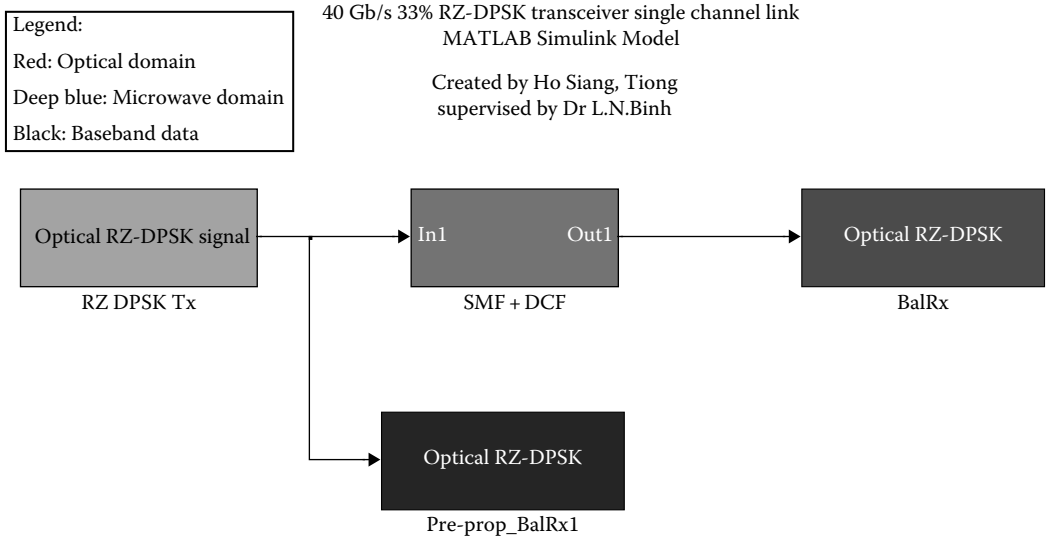

FIGURE 4.2
Generic overview of an optical transmission model on MATLAB® Simulink® platform for generation, Propagation and detection of 40 Gb/s DPSK RZ pulse shaping with 33% pulse with two-bit period ratio.

methods for novel applications in fiber-optic communications. Finally, Section 4.10 discusses the advantages of the developed MATLAB Simulink modeling platform before a summary of this chapter is provided. A generic model of optical transmission system developed on Simulink platform is shown in Figure 4.2.

4.2 Optical Transmitter

An optical transmitter normally consists of a narrow linewidth laser source, external optical modulators, a bit pattern data generator, and optionally an electrical precoder or an electrical shaping filter (see Figure 4.3).

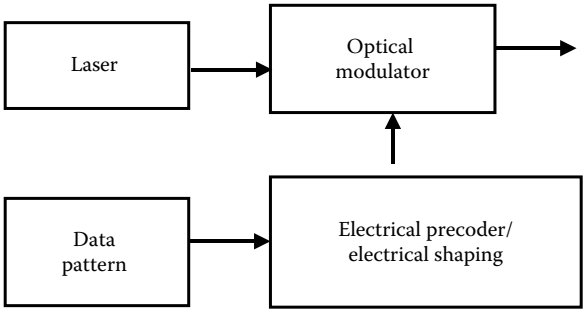

FIGURE 4.3
Generic block diagram of an optical transmitter.

The narrow linewidth laser source is normally a distributed feedback (DFB) laser [6,7] with generated wavelengths complying with the ITU-Grid standard. The laser can be biased at a constant current to provide a continuous-wave (CW) laser, whose optical carrier passes through an external optical modulator for the data modulation process. In simulation, all signals are to be sampled because the simulation model is normally implemented in digital computers and sampling is essential. If an optical carrier with frequency in the range of 200 THz is used then the sampling rate would be of the order of few hundred Tera-Samples/s. At this rate, the computer may run out of memory, and the execution time becomes very long. Thus normally, the amplitude of the data sequence is represented as a complex amplitude whose imaginary part, and hence the phase angle of the carrier, can be incorporated without using the real carrier.

4.2.1 Background of External Optical Modulators

In the 1980s and early 1990s, direct modulation of semiconductor lasers was the main modulation technique. However, this technique faces several limiting factors [8,9]: Direct modulation induces unwanted chirps, resulting in the spectral broadening of the signal and hence causing severe dispersion penalties. Directly modulated optical signals experience fluctuation in the intensity, arising from the relative intensity noise (RIN) of semiconductor laser. Laser phase noise induced from nonzero linewidth of laser sources also limits the application of the direct modulation technique in high-speed transmission systems.

External data modulation has thus been the preferred technique over direct modulation as it minimizes the problems mentioned earlier for digital photonic transmission systems. The external data modulation can be implemented using either electro-absorption modulators (EAMs) or electro-optic modulators (EOMs). EOMs have been preferable because of the advantages of electro-optic materials such as linear response characteristic, high extinction ratio, and in particular, capability to control either phase, frequency, or amplitude of the light wave carrier [10,11]. The operation of EOM is based on principles of Pockels electro-optic effects of solid-state, polymeric, or semiconductor materials [8,10]. Over the years, waveguides of EOMs are mainly integrated on lithium niobate ($LiNbO_3$) material. It has prominent properties such as high electro-optic coefficients, low attenuation, and the possibility of generating chirp-free signals [10,12]. $LiNbO_3$ EOMs have been developed since the early 1980s, but were not popular until the advent of EDFA in the late 1980s [10,13]. They were employed in coherent optical communications to mitigate the problems of broad linewidth and RIN of the laser source in direct modulation, as mentioned earlier. The knowledge of using these external modulators has recently been revisited for the generation of advanced modulation formats in incoherent transmission systems. The data modulation is conducted in photonic domain by using either the optical phase or intensity modulator.

4.2.2 Optical Phase Modulator

An electro-optic phase modulator (EOPM) employs a single electrode as shown in Figure 4.4. Its operation is based on Pockels electro-optic effect, that is, when a driving voltage is applied to the electrode, the refractive index (RI) of electro-optic waveguide changes accordingly, thus slowing down the light waves and hence inducing a delay in the optical waves. Because the delays correspond to phase changes, the EOPM is able to manipulate the phase of the light wave carrier.

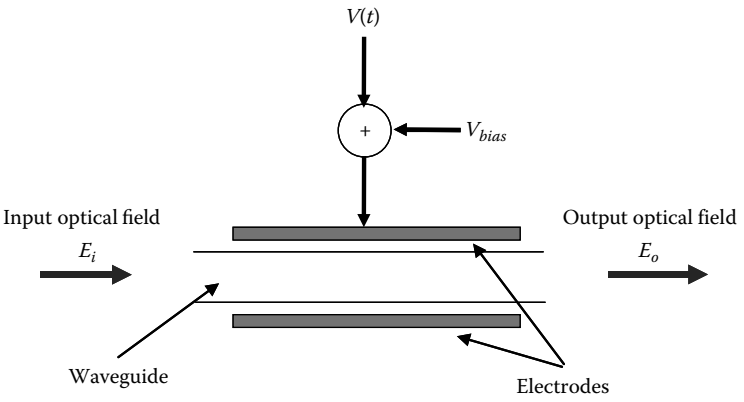

FIGURE 4.4
Electro-optic phase modulator (EOPM).

The induced phase variation corresponding to a particular radio frequency (RF) electrical driving voltage $V(t)$ is given as:

$$\varphi(t) = \pi \frac{\left(V(t) + V_{bias}\right)}{V_\pi} \tag{4.1}$$

where

V_π is the driving voltage required to create a π phase shift on the light wave carrier and has typical values within a range of 3–6 V [12,14]

$V(t)$ is a time-varying driving signal voltage

V_{bias} is a DC bias voltage which is normally coupled with the signal source using a *T*-bias device

The complex-envelope representation of the optical field E_o at the output of EOPM is expressed as:

$$E_o(t) = E_i(t)e^{j\varphi(t)} \tag{4.2}$$

EOPMs operating at high speed, for example, at 40 Gb/s, and using resonant-type electrodes have been recently reported [15,16]. In addition, due to the linear response characteristic of electro-optical materials (reflected in (4.1)). It is possible to modulate the EOPM, and hence the optical frequency by manipulating the slope of the time-varying RF driving signal.

4.2.3 Optical Intensity Modulator

An intensity modulator is composed of two EOPMs in a parallel structure to form a Mach–Zehnder interferometer which is commonly known as Mach–Zehnder intensity modulator (MZIM) (see Figure 4.5).

The field of the input optical wave is split equally when entering the two arms of MZIM. Each arm of the MZIM is actually an EOPM for modulating the phase of the optical carrier.

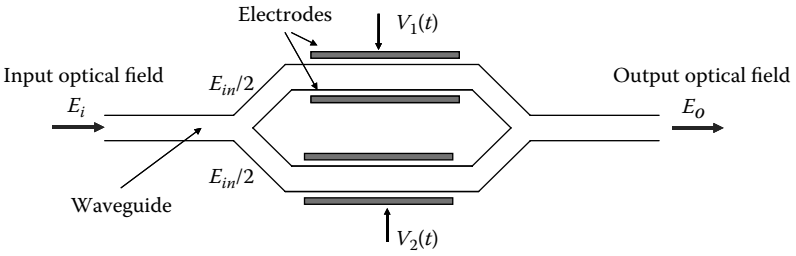

FIGURE 4.5
Optical intensity modulator with a Mach–Zehnder interferometric structure.

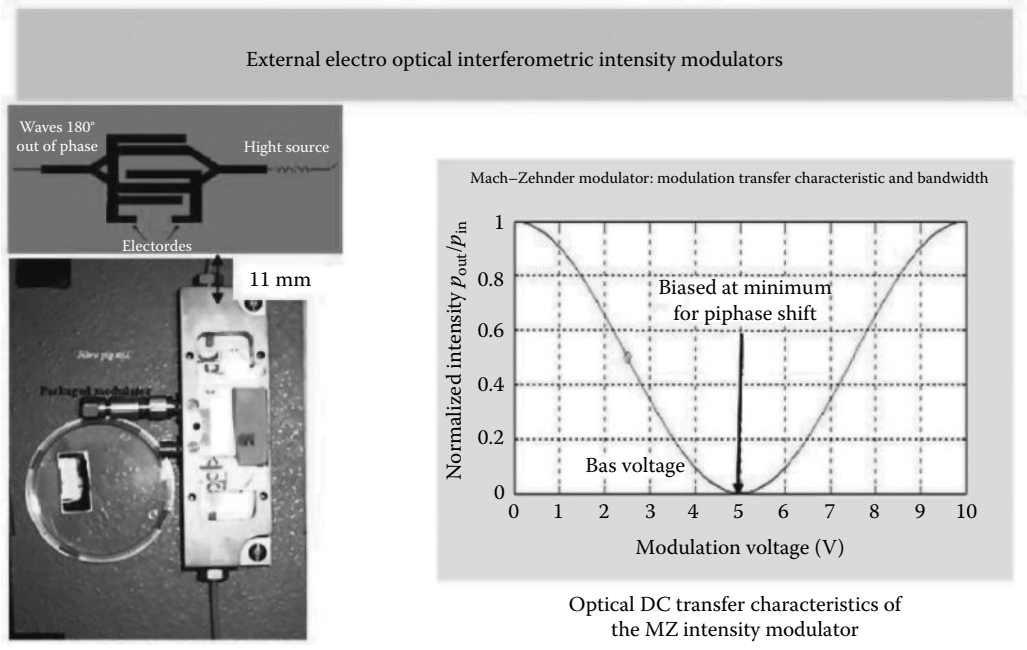

Monash packaged 26 GHz MZI wideband modulator

Optical DC transfer characteristics of the MZ intensity modulator

FIGURE 4.6
A packaged MZIM and its operating the transfer curve.

At the output of MZIM, the optical fields from the two arms are coupled and interfere with each other either constructively or destructively. This enables the "ON–OFF" modulation of the light wave intensity. Figure 4.6 shows a sample of a packaged MZIM and its modulation transfer characteristic [17] whose 3 dB bandwidth reaches 26 GHz.

MZIM can be classified into single-drive and dual-drive types, which are described in the next subsections.

4.2.3.1 Single-Drive MZIM

A single-drive MZIM has only one single driving voltage applied to either arm of MZIM. For instance, it is assumed that there is no voltage driving onto arm 1 while a voltage $V(t)$

is applied on arm 2 (refer to Figure 4.4). The transmitted optical field $E_o(t)$ at the output of a single-drive MZIM is a function of $V(t)$ and a bias DC voltage V_{bias}. Written in the low-pass equivalent format, the expression of $E_o(t)$ is given by

$$E_o(t) = \frac{E_i(t)}{2}\left[1+e^{j\pi\frac{(V(t)+V_{bias})}{V_\pi}}\right] = E_i\cos\left[\frac{\pi}{2}\frac{(V(t)+V_{bias})}{V_\pi}\right]e^{-j\left[\frac{\pi}{2}\frac{(V(t)+V_{bias})}{V_\pi}\right]} \tag{4.3}$$

The phase term in (4.3) implies the existence of the phase modulation of the optical carrier, that is, the chirping effect. Thus, by using a single-drive MZIM, generated optical signals are theoretically not chirp free, particularly in the case of using a *z*-cut $LiNbO_3$ MZIM, which has an asymmetrical structure of field distributions [12]. However, an *x*-cut MZIM can provide a modest amount of chirping thanks to the symmetrical distribution of its electrical fields [12]. In practice, a small amount of chirp might be useful for transmission [8].

4.2.3.2 Dual-Drive MZIM

A dual-drive MZIM has a push–pull arrangement for dual-driving voltages, that is, ($V_1(t)$ and $V_2(t)$ are inverses of each other ($V_2(t) = -V_1(t)$) and hence can completely eliminate the chirping effect in the modulation of the light wave carrier. The transmitted optical field $E_o(t)$ in (4.3) can be rewritten as:

$$E_o(t) = \frac{E_i(t)}{2}\left[e^{j\pi\frac{(V(t)+V_{bias})}{V_\pi}} + e^{j\pi\frac{-(V(t)+V_{bias})}{V_\pi}}\right] = E_i\cos\left[\frac{\pi}{2}\frac{(V(t)+V_{bias})}{V_\pi}\right] \tag{4.4}$$

In (4.4), the phase term no longer exists, indicating that the chirping effect is totally eliminated.

4.3 Impairments of Optical Fiber

4.3.1 Chromatic Dispersion (CD)

This section presents key properties of the CD impairment in a single-mode fiber. The first point to discuss about the CD of a single-mode fiber is the expansion of the mode propagation constant or "wave number" parameter β using the Taylor series [8]:

$$\beta(\omega) = \frac{\omega n(\omega)}{c} = \beta_0 + \beta_1\Delta\omega + \frac{1}{2}\beta_2\Delta\omega^2 + \frac{1}{6}\beta_3\Delta\omega^3 + \cdots + \frac{1}{n!}\beta_n\Delta\omega^n \tag{4.5}$$

where

ω is the angular optical frequency
$n(\omega)$ is the fiber RI

The parameters β_n represent the nth derivative of β and their meanings are described in the following text.

- β_0 involves the phase velocity, v_p, of the optical carrier ω_0 and v_p is defined as

$$v_p = \frac{\omega_0}{\beta_0} = \frac{c}{n(\omega_0)} \tag{4.6}$$

  The subscript 0 of the optical carrier frequency indicates the central frequency component of the carrier. Other frequency differences $\Delta\omega$ indicate the difference of the sideband component and the central carrier.
- β_1 determines the group velocity v_g that is related to β of the guided mode by

$$v_g = \frac{1}{\beta_1} = \left(\frac{d\beta}{d\omega}\bigg|_{\omega=\omega_0} \right)^{-1} \tag{4.7}$$

- β_2 is the derivative of the group velocity v_g with respect to frequency, and hence, β_2 clearly shows the frequency dependence of the group velocity. This means that different frequency components of an optical pulse propagate along the optical fiber at different velocities, thus leading to the spreading of the pulse, that is, the dispersion. The parameter β_2 is commonly known as the group velocity dispersion (GVD). The optical fiber exhibits normal dispersions for $\beta_2 > 0$ or anomalous dispersions for $\beta_2 < 0$. A pulse having the spectral width of $\Delta\omega$ and traveling through a length L of fiber is broadened by an amount of time ΔT given by $\Delta T = \beta_2 L \Delta\omega$ [3]. In practice, a more common factor to represent the CD of a SMF is the dispersion factor D with the unit of ps/(nm·km). D is closely related to GVD β_2 by

$$D = -\left(\frac{2\pi c}{\lambda^2} \right) \beta_2 \tag{4.8}$$

  where λ is the operating wavelength.
- β_3 is the derivative of β_2 and contributes to the dispersion slope $S(\lambda)$ as follows:

$$S = \frac{dD}{d\lambda} = \left(\frac{2\pi c}{\lambda^2} \right) \beta_3 + \left(\frac{4\pi c}{\lambda^3} \right) \beta_2 \tag{4.9}$$

4.3.2 Chromatic Dispersion as a Total of Material Dispersion and Waveguide Dispersion

From the view of fiber design [8,18], D is a sum of material dispersion (D_M) and waveguide dispersion (D_W):

$$D = -\left(\frac{2\pi c}{\lambda^2} \right) \beta_2 \equiv D_M + D_W. \tag{4.10}$$

The following equations describe how D_M and D_W are obtained. In this case, a step-index optical fiber with a core radius a is considered and the RIs of the core and cladding

of the SSMF are denoted as n_1 and n_2, respectively. The significant transverse propagation constants of guided light waves u and v in the core and cladding regions are formulated as:

$$u = a\sqrt{k^2 n_1{}^2 - \beta^2} \tag{4.11}$$

$$v = a\sqrt{\beta^2 - k^2 n_2^2} \tag{4.12}$$

where $k^2 n_1{}^2$ and $k^2 n_2{}^2$ are the plane-wave propagation constants in the core and cladding, respectively. The guided wave number β is calculated as:

$$\beta = \sqrt{k^2 (b(n_1{}^2 - n_2^2) + n_2^2)} \tag{4.13}$$

where b is the normalized propagation constant whose values for guided modes fall within the range of [0, 1] and b is calculated as:

$$b = \frac{\frac{\beta}{k} - n_2}{n_1 - n_2} \tag{4.14}$$

The normalized frequency V is expressed as:

$$V = ak\sqrt{n_1{}^2 - n_2{}^2} \tag{4.15}$$

The waveguide dispersion D_W can be calculated using the following equation [19–21]:

$$D_W = -\left(\frac{n_1 - n_2}{c\lambda}\right)\frac{Vd^2(Vb)}{dV^2} \tag{4.16}$$

where $Vd^2(Vb)/dV^2$ is defined as the normalized waveguide dispersion parameter. An effective approximation based on the polynomial interpolation has been developed to calculate the waveguide dispersion parameter of a multi-cladding DCF [18].

The material dispersion of an optical fiber is due to the wavelength dependence on the RI of the core and the cladding. The RI $n(\lambda)$ is estimated by the Sellmeier's equation [21]:

$$n^2(\lambda) = 1 + \sum_{i=1}^{M} \frac{B_i \lambda^2}{\left(\lambda^2 - \lambda_i^2\right)} \tag{4.17}$$

where

λ_i indicates the ith resonance wavelength
B_i is its corresponding oscillator strength
n stands for n_1 or n_2 for either the core or cladding RIs, respectively

The material dispersion factor D_M is then obtained by

$$D_M = -\frac{\lambda}{c}\left(\frac{d^2 n(\lambda)}{d\lambda^2}\right) \tag{4.18}$$

where c is the light velocity in vacuum. For pure silica and over the wavelength of 1.25–1.66 μm, D_M can also be approximated by an empirical relation [19,21]:

$$D_M = 122\left(1 - \frac{\lambda_{ZD}}{\lambda}\right) \tag{4.19}$$

where λ_{ZD} is the zero material dispersion wavelength which is defined as the wavelength at $D_M(\lambda) = 0$ for instance, $\lambda_{ZD} = 1.276$ μm for pure silica. λ_{ZD} can vary according to various doping concentrations in the core and cladding of different materials such as germanium (Ge) or fluorine (F).

With the demand for reducing the effects of fiber CD, several types of fibers including dispersion-shifted fiber (DSF) and NZDSF were proposed. The latter type requires a non-zero local dispersion value to avoid phase matching between the wavelengths in a DWDM transmission system, that is, avoid the FWM effect. Values of D for various types of fibers within the C-band wavelengths of the ITU-Grid standard are demonstrated in Figure 4.7 and the indicated circle values are located at 1550 nm wavelength.

The optical transmission medium also involves DCF and several other types of fibers such as dispersion-flattened fiber (DFF) and Corning Vascade fibers. DCF is usually used inline with SSMF in a dispersion-managed optical system so that fiber CD is fully compensated within a span. The dispersion factor D of a DCF has negative values. On the other hand, DFF is manufactured for the specific purpose of flattening dispersion factors over a wide range of wavelengths to reduce fiber CH effects. However, these wavelengths travel at nearly the same velocities and thus the phase-matching conditions are easily satisfied. This results in FWM effects with the introduction of a ghost pulse. However, DFF has an important application in the parametric amplification utilizing the FWM nonlinearity [3]. Furthermore, Corning Vascade fibers are designed for ultra long-haul and transoceanic optical transmission systems and they provide a complete built-in CD compensation.

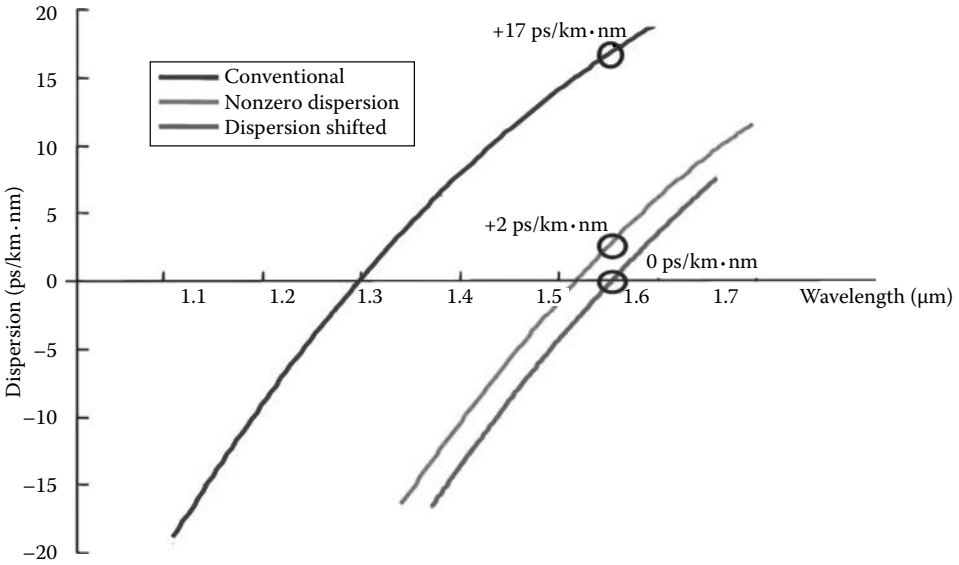

FIGURE 4.7
Typical values of fiber CD for different types of fiber.

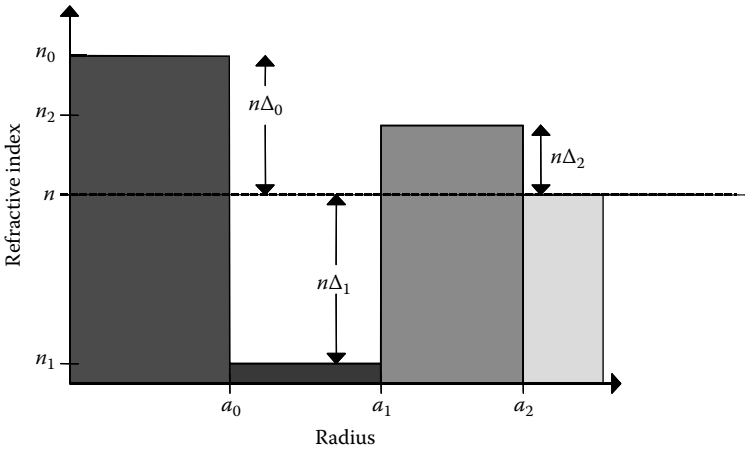

FIGURE 4.8
Index profile of a triple-cladding fiber for a design of DCF or DFF.

The design of DCF and DFF is more complicated than that of SSMF as it involves a multi-cladding/core structure (see Figure 4.8) compared to the simple step-index profile of SSMF [18].

4.3.3 Dispersion Length

An important parameter that governs the effects of fiber CD on optical pulses is the dispersion length L_D. This length corresponds to the distance at which a pulse broadens by one-bit interval [19,22]. For high-capacity and long-haul transmission employing external modulation, L_D can be estimated as [22]:

$$L_D = \frac{10^5}{D \cdot R^2} \tag{4.20}$$

where
R is the bit rate (Gb/s)
D is in ps/(nm · km)
L_D is in km

Equation 4.20 provides a reasonable approximation even though the accurate computation of L_D depends on a number of factors: the modulation format, pulse shaping, and the optical receiver performance. It is found that this transmission limit is inversely proportional to the square of the bit rate. Thus, for 10 Gb/s OC-192 OOK systems (D = ±17 ps/(nm · km)), the dispersion length L_D has a value of approximately 60 km SSMF. This SSMF length corresponds to a residual dispersion of about ±1000 ps/nm. In the case of 40 Gb/s OC-768 systems, L_D is about 4 km or equivalent to ±60 ps/nm.

4.3.4 Polarization Mode Dispersion (PMD)

PMD represents another cause of pulse spreading and relates to the differential group delay (DGD) between two orthogonal principal states of polarizations (PSP) in the propagating optical field, as illustrated in Figure 4.9.

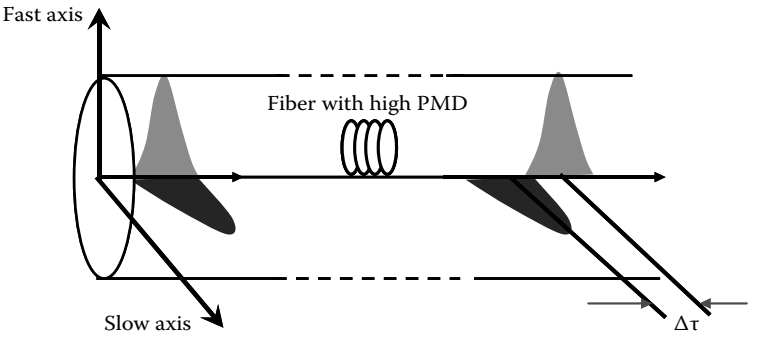

FIGURE 4.9
Delay caused by DGD of two PSPs along the fiber propagation.

Fiber PMD is caused by either the asymmetry of the fiber core or the deformation of optical fibers. These are consequences of defects in the manufacturing process, the external stress to the fiber, the aging problem, or the variation of temperature over time.

The delay between two PSPs is normally negligibly small at 10 Gb/s. However, at high bit rate and in ultra long-haul transmission, PMD severely degrades the system performance [23–26]. The instantaneous value of DGD ($\Delta\tau$) varies along the fiber and follows a Maxwellian distribution [27,28] (see Figure 4.10).

The Maxwellian distribution is governed by the following expression:

$$f(\Delta\tau) = \frac{32(\Delta\tau)^2}{\pi^2 \langle \Delta\tau \rangle^3} \exp\left\{-\frac{4(\Delta\tau)^2}{\pi \langle \Delta\tau \rangle^2}\right\} \quad \Delta\tau \geq 0 \tag{4.21}$$

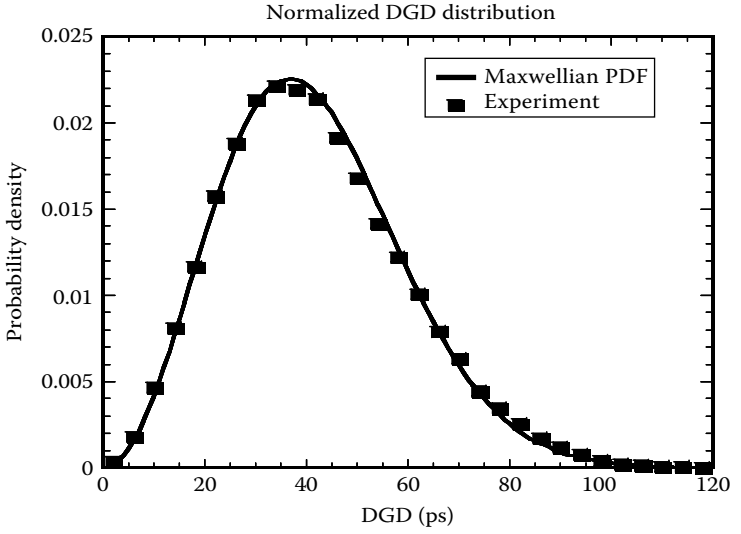

FIGURE 4.10
Maxwellian distribution of PMD random process.

The mean DGD value $\langle \Delta\tau \rangle$ is commonly termed "fiber PMD" and provided in the fiber specifications. The following expression gives an estimate of the maximum transmission limit $L_{\max}$ due to the PMD effect [29]:

$$L_{\max} = \frac{0.02}{\langle \Delta\tau \rangle^2 \cdot R^2} \tag{4.22}$$

where R is the bit rate. Based on (4.22), $L_{\max}$ for both old fibers and contemporary fibers is obtained as follows:

- $\langle \Delta\tau \rangle$ = 1 ps/km (old installed fibers)
  - R = 40 Gb/s; $L_{\max}$ = 12.5 km
  - R = 10 Gb/s; $L_{\max}$ = 200 km
- $\langle \Delta\tau \rangle$ = 0.1 ps/km (contemporary modern fibers)
  - R = 40 Gb/s; $L_{\max}$ = 1250 km
  - R = 10 Gb/s; $L_{\max}$ = 20,000 km

4.3.5 Fiber Nonlinearity

Fiber RI is dependent on both the operating wavelengths and the intensity of the guided mode distributed across the area of the fiber core and cladding. This intensity-dependent phenomenon is known as the Kerr effect and is the cause of fiber nonlinear effects. The power dependence of RI is expressed as [3]:

$$n' = n + \bar{n}_2 (P / A_{eff}) \tag{4.23}$$

where
P is the average optical intensity inside the fiber
$\bar{n}_2$ is the fiber nonlinear coefficient
A_{eff} is the effective area of the fiber

Fiber nonlinear effects include intrachannel SPM, interchannel XPM, FWM, stimulated Raman scattering (SRS), and stimulated Brillouin scattering (SBS). SRS and SBS are not the main degrading factors as their effects are only getting noticeably large with very high optical power. On the other hand, FWM degrades severely the performance of an optical system with the generation of ghost pulses only if the phases of optical signals are matched with each other. However, with high local dispersions such as in SSMF, the effects of FWM become negligible [30]. In terms of XPM, its effects can be considered to be negligible in a DWDM system in the following scenarios [31–35]: (1) highly locally dispersive system and (2) large channel spacing. However, XPM should be taken into account for optical transmission systems deploying NZDSF where local dispersion values are small. Thus, SPM is usually the dominant nonlinear effect for systems employing transmission fibers with high local dispersions, for example, SSMF

and DCF. The effect of SPM is normally coupled with the nonlinear phase shift ϕ_{NL} defined as [3]:

$$\phi_{NL} = \int_0^L \gamma P(z)dz = \gamma L_{eff} P,$$

$$\gamma = \frac{\omega_c \bar{n}_2}{A_{eff} c} \tag{4.24}$$

$$L_{eff} = \frac{1 - e^{-\alpha L}}{\alpha}$$

where

ω_c is the light wave carrier
L_{eff} is the effective transmission length
α is the fiber attenuation factor, which normally has a value of 0.17–0.2 dB/km for the current 1550 nm window of operating wavelengths

The temporal variation of the nonlinear phase ϕ_{NL} results in the generation of new spectral components far apart from the light wave carrier ω_c, indicating the broadening of the signal spectrum. This spectral broadening $\delta\omega$ can be obtained from the time dependence of the nonlinear phase shift as follows:

$$\delta\omega = -\frac{\partial \phi_{NL}}{\partial T} = -\gamma \frac{\partial P}{\partial T} L_{eff} \tag{4.25}$$

Equation 4.25 indicates that $\delta\omega$ is proportional to the time derivative of the average signal power *P*. Additionally, the generation of new spectral components occurs mainly at the rising and falling edges of optical pulses, that is, the amount of generated chirps is larger for an increased steepness of the pulse edges.

4.4 Modeling of Fiber Propagation

4.4.1 Symmetrical SSFM

The evolution of slow varying complex envelopes $A(z, t)$ of optical pulses along a single-mode optical fiber is governed by the nonlinear Schrodinger equation (NLSE) [3]:

$$\frac{\partial A(z,t)}{\partial z} + \frac{\alpha}{2} A(z,t) + \beta_1 \frac{\partial A(z,t)}{\partial t} + \frac{j}{2}\beta_2 \frac{\partial^2 A(z,t)}{\partial t^2} - \frac{1}{6}\beta_3 \frac{\partial^3 A(z,t)}{\partial t^3} = -j\gamma \left|A(z,t)\right|^2 A(z,t) \tag{4.26}$$

where

z is the spatial longitudinal coordinate
α accounts for fiber attenuation
β_1 indicates DGD
β_2 and β_3 represent second- and third-order factors of fiber CD
γ is the nonlinear coefficient

In a single channel transmission, (4.26) includes the following effects: fiber attenuation, fiber CD and PMD, dispersion slope, and SPM nonlinearity. The fluctuation in optical intensity caused by the Gordon–Mollenauer effect [36] is also included in this equation.

The solution of NLSE and hence the modeling of pulse propagation along an SMF are solved numerically by using SSFM [3]. In SSFM, the fiber length is divided into a large number of small segments δz. In practice, fiber dispersion and nonlinearity are mutually interactive at any distance along the fiber. However, these mutual effects are small within δz and thus the effects of fiber dispersion and fiber nonlinearity over δz are assumed to be statistically independent of each other. As a result, SSFM can separately define two operators: (1) the linear operator that involves fiber attenuation and fiber dispersion effects and (2) the nonlinear operator that takes into account fiber nonlinearities. These linear and nonlinear operators are formulated as follows:

$$\hat{D} = -\frac{i\beta_2}{2}\frac{\partial^2}{\partial T^2} + \frac{\beta_3}{6}\frac{\partial^3}{\partial T^3} - \frac{\alpha}{2}$$
$$\hat{N} = i\gamma \mid A \mid^2 \tag{4.27}$$

where

A replaces $A(z, t)$ for simpler notation

$T = t - z/v_g$ is the reference time frame moving at the group velocity

Equation 4.26 can be rewritten in a shorter form, given by

$$\frac{\partial A}{\partial z} = (\hat{D} + \hat{N})A \tag{4.28}$$

and the complex amplitudes of optical pulses propagating from z to $z + \delta z$ are calculated using the approximation in the following:

$$A(z + h, T) \approx \exp(h\hat{D})\exp(h\hat{N})A(z, T). \tag{4.29}$$

Equation 4.29 is accurate to the second order of the step size δz [3]. The accuracy of SSFM can be improved by including the effect of fiber nonlinearity in the middle of the segment rather than at the segment boundary (see Figure 4.11). This modified SSFM is known as the symmetric SSFM.

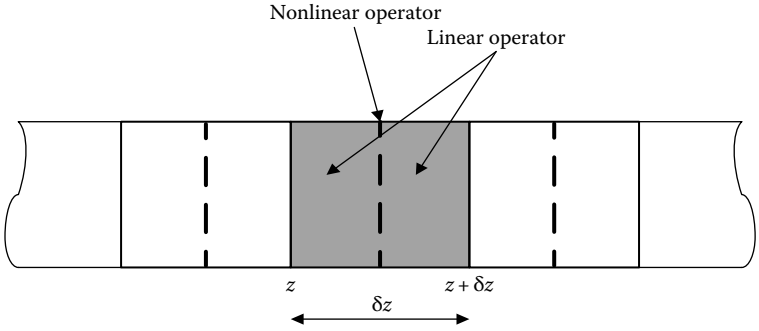

FIGURE 4.11
Schematic illustration of symmetric SSFM.

Equation 4.29 can now be modified as:

$$A(z+\delta z,T)\approx \exp\left(\frac{\delta z}{2}\hat{D}\right)\exp\left(\int_{z}^{z+\delta z}\hat{N}(z')dz'\right)\exp\left(\frac{\delta z}{2}\hat{D}\right)A(z,T) \tag{4.30}$$

This method is accurate to the third order of the step size δz. In symmetric SSFM, the optical pulse propagates along a fiber segment δz in two stages. First, the optical pulse propagates through the linear operator that has a step size of δz/2 that takes into account fiber attenuation and dispersion effects. Then, the fiber nonlinearity is calculated in the middle of the segment. After that, the pulse propagates through the second half of the linear operator. The process continues repetitively in consecutive segments of size δz until the end of the fiber. It should be highlighted that the linear operator is computed in the frequency domain while the nonlinear operator is calculated in the time domain.

4.4.2 Modeling of PMD

First-order PMD can be implemented by modeling the optical fiber as two separate paths representing the propagation of two PSPs. Symmetrical SSFM is carried out on each transmission path before the outputs of these two paths are superimposed to calculate the output optical field. The transfer function to represent the first-order PMD is given by

$$H(f)=H^{+}(f)+H^{-}(f) \tag{4.31}$$

where

$$H^{+}(f)=\sqrt{k}\exp\left[j2\pi f\left(-\frac{\Delta\tau}{2}\right)\right]$$

$$H^{-}(f)=\sqrt{k}\exp\left[j2\pi f\left(-\frac{\Delta\tau}{2}\right)\right]$$

in which k is the power splitting ratio and $k = 1/2$ when using a 3 dB or 50:50 optical coupler/splitter, $\Delta\tau$ is the instantaneous DGD value following a Maxwell distribution (refer to (4.21)).

4.4.3 Optimization of Symmetrical SSFM

4.4.3.1 Optimization of Computational Time

A huge amount of time is spent on symmetric SSFM for FFT and IFFT operations, in particular, when fiber nonlinear effects are involved. In practice, when optical pulses propagate toward the end of a fiber span, the pulse intensity is greatly attenuated due to the fiber attenuation. As a result, fiber nonlinear effects become negligible for the rest of that fiber span and hence, the transmission operates in a linear domain in this range. In this research, a technique to configure symmetric SSFM is proposed to reduce the computational time. If the peak power of an optical pulse is lower than the nonlinear threshold of

the transmission fiber, for example, around −4 dBm, symmetrical SSFM is switched to a linear mode operation. This linear mode involves only fiber dispersions and fiber attenuation and its low-pass equivalent transfer function for the optical fiber is given by

$$H(\varpi) = \exp\left\{-j\left[(1/2)\beta_2\varpi^2 + (1/6)\beta_3\varpi^3\right]\right\} \tag{4.32}$$

If β_3 is not considered in this fiber transfer function, which is normally the case due to its negligible effects on 40 Gb/s and lower bit rate transmission systems, the transfer function given earlier has a parabolic phase profile [37,38].

4.4.3.2 Mitigation of Windowing Effect and Waveform Discontinuity

In symmetric SSFM, mathematical operations of FFT and IFFT play a very significant role. However, because a finite window length is required for FFT and IFFT operations, these operations normally introduce overshooting at the two boundary regions of the FFT window, commonly known as the windowing effect of FFT. In addition, since the FFT operation is a block-based process, there exists the issue of waveform discontinuity, that is, the right-most sample of the current output block does not start at the same position as the left-most sample of the previous output block. The windowing effect and the waveform discontinuity problems are resolved by the following solutions (see Figure 4.12).

- The actual window length for FFT/IFFT operations consists of two blocks of samples (2*N* sample length). The output, however, is a truncated version with the length of one block (*N* samples) and output samples are taken in the middle of the two input blocks.
- The next FFT window overlaps the previous one by one block of the *N* sample.

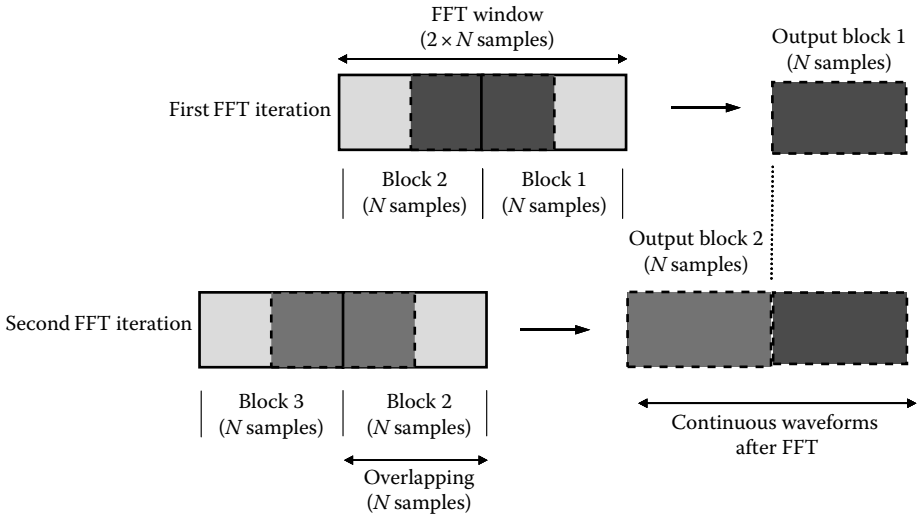

FIGURE 4.12
Proposed solution for mitigating windowing effect and waveform discontinuity caused by FFT/IFFT operations.

4.5 Optical Amplifiers

In the modeling of an EDFA, two key parameters are ASE noise or the noise figure (NF). The following formulation accounts for the average power of ASE noise (N_{ASE}) [8]:

$$N_{ASE} = mn_{sp}hf(G-1)B_o \tag{4.33}$$

where
- f is the optical operating frequency
- G is the amplifier optical gain
- n_{sp} is the spontaneous emission factor
- h is Planck's constant
- m is the number of polarization modes (usually $m = 2$ for systems without polarization multiplexing)
- B_o is the bandwidth of an optical filter

The NF of an EDFA is defined as the ratio between the output OSNR and the OSNR at the input of the EDFA, and is given by

$$NF = \frac{OSNR_{in}}{OSNR_{out}} \approx 2n_{sp} \quad \text{for } G \gg 1. \tag{4.34}$$

Assuming that EDFAs are operating in the saturation regions and by substituting NF from (4.34) into (4.33), the N_{ASE} can be related to NF as follows:

$$N_{ASE} = (NF \cdot G - 1)hfB_o \tag{4.35}$$

The total optical noises of a transmission system are normally measured over a standard noise bandwidth of 0.1 nm or about 12.5 GHz at 1550 nm wavelength region. The common representation is therefore $OSNR_{0.1\ \text{nm}}$, whose noise is measured over a band of 0.1 nm. Details of measurement techniques for noises in optical amplifiers can be found in Ref. [39].

4.5.1 Optical and Electrical Filters

In this research, filtering of noise-corrupted optical signals is conducted with a Gaussian-type optical filter whose impulse response is governed by the following expression:

$$h_{Gauss}(t) = \frac{1}{\sqrt{2\pi}\xi} e^{\left(\frac{-t^2}{2\xi^2}\right)} \tag{4.36}$$

where $\xi = \sqrt{\ln(2)}/2\pi BT$ in which B is a one-sided 3 dB bandwidth of the Gaussian filter and T is the bit period. Variations of these two parameters are reflected by the change in the BT product.

The modeling of an electrical filter can also be implemented with a Gaussian filter having a similar impulse response to (4.36). Alternatively, a fifth-order Bessel filter, which can be

easily designed using the filter design toolbox in MATLAB, is used. The MATLAB pseudocodes for designing a fifth-order Bessel filter are shown as follows:

```
[b, a] = besself(fifth order, 2 * π * BT/sampling_factor)
[bz, az] = impinvar(b, a, 1);
[hf t1] = impz(bz, az, 2 * delay * sampling_factor + 1, sampling_factor)
```

where the *BT* product is defined similar to that of the Gaussian filter.

4.6 Optical Receiver

The original message is recovered in the electrical domain, requiring a conversion of light waves to electrical signals. In optical communications, this process is widely implemented with a *P*-type-Intrinsic-*N*-type (PIN) photodiode for either coherent or incoherent detections. The first type requires a local oscillator to coherently convert modulated light waves from the optical frequency range down to the intermediate frequency (IF) range. On the other hand, the incoherent detection that has been preferred since the last decade is based on the square-law envelope detection of optical signals. The incoherent detection however still requires the recovery of the clock timing. In the model of the digital photonic transmission systems in this research, the ideal clock timing is assumed. Another key parameter of optical receivers is the responsivity parameter of the PIN photodiode, which is a measure for the efficiency of the photonic-electronic conversion. Photodiodes with a high responsivity of around 0.8–0.9 A/W are commercially available. In this research, it is assumed that the responsivity is equal to 1 A/W. Moreover, the induced electrical current is usually amplified with a trans impedance amplifier and then passed through an electrical filter. At this stage, electrical eye diagrams are observed and the sampling process of electrically filtered received signals is carried out for recovering the data information.

Received signals are corrupted by noise from several sources. They include the shot noise (σ^2_{shot}), the electronic noise (σ^2_{elec}), the dark current noise (σ^2_{dark}), and the interactions between signals and ASE noise ($\sigma^2_{signal,ASE}$) as well as between ASE and ASE noise itself ($\sigma^2_{ASE,ASE}$). The summation of these noise sources reflects the total receiver noise.

$$\sigma^2_{total} = \sigma^2_{shot} + \sigma^2_{elec} + \sigma^2_{dark} + \sigma^2_{signal,ASE} + \sigma^2_{ASE,ASE} \tag{4.37}$$

These noise sources are modeled with normal distributions whose variances represent the noise power and they are described as follows:

- *Shot noise* (σ^2_{shot}) is caused by the intrinsic opto-electronic phenomenon of the semiconductor photodiode. A random number of electron-hole pairs are generated with the receipt of photons, causing the randomness of the induced photo current. The shot noise is given by

$$\sigma^2_{shot} = 2 \cdot q \langle i_s \rangle B_e \tag{4.38}$$

  where
  B_e is the 3 dB bandwidth of the electrical filter
  $\langle i_s \rangle$ is the average signal current (with the unit of A/Hz)

- *Electronic noise* source σ^2_{elec} is injected from the trans impedance amplifier. It is modeled by an equivalent noise current i_{Neq} over the bandwidth B_e of the electrical filter. The unit of i_{Neq} is A/$\sqrt{\text{Hz}}$ and the value of σ^2_{elec} is obtained from

$$\sigma^2_{elec} = (i_{Neq})^2 B_e. \tag{4.39}$$

- *Dark current* i_{dark} is normally specified for a photodiode and has the unit of A/Hz. Hence, the noise power σ^2_{dark} is calculated as:

$$\sigma^2_{dark} = 2 \cdot q i_{dark} B_e. \tag{4.40}$$

- The variances of amplitude fluctuations due to the beating of the signal and ASE noise and between ASE and ASE noise itself are given in the following expressions:

$$\sigma^2_{signal,ASE} = 4 \cdot i_S i_N \frac{B_e}{B_{opt}} \tag{4.41}$$

$$\sigma^2_{ASE-ASE} = i_N^2 \frac{B_e}{B_{opt}^2}(2 \cdot B_{opt} - B_e) \tag{4.42}$$

where

B_{opt} is the 3 dB bandwidth of the optical filter

i_N is the noise-induced photo current

In practice, the value of $\sigma^2_{ASE,ASE}$ is normally negligible compared to the value of $\sigma^2_{signal,ASE}$ and can be ignored without affecting the performance of the receiver. In addition, in an optically preamplified receiver, that is, the optical signal is amplified at a stage before the photo detector, the $\sigma^2_{signal,ASE}$ is the dominant factor compared to other noise sources.

A simplified Simulink model is shown in Figure 4.13a and b. The noise equivalent current as seen from the input of the electronic preamplifier is modeled as a random noise source superimposed on the signal input to the receiver. The relevant quantum shot noise is also calculated by the model at each sampled numerical instant.

4.7 Performance Evaluation

The performance of an optical transmission system can be evaluated by using conventional techniques such as the Monte Carlo method and the single Gaussian distribution method. However, these conventional techniques have several limiting factors. The main limitation in the Monte Carlo method is the large amount of time needed for a simulation experiment whereas the single Gaussian method does not take into account distortions caused by dynamic effects of the optical fibers. To cope with these issues, two statistical methods are presented in this research for novel applications in optical fiber communication and they

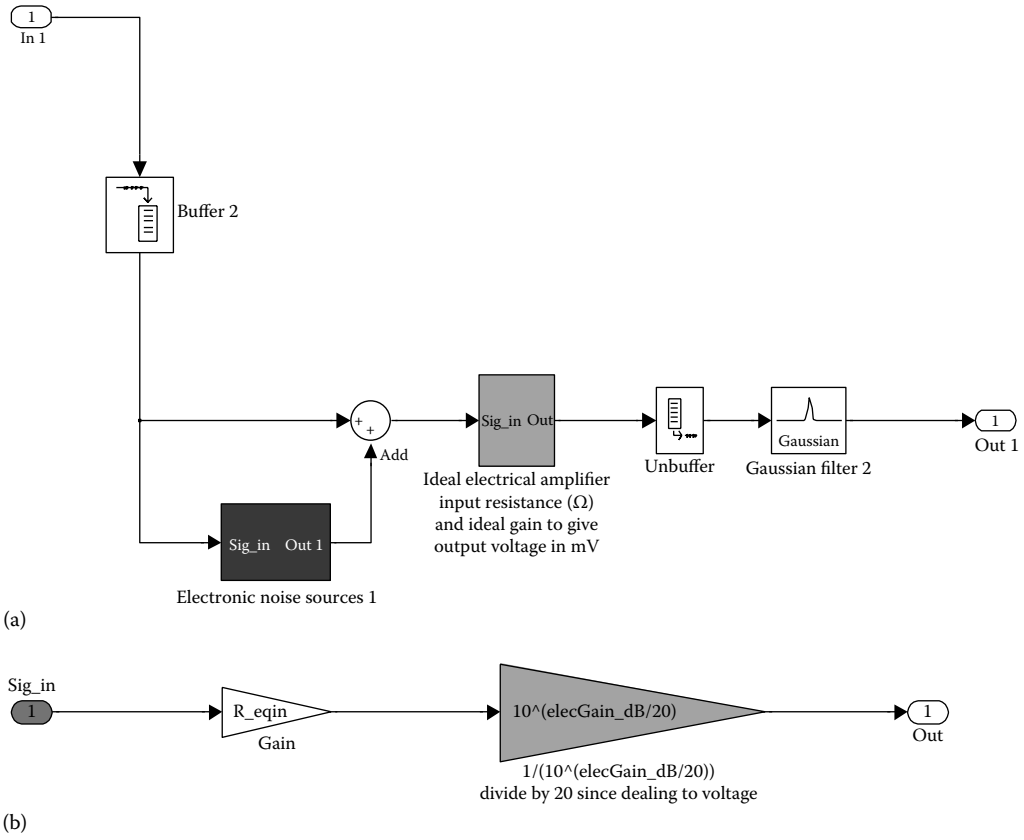

FIGURE 4.13
Simulink® model of optical receiver (a) noise and gain (b) gain section.

offer flexible and fast-processing methods to obtain the BER performance. Several main characteristics on these methods are as follows:

- The first method implements the Expected Maximization (EM) theorem in which the probability distribution function (pdf) of received electrical signals is estimated as a mixture of Multiple Gaussian Distributions (MGD). Although the application of this method in optical communications has recently been reported [40,41], the guidelines for optimizing the accuracy of this method have yet to be presented.
- The second method, which is based on the generalized extreme value (GEV) theorem, is the generalized Pareto distribution (GPD) method. This method predicts the probability of the occurrence of extreme values that occur within the long tail of the signal pdf. Although the GPD method is popularly used in several fields such as finance [42], meteorology [43], and climate forecasting [44], it has not yet been applied in the field of optical communications.

BER values calculated from all of the above-described evaluation methods are normally plotted as a function of OSNR which is discussed in the next subsection.

4.7.1 Optical Signal-to-Noise Ratio (OSNR)

OSNR is a metric for the quality assessment of received signals that are corrupted by the ASE noise of EDFAs. OSNR is defined as the ratio of the average optical signal power to the average optical noise power. For a single EDFA with the output power P_{out} and the noise power N_{ASE}, OSNR is computed as [8]:

$$OSNR = \frac{P_{out}}{N_{ASE}} = \frac{P_{out}}{(NF \cdot G - 1)hf\Delta f} \tag{4.43}$$

where
NF is the noise figure
G is the amplifier gain
hf is the photon energy
Δf is the optical measurement bandwidth

When addressing an OSNR value, it is important to define an optical reference bandwidth for the calculation of OSNR. A bandwidth Δf of 12.5 GHz (or $\Delta\lambda$ = 0.1 nm) is the typical reference bandwidth for calculating OSNR values.

4.7.2 OSNR Penalty

OSNR penalty is obtained from the BER curves and determined at a particular BER. A value of the OSNR penalty is obtained by comparing the values of OSNR before and after the change of the parameters, which are under test, as given by

$$\text{OSNR\_Penalty} = 10\log\left(\frac{OSNR_{before}}{OSNR_{after}}\right) \tag{4.44}$$

4.7.3 Eye Opening (EO)

OSNR is a time-averaged indicator for the ratio of average optical signal power over average optical noise power. Hence, OSNR is used most effectively when noise is the main degrading factor to the system performance. However, as the OSNR metric becomes less accurate, the system degradation is due mainly to waveform distortions. These waveform distortions can originate either from an ISI problem caused by fiber CD and PMD, from fiber nonlinearities, or from the effects of narrowband optical/electrical filtering. In contrast, waveform distortions are taken into account by using the EO metric. The EO is determined from the difference between the "mark" and "space" levels. In addition, EOP is the penalty of an EO when comparing to a reference EO. This reference EO is usually obtained from a back-to-back configuration when signal waveforms are not distorted at all. The EOP is normally in log scale (dB) and given by

$$EOP = 10\log\left(\frac{EO_{ref}}{EO_{received}}\right) \tag{4.45}$$

EO and EOP metrics are useful for noise-free systems as they provide a good measure for pulse distortions. If noise is present, calculations of EO and EOP become less precise.

In addition, the accuracy of EO and EOP calculations relies on the sampling instance. Detected pulses are usually sampled in the middle of the eye diagrams where the EO is widest.

4.7.4 Conventional Evaluation Methods

4.7.4.1 Monte Carlo Method

BER in simulation experiments is computed as the ratio between the number of error occurrences (N_{error}) and the total number of transmitted data bits (N_{tot}):

$$BER = \frac{N_{error}}{N_{trans}} \tag{4.46}$$

The Monte Carlo method provides a precise BER calculation as it takes into account the effects that arise from all the impairment of the fiber. However, the Monte Carlo method requires a huge number of transmitted information bits to obtain low values of BER, thus leading to excessive computational time. A BER of 1e–9, which is considered as "error free" in fiber-optic communications, requires at least 1e–10 transmitted bits. Furthermore, a BER of up to 1e–12 is now becoming more common for modern high-capacity and high-speed digital photonic transmission systems. These huge numbers are difficult to handle for simulation experiments conducted by a personal computer at present. In addition, time-consuming operations such as FFT/IFFT while implementing the symmetrical SSFM also increase the computational time significantly.

However, the Monte Carlo method is still used effectively in simulation experiments because commercial optical transmission systems usually employ forward error correction (FEC) coding schemes to enhance significantly the system performance. Pre-FEC BERs can thus be as low as 2e–3 (the FEC limit), provided that no sign of long-burst errors is observed [22]. Figure 4.14 demonstrates significant improvements in

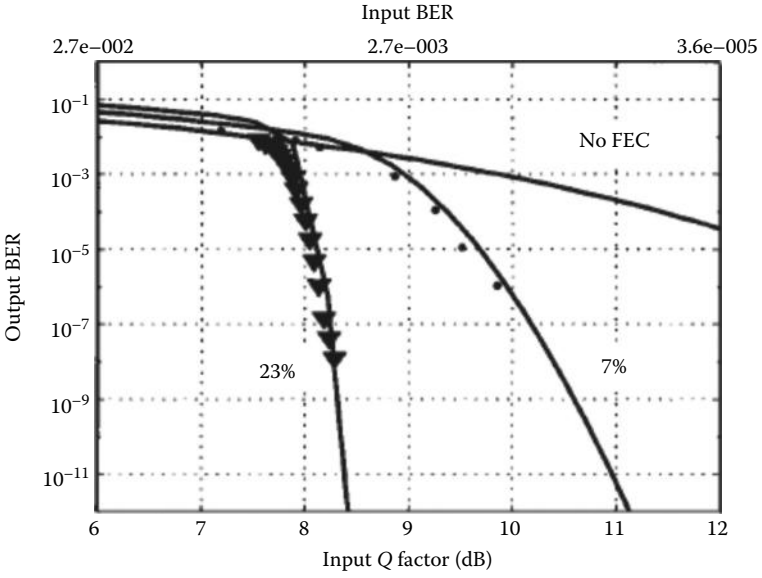

FIGURE 4.14
Demonstration of effectiveness of FEC schemes in improving the system performance.

the system performance by using FEC schemes: 7% single stage and 23% concatenated Reed–Solomon code [22].

With the current processing speed of contemporary personal computers, a BER of up to 1e−6 is of interest for simulation experiments. BERs calculated from the Monte Carlo method are usually taken as benchmarks for BER values computed by other methods.

4.7.4.2 Single Gaussian Statistical Method

This method implements a statistical process to calculate BER. It should be noted that signals are normally in voltage since photodiode induced currents are amplified by a transimpedance electrical amplifier. A particular voltage serves as a reference for distinguishing "0" and "1" levels, known as the threshold voltage (V_{th}). In addition, the received signals are sampled at a particular instance. As a result, based on this V_{th}, normalized histograms of received signals for "0" and "1" are obtained, thus leading to the achievement of the pdf. The pdf normally complies to a distribution such as Gaussian, Chi-square, and so on. The BER is calculated as [45]:

$$BER = P(\text{“1”})P(\text{“0”}|\text{“1”}) + P(\text{“0”})P(\text{“1”}|\text{“0”}) \tag{4.47}$$

where

P("1") is the probability that a bit "1" is sent
P("0"|"1") is the probability of error due to receiving "0" where actually "1" is sent
P("0") is the probability that "0" is sent
P("1"|"0") is the probability of error due to receiving "1" where actually "0" is sent

In the case of binary digital transmission, the probability of transmitting "0" or "1" is equal, that is, P("1") = P("0") = 1/2. P("0"|"1") and P("1"|"0") are calculated from integrating the overlap region of the pdf, which exceeds the threshold voltage.

A popular assumption is that the pdf of received electrical signals follows a Gaussian distribution. This enables a fast calculation for BER values by using the complementary error functions (erfc):

$$BER = \frac{1}{2}\left[erfc\left(\frac{|\mu_1 - V_{th}|}{\sqrt{2}\sigma_1} \right) + erfc\left(\frac{|\mu_0 - V_{th}|}{\sqrt{2}\sigma_0} \right) \right] \tag{4.48}$$

where μ_0, μ_1 and σ_0, σ_1 are means and variances of the Gaussian pdfs of "0" and "1" received signals, respectively.

Apart from BER, the quality (Q) factor is another common measure to assess the system's performance. Q values are calculated from μ_0, μ_1 and σ_0, σ_1 as follows:

$$Q = \frac{\mu_1 - \mu_0}{\sigma_1 - \sigma_0} \tag{4.49}$$

and Q factors are either in linear scale or in dB scale. The BER can be obtained from the Q factor by

$$BER = \frac{1}{2} erfc\left(\frac{Q}{\sqrt{2}} \right) \tag{4.50}$$

4.7.4.2.1 Improving Accuracy of Histograms

The pdfs of "0" and "1" received signals are determined from normalized histograms. The estimation of these normalized histograms affects the BER's accuracy considerably. Thus, a proper estimation for the value of the histograms is very important. A histogram is normally divided into a number of bins with the same bin width. With a sufficiently large number of transmitted bits (N_0), a good estimate for the width (W_{bin}) of each equally spaced histogram bin is given by $W_{bin} = \sqrt{N_0}$ [46].

4.7.5 Novel Statistical Methods

The single Gaussian distribution (the Q factor) method considers only the effects of noise corruption on detected signals while ignoring waveform distortions caused by fiber dispersion and fiber nonlinear effects. These distortions result in multi-peak and non-Gaussian pdfs (see Figure 4.15). Such pdfs cannot be correctly estimated by the conventional single Gaussian distribution method.

This issue is resolved by following two statistical methods: the MGD method based on the expectation maximization (EM) theorem and the GPD method based on the GEV theorem. The implementation of these methods is conducted in MATLAB. It should be noted that the conventional single Gaussian distribution method is a particular case of the MGD method.

4.7.5.1 Multivariate Gaussian Distributions (MGD) Method

One of the most popular applications of the EM theorem is to obtain parameters of mixed probability densities. This theorem is based on the fact that most of deterministic distributions can be considered as a superposition of multiple distributions. The probability distribution function $p(x|\Theta)$ for a set of received data can be expressed as the mixture of M different distributions [47]:

$$p(x|\Theta) = \sum_{i=1}^{M} w_i p_i(x|\theta_i); \quad \Theta = (w_1, \ldots, w_M, \theta_1, \ldots, \theta_M) \tag{4.51}$$

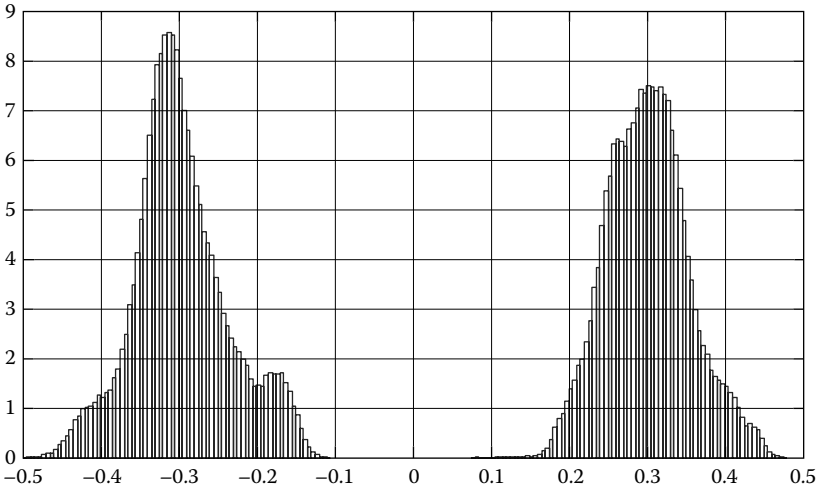

FIGURE 4.15
Demonstration of multi-peak and non-Gaussian distributions of received signals.

where $p_i(x|\theta_i)$ represents the pdf of each distribution in the mixture and each pdf has a weight w_i such that $\sum_{i=1}^{M} w_i = 1$. This weight indicates the probability of each pdf. When adopted for optical communications, the EM algorithm is implemented with a mixture of multiple Gaussian distributions. A critical stage in the MGD method, which affects the accuracy of BER calculations, is to estimate the number of Gaussian distributions for use in the mixture.

4.7.5.1.1 Selection of Number of Gaussian Distributions in MGD Method

The number of Gaussian distributions to be used is estimated by the number of peak and valley pairs in the first and second derivatives of the original data set. This is illustrated in Figure 4.16. This figure is based on the "Heming Lake Pike" example [49,50]. In this example, the data of five age groups give the lengths of 523 pikes and they were sampled in 1965 from Heming Lake, Manitoba, Canada. The components are heavily overlapped, and the resultant pdf is obtained with a mixture of five Gaussian distributions (refer to the top figure of Figure 4.16). The number of Gaussian distributions is then estimated from the number of peak and valley pairs in the first and second derivative curves of the original data set. As seen from Figure 4.16, the first derivative of the mixed pdf shows clearly four

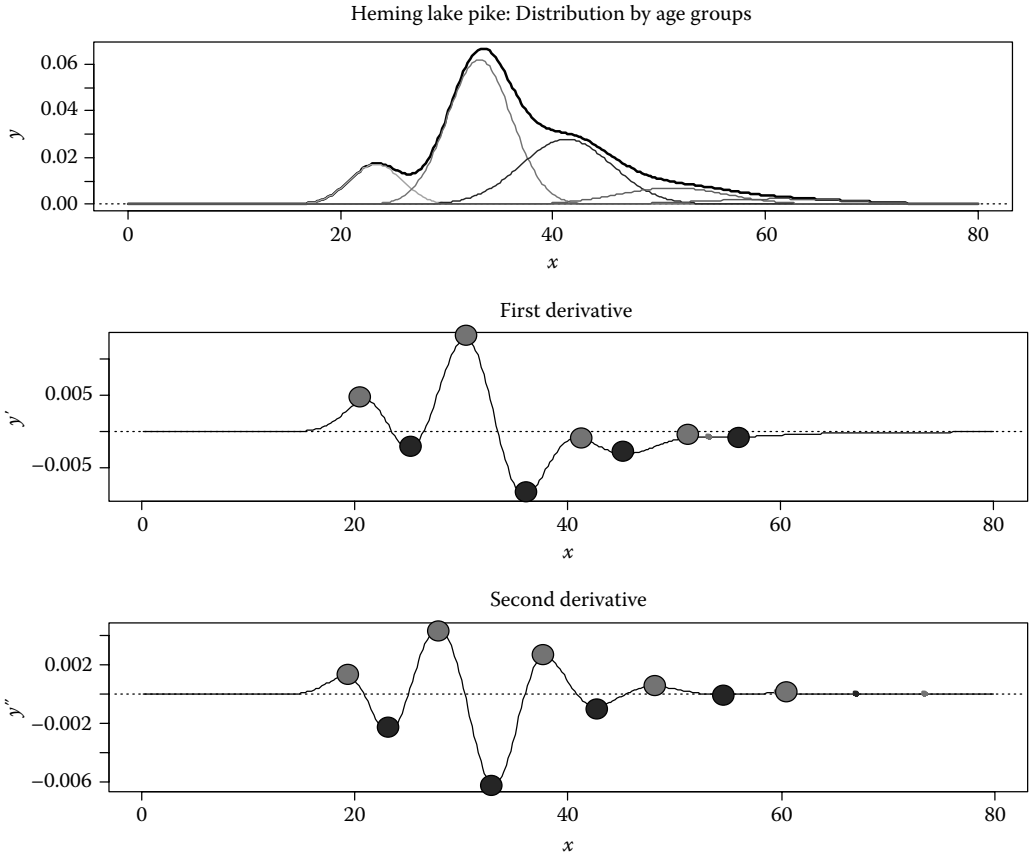

FIGURE 4.16
Process of estimating the number of Gaussian pdfs for MGD fitting based on the number of pairs of inflection peaks and valleys in the first and second derivative curves. (From Glynn, E.F., Mixtures of Gaussians, Stowers Institute for Medical Research, Kansas City, MO, February 2007.)

pairs of peaks (dark dots) and valleys (light dots), suggesting that there should be at least four Gaussian distributions contributing to the original pdf. However, by taking the second derivative, it is realized that there are actually up to five contributed Gaussian distributions.

4.7.5.1.2 Steps for Implementing MGD Method to Obtain BERs

- Obtain the pdf by the normalized histogram of received electrical signals.
- Estimate the number of Gaussian distributions (N_{Gaus}) used for fitting the pdf of the original data set. This selection is based on the guidelines explained in the earlier text.
- Implement the EM algorithm in MATLAB with the mixture of N_{Gaus} Gaussian distributions to calculate the values of mean, variance, and weight for each distribution.
- Calculate BERs by integrating the tails of these Gaussian distributions when these tails cross the threshold value.

4.7.5.2 Generalized Pareto Distribution (GPD) Method

GPD is a subset of the GEV theorem that consists of the GEV and GPD distributions. Both methods can be used to determine the probabilities of extreme events occurring in the tails of the data pdf. However, the key difference between these two methods is that GEV requires the whole signal pdf whereas GPD only needs the tail regions of the signal pdf. There is only one report on the application of the GEV theorem in fiber-optic communications [51]. However, this paper studies the GEV distribution for OOK optical system and only involves noise effects while neglecting the effects of fiber impairments. Moreover, similar to the single Gaussian distribution, the GEV distribution fails to estimate precisely the multi-peak pdf of received signals, which are mainly caused by waveform distortions.

When nonlinearity is the dominant shortcoming to the performance of optical transmission systems, received sample signals usually introduce a long-tailed pdf. This differs from the Gaussian pdf which has slow roll-off tails. As a result, the conventional BER based on the assumption of Gaussian pdf is no longer valid, and often underestimates the BER.

A wide range of analytical techniques have recently been studied for optical communications such as importance sampling, multi-canonical, and covariance matrix methods [52–55]. Although these techniques provide precise BERs, they are quite complicated. In contrast, the GPD method has been widely used in various fields [42,43] and it has become available in recent MATLAB versions (since MATLAB version 7.1). Thus, the GPD provides the potential of a fast and convenient method for evaluating the system performance in both practical and simulation scenarios.

The pdf for the GPD fitting function is defined as follows [56]:

$$y = f(x|k,\sigma,\theta) = \left(\frac{1}{\sigma}\right)\left(1 + k\frac{(x-\theta)}{\sigma}\right)^{-1-\frac{1}{k}} \tag{4.52}$$

$$\text{for } \theta < x \text{ when } k > 0 \text{ or for } \theta < x < \frac{-\sigma}{k} k < 0$$

where

k is the shape parameter ($k \neq 0$)
σ is the scale parameter
θ is the threshold parameter

Key constraints for Equation 4.52 are described as follows

- when $k > 0$ and $\theta < x$ there is no upper bound for x.
- when $k < 0$ and $\theta < x < -\sigma/k$: zero probability for the case $x > -\sigma/k$.
- when $k = 0$, (4.52) turns to

$$y = f(x|0, \sigma, \theta) = \left(\frac{1}{\sigma}\right) e^{-\frac{(x-\theta)}{\sigma}} \quad \text{for } \theta < x \tag{4.53}$$

- when $k = 0$ and $\theta = 0$, the GPD is equivalent to the exponential distribution.
- when $k > 0$ and $\theta = \sigma$, the GPD is equivalent to the Pareto distribution.

Accordingly, the GPD method has three basic classes of the underlying distributions:

- Distributions whose tails decrease exponentially, such as the normal distribution, have shape parameters equal to zero.
- Distributions with tails decreasing as a polynomial, such as Student's t-distribution lead to a positive shape parameter.
- Distributions having finite tails, such as the beta distribution, have negative shape parameters.

The first step and also the most critical step affecting the accuracy of BER calculations is to find the precise threshold for the GPD fitting function.

4.7.5.2.1 Selection of GPD Threshold

The threshold value (V_{GPD}) used for the GPD fitting function indicates the start of the GPD. There have been several suggested guidelines to aid the selection of the GPD threshold [57–59]. However, they are either too complicated or not applicable in optical communications.

In this research, simple guidelines to determine the GPD threshold value are proposed. These guidelines are based on the observation that extreme values in the long tail region normally comply with a slow exponential slope compared to a faster decaying slope when they are close to the peak of the distribution. The interception region of these two slopes gives a good estimate for the GPD threshold value (see Figure 4.17).

The accuracy in the selection of V_{GPD} is evaluated by using the cumulative density function (cdf) and the quantile–quantile plot (Q–Q plot). If there is a high correlation between the distribution of the tail of the original data set and the implemented GPD function, there should be a good fit between the empirical cdf of the original data set and the GPD-fitted cdf (see Figure 4.18). Furthermore, this high correlation is also reflected in a linear trend of Q–Q plot, as observed in Figure 4.19.

Figures 4.20 and 4.21 demonstrate the inaccuracy of the GPD method caused by an improper selection of V_{GPD}. Figure 4.20 shows the discrepancy between the GPD-fitted cdf and the empirical cdf of data while Figure 4.21 clearly displays a nonlinear trend of the Q–Q plot instead of a linear trend.

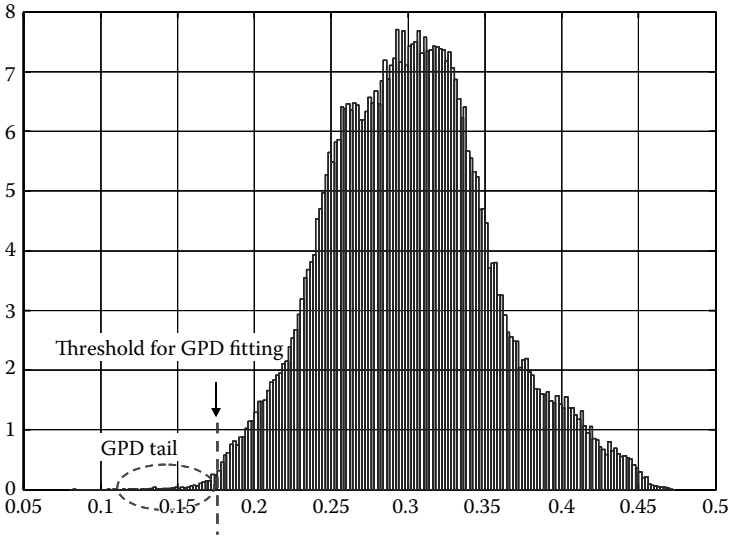

FIGURE 4.17
Selection of threshold for GPD fitting.

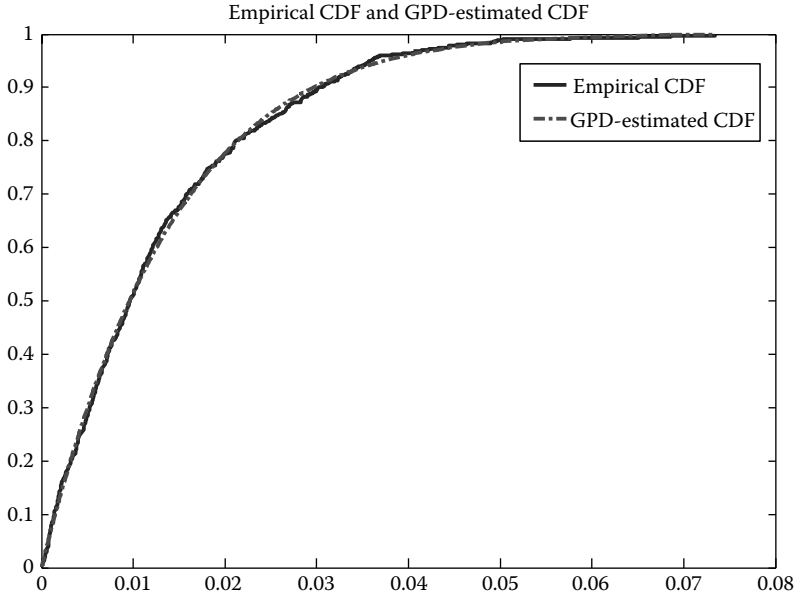

FIGURE 4.18
Demonstration of high correlation between GPD fitted and empirical cdf.

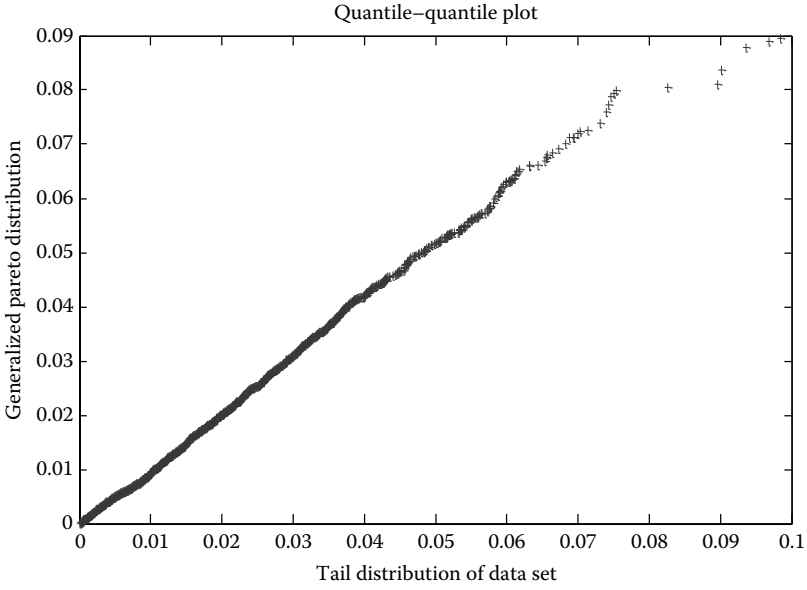

FIGURE 4.19
Q–Q plot of a high correlation GPD fitting function.

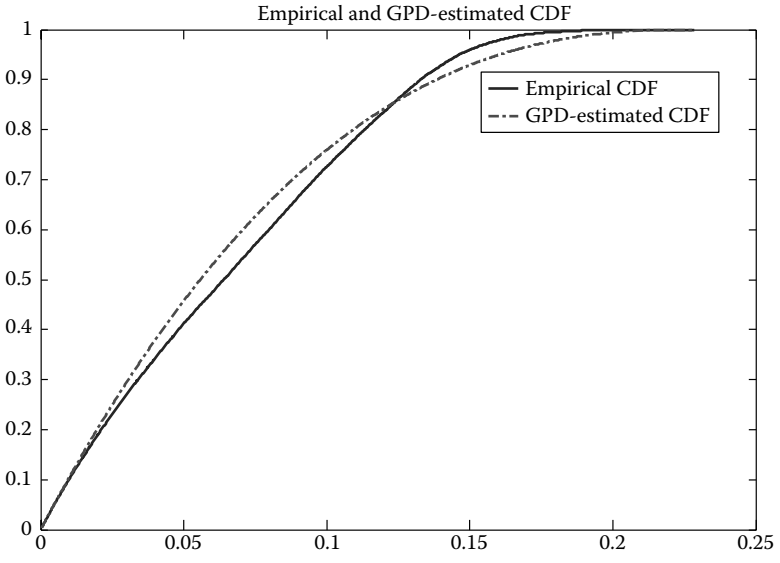

FIGURE 4.20
Demonstration of incompliance between the empirical cdf and the GPD-fitted cdf due to improper selection of V_{GPD}.

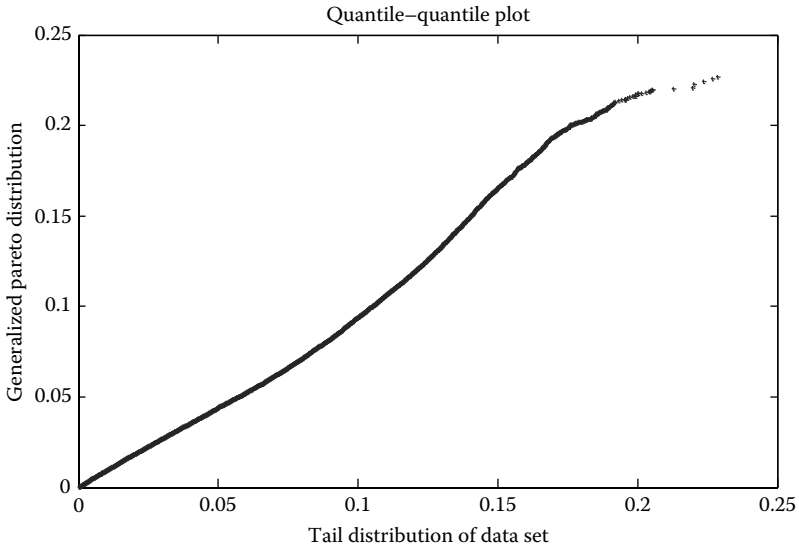

FIGURE 4.21
Nonlinear trend in the Q–Q plot caused by an improper selection of V_{GPD}.

4.8 MATLAB® Simulink® Modeling Platform

4.8.1 General Model

A simulation package can be developed using MATLAB Simulink platform for modeling advanced digital optical transmission systems. The modeling platform developed in this research mainly aims to investigate and verify benefits and shortcomings of advanced modulation formats used in fiber-optic communications. Thus, single-channel optical transmission systems are of main interest in this research. The MATLAB Simulink modeling platform has several advantages as follows:

- The simulator provides toolboxes and block-sets for setting up any complicated transmission configurations. In addition, the initialization process for all key parameters of the subsystem components can be automatically conducted at the start of any simulation. Furthermore, the initialization file is written in a separate MATLAB file; hence, the simulation parameters can be modified easily.
- The signal monitoring can be carried out easily at any point along the propagation path in a simulation with simple plug-and-see monitoring scopes provided by Simulink block-sets.
- Numerical data can be easily stored for post processing in MATLAB. This offers a complete package for generating and processing numerical data for the achievement of BER.

A generic arrangement of an optical fiber transmission system is shown in Figure 4.22. Each major block in this figure represents a subsystem of the transmission model including optical transmitter, fibers spans and propagation model and optical receiver and signal monitoring as shown in Figures 4.23 through 4.25. The reverse is true. That means when the model

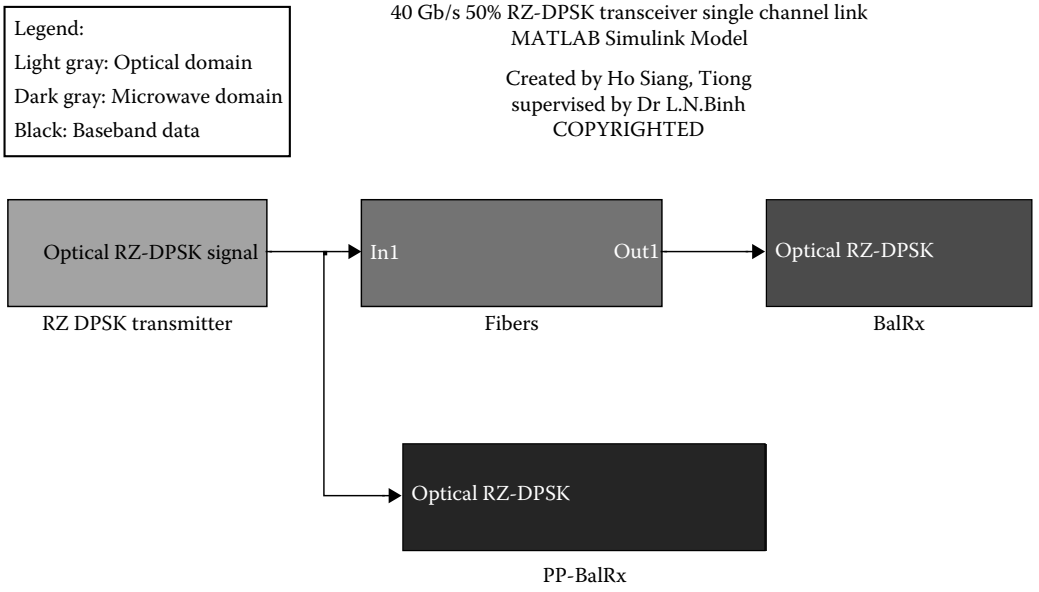

FIGURE 4.22
Overview of an optical fiber transmission system consisting of an optical transmitter generating RZ-DQPSK modulation format, a fiber propagation model including optical amplifiers and dispersion compensating fibers, an optical receiver at the transmission end, and one monitoring at the output of the transmitter.

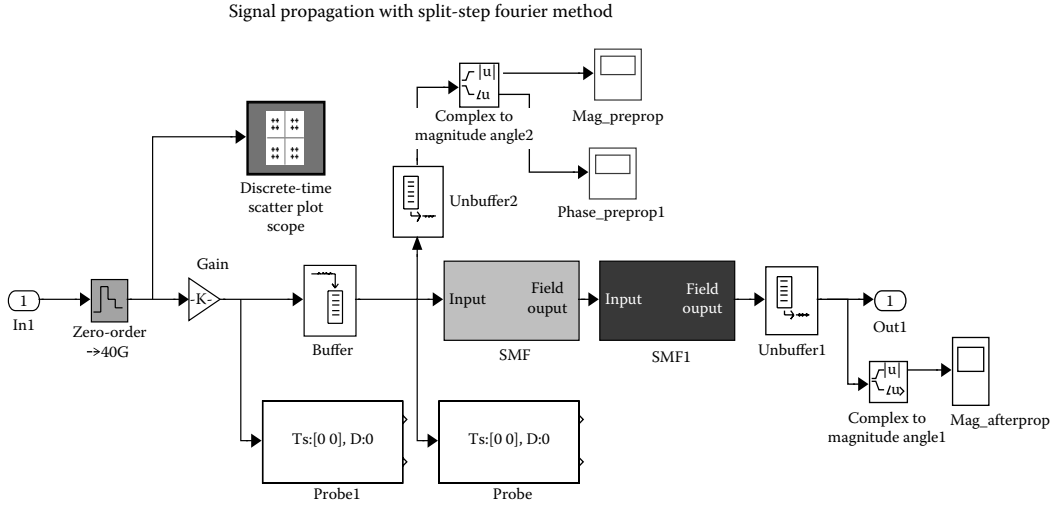

FIGURE 4.23
Fiber propagation model with transmission and dispersion compensating fiber without optical amplifiers.

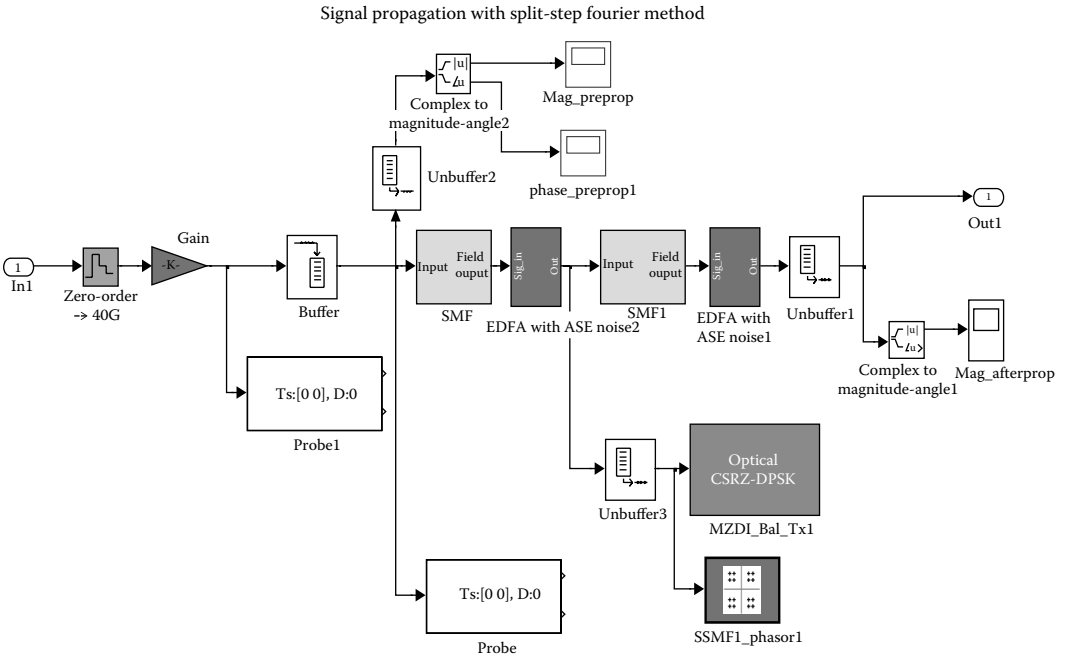

FIGURE 4.24
Fiber propagation model with transmission and dispersion compensating fiber with optical amplifiers integrated with both transmission and dispersion compensating fibers.

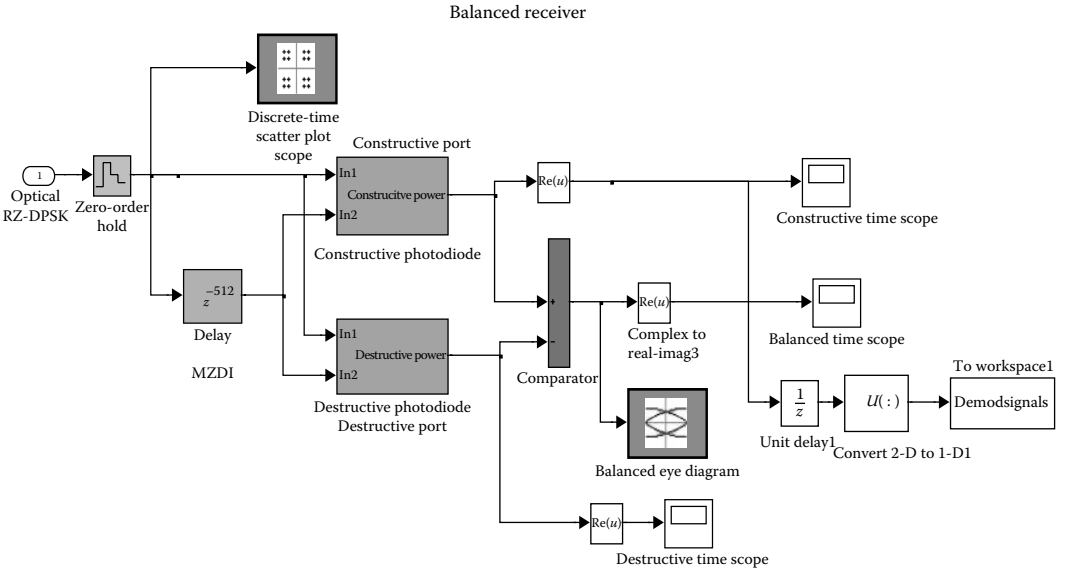

FIGURE 4.25
Balanced optical receiver with a phase comparison at the input to obtain constructive and destructive interfered modes for identification of the "1" and "0" of the phase difference of consecutive bits in differential coded sequence.

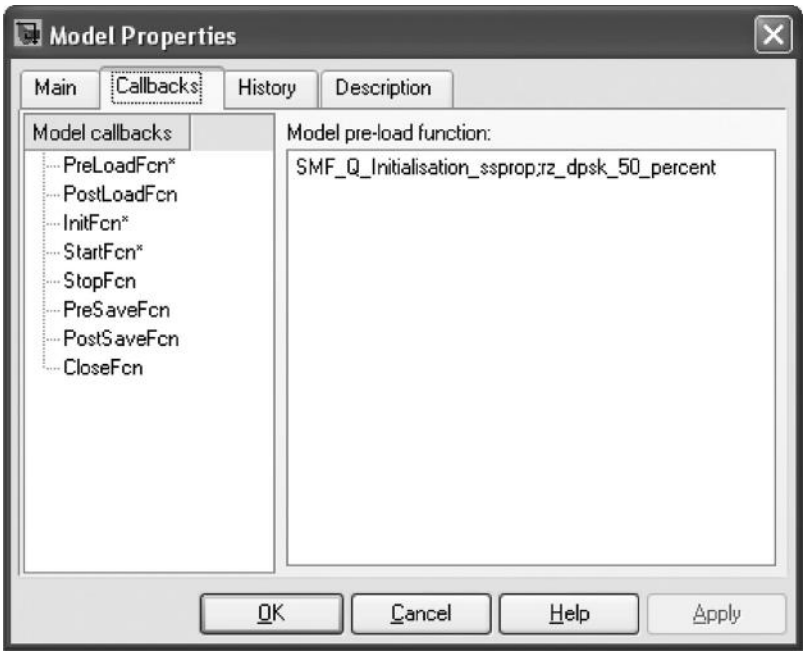

FIGURE 4.26
Model property set up for automatic transfer of parameters in initialization file to Simulink® model.

of each subsystem development is complete one can combine and form a subsystem using "create sub-system" command in Simulink. The data inputs can be loaded to the Simulink model by using an initial initialization file as shown in the next subsection. This initialization file must be included in the Simulink model using the "Model Property" and the "Call Back" in the PreLoadFcn PostLoadFcn and InitFcn as shown in Figure 4.26. SSFM files or any MATLAB files required for the split-step Fourier propagation along fibers or for any blocks of the Simulink model can also be included here.

4.8.2 Initialization File

```
% Initialization file for data and parameters %transfer to Simulink model
% This file also includes parameters required for solving the NLSE for
% pulse propagation in an optical fiber using the split-step
% Fourier given in: GP. Agrawal,"Nonlinear Fiber Optics", 2nd ed., AP
% Agrawal, 1995, Chapter 2.
%
% The following effects are included in the model: group
% velocity dispersion (GVD), GVD-slope / third-order
% dispersion, loss, and self-phase modulation (n2).  The core
% routine is implementing the split-step propagation
clear all
close all
% CONSTANTS
c = 3e8;                        % speed of light (m/s)
% NUMERICAL PARAMETERS
numbitspersymbol = 1;
P0 = 0.003162;                  % peak power (W)
```

```
FWHM = 25                          % pulse width FWHM (ps)
%halfwidth = FWHM/1.6651           % for Gaussian pulse
halfwidth = FWHM                   % for square pulse

bitrate = 1/halfwidth;             % THz
baudrate = bitrate/numbitspersymbol;
signalbandwidth = baudrate;
%%%%%%%%%%%%%%%%%%%%%%%%%%%%%%%%
PRBSlength = 2^5;
% Make sure : FFT time window (=nt*dt) = PRBSlength * FWHM...
% FFTlength nt = PRBSlength/block * numbersamples/bit = PRBSlength *
(FWHM/dt)

% num_samplesperbit = FWHM/dt  should be about 8 - 16 samples/bit
num_samplesperbit = 64;            % should be 2^n
dt = FWHM/num_samplesperbit ;  % sampling time(ps); % time step (ps)
nt = PRBSlength*num_samplesperbit;      % FFT length

dz = 0.1;                          % distance step-size (km)
nz = 10;                           % number of z-steps
maxiter = 20;                      % max # of iterations
tol = 1e-5;                        % error tolerance

% OPTICAL PARAMETERS

nonlinearthreshold = 0.005; % 5mW -- % Nonlinear Threshold Peak Power for
silica core fiber

lambda = 1550;
lambda_carrier = 14648.4375;   % wavelength (nm)with Level 4 group the
carrier freq is scaled down to 500G or 200 GHz
optical_carrier = c/(lambda_carrier*1e-9);     %carrier freq
%dBperkm = 0.2;                    % loss (dB/km)
alpha_indB = 0.001;                % loss (dB/km)
D = 17;                            % NZDSF GVD (ps/nm.km); if anomalous
dispersion(for compensation),D is negative
%D = 17;                           % SSMF GVD (ps/nm.km); if anomalous
dispersion(for compensation),D is negative
beta3 = 0.3;                       % GVD slope (ps^3/km)

ng = 1.46;                         % group index
n2 = 2.6e-20;                      % nonlinear index (m^2/W)
Aeff = 47;                         % effective area (um^2)

% CALCULATED QUANTITIES

T = nt*dt;   % FFT window size (ps) -Agrawal: should be about 10-20 times
of the pulse width
alpha_loss = log(10)*alpha_indB/10;     % alpha (1/km)
beta2 = -1000*D*lambda^2/(2*π*c);       % beta2 (ps^2/km);
%-----------------------------------------------------
% beta 3 can be calculated from the Slope Dispersion (S) as follows:]
% Slope Dispersion S = 0.092;    % ps/(nm^2.km)
```

```
% beta31 = (S - (4*π*c./lambda.^3))./(2*π*c./lambda.^2)
%-----------------------------------------------------
gamma = 2e24*π*n2/(lambda*Aeff);  % nonlinearity coef (km^-1.W^-1)
t = ((1:nt)'-(nt+1)/2)*dt; % vector of t values (ps)
t1 = [(-nt/2+1:0)]'*dt;    % vector of t values (ps)
t2 = [(1:nt/2)]'*dt;       % vector of t values (ps)

w = 2*π*[(0:nt/2-1),(-nt/2:-1)]'/T;      % vector of w values (rad/ps)
v = 1000*[(0:nt/2-1),(-nt/2:-1)]'/T;     % vector of v values (GHz)
vs = fftshift(v);   % swap halves for plotting
v_tmp = 1000*[(-nt/2:nt/2-1)]'/T;

% STARTING FIELD

L = nz*dz

Lnl = 1/(P0*gamma)                % nonlinear length (km)
Ld = halfwidth^2/abs(beta2)       % dispersion length (km)
N = sqrt(abs(Ld./Lnl))            % governing the which one is dominating:
                                  dispersion or Non-linearities
ratio_LandLd = L/Ld               % if L << Ld --> NO Dispersion Effect
ratio_LandLnl = L/Lnl             % if L << Lnl --> NO Nonlinear Effect

% Monitor the broadening of the pulse with relative the Dispersion Length
% Calculate the expected pulsewidth of the output pulse
% Eq 3.2.10 in Agrawal "Nonlinear Fiber Optics" 2001 pp67

FWHM_new = FWHM*sqrt(1 + (L/Ld)^2);

% N<<1 --> GVD ; N >>1 ---> SPM
Leff = (1 - exp(-alpha_loss*L))/alpha_loss;
expected_normPout = exp(-alpha_loss*2*L);
NlnPhaseshiftmax = gamma*P0*Leff ;

betap = [0 0 beta2 beta3]';


% Constants for ASE of EDFA
% PSD of ASE: N(at carrier freq) = 2*h*fc*nsp*(G-1) with nsp = Noise
% Figure/2 (assume saturated gain)
%**************** Standdard Constant ******************************
h = 6.626068e-34;       %Plank's Constant
%******************************************
```

4.9 OCSS©: A MATLAB® Simulation Platform

4.9.1 Overview

The primary objective of this section is to outline a computer simulation platform based strongly on experimental and empirical results, for ultra-long high-speed optical fiber transmission systems. All programs are provided in m-files in the MATLAB platform

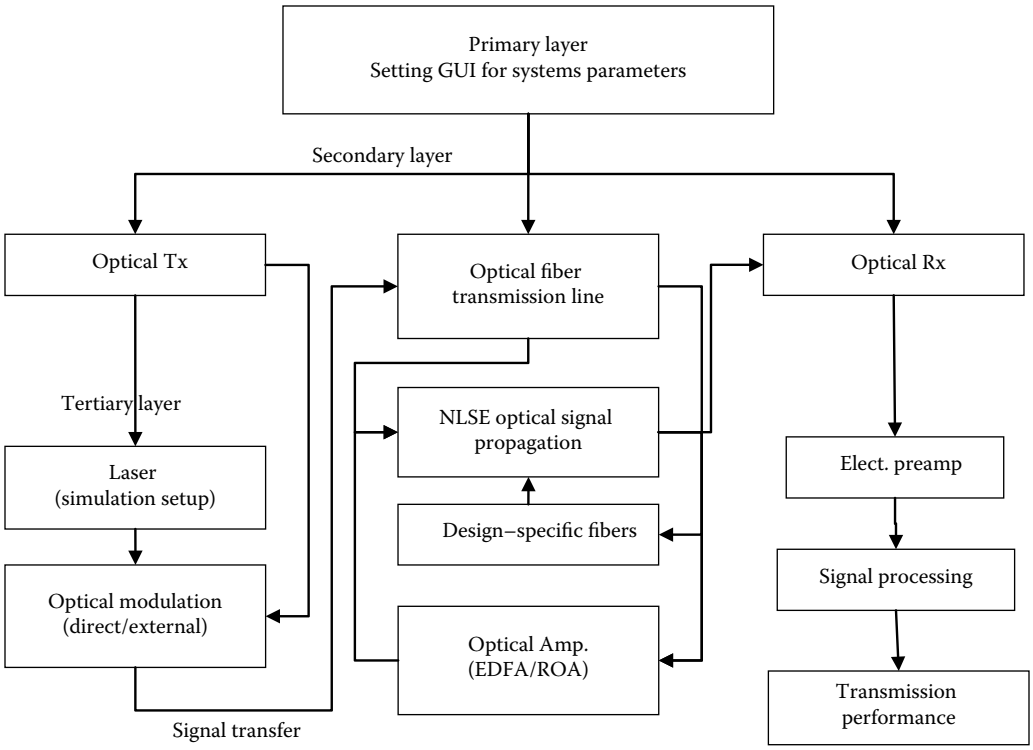

FIGURE 4.27
Structure flow of **OCSS**© simulation platform of all MATLAB® *.m modules and files.

whose structuring schematic flow is shown in Figure 4.27. There are three layers of the simulation platform. Layer 1 as the primary layer outlines the setting up of all graphic units for entering system parameters of the simulation system to be conducted. Layer 2 (secondary layer) then sets the simulation parameters for each subsystem of the simulation system such as the transmitters, the propagation medium (the fiber transmission line), the optical amplification modules, and passes these parameters into the propagation submodule, the optical reception devices, and submodules for performance evaluation.

Unlike the MATLAB Simulink as described in previous sections of this chapter, in the Simulink model an initial file is used to specify all parameters of the whole platform. The **OCSS**© platform given in this section illustrates how to set up the three-layered platform and ways to set up parameters in the submodules.

Optical signal transmitters, optical fibers, and receiver modules are modeled in modular form so that they can be coupled and integrated to form an optical fiber communication system depending on the user's choice. The effectiveness of the simulation package is demonstrated by analysis and investigation of the optical characteristics of each individual optical component and by measuring the performance of real optical systems. These simulated results are confirmed by experimental systems.

The simulation techniques that are presented in the chapters of the book which are designed as modular structures, that is, they are designed to operate independently of each other but can be integrated to form a part or complete optical fiber communication system. Programs and their logical flowcharts are shown to assist users in following and understanding the numerical structures.

Equalizations and compensation techniques are used to extend the IM/DD optical transmission distance to more than a few hundred kilometers using standard single-mode optical fibers and lasers with direct modulation.

We also give, as an example, the optical transmission systems employing optical solitons of both bright and dark soliton types. We have described in detail the theoretical techniques using inverse scattering method where the results obtained are compared with numerical simulation using the time-dependent beam propagation technique.

4.9.2 System Design Using Software Simulation

Researchers and system designers can spend millions of dollars investing in experimental hardware in order to simulate multi-wavelength long-haul fiber transmission systems. One important way to reduce the experimenting cost is to employ simulation techniques to predict system performance prior to any hardware implementation. One would then be able to implement the hardware once the simulated results indicate accurate and logical functioning of the system or network. In this way, we would avoid wasting our resources in unnecessary mistakes or errors, which could contribute to failures.

In fiber optic communication engineering and technology, especially for bit rates reaching multi-Giga-bits/s, most of the experimental hardware are extremely expensive, and therefore, it is much simpler if simulation platforms can be developed to accurately predict the functioning of the transmission systems under considerations. Furthermore since the 1990s, high performance and inexpensive PC-based computer and processing systems are available in most of research and tertiary educational institutions. They are capable of handling massive numerical calculations with random access memory of the order of more than 100G RAM and even multi-core processors and image processing units.

The low loss of optical silica fibers in the two windows of 1300 and 1550 nm allows us to transmit optical information signals over extremely long distances at high bit rate. Several recent experimental demonstrations [60] have reported that optical information can be transmitted over optically amplified multi-span link of more than 4000 km at a bit rate of 100 Gb/s with dispersion compensation incorporated or by coherent detection and signal processing in the digital domain.

Thus, an accurate and detailed theoretical simulation based on experimental results must be developed to study these ultra-long and high-speed optical communication systems.

The primary objective, therefore, of this text is to present the development of a comprehensive simulation software package for a desktop computing environment to accurately simulate optical fiber communication systems. The developed simulation platform is called as "Optical Communication Systems Simulator or **OCSS©**," and is introduced in the following sections.

4.9.3 Optical Communication Systems Simulator: OCSS© Simulation Platform

Optical Communication Systems Simulator (**OCSS©**) is a complete computer simulation package that is developed. The purpose of this package is to design and predict the performance of ultra-long high-speed optical fiber communication systems. **OCSS©** has been developed through an interdisciplinary approach using an appropriate blend of communication analysis, computer science, numerical methods, and digital signal processing (DSP). **OCSS©** is developed by using an existing software package—MATLAB for Windows. MATLAB is a powerful tool for high-performance numerical computation and visualization. It has a especially built-in *signal processing* toolbox and other embedded objects, which

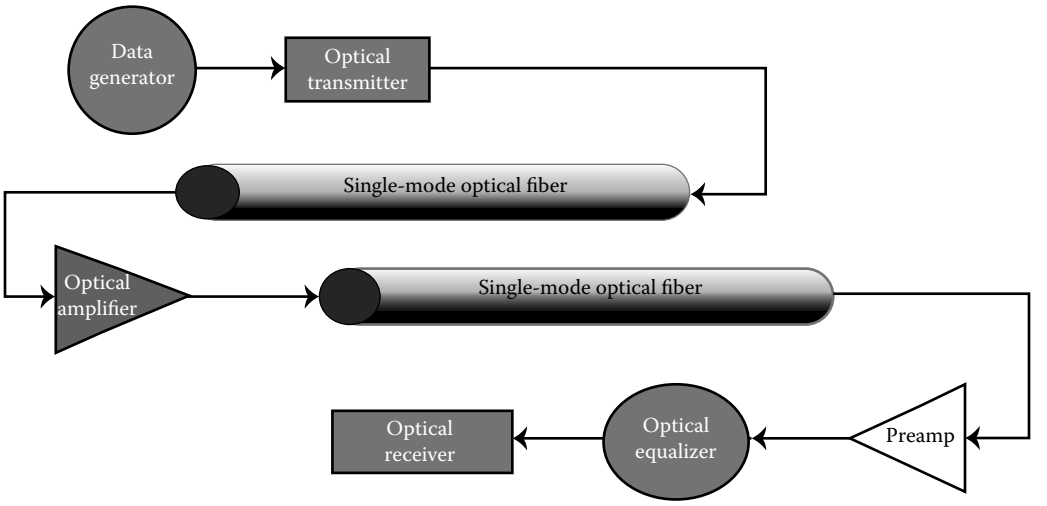

FIGURE 4.28
Block diagram of an optical fiber communication system consisting of an optical transmitter modulated by a data generator, the optical transmission medium, the optical fiber integrated with in-line optical amplifiers, the optical receiver including an electronic or optical amplifier preamplification device, main amplifier, and the data transponder.

can handle most of the communication computation and analysis. Moreover, MATLAB is richly equipped with various mathematical functions that can be used easily.

OCSS© can be used to simulate a large variety of signal processing and communications systems. Some typical applications include modulation and coding, system performance, design, and customization of optical laser source, verification of optical fiber channel specifications, signal equalization and detection, device modeling, and output waveform for each optical subsystems.

Fundamental to developing this simulation package are the concepts of signal sampling and linear systems [61]. This has become familiar to most electrical engineers and many good textbooks in DSP are available. The multitude of processes being modeled are digital signal generation, filtering, and translational frequency, which make fixed step size numerical computation very desirable. This, combined with small simulation step size and, therefore, high accuracy results makes DSP approaches most attractive.

The block diagram of an end-to-end SMF communication system is shown in Figure 4.28. We have developed the simulation package in modular forms so that it can be integrated easily into a complete system. Moreover, new optical components can be inserted easily into the system once the system has been developed. Three main modules, the transmitter module, optical fiber module, and receiver module, all of which are extremely essential for an optical fiber system have been successfully modeled. The flowcharts for the developed modules of the advanced fiber optic communication are also given.

4.9.4 Transmitter Module

The main role of an optical transmitter is to modulate and convert the incoming electrical information signal into the optical domain. Single-mode semiconductor laser is used as an optical transmitting source as it can produce a narrow pulse for a high-speed modulating

system in the gigahertz range. Before the signal is being modulated by the laser, the signal encoder is needed to encode the binary data using either nonreturn zero (NRZ), return zero (RZ), or Manchester (MAN) line coding. We design laser sources with high-speed modulation capability for high-performance optical transmitters. The dynamic response of a laser is governed by the laser rate equations. We look into the various aspects of the characteristic of a laser source. We investigate and analyze the effect of each parameter in laser rate equations on the behavior of a laser. By knowing these effects, we could design our laser source such that it is stable and the chirping effect is negligible.

We have designed and modeled five types of laser sources, which are the 1550nm special laser source, 1550 nm constricted mesa, 1550 nm *DFB* laser, 1300 nm *DFB* laser, and 1300 *FP* laser. In a real system, we need to consider Langevin noise in the laser modulation. Laser chirp is discussed and suggestions are made to overcome the chirp effect. The results of the modulated optical output waveform are compared and found to be comparable with the results published in Ref. [62].

4.9.5 Optical Fiber Module

Optical signals emitted from the laser source are launched into the optical transmission medium, the SMF. Our task is to model an ultra-long high-speed optical communication system, and therefore, it is essential to employ the single-mode fiber in order to overcome various unwanted effects such as dispersion due to different guided modes. Further in this chapter, a design technique for a single-mode fiber with low or near zero dispersion for long-distance transmission has been developed and demonstrated to be an efficient and accurate facility.

For the current state-of-art fiber, the two main fiber windows are the 1300 and 1550 nm, which have intrinsic attenuation loss of 0.3 dB/km down to 0.1 dB/km. Unfortunately at 1550 nm wavelength, the standard optical fiber exhibits a dispersion of at least 17 ps/(nm · km). To transmit optical signals over 200 km at 10 Gb/s, a dispersion factor of 0.5 ps/(nm · km) or better is needed. It is therefore required to design an optical fiber whose dispersion must be close to zero at this wavelength. This type of fiber is usually termed as dispersion-shifted optical fiber.

For high-performance telecommunication systems, the utility of the transmission channels needs to be maximized and therefore, wavelength division multiplexing (WDM) is introduced. Thus, we design a dispersion-flattened triple-clad fiber to tailor to the needs of *WDM* systems which require a low-fiber dispersion profile over a range of operating wavelengths. Because of the intrinsic attenuation loss of the fiber, optical amplifiers may be included in between the optical fibers if the transmitted signal is weak for long-distance transmission. By carefully designing the core radius, the core and cladding refractive index, we achieved the required fiber performance for long-haul high-speed communication channels. Thus, we have developed an algorithm to design the triple-clad optical fiber by analyzing the effect of the radius and the refractive index profiles of the core, first cladding, second cladding, and outer cladding.

4.9.6 Receiver Module

The receiver system is our final and yet complicated module modeled in the **OCSS**© package. The incoming optical signal needs to be detected and converted back into an electrical signal. Thus, we have modeled *PIN* and *APD* photodiodes with high quantum efficiency and high sensitivity in the 1300 and 1550 nm transmission windows. The converted

electrical signal may not necessarily be large because of the power budget of the transmission system. Thus, the signal needs to be amplified by a preamplifier. We have designed and modeled five types of preamplifiers which are the *FET* high impedance, *FET* trans impedance, *BJT* high impedance, *BJT* trans impedance, and *HEMT*-matched noise network. Noises such as shot noise, thermal noise, photodiode dark current, surface leakage current, and channel resistance noise are modeled and included in the receiver modeling because our task is to model a real practical optical receiver system.

HEMT-matched noise network preamplifier is especially modeled for low-noise broadband communication receiver. A third-order circuit is designed by Park using a noise figure concept [63], and this circuit is integrated into our system to match the noise of the receiver. As the name implies, *HEMT* (high-electron mobility transistor) is used for high-frequency amplification. Thus, this design could overcome the system performance limited by the noise factors.

The limited bandwidth is a critical problem for a high bit rate receiver system. Thus, we have designed 5 and 10 GHz electronic equalizers to enhance the system bandwidth as well as to reduce the pulse broadening effect of the pulse due to transmission in the optical fiber. The signal is further processed and amplified by the post amplifier to maintain a sufficiently high signal level for data recovery in the signal decoder submodule.

Finally, the integrated **OCSS**© software package offers an user-friendly simulation environment. All transactions between the user and the computer are done in display menus with the help of a computer mouse. "Help information" and "print facilities" are available in the menus. At the end of each modular subsystem, **OCSS**© provides the facilities to view the output waveforms, analysis results, and so on.

4.9.7 System Simulation

Once we have completed the modeling of the optical modules, we can simulate the optical transmission system as a practical link. Design of transoceanic or long-distance optical fiber cable links has attracted great attention in this decade. Thus, we demonstrate the use of **OCSS**© to obtain results for a real practical system.

We have simulated the transoceanic *TPC*-5 optical fiber cable link from the *USA* to Japan for about 9000 km transmission distance using the *WDM* system.

4.9.8 Equalized Optical Communications Systems

In Chapter 6, we present the foundation of equalization and compensation techniques for extending the high-bit-rate optical transmission systems to the maximum capacity. The equalized and compensated systems are proven to be able to recover the "eye closed" pulses to open thus extending the transmission distance to a remarkable record.

4.9.9 Soliton Optical Communications Systems

Optical solitons play a major part in the transoceanic communications systems because they preserve energy during transmission along optical fibers. We present the use of optical solitons in bright "positive logic" and dark for "negative logic" in optical communication systems. We can show that the transmission distance can be extended beyond the ten thousand(s) kilometers range with a bit rate higher than 10 Gb/s.

The generators and detectors of dark optical solitons are presented in Chapter 8 to complete the study of optical solitons for ultra-high-speed and ultra-long optical communication systems.

4.9.10 Remarks

The principal objective of this book is to develop a new simulation package (**OCSS©**) for ultra-long high-speed optical fiber communication systems. This package, as a design tool, enables us to predict and analyze the results of a real practical system and hence, it determines the best solution and yet a cost-effective system implementation. In summary, we have discussed the following:

- A new development of a comprehensive simulation package (**OCSS©**) for ultra-long high-speed optical fiber communication systems
- Analysis of the effect of parameters in the laser rate equations on the dynamic response or behavior of the single-mode laser source
- An algorithm developed to generate a set of complete waveguide dispersion parameter curves to simulate the dispersion flattening effect of the triple-clad optical fiber. This is the most advanced modeling and design for optical fibers.
- An analysis of the effects of the seven parameters of triple-clad optical fiber on the characteristic of the total dispersion
- The first computer simulation of the low-noise broadband *HEMT*-matched noise network preamplifier
- Equalizations schemes for extending the optical transmission distance for "standard" optical fiber communications systems and dispersion-shifted optical fiber–based systems. Optical dispersion schemes are also included using dispersion management schemes.
- Optical solitons transmission using the equalization of the GVD of light waves of different wavelengths in a dispersion-shifted optical fiber and optical amplifiers to compensate for the optical transmission loss. Both bright and dark solitons systems are modeled.

4.10 Concluding Remarks

This chapter presented an overview of modeling of critical subsystem components of a digital photonic transmission system, starting from the optical transmitter, onto the generic properties of optical fibers as a transmission medium, and to the optical receiver. Detailed descriptions of the fiber impairments including CD, PMD, and Kerr-effect nonlinearities are provided. Moreover, the symmetrical SSFM is optimized to reduce the computational time and mitigate artificial errors induced from the windowing effect of FFT/IFFT. The modeling of ASE noise of optical amplifiers and electronic noises of the receiver are also discussed.

Apart from the conventional evaluation methods such as Monte Carlo and single Gaussian distribution methods, two statistical methods have been adopted for novel application in optical communications. These are the MGD method implementing the EM theorem and the GPD method based on the GEV theorem. The guidelines for optimizing the accuracy of these two methods were provided. These methods offer fast processing techniques to obtain BER values. Last but not least, a MATLAB Simulink modeling model has been developed for advanced digital photonic transmission systems. These models are provided in the chapters. The Simulink platform takes advantages of the user-friendly MATLAB Simulink, thus making it easy for further development.

Samples of simulation platforms for both Simulink and the m-file can be downloaded from CRC Press websites provided that readers can provide evidence of purchase of the original book. These samples can only provide an initial platform for further development of the simulators. Readers must not assume that these platforms provide all features of optical transmission systems as the optical transmission technology has been evolving very fast over time. For example, the long-haul transmission systems are now sufficient to provide the transport medium backbone for optical networks, but the access and metropolitan optical networks need extensive development. Thus, short-haul and low-cost optical transport networks need intensive attention. Thus, the simulation platforms need to be developed further for such environments in which wavelength selective switches (WSS) must be modeled as well as optical filters for muxes and demuxes for network infrastructure. A flexible bandwidth and nonuniform wavelength grid will emerge as the new transport technology for massive Tera-bits/s communication networks.

We must also note that in the DSP modules are not included in these sampled platforms but can be easily incorporated using several DSP modules available in MATLAB Simulink DSP tool boxes. Coherent and DSP-based reception systems provide for the transmission of 100G, 400G, and Tbps channels over hundreds of kilometers of uncompensated fiber transmission lines.

In the chapters of this book, MATLAB files for submodules are referred to from time to time and listed in the Appendices. The source codes can be found in the folders downloadable from CRC Press.

References

1. S. Ten—Corning Inc., Advanced fibers for submarine and long-haul applications, in *Proceedings of IEEE LEOS'04*, Rio Grande, PR, paper WJ2, 2004; S. Ten—Corning Inc., Advanced fibers for submarine networks, in *Proceedings of SubOptic'07*, (invited paper), Baltimore, MD, 2007.
2. S. Ten—Corning Inc., Advanced fibers for submarine networks, in *Proceedings of SubOptic'07*, (invited paper), Baltimore, MD, 2007.
3. G.P. Agrawal, *Nonlinear Fiber Optics*, 3rd ed., Academic Press, San Diego, CA, 2001.
4. K.P. Ho, *Phase-Modulated Optical Communication Systems*, Springer, New York, 2005.
5. A.H. Gnauck and P.J. Winzer, Optical phase-shift-keyed transmission, *IEEE Journal of Lightwave Technology*, 23(1), 115–130, 2005.
6. H. Ghafouri-Shiraz, *Distributed Feedback Laser Diodes*, John Wiley & Sons, New York, 1995.
7. G. Morthier and P. Vankwikelberge, *Handbook of Distributed Feedback Laser Diodes*, Artech House, Norwood, MA, 1995.
8. G.P. Agrawal, *Fiber-Optic Communication Systems*, 3rd ed., John Wiley & Sons, New York, 2002.
9. M. Lax, Rate equations and amplitude noise, *IEEE Journal of Quantum Electronics*, 3, 37, 1967.
10. I.P. Kaminow and T. Li, *Optical Fiber Communications, Volume IVA*, Academic Press/Elsevier Sciene, San Diego, CA, 2002, Chapter 6.
11. T. Kawanishi, T. Sakamoto, and M. Izutsu, High-speed control of lightwave amplitude, phase, and frequency by use of electro-optic effect, *IEEE Journal of Selected Topcis in Quantum Electronics*, 13(1), 79–91, 2007.
12. G.P. Agrawal, *Fiber-Optic Communication Systems*, 3rd ed., Wiley, New York, 2002, Chapter 3.
13. L. Thylen, Integrated optics in $LiNbO_3$: Recent developments in devices for telecommunications, *IEEE Journal of Lightwave Technology*, 6, 847–861, June 1988.
14. SHF AG, Operating manual, DPSK optical transmitter—SHF 5003, SHF Communication Technologies AG, Berlin, Germany, http://www.shf.de/fileadmin/download/46210/datasheet_shf_46210c_v001.pdf, access date August 2014.

15. T. Kawanishi, S. Shinada, T. Sakamoto, S. Oikawa, K. Yoshiara, and M. Izutsu, Reciprocating optical modulator with resonant modulating electrode, *Electronics Letters*, 41(5), 271–272, 2005.
16. R. Krahenbuhl, J.H. Cole, R.P. Moeller, and M.M. Howerton, High-speed optical modulator in $LiNbO_3$ with cascaded resonant-type electrodes, *IEEE Journal of Lightwave Technology*, 24(5), 2184–2189, 2006.
17. L.N. Binh, Tutorial part I on optical systems design, in *Proceedings of ICOCN 2002*, Singapore, November 2002.
18. L.N. Binh, T.L. Huynh, K.Y. Chin, and D. Sharma, Design of dispersion flattened and compensating fibers for dispersion-managed optical communications systems, *International Journal of Wireless and Optical Communications*, 2(1), 63–82, June 2004.
19. G.P. Agrawal, *Fiber-Optic Communication Systems*, 3rd ed., John Wiley & Sons, New York, 2001.
20. J.B. Jeunhomme, *Single Mode Fiber Optics, Principles and Applications*, 2nd ed., Marcel Dekker Publications, New York, 1990.
21. J.A. Buck, *Fundamentals of Optical Fibers*, John Wiley & Sons, New York, 1995.
22. I.P. Kaminow and T. Li, *Optical Fiber Communications, Volume IVB*, Elsevier Science, San Diego, CA, 2002, Chapter 5.
23. J.P. Gordon and H. Kogelnik, PMD fundamentals: Polarization mode dispersion in optical fibers, *PNAS*, 97(9), 4541–4550, April 2000.
24. Corning Inc., An introduction to the fundamentals of PMD in fibers, White Paper, New York, July 2006.
25. A. Galtarossa and L. Palmieri, Relationship between pulse broadening due to polarisation mode dispersion and differential group delay in long singlemode fiber, *Electronics Letters*, 34(5), 492–493, March 1998.
26. J.M. Fini and H.A. Haus, Accumulation of polarization-mode dispersion in cascades of compensated optical fibers, *IEEE Photonics Technology Letters*, 13(2), 124–126, February 2001.
27. A. Carena, V. Curri, R. Gaudino, P. Poggiolini, and S. Benedetto, A time-domain optical transmission system simulation package accounting for nonlinear and polarization-related effects in fiber, *IEEE Journal on Selected Areas in Communications*, 15(4), 751–765, 1997.
28. S.A. Jacobs, J.J. Refi, and R.E. Fangmann, Statistical estimation of PMD coefficients for system design, *Electronics Letters*, 33(7), 619–621, March 1997.
29. J. Leibrich and W. Rosenkranz, Efficient numerical simulation of multichannel WDM transmission systems limited by XPM, *IEEE Photonics Technology Letters*, 15(3), 395–397, 2003.
30. D. Marcuse, A.R. Chraplyvy, and R.W. Tkach, Dependence of cross-phase modulation on channel number in fiber WDM systems, *IEEE Journal of Lightwave Technology*, 12(5), 885–890, 1994.
31. T. Mizuochi, K. Ishida, T. Kobayashi, J. Abe, K. Kinjo, K. Motoshima, and K. Kasahara, A comparative study of DPSK and OOK WDM transmission over transoceanic distances and their performance degradations due to nonlinear phase noise, *IEEE Journal of Lightwave Technology*, 21(9), 1933–1943, 2003.
32. K. Hoon, Cross-phase-modulation-induced nonlinear phase noise in WDM direct-detection DPSK systems, *IEEE Journal of Lightwave Technology*, 21(8), 1770–1774, 2003.
33. S. Bigo, G. Bellotti, and M.W. Chbat, Investigation of cross-phase modulation limitation over various types of fiber infrastructures, *IEEE Photonics Technology Letters*, 11(5), 605–607, 1999.
34. C. Furst, J.P. Elbers, C. Scheerer, and C. Glingener, Limitations of dispersion-managed DWDM systems due to cross-phase modulation, in *Proceedings of Annual Meeting LEOS'00*, Rio Grande, PR, vol. 1, pp. 23–24, 2000.
35. H.J. Thiele, R.I. Killey, and P. Bayvel, Influence of transmission distance on XPM-induced intensity distortion in dispersion-managed, amplified fiber links, *Electronics Letters*, 35(5), 408–409, 1999.
36. J.P. Gordon and L.F. Mollenauer, Phase noise in photonic communications systems using linear amplifiers, *Optics Letters*, 15(23), 1351–1353, December 1990.
37. A.F. Elrefaie and R.E. Wagner, Chromatic dispersion limitations for FSK and DPSK systems with direct detection receivers, *IEEE Photonics Technology Letters*, 3(1), 71–73, 1991.
38. A.F. Elrefaie, R.E. Wagner, D.A. Atlas, and A.D. Daut, Chromatic dispersion limitation in coherent lightwave systems, *IEEE Journal of Lightwave Technology*, 6(5), 704–710, 1988.

39. D.M. Baney, P. Gallion, and R.S. Tucker, Theory and measurement techniques for the noise figure of optical amplifiers, *Optical Fiber Technology*, 6, 122, 2000.
40. D. Ye and W.D. Zhong, Improved BER monitoring based on amplitude histogram and multi-Gaussian curve fitting, *Journal of Optical Networking*, 6(6), 584–598, 2007.
41. L. Ding, W.-D. Zhong, C. Lu, and Y. Wang, New bit-error-rate monitoring technique based on histograms and curve fitting, *Optics Express*, 12(11), 2507–2511, 2007.
42. E. J. Bomhoff, *Financial Forecasting for Business and Economics*, Spiral ed., Academic Press, San Diego, CA, 1995.
43. T. Schneider, Analysis of incomplete climate data: Estimation of mean values and covariance matrices and imputation of missing values, *Journal of Climate*, 14, 853–871, March 2000.
44. B.B. Brabson and J.P. Palutikof, Test of the generalized Pareto distribution for predicting extreme wind speed, *Journal of Applied Meteorology*, 39, 1627–1640, 2000.
45. J.G. Proakis, *Digital Communications*, 4th ed., McGraw-Hill, New York, 2001.
46. W.H. Tranter, K.S. Shanmugan, T.S. Rappaport, and K.L. Kosbar, *Principles of Communication Systems Simulation with Wireless Applications*, Prentice Hall, Upper Saddle River, NJ, 2004.
47. A.P. Dempster, N.M. Laird, and D.B. Rubin, Maximum-likelihood from the incomplete data via the EM algorithm, *Journal of Royal Statistics Society*, 39, 1–38, 1977.
48. E.F. Glynn, Mixtures of Gaussians, Stowers Institute for Medical Research, Kansas City, MO, February 2007.
49. P.D.M. Macdonald, Analysis of length-frequency distributions, in *Age and Growth of Fish*, Iowa State University Press, Ames, IA, pp. 371–380, 1987.
50. P.D.M. Macdonald and T.J. Pitcher, Age-groups from size-frequency data: A versatile and efficient method of analysing distribution mixtures, *Journal of the Fisheries Research Board of Canada*, 36, 987–1001, 1979.
51. Y. Kopsinis, J. Thompson, and B. Mulgrew, Performance evaluation of optical communication systems using extreme value theory, in *Proceedings of IEE Seminar on Optical Fiber Communications and Electronic Signal Processing*, London, U.K., December 2005.
52. Y. Yadin, M. Shtaif, and M. Orenstein, Bit-error rate of optical DPSK in fiber systems by multicanonical Monte Carlo simulations, *IEEE Photonics Technology Letters*, 17(6), 1355–1357, 2005.
53. W. Pellegrini, J. Zweck, C. R. Menyuk, and R. Holzlohner, Computation of bit error ratios for a dense WDM system using the noise covariance matrix and multicanonical Monte Carlo methods, *IEEE Photonics Technology Letters*, 17(8), 1644–1646, 2005.
54. D. Yevick, Multicanonical communication system modeling-application to PMD statistics, *IEEE Photonics Technology Letters*, 14(11), 1512–1514, 2002.
55. N.B. Mandayam and B. Aazhang, Importance sampling for analysis of direct detection optical communication systems, *IEEE Transactions on Communications*, 43(234), 229–239, 1995.
56. MATLAB Helpdesk, Statistical toolbox, generalized Pareto distribution, http://www.mathworks.com/access/helpdesk/help/toolbox/stats. Accessed September, 2006.
57. R.L. Smith, *Handbook of Applicable Mathematics; Extreme Value Theory*, John Wiley & Sons, Chichester, U.K., 1989.
58. A.C. Davidson, Models for exceedances over high thresholds, *Journal of Royal Statistics Society*, B52, 393–442, 1990.
59. R.L. Smith and I. Weissman, Estimating the extremal index, *Journal of Royal Statistics Society*, B56, 515–528, 1999.
60. J.E. Bowers and M.A. Pollack, Semiconductor lasers for telecommunications, in S.E. Miller and I.P. Kaminow (Eds.), *Optical Fiber Telecommunications II*, Academic Press, Boston, MA, pp. 509–568, 1988.
61. J.M. Senior, *Optical Fiber Communications: Principles and Practice*, 2nd ed., Prentice Hall, New York, 1992.
62. G.P. Agrawal, *Fiber Optic Communication Systems*, John Wiley & Sons, New York, 1992.
63. M.S. Park, PhD Thesis Dissertation, Sydney University, Sydney, New South Wales, Australia, 1993.

5

Optical Direct and External Modulation

This chapter deals with the modulation of light wave sources by either direct or external modulation. For direct modulation, the generation of the light wave within the cavity of the laser is manipulated by injection or withdrawing of electrons and hence stimulating the emission process. On the other hand, in the case of external modulation the laser is turned on at all times and the generated optical continuous waves are then modulated, by frequency, phase, or amplitude through an optical modulator. The properties of modulated signals are described. The uses of these transmitters in optical communication transmission systems are given, especially those for long-haul transmissions at very high bit rate. MATLAB® Simulink® models are described. Further, an introduction of external modulators is given for $LiNbO_3$, electro-absorption (EA) type, and silicon-based phase modulation devices that can then form other modulation formats on the guided light waves such as intensity, *I*–*Q* modulator, switches, and so on.

5.1 Introduction

A photonic transmitter would consist of a single or multiple light wave sources, which can be modulated either directly by manipulating the driving current of the laser diode or externally via an integrated optical modulator. These are called direct and external modulation techniques.

This chapter presents the techniques for generation of light waves and modulation techniques of light waves, either directly or externally. Direct modulation is the technique that directly manipulates the stimulated emission from inside the laser cavity, via the use of electro-optic effects. In external modulation, the laser is turned on at all times and the generated light waves are coupled to an integrated optic modulator through which the electro-optic effect is used with the electrical traveling waves, the amplitude, or phase of the light waves being modulated. Advanced modulation formats have recently attracted much attention for the enhancement of the transmission efficiency since the mid-1980s for coherent optical communications. Hence, the preservation of the narrow linewidth of the laser source is critical for operation bit rates in the range of several tens of Gb/s. Thus, external modulation is essential.

For direct modulation, fundamentally, electrical signals inject electronic carriers into the lasing cavity which are converted into optical-modulated light wave signals, which would then be transmitted through the optical fiber transmission lines, the optical fibers.

In this module, a number of practical lasers such as special lasers, constricted-mesa lasers, distributed feedback (DFB) lasers, and Fabry–Perot (FP) lasers are modeled for analysis and simulation of the ultra-long high-speed optical fiber communication system.

A complete analysis and study of the effect of physical parameters of the laser rate equation on its dynamic behavior are described. The simulated results of the laser output are confirmed with the experimental and analytical results published in various literatures.

For external modulation, three typical types of optical modulators are briefly presented in this chapter including the modulation of light waves using lithium niobate ($LiNbO_3$) electro-optic modulators (EOMs). Furthermore, EA modulation types and Si-based integrated modulators are introduced in Section 5.3. Their operating principles, physical structures of the devices, device parameters and their applications, and driving conditions for generation of different modulation formats as well as their impacts on system performance are discussed. Further details of modulation of light waves to generate different modulation formats such as phase- and frequency-shift keying schemes will be treated in the next chapter. However, a MATLAB Simulink model is given in Section 5.3.10 to illustrate how to set up Simulink model for optical modulation devices.

5.2 Direct Modulation

5.2.1 Introductory Remarks

The principal optical component of an optical fiber communication transmitter is the optical source. The crucial role of the optical transmitter is to convert an electrical information input signal into its corresponding optical domain, which would then be launched into an optical communication channel, the single-mode optical fiber (SMF). Most long-haul optical communication systems use semiconductor lasers as optical sources by direct modulation or incorporated with an external modulator for modulation without switching the laser on and off. With no exception, our analysis for ultra-long high-speed optical communication systems examined in this chapter employs semiconductor lasers with direct intensity modulation.

Laser is a coherent source generated by a stimulated emission process and therefore produces a relatively narrow spectral width of emitted light that allows operation in ultra-long high-speed optical fiber communication systems. Light waves emitted from the semiconductor laser can be modulated either directly by controlling the diode-injected current or externally coupled to an optical modulator. Normally, an electro-optic integrated device is used, through which guided light waves are electro-optically modulated by applying a traveling electric wave. The phase-modulated optical light waves are combined with non-modulated phase paths giving amplitude-modulated light waves as output [1–5].

Optical systems operating at Gigabits per second range (up to 100 Gb/s) can be directly modulated without using an external modulator [6], while external modulators such as $LiNbO_3$, Mach–Zehnder interferometric modulator (MZIM), and electro-absorption modulator (EAM) can operate up to several tens of GHz.

Several designs of semiconductor lasers have been produced to cater for ultra-high-speed optical transmission systems, for example, FP laser, DFB laser, and constricted-mesa laser. They are capable of handling approximately 200 Mb/s, 600 Mb/s, and 15 Gb/s system bit rate, respectively [7]. These laser sources are used for modeling the optical transmitter except for the "special" laser source that is modeled in a separate section.

Further information on the semiconductor laser acting as an optical transmitter is presented in Section 5.3. Three laser rate equations, namely, the photon rate equation, the

carrier rate equation, and the optical phase rate equation are described for generating temporally coherent light waves. The effects of each physical parameter of the rate equation on the laser response are studied and analyzed in Section 5.2.2.9.

For ultra-long high-speed optical transmission systems, the dynamic response of the laser source is critical for the output characteristic of an optical source. Relaxation oscillation and switch-on delay are two examples of dynamic responses as covered in Section 5.2.2.9. These effects are simulated and discussed in Section 5.3.10.

To model a real practical system, Langevin force (a noise term) is introduced into each rate equation and noise considerations are given in Section 5.2.2.11. In Section 5.6, eye diagrams of laser output light waves are generated and compared to those obtained in practical systems.

5.2.2 Physics of Semiconductor Lasers

Under normal conditions, all semiconductor materials absorb light rather than emit it. The absorption process can be understood by referring to Figure 5.1, where the energy levels E_1 and E_2 correspond to the ground state and the excited state of atoms, respectively. If the photon energy $h\upsilon$ of the incident light of frequency υ is about the same as the energy difference $E_g = E_1 - E_2$, the photon is absorbed by the atom, which ends up in the excited state.

Excited atoms eventually return to their normal "ground" state and emit light in the process. Light emission can occur through two fundamental processes known as spontaneous emission and stimulated emission. Both are shown schematically in Figure 5.1. In spontaneous emission process, photons are emitted in random directions with no phase relationship, whereas in stimulated emission the process is initiated by an existing photon and the emitted photons match the original photon in energy (or frequency), phase, and direction of propagation. All lasers, including semiconductor lasers, emit light through the process of stimulated emission and are said to emit coherent light. Therefore, over a large number of stimulated emission events, the laser source acts like a linear amplifier [8].

At room temperature, spontaneous emission always dominates over stimulated emission in thermal equilibrium. Thus, it can never emit coherent light. Therefore, lasers should necessarily operate away from thermal equilibrium by pumping lasers with an external energy source. Even for an atomic system pumped externally, stimulated emission may not be the dominant process, since it has to compete with the absorption process. Thus, population inversion is a prerequisite for laser operation where the atomic density in excited states must be relatively greater than at the ground level [3].

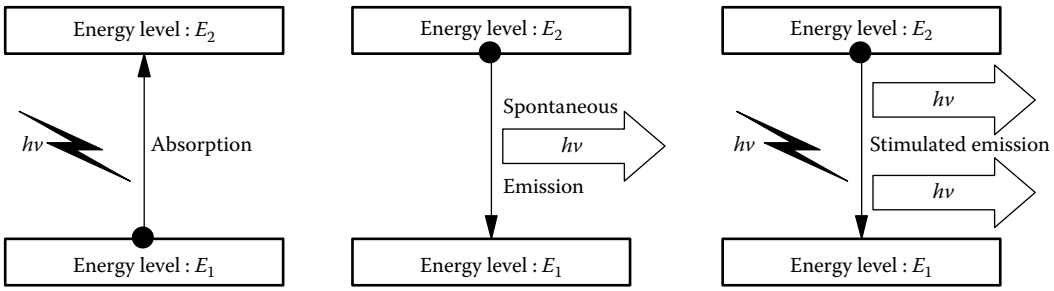

FIGURE 5.1
Three fundamental processes in a semiconductor laser—absorption, spontaneous emission and stimulated emission—occurring between the two energy states of an atom where E_1 and E_2 are the energy levels of valence band and conduction band, respectively, and $E_1 > E_2$.

5.2.2.1 The Semiconductor p–n Junction for Lasing Light Waves

The *p–n* junction as shown in Figure 5.2 is a homojunction type because the same type of semiconductor material is fabricated on both sides of the junction. The disadvantage of a homojunction is that electron-hole recombination can occur over a relatively wide region (10 μm) which is determined by the diffusion length of charged carriers (electron and holes). However, the homojunction structure leads to spatial dispersion of charged carriers and thus nonconfinement to the immediate vicinity of the junction; it is difficult, therefore, to realize high carrier densities.

Shown in Figure 5.3 is the heterojunction in which the carrier confinement occurs as a result of bandgap discontinuity at the junction between two different layers of semiconductors that have the same crystalline structure but different bandgaps. The carrier confinement problem for homojunction can thus be resolved by sandwiching this semiconductor material between the *p*-type and *n*-type layers. This is shown as the lasing active region. The bandgap of the active region is smaller than the layers surrounding it. Therefore, the electron-hole recombination process only occurs in a relatively narrow region (0.1 μm) and high carrier densities can be realized at a given injection current, which is far better than that for the case of the homojunction.

In addition, the refractive index of the active layer is slightly larger than that of the surrounding layers. As a result of the difference in the refractive index, the active layer acts as a dielectric waveguide. The main function of this waveguide and active layer is to confine the generated optical energy within the active layer so that resonance can occur to effectively

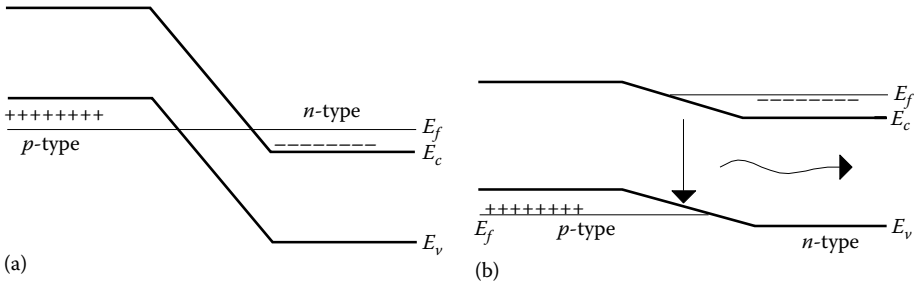

FIGURE 5.2
Energy-band diagram of a *p–n* homo junction of a semiconductor laser: (a) thermal equilibrium, (b) under forward bias.

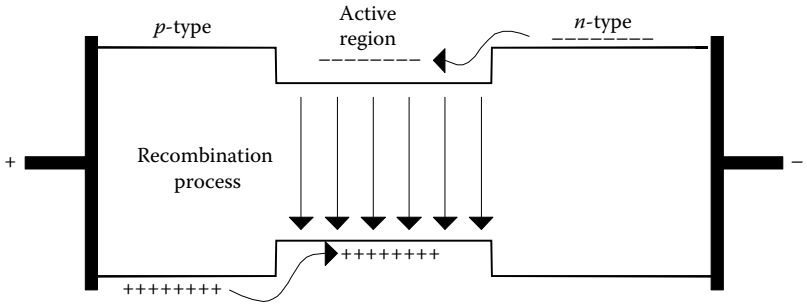

FIGURE 5.3
Energy-band diagram of a heterojunction.

generate light waves in the cavity. Thus, the heterostructure *p–n* junction semiconductor laser is a very efficient device where the optical waves are mostly confined to the active region as also the carriers, thus maximizing stimulated emission and resulting in laser optical gain.

5.2.2.2 Optical Gain Spectrum

Optical gain occurs in the active region when the injected carrier density in the active layer exceeds a certain limit, known as the transparency value where population inversion is realized. Spectra distribution of emitted light affects the performance of optical communication systems through fiber dispersion. The optical gain spectrum is found by considering all possible transitions from conduction to valance band shown in Figure 5.4. The width of the gain spectrum ranges from 30 to 100 nm. It can be further reduced by the laser resonance cavity that consists of two partially reflecting mirrors placed at the ends of a very short lasing length (of the order of 10–40 ppm).

5.2.2.3 Types of Semiconductor Lasers

Semiconductor lasers are mainly classified by their structure. To achieve high bit-rate transmission, one has to narrow the laser spectral width and to improve the optical pulse

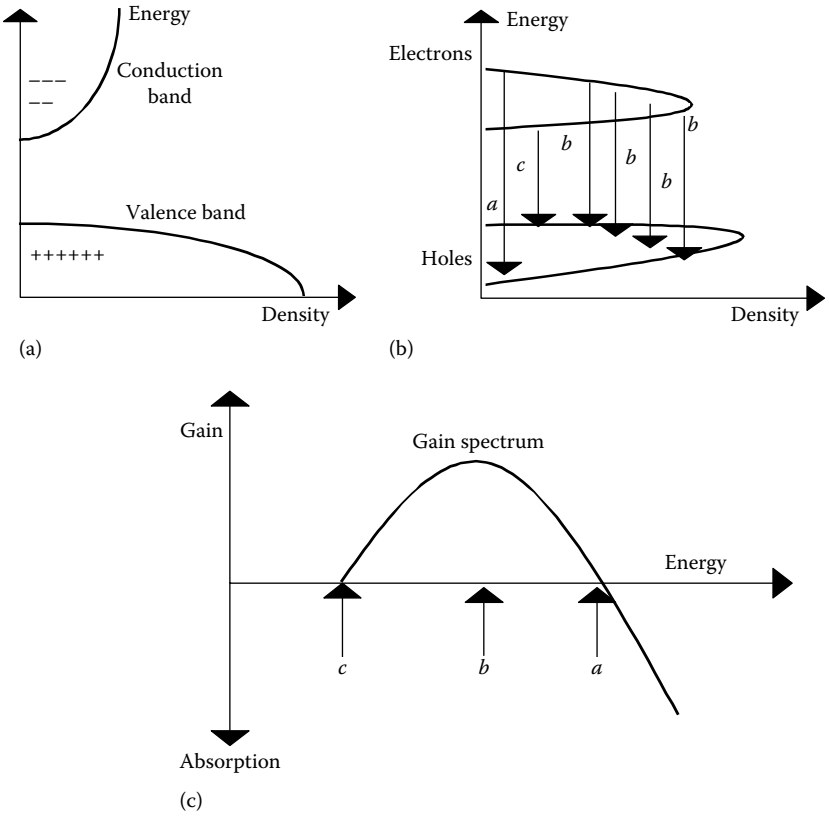

FIGURE 5.4
Optical gain and absorption as a function of bandgap energy (a) energy bands, (b) carrier energy density, (c) gain and absorption with respect to carrier energy.

response the rise-time constant has to be minimized. Some common types of semiconductor lasers, commercially available in the production, are FP lasers, DFB lasers, distributed Bragg reflector (DBR) lasers, single quantum well (SQW) lasers, multi-quantum well (MQW) lasers, constricted-mesa lasers, and buried heterostructure (BH) lasers. In addition, currently coherent transmission systems require narrow linewidth light wave source with a 3 dB bandwidth of around 100 kHz or even less, the external cavity is then to be inserted to reflect only the single-frequency lasing line. External free-space gratings are now commonly employed [9–12].

5.2.2.4 Fabry–Perot (FP) Heterojunction Semiconductor Laser

The optical gain alone is essential but not sufficient for laser operations. The other necessary ingredients are the optical feedback mechanism and the optical guiding in the active layer.

Similar to the resonance in second- and third-order electrical circuitry, the optical energy feedback phenomenon from the two end mirrors located at the end of the guiding cavity as indicated in Figure 5.5a is a positive feedback. This would thus stimulate the optical

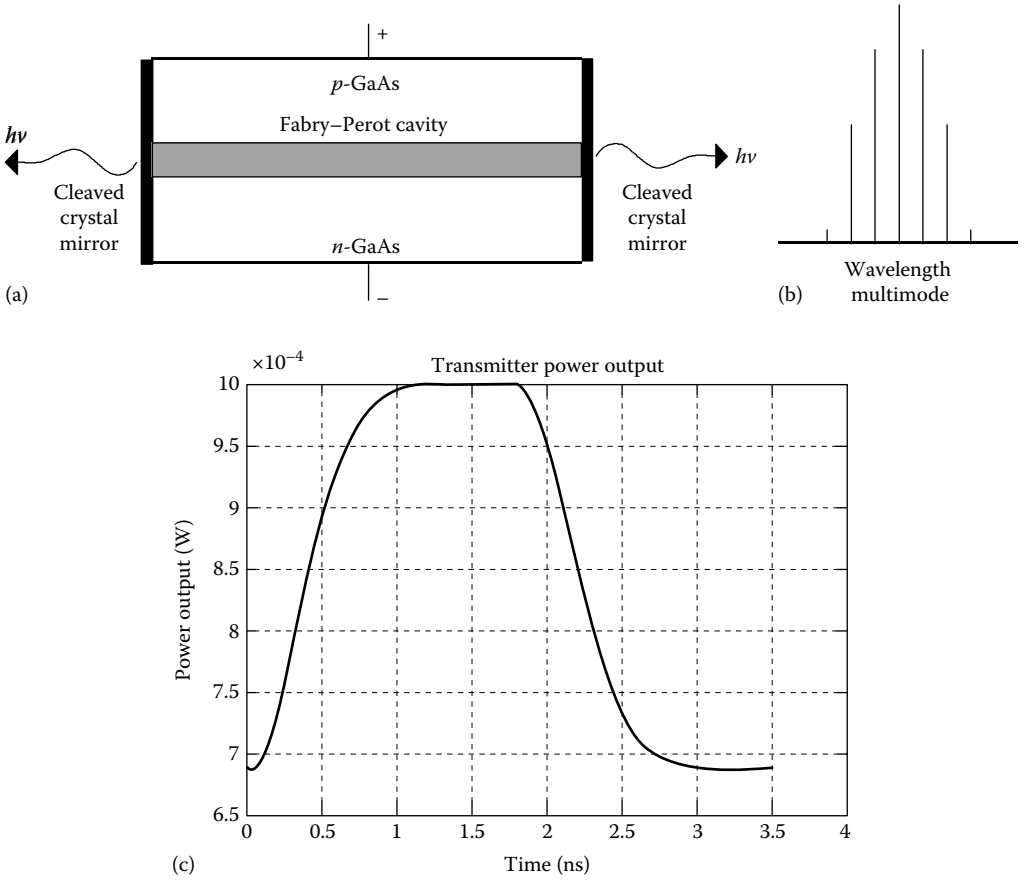

FIGURE 5.5
(a) Schematic diagram of Fabry–Perot laser, (b) FP laser output spectral, (c) FP laser output response (565 MHz) obtained by simulation.

resonance and oscillation. This cavity is commonly known as the FP cavity. Each modal resonance frequency in and along the cavity is called a longitudinal mode. Since a standing wave is formed along the cavity, it is bound to have several longitudinal modes (due to multiple resonance modes) that exist within the gain spectrum of the device (Figure 5.5). However, improved longitudinal mode selectivity can be achieved using structures that give adequate loss discrimination between the desired mode and all of the unwanted modes of the laser resonator, for example, by using short cavity resonator, coupled cavity resonators [13], and DFB. In Figure 5.5, the broad spectral width (≈5 nm) limits the FP lasers transmission rate to about 565 Mb/s for NRZ line coding.

Light waves, reflected and traveling back and forth and confined in the active layer which is an optical waveguide whose refractive index profile is greater than that of the upper and lower layers, the cladding regions. This confinement would give better power conservation and field matching to the fiber pigtail.

5.2.2.5 Distributed-Feedback (DFB) Semiconductor Laser

In a DFB laser, as the name implies, optical energy feedback mechanism is not localized at the facets but is distributed throughout the cavity length. This is achieved through an internal built-in corrugated grating that leads to a periodic perturbation of the refractive index (Figure 5.6a). Feedback occurs by means of Bragg diffraction that couples the waves propagating in the forward and backward directions. We can now refer to Figure 5.6b; each impedance boundary causes a reflection and the grating period (Λ) must satisfy the Bragg condition

$$\Lambda = m\left(\frac{\lambda_B}{2n_{eq}}\right) \tag{5.1}$$

where

n_{eq} denotes equivalent (or effective, normally derived from the eigenvalue of the wave equation) refractive index of the optical guided waves in the active waveguide cavity
λ_B denotes operating wavelength
the integer m represents the order of Bragg diffraction

The region of periodically varying refractive index serves to couple two counter-propagating traveling waves. The coupling is a maximum for wavelengths close to λ_B. First-order gratings provide the strongest coupling, but second-order gratings are sometimes used because they are easier to fabricate, with their larger spatial period (Λ). Thus, DFB lasers by means of Bragg diffraction could produce single-frequency mode with a very narrow spectral width (≈ a few hundred MHz). The modulation rate of DFB lasers can be about 600 Mb/s to 2 Gb/s for NRZ line coding without broadening its linewidth.

5.2.2.6 Constricted-Mesa Semiconductor Laser

Constricted-mesa laser is one component of the family of index-guided lasers. Index-guided laser structure is modified from the gain-guided laser [13] that eliminates the problems of having "kinks," astigmatism, unstable far-field patterns, and self-pulsations. In other words, this is to linearize the optical power-driven current (*P–I*) characteristic of a laser, and hence reduce the distortion of the emitted laser pulse.

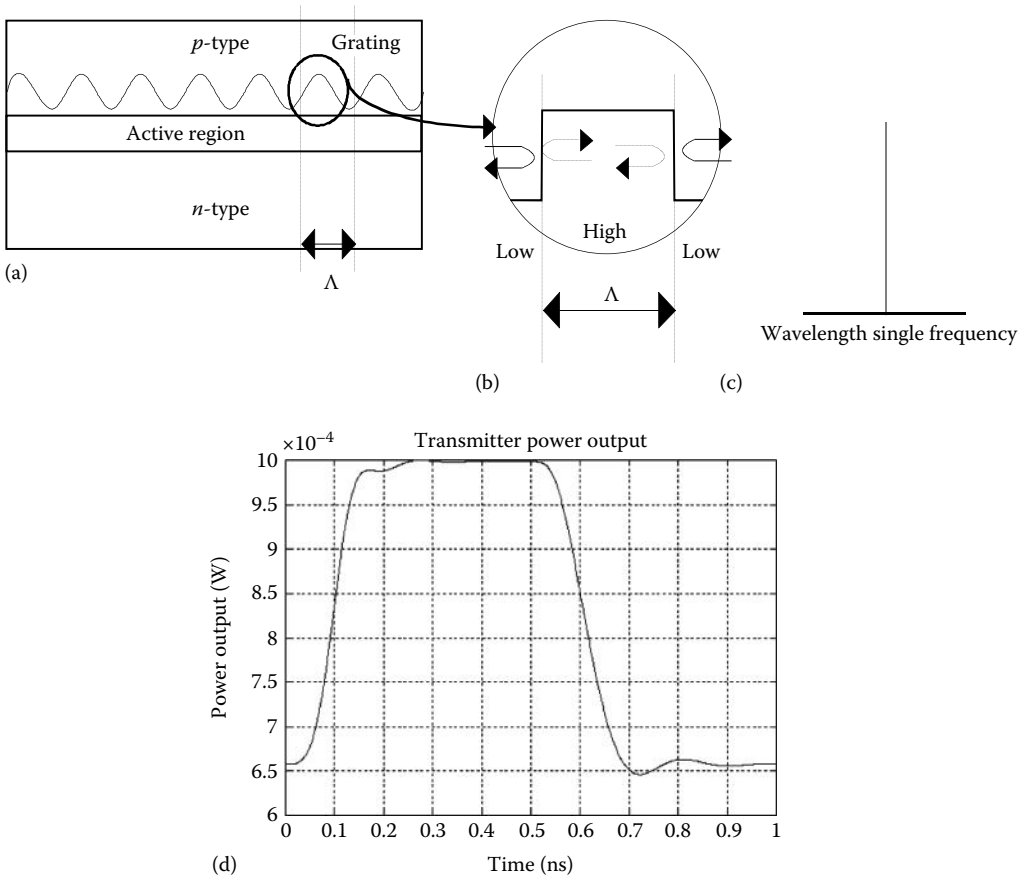

FIGURE 5.6
(a) Schematic diagram of DFB laser, (b) each impedance boundary causes a reflection, (c) DFB laser output spectral, (d) DFB laser output response (2 GHz) by simulation file given in the Appendix of this chapter.

Real refractive index variation is introduced into the lateral structure of the laser to achieve this purpose. In high-speed modulation laser, parasitic capacitance could be the limiting factor in achieving excellent high-speed transmission. In a laser with significant parasitic capacitance, the electrical pulse reaching the laser is broadened, and the capacitance provides a source of current during the time when the photon density is high. Consequently, the laser output may consist of two or more pulses as the electron density is repetitively built up and relaxation oscillations are extinguished. Thus, constricted-mesa lasers are fabricated with current-blocking layers by the regrowth of semi-insulating material, SiO_2 or SiN_x, shown in Figure 5.7. Hence, the modulation speed of 20 GHz for NRZ line coding format can be achieved [14].

5.2.2.7 Special Semiconductor Laser Source

In addition to the lasers available by simulation as mentioned earlier, a "special" semiconductor laser has been modeled, tailored for the analysis of the high-speed ultra-long optical fiber communication systems. With optical confinement factor of 0.9 (which is remarkably higher than that of the normal laser) and narrow spectral linewidth of 0.05 nm, these lasers

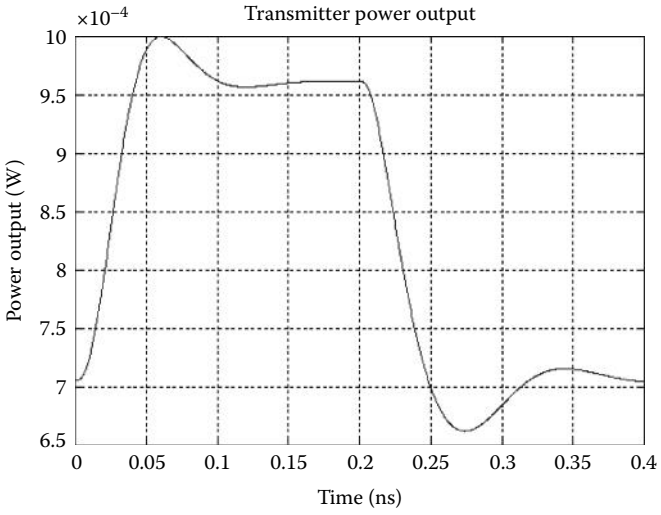

FIGURE 5.7
Constricted-mesa laser output response (5 GHz) from simulation.

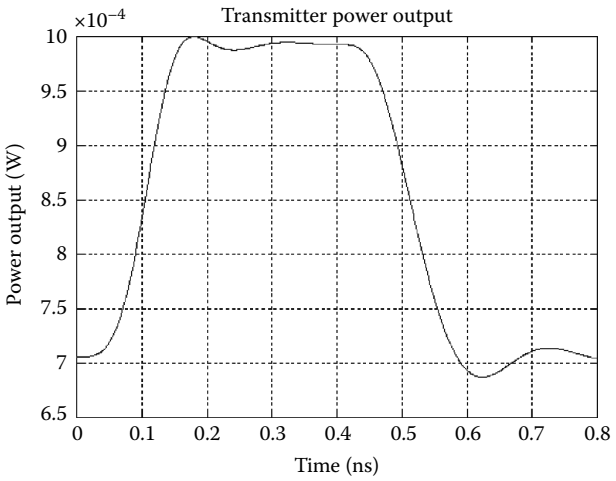

FIGURE 5.8
Special laser output response (5 GHz) by simulation.

enable modulation of very high-speed signal up to 20 GHz without any observable defects. At around 2.5 GHz, it provides a smooth running response with slight relaxation oscillation and overshooting (Figure 5.8). Thus, it produces a reasonable optical pulse shape for us to analyze especially at the fiber output and receiver terminals.

5.2.2.8 Single-Mode Optical Laser Rate Equations

The operating characteristics of semiconductor lasers are well described by a set of rate equations that govern the interaction of photons and electrons inside the active region. A rigorous derivation of these rate equations generally starts from Maxwell's equations

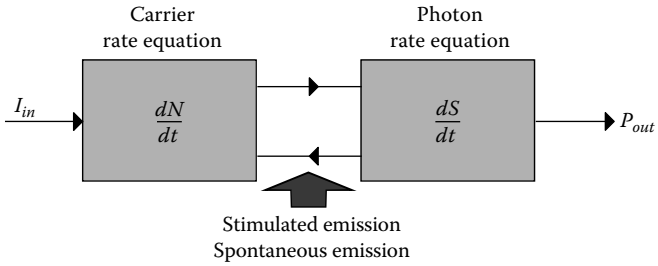

FIGURE 5.9
Single mode laser model as expressed by the rate equations (5.2) through (5.4).

together with a quantum-mechanical approach for the induced polarization. However, the rate equations can also be obtained heuristically by considering the physical phenomena through which the number of photons S and the number of electrons N change with time inside the active region as illustrated in Figure 5.9.

For a single-mode laser, three rate equations are given in (5.2) through (5.4). These rate equations can be used for computer simulation of the frequency chirp and output power waveform.

$$\frac{dN(t)}{dt} = \frac{I(t)}{qV_a} - \frac{N(t)}{\tau_n} - v_0 a_0 \frac{N(t) - N_0}{1 + \varepsilon_C S(t)} S(t) \tag{5.2}$$

$$\frac{dS(t)}{dt} = \left(\Gamma a_0 v_g \frac{N(t) - N_0}{1 + \varepsilon_C S(t)} - \frac{1}{\tau_p} \right) S(t) + \frac{\beta \Gamma N(t)}{\tau_n} \tag{5.3}$$

$$\frac{d\phi_m(t)}{dt} = \frac{\alpha}{2} \left(\Gamma v_g a_0 \left(N(t) - N_0 \right) - \frac{1}{\tau_p} \right) \tag{5.4}$$

where the parameters of the these rate equations are as follows:

Γ is the optical confinement factor
v_g is the guided light wave group velocity
a_0 is the gain coefficient
N_0 is the carrier density at transparency
ε_C is the gain compression factor
τ_p is the photon lifetime
β is the fraction of spontaneous emission coupled into the lasing mode
τ_n is the electronic carrier lifetime
q is the electronic charge
V_a is the active (lasing) layer volume
α is the optical linewidth enhancement factor
ϕ_m is the optical phase

In (5.2), the electron density $N(t)$ increases due to the injection of a current $I(t)$ into the active layer volume V_a and decreases due to stimulated and spontaneous emission

of photon density $S(t)$. Similarly in (5.3), the photon density $S(t)$ is increased by stimulated and spontaneous emission $S(t)$ and decreased by internal and mirror losses with a photon lifetime τ_p given by

$$\tau_p = \frac{1}{v_g\left(\alpha_i + \alpha_m\right)} \tag{5.5}$$

where α_i and α_m denote the waveguide loss coefficients and the mirror loss, respectively. The carrier lifetime, τ_n is related to the loss of electrons due to both spontaneous emission and nonradiative recombination [3] given by

$$\tau_n = \frac{N(t)}{R_{sp} + R_{nr}} \tag{5.6}$$

where
R_{sp} denotes rate of spontaneous emission
R_{nr} denotes nonradiative recombination

The time variations of the optical power output [15] are given by

$$m(t) = \frac{S(t)V_a\eta_0 h\nu}{2\Gamma\tau_p} \tag{5.7}$$

where
$h\nu$ denotes the photon energy
η_0 denotes the total differential quantum efficiency

5.2.2.9 Dynamic Response of Laser Source

The dynamic behavior of the injected laser is critical, especially when it is used in ultralong high-speed optical fiber communication systems. The application of a step current to the device results in a switch-on delay, often followed by high-frequency damped oscillations (≈10 GHz) known as the relaxation oscillations (ROs). RO occurs when the electron (as the carrier) and photon populations within the structure come into equilibrium. This can be illustrated as shown in Figure 5.10. The input electrical pulse causes the electron density to rise to a maximum, which is maintained during a turn-on delay until a large photon density builds up and depletes the carriers. This behavior is easily seen from the carrier rate equations (5.2) through (5.4) and is explained in Section 5.3.

In addition, when a current pulse reaches a laser that has significant parasitic capacitance after the initial delay time, the pulse will be broadened because the capacitance provides a source of current over the period when the photon density is high. The turn-on delay is caused by the initial build-up of photon density resulting from stimulated emission. It is related to the minority carrier lifetime and the current passing through the device. It can be reduced by biasing the laser current near the threshold current level (pre-biasing). However, further increase in laser current will decrease the extinction ratio $P_{\text{“1”}}/P_{\text{“0”}}$. The resonant or oscillating frequency f_{osc} can be increased. The overshooting can be reduced by shaping the electrical input pulse [16] (Figure 5.11).

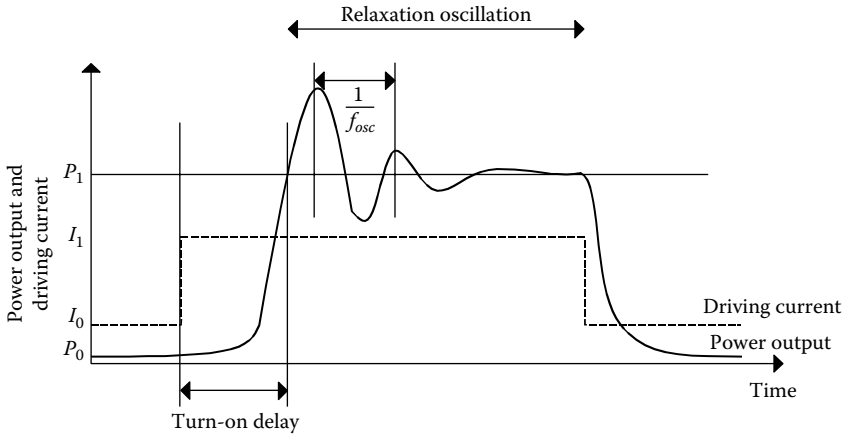

FIGURE 5.10
Typical response to a drive rectangular pulse.

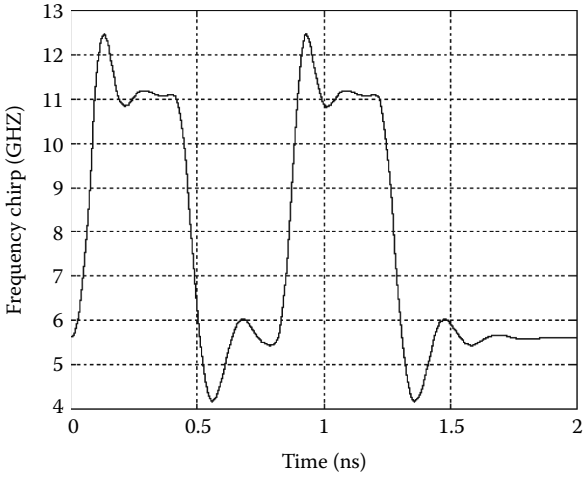

FIGURE 5.11
Frequency chirp effects on direct modulated optical pulses.

5.2.2.10 Frequency Chirp

The direct current modulation of a single longitudinal mode semiconductor laser can cause a dynamic shift in the peak wavelength emitted from the device [17]. This phenomenon, which results in dynamic linewidth broadening under direct modulation of the injected current, is referred to as frequency chirping. It arises from gain-induced variations in the laser refractive index due to the strong coupling between the free carrier density and the index of refraction, which is present in any semiconductor structure [11]. Hence, even small changes in carrier density will result in a phase shift of the optical field, giving an associated change in the resonance frequency within both FP and DFB laser structures.

$$\Delta\nu(t) = \frac{1}{2\pi}\left(\frac{d\phi_m(t)}{dt}\right) = \frac{1}{2\pi}\left[\frac{\alpha}{2}\left(\Gamma v_g a_0 (N(t) - N_0) - \frac{1}{\tau_p}\right)\right] \tag{5.8}$$

where
- $\Delta\nu$ denotes the frequency chirp
- $N(t)$ denotes the carrier density
- $d\phi_m/dt$ denotes optical phase rate equations

A number of techniques can be employed to reduce the frequency chirp effects by:

1. Biasing the laser sufficiently above the threshold so that the modulation current does not drive the device below the threshold where the rate of change of optical output power varies rapidly with time. However, this method gives an extinction ratio penalty of the order of several decibels at the receiver.
2. Damping the relaxation oscillations by shaping the electrical drive pulses that would result in small fluctuations of optical output power [16].
3. Using quantum well lasers, Bragg wavelength detuned DFB lasers, and multi-electrode DFB lasers, all of which provide an improvement in frequency chirp. However, it requires a complex fabrication process.
4. Using external modulators such as $LiNbO_3$, the Mach–Zehnder interferometric amplitude type with the laser source emits continuous light waves of appropriate wavelengths or frequencies [18].

5.2.2.11 Laser Noises

The output of a semiconductor laser exhibits fluctuations in its intensity, phase, and frequency chirp (as described in Section 5.2.2.10) even when the laser is biased at a constant current with negligible current fluctuations. This is due to two fundamental noise mechanisms, the spontaneous emission and the electron-hole recombination (shot noises). Usually, noises generated in semiconductor lasers are dominated by photons randomly generated by spontaneous emission. The intrinsic intensity fluctuation in a semiconductor laser is a noise source in direct modulated optical communication systems and in some specific applications may significantly reduce the signal-to-noise ratio (SNR), whereas phase fluctuation leads to a limited spectral linewidth when semiconductor lasers are operated continuously at a constant current. The rate equations can be used to study laser noises by adding an extra noise term, known as the Langevin force, to each of them. The rate equations become

$$\frac{dS(t)}{dt} = \left(\Gamma a_0 v_g \frac{N(t) - N_0}{1 + \varepsilon_C S(t)} - \frac{1}{\tau_p}\right) S(t) + \frac{\beta\Gamma N(t)}{\tau_n} + F_S(t) \tag{5.9}$$

$$\frac{dN(t)}{dt} = \frac{I(t)}{qV_a} - \frac{N(t)}{\tau_n} - v_g a_0 \frac{N(t) - N_0}{1 + \varepsilon_C S(t)} S(t) + F_N(t) \tag{5.10}$$

$$\frac{d\phi_m(t)}{dt} = \frac{\alpha}{2}\left(\Gamma v_g a_0 \left(N(t) - N_0\right) - \frac{1}{\tau_p}\right) + F_\phi(t) \tag{5.11}$$

where $F_S(t)$, $F_N(t)$, and $F_\phi(t)$ denote the Langevin noise sources due to the spontaneous emission, the carrier generation recombination process in photon number, and the generated phase, respectively [19]. They are assumed to be Gaussian random process with zero mean value. Under the Markovian assumption (the system has no memory), the correlation function of the form given by the Markovian approximation is

$$\langle F_i(t)F_j(t')\rangle = 2D_{ij}\delta(t-t') \tag{5.12}$$

where $i, j = S, N$, or ϕ, angle brackets denote the ensemble average, and Dij is called the diffusion coefficient [17] and are listed as

$$D_{SS} = \frac{\beta V_a N_{sd}\left(V_a S_{sd}+1\right)^3}{\tau_n} \tag{5.13}$$

$$D_{NN} = \frac{V_a N_{sd}}{\tau_n}\left[\beta V_a S_{sd}+1\right] \tag{5.14}$$

$$D_{\phi\phi} = \frac{R_{sp}}{4S} \tag{5.15}$$

where

N_{sd} and S_{sd} represent the steady-state average values of the carrier and photon populations, respectively

R_{sp} denotes the rate of spontaneous emission

$$N_{sd} = \frac{1}{\Gamma a_0 v_g \tau_p} + N_0 \tag{5.16}$$

$$S_{sd} = \frac{\tau_p}{\tau_n} N_{sd}\left(\frac{I(t)}{I_b}-1\right) \tag{5.17}$$

$$R_{sp} = 2\Gamma v_g \sigma_g \left(N(t)-N_0\right) \tag{5.18}$$

where I_b denotes bias current and σ_g, the gain cross section is normally 2×10^{-20} m^2. By making use of the Wiener–Kinchen theorem, which states that the Fourier transform of the autocorrelation function of a process is equal to the power spectral density of that process, we take the Fourier transform of a delta function to be simply white Gaussian noise. For ergodic random process and since $\overline{F_i}^2 = 0$, variance of F_i or var $(F_i) = 2D_{ij}$ (refer to Equation 5.12). Thus, the Langevin force is white Gaussian with a mean of zero and standard deviation of $\sqrt{2D_{ij}}$ given as

$$F_S(t) = N(0,1)\sqrt{2D_{SS}} \tag{5.19}$$

$$F_N(t) = N(0,1)\sqrt{2D_{NN}} \tag{5.20}$$

$$F_\phi(t) = N(0,1)\sqrt{2D_{\phi\phi}} \tag{5.21}$$

where $N(0, 1)$ denotes the Gaussian distributed random process with mean 0 and standard deviation of 1 and these three Langevin forces are to be fitted in (5.19) through (5.21).

The noise power spectrum $s(f)$ of the photon density as a function of the Fourier frequency, f, can be written using the rate equation as

$$s(f) = \frac{\tau_p f_r^4 \left\langle F_N^2 \right\rangle + \Psi^2 \dfrac{\left\langle F_s^2 \right\rangle}{4\pi^2} + \tau_p f_r^4 \Psi \dfrac{\left\langle F_s F_N \right\rangle}{\pi} + \dfrac{\left\langle F_s^2 \right\rangle}{4\pi^2} f^2}{\left(f^2 - f_r^2\right) + \Psi^2 f^2} \tag{5.22}$$

and the relative intensity noise (RIN) of a laser source can be estimated by (Figures 5.12 and 5.13)

$$RIN = 10\mathrm{Log}_{10} \frac{s(f)^2}{S_{sd}^2} \tag{5.23}$$

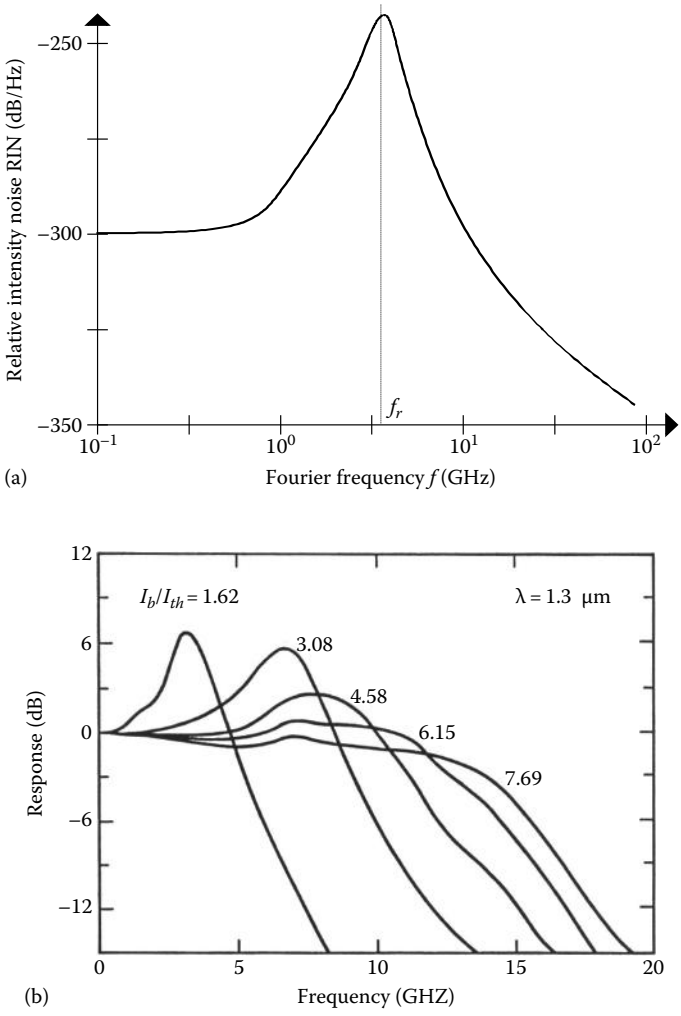

FIGURE 5.12
Relative intensity noise for intensity modulation (a) modeling using rate equations (b) measured frequency response.

where f_r denotes the resonant frequency given by

$$f_r = \frac{1}{2\pi}\sqrt{\frac{1}{\tau_p\tau_n}\left(1+\Gamma a_0 v_g N_0 \tau_p\right)\left(\frac{I(t)}{I_b}-1\right)} \tag{5.24}$$

and $\langle F_S F_N \rangle$ denotes cross-correlation given by

$$\left\langle F_s F_N \right\rangle = -\frac{\beta V_a N_{sd}(V_a S_{sd}+1)}{\tau_N} + \frac{V_a S_{sd}}{\tau_p} \tag{5.25}$$

and constant Ψ denotes

$$\Psi = \frac{1}{2\pi}\left(\Gamma a_0 v_g S_{sd} + \frac{1}{\tau_n}\right) \tag{5.26}$$

The typical relationship between the inject current injected into the lasing cavity and the output intensity of the FP laser and its variation with respect to temperature is shown in Figure 5.13. It is noted that the threshold current varies as the temperature changes. If the laser chip is not cooled by a feedback-controlled mechanism, then the driving current level for a "1" may no longer be at the "ON" level when the temperature changes. Therefore, as shown in Figure 5.14, the packaged laser in which a Peltier cooler or TEC (thermo-electric cooler) is employed is used to maintain the temperature of the laser chip to within 0.1°C. A block diagram of a laser circuit and its control feedback with temperature control and biasing currents at DC (direct current) is shown in Figure 5.15.

5.2.3 Modeling and Development of Optical Transmitter

A typical block diagram of an optical transmitter is shown in Figure 5.15. The input to the optical source is represented by the coded output of a data signal generator. Users are required to specify the binary number input sequence in the *Transmitter Main Menu* (see Appendix 1—files mn_input1.m, mn_input2.m, and mn_input3.m). The source output is coupled to a transmitting optical component block (Figure 5.16). These components may be connectors, couplers, or filters. The optical output power is usually directly modulated by varying the drive current, but external optical modulation is also possible [20].

5.2.3.1 Line Coding

Currently, nonreturn zero (NRZ), return zero (RZ), and Manchester (MAN) are the most common coding schemes used in optical communications [21]. NRZ codes are simple and easy to implement. The RZ and MAN codes increase the bandwidth requirements, but this is not a serious concern at present with SMF transmission. The resulting waveforms of these coding schemes, generated using **OCSS©**,* are shown in Figure 5.16.

* Available for download from CRC Press.com specific website. Contact Publisher for further details. Menu for transmitters in .m files are listed in Appendix 1.

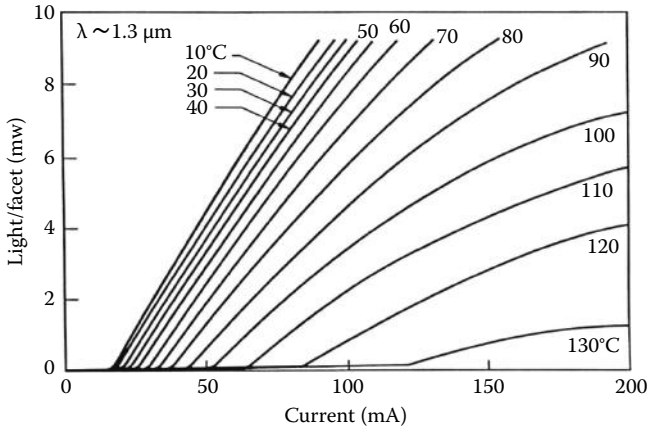

FIGURE 5.13
Laser *P–I* characteristics with temperature as a parameter.

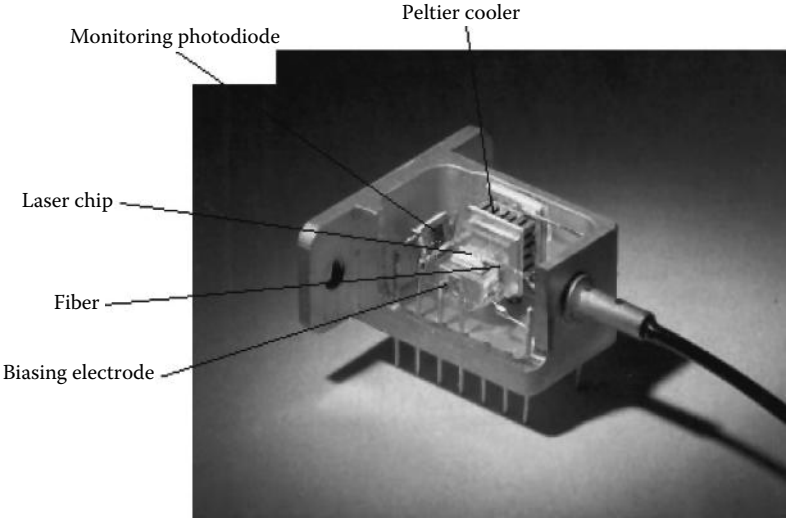

FIGURE 5.14
Packaged semiconductor laser.

When an NRZ code is employed, the binary one level is held for the whole bit period. In this case, there are two bit periods in one wavelength. Hence, the maximum bandwidth B_{max} is one half of the maximum data rate, for example, 10 GHz data rate produces B_{max} of 5 GHz (Figure 5.18). However, when RZ or MAN is considered, the binary one level is held for only half of the bit period. For this signaling scheme, the data rate is equal to the bandwidth, for example, 10 GHz data rate produces B_{max} of 10 GHz (Figure 5.19). The advantage of MAN over RZ or NRZ is to overcome "DC built-up" by having long consecutive input bits stream of all "ones" which could overheat the driving circuitry of the laser source.

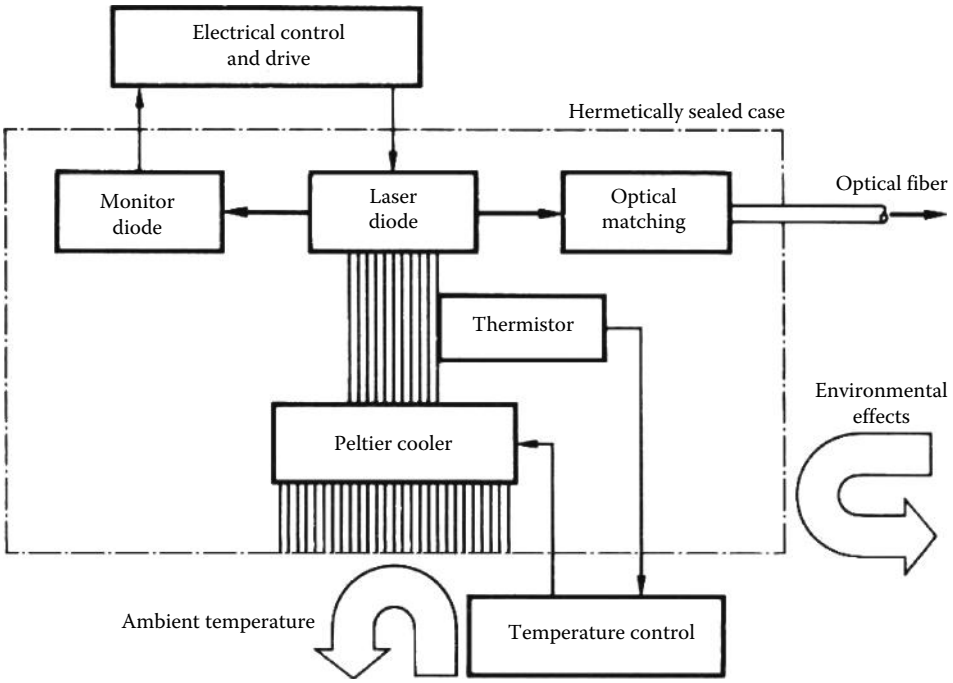

FIGURE 5.15
Schematic of an electrical circuitry for driving a semiconductor laser including biasing current source, cooling by Peltier effects. No AC signal input is shown.

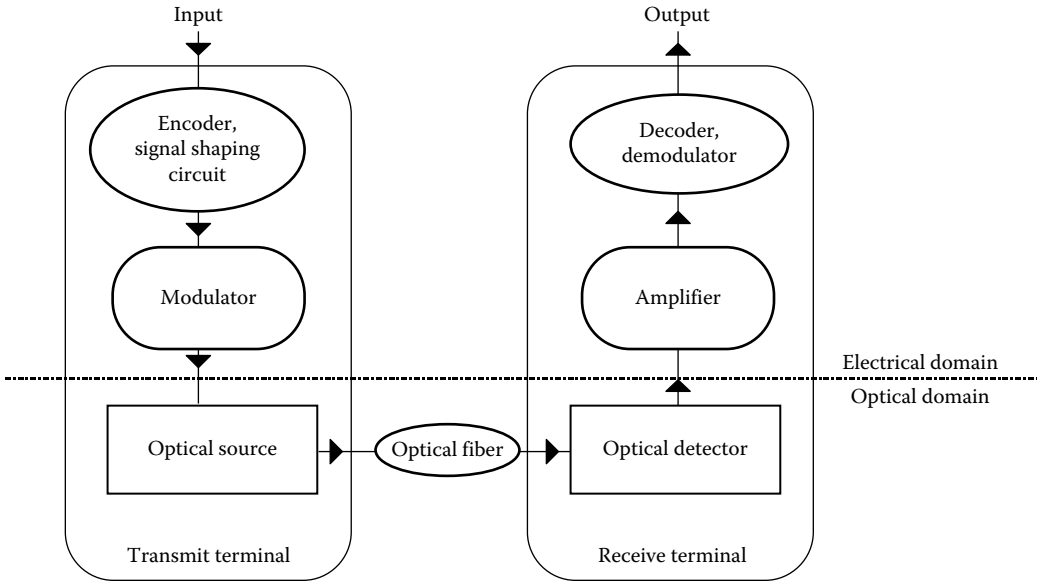

FIGURE 5.16
Transmitter block diagram.

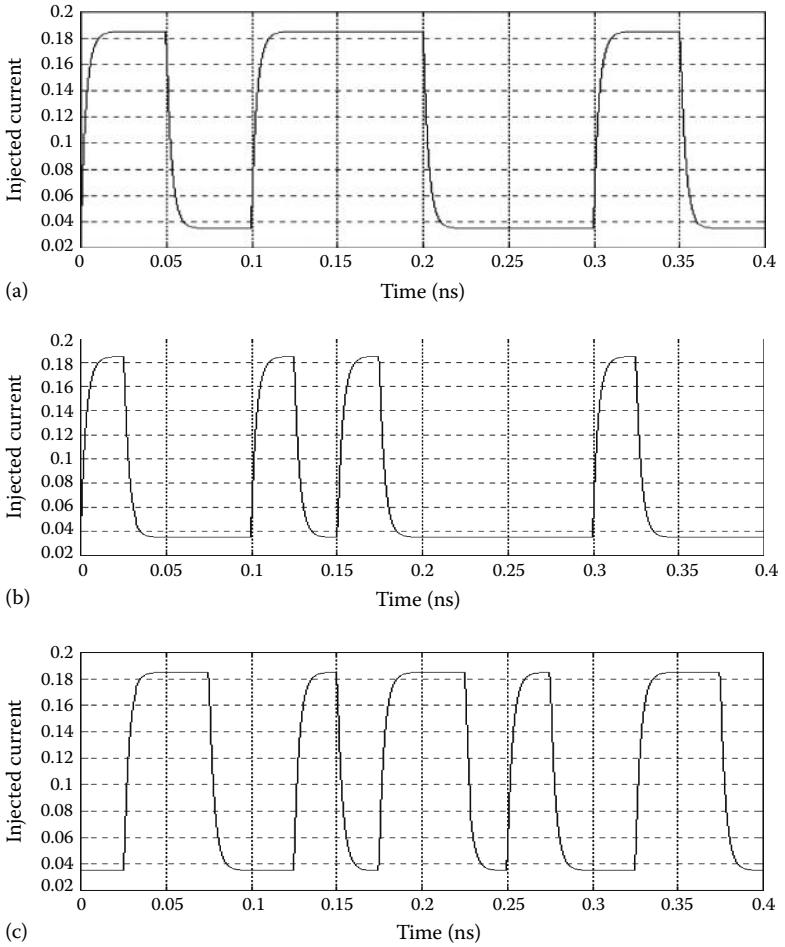

FIGURE 5.17
Output waveform of (a) NRZ, (b) RZ, and (c) MAN line coding.

5.2.3.2 Runge–Kutta Algorithm

Laser rate equations given in Section 5.2.2.8 are in the form of ordinary differential equations. A few differential equations can be integrated exactly to give a solution, which can be written in terms of elementary functions. In general, a numerical method must be used to find an approximate solution to the first-order differential equation which follows the general form

$$\frac{dy}{dt} = f(t, y) \tag{5.27}$$

where f is a given function of both t and y. In these equations, we are seeking an unknown function $y(t)$ which satisfies this equation for all values of t larger than some given initial value t_0, at which the initial value of y is also specified. Available methods to solve these differential equations are Euler's method or the improved Euler method and Runge–Kutta method. To solve the rate equations in this simulation, Runge–Kutta method is used, as in most applications it gives very accurate results provided a very small step size is used for iteration.

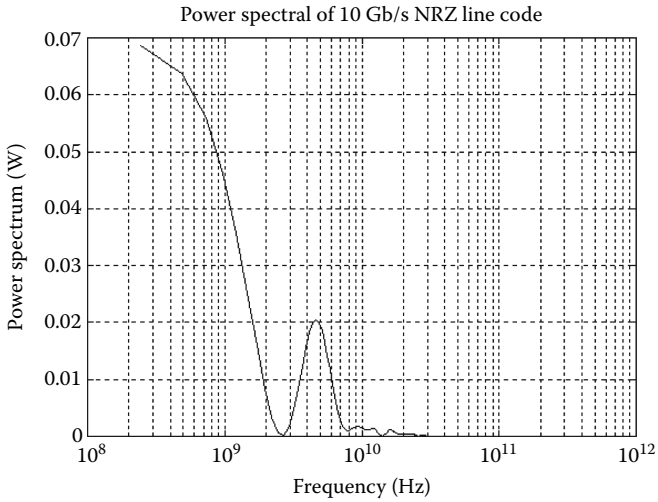

FIGURE 5.18
Bandwidth display of NRZ line code at 10 Gb/s.

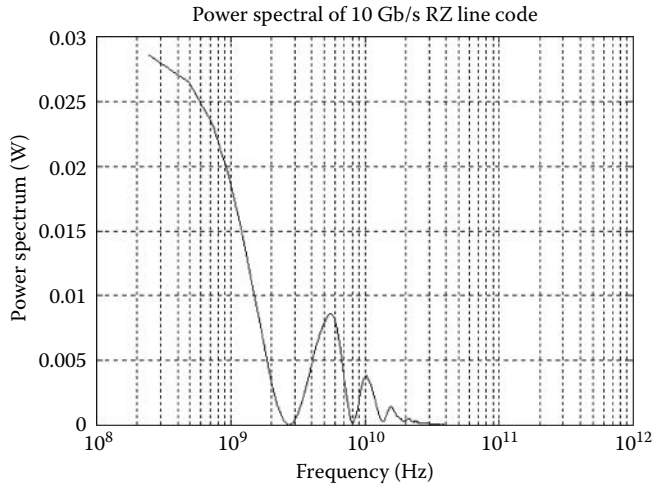

FIGURE 5.19
Bandwidth display of RZ line code at 10 Gb/s.

There are two library files available in MATLAB to solve ordinary differential equations using Runge–Kutta method, *ODE23* and *ODE45*,

ODE23(FunFcn, t0, tfinal, y0, tol, trace)
ODE45(FunFcn, t0, tfinal, y0, tol, trace)

ODE23 integrates a system of ordinary differential equations using second- and third-order Runge–Kutta formulas whereas *ODE45* integrates a system of ordinary differential equations using fourth and fifth order, which appears to provide more accurate numerical solutions but takes longer computation time. *tol* is the desired accuracy for Runge–Kutta

computation and it has value 0.0000001 by default. In **OCSS**©, *ODE45* with $1e^{-7}$ accuracy is adopted for simulation analysis and listed in Section 5.5.2.

5.2.3.3 Optical Source Modeling

A block diagram of the optical transmitter system to be considered is illustrated in Figure 5.16. Input signals are electrically encoded by using laser drive circuit. The optical source is assumed to be single-longitudinal mode semiconductor laser in which the injected laser current $I(t)$ is a digital pulse waveform

$$I(t) = I_{bias} + \sum_{k=-\infty}^{\infty} A_k I_p(t - kT) \tag{5.28}$$

where

A_k is the input data sequence (A_k = 0 or 1 for each k index)
$I_p(t)$ is the transmitted current pulse shape whose format is one of RZ, NRZ and MAN signaling
T is the bit period
I_{bias} is the bias current

Current pulse shape is assumed to be of the form [21]

$$I_p(t) = \begin{cases} 0 & t < 0 \\ I_m\left[1 - \exp\left(-t^2/\tau_r^2\right)\right] & 0 \le t \le T \\ I_m\left[1 - \exp\left(-T^2/\tau_r^2\right)\right] \cdot \exp\left(-t^2/\tau_r^2\right) & t > T \end{cases} \tag{5.29}$$

where

I_m is the peak modulation current
τ_r determines the pulse rise time or fall time

Figure 5.17 depicts typical pulse sequences generated by this simulation section for modulation format NRZ, RZ and MAN. A typical pulse response is shown in Figure 5.20.

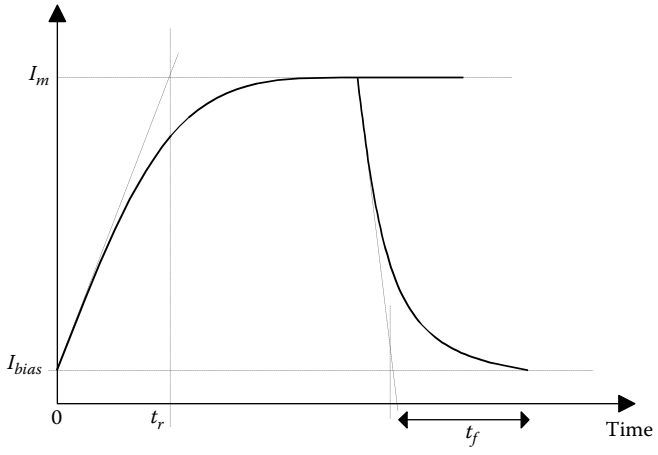

FIGURE 5.20
A typical laser current response showing the t_{rise} and t_{fall}.

The photon density, carrier density, and optical phase of the semiconductor laser, in response to the injected current $I(t)$,* are determined by numerically solving the rate equations, which describe the nonlinear modulation dynamics of the device and have been discussed in Sections 5.2.3 and 5.2.3.1. A *fourth–fifth order Runge–Kutta algorithm* is used to integrate the coupled set of first-order differential equations for the photon density $S(t)$, carrier density $N(t)$, and optical phase $\phi_m(t)$. Laser noise due to spontaneous emission and electron-hole recombination (shot noise) can be represented by Langevin noise which has been discussed in Section 5.2.3.3. **OCSS**©† uses MATLAB's built in Runge–Kutta algorithm to solve these complex rate equations

$$\frac{dS(t)}{dt} = \left(\Gamma a_0 v_g \frac{N(t)-N_0}{1+\varepsilon_C S(t)} - \frac{1}{\tau_p}\right) S(t) + \frac{\beta\Gamma N(t)}{\tau_n} + N(0,1)\sqrt{2\left(\frac{\beta V_a N_{sd}\left(V_a S_{sd}+1\right)^3}{\tau_n}\right)} \tag{5.30}$$

$$\frac{dN(t)}{dt} = \frac{I(t)}{qV_a} - \frac{N(t)}{\tau_n} - v_g a_0 \frac{N(t)-N_0}{1+\varepsilon_C S(t)} S(t) + N(0,1)\sqrt{2\left(\frac{V_a N_{sd}}{\tau_n}\left(\beta V_a S_{sd}+1\right)\right)} \tag{5.31}$$

$$\frac{d\phi_m(t)}{dt} = \frac{\alpha}{2}\left(\Gamma v_g a_0 \left(N(t)-N_0\right) - \frac{1}{\tau_p}\right) + N(0,1)\sqrt{\frac{\Gamma v_g \sigma_g \left(N(t)-N_0\right)}{S(t)}} \tag{5.32}$$

where all the parameters are explained in Sections 5.2.2 and 5.2.3.2, and $N(0, 1)$ denotes the Gaussian-distributed random process with zero mean and standard deviation of unity. The photon density $S(t)$, carrier density $N(t)$, and optical phase $\phi_m(t)$, obtained by simulation platform **OCSS©,** are shown in Figure 5.21. Readers can refer to Appendix B10 for the **OCSS**© Plotting Menu.

In modeling an optical transmitter, the important characteristics are the optical spectrum and the optical power output waveform. The source optical spectrum is one of the inputs needed to calculate the single-mode fiber transfer function. The time variations of the optical signal modulated magnitude and the laser chirp are given by Equations 5.7 and 5.8, respectively.

5.2.4 Conditions for the Laser Rate Equations

In modeling the initial response of the laser source there are two possible initial states as shown in Figure 5.22, the switch-on and continuous states. In the switch-on state, we assume that a step current is introduced to the laser driving circuitry and this causes a switch-on delay explained in Sections 5.2.4.1 and 5.2.4.2. A sharp overshoot may occur before the photons and electrons have reached an equilibrium state. Therefore, this phenomenon is called the *Switch-On* state of the laser.

In the second case, we assume that the laser source has been turned on for a period of time whereby the equilibrium state of the photons and electrons has been reached. Thus, there is no sharp overshoot but switch-on delay is still in effect due to the turn-on period in an earlier point of time. Hence, this phenomenon is called the *continuous* state of the laser. Both states can be modeled by using the basic laser rate equations and with a few boundary conditions.

* It is noted that the capital I is used here to indicate that the current driving the laser I not in a small signal condition at which the lower case is commonly used indicating the linearity operating.

† OCSS = Optical Communication Systems Simulator: the package provided in this chapter.

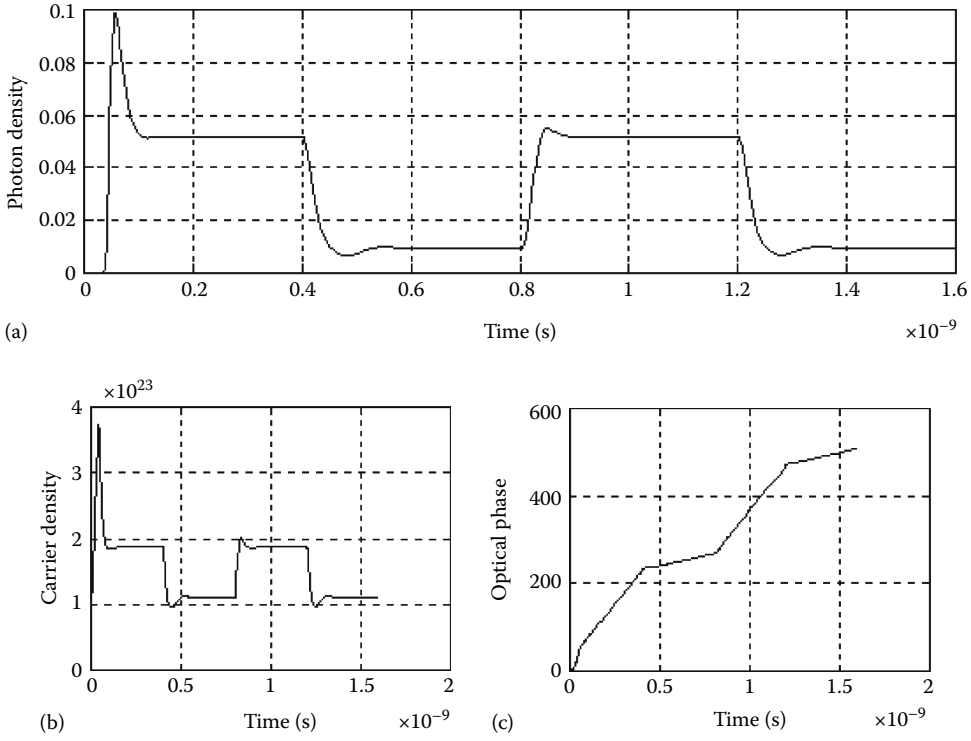

FIGURE 5.21
(a) Photon density, (b) carrier density, and (c) optical phase.

At $t = 0$, the fraction of the photons produced by spontaneous emission can be ignored, then from (5.2) we have

$$\frac{\beta\Gamma N(t)}{\tau_n} = 0 \tag{5.33}$$

Since $dS(t)/dt_{\text{at } t=0}$ must be a positive number, or

$$\left.\frac{dS(t)}{dt}\right|_{t=0} > 0 \tag{5.34}$$

Hence, from (5.2):

$$\Gamma a_0 v_g \frac{N(t) - N_0}{1 + \varepsilon_C S(t)} > \frac{1}{\tau_p} \tag{5.35}$$

$$N(0) = N_0 + \frac{1 + \varepsilon_C S(0)}{\Gamma a_0 v_g \tau_p} \tag{5.36}$$

Thus, the initial state of the carrier density is given by (5.36) which is valid for the following two cases.

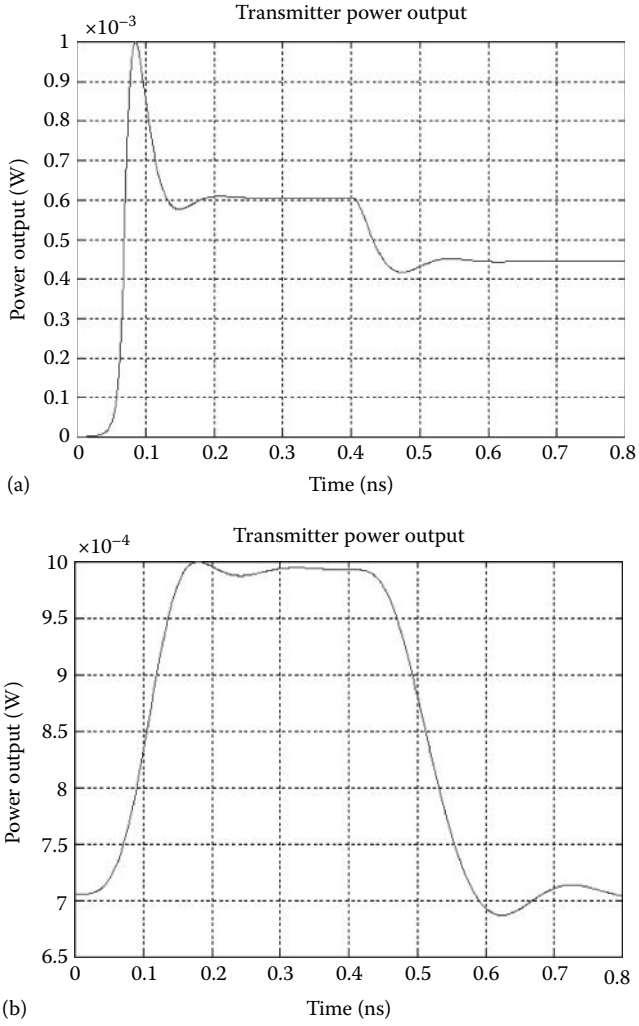

FIGURE 5.22
Optical power output of the laser under the driving conditions (a) switch on state and (b) continuous state.

5.2.4.1 Switch On State

We now define a threshold current as the $I(t)$ required to sustain $N(t) = N_{th}$ when $S(t) = 0$. From (5.2), this leads to

$$\frac{I_{th}}{qV_a} = \frac{N_{th}}{\tau_n} \tag{5.37}$$

This gives the current required to sustain an excess electron concentration, $N(t)$, when spontaneous emission is the only decay mechanism. We can use (5.3) to find $S(t)$ for the *switch-on* state. By substituting (5.37) into (5.2) and using (5.30), we obtain

$$S(t) = \frac{\tau_p}{qV_a}\left(I(t) - I_{th}\right) \tag{5.38}$$

since, $I_m = I_{th}$, $I(0) = 1.1 \times I_m$, $I_{bias} = 1.1I_m$ we have

$$S(0) = \frac{\tau_p}{qV_a}\left(0.1 \times I_m\right) \tag{5.39}$$

Thus, the initial state $S(0)$ for the *switch-on* state is given by (5.39). Readers can refer to Appendix 2 for detailed derivations.

5.2.4.2 Continuous State

The initial conditions for photon density, $S(0)$, and carrier density, $N(0)$, can be obtained by considering the steady-state solutions to the rate equations. These solutions are found by taking

$$\frac{dS(t)}{dt} = 0 \tag{5.40}$$

$$\frac{dN(t)}{dt} = 0 \tag{5.41}$$

Laser source rate equations are given by (5.2) and (5.3). By applying the steady-state conditions at $t = 0$ in (5.40) and (5.41):

$$\Gamma\left(\frac{a_0 v_g N(0)S(0)}{1+\varepsilon_C S(0)} - \frac{N_0 a_0 v_g S(0)}{1+\varepsilon_C S(0)}\right) - \frac{S(0)}{\tau_p} + \frac{\beta\Gamma N(0)}{\tau_n} = 0 \tag{5.42}$$

$I(0) = I_{bias}$,

$$\frac{I_{bias}}{qV_a} - \frac{N(0)}{\tau_n} - \left(\frac{a_0 v_g N(0)S(0)}{1+\varepsilon_C S(0)} - \frac{N_0 a_0 v_g S(0)}{1+\varepsilon_C S(0)}\right) = 0 \tag{5.43}$$

Equating (5.42) and (5.43) gives

$$\frac{I_{bias}\Gamma}{qV_a} - \frac{N(0)\Gamma}{\tau_n} - \frac{S(0)}{\tau_p} + \frac{\beta\Gamma N(0)}{\tau_n} = 0 \tag{5.44}$$

Finally, we have

$$N(0) = \frac{\tau_n}{(\beta-1)}\left(\frac{S(0)}{\Gamma\tau_p} - \frac{I_{bias}}{qV_a}\right) \tag{5.45}$$

Equating (5.45) and (5.36):

$$N_0 + \frac{1}{\Gamma a_0 v_g \tau_p} + \frac{\varepsilon_C S(0)}{\Gamma a_0 v_g \tau_p} = \frac{\tau_n S(0)}{(\beta-1)\Gamma\tau_p} - \frac{\tau_n I_{bias}}{(\beta-1)qV_a} \tag{5.46}$$

$$S(0) = \frac{qV_a(\beta-1)\left[1+N_0\Gamma a_0 v_g \tau_p\right] + \tau_n I_{bias}\Gamma a_0 v_g \tau_p}{qV_a\left[\tau_n a_0 v_g - \varepsilon_C(\beta-1)\right]} \tag{5.47}$$

Thus, the initial state $S(0)$ for *continuous* state is given by (5.47). Refer Appendix 2 for detailed derivations.

5.2.4.3 The Effect of Rate Equation Parameters on the Laser Response

The response of the laser power output is governed by the parameters in the photon rate equation stated in (5.2) and the modulation current stated in (5.28) and (5.29). Each parameter has a significant representation about the physical structure of a semiconductor laser, which would affect its response.

Therefore, to design a laser source, it is essential to know the effect of each parameter on the response of the laser output. Then, we can model the semiconductor laser source without carrying out any tedious or time-consuming experiments. Prior to designing, a considerable amount of knowledge about the effect of the parameters to its output response is needed. Thus, analysis of each parameter is carried out in this section. Parameters that are used in this analysis are as follows: T_{rise}—rise (or fall) time constant, Γ—confinement factor, α—linewidth enhancement factor, η—differential quantum efficiency, τ_p—photon lifetime, τ_n—carrier lifetime, ε_C—gain compression factor. Their effects on the generated optical pulses and detailed analyses are outlined in the following sections.

5.2.4.4 The Effect of Laser Rise-Time Constant

Ultra-long high-speed optical communication systems are very much limited by the laser source rise time constant. For high-speed modulation laser, small laser rise time constant is required. However, smaller laser rise-time constant would cause higher initial overshoot (Figure 5.23). In the case where the rise-time constant is 5 ps, the overshoot is about 75%. No overshoot effect is observed for rise-time constant of 50, 80, and 120 ps, but these lasers render low-speed modulation capability.

The second observable effect is the turn-on delay, which has been illustrated in Figure 5.22 and has been explained in Section 5.2.4.1. As expected, a larger laser rise time constant would give rise to longer turn-on delay and hence, slower laser output response. Referring to Figure 5.22, the average turn-on delay is about 20% of the bit period (5 ns).

Thus, to design a good, reliable, stable, and high-speed modulation laser source, optimum responses should be drawn from the balance effect of the overshoot and the rise time.

5.2.4.5 Effects of the Confinement Factor (Γ)

The optical confinement factor Γ is defined as the ratio of the fractional optical power confined in the core region to the total power. This factor is important for a semiconductor laser having optical gain in the core region, because it is related to the mode gain. In Figure 5.24, it is clearly seen that the optical confinement factor has a great effect on the turn-on delay time. When a laser medium is excited suddenly by a pulsed excitation source, the laser cannot start to oscillate immediately. The laser begins to oscillate after a time delay t_d, the characteristic time it takes for the population to build up to a level corresponding to the threshold.

We can observe from Figure 5.20 that a smaller optical confinement factor contributes considerably to longer delay times of the output pulse. In the case of Γ = 0.1, the delay time

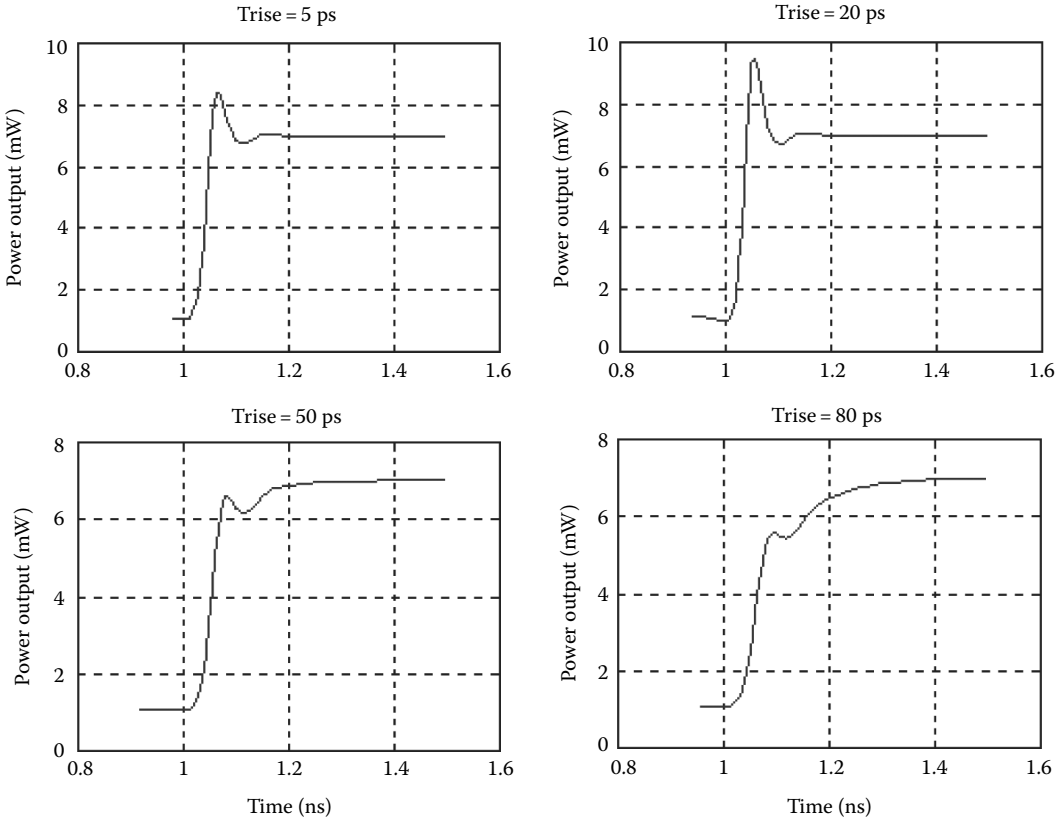

FIGURE 5.23
Power output lightwaves of various rise time constants at 2 Gb/s bit rate.

is about 30% of the bit period (5 ns) whereas when $\Gamma = 1.0$, the delay time is greatly reduced to only 1% of the bit period. Thus, by increasing the optical confinement factor in the active layer of the semiconductor, we can reduce the delay time considerably. Furthermore, for a higher value of the optical confinement factor, the overshoot effect is also reduced. Take, for example, when $\Gamma = 0.1$, the overshoot is about 400% whereas $\Gamma = 1.0$ only gives rise to about 100% overshoot. The final advantage of having a large optical confinement factor is the good damping effect. For $\Gamma = 0.1$, the pulse is oscillating over the whole bit period creating an additional unnecessary bandwidth in the communication channel. This phenomenon is known as the relaxation oscillation, which has been discussed in Section 5.2.3.1 (also see Figure 5.10).

Therefore, a good laser source design should maximize the optical confinement factor in the active layer. With a reasonable value, we can reduce the pulse distortion due to the delay time, overshoot, and relaxation oscillation effect of the response.

5.2.4.6 Effects of the Linewidth Enhancement Factor (α)

Low-frequency chirp, single-frequency laser diodes are extremely important for coherent optical communication systems. The principles of laser chirp have been discussed in Section 5.2.3.2 and various methods of reducing this effect have been recommended.

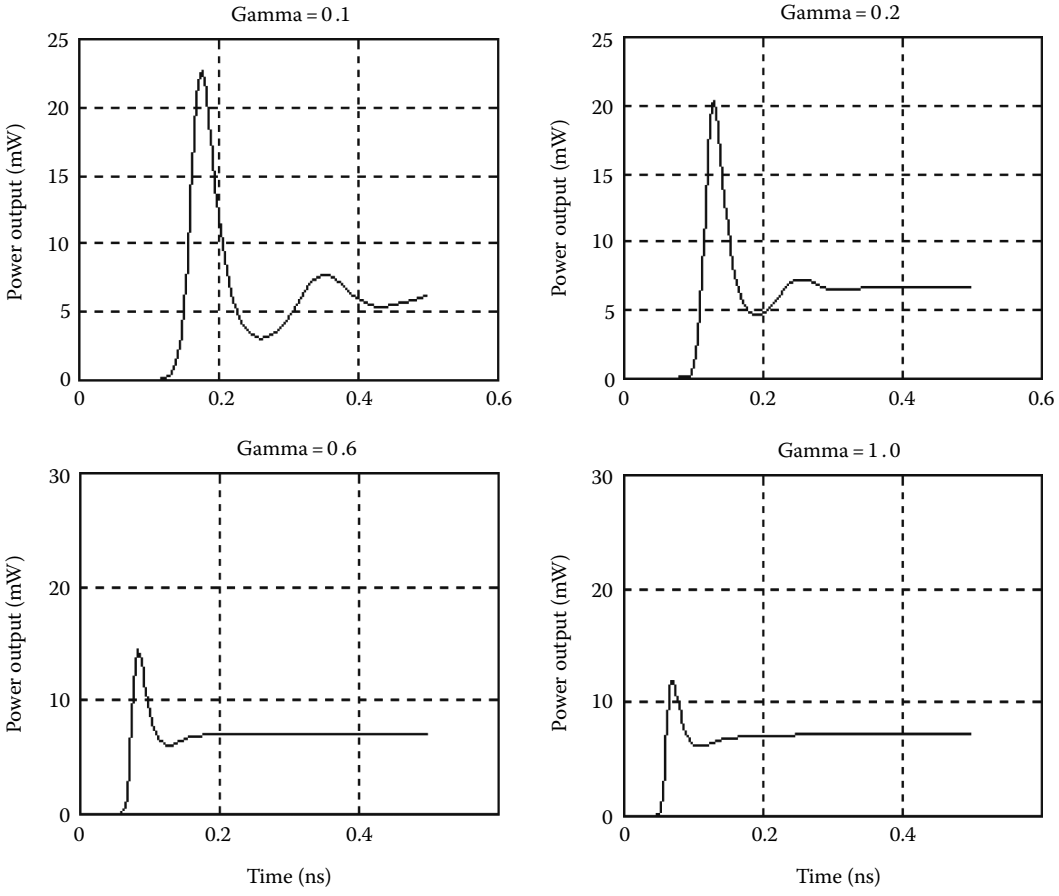

FIGURE 5.24
Power output of various optical confinement factors at 2 Gb/s.

In this section, we analyze the effect of linewidth enhancement factor, α on the frequency chirp. As we can see from Equation 5.8, the magnitude of frequency chirp (measured in Hz) is proportional to α. In this experiment, we assume direct intensity optical modulation scheme. No external modulator is used or otherwise the chirping effect is virtually nonexistent (Figure 5.25).

In Figure 5.21, we expect to see the linear relationship between frequency chirp and the linewidth enhancement factor, α. There is an increase of about 5.5 GHz for each unit increment of alpha. Thus, the frequency chirp (an undesirable effect) can be reduced by minimizing the factor α. We can also deduce from (5.8) that the frequency chirp is proportional to the carrier density, $N(t)$ and hence, to the input pulse. Therefore, in Figure 5.21, the magnitude of the frequency chirp follows the sequence of the input pulse.

In conclusion, design implementation of the laser source should remove the chirping effect as much as possible if not all, by minimizing the value of α. For example, high-performance tunable 1.5 μm InGaAs/InGaAsP multiple-quantum well DFB lasers are designed by AT&T Bell Laboratories in 1988 [27] with the value $\alpha = -3.5$.

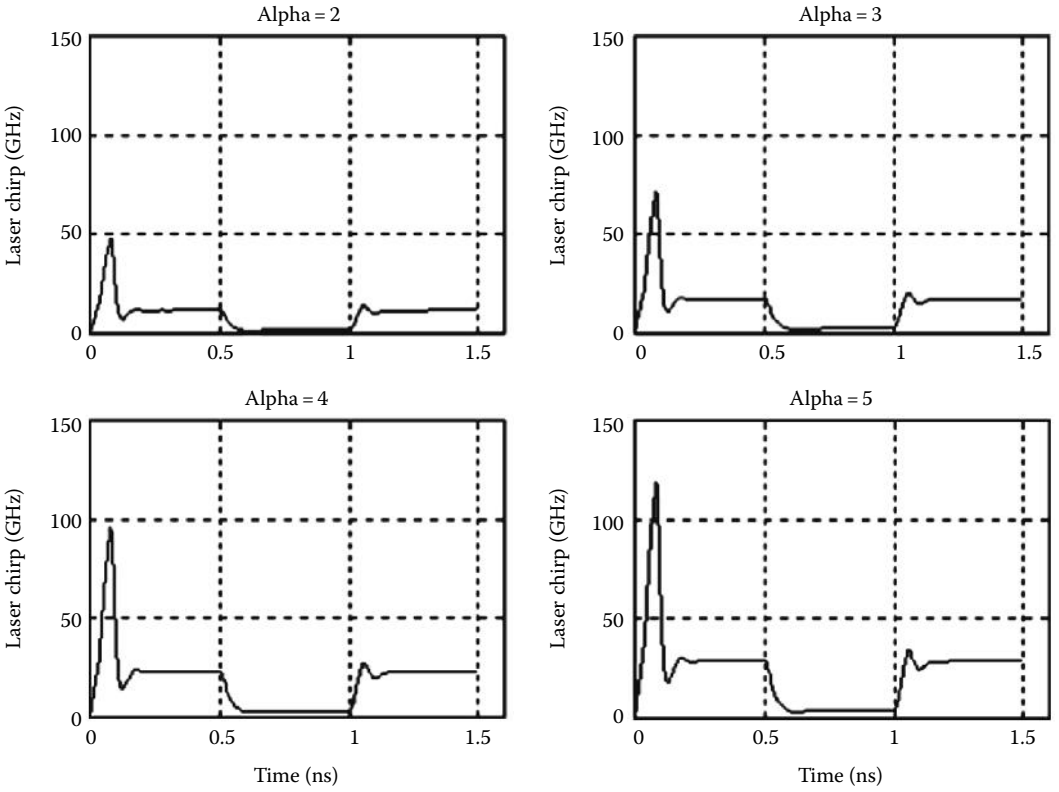

FIGURE 5.25
Power output of various linewidth enhancement factors at 2 Gb/s.

5.2.4.7 Effects of Differential Quantum Efficiency (η)

Differential quantum efficiency η can be best understood by quantifying the proportion of photons generated with respect to the injected electrons. The proposed mechanism giving rise to low differential quantum efficiency such as heating and leakage currents is not sufficient to explain the observed behavior. The linear dependency between η and the injected current has been discovered in GTE Laboratories [28].

From Figure 5.22, we can see that the power output is linearly related to the increment of η in (5.7). However, there are difficulties in designing a laser source with a high differential quantum efficiency. The average η for existing laser source ranges from 0.03 to 0.20 (or 3%–20%) only (Figure 5.26).

5.2.4.8 Effects of the Photon Lifetime (τ_p)

Photon lifetime τ_p is related to the cavity structure of the semiconductor laser (Figure 5.27). A small value of τ_p corresponds to short cavity structure of the laser source. From Equation 5.17, we see that τ_p is inversely proportional to the power output, $m(t)$. In Equation 5.18, we notice that we could reduce frequency chirp by reducing τ_p. And Figure 5.23 tells us that turn-on delay can be improved by reducing τ_p. Thus, it is essential to reduce τ_p by observing the importance of these three considerations.

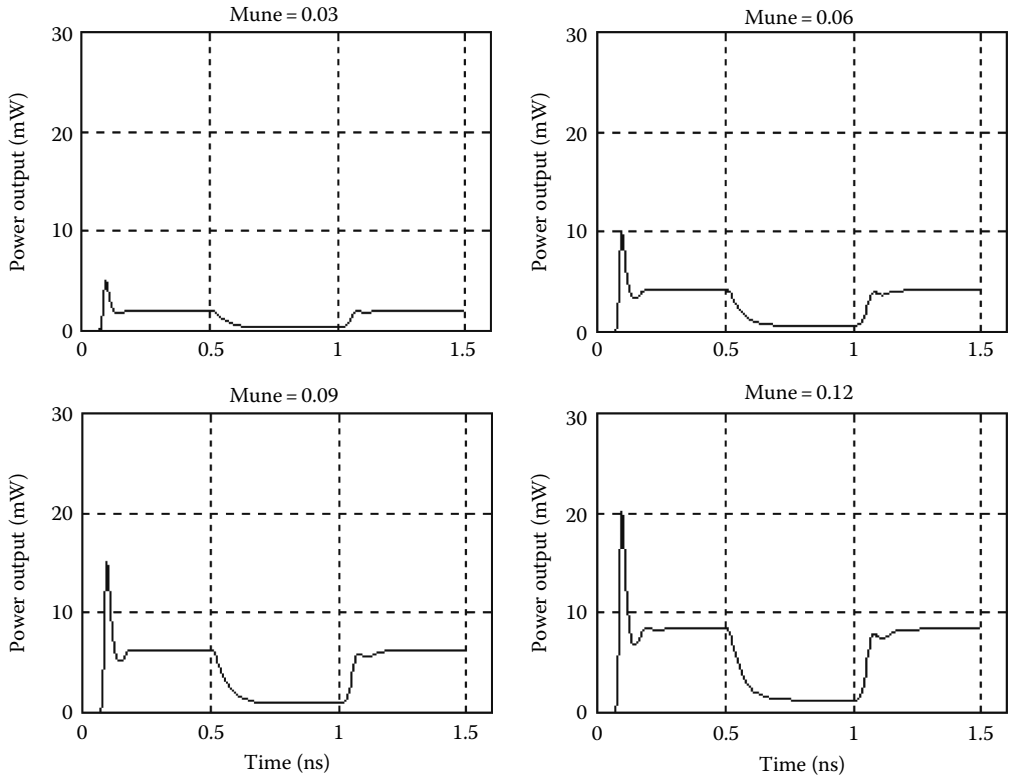

FIGURE 5.26
Power output of various differential quantum efficiencies at 2 Gb/s.

However, referring to Figure 5.23, we notice that a small value of τ_p gives rise to large overshoot in the output response. For instance where $\tau_p = 3$ ps, the overshoot is about 120%, which is undesirable. No overshoot has been observed for τ_p greater than 30 ps but again large values of τ_p would cause severe frequency chirp, turn-on delay, and low power output.

Thus, there is no better solution unless all the factors discussed here are compromised. Therefore, one optimum solution is to be obtained for the design implementation.

5.2.4.9 Effects due to the Carrier Lifetime (τ_n)

The carrier lifetime τ_n is related to the loss of electrons due to both spontaneous emission and nonradiative recombination [2.3]. From Figure 5.24, we notice that the overshoot of the output response is proportional to the carrier lifetime, τ_n. For example where τ_n = 512 ns the overshoot is 230%, compared with τ_n = 0.5 ns where the overshoot is only 100%. Referring to Appendix C17 (overlapped plotting of Figure 5.24), the turn-on delay has no direct relationship with τ_n. However, there seems to be a minimum turn-on delay between τ_n = 0.5 and 2 ns. Therefore, we should reduce τ_n so that we do not have an overshoot effect in our design implementation (Figure 5.28).

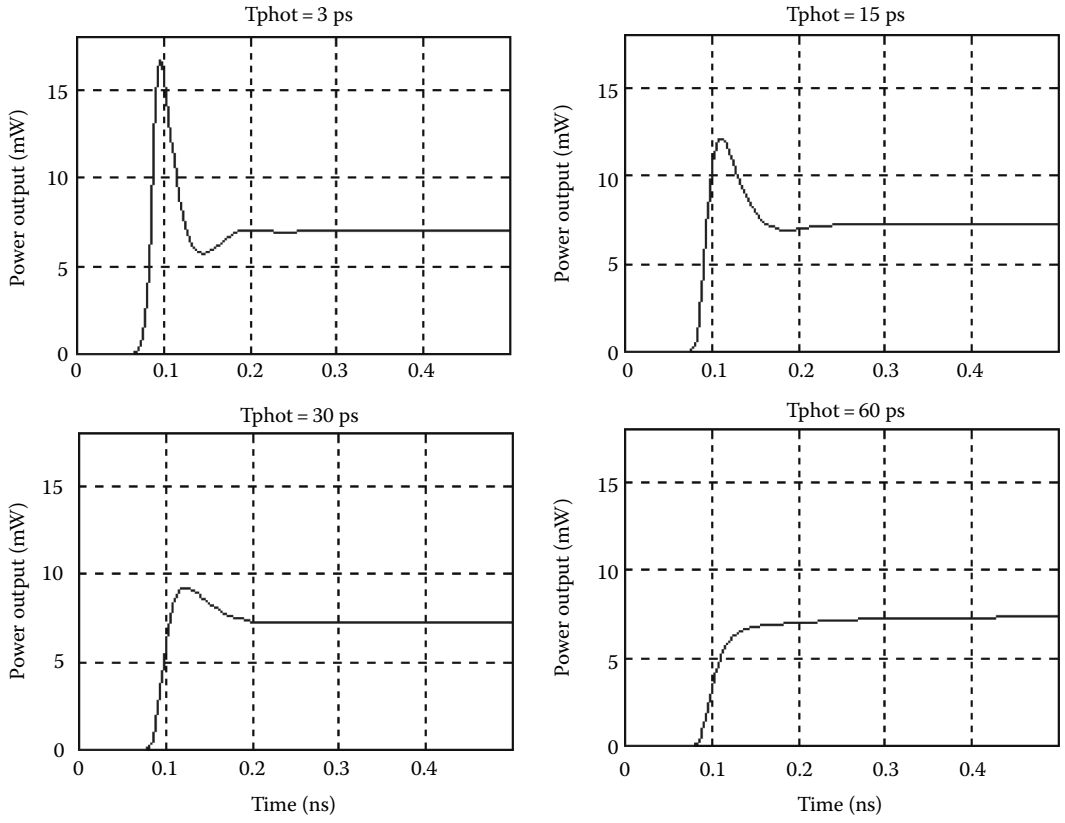

FIGURE 5.27
Power output of various photon lifetimes at 2 Gb/s.

5.2.4.10 Effects due to the Gain Compression Factor (ε)

The inclusion of gain compression factor ε in the laser rate equations (5.2) and (5.3) is a phenomenological approach, which can represent a number of mechanisms, including spatial hole burning and lateral carrier diffusion [2.33], [2.34], spectral hole burning, and other nonlinearities [2.35] (Figure 5.29).

From Figure 5.27 and Figure 5.29, it is clear that a good damping effect (less relaxation oscillations) and a small overshoot can be achieved by having a larger value of ε. For instance, oscillations of four cycles with overshoot of 330% ($\varepsilon_C = 0.5 \times 10^{-23}$) can be reduced to one oscillation cycle with 130% overshoot for the case where $\varepsilon_C = 2.5 \times 10^{-23}$. Thus, one can foresee that the output response will be fully oscillating for $\varepsilon_C = 0$.

In conclusion, a reasonably large value of ε_C is desirable to overcome the relaxation oscillation, which would cause some additional unnecessary bandwidth in the communication system.

5.2.5 Power Output and Eye-Diagram Analysis

Binary input stream pulses are encoded with using RZ, NRZ, or Manchester line coding in the code generator. The encoded input signal current is used to drive the semiconductor

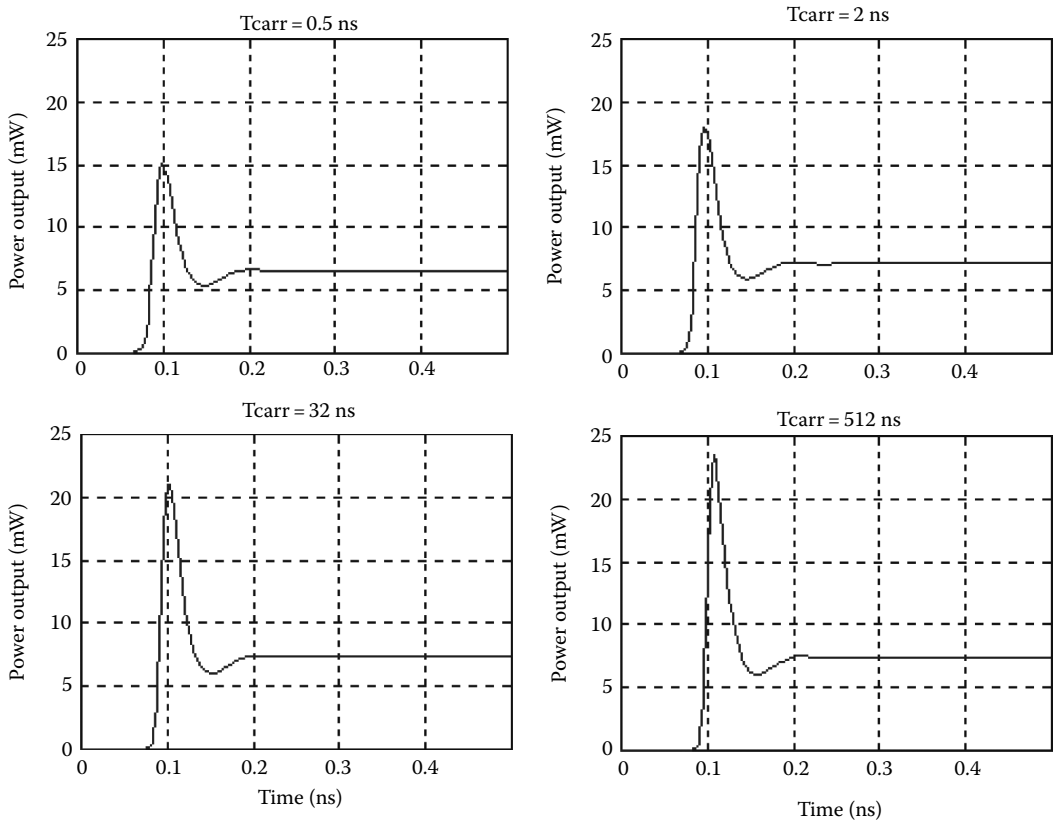

FIGURE 5.28
Power output of various carrier lifetimes at 2 Gb/s.

laser source by using a biasing circuit. This optical power output $m(t)$ will be transmitted into the optical fiber in the next module (Figure 5.30).

Shown in Figure 5.26 is the typical optical power output waveforms. It is encoded with binary bit sequence of 1011 0111 using NRZ format at a transmission rate of 2.5 Gb/s. In Figure 5.26, we notice that the whole output pulse has been shifted by 0.1 ns, that is, by 25% of the bit period (0.4 ns). This delay is due to the turn-on delay time, which has been discussed in Section 5.3.1.

5.2.5.1 Eye-Diagram Analysis

The eye-diagram technique is a simple but powerful measurement method for assessing the data-handling ability of a digital transmission system. This method has been used extensively for evaluating the performance of wire systems and can also be applied to optical fiber data links. To measure the system performance with the eye-diagram method, a variety of word patterns should be provided. A convenient approach is to generate a random data signal. Our simulation platform uses eight different 3-bit long combinations to simulate the eye diagrams. The output of each is overlapped and hence the eye diagram (see MATLAB program in the Appendix) (Figure 5.31).

Shown in Figure 5.27 are the simulated eye diagrams of various bit rates for a particular laser source with rise time 130 ps. As the transmission bit rate increases, the eye opening

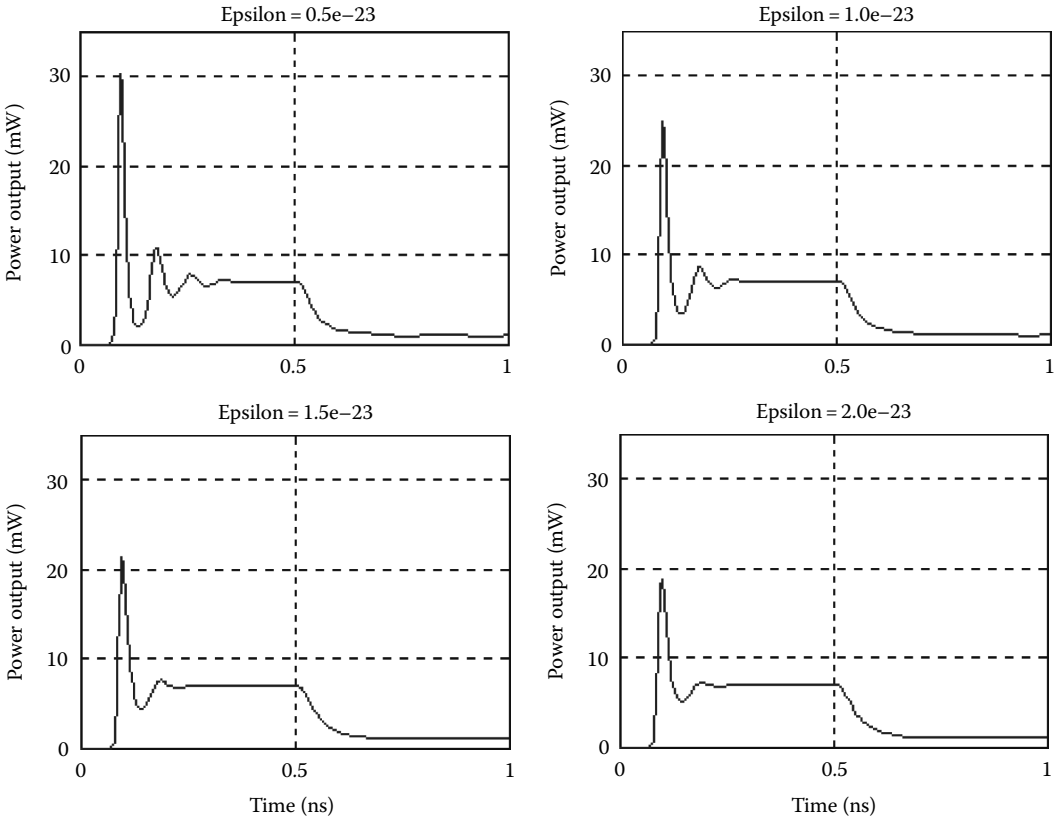

FIGURE 5.29
Power output of various gain compression factors at 2 Gb/s.

reduces to a limit where the eye does not exist anymore. Due to the indecisive decision level, it is impossible for the receiver to decode the optical signal correctly. The performance probability related to this is known as the *bit error rate* (BER) that is discussed in Chapter 4. Thus, the performance of a laser source is limited by the transmission rate. In Figure 5.27, the performance of the 5 Gb/s transmission is undesirable. Hence, this particular laser source could only afford to transmit at 3.3 Gb/s or below. However, it is recommended to place the limit at 1 Gb/s as the signal will be further distorted by the dispersion of optical fiber, which in turn would produce a bad undesirable eye diagram at the receiving end.

The same laser source is used for this analysis. Notice that the maximum achievable transmission bit rate for Manchester line coding is half of NRZ. Basically, it is because only a minimum half of the bit period is used to encode a pulse. Thus, we conclude that the system performance of an optical transmitter measured by eye-diagram technique is limited by the laser rise time constant as well as the choice of line coding.

5.2.5.2 Recent Research and Development in Optical Laser Source

Research and development in optical laser sources have been conducted by various photonics laboratories and research centers in both hardware and software environments.

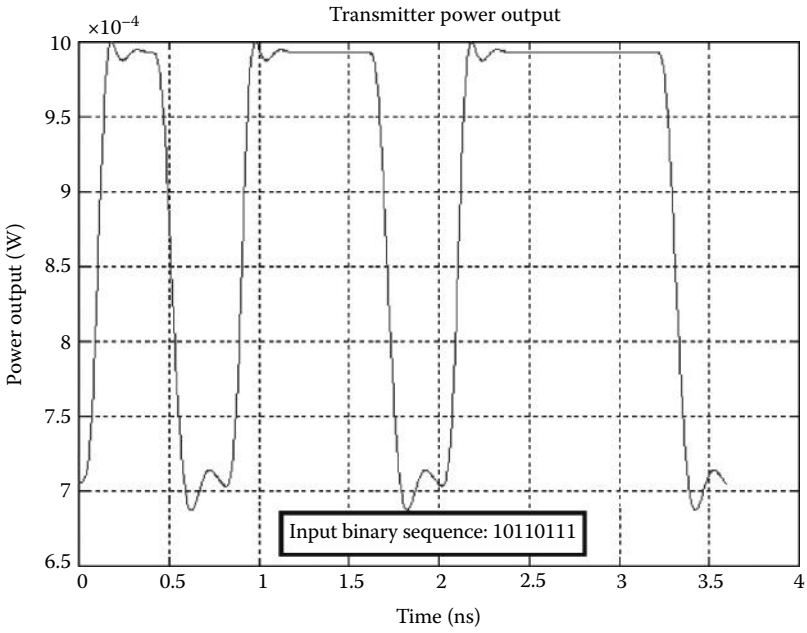

FIGURE 5.30
Power output of the optical transmitter with input bits 1011 0111 for NRZ format.

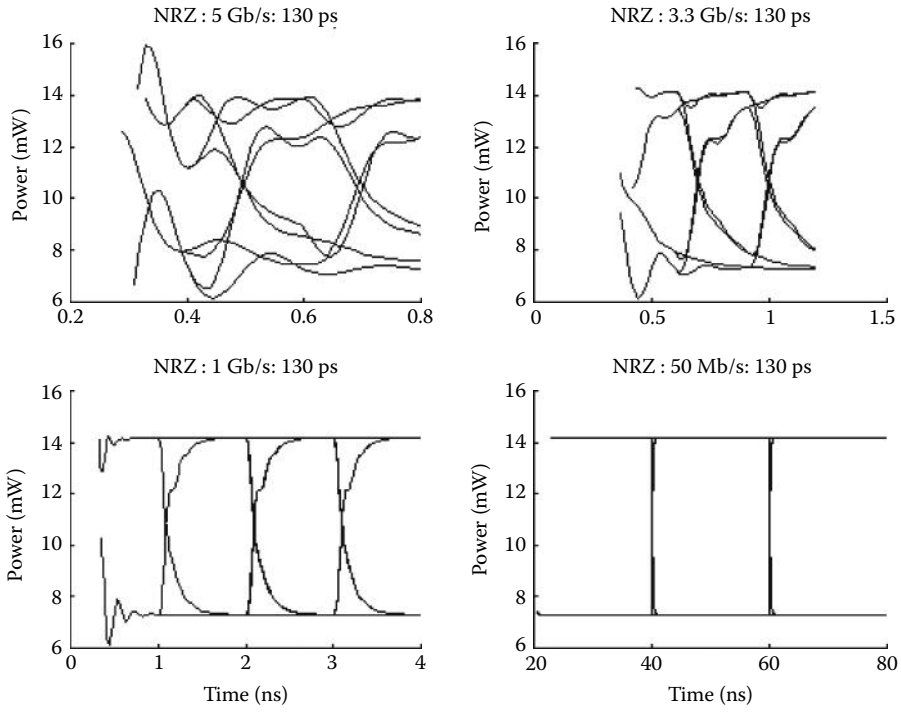

FIGURE 5.31
Eye diagrams of the optical transmitter at various bit rates.

Hardware simulation involves designing and inventing better performance optical laser sources that are capable of handling high-speed transmission systems. Software simulation involves modeling and developing software packages to assist researchers to design the hardware. In a way, software simulation can offer an important role to save the cost in the development of new products since experimenting with hardware requires a higher cost of investment.

5.2.5.3 Simulation Software

A new noise equivalent circuit model for laser diode is presented. It enables the noise analysis of laser diode and its relevant circuit to be complemented in a unified manner using circuit analytical software SPICE and allows the straightforward calculation of the intrinsic shot noise together with modulation response, terminal impedance, transient response, and nonlinear distortion. A concept of equivalent input intrinsic shot noise of laser diode is proposed to establish this model [12].

5.2.5.4 Hardware

There has been a growing interest in employing directly modulated semiconductor lasers, capable of being modulated at microwave frequencies (in GHz range) for transmission over fiber optic links.

A 20 GHz bandwidth 1.3 μm InGaAsP/InP Straight-Wall Mass-Transport Buried Heterostructure (SW-MTBH) laser diode was developed to operate in a microwave fiber optic link [6]. This laser diode has wide bandwidth, high dynamic range, low-noise, and good modulation properties which make it an attractive optical source for microwave fiber optic applications. Even though there are many lasers that are capable of transmitting at a higher bit rate (Table 5.1), SW-MTBH laser is claimed to be the best due to its overall performance, which includes reliability in a wide range of operating temperatures and low cost of production.

TABLE 5.1

Statistic of Recent Developments in Optical Laser Source

Laser Type	Abbr.	Bandwidth (GHz)	Year	Ref.
Buried heterostructure	BH	4	1982	[16]
Ridge waveguide	RW	4.5	1984	[18]
Etched mesa buried heterostructure	EMBH	7	1984	[18]
Constricted mesa (V-groove mass transport buried heterostructure)	V-MTBH	15	1987	[15]
Vapor-phase-regrown buried heterostructure	VPR-BH	24	1990	[13]
Multi-quantum well active region	MQW	20	1992	[13]
P-doped strained multi-quantum well active region	pS-MQW	25	1992	[14]
Semi-insulating buried crescent	SIBC	22	1992	[16]
Straight-wall mass transport buried heterostructure	SW-MTBH	20	1994	[6]

5.3 Introduction to Optical External Modulation

The modulation of light waves via an external optical modulator can be classified into three types depending on the special effects that alter the property of light waves, especially the intensity or the phase of the light wave carrier. In an external modulator, the intensity is normally manipulated by manipulating the phase of the carrier light waves guided in one path of an interferometer. Mach–Zehnder interferometric structure is the most common type [6,22–25]. See also Appendix 1 for some details of electrode arrangements with respect to optical waveguides.

EAM employs the Franz and Keldysh effect which is observed as lengthening the wavelength of the absorption edge of a semiconductor medium under the influence of an electric field [26–28]. In quantum structures, such as the multi-quantum well structure, this effect is called the Stark effect or the electro-absorption (EA) effect. The EAM can be integrated with a laser structure on the same integrated circuit chip. For $LiNbO_3$ modulator, the device is externally connected to a laser source via an optical fiber.

The total insertion loss of semiconductor intensity modulator is about 8–10 dB including fiber-waveguide coupling loss which is rather high. However, this loss can be compensated by a semiconductor optical amplifier (SOA) that can be integrated in the same circuit. In the case of LiNbO3 optical modulators, the total insertion loss is about 3–4 dB for a single MZIM structure and up to 11 dB for more complex modulators such as the polarization division multiplexed in-phase–quadrature modulator (PDM-IQ). However, these losses can now be compensated by using Er-doped fiber amplifier (EDFA), as described in Chapter 9.

The driving voltage for the EAM is usually lower than that required for $LiNbO_3$. However, the extension ratio is not as high as that of $LiNbO_3$ type which is about 25 dB as compared to 10 dB for the EAM. This feature contrasts the operating characteristics of the $LiNbO_3$ and EA modulators. Although the driving voltage for the EAM is about 3–4 and 5–7 V for $LiNbO_3$, the former type would be preferred for intensity or phase modulation formats due to this extinction ratio that offers a much lower "zero" noise level and hence, high-quality factor.

It is noted here that the extension ratio by EA modulation is normally about 11 dB to 14 dB, but for MZIM this ratio can reach 27–30 dB. This is due to the destructive interference and external modulation without too much of a contribution from the cavity noises as in direct modulation. However, the linearity of the transfer curve of the EA is much better than that of the $\cos^2$ transfer characteristics of the MZIM. If multi-level pulse amplitude modulation *M*-ary-PAM is employed then the EAM may offer a better total harmonic distortion than the MZIM.

In the following subsections, we outline the main modulation effects on light waves guided through optical waveguides. These phenomena are then employed to generate by modulation different optical modulation formats for long-haul terrestrial and short-haul metropolitan transmission systems and networks.

5.3.1 Phase Modulators

The phase modulator is a device which manipulates the "phase" of optical carrier signals under the influence of an electric field created by an applied voltage. When voltage is not applied to the RF electrode, the number of periods of the light waves, n, exists in a certain path length. When voltage is applied to the RF electrode, one or a fraction of one period of the wave is added, which now means that $(n + 1)$ waves exist in the same length. In this

case, the phase has been changed by 2π and the half voltage of this is called the driving voltage. In case of long-distance optical transmission, the waveform is susceptible to degradation due to a nonlinear effect such as self-phase modulation. A phase modulator can be used to alter the phase of the carrier to compensate for this degradation. The magnitude of the change of the phase depends on the change of the refractive index created via the electro-optic effect that in turn depends on the orientation of the crystal axis with respect to the direction of the established electric field by the applied signal voltage.

An integrated optic phase modulator operates in a similar manner except that the light wave carrier is guided via an optical waveguide in a diffused or an ion-exchange confined region for $LiNbO_3$ and via rib-waveguide structures for semiconductor type. Two electrodes are deposited so that an electric field can be established across the waveguiding cross section so that a change in the refractive index can be effected via the electro-optic or EA effect as shown in Figure 5.32. For ultra-fast operation, one of the electrodes is a traveling wave type or hot electrode and the other is a ground electrode. The traveling wave electrode must be terminated with matching impedance at the end so as to avoid wave

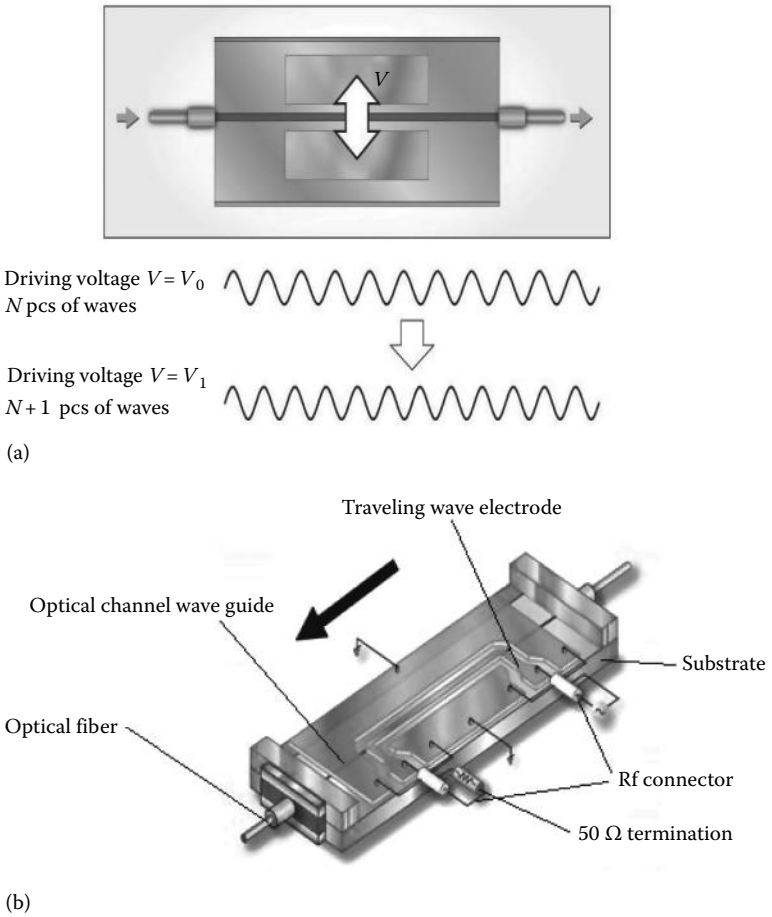

FIGURE 5.32
Electro-optic phase modulation in an integrated modulator using $LiNbO_3$. Electrode impedance matching is not shown (a) schematic diagram, (b) integrated optic structure.

reflection. Usually, a quarter wavelength impedance is used to match the impedance of the traveling wave electrode to that of the 50 Ω transmission line.

A phasor representation of a phase-modulated light wave can be made by the circular rotation at an angular frequency ω_C. Thus, the vector with an angle ϕ represents the magnitude and phase of the light wave.

5.3.2 Intensity Modulators

Basic structured $LiNbO_3$ modulator comprises (1) two waveguides, (2) two *Y*-junctions, and (3) RF/DC traveling wave electrodes. Optical signals coming from the light wave source is launched into the $LiNbO_3$ modulator through the polarization maintaining fiber; it is then equally split into two branches at the first *Y*-junction on the substrate. When no voltage is applied to the RF electrodes, the two signals are recombined constructively at the second *Y*-junction and coupled into a single output. In this case, output signals from the $LiNbO_3$ modulator are recognized as "ONE." When voltage is applied to the RF electrode, due to the electro-optic effects of the $LiNbO_3$ crystal substrate, the waveguide refractive index is changed, and hence, the carrier phase in one arm is advanced though retarded in the other arm. Thence, the two signals are recombined destructively at the second *Y*-junction, and they are transformed into higher-order mode and radiated at the junction. If the phase retarding is a multiple odd factor of π, the two signals are completely out of phase, the combined signals are radiated into the substrate, and the output signal from the $LiNbO_3$ modulator is recognized as a "ZERO." The voltage difference that induces this "ZERO" and "ONE" is called the driving voltage of the modulator and is one of the important parameters in deciding the modulator's performance.

5.3.3 Phasor Representation and Transfer Characteristics

Consider an interferometic intensity modulator that consists of an input waveguide split into two branches and then recombined to a single output waveguide (Figure 5.33). If the two electrodes are initially biased with voltages V_{b1} and V_{b2} then the initial phases exerted on the light waves would be $\phi_1 = \dfrac{\pi V_{b1}}{V_\pi} = -\phi_2$ which are indicated by the bias vectors shown in Figure 5.34a and b. From these positions, the phasors are swinging according to the magnitude and sign of the pulse voltages applied to the electrodes (Figure 5.34a). They can

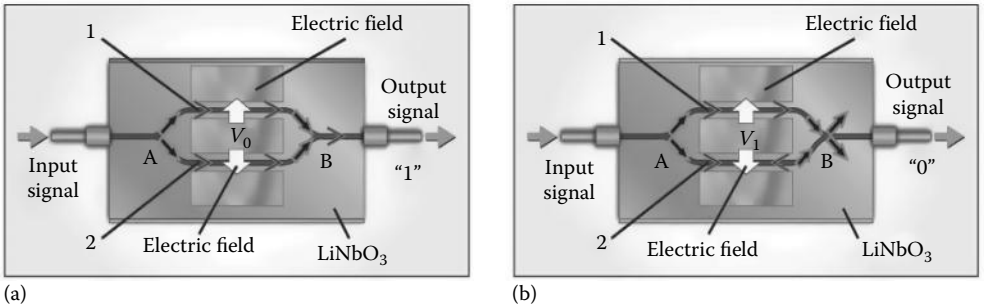

FIGURE 5.33
Intensity modulation using interferometric principles in guide wave structures in $LiNbO_3$ (a) ON—constructive interference mode, (b) destructive interference mode—OFF. Optical guided wave paths 1 and 2. Electric field is established across the optical waveguide.

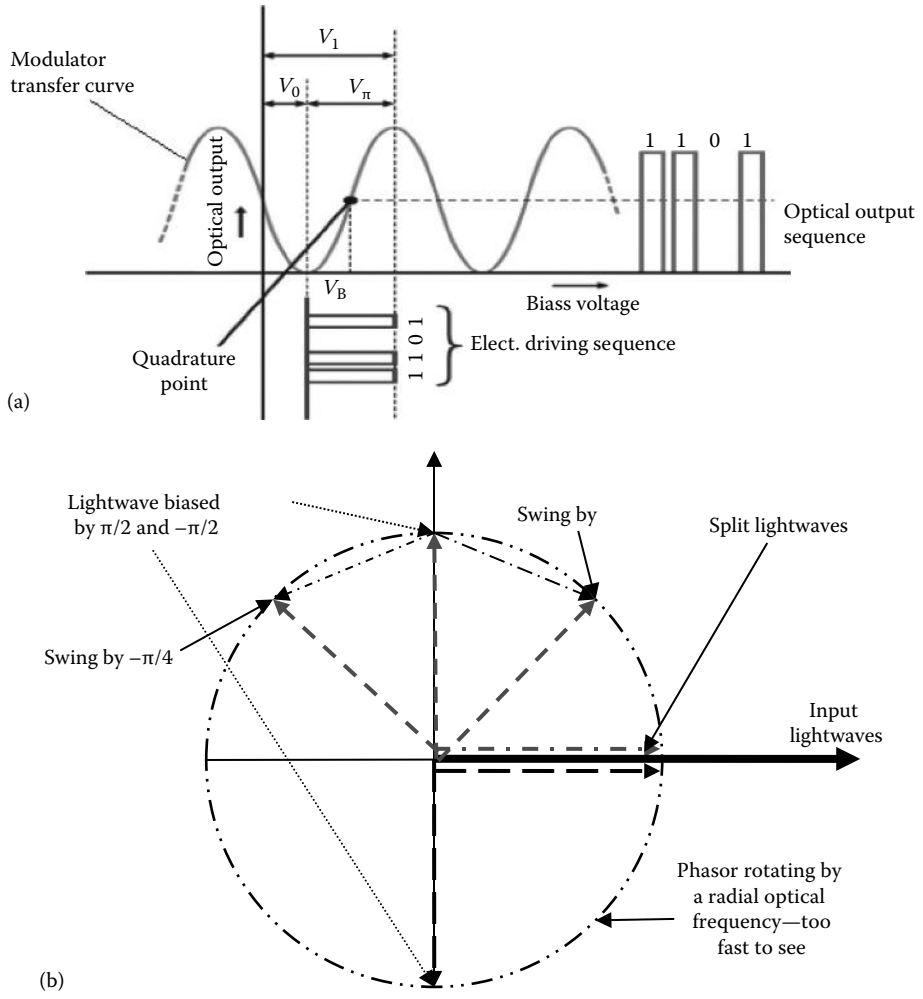

FIGURE 5.34
Electrical to optical transfer curve of an interferometric intensity modulator (a) transfer curve: optical output versus voltage input; (b) phasor diagram with vectors representing the initial biasing phase by bias applied voltages and the vectors indicating the AC swing by the amplitudes of the RF signals. Note that these RF vectors swing at RF frequency, and hence not represented but by a static maximum position.

be switched to two positions that can be constructive or destructive. The output field of the light wave carrier can be represented by

$$E_0 = \frac{1}{2} E_{iRMS} e^{j\omega_c t} \left(e^{j\phi_1(t)} + e^{j\phi_2(t)} \right) \tag{5.48}$$

where

ω_c is the carrier radial frequency
E_{iRMS} is the root mean square value of the magnitude of the carrier
$\phi_1(t)$ and $\phi_2(t)$ are the temporal phases generated by the two time-dependent pulse sequences applied to the two electrodes

With the voltage levels varying according to the magnitude of the pulse sequence one can obtain the transfer curve as shown in Figure 5.34b. This phasor representation can be used to determine the biasing conditions exactly and the magnitude of the RF or digital signals required for driving the optical modulators to achieve 50%, 33% or 67% bit period pulse shapes.

The power transfer function of Mach–Zehnder modulator is expressed as*

$$P_0(t) = \alpha_M P_i \cos^2 \frac{\pi V(t)}{V_\pi} \tag{5.49}$$

where

$P_0(t)$ is the output transmitted power
α_M is the modulator total insertion loss
P_i is the input power (usually from the laser diode)
$V(t)$ is the time-dependent signal applied voltage
V_π is the driving voltage such that a π phase shift is exerted on the light wave carrier along the optical path of the MZIM

It is necessary to set the static bias on the transmission curve through the Bias electrode. It is common practice to set the bias point at the 50% transmission point or a $\pi/2$ phase difference between the two optical waveguide branches, the quadrature bias point. As shown in Figure 5.34a and b, the electrical digital signals are transformed into optical digital signals by switching voltage to both ends of quadrature points on the positive and negative side.

5.3.4 Bias Control

One factor that affects the modulator performance is the drift of the bias voltage. For the MZIM type, it is very critical when it is required to bias at the quadrature point or at a minimum or maximum location on the transfer curve. DC drift is the phenomenon that occurs in $LiNbO_3$ due to the build-up of charges on the surface of the crystal substrate. Under this drift, the transmission curve gradually shifts in the long term [29,30]. In the case of the $LiNbO_3$ modulator, the bias point control is vital as the bias point will shift in the long term. To compensate for the drift, it is necessary to monitor the output signals and feed it back into the bias control circuits to adjust the DC voltage so that operating points stay at the same point as shown in Figure 5.35; for example, the quadrature point. It is the manufacturer's responsibility to reduce DC drift so that DC voltage is not beyond the limit throughout the lifetime of the device.

5.3.5 Chirp-Free Optical Modulators

Due to the symmetry of the crystal refractive index of the uniaxial anisotropy of the class m of $LiNbO_3$, the crystal cut and the propagation direction of the electric field affect both the modulator efficiency, denoted by the driving voltage, and the modulator chirp. The uniaxial property of $LiNbO_3$ is shown in Figure 5.36. As shown in Figure 5.37, in the case

* Note that this equation is represented for single-drive MZIM—it is the same for dual-drive MZIM provided that the bias voltages applied to the two electrodes are equal and opposite in signs. The transfer curve of the field representation would have half the periodic frequency of the transmission curve shown in Figure 5.34.

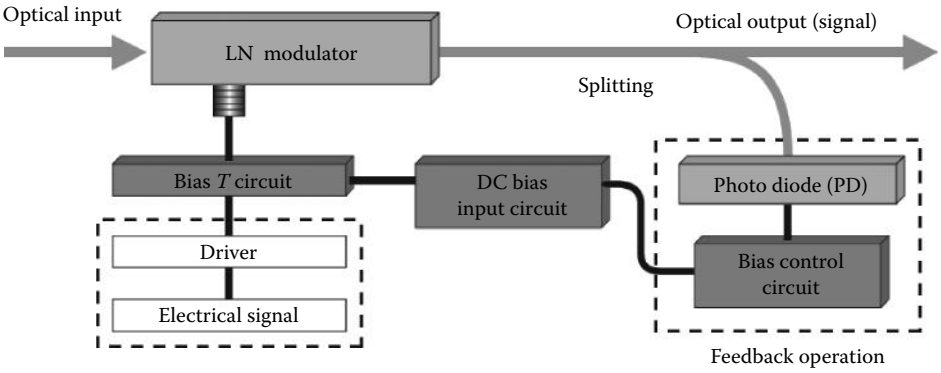

FIGURE 5.35
Arrangement of bias control by feedback signals from optoelectronic detector fed by tapped optical waves at the output of the MZIM.

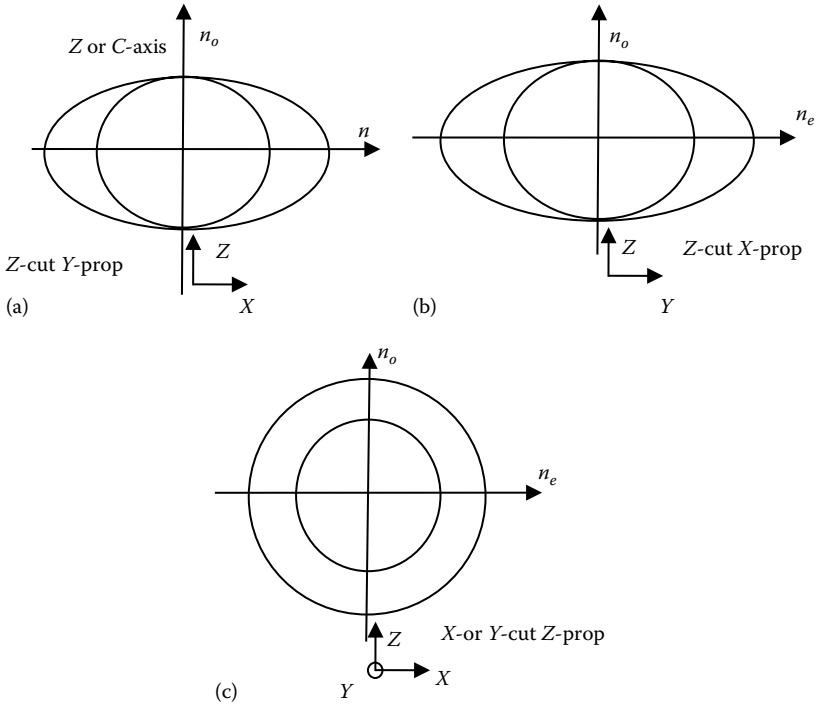

FIGURE 5.36
Refractive index contours of $LiNbO_3$ uniaxial crystal with *Z* or *C* denoting as the principal axis: (a) lightwaves propagation in the *Z*-axis polarize along *Y*-cut $LiNbO_3$, (b) propagation direction *Z*-axis and *X*-cut crystal, (c) *Y*-prop and *Y*-cut crystal.

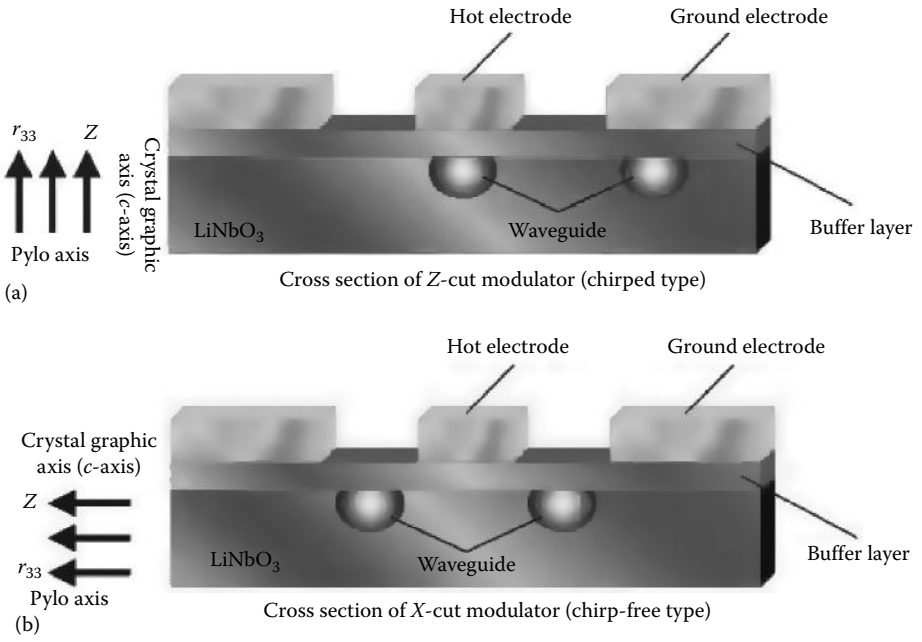

FIGURE 5.37
Different crystal cuts of $LiNbO_3$-integrated structures: (a) integration of electrodes and optical waveguides in *Z*-cut and (b) *X*-cut.

of the *Z*-cut structure, as the hot electrode is placed on top of the waveguide, the RF field flux is more concentrated, and this results in the improvement of overlap between RF and the optical field. However, overlap between RF in the ground electrode and the waveguide is reduced in the *Z*-cut structure so that the overall improvement in driving voltage for the *Z*-cut structure as compared to the *X*-cut is approximately 20%. The different overlapping area for the *Z*-cut structure results in a chirp parameter of 0.7, whereas the *X*-cut and *Z*-propagation has almost zero chirp due to its symmetric structure. A number of commonly arranged electrode and waveguide structures, as shown in Figure 5.38, maximize the interaction between the traveling electric field and the optical guided waves.

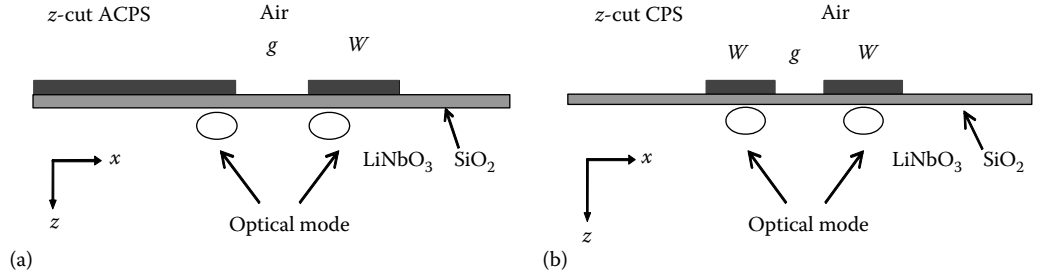

FIGURE 5.38
Commonly used electrode structure and crystal orientation for interferometric modulation to maximize the use of the overlap integral between the optical guided mode and the electric field distribution for largest electro-optic coefficients: (a) ACPS and (b) CPS.

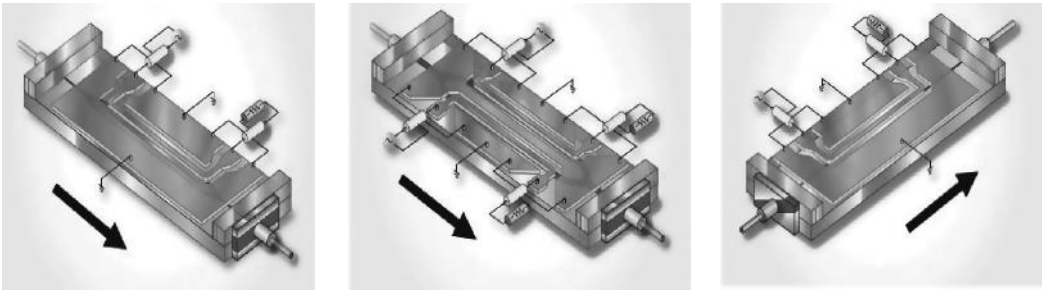

(a) (b) (c)

FIGURE 5.39
Intensity modulators using $LiNbO_3$ (a) single-drive electrode, (b) dual electrode structure, (c) electro-optic polarization scrambler using $LiNbO_3$.

Furthermore, a buffer layer, normally SiO_2, is used to match the velocities between these waves so as to optimize the optical modulation bandwidth.

5.3.6 Structures of Photonic Modulators

Figure 5.39a and b shows the structure of an MZ intensity modulator using single and dual electrode configurations, respectively. The thin line electrode is called the "hot" electrode or traveling wave electrode. RF connectors are required for launching the RF data signals to establish the electric field required for electro-optic effects. Impedance termination is also required. Optical fiber pig tails are also attached to the end faces of the diffused waveguide. The mode spot size of the diffused waveguide is not symmetric and hence, some diffusion parameters are controlled so that maximizing the coupling between the fiber and the diffused or rib waveguide can be achieved. Due to this mismatching between the mode spot sizes of the circular and diffused optical waveguides, there occurs coupling loss. Furthermore, the difference between the refractive indices of the fiber and $LiNbO_3$ is quite substantial and thus, Fresnel reflection loss is also incurred.

Figure 5.39c shows the structure of a polarization modulator, which is essential for multiplexing two polarized data sequences so as to double the transmission capacity, for example, 40G to 80 Gb/s. Furthermore, this type of polarization modulator can be used as a polarization rotator in a polarization dispersion compensating subsystem [31,32].

5.3.7 Typical Operational Parameters (Table 5.2, Figure 5.40)

5.3.8 Electro-Absorption Modulators

Because the electric field in the active region modulates not only the absorption characteristics but also the refractive index, the EAM produces some chirp. However, this chirp usually is much less than that of a directly modulated laser. A small on-state (bias) voltage of around 0–1 V often is applied to minimize the modulator chirp.

EAM employs the Franz and Keldysh effect which is observed as lengthening the wavelength of the absorption edge of a semiconductor medium under the influence of an electric field [33]. In quantum structure such as the multi-quantum well structure, this effect is called the Stark effect or the electro-absorption (EA) effect. The EAM can be integrated with a laser structure on the same integrated circuit chip. For $LiNbO_3$ modulator, the device is externally connected to a laser source via an optical fiber.

TABLE 5.2

Typical Operational Parameters of Optical Intensity Modulators

Parameters	Typical Values	Definition/Comments
Modulation speed	10 Gb/s	Capability to transmit digital signals
Insertion loss	Max. 5 dB	Defined as the optical power loss within the modulator
Driving voltage	Max. 4 V	The RF voltage required to have a full modulation
Optical bandwidth	Min. 8 GHz	3 dB roll-off in efficiency at the highest frequency in the modulated signal spectrum
ON/OFF extinction ratio	Min. 20 dB	The ratio of maximum optical power (ON) and minimum optical power (OFF)
Polarization extinction ratio	Min. 20 dB	The ratio of two polarization states (TM- and TE-guided modes) at the output

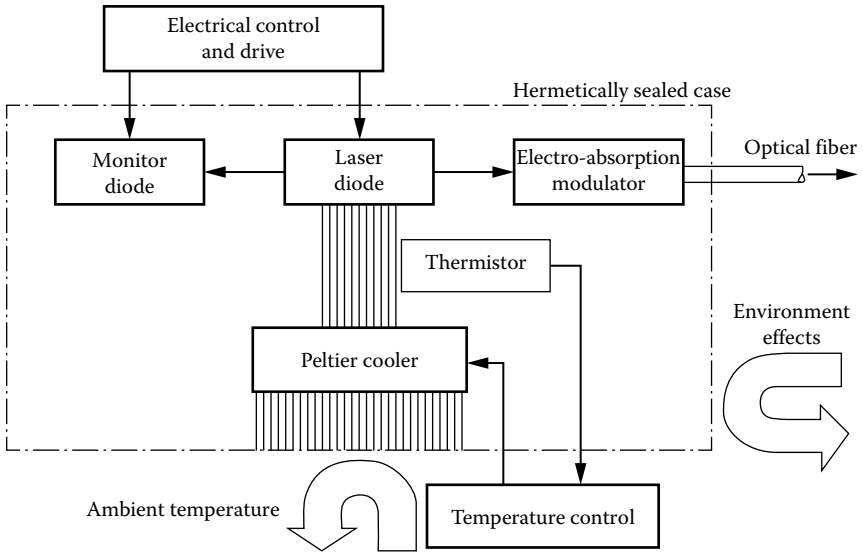

FIGURE 5.40
Block diagram of driving circuitry for a semiconductor laser and the EA modulator.

The total insertion loss of semiconductor intensity modulator is about 8–10 dB including fiber-waveguide coupling loss, which is rather high. However, this loss can be compensated by a semiconductor optical amplifier (SOA) that can be integrated on the same chip dye. This kind of integrated laser-EA-SOA device is now commonly known as EML (electro-absorption modulator laser).

The driving voltage for EAM is usually lower than that required for $LiNbO_3$. However, the extension ratio is not as high as that of the $LiNbO_3$ type which is about 25 dB as compared to 10 dB for the EAM. This feature contrasts the operating characteristics of the $LiNbO_3$ and EA modulators. Although the driving voltage for EAM is about 3–4 and 5–7 V for $LiNbO_3$, the former type would be preferred for intensity or phase modulation formats due to its high extinction ratio, which offers much lower "zero" noise level and hence, high-quality factor.

EAM is small and can be integrated with the laser on the same substrate as shown in Figure 5.41. An EAM combined with a CW laser source is known as an electroabsorption modulated laser (EML).

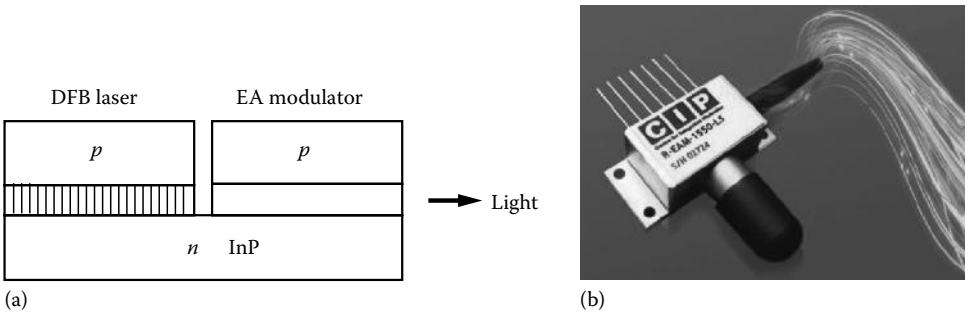

FIGURE 5.41
(a) Typical structure of EAM integrated with a distributed feedback laser on the same InP substrate; (b) package EAM of Huawei Center for Integrated Photonics of England.

An EML consists of a CW DFB laser followed by an EAM, as mentioned in the earlier text. Both devices can be integrated monolithically on the same InP substrate, leading to a compact design and low-coupling losses between the two devices. The EAM consists of an active semiconductor region sandwiched in between a *p*- and *n*-doped layer, forming a *p*–*n* junction. As mentioned earlier, the EAM works on the principle known as Franz–Keldysh effect, according to which the effective bandgap of a semiconductor decreases with an increasing electric field.

Without bias voltage across the *p*–*n* junction, the bandgap of the active region is just wide enough to be transparent at the wavelength of the laser light. However, when a sufficiently large reverse bias is applied across the *p*–*n* junction, the effective bandgap is reduced to the point where the active region begins to absorb the laser light and thus becomes opaque.

In practical EAMs, the active region usually is structured as a multi-quantum well (MQW), providing a stronger field-dependent absorption effect, which is known as the quantum-confined Stark effect.

The relationship between the optical output power, P_{out}, and the applied reverse voltage, V_m, of an EAM is described by the so-called switching curve as shown in Figure 5.42a, which illustrates such a curve together with the achievable ER for a given switching

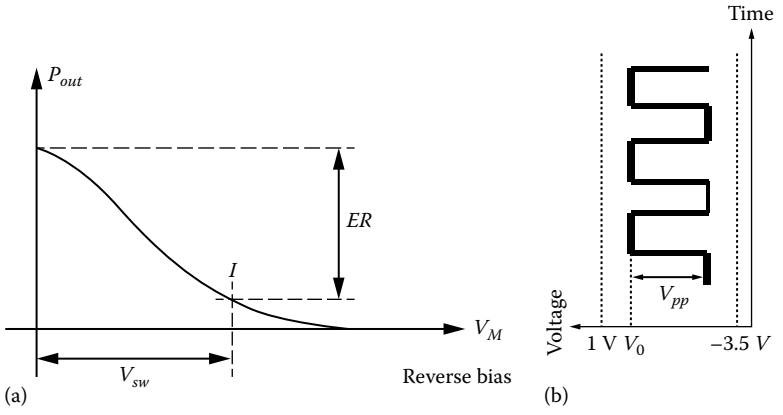

FIGURE 5.42
Power versus applied voltage of EAM (a) voltage-optical power transfer curve; (b) time domain signal to be injected into the EA with V_{pp} fallen within the liner region of the transfer curve.

voltage, V_{SW}. Figure 5.42b shows the signal in time domain that should be employed so that the optical output signal can be in the nonchirp and linear behavior.

The voltage for switching the modulator from the on state to the off state, the switching voltage V_{SW} is typically in the range of 1.5–4 V, and the dynamic ER is usually in the range of 11–13 dB.

Compared to the EOM described in details in the following text, EAMs can operate with much lower voltages, a few volts instead of ten volts or more. They can be operated at very high speed; a modulation bandwidth of tens of GHz can be achieved, which makes these devices useful for optical fiber communication. A convenient feature is that an EAM can be integrated with the DFB laser diode on a single chip to form a data transmitter in the form of a photonic integrated circuit. Compared with direct modulation of the laser diode, a higher bandwidth and reduced chirp can be obtained. One major drawback of the EAM is that the extinction ratio is not that high as compared with EOM. But the linear relationship between the applied voltage and output power is high.

In simple terms, the operation of an EAM can be considered as that of an optical attenuator at very high speed depending on the level of the reverse bias.

The modern optical transmitter for low-cost 100 Gb/s access and metro transmission optical networks now employ integrated lasers in line with an EAM so as to achieve the transmission of 28 Gsystems/s. Then with the use of four laser and inline EAMs, a 100G module can be created. This type of transmitter is called TOSA (Transmitter Optical Sub Assemblies) and its counterpart is ROSA (*R* = stands for Receiver).

5.3.9 Silicon-Based Optical Modulators

Currently, in the first two decades of the twenty-first century intensive research and development attention is paid to the use of silicon as a base material platform for integrated photonic circuits to reduce the cost of transmitters, transponders for ultra-broadband access systems, and long-haul transmission networks.

Silicon waveguides can be generated by ridge-type structures with carrier injection, depletion, or MOS (metal oxide) as shown in Figure 5.43. The injection mode operates by injection of the carrier by forward biasing with an applied voltage and a time-varying high-frequency signal. On the other hand, the depletion mode type modulator operates on the principles of depletion of the carrier in the ridge structure and then the electro-optic modulation effects created by the electric field of the traveling wave electrode pair are deposited on the two sides of the wave guide as shown. Similarly, the MOS waveguide modulator operates on the attraction of the carrier to the surface just below the oxide layer between the p and n layer

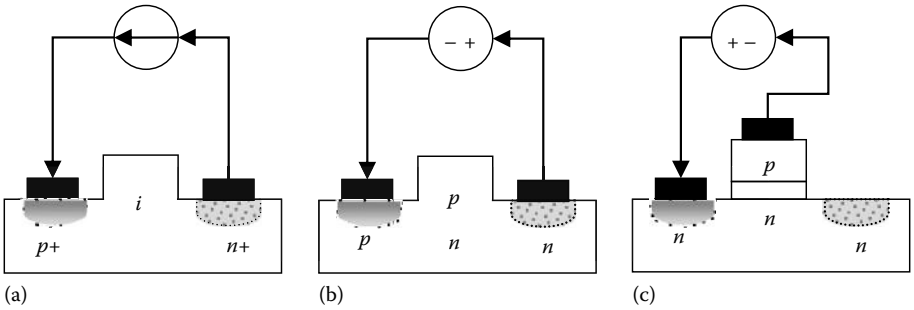

FIGURE 5.43
Basic structure of Si-modulation devices (a) by carrier injection into an intrinsic rib guide; (b) by carrier depletion; and (c) MOS and channel depletion.

shown in Figure 5.43c. Under the electro-optic modulation of the phase of the guided lightwaves, an electric field is applied across the waveguide via the electrode pair, hence there is modulation of the phase of the lightwave guided through the waveguide ridge structure.

Silicon is a class IV material and so, the EO coefficient is small. However, because of the large refractive index difference between the waveguide material Si and the cover layer which is normally SiO_2, the mode of confinement is very strong and thus the waveguide cross section can be made small enough, and the modulation can be effective with $V_\pi L$ = 25 V-mm. This leads to a V_π of 1.0 V for a 25 mm long electrode pair.

Once the phase modulation can be achieved in such an Si waveguide and modulator, several modulation structures can be formed such as the MZIM, the *I*–*Q* modulator, and the PDM-IQ modulators as described in the previous sections. With such traveling wave electrodes properly designed, the modulator 3 dB bandwidth can reach 40 GHz without much of a problem [34].

Si-integrated photonics can be established to take advantage of the matured Si-integrated circuit technology to produce low-cost high-speed transponder integrated with ADC and DAC based on Si–Ge technology.

Si–IP can not only provide optical modulators for advanced modulation formats, but it can also provide compact integrated optical switches and switching matrices for routing of optical channels in the optical domain without resorting to the intermediate electronic plane. Figure 5.44 shows the generic structure of different types of optical switches. Figure 5.44a shows the schematic structure of a directional coupler with cross coupling or switching occurring by applying a control voltage signal to change the waveguide mode distribution profile. The evanescent field is then coupled through to the other waveguide and a complete power transfer occurs when the phase of $\pi/2$ is achieved. Figure 5.44b also shows a directional coupler optical switch but with the active electrodes arranged in

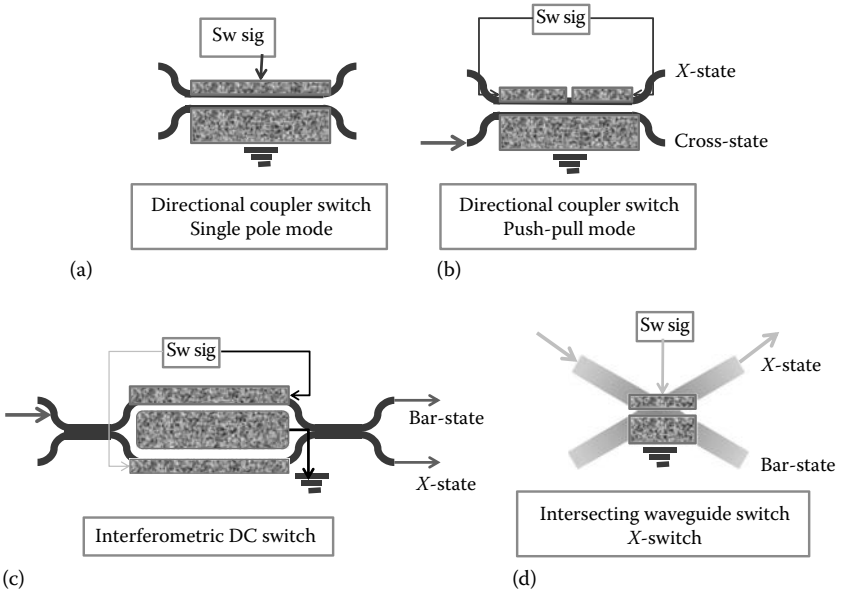

FIGURE 5.44
2 × 2 optical switches by integrated optic structures: 2 × 2 directional coupler switch structure (a) without and (b) with push pull operation; (c) 2 × 2 optical switch by Mach–Zehnder interferometric mechanism consisting of a Mach–Zehnder structure plus two 2 × 2 couplers for splitting switched channels; and (d) cross over X-switch.

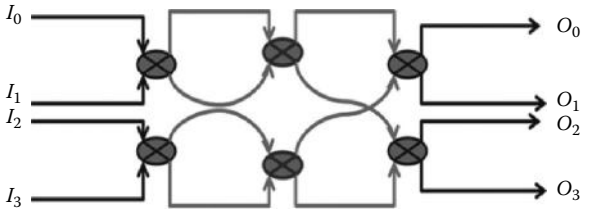

FIGURE 5.45
Structure of an optical switching matrix using Si-IP.

a push-pull mode so that the switching voltage can be reduced, hence requiring less RF amplification for operating at high frequencies. On the other hand, the X-switch shown in Figure 5.44d can also be implemented, but due to short active length in the cross region this requires high voltage amplitude signal. Figure 5.44c shows the interferometric switch with two input ports and two output ports. The switching occurs when there is depletion of the output waves due to the phase generated by applying the switching signal. Thus, 3 dB may be lost due to this destructive interference. This type of switch offers a truly 2 × 2 optical switch and can be easily implemented in Si–IP platform. Figure 5.45 shows how 2 × 2 optical switches can be used to structure nonblocking 4 × 4 switching structure. Higher-order $N \times N$ optical switching matrices can also be formed in this way.

5.3.10 MATLAB® Simulink® Models of External Optical Modulators

5.3.10.1 Phase Modulation Model and Intensity Modulation

In MATLAB Simulink, there are a number of blocksets such as Simulink Common blockset, Communications Blockset, Control System Blockset, and Signal Processing Blockset. A phase modulation section of optical waveguide can be implemented by using the phase shift block given in "Utility Blocks" of the Communication Blockset as shown in Figure 5.46.

The integration of phase shift blocks to form an intensity modulator is shown in Figure 5.47.

This data modulator can be integrated with another optical modulator, the pulse carver to generate the RZ pulse shaping with or without carrier suppression. This is implemented by setting an appropriate biasing of the pulse carver as shown in Figure 5.48. Note that the sinusoidal signal generators fed into the two phase shifters of the modulator complement each other and the voltage peak-to-peak magnitude must be two V_p in order to create a periodic sequence with suppression of the carrier. The output pulse period is half of that of the input sinusoidal wave, thus giving rise to a frequency doubling effect due to the nonlinear property of the voltage-output intensity transfer characteristics of the intensity

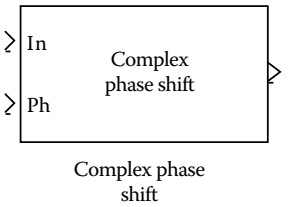

FIGURE 5.46
Phase shift block to be used for phase modulation in optical phase modulators or intensity modulators.

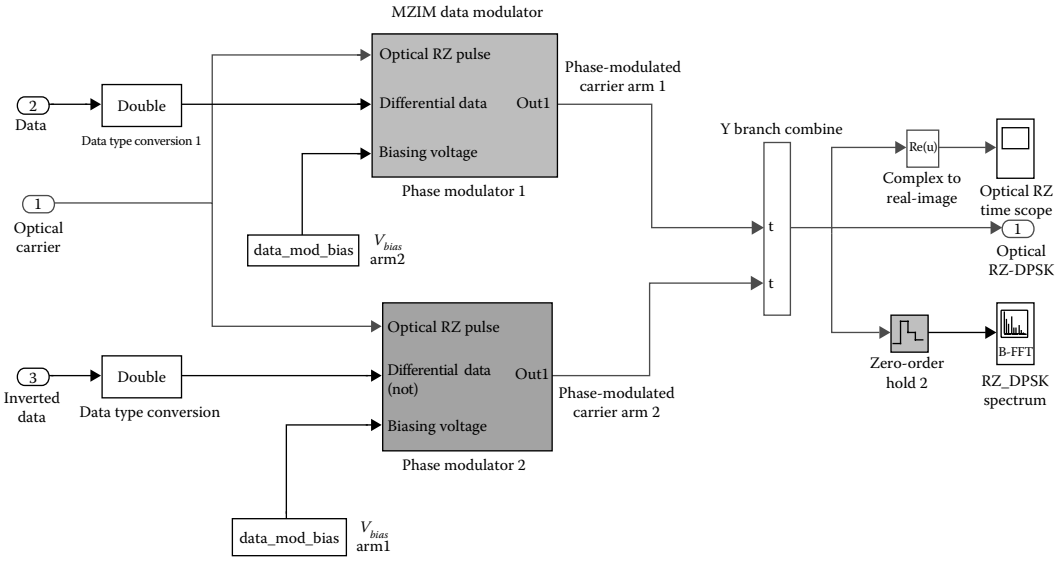

FIGURE 5.47
MATLAB® Simulink® model of an intensity optical modulator using dual electrode structures represented as two phase shift blocks with phase bias, laser lightwave input port and electrical data modulation port.

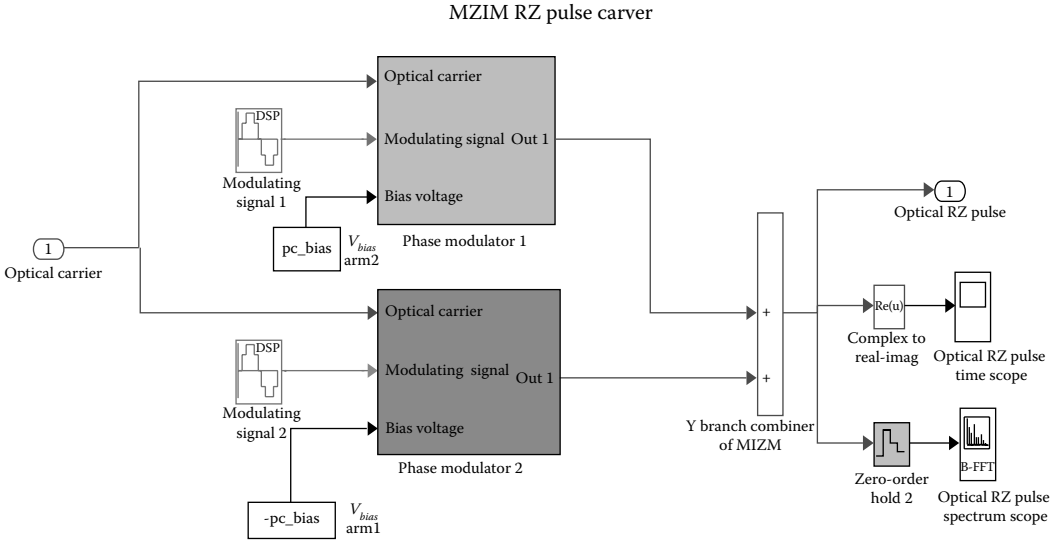

FIGURE 5.48
MATLAB® Simulink® model of an optical pulse carver for generation of RZ pulse shaping.

modulator. If a dual-drive modulator is used then the biasing voltage must be at $\pi/2$ so that there is always a π phase difference between the two arms of the Mach–Zehnder interferometer. The overall transmitter is shown in Figure 5.49. In addition to the optical modulation, for DPSK there must be a differential coder as shown in Figure 5.50 for coding the different features of the bit sequence to map two bits into the port representing the in-phase and quadrature components to be fed into the optical modulator.

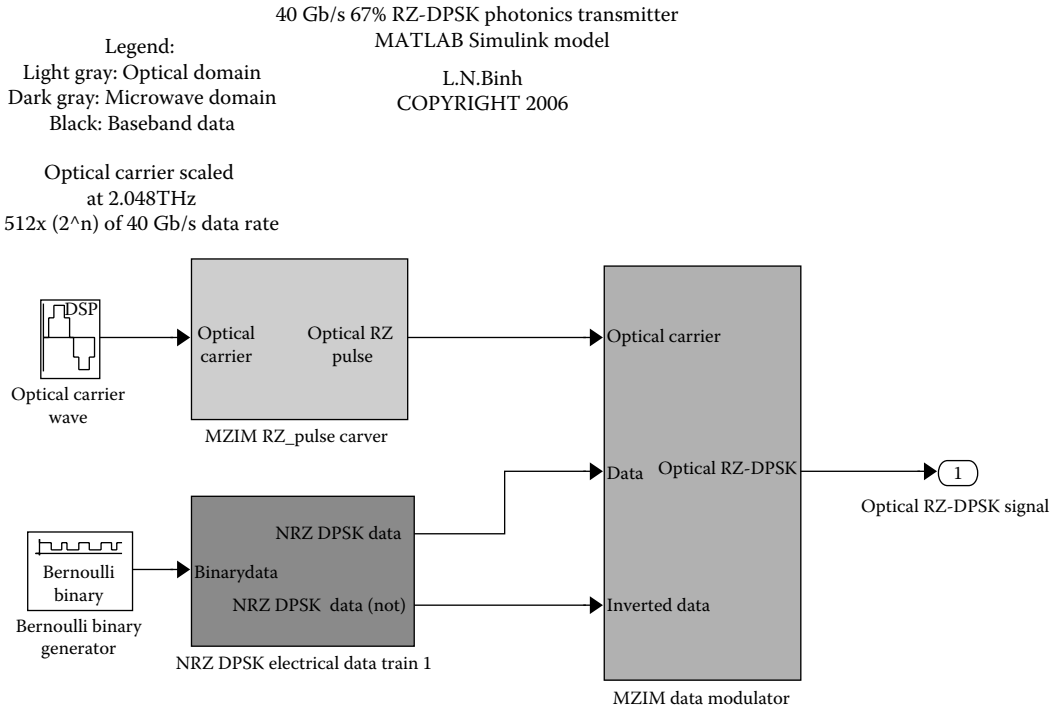

FIGURE 5.49
Photonic transmitters for carrier suppressed RZ and data modulation using DPSK modulation scheme.

5.3.10.2 DWDM Optical Multiplexers and Modulators

In DWDM transmission systems, the optical transmitters are multiplexed before conduction of the transmission via optical transmission spans. The Simulink model is shown in Figure 5.51. Different modulation formats, the MSK and DNPSK transmitters, are employed in this model. It is noted that the optical spectrum analyzer shown in this figure should be set sufficiently wide to accommodate the spectrum of all multiplexed channels. The 1/z block is required for sampling the waveform for appropriate setting for observation in the spectrum analyzer.

5.4 Remarks

In the first section of this chapter, we have mainly discussed the principles of laser and the technique of direct modulation of a semiconductor laser source including all essential rate equations describing the lasing phenomenon. Furthermore, the development of the simulation platform **OCSS**© for optical transmitter module as well as the discussion of the simulated results is given in Sections 5.2.3 through 5.2.5.

The lasing principles of different structures of semiconductor lasers (FP, DFB, and Constricted Mesa) have been described in this chapter. Laser source has been successfully modeled by using laser rate equations that can be solved by employing the well-known

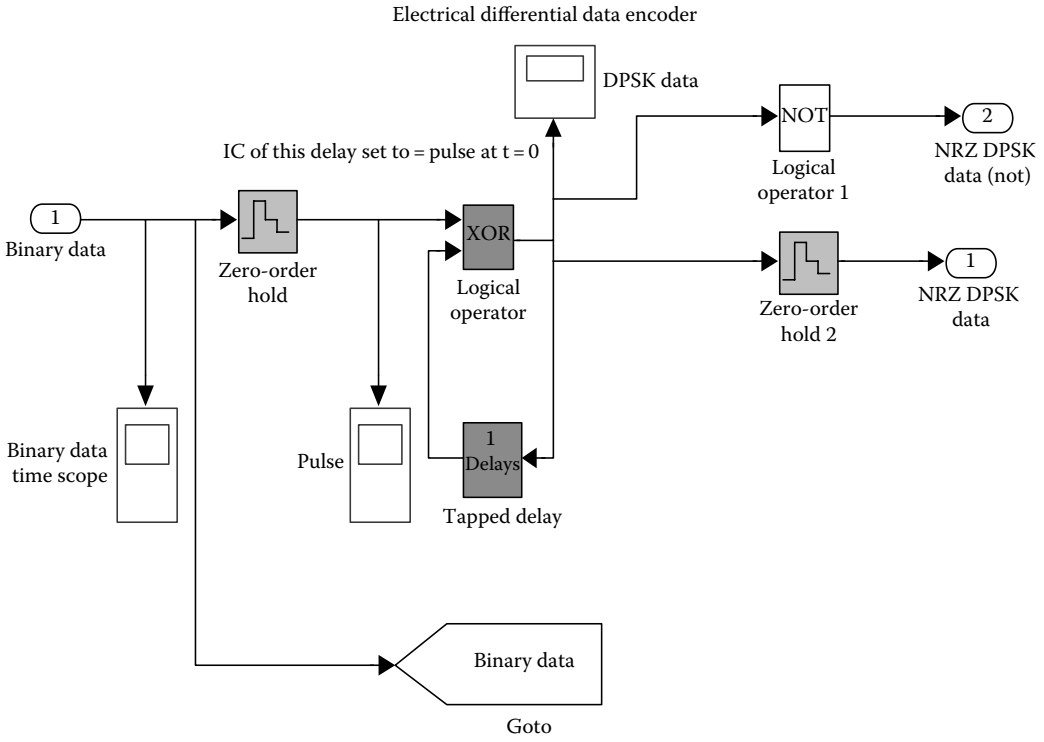

FIGURE 5.50
Electrical differential encoder for DPSK modulation scheme.

Runge–Kutta algorithm. In order to simulate the real system, laser noise (*Langevin force*) is incorporated into the rate equations. A special laser source is being modeled for the purposes of the simulation analysis. The dynamic responses of the lasers, for example, relaxation oscillations, frequency chirp, and turn-on delay are simulated and confirmed with the experimental results as reported in Ref. [51].

The effect of each parameter of the laser rate equations to the response of the laser source has been analyzed and discussed in details. All these results can be used as a guideline to design a laser source. A design menu has been developed and is available in **OCSS**© for design purposes. The generation of the eye diagrams has been developed and it can be used to measure the performance of a particular optical transmitter system.

Direct modulation of a laser source is described with modeling and practical considerations. These light wave sources dominate the optical communications in the bit rate up to 2.5 Gb/s but are no longer capable of operating in the higher bit rates, especially at greater than 10 Gb/s. In this case, external modulators are employed. These modulators have been described and coupled with advanced modulation techniques as given in the rest of the chapter.

Since the proposed of dielectric waveguide and the advent of optical circular waveguide, the employment of modulation techniques has been extensively exploited recently since the availability of optical amplifiers. The modulation formats allow the transmission efficiency, and hence the economy of ultra-high capacity information telecommunications. Optical communications have evolved significantly through several phases from single-mode systems to coherent detection and modulation, which was developed with the main aim of improving on the optical power. The optical amplifiers defeated that main objective of

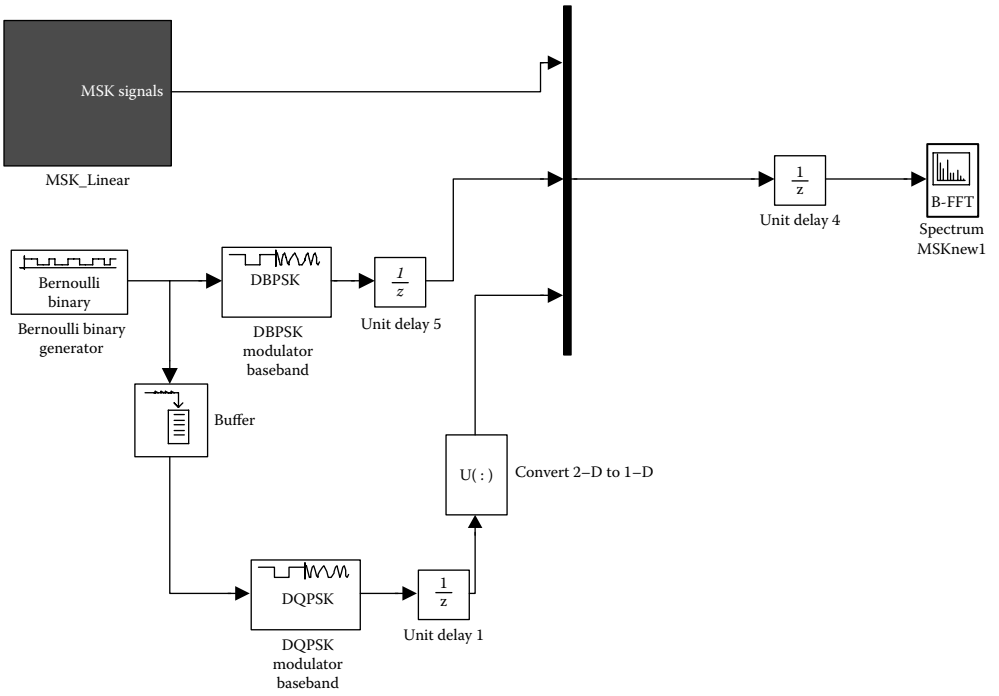

FIGURE 5.51
Simulink® model for multiplexing of different modulation formats.

modulation formats and allow the possibility of incoherent and all possible formats employing the modulation of the amplitude, the phase, and frequency of the lightwave carrier.

Currently, photonic transmitters play a principal part in the extension of the modulation speed into several GHz range and make possible the modulation of the amplitude, the phase, and frequency of the optical carriers and their multiplexing. Photonic transmitters using $LiNbO_3$ have been proven in laboratory and installed systems. The principal optical modulator is the MZIM, which can be a single or a combined set of these modulators whereby binary or multilevel amplitude or phase modulation can be formed, which are even more effective for discrete or continuous phase-shift keying techniques.

Optical modulators employed for the generation of optical signals using advanced modulation techniques at ultra-high speed are presented in Chapter 6. The effects of the modulation on transmission performance are given. MATLAB Simulink assists the modeling of the photonic transmitters. Optical modulation can be implemented using the phase shift blocks. These techniques are further developed in Chapter 6 for the implementation of models for advanced modulation formats and pulse shaping.

5.A Appendices

5.A.1 OCSS Simulation Platform

This appendix gives the main files of the OCSS-2014 for the simulation platform "Optical Communications Systems Simulator" including setting the graphic interface and source files and function files to set up the simulator. CRC Press does have a website address for

downloading the simulators provided that readers can provide evidence of purchase of this book. Descriptions of files are given from time to time in the book chapters and it is recommended that readers set up the files in new MATLAB platform such as MATLAB-2012 or a newer version. Some commands included in the MATLAB files given here were from MATLAB-2007 and some by MATLAB-1995. The author is unable to update these files to the current MATLAB version but has substantially tested the model with his graduate students over the year.

5.A.1.1 MATLAB® File for Starting Simulation "Start1.m," "Start2" and "Start3": Setting Graphical Interface Platform

```
%%%%%%%%%% start1.m %%%%%%%%%
% setting up graphic screen for entering essential %parameters for simulation

global etx
global Wuzere
global Recall1

close all
clear all
etx=0;
Wuzere=0;

%pack
 figure(6)

 frm_main = uicontrol('Style','frame','Position',[30 220 500 180]);
 frm_main = uicontrol('Style','frame','Position',[30 60 500 120]);

 ee = uicontrol(gcf,'Style','text','Position',[35 350 480 35],...
                    'String',...
                    'OPTICAL COMMUNICATION SYSTEMS SIMULATOR');

 ee = uicontrol(gcf,'Style','text','Position',[40 300 480 50],...
                    'String',...
                    'OCSS-2012');

 ee = uicontrol(gcf,'Style','text','Position',[40 270 480 40],...
                    'String',...
                    'A SIMULATOR FOR HIGH-SPEED DIRECT IM/DD');

 ee = uicontrol(gcf,'Style','text','Position',[40 250 480 30],...
                    'String','OPTICAL FIBER COMMUNICATION SYSTEMS');

 ee = uicontrol(gcf,'Style','text','Position',[40 130 480 30],...
                    'String',...
                    'Created By Le BINH 2012');

 ee = uicontrol(gcf,'Style','text','Position',[40 100 480 30],...
                    'String',...
                    'Simulation & Development Director LeBinh');
```

```
 ee = uicontrol(gcf,'Style','text','Position',[40 80 480 20],...
                    'String',...
                    'Modified and Updated 2012');
 ee    = uicontrol(gcf,'Style','push','Position',[70 25 170 25],...
                    'String','<<< ...CLICK HERE TO EXIT','CallBack','close all');
 aa    = uicontrol(gcf,'Style','push','Position',[330 25 170 25],...
                    'String','CLICK HERE TO BEGIN  >>>','CallBack',['mn_inp1;']);
%%%%%%%% Copyright DEC-2013 Le Nguyen Binh CRC Press  %%%%%%%%%%

%%%%%%%%%% start2.m %%%%%%%%%%
% setting some common parameters

close all
clear

global BitRate
global InPulse
global OpLamda
global Seconds
global BitPeriod
global Recall1
global TotLength


mn_fib1

%%%%%%%% Copyright DEC-2013 Le Nguyen Binh CRC Press %%%%%%%%%%

%%%%%%%%%% start3.m %%%%%%%%%%

% start3 setting parameters for optical receiver

clear
close all
global PowReceived

h=figure('Position',[0 0 639 439]);  %main menu - recovering   1
h=figure('Position',[0 0 639 439]);  %plot menu - recovering   2
h=figure('Position',[0 0 639 439]);  %receiver main menu       3
h=figure('Position',[0 0 639 439]);  %more info                4
h=figure('Position',[0 0 639 439]);  %amplifier menu           5
h=figure('Position',[0 0 639 439]);  %display                  6
h=figure('Position',[0 0 639 439]);  %mn_plot3 menu            7

load end2
PowReceived = OutFiber ;

mn_rec1

%%%%%%%% Copyright DEC-2013 Le Nguyen Binh CRC Press %%%%%%%%%%

%%%%%%%%%% start4.m  %%%%%%%%%%
```

```
% start4 setting performance anaylusis

close all

h=figure('Position',[0 0 639 439]);   %performance analysis    1
h=figure('Position',[0 0 639 439]);   %plotting display        2
h=figure('Position',[0 0 639 439]);   %SNR menu                 3
h=figure('Position',[0 0 639 439]);   %SUMMARY                  4

load end2
analysis

%%%%%%%% Copyright DEC-2013 Le Nguyen Binh CRC Press %%%%%%%%%%
```

5.A.1.2 MATLAB® Program for Solving the Laser Rate Equation

```
%%%%%%%%%%%%%%%%%%%%%%%%%%%%%%%%%%%%%%%%%%%%%%%%%%%%%%%%%%%%%%%%%%%%%%%
% D F B L A S E R D I O D E P A R A M E T E R S
% 1.55micron ; InGaAsP/InP ; 2 Gbit/s ; 40 Km
%%%%%%%%%%%%%%%%%%%%%%%%%%%%%%%%%%%%%%%%%%%%%%%%%%%%%%%%%%%%%%%%%%%%%%%
global q
global Vg
global Beta
global Imax
global Mune
global Gamma
global Anull
global Nnull
global Epsil
global Tphot
global Tcarr
global Vactv
global Alpha
global Trise
global Ibias
global MidLamda
global SpecWidth

Gamma  = 0.8    ;    % OPTICAL CONFINEMENT FACTOR    0.8 %
Anull  = 3.2e-20;    % GAIN COEFFICIENT                        %
Vg     = 7.5e+7 ;    % GROUP VELOCITY                          %
Nnull  = 1.0e+12;    % CARRIER DENSITY AT TRANSPARENCY         %
Epsil  = 2.5e-23;    % GAIN COMPRESSION FACTOR                 %
Tphot  = 3.0e-12;    % PHOTON LIFE-TIME                        %
Beta   = 3.0e-5 ;    % FRACTION OF SPONTANEOUS EMISSION        %
Tcarr  = 0.3e-9 ;    % CARRIER LIFE-TIME                       %
q      = 1.6e-19;    % ELECTRON CHARGE                         %
Vactv  = 1.5e-16;    % ACTIVE VOLUME LAYER                     %
Alpha  = 5      ;    % LINE WIDTH ENHANCEMENT FACTOR           %
Trise  = 1e-12;     % RISE TIME - 1 ps version oc2000_1

Ith = q/Tcarr*Vactv*(Nnull+1/Gamma/Anull/Vg/Tphot); % Threshold current
```

```
Ibias = 7.1*Ith ;     % BIAS CURRENT
Imax     = 9.0*Ith ;  % Maximum Input Current
Mune     = 0.042 ;    % TOTAL DIFFERENTIAL QUANTUM EFFICIENCY %
% if Channel ==1
% MidLamda = 1553.3*1e-9;    % Operating Wavelength of Laser Source =
1553.8 nm to match with centre of AWG see mulplex %
% change from 1553.8nm to 1553.3nm to match with ITU-grid AC and GA
% else
    MidLamda= OpLamda(Channel);
% end

SpecWidth = 40e-15; % Laser Source Spectral Line Width = 10 MHz linewidth
set
%%%%%%%%%%%%%%%    Solving The Rate equations    %%%%%%%%%
function rate=rate_equ(t,y)
global q
global Vg
global Nsd
global Ssd
global Beta
global Gamma
global Anull
global Nnull
global Epsil
global Tphot
global Tcarr
global Vactv
global Alpha
global Trise
global Ibias
global Sigma

global Imax
global dummy
global Initial
global InPulse
global BitPeriod

Nsd    = 1/(Gamma*Anull*Vg*Tphot)+Nnull ;
Ssd    = (Tphot/Tcarr)*Nsd*(Imax/Ibias-1) ;
Sigma  = 2e-20 ;

%---- Computing the Rate Equations ------------------------------
rate = zeros(3,1);

rate(1) = (Gamma*Anull*Vg*((y(2)-Nnull)/...
          (1+Epsil*y(1)))-1/Tphot)*y(1)+Beta*Gamma*y(2)/Tcarr + ...
           randn*sqrt(2*Beta*Vactv*Nsd*(Vactv*Ssd+1)^3/Tcarr) ;

rate(2) = dgcoding(t,InPulse)/(q*Vactv)-y(2)/...
          Tcarr-Vg*Anull*y(1)*(y(2)-Nnull)/(1+Epsil*y(1)) + ...
          randn*sqrt(2*Vactv*Nsd/Tcarr*(Beta*Vactv*Ssd+1)) ;
```

```
rate(3) = Alpha*(Gamma*Vg*Anull*(y(2)-Nnull)-1/Tphot)/2 +...
          randn*sqrt(Gamma*Vg*Sigma*(y(2)-Nnull)/y(1)) ;

  if t<0
   rate=Initial;
  end

  dummy=dummy+1;
  if dummy>=50
%    waitbar(t/(BitPeriod*size(InPulse,2))) ;
    dummy=0 ;
  end

%%% Copyright Le Nguyen Binh, CRC Press 2014 %%%%%%%%%%%%%%%%%%%%
```

5.A.1.3 MATLAB® Files for elect.signal Coding into NRZ or RZ and Decoding

```
%%%%%%%%%%%%%%%%%%%%%%%%%%%%%%%%%%%%%%%%%%%%%%%%%%%%%%%%%%%%%%%%%%%%
%      DIGITAL CODING      --------      R Z    and    N R Z
%%%%%%%%%%%%%%%%%%%%%%%%%%%%%%%%%%%%%%%%%%%%%%%%%%%%%%%%%%%%%%%%%%%%

function I=dgcoding(t,InPulse)

global I0
global Imax        % INPUT CURRENT AMPLITUDE      %
global Trise       % RISE TIME                     %
global Ibias       % BIAS CURRENT                  %
global SWcode      % DIGITAL CODING SELECTION      %
global BitPeriod   % BIT PERIOD                    %

timing = rem(t,BitPeriod)   ;  %fraction of time within BitPeriod
n      = fix(t/BitPeriod)+1 ;  %extract input sequence number

%---- RZ Line Coding ------------------------------------------

if SWcode == '#rz'                    %%% RZ line coding %%%

       if timing<=BitPeriod/2
          I=Ibias+InPulse(n)*Imax*(1-exp(-timing.^2/Trise^2));
          I0=I-Ibias;
       else
          I=Ibias+I0*exp(-(timing-BitPeriod/2).^2/Trise^2);
       end


%---- NRZ Line Coding ------------------------------------------

elseif SWcode == 'nrz'     %%% NRZ line coding %%%
       if n==1
          I=Ibias+InPulse(n)*Imax*(1-exp(-timing.^2/Trise^2));
          I0=I-Ibias;
       elseif InPulse(n-1)==1
```

```
          if InPulse(n)==1
           I=Ibias+Imax*(1-exp(-(timing+BitPeriod).^2/Trise^2));
           I0=I-Ibias;
          else
           I=Ibias+I0*exp(-timing.^2/Trise^2);
          end
        elseif InPulse(n-1)==0
          if InPulse(n)==0
           I=Ibias+I0*exp(-(timing+BitPeriod).^2/Trise^2);
          else
           I=Ibias+Imax*(1-exp(-timing.^2/Trise^2));
           I0=I-Ibias;
          end
        end

%---- Manchester Line Coding ----------------------------------

elseif SWcode == 'man'
 timing = rem(t-BitPeriod/2,BitPeriod);  %fraction of time
 n      = fix((t-BitPeriod/2)/BitPeriod)+1 ; %extract input sequence number

        if n==size(InPulse,2)
          if InPulse(n)==0
            I=Ibias+I0*exp(-timing.^2/Trise^2);
          else
            I=Ibias+Imax*(1-exp(-timing.^2/Trise^2));
          end
        elseif timing < 0
           if InPulse(1)==1,I=Ibias;
           else
             I = Ibias+Imax;
             I0= Imax;
           end
        elseif InPulse(n)==1
          if InPulse(n+1)==0
            I=Ibias+Imax*(1-exp(-timing.^2/Trise^2));
            I0=I-Ibias;
          elseif InPulse(n+1)==1
            if timing < BitPeriod/2
              I=Ibias+Imax*(1-exp(-timing.^2/Trise^2));
              I0=I-Ibias;
            else
              I=Ibias+I0*exp(-(timing-BitPeriod/2).^2/Trise^2);
            end
          end
        elseif InPulse(n)==0
          if InPulse(n+1)==1
            I=Ibias+I0*exp(-timing.^2/Trise^2);
          elseif InPulse(n+1)==0
            if timing < BitPeriod/2
              I=Ibias+I0*exp(-timing.^2/Trise^2);
            else
```

```
            I=Ibias+Imax*(1-exp(-(timing-BitPeriod/2).^2/Trise^2));
            I0=I-Ibias;
          end
        end
      end
end

%%%%% END CODING %%%% Dec 2014 Copyright Le Nguyen Binh CRC Press


%%%%%%%%%%%%%%%%%%%%%%%%%%%%%%%%%%%%%%%%%%%%%%%%%%%%%%%%%%%%%%%%%%%%%%%
%           D I S P L A Y      D E C O D E D       B I N A R Y
%%%%%%%%%%%%%%%%%%%%%%%%%%%%%%%%%%%%%%%%%%%%%%%%%%%%%%%%%%%%%%%%%%%%%%%

global OutPulse
 ee = uicontrol(gcf,'Style','push','Position',[330 414 80 25],...
 'String','Output >>');
 ee = uicontrol(gcf,'Style','text','Position',[415 419 160 15],...
 'String',num2str(OutPulse));

%%%%%%%%%%%%%%%%%%%%%%%%%%%%%% Dec2013 %%%%%
```

5.A.1.4 MATLAB® Files for "Transmitter Menu"

```
%%%%%%%%%%%%%%%%%%%%%%%%%%%%%%%%%%%%%%%%%%%%%%%%%%%%%%%%%%%%%%%%%%%%%%%
% T R A N S M I T T E R   M O D U L E : M A I N   M E N U - I
% File name mn_input1.m
%%%%%%%%%%%%%%%%%%%%%%%%%%%%%%%%%%%%%%%%%%%%%%%%%%%%%%%%%%%%%%%%%%%%%%%
figure(1)
clear all
global Mod
global Source
global SWcode
global Wuzere
global OpLamda
global InPulse
global Accepted
global IniState
global BitPeriod
global BitRate

clear input
clear rate41

if Accepted == 1, mn_inp2 ;
 else
 frm_main = uicontrol('Style','frame','Position',[50 0 550 440]);

%---- LINE CODING ------------------------------------------------
ee = uicontrol(gcf,'Style','frame','position',[260 240 170 100]);
ee = uicontrol(gcf,'Style','push','String','Select line coding',...
                    'Position',[260 340 170 20]);
```

```
 rz       = uicontrol(gcf,'Style','radio','String','RZ   - Return Zero',...
                      'Position',[265 315 160 20],...
                      'CallBack',['set(rz ,''Value'',1),'...
                                  'set(nrz,''Value'',0),'...
                                  'set(man,''Value'',0),'...
                                  'SWcode = ''#rz'';']);
 nrz      = uicontrol(gcf,'Style','radio','String','NRZ - Non Return Zero',...
                     'Position',[265 295 160 20],...
                     'CallBack',['set(nrz,''Value'',1),'...
                                 'set(rz ,''Value'',0),'...
                                 'set(man,''Value'',0),'...
                                 'SWcode = ''nrz'';']);
 man      = uicontrol(gcf,'Style','radio','String','MAN - Manchester',...
                      'Position',[265 275 160 20],...
                      'CallBack',['set(nrz,''Value'',0),'...
                                  'set(rz ,''Value'',0),'...
                                  'set(man,''Value'',1),'...
                                  'SWcode = ''man'';']);

%ee = uicontrol('Style','frame','Position',[260 210 170 120]);
%---- INPUT BIT SEQUENCE ----------------------------------------
 ee       = uicontrol(gcf,'Style','push','String',...
                      'Input Bit Sequence  >>>',...
                      'Position',[85 373 170 20]);
 input    = uicontrol('Style','edit','String','[   ]',...
                      'HorizontalAlignment','Right',...
                      'Position',[260 373 150 20],...
                      'Callback',...
                      ['InPulse = str2num(get(input,''String''));',...
                      'InPulse = [InPulse 0];']);
 %ee      = uicontrol('Style','frame','Position',[75 345 355 35]);

%---- INITIAL STATE ---------------------------------------------
ee        = uicontrol(gcf,'Style','frame','Position',[455 395 120 20]);
ee        = uicontrol(gcf,'Style','push','String','Initial State',...
                      'Position',[455 395 120 20]);

 swon     = uicontrol(gcf,'Style','radio','String','Swicth On',...
                      'Position',[465 380 110 15],...
                      'CallBack',['set(swon,''Value'',1),'...
                                  'set(cont,''Value'',0),'...
                                  'IniState = ''swon'';']);
 cont     = uicontrol(gcf,'Style','radio','String','Continuous',...
                     'Position',[465 360 110 15],...
                     'CallBack',['set(swon,''Value'',0),'...
                                 'set(cont,''Value'',1),'...
                                 'IniState = ''cont'';']);
% ee = uicontrol('Style','frame','Position',[455 345 120 65]);

%---- BIT PERIOD ------------------------------------------------
 ee       = uicontrol(gcf,'Style','push','String','Transmission rate',...
                      'Position',[75 240 160 100]);
```

```
 rate1     = uicontrol(gcf,'Style','radio','String','2.5Gbps(400ps)',...
                       'Position',[80 315 150 20],...
                       'CallBack',['set(rate1,''Value'',1),'...
                                   'set(rate2,''Value'',0),'...
                                   'set(rate3,''Value'',0),'...
                                   'set(rate4,''Value'',0),'...
                                   'BitRate   = 2.5;',...
                                   'BitPeriod = 1e-9/BitRate;']);
 rate2     = uicontrol(gcf,'Style','radio','String','10Gbps (100ps)',...
                       'Position',[80 295 145 20],...
                       'CallBack',['set(rate1,''Value'',0),'...
                                   'set(rate2,''Value'',1),'...
                                   'set(rate3,''Value'',0),'...
                                   'set(rate4,''Value'',0),'...
                                   'BitRate   = 10;',...
                                   'BitPeriod = 1e-9/BitRate;']);
 rate3     = uicontrol(gcf,'Style','radio','String','25Gbps  (40ps)',...
                       'Position',[80 275 145 20],...
                       'CallBack',['set(rate1,''Value'',0),'...
                                   'set(rate2,''Value'',0),'...
                                   'set(rate3,''Value'',1),'...
                                   'set(rate4,''Value'',0),'...
                                   'BitRate   = 25;',...
                                   'BitPeriod = 1e-9/BitRate;']);
 rate4     = uicontrol(gcf,'Style','radio','String','other(Gbit/s)',...
                       'Position',[80 250 90 20],...
                       'CallBack',['set(rate1,''Value'',0),'...
                                   'set(rate2,''Value'',0),'...
                                   'set(rate3,''Value'',0),'...
                                   'set(rate4,''Value'',1),']);
 rate40    = uicontrol('Style','frame','Position',[175 245 55 25]);
 rate41    = uicontrol('Style','edit','String','',...
                       'Position',[180 250 45 15],...
                       'Callback',[...
                       'set(rate1,''Value'',0),'...
                       'set(rate2,''Value'',0),'...
                       'set(rate3,''Value'',0),'...
                       'set(rate4,''Value'',1),'...
                       'BitRate   = str2num(get(rate41,''String''));',...
                       'BitPeriod = 1e-9/BitRate;']);

 %ee = uicontrol('Style','frame','Position',[75 210 160 120]);
%---- LASER OPTICAL SOURCE types -------------------------------
ee       = uicontrol(gcf,'Style','frame','Position',[75 15 355 150]);

ee       = uicontrol(gcf,'Style','push','String',...
                     'Choose a laser source    [InGaAsP/InP]',...
                     'Position',[75 165 355 20]);

src0     = uicontrol(gcf,'Style','radio','String',...
                     'Special Laser Source',...
                     'Position',[80 145 210 15],...
```

```
                    'CallBack',['set(src1,''Value'',0),'...
                                'set(src0,''Value'',1),'...
                                'set(src2,''Value'',0),'...
                                'set(src3,''Value'',0),'...
                                'set(src4,''Value'',0),'...
                                'Source = ''SourceT'';']);

%aa      = uicontrol(gcf,'Style','push','Position',[295 125 110 15],...
             %'String','>> more info','CallBack','msg_mesa');
src1     = uicontrol(gcf,'Style','radio','String',...
             'Constricted Mesa    :',...
                    'Position',[80 125 210 15],...
                    'CallBack',['set(src1,''Value'',1),'...
                                'set(src0,''Value'',0),'...
                                'set(src2,''Value'',0),'...
                                'set(src3,''Value'',0),'...
                                'set(src4,''Value'',0),'...
                                'Source = ''Source0'';']);

%aa = uicontrol(gcf,'Style','push','Position',[295 105 110 15],...
              % 'String','>> more info','CallBack','msg_fp');
src2     = uicontrol(gcf,'Style','radio','String',...
           'Fabry Perot (FP)      :',...
                    'Position',[80 105 210 15],...
                    'CallBack',['set(src1,''Value'',0),'...
                                'set(src0,''Value'',0),'...
                                'set(src2,''Value'',1),'...
                                'set(src3,''Value'',0),'...
                                'set(src4,''Value'',0),'...
                                'Source = ''Source1'';']);

%aa = uicontrol(gcf,'Style','push','Position',[295 85 110 15],...
 %              'String','>> more info','CallBack','msg_dfb1');
src3     = uicontrol(gcf,'Style','radio','String',...
           'DFB1 NEL NTT NLK5C5E2KA... ',...
                    'Position',[80 105 210 15],...
                    'CallBack',['set(src1,''Value'',0),'...
                                'set(src0,''Value'',0),'...
                                'set(src2,''Value'',0),'...
                                'set(src3,''Value'',1),'...
                                'set(src4,''Value'',0),'...
                                'Source = ''Source2'';']);

%aa = uicontrol(gcf,'Style','push','Position',[295 65 110 15],...
 %              'String','>> more info','CallBack','msg_dfb2');
src4     = uicontrol(gcf,'Style','radio','String',...
                    'DFB2....:',...
                    'Position',[80 75 210 15],...
                    'CallBack',['set(src1,''Value'',0),'...
                                'set(src0,''Value'',0),'...
                                'set(src2,''Value'',0),'...
                                'set(src3,''Value'',0),'...
                                'set(src4,''Value'',1),'...
                                'Source = ''Source3'';']);
```

```
%src5   = uicontrol(gcf,'Style','radio','String','',...
                    %'Position',[80 45 20 15],...
                    %'CallBack',['set(src1,''Value'',0),'...
                     %          'set(src0,''Value'',0),'...
                      %         'set(src2,''Value'',0),'...
                       %        'set(src3,''Value'',0),'...
                        %       'set(src4,''Value'',0),'...
                         %      'set(src5,''Value'',1),'...
                          %     'Source = ''Source4'';']);
 % if Wuzere==0
  %     src51     = uicontrol(gcf,'Style','push',...
    %                          'String',...
     %                         '>>>  Design and Customize Laser Source
(Press)',...
      %                        'Position',[100 40 325 20],...
       %                       'Callback',[...
        %                      'set(src0,''Value'',0),'...
         %                     'set(src1,''Value'',0),'...
          %                    'set(src2,''Value'',0),'...
           %                   'set(src3,''Value'',0),'...
            %                  'set(src4,''Value'',0),'...
             %                 'set(src5,''Value'',1),'...
              %                'Source = ''Source4'';',...
               %               'src_cust';]);
  %else
   % src51      = uicontrol(gcf,'Style','push',...
                      %      'String',...
                      %      '>>>   Design and Customize Laser Source
(Press)',...
                      %      'Position',[100 40 325 20],...
                      %%     'Callback',[...
                      %      'set(src0,''Value'',0),'...
                      %      'set(src1,''Value'',0),'...
                       %     'set(src2,''Value'',0),'...
                        %    'set(src3,''Value'',0),'...
                         %   'set(src4,''Value'',0),'...
                          %  'set(src5,''Value'',1),'...
                           %'Source = ''Source4'';',...
                           %'figure(3)';]);
  %end

 %ee = uicontrol('Style','frame','Position',[75 35 355 140]);

%---- MODULATION TECHNIQUE -------------------------------------
 ee       = uicontrol(gcf,'Style','push','String','',...
                'Position',[460 240 120 100]);

 dir      = uicontrol(gcf,'Style','radio','String','DirectMod',...
                'Position',[465 309 120 15],...
                'CallBack',['set(dir,''Value'',1),'...
                            'Mod    = ''dir'';']);
 %ee = uicontrol(gcf,'Style','text','Position',[485 290 60 15],...
 %                 'String','Int-Mod');
 Mod='dir';
```

```
% ext  = uicontrol(gcf,'Style','radio','String','External',...
%                              'Position',[460 240 80 20],...
%                              'CallBack',['set(dir,''Value'',0),'...
%                                          'set(ext,''Value'',1),'...
%                                          'Mod    = ''ext'';']);
% ee = uicontrol(gcf,'Style','text','Position',[467 220 80 20],...
% 'String','Modulator');

 %ee = uicontrol('Style','frame','Position',[455 210 120 120]);

 %---- Display Banner ------------------------------------------

 ee = uicontrol(gcf,'Style','push','Position',[50 420 550 25],...
 'String',...
 'OPTICAL COMMUNICATION SYSTEMS SIMULATOR - OCSS-2012');

 ee = uicontrol(gcf,'Style','push','Position',[75 390 355 25],...
 'String',...
 'TRANSMITTER MODULE : MAIN');

 ee = uicontrol(gcf,'Style','push','Position',[50 0 550 25],...
 'String',...
 'SIMULATION  MODELLED BY LN Binh - Huawei Technologies ERC -2012');

 %---- Closing -------------------------------------------------
 aa   = uicontrol(gcf,'Style','push','Position',[455 125 120 25],...
 'String','Calculate','CallBack',['Accepted=1;','calc;']);

 ee   = uicontrol(gcf,'Style','push','Position',[455 35 120 25],...
 'String','<< BACK','CallBack','figure(6)');

 end
%%%%%%%%%%% Dec-2013 Copyright Le Nguyen Binh CRC Press %%%%%%%


%%%%%%%%%%%%%%%%%%%%%%%%%%%%%%%%%%%%%%%%%%%%%%%%%%%%%%%%%%%%%%%%%%%%
% T R A N S M I T T E R   M O D U L E : M A I N   M E N U - II
% File mn_input2.m
%%%%%%%%%%%%%%%%%%%%%%%%%%%%%%%%%%%%%%%%%%%%%%%%%%%%%%%%%%%%%%%%%%%%
figure(1)

global Accepted

aa   = uicontrol(gcf,'Style','push','Position',[455 125 120 25],...
'String','Calculate','CallBack',['Accepted=1;','calc;']);

bb   = uicontrol(gcf,'Style','push','Position',[455 95 120 25],...
'String','ReSelect','CallBack',['Accepted=0;','mn_inp1;']);

cc   = uicontrol(gcf,'Style','push','Position',[455 65 120 25],...
'String','Plot','CallBack','mn_plot1');
```

```
dd   = uicontrol(gcf,'Style','push','Position',[455 35 120 25],...
'String','EXIT','CallBack','exit');

ee   = uicontrol(gcf,'Style','push','Position',[455 160 120 40],...
'String','<< TRANSMIT >>','CallBack',['mn_inp3']);


%---- Closing -----------------------------------------------
%%%%%%%%%%% DEC-2013 Copyright Le Nguyen Binh CRC Press  %%%%%%%


%%%%%%%%%%%%%%%%%%%%%%%%%%%%%%%%%%%%%%%%%%%%%%%%%%%%%%%%%%%%%%%%%%%%%%%
% T R A N S M I T T E R : C H E C K - L I S T  M E N U
% File name mn_input3.m
%%%%%%%%%%%%%%%%%%%%%%%%%%%%%%%%%%%%%%%%%%%%%%%%%%%%%%%%%%%%%%%%%%%%%%%
figure(5)

global Mod
global Source
global SWcode
global OpLamda
global InPulse
global BitRate
global TimeStep
global SpecWidth
global SampleSize

%---- Rewrite Parameters to String Format -----------------------
BitRateLB  = [num2str(BitRate),' Gbit/s'];
OpLamdaLB  = [num2str(OpLamda*1e6),' micron'];
SpectraLB  = [num2str(SpecWidth/1e-9),' nanometer'];
InPulsePrint=InPulse;
InPulsePrint(length(InPulse))=[];

if Mod=='dir' ModLB='Direct Intensity';   end
if Mod=='ext' ModLB='External Modulator'; end

if SWcode=='nrz' SWcodeLB='Non Return Zero -- NRZ';   end
if SWcode=='#rz' SWcodeLB='Return Zero -- RZ';        end
if SWcode=='man' SWcodeLB='Manchester Code -- MAN';   end

if Source=='SourceT' SourceLB='Special Laser Source';    end
if Source=='Source0' SourceLB='Constricted Mesa Laser';  end
if Source=='Source1' SourceLB='Fabry Perot Laser';       end
if Source=='Source2' SourceLB='Distributed Feedback';    end
if Source=='Source3' SourceLB='Distributed Feedback';    end
if Source=='Source4' SourceLB='Customized Laser Source'; end

%---- Display Banner ----------------------------------------
 ee = uicontrol(gcf,'Style','push','Position',[50 420 550 25],...
 'String',...
 'OPTICAL COMMUNICATION SYSTEMS SIMULATOR - OCSS-2012');
```

```
 ee = uicontrol(gcf,'Style','push','Position',[213 395 234 25],...
 'String',...
 'TRANSMITTER : CHECK-LIST MENU');

 ee = uicontrol(gcf,'Style','push','Position',[50 0 550 15],...
 'String',...
 'SIMULATION  MODELLED  BY    LeBinh 2012');
%---- Check-List ---------------------------------------------
 ee = uicontrol(gcf,'Style','push','Position',[120 345 200 25],...
 'String','Input Binary Sequence >>');
 ee = uicontrol(gcf,'Style','text','Position',[330 350 180 15],...
 'String',num2str(InPulsePrint));

 ee = uicontrol(gcf,'Style','push','Position',[120 315 200 25],...
 'String','Transmission Bit Rate >>');
 ee = uicontrol(gcf,'Style','text','Position',[330 320 180 15],...
 'String',BitRateLB);

 ee = uicontrol(gcf,'Style','push','Position',[120 285 200 25],...
 'String','Digital Line Coding   >>');
 ee = uicontrol(gcf,'Style','text','Position',[330 290 180 15],...
 'String',SWcodeLB);

 ee = uicontrol(gcf,'Style','push','Position',[120 255 200 25],...
 'String','Optical Laser Source  >>');
 ee = uicontrol(gcf,'Style','text','Position',[330 260 180 15],...
 'String',SourceLB);

 ee = uicontrol(gcf,'Style','push','Position',[120 225 200 25],...
 'String','Laser Spectral Line Width   >>');
 ee = uicontrol(gcf,'Style','text','Position',[330 230 180 15],...
 'String',SpectraLB);
 ee = uicontrol(gcf,'Style','push','Position',[120 195 200 25],...
 'String','Operating Wavelength  >>');
 ee = uicontrol(gcf,'Style','text','Position',[330 200 180 15],...
 'String',OpLamdaLB);

 ee = uicontrol(gcf,'Style','push','Position',[120 165 200 25],...
 'String','Modulation Technique  >>');
 ee = uicontrol(gcf,'Style','text','Position',[330 170 180 15],...
 'String',ModLB);

%---- Closing ------------------------------------------------
 aa   = uicontrol(gcf,'Style','push','Position',[230 115 200 40],...
 'String','PROCEED TO TRANSMIT','CallBack',...
 ['save end1 BitPeriod BitRate OpLamda Tstep mstep TimeStep
SampleSize',...
   ' t m InPulse Mod Phase Phasestep SpecWidth q Vg Beta Imax Mune
Gamma',...
   ' Anull Nnull Epsil Tphot Tcarr Vactv Alpha Trise Ibias IniState',...
   ' AtStep SWcode;','start2']);
```

```
 bb    = uicontrol(gcf,'Style','push','Position',[230 70 200 40],...
 'String','VIEW OUTPUT WAVEFORM','CallBack',[...
                    'figure(4);',...
                    'subplot(111),plot(Tstep/1e-9,abs(AtStep),''y.'');',...
                    'xlabel(''time (nsec)'');',...
                    'ylabel(''Power Output (W)'');',...
                    'title(''TRANSMITTER POWER OUTPUT'');',...
                    'grid;',...
                    'figure(4);',...
                    'plot(Tstep/1e-9,abs(AtStep),''g'');',...
                    'xlabel(''time (nsec)'');',...
                    'ylabel(''Power Output (W)'');',...
                    'title(''TRANSMITTER POWER OUTPUT'');',...
                    'grid;','pause;','clg;','figure(5);',...
                    'clear SourceLB SWcodeLB OpLamdaLB BitRateLB ModLB;']);

cc     = uicontrol(gcf,'Style','push','Position',[230 25 200 40],...
  'String','EXIT TO MAIN MENU','CallBack',[...
  'clear SourceLB SWcodeLB OpLamdaLB BitRateLB
ModLB;','clf;','figure(1)']);
%%%%%%%% Dec-2013 Copyright Le Nguyen Binh CRC Press %%%%%
```

5.A.2 Initial Conditions for Photon Density, *S*(*t*) and Carrier Density, *N*(*t*)

The initial conditions for photon density $S(0)$ and Carrier Density $N(0)$ can be obtained by considering the steady-state solutions to the rate equations.. These solutions are found by taking:

$$\frac{dS(t)}{dt} = 0 \tag{5.50a}$$

$$\frac{dN(t)}{dt} = 0 \tag{5.50b}$$

Laser source rate equations are given by

$$\frac{dS(t)}{dt} = \left(\Gamma a_0 v_g \frac{N(t) - N_0}{1 + \varepsilon_C S(t)} - \frac{1}{\tau_p} \right) S(t) + \frac{\beta \Gamma N(t)}{\tau_n} \tag{5.51}$$

$$\frac{dN(t)}{dt} = \frac{I(t)}{qV_a} - \frac{N(t)}{\tau_n} - v_g a_0 \frac{N(t) - N_0}{1 + \varepsilon_C S(t)} S(t) \tag{5.52}$$

By applying the steady-state conditions at $t = 0$ in (5.50a) and (5.50b), we have

$$\Gamma\left(\frac{a_0 v_g N(0)S(0)}{1+\varepsilon_C S(0)} - \frac{N_0 a_0 v_g S(0)}{1+\varepsilon_C S(0)}\right) - \frac{S(0)}{\tau_p} + \frac{\beta\Gamma N(0)}{\tau_n} = 0 \tag{5.53}$$

Then when $I(0) = I_{bias}$ we have

$$\frac{I_{bias}}{qV_a} - \frac{N(0)}{\tau_n} - \left(\frac{a_0 v_g N(0)S(0)}{1+\varepsilon_C S(0)} - \frac{N_0 a_0 v_g S(0)}{1+\varepsilon_C S(0)}\right) = 0 \tag{5.54}$$

$$\Gamma\left(\frac{a_0 v_g N(0)S(0)}{1+\varepsilon_C S(0)} - \frac{N_0 a_0 v_g S(0)}{1+\varepsilon_C S(0)}\right) = \left(\frac{I_{bias}}{qV_a} - \frac{N(0)}{\tau_n}\right)\Gamma \tag{5.55}$$

Equating (5.55) and (5.53) leads to

$$\frac{I_{bias}\Gamma}{qV_a} - \frac{N(0)\Gamma}{\tau_n} - \frac{S(0)}{\tau_p} + \frac{\beta\Gamma N(0)}{\tau_n} = 0 \tag{5.56}$$

$$N(0)\left(\frac{\beta\Gamma}{\tau_n} - \frac{\Gamma}{\tau_n}\right) = \frac{S(0)}{\tau_p} - \frac{I_{bias}\Gamma}{qV_a} \tag{5.57}$$

$$\frac{N(0)\Gamma}{\tau_n}(\beta - 1) = \frac{S(0)}{\tau_p} - \frac{I_{bias}\Gamma}{qV_a} \tag{5.58}$$

$$N(0) = \frac{\tau_n S(0)}{\Gamma\tau_p(\beta - 1)} - \frac{\tau_n I_{bias}}{qV_a(\beta - 1)} \tag{5.59}$$

Finally, we have

$$N(0) = \frac{\tau_n}{(\beta - 1)}\left(\frac{S(0)}{\Gamma\tau_p} - \frac{I_{bias}}{qV_a}\right) \tag{5.60}$$

At $t = 0$, a fraction of the photons produced by spontaneous emission can be ignored, that is, the second term of (5.51):

$$\frac{\beta\Gamma N(t)}{\tau_n} = 0 \tag{5.61}$$

Since $dS(t)/dt$ at $t = 0$ must be a positive number:

$$\left.\frac{dS(t)}{dt}\right|_{t=0} > 0 \tag{5.62}$$

Hence, from (5.51):

$$\Gamma a_0 v_g \frac{N(t)-N_0}{1+\varepsilon_C S(t)} > \frac{1}{\tau_p} \tag{5.63}$$

$$N(0) = N_0 + \frac{1+\varepsilon_C S(0)}{\Gamma a_0 v_g \tau_p} \tag{5.64}$$

5.A.2.1 Case 1: Switch On State

We now define a threshold current as $I(t)$ required to sustain $N(t) = N_{th}$ when $S(t) = 0$. From (5.51), this requires

$$\frac{I_{th}}{qV_a} = \frac{N_{th}}{\tau_n} \tag{5.65}$$

This gives the current required to sustain an excess electron concentration, $N(t)$, when spontaneous emission is the only decay mechanism. We can use (5.52) to find $S(t)$ for the "switch-on" state. By substituting (5.59) into (5.51) and considering (5.57), we obtain

$$0 = \frac{I(t)}{qV_a} - \frac{N_{th}}{\tau_n} - v_g a_0 \frac{N(t)-N_0}{1+\varepsilon_C S(t)} S(t) \tag{5.66}$$

$$0 = \frac{I(t)}{qV_a} - \frac{I_{th}\tau_n}{qV_a\tau_n} - \frac{1}{\tau_p} S(t) \tag{5.67}$$

$$S(t) = \frac{\tau_p}{qV_a}\left(I(t) - I_{th}\right) \tag{5.68}$$

since $I_m = I_{th}$; $I_{bias} = 1.1I_m$; $I(0) = 1.1I_m$ we have from (5.68)

$$S(0) = \frac{\tau_p}{qV_a}\left(I(0) - I_m\right) = \frac{\tau_p}{qV_a}\left(1.1\times I_m - I_m\right) \rightarrow S(0) = \frac{\tau_p}{qV_a}\left(0.1\times I_m\right) \tag{5.69}$$

Thus, the initial state $S(0)$ for "switch-on" state is given by (5.62).

5.A.2.2 Case 2: Continuous State

Equating Equations 5.57 and 5.59:

$$N_0 + \frac{1}{\Gamma a_0 v_g \tau_p} + \frac{\varepsilon S(0)}{\Gamma a_0 v_g \tau_p} = \frac{\tau_n S(0)}{(\beta-1)\Gamma\tau_p} - \frac{\tau_n I_{bias}}{(\beta-1)qV_a} \tag{5.70}$$

$$S(0)\left(\frac{\tau_n}{(\beta-1)\Gamma\tau_p}-\frac{\varepsilon_C}{\Gamma a_0 v_g \tau_p}\right)=N_0+\frac{1}{\Gamma a_0 v_g \tau_p}+\frac{\tau_n I_{bias}}{(\beta-1)qV_a} \tag{5.71}$$

$$S(0)\left(\frac{\tau_n a_0 v_g-\varepsilon_C(\beta-1)}{(\beta-1)\Gamma\tau_p a_0 v_g}\right)=\frac{N_0\Gamma a_0 v_g\tau_p(\beta-1)qV_a+(\beta-1)qV_a+\tau_n I_{bias}\Gamma a_0 v_g\tau_p}{\Gamma a_0 v_g\tau_p(\beta-1)qV_a} \tag{5.72}$$

$$S(0)\left[\tau_n a_0 v_g-\varepsilon_C(\beta-1)\right]=\frac{N_0\Gamma a_0 v_g\tau_p(\beta-1)qV_a+(\beta-1)qV_a+\tau_n I_{bias}\Gamma a_0 v_g\tau_p}{qV_a}$$

Therefore

$$S(0)=\frac{N_0\Gamma a_0 v_g\tau_p(\beta-1)qV_a+(\beta-1)qV_a+\tau_n I_{bias}\Gamma a_0 v_g\tau_p}{qV_a\left[\tau_n a_0 v_g-\varepsilon_C(\beta-1)\right]}$$

then

$$S(0)=\frac{qV_a(\beta-1)\left[1+N_0\Gamma a_0 v_g\tau_p\right]+\tau_n I_{bias}\Gamma a_0 v_g\tau_p}{qV_a\left[\tau_n a_0 v_g-\varepsilon_C(\beta-1)\right]} \tag{5.73}$$

Thus, $N(0)$ and $S(0)$ are given by (5.59) and (5.63), respectively.

References

1. G.P. Agrawal, *Fiber Optic Communications Systems*, 3rd ed., Academic Press, New York, 2003.
2. J.E. Bowers and M.A. Pollack, Semiconductor lasers for telecommunications, in S.E. Miller and I.P. Kaminow (Eds.), *Optical Fiber Telecommunications II*, Academic Press, San Diego, CA, pp. 509–568, 1988.
3. J.M. Senior, *Optical Fiber Communications: Principles and Practice*, 2nd ed., Prentice Hall, New York, 1992.
4. W.B. Jr. Jones, *Introduction to Optical Fibre Communications*, Holt, Rinehart and Winston, New York, 1988.
5. D.A. Atlas, B. de Largy, A. Rosiewicz, and R. Panock, 20 GHz bandwidth high dynamic range 1.3 μm buried heterostructure laser modules, *Journal of Optical Communications*, 15(6), 231–237, 1994.
6. M. Rizzi and B. Castagnolo, Electro-optic intensity modulator for broadband optical communications, *Fiber and Integrated Optics*, 21, 243–251, 2002.
7. H. Lipsanen et al., High-speed InGaAsP/InP multiple quantum well lasers, *Photonics Technology Letters*, 4(7), 673–675, 1992.
8. A. Lowery, Spectral and dynamic behaviour of semiconductor lasers, in *19th Australian Conference on Optical Fibre Technology (ACOFT'94)*, Melbourne, Victoria, Australia, 1994.
9. K. Vahala, K. Kyuma, A. Yariv, A., and S. Kwong, Narrow linewidth, single frequency semiconductor laser with a phase conjugate external cavity mirror, *Applied Physics Letters*, 49(23), 1563–1565, December 1986.

10. S.D. Saliba and R.E. Scholten, Linewidths below 100 kHz with external cavity diode lasers, *Applied Optics*, 48(36), 6961–6966, 2009.
11. C. Ye, *Tunable External Cavity Diode Lasers*, World Scientific, Hackensack, NJ, 2004, Google books, access date December 2013.
12. J. Kim, A. Shinya, K. Nozaki, H. Taniyama, C.-H. Chen, T. Sato, S. Matsuo, and M. Notomi, Narrow linewidth operation of buried-heterostructure photonic crystal nanolaser, *Optics Express*, 20(11), 11643–11651, May 21, 2012.
13. G.P. Agrawal and N.K. Dutta, *Long-Wavelength Semiconductor Lasers*, Van Nostrand Reinhold, New York, 1986.
14. R.S. Tucker and I.P. Kaminow, High-frequency characteristics of directly modulated InGaAsP ridge waveguide and buried heterostructure lasers, *IEEE Journal Lightwave Technology*, 2(4), 385–393, 1984.
15. K. Hagimoto, N. Ohta, and K. Nakagawa, 4 Gb/s direct modulation of 1.3 μm InGaAsP/InP semiconductor lasers, *Electronics Letters*, 796–797, 1982.
16. L. Bickers and L.P. Westbrook, Reduction in laser chirp in 1.5um DFB lasers by modulation pulse shaping, *Electronics Letters*, 103–104, 1985.
17. R.A. Linke, Modulation induced transient chirping in single frequency lasers, *IEEE Journal of Quantum Electronics*, 593–597, 1985.
18. F. Koyama, Frequency chirping in external modulators, *IEEE Journal of Lightwave Technology*, 87–93, 1988.
19. R. Xin-Gen and X. Guo-Ping, SPICE model for the intrinsic noise of laser diodes, *Journal of Optical Communications*, 135–137, 1994.
20. J. Miller et al., Part II: Devices and system consideration, *Proceedings of IEEE*, 1726–1751, 1973.
21. A.F. Elrefaie et al., Computer simulation of digital lightwave links, *IEEE Journal on Selected Areas in Communications*, 94–105, 1988.
22. R.C. Alferness, Optical guided-wave devices, *Science*, 234(4778), 825–829, November 14, 1986.
23. H. Takara, High-speed optical time-division-multiplexed signal generation, *Optical and Quantum Electronics*, 33(7–10), 795–810, July 10, 2001.
24. E.L. Wooten et al., A review of lithium niobate modulators for fiber-optic communications systems, *IEEE Journal of Selected Topics in Quantum Electronics*, 6(1), 69–80, January/February 2000.
25. K. Noguchi, O. Mitomi, H. Miyazawa, and S. Seki, A broadband Ti: $LiNb0_3$ optical modulator with a ridge structure, *Journal of Lightwave Technology*, 13(6), 1164–1168, June 1999.
26. S.G. Carter, Quantum coherence in an optical modulator, *Science*, 310, 651, 2005.
27. I.B. Akca, Electro-optic and electro-absorption characterization of InAs quantum dot waveguides, *Optics Express*, 16, 3439, 2008.
28. X. Xu, Coherent optical spectroscopy of a strongly driven quantum dot, *Science*, 317, 929, 2007.
29. T. Kawanishi, S. Shinada, T. Sakamoto, S. Oikawa, K. Yoshiara, and M. Izutsu, Reciprocating optical modulator with resonant modulating electrode, *Electronics Letters*, 4(5), 271–272, 2008.
30. R. Krahenbuhl, J.H. Cole, R.P. Moeller, and M.M. Howerton, High-speed optical modulator in $LiNbO_3$ with cascaded resonant-type electrodes, *IEEE Journal of Lightwave Technology*, 24(5), 2184–2189, 2007.
31. R. Krahenbuhl, J.H. Cole, R.P. Moeller, and M.M. Howerton, High-speed optical modulator in $LiNbO_3$ with cascaded resonant-type electrodes, *Journal of Lightwave Technology*, 24(5), 2184–2189, 2009.
32. O. Painter, P.C. Sercel, K.J. Vahala, D.W. Vernooy, and G.H. Hunziker, Resonant optical modulators, US Patent No. WO/2002/050575, June 27, 2002.
33. M. Suzuki, Y. Noda, H. Tanaka, S. Akiba, Y. Kuahiro, and H. Isshiki, Monolithic integration of InGaAsP/InP distributed feedback laser and electroabsorption modulator by vapor phase epitaxy, *IEEE Journal of Lightwave Technology*, LT-5(9), 127, September 1987.
34. G. Roelkens et al., III-V/Si photonics by die-to-wafer bonding, *Material Today*, 10(7–8), 36–43, July–August 2007.

6

Advanced Modulation Format Optical Transmitters

Following the presentation of optical modulation in the direct and external modulation in Chapter 5, this chapter presents advanced modulation formats of light wave sources via external modulators. This is an extension of the modulation employing optical modulators connected at the output of a continuous-wave (CW) laser source. The laser is thus turned on at all times and the generated optical CWs are then modulated in terms of frequency, phase, and/or amplitude through an external optical modulator. Hence, the pulse sequence that envelops the carrier phase or frequency underneath can be varied according to the modulation schemes. The uses of these transmitters in optical communication transmission systems are given, especially those for long-haul transmissions at a very high bit rate. MATLAB® Simulink® models are described for generation of advanced modulation format in the optical domain.

These photonic transmitters can be used for both direct detection and coherent reception except for the requirement of narrowness of the linewidth of the laser source.

6.1 Introduction

A photonic transmitter would consist of a single or multiple lightwave source, which can be modulated either directly by manipulating the driving current of the laser diode or externally via an integrated optical modulator. These are called direct and external modulation techniques.

This chapter presents the techniques for generation of light waves and modulation techniques of light waves, either directly or externally. Direct modulation is the technique that directly manipulates the stimulated emission from inside the laser cavity, by the use of electro-optic effects. In external modulation, the laser is turned on at all times, and the generated light waves are coupled to an integrated optic modulator through which the electro-optic effect is used. With the electrical traveling waves that incorporate the coded information signals, the amplitude and/or phases of the light waves are modulated. Advanced modulation formats have recently attracted much attention for the enhancement of the transmission efficiency for coherent optical communications. Hence, the preservation of the narrow linewidth of the laser source is critical for operation bit rates in the range of several tens of Gb/s, making external modulation essential.

In Chapter 5, we introduced both direct and external modulation. External modulation is considered to be essential to preserve the linewidth of the laser, and hence, the bandwidth of the baseband signal is the principal factor influenced by the dispersion phenomena when travelling through the fiber medium.

This chapter describes the modulation techniques for optical communication systems employing mainly the external modulators—modulation of the phase and amplitude of

light waves, pulse shaping nonreturn-to-zero (NRZ) or return-to-zero (RZ), and schemes such as amplitude-shift keying (ASK), differential phase-shift keying (DPSK), minimum-shift keying (MSK), frequency-shift keying (FSK), multilevel amplitude and phase modulation such as quadrature amplitude modulation (QAM), and multicarriers such as orthogonal frequency division modulation (OFDM). Appropriate Simulink models are given for different modulation schemes.

6.2 Digital Modulation Formats

In this chapter, we focus on digital modulation formats as a way of carrying information over long distances through the optical carrier. These modulation formats have been developed over the last 50 years and now are well known. However, for completeness a brief revision of the concepts is given as these will lead to further detailed understanding of the modulation of the light waves in the optical domain. The modulation of the light wave carrier can be in the following forms:

The optical signal field has the ideal form during the duration of the one-bit period given by

$$E_s(t) = E_P(t)a(t)\cos\left[\omega(t)t + \theta(t)\right], \quad \text{for } 0 \le t \le T \tag{6.1a}$$

where $E_s(t)$, $E_P(t)$, $a(t)$, $\omega(t)$, and $\theta(t)$ are the signal optical field, the polarized field coefficient as a function of time, the amplitude variation, the optical frequency change with respect to time, and the phase variation with respect to time. Depending on the modulation of the carrier by amplitude, frequency, or phase it follows that (Figure 6.1):

- For ASK, the amplitude $a(t)$ takes the value $a(t) > 0$ for a "1" symbol and the value of 0 for a "0" symbol. Other values such as the angular frequency and the phase parameter remain unchanged over the one-bit period.
- For PSK, the phase angle $\theta(t)$ takes a value of some radians for a "1" symbol and zero radian for the symbol "0" so that the distance between these symbols on the phase plane is a maximum and hence, minimum interference or error can be obtained. These values are changed accordingly if the number of phase states is increased. The values of $a(t)$, $\omega(t)$, and $E_p(t)$ remain unchanged.
- For FSK, the value of $\omega(t)$ takes the value ω_1 for the "1" symbol and ω_2 for the "0" symbol. The values of $a(t)$, $\theta(t)$, and $E_p(t)$ remain unchanged. Indeed, FSK is a form of phase modulation when the phase is continuous. Sometimes, continuous phase modulation is also used as the term for FSK. In the case that the frequency spacing between ω_1 and ω_2 equals to a quarter of the bit rate then the FSK is called minimum-shift keying (MSK).
- For polarization-shift keying (PolSK), we have $E_p(t)$ taking one direction for the "1" symbol and the other for the "0" symbol. Sometimes, continuous polarization of a light wave is used to multiplex two optically modulated signal sequences to double the transmission capacity.
- Furthermore, to increase the transmission capacity there is a possibility of increasing the number of bits per symbol by using M-ary QAM such as 16 QAM, 32, or 64 QAM whose constellations are shown in Figure 6.2. However, the limitation is

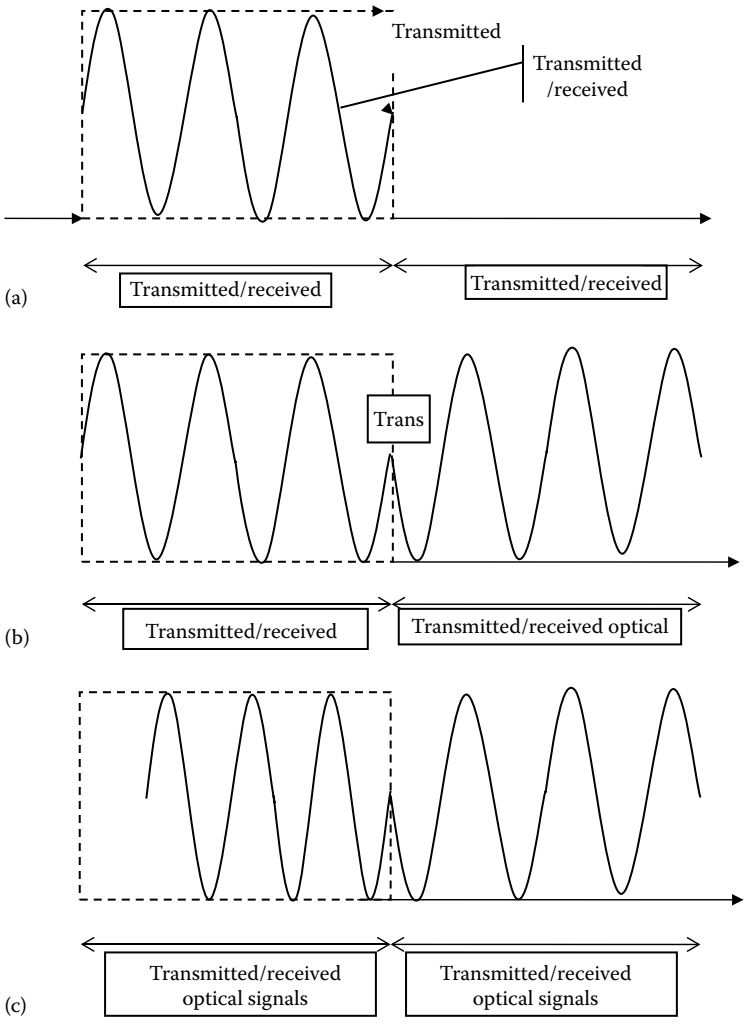

FIGURE 6.1
Illustration of ASK, PSK, and FSK with the symbol and variation of the optical carrier: (a) amplitude, (b) phase, and (c) frequency.

that the required optical signal to noise ratio (OSNR) would be increased accordingly. For example, an extra 6–7 dB would be required for 16 QAM as compared to QPSK which is 4 QAM. The estimated theoretical BER versus SNR can be depicted as in Figure 6.3 by using the bertoool.m in MATLAB communications tool boxes.

Clearly, we can observe that at a BER of 1e–4, the required energy per bit of 16 QAM is about 5 dB above that required for QPSK. So, where can we get this energy for a symbol in the optical domain? We can increase the carrier power to achieve this but this will hit the threshold level of nonlinear effects, thus acquiring further penalty. This can be resolved by a number of techniques that would be explained in detail in the chapters related to transmission systems.

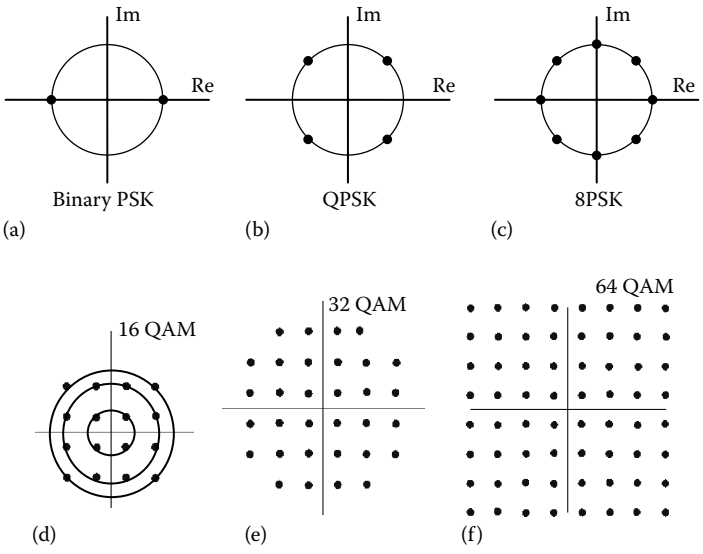

FIGURE 6.2
Constellations of the inphase and quadrature phases of the light wave carrier under modulation formats: (a) with π phase shift of the BPSK at the edge of the pulse period, (b) QPSK, (c) 8 PSK, (d) 16 QAM with three rings, (e) 32 QAM, (f) 64 QAM.

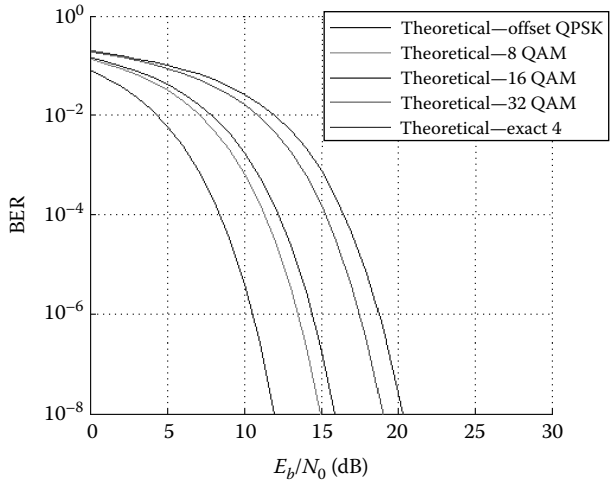

FIGURE 6.3
BER versus SNR for multilevel *M*-ary-QAM.

6.3 ASK Modulation Formats and Pulse Shaping

6.3.1 Return-to-Zero Optical Pulses

Figure 6.4 shows the conventional structure of an RZ–ASK transmitter in which two external $LiNbO_3$ MZIMs can be used. The MZIM shown in this transmitter can be either a single- or dual-drive (push pull) type. Operational principles of the MZIM were presented in Section 5.2. The optical OOK transmitter would normally consist of a narrow linewidth laser source to generate light waves whose wavelength satisfies the ITU grid standard.

The first MZIM, commonly known as the pulse carver, is used to generate the periodic pulse trains with a required RZ format. The suppression of the light wave carrier can also be carried out at this stage if necessary, commonly known as the carrier-suppressed RZ (CSRZ). Compared to other RZ types, CSRZ pulse shape is found to have attractive attributes for long-haul WDM transmissions including the π phase difference of adjacent modulated bits, suppression of the optical carrier component in optical spectrum, and narrower spectral width.

Different types of RZ pulses can be generated depending on the driving amplitude of the RF voltage and the biasing schemes of the MZIM. The equations governing the RZ pulses electric field waveforms are

$$E(t)=\begin{cases}\sqrt{\dfrac{E_b}{T}}\sin\left[\dfrac{\pi}{2}\cos\left(\dfrac{\pi t}{T}\right)\right] & \text{67\% duty-ratio RZ pulses or CSRZ}\\ \sqrt{\dfrac{E_b}{T}}\sin\left[\dfrac{\pi}{2}\left(1+\sin\left(\dfrac{\pi t}{T}\right)\right)\right] & \text{33\% duty-ratio RZ pulses or RZ33}\end{cases} \tag{6.1b}$$

where

E_b is the pulse energy per transmitted bit
T is the one-bit period

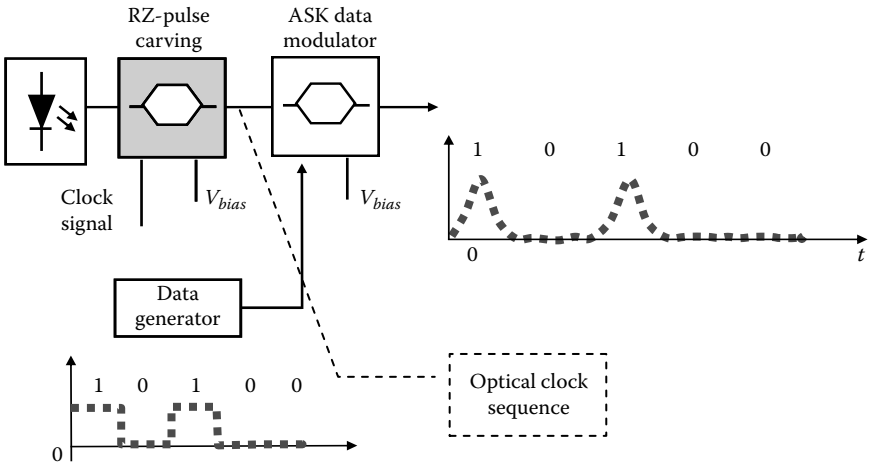

FIGURE 6.4
Conventional structure of an OOK optical transmitter utilizing two MZIMs.

The 33% duty-ratio RZ pulse is denoted by RZ33 pulse whereas the 67% duty cycle RZ pulse is known as the CSRZ type. The art the in generation of these two RZ pulse types stays at the difference of the biasing point on the transfer curve of an MZIM.

The pulse shape of these two RZ types can be generated with the carrier suppression and nonsuppression of the maximum-level carrier. This can be implemented with the biasing points at the minimum and maximum transmission points of the transmittance characteristics of the MZIM, respectively. The peak-to-peak amplitude of the RF-driving voltage is $2V_\pi$ where V_π is the required driving voltage to obtain a π phase shift on the light wave carrier. Another important point is that the RF signal must operate at only a half of the transmission bit rate and via the nonlinear transfer characteristic curve of the MZIM as a frequency double occurs, thus generating the RZ optical clock sequence at a repetition rate equal to the bit rate. Hence, pulse carving is obtained by implementing the frequency doubling. The generations of RZ33 and CSRZ pulse train are demonstrated in Figure 6.5a and b.

The pulse carver can also utilize a dual-drive MZIM which is driven by two complementary sinusoidal RF signals. This pulse carver is biased at $-V_{\pi/2}$ and $+V_{\pi/2}$ with the peak to peak amplitude of $V_{\pi/2}$. Thus, a π phase shift is created between the state "1" and "0" of the pulse sequence and hence, the RZ has an alternating phase 0 and π. If carrier suppression is required then the two electrodes are applied with voltages V_π and swing voltage amplitude of V_π.

Although RZ modulation offers improved performance, RZ optical systems usually require more complex transmitters than the NRZ ones. Compared to only one stage for modulating data on the NRZ optical signals, two modulation stages are required for generation of RZ optical pulses.

Recalling Equation 6.1a and b, we have

$$E_o = \frac{E_i}{2}\left[e^{j\varphi_1(t)} + e^{j\varphi_2(t)}\right] = \frac{E_i}{2}\left[e^{j\pi v_1(t)/V_\pi} + e^{j\pi v_2(t)/V_\pi}\right] \tag{6.2}$$

It can be seen that the modulating process for generation of RZ pulses can be represented by a phasor diagram as shown in Figure 6.6. This technique gives a clear understanding of the superposition of the fields at the coupling output of two arms of the MZIM. Here, a dual-drive MZIM is used, that is, the data driving signals $[V_1(t)]$ and inverse data ($\overline{\text{data}}$: $V_2(t) = -V_1(t)$) are applied into each arm of the MZIM, respectively, and the RF voltages swing in inverse directions. Applying the phasor representation, vector addition, and simple trigonometric calculus, the process of generation of RZ33 and CSRZ is explained in detail and verified.

The width of these pulses is commonly measured at the position of full-width half maximum (FWHM). It is noted that the measured pulses are intensity pulses whereas we are considering the addition of the fields in the MZIM. Thus, the normalized E_o field vector has the value of $\pm 1/\sqrt{2}$ at the FWHM intensity pulse positions and the time interval between these points gives the FWHM values.

6.3.2 Phasor Representation of CSRZ Pulses

Key parameters including the V_{bias}, the amplitude of the RF driving signal are shown in Figure 6.7a. Accordingly, its initialized phasor representation is demonstrated in Figure 6.7b.

The values of the key parameters are outlined as follows: (1) V_{bias} is $\pm V_\pi/2$; (2) Swing voltage of driving RF signal on each arm has an amplitude of $V_\pi/2$ (i.e., $V_{p-p} = V_\pi$); (3) RF

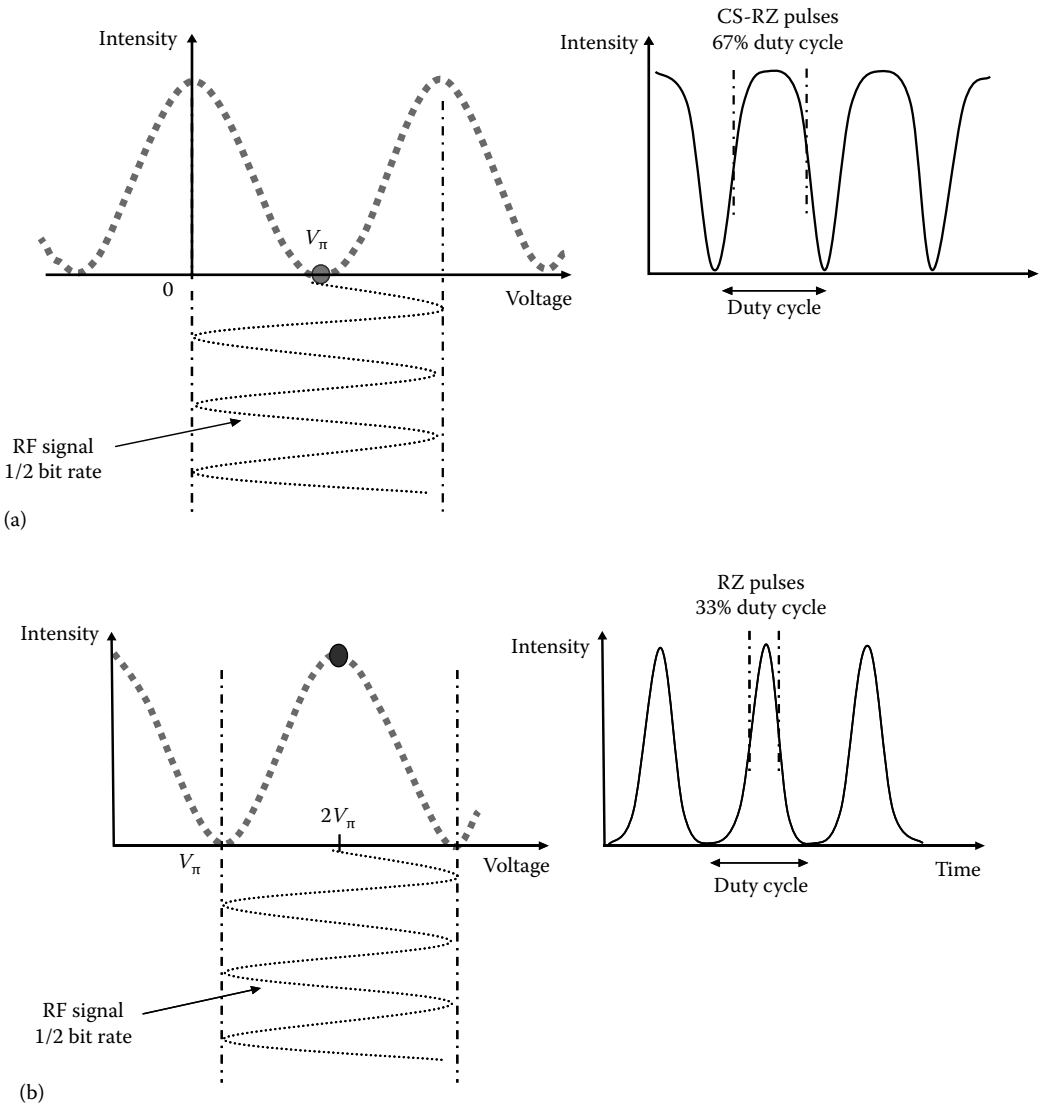

FIGURE 6.5
Bias point and RF driving signals for generation of (a) CSRZ and (b) RZ33 pulses.

signal operates at half of bit rate ($B_R/2$); (4) At the FWHM position of the optical pulse, the $E_{out} = \pm 1/\sqrt{2}$ and the component vectors V_1 and V_2 form with the vertical axis a phase of π/4 as shown in Figure 6.8.

Considering the scenario for generation of 40 Gb/s CSRZ optical signal, the modulating frequency is f_m ($f_m = 20$ GHz $= B_R/2$). At the FWHM positions of the optical pulse, the phase is given by the following expressions:

$$\frac{\pi}{2}\sin(2\pi f_m) = \frac{\pi}{4} \Rightarrow \sin 2\pi f_m = \frac{1}{2} \Rightarrow 2\pi f_m = \left(\frac{\pi}{6}, \frac{5\pi}{6}\right) + 2n\pi \tag{6.3}$$

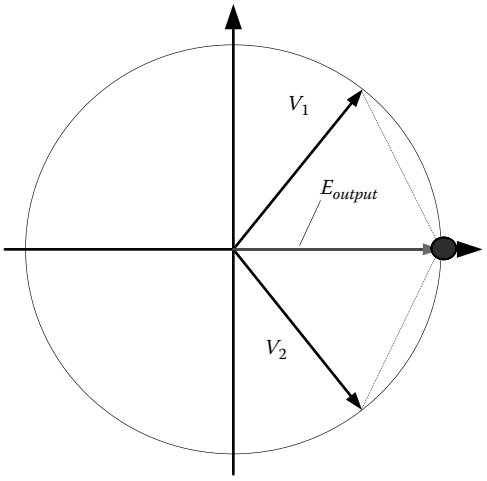

FIGURE 6.6
Phasor representation for generation of output field in dual-drive MZIM.

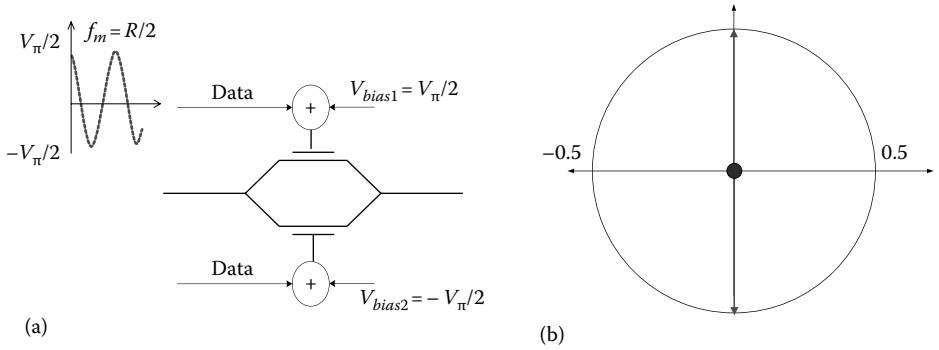

FIGURE 6.7
Initialized stage for generation of CSRZ pulse: (a) RF driving signal and the bias voltages; (b) Initial phasor representation.

Thus, the calculation of TFWHM can be carried out and hence, the duty cycle of the RZ optical pulse can be obtained as given in the following expressions:

$$T_{FWHM} = \left(\frac{5\pi}{6} - \frac{\pi}{6}\right)\frac{1}{R2\pi} = \frac{1}{3}\pi \times \frac{1}{R} \Rightarrow \frac{T_{FWHM}}{T_{BIT}} = \frac{1.66 \times 10^{-4}}{2.5 \times 10^{-11}} = 66.67\% \tag{6.4}$$

The result obtained in (6.6) clearly verifies the generation of CSRZ optical pulses from the phasor representation.

6.3.3 Phasor Representation of RZ33 Pulses

Key parameters including the V_{bias}, the amplitude of driving voltage, and its correspondent initialized phasor representation are shown in Figure 6.9a and b, respectively.

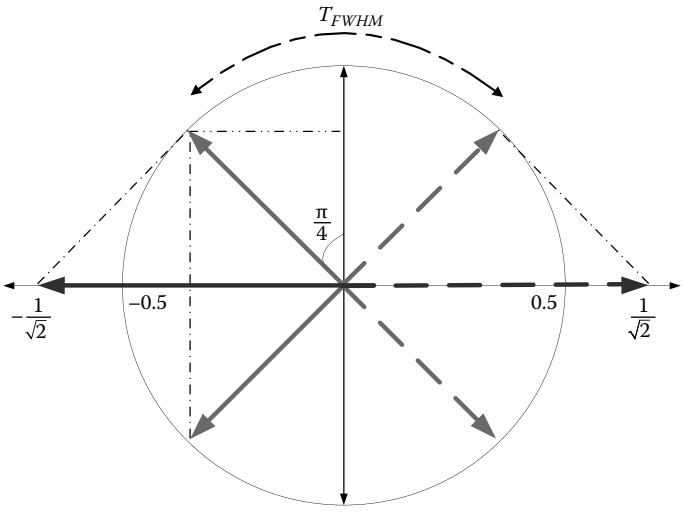

FIGURE 6.8
Phasor representation of CSRZ pulse generation using dual-drive MZIM.

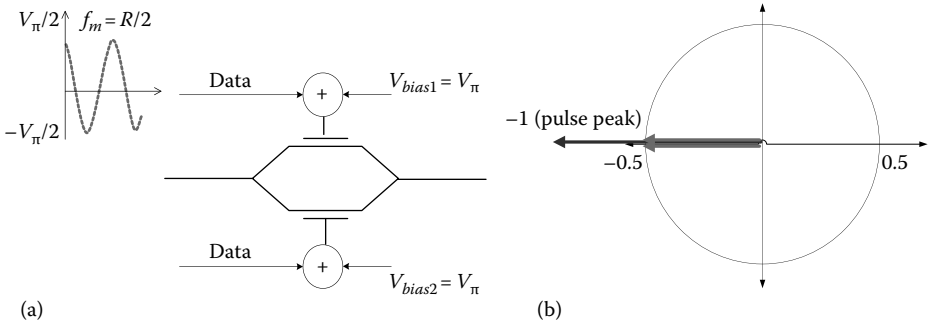

FIGURE 6.9
Initialized stage for generation of RZ33 pulse: (a) RF driving signal and the bias voltage; (b) Initial phasor representation.

The values of the key parameters are as follows: (1) V_{bias} is V_π for both arms; (2) Swing voltage of driving RF signal on each arm has the amplitude of $V_\pi/2$ (i.e., $V_{p-p} = V_\pi$); (3) RF signal operates at half of bit rate ($B_R/2$).

At the FWHM position of the optical pulse, the $E_{output} = \pm 1/\sqrt{2}$ and the component vectors V_1 and V_2 form with the horizontal axis a phase of $\pi/4$ as shown in Figure 6.10.

Considering the scenario for generation of 40 Gb/s CSRZ optical signal, the modulating frequency is f_m ($f_m = 20$ GHz $= B_R/2$). At the FWHM positions of the optical pulse, the phase is given by the following expressions:

$$\frac{\pi}{2}\cos(2\pi f_m t) = \frac{\pi}{4} \Rightarrow t_1 = \frac{1}{6f_m} \tag{6.5}$$

$$\frac{\pi}{2}\cos(2\pi f_m t) = -\frac{\pi}{4} \Rightarrow t_2 = \frac{1}{3f_m} \tag{6.6}$$

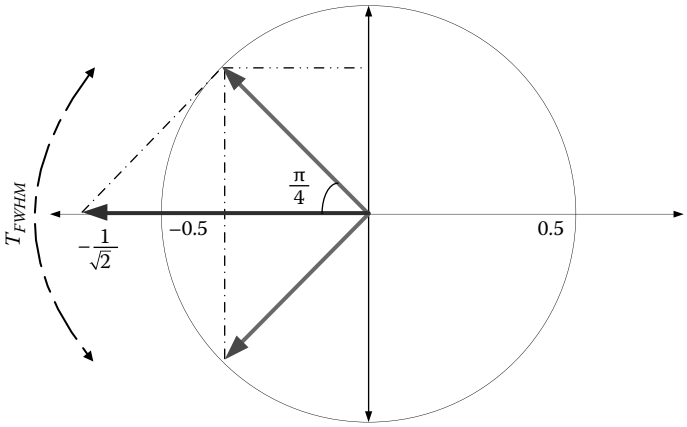

FIGURE 6.10
Phasor representation of RZ33 pulse generation using dual-drive MZIM.

$$S_0 = \overline{b_n}\,\overline{S_0'}\,\overline{S_1'} + b_n\,\overline{S_0'}S_1' + \overline{b_n}S_0'S_1' + b_nS_0'\,\overline{S_1'} \tag{6.7}$$

Thus, the calculation of TFWHM can be carried out and hence, the duty cycle of the RZ optical pulse can be obtained. The result obtained in (6.7) clearly verifies the generation of RZ33 optical pulses from the phasor representation.

6.4 Differential Phase Shift Keying

6.4.1 Background

Digital encoding of data information by modulating the phase of the light wave carrier is referred to as optical PSK. In early days, optical PSK was studied extensively for coherent photonic transmission systems. This technique requires the manipulation of the absolute phase of the light wave carrier. Precise alignment of the transmitter and demodulator center frequencies is required for coherent detection. These coherent optical PSK systems face severe obstacles such as broad linewidth and chirping problems of the laser source. Meanwhile, the DPSK scheme overcomes those problems, since the DPSK optically modulated signals can be detected incoherently. This technique only requires the coherence of the light wave carriers over one-bit period for the comparison of the differentially coded phases of the consecutive optical pulses.

A binary "1" is encoded if the present input bit and the past encoded bit are of opposite logic whereas a binary 0 is encoded if the logics are similar. This operation is equivalent to an XOR logic operation. Hence, an XOR gate is employed as a differential encoder. NOR can also be used to replace XOR operation in differential encoding as shown in Figure 6.11a. In DPSK, the electrical data "1" indicates a π phase change between the consecutive data bits in the optical carrier, while the binary "0" is encoded if there is no phase change between the consecutive data bits. Hence, this encoding scheme gives rise to two points located exactly at a phase difference of π with respect to each other

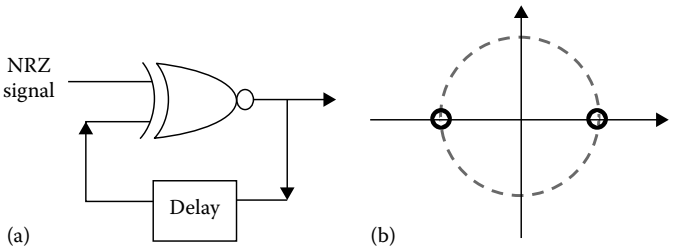

FIGURE 6.11
(a) DPSK precoder, (b) Signal constellation diagram of DPSK.

in the signal constellation diagram. For continuous PSK such as the MSK, the phase evolves continuously over a quarter of the section and results in a phase change of $\pi/2$ between one phase state to the other. This is indicated by the inner bold circle as shown in Figure 6.11b.

6.4.2 Optical DPSK Transmitter

Figure 6.12 shows the structure of a 40 Gb/s DPSK transmitter in which two external $LiNbO_3$ MZIM are used. Operational principles of an MZIM were presented earlier. The MZIMs shown in Figure 6.12 can be of either single- or dual-drive type. The optical DPSK transmitter also consists of a narrow linewidth laser to generate a lightwave whose wavelength conforms to the ITU grid.

The RZ optical pulses are then fed into the second MZIM through which the RZ pulses are modulated by the precoded binary data to generate RZ–DPSK optical signals. Electrical data pulses are differentially precoded in a precoder using the XOR coding scheme. Without the pulse carver, the structure shown in Figure 6.12 is an optical NRZ–DPSK

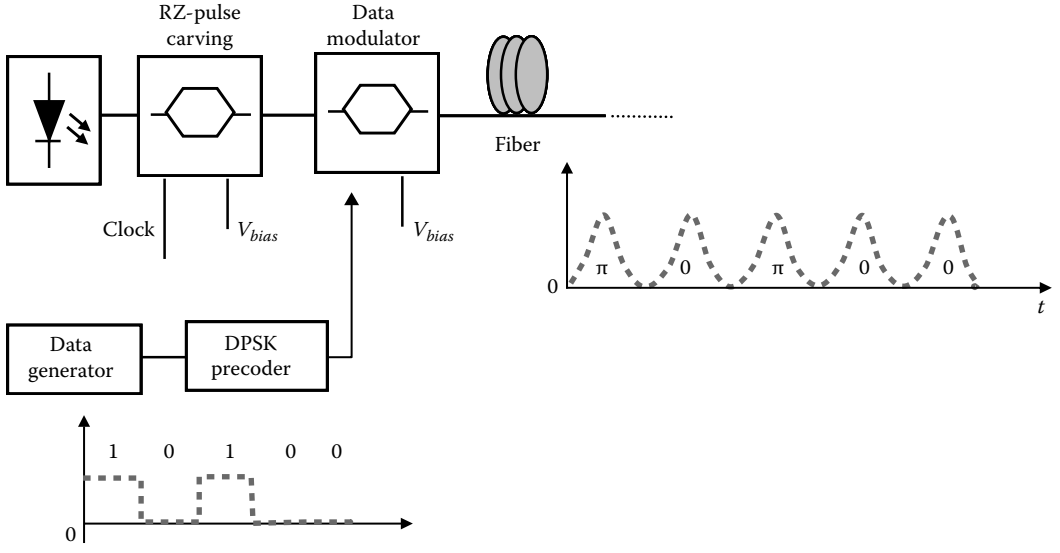

FIGURE 6.12
DPSK optical transmitter with RZ pulse carver.

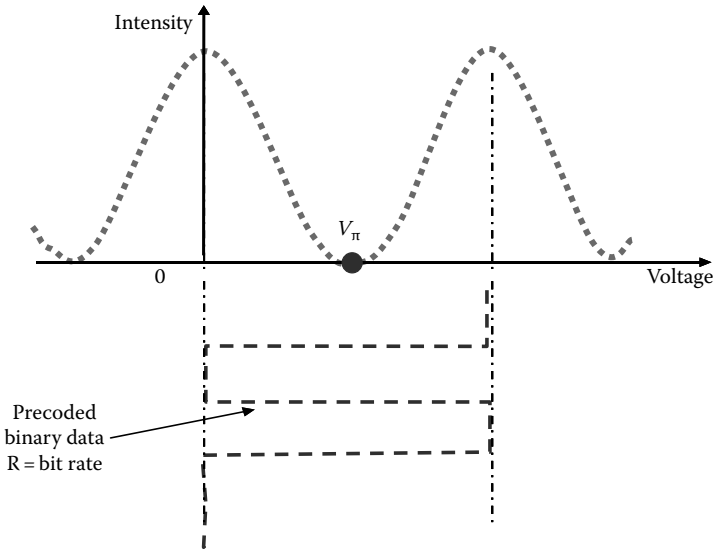

FIGURE 6.13
Bias point and RF driving signals for generation of optical DPSK format.

transmitter. In data modulation for DPSK format, the second MZIM is biased at the minimum transmission point. The precoded electrical data have peak-to-peak amplitude equal to $2V\pi$ and operate at the transmission bit rate. The modulation principles for generation of optical DPSK signals are demonstrated in Figure 6.13.

The electro-optic phase modulator might also be used for generation of DPSK signals instead of MZIM. Using optical phase modulator, the transmitted optical signal is chirped whereas using MZIM, especially the X-cut type with Z-propagation, chirp-free signals can be produced. However, in practice, a small amount of chirp might be useful for transmission [1].

6.5 Generation of Modulation Formats

Modulation is the process of facilitating the transfer of information over a medium, for example, a wireless or optical environment. Three basic types of modulation techniques are based on the manipulation of a parameter of the optical carrier to represent the information digital data. These are ASK, PSK, and FSK. In addition to the manipulation of the carrier, the occupation of the data pulse over a single period would also determine the amount of energy concentrates and the speed of the system required for transmission. The pulse can remain constant over a bit period or return to zero level within a portion of the period. These formats would be named NRZ or RZ. They are combined with the modulation of the carrier to form various modulation formats, which are presented in this section.

Figure 6.14 shows the baseband signals of the NRZ and RZ formats and its corresponding block diagram of a photonic transmitter.

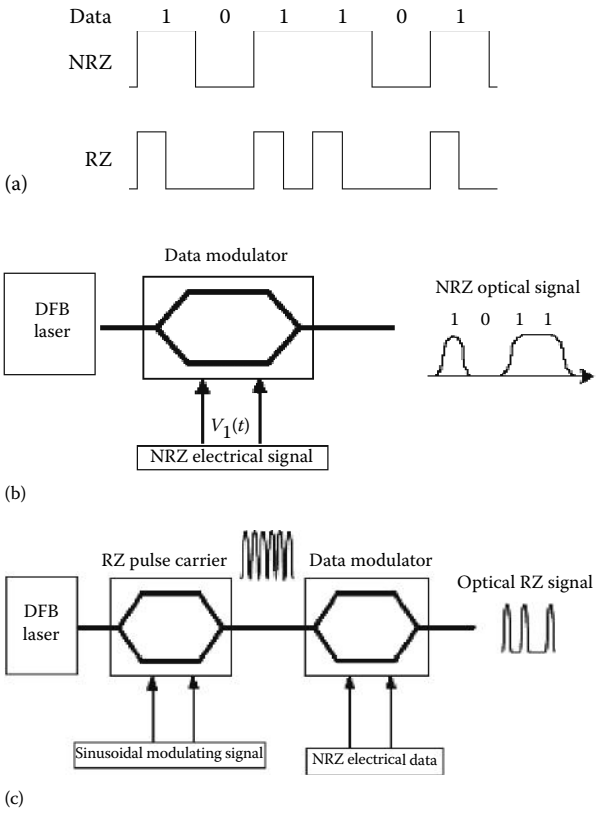

FIGURE 6.14
(a) Baseband NRZ and RZ line coding for 101101 data sequence, (b) block diagram of NRZ photonics transmitter, and (c) RZ photonics transmitter incorporating a pulse carver.

6.5.1 Amplitude–Modulation ASK–NRZ and ASK–RZ

There are a number of advanced formats used in advanced optical communications based on the intensity of the pulse which include NRZ, RZ, and duobinary. These ASK formats can also be integrated with the phase modulation to generate discrete or continuous phase NRZ or RZ formats. Currently, the majority of 10 Gb/s installed optical communication systems have been developed with NRZ due to its simple transmitter design and bandwidth efficient characteristic. However, RZ format has higher robustness to fiber nonlinearity and polarization mode dispersion (PMD). In this section, the RZ pulse is generated by MZIM commonly known as *pulse carver* as arranged in Figure 6.15. There are a number of variations in the RZ format based on the biasing point in

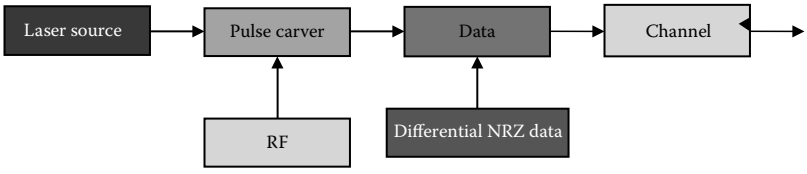

FIGURE 6.15
Block diagrams of RZ–DPSK transmitter.

TABLE 6.1

Summary of RZ Format Generation and Characteristics of Single-Drive MZIM Based on Biasing Point, Drive Signal Amplitude, and Frequency

Biasing Point in the $\cos^2$ Transmission Transfer Curve	RZ Generation Characteristics	Phasor Representation
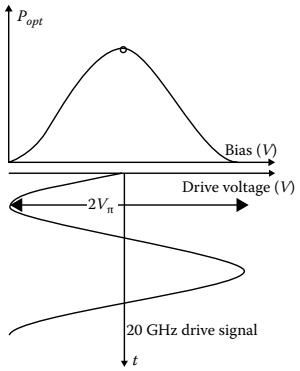	(a) Biasing point: Maximum, $V_{2\pi}$ (b) Drive signal amplitude: $2V_\pi$ (c) Drive sinusoidal signal frequency: 20 GHz (d) Pulse width: 9–10 ps about 70% of half the data rate (e) RZ pulse frequency: 40 GHz frequency doubling effect.	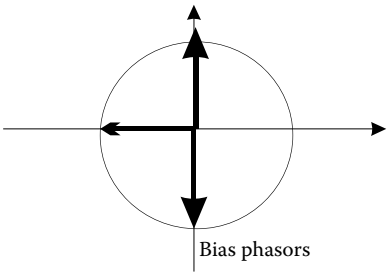
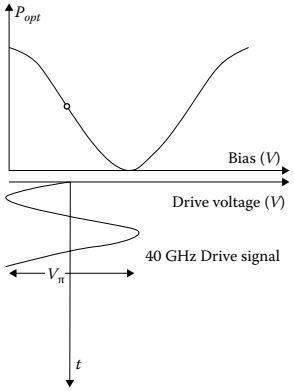	(a) Biasing point: linear region, $V_{\pi/2}$ (b) Drive signal amplitude: V_π (c) Drive sinusoidal signal frequency: 20 GHz (d) Pulse width: 9–10 ps or about 70% of half the data rate (e) RZ pulse frequency: 20 GHz	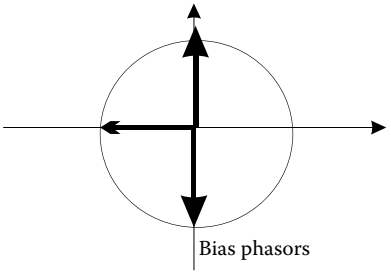
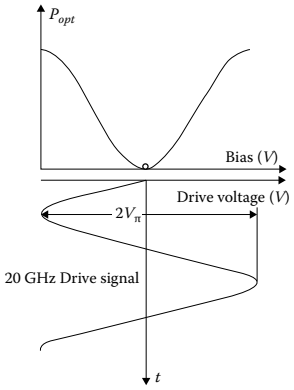	(a) Biasing point: minimum, V_π (b) Drive signal amplitude: $2V_\pi$ (c) Drive sinusoidal signal frequency: 20 GHz (d) Pulse width: 9–10 ps about 70% of half the data rate (e) RZ pulse frequency: 40 GHz frequency doubling effect. (Carrier suppressed RZ is generated using this scheme)	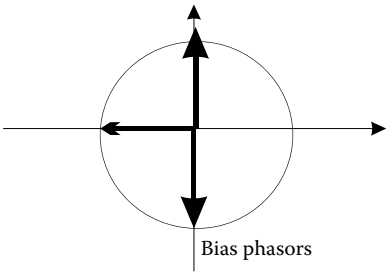

the transmission curve shown in Table 6.1. The phasor representation of the biasing and driving signals can also be observed in this table.

CSRZ has been found to have more attractive attributes in long-haul WDM transmissions compared to conventional RZ format because of the possibility of reducing the upper level of the power contained in the carrier that serves no purpose in the transmission but

only increases the total energy level so as to approach the nonlinear threshold level faster. CSRZ pulse has an optical phase difference of π in adjacent bits, removing the optical carrier component in optical spectrum and reducing the spectral width. This offers an advantage in compact WDM channel spacing.

6.5.1.1 Amplitude–Modulation Carrier-Suppressed RZ (CSRZ) Formats

The suppression of the carrier can be implemented by biasing the MZ interferometer in such a way so that there is a π phase shift between the two arms of the interferometer. The magnitude of the sinusoidal signals applied to an arm or both arms would determine the width of the optical output pulse sequence. The driving conditions and phasor representation are shown in Table 6.1.

6.5.2 Discrete Phase–Modulation NRZ Formats

The term discrete phase modulation refers to the DPSK whether DPSK or quadrature DPSK (DQPSK) to indicate the states of the phases of the light wave carrier as it switches from one distinct location on the phasor diagram to another state, for example, from 0 to π or $-\pi/2$ to $-\pi/2$ for binary PSK (BPSK), or even more evenly spaced PSK levels as in the case of *M*-ary PSK.

6.5.2.1 Differential Phase-Shift Keying (DPSK)

Information encoded in the phase of an optical carrier is commonly referred to as optical PSK. In early days, PSK required precise alignment of the transmitter and demodulator center frequencies. Hence, PSK system is not widely deployed. With DPSK scheme introduced, coherent detection is not critical since DPSK detection only requires source coherence over one-bit period by comparison of two consecutive pulses.

A binary "1" is encoded if the present input bit and the past encoded bit are of opposite logic and a binary 0 is encoded if the logic is similar. This operation is equivalent to XOR logic operation. Hence, an XOR gate is usually employed in differential encoder. NOR can also be used to replace XOR operation in differential encoding as shown in Figure 6.16.

In optical application, electrical data "1" is represented by a π phase change between the consecutive data bits in the optical carrier, while state "0" is encoded with no phase change between the consecutive data bits. Hence, this encoding scheme gives rise to two points located exactly at π phase difference with respect to each other in the signal constellation diagram as indicated in Figure 6.16b.

A RZ–DPSK transmitter consists of an optical source, pulse carver, data modulator, differential data encoder, and a channel coupler. The channel coupler model is not developed in simulation by assuming no coupling losses when optical RZ–DPSK modulated signal is launched into the optical fiber. This modulation scheme has combined the functionality of the dual-drive MZIM modulator of pulse carving and phase modulation.

The pulse carver, usually an MZ interferometric intensity modulator, is driven by a sinusoidal RF signal for single-drive MZIM and two complementary electrical RF signals for dual-drive MZIM to carve pulses out from optical carrier signal forming RZ pulses. These optical RZ pulses are fed into the second MZ intensity modulator where RZ pulses are modulated by differential NRZ electrical data to generate RZ–DPSK. This data phase modulation can be performed using straight line phase modulator but the MZ waveguide structure has several advantages over the phase modulator because of its chirpless property. Electrical data pulses are differentially precoded in a differential precoder as

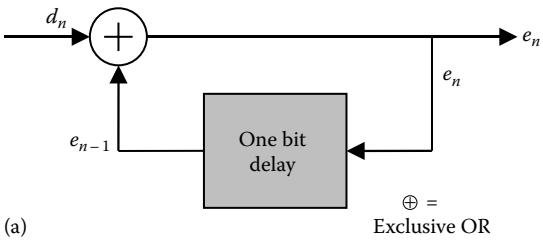

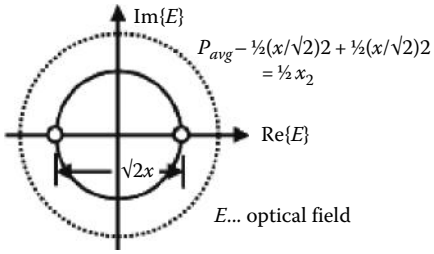

(b) Differential phase-shift keying (DPSK)

FIGURE 6.16
(a) The encoded differential data are generated by $e_n = d_n \oplus e_{n-1}$, (b) signal constellation diagram of DPSK.

shown in Figure 6.16a. Without the pulse carver and sinusoidal RF signal, the output pulse sequence follows NRZ–DPSK format, that is, the pulse occupies 100% of the pulse period and there is no transition between the consecutive "1s."

6.5.2.2 Differential Quadrature Phase-Shift Keying (DQPSK)

This differential coding is similar to DPSK except that each symbol consists of two bits that are represented by the two orthogonal axial discrete phases at (0, π) and (–π/2, +π/2) as shown in Figure 6.17 or two additional orthogonal phase positions are located on the imaginary axis of Figure 6.16b.

6.5.2.3 NRZ–DPSK

Figure 6.18 shows the block diagram of a typical NRZ–DPSK transmitter. The differential precoder of electrical data is implemented using the logic explained in the previous

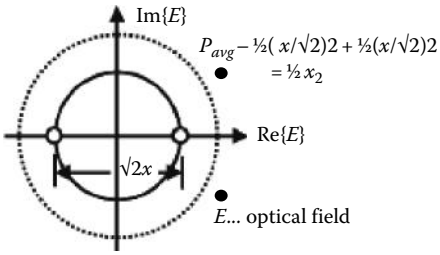

Differential phase-shift keying (DPSK)

FIGURE 6.17
Signal constellation diagram of DQPSK. Two bold dots are orthogonal to the DPSK constellation.

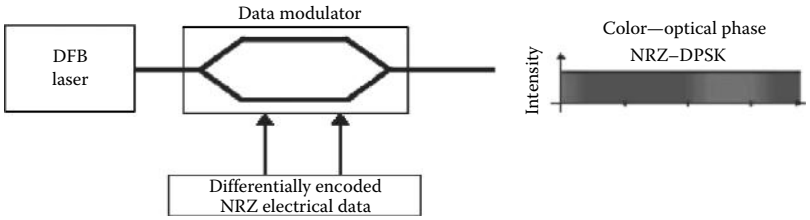

FIGURE 6.18
Block diagram of NRZ–DPSK photonics transmitter.

section. In phase modulating the optical carrier, MZ modulator known as data phase modulator is biased at the minimum point and driven by the data swing of $2V_\pi$. The modulator showed excellent behavior showing that the phase of the optical carrier will be altered by exactly π when the signal transits the minimum point of the transfer characteristic.

6.5.2.4 RZ–DPSK

The arrangement of RZ–DPSK transmitter is essentially similar to RZ–ASK as shown in Figure 6.19 with the data intensity modulator replaced by data phase modulator. The difference between them is the biasing point and the electrical voltage swing. Different RZ formats can also be generated.

6.5.2.5 Generation of M-Ary Amplitude Differential Phase-Shift Keying (M-Ary ADPSK) Using One MZIM

As an example, a 16-ary MADPSK signal can be represented by a constellation shown in Figure 6.20. It is, indeed, a combination of a 4-ary ASK and a DQPSK scheme. At the transmitting end, each group of four bits $[D_3D_2D_1D_0]$ of user data is encoded into a symbol, among them two least significant bits $[D_1D_0]$ are encoded into four phase states and the other two most significant bits, $[D_3D_2]$, are encoded into four amplitude levels. At the receiving end, as MZ delay interferometers (MZDI) are used for phase comparison and detection, a diagonal arrangement of the signal constellation shown in Figure 6.20a is preferred. This simplifies the design of transmitter and receiver, and minimizes the number of phase detectors, hence leading to high receiver sensitivity.

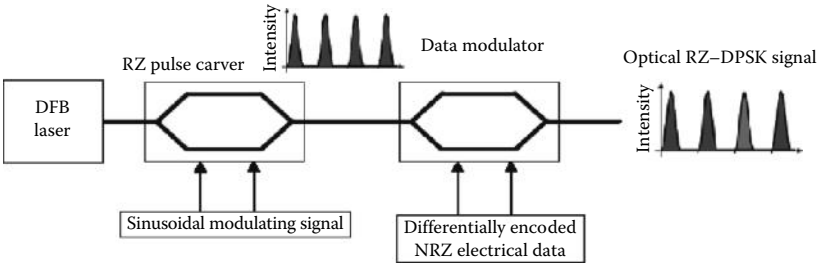

FIGURE 6.19
Block diagram of RZ–DPSK photonics transmitter.

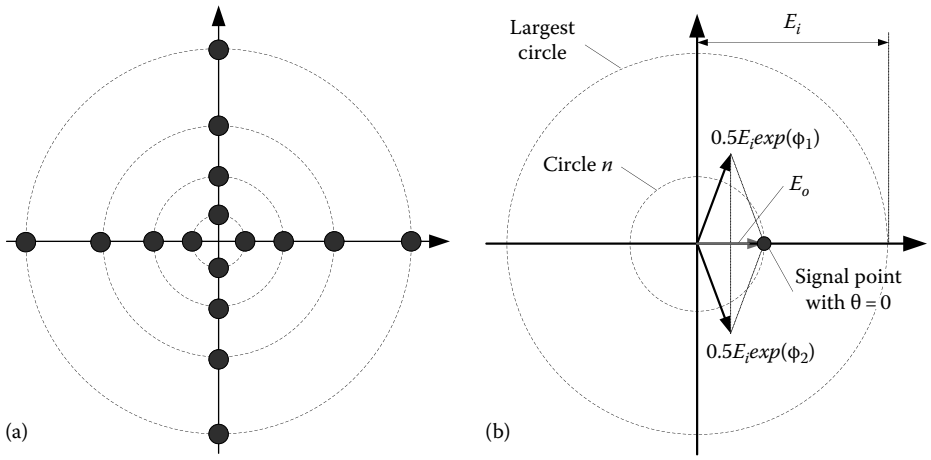

FIGURE 6.20
Signal constellation of 4-ary ADPSK format and phasor representation of a point on the constellation for driving voltages applied to dual-drive MZIM (a) constellation diagram and (b) Phasor diagram for generation of constellation.

To balance the bit error rate (BER) between ASK and DQPSK components, the signal levels corresponding to the four circles of the signal space should be adjusted to a reasonable ratio which depends on the noise power at the receiver. As an example, if this ratio is set to $[I_0/I_1/I_2/I_3] = [1/1.4/2/2.5]$, where I_0, I_1, I_2, and I_3 are the intensities of the optical signals corresponding to circle 0, circle 1, circle 2, and circle 3, respectively, then by selecting E_i equal to the amplitude of the circle 3 and V_π equal to 1, the driving voltages should have the values given in Table 6.2. Conversely, one can set the outermost level such that its peak value is below the nonlinear SPM threshold, and the voltage level of the outermost circle is determined. The innermost circle is limited to the condition that the largest signal to noise ratio (SNR) should be achieved. This is related to the optical SNR (OSNR) required for a certain BER. Thus, from the largest amplitude level and smallest amplitude level we can then design the other points of the constellation.

Furthermore, to minimize the effect of intersymbol interference, 66%-RZ and 50%-RZ pulse formats are also used as alternatives to the traditional NRZ pulse format. These RZ pulse formats can be created by a pulse carver that precedes or follows the dual-drive MZIM modulator. Mathematically, waveforms of NRZ and RZ pulses can be represented

TABLE 6.2
Driving Voltages for 16-Ary MADPSK Signal Constellation

Circle 0			Circle 1			Circle 2			Circle 3		
Phase	$V_1(t)$, V	$V_2(t)$, V	Phase	$V_1(t)$, V	$V_2(t)$, V	Phase	$V_1(t)$, V	$V_2(t)$, V	Phase	$V_1(t)$, V	$V_2(t)$, V
0	0.38	−0.38	0	0.30	−0.30	0	0.21	−0.21	0	0.0	0.0
π/2	0.88	0.12	π/2	0.80	0.20	π/2	0.71	0.29	π/2	0.5	0.5
π	−0.62	0.62	π	−0.7	0.70	π	−0.79	0.79	π	−1.0	1.0
3π/2	−0.12	−0.88	3π/2	−0.20	−0.8	3π/2	−0.29	−0.71	3π/2	−0.5	−0.5

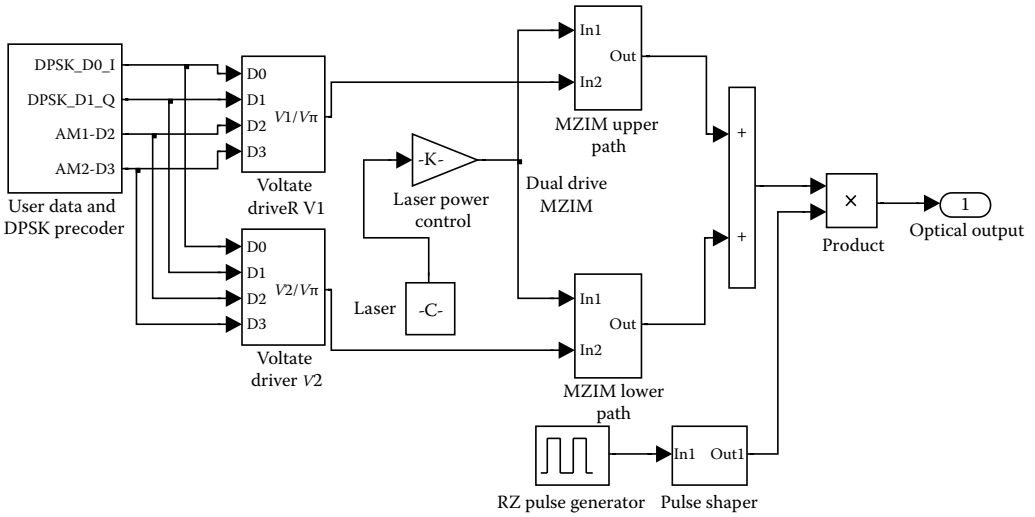

FIGURE 6.21
MATLAB® Simulink® model of a MADPSK photonic transmitter. The MZIM is represented by two phase shifter blocks.

by the following equations, where E_{on}, $n = 0, 1, 2, 3$ are peak amplitudes of the signals in the circle 0, circle 1, circle 2, and circle 3 of the constellation, respectively:

$$p(t) = \begin{cases} E_{on} & \text{for NRZ} \\ E_{on}\cos\left(\dfrac{\pi}{2}\cos^2\left(\dfrac{1.5\pi t}{T_s}\right)\right) & \text{for 66\%-RZ} \\ E_{on}\cos\left(\dfrac{\pi}{2}\cos^2\left(\dfrac{2\pi t}{T_s}\right)\right) & \text{for 50\%-RZ} \end{cases} \tag{6.8}$$

A typical arrangement of the signals of the precoder and driving signals for the MZIM is shown in Figure 6.21.

6.5.2.6 Continuous Phase–Modulation PM–NRZ Formats

In the previous section, the optical transmitters for discrete PSK modulation formats have been described. Obviously, the phase of the carrier is used to indicate the digital states of the bits or symbols. These phases are allocated in a noncontinuous manner around a circle corresponding to the magnitude of the wave. Alternatively, the phase of the carrier can be continuously modulated and the total phase changes at the transition instants, usually at the ends of the bit periods, would be the same as those for discrete cases. Since the phase of the carrier varies continuously during the bit period, this can be considered as an FSK modulation technique, except that the transition of the phase at the end of one bit and the beginning of the next bit would be continuous. The continuity of the carrier phase at these transitions would reduce the signal bandwidth and hence become more tolerant of dispersion effects and higher energy concentration for effective transmission over the

optical guided medium. One of the examples of the reduction of the phase at the transition is the offset DQPSK, which is a minor but important variation of the QPSK or DQPSK. In OQPSK, the Q channel is shifted by half a symbol period so that the transition instants of I and Q channel signals do not occur at the same time. The result of this simple change is that the phase shifts at any one time are limited and hence, the offset QPSK is a more constant envelope than the normal QPSK.

The enhancement of the efficiency of the bandwidth of the signals can be further improved if the phase changes at these transitions are continuous. In this case, the change in the phase during the symbol period is made continuous by using half-cycle sinusoidal driving signals with the total phase transition over a symbol period being a fraction of π, depending on the levels of this PSK modulation. If the change is π/2, then we have an MSK scheme. The orthogonality of the I and Q channels will also reduce further the bandwidth of the carrier-modulated signals. In this section, we describe the basic principles of optical MSK and the photonic transmitters for these modulation formats. Ideally, the driving signal to the phase modulator should be a triangular wave so that a linear phase variation of the carrier in the symbol period is linear. However, when a sinusoidal function is used there are some nonlinear variations; we term this type of MSK as a nonlinear MSK format. This nonlinearity contributes to some penalty in the optical signal to noise ratio (OSNR), which is explained in a later chapter. Furthermore, the MSK as a special form of ODQPSK is also described for optical systems.

6.5.2.7 Linear and Nonlinear MSK

6.5.2.7.1 Signals and Precoding

MSK is a special form of continuous phase FSK (CPFSK) signal in which the two frequencies are spaced in such a way that they are orthogonal, have minimum space between them, and are defined by

$$s(t) = \sqrt{\frac{2E_b}{T_b}} \cos\left[2\pi f_1 t + \theta(0)\right] \quad \text{for symbol 1,} \tag{6.9}$$

$$s(t) = \sqrt{\frac{2E_b}{T_b}} \cos\left[2\pi f_2 t + \theta(0)\right] \quad \text{for symbol 0.} \tag{6.10}$$

As shown by these equations, the signal frequency change corresponds to higher frequency for data-1 and lower frequency for data-0. Both frequencies, f_1 and f_2, are defined by

$$f_1 = f_c + \frac{1}{4T_b} \quad \text{and} \quad f_2 = f_c - \frac{1}{4T_b} \tag{6.11}$$

Depending on the binary data, the phase of the signal changes; data-1 increases the phase by π/2, while data-0 decreases the phase by π/2. The variation of phase follows paths of a sequence of straight lines in phase trellis (Figure 6.22), in which the slopes represent frequency changes. The change in carrier frequency from data-0 to data-1, or vice versa, is equal to half the bit rate of incoming data. This is the minimum frequency spacing that allows the two FSK signals representing symbols 1 and 0 to be coherently orthogonal in the sense that they do not interfere with one another in the process of detection.

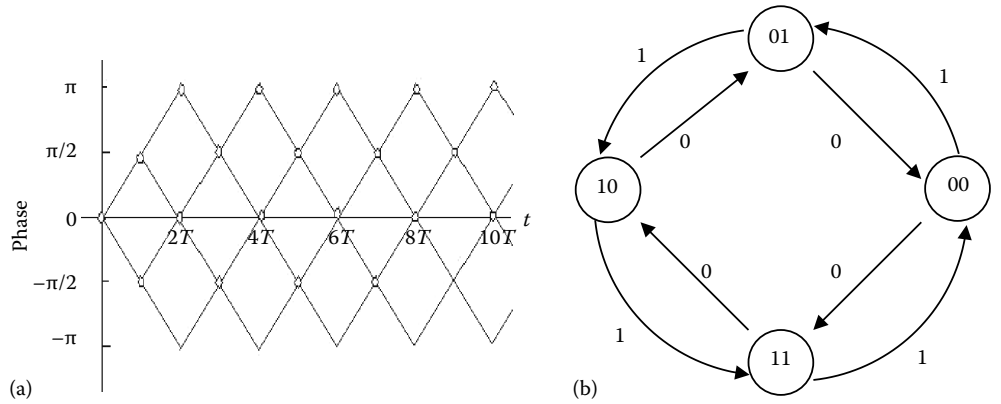

FIGURE 6.22
(a) Phase trellis for MSK, (b) state diagram for MSK.

An MSK signal consists of both *I* and *Q* components, which can be written as

$$s(t) = \sqrt{\frac{2E_b}{T_b}} \cos\left[\theta(t)\right]\cos\left[2\pi f_c t\right] - \sqrt{\frac{2E_b}{T_b}} \sin\left[\theta(t)\right]\sin\left[2\pi f_c t\right] \tag{6.12}$$

The in-phase component consists of half-cycle cosine pulse defined by

$$s_I(t) = \pm\sqrt{\frac{2E_b}{T_b}} \cos\left(\frac{\pi t}{2T_b}\right), \quad -T_b \le t \le T_b \tag{6.13}$$

while the quadrature component would take the form

$$s_Q(t) = \pm\sqrt{\frac{2E_b}{T_b}} \sin\left(\frac{\pi t}{2T_b}\right), \quad 0 \le t \le 2T_b. \tag{6.14}$$

Between even-bit intervals, the *I* component consists of the positive cosine waveform for phase of 0, and the negative cosine waveform for phase of π; between odd-bit intervals, the *Q* component consists of positive sine waveform for phase of π/2, and negative sine waveform for phase of −π/2 (see Figure 6.22). Any of the four states can arise: 0, π/2, −π/2, π. However, only state 0 or π can occur during any even-bit interval and only π/2 or −π/2 can occur during any odd-bit interval. The transmitted signal is the sum of *I* and *Q* components and its phase is continuous with time.

Two important characteristics of MSK are that each data bit is held for two bit periods, meaning the symbol period is equal to two bit periods ($h = 1/2$) and the *I* and *Q* components are interleaved. *I* and *Q* components are delayed by 1-bit period with respect to each other. Therefore, only the *I* or *Q* component can change at a time (when one is at zero crossing, the other is at maximum peak). The precoder can be a combinational logic as shown in Figure 6.23.

A truth table can be constructed based on the logic state diagram and combinational logic diagram given earlier. For the positive half-cycle cosine wave and the positive half

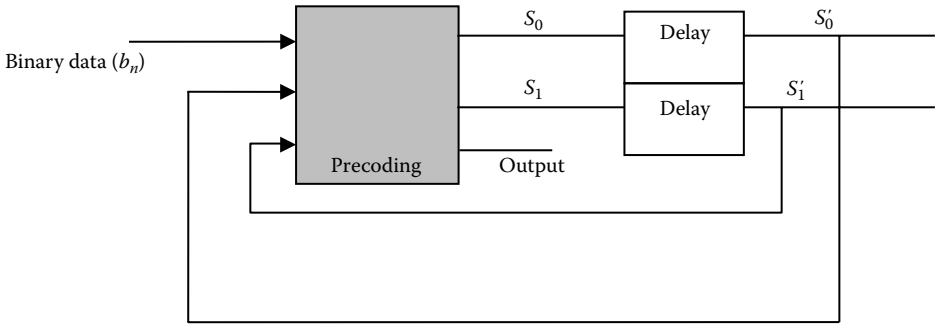

FIGURE 6.23
Combinational logic, the basis of the logic for constructing the precoder.

TABLE 6.3
Truth Table Based on MSK State Diagram

$b_nS_0'S_1'$	$S_0'S_1'$	Output
100	01	1
001	00	1
100	01	1
101	10	0
010	01	1
101	10	0
110	11	0
111	00	1
000	11	0
011	10	0

cycle sine wave, the output is 1; for the negative half-cycle cosine wave and the negative half-cycle sine wave, the output is 0. Then, a *K*-map can be constructed to derive the logic gates of the precoder, based on the truth table (Table 6.3). The following three precoding logic equations are derived:

$$S_0 = \overline{b_n}\,\overline{S_0'}\,\overline{S_1'} + b_n\,\overline{S_0'}S_1' + \overline{b_n}S_0'S_1' + b_nS_0'\,\overline{S_1'} \tag{6.15}$$

$$S_1 = \overline{S_1'} = \overline{b_n}\,\overline{S_1'} + b_n\,\overline{S_1'} \tag{6.16}$$

$$Output = \overline{S_0} \tag{6.17}$$

The resultant logic gates construction for the precoder is as shown in Figure 6.23.

6.5.2.7.2 MSK as a Special Case of Continuous Phase FSK (CPFSK)

CPFSK signals are modulated in the upper and lower sideband frequency carriers f_1 and f_2, which can be expressed as

$$s(t) = \sqrt{\frac{2E_b}{T_b}}\cos\left[2\pi f_1 t + \theta(0)\right] \quad \text{symbol "1"} \tag{6.18}$$

$$s(t) = \sqrt{\frac{2E_b}{T_b}} \cos\left[2\pi f_2 t + \theta(0)\right] \quad \text{symbol "0"} \tag{6.19}$$

where

$$f_1 = f_c + \frac{1}{4T_b}$$

$$f_2 = f_c + \frac{1}{4T_b}$$

T_b is the bit period.

The phase slope of the light wave carrier changes linearly or nonlinearly with the modulating binary data. In the case of linear MSK, the carrier phase changes linearly by π/2 at the end of the bit slot with data "1," while it decreases linearly by π/2 with data "0." The variation of phase follows paths of well-defined phase trellis in which the slopes represent frequency changes. The change in carrier frequency from data-0 to data-1, or vice versa, equals half the bit rate of incoming data. This is the minimum frequency spacing that allows the two FSK signals representing symbols 1 and 0 to be coherently orthogonal in the sense that they do not interfere with one another in the process of detection. The MSK carrier phase is always continuous at bit transitions. The MSK signals in (6.18) and (6.19) can be simplified as:

$$s(t) = \sqrt{\frac{2E_b}{T_b}} \cos\left[2\pi f_c t + d_k \frac{\pi t}{2T_b} + \Phi_k\right], \quad kT_b \le t \le (k+1)T_b \tag{6.20}$$

and the baseband equivalent optical MSK signal is represented by

$$\tilde{s}(t) = \sqrt{\frac{2E_b}{T_b}} \exp\left\{j\left[d_k \frac{\pi t}{2T} + \Phi(t,k)\right]\right\}, \quad kT \le t \le (k+1)T$$

$$= \sqrt{\frac{2E_b}{T_b}} \exp\left\{j\left[d_k 2\pi f_d t + \Phi(t,k)\right]\right\} \tag{6.21}$$

where

$d_k = \pm 1$ are the logic levels

f_d is the frequency deviation from the optical carrier frequency

$h = 2f_dT$ is defined as the frequency modulation index

In case of optical MSK, $h = 1/2$ or $f_d = 1/(4T_b)$.

6.5.2.8 MSK as Offset Differential Quadrature Phase–Shift Keying (ODQPSK)

Equation 6.21 can be rewritten to express MSK signals in the form of *I*–*Q* components as:

$$s(t) = \pm\sqrt{\frac{2E_b}{T_b}} \cos\left(\frac{\pi t}{2T_b}\right)\cos\left[2\pi f_c t\right] \pm \sqrt{\frac{2E_b}{T_b}} \sin\left(\frac{\pi t}{2T_b}\right)\sin\left[2\pi f_c t\right] \tag{6.22}$$

The I and Q components consist of half-cycle sine and cosine pulses defined by [2,3]

$$s_I(t) = \pm\sqrt{\frac{2E_b}{T_b}}\cos\left(\frac{\pi t}{2T_b}\right) \quad -T_b < t < T_b \tag{6.23}$$

$$s_Q(t) = \pm\sqrt{\frac{2E_b}{T_b}}\sin\left(\frac{\pi t}{2T_b}\right) \quad 0 < t < 2T_b \tag{6.24}$$

During even-bit intervals, the in-phase component consists of positive cosine waveform for phase of 0 while negative cosine waveform for phase of π. During odd-bit intervals, the Q component consists of the positive sine waveform for phase of π/2 and the negative sine waveform for phase of −π/2. Any of the four states can arise: 0, π/2, −π/2, π. However, only state 0 or π can occur during any even-bit interval and only π/2 or −π/2 can occur during any odd-bit interval. The transmitted signal is the sum of I and Q components and its phase is continuous in time.

Two important characteristics of MSK are that each data bit is held for two-bit period, mseaning the symbol period is equal to two bit periods (h = 1/2) and the I component and Q component are interleaved. I and Q components are delayed by one-bit period with respect to each other. Therefore, only I or Q component can change at a time (when one is crossing zero, the other is at maximum peak).

6.6 Photonic MSK Transmitter Using Two Cascaded Electro-Optic Phase Modulators

Electro-optic phase modulators and interferometers that can operate at high frequency using resonant-type electrodes have been studied and proposed in Ref. [4]. In addition, high-speed electronic driving circuits evolved with ASIC technology using 0.1 μm GaAs P-HEMT or InP HEMTs enables realization of the optical MSK transmitter structure. The baseband equivalent optical MSK signal can be generated.

The first electro-optic phase modulator (E-OPM) enables the frequency modulation of data logics into upper sidebands (USB) and lower sidebands (LSB) of the optical carrier with frequency deviation of f_d. Differential phase precoding is not necessary in this configuration because of the nature of the continuity of the differential phase trellis. By alternating the driving sources $V_d(t)$ to sinusoidal waveforms for simple implementation or combination of sinusoidal and periodic ramp signals, which was first proposed by Amoroso in 1976 [2], different schemes of linear and nonlinear phase–shaping MSK transmitted sequences whose spectra are shown in Figure 6.35 can be generated.

The second E-OPM enforces the phase continuity of the light wave carrier at every bit transition. The delay control between the E-OPMs is usually implemented by the phase shifter shown in Figure 6.24. The driving voltage of the second E-OPM is precoded to fully compensate the transitional phase jump at the output $E_{01}(t)$ of the first

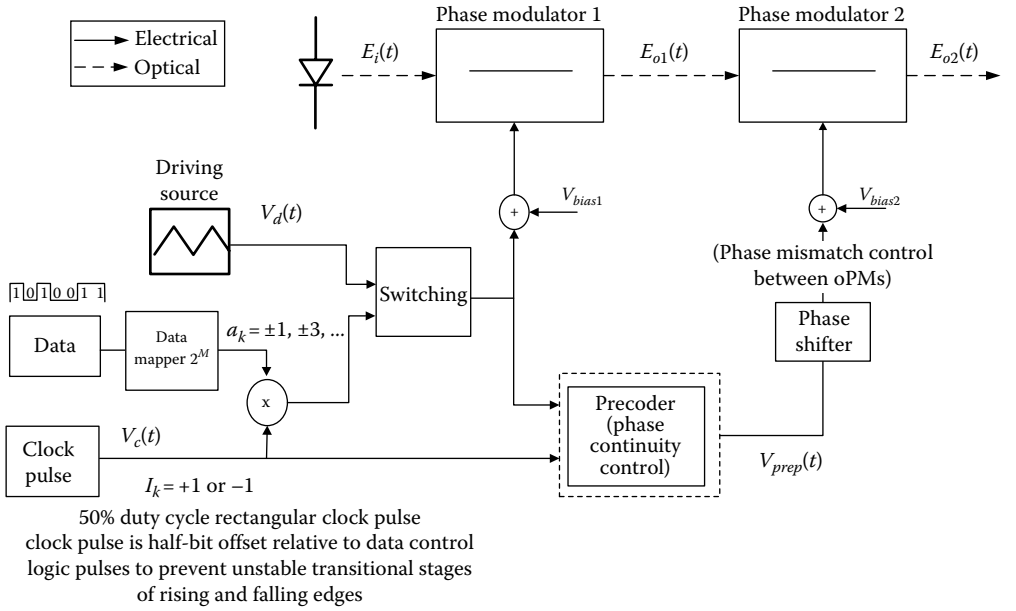

FIGURE 6.24
Block diagram of optical MSK transmitter employing two cascaded optical phase modulators.

E-OPM. Phase continuity characteristic of the optical MSK signals is determined by the algorithm for MSK [5]

$$\Phi(t,k) = \frac{\pi}{2}\left(\sum_{j=0}^{k-1} a_j - a_k I_k \sum_{j=0}^{k-1} I_j\right) \tag{6.25}$$

where

$a_k = \pm 1$ are the logic levels
$I_k = \pm 1$ is a clock pulse whose duty cycle is equal to the period of the driving signal $V_d(t)$
f_d is the frequency deviation from the optical carrier frequency
$h = 2f_dT$ is previously defined as the frequency modulation index

In case of optical MSK, $h = 1/2$ or $f_d = 1/(4T)$. The phase evolution of the continuous-phase optical MSK signals is explained in Figure 6.24. In order to mitigate the effects of the rising and falling edges of the electronic circuits, the clock pulse $V_c(t)$ is offset with the driving voltages $V_d(t)$ (Figure 6.25).

6.6.1 Optical MSK Transmitter Using Mach–Zehnder Intensity Modulators: *I–Q* Approach

The conceptual block diagram of the optical MSK transmitter is shown in Figure 6.26. The transmitter consists of two dual-drive electro-optic MZM modulators generating chirpless *I* and *Q* components of MSK-modulated signals, which is a special case of staggered or offset QPSK. The binary logic data are precoded and deinterleaved into even- and odd-bit streams, which are interleaved with each other by one bit duration offset.

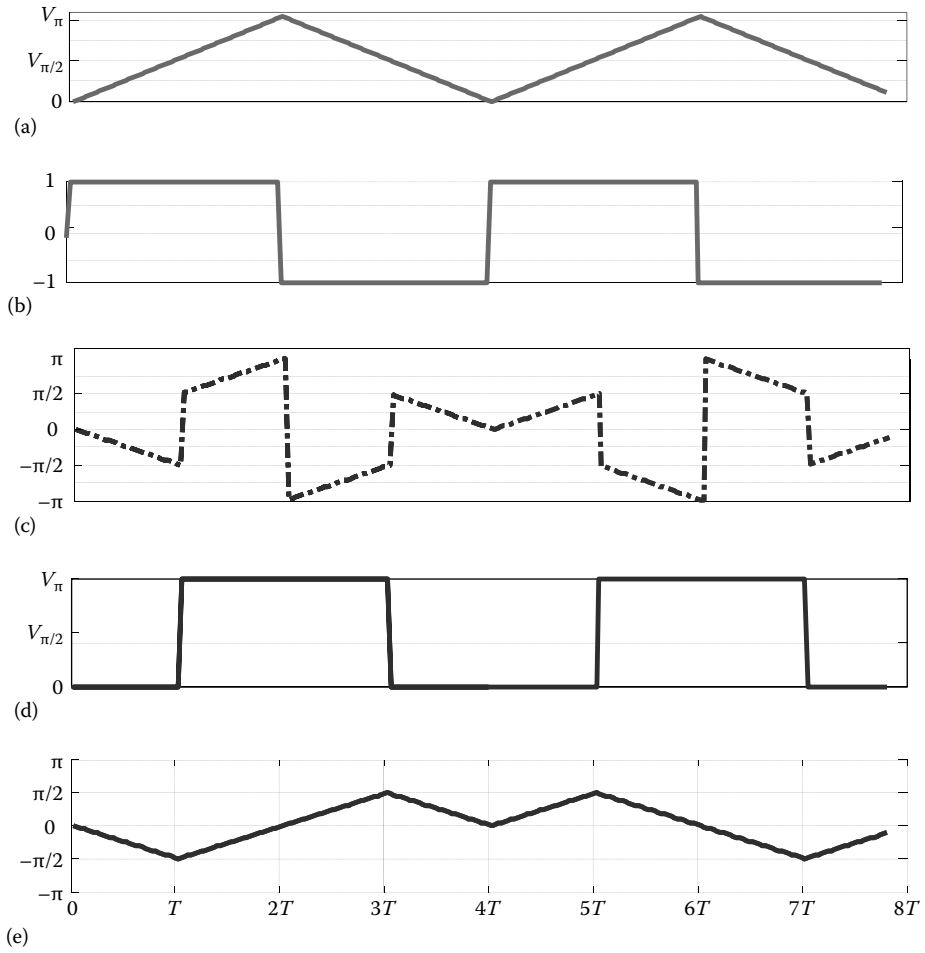

FIGURE 6.25
Evolution of time-domain phase trellis of optical MSK signal sequence [–1 1 1 –1 1 –1 1 1] as inputs and outputs at different stages of the optical MSK transmitter. The notation is denoted in Figure 6.24 accordingly; (a) $V_d(t)$: periodic triangular driving signal for optical MSK signals with duty cycle of 4-bit period, (b) $V_c(t)$: the clock pulse with duty cycle of 4T, (c) $E_{01}(t)$: phase output of oPM1 (d) $V_{prep}(t)$: precomputed phase compensation driving voltage of oPM2, and (e) $E_{02}(t)$: phase trellis of a transmitted optical MSK sequences at output of oPM2.

Two arms of the dual-drive MZM modulator are biased at $V_\pi/2$ and $-V_\pi/2$ and driven with *data* and $\overline{data}$. Phase-shaping driving sources can be a periodic triangular voltage source in case of linear MSK generation or simply a sinusoidal source for generating a nonlinear MSK-like signal, which also have the linear phase trellis property but with small ripples introduced in the magnitude. The magnitude fluctuation level depends on the magnitude of the phase-shaping driving source. High spectral efficiency can be achieved with tight filtering of the driving signals before modulating the electro-optic MZMs. Three types of pulse shaping filters are investigated including Gaussian, raised cosine, and squared-root raised cosine filters. The optical carrier phase trellis of linear and nonlinear optical MSK signals is shown in Figure 6.27.

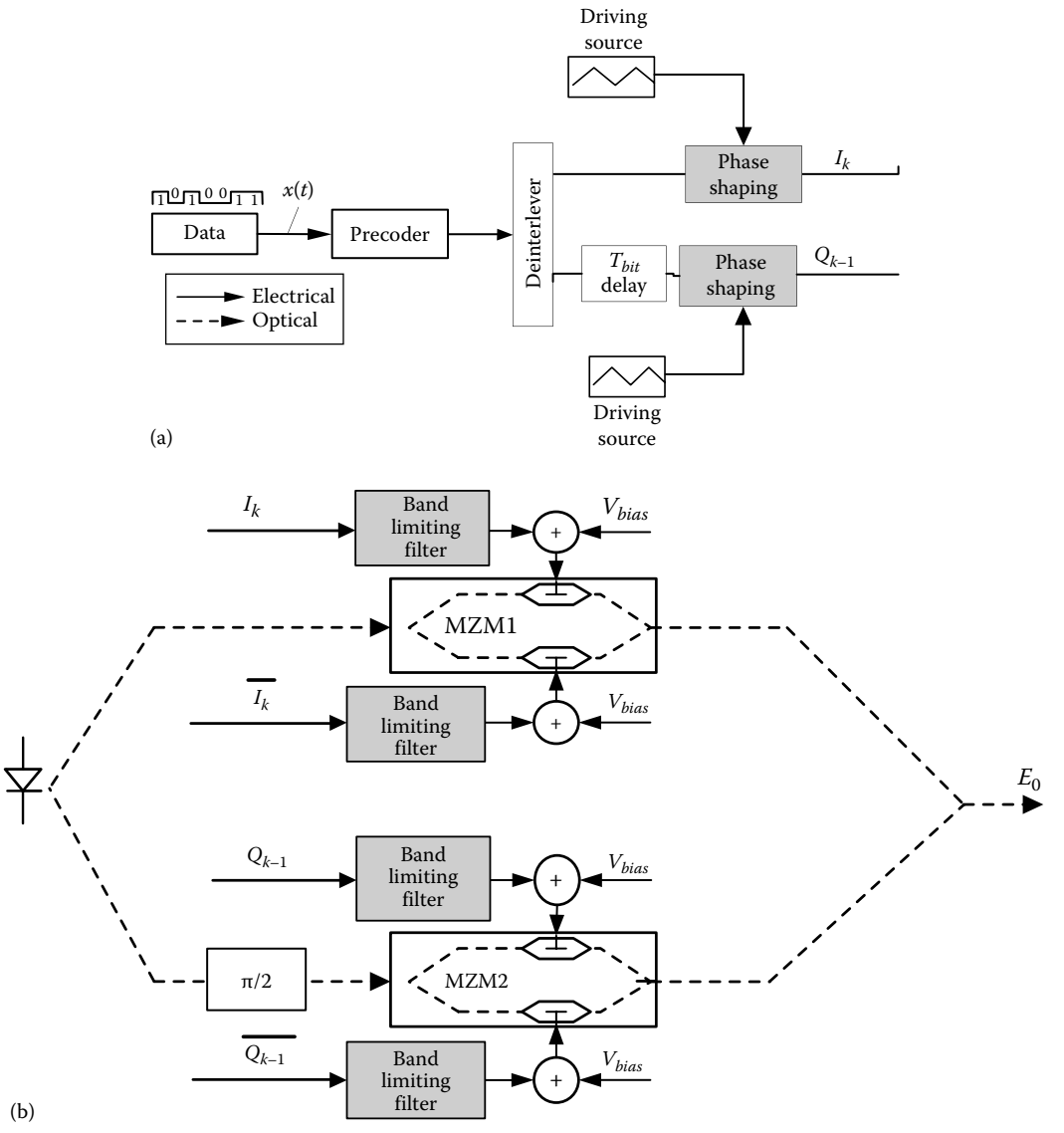

FIGURE 6.26
Block diagram configurations of band-limited phase-shaped optical MSK: (a) Encoding circuit and pulse shaping, (b) parallel MZIM optical modulators.

6.6.2 Single Sideband (SSB) Optical Modulators

An SSB modulator can be formed using a primary interferometer with two secondary MZM structures, the optical Ti-diffused waveguide paths that form a nested primary MZ structure as shown in Figure 6.28. Each of the two primary arms contains an MZ structure. Two RF ports are for RF modulation and three DC ports are for biasing the two secondary MZMs and one primary MZM. The modulator consists of an X-cut Y-propagation $LiNbO_3$ crystal, where you can produce an SSB modulation just by driving each MZ. DC voltage is supplied to produce the π phase shift between the upper and lower arms. DC bias voltages

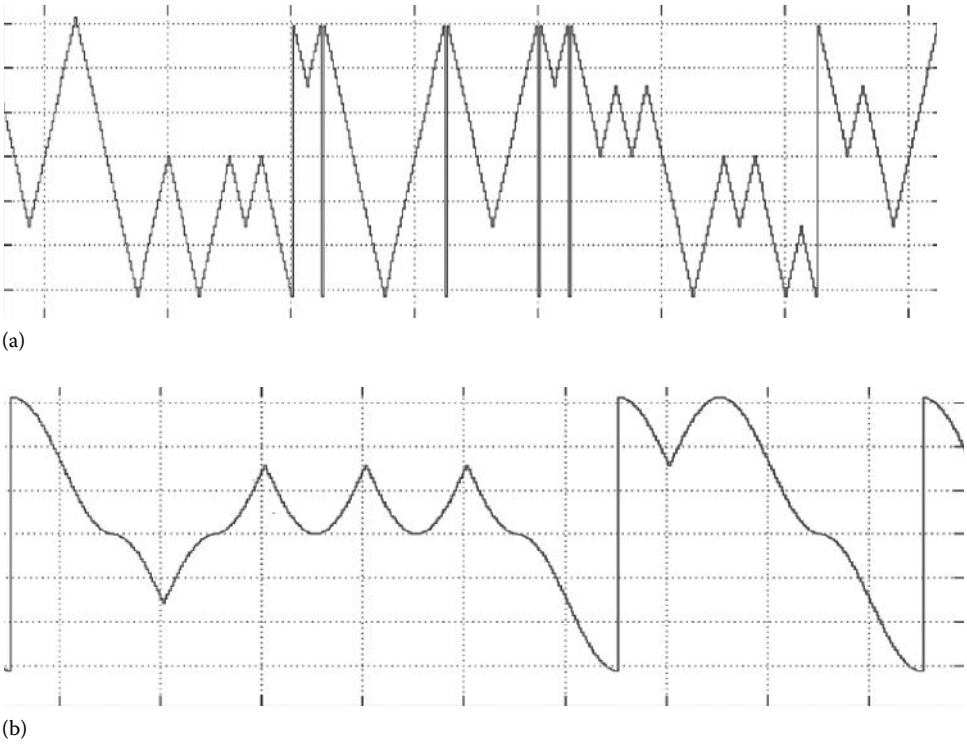

FIGURE 6.27
Phase trellis of linear and nonlinear MSK transmitted signals, (a) ideal phase state evolution by linear modulation and (b) practical phase evolution using sinusoidal modulation.

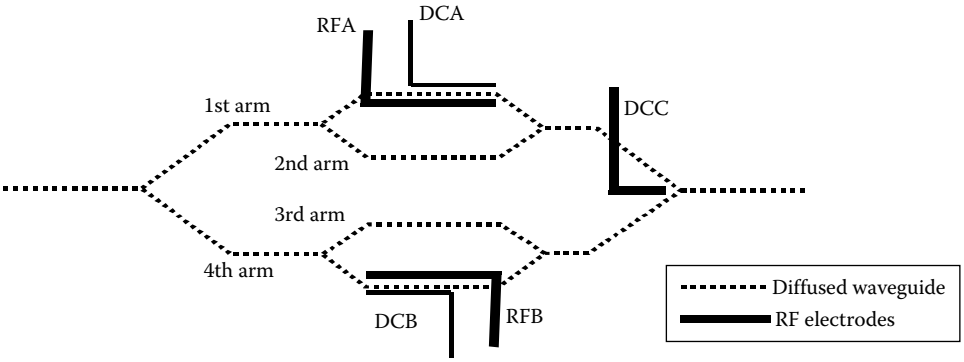

FIGURE 6.28
Schematic diagram (not to scale) of a single sideband (SSB) FSK optical modulator formed by nested MZ modulators.

are also supplied from DC_B to produce the phase shift between the third and fourth arms. A DC bias voltage is supplied from DC_C to achieve a $\pi/2$ phase shift between $MZIM_A$ and $MZIM_B$. The RF voltages applied, $\Phi_1(t) = \Phi \cos \omega_m t$ and $\Phi_2(t) = \Phi \sin \omega_m t$, are inserted from RF_A and RF_B, respectively, by using a wideband $\pi/2$ phase shifter. Φ is the modulation level and ω_m is the RF angular frequency.

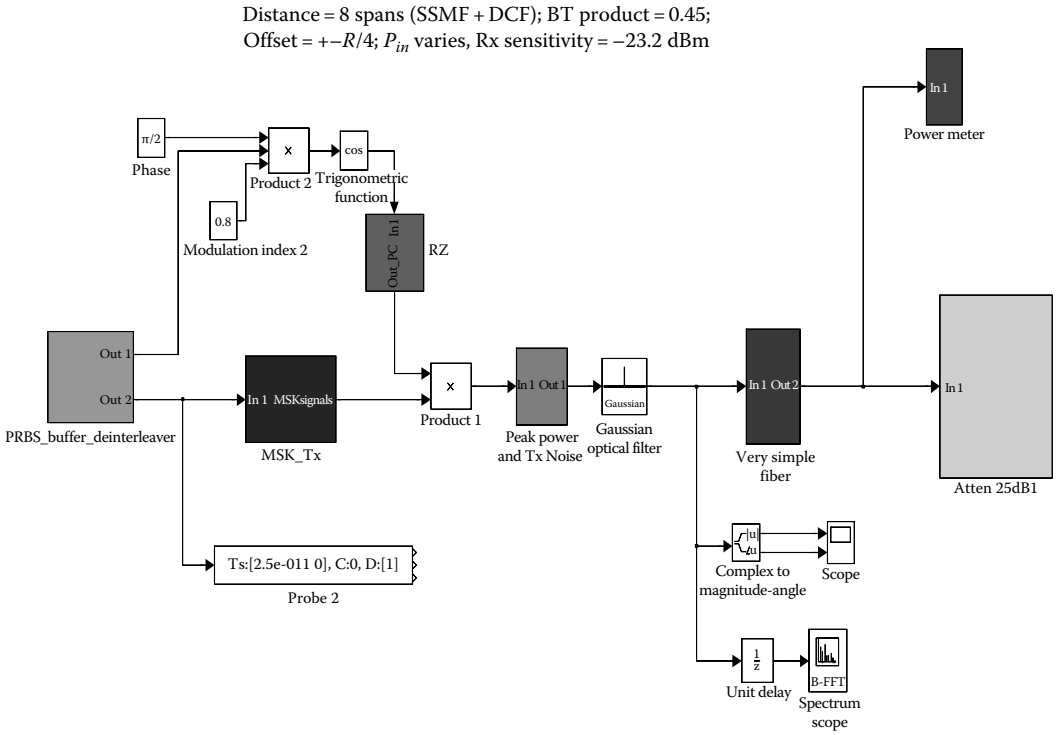

FIGURE 6.29
MATLAB® Simulink® model of an RZ–MSK optical transmission system.

6.6.3 Optical RZ–MSK

The RZ format of the optical MSK modulation scheme can also be generated. A bit is used to generate the ASK-like feature of the bit. A Simulink structure of such a transmitter is shown in Figure 6.29. The encoder as shown in the far left of the model provides two outputs, one for MSK signal generation and the other for amplitude modulation for generation of the RZ or NRZ format. The amplitude and phase of the RZ signals at the receivers are shown in Figure 6.30 after the one 100 km span transmission and fully compensated. The phase of the RZ–MSK must be nonzero so as to satisfy the continuity of the phase between one state and the other.

6.6.4 Multi-Carrier Multiplexing (MCM) Optical Modulators

Another modulation format that can offer much higher single channel capacity and flexibility in dispersion and nonlinear impairment mitigation is the employment of multi-carrier multiplexing. These subcarrier channels are orthogonal, and hence, the term orthogonal frequency division multiplexing (OFDM) is used.

Our motivation in the introduction of OFDM is because of its potential as a ultra-high capacity channel for the next generation Ethernet, the optical Internet. The network interface cards for 1 and 10 Gb/s Ethernet are readily commercially available. Traditionally, the Ethernet data rates have grown in 10 Gb/s increments, so the data rate of 100 Gb/s can be expected as the speed of the next generation of Ethernet. The 100 Gb/s all-electrically time-division-multiplexed (ETDM) transponders are becoming increasingly important because

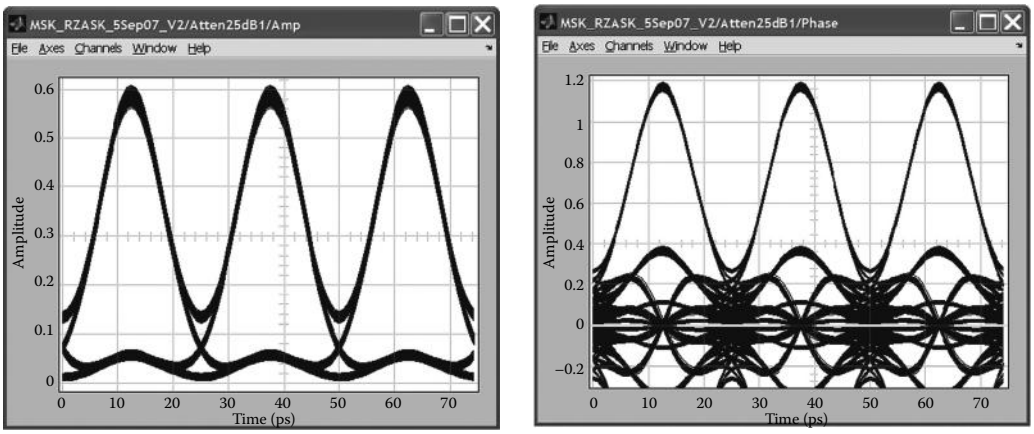

FIGURE 6.30
RZ eye diagram at outputs of the amplitude receiver (a) and phase detection (b).

they are viewed as a promising technology that may be able to meet speed requirements of the new generation of Ethernet. Despite the recent progress in high-speed electronics, ETDM [6] modulators and photodetectors are still not widely available, so that alternative approaches to achieving a 100 Gb/s transmission using commercially available components and QPSK are very attractive.

OFDM is a combination of multiplexing and modulation. The data signal is first split into independent subsets and then modulated with independent subcarriers. These subchannels are then multiplexed to form OFDM signals. OFDM is thus a special case of FDM but instead like one stream, it is a combination of several small streams in one bundle.

A schematic signal flow diagram of an MCM is shown in Figure 6.31. The basic OFDM transmitter and receiver configurations are given in Figure 6.32a and b, respectively. Data streams (e.g., 1 Gb/s) are mapped into a 2D signal point from a point signal constellation such as QAM. The complex-valued signal points from all subchannels are considered as the values of the discrete Fourier transform (DFT) of a multi-carrier OFDM signal. By selecting the number of subchannels, sufficiently large, the OFDM symbol interval can be made much larger than the dispersed pulse width in a single-carrier system, resulting in an arbitrary small intersymbol interference (ISI). The OFDM symbol, shown in Figure 6.33,

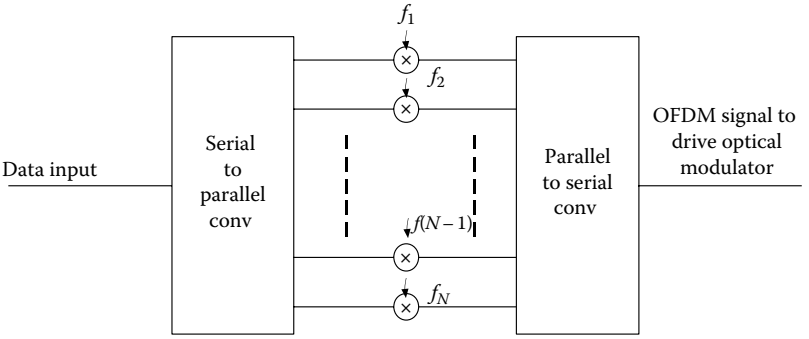

FIGURE 6.31
Multi-carrier FDM signal arrangement. The middle section is the RF converter as shown in Figure 6.2.

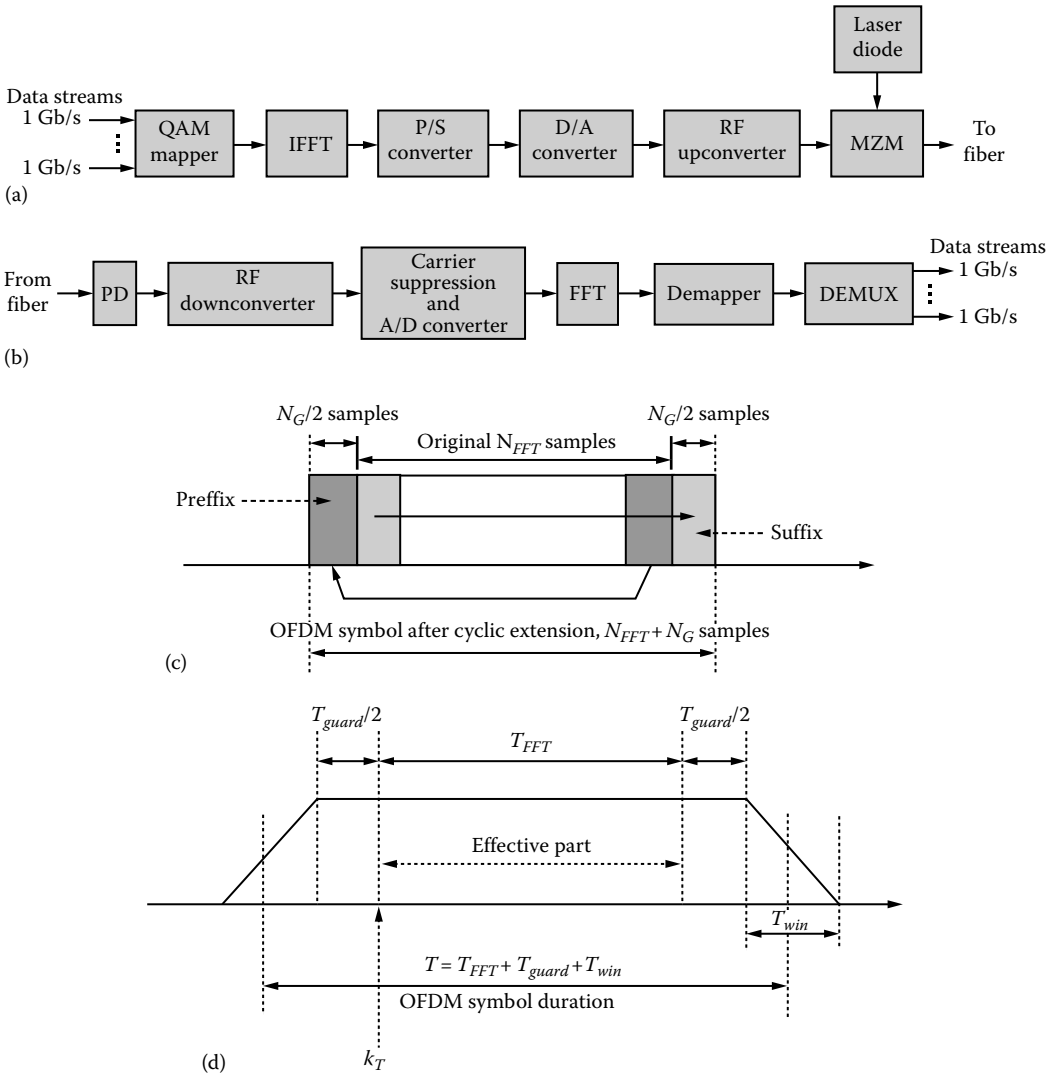

FIGURE 6.32
Schematic diagram of the principles of generation and recovery of OFDM signals: (a) Electronic processing and optical transmitter; (b) opto-electronic and receiver configurations; (c) OFDM symbol cyclic extension; (d) OFDM symbol after windowing. (Adapted from Djordjevic, I.B. and Vasic, B., *IEEE Photon. Tech. Lett.*, 18(15), 1576, August 1, 2009.)

is generated under software processing, as follows: input QAM symbols are zero padded to obtain input samples for inverse fast Fourier transform (IFFT), the samples are inserted to create the guard band, and the OFDM symbol is multiplied by the window function (raised cosine function can be used). The purpose of cyclic extension is to preserve the orthogonality among subcarriers even when the neighboring OFDM symbols partially overlap as a result of dispersion.

A system arrangement of the OFDM for optical transmission in laboratory demonstration is shown in Figure 6.34. Each individual channel at the input would carry the same data rate sequence. These sequences can be generated from an arbitrary waveform

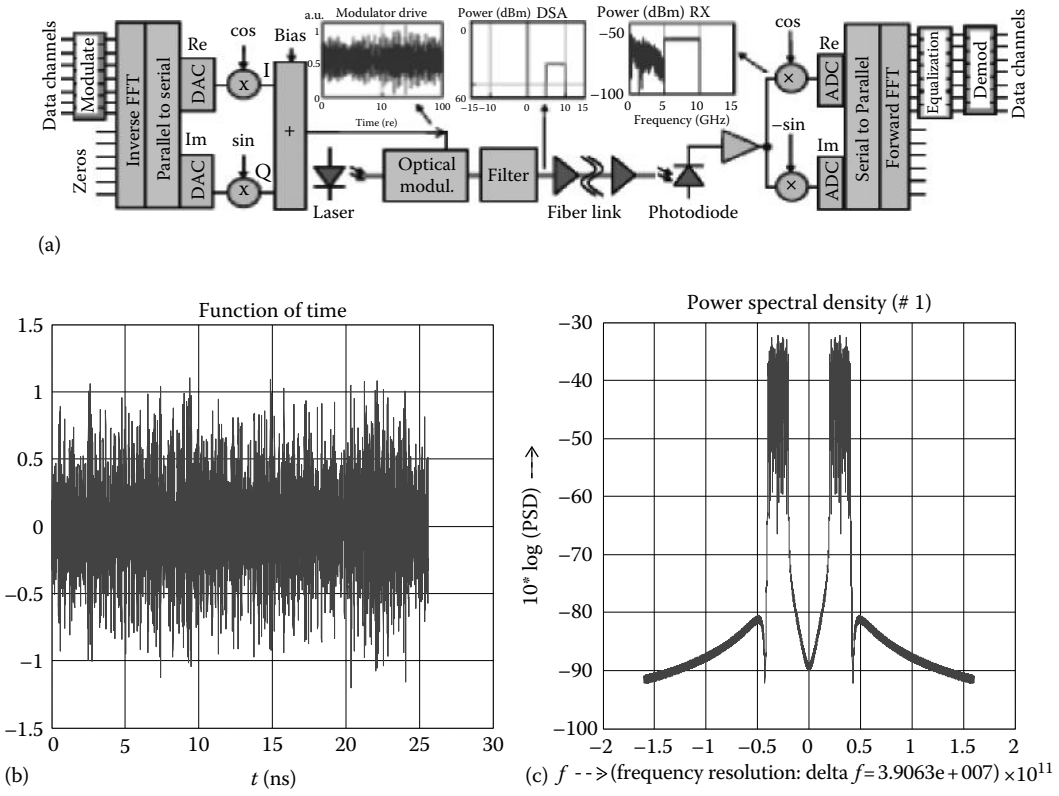

FIGURE 6.33
An optical FFT/IFFT–based (a) OFDM system including representative waveforms and spectra. (Extracted from [18].) (b) Typical time-domain OFDM signals. (c) Power spectral density of OFDM signal with 512 subcarriers a shift of 30 GHz for the line rate of 40 Gb/s and QPSK modulation.

generator or a digital to analogue converter, for example, a Fijitsu DAC [8]. The multiplexed channels are combined and converted to the time domain using the IFFT module and then converted to the analog version via the two digital to analog converters. These orthogonal data sequences are then used to modulate *I*- and *Q*-optical waveguide sections of the electro-optical modulator to generate the orthogonal channels in the optical domain. Similar decoding of *I* and *Q* channels is performed in the electronic domain after the optical transmission and optical–electronic conversion via the photodetector and electronic amplifier.

In OFDM, the serial data sequence, with a symbol period of *Ts* and a symbol rate of 1/*Ts*, is split up into *N*-parallel substreams (subchannels).

6.6.5 Spectra of Modulation Formats

Utilizing this double phase modulation configuration, different types of linear and nonlinear CPM phase–shaping signals including MSK, weakly nonlinear MSK, and linear-sinusoidal MSK can be generated. In the third scheme, introduced by Amoroso [2], the side lobes decay with a factor of 8 compared to 4 of MSK. The simulated optical spectra of DBPSK and MSK schemes at 40 Gb/s are contrasted in Figure 6.35. Table 6.4 outlines the characteristics and spectra of all the different modulation schemes.

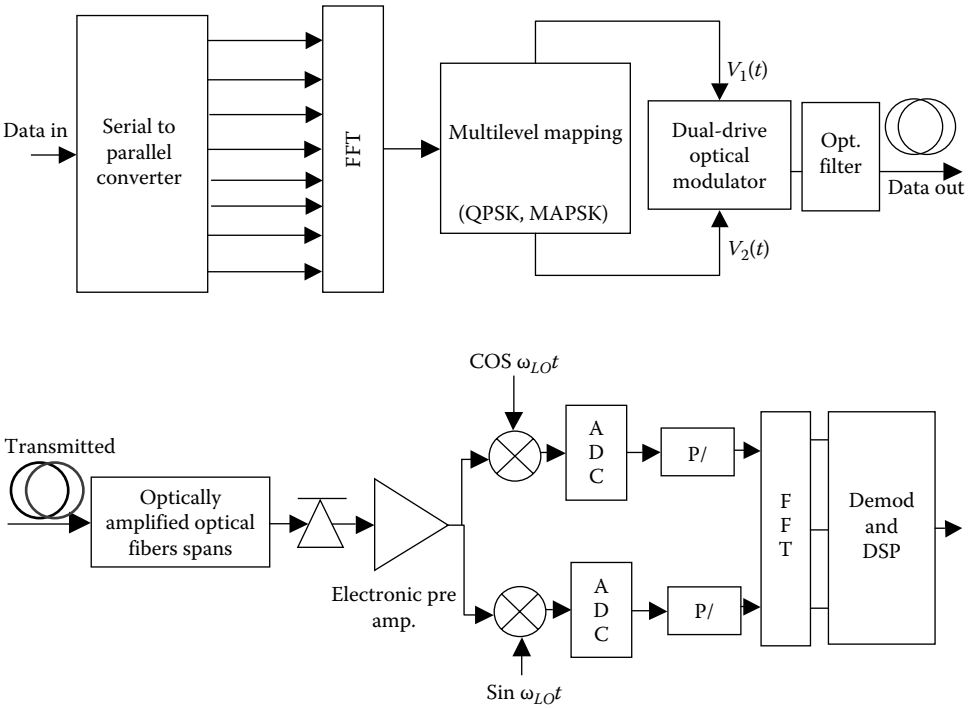

FIGURE 6.34
Schematic diagram of an optical FFT/IFFT–based OFDM system. S/P and P/S ~ serial to parallel conversion and vice versa.

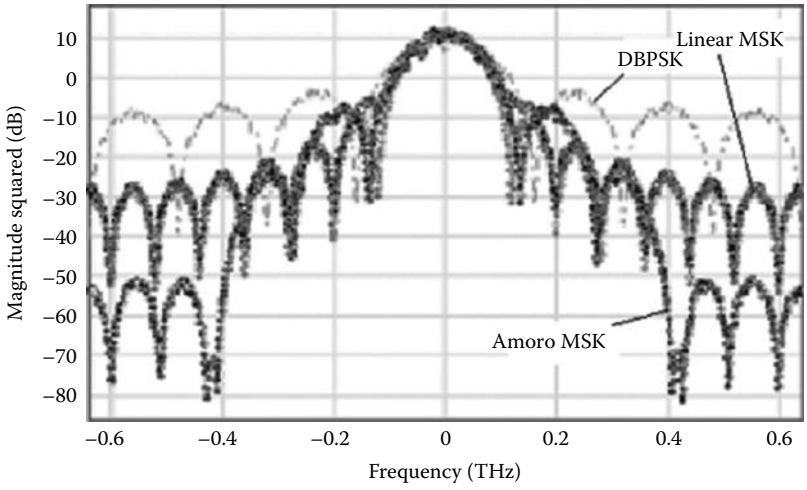

FIGURE 6.35
Spectra of 40 Gb/s DBPSK and linear and nonlinear MSK.

TABLE 6.4

Typical Parameters of Optical Intensity Modulators for Generation of Modulation Formats

Modulation Format	Spectra	Formats	Definition/Comments
Amplitude modulation—ASK–NRZ	DSB + carrier	ASK–NRZ	Biased at quadrature point or offset for prechirp.
AM–ASK–RZ	DSB + carrier	ASK–RZ	Two MZIMs required—one for RZ pulse sequence and the other for data switching.
ASK–RZ-carrier suppressed	DSB–CSRZ	ASK–RZCS	Carrier suppressed, biased at π phase difference for the two electrodes.
Single sideband	SSB + carrier	SSB–NRZ	Signals applied to MZIM are in phase quadrature to suppress one sideband. Alternatively, an optical filter can be used.
CSRZ–DSB	DSB—carrier	CSRZ–ASK	RZ pulse carver is biased such that a π phase shift between the two arms of the MZM to suppress the carrier and then switch on and off or phase modulation via a data modulator.
DPSK–NRZ, DPSK–RZ, CSRZ–DPSK		Differential BPSK–RZ or NRZ/RZ-carrier suppressed	
DQPSK		DQPSK–RZ or NRZ	Two bits per symbol.
MSK	SSB equivalent	Continuous phase modulation with orthogonality	Two bits per symbol and efficient bandwidth with high side-lobe suppression.
Offset-DQPSK		Oriented $\pi/4$ as compared to DQPSK constellation	Two bits/symbol.
MCM (Multi-carrier multiplexing—e.g., OFDM)	Multiplexed bandwidth—base rate per subcarrier		
Duo-binary	Effective SSB		Electrical low-pass filter required at the driving signal to the MZM.
FSK	Two distinct frequency peaks		
Continuous phase FSK	Two distinct frequency peaks with phase continuity at bit transition	Minimum-shift keying	When the frequency difference equals to a quarter of the bit rate, the signals for "1" and "0" are orthogonal and called MSK.
Phase modulation (PM)	Chirped carrier phase		Chirpless MZM should be used to avoid inherent crystal effects, hence, carrier chirp.

Figure 6.37 shows the power spectra of the DPSK-modulated optical signals with various pulse shapes including NRZ, RZ33, and CSRZ types. For the convenience of the comparison, the optical power spectra of the RZ OOK counterparts are also shown in Figure 6.35.

Several key notes observed from Figures 6.36 and 6.37 are outlined as follows: (1) The optical power spectrum of the OOK format has high power spikes at the carrier frequency or at signal modulation frequencies, which contribute significantly to the severe penalties

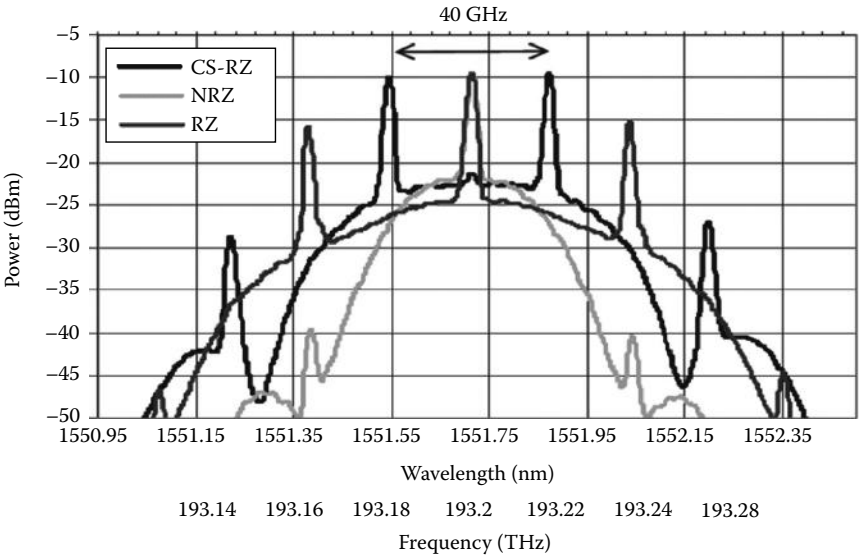

FIGURE 6.36
Spectra of CSRZ/RZ/NRZ—OOK modulated optical signals.

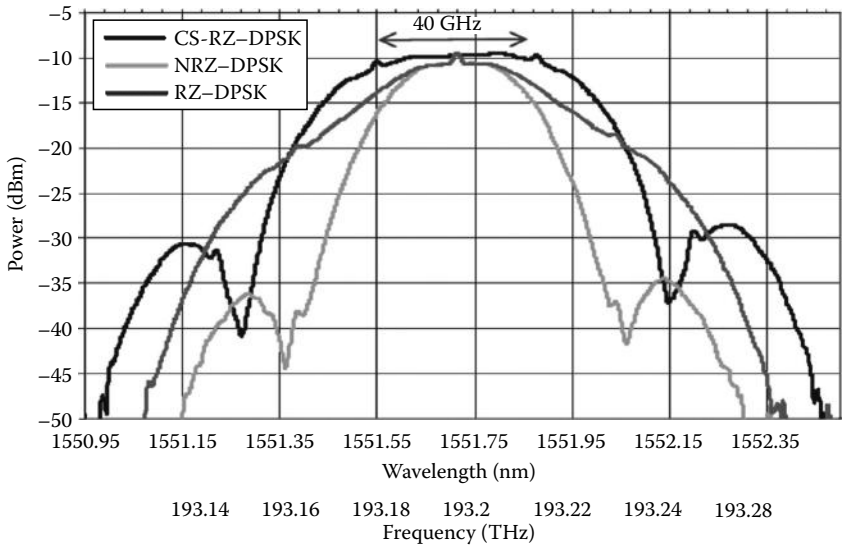

FIGURE 6.37
Spectra of CSRZ/RZ33/NRZ—DPSK modulated optical signals.

caused by the nonlinear effects. The DPSK optical power spectra, however, do not contain these high power frequency components. (2) RZ pulses are more sensitive to fiber dispersion because of their broader spectra. In particular, RZ33 pulse type has the broadest spectrum at the point of –20 dB down from the peak. This property of the RZ pulses thus leads to faster spreading of the pulse when propagating along the fiber. Thus, the peak values of the optical power of these CSRZ or RZ33 pulses decrease much more quickly than the NRZ counterparts. As a result, the peak optical power quickly turns out to be lower than the nonlinear threshold of the fiber, which means that the effects of fiber nonlinearity are significantly reduced. (3) However, NRZ optical pulses have the narrowest spectrum. They are expected to be most robust in response to fiber dispersion. As a result, there is a trade-off between RZ and NRZ pulse types. RZ pulses are much more robust to nonlinearity but less tolerant to fiber dispersion. The RZ33/CSRZ—DPSK optical pulses are proven to be more robust against impairments especially self-phase modulation and polarization mode dispersion compared to the NRZ–DPSK and the CSRZ/RZ33–OOK counterparts.

Optical power spectra of three *I*–*Q* optical MSK modulation formats that are linear, weakly nonlinear, and strongly nonlinear are shown in Figure 6.38. It can be observed that there are no significant distinctions of the spectral characteristics between these three schemes. However, the strongly nonlinear optical MSK format does not suppress the side lobe as highly compared to the linear MSK type. All three formats offer better spectral efficiency compared to their DPSK counterpart as shown in Figure 6.39. This figure compares the power spectra of three modulation formats: 80 Gb/s dual-level MSK, 40 Gb/s MSK, and NRZ–DPSK optical signals. The normalized amplitude levels in the two optical MSK transmitters comply with the ratio of 0.75/0.2.

Several key notes that can be observed from Figure 6.39 are outlined as follows: (1) The power spectrum of the optical dual-level MSK format has identical characteristics to that

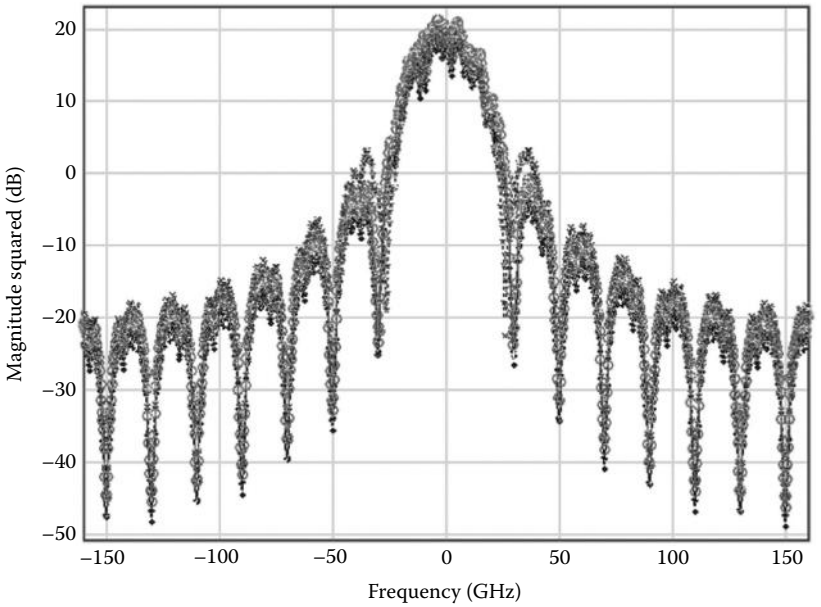

FIGURE 6.38
Optical power spectra of three types of *I*–*Q* optical MSK formats: linear (* dark gray), weakly nonlinear (o light gray), and strongly nonlinear (x black).

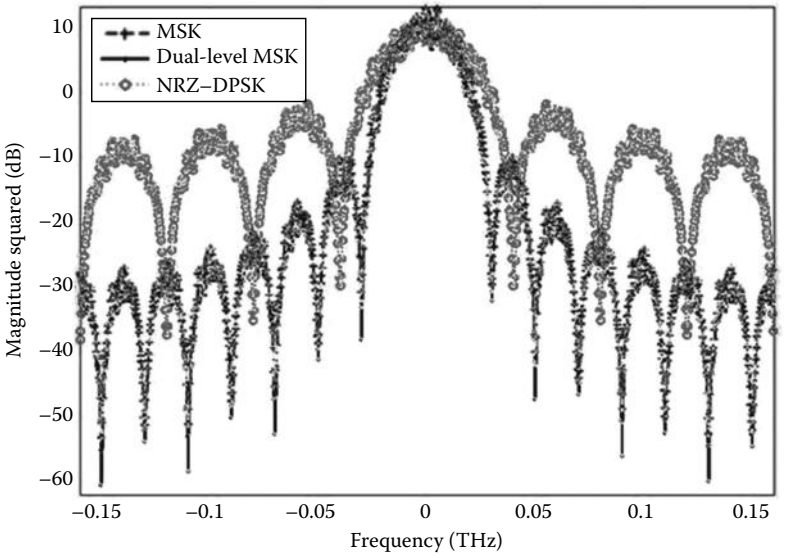

FIGURE 6.39
Spectral properties of three modulation formats: MSK (dash), dual-level MSK (black, solid), and DPSK (dot).

of the MSK format. The spectral width of the main lobe is narrower than that of the DPSK. The base width takes a value of approximately ±32 GHz on either side compared to ±40 GHz in the case of the DPSK format. Hence, the tolerance to the fiber dispersion effects is improved. (2) High suppression of the side lobes with a value approximately greater than 20 dB in the case of 80 Gb/s dual-level MSK and 40 Gb/s optical MSK power spectra, thus, provides more robustness to interchannel cross talk between DWDM channels. (3) The confinement of signal energy in the main lobe of the spectrum leads to a better signal to noise ratio. Thus, the sensitivity to optical filtering can be significantly reduced [9]. A summary of the spectra of different modulation formats is given in Table 6.4.

6.7 Generation of QAM Signals

6.7.1 Generation

I–*Q* modulators are essential for modulation of light waves in both the in-phase and quadrature-phase components so that quadrature amplitude modulation scheme can be implemented. *I*–*Q* modulators can be fabricated consisting of a master and two slave Mach–Zehnder interferometric modulation (MZIM) sections as shown in Figure 6.40. The electrodes are arranged in such a way that either single drive or dual drive can be employed. Thus, differential driving conditions can be designed so that QAM constellations can be generated.

This section gives a detailed description of the operation of an *IQ* modulator for generation of *M*-ary QAM constellations. The phase diagrams and operation for the generation of the 16 QAM constellation can be illustrated as shown in Figure 6.41. This diagram is also valid for a dual-drive MZIM.

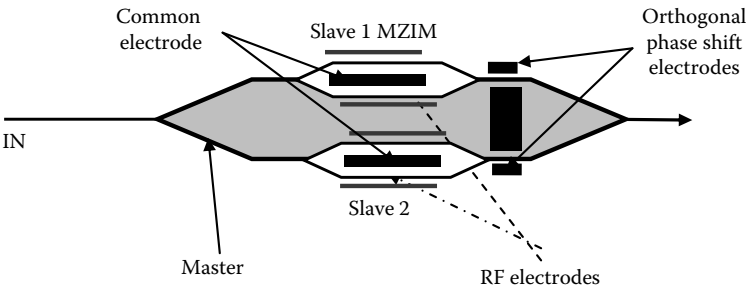

FIGURE 6.40
Structure of optical waveguides and electrodes of an *I*–*Q* modulator using master and slave MZIM and DC plus AC electrode arrangement.

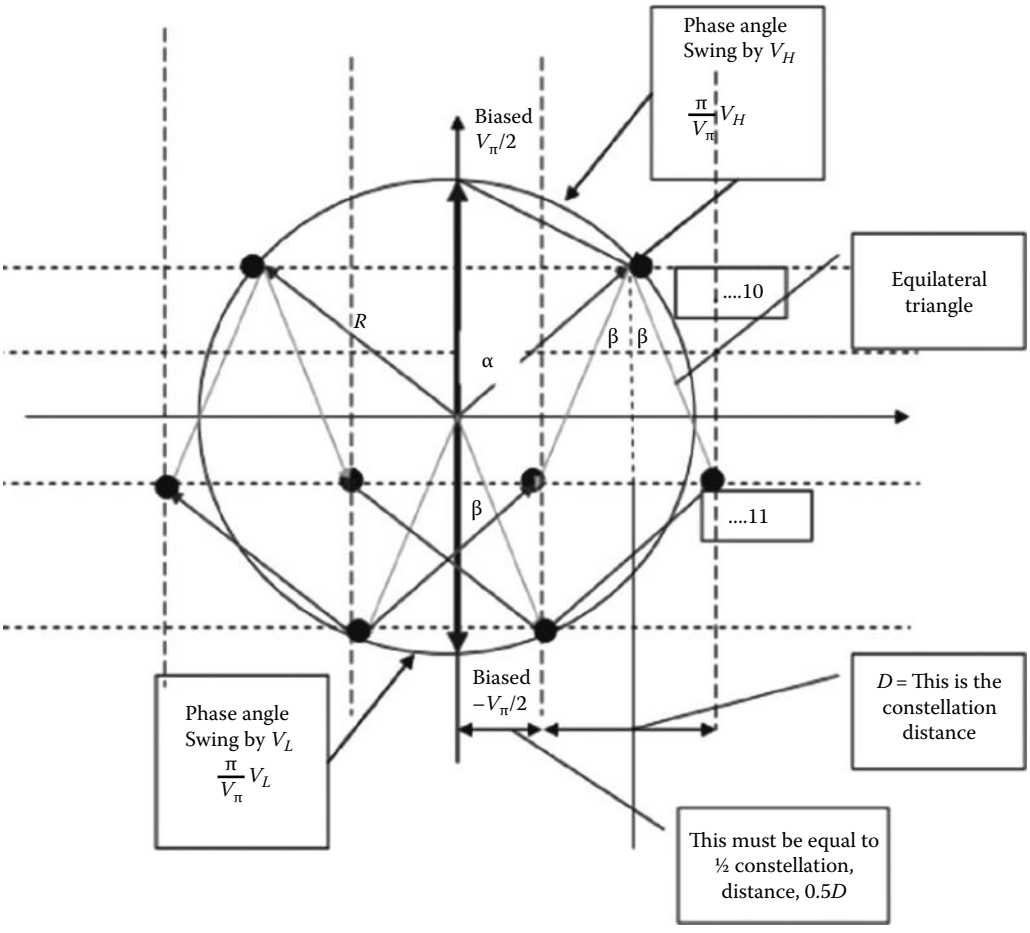

FIGURE 6.41
Constellation of one row of the 16 QAM as generated by one branch of the *I*–*Q* modulator, differential drive. V_H,V_L are amplitudes of the signal sequence applied to the upper and lower electrodes, respectively, and their corresponding phases $V_H \frac{\pi}{V_\pi}, V_L \frac{\pi}{V_\pi}$.

The operation principles for generation of the 16 QAM constellation using *I*–*Q* modulators whose structures are shown in Figures 6.41 and 6.40 are as follows:

1. Consider only one slave MZIM of one arm of the master MZIM. One needs to bias the MZIM in such a way that they operate in a push–pull mode. So, if the slave MZIM is biased with $V_\pi/2$ and $-V_\pi/2$, then a null point setup is established. The "red" vectors in Figure 6.41 show the locations of the biasing phases of the two branches of the slave MZIM.
2. From these two DC biasing phases, the driving ac signals are then applied or superimposed. The swing of the ac signals from negative to positive with amplitude V_H or V_L would then shift the phases of the light waves passing through the two branches to the locations shown as "blue" vector and "orange" vector, respectively.
3. With the low and high states of the phase variations, these vectorial phases are then added up to give the constellation points as shown in Figure 6.41.
4. Thus, we have the 4 ASK constellation. It is noted that the amplitude of the ac signals to be superimposed on the biased voltages must be at appropriate levels, for example, the high-level signals at $V_\pi/4$ and low-level amplitude at $V_\pi/8$ would give an equidistant constellation as shown in Figure 6.41. Other distances can be designed by changing the magnitude of the ac signals.
5. For the Quadrature 4 ASK the procedures are similar. We can obtain the 16 QAM constellation from this.
6. The 16 QAM constellation can be tilted by changing the biasing of the slave MZIM retaining a π phase difference or effectively, the "red" axis of Figure 6.40 can be tilted.

The constellations can be obtained as shown in Figure 6.42 for square and tilted cases [10].

Instead of the *I*–*Q* modulator, a dual-drive MZIM can be used and the biased phase and amplitude of the driving signals applied to the upper and lower electrodes of the two branches of the MZI can be implemented in a similar manner. Any variations of the amplitudes of the electrical signal applied to the electrodes can generate a tilted constellation of the 16 QAM as shown in Figure 6.42b. The geometrical aspect ratio of the constellation can be estimated from a geometrical diagram structured from the magnitudes and phases generated.

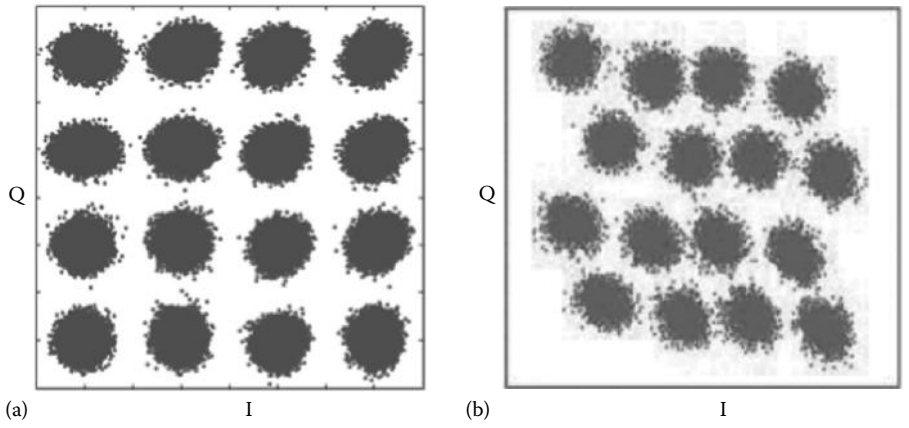

FIGURE 6.42
16 QAM (a) square constellation and (b) tilted constellation. (Adapted from Refs. [23,24].)

6.7.2 Optimum Setting for Square Constellations

The setting of the phase angle α, β as indicated in the diagram of Figure 6.41 can be estimated by using a few principles of geometry and trigonometry such as equilateral triangles and triangles with one angle equal to 90°. We can arrive at the two conditions for α, β that satisfy a square constellation as:

$$\begin{aligned} &\cos\alpha = 2\sin\beta \\ &\sin\beta - \cos\beta = -\cos\alpha \end{aligned} \tag{6.26}$$

Thus, combing these two conditions leads to

$$\begin{aligned} &\tan\beta = \frac{1}{3} \rightarrow \beta = 0.3218 \text{ rad} \sim \beta = 18.43^\circ \\ &\rightarrow \alpha \sim 49.88^\circ \end{aligned} \tag{6.27}$$

These two angles correspond to the phase of the low and high levels of the square constellation. The voltage amplitude level of the RF waves of the data sequence to be applied to the electrodes of the slave MZIM can then be deduced.

Thus, from (6.28) we can derive the values of the high and low amplitudes of the RF data sequence to be applied to the electrodes as:

$$\begin{aligned} &\tan\beta = \frac{1}{3} \rightarrow \beta = 0.3218 \text{ rad} \sim \beta = 18.43^\circ \\ &\rightarrow \alpha \sim 49.88^\circ \\ &\rightarrow V_L \frac{\pi}{V_\pi} = 0.321 \rightarrow V_L = \frac{0.321 V_\pi}{\pi} \\ &\rightarrow V_H \frac{\pi}{V_\pi} \rightarrow V_L = \frac{0.8770 V_\pi}{\pi} \end{aligned} \tag{6.28}$$

The arrangement of an experimental platform using SHF BPG [11] unit at 56 Gb/s and an ultra-wideband *I*–*Q* modulator or MZIM modulator can be arranged as follows (Figure 6.43):

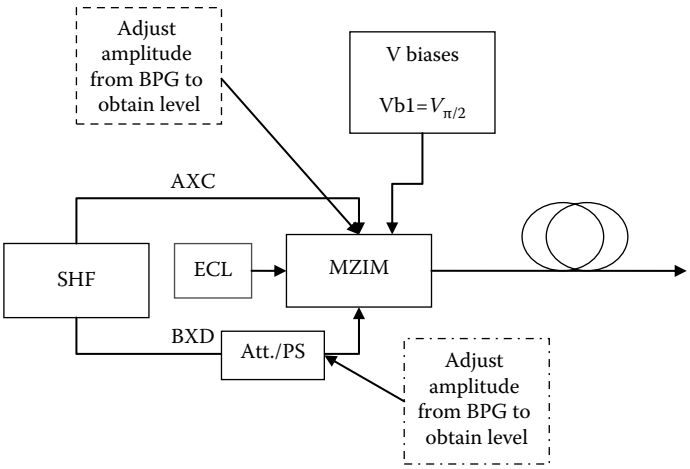

FIGURE 6.43
Driving signal arrangement for generation of 16 QAM using dual-drive MZIM.

6.8 Remarks

Since the advent of the optical circular waveguide and the proposed dielectric waveguide now, the employment of modulation techniques is extensively exploited because of the availability of optical amplifiers. The modulation formats allow transmission efficiency, and ultra-high capacity information telecommunications has become more economical. Optical communications have evolved significantly through several phases from single-mode systems to coherent detection and modulation, developed with the main aim of improving optical power. The optical amplifiers defeated the main objection to modulation formats and allow the possibility of incoherent as well as other possible formats employing the modulation of the amplitude, the phase, and frequency of the light wave carrier.

Currently, photonic transmitters play a principal part in the extension of the modulation speed into several GHz range and make possible the modulation of the amplitude, the phase, and frequency of the optical carriers and their multiplexing. Photonic transmitters using $LiNbO_3$ have been proven in laboratory and installed systems. The principal optical modulator is the MZIM, which can be a single or a combined set of these modulators to form binary or multilevel amplitude or phase modulations and is even more effective for discrete or continuous PSK techniques. The effects of the modulation on transmission performance are given in the next chapters.

Spectral properties of the optical 80 Gb/s dual-level MSK, 40 Gb/s MSK, and 40 Gb/s DPSK with various RZ pulse shapes are compared. The spectral properties of the first two formats are similar. Compared to the optical DPSK, the power spectra of optical MSK and dual-level MSK modulation formats have more attractive characteristics. These include the high spectral efficiency for transmission, higher energy concentration in the main spectral lobe, and more robustness to interchannel cross talk in DWDM because of greater suppression of the side lobes. In addition, the optical MSK offers the orthogonal property, which may offer a great potential in coherent detection, in which the phase information is reserved via the *I* and *Q* components of the transmitted optical signals. In addition, the multilevel formats would permit the lowering of the bit rate and hence, a substantial reduction of the signal effective bandwidth and the possibility of reaching the highest speed limit of the electronic and the digital signal processing, for equalization and compensation of distortion effects. The demonstration of ETDM receiver at 80 G and higher speed [6] would allow the applications of these modulation formatted schemes every potential in ultra-high-speed transmission.

6.A Appendix: Structures of Mach–Zehnder Modulator

It is clearly shown that the electric field lines are along the *Z*-axis and the electrode of the driving signal is located on either side of the optical waveguide. This configuration is driven by only one electrical drive (data) and it is chirp free because of the symmetrical structure that leads to intrinsic balance as shown in Figures 6.44 and 6.45.

There is a distinct difference from the *X*-cut where the electrode of the driving signal is located exactly on top of the optical waveguide. The *Z*-cut has better coupling efficiency between the electric field and optical waveguide. Dual-drive configuration or push–pull structure employs two electrical drives (data and inverted data) to perform the modulation. If the electrical fields are perfectly matched, that is, the driving signal amplitude has to be

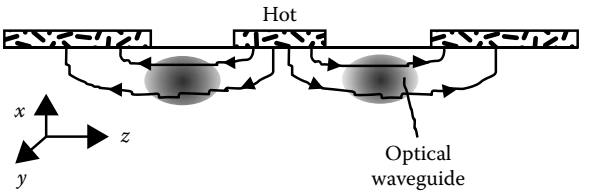

FIGURE 6.44
X-cut single-drive configuration. (Adopted from Nagata, H. et al., *IEEE Photon. Tech. Lett.*, 16(10), 2233, October 2004.)

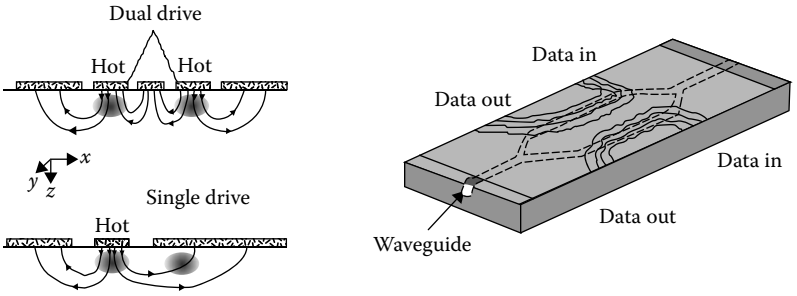

FIGURE 6.45
Z-cut single-drive and dual-drive configuration.

of the same amplitude but of opposite phase, the dual-drive configuration will be chirp free. Nonetheless, the Z-cut single-drive configuration has nonzero chirp coefficient because the electric field lines pass through two optical waveguides that are often not similar. Table 6.5 gives typical configurations and applications of various types of optical modulators.

MATLAB Simulink models of these optical modulators are presented in Chapter 12 in association with the modulation formats such as ASK for amplitude shift keying, DPSK, DQPSK as discrete differential phase modulation, and MSK and CPFSK as continuous phase modulation.

TABLE 6.5

Summary of Advantages, Disadvantages, and Application of X-Cut, Z-Cut, and EA Modulator

Configuration	Advantage	Disadvantage	Application
• $LiNbO_3$ • Z-cut	• Lower and well-behaved frequency chirp than EA modulator • Lower $V\pi$	• Chirped (un-chirped only by balanced driving) • More DC drift than X-cut • Buffer layer required • Single drive not for PSK	• Traditionally used for RZ and NRZ (balance driven)
• $LiNbO_3$ • X-cut	• Intrinsically balanced—chirp free • No need to align the delay (phase) of two signals	• Electro-optical efficiency lower than Z-cut • Buffer layer required • Higher driving voltage	• Suitable for modulation, required absolute chirp free
• EA modulator	• Large linear region	• Chirp is high and dynamic • Changing with bias • High insertion loss • Modulation <1.0	• Cannot be used for PSK

Problems

6.1 Refer to a *carrier-suppressed RZ* optical transmitter shown in Figure 6.46:

(a) Sketch the time-domain pulse sequence over the 10-bit period for a bit rate of 40 Gb/s at the output of the pulse pattern generator.

(b) Give a brief description of the principles of suppression of the carrier. Which component of the transmitter would implement the suppression?

(c) What are the functions of the laser, the modulator, and the push–pull modulator? If V_π for the two modulators is 5 V, sketch the transfer characteristics of the modulators—that is, the output power versus the input driving voltage. Make sure that you set appropriate biasing voltages for the modulators. The output power of the laser is 10 dBm and the total insertion loss for each modulator is 4 dB. For the pulse pattern generator, the output power at the output port data is 10 dBm and that at the clock output port is $2V_{p-p}$. All line impedances are 50 Ω.

(d) Is it necessary to use a booster optical amplifier to increase the total average power launching into an optical fiber for transmission? If it does then what is the gain and noise of the optical amplifier. Note that the nonlinear limit of an SSMF is around 5 dBm.

(e) Sketch the spectra at the outputs of the laser, the modulator, and the push–pull modulator.

6.2 Optical modulator and phasor diagram—dual-drive MZM.

(a) Repeat Question 3 with a bias voltage of $V_b = V_\pi/2$ and V_π and a time-varying signal of $v_s(t) = V_\pi/2 \cos \omega_s t$ with $\omega_s = 2\pi f_s$ and $f_s = 20$ GHz.

(b) Now if the modulator is a dual-drive MZM, repeat Question 1 with a bias voltage of $V_b = V_\pi/2$ and V_π and a time-varying signal of $v_s(t) = V_{\pi/2} \cos \omega_s t$ with $\omega_s = 2\pi f_s$ and $f_s = 20$ GHz.

6.3 An optical fiber communication system consists of (1) an optical transmitter using a 1550 nm DFB laser with a linewidth of 10 pm (pico-meters), an external optical modulator whose bandwidth is 20 GHz, and a total insertion loss of 5 dB. (2) The modulator is driven by a bit-pattern-signal generator with a 10 dBm electrical power output into a 50 Ω line. A microwave amplifier is used to boost the electrical data

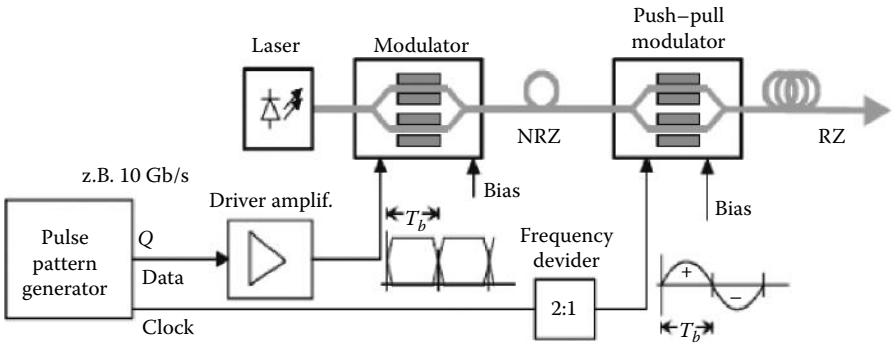

FIGURE 6.46
Figure Question 6.1.

pulse to an appropriate level for driving the optical modulator. The data bit rate is 10 Gb/s and its format is NRZ and (3) An 80 km SSMF is used for the transmission of the modulated signals.

Sketch the block diagram of the transmission system.

If the V_π of the external modulator is 5 V, what is the gain of the microwave amplifier so that an extension ratio of 20 dB can be achieved for the output pulses of "1" and "0" at the output of the modulator. Make sure that you sketch the amplitude and power output of the modulator versus the driving voltage into the modulator. What type of connector that you would use to connect the microwave amplifier to the modulator and that to the bit-pattern generator?

If the DFB laser emits 0 dBm optical power at its pig tail output then what is the average of optical power contained in the signal spectrum? You may assume that the pulse sequence generated at the output of the bit pattern generator is a perfect rectangular shape. What is the effective 3 dB bandwidth of the signal power spectrum? Hence, estimate the total pulse broadening of the pulse sequence at the end of the 80 km fiber length. Similarly, estimate the pulse sequence if the bit rate is 40 Gb/s.

Now if a dispersion compensating fiber of 20 km is used to compensate for the signal distortion in the 80 km fiber, what is the required dispersion factor for this fiber so that there would be no distortion? If the loss of the dispersion compensating fiber is 1.0 dB/km at 1550 nm, estimate the average optical power of the signal at the output of the dispersion compensating fiber.

On the basis of the dispersion limit given here, plot the dispersion length as a function of the bit rate for NRZ format.

Hint: The dispersion limit, under linear regime operation, can be estimated by the equation $L_D = \frac{c}{\lambda}\frac{\rho}{B_R^2 D}$ where B_R is the bit rate, D is the dispersion factor (s/m^2), ρ is the duty cycle ratio, that is, the ratio between the "ON" and "OFF" in a bit period, and L_D is in meters.

6.4 Repeat Question 6 for RZ format and ASK modulation. Sketch the structure of the RZ optical transmitter, note that an extra optical modulator must be used and coupled with the data modulator of Question 1, the optical pulse carver. Give details of the pulse carver including, driving voltage, driving signal, and synchronization with the data generator.

6.5 Spectral efficiency

(a) A DWDM optical transmission system can transmit optical channels whose channel spacing is 100 GHz. What is the spectral efficiency if the bit rate of each channel is 40 Gb/s and the modulation is NRZ–ASK?

(b) Repeat (a) for RZ–ASK modulation format.

(c) Repeat (a) and (b) for the channel spacing of 50 GHz.

6.6 Give a structure of an optical transmitter for generation of RZ–ASK modulation format. Make sure that you assign the optical power of light waves generated from the light source at the output of the optical modulators so that a maximum of 10 dBm of optical power is launched into the SSMF so that it is below the nonlinear SPM effect limit.

Describe the operation of the optical modulator, the pulse carver, so that it can generate periodic pulse sequence before feeding into the data generator. Make sure

that you provide the amplitude and intensity levels versus the driving signal voltage levels, which are used to drive the optical modulators.

6.7 Nonlinear SPM effect

The nonlinear refractive index coefficient of silica-based SSMF is $n_2 = 2.5 \times 10^{-20}$ m^2/W.

What is the effective area of the SSMF—you can refer to the technical specification of the Corning SMF-28 and its mode field diameter to estimate this area.

Estimate the change in the refractive index as a function of the average optical power. Hence, estimate the total phase change as a resut of this nonlinear effect after propagating through a length L (in km) of this fiber.

Hence, estimate the maximum length L of the SSMF that the light waves can travel so that the phase change on this light wave carrier would be no higher than 0.1 rad.

Show how you can generate a format that would have an RZ format and a suppression of the light wave carrier. Show that the width of the RZ pulse in this case is 67% of the bit period. *Hint*: you may represent the light waves in the path of the optical modulator, an optical interferometer by using phasors. First sketch the phasor of the input light wave, then those of the two paths, and then the phase applied onto these paths. Then sum up at the output to give the resultant output. For the pulse width you can estimate the width over which the amplitude fall to $1/\sqrt{2}$ of its maximum.

Now show you can generate RZ pulse sequence with 50% and 33% pulse width of the bit period.

6.8 Balanced receiver

(a) Sketch the schematic diagram of an optical balanced receiver—a balanced receiver would consist of a delay interferometer and a back-to-back connected pair of photo detectors with its output connected to the input of an optical preamplifier.

(b) What is the functionality of the delay interferometer. What is the temporal length of the delay unit?

(c) What are the roles of the two optical couplers and their ideal coupling coefficients?

(d) What is the relationship between the two output ports of the delay interferometer?

Assume that a sequence of 4 bits of a DPSK 10 Gb/s data channel is presented at the input of a balanced receiver. The phases of the light wave carrier contained within these four bits are π, π, o, π at the transition of the bit period.

Sketch the carrier wave and the pulse envelope. The light wave has a wavelength of 1550 nm—however, to illustrate the wave you are expected to sketch only a few periods of the waves contained within the bit period at the input of the receiver.

Sketch the electrical signal at the output of the electronic preamplifier not including noises.

Now assuming that an optical amplifier, used as an optical preamplifier, is placed at the input of the balanced receiver that would give an optical signal power of –10 dBm for the "0" and "1" of the DPSK sequence. The responsibility of the photo detector is 0.9 and the electronic preamplifier has a trans impedance of 150 Ω and a total equivalent noise current spectral density of 2 pA/(Hz)$^{1/2}$ and a bandwidth of 15 GHz. Sketch the signal waveform at the output of the electronic preamplifier.

6.9 Duobinary modulation format

Design a block diagram of a precoder that would generate tri-level modified duobinary format signals. Make sure that the coefficients of the filters are specified. *Hint*: you may refer to pages 8–11 of the lectures notes. Hence, derive the spectrum of the signals after the precoder of the modified duobinary.

If possible obtain the precoders for AMI and duobinary and their frequency responses. Compare the frequency responses of the three modulation schemes.

Sketch the structure of the tri-level duobinary precoder with its output of –1, 0, +1.

Show how to use the coded signals to drive a dual-drive MZIM to generate optical duobinary signals.

6.10 Duobinary modulation format

A modulation format that would allow the detection of the modulated signals is a duobinary, which is a special case of partial response coding as shown in Figure 6.47.

Give a brief account of the principles of operation of this line code.

A duobinary coder using a delay and coding structures is shown here. If three-level duobinary-coded signals are required, design the precoder for this type of modulation.

Now if delay time Tb is that of a bit period, transform the structure into the z-transform diagram and hence, obtain the transfer function of the coder in the z-domain, and the the frequency response of this coder. Plot the frequency response of the transfer function of the filter in the continuous domain.

Find the impulse response of the coder, and hence, the term partial response.

Sketch a block diagram that shows the functionality of precoding, coding, tri-level conversion (offset), and decoding.

A binary sequence $d(k)$ = {0 0 1 1 0 1 0 0 1} is applied to the input of the duobinary coder. Determine the data sequences $b(K)$, $c(k)$, and $c'(k)$ in the electrical domain that can be used to modulate an optical modulator.

Assuming that there is no dispersion in the transmission of the duobinary data sequence, find the output pulse sequence at the output of the decoder. What is the physical realization of the decoder? Sketch the sequence at the output of a decision circuit.

Now the electrical signals are applied to a microwave amplifier that would condition the signals to appropriate signal levels so as to modulate the optical modulator. The measured spectra are recorded as shown in the diagrams in the following.

Determine the points in the block diagram of the transmission system (as per attached diagram) to which each spectrum belongs.

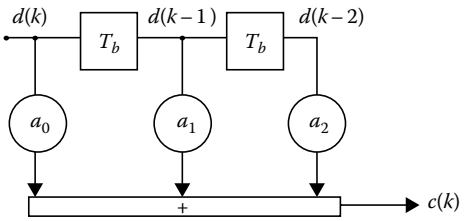

FIGURE 6.47
Figure Question 10.

6.11 DQPSK

DQPSK is a 2-bit per symbol modulation, that is, 2 bits/symbol, and the scheme is spectral efficient.

Give a brief account of the modulation schemes DPSK and DQPSK.

Give the structure of a precoder for DPSSK—that give a differential modulation with phase as the codes for "1" and "0."

Now extend this precoder and the phase quadrature modulation technique to the structure of a DQPSK optical transmitter.

6.12 SSB and DSB modulation

Refer to the diagram (Figure 6.48) shown here for generation of optical signals with SSB.

State the functionality of the Hilbert transformer. Hence, can you deduce a general principle for suppression of a sideband to generate single sideband signals?

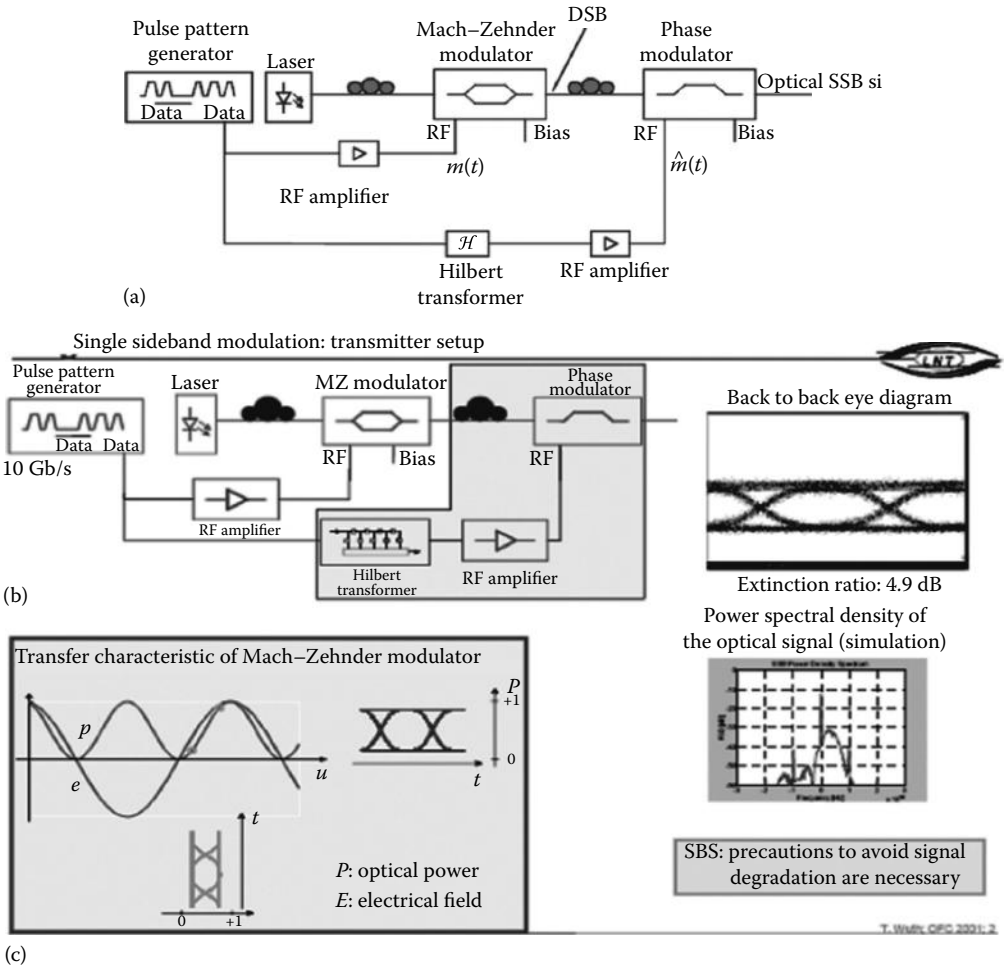

FIGURE 6.48
SSB modulation and generation using (a) transform in optical domain, (b) transform in electrical domain, (c) realization of an SSB optical transmitter.

What is the role of the phase shifter π/2?

Explain the operation of the optical SSB transmitter, in both the time and frequency domain. Confirm that the spectrum is correct.

6.13 Coherent optical communication systems

Sketch a structure of an optical coherent receiver. Give a brief description of the roles of each component in your system.

What is the typical modern linewidth of the laser that acts as the local oscillator?

Give a distinction between the homodyne and heterodyne coherent system.

A homodyne optical receiver has the following parameters:

A photodetector with a responsivity of 0.9 is followed by an electronic preamplifier whose total equivalent noise spectral density is 5 pA/(Hz)$^{1/2}$ and an electrical bandwidth of 15 GHz. The transmission bit rate is 10 Gb/s.

The local oscillator is a tunable laser source with a linewidth of 100 MHz. The wavelength in vacuum of both the signals and the local oscillator is 1550.92. The average optical power of the local oscillator coupled with the photodetector is 0 dBm. Sketch the structure of the receiver and then its equivalent small signal circuit, which includes the generated electronic signal current at the output of the photodetector, the total noise currents looking from the input of the electronic preamplifier. What is the dominant noise source of the receiver?

For an optical signal with an average power of –20 dBm, estimate the signal to noise ratio at the output of the photodetector. Recalculate the SNR of the receiver if the frequency of the local oscillator is 20 GHz away from that of the signal carrier frequency.

References

1. Y. Yamada, H. Taga, and K. Goto, Comparison between VSB, CS-RZ and NRZ format in a conventional DSF based long haul DWDM system, in *Proceedings of ECOC'02*, Copenhagen, Denmark, vol. 4, pp. 1–2, 2002.
2. F. Amoroso, Pulse and spectrum manipulation in the minimum frequency shift keying (MSK) format, *IEEE Transactions on Communications*, 24, 381–384, March 1976.
3. L.N. Binh, *Digital Optical Communications Systems*, CRC Press, Boca Raton, FL, 2008.
4. L.N. Binh, *Digital Processing: Optical Transmission and Coherent Receiving Techniques*, CRC Press, Boca Raton, FL, 2013.
5. K.K. Pang, *Digital Transmission*, Mi-Tec Publishing, Melbourne, Victoria, Australia, p. 58, 2002.
6. C. Schubert, R.H. Derksen, M. Möller, R. Ludwig, C.-J. Weiske, J. Lutz, S. Ferber, A. Kirstädter, G. Lehmann, and C. Schmidt-Langhorst, Integrated 100-Gb/s ETDM receiver, *IEEE Journal of Lightwave Technology*, 25(1), 122–130, January 2007.
7. I.B. Djordjevic and B. Vasic, *IEEE Photonics Technology Letters*, 18(15), 1576–1578, August 1, 2009.
8. http://www.fujitsu.com/downloads/MICRO/fme/dataconverters/OFC-2010–56Gss-ADC-Enabling-100GbE.pdf. Accessed March, 2014, in *Presented at OFC 2010*, Los Angeles, CA.
9. L.N. Binh, T.L. Huynh, K.K. Pang, and T. Sivahumaran, MLSE equalizers for frequency discrimination receiver of MSK optical transmission system, *IEEE Journal of Lightwave Technology*, 26(12), 1586–1595, 2008.

10. S. Yan, D. Wang, Y. Gao, and C. Lu, A.P. Tao Lau, L. Liu, and X. Xu, Generation of square or hexagonal 16-QAM signals using a single dual drive IQ modulator driven by binary signals, *Optics Express*, 20(27), 29023, December 17, 2012.
11. http://www.shf.de/communication/support/news_details/article/138/1/129ccd2f82227f162374f8a0973ac47a/. Accessed March, 2014.
12. H. Nagata, Y. Li, W.R. Bosenberg, and G.L. Reiff, DC drift of x-cut $LiNbO_3$ modulators, *IEEE Photonics Technology Letters*, 16(10), 2233–2335, October 2004.

7

Direct Detection Optical Receivers

This chapter describes the fundamental understanding of the detection of optical signals using direct techniques. In this detection process, the lightwave power is absorbed by the semiconductor active area in which the absorption would result in the generation of positive and negative carriers which are then collected by either the cathode or anode of the photodetector (PD) junction under reverse bias. On the other hand, the detection of the optical input field can be mixed with a local oscillator so that the total field can be detected in the PD under the square-law relation. This square law results in a few DC components and two AC components whose frequency can be either the sum or difference of the signal and the local laser. The difference term will bring the detected signals back to the baseband when the carrier frequency of the local laser and the signal carrier is the same, the homodyne coherence detection. A schematic of the structures of the direct detection and coherent detection subsystems is shown in Figure 7.1a and b, respectively, in which the fields of the signals are local oscillators denoted as $\tilde{E}_s$ and $\tilde{E}_{LO}$. It is obvious in direct detection that the generated current source is proportional to the power of the signal source while that current is proportional to the square of the total optical field of the signal and the local oscillator. This coherent mixing allows the boosting of the magnitude of the generated current by the magnitude of the local oscillator and preserve the phase ϕ_s of the signals as shown in the diagram.

The coherent reception transmission systems are described in Chapter 8. Optical preamplification at the input of the optical receivers is not treated here but later in Chapter 10. MATLAB® Simulink® models are described wherever appropriate.

7.1 Introduction

Optical receivers are important components in optical fiber communication systems and networks. Optical receivers are normally placed at the far end of the transmission links or they are used in the front end of an optical repeater in terrestrial optical systems and at terminal front ends in optical networks. Their principal function is conversion of optical signals into electronic forms for further electronic amplification and signal processing such as clock recovery, retiming, digital level detection, and sampling.

The typical arrangement of an optical receiver is that the optical signals are detected by a photodiode (a pin diode or APD or a photon counting device), electrons generated in the PD are then electronically amplified through a front-end electronic amplifier. The electronic signals are then decoded for the recovery of the original format.

Optical coherent communication systems have also been reviving dramatically due to electronic processing and availability of stable narrow linewidth lasers. We also describe

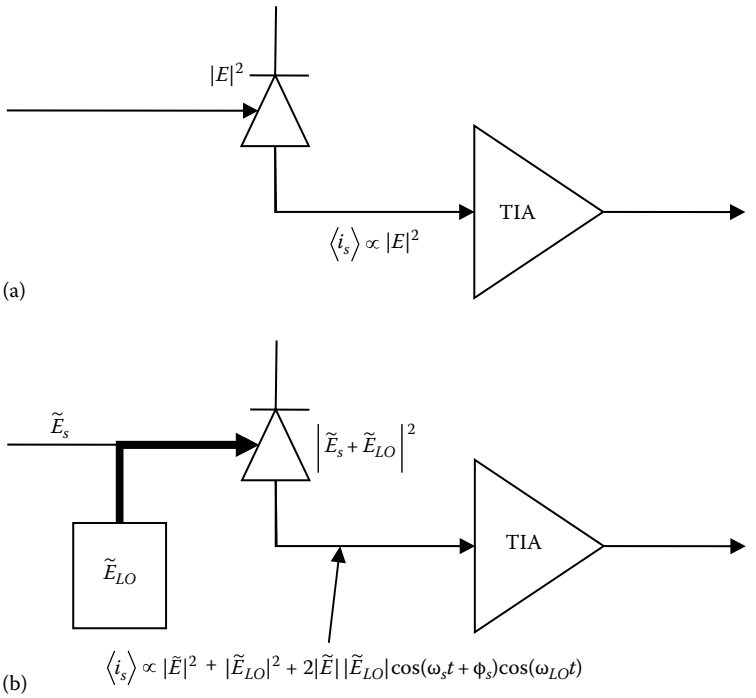

FIGURE 7.1
Schematic of (a) direct and (b) coherent detection.

the coherent detection techniques in association with digital signal processing (DSP) method in the next chapter so as to update readers with this emerging trend in the twenty-first century.

This chapter deals with the analysis and design of electronic amplifiers (the transimpedance amplifying device [TIA]) incorporated with the photodetection device as the fundamental elements of an optical receiver. In recent years, the development of optical amplifiers, particularly the rare-earth-doped optical fiber amplifiers, has advanced to a particle stage that these fiber amplifiers are coming to be a standard photonic component in most terrestrial optical fiber communication systems. With this in mind, we need to include the design of optical amplifiers as a stand-alone system or in-line optical receivers acting as an optical repeater or as a preamplifier front end placed before the PD and followed by an electronic amplifier.

Noises generated in the electronic preamplifier lower the signal-to-noise ratio or reduce the eye opening of the received digital signals at its output. The equivalent noise power of the electronic preamplifier increases as a square function of the frequency. It is necessary to reduce this frequency-dependent noise. A noise matching network can be placed at the front end which would act as a noise filter. An example for high-frequency electronic preamplifier is given in Section 7.5.

Optical amplifiers, the rare-earth-doped optical fiber amplifiers, technologically more advanced now, provide a boost in opto-electronic detection. The integration of an OA would further improve the coherent detection and a treatment of this optically preamplified detection process is given here. The invention of optical amplifiers in the 1990s has

thus revolutionized the design of optical transmission over long haul as they offer significant optical gain that would compensate for fiber and other losses of optical components. Optically preamplified receivers are discussed in Chapter 9.

This chapter is organized as follows: Section 7.2 gives an overview of the roles of the optical receiver in various optical transmission systems and their applications in networking. Section 7.3 then gives an account of optical components of an optical receiver for direct detection. Noises in PD and integration with electronic preamplifiers are described in this section. Methods for calculation of receiver noises are also described in Section 7.4. The performance evaluation of the binary optical receiver is given in terms of noise and signal power as the output of the receiver is described in Section 7.5. Two examples of the design and noise estimation when FET or BJT is used as the front-end electronic amplification device are illustrated.

Section 7.6 gives the method to match the network at the front end of the transimpedance amplifier to reduce the noises over the high frequency band of broadband amplifiers. This is very critical for TIA employed in ultra-wideband receivers for 100G, 400G channels. Further, differential TIA is also described in Section 7.7 as a new and emerging TIA with differential input ports and differential output ports. This type of TIA offers significant transimpedance gain reaching more than 3000 Ω which is about 20 times higher than that offered by single-end TIA. The noise of differential TIA is about twice the value of that of the single-end type.

Finally, Section 7.8 provides the concluding remarks.

7.2 Optical Receivers in Various Systems

In modern optical and photonic communication systems, optical amplifiers can be incorporated in front of a front-end opto-electronic receiver to form an optical amplified preamplifier. This type of optical receivers is treated in Chapter 10 which deals with optical amplification.

The ultimate goals of the design of optical receiver are to determine the minimum optical energy in terms of the number of photons per bit period required at the input of the PD so that it would satisfy a certain optical signal-to-noise ratio for an analog optical system or the sensitivity of a digital optical communication system satisfying a certain bit error rate (BER). In other words, the minimum optical power is required at a certain bit rate in a digital communication system so that the decision circuitry can be detected with a specified BER, for example, $BER = 10^{-9}$ or 10^{-12}.

Table 7.1 shows the important requirement for optical receivers in various communication systems from a terrestrial to a local and wide area network to undersea submarine systems.

The electronic amplifier is considered a block diagram rather than the detail circuit configuration. However, for completeness, a section is dedicated to the design of the electronic front-end amplifier. This is essential for a generic approach to the design of optical receivers, which is the ultimate objective of this chapter. More details of DSP subsystems to be cascaded with the optical reception unit are described in the next chapter dealing with coherent reception. However, DSP works for both direct and coherent reception systems. This is explained in the next chapter.

TABLE 7.1

Optical Receiver Characteristics and Their Relative Importance in Typical Optical-Fiber Communications Systems

	Features	Undersea Optical Communications	Terrestrial Communications and WAN	Point-to-Point	LAN
High receiver sensitivity	Maximum repeater spacing	Critical	Moderately critical	Moderate	Moderate
Wide dynamic range	Flexible and convenient systems configurations	Moderate	Moderately critical	Moderately critical	Critical
Bit rate transparency	Variable bit rate operation	Not required	Not required	Desirable	Desirable
Bit rate dependency	Flexible	Accommodated by the use of appropriate line codes and scrambling/descrambling		Desirable	Desirable
Fast acquisition time	Short preamble bit sequence	Not required	Not required	Moderately critical	Moderately critical
DSP: dispersion compensation (linear)	Non-DCF multi-span links	Essential for 100G	Essential for 100G to Tera-bit per second	Essential in metro- and access networks	Not essential
DSP: compensation for nonlinear impairment	Non-DCF multi-span DWDM/flex OTN[a]	Essential	Essential for non-DCF multi-span link	Not very critical	Not essential
DSP: carrier phase and clock recovery	Non-DCF multi-span link	Essential	Essential	Essential in short and moderate link	Possibly required when DSP is inexpensive

[a] OTN: Optical transport networks or IP_DWDM—GMPLS: Internet protocol over dense wavelength division multiplexing—General multi-protocol label/lamda switching.

7.3 Receiver Components

The design of an optical receiver depends on the modulation format of the signals and is transmitted through the transmitter. In particular, it is dependent on the modulation in analog or digital, Gaussian, or exponential pulse shape, on–off keying or multiple levels, and so on.

Optical signals treated in this chapter are part of intensity modulated and direct detection (IM/DD) ON/OFF keying (OOK) systems. They are treated with an assumption that light waves that arrive at the receiver are assumed to be polarization-independent and that their polarization plays no part in the degradation of the optical signals, except due to the polarization mode dispersion, which is independently discussed in the Optical Fiber chapter. Coherent optical systems have been treated in many other textbooks on optical communications where the polarization and the coherence of the optical source play a very significant part in the design and implementation of the optical fiber communication systems. These coherent optical communications were of great interest to the research and

development community in early to mid-1980s but is of little interest now because of the invention of the Erbium-doped optical amplifiers (EDFA) in the late 1980s.

Figure 7.2 shows the schematic diagram of a digital optical receiver. An optical receiver front end consists of a PD for converting lightwave energy into electronic currents, an electronic preamplifier for further amplification of the generated electronic current, usually in voltage form, a main amplifier for further voltage amplification, a clock recovery circuitry for regenerating the timing sequence, and a voltage-level decision circuit for sampling the waveform for the final recovery of the transmitted and received digital sequence. Therefore, the opto-electronic preamplifier is followed by a main amplifier with an automatic control to regulate the electronic signal voltage to be filtered and then sampled by a decision circuit with synchronization by a clock recovery circuitry as shown in Figure 7.2a.

In case the DSP is used, an analog to digital converter (ADC) is employed to generate sampled digital data sequence and then fed into a DSP subsystem in which compensation algorithms may be used to compensate for distortion due to impairment, clock recovery, decoding of FEC-encoded sequence as well as the bit sequence as shown in Figure 7.2b. Currently, 100G receivers or transponders have been developed with four lanes each carrying 25G or 28G (including forward error coding [FEC]). Thus, the sampling rate must be at least 50 or 56 GS/s and real-time DSP can be cascaded or in parallel if the sampling speed

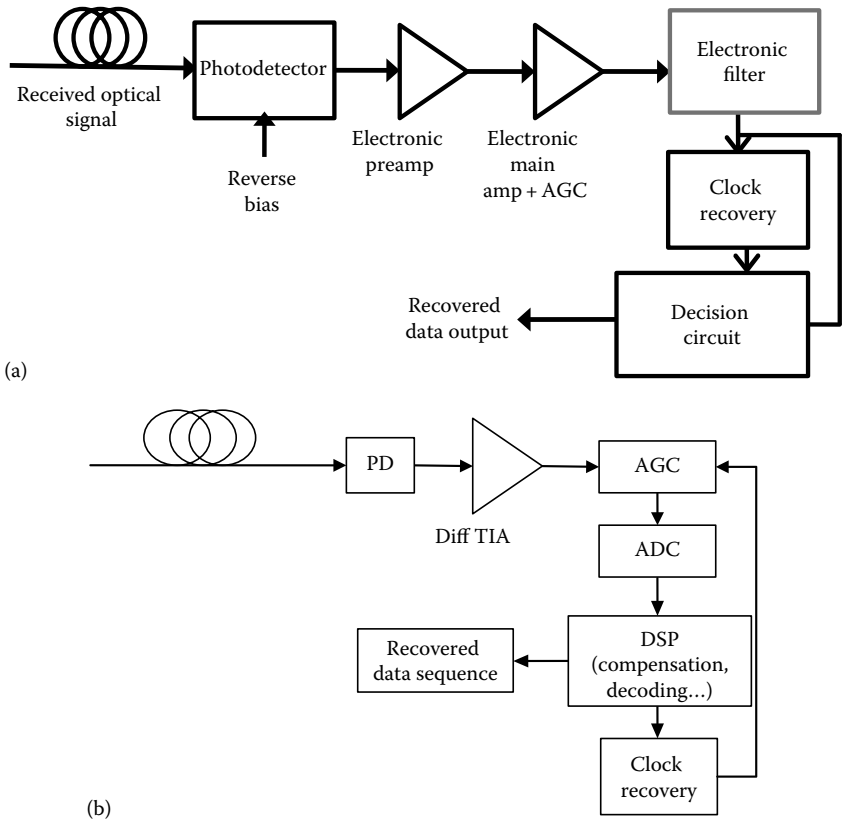

FIGURE 7.2
Schematic diagram of the digital optical receiver IM/DD (a) without incorporating a DSP subsystem and (b) with a DSP subsystem. ADC = analog to digital converter.

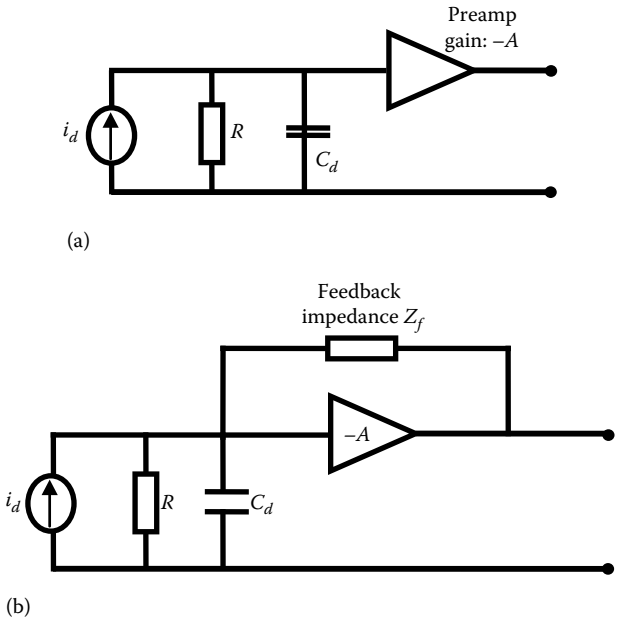

FIGURE 7.3
Schematic diagram of electronic preamplifier in an optical receiver: (a) High Impedance (HI) optical front-end receiver. (b) Transimpedance (TI) optical front-end receiver. The current source represents the electronic current generated in the photodetector. C_d = photodiode capacitance.

of these DSPs does not reach this rate. Alternatively, FPGAs can be structured in parallel form to perform real-time processing.

In in-line fiber, an optical amplifier can be incorporated in front of the PD to form an optical receiver with an optical amplifier front end to improve its receiving sensitivity. This optical amplification at the front end of an optical receiver will be treated in the chapter dealing with optical amplification processes.

The structure of the receiver consists of three parts, namely, the front end section, the linear channel of the main amplifier, and AGC and the Data Recovery section. These sections are described in order in the following text (Figure 7.3).

7.3.1 Photodiodes

A PD detects and converts the optical input power into an electric current output. The ideal PD would be highly quantum efficient, would, ideally, add no noises to the received signals, respond uniformly to all signals with different wavelengths within the transparent windows of optical fibers around 1300 and 1550 nm, and finally would not be saturated and behave linearly as a function of a signal amplitude. There are several different types of PDs which are commercially available. In the semiconductor-based types, the photodiode is used almost exclusively for high-speed fiber optic systems due to its compactness and extremely high bandwidth. The two most commonly used types of photodiodes are the PIN and avalanche photodiode (APD). Detailed reviews of these photodiodes have been presented in well-known published literature [1–3]. The fundamental characteristics of these two device types are briefly described for completeness.

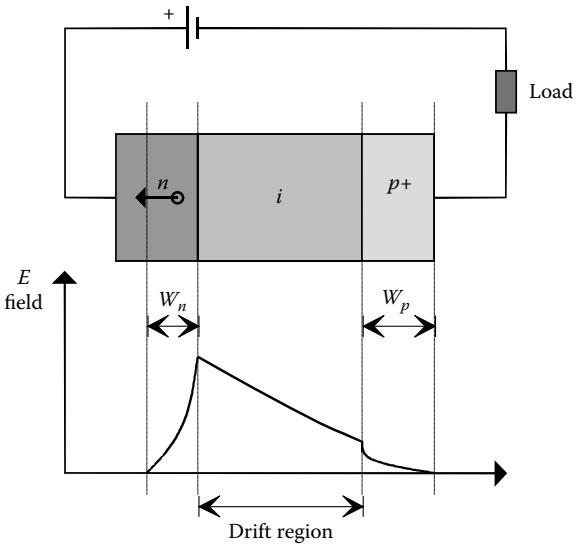

FIGURE 7.4
Schematic diagram of a *p–i–n* photodiode.

7.3.1.1 p–i–n Photodiode

A pin PD consists of three regions of semiconductors, the heavily doped *p*, the intrinsic *i*, and the *n* doped sections. It is essential that the *p–n* junction is reverse-biased to cause mobile electrons and holes to move away from the junction, increasing the width of the depletion layer as a result of which a high electric field is produced by the immobile charges at both ends. If lightwaves are incident on the PIN surface and absorbed in the *high-field depleted* region, the electron-hole pairs generated will move at saturation-limited velocity. No great contribution is seen if the photons fall in other regions. Thus, since the width of the *p* region, W_p, is inversely proportional to its doping concentration, decreasing the doping level to intrinsic behavior would widen W_p, and the depleted region will now be wider and compatible with the absorption region to produce large photon-generated current. A p^+ region must be added to make good ohmic contact. A wider intrinsic region gives higher quantum efficiency, η but lower response rates (Figure 7.4).

7.3.1.2 Avalanche Photodiodes (APDs)

High-field multiplication region is added adjacent to the lightly doped depletion region—intrinsic as in contrast with the PIN structure. Photons absorbed in the intrinsic region produce electron-hole pairs. These pairs drift to the high-field region whereby they gain sufficient energy (the *E* field must be above the threshold for impact ionization to occur) so as to ionize bound electrons in the valence band upon colliding with them. The avalanche effect occurs only when the electric field in the high-field multiplication region is above the threshold for impact ionization (Figure 7.5). A guard ring is usually added to prevent the leakage of surface current, I_{surf}.

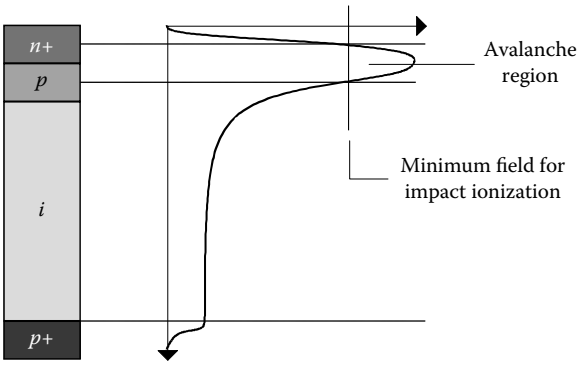

FIGURE 7.5
Schematic diagram of an avalanche photodiode (APD).

7.3.1.3 Quantum Efficiency and Responsivity

Two most important characteristics of a PD are its quantum efficiency and its response speed. These parameters depend on the material band gap, the operating wavelength, the doping and thickness of the *p*, *i*, and *n* regions of the device. The quantum efficiency, η, is the number of electron-hole carrier pairs generated per incident photon of energy $h\nu$ and is given by

$$\eta = \frac{\text{Number of electron pairs generated}}{\text{Number of incident photons}} = \frac{I_p/q}{P_o/h\upsilon} = \frac{I_p h\upsilon}{P_o q} \tag{7.1}$$

where
I_p is the photocurrent
P_o is the incident optical power

The performance of a photodiode is often characterized by its responsivity $\Re$ which is related to the quantum efficiency by

$$\Re = \left(\frac{I_P}{P_o}\right)G = \left(\frac{\eta q}{h\upsilon}\right)G = \left(\frac{\eta q \lambda}{hc}\right)G \tag{7.2}$$

where G is the *APD average multiplication factor* and $G = 1$ for the *non-APD* case. The optical power is given by

$$P_o = \frac{i_s}{G\Re} \tag{7.3}$$

which implies that for the same incident optical power, APD could produce higher photocurrent than PIN.

7.3.1.4 High-Speed Photodetectors

When the speed of the PDs is increased, for example, when used in high-speed systems above 10 Gb/s, pin detectors are normally used and the effective receiving area is smaller to reduce the junction capacitance. This decreased area then forces the detector to have a lower breakdown voltage.

7.4 Detection and Noises

The front-end subsystem is the most important component because noise contributed by this part severely affects the overall performance of the system. The design of an amplifier front end depends on the sensitivity required and the bandwidth of the system. For example, an optical front-end amplifier for an optical time domain reflectometer would require a very high-sensitive front end while its bandwidth is not critical. On the other hand, a front-end optical amplifier for a high bit rate optical communication system requires a wide bandwidth amplifier as well as a reasonably high sensitivity and low-noise contribution. In Table 7.1, optical front-end amplifiers and the demands on their characteristics with their limits are given.

In general, optical amplified front ends are required for two types of optical systems: the short link in the local area or metropolitan area networks and the terrestrial link systems. The former requires high data accumulation rate and the latter requires a fast acquisition rate and reasonable sensitivity.

Thus, electronic preamplifiers can take two typical structures: the high impedance (HI) and the transimpedance (TI) front end. The difference is that in TI configuration there is a shunt feedback from the output to the input. This TI configuration offers a wide bandwidth. The HI provides a high sensitivity due its noise, which is almost negligible compared to the TI model. The TI and HI configurations are shown in Figure 7.3.

A PD is represented by a current source and a capacitor in parallel. The noise current (quantum shot noise) is not shown. A diode capacitance dropped across the depletion region of the p–n junction is also included. In fact, this diode capacitance C_d is a critical component for the design of the PD.

The HI front end would have very high impedance Z_i as the input impedance of the electronic amplifier. This high impedance would limit the bandwidth of the overall amplifier. Usually, Z_i would be a few hundred ohms. Whereas a TI front end offers lower receiver sensitivity, the bandwidth is increased by a factor of A, the amplifier linear gain.

7.4.1 Linear Channel

The linear channel in optical receivers consists of a main electronic amplifier and a low-pass filter or an equalizer whose objectives are to reduce the noise or distortion in the channel without incurring further intersymbol interference (ISI). The preamplifier and main amplifier have the bandwidth normally wider than that of the system. Thus, in calculating the total noise contribution the noise spectra density must be integrated over the electronic amplifier bandwidth.

7.4.2 Data Recovery

Once the optical signals are detected and amplified, the data streams are sampled with respect to the time interval recovered by a clock recovery circuit, by using a surface acoustic wave filter if the bit rate is high, and then amplified and fed into a triggering circuit. In several high-speed optical receivers, its components are usually integrated in a chip or by using a hybrid circuit if the bit rate is higher than 2.5 Gb/s.

7.4.3 Noises in Photodetectors

The most important noise source in the PD is the fundamental quantum or shot noise caused by the intrinsic fluctuations in the photo excitation of electronic carriers. In any

interval of T seconds, the probability in which exactly N primary electrons are generated is given by the time-varying Poisson distribution

$$P[N,(t_0,t_0+T)]=\frac{\Lambda^N e^{-\Lambda}}{N!} \tag{7.4}$$

where $\Lambda=\int_{t_0}^{t_0+T}\lambda(t)dt \xrightarrow{\text{where}} \lambda(t)=\frac{\eta}{\hbar\nu}p(t)+\lambda_d$ and λ_d is the number of electrons generated under dark conditions, or the dark current electrons of the PD; thus, Λ is the average number of primary electrons produced during the interval.

For APD, the internal avalanche multiplication factor is also a random process. The variation of the avalanche gain gives rise to excess noise. The probability of distribution of the avalanche gain depends on the types of APD. In particular, it is a function of the ratio of hole ionization probability to that of the electron, the factor k. The extra noise is represented by an excess noise factor $F(g)$ given by

$$\begin{aligned}&\left\langle g^2\right\rangle = F(g)G^2\\ &\text{with } G=\left\langle g\right\rangle\end{aligned} \tag{7.5}$$

The term $F(g)$ is usually determined by experimental works and can be approximated as

$$F(G)\simeq kG+\left(2-\frac{1}{G}\right)(1-k) \tag{7.6}$$

and usually, $F(G)$ can be estimated by

$$F(G)\simeq G^x \tag{7.7}$$

For Ge APD $x \sim 1$ while for well-designed Si APD $x \sim 0.4$ or 0.5.

7.4.4 Receiver Noises

Before proceeding to the systems calculations to determine the performance of optical receivers, it is necessary that the noises generated in the PD and the preamplifier front end are considered.

Readers can in fact consider investigating the system calculation and returning back to the noise calculation provided they take either the total equivalent noise spectral density at the input of the detector or its noise. This section describes all noise mechanisms related to the photodetection process including the electronic noise associated with the receiver.

Shot noises and thermal noises are the two most significant noises in optical detection systems. Shot noises are generated by either quantum process or electronic biasing. The noises are specified in noise spectral density that is the square of the noise current per unit frequency (in Hz). Thus, the noise spectral density is to be integrated over the total amplifier bandwidth to obtain the equivalent noise currents.

7.4.4.1 Shot Noises

Electrical shot noises are generated by the random generation of streams of electrons (current). In optical detection, shot noises are generated by (1) biasing currents in electronic devices and (2) photo currents generated by the photodiode

For a bias current I, the spectral current noise density S_I is given by

$$S_I = \frac{d\left(i_{N,I}^2\right)}{df} = 2qI \text{ A}^2/\text{Hz} \tag{7.8}$$

where q is the electronic charge. The current $i_{N,I}$ represents the noise current due to the biasing current I.

7.4.4.2 Quantum Shot Noise

The average current $\left\langle i_s^2 \right\rangle$ generated by the PD by an optical signal with an average optical power P_{in} is given by

$$S_Q = \frac{d\left\langle i_s^2 \right\rangle}{df} = 2q\left\langle i_s^2 \right\rangle \text{ A}^2/\text{Hz}. \tag{7.9a}$$

When the APD is used then the noise spectral density is given by

$$S_Q = \frac{d\left\langle i_s^2 \right\rangle}{df} = 2q\left\langle i_s^2 \right\rangle \left\langle G_n^2 \right\rangle \text{ A}^2/\text{Hz} \tag{7.9b}$$

with $\left\langle G_n^2 \right\rangle$ as the average avalanche gain of the detector. It is noted here again that the dark currents generated by the PD must be included in the total equivalent noise current at the input after it is evaluated. These currents are generated even in the absence of the optical signal. The dark currents can be eliminated by cooling the PD to at least below the temperature of liquid nitrogen (77 K).

7.4.4.3 Thermal Noise

At a certain temperature, the conductivity of a conductor varies randomly. This random movement of electrons generates a fluctuating current even in the absence of an applied voltage. The thermal noise of a resistor R is given by

$$S_R = \frac{d\left(i_{N,R}^2\right)}{df} = \frac{2k_BT}{R} \text{ A}^2/\text{Hz} \tag{7.10}$$

where

k_B is the Boltzmann's constant
T is the absolute temperature (in K)
R is the resistance (in ohms)
$i_{N,R}^2$ denotes the noise current due to resistor R

7.4.5 Noise Calculations

In this section, the design of a receiver for use in a digital communication system and the methods for noise calculations are described. Binary and multi-level operations are also given.

A schematic of an optical preamplifier of the receiver and an electronic analog equalizer for the detection of optical digital modulated signals is shown in Figure 7.6. An equalizer is considered to extend the bandwidth of the receiver to the range of several GHz for ultra-high-speed operations of these digital optical receivers. This is similar to earlier design considerations of optical receivers when multimode fibers were used in the first generation of optical fiber communication systems [4–6]. The noise sources and small amplification circuit model can be simplified as shown in Figure 7.7 in which all the noise sources of the electronic amplifier and the PD are presented and grouped into total noise current sources at the input and output of the amplifier. These sources are then transferred to a total equivalent current source as seen in the input of the amplifier. The signal to noise ratio and contribution of noises from the electronic amplification process and the quantum shot noise process in the detection of optical signals can thus be calculated very easily.

Our goal is to obtain an analytical expression of the noise spectral density equivalent to a source like the electronic amplifier including the quantum shot noises of the PD.

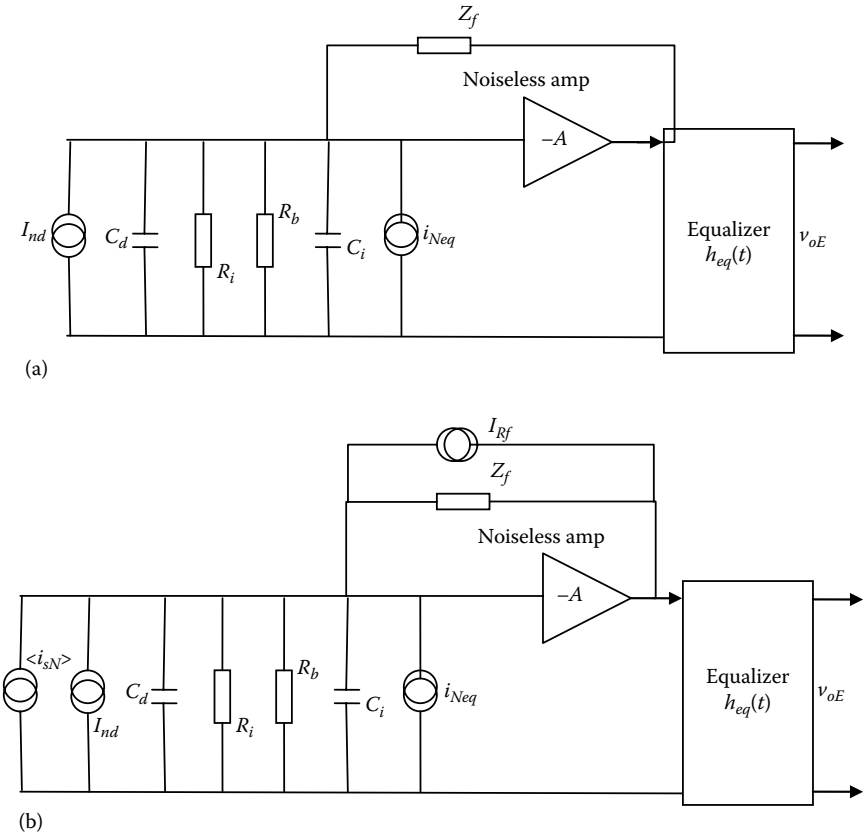

FIGURE 7.6
Optical receiver small-signal model and associate noise sources. (a) Without and (b) with noise source contributed by the shunt feedback impedance.

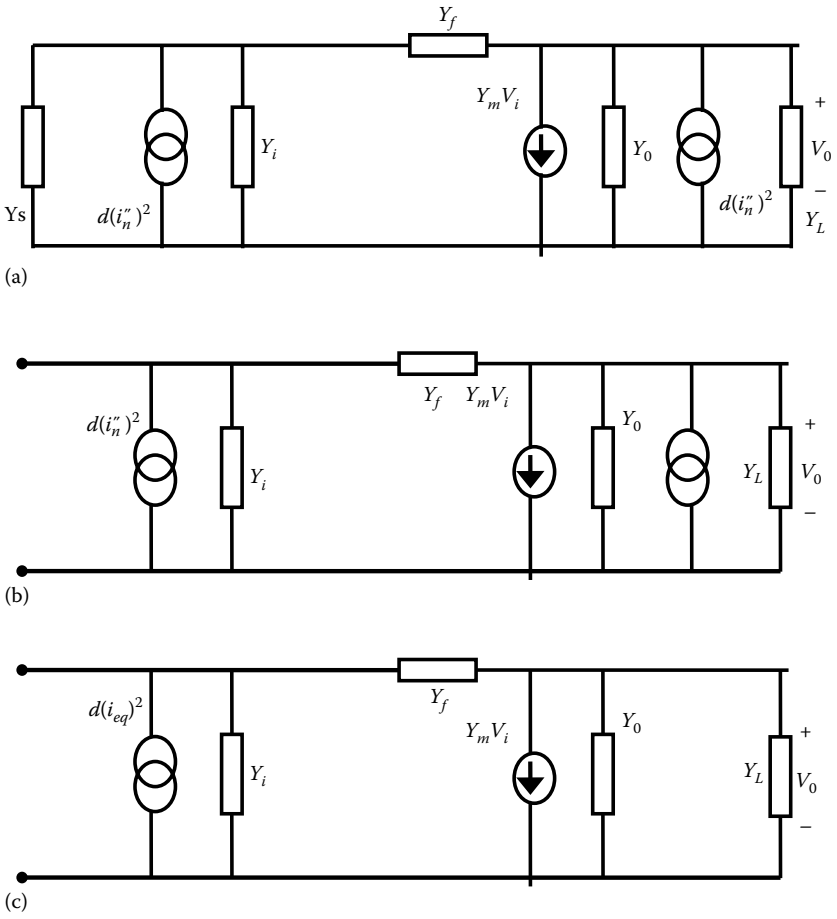

FIGURE 7.7
Small equivalent circuits including noise sources: (a) *Y*-parameter model representing the ideal current model and all current noise sources at the input and output ports, (b) with noise sources at input and output ports, and (c) with a total equivalent noise source at the input.

A general method for deriving the equivalent noise current at the input is by representing the electronic device by a *Y*-equivalent linear network as shown in Figure 7.7. The two current noise sources $d\left(i_N'^2\right)$ and $d\left(i_N''^2\right)$ represent the summation of all noise currents at the input and the output of the *Y*-network. This can be transformed into a *Y*-circuit with the noise current at the input as follows.

The output voltages V_o of Figure 7.7a can be written as:

$$V_o = \frac{i_N'(Y_f - Y_m) + i_N''(Y_i + Y_f)}{Y_f(Y_m + Y_i + Y_o + Y_L) + Y_i(Y_o + Y_L)} \tag{7.11a}$$

and for Figure 7.7b

$$V_o = \frac{(i_N')_{eq}(Y_f - Y_m)}{Y_f(Y_m + Y_i + Y_o + Y_L) + Y_i(Y_o + Y_L)} \tag{7.11b}$$

Comparing these two equations, we can deduce the equivalent noise current at the input of the detector is:

$$i_{Neq} = i'_N + i''_N \frac{Y_i + Y_f}{Y_f - Y_m} \tag{7.12a}$$

Then reverting to mean square generators for a noise source, we have

$$d(i_{Neq})^2 = d(i'_N)^2 + d(i''_N)^2 \left| \frac{Y_i + Y_f}{Y_f - Y_m} \right|^2 \tag{7.12b}$$

It is therefore expected that if the *Y*-matrix of the front-end low-noise amplifier is known the equivalent noise at the input of the amplifier can be obtained using (7.12b).

7.5 Performance Calculations for Binary Digital Optical Systems

As described earlier, the noises of the optical receivers consist of the thermal noises and quantum shot noises due to the bias currents and the photocurrent generated by the PD with and without the optical signals. This quantum shot noise is strongly signal dependent.

These noises degrade the sensitivity of the receiver and thus a penalty can be estimated. Another source of interference that also results in signal penalty is the ISI. The goal of this section is to obtain an analytical expression for the receiver sensitivity of the optical receiver in an IM/DD pulse-code-modulated system.

7.5.1 Signals Received

Assuming that the received signal power is

$$p(t) = \sum_j a_j h_p(t - jT_B) \tag{7.13}$$

T_B is the bit period. The average output voltage is thus given by

$$\langle v_o \rangle = \Re \langle G_n \rangle \left[\sum_j a_j \frac{1}{T_B} \int_{-T_b/2}^{T_b/2} h_p(t - jT_B) dt \right] R_I A \tag{7.14}$$

where

$h_p(t - jT_B)$ is the impulse response of the system evaluated at each time interval

R_I is the input resistance of the overall amplifier of the system including both the front end and linear channel amplifier

It is assumed that the overall amplifier has a flat gain response A over the bandwidth of the system.

$$a_j\Big|_{t=0} = \begin{cases} b_o \approx 0 \\ b_1 \end{cases} \tag{7.15}$$

where
b_o is the energy when a transmitted "0" is received
b_1 is the energy when a transmitted "1" is received

In the summation over a number of periods, it is necessary to take the contribution of adjacent optical pulses into account.

We now have to distinguish between two cases when a "0" or a "1" is transmitted and received.

Case (a): OFF or a transmitted "0" is received
Using (7.14) and (7.15), we have

$$\langle v_o \rangle_0 = v_{oo} = \Re \frac{b_0}{T_B} G R_I A \cong 0 \tag{7.16}$$

with the total equivalent noise voltage at the output, v_{NTo}^2 is

$$v_{NTo}^2 = v_{NA}^2 = i_{Neq}^2 R_I^2 A^2 \tag{7.17}$$

Case (b): ON or a transmitted "1" received
In this case, the average signal voltage at the output is received as

$$\langle v_o \rangle_1 = v_{01} = \Re \frac{b_1}{T_b} \langle G_n \rangle R_I A \tag{7.18}$$

with a total noise equivalent mean voltage at the output is given by

$$v_{NT1}^2 = v_{oSN}^2 + v_{NA}^2 \tag{7.19}$$

where v_{oSN}^2 is the signal-dependent shot noise. v_{NA}^2 is the amplifier noise at the output and is given by

$$v_{NA}^2 = i_{Neq}^2 R_I^2 A^2 B \tag{7.20}$$

The signal-dependent noise is in fact the quantum shot noise and is given by

$$v_{oSN}^2 = \int_0^B 2q\langle i_s\rangle_1 \left\langle G_n^2\right\rangle R_I^2 A^2 df \tag{7.21}$$

where

B is the 3 dB bandwidth of the overall amplifier

$\langle i_s\rangle_1$ is the average photocurrent current received when a "1" was transmitted

This current is estimated as follows:

$$\langle i_s\rangle_1 = \sum_{-\infty}^{\infty} \Re \frac{b_1}{T_B} \int_{-T_b/2}^{T_b/2} h_p(t - jT_B)dt \tag{7.22}$$

or

$$\langle i_s\rangle_1 = \Re \frac{b_1}{T_B} \int_{-\infty}^{\infty} h_p(t)dt \tag{7.23}$$

Using normalization with $\int_{-\infty}^{\infty} h_p(t)dt = 1$, (7.23) becomes

$$\langle i_s\rangle_1 = \Re \frac{b_1}{T_B} \tag{7.24}$$

7.5.2 Probability Distribution

The optical systems under consideration are typical IM/DD systems in which the optical energy of each pulse period is equivalent to that of at least a few hundred photons. This number is large enough so that a Gaussian distribution of the probability density is warranted.

The probability density function of a "0" transmitted and received by the optical receiver is thus given by Equation 7.25 and illustrated in Figure 7.8.

$$p\left[v_o \middle| \text{"0"}\right] = \frac{1}{\left(2\pi v_{NT0}^2\right)^{1/2}} \exp\left[\frac{-(v_0 - v_{00})^2}{2v_{NT0}^2}\right] \tag{7.25}$$

and similarly for transmission of a "1" it is given by Equation 7.26

$$p\left[v_o \middle| \text{"1"}\right] = \frac{1}{\left(2\pi v_{NT1}\right)^{1/2}} \exp\left[\frac{-(v_0 - v_{01})^2}{2v_{NT1}^2}\right] \tag{7.26}$$

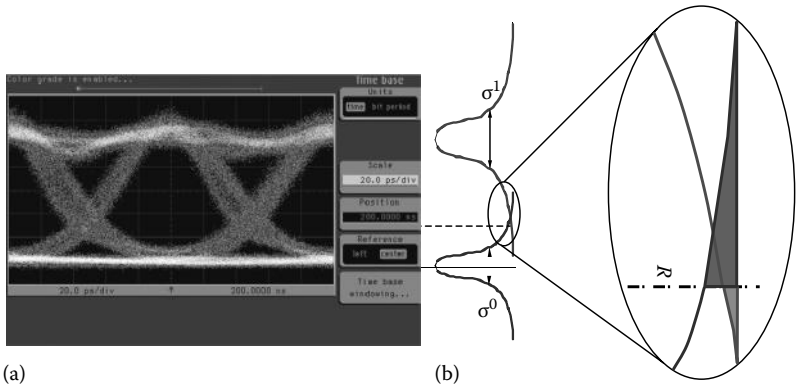

FIGURE 7.8
(a) Time-dependent fluctuating signal in the receiver in response to the random digital bit stream, the eye diagram, and (b) the corresponding probability density distribution as a function of the output voltage level and the decision level for recovery of the transmitted signals.

The total probability of error or a bit error rate (BER) is defined [7,8] as

$$BER = p(1)p(0/1) + p(0)p(1/0) \tag{7.27}$$

where

$p(1)$ and $p(0)$ are the probabilities of receiving "1" and "0", respectively
$p(1/0)$ and $p(0/1)$ are the probabilities of deciding "1" when "0" is transmitted and vice versa

In a binary bit stream, "1" and "0" are likely to occur equally, that is, $p(1) = p(0) = 0.5$, then (7.27) becomes

$$BER = \frac{1}{2}[p(0/1) + p(1/0)] \tag{7.28}$$

As it is assumed that the probability of transmitting "0" and "1" is equal then for a decision voltage level of d as indicated in Figure 7.5 the total probability of error P_E is the summation of the errors of deciding "0" or "1" by integrating the probability density function over the shaded regions, and is given by

$$BER = P_E = \frac{1}{2}\int_{d}^{\infty} p\left[v_0 \middle| \text{"0"}\right] dv_0 + \frac{1}{2}\int_{-\infty}^{d} p\left[v_0 \middle| \text{"1"}\right] dv_0 \tag{7.29}$$

Substituting for the probability distribution using (7.27) leading to

$$BER = \frac{1}{2\sqrt{\pi}} \int_{\frac{d-v_{00}}{v_{NT0}}}^{\infty} e^{-\frac{x^2}{2}} dx + \frac{1}{2\sqrt{\pi}} \int_{\frac{v_{01}-d}{v_{NT1}}}^{d} e^{-\frac{x^2}{2}} dx \tag{7.30}$$

The functions in (7.30) have the standard form of the complementary error function $Q(\alpha)$ defined as

$$Q(\alpha) = \frac{1}{\sqrt{2\pi}} \int_{\alpha}^{\infty} e^{-x^2/2} dx \tag{7.31}$$

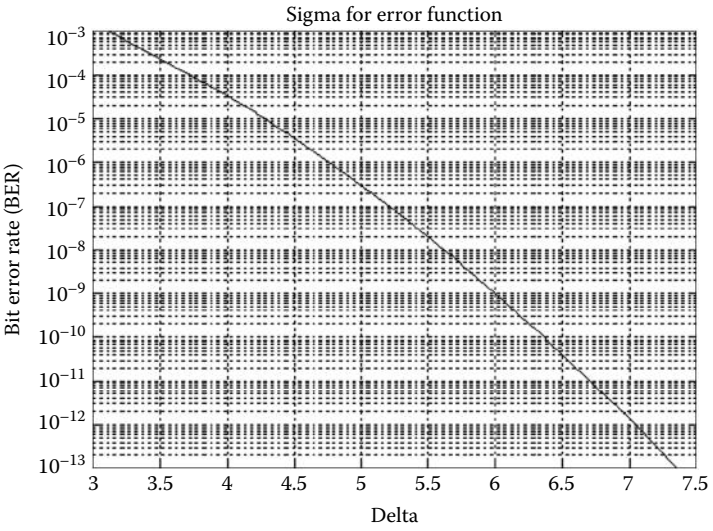

FIGURE 7.9
BER as a function of the δ parameter. Sometimes δ is assigned as the system *Q* Magnum function.

then Equation 7.30 becomes

$$BER = \frac{1}{2}\left[Q\left(\frac{d}{v_{NT0}} \right) + Q\left(\frac{v_{01} - d}{v_{NT1}} \right) \right] \tag{7.32}$$

The $Q(\delta)$ function is a standard function and this curve is shown in Figure 7.9. It is noted that for a *BER* = 1e−9 the value of δ is about 6 which is the normal standard for communications at bit rate of 155 Mb/s to 40 Gb/s. However, in laboratory demonstration it requires a BER of 10^{-12} to correspond to a δ of 7.

7.5.3 Minimum Average Optical Received Power

Again using the condition $p[v_o/\text{“0”}] = p[v_o/\text{“1”}]$ we have from (7.32)

$$\frac{d}{v_{NT0}} = \frac{v_{01} - d}{v_{NT1}} \equiv \delta \tag{7.33}$$

Now assuming $v_{00} = 0$, hence

$$BER = Q(\delta) \tag{7.34}$$

Thus by eliminating the variable *d* from (7.33) we obtain

$$\delta = \frac{v_{01} - \delta v_{NT0}}{v_{NT1}} \tag{7.35}$$

Or alternatively

$$v_{01} = \delta(v_{NT0} + v_{NT1}) \tag{7.36}$$

substituting v_{01}, v_{NT1}, v_{NT0} we have

$$\Re \frac{b_1}{T_b} \langle G_n \rangle R_I A = \partial \left\{ \left[2\Re q \frac{b_1}{T_B} \left\langle G_n^2 \right\rangle B R_I^2 A^2 + v_{NA}^2 \right]^{1/2} + v_{NA} \right\} \tag{7.37}$$

However, the amplifier noise voltage v_{NA} is given by $v_{NA} = i_{Neq} R_I A B^{1/22}$. By substituting this noise voltage and eliminating $R_I A$ and solving for the energy essential for the "1" transmitted and received at the PD, the energy b_1 can be written as

$$b_1 = \frac{q}{\Re} \left[\delta^2 G^x + \frac{2\delta i_{Neq} T_B}{qG} \right] \tag{7.38}$$

where we have used the approximation $\langle G_n \rangle = G$ and $\left\langle G_n^2 \right\rangle = \langle G \rangle^{2+x}$ and x is the factor dependent on the ionization ratio in an APD. For pin PD $G = 1$.

The optical receiver sensitivity, denoted as RS, can thus be defined as

$$\text{Receiver sensitivity} = RS = 10\text{Log}_{10} \frac{P_{av}}{P_o} \text{ in dBm} \tag{7.39}$$

where

$P_{av} = b_1/T_b$

$P_o = 1.0$ mW (the reference power level for evaluating power in dBm)

This is the optical receiver sensitivity which is defined as the minimum optical power required for the receiver to operate reliably with a BER below a specified value.

In Equation 7.39, there are two terms clearly specifying the dependence of the signal dependence δ and the amplifier noise contribution. Recall that the term b_1 represents the optical energy of the "1" required for the optical receiver to detect with a certain BER. The term q/R in the RHS of (7.38) is equivalent to the optical power required to generate one electron, or the number of photons required at the optical receiver to generate one electron. A typical measure for the optical receiver is the number of photons required for it to operate with a specified BER. Thus, the term $[\delta^2 G^x]$ indicates the number of photons required to overcome the opening of the eye at a particular BER and the term $(2\delta i_{Neq} T_b)/qG$ indicates the number of photons required to overcome the noises of the electronic preamp at a specific BER. With the avalanche PD, the avalanche gain also contributes to an increase in the noise level and hence to a higher power. However, the current avalanche gain would compensate for this.

We note that the analysis here has not taken into account the effects of pulse shape and the transfer function characteristics of the receiver. In this case, an equivalent current noise power as seen from the input port of the electronic preamplifier would simplify the analysis of the optical receiver sensitivity or SNR. The effects of the pulse shape and transfer function of the receiver are considered in the next few sections.

7.5.3.1 Fundamental Limit: Direct Detection

Referring to (7.38) we see that in the case when there are no electronic noises then the first term is the number of photons in the quantum limit of the direct detection receiver. Thus, we have

$$n_p = \left[\delta^2 G^x \right] \tag{7.40}$$

For a PIN detector and a BER of 1e–9 the number of photons of the quantum limit is 36.

Examples:

For an ASK-modulated optical signal at a bit rate of 10 Gb/s, estimate the number of photons required for the incoming symbol "1" so that a BER of 1e–9 can be achieved.

7.5.3.2 Equalized Signal Output

Recalling the optical signal $p(t)$ fallen on the input of the PD as

$$p(t) = \sum_{k=-\infty}^{\infty} a_k h_p(t' - kT_B) \tag{7.41}$$

where T_B is signal bit period, and $h_p(t)$ is the input optical shape constrained by

$$\int_{-\infty}^{+\infty} h_p(t)dt = 1 \tag{7.42}$$

It is noted that this function represents the optical power variation as a function of time and is always positive.

Now neglecting the DC component due to dark current, the signal at the output of the equalizer can be written as:

$$\left\langle v_{0E}(t) \right\rangle = \Re G p(t) * h_{fe}(t) * h_{eq}(t) \tag{7.43}$$

where

$h_{fe}(t)$ is the impulse response of the optical receiving subsystem
$h_{eq}(t)$ is the impulse response of the electronic equalizer
* indicates the convolution

The optical receiver is usually dominated by the pole contributed by the diode capacitance C and associated resistance of the network. It can be shown without difficulty that (refer to Figure 7.6) the frequency domain transfer function is given by

$$H_{fe}(\omega) = -\frac{R_f}{1 + j\omega \dfrac{R_f C}{A}} \tag{7.44}$$

where

A is the open loop voltage gain of the electronic preamplifier
R_f is the feedback resistance
C is the total input equivalent capacitance at the input port of the amplifier

Knowing the input optical shape, the equalizer transfer function for a given pulse shape can be determined by multiplying the transfer function of the receiver and that of the equalizer. It is noted that the 3 dB bandwidth of a feedback receiver is given by A/R_fC which is about A times the bandwidth of the receiver without feedback. Thus, the demand on the equalizer is much less for this case.

7.5.3.3 Photodiode Shot Noise

The output noise power due to the random fluctuation of the multiplied Poisson nature of the current produced by the PD can be written [4] as:

$$\left\langle i_{sN}^2 \right\rangle = \int_{-\infty}^{+\infty} qG^{2+x}\Re\left\{\sum_{k=-\infty}^{\infty} a_k h_p(t'-kT_B)+\lambda_d\right\} h_I^2(t-t')dt' \tag{7.45}$$

where

$h_I(t) = h_{fe}(t)^* h_{eq}(t)$ is the overall *current* impulse response of the optical preamplifier and the equalizer in cascade

λ_d is the electron/s generated by the PD when no lightwave is shined on the PD

It is important to note that the quantum shot noise power depends on the signal levels $\{a_k\}$ and the time t, that is, the noise is signal dependent and nonstationary.

Without loss of generality, we can consider the output quantum shot noise at the instant $t = 0$, then by replacing $t = 0$ and $t' = \tau$, (7.45) becomes

$$\left\langle i_{sN}^2(0) \right\rangle = \int_{-\infty}^{+\infty} qG^{2+x}\Re\left\{\sum_{k=-\infty}^{\infty} a_k h_p(\tau-kT)h_I^2(-\tau)\right\} d\tau + \int_{-\infty}^{+\infty} qG^{2+x}\Re\lambda_d h_I^2(\tau)d\tau \tag{7.46}$$

The first term is contributed by the signal amplitude, the signal-dependent shot noise and the second term indicates the contribution of the dark current of the PD.

The shot noise power due to the signal sequence $\{a_k\}$ at the time $t = 0$ can thus be rewritten as

$$\left\langle i_{SN}^2(0) \right\rangle = qG^{2+x}\Re\left\{\sum_{k=-\infty}^{\infty} a_k (h_p * h_I^2)(-kT_B)\right\} \tag{7.47}$$

$$\left\langle i_{SN}^2(0) \right\rangle = qG^{2+x}\Re\left\{\sum_{k=-\infty}^{\infty} a_k (h_p * h_I^2)(-kT_B)\right\} = qG^{2+x}\Re a_0 g(0) + qG^{2+x}\Re\left\{\sum_{\substack{k=-\infty \\ k\neq 0}}^{\infty} a_k g(-kT_B)\right\}$$

$$\text{with } (h_p * h_I^2)(-kT_B) = g(-kT_B) \tag{7.48}$$

The first term is the quantum shot noise due to the pulse under consideration and the second term is due to the preceding and succeeding signal pulses. The effects of the succeeding pulses on the noise at $t = 0$ are likely since there is some delay due to the signal

traveling through the system. This dependence of noise power on preceding and succeeding pulses is similar to intersymbol interference. However, it is important to note that this effect cannot be eliminated by equalizing the pulse to obtain zero ISI, since $h_0(kT) = 0$ does not imply that $g(kT) = 0$. The exact estimation of the noise power contributed to the considered pulse $\left\langle i_{SN}^2(0)\right\rangle$ requires statistical knowledge of the distribution of the pulse sequence. This is not generally known, and thus, some criteria must be used. The worst case that would contribute the largest noise effect is when the sequence $\{a_k\}$ has the adjacent symbols of maximum value b_M. In this case, we have

$$\left\langle i_{SN}^2(0)\right\rangle = qG^{2+x}\Re a_0 g(0) + qG^{2+x}\Re\left\{\sum_{\substack{k=-\infty\\k\neq 0}}^{\infty} b_M g(-kT_B)\right\} \tag{7.49}$$

The frequency domain of the noise power can be estimated as

$$\left\langle\left[i_{SN}^F(0)\right]^2\right\rangle = qG^{2+x}\Re\left\{\frac{b_M}{T_B}\sum_{\substack{k=-\infty\\k\neq 0}}^{\infty} b_M G\left(\frac{2\pi N}{T_B}\right) - \frac{b_M - a_0}{2\pi}\int_{-\infty}^{\infty} G(\omega)d\omega\right\} \tag{7.50}$$

where

$$\begin{aligned} G(\omega) &= \Im[g(t)] \\ G(\omega) &= \frac{1}{2\pi}H_p(\omega)[H_I(\omega) * H_I(\omega)] \\ \sum_{k=-\infty}^{\infty} g(-kT_B) &= \frac{1}{T_B}\sum_{n=-\infty}^{\infty} b_M G\left(\frac{2\pi N}{T_B}\right) \end{aligned} \tag{7.51}$$

The worst case total noise power is therefore given by

$$\left\langle\left[i_{SN}^F(0)\right]^2\right\rangle = \left\langle i_{sd}^2\right\rangle + \left\langle i_{SN}^2(0)\right\rangle \tag{7.52}$$

where $\left\langle i_{SD}^2\right\rangle$ is the shot noise due to the dark current of the PD.

7.5.4 Total Output Noises and Pulse Shape Parameters

It is now advantageous to normalize the input optical pulse and the output equalized pulse as follows:

$$\begin{aligned} h_p'(t) &= T_B h_p(tT_B) \\ h_o'(t) &= T_B h_o(tT_B) \end{aligned} \tag{7.53}$$

Or equivalently in the frequency domain

$$H'_p(f) = H_p\left(\frac{2\pi f}{T_B}\right)$$
$$H'_o(f) = \frac{1}{T_B} H_o\left(\frac{2\pi f}{T_B}\right) \tag{7.54}$$

These temporal and spectral functions depend only on the shapes of the input and output pulses and not on the epoch *T*. The normalization can be achieved by setting:

$$H'_p(0) = 1 \tag{7.55}$$

While the requirement on $H'_o(f)$ for zero intersymbol interference is

$$\sum_{-\infty}^{\infty} H'_0(f+k) = 1 \quad \text{for } |f| < 0.5 \tag{7.56}$$

all the output noises can be expressed in terms of these normalized functions. We can thus obtain from (7.51):

$$H_I\left(\frac{2\pi f}{T_B}\right) = \frac{T_B}{\Re G} H'(f)$$
$$\text{with } H'(f) = \frac{H'_o(f)}{H'_p(f)} \tag{7.57}$$

The normalized effects of the pulse shaping are given as:

$$I_1 = \int_{-\infty}^{\infty} H'_p[H' * H'(f)]df$$
$$I_2 = \int_{-\infty}^{\infty} |H'(f)|^2 \, df \tag{7.58}$$
$$I_2 = \int_{-\infty}^{\infty} |H'(f)|^2 \, f^2 df$$

The term I_1 influences the quantum shot noise of the PD from the optical signal received at the input, the term I_2 influences the dark current shot noises and the thermal noises due to the input resistance of the preamplifier, and the term I_3 influences the frequency dependent parts of the transfer function of the electronic preamp.

7.5.4.1 FET Front-End Optical Receiver

As an example of the estimation of noises at the output of the optical receiver we illustrate by the example of an optical receiver with a PD followed by an FET front end. Referring to Figure 7.6 for an FET front end we have the following parameters:

$$C = C_a + C_d \tag{7.59}$$

$$R_p = R_b R_i/(R_b + R_i) \tag{7.60}$$

where
R_b is the bias resistance
R_i is the input resistance of the amplifier at midband
C_d is the diode capacitance under reverse bias
C_a is the input capacitance of the amplifier

The spectral density of the thermal noises due to the bias resistance and the feedback resistance R_f are given by

$$S_R = \frac{2k_BT}{R_f}$$
$$S_{R_b} = \frac{2k_BT}{R_b} \tag{7.61}$$

where
T is the temperature
k is the Boltzmann's constant

Then the noise power at the equalizer output is given by

$$\left\langle i_{RN}^2 \right\rangle = 2k_BT\left(\frac{1}{R_f}+\frac{1}{R_b}\right)\cdot\int_{-\infty}^{\infty}\left|H_I(2\pi f)\right|^2 df = 2k_BT\left(\frac{1}{R_f}+\frac{1}{R_b}\right)\cdot\left(\frac{1}{\Re G}\right)^2 I_2 T_b \tag{7.62}$$

where
T_b is the bit period
T is the absolute temperature

The noise due to the transconductance of the FET is given by

$$\left\langle i_{g_mN}^2 \right\rangle = \frac{2k_BT\Gamma P}{g_m}\cdot\frac{1}{2\pi}\int_{-\infty}^{\infty}\left|H_I(2\pi f)\right|^2\left(\frac{1}{R_f^2}+\omega^2C^2\right)d\omega$$
$$= \frac{2k_BT\Gamma P}{g_m}\cdot\left(\frac{1}{\Re G}\right)^2\left(\frac{T_bI_2}{R_f^2}+\frac{(2\pi C)^2}{T_b}I_3\right) \tag{7.63}$$

where
g_m is the transconductance of the FET
$\Gamma \sim 0.7$ is the factor-related material and 0.7 for GaAs
P is the imperfection factor of the FET device

The quantum shot noise of the PD is given by

$$\left\langle \left[i_{SN}^{F}(0) \right]^2 \right\rangle = qG^{2+x}\Re \left\{ \frac{b_M}{T} \sum_{\substack{k=-\infty \\ k\neq 0}}^{\infty} b_M G\left(\frac{2\pi N}{T} \right) - \frac{b_M - a_0}{2\pi} \int_{-\infty}^{\infty} G(\omega) d\omega \right\}$$

$$= \frac{q}{\Re} G^x \left[a_0 I_1 + b_M \left(\sum_1 - I_1 \right) \right] \tag{7.64}$$

$$\text{with} \quad \sum_1 = \sum_{-\infty}^{\infty} H_p'(k)\left[H'(k) * H'(k) \right]$$

7.5.4.2 BJT Front-End Optical Receiver

Bipolar junction transistor (BJT) can also be employed as the front-end amplification stage of the optical receivers. A typical circuit design of such a receiver can be shown in Figure 7.10 in which three BJTs have been used with a direct coupled pair and a peaking stage to extend the bandwidth of the overall gain and then a shunt feedback to form a trans impedance configuration.

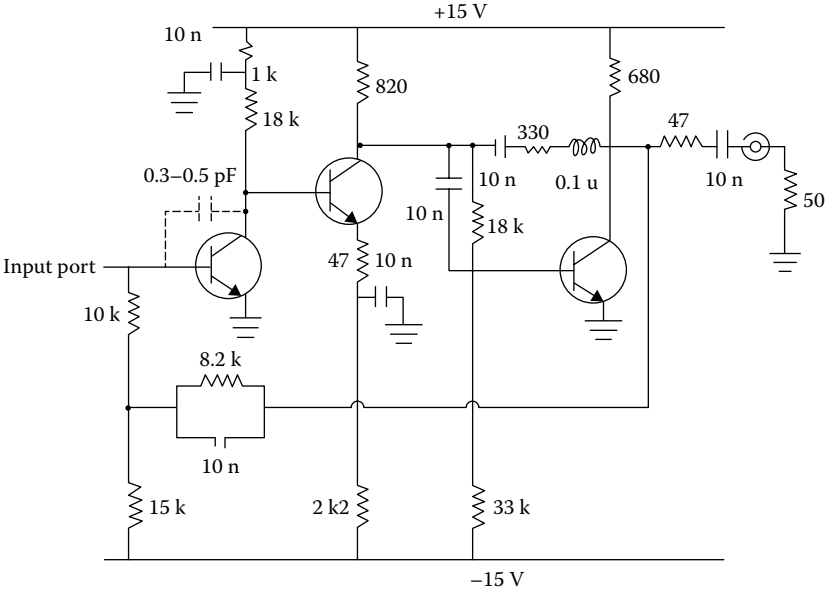

FIGURE 7.10
Design circuit of the electronic preamplifier for the balanced optical amplifier. All BJTs are either of type Phillips BFR90A or BFT24.

7.5.4.2.1 Noise Generators

Electrical shot noises are generated by the random generation of streams of electrons (current). In optical detection, shot noises are generated by (1) biasing currents in electronic devices and (2) photocurrents generated by the photodiode.

A biasing current I generates a spectral current density S_I given by

$$S_I = \frac{d(i_I^2)}{df} = 2qI \text{ in A}^2/\text{Hz} \tag{7.65}$$

where q is the electronic charge. The quantum shot noise $\langle i_s^2 \rangle$ generated by the PD by an optical signal with an average optical power P_{in} is given by

$$S_Q = \frac{d\langle i_s^2 \rangle}{df} = 2q\langle i_s^2 \rangle \text{ in A}^2/\text{Hz} \tag{7.66}$$

When APD is used then the noise spectral density is given by

$$S_Q = \frac{d\langle i_s^2 \rangle}{df} = 2q\langle i_s^2 \rangle \langle G_n^2 \rangle \text{ in A}^2/\text{Hz} \tag{7.67}$$

It is noted here again that the dark currents generated by the PD must be included to the total equivalent noise current at the input after it is evaluated. These currents are generated even in the absence of the optical signal. These dark currents can be eliminated by cooling the PD to at least below the temperature of liquid nitrogen (77 K).

At a certain temperature, the conductivity of a conductor varies randomly. The random movement of electrons generates a fluctuating current even in the absence of an applied voltage. The thermal noise spectral density of a resistor R is given by

$$S_R = \frac{d\left(i_R^2\right)}{df} = \frac{4k_BT}{R} \text{ in A}^2/\text{Hz} \tag{7.68}$$

where

k_B is the Boltzmann's constant
T is the absolute temperature (in K)
R is the resistance (in ohms)
i_R denotes the noise current due to resistor R

7.5.4.2.2 Equivalent Input Noise Current

Our goal is to obtain an analytical expression of the noise spectral density equivalent to a source like the electronic amplifier including the quantum shot noises of the PD. A general method for deriving the equivalent noise current at the input is by representing the electronic device by a Y-equivalent linear network as shown in Figure 7.23 of Appendix 7.A. The two current noise sources $di_n'^2$ and $di_n''^2$ represent the summation of all noise currents

at the input and at the output of the *Y*-network. This can be transformed into a *Y*-network circuit with the noise current referred to the input as follows.

The output voltages V_0 as referred to Figure 7.7 can be written as:

$$V_0 = \frac{i'_N(Y_f - Y_m) + i''_N(Y_i + Y_f)}{Y_f(Y_m + Y_i + Y_o + Y_L) + Y_i(Y_o + Y_L)} \tag{7.69}$$

and then using the equivalent model, we have

$$V_0 = \frac{(i'_N)_{eq}(Y_f - Y_m)}{Y_f(Y_m + Y_i + Y_o + Y_L) + Y_i(Y_o + Y_L)} \tag{7.70}$$

Comparing these two equations we can deduce the equivalent noise current at the input of the detector as:

$$i_{Neq} = i'_N + i''_N \frac{Y_i + Y_f}{Y_f - Y_m} \tag{7.71}$$

then reverting to mean square generators for a noise source we have

$$d(i_{Neq})^2 = d(i'_N)^2 + d(i''_N)^2 \left| \frac{Y_i + Y_f}{Y_f - Y_m} \right|^2 \tag{7.72}$$

It is therefore expected that if the *Y*-matrix of the front-end low-noise amplifier is known, the equivalent noise at the input of the amplifier can be obtained by using (7.72).

For a given source, the input noise current power of a BJT front end can be found from (see also the Appendix)

$$i_{Neq}^2 = \int_0^B d(i_{Neq})^2 = a + \frac{b}{r_E} + cr_E \tag{7.73}$$

where

B is the bandwidth of the electronic preamplifier
r_E is the emitter resistance of the front-end transistor of the preamplifier
a, b, and c are the parameters depending on the circuit elements and amplifier bandwidth

Hence, an optimum value of r_E can be found by setting an optimum biasing current for the collector current of the BJT such that i_{Neq}^2 is at a minimum.

$$r_{Eopt} = \sqrt{\frac{b}{c}} \quad \text{hence} \quad \rightarrow i_{Neq}^2\Big|_{r_E = r_{Eopt}} = a + 2\sqrt{bc} \tag{7.74}$$

If two types of BJTs are considered , for example, Phillips BFR90A and BFT24, then a good approximation of the equivalent noise power can be found as:

$$\begin{aligned} a &= \frac{8\pi B^3}{3}\left\{r_B C_s^2 + \left(C_s + C_f + C_{tE}\right)\tau_T\right\} \\ b &= \frac{B}{\beta_N} \\ c &= \frac{4\pi B^3}{3}\left(C_s + C_f + C_{tE}\right)^2 \end{aligned} \tag{7.75}$$

The theoretical estimation of the transistors can be derived from the measured scattering parameters as given by the manufacturer as

$$\begin{aligned} &\text{BFR90A} \\ &r_{Eopt} = 59\ \Omega \\ &I_{Eopt} = 0.44\ \text{mA} \\ &I_{eq}^2 = 7.3\times10^{-16}\ \text{A}^2 \longrightarrow \frac{I_{eq}^2}{B} = 4.9\times10^{-24}\ \text{A}^2/\text{Hz} \\ &I_{eq} = 27\ \text{nA} \longrightarrow \frac{I_{eq}}{\sqrt{B}} = 2.21\ \text{pA}/\sqrt{\text{Hz}} \end{aligned} \tag{7.76}$$

$$\begin{aligned} &\text{BFT24} \\ &r_{Eopt} = 104\ \Omega \\ &I_{Eopt} = 0.24\ \text{mA} \\ &I_{eq}^2 = 79.2\times10^{-16}\ \text{A}^2 \longrightarrow \frac{I_{eq}^2}{B} = 6.1\times10^{-24}\ \text{A}^2/\text{Hz} \\ &I_{eq} = 30.2\ \text{nA} \longrightarrow \frac{I_{eq}}{\sqrt{B}} = 2.47\ \text{pA}/\sqrt{\text{Hz}} \end{aligned} \tag{7.77}$$

Note that the equivalent noise current depends largely on some not well-defined values such as the capacitance, the transit times, and the base-spreading resistance and the short circuit current gain β_N. The term $I_{eq}/\sqrt{B}$ is usually specified as the noise spectral density equivalent, as referred to the input of the electronic preamplifier.

7.6 An HEMT-Matched Noise Network Preamplifier

7.6.1 Matched Network for Noise Reduction

A third-order noise-matching network (shown in Figure 7.11) has been obtained by Park [9] to tailor for 10 GHz low-noise optical receiver. This network is inserted in our preamplifier modeling and the electronic circuit is connected as shown in Figure 7.12.

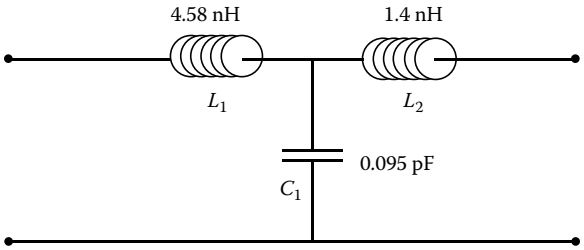

FIGURE 7.11
Third-order noise-matching network.

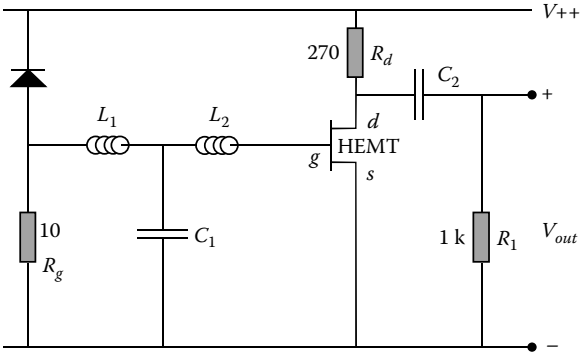

FIGURE 7.12
Electronic circuit of HEMT noise–matched network preamplifier.

For receiving high bit rate, we need to design a preamplifier with high frequency response. In electronics, the drain-to-source HEMT parasitic capacitance, C_{ds}, is negligibly small at high frequency. Further, we could reduce the complexity of solving this circuit by considering the *Miller effect* capacitance. We can then construct the small-signal high frequency response equivalent circuit for the electronic circuit and the simplified equivalent circuit is shown in Figure 7.13.

The equivalent circuit shown in Figure 7.13 can be further simplified as shown in Figure 7.14.

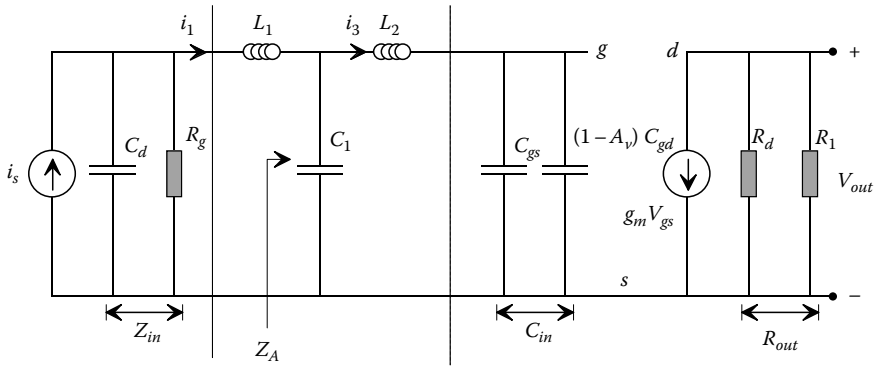

FIGURE 7.13
Equivalent circuit of HEMT noise–matched network preamplifier.

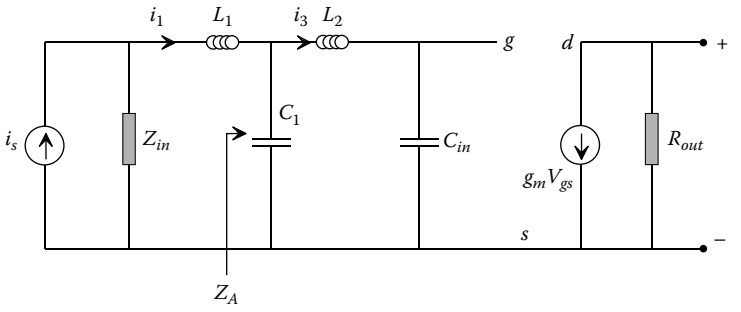

FIGURE 7.14
Simplified equivalent circuit of HEMT noise–matched network preamplifier.

Thus, the required preamplifier's transfer function can be obtained by the following:

$$i_3 = \left(\frac{sC_{in}}{s^3 L_2 C_1 C_{in} + sC_1 + sC_{in}} \right) \cdot i_1 \tag{7.78}$$

$$i_1 = \left(\frac{Z_{in}}{Z_{in} + Z_A} \right) \cdot i_s \tag{7.79}$$

By substituting (7.79) into (7.78), we obtain the transfer function of the HEMT-matched noise network preamplifier (Figure 7.15),

$$H_{HEMT} = \frac{V_{out}}{i_s} = -g_m R_{out} \left(\frac{1}{s^3 L_2 C_1 C_{in} + sC_1 + sC_{in}} \right) \cdot \left(\frac{Z_{in}}{Z_{in} + Z_A} \right) \tag{7.80}$$

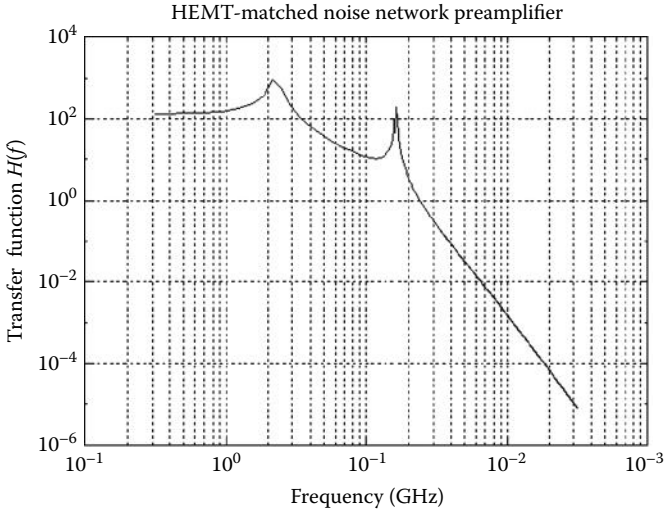

FIGURE 7.15
Frequency response of the HEMT noise–matched network preamplifier.

where

$$R_{out} = \frac{R_d R_l}{R_d + R_l} \tag{7.81}$$

$$Z_{in} = \frac{R_g}{sR_g C_d + 1} \tag{7.82}$$

$$Z_A = sL_1 + \frac{\left(\frac{1}{sC_1}\right)\cdot\left(sL_2 + \frac{1}{sC_{in}}\right)}{\frac{1}{sC_1} + \frac{1}{sC_{in}} + sL_2} = \frac{s^4 L_1 L_2 C_1 C_{in} + s^2 L_1 C_1 + s^2 L_1 C_{in} + s^2 L_2 C_{in} + 1}{s^3 L_2 C_1 C_{in} + s\left(C_1 + C_{in}\right)} \tag{7.83}$$

7.6.2 Noise Theory and Equivalent Input Noise Current

Circuit diagram in Figure 7.20 can be represented with the reflection coefficients shown in Figure 7.17. We denote the reflection coefficient of Z_{ph}, Z_S, Z^*_{opt} by $\Gamma_{ph}, \Gamma_S, \Gamma^*_{opt}$, which are normalized to Z_0 and defined by

$$\Gamma_x = \frac{Z_x - Z_0}{Z_x + Z_0} \tag{7.84}$$

where $x = ph$, s, and opt. It is useful to obtain the S parameters of the third-order noise-matching network defined in the matrix form as shown in Equation 7.85 and Figure 7.16.

$$S = \begin{bmatrix} S_{11} & S_{12} \\ S_{21} & S_{22} \end{bmatrix} \tag{7.85}$$

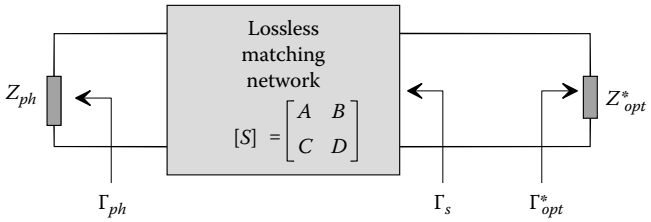

FIGURE 7.16
Lossless matching network with source and load impedances.

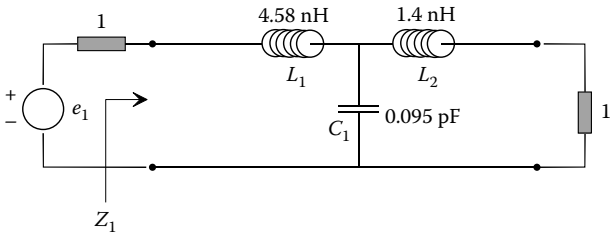

FIGURE 7.17
Matched third-order noise-matching network to find the *S* parameters.

From Figure 7.17, we find Z_1 given by

$$Z_1 = sL_1 + \left(sC_1 + \frac{1}{1+sL_2} \right)^{-1} = \frac{s^3 C_1 L_1 L_2 + s^2 C_1 L_1 + s\left(L_1 + L_2\right) + 1}{s^2 C_1 L_2 + sC_1 + 1} \tag{7.86}$$

Applying the circuit theory of the *T*-Network and by substituting (7.85), we obtain

$$S_{11} = \frac{Z_1 - 1}{Z_1 + 1} = \frac{s^3 C_1 L_1 L_2 + s^2\left(C_1 L_1 - C_1 L_2\right) + s\left(L_1 + L_2 - C_1\right)}{s^3 C_1 L_1 L_2 + s^2\left(C_1 L_1 + C_1 L_2\right) + s\left(L_1 + L_2 + C_1\right) + 2} \tag{7.87}$$

From circuit theory, S_{21} is given by

$$S_{21} = 2\sqrt{\frac{r_1}{r_2}}\left(\frac{V_2}{e_1}\right) \tag{7.88}$$

From Figure 7.17, we can obtain

$$\frac{V_2}{e_1} = \frac{1}{s^3 C_1 L_1 L_2 + s^2\left(C_1 L_1 + C_1 L_2\right) + s\left(L_2 + L_1 + C_1\right) + 2} \tag{7.89}$$

Hence, by substituting (7.89) into (7.87), we have

$$S_{21} = \frac{2}{s^3 C_1 L_1 L_2 + s^2\left(C_1 L_1 + C_1 L_2\right) + s\left(L_2 + L_1 + C_1\right) + 2} \tag{7.90}$$

Using the symmetrical property, the other two *S* parameters can be obtained as follows:

$$S_{22} = S_{11} = \frac{s^3 C_1 L_1 L_2 + s^2\left(C_1 L_1 - C_1 L_2\right) + s\left(L_1 + L_2 - C_1\right)}{s^3 C_1 L_1 L_2 + s^2\left(C_1 L_1 + C_1 L_2\right) + s\left(L_1 + L_2 + C_1\right) + 2} \tag{7.91}$$

$$S_{12} = S_{21} = \frac{2}{s^3 C_1 L_1 L_2 + s^2\left(C_1 L_1 + C_1 L_2\right) + s\left(L_2 + L_1 + C_1\right) + 2} \tag{7.92}$$

By using Equation 7.84, we can derive all the required reflection coefficients. First of all, consider the equivalent photodiode circuit shown in Figure 7.18.

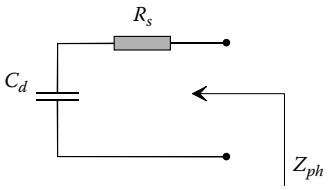

FIGURE 7.18
Equivalent circuit for photodiode.

Then, Z_{ph} can be found as

$$Z_{ph} = R_s + \frac{1}{sC_d} \tag{7.93}$$

From Equation 7.93, we have

$$\Gamma_{ph} = \frac{Z_{ph} - Z_0}{Z_{ph} + Z_0} \tag{7.94}$$

Then, we substitute Z_{ph} from (7.93):

$$\Gamma_{ph} = \frac{sC_d\left(R_s - 1\right) + 1}{sC_d\left(R_s + 1\right) + 1} \tag{7.95}$$

Knowing the S parameters and Γ_{ph}, we can obtain Γ_S as

$$\Gamma_s = S_{22} + \frac{S_{12}S_{21}\Gamma_{ph}}{1 - \Gamma_{ph}S_{11}} \tag{7.96}$$

and

$$\Gamma_{opt} = \Gamma_s = S_{22} + \frac{S_{12}S_{21}\Gamma_{ph}}{1 - \Gamma_{ph}S_{11}} \tag{7.97}$$

The equivalent input noise current density appearing across the photodiode junction capacitance can be expressed in terms of the reflection coefficients [9] as

$$i_{eq}^2 = 4kTR_s\left(\omega C_d\right)^2 \frac{\left(1 - \left|\Gamma_{opt}^*\right|^2\right)}{G_M\left|1 - \Gamma_s\Gamma_{opt}^*\right|^2}\left\{F_{\min}\left(1 - \left|\Gamma_s\right|^2\right) + \frac{4R_n}{Z_0}\frac{\left|\Gamma_s - \Gamma_{opt}\right|^2}{\left|1 + \Gamma_{opt}\right|^2}\right\}\Delta f \tag{7.98}$$

where

$F_{\min}$ and R_n can be obtained from the given data in Table 7.2
G_M is the transducer power gain of the lossless matching network

TABLE 7.2

Noise Parameters of the Packaged HEMT with 0.3 μm Gate Length

	Γ_{opt}			
Frequency (GHz)	**(Mag)**	**(Ang)**	$F_{\min}$ **(dB)**	R_n **(Ω)**
2	0.79	30	0.33	29
4	0.73	59	0.35	21
6	0.68	87	0.44	14.5
8	0.63	119	0.55	9.5
10	0.59	139	0.66	6
12	0.55	164	0.75	4

Our goal is to minimize the equivalent input noise current density. This can be done by minimizing the photodiode junction capacitance C_d, the series resistance R_s of the photodiode, the noise figure $F_{\min}$, and the noise resistance R_n, and by maximizing the transducer power gain. Among these parameters in Equation 7.98, only the transducer power gain G_M and the output reflection coefficient Γ_s are related to the noise-matching network and these may be optimized by design. The transducer power gain can be expressed in terms of the reflection coefficients [9] and is defined by

$$G_M = 1 - \left| \frac{(1+\Gamma_s)(1-\Gamma_{opt}) - (1-\Gamma_s)(1+\Gamma_{opt})}{(1+\Gamma_s)(1-\Gamma_{opt}^*) + (1-\Gamma_s)(1+\Gamma_{opt}^*)} \right|^2 \tag{7.99}$$

The transducer power gain has its maximum value of unity when $\Gamma_s = \Gamma_{opt}$. This condition is equivalent to the output admittance of the noise-matching network being conjugately matched to the complex conjugate of the optimum source admittance to suppress the noise spectral density at high frequency region (Figure 7.19).

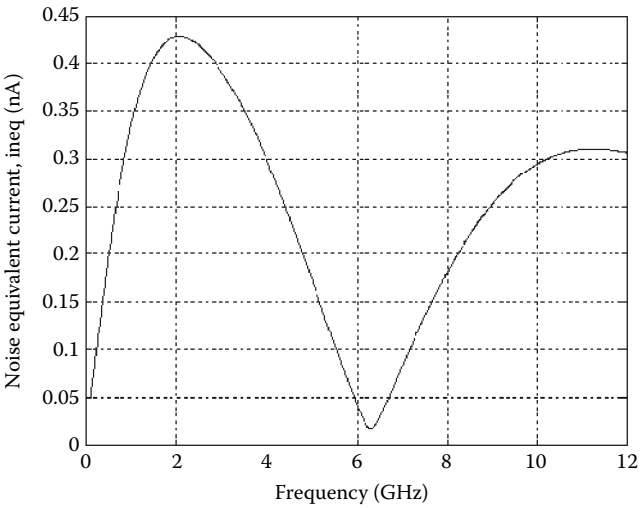

FIGURE 7.19
Equivalent input noise current density of the HEMT noise–matched front-end receiver.

7.7 Trans Impedance Amplifier: Differential and Nondifferential Types

The trans impedance amplifier (TIA) is the critical amplifying device, which is to be connected in cascade with a high-speed PD to provide the preamplification of the current produced in the PD to the voltage output whose level would be appropriate for an analog to digital conversion so that digitized signals can then be processed in the digital domain by a digital signal processor (DSP). The total equivalent noises referred to the input port of this amplifier are very critical to the impact of the SNR of the optical receiver. The method for calculations of noise processes and noise currents as well as the total equivalent noises referred to the input is given in Section 7.4.4.

Traditionally, single input or nondifferential input TIA has been extensively exploited over the years [10]. However, currently, differential TIAs (DTIA) offer wider bandwidth and high differential trans impedance gain of around 3000–5000 Ω over the 30–40 GHz bandwidth by Si–Ge technology so that the transition frequency f_T can reach 280 GHz* [11,12]. However, these differential TIAs [13] are limited in their dynamic range and normally an automatic gain control stage would be required. A typical setup of PD pair and a differential TIA is shown in Figure 7.20. Typical circuit diagrams of the DTIA employing Si–Ge and InP are shown in Figure 7.21a and b, respectively, in which the main differential long-tail pair is followed by two common collector stages connected to the differential output of this long-tail pair. The outputs of these stages are then fed back in by a shunt feedback to obtain the highest transfer impedance and wideband property. The outputs are used as feedback for the differential input. These differential ports are then fed into a further differential voltage gain stage (without any feedback stage).

The DTIA can offer a transfer impedance of 4000–5000 Ω. Thus, with an optical signal average power input of 0 dBm (or 1 mW) and a responsivity of the PD of 0.9–1.0 A/W, a current of

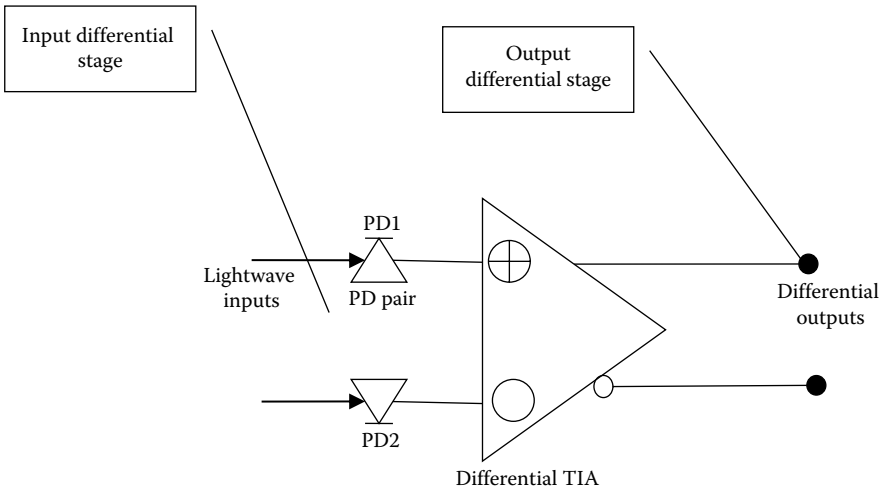

FIGURE 7.20
Generic schematic of differential TIA and a PD pair.

* The transition frequency f_T is defined as the frequency at which the short-circuit current gain of a transistor equals unity.

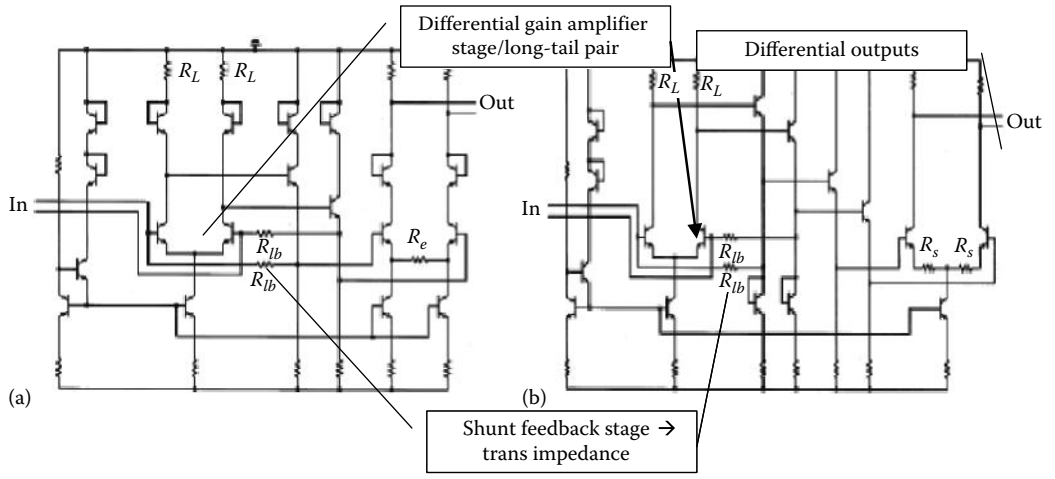

FIGURE 7.21
Typical circuit topologies of (a) DTIA by Si–Ge and (b) InP technology. (Extracted from Ref. [14].)

1 mA is produced and fed into the differential TIA. This in turn produces a differential voltage of 4–5 V signals at the output. Unfortunately, this level will saturate the outputs of the DTIA. So, normally an automatic gain control stage is employed to increase the dynamic range of the optical receiver. The parameters of differential TIA with the input-referred current noise of the InP TIA are approximately 25 $\text{pA}/\sqrt{\text{Hz}}$ on average to a bandwidth of 40 GHz.

It is noted that one of the main problems with DTIA is the high transimpedance gain that would lead to the saturation level of the output voltage, which results in significant errors. The saturated level would remain high for some time after the "1" level returning back to "0" level. Users of differential TIA must pay attention to this problem to consider DTIA with incorporated automatic gain control (AGC) stage.

7.8 Concluding Remarks

This chapter has addressed optical receivers in which the electronic currents are generated when the optical energy/power from the modulated optical signals is absorbed by the photosensitive regions directly. The noise generation process is described as are related to small-signal models of electronic preamplifiers. An equivalent noise current as seen at the input port of the electronic preamplifier is presented as well as the method to derive it for the front-end amplifier. Both FET and BJT types are given. Further, the effects of the pulse shape on the output signals are also given as related to the transfer function of the electronic preamplifier. A noise-matching network at the front end of the optical preamplifier would reduce the noise effects at high frequency and this is crucial in the design of ultra-wide band optical receiver.

These noise models can be integrated into coherent receivers, which are described in the chapter 8. For coherent optical receiver a local oscillator, a powerful laser, mixes the optical signals with its output field and gives a beating signal in the PD as a result of the

square-law property. The phase and amplitude of the optical signals are preserved in the electronic domain and thus processing in the electronic domain can be performed to extract the digital and analog property of the original signals.

7.A Appendix: Noise Equations

Referring to the small signal and noise model given in Figures 7.22 and 7.23, the noises generated in a transistor can be expressed as:

$$\begin{aligned} di_1^2 &= 4k_B T g_B df \\ di_2^2 &= 2qI_C df \simeq 2k_B T g_m df \\ di_3^2 &= 2qI_B df \simeq 2k_B T(1-\alpha_N) g_m df \\ di_4^2 &= \text{shot noise of diodes and thermal noise of bias in } g_B \text{ resistors} \end{aligned} \tag{7.100}$$

where
g_B is the base conductance
I_C is the collector bias current
I_B is the base bias current

From nodal analysis of the small-signal equivalent circuit given in Figure 7.23, we can obtain the relationship

$$\begin{bmatrix} Y_s + g_B & -g_B & 0 \\ -g_B & g_B + y_1 + y_f & -y_f \\ 0 & g_m - y_f & y_f + y_2 \end{bmatrix} \begin{bmatrix} V_1 \\ V_2 \\ V_3 \end{bmatrix} = \begin{bmatrix} i_{eq} - i_{N1} \\ i_{N1} + i_{N3} \\ i_{N2} \end{bmatrix} \tag{7.101}$$

Hence, V_3, V_2, and V_1 can be found by using Euler's rule for the matrix relationship

$$V_3 = \frac{\Delta_{13}}{\Delta}(i_{eq} - i_{N1}) + \frac{\Delta_{23}}{\Delta}(i_{N1} + i_{N3}) + \frac{\Delta_{33}}{\Delta}(i_{N2}) \tag{7.102}$$

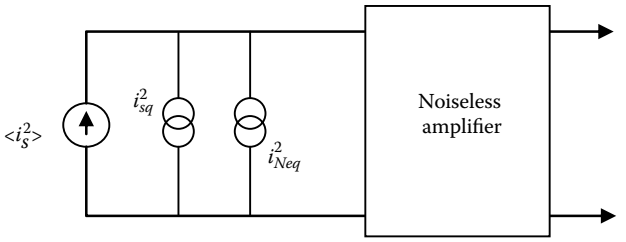

FIGURE 7.22
Equivalent noise current at the input and noiseless amplifier model, i_{Sq}^2 is the quantum shot noise, which is signal dependent, i_{Neq}^2 is the total equivalent noise current referred to the input of the electronic amplifier.

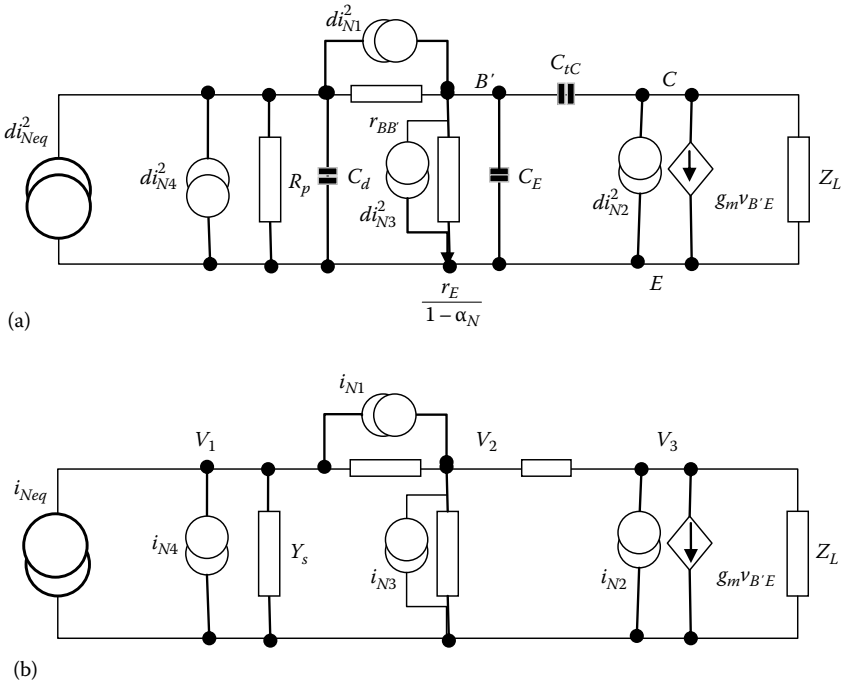

FIGURE 7.23
(a) Approximated noise equivalent and small-signal model of a BJT front end. (b) Generalized noise and small-signal model circuit. Note that $r_B = r_{sd} + r_{BB'}$ and $C_d = C_p + C_i$ with $r_{BB'}$ is the base resistance, r_{sd} is the diode resistance, C_d is the photodiode capacitance, and C_i is the input capacitance.

Hence, the noise currents as referred to the input are

$$d(i_1'^2) = \left|\frac{Y_s}{g_B}\right|^2 dI_1^2 = \omega_2 C_s^2 r_B 4kTdf \tag{7.103}$$

$$d(i_2'^2) = \left|(Y + y_1 + y_f) + \frac{Y_s}{g_B}(y_1 + y_f)\right|^2 \left|\frac{1}{y_f - g_m}\right|^2 = \left|\frac{1}{y_f - g_m}\right|^2 dI_2^2$$

$$= \left(\frac{1}{\beta_N r_E^2} + \omega^2\left(C_0^2 - \frac{2C_B r_B}{\beta_N r_E}\right) + \omega^4 2C_s r_B C_B^2\right) 2kTr_E df \tag{7.104}$$

$$d(i_3'^2) = \left|\frac{Y_s}{g_B} + 1\right|^2 dI_3^2 = \left(\omega C_s^2 r_B^2 + 1\right)\frac{2kT}{\beta r_E} df \tag{7.105}$$

in which we have assumed that $\omega C_f \ll g_m$.

Problems

7.1 Suppose that we have an ideal PD that produces no dark current, that is, no electron-hole pairs are generated in the absence of an optical pulse. Assume that an optical pulse of energy b_1 falls on the PD in an interval T. This can be interpreted by the receiver as a "0" pulse if no electron-hole pairs are generated with the present pulse. Show that if the probability of this pulse being interpreted as a "0" is 10^{-9} then $b_1 = 36h\upsilon/\eta$ where η is the quantum efficiency of the PD.

Assume that the average power detected, $p(t)$, with this PD is given by $b_1 B_r/2$, where B_r is the system bit rate, and also assume that an equal number of "1s" and "0s" is received. Show that if the quantum efficiency is 1.0, the minimum optical power required at a BER of 10^{-9} for a bit rate of 155 Mb/s is about −63 dBm at an operating wavelength of 810 nm. What is the required optical power for the system operating at 1300 nm?

7.2 A 1310 nm digital optical receiver is operating at 2.2 Gb/s and has an effective noise bandwidth of 1.5 GHz. The pin photodiode has negligible dark current and 90% quantum efficiency. The equivalent input resistance is 100 Ω and the equivalent noise current is 2.5 pA/(Hz)$^{1/2}$. Calculate the receiver sensitivity corresponding to a BER of 10^{-9}. How much does it change if the receiver is designed to operate reliably up to a BER of 10^{-12}.

7.3 Consider an optical receiver operating at 140 Mb/s in PCM systems. It has an APD with an x-factor of 0.8 and a responsivity of 0.7 A/W; its avalanche gain depends on the bias reverse voltage. An electronic amplifier, which follows the PD, has an equivalent noise current density of 10.0 nA/(Hz)$^{1/2}$ and a 3 dB bandwidth of 100 MHz. For a system BER of 10^{-9}, calculate and plot the receiver sensitivity as a function of the avalanche gain between 10 and 70. Comment on the receiver performance with this range of avalanche gain.

7.4 An optical receiver consists of a pin photodiode or an APD followed by an electronic amplifier with the following characteristics:

PIN-PD

- InGaAs type with a quantum efficiency of 0.8 average over the wavelength region of 1.2–1.7 μm
- Dark current noise of 0.05 nA
- Total rise time and fall time of 1.0 ns
- Diode capacitance at a typical reverse bias of 0.5 pF.

APD

- Ge type with an x-factor of 0.9
- An average avalanche gain of 30 over the wavelength range of 1200–1700 nm
- Total dark current of 7.0 nA
- Total rise and fall time of 1.0 ns

Electronic amplifier

High impedance type front end followed by a main amplifier and equalizer with a total equivalent noise spectral density of 0 pA/(Hz)$^{1/2}$ and an overall bandwidth of 200.0 MHz.

For a PCM system bit rate of 140 Mb/s and a BER of 10^{-9}, find the energy of the "1" pulse required at the input of the PD. You may assume that the probability density distribution of receiving "1" and "0" are Gaussian and equal. Hence, deduce the receiver sensitivity in dBm.

This receiver is to be considered for a new receiver configuration that is to be specified for two optical communication links with the following requirements:

(b1) Link 1: Optical communications between two supercomputers operating at a bit rate of 1.2 Gb/s.

(b2) Link 2: PCM 140 Mb/s optical communication transmission systems using a single-mode optical fiber for linking two towns *A* and *B* 200 km apart. Bi-directional transmission at 1300 and 1550 nm wavelength regions. The specification of the standard fiber is given in the ECS4344 lectures.

A number of optoelectronic components such as PDs and sources by Fujitsu are available. Select appropriate components and design the link.

7.5 An optical fiber communications link has the following components:

- Optical transmitter: InGaAsP laser diode operating in the region of about 1320 nm with a spectral width of 2.0 nm.
- The laser power coupled to the single-mode fiber of 10 mm diameter pigtail of 1.0 mW.
- The fiber is single mode at 1300 nm wavelength with a cutoff wavelength of 1190 nm.
- The total fiber loss is 0.35 dB/km.
- The receiver consisting of an InGaAs pin photodiode, which has a sensitivity of P dBm approximately given by $P = 18.5\ \text{Log10}\ (B) - 68.5$ dBm where *B* is the bit rate in Mb/s.

For a bit rate of 1–1000 Mb/s, plot the attenuation-limited transmission distance including a 0.1 dB connector loss at each end and a 3.0 dB system operating margin.

References

1. R.C. Alferness, Waveguide electrooptic modulators, *IEEE Journal of Microwave Theory and Techniques*, MTT-30, 1121–1137, 1982.
2. R.C. Booth, $LiNbO_3$, integrated optic devices for coherent optical fiber systems, *Thin Solid Films*, 126, 167–176, 1985.
3. S. Ritchie and A.G. Steventon, The potential of semiconductors for optical-integrated circuits, in *Proceedings of the Conference on Digital Optical Circuit Technology*, NATO, France, vol. 362, pp. 1111–1120, 1985.
4. S.D. Personick, Receiver design for digital fiber optic communications systems, *Bell System Technical Journal*, 52, 843–886, July–August 1973.
5. S.D. Personick, Optical detectors and receivers, *IEEE Journal of Lightwave Technology*, 26(9), 1005–1020, 2008.
6. J.L. Hullet and T.V. Muoi, A feedback receive amplifier for optical transmission systems, *IEEE Transactions on Communications*, 24(10), 1180–1185, 1976.
7. R. Dogliotti, G. Luvison, and G. Pirani, Error probability in optical fiber transmission systems, *IEEE Transactions on Information Theory*, IT-25(2), 170–178, 1979.

8. S.D. Personick, *Optical Fiber Transmission Systems*, Plenum Publishing, New York, 1980.
9. Y. Yamamoto, Receiver performance evaluation of various digital optical modulation-demodulation systems in the 0.5–1.0 μm wavelength region, *IEEE Journal of Quantum Electronics*, QE-16, 1251–1259, 1980.
10. T. van Muoi, Receiver design for high speed optical fiber systems, *IEEE Journal of Lightwave Technology*, 2(3), 243–266, 1984.
11. P. Kempf and M. Racanelli, Silicon germanium BiCMOS technology, *IEEE GaAs IC Symposium Digital*, 3–6, October 2002.
12. B. Jagannathan et al., Self-aligned site NPN transistors with 285 GHz $f_{\max}$ and 207 GHz f_T in a manufacturable technology, *IEEE Electron Device Letters*, 23, 258–260, May 2002.
13. J.S. Weiner et al., SiGe differential trans-impedance amplifier with 50-GHz bandwidth, *IEEE Journal of Solid-State Circuits*, 38(9), 1512, September 2003.
14. Maruf Newaz Ahmed, Transimpedance amplifier (TIA) design for 400 Gb/s optical fiber communications, Master thesis dissertation, Virginia Polytechnic Institute and State University, Blacksburg, VA, May 2013.

8

Digital Coherent Optical Receivers

Chapter 7 has presented the detection of optical signals by direct conversion of optical signal power into electronic current in the photodiode (PD) and then electronic preamplification. This chapter describes the fundamentals of coherent receivers including the detection of optical signals by mixing optical fields with that of a local oscillator (LO), a higher amplitude laser of the same or different frequency so that their beating product would result in demodulated signals preserving the signals in both phase and amplitude characteristics in the electronic domain. When the frequencies of the signal and LO are the same, then the reception is a homodyne type. If they are different, then the process is a heterodyne type. Under practical homodyne reception, there would be some small frequency difference and this is normally termed as intradyne reception. Optical preamplification for coherent detection is treated in Chapter 9. The electrical output of the coherent reception stage is then converted into the digital domain via an analog-to-digital converter (ADC) and then processed in digital signal processing (DSP) systems. This type of optical receiver is termed as the Digital Coherent Optical Receiver.

8.1 Introduction

With the exponential increase in data traffic, especially due to the demand for ultrabroad bandwidth driven by multimedia applications, cost-effective ultra-high-speed optical networks have become highly desired. It is expected that Ethernet technology will not only dominate access networks but will also become the key transport technology of the next generation metro/core networks. 100 Gigabit Ethernet (100 GbE) is currently considered to be the next logical evolution after 10 Gigabit Ethernet (10 GbE). Based on the anticipated 100 GbE requirements, 100-Gb/s data rate of serial data transmission per wavelength is required. To achieve this data rate while complying with current system design specifications such as channel spacing, chromatic dispersion, and polarization mode dispersion (PMD) tolerance, coherent optical communication systems with multilevel modulation formats will be desired, since they can provide high spectral efficiency, high receiver sensitivity, and potentially high tolerance to fiber dispersion effects [1]. Compared to conventional direct detection in intensity-modulation/direct-detection (IMDD) systems, which only detect the intensity of the light of the signal via the square law detection in the PD, coherent detection can retrieve the phase information of the light via the beating product of the signal and the LO, and therefore, can tremendously improve receiver sensitivity.

Coherent optical receivers are important components in long haul optical fiber communication systems and networks to improve the receiver sensitivity and achieve extra transmission distance. Coherent techniques were considered for optical transmission systems in the 1980s when the extension of repeater distance between spans was pushed to 60 km instead of 40 km for single-mode optical fiber at the bit rate of 140 Gb/s. However,

in the late 1980s the invention of optical fiber amplifiers overtook this attempt, and coherent transmission was no longer of much interest for further development at the time. Transmission systems over optically amplified and dispersion compensating multiple spans were then extensively deployed for terrestrial and underseas networks with bit rates reaching 10Gbps and 40Gbps and dense-wavelength division multiplexing (DWDM) technique to offer total capacity in the Tera-bits/s. However, the accumulation of the amplified stimulated emission (ASE) over the link limits the transmission distance.

Recently, interests in coherent optical communications have attracted significant and deployment of ultra-high bit rate (multi-Tera-bps) DWDM optical systems and networks. The motivation has been the result of (1) the use of optical amplifiers in cascade fiber spans has added significant noises and limited the transmission distance; (2) the advances in digital signal processors whose sampling rate can reach few tens of Giga-samples/s, allowing the processing of beating signals to recover the phase or phase estimation (PE); (3) the availability of advanced signal processing algorithms such as Viterbi and Turbo algorithms; and (4) the differential coding and modulation and detection of such signals not requiring optical phase lock loop (OPLL), and allowing self-coherent and digital signal processing to recover transmitted signals.

As described in Chapter 7, in a typical arrangement of an optical receiver, the optical signals are detected by a PD (a PIN diode or APD or a photon counting device) and electrons generated in the photodetector are then electronically amplified through a front-end electronic amplifier. The electronic signals are then decoded for recovery of original format. However, when the fields of incoming optical signals are mixed with those of a LO whose frequency can be identical or different to that of the carrier, the phase and frequency property of the resultant signals reflect those of the original signals. Coherent optical communication systems have also been reviving dramatically due to electronic processing in the digital domain (DSP) following an ultra-high sampling ADC. Furthermore, availability of stable narrow linewidth has also accelerated this DSP-based coherent reception.

This chapter deals with the analysis and design of coherent receivers with OPLL and the mixing of optical signals and that of the LOs in the optical domain and detection by the opto-electronic receivers following this mixing. Both the optical mixing and photodetection devices act as the fundamental elements of a coherent optical receiver. Depending on the frequency difference between the lightwave carrier of the optical signals and that of the LO, the coherent detection can be termed as heterodyne or homodyne detection. For heterodyne detection, there is a difference in the frequency and thus the beating signal falls in a passband region in the electronic domain. Thus, all the electronic processing at the front end must happen in this passband region. In homodyne detection, there is no frequency difference and thus the detection is in the base band of the electronic signal. Both cases would require a locking of the LO and carrier of the signals. An OPLL is thus briefly treated in this chapter.

DSP for coherent transmission systems and its reception subsystems is very critical for overcoming several difficulties of the originally proposed coherent techniques in the 1980s. This is due to the advanced technological development of ultra-high-speed ADC converters and digital-to-analog (DAC) converters, which enables the predistortion and pulse shaping of the input sequence so as to effectively use the spectrum and compensation of the linear distortion impairment. Hence, algorithms employed in wireless communication systems have been extensively applied for DSP-based coherent transmission. A number of basic algorithms are given here in this chapter. In Chapter 15, more advanced algorithms will be described.

This chapter is organized as follows: Section 8.2 gives an account of the components of coherent receivers; Section 8.3 outlines principles of optical coherent detection under heterodyne or homodyne technique; and Section 8.4 gives details of OPLL, which is a very important development in modern optical coherent detection. Section 8.5 presents some basic processing algorithms for coherent reception. This is followed by Section 8.6 dealing with the analysis of coherent reception. Finally, Section 8.7 gives some concluding remarks. A self-homodyne reception Simulink® model is available (see Section 8.4) for readers who can modify with additional LO source and a hybrid coupler in Simulink. In association with other widely available Simulink "signal processing" tool boxes, readers can further develop alternative models for treatments of distorted signals propagating through fibers under linear or nonlinear impairments as well as other physical effects in ADC or DAC or delay skew short falls under sampling at ultra-high speeds.

8.2 Coherent Receiver Components

The design of an optical receiver depends on the modulation format of the signals that are transmitted through the transmitter. The modulation of the optical carrier can be in the form of amplitude, phase, and frequency. Furthermore, phase shaping also plays a critical role in the detection and the bit error rate of the receiver and, consequently, the transmission systems. In particular, it is dependent on the modulation in analog or digital, Gaussian or exponential pulse shape, on–off keying or multiple levels, and so on.

Figure 8.1 shows the schematic diagram of a digital coherent optical receiver, which is similar to the direct detection receiver but with an optical mixer at the front end. However, the phase of the signals at the base or passband of the detected signals in the electrical domain would remain in the generated electronic current and voltages at the output of the electronic preamplifier. An optical front end is an optical mixer combining the fields of the optical waves of the local laser and the optical signals so that the envelope of the optical signals can beat with each other to a product with the sum and difference of the frequencies of the lightwaves. Only the lower-frequency term that falls within the absorption range of the photodetector is converted into the electronic current preserving both the phase and amplitude of the modulated signals.

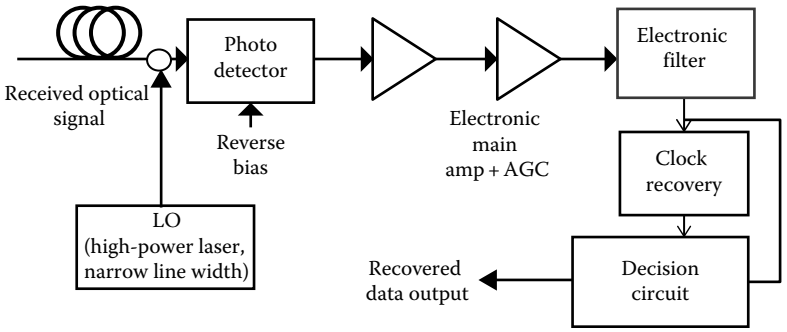

FIGURE 8.1
Schematic diagram of a digital optical coherent receiver with an additional LO mixing with the received optical signals before detection by an optical receiver.

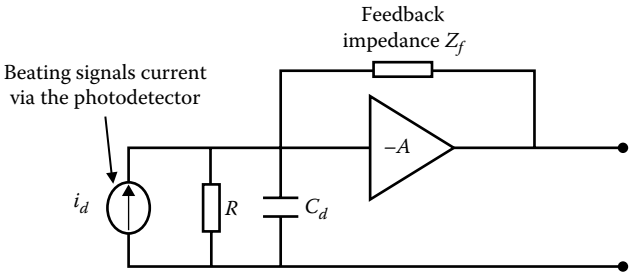

FIGURE 8.2
Schematic diagram of the electronic preamplifier in an optical receiver with transimpedance electronic amplifier at the front end. The current source represents the electronic current generated in the photodetector due to the beating of the LO and the optical signals. C_d, is the PD capacitance.

The front end of an optical receiver, very much the same as that of the direct detection, is connected to the optical processing front end consisting of a photodetector for converting lightwave energy into electronic currents; an electronic preamplifier for further amplification of the generated electronic current; an electronic equalizer for bandwidth extension, usually in voltage form; a main amplifier for further voltage amplification; a clock recovery circuitry for regenerating the timing sequence; and a voltage-level decision circuit for sampling the waveform for the final recovery of the transmitted and received digital sequences. Therefore, the opto-electronic preamplifier is followed by a main amplifier with an automatic control to regulate the electronic signal voltage to be filtered and then sampled by a decision circuit with synchronization by a clock recovery circuitry (Figures 8.1 and 8.2).

In in-line fiber, the optical amplifier can be incorporated in front of the photodetector to form an optical receiver with an optical amplifier front end to improve its receiving sensitivity. This optical amplification at the front end of an optical receiver will be treated in the chapter dealing with optical amplification processes.

The structure of the receiver consists of four parts: the optical mixing front; the front end section; the linear channel of the main amplifier and AGC, if necessary; and the data recovery section. The optical mixing front end performs the summation of the optical fields of the LO and that of the optical signals. Polarization orientation between these lightwaves is very critical in order to maximize the beating of the additive field in the PD. Depending on whether the frequency difference is finite or null between these fields when the resulting electronic signals are derived from the detector, the electronic signals can be in the base band or the pass band, and the detection technique is termed as the heterodyne or homodyne technique, respectively.

8.3 Coherent Detection

Optical coherent detection can be distinguished by the "demodulation" scheme in communication techniques in association with following definitions: (1) Coherent detection is the mixing between two lightwaves or optical carriers, one is information bearing lightwaves and the other an LO with an average energy much larger than that of the signals; while (2) Demodulation refers to the recovery of baseband signals from the electrical signals.

A typical schematic diagram of a coherent optical communication employing guided wave medium and components is shown in Figure 8.1 in which a narrow-band laser incorporating an optical isolator cascaded with an external modulator is usually the optical transmitter. Information is fed via a microwave power amplifier to an integrated optic modulator, commonly used $LiNbO_3$ or electro-absorption (EA) types. The coherent detection is a principal feature of coherent optical communications which can be further distinguished with heterodyne and homodyne techniques depending on whether there is a difference or not between the frequencies of the LO and that of the carrier of the signals. An LO is a laser source whose frequency can be tuned and made approximately equivalent to a monochromatic source, using a polarization controller also to match its polarization with that of the information-bearing carrier. The LO and the transmitted signal are mixed via a polarization maintaining coupler and then detected by a coherent optical receiver. Most of the previous coherent detection schemes are implemented in a mixture of a photonic domain and an electronic/microwave domain.

Coherent optical transmission returns into the focus of research. One significant advantage is the preservation of all the information of the optical field during detection, leading to enhanced possibilities for optical multilevel modulation. This chapter investigates the generation of optical multi-level modulation signals. Several possible structures of optical *M* phase-shift keying (*M*-PSK) and *M* quadrature amplitude modulation (*M*-QAM) transmitters are shown and theoretically analyzed. Differences in the optical transmitter configuration and the electrical driving lead to different properties of the optical multilevel modulation signals. This is shown by deriving general expressions applicable to every *M*-ary-PSK and *M*-ary-QAM modulation format and exemplarily clarified for Square-16-QAM modulation.

Coherent receivers are classified as synchronous and asynchronous. Synchronous detection requires an OPLL that recovers the phase and frequency of the received signals to lock the LO to that of the signal so as to measure the absolute phase and frequency of the signals relative to that of the LO. Thus synchronous receivers allow direct mixing of the bandpass signals and the base band; this technique is termed as homodyne reception. For asynchronous receivers, the frequency of the LO is approximately the same as that of the receiving signals and no OPLL is required. In general, the optical signals are first mixed with an intermediate frequency (IF) oscillator that is about two to three times that of the 3 dB passband. The electronic signals can then be recovered using an electrical phase lock loop (PLL) at a lower carrier frequency in the electrical domain. The mixing of the signals and an LO of an IF frequency is referred to as heterodyne detection.

If no LO is used for demodulating the digital optical signals, then differential or self-homodyne reception may be utilized, or classically termed as autocorrelation reception process or self-heterodyne detection.

Coherent communication was an important technique in the 1980s and the early 1990s, but the research was interrupted with the advent of optical amplifiers in the late 1990s that offered up to 20 dB gain without difficulty. However, at present, coherent systems have emerged again into focus, because of the availability of digital signal processing, low-priced components, the partly relaxed receiver requirements at high data rates, and several other advantages that coherent detection provides. The preservation of the temporal phase of coherent detection has enabled new methods for adaptive electronic compensation of chromatic dispersion. With regard to wavelength division multiplexing (WDM) systems, coherent receivers offer tunability and allow channel separation via steep electrical filtering. Furthermore, only the use of coherent detection permits the convergence to the ultimate limits of spectral efficiency. To reach higher spectral efficiencies, the use of multilevel modulation is required. Here, again coherent systems are beneficial because all the information of

the optical field is available in the electrical domain. That way, complex optical demodulation with interferometric detection—which has to be used in direct detection systems—can be avoided, and the complexity transferred from the optical to the electrical domain. Several different modulation formats based on the modulation of all four quadratures of the optical field were proposed in the early 1990s, describing the possible transmitter and receiver structures and calculating the theoretical bit error rate (BER) performance. However, a more detailed and practical investigation of multilevel modulation coherent optical systems for today's networks and data rates is missing so far.

Currently, coherent reception has attracted significant interest for the following reasons: (1) the received signals of the coherent optical receivers are in the electrical domain that is proportional to that in the optical domain. This, in contrast to the direct detection receivers, allows exact electrical equalization or exact PE of the optical signals. (2) Using heterodyne receivers, DWDM channels can be separated in the electrical domain by using electrical filters with a sharp roll of the passband to the cut-off band. Presently, the availability of ultra-high sampling rate DSP allows users to conduct filtering in the DSP in which the filtering can be effected with ease.

However, there are disadvantages in using coherent receivers, namely: (1) Coherent receivers are polarization sensitive and require polarization tracking at the front end of the receiver; (2) Homodyne receivers require OPLL and electrical PLL, and heterodyne receivers need control and feedback circuitry, optical or electrical, which may be complicated; and (3) For differential detection, the compensation may be complicated because of the differentiation nature of the receiver.

In a later chapter, where some advanced modulation formats are presented for optically amplified transmission systems, the use of photonic components is extensively exploited to take advantage of the advanced technology of integrated optics, planar lightwave circuits. Modulation formats of signals depend on whether the amplitude, the phase, or the frequency of the carrier is manipulated as mentioned in Chapter 2. In this chapter, the detection is coherently converted into the IF range in the electrical domain and the signal envelope. The down-converted carrier signals are detected and then recovered. Both binary-level and multilevel modulation schemes employing amplitude, phase, and frequency shift keying modulation are described in this chapter (Figure 8.3).

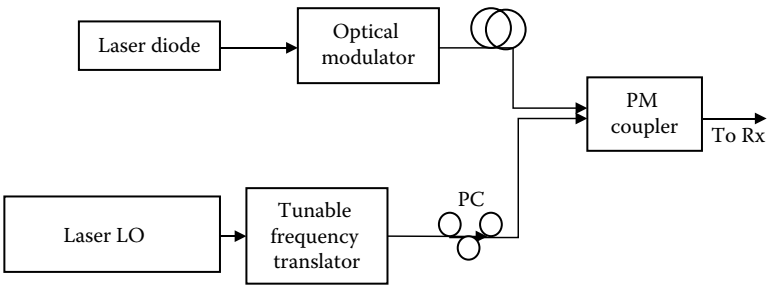

FIGURE 8.3
Typical arrangement of coherent optical communications systems. Laser diode/laser cavity (LD/LC) is a very narrow linewidth laser diode as a LO without any phase locking to the signal optical carrier. Phase modulator (PM) coupler is the polarization maintaining fiber-coupled device. PC, polarization controller. (From Alferness, R.C., *IEEE J. Quant. Electron*., QE-17, 946, 1981; Stallard, W.A. et al., *IEEE J. Lightwave Tech*., LT-4(7), 852, July 1986.)

8.3.1 Optical Heterodyne Detection

The basic configuration of optical heterodyne detection is shown in Figure 8.4. The LO whose frequency can be higher or lower than that of the carrier is mixed with the information-bearing carrier thus allowing down or up conversion of the information signals into the IF range. The down-converted electrical carrier and signal envelope is received by the photodetector. This combined lightwave is converted by the PD into electronic current signals that are then filtered by an electrical bandpass filter (BPF) and then demodulated by a demodulator. A low-pass filter (LPF) is also used to remove higher-order harmonics of the nonlinear detection photodetection process, the square-law detection. Under the use of an envelope detector, the process is asynchronous, hence the name term asynchronous detection. If the down-converted carrier is recovered and then mixed with IF signals, then this is synchronous detection. It is noted that the detection is conducted at the IF range in electrical domain, hence there needs of controlling of the stability of the frequency spacing between the signal carrier and that of the LO. That means the mixing of these carriers would result in an IF carrier in the electrical domain prior to the mixing process or envelope detection to recover the signals.

The coherent detection thus relies on the electric field component of the signal and the LO. The polarization alignment of these fields is critical for optimum detection. The electric field of the optical signals and the LO can be expressed as

$$E_s(t) = \sqrt{2P_s(t)}\cos\{\omega_s t + \phi_s + \phi(t)\} \tag{8.1}$$

$$E_{LO} = \sqrt{2P_{LO}}\cos\{\omega_{LO} t + \phi_{LO}\} \tag{8.2}$$

where

$P_s(t)$ and P_{LO} are the instantaneous signal power and average power of the signals and LO, respectively
$\omega_s t$ and ω_{LO} are the angular frequencies of the signal and LO, respectively
ϕ_s and ϕ_{LO} are the phases including any phase noise of the signal and the LO, respectively
$\phi(t)$ is the modulation phase

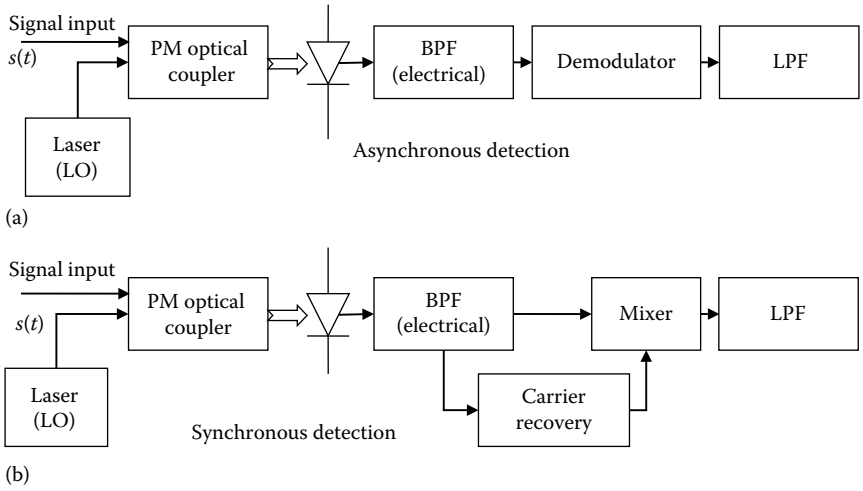

FIGURE 8.4
Schematic diagram of optical heterodyne detection: (a) asynchronous and (b) synchronous receiver structures. LPF, low-pass filter; BPF, bandpass filter; PD, photodetector.

The modulation can be the amplitude with the switching on and off (amplitude shift keying—ASK) of the optical power or phase or frequency with the discrete or continuous variation of the time-dependent phase term. For discrete phase, it can be phase shift keying (PSK), differential PSK (DPSK), or differential quadrature PSK (DQPSK), and when the variation of the phase is continuous, we have frequency shift keying if the rate of variation is different for the bit "1" and bit "0" as given in Chapter 4.

Under an ideal alignment of the two fields, the photodetection current can be expressed by

$$i(t) = \frac{\eta q}{h\upsilon}\left[P_s + P_{LO} + 2\sqrt{P_s P_{LO}}\cos\left\{(\omega_s - \omega_{LO})t + \phi_s - \phi_{LO} + \varphi(t)\right\}\right] \tag{8.3}$$

where the higher-frequency term (the sum) is eliminated by the photodetector frequency response, η is the quantum efficiency, q is the electronic charge, h is Plank's constant, and ν is the optical frequency.

Thus, the power of the LO dominates the shot noise process and at the same time boosts the signal level, hence enhancing the signal-to-noise ratio (SNR). The oscillating term is the beating between the LO and the signal and is proportional to the amplitude, which is the square root of the product of the power of the LO and the signal.

The electronic signal power S and shot noise N_s can be expressed as

$$\begin{aligned} S &= 2\Re^2 P_s P_{LO} \\ N_s &= 2q\Re(P_s + P_{LO})B \\ \Re &= \frac{\eta q}{h\nu} = \text{responsivity} \end{aligned} \tag{8.4}$$

where B is the 3 dB bandwidth of the electronic receiver. Thus, the optical signal to noise ratio (OSNR) can be written as

$$OSNR = \frac{2\Re^2 P_s P_{LO}}{2q\Re(P_s + P_{LO})B + N_{eq}} \tag{8.5}$$

where N_{eq} is the total electronic noise equivalent power at the input to the electronic preamplifier of the receiver. From this equation, we can observe that if the power of the LO is significantly increased so that the shot noise dominates over the equivalent noise, at the same time increasing the SNR, the sensitivity of the coherent receiver can only be limited by the quantum noise inherent in the photodetection process. Under this quantum limit, the $OSNR_{QL}$ is given by

$$OSNR_{QL} = \frac{\Re P_s}{qB} \tag{8.6}$$

8.3.1.1 ASK Coherent System

Under the ASK modulation scheme, the demodulator of Figure 8.4 is an envelope detector (in lieu of the demodulator) followed by a decision circuitry. That is the eye diagram is obtained and a sampling instant is established with a clock recovery circuit.

The synchronous detection would require a locking between the carrier frequencies, which is then tuned to the LO frequency to track the frequency component of the signal. The amplitude demodulated envelope can be expressed as

$$\begin{aligned} r(t) &= 2\Re\sqrt{P_s P_{LO}}\cos(\omega_{IF})t + n_x\cos(\omega_{IF})t + n_y\sin(\omega_{IF})t \\ \omega_{IF} &= \omega_s - \omega_{LO} \end{aligned} \tag{8.7}$$

The IF ω_{IF} is the difference between those of the LO and the signal carrier, n_x and n_y are the expected values of the orthogonal noise power components which are random variables:

$$\begin{aligned} r(t) &= \sqrt{[2\Re P_s P_{LO} + n_x]^2 + n_y^2}\cos(\omega_{IF}t + \Phi)t \\ \text{with } \Phi &= \tan^{-1}\frac{n_y}{2\Re P_s P_{LO} + n_x} \end{aligned} \tag{8.8}$$

8.3.1.1.1 Envelope Detection

The noise power terms can be assumed to follow a Gaussian probability distribution and are independent of each other with a mean zero and a variance σ, the probability density function (PDF) can thus be given as

$$p(n_x, n_y) = \frac{1}{2\pi\sigma^2}e^{\frac{-\left(n_x^2+n_y^2\right)}{2\sigma^2}} \tag{8.9}$$

and with respect to the phase and amplitude this equation can be written as [3]

$$p(\rho, \phi) = \frac{\rho}{2\pi\sigma^2}e^{\frac{-(\rho^2+A^2-2A\rho\cos\phi)}{2\sigma^2}} \tag{8.10}$$

where

$$\begin{aligned} \rho &= \sqrt{\left[2\Re\sqrt{P_s(t)P_{LO}} + n_s(t)\right]^2 + n_y^2(t)} \\ A &= 2\Re\sqrt{P_s(t)P_{LO}} \end{aligned} \tag{8.11}$$

The PDF of the amplitude can be obtained by integrating the phase amplitude PDF over the range of 0–2π and given as

$$p(\rho) = \frac{\rho}{\sigma^2}e^{\frac{-(\rho^2+A^2)}{2\sigma^2}}I_0\left\{\frac{A\rho}{\sigma^2}\right\} \tag{8.12}$$

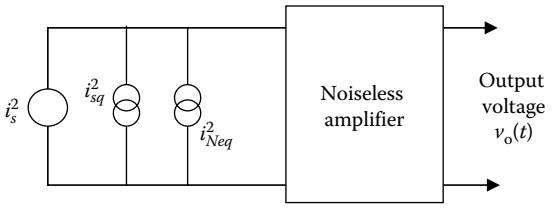

FIGURE 8.5
Equivalent current model at the input of the optical receiver, average signal current, and equivalent noise current of the electronic preamplifier as seen from its input port.

where I_0 is the modified Bessel function. If a decision level is set to determine the "1" and "0" level, then the probability of error and then the bit error rate BER can be obtained if assuming an equal probability of error between the "1s" and "0s" is equal, as

$$BER = \frac{1}{2}P_e^1 + \frac{1}{2}P_e^0 = \frac{1}{2}\left[1 - Q\left(\sqrt{2\delta}, d\right) + e^{-\frac{d^2}{2}}\right] \tag{8.13}$$

where Q is the Magnum function given in Chapter 7 and δ is given by

$$\delta = \frac{A^2}{2\sigma^2} = \frac{2\Re^2 P_s P_{LO}}{2q\Re\left(P_s + P_{LO}\right)B + i_{N_{eq}}^2} \tag{8.14}$$

When the power of the LO is much larger than that of the signal and the equivalent noise current power, then this SNR becomes

$$\delta = \frac{\Re P_s}{qB} \tag{8.15}$$

The physical representation of the detected current and the noises current due to the quantum shot noise and the noise equivalent of the electronic preamplification can be seen in Figure 8.5. The signal current can be derived from the output of the detection scheme, that from a photodetector or a back-to-back pair of photodetectors of a balanced receiver for detecting the phase difference of DPSK or DQPSK or continuous phase frequency shift keying (CPFSK) signals and converting to amplitudes.

The BER is optimum when setting its differentiation with respect to the decision level δ; an approximate value of the decision level can be obtained as

$$d_{opt} \cong \sqrt{2 + \frac{\delta}{2}} \quad \Rightarrow \quad BER_{ASK-e} \cong \frac{1}{2}e^{-\frac{\delta}{4}} \tag{8.16}$$

8.3.1.1.2 Synchronous Detection

ASK can be detected using synchronous detection,* and the BER is given by

$$BER_{ASK-S} \cong \frac{1}{2}erfc\frac{\sqrt{\delta}}{2} \tag{8.17}$$

* Synchronous detection is implemented by mixing the signals and a strong LO in association with the phase locking of the LO to that of the carrier.

8.3.1.2 PSK Coherent System

Under the phase shift keying modulation format, the detection is similar to that of Figure 8.4 for heterodyne detection, but after the BPF, an electrical mixer is used to track the phase of the detected signal (Figure 8.6). The received signal is given by

$$r(t) = 2\Re\sqrt{P_s P_{LO}}\cos[(\omega_{IF})t + \varphi(t)] + n_x \cos(\omega_{IF})t + n_y \sin(\omega_{IF})t \tag{8.18}$$

The information is contained in the time-dependent phase term $\phi(t)$.

When the phase and frequency of the voltage control oscillator (VCO) are matched with those of the signal carrier, then the received electrical signal can be simplified to

$$\begin{aligned} r(t) &= 2\Re\sqrt{P_s P_{LO}}\, a_n(t) + n_x \\ a_n(t) &= \pm 1 \end{aligned} \tag{8.19}$$

Under Gaussian statistical assumption, the probability of the received signal being a "1" is given by

$$p(r) = \frac{1}{\sqrt{2\pi\sigma^2}} e^{-\frac{(r-u)^2}{2\sigma^2}} \tag{8.20}$$

Furthermore, the probabilities of the "0" and "1" are assumed to be equal. We can obtain the BER as the total probability of the received "1" and "0" as

$$BER_{PSK} = \frac{1}{2} erfc(\delta) \tag{8.21}$$

8.3.1.2.1 Differential Detection

As observed in synchronous detection, there is a need for a carrier recovery circuitry, usually implemented using a PLL, which complicates the overall receiver structure. It is possible to detect the signal by a self-homodyne process by beating the carrier of one bit period onto that of the next consecutive bit; this is called differential detection. The detection process can be modified as shown in Figure 8.7 in which the phase of the IF carrier of one bit is compared with that of the next bit and a difference is recovered to represent the bit "1" or "0".

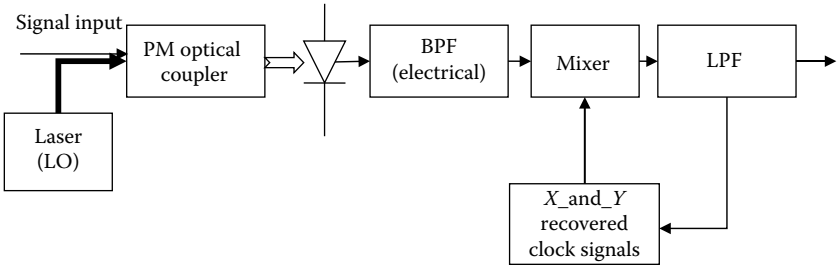

FIGURE 8.6
Schematic diagram of the optical heterodyne detection for PSK format.

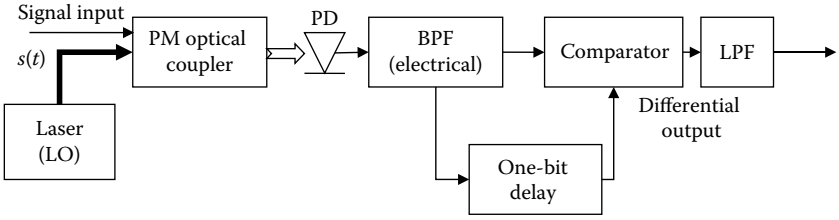

FIGURE 8.7
Schematic diagram of optical heterodyne and differential detection for PSK format.

This requires a differential coding at the transmitter and an additional phase comparator for the recovery process. In a later chapter on differential PSK, the differential decoding is implemented in the photonic domain via a photonic phase comparator in the form of an asymmetric Mach–Zehnder (MZ) interferometer incorporating a thermal tuning optical delay line in one path. The main motivation of the differential mode format is to eliminate the effects of degradation due to the variation in the frequency of the signal carrier. The BER can be expressed as

$$BER_{DPSK-e} \cong \frac{1}{2} e^{-\delta} \tag{8.22}$$

$$r(t) = 2\Re\sqrt{P_s P_{LO}}\cos[\pi A_k s(t)] \tag{8.23}$$

where
$s(t)$ is the modulating waveform
A_k represents the bit "1" or "0"

This is equivalent to the baseband signal, and the ultimate limit is the BER of the baseband signal.

The noise is dominated by the quantum shot noise of the LO with its square noise current given by

$$i_{N-sh}^2 = 2q\Re(P_s + P_{LO})\int_0^\infty |H(j\omega)|^2 d\omega \tag{8.24}$$

where $H(j\omega)$ is the transfer function of the overall receiver, normally a transimpedance of the electronic preamp and that of the following matched filter. As the power of the LO is much larger than the signal, integrating over the 3 dB bandwidth of the transfer function, this current can then be approximated by

$$i_{N-sh}^2 \simeq 2q\Re P_{LO} B \tag{8.25}$$

Hence, the SNR (power) is given by

$$SNR \equiv \delta \simeq \frac{2\Re P_s}{qB} \tag{8.26}$$

The BER is the same as that of a synchronous detection and is given by

$$BER_{homodyne} \cong \frac{1}{2} erfc\sqrt{\delta} \tag{8.27}$$

The sensitivity of the homodyne process is at least 3 dB better than that of the heterodyne, and the bandwidth of the detection is half of its counterpart due to the double-sideband nature of the heterodyne detection.

8.3.1.3 FSK Coherent System

The nature of frequency shift keying (FSK) is based on the two frequency components that determine the bits "1" and "0". There are a number of formats related to FSK depending on whether the change in the frequencies representing the bits is continuous or noncontinuous, the FSK or CPFSK modulation formats. For noncontinuous FSK, the detection is usually performed by a structure of dual frequency discrimination as shown in Figure 8.8 in which two narrow-band filters are used to extract the signals. For CPFSK, both the frequency discriminator and balanced receiver for PSK detection can be used. The frequency discrimination is indeed preferred as compared with the balanced receiving structures because it would eliminate the phase contribution by the LO or optical amplifiers which may be used as an optical preamp. We highlight the performance of these detection schemes for modulation format using noncoherent techniques in the next chapters.

8.3.2 Optical Homodyne Detection

Optical homodyne detection matches the transmitted signal phases to that of the LO phase signal. A schematic of the optical receiver is shown in Figure 8.9. The field of the incoming optical signals is mixed with the LO whose frequency and phase are locked with that of the signal carrier waves via a PLL. The resultant electrical signal is then filtered, and a decision circuit is formed.

8.3.2.1 Detection and Optical PLL

Optical homodyne detection requires phase matching of the frequency of the signal carrier and that of the LO. In principle, this type of detection would yield very high sensitivity requiring an energy of only 9 photons/bit. Implementation of such a system would normally require an OPLL whose structure in a recent development [4] is as shown in Figure 8.10. The LO frequency is locked into the carrier frequency of the signals by shifting

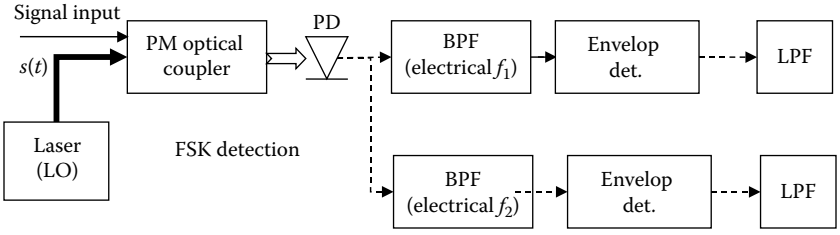

FIGURE 8.8
Schematic diagram of optical homodyne detection of FSK format with demodulation in the electrical domain.

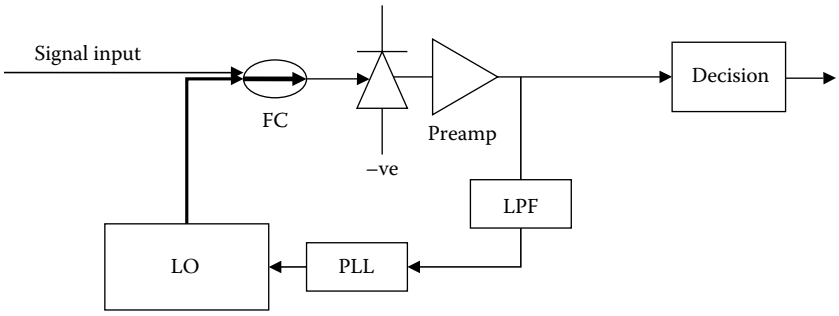

FIGURE 8.9
General structure of an optical homodyne detection system. FC, fiber coupler; LPF, low-pass filter; PLL, phase lock loop.

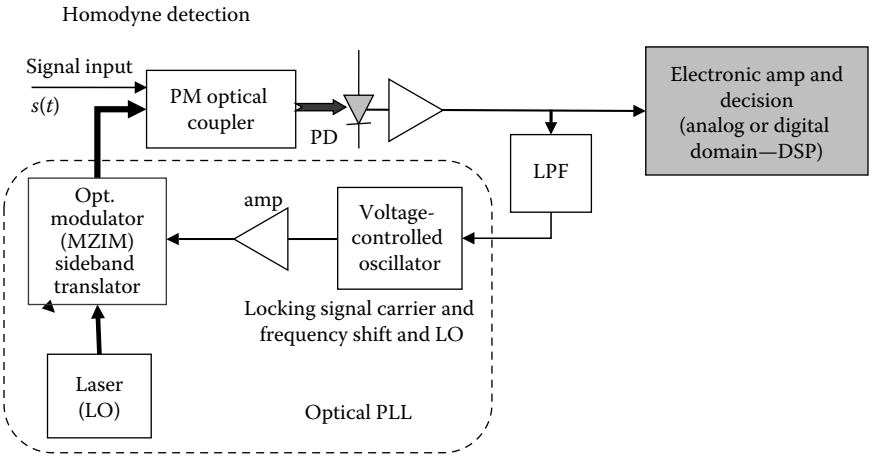

FIGURE 8.10
Schematic diagram of optical homodyne detection—electrical line (dashed) and optical line (continuous and solid) using an OPLL. *Note:* MZIM, Mach-Zehnder interferometric modulator.

it to the modulated sideband component via the use of the optical modulator. A single-sideband optical modulator is preferred. However, a double sideband may also be used. This modulator is excited by the output signal of a voltage-controlled oscillator whose frequency is determined by the voltage level of the output of an electronic BPF condition to meet the required voltage level for driving the electrode of the modulator. The frequency of the LO is normally tuned to the region such that the frequency difference with respect to the signal carrier falls within the passband of the electronic filter. When the frequency difference is zero, then there is no voltage level at the output of the filter signifying that the optical PLL has reached the final stage of locking. The bandwidth of the optical modulator is important so that it can extend the locking range between the two optical carriers.

Any difference in frequency between the LO and the carrier is detected, and the noise is filtered by the LPF. This voltage level is then fed to a VCO to generate a sinusoidal wave, which is then used to modulate an intensity modulator modulating the lightwaves of the LO. The output spectrum of the modulator would exhibit two sidebands and the LO light-wave. One of these components would then be locked to the carrier. A close loop would ensure a stable locking. If the intensity modulator is biased at the minimum transmission

point and the voltage level at the output of the VCO is adjusted to 2 Vπ with driven signals of π/2 phase shift with each, other then we would have carrier suppression and sideband suppression. This eases the confusion of the closed-loop locking.

Under a perfect phase matching, the received signal is given by

$$i_s(t) = 2\Re\sqrt{p_s P_{LO}}\cos\{\pi a_k s(t)\} \tag{8.28}$$

where

a_k takes the value ±1

$s(t)$ is the modulating waveform

This is a baseband signal; thus, the error rate is the same as that of the baseband system.

The shot noise power induced by the LO and the signal power can be expressed as

$$i_{NS}^2 = 2q\Re(p_s + P_{LO})\int_0^\infty |H(j\omega)|\, d\omega \tag{8.29}$$

where $|H(j\omega)|$ is the transfer function of the receiver whose expression, if under a matched filtering, can be

$$|H(j\omega)|^2 = \left[\frac{\sin(\omega T/2)}{\omega T/2}\right]^2 \tag{8.30}$$

where T is the bit period. Then the noise power becomes

$$i_{NS}^2 = q\Re(p_s + P_{LO})\frac{1}{T} \simeq \frac{q\Re P_{LO}}{T}$$
$$\text{when } p_s \ll P_{LO} \tag{8.31}$$

Thus, the SNR is

$$SNR = \frac{2\Re p_s P_{LO}}{q\Re P_{LO}/T} = \frac{2p_s T}{q} \tag{8.32}$$

and hence, the BER can be obtained as

$$P_E = \frac{1}{2}erfc(\sqrt{SNR}) \rightarrow BER = erfc(\sqrt{SNR}) \tag{8.33}$$

8.3.2.2 Detection of Quantum Limit

For homodyne detection, a super quantum limit can be achieved. In this case, the LO is used in a very special way that matches the incoming signal field in polarization, amplitude, and frequency and is assumed to be phase locked to the signal. Assuming that the

phase signal is perfectly modulated such that it acts in phase or in counterphase with the LO, the homodyne detection would give a normalized signal current of

$$i_{sC} = \frac{1}{2T}\left[\mp\sqrt{2n_p} + \sqrt{2n_{LO}}\right]^2 \quad \text{for } 0 \le t \le T \tag{8.34}$$

Assuming further that $n_p = n_{LO}$, the number of photons for the LO for generation of detected signals, then the current can be replaced with $4n_p$ for the detection of a "1" and nothing for a "0" symbol.

8.3.2.3 Linewidth Influences

8.3.2.3.1 Heterodyne Phase Detection

When the linewidth of the light sources is significant, the IF deviates due to a phase fluctuation and the PDF is related to this linewidth conditioned on the deviation δω of the IF. For a RMS signal power of p_s, the total probability of error is given as

$$P_E = \int_{-\infty}^{\infty} P_C(p_s, \partial\omega) p_{IF}(\partial\omega)\partial\omega \tag{8.35}$$

The PDF of the IF under a frequency deviation can be written as [5]

$$p_{IF}(\partial\omega) = \frac{1}{\sqrt{\Delta\nu BT}} e^{-\frac{\partial\omega^2}{4\pi\Delta\upsilon B}} \tag{8.36}$$

where

$\Delta\nu$ is the full IF linewidth at FWHM of the power spectral density
T is the bit period

8.3.2.3.2 Differential Phase Detection

The DPSK detection requires an Mach–Zehnder delay interferometer (MZDI) and a balanced receiver either in the optical domain or in the electrical domain. If in the electrical domain, then the beating signals in the PD between the incoming signals and the LO would give the beating electronic current, which is then split and one branch is delay by one bit period and then summed up. The heterodyne signal current can be expressed as [6]

$$i_s(t) = 2\Re\sqrt{P_{LO}p_s}\cos(\omega_{IF}t + \phi_s(t)) + n_x(t)\cos\omega_{IF}t - n_y(t)\sin\omega_{IF}t \tag{8.37}$$

The phase $\phi_s(t)$ is expressed by

$$\phi_s(t) = \varphi_s(t) + \{\varphi_N(t) - \varphi_N(t+T)\} - \{\varphi_{pS}(t) - \varphi_{pS}(t+T)\} - \{\varphi_{pL}(t) - \varphi_{pL}(t+T)\} \tag{8.38}$$

The first term is the phase of the data and takes the value 0 or π. The second term represents the phase noise due to shot noise of the generated current, and the third

and fourth terms are the quantum shot noises due to the LO and the signals. The probability of error is given by

$$P_E = \int_{-\pi/2}^{\pi/2} \int_{-\infty}^{\infty} p_n(\phi_1 - \phi_2) p_q(\phi_1) \partial\phi_1 \partial\phi_1 \tag{8.39}$$

where

$p_n(.)$ is the PDF of the phase noise due to the shot noise
$p_q(.)$ is for the quantum phase noise generated from the transmitter and the LO [7]

The probability of error can be written as

$$p_N(\phi_1 - \phi_2) = \frac{1}{2\pi} + \frac{\rho e^{-\rho}}{\pi} \sum_{m=1}^{\infty} a_m \cos\left(m(\phi_1 - \phi_2)\right)$$

$$a_m \sim \left\{ \frac{2^{m-1}\Gamma\left[\frac{m+1}{2}\right]\Gamma\left[\frac{m}{2}+1\right]}{\Gamma\left[m+1\right]} \left[I_{m-1/2}\frac{\rho}{2} + I_{(m+1)/2}\frac{\rho}{2} \right] \right\}^2 \tag{8.40}$$

where $\Gamma(.)$ is the gamma function and it is the modified Bessel function of the first kind. The PDF of the quantum phase noise can be given as [8]

$$p_q(\phi_1) = \frac{1}{\sqrt{2\pi D\tau}} e^{\frac{\phi_1^2}{2D\tau}} \tag{8.41}$$

With D is the phase diffusion constant, the standard deviation from the central frequency is given as

$$\Delta\nu = \Delta\nu_R + \Delta\nu_L = \frac{D}{2\pi} \tag{8.42}$$

which is the sum of the transmitter and the LO FWHM linewidth. Substituting (8.41) and (8.40) into (8.39) we obtain

$$P_E = \frac{1}{2} + \frac{\rho e^{-\rho}}{2} \sum_{n=0}^{\infty} \frac{(-1)^n}{2n+1} e^{-(2n+1)^2 \pi\Delta\upsilon T} \left\{ I_{n-1/2}\frac{\rho}{2} + I_{(n+1)/2}\frac{\rho}{2} \right\}^2 \tag{8.43}$$

This equation gives the probability of error as a function of the received power. The probability of error is plotted against the receiver sensitivity and the product of the linewidth with the bit rate (or the relative bandwidth of the laser line width and the bit rate) are shown in Figure 8.11 for DPSK modulation format at 140 Mb/s bit rate and the variation of the laser linewidth from 0 to 2 MHz.

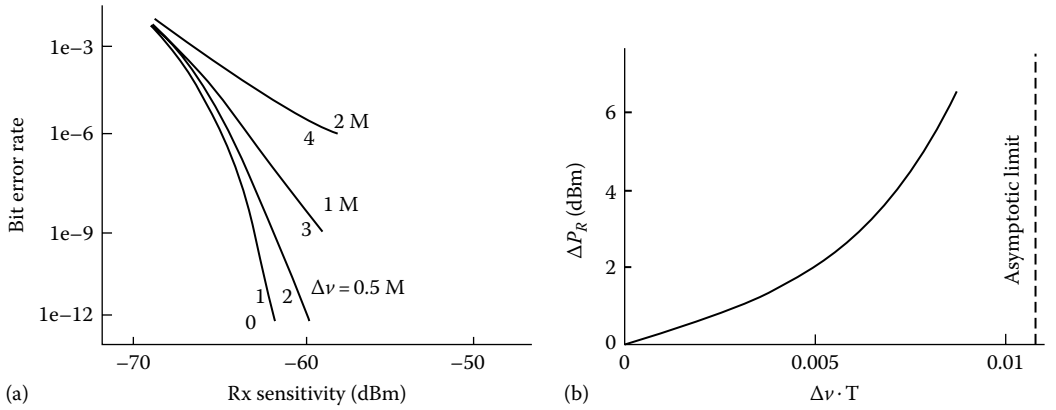

FIGURE 8.11
(a) Probability of error versus receiver sensitivity with linewidth as a parameter in MHz. (b) Degradation of optical receiver sensitivity at *BER* = 1e-9 for DPSK systems as a function of the linewidth and bit period—bit rate = 140 Mb/s. (Extracted with permission from Nicholson, G., *Electron. Lett*., 20(24), 1005, November 1984.)

8.3.2.3.3 Self-Coherent Differential Phase Detection

Recently, the laser linewidth requirement for DQPSK modulation and differential detection for DQPSK have also been studied, and no LO is used implying self-coherent detection. It has been shown that for the linewidth of up to 3 MHz of the transmitter, laser would not significantly influence the probability of error as shown in Figures 8.12 and 8.13 [8].

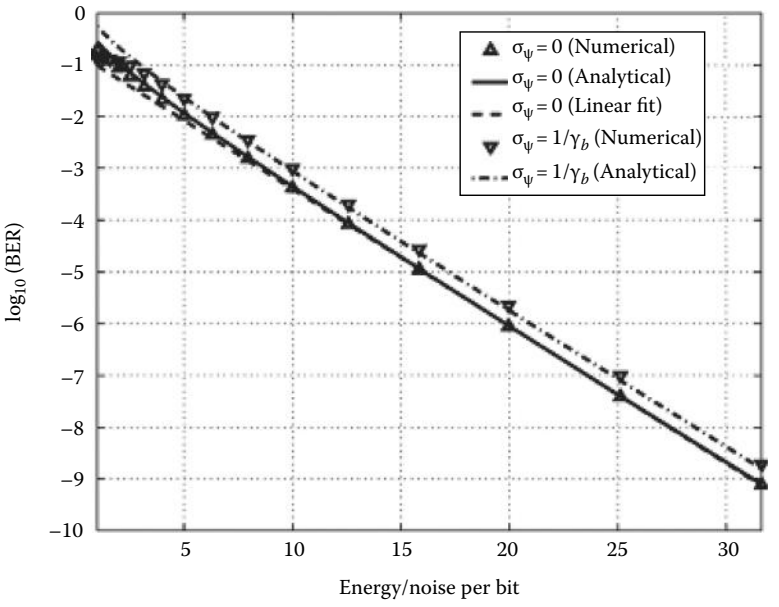

FIGURE 8.12
Analytical approximation (solid line) and numerical evaluation (triangles) of the BER versus the energy per bit for the cases of zero linewidth and that required to double the BER. The dashed line is the linear fit for zero linewidth. Bit rate 10 Gb/s per channel. (Extracted with permission from Savory, S. and Hadjifotiou, T., *IEEE Photon. Tech. Lett*., 16(3), 930, March 2004.)

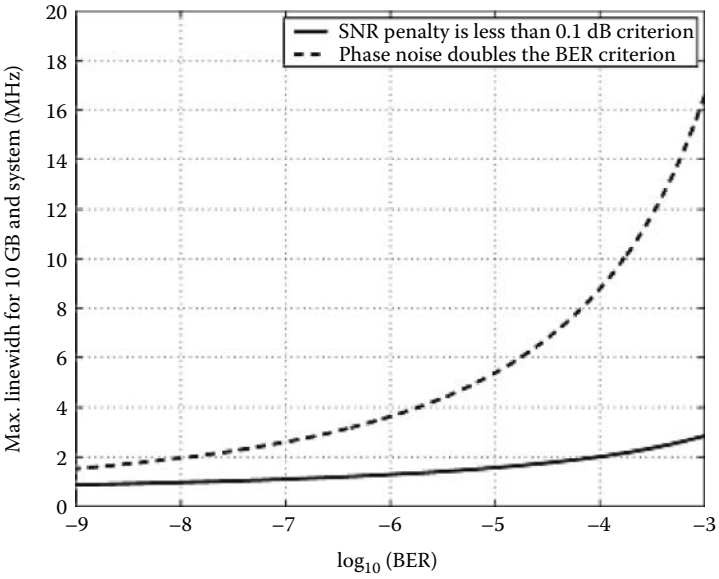

FIGURE 8.13
Criteria for neglecting linewidth in a 10-Gsymbol/s system. The loose bound is to neglect linewidth if the impact is to double the BER with the tighter bound to neglect linewidth if the impact is a 0.1 dB SNR penalty. Bit rate is 10 Gsymbol/s. (Extracted with permission from Yamamoto, Y. and Kimura, T., *IEEE J. Quant. Electron.*, QE-17, 919, 1981.)

8.3.2.3.3.1 Differential Phase Coherent Detection of Continuous Phase FSK Modulation Format The probability of error of CPFSK can be derived by taking into consideration the delay line of the differential detector, the frequency deviation, and the phase noise [10]. Similar to Figure 8.8, the differential detector configuration is shown in Figure 8.14a and the conversion of frequency to voltage relationship in Figure 8.14b. If heterodyne detection is employed, then a BPF is required to bring the signals back to the electrical domain.

The detected signal phase at the shot noise limit at the output of the LPF can be expressed as

$$\phi(t) = \omega_c t + a_n \frac{\Delta\omega}{2}\tau + \varphi(t) + \varphi_n(t)$$
$$\text{with } \omega_c = 2\pi f_c = (2n+1)\frac{\pi}{2\tau} \tag{8.44}$$

And, τ is the differential detection delay time, $\Delta\omega$ is the deviation of the angular frequency of the carrier for the "1" or "0" symbol, $\phi(t)$ is the phase noise due to the shot noise, and $n(t)$ is the phase noise due to the transmitter and the LO quantum shot noise and takes the values of ±1, the binary data symbol.

Thus, by integrating the detected phase from $-\frac{\Delta\omega}{2}\tau \longrightarrow \pi - \frac{\Delta\omega}{2}\tau$, we obtain the probability of error as

$$P_E = \int_{-\frac{\Delta\omega}{2}\tau}^{\pi-\frac{\Delta\omega}{2}\tau/2} \int_{-\infty}^{\infty} p_n(\phi_1 - \phi_2) p_q(\phi_1)\, \partial\phi_1 \partial\phi_1 \tag{8.45}$$

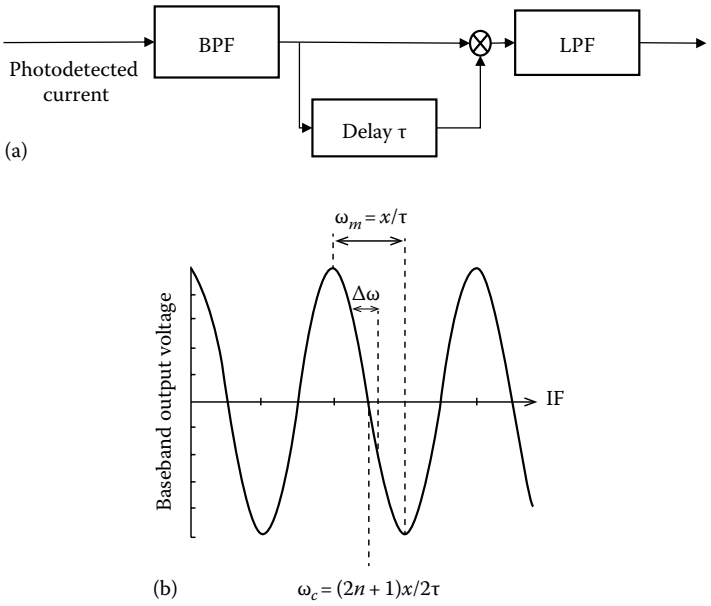

FIGURE 8.14
(a) Configuration of a CPFSK differential detection and (b) frequency to voltage conversion relationship of FSK differential detection. (Extract with permission from Iwashita, K. and Masumoto, T., *IEEE J. Lightwave Tech.*, LT-5/4, 452, 1987.)

Similar to the case of DPSK system, substituting (8.40) and (8.41) into (8.45) we obtain

$$P_E = \frac{1}{2}\frac{\rho e^{-\rho}}{2}\sum_{n=0}^{\infty}\frac{(-1)^n}{2n=1}e^{-(2n+1)^2\pi\Delta\upsilon\tau}\left\{I_{n-1/2}\frac{\rho}{2}+I_{(n+1)/2}\frac{\rho}{2}\right\}^2 e^{-(2n+1)^2\pi\Delta\upsilon\tau}\cos\{(2n+1)\alpha\} \tag{8.46}$$

$$\alpha = \frac{\pi(1-\beta)}{2} \quad \text{and} \quad \beta = \frac{\Delta\omega}{\omega_m} = \frac{2\pi\tau}{T_0}$$

where
ω_m is the deviation of the angular frequency with m as the modulation index
T_0 is the pulse or bit period

The modulation index parameter β is defined as the ratio of the actual frequency deviation to the maximum frequency deviation. The variation of the power penalty of the system with respect to the modulation index is depicted in Figure 8.15.

8.4 Self-Coherent Detection and Electronic DSP

The coherent techniques described earlier offer significant improvement but face a setback due to the unavailability of stable LO and an OPLL for locking the frequency of the LO and that of the signal carrier.

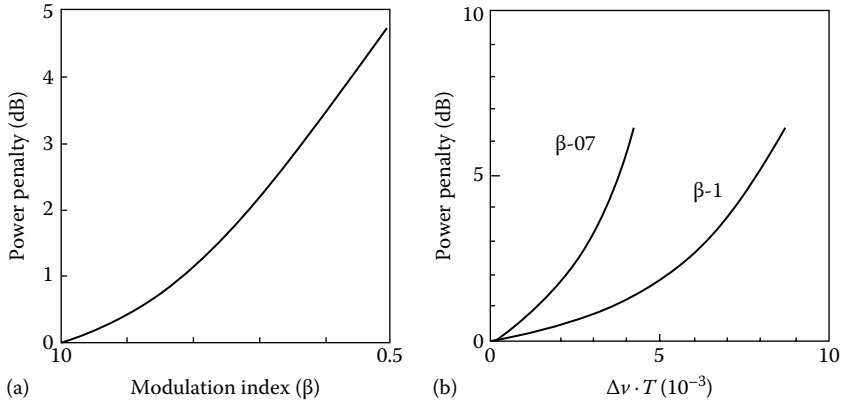

FIGURE 8.15
(a) Dependence of receiver power penalty at BER of 1e-9 on modulation index β (ratio between frequency deviation and maximum frequency spacing between f_1 and f_2) and (b) receiver power penalty at BER 1e-9 as a function of the product of beat bandwidth and bit delay time—effects excluding LD phase noise. (Extracted with permission from Iwashita, K. and Masumoto, T., *IEEE J. Lightwave Tech.*, LT-5/4, 452, 1987.)

DSP, which has been widely used in wireless communications, has a key role to play in the implementation of coherent optical communication systems. DSP techniques are applied to coherent optical communication systems to overcome the difficulties of OPLL and also to improve the performance of the transmission systems in the presence of fiber degrading effects such as chromatic dispersion, PMD, and fiber nonlinearities.

Coherent optical receivers have the following advantages: (1) the shot-noise-limited receiver sensitivity can be achieved with sufficient LO power; (2) closely spaced WDM channels can be separated with electrical filters having sharp roll-off characteristics; and (3) the ability of phase detection can improve the receiver sensitivity compared with the IMDD system [13]. In addition, any kind of multilevel phase modulation formats can be introduced by using the coherent receiver. While the spectral efficiency of binary modulation formats is limited to 1 bit/s/Hz/polarization (which is called the Nyquist limit), multilevel modulation formats with N bits of information per symbol can achieve spectral efficiency up to N bit/s/Hz/polarization. Recent research has focused on M-ary-PSK and even QAM with coherent detection, which can increase the spectral efficiency by a factor of $\log_2 M$ [14–16]. Moreover, for the same bit rate, since the symbol rate is reduced, the system can have higher tolerance to chromatic dispersion and PMD.

However, one of the major challenges in coherent detection is to overcome the carrier phase noise when using an LO to beat with the received signals to retrieve the modulated phase information. Phase noise can result from lasers, which cause a power penalty to the receiver sensitivity. A self-coherent multisymbol detection of optical differential M-ary PSK is introduced to improve the system performance; however, higher analog-to-digital conversion resolution and more digital signal processing power are required as compared to a digital coherent receiver [17]. Further, differential encoding is also necessary in this scheme. As for the coherent receiver, initially, an OPLL is an option to track the carrier phase with respect to the LO carrier in homodyne detection. However, an OPLL operating at optical wavelengths in combination with distributed feedback (DFB) lasers may be quite difficult to implement because the product of laser linewidth and loop delay is too large [18]. Another option is to use electrical PLL to track the carrier phase

after down converting the optical signal into an intermediate frequency (IF). IF electrical signal in a heterodyne detection receiver as mentioned earlier. Compared to heterodyne detection, homodyne detection offers better sensitivity and requires a smaller receiver bandwidth [17]. On the other hand, coherent receivers employing high-speed ADCs and high-speed baseband DSP units are becoming increasingly attractive rather than using an OPLL for demodulation. Conventional block *M*th power PE scheme is proposed in Refs. [12,19] to raise the received *M*-ary PSK signals to the *M*th power to estimate the phase reference in conjunction with a coherent optical receiver. However, this scheme requires nonlinear operations, such as taking the *M*th power and the $\tan^{-1}(\cdot)$, and resolving the $\pm 2\pi/M$ phase ambiguity, which results in a large latency to the system. Such nonlinear operations would limit further potential for real-time processing of the scheme. In addition, nonlinear phase noises always exist in long-haul systems due to the Gordon–Mollenauer effect [20], which severely affects the performance of a phase-modulated optical system [21]. The results in Ref. [22] show that such *M*th power PE techniques may not effectively deal with nonlinear phase noise.

The maximum likelihood (ML) carrier phase estimator derived in Ref. [23] can be used to approximate the ideal synchronous coherent detection in optical PSK systems. The ML phase estimator requires only linear computations, and hence, is more suitable for online processing for real systems. Intuitively, one can show that the ML estimation receiver outperforms the *M*th power block phase estimator and conventional differential detection, especially when the nonlinear phase noise is dominant, thus significantly improving the receiver sensitivity and tolerance to the nonlinear phase noise. The algorithm of ML phase estimator is expected to improve the performance of coherent optical communication systems using different *M*-ary PSK and quadrature amplitude modulation (QAM) formats. The improvement by DSP at the receiver end can be significant for the transmission systems in the presence of fiber degrading effects, such as chromatic dispersion, PMD, and nonlinearities for both single channel and also DWDM systems.

8.4.1 Coherent and Incoherent Receiving Techniques

Coherent or noncoherent or direct reception of the modulated and transmitted signals is currently considered, but the choice depends on the environment of applications and employment whether they are in the long haul (carrier side), metropolitan access (client side), or access networks. Direct modulation should also be considered as it is significantly inexpensive for deployment in metro networks while coherent solutions offer significant advantages to long-haul transmission systems in term of reach and symbol rates or baud rates. Both incoherent and coherent systems can employ digital processing techniques to improve the receiver sensitivity and error coding to achieve coding gain, resulting in longer transmission distances. We have witnessed the development of chirp-managed lasers by taking advantage of the biasing of distributed feedback (DFB) laser about 4–5 times the level of the laser threshold so that the inverse non-return to zero (NRZ) driving of the DFB would produce chirp and then the phase difference between the "1" and "0" would be about π_rads. Hence, any dispersion due to these pulses over long distances of fiber would be canceled out, thus managing the dispersion tolerance of the chirp the laser by direct modulation.

The constellation of different QAM modulation formats shown in Figure 8.16 results in different demands on the ratio of the energy per bit to the noise per bit as estimated theoretically in Figure 8.17. Indeed, from this ratio, the receiver sensitivity must

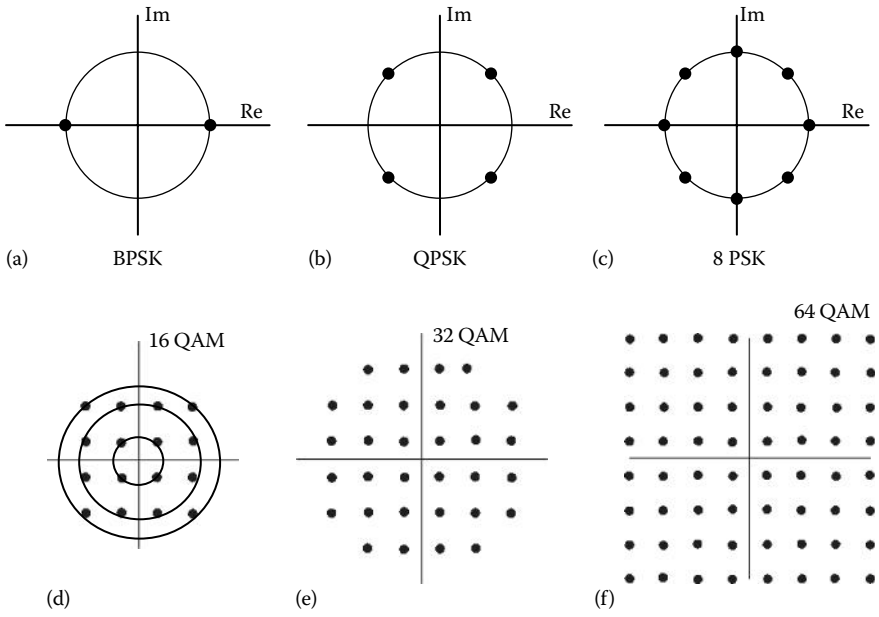

FIGURE 8.16
Constellations of the in phase and quadrature phase of lightwave carrier under modulation formats (a) with π phase shift of the BPSK at the edge of the pulse period, (b) QPSK, (c) 8 PSK, (d) 16 QAM with three rings, (e) 32 QAM, and (f) 64 QAM.

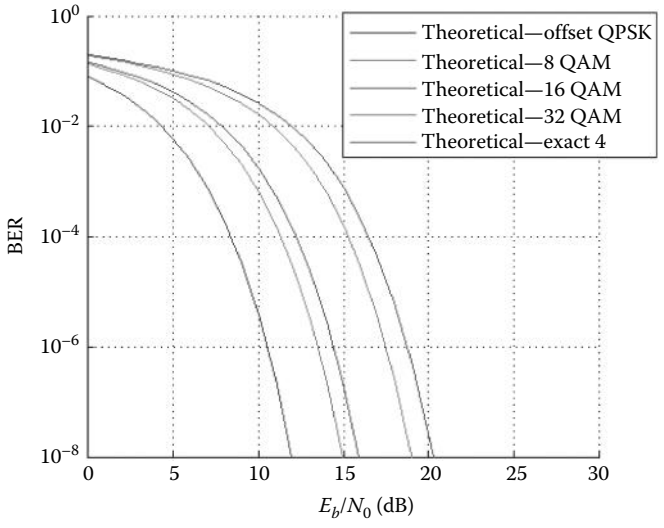

FIGURE 8.17
BER versus SNR for multilevel *M*-ary-QAM.

be satisfied. This curve is valid for coherent detection in which the phase of the modulated carrier must be demodulated.

Clearly, we can observe that at a BER of 1e-4 the required energy per bit of 16 QAM is about 5 dB above that required for quadrature PSK (QPSK). So, where can we get this energy for a symbol in the optical domain? We can naturally increase the carrier power to achieve this, but this will hit the threshold level of nonlinear effects, resulting in further penalty.

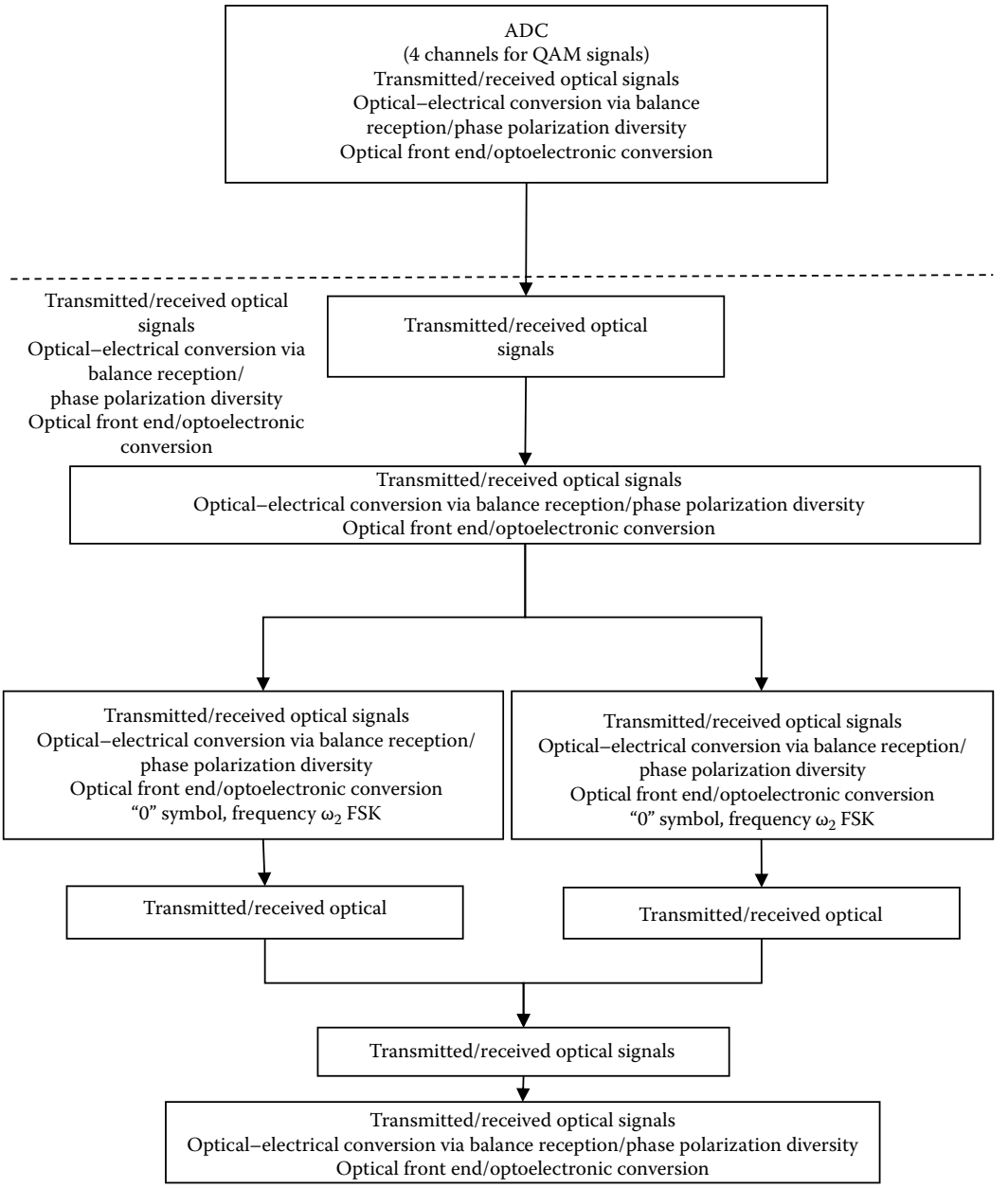

FIGURE 8.18
Flow Chart of Block Schematic of the optical digital receiver and DSP.

This can be resolved by a number of techniques that would be explained in detail in the corresponding chapters related to transmission systems.

8.4.2 Digital Processing in Advanced Optical Communication Systems

A generic block diagram of the digital coherent receiver and associated DSP techniques is shown in the flow chart given in Figure 8.18. Obviously, the reception of the modulated and transmitted signals is conducted via an optical receiver in coherent mode. Homodyne, heterodyne, and now intradyne are well-known coherent reception techniques that are dependent on the frequency difference between the LO and that of the carrier of the receiving channel. For homodyne coherent detection, the frequency difference is nil, thus locking the LO frequency to that of the carrier of the channel, while for heterodyne coherent detection there is a frequency difference that is outside the 3 dB bandwidth of the channel. When the frequency difference is less than the 3 dB and can be close to the carrier, then the coherent reception is of the intradyne type. Indeed, this difference has degraded the first-generation coherent reception systems for optical fiber communications of the mid-1980s. With the digital signal processing, the phase carrier recovery techniques can be developed and these difficulties can be overcome. Heterodyne reception would require an electrical filter to extract the beating channel information outside the signal band and is more troublesome with problems such as cross talks between channels. With the bit rate and symbol rate now expected to reach several tens of GHz, the heterodyne detection is not the preferred technique in view of its complexity.

For DSP-based coherent receiver the availability of high-speed sampling rate ADC is a must. However, with tremendous progresses in digital technology, ADC at 56–64 GSa/s is available and the sampling speed is expected to rise when 28 nm SiGe technology is employed. In addition, significant progress in the development of algorithms for processing the received sampled data sequence in real time must be made so that real-time recovery of data sequences can be realized. Currently, off-line processing is being done to ensure the availability of processing algorithms. Real-time processing must be implemented using application-specific integrated circuits (ASIC) technology for real system implementation.

8.5 Digital Signal Processing associated with Coherent Optical Receiver

8.5.1 Overview DSP-Assisted Coherent Reception

A generic block diagram of the digital coherent receiver and associated DSP techniques is shown in the flow chart given in Figure 8.18. Obviously, the reception of the modulated and transmitted signals is conducted via an optical receiver in coherent mode. Commonly known coherent reception techniques are homodyne, heterodyne and now intradyne that are dependent on the frequency difference between the LO and that of the carrier of the received channel. For homodyne coherent detection, the frequency difference is nil, thus locking the LO frequency to that of the carrier of the channel is essential, while for heterodyne coherent detection, there is a frequency difference that is outside the 3 dB bandwidth of the channel. When the frequency difference is less than the 3 dB and can be close to

the carrier, then the coherent reception is of intradyne type. Indeed, this difference has degraded the first-generation coherent reception systems for optical fiber communications in the mid-1980s. With the digital signal processing, the phase carrier recovery techniques can be developed and overcome these difficulties. Heterodyne reception would require electrical filter to extract the beating channel information outside the signal band and hence much troublesome as well as cross talks between received channels. With the bit rate and symbol rate now expected to reach several tens of GHz the heterodyne detection is not the preferred techniques and also due to its complexity.

For DSP-based coherent receiver, the availability of high-speed sampling rate ADC is a must. However, with tremendous progresses in digital technology, ADC at 56–64 GSa/s is available and the sampling sped is expected to rise when 28 nm SiGe technologies are employed. In addition, significant progresses in the development of algorithm for processing the received sampled data sequence in real time must be made so that real-time recovery of data sequences can be realized. Currently, off-line processing has been done to ensure the availability of processing algorithms (Figure 8.19).

8.5.2 Polarization Multiplexed Coherent Reception: Analog Section

A schematic of synchronous coherent receiver using ML PE for coherent optical communications is shown in Figure 8.20 [25]. Optical differential QPSK (DQPSK) system can be used as an example. Phase diversity receivers are usually employed to retrieve in-phase (I) and quadrature-phase (Q) signals in coherent lightwave systems with phase modulation. Such a receiver comprises a 90° optical hybrid coupler to mix the incoming signal with the four quadruple states associated with the LO inputs in the complex-field space. A $\pi/2$ phase shifter is used to extract the quadrature component of the optical signal. The optical hybrid then provides four lightwave signals to two pairs of balanced photodetectors to reconstruct the I and Q information of the transmitted signal. This is equivalent to self-homodyne detection as in the balanced receiver there would be a delay interferometer to compare the phases of the two consecutive bits. We can assume a complete matching of the polarization between the signal and the LO fields so that only the impact of phase noise has to be considered. The ML algorithm is nothing but the modern maximum likelihood sequence estimation (MLSE) technique [5].

The output signal reconstructed from the photocurrents can be represented by

$$r(k) = E_0 \exp[j(\theta_s(k) + \theta_n(k))] + \tilde{n}(k) \tag{8.47}$$

where k denotes the kth sample over the time interval $[kT, (k + 1)T]$ (T is the symbol duration); $E_0 = \Re\sqrt{P_{LO} p_s}$, where R is the PD responsivity, P_{LO} and p_s are the power of LO and received signal, respectively; $\theta_s(k) \in \{0, \pi/2, \pi, -\pi/2\}$ is the modulated phase, the phase difference carrying the data information; $\theta_n(k)$ is the phase noise during the transmission; and $\{\tilde{n}(k)\}$ is a complex white Gaussian random variables with $E[\tilde{n}(k)] = 0$ and $E[|\tilde{n}(k)|^2] = N_0$.

To retrieve information from the phase modulation $\theta_s(k)$ at time $t = kT$, the carrier phase noise $\theta_n(k)$ is estimated based on the received signal over the immediate past L symbol intervals, that is, based on $\{r(l), k - L \le l \le k - 1\}$. In the decision feedback strategy, a complex phase reference $v(k)$ is computed by the correlation of the L received

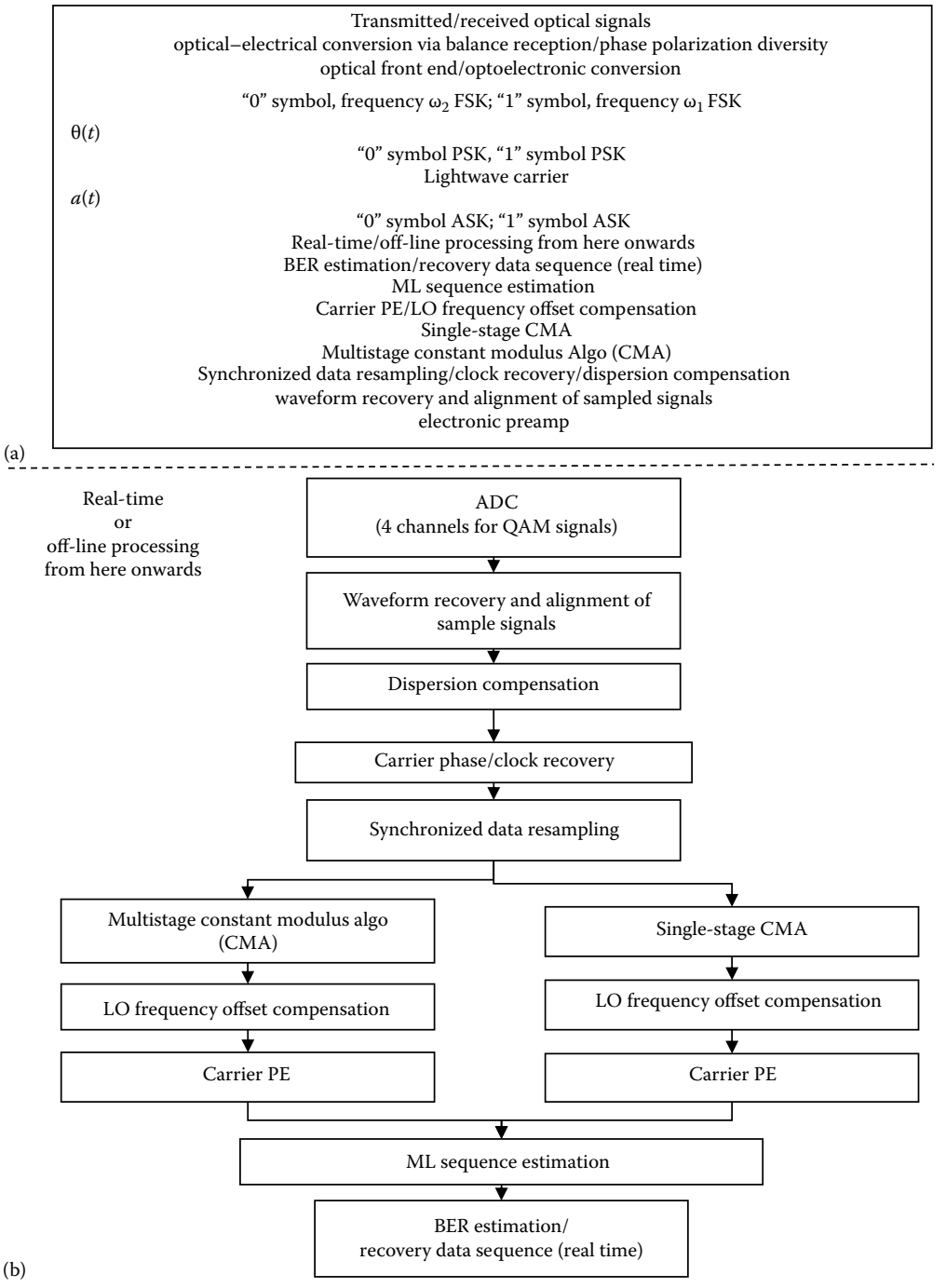

FIGURE 8.19
Flow Chart of Block Schematic of the optical digital receiver and DSP: (a) general sequence of processing from analog to digital and (b) DSP sequence of algorithms.

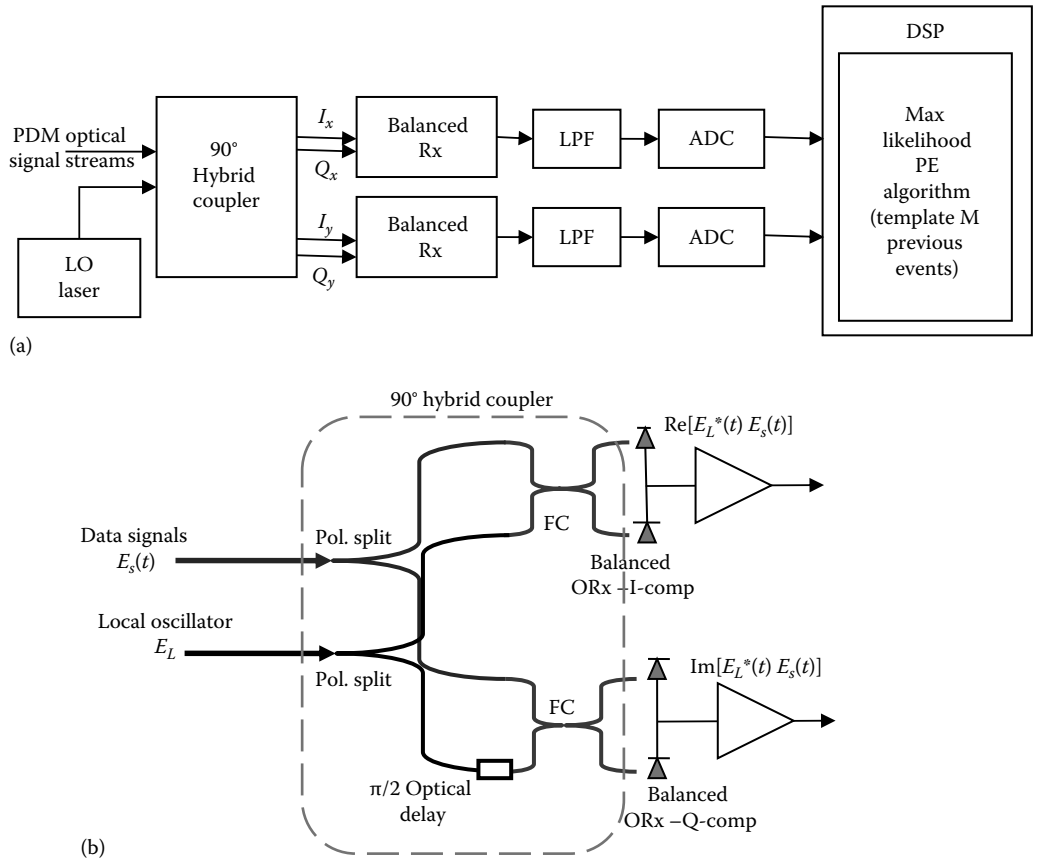

FIGURE 8.20
Scheme of a dual-polarization synchronous coherent receiver using digital signal processing for PE for coherent optical communications. (Adapted from Zhang, S. et al., A comparison of PE in coherent optical PSK system, *Photonics Global'08*, Paper C3-4A-03, Singapore, December 2008; Zhang, S. et al., Adaptive decision-aided ML PE in coherent optical DQPSK system, in *OptoElectronics and Communications Conference (OECC)'08*, Paper TuA-4, Sydney, New South Wales, Australia, July 2008, pp. 1–2.) (a) Generic scheme and (b) detailed optical receiver.

signal samples $r(l)$ and the L symbol decisions $\{m(l), k-L \le l \le k-1\}$, where $\hat{m}(l)$ is the receiver's decision onexp($j\theta_s(l)$):

$$v(k) = \sum_{l=k-L}^{k-1} r(l)\,\hat{m}^*(l) \tag{8.48}$$

Here, the asterisk symbol denotes the complex conjugation. An initial L symbol (long-known data sequence) is sent to initiate the processor/receiver. Alternatively, the ML decision processor can be trained prior to the transmission of the data sequence. It is important to note that not only can the π/4-radian phase ambiguity be resolved but also the decision-aided method is now totally linear and efficient to implement based on (8.48). To some extent, the reference $v(k)$ assists the receiver to acquire the channel characteristic. With the assumption that $\theta_n(k)$ varies slowly compared to the symbol rate, the computed complex

reference $v(k)$ from the past L symbols forms a good approximation to the phase noise phasor $\exp(j\theta_n(k))$ at time $t = kT$.

Using the phase reference $v(k)$ from (8.48), the decision statistic of the ML receiving processor is given as

$$q_i(k) = r(k)C_i^* \cdot v(k), \quad i = 0, 1, 2, 3 \tag{8.49}$$

where

$C_i \in \{\pm 1, \pm j\}$ is the DQPSK signal constellation

$\cdot$ denotes inner product of two vectors

The detector declares the decision $\hat{m}(k) = C_k$ if $q_k = \max q_i$. This receiver/processor has been shown to achieve coherent detection performance if the carrier phase is a constant and the reference length L is sufficiently long.

The performance of ML the receiving processor can be evaluated by simulation using Monte Carlo simulations in two cases: a linear phase noise system and a nonlinear phase noise system. For comparison, the Mth power phase estimator and differential demodulation can also be employed.

The nonlinear effects in a single-mode optical fiber can be ignored when the launch optical power is below the nonlinear self phase modulation (SPM) threshold, so the single mode fiber (SMF) can be modeled as a linear channel. The phase noise difference in two adjacent symbol intervals, i.e., $\theta_n(k) - \theta_n(k-1)$, obeys a Gaussian distribution with the variance σ^2 determined by the linewidth of the transmitter laser and the LO, given by the Lorentzian linewidth formula $\sigma^2 = 2\pi\Delta vT$, where Δv is the total linewidth of the transmitter laser and the LO [23]. In the simulations, σ can be set to 0.05, corresponding to the overall linewidth $\Delta v = 8$ MHz when the bit rate is 40 Gsymbol/s.

As observed in Figure 8.21, the ML processor outperforms the phase estimator and differential demodulation by about 0.25 and 1 dB, respectively. Although the performance gap between ML processor and Mth power PE is not very large in the case of this multi-phase shift keying (MPSK) system, the Mth power phase estimator requires more nonlinear computations, such as an arctan(·), which results in a large latency in the system and leads to phase ambiguity in estimating the block phase noise. On the contrary, the ML processor is a linear and efficient algorithm, and there is no need to deal with the $\pi/4$-radian phase ambiguity, and is thus more feasible for online processing for real systems. We also extend our ML PE technique to the QAM system. The conventional Mth-power PE scheme suffers from performance degradation in QAM systems since only a subgroup of symbols with phase modulation $\pi/4 + n \cdot \pi/2 (n = 0, 1, 2, 3)$ can be used to estimate the phase reference. The maximum tolerance of linewidth per laser in Square 16-QAM can be improved 10 times compared to the Mth-power phase estimator scheme.

Let us now consider the case with nonlinear phase noise. In a multispan optical communication system with erbium-doped fiber amplifiers (EDFAs), the performance of the optical DQPSK is severely limited by the nonlinear phase noise converted by the amplified ASE noise because of the nonlinearity of the fiber [23]. The laser linewidth is excluded only to consider the impact of the nonlinear phase noise on the receiver. The transmission system comprises a single-channel DQPSK-modulated optical signal transmitted at 10–40 Gsymbol/s over N 100 km equally spaced amplified spans which are fully compensated for chromatic dispersion and equalized gain of optical power along the fiber as shown in Figure 8.22. We set the following parameters: $N = 20$, fiber nonlinear coefficient $\gamma = 2$ W/km,

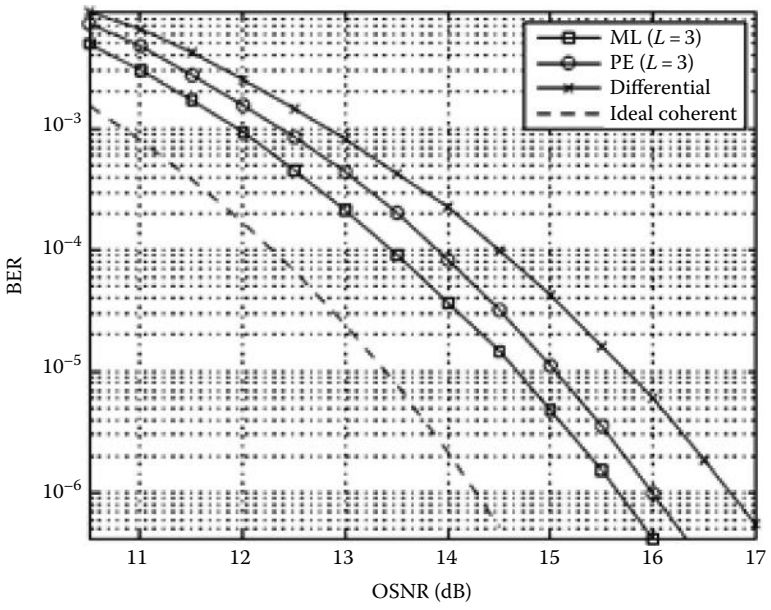

FIGURE 8.21
Simulated BER performances of a 10-Gsymbol/s DQPSK signal in linear optical channel with laser linewidth 2 MHz (σ = 0.05) and decision-aided length L = 3. (Extracted with permission from Zhang, S. et al., A comparison of PE in coherent optical PSK system, *Photonics Global'08*, Paper C3-4A-03, Singapore, December 2008.)

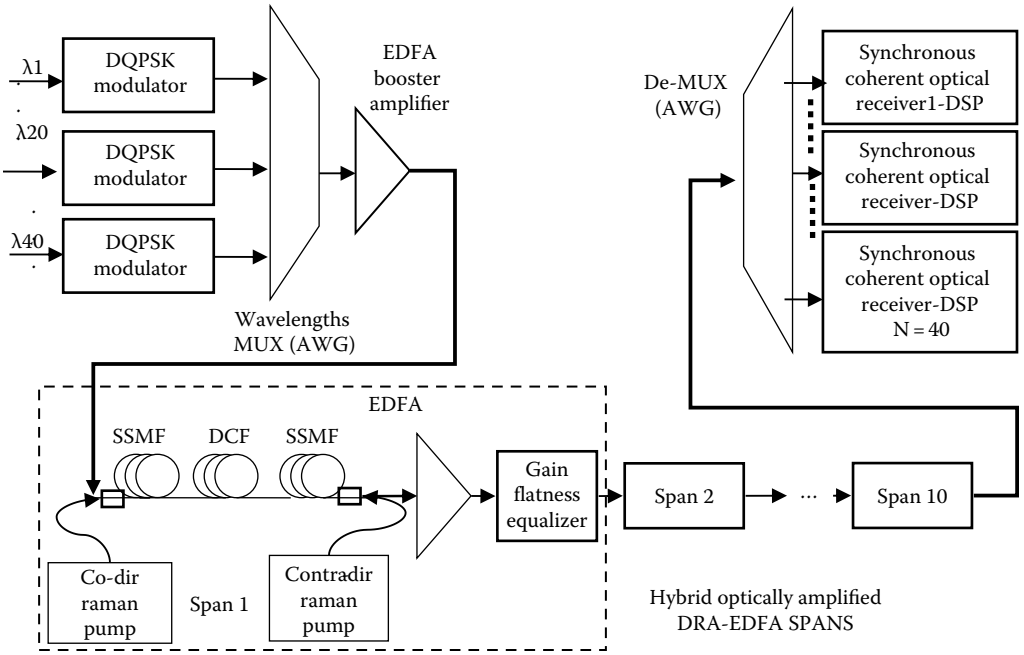

FIGURE 8.22
DWDM Optical DQPSK system with N-span optic fibers using synchronous coherent receiver to compensate nonlinear phase noise under both the Raman amplification and EDF amplification.

fiber loss α = 0.2 dB/km, the amplifier gain is G = 20 dB, the noise figure (NF) is 6 dB, the optical wavelength λ = 1553 nm, and the bandwidth of optical filter and electrical filter are set to Δλ = 0.1 nm and 7 GHz, respectively. The OSNR is defined as the ratio between the signal power and the noise power in two polarization states within a 0.1 nm bandwidth. As shown in Figure 8.23a, the receiver sensitivity of the ML processor has improved by about 0.5 and 3 dB over PE and differential demodulation, respectively, at the BER level of 10^{-4}. Besides, it is noteworthy that differential demodulation has exhibited an error floor because of the severe nonlinear phase noise with high launch optical power at the transmitter.

To obtain the impact of the nonlinear phase on the demodulation methods and the noise loading effects, the number of amplifiers can be increased to N = 30. The Q factor is used

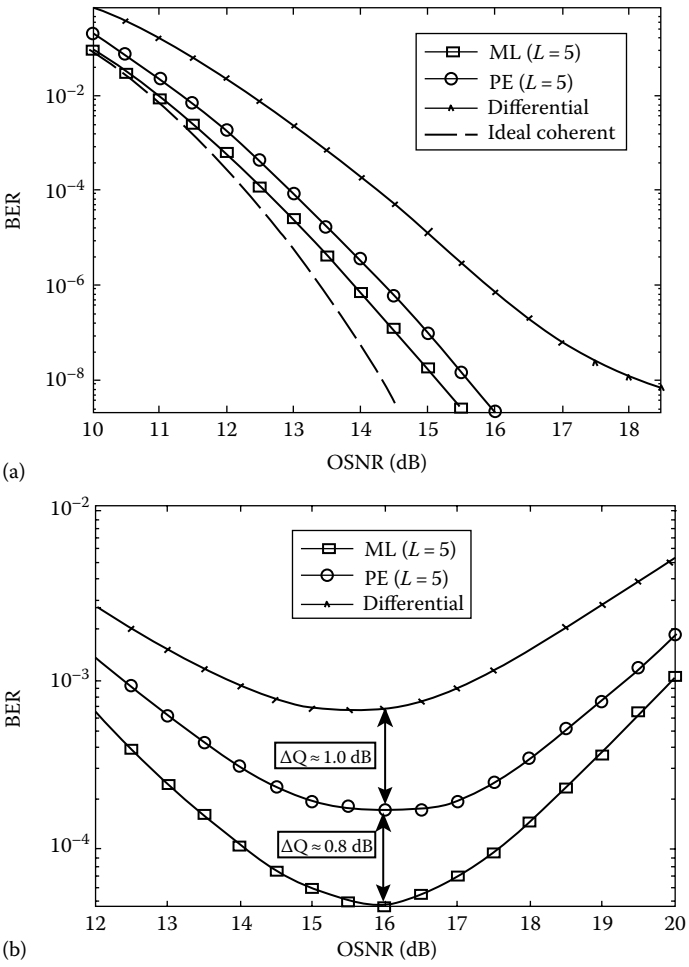

FIGURE 8.23
Monte Carlo Simulated BER of a 10-Gsymbol/s DQPSK signal in an N-span optical fiber system with template length L = 5: (a) N = 20 and (b) N = 30 under different detection schemes of ML estimator, phase estimator, differential demodulation, and ideal coherent detection. ML, maximum likelihood; PE, phase estimation. (Extracted from Zhang, S. et al., A comparison of PE in coherent optical PSK system, *Photonics Global'08*, Paper C3-4A-03, Singapore, December 2008.)

to show a numerical improvement of the ML processor/receiver. As shown in Figure 8.23b, with the increase in launch power, the ML receiver/processor approximates the optimum performance because of the reduced variance of the phase noise. At the optimum point, the ML receiver/processor outperforms the *M*th power phase estimator by about 0.8 dB while having about 1.8 dB receiver sensitivity improvement compared to the differential detection. It is also found that the optimum performance occurs at an OSNR of 16 dB when the nonlinear phase shift is almost 1 radian. With the launch power exceeding the optimum level, nonlinear phase noise becomes severe again. Only the ML phase estimator can offer BER beyond 10^{-4}, while both the *M*th power phase estimator and differential detection exhibit error floor before BER reaches 10^{-4}. From the numerical results, the ML processor carrier PE shows a significant better receiver sensitivity than the *M*th power phase estimator and conventional differential demodulation for optical DQPSK signal in nonlinear phase noise–dominant systems. Again, we want to emphasize that the ML estimator is a linear and efficient algorithm, and there is no need to deal with the π/4-radian phase ambiguity, making it feasible for online processing for the real systems.

In summary, the performance of synchronous coherent detection with the ML processor carrier PE may offer a linear phase noise system and a nonlinear optical noise system separately. The ML DSP PE can replace the OPLL, and the receiver sensitivity is improved compared to conventional differential detection and *M*th power phase estimator. The receiver sensitivity is improved by approximately 1 and 3 dB in these 2 channels (20 spans for the nonlinear channel), respectively, compared to differential detection for the 30-span nonlinear channel. Only the ML processor can offer BER beyond 10^{-4} (using the Monte Carlo simulation) while both the *M*th power phase estimator and differential detection exhibit error floor before BER reaches 10^{-4}. At the optimum point of the power, the *Q* factor of the ML receiver/processor outperforms the *M*th power PE by about 0.8 dB. In addition, an important feature is the linear and efficient computation of the ML PE algorithm, which enables the possibility of real-time online DSP processing.

8.5.3 DSP-Based Phase Estimation and Correction of Phase Noise and Nonlinear Effects

Kikuchi's group [26] at the University of Tokyo uses electronic signal processing based on the *M*th power PE to estimate the carrier phase. However, DSP circuits for the *M*th power PE need nonlinear computations, thus impeding the potential possibility of real-time processing in the future. Furthermore, the *M*th power PE method requires dealing with the π/4-radian phase ambiguity when estimating the phase noise in adjacent symbol blocks. While the electronic DSP is based on the ML processing for carrier PE to approximate the ideal synchronous coherent detection in optical phase modulation systems, which require only linear computations, it eliminates the OPLL and is more feasible for online processing for real systems. Our initial simulation results show that the ML receiver/processor outperforms the *M*th power phase estimator especially when the nonlinear phase noise is dominant, thus significantly improving the receiver sensitivity and tolerance to the nonlinear phase noise.

Liu's group [27,28] at Alcatel-Lucent Bell Labs uses optical delay differential detection with DSP to detect differential BPSK (DPSK) and DQPSK signals. Since direct detection only detects the intensity of the light, the improvement of DSP is limited after direct detection. After the synchronous coherent detection of our technique, the DSP, such as electronic equalization of chromatic dispersion and PMD, offers better performance since the phase information is retrieved. And as the level of phase modulation increases, it becomes

more and more difficult to apply the optical delay differential detection because of the rather complex implementation of the receiver and the degraded SNR of the demodulated signal, while the ML estimator/processor can still demodulate other advanced modulation formats such as 8-PSK, 16-PSK, 16-QAM, and so on.

8.5.4 DSP-Based Forward Phase Estimation of Optical Coherent Receivers of QPSK Modulation Format

Recent progress in DSP [17,29] with the availability of ultra-high sampling rate allows the possibility of DSP-based PE and polarization management techniques that make the coherent detection robust and practical. This section is dedicated to the new emerging technology that will significantly influence the optical transmission and detection of optical signals at ultra-high speed.

Recall the schematic of a coherent receiver of Figure 8.20. Figure 8.24 shows a coherent detection scheme for QPSK optical signals in which they are mixed with the LO field. In the case of modulation format QPSK or DQPSK, a $\pi/2$ optical phase shift is needed to extract the quadrature component; the real and imaginary parts of a phase shift–keyed signals can be deduced at the output of a balanced receiver from a pair of identical PDs connected back to back. Note that for a balanced receiver, the quantum shot noise contributed by the photodetectors is double as noise is always represented by the noise power and no current direction must be applied (Figure 8.25).

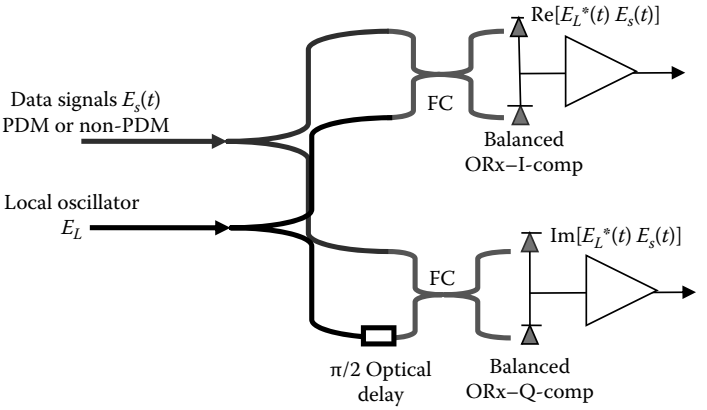

FIGURE 8.24
Schematic of a coherent receiver using balanced detection techniques for I–Q component phase and amplitude recovery. PDM, polarization division multiplexing.

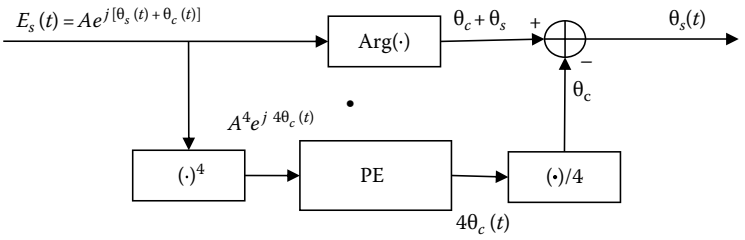

FIGURE 8.25
Schematic of a QPSK coherent receiver.

When the received signal is raised to the quadratic power, the phase of the signal disappears because $e^{j4\theta s(t)} = 1$ for DQPSK whose states are 0, π/2, π, and 2π. The data phase is excluded, and the carrier phase can be recovered with its fluctuation with time. This estimation is computed using the DSP technique. The estimated carrier phase is then subtracted with the detected phase of the signal and the carrier to give only the phase states of the signals as indicated in the diagram. This is a feedforward PE and suitable for DSP implementation.

8.6 Coherent Receiver Analysis

At ultra-high bit rate, the laser must be externally modulated such that the phase of the lightwave is conserved along the fiber transmission line. The detection can be direct detection, self-coherent, or homodyne and heterodyne. The sensitivity of the coherent receiver is also important for the transmission system, especially the PSK scheme under both homodyne and heterodyne transmission techniques. This section gives the analysis of receiver for synchronous coherent optical fiber transmission systems. Consider that the optical fields of the signals and LO are coupled via a fiber coupler with two output ports 1 and 2. The output fields are then launched into two photodetectors connected back to back, and then the electronic current is amplified using a transimpedance type and further equalized to extend the bandwidth of the receiver. Our objective is to obtain the receiver penalty and its degradation because of imperfect polarization mixing and unbalanced effects in the balanced receiver (Figure 8.26).

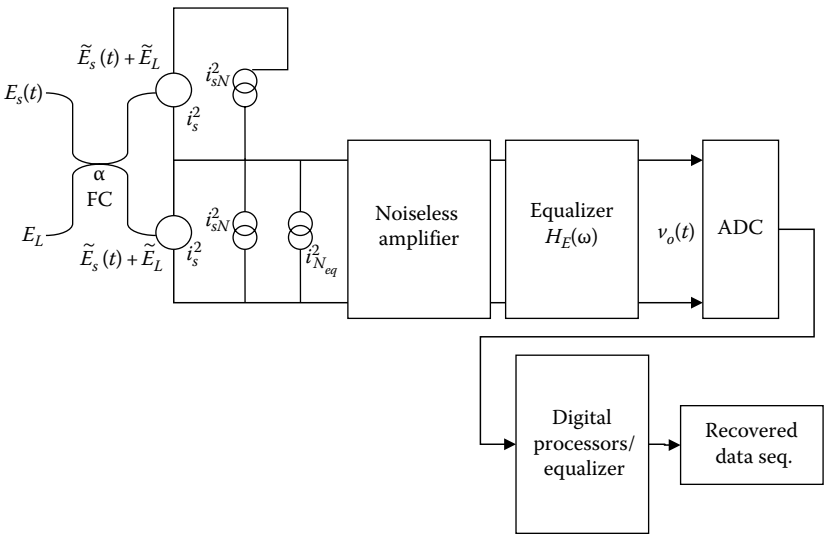

FIGURE 8.26
Equivalent current model at the input of the optical balanced receiver under coherent detection, average signal current, and equivalent noise current of the electronic preamplifier as seen from its input port and equalizer. FC, fiber coupler.

The following parameters are used in the analysis:

E_s	Amplitude of signal in the optical field at the receiver
E_L	Amplitude of LO in the optical field
p_s,P_L	Optical power of signal and LO at the input of the photodetector
$s(t)$	The modulated pulse
$\langle i_{NS}^2(t)\rangle$	Mean square noise current (power) produced by the total optical intensity on the photodetector
$\langle i_s^2(t)\rangle$	Mean square current produced by the photodetector by $s(t)$
$S_{NS}(t)$	Shot noise spectral density of $\langle i_s^2(t)\rangle$ and LO power
$i_{N\,eq}^2(t)$	Equivalent noise current of the electronic preamplifier at its input
$Z_T(\omega)$	Transfer impedance of the electronic preamplifier
$H_E(\omega)$	Voltage transfer characteristic of the electronic equalizer following the electronic preamplifier

The combined field of the signal and LO via a directional coupler can be written with their separate polarized field components as

$$\begin{aligned} E_{sX} &= \sqrt{K_{sX}}E_S\cos(\omega_s t - \phi_{m(t)}) \\ E_{sY} &= \sqrt{K_{sY}}E_S\cos(\omega_s t - \phi_{m(t)} + \delta_s) \\ E_{LX} &= \sqrt{K_{LX}}E_L\cos(\omega_L t) \\ E_{LY} &= \sqrt{K_{LY}}E_L\cos(\omega_L t + \delta_L) \\ \phi_{m(t)} &= \frac{\pi}{2}K_m s(t) \end{aligned} \tag{8.50}$$

where

$\phi_{m(t)}$ represents the phase modulation
K_m is the modulation depth
K_{sX}, K_{sY}, K_{LX}, and K_{LY} are the intensity fraction coefficients in the X and Y directions of the signal and LO fields, respectively

Thus, the output fields at ports 1 and 2 of the coupler in the *X-plane* can be obtained using the matrix transfer as

$$\begin{bmatrix} E_{R1X} \\ E_{R2X} \end{bmatrix} = \begin{bmatrix} \sqrt{K_{sX}(1-\alpha)}\cos(\omega_s t - \phi_{m(t)}) & \sqrt{K_{LX}\alpha}\sin(\omega_L t) \\ \sqrt{K_{sX}\alpha}\sin(\omega_s t - \phi_{m(t)}) & \sqrt{K_{LX}(1-\alpha)}\cos(\omega_L t) \end{bmatrix} \begin{bmatrix} E_s \\ E_L \end{bmatrix} \tag{8.51}$$

$$\begin{bmatrix} E_{R1Y} \\ E_{R2Y} \end{bmatrix} = \begin{bmatrix} \sqrt{K_{sY}(1-\alpha)}\cos(\omega_s t - \phi_{m(t)}) & \sqrt{K_{LY}\alpha}\sin(\omega_L t + \delta_L) \\ \sqrt{K_{sY}\alpha}\sin(\omega_s t - \phi_{m(t)}) & \sqrt{K_{LY}(1-\alpha)}\cos(\omega_L t) + \delta_L \end{bmatrix} \begin{bmatrix} E_s \\ E_L \end{bmatrix} \tag{8.52}$$

where α is the intensity coupling ratio of the coupler. Thus, the field components at ports 1 and 2 can be derived by combining the *X_and_YX_and_Y* components from (8.51) and (8.52), and the total power at ports 1 and 2 are given as

$$\begin{aligned} P_{R1} &= P_s(1-\alpha) + P_L\alpha) + 2\sqrt{P_sP_L\alpha(1-\alpha)K_p}\,\sin(\omega_{IF}t + \phi_{m(t)} + \phi_p - \phi_c) \\ P_{R2} &= P_s\alpha + P_L(1-\alpha) + 2\sqrt{P_sP_L\alpha(1-\alpha)K_p}\,\sin(\omega_{IF}t + \phi_{m(t)} + \phi_p - \phi_e + \pi) \\ \text{with } K_p &= K_{sX}K_{LX} + K_{sY}K_{LY} + 2\sqrt{K_{sX}K_{LX}K_{sY}K_{LY}}\cos(\delta_L - \delta_s) \\ \phi_p &= \tan^{-1}\left[\frac{\sqrt{K_{sX}K_{LY}}\sin(\delta_L - \delta_s)}{\sqrt{K_{sX}K_{LX}} + \sqrt{K_{sY}K_{LY}}\cos(\delta_L - \delta_s)}\right] \end{aligned} \tag{8.53}$$

where

ω_{IF} is the intermediate angular frequency and equals the difference between the frequencies of the LO and the carrier of the signals
ϕ_e is the phase offset
$\phi_p - \phi_e$ is the demodulation reference phase error

In (8.53), the total field of the signal and the LO are added, and then the product of the field vector and its conjugate are taken to obtain the power. Only the term with frequency that falls within the sensitive range of the photodetector would produce the electronic current. Thus, the term with the sum of the frequency of the wavelength of the signal and LO would not be detected, and only the product of the two terms would be detected as given.

Now assuming a binary PSK (BPSK) scheme, the pulse has a square shape with amplitude +1 or –1, the PD is a *p-i-n* type, and the PD bandwidth is larger than the 3 dB signal bandwidth, an equalized electronic preamplifier. The signal at the output of the electronic equalizer or the input of the decision circuit is given by

$$\begin{aligned} \hat{v}_D(t) &= 2K_HK_p\sqrt{P_sP_L\alpha(1-\alpha)K_p}\int_{-\infty}^{\infty}H_E(f)\,df\int_{-\infty}^{\infty}(t)\,dt\,\sin\left(\frac{\pi}{2}K_m\right)\cos(\phi_p - \phi_e) \\ &\xrightarrow[\text{the integral}]{\text{substituting} \rightarrow} \hat{v}_D(t) = 2K_HK_p\sqrt{P_sP_L\alpha(1-\alpha)K_p}\,\sin\left(\frac{\pi}{2}K_m\right)\cos(\phi_p - \phi_e) \end{aligned} \tag{8.54}$$

$$K_H = 1 \text{ for homodyne; } K_H = 1/\sqrt{2} \text{ for heterodyne}$$

For a completely balanced receiver K_B α = 0.5, otherwise K_B = 1. The integrals of the first line in (8.54) are given by

$$\begin{aligned} &\int_{-\infty}^{\infty}H_E(f)\,df = \frac{1}{T_B} \quad \text{since} \quad H_E(f) = \sin c(\pi T_B f) \\ &\int_{-\infty}^{\infty}s(t)\,dt = 2T_B \end{aligned} \tag{8.55}$$

where

$H_E(f)$ is the transfer function of the matched filter for equalization
T_B is the bit period

The total noise current equals the sum of the quantum shot noise currents generated by both the signal and the LO, and the total equivalent noise current referred to the input of the electronic preamplifier. This total noise current is then transferred to a noise voltage at the output of the equalizer, given by

$$\left\langle v_N^2(t)\right\rangle = \frac{\left[K_B\alpha S'_{IS} + (2-K_B)S_{IX} + S_{IE}\right]\int_{-\infty}^{\infty}\left|H_4(f)\right|^2 df}{K_{IS}^2}$$

or

$$\left\langle v_N^2(t)\right\rangle = \frac{\left[K_B\alpha S'_{IS} + (2-K_B)S_{IX} + S_{IE}\right]}{K_{IS}^2 T_B} \tag{8.56}$$

For homodyne and heterodyne detections, we have

$$\left\langle v_N^2(t)\right\rangle = \Re q\frac{P_L}{\lambda T_B}\left[K_B\alpha S'_{IS} + (2-K_B)S_{IX} + S_{IE}\right] \tag{8.57}$$

where the spectral densities S'_{IX} and S'_{IE} are given by

$$\begin{aligned} S'_{IX} &= \frac{S_{IX}}{S'_{IS}} \\ S'_{IE} &= \frac{S_{IE}}{S'_{IS}} \end{aligned} \tag{8.58}$$

Thus, the receiver sensitivity for BPSK, equiprobable detection, and a Gaussian density distribution we have

$$P_e = \frac{1}{2}erfc\left(\frac{\delta}{\sqrt{2}}\right) \tag{8.59}$$

where δ is given by

$$P_e = \frac{1}{2}erfc\left(\frac{\delta}{\sqrt{2}}\right)$$

and (8.60)

$$\delta = \frac{\hat{v}_D}{2\sqrt{\left\langle v_N^2\right\rangle}}$$

Thus, we have the receiver sensitivity given by

$$P_s = \langle P_s(t) \rangle = \frac{\Re q \delta^2}{4\lambda T_B K_H^2} \frac{\left[K_B \alpha S'_{IS} + (2 - K_B) S_{IX} + S_{IE}\right]}{\eta K_p (1-\alpha)\alpha K_B^2 \sin^2\left(\frac{\pi}{2} K_m\right) \cos^2(\phi_p - \phi_e)} \tag{8.61}$$

8.6.1 Shot-Noise-Limited Receiver Sensitivity

In the case that the power of the LO dominates the noise of the electronic preamplifier and the equalizer, the receiver sensitivity is given by

$$P_s = \langle P_{sL} \rangle = \frac{\Re q \delta^2}{4\lambda T_B K_H^2} \tag{8.62}$$

This shot-noise-limited receiver sensitivity can be plotted as shown in Figure 8.27.

We can now consider the receiver sensitivity of the reception system under nonideal conditions. Under nonideal conditions, the receiver sensitivity loses its sensitivity to the shot noise and is characterized by the receiver sensitivity penalty PD_T as

$$PD_T = 10 \text{ Log} \frac{\langle P_s \rangle}{\langle P_{sL} \rangle} \text{ in dB} \tag{8.63}$$

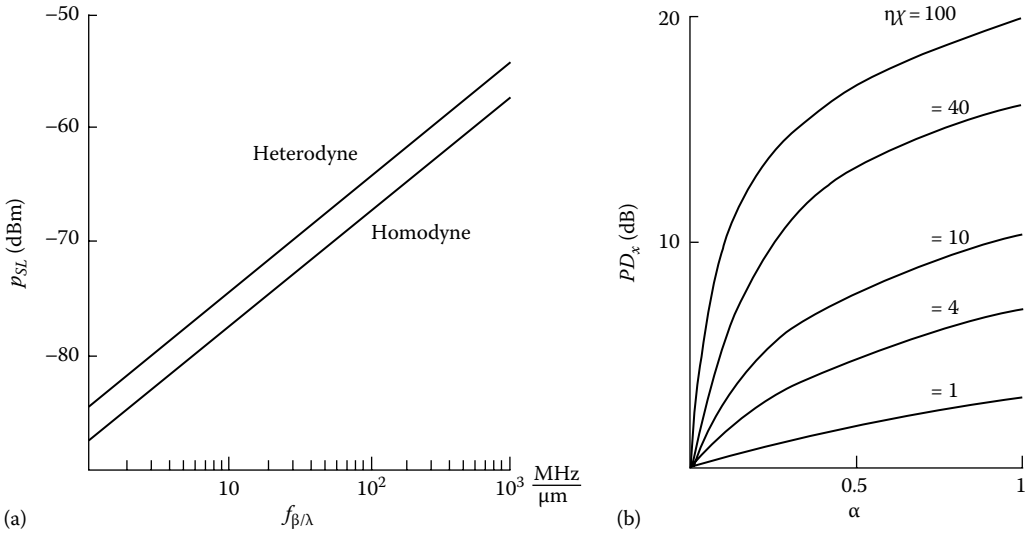

FIGURE 8.27
(a) Receiver sensitivity of coherent homodyne and heterodyne detections, signal power versus bandwidth over the wavelength. (b) Power penalty of the receiver sensitivity from the shot-noise-limited level as a function of the excess noise of the LO. (Extracted with permission from Hodgkinson, I., *IEEE J. Lightwave Tech.*, 5(4), 573, 1987.)

$$PD_T = 10\ \mathrm{Log}_{10}\left[\frac{K_B\alpha S'_{IS} + (2-K_B)S_{IX} + S_{IE}}{K_B\alpha}\right] - 10\ \mathrm{Log}_{10}\left[K_B(1-\alpha)\right]$$

$$-10\ \mathrm{Log}_{10}\left([\eta][K_p]\sin^2\left(\frac{\pi}{2}K_m\right)\cos^2(\phi_p-\phi_e)\right) \tag{8.64}$$

where η is the LO excess noise factor.

The receiver sensitivity plotted against the ratio f_B/λ in the case of homodyne and heterodyne detections is shown in Figure 8.27a, and the power penalty of the receiver sensitivity plotted against the excess noise factor of the LO is shown in Figure 8.27b. Receiver power penalty can be deduced as a function of the total electronic equivalent noise spectral density, and its reduction as a function of the rotation of the polarization of the LO can be found in Ref. [30]. Furthermore, from Ref. [27], it can be seen that the receiver power penalty and the normalized heterodyne center frequency vary as a function of the modulation parameter, and its variation as a function of the optical power ratio at the same polarization angle can also be found.

8.7 Remarks

We have described the principles of coherent detection, homodyne, heterodyne, and self-homodyne techniques. The receiver sensitivity and probability of error of these optical receivers have been given. OPLL and the methods of its implementation in modern optical transmission systems are described briefly. This is essential when there is some uncertainty in the matching of the frequencies of the LO and the signal carrier. If this difference is small enough, then the DSP can be employed to eliminate this effect as described in Chapter 15. Coherent optical receivers without using a LO, the self-coherent detection techniques suitable for differential phase modulation has emerged as a potential detection system if associated with digital signal processing and advanced equalization. PE such as the MLSE can offer significant improvement in receiver sensitivity and in reducing the bit error rate. Coherent detection will thus offer significant development in modern optical communications. Theoretically, coherent PSK detection can reach the quantum limit of about 16 photons/bit, although this remains to be proven in practice. As mentioned in the introductory remarks at the beginning, Simulink models for coherent reception can be developed without much difficulty by using the self-coherent reception model in Section 8.4 with some additional LO lasers and a hybrid coupler. Furthermore, there are several Simulink models available from the "Signal processing tool boxes" of MATLAB® which can be integrated into Simulink models to test the effectiveness of DSP algorithms. It is recommended that readers employ these algorithms, including the complex MLSE procedures. Chapter 15 describes DSP algorithms in greater detail.

Problems

8.1 Coherent optical communication systems

(a) Sketch a structure of an optical coherent receiver employing either the homodyne or heterodyne technique. Give a brief description of the roles of each component in your system.

(b) What is the typical modern linewidth of the laser that acts as the LO?

(c) Draw a distinction between the homodyne and heterodyne coherent systems.

(d) A homodyne optical receiver has the following parameters: A photodetector with a responsivity of 0.9 is followed by an electronic preamplifier whose total equivalent noise spectral density referred to its input is $5\,\text{pA}/\sqrt{\text{Hz}}$ and an electrical bandwidth of 15 GHz. The transmission bit rate is 10 Gb/s. The LO is a tunable laser source with a line width of 100 MHz. The wavelength in vacuum of both the signals and the LO is 1550.92. The average optical power of the LO coupled to the photodetector is 0 dBm.

Sketch the structure of the receiver and then its equivalent small signal circuit which includes the generated electronic signal current at the output of the photodetector, the total noise currents from the input of the electronic preamplifier. What is the dominant noise source of this receiver? For an optical signal with an average power of –20 dBm estimate the SNR at the output of the photodetector. Re-calculate the SNR of the receiver if the frequency of the LO is 20 GHz away from that of the signal carrier frequency.

8.2 Concept of homodyne and heterodyne coherent detections

A BPSK modulation transmission uses an optical carrier at λ = 1550 nm. The average optical power is 0 dBm. The bit rate is 10 Gb/s, assuming that the signals are dispersion compensated perfectly and gain equalized by optical amplifiers with negligible ASE noises. The receiver responsivity is 0.9 A/W. At the receiver, an LO is employed to mix with the optical signals. The frequency of the LO can be assumed to be identical to that of the signal carrier:

(a) Sketch a schematic diagram of the receiver and indicate the signal magnitude level in either the optical or electrical domain.

(b) Repeat (a) if the frequency difference between the LO and the carrier is 40 GHz.

(c) Estimate the current magnitude of the optical signals at the output of the photodetector for (a) and (b).

8.3 Homodyne ASK

Calculate the sensitivity of a homodyne receiver for binary ASK system with *BER* = 1e-9. The data bit rate is 10 Gb/s, and the wavelength is 1550 nm. It uses a *p-i-n* photodetector of a responsivity of 0.8 A/W and a dark current of 2 nA. The PIN load resistance is 100 Ω, and the receiver noise bandwidth is 15 GHz. The amplifier total noise equivalent at the input is about five times that of the thermal resistance at the input. You may assume equal probability of the "1" and "0". The relative phase between the LO and the incoming lightwave is not larger than 10°.

References

1. A.H. Gnauck and P.J. Winzer, Optical phase-shift-keyed transmission, *Journal of Lightwave Technology*, 23, 115–130, 2005.
2. R.C. Alferness, Guided wave devices for optical communication, *IEEE Journal of Quantum Electronics*, QE-17, 946–959, 1981.
3. W.A. Stallard, A.R. Beaumont, and R.C. Booth, Integrated optic devices for coherent transmission, *IEEE Journal of Lightwave Technology*, LT-4(7), 852, July 1986.
4. V. Ferrero and S. Camatel, Optical phase locking techniques: An overview and a novel method based on single sideband sub-carrier modulation, *Optics Express*, 16(2), 818–828, January 21, 2008.
5. I. Garrett and G. Jacobsen, Theoretical analysis of heterodyne optical receivers for transmission systems using (semiconductor) lasers with nonneglible linewidth, *IEEE Journal of Lightwave Technology*, LT-3/4, 323–334, 1986.
6. G. Nicholson, Probability of error for optical heterodyne DPSK system with quantum phase noise, *Electronics Letters*, 20(24), 1005–1007, November 1984.
7. S. Shimada, *Coherent Lightwave Communications Technology*, Chapman and Hall, London, U.K., 1995, p. 27.
8. Y. Yamamoto and T. Kimura, Coherent optical fiber transmission system, *IEEE Journal of Quantum Electronics*, QE-17, 919–934, 1981.
9. S. Savory and T. Hadjifotiou, Laser linewidth requirements for optical DQPSK optical systems, *IEEE Photonics Technology Letters*, 16(3), 930–932, March 2004.
10. K. Iwashita and T. Masumoto, Modulation and detection characteristics of optical continuous phase FSK transmission system, *IEEE Journal of Lightwave Technology*, LT-5/4, 452–462, 1987.
11. K. Iwashita and T. Masumoto, Modulation and detection characteristics of optical continuous phase FSK transmission system, *IEEE Journal of Lightwave Technology*, LT-5/4, 452–462, 1987. (Fig. 1.)
12. K. Iwashita and T. Masumoto, Modulation and detection characteristics of optical continuous phase FSK transmission system, *IEEE Journal of Lightwave Technology*, LT-5/4, 452–462, 1987. (Fig. 2&3.)
13. D.-S. Ly-Gagnon, S. Tsukamoto, K. Katoh, and K. Kikuchi, Coherent detection of optical quadrature phase-shift keying signals with carrier phase estimation, *Journal of Lightwave Technology*, 24, 12–21, 2006.
14. E. Ip and J.M. Kahn, Feedforward carrier recovery for coherent optical communications, *Journal of Lightwave Technology*, 25, 2675–2692, 2007.
15. L.N. Binh, Dual-ring 16-star QAM direct and coherent detection in 100 Gb/s optically amplified fiber transmission: Simulation, *Optical and Quantum Electronics*, 40(10), 707–732, August 5, 2008. Accepted December 2008.
16. L.N. Binh, Generation of multi-level amplitude-differential phase shift keying modulation formats using only one dual-drive Mach-Zehnder interferometric optical modulator, *Optical Engineering*, 48(4), 045005, 2009.
17. M. Nazarathy, X. Liu, L. Christen, Y.K. Lize, and A. Willner, Self-coherent multisymbol detection of optical differential phase-shift-keying, *Journal of Lightwave Technology*, 26, 1921–1934, 2008.
18. R. Noe, PLL-free synchronous QPSK polarization multiplex/diversity receiver concept with digital I&Q baseband processing, *IEEE Photonics Technology Letters*, 17, 887–889, 2005.
19. L.G. Kazovsky, G. Kalogerakis, and W.-T. Shaw, Homodyne phase-shift-keying systems: Past challenges and future opportunities, *Journal of Lightwave Technology*, 24, 4876–4884, 2006.

20. J.P. Gordon and L.F. Mollenauer, Phase noise in photonic communications systems using linear amplifiers, *Optic Letters*, 15, 1351–1353, 1990.
21. H. Kim and A.H. Gnauck, Experimental investigation of the performance limitation of DPSK systems due to nonlinear phase noise, *IEEE Photonics Technology Letters*, 15, 320–322, 2003.
22. S. Zhang, P.Y. Kam, J. Chen, and C. Yu, Receiver sensitivity improvement using decision-aided maximum likelihood phase estimation in coherent optical DQPSK system, in *Conference on Lasers and Electro-Optics/Quantum Electronics and Laser Science and Photonic Applications Systems Technologies*, Paper CThJ2, Technical Digest (CD), Optical Society of America, Baltimore, MD, 2008.
23. P.Y. Kam, Maximum-likelihood carrier phase recovery for linear suppressed-carrier digital data modulations, *IEEE Transactions on Communications*, COM-34, 522–527, June 1986.
24. S. Zhang, P.Y. Kam, J. Chen, and C. Yu, A comparison of phase estimation in coherent optical PSK system, in *Photonics Global'08*, Paper C3-4A-03, Singapore, December 2008.
25. S. Zhang, P.Y. Kam, J. Chen, and C. Yu, Adaptive decision-aided maximum likelihood phase estimation in coherent optical DQPSK system, in *OptoElectronics and Communications Conference (OECC)'08*, Paper TuA-4, pp. 1–2, Sydney, New South Wales, Australia, July 2008.
26. A.P. Clark, *Equalizers for Digital Modem*, Pentec Press, London, U.K., 1985.
27. X. Liu, X. Wei, R.E. Slusher, and C.J. McKinstrie, Improving transmission performance in differential phase-shift-keyed systems by use of lumped nonlinear phase-shift compensation, *Optic Letters*, 27(18), 1351–1353, September 2002.
28. X. Wei, X. Liu, and C. Xu, Numerical simulation of the SPM penalty in a 10-Gb/s RZ-DPSK system, *IEEE Photonics Technology Letters*, 15(11), 1636–1638, November 2003.
29. E. Ip and J.M. Kahn, Digital equalization of chromatic dispersion and polarization mode dispersion, *IEEE Journal of Lightwave Technology*, 25, 2033–2043, 2007.
30. I. Hodgkinson, Receiver analysis for optical fiber communications systems, *IEEE Journal of Lightwave Technology*, 5(4), 573–587, 1987.
31. I. Hodgkinson, Receiver analysis for optical fiber communications systems, *IEEE Journal of Lightwave Technology*, 5(4), 573–587, 1987. (Fig. 1&2.)

9

EDF Amplifiers and Simulink® Models

Optical fiber amplifiers are dominating the loss compensation in fiber-optic communication systems, especially the erbium-doped types for communication spectrum based on silica fibers. Several models have been developed for such photonic amplification devices. However, there are no comprehensive models developed in MATLAB® Simulink® platform. This chapter describes in detail the development of a Simulink model for erbium-doped fiber amplifiers (EDFAs) operating under steady state and dynamic condition.

The equations that govern the pump and signal propagation in the doped fiber are derived and tabulated with corresponding amplifier parameters. The model blocks are then described under the Simulink environment. Simulation results are compared with experimental values, and their close agreements indicate the validity of the Simulink EDFA models. The model is tested to see if it is user friendly and easy to use in research and teaching laboratories.

9.1 Introductory Remarks

Since 1989, the rare earth metal–doped fibers have been exploited as the optical amplification media and source of lasers both in experimental and theoretical aspects. The EDFAs are the amplifying devices employed in commercial optical transmission systems. Several models have been developed for design and system simulation and have also been reported.

The mathematical laboratory MATLAB has also been developed and improved over the last two decades. It is now considered the standard mathematical tool in teaching and R&D laboratories around the world. Recently, it has added the Simulink tool boxes. This gives an additional and powerful tool for simulation of physical systems. The Laboratory for Optical Communications and Applied Photonics of Monash University has developed several packages under MATLAB and Simulink for simulation of photonic devices and optical communication system for both research and training purposes.

Why should Simulink be developed while there are a number of commercial simulation packages available such as VPI Systems? Simulink is a modular tool box attached to MATLAB which is now used as a universal computing tool in global universities. Its communication blockset contains many tools for digital communications in the base band as well as the passband. Thus, these toolboxes can be used as a modular set for generation and detection of light wave signals. As the frequency of the light waves is much higher than the base band signals, it is not likely that the carrier will be contained under the envelope of the signals because an extremely high sampling rate would be required, which is currently not possible in computing systems. Thus complex envelope signals are used to represent the phase of the carrier. Therefore, the simulation models for digital optical communications can be modeled very accurately and with ease because of the modular

nature of Simulink. The Simulink techniques and samples of models may be made available as a toolbox in MATLAB in the future so that global laboratories can use them to facilitate teaching and research activities. Thus, the Simulink models, especially the toolset, described in this book can be easily integrated into standard MATLAB software packages in the university, research, and engineering laboratories as well as in the field. The Digital Optical Communications MATLAB Simulink models are globally affordable for researchers and students of advanced-level applied physics and telecommunications engineering.

This chapter describes the comprehensive and successful implementation of the EDFA over the Simulink MATLAB 7 R14. The report has been organized as follows: The fundamental and theoretical expressions representing the optical amplification and the rate of transitions of the erbium ions and light wave propagation over the amplifying medium are described in Section 9.2. Both forward and backward pumping configurations are given. Section 9.3 gives an account of the Simulink models for the amplifiers in the steady state and dynamic environments. Section 9.4 then illustrates the samples of the Simulink simulator; Section 9.4 presents details of the simulation results to validate the developed models with experimental data obtained from EDFA constructed in the laboratory as well as those specified by commercial manufacturers.

The proposed MATLAB Simulink models are proven to be user friendly and easy to use [9,10]. It would be a good tool for researchers and teaching graduates at advanced levels in the field of photonics and optical communications.

9.2 Fundamental and Theoretical Issues of EDFAs

In this section, basic theoretical analyses of the EDFA are described for the development of EDFA simulation modeling. Several technical terms such as Pumping Scheme, Population inversion factor, and amplified spontaneous emission (ASE) noise are defined.

9.2.1 EDFA Configuration

EDFA is constructed mainly by a short length of optical fiber whose core has been doped with less than around 0.1% erbium, an optically active rare earth element, which has many unique intrinsic properties for optical amplification [6,7]. The optical fiber used is named erbium-doped fiber. The optical amplifier engineer chooses appropriate erbium-doped fiber during the EDFA development. Different doped fibers have different characteristics of the absorption and emission factors, which are identified and discussed in a later section.

An EDFA consists of an erbium-doped silica fiber and other photonic components such as the pump source, the optical isolators, and the WDM coupler as shown in Figure 9.1. An enhanced EDFA Module consists of an erbium-doped fiber, a wavelength-dependent coupler (WSC), and a polarization-insensitive optical isolator (OI). An optical filter may be required to improve EDFA performance [13] depending on specific applications. The optical filter is used to reduce the ASE noise and protect the amplifier from saturation caused by ASE accumulated in an in-line-amplification system. The OI is used for achieving a stable amplified operation to prevent spurious oscillations and reflection. The pump source is used for pumping the erbium ions to the next higher-energy level; several proper pumping wavelength laser diodes exist at present. Both 1480 and 980 nm

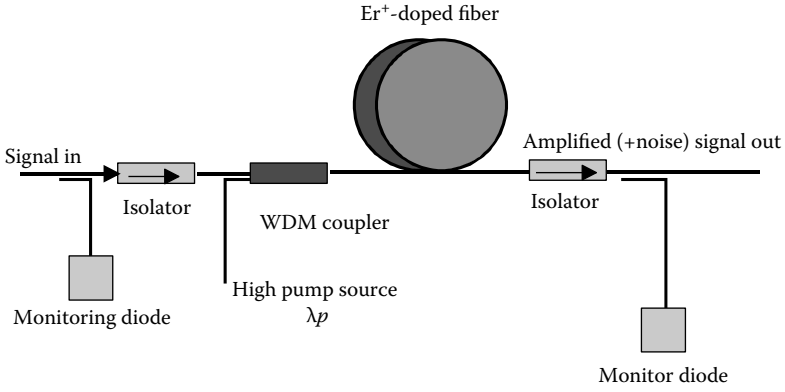

FIGURE 9.1
Standard forward pumped EDFA. (From Scholten, R., Quantum & advanced optics laser, School of Physics, University of Melbourne, Melbourne, Victoria, Australia, 2003.)

pumping laser diodes can provide high pump gain, investigations of which are described in a later section. The WSC/WDM is used to combine the pump sources and the incoming signal. The pump light waves are guided and propagating along the EDF length and the depleted erbium ions then rise to an excited state by absorbing the energy. As the signal propagates through the erbium-doped fiber (EDF), it stimulates emission of light from the excited ions, thereby amplifying the signal. The tap coupler is used as a separator taping the pumping power to protect the receiver, normally used in preamplifier.

Two pumping configurations can be used in EDFAs, the backward pumping and dual backward and forward pumping as shown in Figure 9.2.

The only difference between the three configurations is the pumping propagation direction. As the name of the configuration suggests, in forwarding pumping, the signal light co-propagates with the pump light, whereas in backward pumping it counter-propagates relative to the pump light, and dual pumping would pump bi-directional. With reference

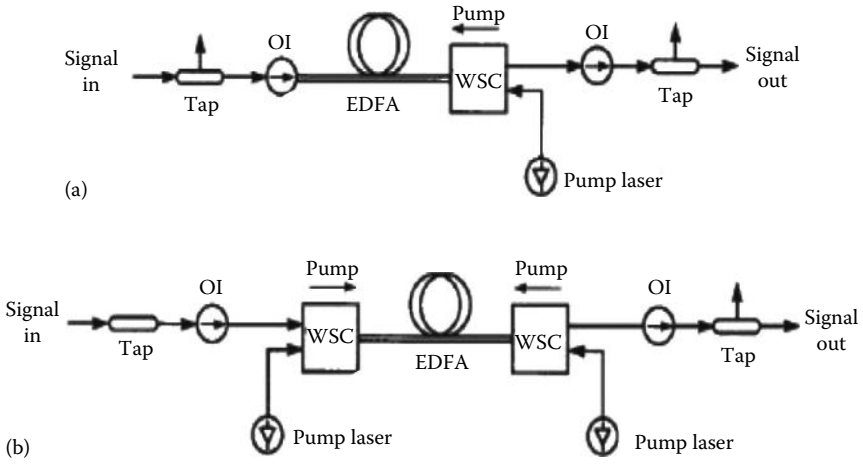

FIGURE 9.2
(a) Backward pumping and (b) dual pumping. (Adopted from Scholten, R., Quantum & advanced optics laser, School of Physics, University of Melbourne, Melbourne, Victoria, Australia, 2003.)

to the noise performance, the forward pumping can produce optical amplification with low noise but may offer lower amplification gain due to fluctuation in the pump power and signal power. On the other hand, the backward pumping may be effective for high power output, but it suffers higher ASE noise. Thus, there is an enhanced model in which bi-directional pumping or dual pumping can be combined.

9.2.2 EDFA Operational Principles

The basic operation principle of EDFA is based on the fact that the erbium ions can exist in several energy states. When they are in a high-energy state, some photons could be stimulated to give up some of their energy (as light) and return to a lower-energy (more stable) state, thereby creating photonic amplification [14].

9.2.3 Pump Wavelength and Absorption Spectrum

The pump wavelength can be either 980 or 1480 nm depending on the availability of these lasers sources. Why do most EDFAs use these two as their pumping wavelengths and not others? Before answering, let us see the energy levels of the triply ionized erbium ion Er^{3+}, the absorption band of Er^{3+}, and the pump efficiency.

There are several states as shown in Figure 9.3a to which the erbium ions could be pumped using different sources of wavelengths such as those operating at 1490, 980, and 850 nm. However, in real light wave systems, the pump wavelength must provide high power to achieve high gain per pump. The commonly available laser diodes can operate

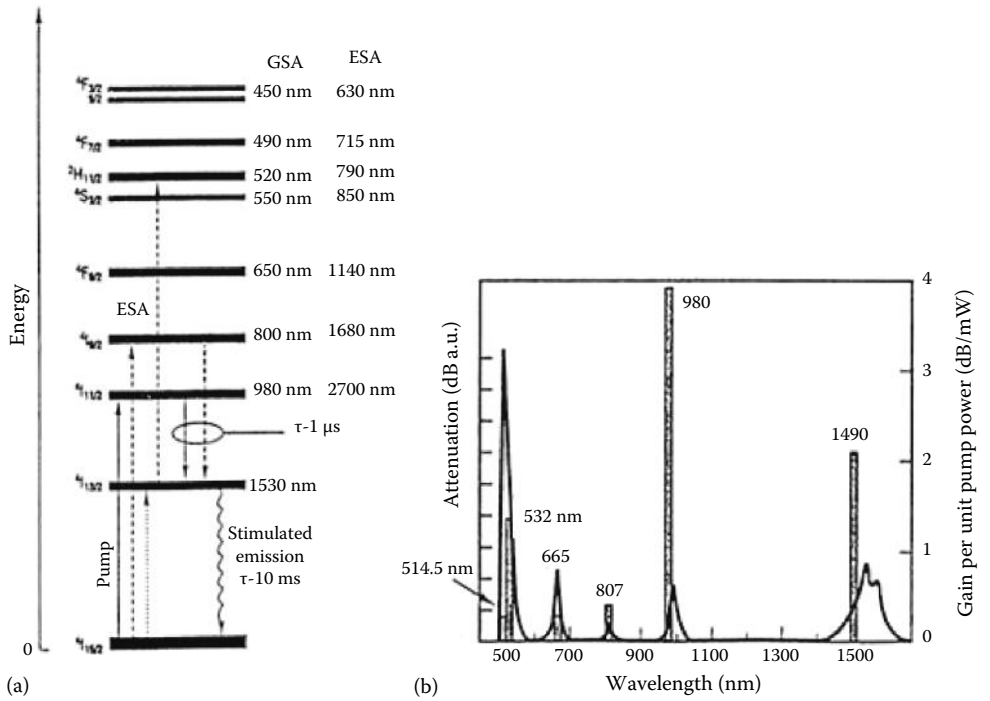

FIGURE 9.3
(a) Energy levels of Er^{3+} ions and (b) gain and attenuation spectra and possible pumping source wavelength.

at 800, 980, and 1480 nm, but the pump efficiency can go more than 1 dB/mW with low attenuation depending on the pump frequency. The only pump wavelength laser source that can give a high pumping efficiency with lower attenuation is that operating at 980 or 1490 nm. In practice, the 980 nm pumping source is commonly used due to its high gain coefficient (4 dB/mW). The model given in this report employs both 980 and 1480 nm pumping sources. The different effects of those two wavelength sources are mainly caused by the absorption and emission factors.

9.2.3.1 Pump Mechanism

Amplification mechanism is the key for developing the EDFA simulation model. The optical amplification gain is supplied by the excited erbium ions (Er^{+}) when the amplifier is pumped to achieve population inversion. Depending on the energy states of the dopant, pumping schemes can be classified as a two-level or three-level scheme. The main difference between the two-level and three-level pumping schemes is related to energy state occupied by the stimulated-emission event. In the case of a three-level scheme, the lower level is ground, whereas it is an excited state with a fast relaxation time in the two-level scheme.

As shown in Figure 9.4, erbium ions are pumped to an upper energy level by the absorption of light wave energy from the pump source at either 980 or 1480 nm to regain the equilibrium distribution [13].

Stage 1

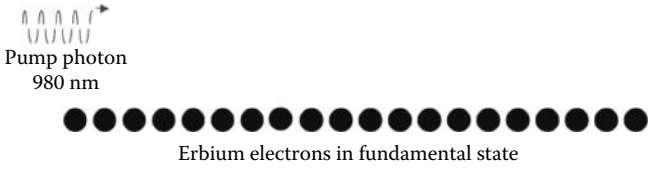

FIGURE 9.4
The pump photon starts propagating through the erbium fiber, and all the erbium electrons are now in the fundamental state (ground state). (Adopted from Scholten, R., Quantum & advanced optics laser, School of Physics, University of Melbourne, Melbourne, Victoria, Australia, 2003.)

Stage 2 (Figure 9.5)

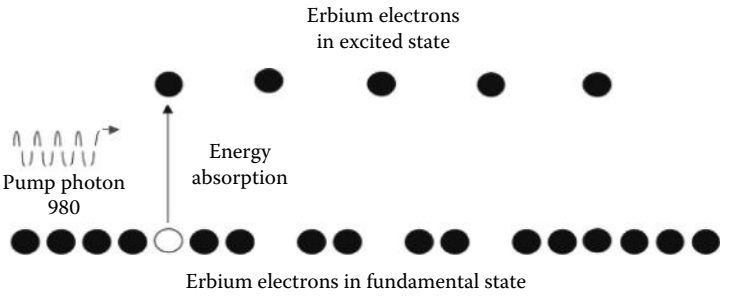

FIGURE 9.5
The erbium electrons that are pumped to higher-level energy states. (Adopted from Scholten, R., Quantum & advanced optics laser, School of Physics, University of Melbourne, Melbourne, Victoria, Australia, 2003.)

Stage 3 (Figure 9.6)

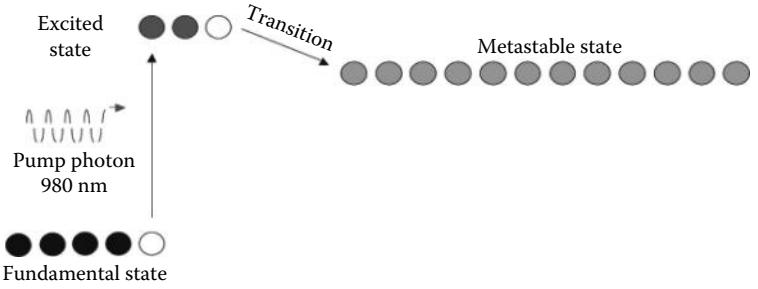

FIGURE 9.6
The erbium electrons now revert to lower states (metastable state) spontaneously after some mean lifetimes t – 1 ms (spontaneous emission). (Adopted from Scholten, R., Quantum & advanced optics laser, School of Physics, University of Melbourne, Melbourne, Victoria, Australia, 2003.)

Stage 4 (Figure 9.7)

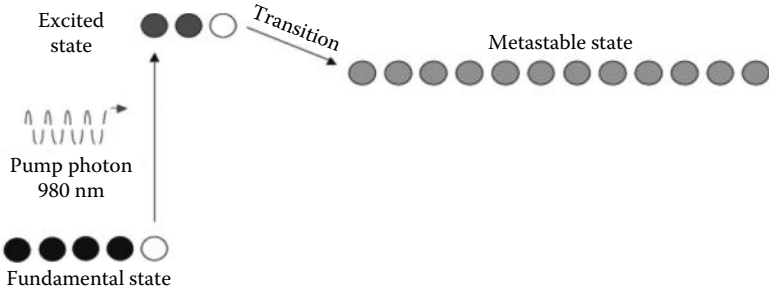

FIGURE 9.7
The erbium electrons revert to the fundamental state spontaneously (spontaneous emission) and stimulated to do so by some incident photons (signal) of exactly the energy corresponding to the drop to lower state (stimulated emission). (Adopted from Scholten, R., Quantum & advanced optics laser, School of Physics, University of Melbourne, Melbourne, Victoria, Australia, 2003.)

The coherence of pump sources and signals implies that the incident photon and the stimulated one have the same frequency, phase, propagation direction, and polarization [15, 16]. The optical gain is achieved when the population inversion reaches a sufficiency high level at which the absorption from the ground state is considerably reduced. This can be readily achieved with available pump lasers because the metastable state exists in Er^{3+} thus rendering the population inversion possible. In addition, the photon lifetime from the metastable state to fundamental state is longer than that from excited state to metastable state, which is normally around 10–10.5 ms whereas the lifetime from excited state to metastable state is normally about 1 ms. Therefore, the ions are accumulated in the metastable state and the ion population in the excited state is negligibly small. This fact is critical in the design of the simulator.

9.2.3.2 Amplifier Noises

During the signal amplification process, noises are generated. The dominant amplification noise source is the ASE noise (amplifier-stimulated emission noise). When ions are on

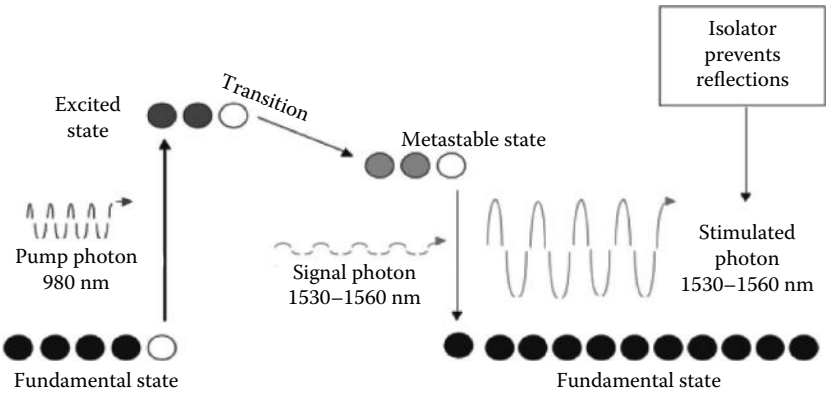

FIGURE 9.8
ASE photons demonstration. (Adopted from Scholten, R., Quantum & advanced optics laser, School of Physics, University of Melbourne, Melbourne, Victoria, Australia, 2003.)

transition from the excited state to the fundamental state, some excited erbium ions decay to the fundamental state with spontaneous emission before amplifying the injecting signal photons. These photons are emitted with random phase and direction [13] (Figure 9.8).

The ASE spectral range is very wide and covers almost all of the C- and L-bands covering the gain spectrum of the amplifier as shown in Figure 9.9a with and without signal injection. Figure 9.9b shows the gain and absorption spectrum of the EDFA so that one can select the pump wavelength at which the absorption is highest to achieve the most effective amplification factor.

This will reduce the available gain for the signal field. Figure 9.10 shows the saturated gain has been reduced by the ASE. That is due to the incoherence of the excited erbium ions with the signal photons. The ASE noises cause degradation to the signal and noise ratio (SNR).

EDFAs are employed in long-haul transmission systems, and the ASE level grows after a cascade of amplifiers and begins to saturate the optical amplifiers and reduce the signal gain. This is because the total power is almost equal to the pump power plus the ASE power.

9.2.3.3 Amplifier Gain Modulation

The gain modulation of EDFAs can provide an attractive approach for implementing status and control communication in modern dense wavelength division multiplexing (DWDM) communication networks. The desired control signal is imposed as amplitude over modulation on the payload communication signals propagating down the system, via modulation of the EDFA pump power [2]. We report here in this chapter the impacts of pump modulation and signal modulation on EDFA gain.

9.3 EDFAs in Long-Haul Transmission Systems

Optical amplifiers can be employed with three different types of optical transmission systems as a booster amplifier, an in-line amplifier regenerator, and as an optical preamplifier at the receiver as shown in Figure 9.11:

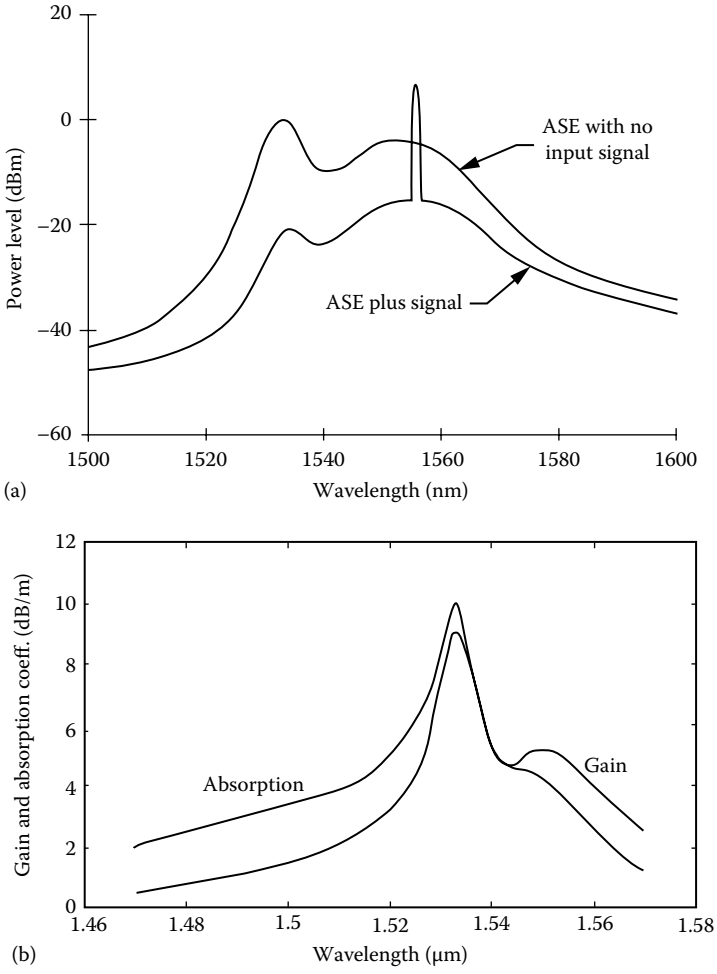

FIGURE 9.9
(a) ASE noise spectrum. (Adopted from Scholten, R., Quantum & advanced optics laser, School of Physics, University of Melbourne, Melbourne, Victoria, Australia, 2003.) (b) Absorption and gain spectra.

- The booster amplifier: This increases and provides a high optical power signal prior to transmission. In long-haul optical communication system, the use of a booster amplifier can increase the link power budget and reduce the number of regenerators required.
- In-line optical amplifiers: The main function of the in-line amplifier is to compensate for the fiber loss of the fiber span or the dispersion compensating fibers thereby overcoming the need for O/E regeneration.
- Optical preamplifier: The main function of the optical preamplifier is to increase the power level of a signal before detection and, as a consequence, the receiver sensitivity.

9.3.1 EDFA Simulation Model

In this section, the mathematical expressions for developing EDFA simulation model are described. In general, the simulation models can be classified into steady state and

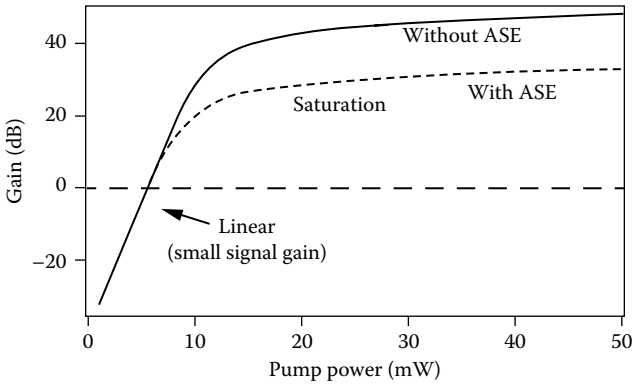

FIGURE 9.10
Optical gain reduction by the contribution of ASE. (Adopted from Scholten, R., Quantum & advanced optics laser, School of Physics, University of Melbourne, Melbourne, Victoria, Australia, 2003.)

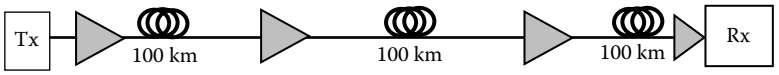

FIGURE 9.11
The employment of three types of amplifiers and related monitoring equipment.

dynamic models and/or perturbation modes [6,7]. In this report, only the first two models are used for EDFAs simulation. The models of single EDFA are investigated; a cascade of EDFAs can be implemented without difficulty and left for users to construct.

9.3.2 Amplifier Parameters

A number of parameters can clarify the principles of the simulation model as shown in Tables 9.1 and 9.2.

TABLE 9.1
Erbium-Doped Fiber Parameters

Physical Meaning	Expression	Symbol and Unit
Erbium-doped fiber parameters (Part I)		
Core radius of erbium-doped fiber		r (μm)
Core area of EDF		A (m^2)
Overlap factor of EDFA at wavelength (λ)		Γ_λ
Ion density of erbium-doped fiber		ρ (ions/m^3)
Florescence lifttime of EDFA		τ (ms)
Absorption cross section at wavelength (λ)		σ_λ^α (m^2)
Emission cross section at wavelength (λ)		σ_λ^e (m^2)
Absorption coefficient at wavelength (λ)	$\rho\Gamma_\lambda\sigma_\lambda^\alpha$	α_λ (m^{-1})
Absorption over length L at wavelength (λ)	$\alpha_\lambda \times L$	
Plank constant	6.626e-34	h (J·s)
Speed of light		c (ms^{-1})

TABLE 9.2

Glossary of EDFA Parameters

Physical Meaning	Expression	Symbol and Unit
Erbium-doped fiber parameters (Part II)		
Length of the erbium fiber		L (m)
Population density in fundamental state		n_1 (ions/m^3)
Population density in excited state (assume 980 nm pump)		n_3 (ions/m^3)
Population density in metastable state		n_2 (ions/m^3)
Signal power		P_{in} (mW)
Pump power		P_{out} (mW)
Signal power in simulation	$N_s = \frac{P_{signal}^{in} c}{h\lambda_s}$	N_s (photons/s)
Pump power in simulation	$N_p = \frac{P_{pump}^{in} c}{h\lambda_p}$	N_p (photons/s)

Bononi and Rusch have developed a dynamic model based on the one-dimensional ordinary nonlinear differential equation for the time-dependent population of excited state erbium ions in EDFAs [3]. With the three level states, the amplification in erbium-doped fiber is based on the stimulated erbium ions; thus, the state population would have discrepancy. Simplifying the schemes to be a three-level pumping, the three populations of erbium atoms are ground state (the fundamental state with population density n_1), level state 2 (the excited state population density, also called metastable state with signal frequency n_2), and level state 3 (the excited state population with pump frequency n_3). The rate equation for these three states can be defined and given as follows [6,7,14]:

Ground state 1 population

$$\frac{\partial n_1}{\partial t} = -W_{1-3} * n_1 - W_{1-2} * n_1 + W_{2-1} * n_2 + \frac{n_2}{\tau_{2-1}} + W_{3-1} n_3 + \frac{n_3}{\tau_{3-2}} \tag{9.1}$$

State 2 population

$$\frac{\partial n_2}{\partial t} = W_{1-2} * n_1 - W_{2-1} * n_2 + W_{3-2} * n_3 - \frac{n_2}{\tau_{2-1}} \tag{9.2}$$

and finally, the state 3 population equation

$$\frac{\partial n_3}{\partial t} = W_{1-3} * n_1 - W_{3-2} * n_3 + W_{3-1} * n_3 - \frac{n_3}{\tau_{3-2}} \tag{9.3}$$

The transition from state 3 to 2 (W_{3-2}) has a greater influence on the EDFA gain than the transition down to the fundamental state (W_{3-1}). The transition rate W_{3-1} can be neglected (Table 9.3). The transition W_{1-3} is associated with the pump source. Furthermore, we can refer to Figure 9.8, the florescence lifetime for transition (W_{3-2}) is short enough (1 μs) compared with that of the transition (W_{2-1}) (10 ms); thus, the erbium ions can be accumulated

TABLE 9.3

Transition Rates between States of a Stimulated Er^{3+} Ion

Physical Meaning	Symbol	Expression	Comment
Transition rate from state 1 to state 2	W_{1-2}	$W_{1-2} = \frac{\Gamma_s \sigma_{1-2} N_s}{A}$	Transition associate by the signal
Transition rate from state 1 to state 3	W_{1-3}	$W_{1-3} = \frac{\Gamma_p \sigma_{1-3} N_p}{A}$	Transition associate by the pump (980 nm)
Transition rate from state 2 to state 1	W_{2-1}	$W_{2-1} = \frac{\Gamma_s \sigma_{2-1} N_s}{A}$	Transition associate by the signal (C-band) 1525–1565 nm (L-band) 1566–1605 nm
Transition rate from state 3 to state 2	W_{3-2}	$W_{3-2} = \frac{\Gamma_p \sigma_{3-2} N_p}{A}$	Transition associate by the pump (980 nm)
Transition rate from state 3 to state 1	W_{3-1}	$W_{3-1} = \frac{\Gamma_p \sigma_{3-1} N_p}{A}$	Transition associate by the pump (980 nm)

in state 2. Hence, the transition rate W_{1-3} should be very close to transition W_{3-2} due to the shorter lifetime. We thus have $W_{3-2} \cong W_{1-3}$. Substituting this into Equation (9.2) we have

$$\frac{\partial n_2}{\partial t} = W_{1-2} * n_1 - W_{2-1} * n_2 + W_{1-3} * n_3 - \frac{n_2}{\tau_{2-1}} \tag{9.4}$$

In fact, n_3, n_2, and n_1 are independent. However, as mentioned earlier, the erbium ions are accumulated in state 2 and the population density in n_3 thus can be negligible. The total population density ρ of the fiber is a constant value. Therefore, if $n_3 \approx 0$, then n_1 and n_2 are no longer independent of each other and are under the constraint that the sum of the two equals the total erbium ions in the fiber $n_1 + n_2 = \rho$. In particular, the populations are functions of both time and linear distance along the erbium-doped fiber [3,6,7,14].

The relationship between the input power and the population has to be determined next. Figure 9.12 illustrates how the input power is evaluated along the EDF.

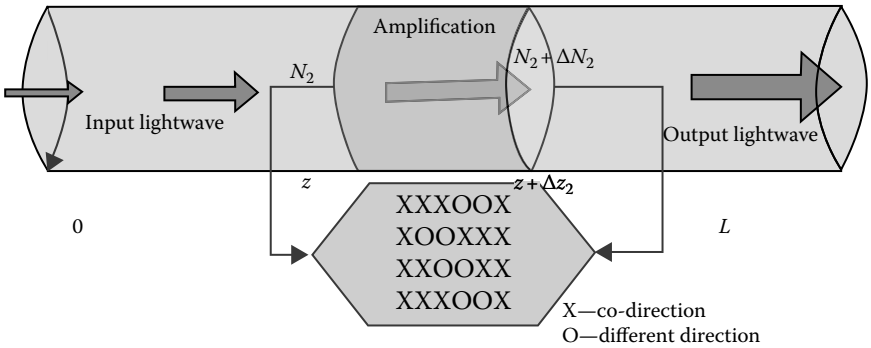

FIGURE 9.12
Power evolution of the signal under the amplification process along EDF.

Refer to Figure 9.12; the input light is amplified along the distance during the time. Hence, the optical power through the erbium-doped fiber is determined [2] by

$$\frac{\partial P_p}{\partial z} = -\Gamma_p * \sigma_{1-3} n_1 * P_p - \gamma_p * p_p \tag{9.5}$$

$$\frac{\partial P_s}{\partial z} = -\Gamma_s * \sigma_{1-2} n_1 * P_s + \Gamma_s * \sigma_{2-1} n_2 * P - \gamma_s * p_s \tag{9.6}$$

where Γ_γ denotes the scattering and other losses of the EDF. As shown in Figure 9.2, X stands for the co-directional photon. O is the photon simulation in a different direction, generating noises, reflection power, and scattering.

9.3.3 EDFAs Dynamic Model

In our simulator, the EDFAs, dynamic modeling is focused on the steady-state modeling as "EDFAs with high output powers for multiple channel optical network are strongly saturate and the resultant effective time constant are reduce to the order of tens of microsecond which is 1000 times shorter than its lift time" [6,7]. The time-dependent problem is especially important in the optical network where the optical channels are constantly reconfigured. Dynamic modeling can predict that the EDFA gain more accurately during multichannel amplification. This section describes the essential Bononi–Rusch approach and develops it to accommodate the time varying pump and communication signal. Multichannel amplification modeling principle is also considered in this section.

First, we note that Equations 9.1 through 9.6 can be typically solved by obtaining the population in a different state as a function of the transition rates. $W_{1-2} = \frac{\Gamma_s \sigma_{1-2} N_s}{A}$, $W_{1-3} = \frac{\Gamma_p \sigma_{1-3} N_p}{A}$, and $W_{2-1} = \frac{\Gamma_s \sigma_{2-1} N_s}{A}$.

Substituting into (9.5) and (9.6), we have

$$\frac{\partial P_p}{\partial z} = -W_{1-3} * n_1 * A - \gamma_p * p_p \tag{9.7}$$

$$\frac{\partial P_s}{\partial z} = -W_{1-2} * n_1 * A + W_{2-1} * n_2 * A - \gamma_p * p_p \tag{9.8}$$

Multiplying (9.4) by the fiber effective core area and substituting (9.7) and (9.8) [12], we have

$$\frac{\partial N_2}{\partial t} = P_s(0,t) * (1 - e^{G_s}) + P_s(0,t) * (1 - e^{G_p}) - \frac{N_2}{\tau} - \gamma_p * p_p - \gamma_s * p_s \tag{9.9}$$

where G_s and G_p are the amplification gains of the power evolution, respectively. The increment of the power along the EDFA is nonlinear and assumed to vary exponentially, and hence we have [1]

$$P_p(L,t) = P_p(0,t) e^{\frac{\Gamma_p \sigma_{1-3}}{A} N_2 - \Gamma_p \sigma_{1-3} \rho L - \gamma_p} \tag{9.10}$$

$$P_s(L,t) = P_s(0,t) e^{\frac{\Gamma_s (\sigma_{1-2} + \sigma_{2-1})}{A} N_2 - \Gamma_s \sigma_{1-2} \rho L - \gamma_s} \tag{9.11}$$

Assuming $\gamma = 0$ leads to

$$G_p = \frac{\Gamma_p(\sigma_{1-3} + \sigma_{3-1})}{A} N_2 - \Gamma_p \sigma_{1-3} \rho L \tag{9.12}$$

$$G_s = \frac{\Gamma_s(\sigma_{1-2} + \sigma_{2-1})}{A} N_2 - \Gamma_s \sigma_{1-2} \rho L \tag{9.13}$$

Input channels with different wavelengths have different EDFA gains as a result of the spectral dependence of the absorption and emission cross sections and the overlap factor. For the three-level transition schemes (980 nm pump), σ_{1-2} and σ_{2-1} are the absorption and emission factors, respectively, at the signal wavelength, and σ_{1-3} and σ_{3-1} correspond to the absorption and emission due to the pump wavelength, respectively. σ_{3-1} is assumed to be negligible over the short transition time. For the two-level scheme, the pump source is normally operating in the spectral region 1480–1490 nm; the rate equations are similar to those obtained for the three-level scheme, but the absorption and emission factors $[\sigma_{1-3} \quad \sigma_{3-1}]$ are to be matched with the corresponding wavelength. Rewriting these matrices to $[\sigma_a \quad \sigma_e]$, the $[\sigma_a \quad \sigma_e]$ for the pump wavelength is $[\sigma_{a_p} \quad \sigma_{e_p}]$, where σ_{e_p} is nonzero and refers to the spectrum of absorption and emission factors. For multichannel amplification, the modeling equations are integrated and summarized as

$$\frac{\partial N_2}{\partial t} = \sum_{\lambda_o}^{\lambda_n} P_\lambda(0,t) * (1 - e^{G_\lambda}) - \sum_{\lambda_o}^{\lambda_n} \gamma_\lambda * p_\lambda - \frac{N_2}{\tau} \tag{9.14}$$

9.3.3.1 EDFA Steady-State Modeling Principles

It is well known that one of the advantages of EDFA is its slow dynamics as a result of the long spontaneous lift time of around 10 ms. This is also the reason why steady-state models play an important role in the dynamic analysis of EDFA properties for system applications [5]. The EDFA steady-state modeling has been widely used. An EDFA operates in a steady-state condition when $\frac{\partial N_2}{\partial t} = 0$, that is when there are no population increments and the EDFA gain reaches the saturation mode. Hence, to model the EDFA in steady state, we have

$$0 = \sum_{\lambda_o}^{\lambda_n} P_\lambda^{saturation}(0,t) * (1 - e^{G_\lambda^{saturation}}) - \sum_{\lambda_o}^{\lambda_n} \gamma_\lambda * p_\lambda^{saturation}(0,t) - \frac{N_2^{steady\text{-}state}}{\tau} \tag{9.15}$$

which can be simplified to

$$P_p(L,t) = \sum_{\lambda_0}^{\lambda_n} P_{\lambda_p}^{steady}(0,t) e^{\frac{\Gamma_p \sigma_{a\lambda_p}}{A} N_2^{steady} - \Gamma_p \sigma_{a\lambda_p} \rho L - \gamma_p} \tag{9.16}$$

$$P_s(L,t) = \sum_{\lambda_0}^{\lambda_n} P_{\lambda_s}^{steady}(0,t) e^{\frac{\Gamma_s(\sigma_{a\lambda_s} + \sigma_{e\lambda_s})}{A} N_2^{steady} - \Gamma_s \sigma_{a\lambda_s} \rho L - \gamma_s} \tag{9.17}$$

This model thus can predict the onset of steady state of the amplification gains and pump absorption in an optical amplifier containing an arbitrary number of pumps and signals for co- and contra-propagating scenarios.

9.3.3.2 Population Inversion Factor

Population inversion indicates the number of ions inverted from state 1 to state 2 excited by the pumping energy. To obtain the amplification gain, the number of photons gained by stimulated emission from the metastable state to the fundamental state must be greater than those by absorption from the fundamental state to state 2. This condition implies that the population in the metastable state must be maintained at a greater level than that in the fundamental state. The degree of population inversion can thus be expressed by the population inversion factor n_{sp} [14] as

$$n_{sp} = \frac{N_2}{N_2 - \frac{\sigma_e}{\sigma_a} N_1} \tag{9.18}$$

where n_{sp} is related to the pump and signal power and is the key factor of the amplifying spontaneous emission noise (ASE).

9.3.4 Amplifier Noises

In the previous section, the production of the ASE photons has been described. The noise statistics of the amplified light waves follows a Gaussian distribution. By considering noise as a random variable generated by various independent sources, it can be assumed that in general the probability density function of their sum also approaches Gaussian. The effect of the amplifier noise can, therefore, be modeled as a Gaussian random process with a noise variance.

9.3.4.1 ASE Noise Model

The ASE noise as a random noise can be modeled by generating complex spectral components whose real and imaginary random variables follow a Gaussian probability density function with the variance P_{ase} corresponding to the average noise. The ASE noise spectral power can be estimated over a bandwidth Δf as

$$P_{ase} = n_{sp}(G-1)hf_s\Delta f = N_0\Delta f \tag{9.19}$$

where it is assumed that a sufficiently large bandwidth on ASE detection is used and is sensitive within the spectral region 1480–1605 nm and G is the small signal amplification gain. To model the ASE noise, a Gaussian wave with ASE mean power and variance are used, which are described in the next section.

9.3.4.2 Other Noise Sources

In practice, an optical BPF is usually incorporated into the EDFA to reduce the ASE noise contribution. Two noise sources contribute to the ASE-induced noise: (1) spontaneous–spontaneous beat noise, *sp–sp* beat noise, caused by the self-interference of the generated spontaneous photons and given by $P_{sp-sp} = 2n_{sp}^2(G-1)^2e^2\Delta f$; and (2) signal–spontaneous beat noise, *s–sp* beat noise, produced by the beating between the signal photons and those of spontaneous emission and given by $P_{s-sp} = 4e^2\frac{P_{in}}{hf}n_{sp}(G-1)G$.

As the *s–sp* term dominates the ASE noise, we have

$$N_{s-sp} = 4e^2N_{in}n_{sp}(G-1)G \tag{9.20}$$

9.4 EDFA Simulation Model

This section gives the evaluation of the numerical data resulting from our EDFA simulator and EDFA Module; experimental results are compared with those generated by our models. The principal advantage of the Simulink EDFA simulator is its versatility and ease of use. These results are by no means exhaustive.

9.4.1 EDFA MATLAB® Simulink® Model

On the basis of the simulation modeling principle from the previous section, we focus here on how to implement EDFA simulation on MATLAB Simulink. This section documents the Simulink simulation design and developments, explaining how each of the blocks within the simulator is brought together. Figures 9.13 and 9.14 illustrate the EDFA Simulator and EDFA Modules and associated monitoring equipment. The explorer views of the subsystem within the Simulink model are available to the user on request.

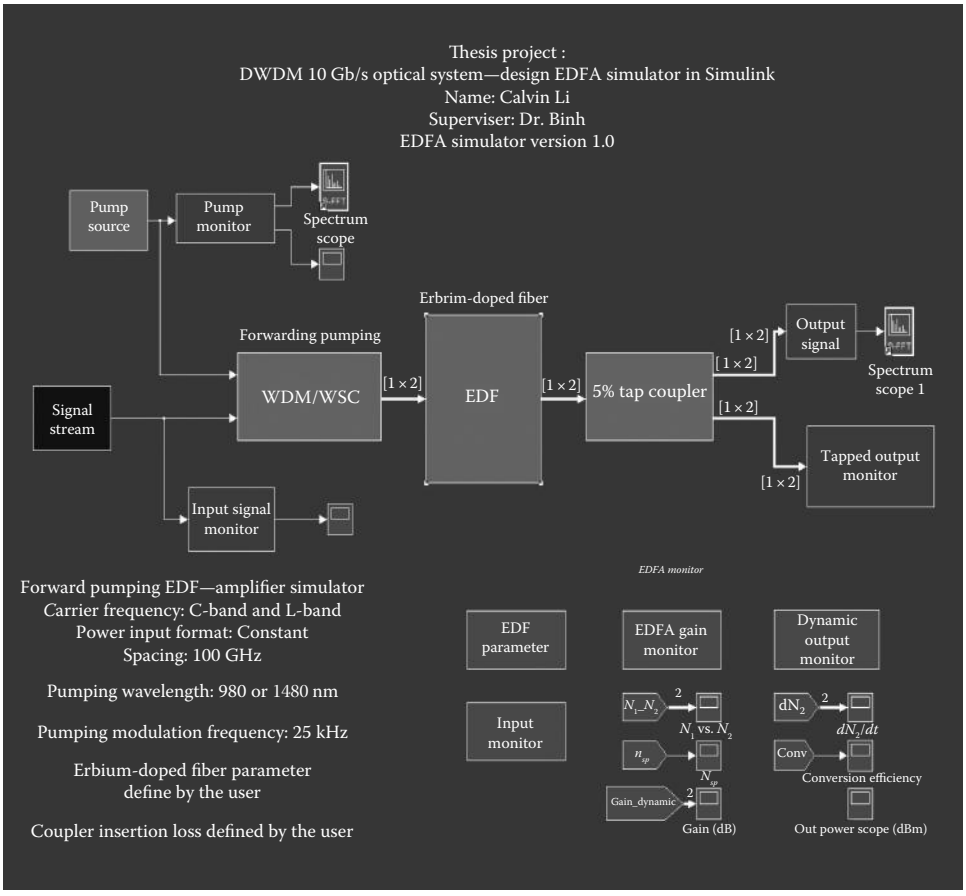

FIGURE 9.13
The EDFA simulator model: amplifier general layout.

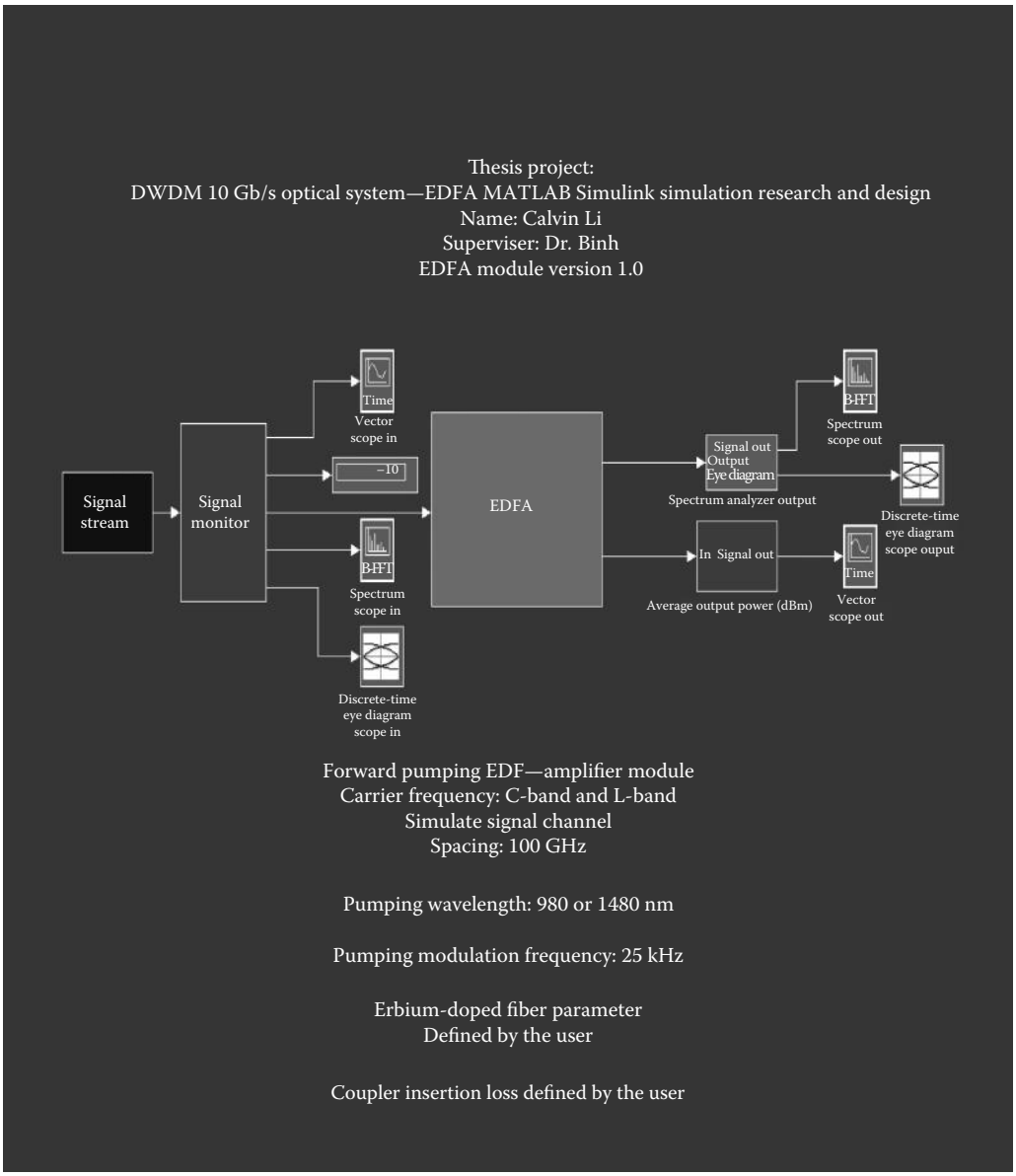

FIGURE 9.14
EDFA module amplifier and monitoring systems.

9.4.2 Simulator Design Outline

Simulink is easier for a user familiar with the programmer's methods or general programming techniques, that is, operators or system technicians. This reduces the likelihood of human-induced error when modeling the system of choice, important in the rapidly changing area of information transmission.

The Simulink simulation model in this chapter is basically divided into two parts: (1) EDFA Simulator and (2) EDFA Module. The EDFA Simulator simulates the details of amplification

along the erbium-doped fiber to investigate and scope how the signal can be pumped along the fiber and also to observe the effect in gain modulation during the amplification. The EDFA simulator development is based on the EDFA dynamic modeling, and the EDFA module is used with the whole optical system simulation for predicting the amplification output and its noise scoping. EDFA Module development is based on the EDFA steady-state modeling. Thus, the function of those two simulations is different. EDFA model can be easily combined with the transmitter simulator and fiber simulator to form an optical communication link.

9.4.3 Simulator Design Process

Intrinsically, MATLAB Simulink is a very powerful design tool. Initially, the first task of the model setup focuses on how to simulate the pumping schemes of the EDF. This is the primary goal and also the principal part of our simulator. The simulator is divided into a number of stages. The flowchart in Figure 9.15 outlines the design process.

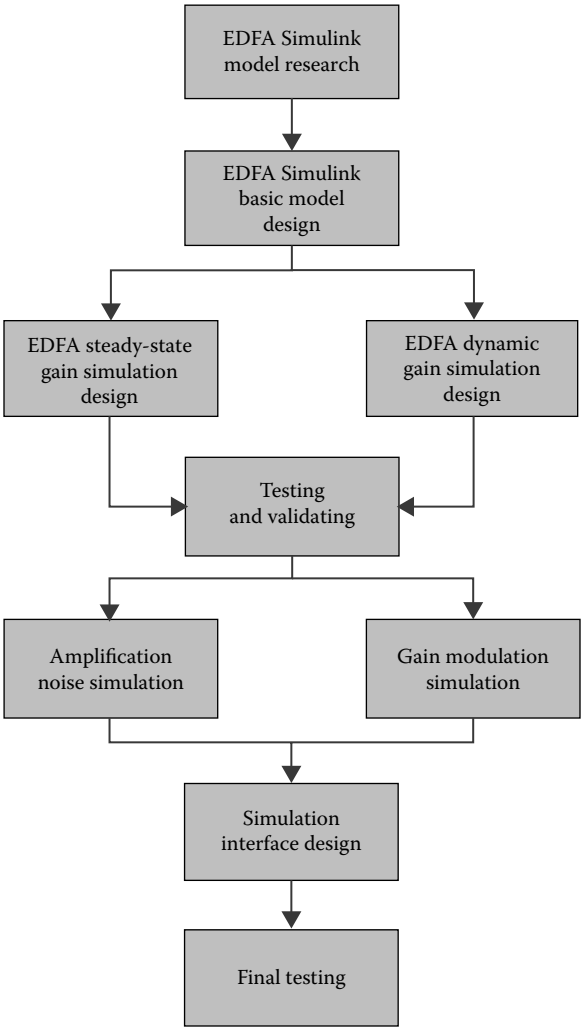

FIGURE 9.15
Simulation design flow chart.

9.4.4 Simulator Requirement

In this section, the requirement related to the basic issues such as software compatibility and simulation efficiency on the MATLAB Simulink software is described. First, the EDFA Simulink simulation is designed based on MATLAB Simulink MATLAB 7. Running the simulator in MATLAB Simulink is the first requirement. As there are many versions of MATLAB Simulink available, running an incorrect Simulator version may cause bug/hang or jams.

Second, the blocksets of the Simulink library must be included and activated. Running without the relevant blockset libraries initialized on the user's platform, the Simulink simulation can be opened. The specific blocksets necessary to assure the operation are Simulink DSP blocksets, Simulink Sink, Simulink Communications Blocksets, and the Simulink Extras Blocksets.

9.4.5 Simulator Design Assumptions

9.4.5.1 Sampling Time Assumption

In the design of the simulator, a discrete rather than continuous sampling method is employed, primarily for practical reasons. In particular, a discrete sampling system would decrease the processing power required to execute simulations and reduce execution time.

According to the well-known sampling theorem, all data are sampled at or above the Nyquist frequency. That is, all sampling is performed at least twice the highest frequency within the simulator (the sampling frequency applied in this chapter was up to seven times the highest frequency). The use of discrete sampling periods ensures synchronization of various system components as the data signal is propagated, an important consideration in optical systems. A study of optical transmission system parameters shows the highest frequency to be that of the carrier waveform. For the purpose of this model, the carrier frequency is located in the C-band and L-band, which is around 0.2 Peta-Hz (PHz). Thus, sampling within the system needs to be at seven times this rate, that is, approximately 1.4 PHz to ensure that signal aliasing does not affect the sample and more accurate results are possible. All blocksets require a discrete sampling time at which to generate data. Unfortunately, this sampling rate is very high and may cause slowing down of the execution time.

9.4.5.2 Signal Streams

Signal streams in EDFA simulator are not defined during the simulation; the EDFA simulator assumes the average signal power. The signal stream simulating in EDFA simulator would be a constant value with superimposed noise on Gaussian pulses. Hence, the determination in the output power is the average signal power.

Signal stream in EDFA Module is developed as the phase shift key (PSK) modulation signal with Gaussian noise. The carrier is defined to be a 192.5 THz sinusoidal waveform. The data stream is assumed at 10 Gb/s (or even higher to 40 Gb/s) binary pulse.

9.4.5.3 EDFA Simulink® Simulation Model Assumption

In the development of the EDFA Dynamic Gain simulator, a number of assumptions have been made: (1) As the pumping wavelengths 980 and 1480 nm can provide a high gain amplification and lower noise, we assume that the EDFA can be pumped with either 980 or

1480 nm sources; (2) Because the transient lifetime from excited state to metastable state is sufficiently short, we can assume that the erbium atoms operate at only two levels relevant for the amplification process; (3) The effective area of the erbium-doped active region is small compared to that of the optical mode at each wavelength of interest. This assumption for the Er-doped core allows us to treat the overlap factor to be a constant value, independent of the energy level and optical power; (4) As the ASE is randomly generated in the simulator we assume the stimulated ions are propagating in one direction to estimate the average mean ASE noise power; and finally (5) No reflection occurs during the amplification process.

Assumptions for the modeling of the steady-state EDFA gain are also made: (1) As the pumping wavelengths of 980 and 1480 nm can provide high amplification gain and lower noise, it is assumed that the EDFA is pumped with either a 980 or 1480 nm source; (2) Because the transient lifetime from excited state to metastable state is short, again we assume two levels operation of the doped ions; (3) As excited state absorption only affects the pump absorption along the fiber, it can be neglected; (4) The response of each individual ion in the collection is equally broad on a picosecond time scale; (5) ASE noise is assumed to be small so that it does not saturate the EDFA amplifier; (6) The effective area of the erbium-doped active region is small compared to that of the optical mode at each wavelength of interest. This assumption for the Er-doped core allows the assumption of a constant overlapping factor independent of the energy level; and finally, (7) As in the steady-state model, the population increment delta N_2 is assumed to be zero.

9.4.5.4 System Initialization

To operate the simulator correctly, an initialization process is required. Written as an m-file, this loads parameters and variables required for the simulator operation. Titled "initialization," the user needs to run this file before starting the Simulink simulation. Failing to do so will result in an error warning. It is within the initialization file that the user can modify system parameters. There are several data to be defined in the initialization file. Table 9.4 gives the input data that can be defined before the simulation. Table 9.5 gives the glossary for input signals.

The use of the initialization file simplifies operation for users. All variable parameters are contained here and automatically updated in the Simulink platform upon execution (saved in to the MATLAB memory called "workspace"). Not incorporating the initialization file will require the user to input the same variable in multiple blocks, increasing the possibility of errors, and complicating the operation of the simulator.

TABLE 9.4

Parameter Set for the Er-Doped Fiber

Physical Meaning	Symbol Defined in Initialize File
Erbium-doped fiber parameters	
Core radius of erbium-doped fiber	*r* (um)
Overlap factor of EDFA at wavelength (*k*)	Gamma
Ion density of erbium-doped fiber	*p*
Peak absorption at 1530 nm	Peak_absorsion
Peak absorption at 980 nm	Peak_absorsion_pump
Length of the fiber	*L* (m)

TABLE 9.5

Input Parameter Set

EDFA Input Initialize	Symbol Defined in Initialize File
Input signal power	Signal_Power (dBm)
Input pump power	Pump_Power (mW)
Input wavelength	Index
Pump wavelength	Pump_wavelength
Number of channel input	*N*
Pump modulation index	mod
Pump modulation frequency	Mod_freq

9.4.6 EDFA Simulator Modeling

The EDFA simulator is combined with various segments as referred to in the prototype of Figure 9.13. Each block presents different segments of the EDFA simulator, for example, the input signal stream is represented by a block, which is named [Signal Stream]. Each block consists of more than one subsystem inside; the design inside can be checked by double clicking the block. The EDFA in the Simulink simulation is implemented according to those subsystems, and they are called from a main program. The following demonstrate the input and output ports in the EDFA simulator and EDFA Module.

9.4.6.1 Using the EDFA Simulator

Input: (1) signal stream—power of signal (includes C-band and L-band signals), and (2) pump source—power of the pump (includes pump modulation, 980 nm pump source and 1480 pump source).

Output: All the output displayers have been put into the block named monitor, and readers can check the output values by opening the Monitor block. (1) EDF parameter (EDF parameters monitor)—the parameters of the erbium-doped fiber such as radius and ions density; (2) EDFA gain monitor—dynamic gain and steady-state gain scope (all the gain data have been put in order [ascent]); (3) EDFA dynamic gain monitor—output signal power, output pump power, average ASE power, noise figure, SNR, and other noise power.

It also displays the evolution of the signal. The rest of this section discusses the simulator segment by segment.

9.4.6.2 Signal Data Stream Modeling

As illustrated in Figure 9.16, the signal stream basically models the C-band and L-band light wave signals. As we have assumed that the system uses 100 GHz optical frequency spacing (0.8 nm) between light wave carriers, the C-band is also assumed to have the wavelength window 1525–1565 nm. There are around 51 channels that can be used as optical carriers over this band. We can see from Figure 9.17 that there are five signal power blocks shown by a bold line, and the last one is not marked by a bold line. The bold lines are multidimensional vector time series lines associated with 10 channels of each signal block. The wavelength section is used for conversion of the signal power in mW units into the number of photons (photon energy per bit period). The input signal power of each channel has been defined as a constant mean power.

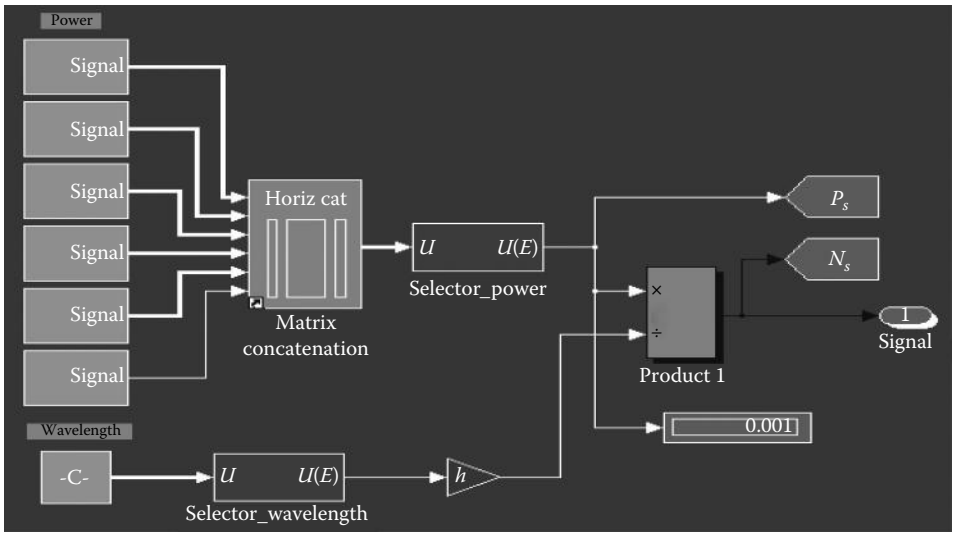

FIGURE 9.16
Signal stream prototype.

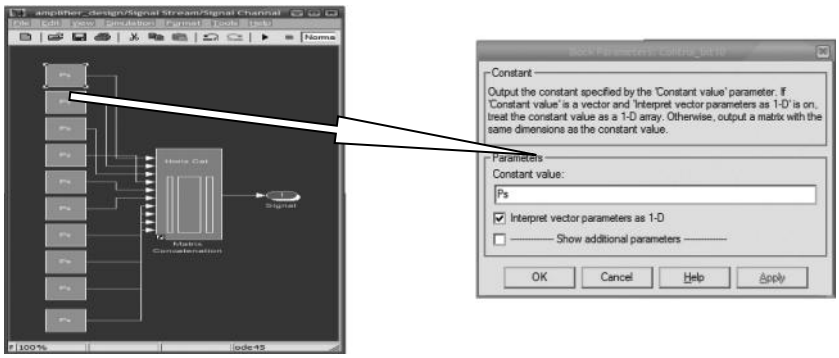

FIGURE 9.17
Signal block prototype.

The value of the mean signal power is defined in the file [Simulation_initailise.m]. The signal carrier frequency is ultra high, around 192.5 THz. If we inject a signal generator with a real 192.5 THz signal (e.g., sinuous wave at 192.5 THz), the Simulink generates the output based on each sampling point of this signal wave, and it may take a long time (maybe more than 2 days!) to generate the output result, which is naturally very inconvenient. On the other hand, predicting the average output power after the amplifier is good enough for the design of the amplifier. Therefore, an average mean input signal power can be used under our conditions.

9.4.7 Pump Source

Pump power also has been set as a constant mean power for simulation. In the previous section, we have identified that there are three different EDFA configurations: forward pump, backward pump, and dual (or bidirectional) pumping. Only forward pumping is

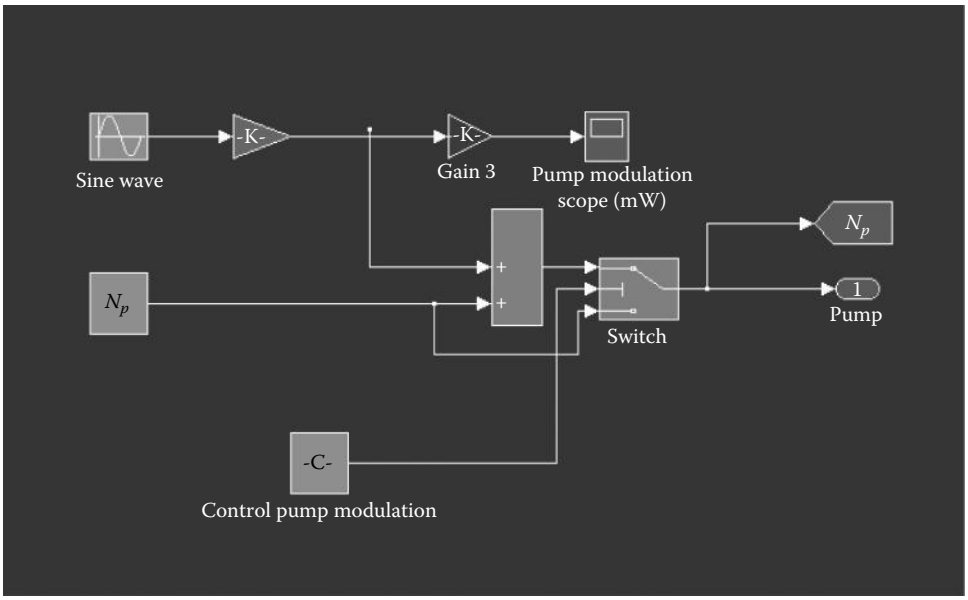

FIGURE 9.18
Pump source prototype.

described in this section as the others can be understood easily following this reasoning. The Simulink model for the pump source is shown in Figure 9.18.

9.4.7.1 Pumping Wavelength

As described in the earlier text, there are two pump wavelengths that can offer high amplifier gain. In our simulation, the wavelength model is implemented within the initialization file. The following is the instruction code for setting the event when different wavelength channels are propagating through the EDFA.

Algorithm:

If Pump wavelength = 980e-9
Absorption factor 980 nm
Emission factor 980 nm
Else if Pump wavelength = 1480e-9
Absorption factor 1480 nm
Emission factor 1480 nm
Else
Reset

According to the absorption and emission characteristics, the absorption and emission properties of the fiber change with different wavelength propagations. The absorption factor is normally given by the fiber manufacturer or measured.

9.4.7.2 Pump Modulation

Pump modulation can be added, and its effects on gain modulation can be investigated. References [3,4] use a dimensionless number called "modulation index" to measure the power

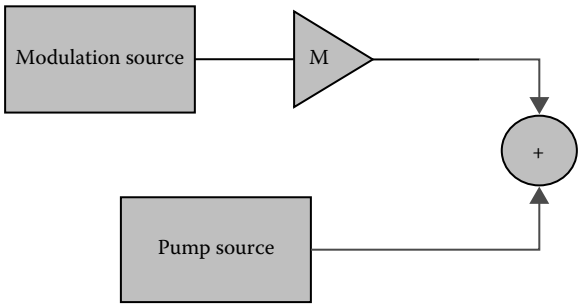

FIGURE 9.19
Pump modulation module.

in the modulated signal. Using this definition, the input pump time series has the form $P_p(0,t) = P_p(0) + P_p^0(0)m_p \cos \omega t$, where $P_p^0(0)$ refers to the initial pump power (in Watts) and m_p is the modulation index. As the mean pump power given here is of a constant value, this is added to the term $m_p P_p^0(0) \cos \omega t$ at the summation box as illustrated in Figure 9.19.

$P_p(0)m_p \cos \omega t$ is the output of the sine wave generator in Figure 9.19. The gain labeled with [M] is the modulation index m_p. N_p is the constant mean pump power; here, the unit of the pump power is in photons/s. The method for converting Watts into the number of photons/s has been given in the previous section.

9.4.7.3 EDF Modeling

We have now described the theoretical EDF model. This section gives the Simulink simulation model design. The Simulink simulation models are based on the rate equations given in Section 9.2. The characteristic of the EDF depends on two factors: the EDFA gain and ASE noise characteristics. The gain characteristic depends on the absorption and emission factors at different wavelengths. Because different erbium-doped fibers provide different absorption and emission characteristics, simulating the absorption and emission spectrum would be the first steps.

The existing absorption spectra given in Refs. [2,6–8,17] can be used. The absorption spectrum is illustrated in Figure 9.9. Although all the data from those references are different, yet the slopes of those spectrums are quite similar. On the basis of this assumption, normalization of these curves would be the first choice for simulation of the spectrum. The normalized spectra simulation is shown in Figure 9.20 Refs. [18–21].

The EDF simulation can be started after these spectra. Figure 9.21 illustrates the prototype of EDF simulation.

9.4.7.4 EDFAs Dynamic Gain Model

The equations for solving the dynamic gain model can now be modeled using Simulink to obtain the gain factors. This section describes how all the blocks are integrated. As we mentioned earlier in this section, the gain in the EDFA is based on the following equations:

$$G_p = \frac{\Gamma_p(\sigma_{1-3} + \sigma_{3-1})}{A} N_2 - \Gamma_p \sigma_{1-3} \rho L - \gamma_p G_p \quad \text{and} \quad G_s = \frac{\Gamma_s(\sigma_{1-2} + \sigma_{2-1})}{A} N_2 - \Gamma_s \sigma_{1-2} \rho L - \gamma_s G_s.$$

In our simulation, the Simulink model representing these expressions is given in Figure 9.22.

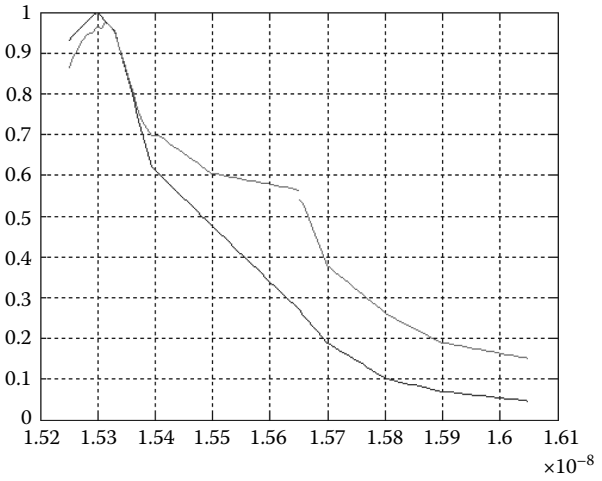

FIGURE 9.20
The absorption and emission factors of the normalized spectra (C-band and L-band).

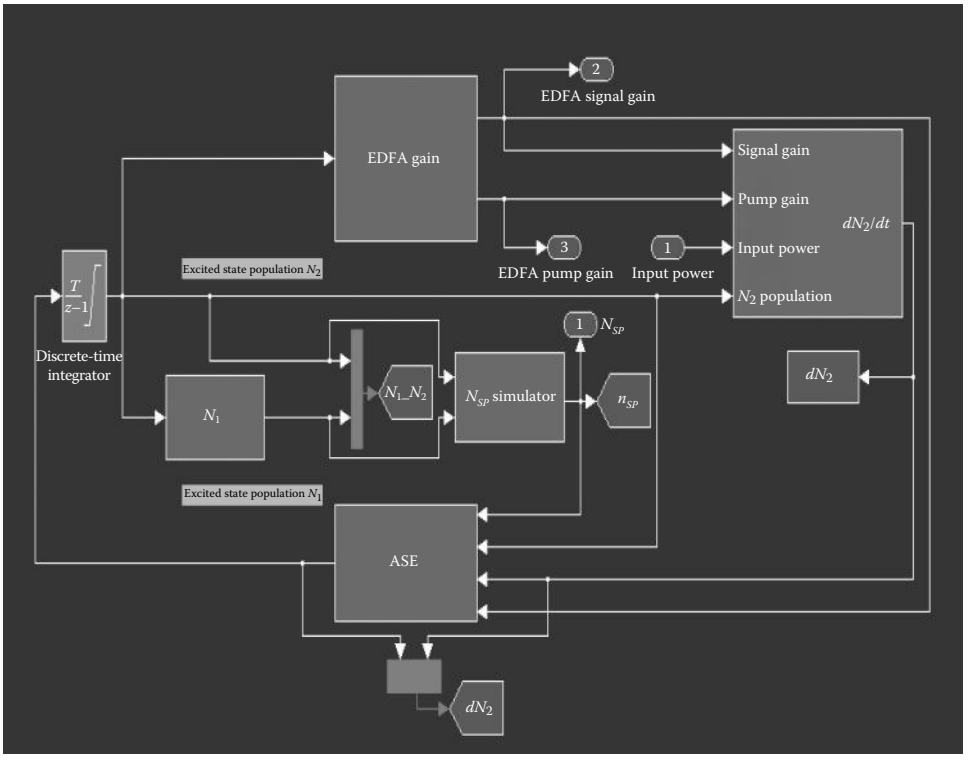

FIGURE 9.21
EDF simulation prototype.

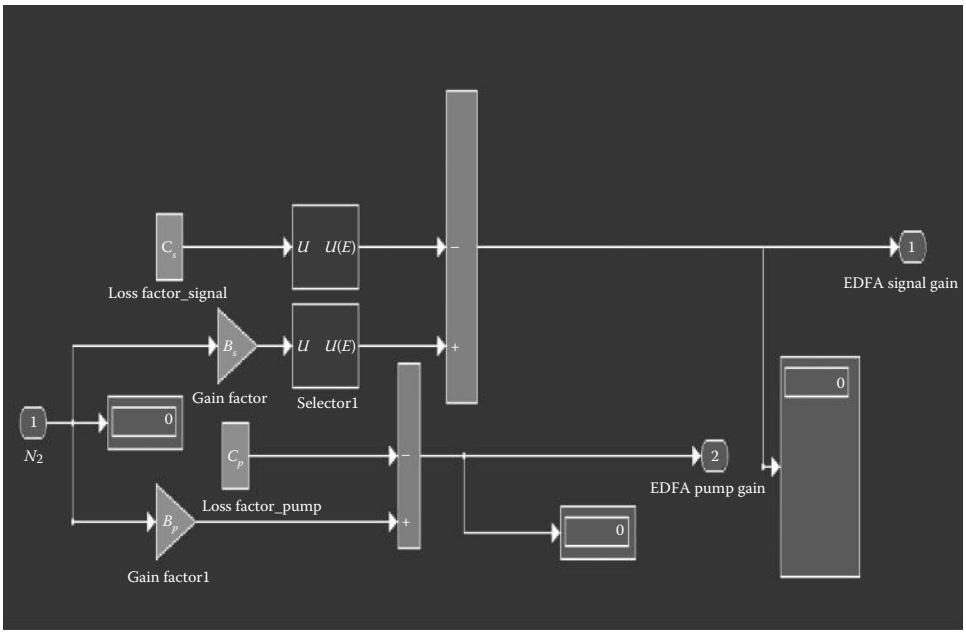

FIGURE 9.22
EDFAs dynamic gain modeling corresponding to Figure 9.21.

In Figure 9.22, B_s and B_p are expressed by the matrix of $\Gamma(\sigma + \sigma)/A$, and similarly C_s and C_p are expressed by the matrix of $\Gamma\sigma\rho L - \gamma G$. Because of the characteristics of absorption and emission, different wavelength signals propagating through the EDF would cause a change in the absorption and emission factors. So, C_s and B_s *act as* the memory locations that store all the absorption and emission values. The following selector is an artificial intelligent block which can select the correspondent values to match the wavelengths. The selector block works by outputting with a selected reference indices that form the B_s matrix, like [B_{s1} B_{s2} B_{s3} … B_{s51}]. Selected [index 1] => Output – B_{s1}. Accordingly, the absorption and emission factors change with respect to different wavelengths.

As shown in the block diagram of Figure 9.23, the loop continues the execution till the difference of the input power and output power is the same as that of N_2/τ that means N_2 is saturated. Thus, the gain remains in the steady state. The data inside the discrete-time integrator block are setting the step time for each increment; here, we set 3.25e-7 as the sampling step. The output of the model is given in Figure 9.24.

9.4.7.5 EDFAs Steady State Gain Model

In steady state, $dN_2/dt = 0$, the Simulink model can be illustrated as in Figure 9.25.

The signal gain here is equal to $B_s * N_2$ (*saturate*) – C_s, and the pump gain here is equal to $B_p * N_2$ (*saturate*) – C_p. The Simulink development is similar to the EDFA dynamic model. The output would be the same as given in Figure 9.24.

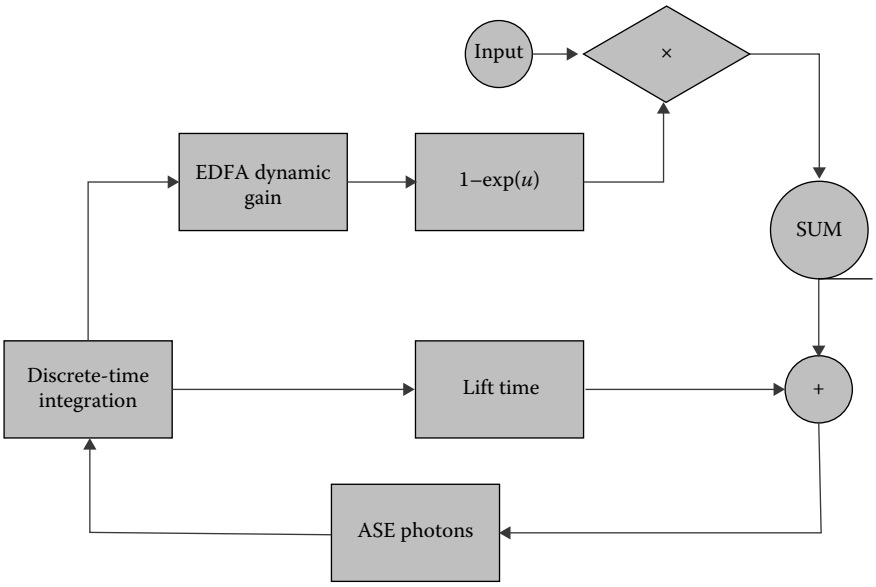

FIGURE 9.23
dN_2/dt simulation block diagram.

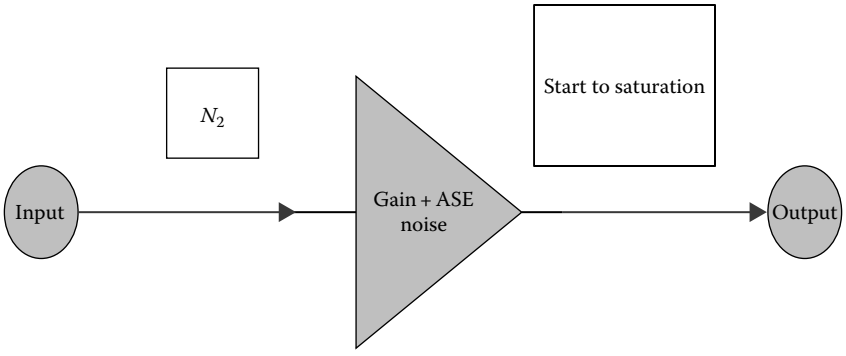

FIGURE 9.24
Output algorithm.

9.4.7.6 Population Inversion Factor Modeling

- N_1 simulation.
  Recall the three state populations and the assumption that N_3 is zero. The relation between N_1 and N_2 is then $N_1 = N_{total} - N_2$ (Figure 9.26).
- N_{sp} simulation (Figure 9.27)
  According to the population inversion factor equation, N_1 would equal N_2. This would lead to the result approaching infinity. Therefore, the [if statement] could limit the result to under 10. Also, the population inversion factor would be greater than 10 in practice.

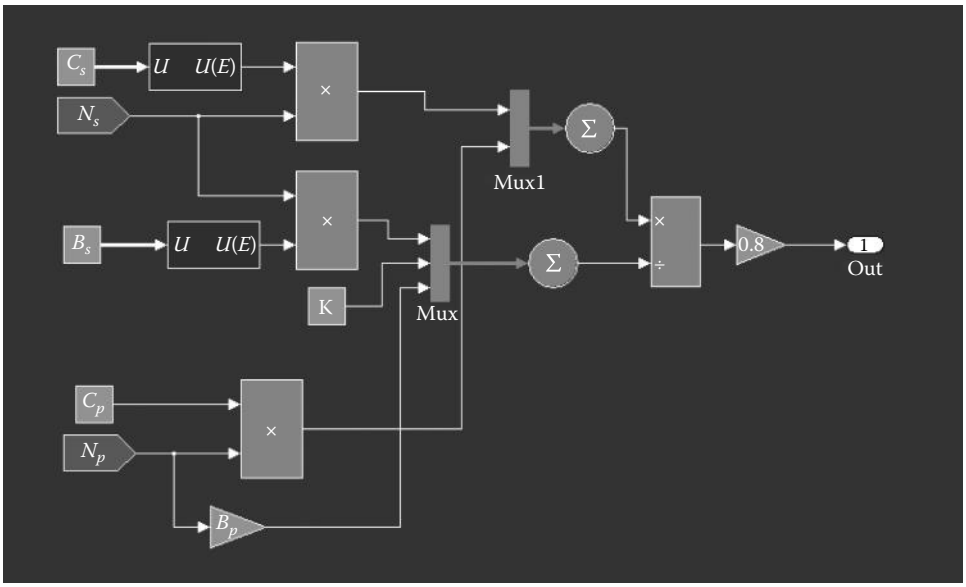

FIGURE 9.25
EDFA steady-state N_2 model.

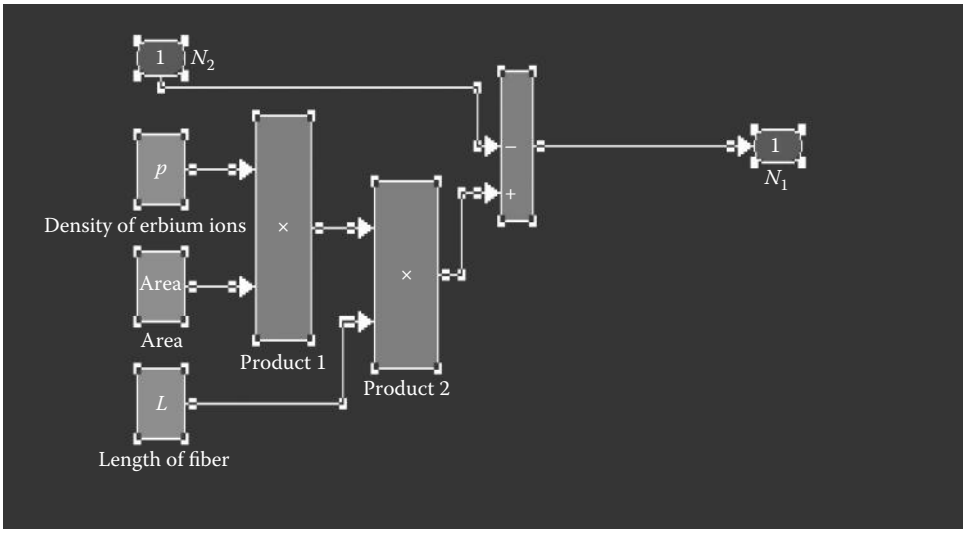

FIGURE 9.26
Representation of N_1 in the simulator.

9.4.7.7 Amplifier Noise Modeling

In the previous section, we have mentioned the method for simulation of the amplification noise. Therefore, to simulate the ASE noise, determining the average mean ASE power is the first action. For the dynamic gain modeling in Simulink, the process is divided into three sections by time (Figure 9.28).

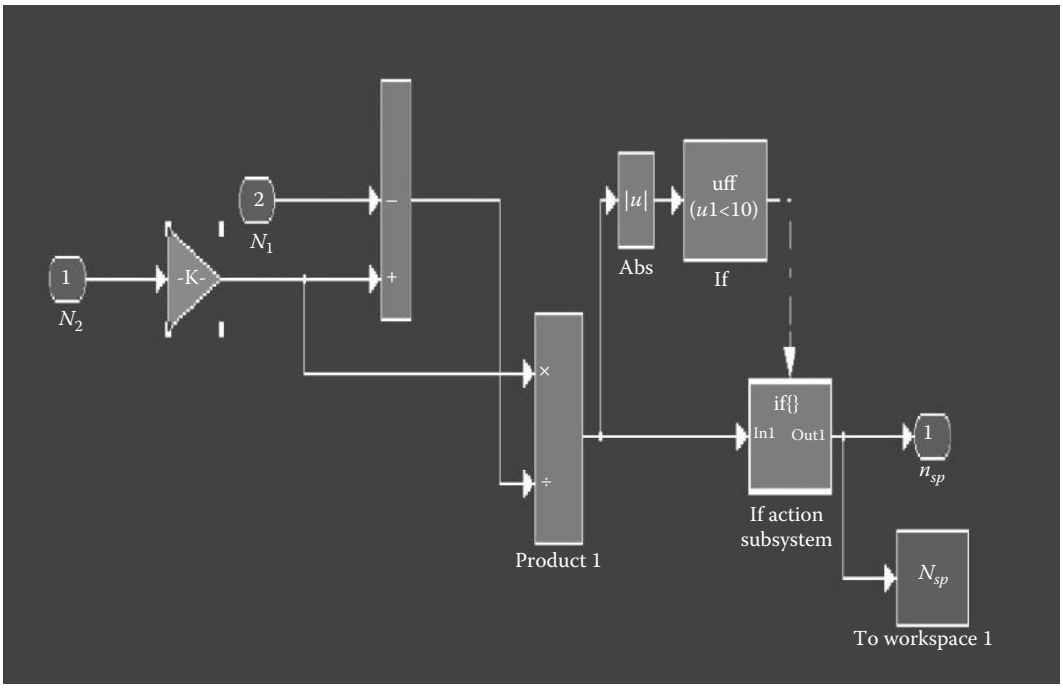

FIGURE 9.27
Representation of n_{sp} in the simulator.

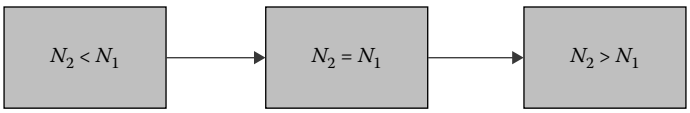

FIGURE 9.28
Amplified population in sequential process.

The calculation for determining the ASE is conducted in three different statements. In the simulation, the following is the algorithm for simulating the ASE mean power (Figure 9.29).

After determining the ASE mean power, the Gaussian assumption of ASE mean power is used to set the variance to model the ASE power and the number of randomly generated photons as shown in Figures 9.30 and 9.31.

9.4.8 Simulink® EDFA Simulator: Execution Procedures

The simulator consists of three major parts: the initialization file [EDFA_initialisation.m], EDFA simulator [EDFA_simulator.mdl], and EDFA Module [EDFA_module.mdl].

Steps for executing a simulation are as follows:

1. Access MATLAB 7.0 R14 or any later version. Open the initialization file from its stored disk, using file, then open, as per normal.
2. This step brings the MATLAB coded initialization file on screen. Refer to the appendices for a hard copy of this file. This file allows the user to define all variables pertaining to the optical simulator. The user is free to modify any value

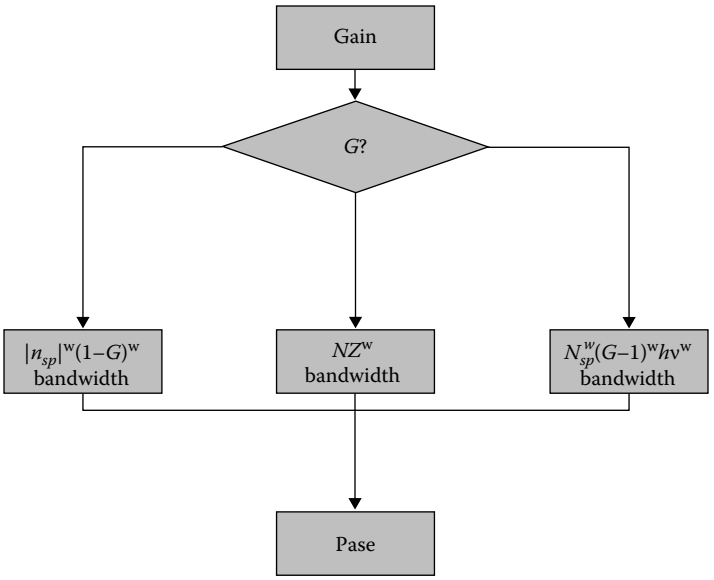

FIGURE 9.29
Modeling flowchart for the ASE noise power; $G < 1$.

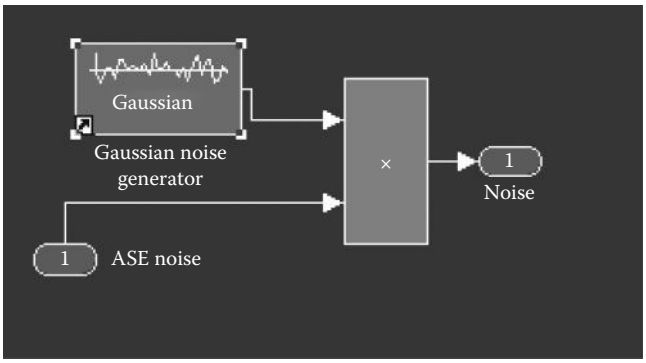

FIGURE 9.30
ASE model.

within this file. The file has been commented so as to instruct the user and future designers of the simulators operation.

3. To run a simulation, enter the required parameter values, then from the debug menu select save and run. This will run the file and load the relevant values into both the MATLAB workspace and the Simulink simulator. The simulator should also open in the Simulink workspace. To analyze the initialized system, simply open the input monitor block and EDF parameter, the initialized input will present there.
4. To inspect the result of the EDFA simulator, either double click the output monitor block or open the scope to see the dynamic evolution. Indeed, all results are saved in the workspace for further investigation.
5. To inspect the results of the EDFA Module, scopes pop up automatically; if they do not, just double click the scope.

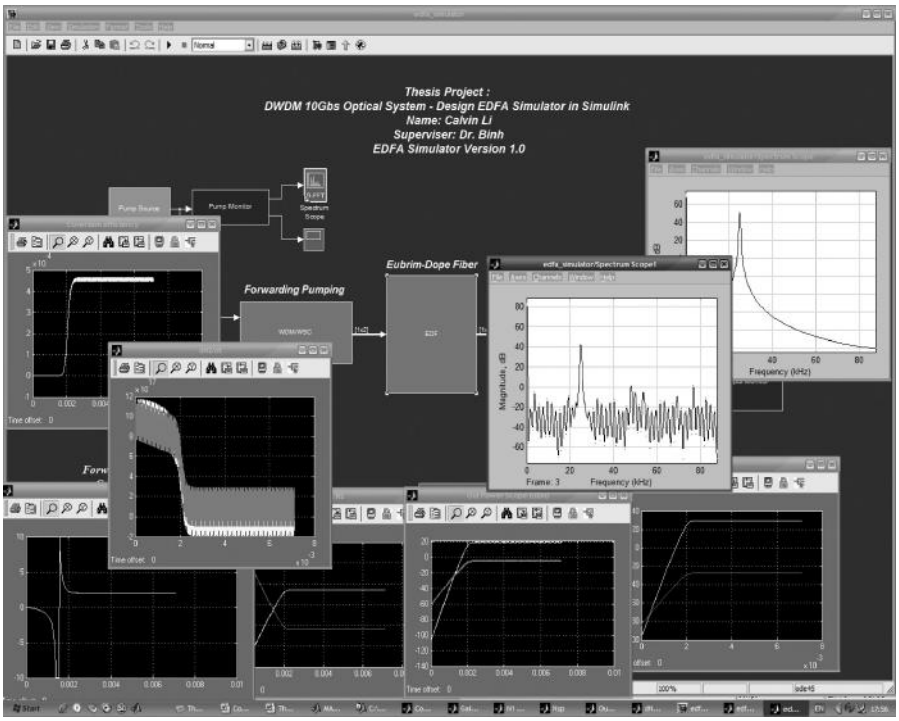

FIGURE 9.31
Samples of the screen shots of the EDFA simulator.

Notes: As the EDFA module can combine with other simulation blocks, the input data stream can be replaced by any other device simulator block. To increase the execution time, the run type in [normal mode], [accelerating mode], [from outside] in the option menu can be changed.

Typical simulator screen shots of the Simulink EDFA simulator are given in Figures 9.31 and 9.32.

The simulated results are based on practical EDFA parameters constructed in our laboratory and some commercial amplifiers operating in the C-band. Table 9.6 gives a set of the parameters employed in the simulator, and the power generated at the output of the EDFA plotted versus the input signal power with the wavelength of the input channel as a parameter is given in Figures 9.33 and 9.34. The saturation is set at around –14 dBm as expected.

The EDFA gain obtained from the simulation agrees with that from the experiment, and the only discrepancy is during low signal input power, this might be due to the internal setting of the commercial device, which is unknown; all the other factors such as the absorption and emission spectrum in the commercial EDFA may be slightly different from the simulator (Table 9.7, Figure 9.35).

The spectral gain is dependent on the stimulation emission factor. As the population inversion rate changes with the signal wavelength, the gain peaks at 1528 nm (Tables 9.8 and 9.9).

Gain does not increase infinitely with the increasing pump power as the ion density in erbium-doped fiber is constant. The power pump just pushes the energy pumping ions to the higher energy state. Thus, if all the ions have been pumped to the high state, then even

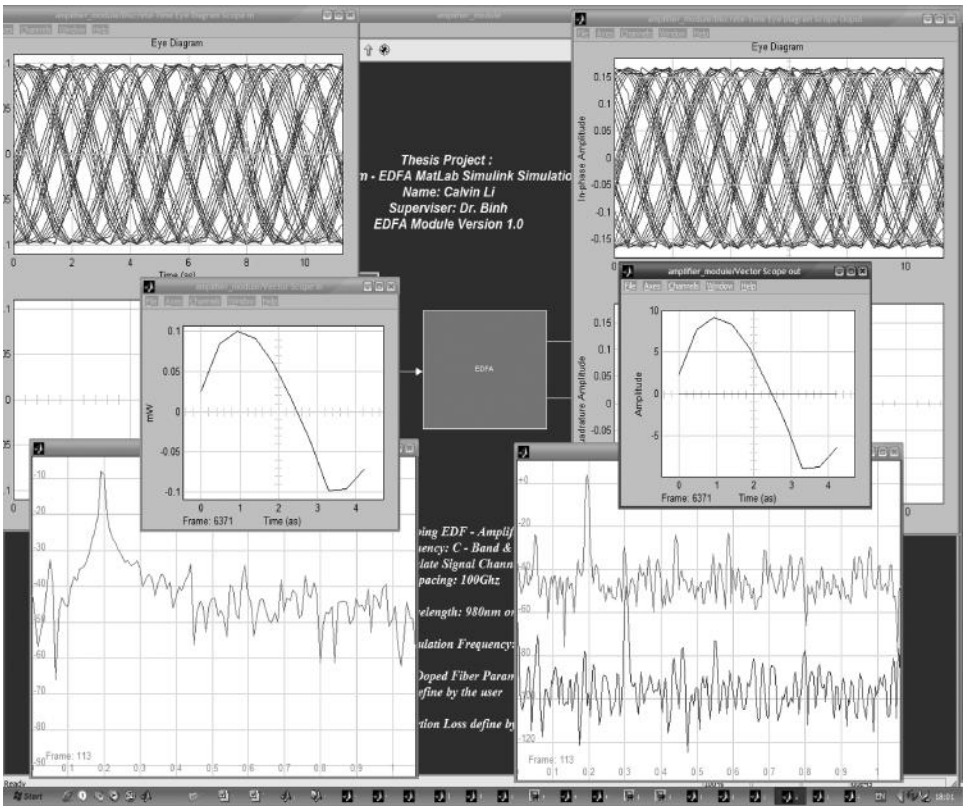

FIGURE 9.32
Samples of the screen shot of the EDFA simulator in the time domain.

TABLE 9.6
EDFA Simulator Parameters

Single Channel	C-Band	EDF Parameter		
Pump wavelength (nm)	980	MFD = 5.9 μm at 1550 nm		
EDF length (m)	16	Cutoff wavelength	940 nm	
Pump power (mW)	195	Peak absorption	6.09 dB/m	At 1530 nm
Without gain modulation			5.24 dB/m	At 979 nm

if the pump power is increased, the number of simulated photons still remains the same, resulting in gain saturation as illustrated (Figure 9.36).

9.4.8.1 Amplification in the L-Band

We compared the L-band signal with the C-band signal and tabulated the values in Table 9.10, and the gain is plotted over the C- and L-bands in Figures 9.37 and 9.38.

The pump power is varied, and the EDFA gain in the L-band is plotted in Figures 9.39 and 9.40 with the parameters of the amplifier given in Table 9.11.

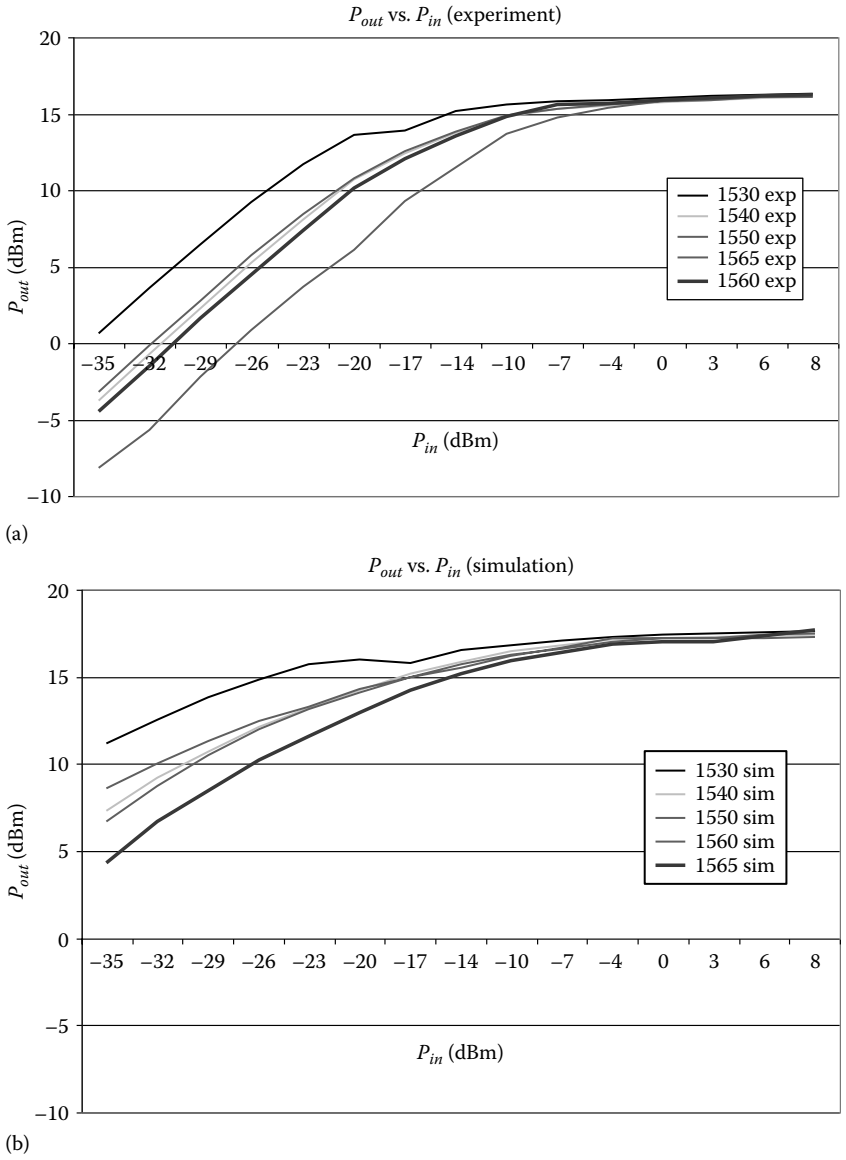

FIGURE 9.33
(a) Experimental results: EDFA output power versus input power level with channel wavelength as a parameter. (b) Simulation results: EDFA output power is plotted against the input signal level with the input channel wavelength as a parameter.

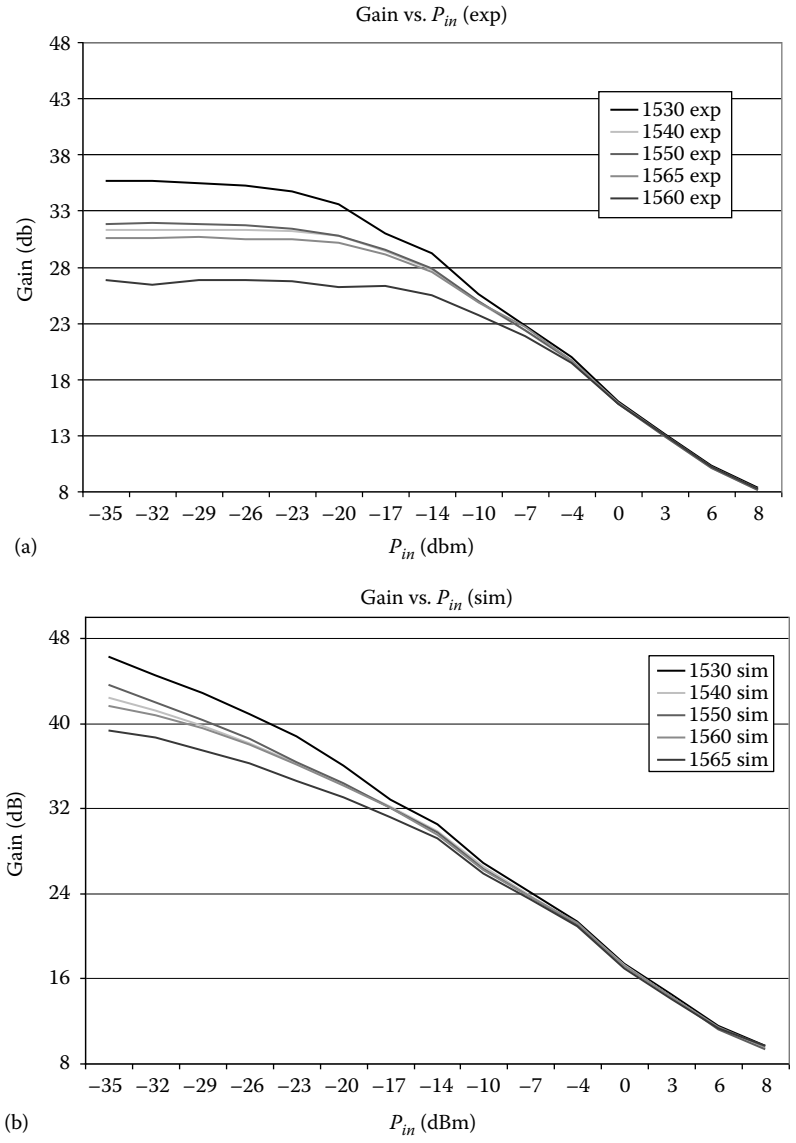

FIGURE 9.34
(a) Experimental results of the amplification gain. (b) Simulation result of amplification gain.

TABLE 9.7
EDFA Simulator Parameters

Single Channel	**C-Band**	**EDF Parameter**		
Pump wavelength (nm)	980	MFD = 5.9 μm at 1550 nm		
EDF length (m)	16	Cutoff wavelength	940 nm	
Pump power (mW)	195	Peak absorption	6.09 dB/m	At 1530 nm
Signal input power (dBm)	−20		5.24 dB/m	At 979 nm

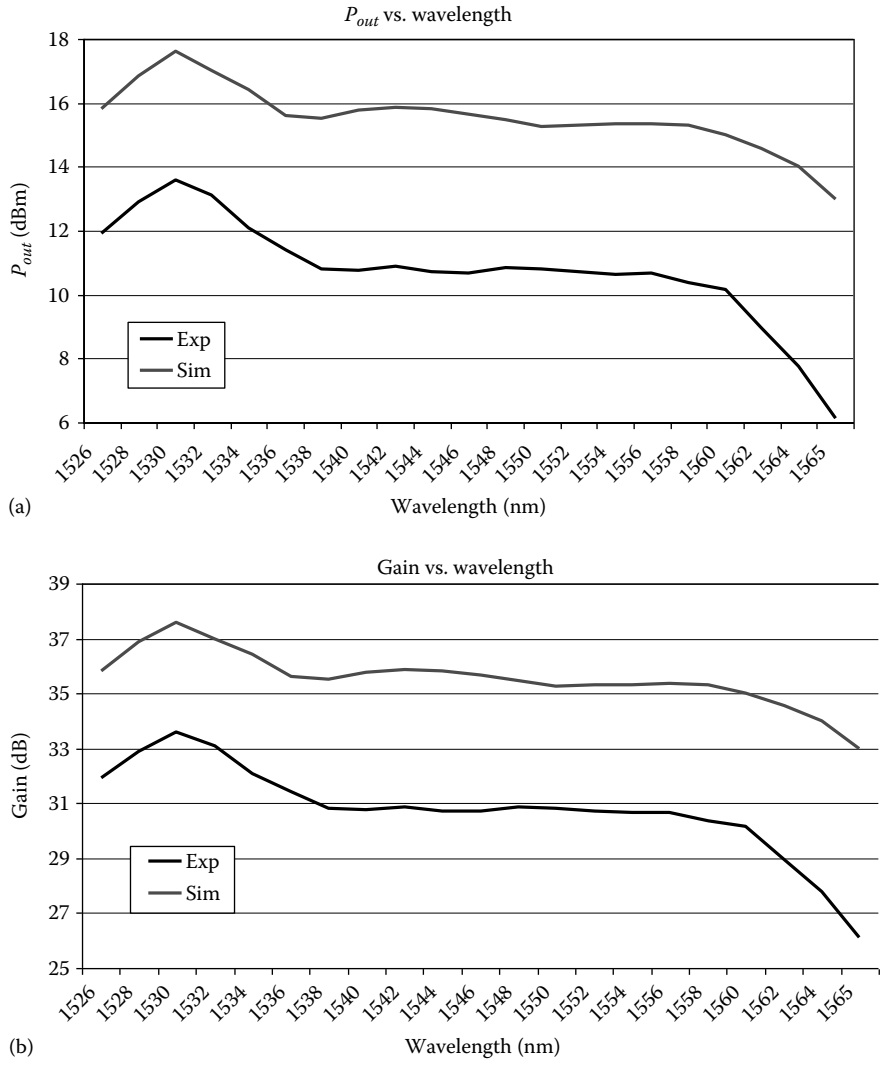

FIGURE 9.35
Spectral properties of (a) output signal power (b) EDFA gain.

TABLE 9.8
EDFA Simulator Testing Parameter

Single Channel	C-Band	EDF Parameter		
Pump wavelength (nm)	980	MFD = 5.9 μm at 1550 nm		
EDF length (m)	16	Cutoff wavelength	940 nm	
Signal wavelength	1565	Peak absorption	6.09 dB/m	At 1530 nm
Signal input power (dBm)	–20		5.24 dB/m	At 979 nm

TABLE 9.9

EDFA Simulator Testing Parameter

Single Channel	L-Band	EDF Parameter		
Pump wavelength (nm)	980	MFD = 5.9 μm at 1550 nm		
EDF length (m)	16	Cutoff wavelength	940 nm	
Pump power (mW)	195 (22.9 dBm)	Peak absorption	6.09 dB/m	At 1530 nm
Without gain modulation			5.24 dB/m	At 979 nm

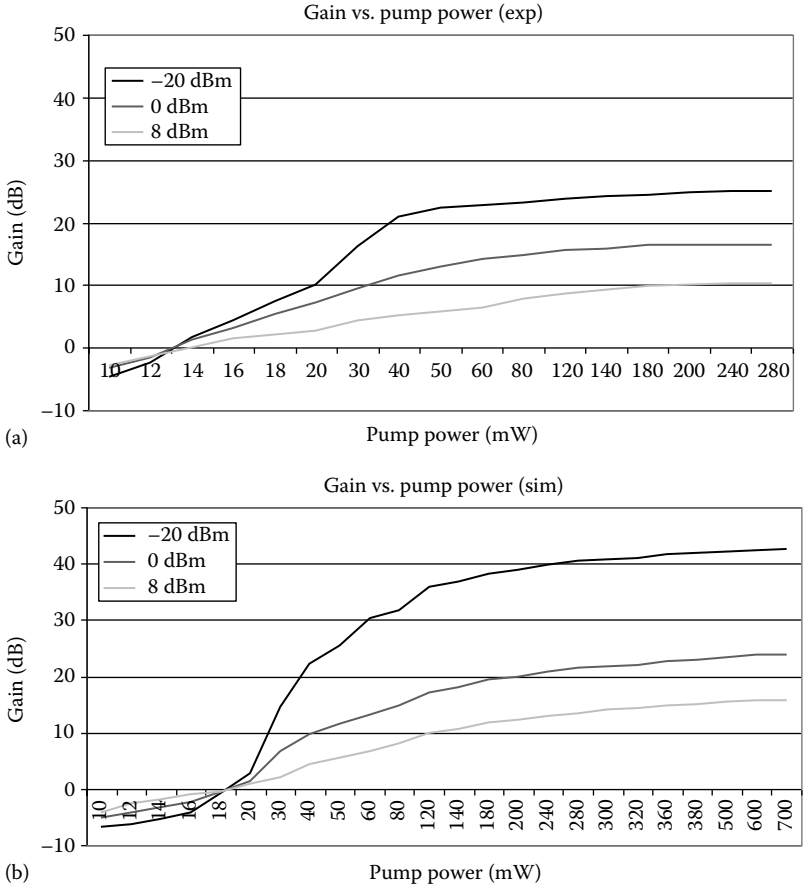

FIGURE 9.36
Pump power plotted against the amplification gain with the signal power as a parameter (a) and (b).

TABLE 9.10

Signal Level/Wavelength		1530	1540	1550	1560	1565
−20 dBm	Output power (dBm)	16.01	14.22	14.3	−2.709	12.97
		1566	**1570**	**1580**	**1590**	**1600**
−20 dBm	Output power (dBm)	18.24	13.8	3.838	−2.709	−5.115

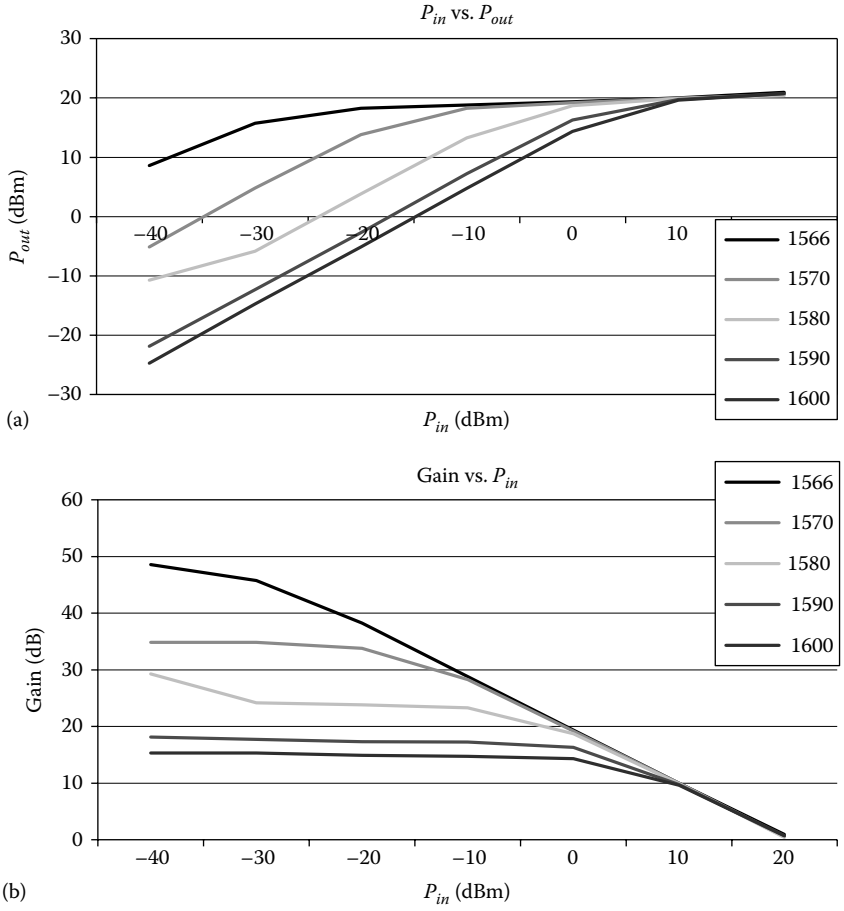

FIGURE 9.37
EDFA gain versus input signal power level for L-band (a) output power versus input level (b) gain against input power level.

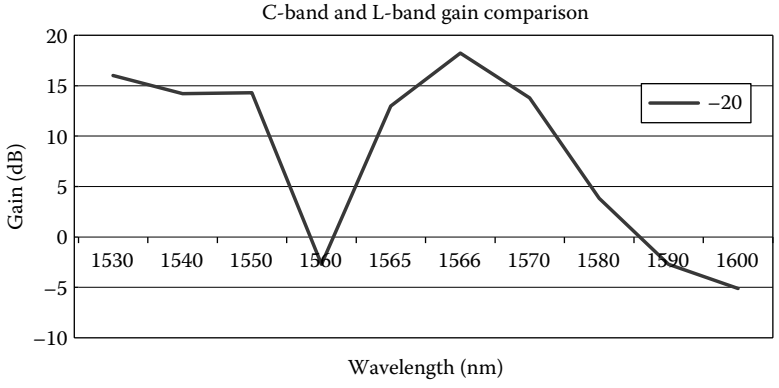

FIGURE 9.38
EDFA gain spectrum.

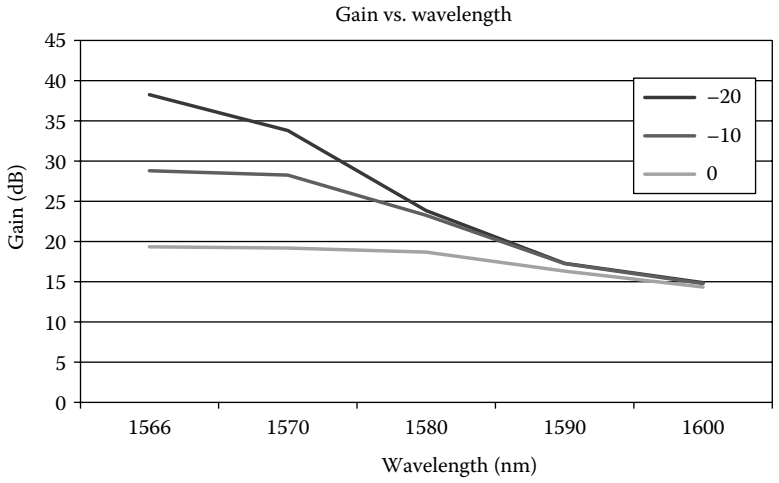

FIGURE 9.39
L-band gain spectrum.

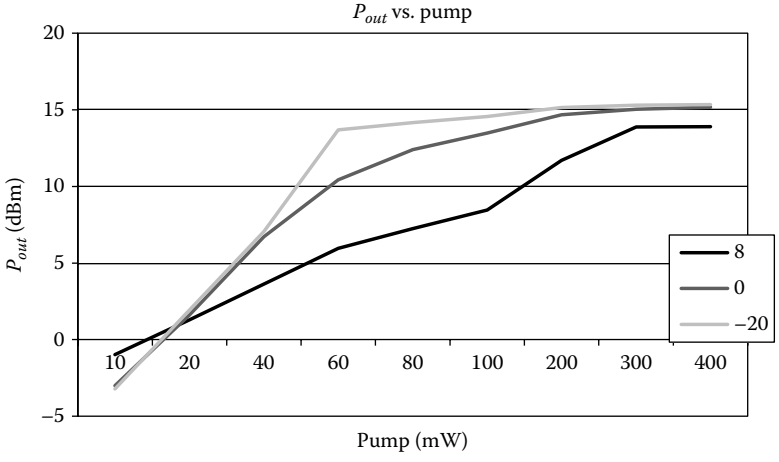

FIGURE 9.40
Output power of the EDFA as a function of the pump power with input power level as a parameter.

TABLE 9.11

EDFA Simulator Testing Parameter

Single Channel	**C-Band**	**EDF Parameter**		
Pump wavelength (nm)	980	MFD = 5.9 μm at 1550 nm		
EDF length (m)	16	Cutoff wavelength	940 nm	
Signal wavelength	1565	Peak absorption	6.09 dB/m	At 1530 nm
Signal input power (dBm)	−20		5.24 dB/m	At 979 nm

Operating wavelength = 1565 nm.

9.4.8.2 Multi-Channel Operation of EDFA (Table 9.12, Figure 9.41)

TABLE 9.12

EDFA Simulator Testing Parameters for Results of Figure 9.41

Multichannel	C-Band	EDF Parameter		
Pump wavelength (nm)	980	MFD = 5.9 μm at 1550 nm		
EDF length (m)	16	Cutoff wavelength	940 nm	
Pump power (mW)	195	Peak absorption:	6.09 dB/m	At 1530 nm
Without gain modulation			5.24 dB/m	At 979 nm

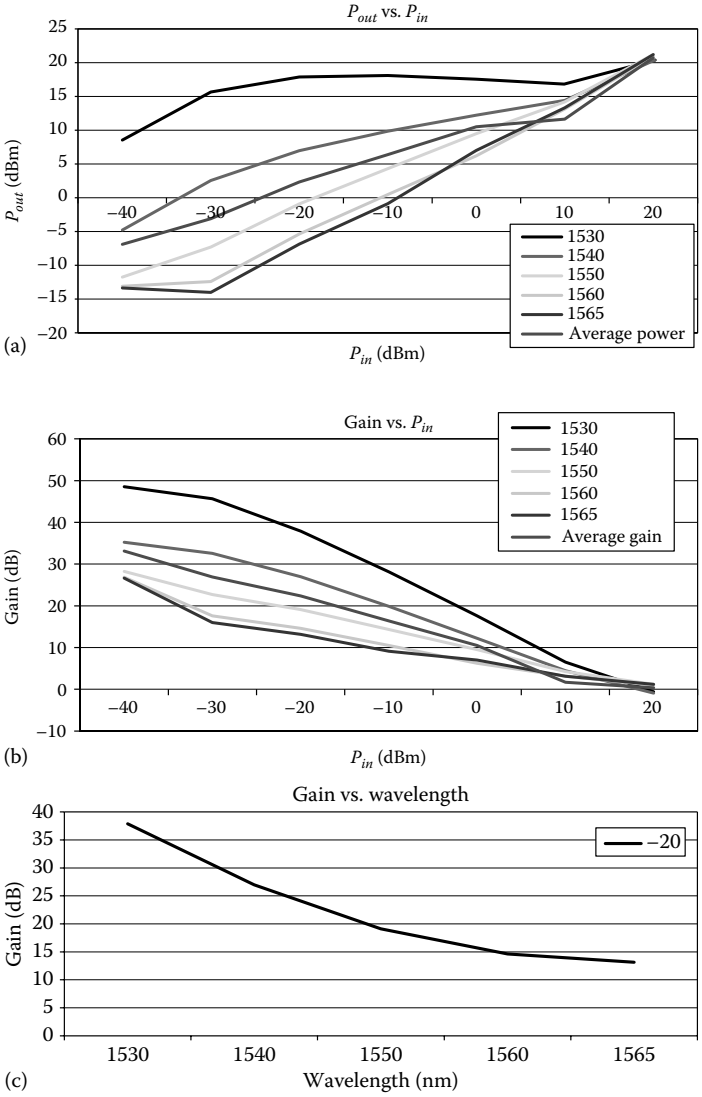

FIGURE 9.41
EDFA characteristics: (a) output power as a function of input signal power level for different channel wavelengths, (b) gain variation as a function of input level, and (c) gain spectra.

9.4.8.3 ASE Measurement (Table 9.13, Figure 9.42)

TABLE 9.13

EDFA Simulator Parameters for the ASE Simulation Results of Figure 9.42

Signal Channel	C-Band	EDF Parameter		
Pump wavelength (nm)	980	MFD = 5.9 μm at 1550 nm		
EDF length (m)	16	Cutoff wavelength	940 nm	
Pump power (mW)	195 (22.9 dBm)	Peak absorption	6.09 dB/m	At 1530 nm
Without gain modulation			5.24 dB/m	At 979 nm
Signal power (dBm)	−20			

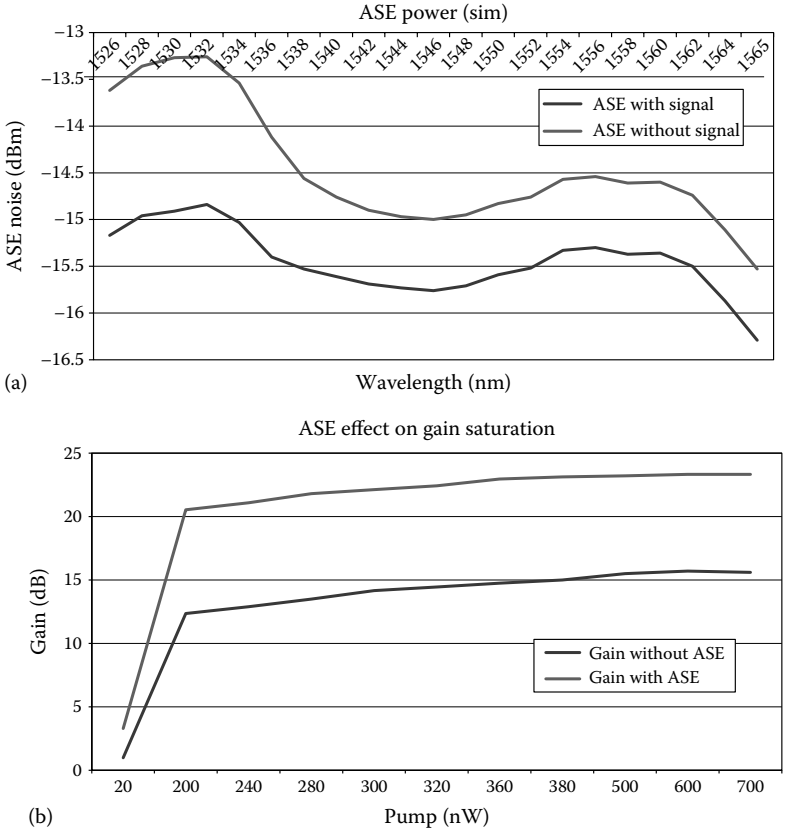

FIGURE 9.42
ASE noise: (a) spectral property and (b) as a function of pump power.

9.4.8.4 Pump Wavelength Testing (Table 9.14, Figure 9.43)

TABLE 9.14

EDFA Simulator Testing Parameters Used for Figure 9.43

Result of EDFA Amplifier		EDF Parameter		
Pump wavelength (nm)	1480	MFD = 5.9 μm at 1550 nm		
EDF length (m)	16	Cutoff wavelength	940 nm	
Pump power (mW)	195	Peak absorption	6.09 dB/m	At 1530 nm
Signal input power (dBm)	−20		5.24 dB/m	At 979 nm

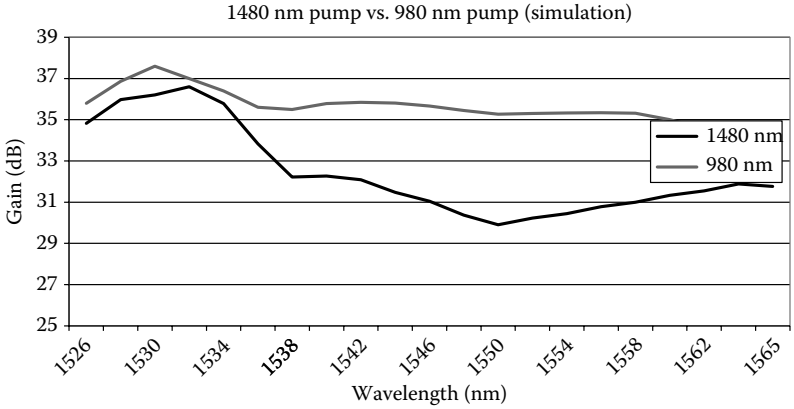

FIGURE 9.43
EDFA gain variation with pumps at 980 and 1480 nm.

9.4.8.5 Gain Pump Modulation Effect (Figures 9.44 and 9.45)

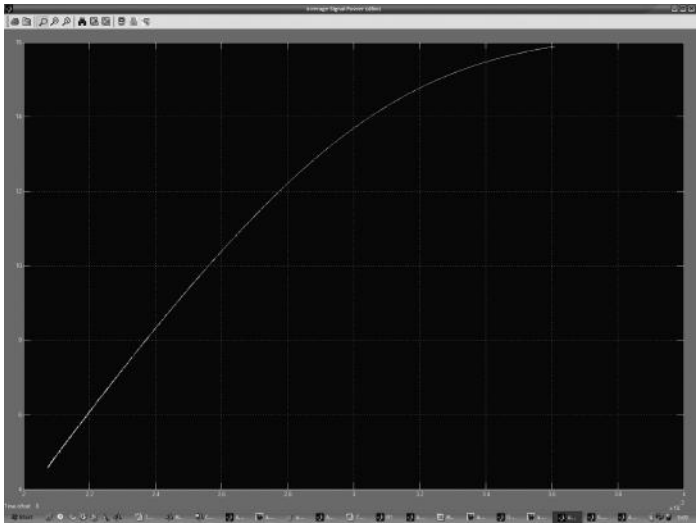

FIGURE 9.44
Output signal without pump source modulation (time dependent).

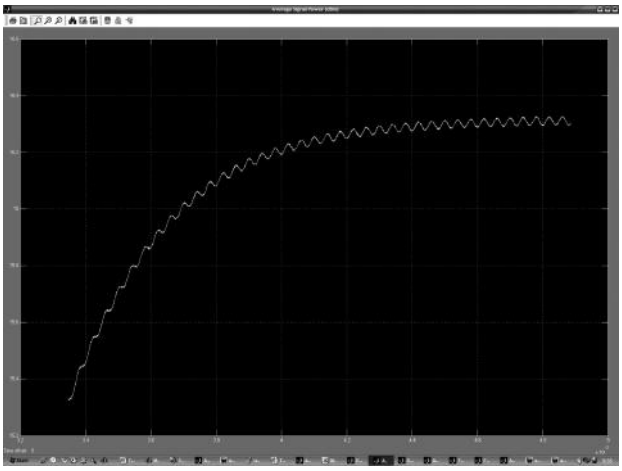

FIGURE 9.45
Output signal with pump source modulation (time dependent).

9.4.9 Samples of the Simulink® Simulator

This section shows the output scope observed from the Simulink simulator. They can be divided into two subsections: EDFA simulation scoping and EDFA module scoping. Here, we demonstrate the operation of the Simulink EDFA simulator as an example incorporating simulated results. This provides the user with an example to follow when using the simulator. The example assumes the system parameters defined in the initialization file. Those parameters are loaded using the run command in the debug menu. This allows the loading of the initialization file of the simulation values in the MATLAB platform.

9.4.9.1 The EDFA Simulator (Figure 9.46)

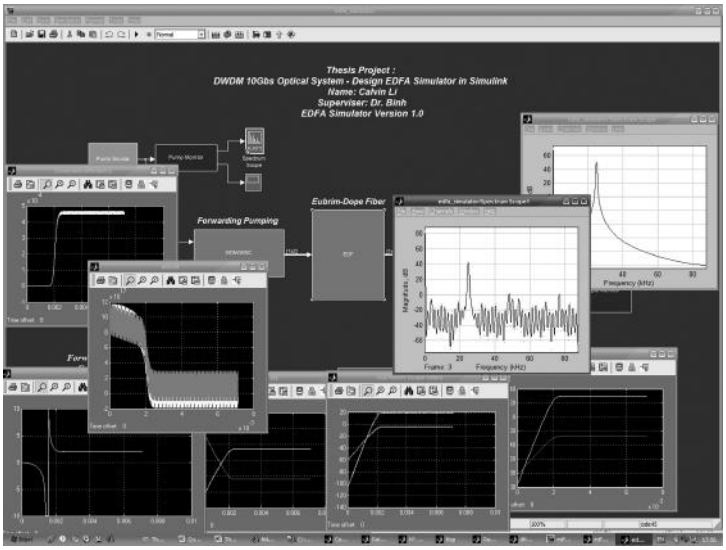

FIGURE 9.46
Sample screen shot of the EDFA simulator.

9.4.9.2 EDFA Simulator Inspection Scopes (Figures 9.47 and 9.48)

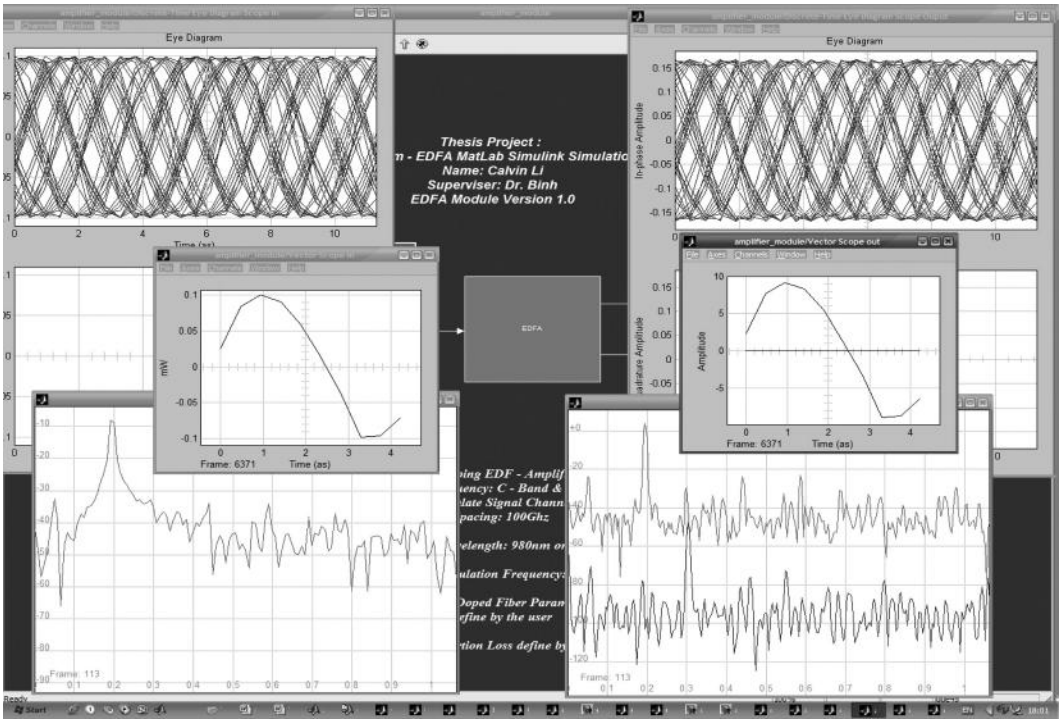

FIGURE 9.47
Sample screen of the EDFA simulator in the time domain.

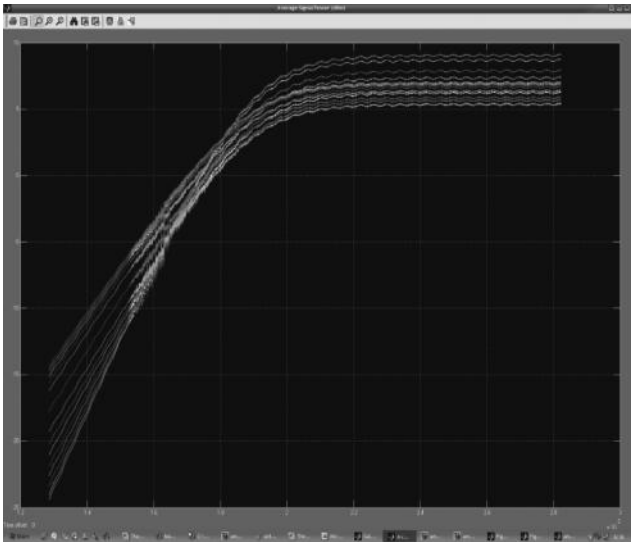

(a)

FIGURE 9.48
Sampled outputs of EDFA gain versus pump power (a and b) constant pump power and gain of different wavelength channels (c and d) time-dependent pumps. *(Continued)*

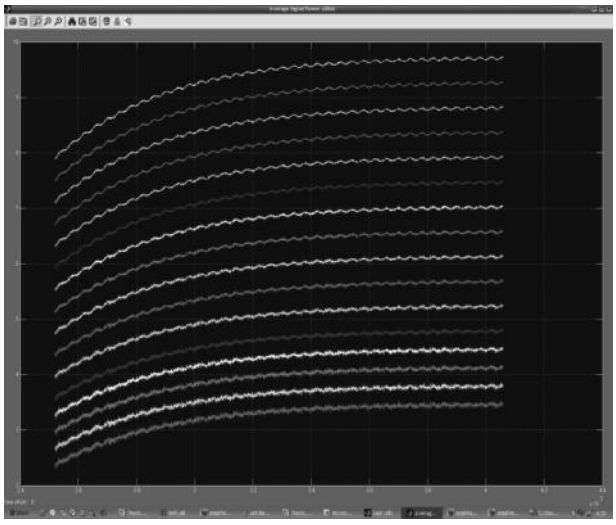

(b)

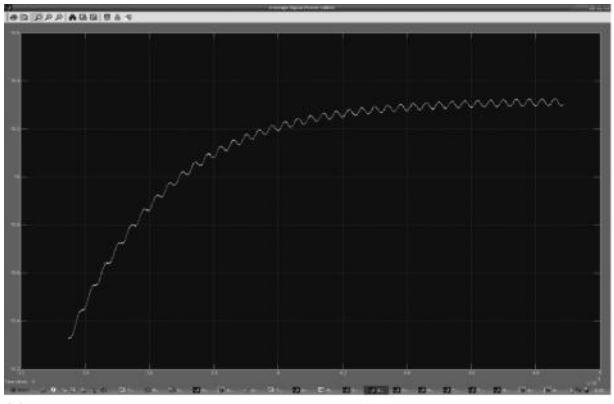

(c)

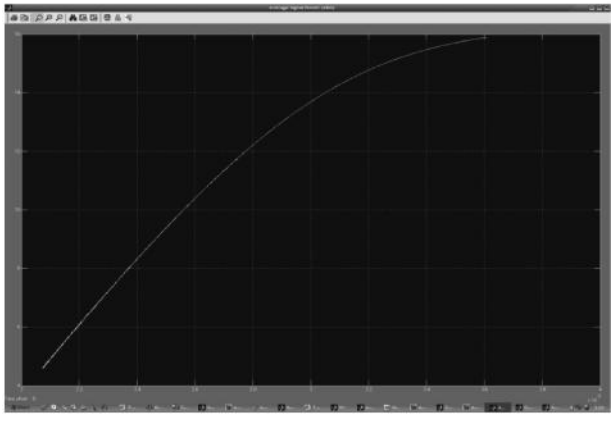

(d)

FIGURE 9.48 (*Continued*)
Sampled outputs of EDFA gain versus pump power (a and b) constant pump power and gain of different wavelength channels (c and d) time-dependent pumps.

9.5 Concluding Remarks

This report demonstrates the successful implementation of the modeling of the EDFA operating under the dynamic and steady states using MATLAB Simulink. The model has been used to investigate the characteristic of the EDFAs over the C- and L-band spectral regions. Predicted results by varying the parameter settings are shown to be in good agreement with those obtained from experiments. The MATLAB Simulink toolboxes for simulating the dynamic system offer significant advantages of being well known and available in worldwide teaching and research laboratories. Multiple-wavelength signal propagation and ASE noise simulations have been taken into account in our EDFA SIMULATOR. Although we have demonstrated only the Simulink [EDFA Module] using the wavelength for one pump and for one signal, it is straightforward to modify the simulation to achieve the multiple-channel propagation as [EDFA Simulator]. The only limitation is the computer memory and the CPU runtime. Cascaded EDFA systems can also be connected, and the effects of propagation loss and noise in such systems can be modeled with ease.

Primarily, a powerful simulator of the modern optical amplifier modules and their various components has been established. Future works will aim to incorporate a number of optimization components into the EDFA simulator, further enhancing the uses of the simulator. Multiple-channel propagation simulation in EDFA Module is also incorporated. The developed EDFA SIMULATOR and the EDFA Modules will provide the framework for development of the Raman amplifier simulation in the near future using MATLAB Simulink.

References

1. C.R. Giles and E. Desurvire, Modeling erbium-doped fiber amplifiers, *IEEE Journal of Lightwave Technology*, 9(2), 271–283, 2002.
2. S. Novak and R. Gieske, SimuLink model for EDFA dynamics applied to gain modulation, *IEEE Journal of Lightwave Technology*, 20(6), 986–992, June 2002.
3. S. Novak and R Gieske, Analytic model for gain modulation in EDFAs, *IEEE Journal of Light wave Technology*, 20(6), 975–985, June 2002.
4. S. Yamashita and M. Nishihara, L-band erbium-doped fiber amplifier incorporating an inline fiber grating laser, *IEEE Journal of Quantum Electronics*, 7(1), 44–48, January/February 2001.
5. Y. Sum, J.L. Zyskind, and A.K. Srivastava, Average inversion level, modelling, and physics of erbium-doped fiber amplifiers, *IEEE Journal of Selected Topics in Quantum Electronics*, 3(4), 991–1007, August 1997..
6. A.A. Saleh, R.M. Jopson. J.D. Evankow, and J. Aspell, Modelling of gain erbium-doped fiber amplifier, *IEEE Photonic Technology Letters*, 2, 714, 1990.
7. K. Izuka, Experiment on erbium-doped fiber amplifiers, Advanced Labs for Special Topic in Photonics (ECE 1640H), University of Toronto, Toronto, Ontario, Canada, April 28, 1998.
8. K. Izuka, Erbium-doped fiber amplifier, Advanced Labs for Special Topic in Photonics (ECE 1640H), University of Toronto, Toronto, Ontario, Canada, April 28, 2003.
9. L.N. Binh, Modelling of dispersion managed WDM optical communication systems, Electrical and Computer System Engineering Faculty, Monash University, Melbourne, Victoria, Australia, 2003.

10. R. Scholten, Quantum & advanced optics laser, School of Physics, University of Melbourne, Melbourne, Victoria, Australia, 2003.
11. V. Mehta, Amplified spontaneous emission tutorial, ECE1654: Optical Networks, University of Toronto, Toronto, Ontario, Canada, 2003.
12. Celion Network, Inc., Overview of optical fiber transmission using DWDM technology, White Paper, Richardson, TX, 2003.
13. W.J. Miniscalco, Erbium-doped glass for fiber amplifiers at 1500 nm, *IEEE Journal of Lightwave Technology*, 9, 234, 1991.
14. G.P. Agrawal, *Fiber-Optic Communication Systems*, 2nd ed., John Wiley & Sons, Sydney, New South Wales, Australia, 1997.
15. Kreyszig, E., *Advanced Engineering Mathematics*, 7th ed., John Wiley & Sons, New York, 1993.
16. ADVA EDFA specification data sheet, Optical Service & Solution (ADVA), Ramsey, NJ.
17. L.N. Binh, ECE 4405 Lecture notes on optical transmitter and receiver for Gb/s broadband communication system and network, Monash University, Melbourne, Victoria, Australia, 2004.
18. L.N. Binh, ECE 4405 Lecture notes on optical repeater, regenerator and amplifier, Monash University, Melbourne, Victoria, Australia, 2004.
19. MATLAB SimuLink Help Files, refer SimuLink programming. MathWorks,.Inc., Natick, MA, 2006.
20. *MATLAB SimuLink Reference Books*. MathWorks,.Inc., Natick, MA, 2006.
21. *MATLAB SimuLink Dynamics Model Design Handbook*. MathWorks,.Inc., Natick, MA, 2006.

10

MATLAB® Simulink® Modeling of Raman Amplification and Integration in Fiber Transmission Systems

Dynamic modeling of optical transmission systems is very important in the ultra-high-speed optically amplified communication systems. Systems operating at bit rates above 40 Gb/s require detailed and accurate modeling. Therefore, the modeling of the Raman gain amplification must be integrated into the propagation of modulated optical signals over the models of multispan transmission link.

This chapter describes the Raman amplification in various types of transmission and dispersion compensating fibers including (1) the physical properties and operational characteristics and (2) its implementation in the lightwave-modulated envelop propagation equation for transmission of 40 Gb/s signals in dense wavelength division multiplexing (DWDM) optical systems. We demonstrate the integration of the Raman amplification gain and noises into the transmission system with the following material.

(1) Numerical techniques to solve these design parameters for a single-channel bidirectionally pumped system operating in the C-band (1525–1565 nm) range at 1550 nm are presented.

(2) Investigations of Raman amplification of different commercially available fibers for obtaining the Raman design parameters of gain, noise figure (NF), and dispersion in distributed and discrete Raman configurations are detailed. Comparisons are contrasted with published documents and existing optical amplification technology.

(3) The numerical solution is adapted from average power to a Gaussian pulse operating at 40 Gb/s and propagated along the length of the fiber using the split-step Fourier method (SSFM), to allow for integration into the amplitude-shift keying (ASK) and multiple-shift keying (MSK) MATLAB® Simulink® Models.

(4) Improvements in transmission link distance and noise performance are described.

10.1 Introduction

Stimulated Raman scattering (SRS), or the Raman effect, is an optical phenomenon, which only recently has attracted commercial interest for its potential in engineering. The interest has been sparked by the increasing demands of the Internet, as a communication tool for both business and personal needs. However, the increased demands have elucidated the limitations of existing modern systems in terms of higher-capacity data transport [1–6].

The Raman scattering phenomenon is associated with the molecular diffraction of light, where photons interact with molecules to induce transitions in energy states. Typically, the photons scattered from these interactions are of the same energy and display the same characteristics as the incident light, in particular, in the wavelength. This type of occurrence is known as Rayleigh or elastic scattering. However, a small fraction of light, approximately 1 in 10^7, is scattered at different optical frequencies and are at a much lower energy level than that of the incident photons. This inelastic effect is referred to as Raman scattering [7]. The optical effects associated with the Raman scattering are of particular importance in the design of modern lightwave systems. The requirements to upgrade existing systems to accommodate for increased signal transmission and transmission quality over longer distances are becoming increasingly important [8].

In modern long-haul fiber-optic communication systems, the transmission distance is limited by fiber loss and dispersion. Traditional methods to overcome this limitation, which use electrical conversion of the optical signal with repeaters to retransmit signals at progressive stages, are becoming increasingly complex and expensive. In the 1990s, optical amplifiers, which directly amplified the transmission signal, became widespread minimizing system intricacies and cost. Although upgrades in transmission fiber design, in particular, in dispersion-compensating fibers (DCF), has minimized linear phase distortions in the signal, in modern systems, existing erbium-doped fiber amplification (EDFA) lumped optical amplifiers are employed to ensure the quality of the transmitted signals [8–11].

The Raman scattering has become important in the application of optical amplification because of several important reasons in comparison to other similar methods [11,12]. Raman optical amplification (ROA) can be described simply as a pump laser that emits lightwaves down an optical fiber; this signifies that it can be compatible with most available transmission systems. The operation of the pump laser is dependent on the gain that is achieved, in particular the pump wavelength. This means that the medium of transmission is completely independent, in contrast to the EDFA. The fact that the gain is dependent on the pump wavelength theoretically means that amplification is achievable for any frequency. It is important to note that using a number of lasers at variable frequencies in a system will provide a broad gain in bandwidth. There are also advantages to ROA from EDFA in low noise characteristics, which can improve the overall signal quality.

The simulation of the amplification processes and generation of gain and noises of the ROA are important for integration of these properties into optical transmission systems, especially in multispan optically amplified transmission systems employing DWDM technique. Further, advanced modulation formats have attracted significant interest in the combat of impairments such as dispersion and nonlinear effects. The performance of these modulation format schemes under the ROA of the long-haul transmission systems has not been demonstrated when both forward and backward amplification sections are used in the same span. It is, therefore, necessary to integrate the ROA into the transmission model for simulation of the transmission performance of advanced modulation formats in multispan ROA and EDFA optically amplified long-haul transmission links.

This chapter comprises three separate components: (1) the physical model of Raman amplification, (2) the system transmission model integrating Raman amplification, and (3) integration of the ROA in the transmission link model operating under advanced modulation formats.

Therefore, the objectives of this chapter are (1) to investigate the physical properties of Raman amplification, apply it to a system model, such as ASK or MSK, and compare results against different system configurations to determine if the ROA is beneficial in expanding

span transmission reach and capacity; (2) to focus on the physical modeling of ROA in terms of the operational principles of ROA, in particular the optical distributed gain and its noise figure; (3) to use MATLAB to numerically solve and analyze these parameters, comparing results of modeling with published documents and other commercially available forms of optical amplification, such as EDFA; (4) to transpose these results into a dynamic Simulink transmission system model employing amplitude, phase or frequency shift keying techniques such as ASK, discrete and continuous phase shift keying such as DPSK, and minimum shift keying (MSK) to prove the effectiveness of our modeling techniques and integration of ROA in long-haul transmission systems; and (5) to provide a case study of ROA long-haul transmission systems along the coastal line of Vietnam, illustrated with the transmission performance.

10.2 ROA versus EDFA

The comparisons between existing lumped EDFA and distributed ROA systems are based on the signal power evolution with the loss and gain compensated by each other along the fiber length. Both forms of optical amplification provide gain to a signal power and are iterated over the span of the fiber. There are important differences: in lumped EDFA, the gain (1) characteristics depend on a large number of device parameters and (2) are amplified to the signal at the start of the segment, and because of the effective length of EDFA (a few tens of meters), are amplified immediately; whereas in distributed ROA, the gain (1) characteristics are dependent on the transmission medium, the silica fiber, and (2) are delivered backward from the end of the first lumped circuit, and because of the effective length of the ROA (in kilometers), are distributed gradually.

The advantages of distributed ROA are the gains obtainable in almost all types of transmission fibers, ease of gain clamping, low noise characteristics, improvement in optical signal-to-noise ratio (OSNR), gain nonresonance, very wide gain bandwidth Δv_g of more than 6 THz (or about 50 nm in the 1550 nm spectral region) achievable by using multiple pumps at different wavelengths, possibility of extending power budget margins. However, the disadvantages of the ROA are the requirement of high pump powers; poor pumping efficiency at lower powers; fast response time, hence new noises; and effects of nonlinearities not negligible.

Advantages of lumped EDFA can be listed as (1) integrated well into existing systems, due to intrinsic properties of silica; (2) good pumping efficiency at lower powers; and (3) widely studied and deployed in WDM systems. The disadvantages of lumped EDFA can be listed as (1) gain resonance and bandwidth limited to C- and L-bands (1525–1605 nm), (2) gain equalization necessary for ultra-wideband DWDM, (3) fiber nonlinearities and noises, and (4) difficulty in gain clamping.

It is important to realize [13–15] that although there are some disadvantages to ROA, advancements in fiber technology, which minimize these issues, are in the experimental stage. A design issue that is considered in this chapter is the incorporation of dispersion compensation fiber (DCF) into the system model. The advantages of DCF in the ROA include (1) high negative dispersion characteristics, which compensate the dispersion induced in the fiber from the group velocity dispersion (GVD) and self phase modulation (SPM). (2) small effective area—hence, lower pump power necessary; and (3) high germanium (Ge) concentration in the silica fiber.

10.3 Raman Amplification

10.3.1 Principles

SRS is a nonlinear effect as a result of interactions between lightwaves with molecular vibrations in silica fiber and occurs when the transmitted power of a channel exceeds the threshold power. For a single channel

$$P_{th} = \frac{16 \cdot A_{eff}}{K_p \cdot L_{eff} \cdot g_r} \tag{10.1}$$

where K_p is the polarization constant and is assumed to be equal to 2 for a completely unscrambled signal. Scattering occurs when the polarization of the molecule changes with the vibrational motion. This is caused when an electric field distorts the electrons of the molecule to create an induced dipole moment, $\mu = \alpha \cdot E$, and for a diatomic molecule $\alpha = \alpha_0 + \left(\partial\alpha/\partial q\right)_0 q + \cdots$. If the molecule is vibrating with frequency v_0, then $q = A\cos(2\pi v_0 t)$, and there is an oscillating electric field at frequency v_i, $E = E_0\cos(2\pi v_i t)$, then the induced dipole moment becomes

$$\begin{aligned}\mu &= E_0 \cdot \alpha_0 \cos(2\pi v_i t) + E_0\left(\frac{\partial\alpha}{\partial q}\right)_0 A\cos(2\pi v_i t)\cos(2\pi v_0 t) \\ &= E_0 \cdot \alpha_0 \cos(2\pi v_i t) + \frac{1}{2}E_0 A\left(\frac{\partial\alpha}{\partial q}\right)_0 [\cos 2\pi(v_i - v_0)t + \cos 2\pi(v_i + v_0)]\end{aligned} \tag{10.2}$$

This shows that the moment can oscillate at three frequencies and can, therefore, emit light at these frequencies, corresponding to Rayleigh scattering (v_i), Stokes scattering ($v_i - v_0$), and anti-Stokes scattering (AS) ($v_i + v_0$). The emission of light is in the form of energy transitions that will depend on the interaction or collisions between the incident light and the quantum of vibrational energy. In SRS, the scattered photons will gain or lose energy by the incident photon. If the incident photon excites a transition of vibration energy in the molecule, the scattered photons experience a gain and a downshift to the Stokes frequency. In contrast, if vibration energy already exists in the molecule, the incident photon can absorb it, which causes a loss in the scattered photons and an up-shift to the AS frequency. The excited vibration level is populated following a Boltzmann distribution. As the anti-Stoke scattering is initiated in the excited vibration level, its transition rate is also proportional to this distribution. The relative intensities and the Stokes shift are essential elements in the design of Raman amplifiers. The physical model of ROA including the Raman gain, the associated noises in the system, and the dispersion incurred along the fiber can be briefly presented.

The frequency difference, $\Omega_R = v_i - v_0$, known as the Stokes shift is, as mentioned earlier, an essential element in Raman gain. The intrinsic properties of glass, usually fused silica, in the transmission medium also provides a range within which the frequency of the pump, $v_p = v_i$, and frequency of the signal, $v_s = v_0$, can differ.

The Raman gain in silica-based fiber can reach up to 20 THz in which the Stokes shift can happen. The maximum Raman gain, g_R, is observed at 13.2 THz; this corresponds to a wavelength difference of 100 nm between the pump and signal. As $f = c/\lambda$, the wavelength is inversely proportional to frequency, and larger frequencies result in smaller wavelengths. The Raman gain bandwidth $\Delta v_g = 6$ THz is defined as the full-width half maximum (FWHM) of the dominant peak in the gain spectrum. The overall optical gain can be expressed in terms of the pump intensity I_p:

$$g(v) = g_R(v) \cdot I_p = g_R(v) \cdot \left(\frac{P_p}{A_{eff}} \right) \tag{10.3}$$

This gain is thus dependent on the frequency and pump power. The parameter Raman gain efficiency $g_{R\_eff} = g_R/A_{eff}$ is a critical design parameter. Different fibers have different gain efficiencies due to smaller effective areas and higher germanium (Ge) concentrations, which increase the overall Raman gain efficiency, and hence the optical gain and lower the threshold power required to initiate lasing and the SRS process.

10.3.2 Raman Amplification Coupled Equations

The power evolution of the pump and signal power along a length of a fiber, z, can be modeled by two coupled equations, respectively:

$$\begin{aligned} \frac{dP_S}{dz} &= -\alpha_S P_S + \left(\frac{g_R}{A_{eff}} \right) P_P P_S \\ \xi \frac{dP_P}{dz} &= -\alpha_P P_P - \left(\frac{v_P}{v_S} \right) \left(\frac{g_R}{A_{eff}} \right) P_S P_P \end{aligned} \tag{10.4}$$

It illustrates that the pump power provides the energy for amplification and depletes as signal power increases. As pump power approaches the signal power, the optical gain is reduced and gain saturation occurs. In ROA, the laser can be pumped from either end of the fiber by changing the polarization, $\xi = -1$. The schematic drawing of the pumping configurations is shown in Figure 10.1. Pumping in different directions changes the signal power evolution along the length of the fiber.

The power along the length of the fiber is reduced by the fiber losses, which occur in the medium due to its intrinsic properties. These result in microscopic fluctuations in the density of the core, which affects the refractive index. Doping the fiber with dopants such as germanium further increases these losses. It is also a limiting factor in transmission distance lengths as optical receivers require minimum amounts of power to recover the signal [15,16].

This attenuation coefficient $\alpha_{P,S}$ includes all sources of power attenuation and is expressed in units of dB/km by the relation α (dB/km) = $10\log(e)\alpha \approx 4.343\alpha$. If pump depletion can be neglected, that is, in small-signal amplification, the pump power for forward pumping becomes

$$P_P(z) = P_0 \exp(-\alpha_P z) \tag{10.5}$$

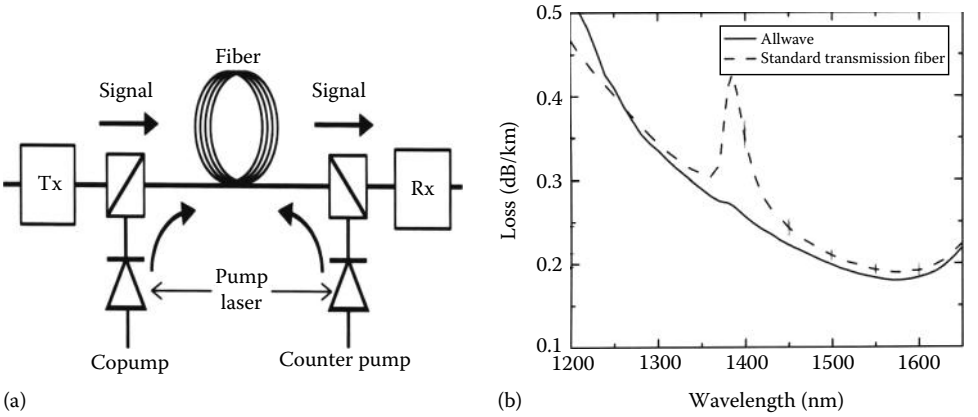

FIGURE 10.1
(a) Schematic of the ROA using the bidirectional configuration and (b) attenuation spectrum of two types of transmission fibers.

with P_0 as the input pump power. Hence, the signal intensity at the output of the amplifier of length L is determined as

$$P_S(L) = P_S(0)\exp\left(\frac{g_R P_0 L_{eff}}{A_{eff}} - \alpha_S L\right) \tag{10.6}$$

The effective length, L_{eff}, is the length where the nonlinearities exist or SRS occurs in the fiber and is defined as

$$L_{eff} = \frac{1-\exp(-\alpha_P L)}{\alpha_P} \tag{10.7}$$

As fiber losses exist at the pump wavelength, it is less than the actual length and can be approximated by $L_{eff} \approx 1/\alpha_P$ if $\alpha_P L \gg 1$. Hence, the gain amplification, the ratio of the power of the signal with and without Raman amplification, is given by

$$G_A = \frac{P_S(L)}{P_S(0)\exp(-\alpha_S L)} = \exp(g_o L) \tag{10.8}$$

This is referred to as the on–off Raman gain and can be determined from Figure 10.4 from the difference in dBm of the Raman pumped fiber and the passive fiber without amplification. The difference from the figure is approximately 20 dB. Hence, the small signal gain, g_o, can be obtained. The signal power evolution along the total length of the fiber can be imagined to be distributed gradually and exponentially to equalize that of the fiber attenuation.

In Raman amplification of the signal, the noises are contributed by the following processes. In the SRS process, noise is added to the amplified signal because of random phases associated with spontaneously generated photons. The spontaneous scattering factor is dependent on the temperature of the amplifier given by $n_{sp} = 1/\left(1-\exp\left(-h\Omega_R/k_B T\right)\right)$.

For a Raman amplifier, $n_{sp} \sim 1.13$ as it is always a fully inverted amplifier. The noise incurred by the spontaneous Raman scattering across the length of the fiber is accumulated and is known as amplified spontaneous emission (ASE).

Rayleigh backscattering occurs in all fibers and is the fundamental loss in signal power. Typically, it is seen as ASE propagating in the backward direction as it is small in comparison to the power of the signal and of no concern. In ROA, however, as a result of large transmission spans, it can cause the ASE to be reflected back in the forward direction and re-amplified enhancing the overall noise; this is known as double Rayleigh backscattering (DBS), and because it can occur anywhere along the fiber, it is referred to as multipath interference (MPI).

In ROA, the short upper state lifetime results in instantaneous gain leading to coupling of the pump fluctuations with the signal. To avoid this, backward pumping configurations are adopted, which changes the upper-state lifetime to the transit time. If forward pumping is to be used, pumps with low noise are required. NF is the determination of the signal denigration over the length of the transmission span. It is the SNR of input over output and in ROA it is dependent on the pumping power and the net gain of the system by

$$NF = 2n_{sp}\frac{g_R}{A_{eff}}\int_0^L \frac{P_p dz}{G(z)}dz + \frac{1}{G_L} \tag{10.9}$$

where

$G(z)$ is the net gain at distance z along the fiber

G_L is the net gain at the end of the fiber

10.4 Raman and Fiber Propagation under Linear and Nonlinear Fiber Dispersions

10.4.1 Propagation Equation

In optical amplifiers, lightwaves are beamed down a length of fiber to transmit a signal. Fiber dispersion properties can vary according to their refractive index profiles of either graded or step distribution and geometrical structure. Furthermore, dispersion can also occur due to nonlinear effects, for example, nonlinear SRS (stimulated Brilloin scattering) can occur in a fiber due to an increase in total channel signal power. In geometrical optics description, dispersion or pulse broadening is caused by different rays following different paths and not arriving at the output end of the fiber at the same time. In modal description, dispersion is related to the group velocities associated with different modes. The GVD is caused by chromatic dispersion, which exists in fibers that support only the fundamental mode. It causes pulse broadening whereby different spectral components of the pulse are propagating at different velocities and arrive at different output of fiber length at different times. It is expressed by $v_g = (d\beta/dw)^{-1}$, where β is the propagation constant. The derivative of the propagation constant in terms of frequency determines the GVD parameter: $\beta_2 = d^2\beta/bw^2$. This parameter determines the pulse broadening effects especially when the pulse is short in ultra-high-speed transmission over the propagating long distance. This can be related to the dispersion parameter D. As dispersion can be both negative and

positive, it can also be designed at a wavelength of zero dispersion λ_{ZD}, which is approximately 1.3 μm. It is important that while dispersion is minimized in design, it cannot be completely removed as it also minimizes the other nonlinear effects in the fiber, such as SPM and cross phase modulation (XPM). The SPM causes a phase shift in the fiber, the accumulated nonlinear phase shift (NLPS) can be solved by

$$\varphi_{NL} = \gamma P_{S0} \int_0^L G(z)dz \tag{10.10}$$

where γ the nonlinear parameter responsible for SPM is defined by $\gamma = 2\pi n_2/\lambda_S A_{eff}$ where $n_2 = 2.6\times10^{-20}$ is the cladding refractive index in fused silica. The NLPS due to ROA, that is the ratio with ROA and without ROA, can be determined by

$$R_{NL} = \frac{\varphi_{NL}(\text{on})}{\varphi_{NL}(\text{off})} = \frac{1}{L_{eff}} \int_0^L G(z)dz \tag{10.11}$$

Pulse broadening can be described by using the wave equation, expressed as

$$\frac{\partial A}{\partial z'} + \frac{i}{2}\beta_2 \frac{\partial^2 A}{\partial t'^2} - \frac{1}{6}\beta_3 \frac{\partial^3 A}{\partial t'^3} = 0 \tag{10.12}$$

where

β_3 is the dispersion slope
$A(t, z)$ is a slowly varying amplitude

To incorporate nonlinear effects into the pulse broadening equation and compensate for dispersion, solitons are integrated in the form of the Schrodinger equation:

$$\frac{\partial A}{\partial z} = \frac{i}{2}\beta_2 \frac{\partial^2 A}{\partial t^2} + \frac{1}{6}\beta_3 \frac{\partial^3 A}{\partial t^3} + i\left|A\sqrt{\gamma}\right|^2 + \frac{1}{2}\left[g(\xi) - \alpha\right] + iTR\frac{\partial\left|A\sqrt{\gamma}\right|^2}{\partial t} \tag{10.13}$$

This is the unnormalized nonlinear Schrodinger equation (NLSE), which includes the effects of distributed amplification and dispersion management.

10.4.2 SSMF and DCF as Raman Fibers

The Raman gain coefficients for various types of fibers as standard single mode fiber (SSMF) have been measured and are tabulated in Table 10.1 and illustrated in Figure 10.2. In long-haul transmission, it becomes necessary to compensate for dispersion. Dispersion can be seen as a linear process whereby pulse spreading can be negated by introducing a fiber with the same degree of GVD but of opposite polarization. DCF exists to manage the impact of dispersion with an opposite sign of dispersion and dispersion slope in comparison to single mode fiber (SMF). It also has a higher attenuation in comparison to SMF and, therefore, will add greater loss, which will result in increased noise power. The power evolutions of the pump and signal in Raman amplification can be described as a set of ordinary differential equations (ODEs).

TABLE 10.1

Different Commercial Fibers and Their Parameters Used for Numerical Solutions to Obtain Raman Amplification

Type of Fiber	Raman Gain Efficiency (1/W·km)	Effective Area (μm²)
Allwave	0.35	84.95
Corning NZDSF	0.72	80
LEAF (NZDSF)	0.45	72
SMF-28 (NDSF)	0.38	84.95
Truewave RS (NDSF)	0.58	60
Truewave reach fiber	0.6	55
OFS Raman fiber	2.5	18.7

Note: NZDSF, nonzero dispersion shifted fiber; NDSF, non dispersion shifted fiber.

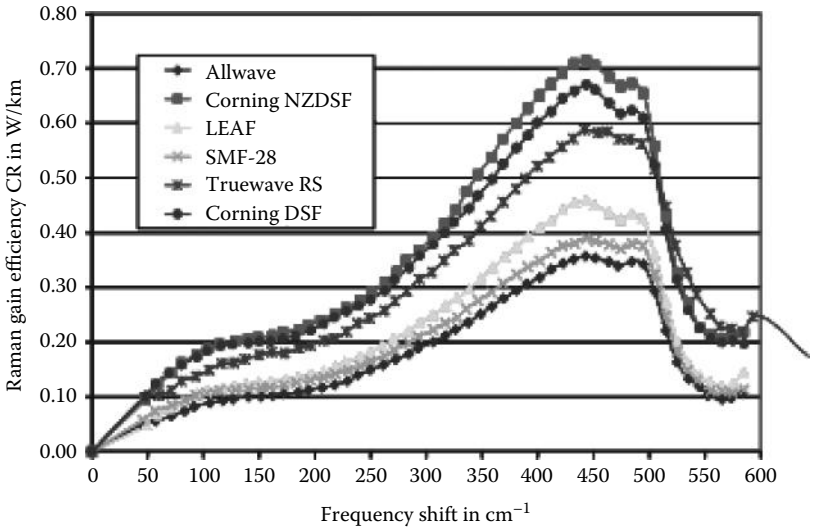

FIGURE 10.2
Measured Raman gain efficiency of different transmission optical fibers.

$$\frac{\partial P_S}{\partial z} = -(\alpha_{RS} + \alpha_S)P_S + \frac{g_R}{A_{eff}} P_P P_S$$

$$\frac{\partial N_S}{\partial z} = \left(-\alpha_{RS} - \alpha_S + \frac{g_R}{A_{eff}} P_P \right) N_S + \frac{g_R}{A_{eff}} (2P_P N_P)^{1/2} P_S + \left(\alpha_{RS} + \alpha_S + \frac{g_R}{A_{eff}} P_P \right) \frac{h\omega_S}{2} B_0$$

$$\frac{\partial P_P}{\partial z} = -(\alpha_{RP} + \alpha_P)P_P - \frac{\omega_S}{\omega_P} \frac{g_R}{A_{eff}} \left(P_S + N_S + \frac{h\omega_S}{2} B_0 \right) P_P \tag{10.14}$$

$$\frac{\partial N_P}{\partial z} = -(\alpha_{RP} + \alpha_P)N_P - \left(\frac{\omega_S}{\omega_P} \frac{g_R}{A_{eff}} P_S \right) (2P_P N_P)^{1/2} + (\alpha_{RP} + \alpha_P) \frac{h\omega_S}{2} B_0$$

$$+ \left(\frac{\omega_S}{\omega_P} \frac{g_R}{A_{eff}} P_S \right) \left(2P_P \frac{h\omega_S}{2} B_0 \right)^{1/2}$$

To model these equations, classical numerical techniques need to be utilized as these equations represent a complex system, which cannot be solved for analytically. The particular choice of numerical approximation (Runge–Kutta, etc.) depends on the method needed to solve it (i.e., initial value ODEs), the accuracy required, and the consideration of simulation time in processing. This last consideration is especially important when implementing from MATLAB to systems in Simulink. The function ode45.m of MATLAB can be used to obtain the initial value by using ODEs employing the Dormand–Prince formula that meets the requirements of accuracy in approximation and in processing speed.

The assumptions made in our modeling platform include the following: (1) forward and backward noise powers are typically less than input signal powers by 30 dB; (2) backscattering powers of pumps and signals are usually about 20–30 dB lower than their original powers; (3) noise effects such as spontaneous Raman scattering, Rayleigh backscattering, and thermal factor can be reasonably ignored when simulating the Raman gain profile; and (4) $\alpha_{RS} = \alpha_{RP}$ for simplicity.

The coupled noise equations (10.2) and (10.4) include the fundamental noise sources including zero-point fluctuations, amplification of noise, partition noise, and Rayleigh scattering. The Raman gain coefficient is dependent on the difference between the pump and the signal frequencies. In the case where the pump is co-pump with the signal at 1450 nm in nonzero dispersion shifted fiber (NZDSF), the effects of different shifting frequencies for the signal on the Raman gain are highlighted as shown in Table 10.2.

Figure 10.3 confirms that Raman amplification is possible over a wide range of signal frequencies for a single pump, with a peak coefficient existing at 13.2 THz from the pump or 100 nm wavelength. Because optical amplification is directly proportional to the Raman coefficient, gain is also distributed across a large bandwidth of signal frequencies. In the single pumped configuration, to determine the performance the gain ripple was determined over the Raman bandwidth. Figure 10.3b shows that gain ripple is approximately 6 dB.

As Raman amplification is theoretically possible at any wavelength, careful consideration of pumping wavelengths and Raman pumping power when using multiple pump lasers (see Figure 10.4) of different wavelengths can provide broadband and flat gain as shown in Figure 10.5. This is possible because individual gain spectra accumulate at different wavelengths to provide the total system gain.

To model ROA in all configurations, forward, backward, and bidirectional, two ode45 functions in MATLAB can be implemented for backward and forward pumping, respectively. This was achieved by changing the pump direction. The signal power always propagates in the same direction. To achieve bidirectional pumping, the effects of the co- and counterpropagating pump powers are accumulated to give the total pump power.

TABLE 10.2

Shows the Effects of Signal Frequency Shifting on the Effective Raman Coefficient and Total Raman Gain

Shifting Frequency		Signal Frequency	Signal Wavelength	Effective Raman	Raman Gain
THz	1/cm	THz	nm	1/W·km	dB
6	200	200.9	1493.3	0.24	6.61
10.5	350	196.4	1527.5	0.5	13.86
13.2	450	193.7	1548.8	0.72	20.13
16.5	550	190.4	1575.6	0.22	6.06

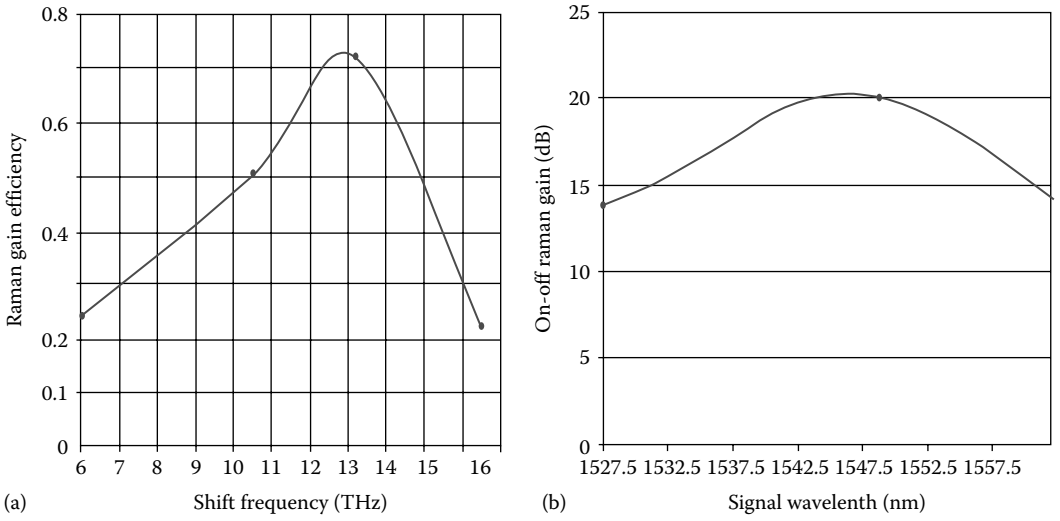

FIGURE 10.3
(a) Effective Raman gain coefficient versus shifting frequency for NZDSF fiber. (b) Gain over the Raman bandwidth.

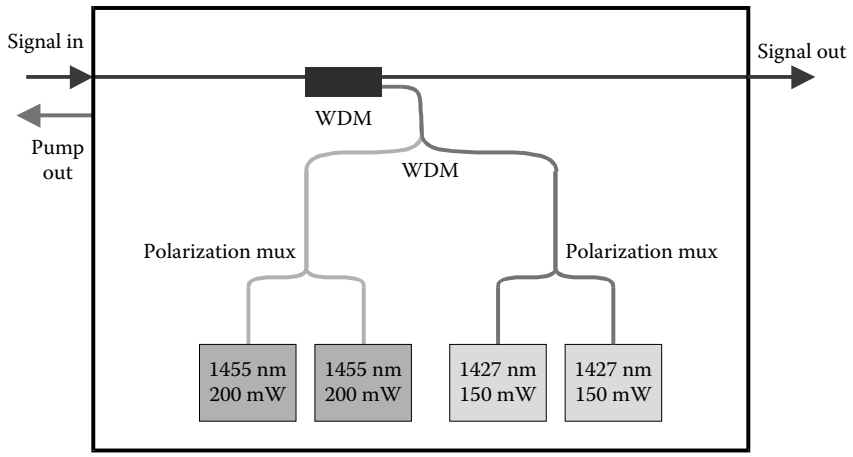

FIGURE 10.4
Multiple pump sources arrangement for Raman amplification in DWDM transmission. Operating band: 1530–1565 nm; Raman pump: multiplexed semiconductor lasers; pump power up to 500 mW; gain ripple: 0.8 dB; small signal gain: 11 dB; OSNR improvement: 4.5 dB; PMD: 0.2 ps, PDG: 0.1 dB.

Figure 10.6 shows the evolution of the distributed gain under both backward and forward pumping. The pump power is shown to reduce to provide gain for the signal power; this is due to pump depletion as shown in Figure 10.7.

The signal power evolution shows how it changes the attenuation map in comparison to the passive fiber, with no Raman amplification. In the forward configuration, there is a large gain in power at the beginning of the fiber length. This results in increasing effects of nonlinearities in the fiber because of the power dependence of the refractive indices of the core and cladding, $n'^{j} = n^{j} + \bar{n}_2(P/A_{eff})$ with $j = 1, 2$. In the backward configuration, the

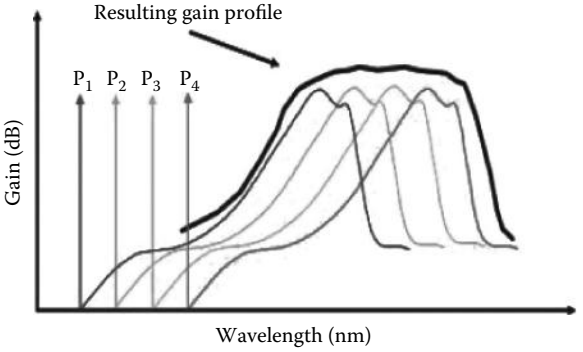

FIGURE 10.5
Raman gain with multiple pump.

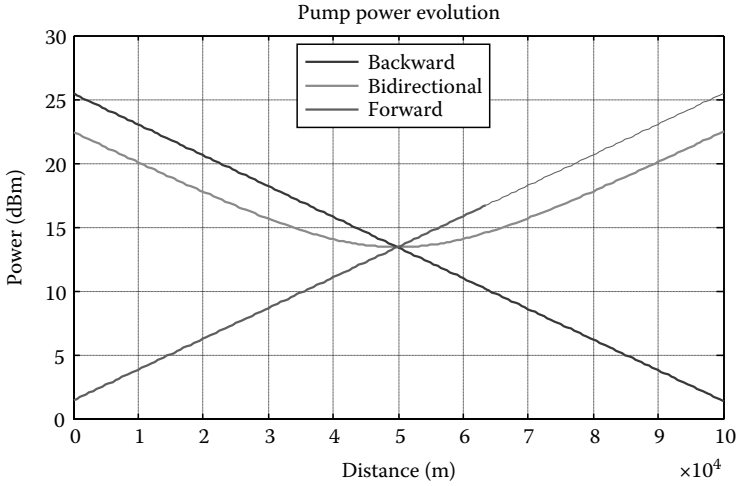

FIGURE 10.6
The power evolution of the pump along the total length of the Corning NZDSF fiber for forward, backward, and bidirectional configurations, dark gray, medium gray, and light gray, respectively.

gain occurs toward the end of the fiber after a substantial power loss. This power loss will increase the possibility of noises altering the quality of the signal. The bidirectional configuration shows a balanced result in terms of noises and nonlinearities. Another important aspect to consider is the on–off Raman gain provided by amplification, in other words, the gain experienced with Raman in comparison to gain experienced without Raman. The evolution of gain along the total length of the fiber can be solved through the decibel difference.

The on–off Raman gain evolution is the important parameter that needed to be implemented using the SSFM for Gaussian pulse and ASK testing in Simulink. It also needs to compensate for the passive fiber losses (net gain = 0). This is important because if the signal has a net gain or loss it will be affected detrimentally when it propagates through numerous spans. Table 10.3 shows the net gain and pumping conditions in different types of fibers over a 100 km span where typical Raman lasers operate at <500 mW; this limits the transmission spans of LEAF, SMF-28, and Allwave.

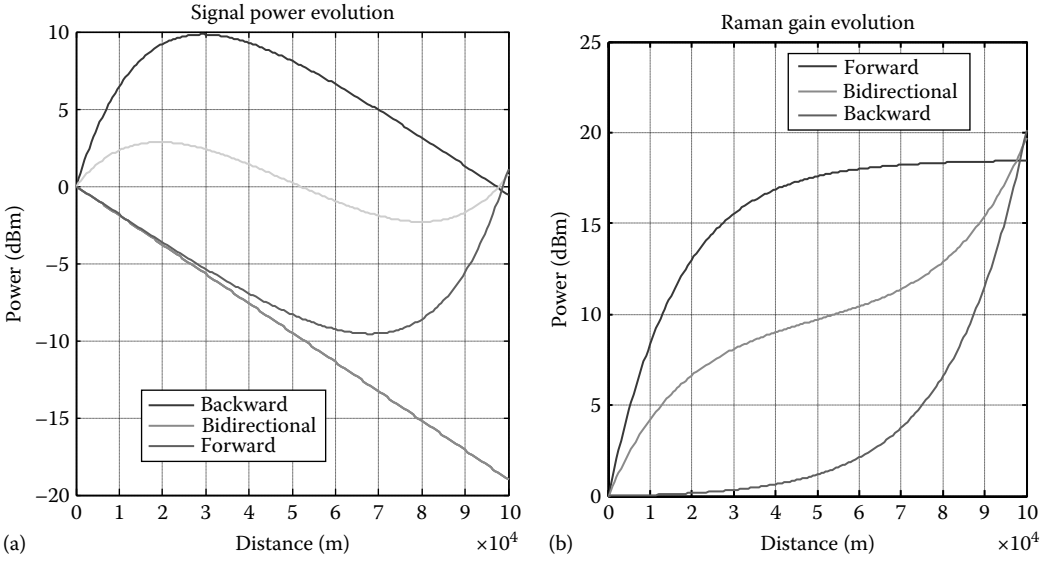

FIGURE 10.7
(a) Power evolution of the signal along the total length of the fiber for forward, backward, and bidirectional configurations, blue, magenta, and cyan, respectively. The red line represents a passive fiber with no gain, α = 0.19 dB/km. (b) Gain evolution over the total length of the fiber due to Raman amplification for forward, backward, and bidirectional configurations.

TABLE 10.3

Final Net Gain for Different Commercial Fibers and the Required Pump Power to Pump the Fiber over the Span Just Compensating Fiber Losses

	Average Power (dBm)			Required Pump Power
Type of Fiber	**Forward**	**Backward**	**Bidirectional**	**(Net Gain = 0) ~ mW**
Allwave	−9.502	−9.327	−9.397	700
Corning NZDSF	−0.551	1.128	0.707	350
LEAF (NZDSF)	−6.879	−6.529	−6.654	550
SMF-28 (NDSF)	−8.707	−8.491	−8.574	650
Truewave RS (NDSF)	−3.638	−2.864	−3.099	425
Truewave reach fiber	−3.165	−2.297	−2.554	425

To illustrate the numerical solutions, an analytical solution was derived from the coupled equations ignoring the pump depletion. It was determined that pump depletion reduces the transfer of power from the pump to the signal as the pump power depletes sooner. To further investigate the initial input, the signal power was increased to approach the initial pump power, and it was observed that there was a greater reduction in signal gain because of gain saturation. Figure 10.8a and b shows the signal power evolution along the fiber under the Raman pumped gain and loss.

Numerically solving the coupled equations using the ode45 function in MATLAB, the signal and power evolution for average power can be obtained. To implement into the Simulink ASK model, this solution needs to be applied to a Gaussian pulse at the correct bit rate of 40 Gb/s, which could be propagated using the SSFM.

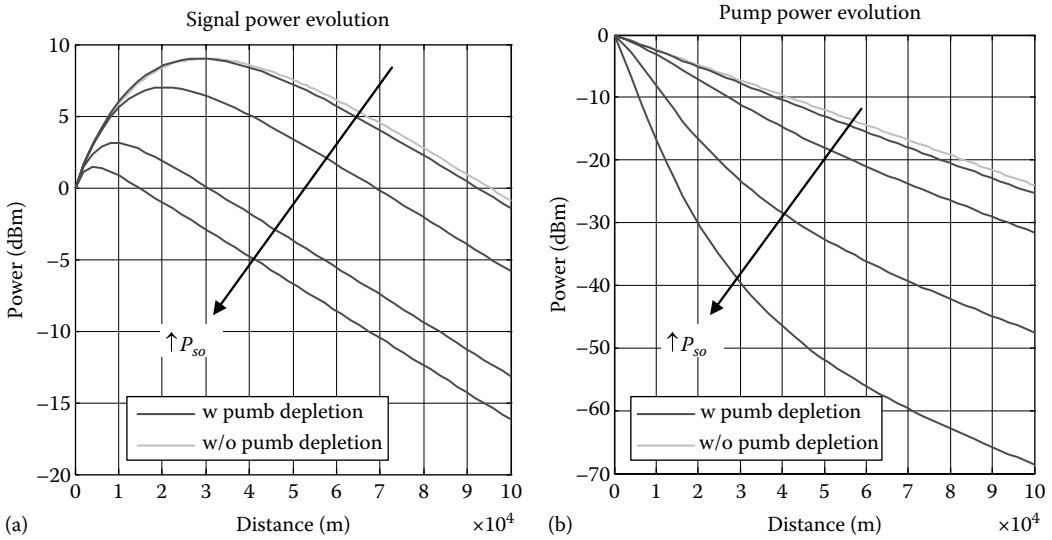

FIGURE 10.8
(a) Power evolution of the signal along the total length of the fiber with and without the effects of pump depletion, blue and green, respectively. (b) Power evolution of the pump along the total length of the fiber with and without the effects of pump depletion, blue and green, respectively.

To implement the Raman in the beam propagation, the NLSE file is modified to include Raman amplification. This is achieved by changing the SSFM half-step parameter that is the gradient of the attenuation iterated over a number of segments along the fiber. In the passive fiber case, the half step is constant; to include ROA, the Raman gain contribution at each point is added to this half step.

10.4.3 Noise Figure

Modeling the noise profile, the noise power evolution of the signal along the total length of the fiber can be determined as depicted in Figure 10.9. The resulting signal noise agrees with published results [13]; discrepancies are a result of the fact that the numerical equations modeled included Rayleigh scattering and pertinent noises other than ASE. Investigating the signal noise evolution along the fiber is essential because it provides an NF of the system. It is a value of the signal denigration over the total span and is proportional to the attenuation and length. Typically for distributed Raman amplification (DRA), the transmission link is greater than 50 km and the net gain of the signal is below 1. Therefore, from Figure 10.10, it is shown that the NF is typically large for amplification over these lengths.

Distributed amplification is analogous to numerous discrete amplifiers providing gain along the length of the fiber; ideally, if the loss at each point in the span could be corrected, the ideal NF could be determined. Theoretically it is described by $NF\big|_{dB} \approx 10\log(2\alpha + 1)$. For a passive fiber with no DRA (on–off gain = 0) over 100 km the NF degrades by 20 dB. By counterpumping with an on–off gain of 20 dB, the NF is reduced to 17 dB. Though there is a high NF, it does not mean that distributed amplifiers are noisier than lumped.

To evaluate the performance of the DRA in relation to a passive fiber or discrete Raman/EDFA amplifier, it is useful to define the *effective NF*: $NF_{eff} = NF_R - \alpha_S L$. It accounts for the attenuation of the fiber and numerically equates the result to an equivalent discrete NF. Therefore, from Figure 10.11, it can be observed that the NF_{eff} for backward DRA is equal

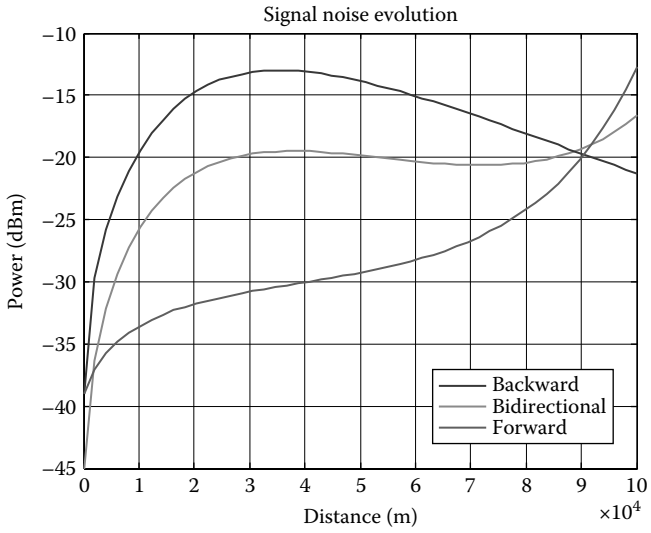

FIGURE 10.9
The noise power associated with the signal along the total length of the fiber for forward, backward, and bidirectional configurations.

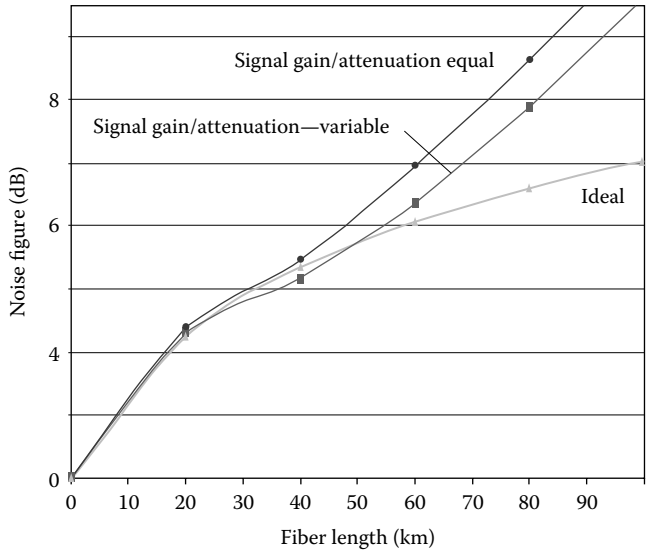

FIGURE 10.10
Noise figure versus on–off Raman gain for backward pumping case and investigating practical and ideal configurations.

to −3 dB for Corning NZDSF. Comparing to a lumped amplifier with an NF limit of at least 3 dB, the overall improvement of distributed amplifiers is at least 6 dB for backward pumping.

The NF is also dependent on the pumping configuration as it is dependent on accumulation of the pumping power and net gain along the fiber. In backward pumping methods, the power reduction in signal and, therefore, the net gain is much more dominant, and

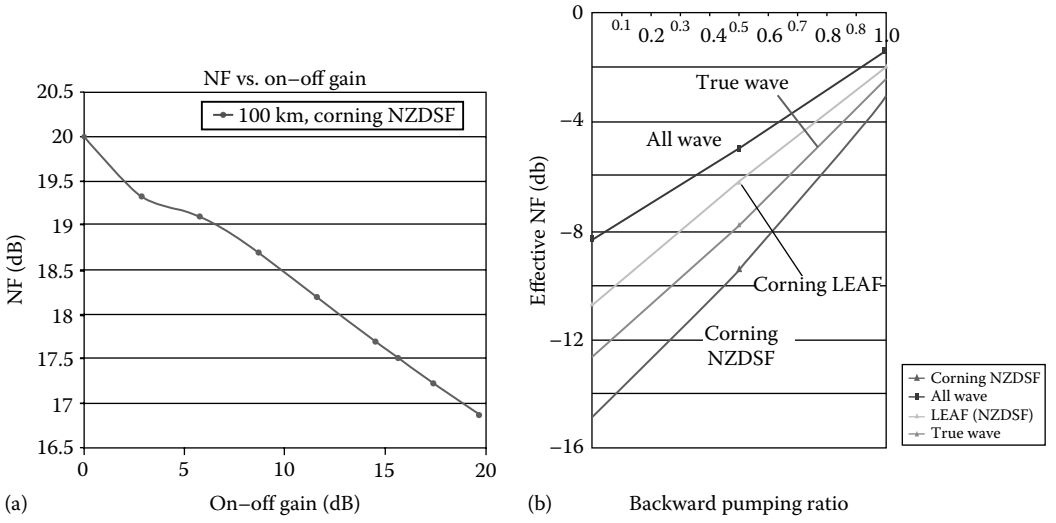

FIGURE 10.11
(a) Noise figure versus on–off Raman gain for a 100 km fiber varying input pump power using Corning NZDSF. (b) Noise Figure versus backward pumping ratio for different fibers over a 100 km transmission link.

therefore, the NF is expected to be much higher. Figure 10.11 illustrates the impact these configurations have on total NF. It shows an improvement of over 10 dB for forward pumping configurations. When varying the backward pumping ratio for different fibers over the span, the different values of NF were determined and showed that for reduced Raman gain coefficient, g_R, values, the impact of the pumping scheme, forward to backward, on the NF was reduced. As the NF is dependent on the pumping power and the net gain, if it is used in a hybrid system configuration, an EDFA pumping gain at the start of the fiber, the NF for ROA can be lowered (Table 10.4). These results assume an ideal EDFA, hence NF = 3 dB is included in the total NF.

TABLE 10.4

Noise Figure of 100 km Backward-Pumped ROA in Hybrid Configuration with Ideal EFDA Gain Using Corning NZDSF

Ideal EDFA Gain (dB)	Noise Figure (dB)
0	17
1	19.13
2	18.27
3	17.46
4	16.6
5	15.8
6	15
7	14.09
8	13.25
9	12.45

TABLE 10.5

Dispersion Characteristics for Two Commercial Fibers with Different Properties in a 100 km Span

	Corning NZDSF		Allwave	
	NLPS (rad)	**Raman NLPS (dB)**	**NLPS (rad)**	**Raman NLPS (dB)**
Forward	7.00E−04	13.79	8.00E−04	14.28
Bidirectional	1.52E−04	7.09	1.53E−04	7.35
Backward	4.28E−05	1.58	4.14E−05	1.7

Source: Headley, C. and Agrawal, G.P., *Raman Amplification in Fibre Optical Communication Systems*, Elsevier Publications, San Diego, CA, 2005.

10.4.4 Dispersion

Another important aspect to consider is the effects of dispersion in the fiber. This was tested for all types of system configurations for two fibers with very different fiber properties (Table 10.5).

It demonstrates that in the forward pumping scheme Raman amplification causes the most nonlinear effects as a result of the increased signal power gained throughout the fiber.

10.5 Nonlinear Raman Gain/Scattering Schrödinger Equation

As can be seen, the model incorporates SSMF and DCF. The system revolves around the NLSE as it governs propagation of optical pulses inside fibers. Thus, if any distributed amplification is to take place, this equation must be transformed to incorporate Raman amplification. The NLSE as solved for the ASK model before manipulation is

$$\frac{\partial A}{\partial z} = -\frac{i}{2}\beta_2 \frac{\partial^2 A}{\partial t^2} + \frac{1}{6}\beta_3 \frac{\partial^3 A}{\partial t^3} - \frac{\alpha}{2}A + i\gamma\left(|A|^2 A + \frac{i}{\omega_0}\frac{\partial}{\partial T}\left(|A|^2 A\right) - T_R A \frac{\partial |A|^2}{\partial T}\right) \tag{10.15}$$

The NLSE incorporates fiber losses through the use of the attenuation factor α and second- and third-order dispersion (TOD) effects through the use of β_2 and β_3, *respectively*. T_R becomes negligible as it is almost insignificant. The NLSE that incorporates distributed amplification and dispersion management is

$$\frac{\partial u}{\partial \xi} = \frac{j}{2}\frac{\partial^2 u}{\partial \tau^2} + \delta \frac{\partial^3 u}{\partial t^3} + j|u|^2 u + \frac{L_D}{2}\left(g(\xi) - \alpha\right) - j\tau_R \frac{\partial |u|^2}{\partial \tau} \tag{10.16}$$

The first Schrödinger equation is unnormalized, meaning that it can be subjected to modeling techniques as it is represented in its raw entirety. The second equation is normalized, meaning that it has to go under the microscope and be transformed into its unnormalized state.

This alone was a hard task and took hours upon hours of complex formulation. This formulation can be seen in the appendices, but the overall result is shown in the following equation:

$$\frac{\partial A}{\partial z} = \frac{i}{2}\beta_2 \frac{\partial^2 A}{\partial t^2} + \frac{1}{6}\beta_3 \frac{\partial^3 A}{\partial t^3} + i\left|A\sqrt{\gamma}\right|^2 + \frac{1}{2}\left[g(\xi) - \alpha\right] + iTR\frac{\partial\left|A\sqrt{\gamma}\right|^2}{\partial t} \tag{10.17}$$

where

$$\gamma = 2\pi n_2/\lambda A_{eff}$$

$$\xi = z/L_D$$

$$L_D = T_0{}^2/|\beta_2|$$

Due to operating parameters, the T_R term can be neglected, resulting in the equations shown earlier. To make calculations simpler, the $\beta_1 z$ term cancels as β_1 equals zero. It must also be noted that the $g(\xi)$ term can be solved for the three cases of forward, bidirectional, and backward pumping.

10.5.1 Fiber Nonlinearities

Fiber nonlinearities are very important when considering Raman amplification within the transmission fiber. The refractive index of Germano-silicate fibers changes with the intensity of the light propagating through the fiber. The nonlinear propagation effects relevant to the evolution of the electric field amplitude involve a cubic term in the electric field, which can be seen in the NLSE. In a communication system with multiple signal channels, the nonlinear effects are typically classified by the number of field amplitudes involved in the process, each associated with its own frequency. Three fiber nonlinearities that are caused by the power being dependent on the refractive index are the following. (1) SPM—this term is used if all three fields belong to the same frequency as the channel of interest. If SPM occurs, the phase of a given channel is modulated by the signal itself and causes broadening of the pulse in the frequency domain if there is an absence of GVD. In certain conditions, SPM can be used to counteract the effect of GVD on a soliton. In other conditions, it causes unwanted pulse distortion. (2) XPM—this is when a phase change appearing on a signal channel is also caused by signals, a tone, or two other channels. The phase modulation caused by other signal channels causes a signal distortion and hence, degradation of the system performance. The XPM is strongly dependent on the walk-off between the signal channel and the channels causing the XPM. It, therefore, depends on the channel's spacing, the GVD, and the polarization of the channels. (3) Four wave mixing (FWM)—occurs when all three amplitudes in the cubic nonlinear term belong to channels other than the one considered. In this process, power is transferred to new frequencies from the signal channels. The appearance of additional waves and the depletion of the signal channels will degrade the system performance through both cross talk and depletion. The efficiency of the FWM depends on channel dispersion and channel spacing.

Other types of nonlinearities are the two major scattering effects that take place because of the intrinsic properties of the optic fiber are the stimulated Brillion scattering (SBS) and stimulated Raman scattering (SRS). Both scattering effects shift the frequency of the signal downwards. These effects are considerably more dominant at high pump powers as the intensity of scattered light grows exponentially once a power threshold is exceeded. Throughout

this chapter, SRS has been the theoretical foundation behind the amplification process and requires a large pump power to be produced. This is the reason why such high pump powers are required when implementing the Raman amplification techniques. SRS does not contribute to fiber losses like SBS does. Input powers less than 10 mW are low enough for SRS not to take place, whereas SBS does not need high pump powers to provide loss to the signal.

10.5.2 Dispersion

From the start of its invention, optic fiber has been taken advantage of and has been stretched to reach its limits. The limits of the optic fiber were not realized until its full implementation and greater transmission rates were passed through it. Dispersion is a term that has been rarely mentioned in this document but is of great importance in transmission systems. Dispersion can be classified into two separate effects", chromatic and polarization mode.

Chromatic dispersion represents the fact that different colors or wavelengths travel at different speeds, even within the same mode. Chromatic dispersion is the result of material dispersion, waveguide dispersion, or profile dispersion. Polarization mode dispersion (PMD) is another complex optical effect that can occur in single-mode optical fibers. Single-mode fibers support two perpendicular polarizations of the original transmitted signal. If it were perfectly round and free from all stresses, both polarization modes would propagate at exactly the same speed, resulting in zero PMD. However, practical fibers are not perfect; thus, the two perpendicular polarizations may travel at different speeds and, consequently, arrive at the end of the fiber at different times [10]. Generally, the effects of PMD are smaller than any given data rate and hence, would be ignored.

10.5.3 Split-Step Fourier Method

The numerical method used to solve the NLSE is known as the SSFM. It accurately models the fiber nonlinearities within the system. This method only applies to the unnormalized expression of the Schrödinger equation and requires the NLSE to be transformed into

$$\frac{dA}{dz} = A\left(\widehat{D} + \widehat{N}\right) \tag{10.18}$$

where

- $\widehat{D}$ represents the differential operator that accounts for dispersion and absorption in a linear regime
- $\widehat{N}$ is a nonlinear operator that governs the effect of fiber nonlinearities

The resulting unnormalized NLSE in split-step form can be represented as

$$\begin{aligned} \widehat{D} &= \frac{i}{2}\frac{\partial^2\left|\beta_2\right|}{\partial t} + \frac{1}{6}\frac{\partial^3\beta_3}{\partial t} + \frac{1}{2}\left[g(\xi) - \alpha\right] \\ \widehat{N} &= i\left|A\sqrt{\gamma}\right|^2 + iTR\frac{\partial\left|A\sqrt{\gamma}\right|^2}{\partial t} \end{aligned} \tag{10.19}$$

In theory, the nonlinear effects and dispersion work in conjunction within the transmission fiber. As SSFM is only an approximation method, these two factors can be broken up and solved individually. The fiber transmission distance is partitioned into a large number of segments of width *h*. Within a segment, the effect of nonlinearity is included at the mid-plane shown by a dashed line indicated in Figure 3.20 of Chapter 3 . Both dispersion and nonlinearity can be solved through an analytical approach, which involves converting from the time domain to the Fourier domain, then the inverse Fourier domain and back into time domain. This is shown in the MATLAB code in the appendix.

10.5.4 Gaussian Pulses, Eye Diagrams, and Bit Error Rate

Testing the SSFM is quite a challenge as the runtime in Simulink is quite slow. Another way of testing the propagation program is to send a theoretical Gaussian pulse through the fiber and check whether the Gaussian pulse that is theoretically transmitted is coming back out with either a gain or loss, depending on the initialization parameters. The full code for this process is shown in the appendices. As illustrated later in the next section, a depiction of the typical Gaussian curve illustrating the FWHM and the amplitude (Figures 10.13 through 10.15); the eye diagram can also be used to examine signal integrity (see Figure 10.17) [11]. The resultant Gaussian pulses from the propagation program are compared to the eye diagrams from the ASK model, which are both in turn compared to that of the numerical solution. This numerical solution has to be added to give gain to both the system and propagation models.

10.6 Raman Amplification and Gaussian Pulse Propagation

10.6.1 Fiber Profiles

Before any system design can take place, the right fiber parameters have to be implemented in the program. Table 10.6 depicts the typical optical fibers found in the industry and the required pump powers to make the signal reach back to a net gain of zero for a length of 100 km of fiber.

Table 10.6 offers no surprises as the required pump power decreases when the Raman gain coefficient is increased. Thus, the ideal fiber for the modeling application is the Corning NZDSF. Testing for these parameters took place with my colleague's program, which used numerically solved coupled equations that govern Raman amplification. This program was later incorporated into the Gaussian propagating program and then the ASK model.

TABLE 10.6

Fiber Properties

Type of Fiber	Raman Gain Efficiency (g_{eff})	Effective Area (μm²)	Required Pump Power for Net Gain = 0 (mW)
Allwave	0.35	84.95	700
Corning NZDSF	0.72	80	350
LEAF (NZDSF)	0.45	72	550
SMF-28 (NDSF)	0.38	84.95	650
Truewave RS (NDSF)	0.58	60	425
Truewave reach fiber	0.6	55	425

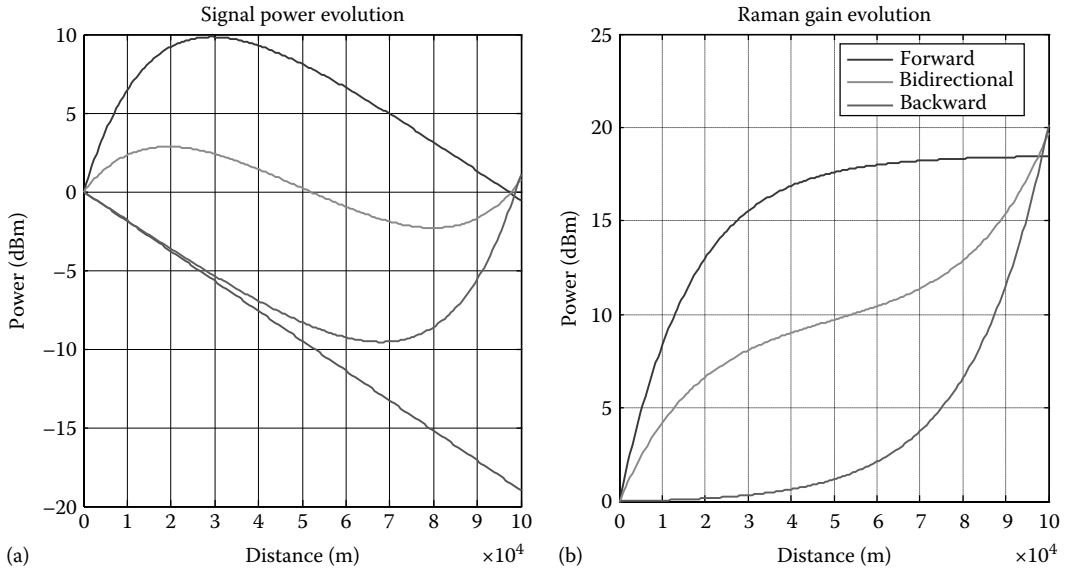

FIGURE 10.12
(a) The power evolution of the signal along the total length of the fiber. (b) The gain evolution over the total length of the fiber due to Raman amplification.

For Corning fiber, the dispersion factor can be estimated using the characteristics $D_\lambda = \frac{S_0}{4}\left(\lambda - \frac{\lambda_0^4}{\lambda^3}\right)$ (see Chapter 1), where S_0 = 0.093 ps/(nm²·km), λ_0 = 1302–1322 nm, and λ = 1550 nm (operating wavelength). Thus, the dispersion calculated is approximately equal to 17 ps/(nm·km). The dispersion effects on other wavelength channels can be estimated.

The gain profile obtained from MATLAB is transferred into the propagation program in the Simulink model to help add gain to the NLSE, which in turn underwent the SSFM. The following are some of the results achieved by the numerical solution of the coupled equations. Note: For all testing, α_S = 0.19 dB/km, α_P = 0.24 dB/km, effective area (A_{eff}) = 80 μm², and Raman gain coefficient = 0.72 W/km. The plot above depicts the power over the length of the fiber. Forward (blue), backward (magenta), bidirectional (cyan) pumping techniques are shown, along with passive fiber (red). The typical net gain at the end of the fiber is approximately zero.

Figure 10.12a shows the evolution of the signal power along the SSMF under Raman amplification, whose gain is depicted in Figure 10.12b. As the attenuation due to the signal is constant over the fiber, it can be considered a constant gradient. To incorporate the gain into the NLSE, it too had to be converted into gradients, so it could be simply added to the attenuation map. This can be seen in any of the Raman ssprop programs in the appendices.

10.6.2 Gaussian Pulse Propagation

Once the NLSE incorporated the Raman gain and was solved using the SSFM propagation program, it needed to be tested in a system setting, before being implemented in the ASK model. The best way to test the SSFM is with a single Gaussian pulse. Before testing

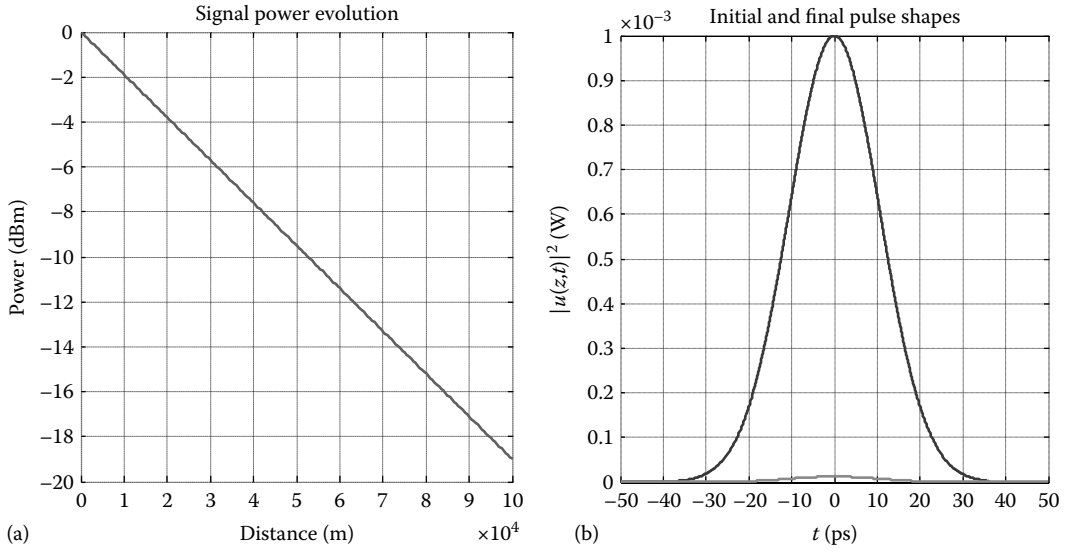

FIGURE 10.13
(a) Attenuation map of a passive fiber over the total length without amplification, α = 0.19 dB/km. (b) Gaussian pulse before and after transmission.

the single pulse on the Raman induced fiber, it was tested on passive fiber, where the end result is known. The plots are shown in Figure 10.13.

In all the Gaussian testing cases presented throughout the results section, the input pulse is depicted in blue and the output in green. In this first case, the input pulse was 1 mW and the output 0.01258 mW. The power lost over 100 km of SMF fiber should be 19 dB. Actual power lost in Gaussian system transmission is $10\log_{10}(0.01258/1) = -19.0032$ dB. As the result was within an acceptable range, the Gaussian program was ready for further testing. The next type of testing with the Gaussian pulse inputs was the three configurations of Raman amplification. The lengths were left the same, and the pump power maximum used was 350 mW in either forward or backward case or 175 mW at both ends when bidirectional.

10.6.2.1 Bidirectional Pumping Case

Figure 10.14 shows the signal power evolution over the length of the fiber. As can be seen, the fiber experiences backward and forward power gains, due to the power from the pumps being implemented in the forward and backward directions, hence the term bidirectional. At the end of the fiber, the expected output is 0.7075 dB. To check to see whether the output obtained from the split-step method is correct, one must look at the output Gaussian pulse. The peak at the output is 1.104 mW, which in turn correlates to $10\log_{10}(1.104/1) = 0.4297$ dB. The expected output is 0.7075 dB, showing that there is a little bit of a discrepancy between the two functions.

10.6.2.2 Forward Pumping Case

The output of the signal obtained from the end of the fiber is −0.5503 dB after undergoing forward gain. The output as seen by the graph in Figure 10.15 is 0.8803 mW. This in turn correlates to a gain of $10\log_{10}(0.8803/1) = -0.5537$ dB. This means that the forward case is almost identical to the numerical model result of −0.5503 dB.

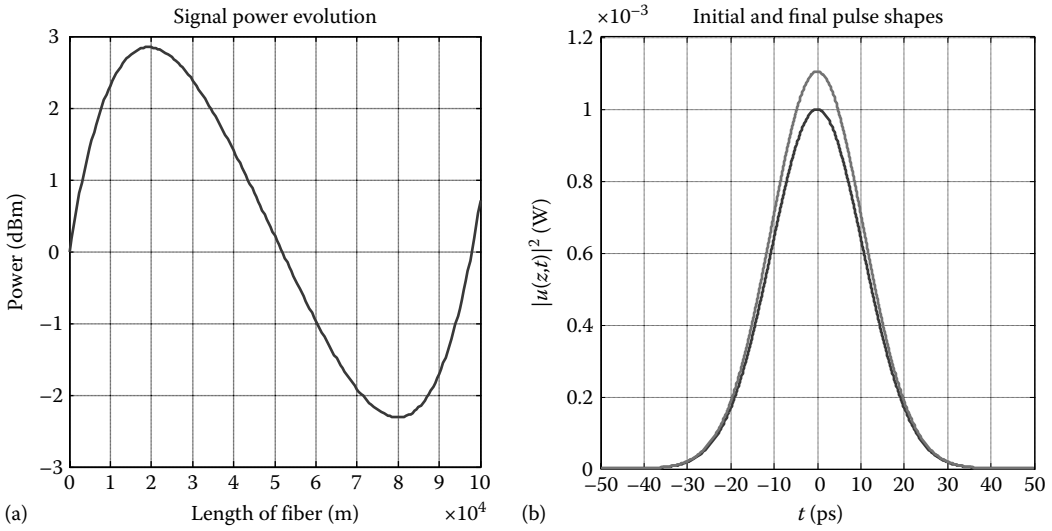

FIGURE 10.14
(a) Signal power evolution: bidirectional pumping. (b) Gaussian: bidirectional pumping.

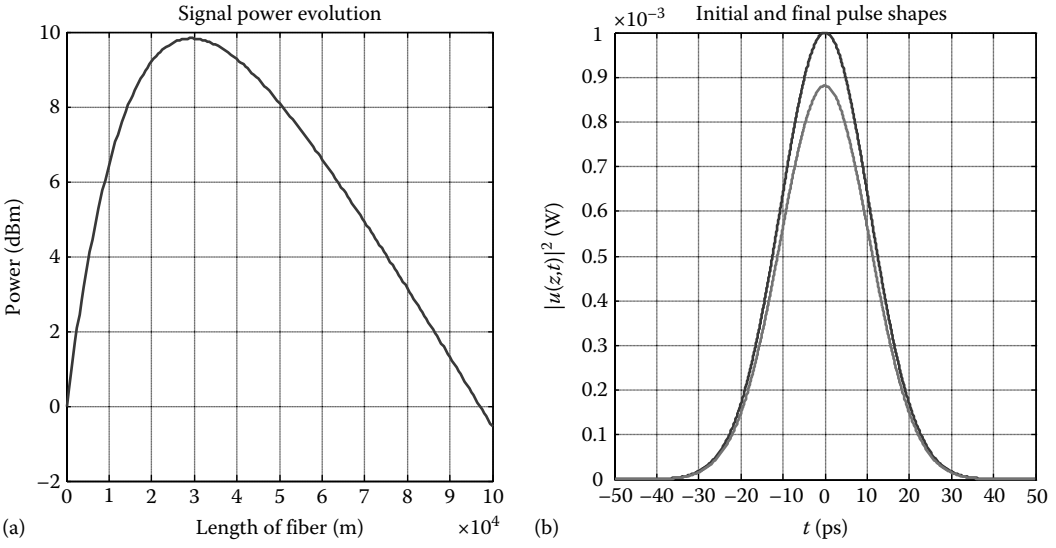

FIGURE 10.15
(a) Signal power evolution: forward pumping. (b) Gaussian: forward pumping.

10.6.2.3 Backward Pumping Case

The output of the signal obtained from the end of the fiber is 1.128 dB after undergoing backward gain, whereas a final pulse of 1.141 mW on the Gaussian correlates to $10\log_{10}$ (0.8803/1) = 0.5729 dB. As can be observed in Figure 10.16, there are inaccuracies in the three pumping techniques presented. This is due to a number of factors including the numerical approximation of the gain curves, the gradients used from the gain curves,

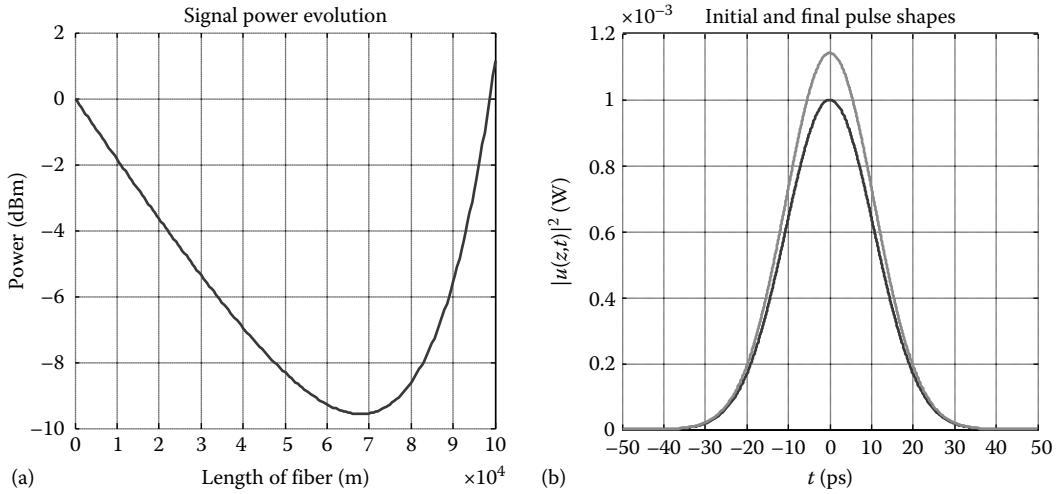

FIGURE 10.16
(a) Signal power evolution: backward pumping. (b) Gaussian: forward pumping.

and the implementation of the fast Fourier transform (FFT) used to solve the NLSE. All three estimation factors contribute to significant dissimilarities between propagating techniques.

10.6.2.4 Back-to-Back Performance

The initial characteristics of the ASK model need to be tested before simulation can take place. The first back-to-back eye diagram is an illustration of the input from the system (Figure 10.17).

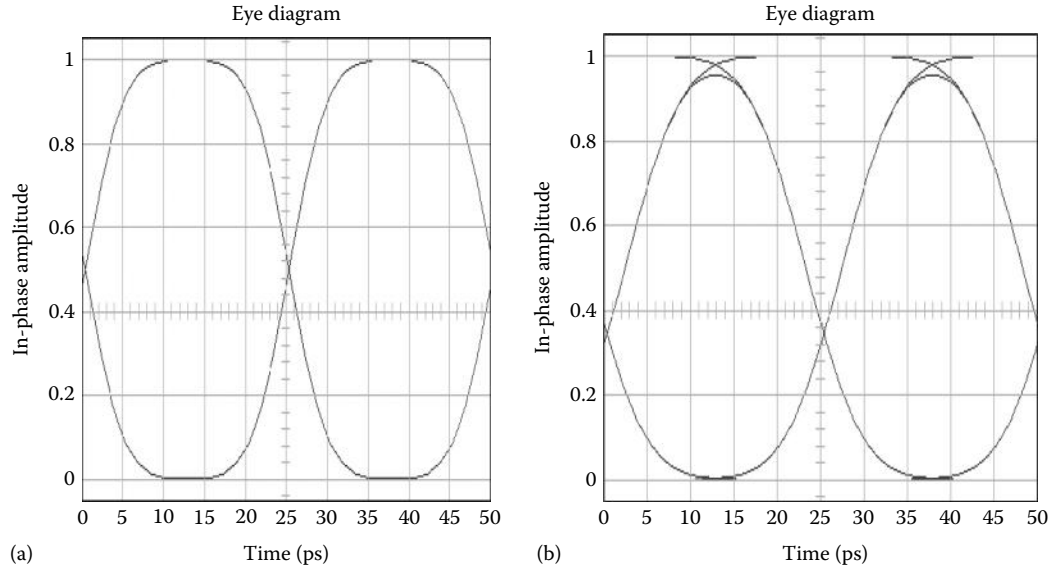

FIGURE 10.17
(a) Input signal from the ASK transmitter. (b) Output signal at the ASK receiver.

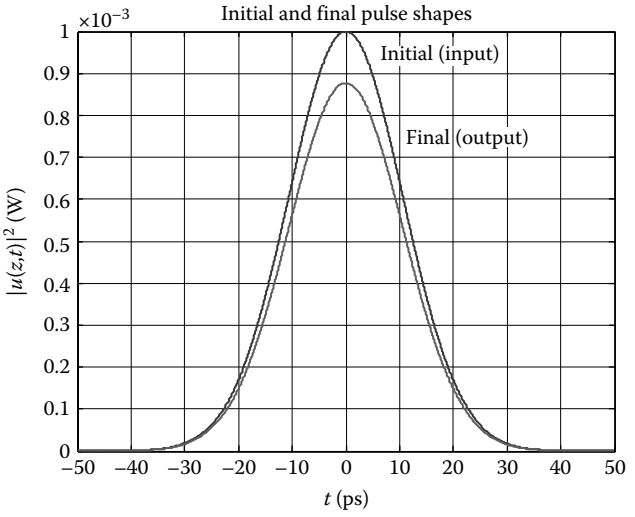

FIGURE 10.18
Gaussian: 3 km passive fiber.

The output eye diagram is as expected even though the output is dilated, the eye is clearly distinguishable, and thus what is transmitted is being received. Note that the pulse width is as initialized, 25 ps.

10.6.2.5 Propagation under No Amplification

The plots in Figure 10.18 represent the ASK model working over fiber, but no amplification is taking place. The first plot represents the Gaussian output over 3 km of fiber with $P_0 = 1$ mW and a total length of fiber = 3 km.

As observed from Figure 10.17, both the eye diagram at the output stage and the Gaussian pulse correlate well. At the output stages, both diagrams show amplitudes of approximately 0.88 mW correlating to a loss of 0.5552 dB. The theoretical foundation depicts the loss at 0.57 dB, leaving only a small room for error.

10.6.2.6 Propagation under Fiber Raman Amplification

Forward pump power = 0.4 W and backward pump power = 0 W (Figure 10.19).

As can be seen from the signal power graph in Figure 10.19, the expected output is 2.883 dB. On the Gaussian plot, the output obtained is $10\log_{10}(1.928) = 2.8511$ dB, which also matches that of the output eye diagram.

The output shows that the amplitude of the eye diagram is correlating with that of the Gaussian pulse. This is no surprise as the signal runs through the same process as the Gaussian pulse. As indicated earlier, the noise experienced in the ASK model is to the result of the numerical approximation of the gain curves, the gradient functions used from the gain curves, and the implementation of the FFT used to solve the NLSE and therefore cannot be solved, but only minimized when using this estimation technique.

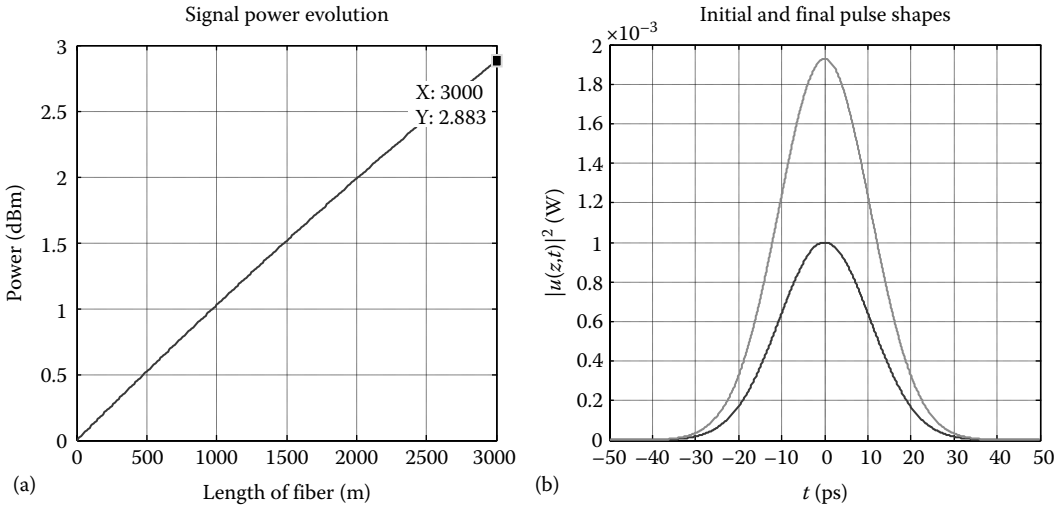

FIGURE 10.19
(a) Signal power evolution: forward pumping. (b) Gaussian: 3 km forward pumped fiber.

10.6.2.7 EDFA Amplification over 99 km Fiber (1 km Mismatch)

Figure 10.20a shows the results that were obtained after running the ASK model that was originally given to the group. As it was, it contained 50 km SMF fiber, an EDFA, 49 km DCF, and then another EDFA. The eye diagram for the input can be seen in the figure. The reason that there is a mismatch between the fibers is because of the system requiring dispersion to reduce nonlinear effects within the fiber. The pulse width is 25 ps, which is the expected result after the initialization file is run. This corresponds to a 40 Gb/s transmission rate. The plot shown in Figure 10.20b depicts what is received after transmission is complete.

The input power into this system is 1 mW; thus, there is quite a large gain as the output is approximately 0.13 W, which equates to an overall system gain of $10\log(0.13/0.001) = 21.1394$ dB. This is quite unrealistic and exceeds the power needed at the receiving end; thus, the overall system gain should be dropped back down to approximately zero. There are two ways of achieving this: increasing the length of the fiber and decreasing the amount of gain that the amplifiers provide. As there needs to be a comparison between the ASK model with EDFAs and DRA, the length was kept consistent, and the EDFA gains were changed from 20 to 9.5 dB and noise kept at the same ratio, thus decreasing it to 2.375 dB. The eye diagram is also obtained, showing a signal peak of approximately 1 mW. This is more realistic as the input signal is the same as the received signal and falls within a reasonable operating range. It must also be noted that the signal becomes a lot less noisy because the EDFA is not providing too much gain, which in turn provides greater noise in the system.

10.6.2.8 Distributed Raman Amplification over 99 km Fiber (1 km Mismatch)

Figure 10.20c depicts the output of the ASK model when using DRA (input is the same as that of the previous model). The output peak power of this particular model correlates to that of the input. The accuracy of the result could be made a lot clearer than what is presented. But, as mentioned before, the use of the FFT degrades the accuracy of the algorithm taking place, the SSFM. It must be noted that the Raman amplification model implemented in this section did not account for any noises that could have been added to the transmission signal.

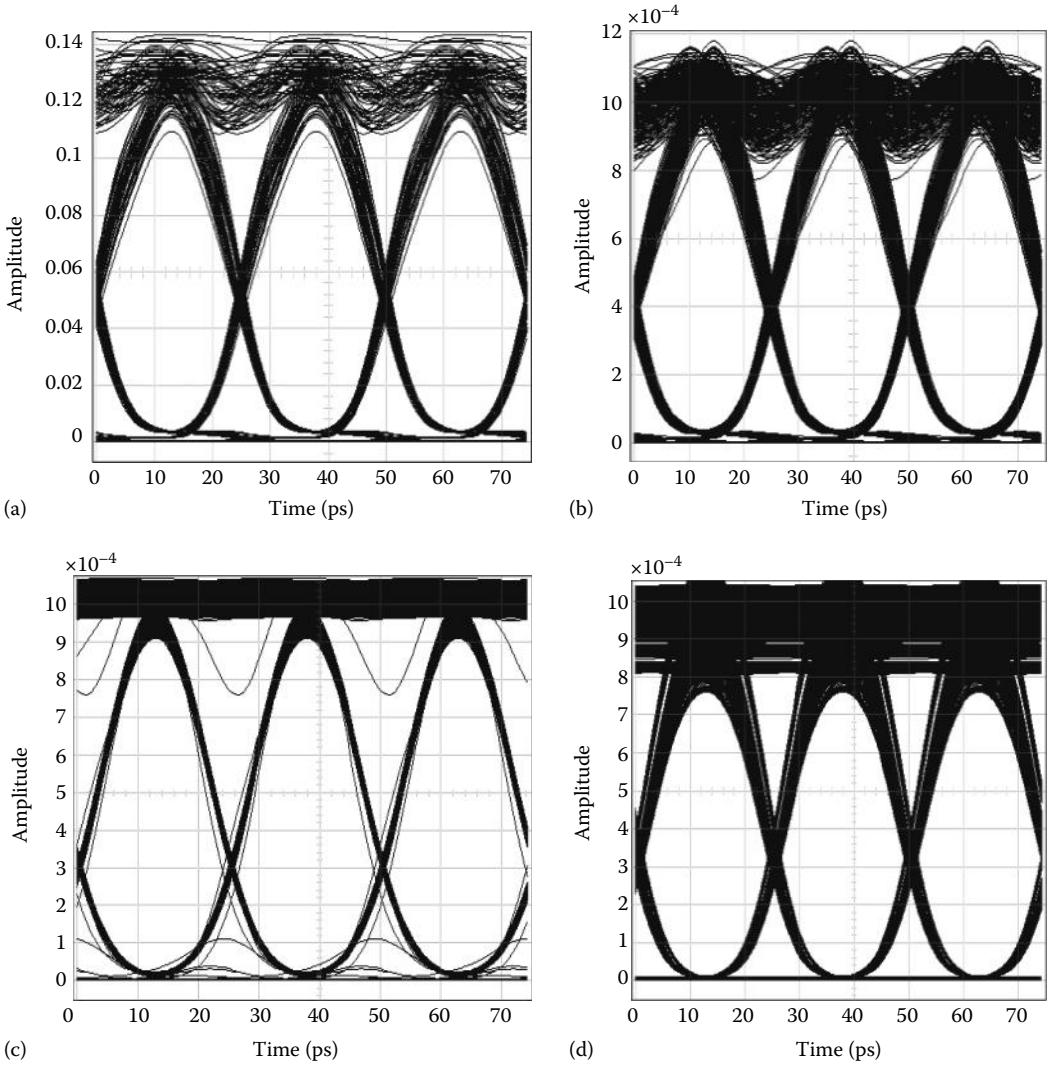

FIGURE 10.20
(a) Output signal of ASK model (20 dB gain EDFA only). (b) Output signal of ASK model (9.5 dB gain EDFA only). (c) Output signal of ASK model (DRA model). (d) Output signal of ASK model (hybrid model).

When taking bit error rates (BERs) into account, the noise of Raman amplification must be added. To check the differences in BER between Raman models with/without noise, both of them have been included with the EDFA model. This process gives an estimated description as to what the effects of noise are on the transmitted signal. The BERs for the three systems have been calculated using the equations as given by Agrawal [3]. To make the process of calculation easier, these equations were made into a MATLAB program, which can be seen in the appendices. Table 10.7 shows the BERs for the two systems and the effect that mismatching has upon the system.

Table 10.7 illustrates the differences between the three models' error rates after undergoing changes in mismatching. All three amplification techniques have low BERs when the mismatch is zero, then starts to increase as the mismatch increases. This correlates in

TABLE 10.7

BER and *Q* Factor for Different Mismatching

	BER			*Q* Parameter		
Kilometer Mismatch	EDFA	Raman No Noise	Raman with Noise	EDFA	Raman No Noise	Raman with Noise
0	1.33E−77	8.03E−268	4.34E−117	23.8123	47.4096	31.9322
1	4.76E−62	7.01E−164	3.04E−94	22.9173	33.6381	26.9262
2	2.05E−54	1.21E−144	1.22E−71	19.1478	28.6273	20.9189
3	1.04E−41	5.77E−83	2.79E−49	14.174	23.3518	16.129
4	9.41E−17	3.90E−22	3.49E−19	11.3113	11.5046	11.7835
5	9.85E−15	4.90E−13	4.93E−13	8.939	7.5701	7.4943

accordance with theoretical foundations—as the *Q* parameter increases, the BER improves, thus *Q* is inversely proportional to BER.

10.6.2.9 Hybrid Amplification

Hybrid testing of the system involved the addition of Raman amplification and EDFAs to coexist in a single-system model. The EDFA was implemented after both the SMF and DCF fibers. The length of the fiber was increased to 100 km (span = 200 km), and the pump power was decreased to 100 mW in the backward direction; therefore, the gain required by the EDFAs is 13.26 dB. This was found out by first testing the Raman amplification in the Gaussian program and then deducing the amount of gain required to boost the signal back to a net gain of zero.

The resultant *Q* parameter and BER are 10.8830 and 4.8712e−013, respectively. This is noticeably higher than that of the Raman and EDFA models when they were in the same position. This could be due to a number of reasons like the amount of noise being added to the system being considerably higher because of both amplification techniques working in tandem. Thus, from the results obtained, it would be safe to say that only the Raman amplification is a good model for use in transmission.

It must be noted that this model uses span length of 100 km, which in turn should not be compared to that of the previous section. When the length of the fibers is decreased to 50 km each (span = 100 km), the total BER and *Q* parameter were 4.8712e−013 and 9.8450, respectively. This is considerably higher but gives a much more accurate depiction as to what values should be obtained.

10.6.3 Long-Haul Optically Amplified Transmission

The final set of demonstrations for the effectiveness of our design of the ROA is integration of TOA sections and EDFAs into a long-haul undersea jump transmission backbone where the Raman amplification can take the transmission signal without regeneration. It is found to be approximately 2000 km with the modulation scheme of ASK.

The Raman amplification subsystems as described earlier are used in the modeling of optical transmission along a coastal line jumping from one inland node to the next. The route is divided into a number of spans that can be implemented by optical amplifiers using EDFA or Raman distributed amplification with incorporated pump lasers placed on land. The modulation scheme is DPSK, and the bit rate is 40 Gb/s.

Shown in Figures 10.21 and 10.22 are the geographical route and the layout of the design of a long-haul undersea jump multispan Raman and EDFA optically amplified transmission system for the coastal undersea jump of Vietnam North–South route. Each span consists of two optical transmission lengths under Raman pump placed at two ends of the span and a transmission fiber with an average length of around 120 km. Thus, the total length of each span is about 250–300 km. Optical amplifiers EDFAs are used at the two ends to boost the optical signals and compensate for the losses at the end of the transmission span, especially the loss of the undersea transmission length in which no Raman gain is achieved. The Simulink model of each span is shown in Figure 10.23. Figure 10.24 shows

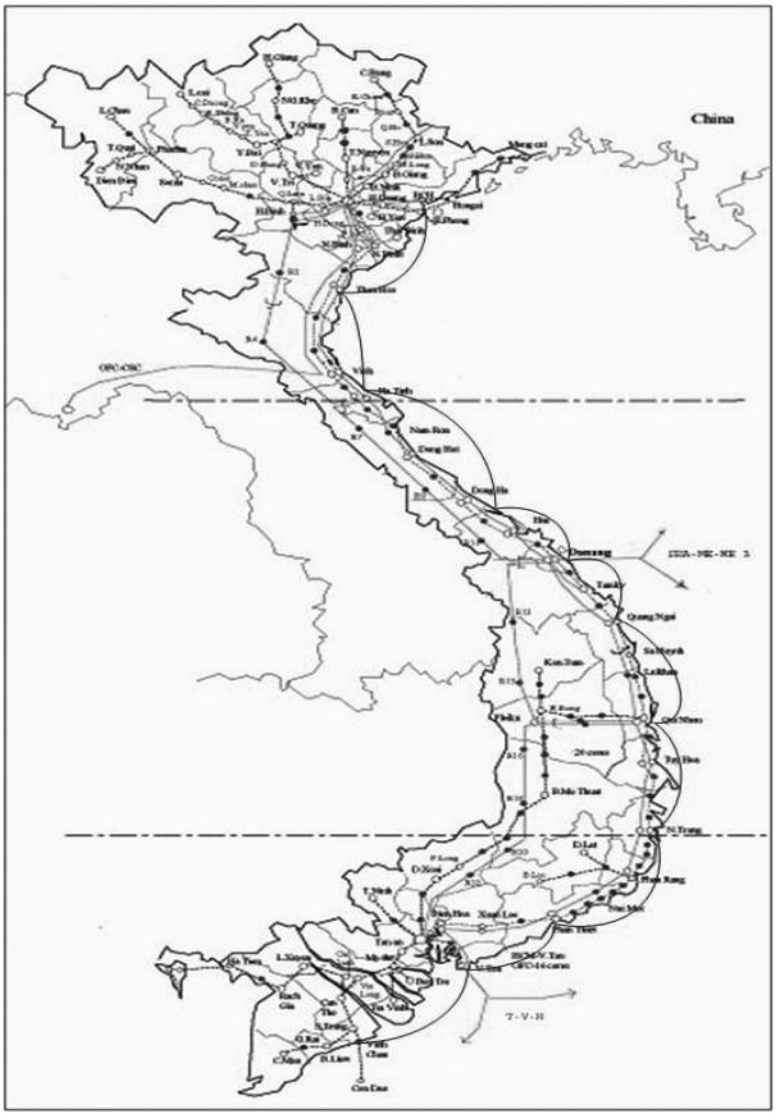

FIGURE 10.21
Geographical route of coastal line of Vietnam for the design of Raman optically amplified transmission backbone network. Jumping lines indicated by blue for undersea fiber routes.

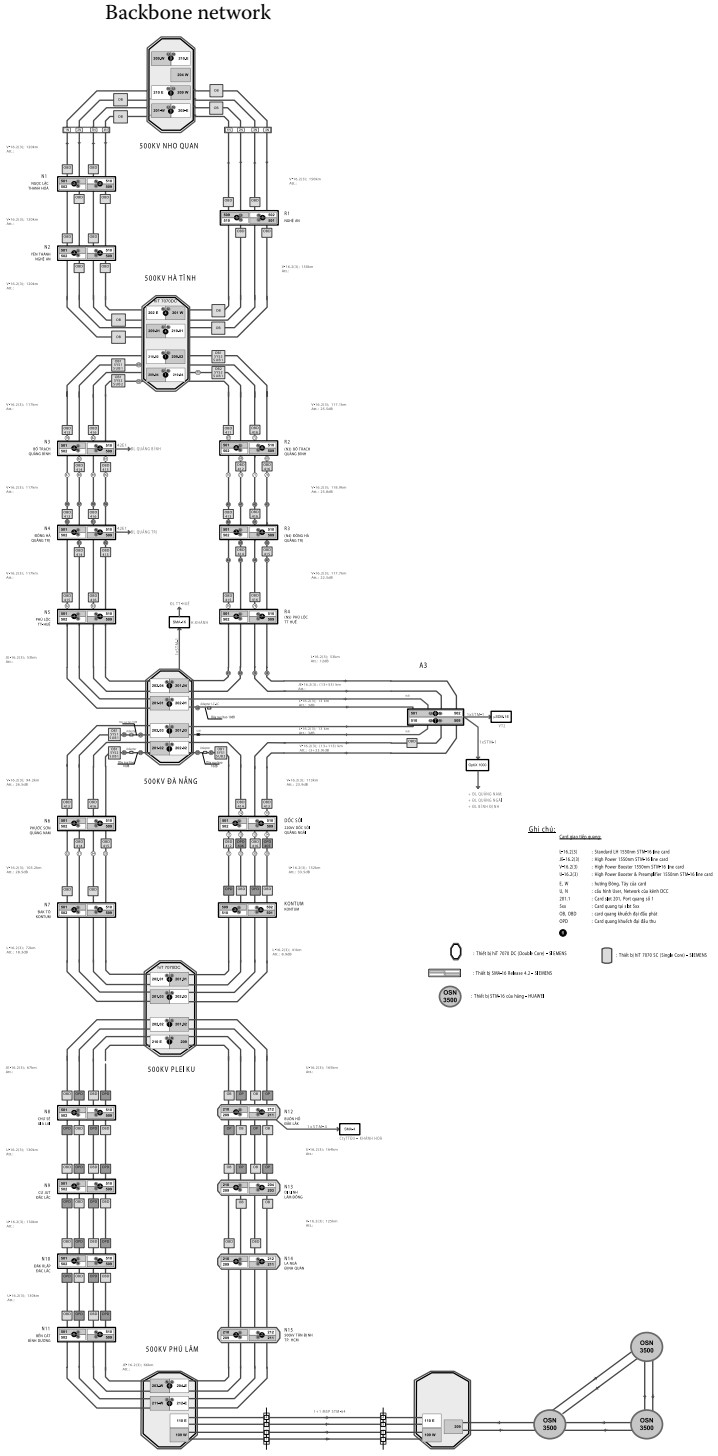

FIGURE 10.22
Lay out of the Raman optically amplified EDFA multispan transmission system of undersea jump coastal telecommunication backbone of Figure 10.21.

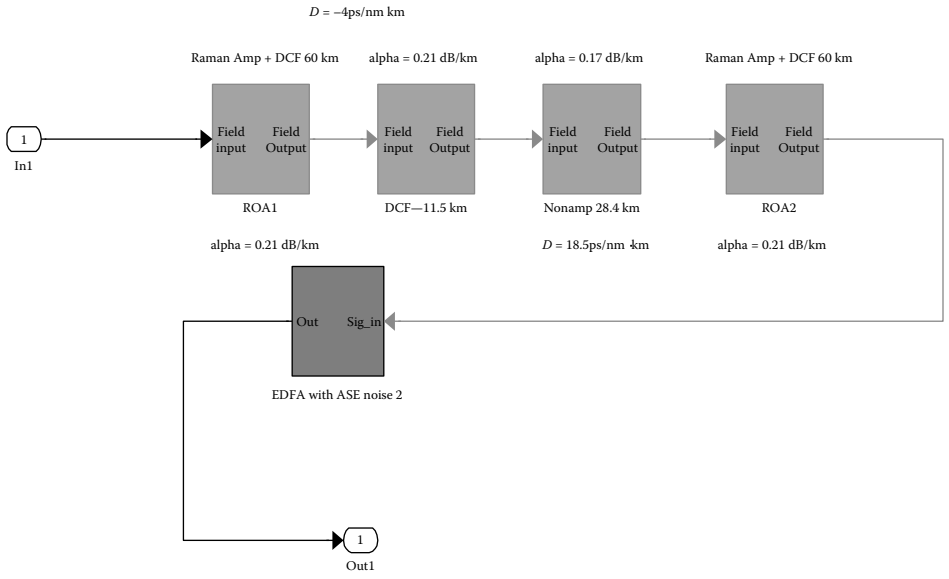

FIGURE 10.23
Simulink® model of an optically amplified span. EDFA is inserted at the end of each span. Other blocks at the two ends are Raman amplified transmission fibers, and the middle blocks are transmission spans without any amplification provision.

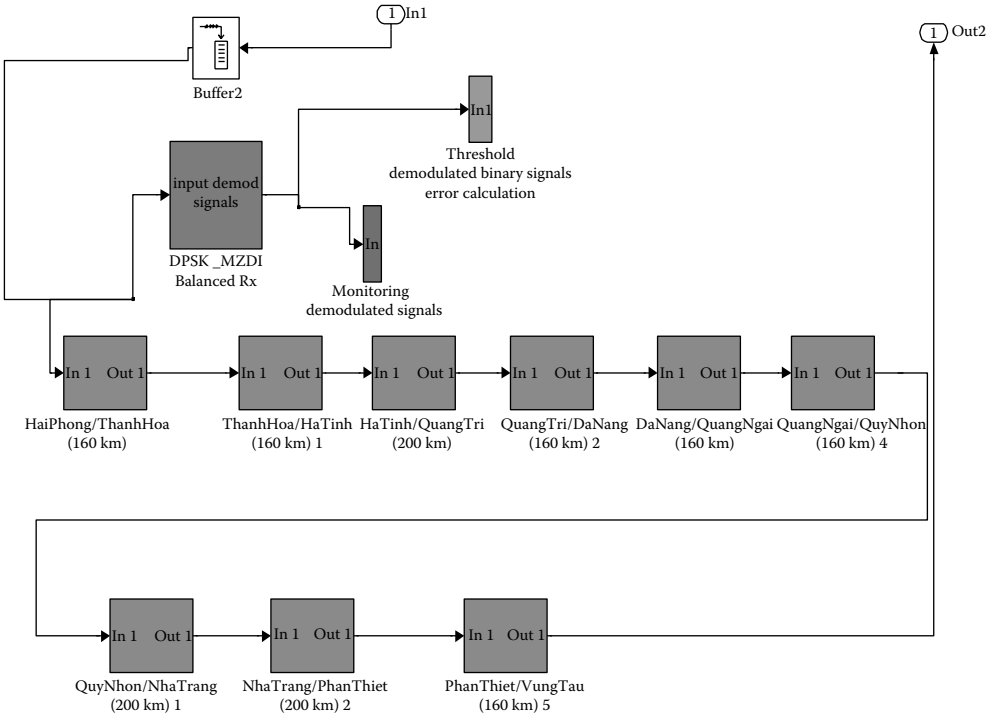

FIGURE 10.24
Simulink® model of the overall optically amplified multispan undersea transmission system.

the arrangement of the multispan transmission systems in which each span incorporates Raman pumps and EDFAs (Figure 10.25). Our design is based on a strategy that the signal power at the input of each span is the same so that there needs to be only one span design with the adjustment of the gains of the EDFA and the ROA as well as the dispersion compensation. ROA is implemented in the dispersion compensating length. It is obvious that the DCF lengths are used at both ends of the span and the transmission fibers are inserted in the middle of the span. A Simulink model of the fiber under ROA and transmission is shown in Figure 10.26. The MATLAB program is included in the Appendix. Figure 10.26a and b shows the phasors of the lightwave signal envelop at the input of the balanced receiver, that is at the end of the optically amplified transmission line and the eye diagram of the DPSK under direct detection and a Mach–Zehnder delay interferometer (MZDI). The phase scatter plot (Figure 10.26b) shows that the scattering of the phase noise of the amplifiers, especially the ROA does not affect significantly the errors of the phase detection of the data sequence. BER is determined from the diagram after the transmission of 2^{31}–1 bit sequence. The probability distribution function is assumed to be Gaussian. Noises contributed by the EDFAs and the electronic receivers are included in our Simulink model. A 20 pA^2/Hz is used as the total equivalent noise spectral density as seen from the input port of the wideband microwave amplifier following the high-speed photodetector pair connected back to back for balanced detection.

The transmission performance illustrated with the BER is plotted against the input launched power and shown in Figure 10.27. Similarly the dispersion tolerance of the

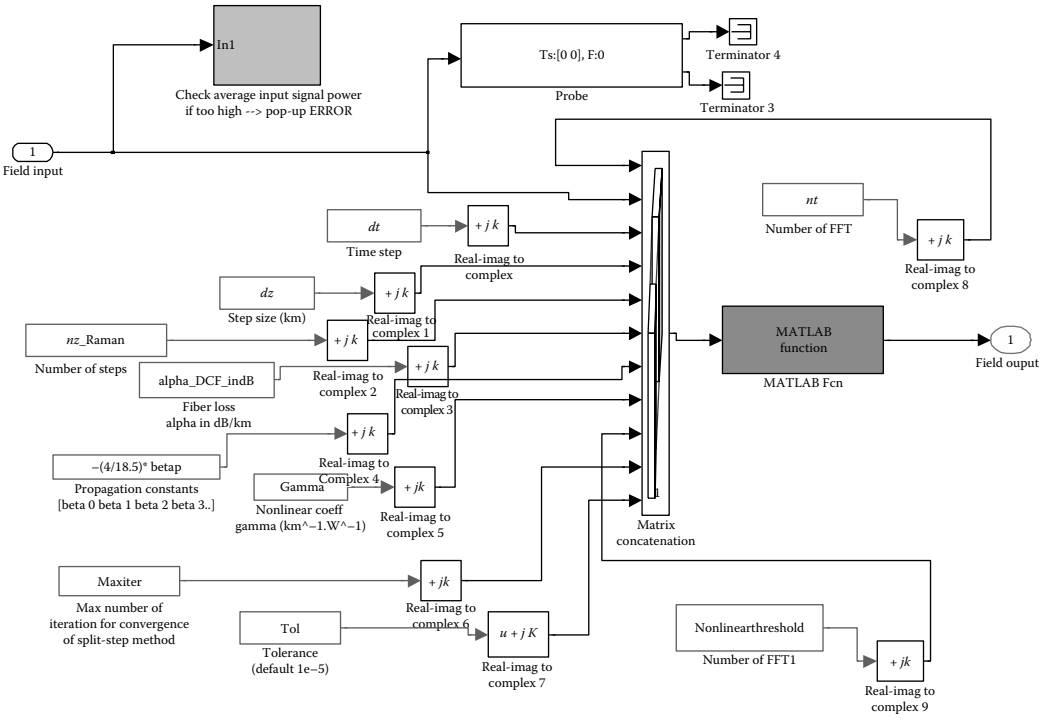

FIGURE 10.25
SSFM model for fiber propagation with Raman amplification.

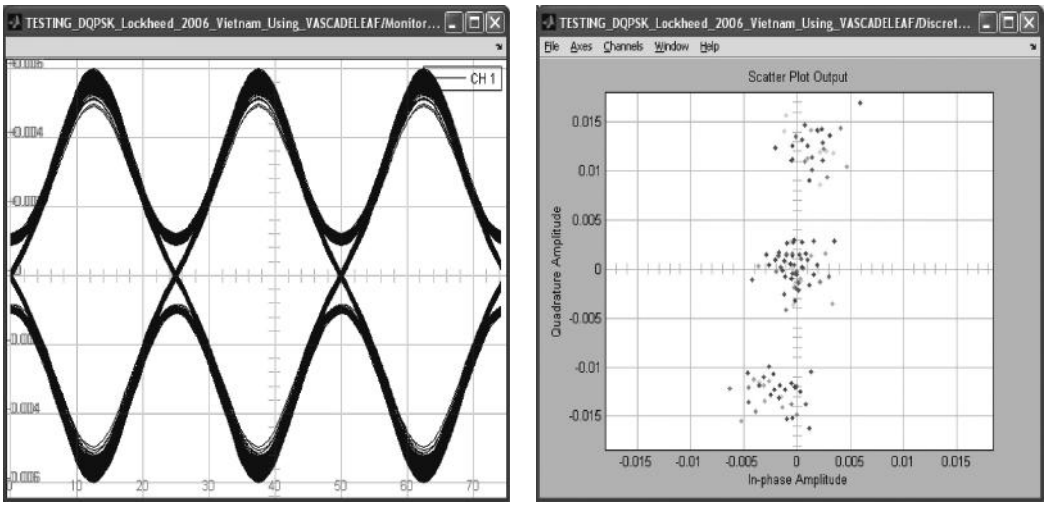

(a) (b)

FIGURE 10.26
(a) DPSK eye diagram obtained at the output of a balance receiver after 1200 km four ROA and EDFA spans. (b) Scatter plot at input of the receiver.

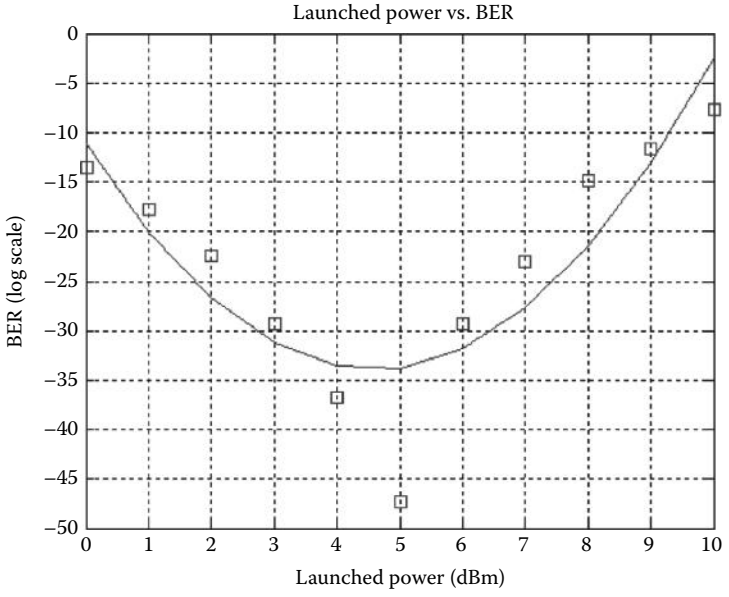

FIGURE 10.27
BER versus launched power to the end of each span. Modulation format ASK, 40 Gb/s.

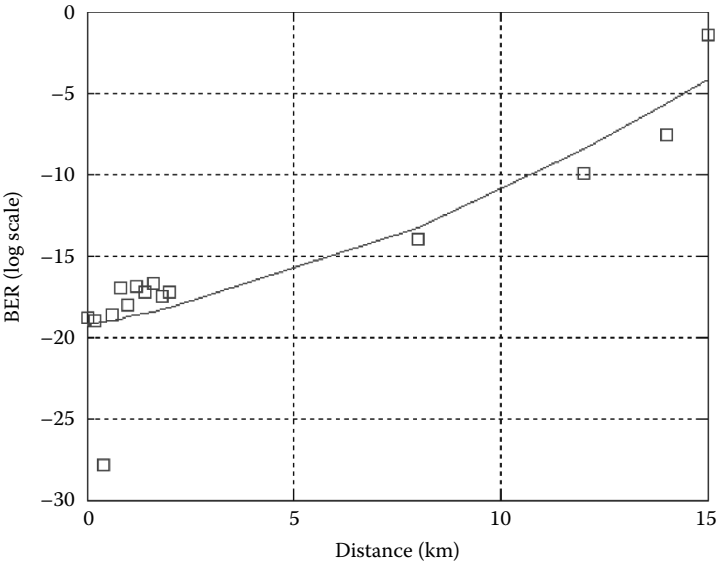

FIGURE 10.28
Dispersion tolerance over the multispan EDFA and ROA optically amplified transmission link. Distance is equivalent to SSMF length. Dispersion is this length multiplied with 17 ps/nm/km. Modulation format ASK 40 Gb/s.

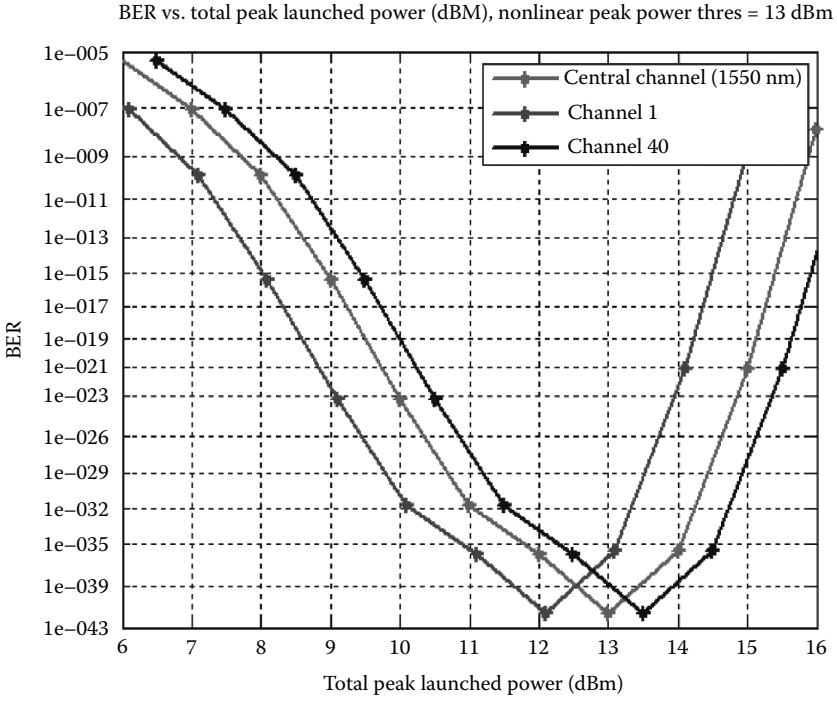

FIGURE 10.29
BER as a function of launched power of two border channels, channel 1 and channel 40, and central channel. Modulation format DPSK 40 Gb/s, total transmission distance 1994 km over 10 spans of 240 km on average hut-skipped distance.

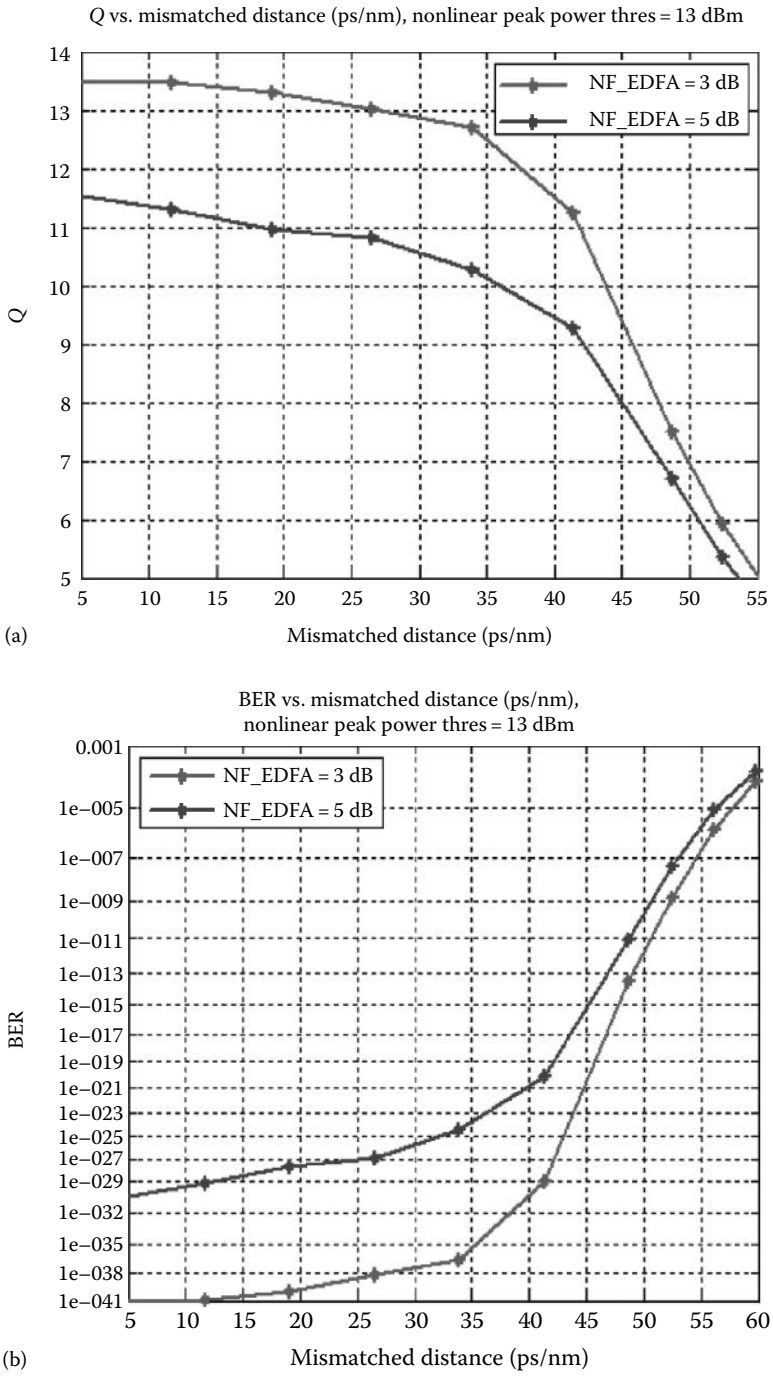

FIGURE 10.30
Dispersion tolerance of the hybrid EDFA–ROA optically amplified transmission system: (a) quality factor variation and (b) BER variation. Modulation format DPSK 40 Gb/s over total transmission distance of 1994 km over 10 spans of 240 km on average hut-skipped distance.

fully compensated ROA, EDFA amplification transmission multispan link is shown in Figure 10.28 for ASK 40 Gb/s modulation format and bit rate. A 170 ps/nm dispersion tolerance is obtained for this multispan ASK 40 Gb/s transmission can be observed. This is more than 30% improvement as compared to EDFA only optically amplified transmission over 12 × 100 km transmission system with dispersion compensating fibers inserted into each span and two EDFAs employed to compensate for the SSMF and DCF losses. Thus, Raman optical amplifiers offer improvement over all EDFA multispan transmission.

DPSK modulation format performance is much superior as compared to that by ASK. It is impossible to obtain an error-free (BER < 1e−9) with ASK modulation scheme at 40 Gb/s as the noise level is quite high.

Over a total transmission distance of 1994 km with 10 spans and average hut-skipped distance of 240 km with EDFAs located in land and Raman pumped at two sides of the landing ends. We can optimize the transmission and dispersion compensating fibers using Corning Vascade fibers S1000. The variation of the BER with the launched power of 40 channels at 40 Gb/s and 50 GHz channel spacing can be achieved error free as shown in Figure 10.29. The dispersion tolerance of this modulation format is also shown in Figure 10.30.

10.7 Concluding Remarks

By numerically solving the set of ODEs for pump and signal power and noises in both distributed and discrete ROA, the design concerns of gain, NF, and dispersion were examined. Distributed amplification can be shown to be useful for 100 km and longer spans using different commercial fibers. The required pump power for each fiber type for net gain to compensate for fiber losses is examined under pump lasers operating at 500 mW. It shows that the transmission span length for Corning NSDSF and Truewave could be well extended beyond 100 km in a purely distributed ROA.

Typically, SMF transmission spans of 100–120 km with effective gain length of about 20 km can be used because the NF is close to that of an ideal distributed NF, that is, if the loss is corrected at every point along the fiber. In 100 km long spans of fiber, the NF for distributed ROA in comparison to lumped amplifiers is improved by between 6 and 16 dB depending on the configuration. It was determined that fibers with higher values of g_R provide lower system NFs. Forward pumping achieves an NF improvement of nearly 10 dB in comparison to backward pumping. It can be further improved by using a hybrid configuration, such as an EDFA to provide a fraction of the gain to the signal. It increases the overall net gain along the fiber and lowers the required pump power for ROA.

Dispersion is also determined, and it is shown that for the different types of fibers there is no real benefit; however, in using different pumping configurations, the total nonlinear phase shift along the fiber could be reduced. There is an approximate benefit of about 12.5 dB in using a backward-pumping configuration. For discrete Raman amplifiers, typically less than 25 km high gains of up to 40 dB could be achieved using specially designed Raman fiber or DCF with high Raman gain efficiencies and small affective areas. The comparison of NF in discrete Raman amplifiers shown for different pumping schemes larger span transmissions resulted in a greater discrepancy of up to 7 dB. It has been determined that larger gain efficiencies cause less net gain and more gain saturation to occur.

The parameters of gain and NF can be integrated into a Gaussian pulse and propagated down the fiber using the SSFM to convert the average powers of the numerical solutions into pulses. This has been achieved by changing the half-step SSFM parameter to include ROA by adding the on–off Raman gain gradient at each step size along the fiber as referred to the MATLAB algorithm given in the Appendix. The associated NFs could be added to the system as discrete values. They could then be analyzed using MATLAB Simulink models.

Further, the most reliable form of pumping in a system model setting is the bidirectional configuration. This pumping scheme finds the trade-off between adding additional noise and superimposing the nonlinear effects. The overall distance in which the signal can propagate without regeneration has been found to be around 2000 km under multiple dispersion compensating spans. The accuracy of this figure depends on many factors such as the fiber property, for example, SSFM, the sampling of the gradients, and the dependency on other numerical runtimes under simulation.

We have shown that through estimation and simulation there can be an accurate depiction of Raman amplification in SMF, as it utilizes the fiber in which the signal propagates, to achieve amplification. All the BERs obtained concur with theoretical models and were well below that of the minimum required to acquire accurate eye diagrams.

Finally, a multispan ROA and EDFA optically amplified transmission system is demonstrated to prove the effectiveness of ROA over multispan transmission link. This is essential for the system that requires undersea hut-skipped spans such as in the Vietnam coastal backbone to avoid problems on land acquisition for cable installation.

Raman distributed amplifiers can provide about 11–14 dB gain by each pump direction. So, when bidirectional pumps are used, then the total gain can reach 25 dB. With these distributed gains, the ROA can be employed in association with EDFAs as described in Chapter 9 to extend the span length to 250–300 km. This is of great interest in engineering transmission systems crossing from mainland to islands such as from Victoria State of Australia to Tasmania State crossing the Tasman Sea.

Problems

10.1 Give an account of the optical amplification of lightwaves in an Er-doped optical fiber amplifier including the structure of the fiber amplification medium, the energy diagram of the erbium ion, and the amplification and noise generation process.

10.2 Repeat Question 1 for a Raman distributed optical fiber amplifier.

10.3 (a) Search and download technical specifications from Avenex.com or jdsu.com of EDFAs that can be used as in-line optical amplifiers, booster amplifiers, and optical preamplifiers for optical receivers.

(b) Contrast their optical properties, for example, optical gain, noise figure, saturation region, minimum input power range, total maximum output power, spectral gain region, and gain ripple.

10.4 Repeat Question 3, for Raman optical amplifiers, especially the pump laser source.

10.5 From the gain and the optical input and output power sketch the curve represent the input and output powers for the optical amplifiers of Problems 3 and 4.

10.6 A span in a long-haul optical communication system consists of a transmission fiber of 100 km SSMF and a DCF with dispersion factor at 1550 nm of −85 ps/nm/km.

(a) What is the length of the DCF for full compensation at 1550 nm?

(b) Assume that the DCF has a core diameter of 2.5 μm. Referring to the technical specification of SSMF (SMF-28) as given in Chapter 2 state the core diameter of the SSMF and hence the spot size. Calculate the nonlinear SPM threshold of SSMF and then DCF.

(c) Show that two optical amplifiers would be needed to equalize the losses in SSMF and DCF. Obtain the gain and minimum and maximum optical powers of the two amplifiers.

10.A Appendices

Two *.m files are given in this appendix—one for the propagation of signal sequence through a single-mode optical fiber with Raman pump. That means that the propagation equations given in (10.17) through (10.19) are employed. This module can be used to replace the module for the NLSE without Raman pumping in the Simulink model. The other *.m file is for initialization when the Raman pumping is employed.

10.A.1 Raman Amplification and Split-Step Fourier Method: MATLAB® Program

```
function output = ssprop_matlabfunction_raman(input)


nt = input(1);
u0 = input(2:nt+1);
dt = input(nt+2);
dz = input(nt+3);
nz = input(nt+4);
alpha_indB = input(nt+5);
betap = input(nt+6:nt+9);
gamma = input(nt+10);
P_non_thres = input(nt+11);
maxiter = input(nt+12);
tol = input(nt+13);
%Ld = input(nt+14);
%Aeff = input(nt+15);
%Leff = input(nt+16);

tic;
%tmp = cputime;

%------------------------------------------------------------
%
```

```
%
% The following effects are included in the model: group velocity
% dispersion (GVD), higher order dispersion, loss, and self-phase
% modulation (gamma).
%
% USAGE
%
% u1 = ssprop(u0,dt,dz,nz,alpha,betap,gamma);
% u1 = ssprop(u0,dt,dz,nz,alpha,betap,gamma,maxiter);
% u1 = ssprop(u0,dt,dz,nz,alpha,betap,gamma,maxiter,tol);
%
% INPUT
%
% u0 - starting field amplitude (vector)
% dt - time step - [in ps]
% dz - propagation stepsize - [in km]
% nz - number of steps to take, ie, ztotal = dz*nz
% alpha - power loss coefficient [in dB/km], need to convert to linear to
  have P=P0*exp(-alpha*z)
% betap - dispersion polynomial coefs, [beta_0 ... beta_m] [in ps^(m-1)/km]
% gamma - nonlinearity coefficient [in (km^-1.W^-1)]
% maxiter - max number of iterations (default = 4)
% tol - convergence tolerance (default = 1e-5)
% OUTPUT
% u1 - field at the output
%---------------
% Convert alpha_indB to alpha in linear domain
%---------------
alpha = 1e-3*log(10)*alpha_indB/10;      % alpha (1/km) - see Agrawal p57
%---------------
%P_non_thres = 0.0000005;
ntt = length(u0);
w = 2*π*[(0:ntt/2-1),(-ntt/2:-1)]'/(dt*nt);
%t = ((1:nt)'-(nt+1)/2)*dt;
gain = numerical_gain_hybrid(dz,nz);
for array_counter = 2:nz+1
    grad_gain(1) = gain(1)/dz;
    grad_gain(array_counter) = (gain(array_counter)-gain(array_
counter-1))/dz;
end
gain_lin = log(10)*grad_gain/(10*2);
clear halfstep
  halfstep = -alpha/2;
    for ii = 0:length(betap)-1;
         halfstep = halfstep - j*betap(ii+1)*(w.^ii)/factorial(ii);
    end
     square_mat = repmat(halfstep, 1, nz+1);
     square_mat2 = repmat(gain_lin, ntt, 1);
     size(square_mat);
     size(square_mat2);
     total = square_mat + square_mat2;

clear LinearOperator
    % Linear Operator in Split Step method
```

```
    LinearOperator = halfstep;
    halfstep = exp(total*dz/2);

u1 = u0;
ufft = fft(u0);
% Nonlinear operator will be added if the peak power is greater than the
% Nonlinear threshold
iz = 0;
while (iz < nz) && (max((gamma*abs(u1).^2 + gamma*abs(u0).^2)) > P_non_
thres)
  iz = iz+1;

  uhalf = ifft(halfstep(:,iz).*ufft);

  for ii = 1:maxiter,
    uv = uhalf .* exp((-j*(gamma)*abs(u1).^2 + (gamma)*abs(u0).^2)*dz/2);
    ufft = halfstep(:,iz).*fft(uv);
    uv = ifft(ufft);

    if (max(uv-u1)/max(u1) < tol)
     u1 = uv;
     break;
    else
     u1 = uv;
    end

  end
  % fprintf('You are using SSFM\n');
  if (ii == maxiter)
    fprintf('Failed to converge to %f in %d iterations',tol,maxiter);
  end

  u0 = u1;

end

if (iz < nz) && (max((gamma*abs(u1).^2 + gamma*abs(u0).^2)) < P_non_
thres)

% u1 = u1.*rectwin(ntt);
  ufft = fft(u1);
  ufft = ufft.*exp(LinearOperator*(nz-iz)*dz);
  u1 = ifft(ufft);

  %fprintf('Implementing Linear Transfer Function of the Fibre
  Propagation');
end

%toc;

output = u1;
```

10.A.2 Initialization *.m File

```
This file defines the parameters for Simulink model for transmission of
% DWDM channels over llong haul transmission fiber spans.

%It also gives parameters for solving the nonlinear Schrodinger equation
% for pulse propagation in an optical fiber using the split-step
% Fourier method described in:
% Agrawal, Govind.  Nonlinear Fiber Optics, 2nd ed.  Academic
% Press, 1995, Chapter 2
%
% The following effects are included in the model: group
% velocity dispersion (GVD), GVD-slope / third-order
% dispersion, loss, and self-phase modulation (n2).  The core
% routine for implementing the split-step propagation is
% called sspropc.m


clear all
close all
% CONSTANTS
c = 299792458;                          % speed of light (m/s)
qe = 1.6*10^(-19);                      % electronic charge charge (Coulomb)
% NUMERICAL PARAMETERS
numbitspersymbol = 1
P0_dBm = 12;
P0 = 1/40*1e-3*(10^(P0_dBm/10));        % peak power (W)
FWHM = 25                               % pulse width FWHM (ps)
%halfwidth = FWHM/1.6651                % for Gaussian pulse
halfwidth = FWHM                        % for square pulse

bitrate = 1/halfwidth;                  % THz
baudrate = bitrate/numbitspersymbol;
signalbandwidth = baudrate;


%%%%%%%%%%%%%%%%%%%%%%%%%%%%%%%%
% for DPSK
Vπ=5;
halfVπ = Vπ/2;
twoVπ=Vπ*2;


% nt = 2^8;                             % number of points in FFT
PRBSlength = 2^5;


% Make sure : FFT time window (=nt*dt) = PRBSlength * FWHM...
% FFTlength nt = PRBSlength/block * numbersamples/bit = PRBSlength *
(FWHM/dt)
% num_samplesperbit = FWHM/dt  should be about 8 - 16 samples/bit
num_samplesperbit = 32;                 % should be 2^n
dt = FWHM/num_samplesperbit ;           % sampling time(ps); % time step (ps)
nt = PRBSlength*num_samplesperbit;  % FFT length
```

```
% nt = 2^9;
% nt =num_samplesperbit;

dz = 0.2;     % distance stepsize (km)
nz = 500;

% %%%%%%%%%%%%%%%%
% Fiber Link
% Using Vascade Fiber
% Vascade S1000 - alpha = 0.24 dB/Km; D = -37 ps/nmKm; Aeff = 26 um^2
% Vascade L1000 - alpha = 0.19 dB/Km; D = +18.5 ps/nmKm; Aeff = 101 um^2
% %%%%%%%%%%%%%%%%
% Raman distance
% We assume Raman will be effective on a 79Km-long distance
% Ref. Calculation Fiber Length.xls and Tech. Report for more details

nz_Raman_SMF_160Km = 266;
nz_Raman_DCF_160Km = 128;

nz_Raman_SMF_180Km = 300;
nz_Raman_DCF_180Km = 95;

nz_Raman_SMF_210Km = 350;
nz_Raman_DCF_210Km = 45;

nz_Raman_SMF_237Km = 395;
nz_Raman_DCF_237Km = 0;

% For convinience, we will have 4 variation distances to be managed
% Ref. Calculation Fiber Length.xls and Tech. Report for more details

nz_DCF_160Km = 10;
nz_DCF_180Km = 110;
nz_DCF_210Km = 260;
nz_DCF_237Km = 395;

% For all purpose, NF_EDFA is the global parameter of the system
NF_EDFA = 3;

% number of z-steps
maxiter = 10;                       % max # of iterations
tol = 1e-5;                         % error tolerance

% OPTICAL PARAMETERS
nonlinearthreshold_dBm = 15;
nonlinearthreshold = 1/40*1e-3*(10^(nonlinearthreshold_dBm/10));

lambda = 1550;      % wavelength (nm)
optical_carrier = c/(lambda*1e-9);
% %%%%%%%%%%%%%%%%
% Used Vascade Fiber
% Vascade S1000 - alpha = 0.24 dB/Km; D = -37 ps/nmKm; Aeff = 26 um^2
% Vascade L1000 - alpha = 0.19 dB/Km; D = +18.5 ps/nmKm; Aeff = 101 um^2
```

```
% %%%%%%%%%%%%%%%

alpha_indB = 0.19;              % Vascade Leaf loss (dB/km)
alpha_DCF_indB = 0.24;          % Vascade EX1000 loss (dB/km)
% For testing channel dispersion. Ref. to fiber datasheet Dipersion slope
% Dispersion slope = 0.06 for SMF and -0.12 for DCF
% D = 18.5-0.06*8;              % GVD (ps/nm.km); if anomalous
dispersion(for compensation),D is negative
% DDCF = -37+0.12*8;

D = 18.5;                       % dispersion factor unit ps/nm/km
DDCF = -37;

beta3 = 0.06;                   % GVD slope (ps^3/km)

ng = 1.46;                      % group index
n2 = 2.6e-20;                   % nonlinear index (m^2/W)
Aeff = 72;                      % effective area (um^2)

% Leaf: 70um^2, EX1000: 76um^2
% CALCULATED QUANTITIES
T = nt*dt;                      % FFT window size (ps) -Agrawal: should be
                                about 10-20 times of the pulse width
alpha_loss = log(10)*alpha_indB/10;     % alpha (1/km)
beta2 = -1000*D*lambda^2/(2*π*c);       % beta2 (ps^2/km);

%-----------------------------------------------------
% beta 3 can be calculated from the Slope Dispersion (S) as follows:]
% Slope Dispersion
% S = 0.092; % ps/(nm^2.km)
% beta31 = (S - (4*π*c./lambda.^3))./(2*π*c./lambda.^2)
%-----------------------------------------------------
gamma = 2e24*π*n2/(lambda*Aeff);      % nonlinearity coef (km^-1.W^-1)
t = ((1:nt)'-(nt+1)/2)*dt;            % vector of t values (ps)
t1 = [(-nt/2+1:0)]'*dt;               % vector of t values (ps)
t2 = [(1:nt/2)]'*dt;                  % vector of t values (ps)

w = 2*π*[(0:nt/2-1),(-nt/2:-1)]'/T;   % vector of w values (rad/ps)
v = 1000*[(0:nt/2-1),(-nt/2:-1)]'/T;  % vector of v values (GHz)
vs = fftshift(v);                     % swap halves for plotting
v_tmp = 1000*[(-nt/2:nt/2-1)]'/T;

% STARTING FIELD
% P0 = 0.001                          % peak power (W)
% FWHM = 20                           % pulse width FWHM (ps)
%halfwidth = FWHM/1.6651              % for Gaussian pulse

%For square wave input, the FWHM = Half Width
%halfwidth = FWHM;

L = nz*dz

Lnl = 1/(P0*gamma)                    % nonlinear length (km)
```

```
Ld = halfwidth^2/abs(beta2)     % dispersion length (km)
N = sqrt(abs(Ld./Lnl))          % governing the which one is dominating:
dispersion or Non-linearities
ratio_LandLd = L/Ld             % if L << Ld --> NO Dispersion Effect
ratio_LandLnl = L/Lnl           % if L << Lnl --> NO Nonlinear Effect
% Monitor the broadening of the pulse with relative the Dispersion Length
% Calculate the expected pulsewidth of the output pulse
% Eq 3.2.10 in Agrawal "Nonlinear Fiber Optics" 2001 pp67
FWHM_new = FWHM*sqrt(1 + (L/Ld)^2)

% N<<1 --> GVD ; N >>1 ---> SPM
Leff = (1 - exp(-alpha_loss*L))/alpha_loss
expected_normPout = exp(-alpha_loss*2*L)
NlnPhaseshiftmax = gamma*P0*Leff

betap = [0 0 beta2 beta3]';
betapDCF = [0 0 beta2*DDCF/D -beta3]';

% Constants for ASE of EDFA
% PSD of ASE: N(at carrier freq) = 2*h*fc*nsp*(G-1) with nsp = Noise
% Figure/2 (assume saturated gain)
%***************** Standdard Constant ********************************
h = 6.626068e-34;   %Plank's Constant
%*****************************************
```

References

1. C. Headley and G.P. Agrawal, *Raman Amplification in Fibre Optical Communication Systems*, Elsevier Publications, San Diego, CA, 2005.
2. M.N. Islam, *Raman Amplifiers for Telecommunications 1-Physical Principles*, Springer-Verlag Publications, Berlin, Germany, 2004.
3. G.P. Agrawal, *Fiber-Optic Communications Systems*, 3rd ed., John Wiley & Sons, New York, 2002.
4. P.L. Kelley, *Nonlinear Fiber Optics*, 3rd ed., Academic Press, San Diego, CA, 1995.
5. D.J. Blumenthal, Distributed Raman amplification for ultra-high speed fiber cross-phase-modulation wavelength converters, Project Report, 2001–2002.
6. Y. Aoki, Properties of fiber Raman amplifiers and their applicability to digital optical communication systems, *IEEE Journal of Lightwave Technology*, 6, 1225–1239, 1988.
7. M.L. Dakss and P. Melman, Amplified spontaneous Raman scattering and gain fiber Raman amplifiers, *IEEE Journal of Lightwave Technology*, 6, 806–813, 1985.
8. M. Menif, M. Karasek, and L.A. Rusch, Cross-gain modulation in Raman fiber amplifier: Experimentation and modeling, *Photonics Technology Letters, IEEE*, 14(9), 1261–1263, September 2002.
9. J. Bromage, Raman amplification for fiber communications systems, *IEEE Journal of Lightwave Technology*, 6, 79–93, 2004.
10. S. Namiki and Y. Emori, Ultra-broadband Raman amplifiers pumped and gain-equalized by wavelength-division-multiplexed high-power laser diodes, *IEEE Journal of Selected Topics in Quantum Electronics*, 7(1), 3–16, January/February 2001.

11. R.H. Stolen, Relation between the effective area of a single-mode fiber and the capture fraction of spontaneous Raman scattering, *Journal of the Optical Society of America*, 19(3), 498–501, 2002.
12. H. Suzuki, N. Takachio, H. Masuda, and K. Iwatsuki, Super-dense WDM transmission technology in the zero-dispersion region employing distributed Raman amplification, *IEEE Journal of Lightwave Technology*, 4(4), 973–981, April 2003; H. Suzuki, J.-I. Kani, H. Masuda, N. Takachio, K. Iwatsuki, Y. Tada, and M. Sumida, 1-Tb/s (100×10 Gb/s) super-dense WDM transmission with 25-GHzchannel spacing in the zero-dispersion region employing distributed Raman amplification technology, *IEEE Photonics Technology Letters*, 12(7), 903–905, July 2000.
13. D. Dahan and G. Eisenstein, The properties of amplified spontaneous emission noise in saturated fiber Raman amplifiers operating with CW signals, *Optics Communications*, 236, 279–288, 2004.
14. P. Gallion, Study of noise properties in optical distributed Raman amplifiers using a semiclassical model, in *Proceedings SPIE*, San Jose, CA, vol. 4646, Photonics West, Optoelectronics, pp. 618–629, January 2002.
15. A.V. Wesson and R.I. Killey, Calculation of the effect of pump depletion in WDM systems with distributed Raman gain, in *Proceedings of London Communications Symposium 2001*, London, U.K., pp. 59–62, 2001, UCL Press Ltd.
16. L. Xueming, Optimization for various schemes of distributed fibre Raman amplifiers, *Journal of Optics A: Pure and Applied Optics*, 6, 1017–1026, 2004.

11

Digital Optical Modulation Transmission Systems

Since the invention of optical fibers, the modulation of light waves for transmission in optical communication systems has been based mainly on the on–off switching of the intensity of the waves, rather than manipulating the phase or frequency of the field of the waves. In the 1980s, interest in extending the repeater-less distance from 40 km to longer than 60 km using coherent reception and transmitting techniques attracted the use of modulation in the carrier wave. However, sufficiently narrow line width laser and integrated optical components that would facilitate the development of such techniques were not available. Then, the invention of optical amplification devices diverted the attention of coherent communications, till recently when the bit rate was extended to 40 Gb/s. With that the necessity of narrowing the signal bandwidth to minimize the dispersion effects has encouraged the exploitation of modulation techniques for direct detection systems. Several modulation techniques have been studied. Coherent communications have also been revived in this trend and are associated with electronic processing for estimation of the phase of the demodulated signals. Digital signal processing (DSP) associated with coherent receptions has overcome several hurdles confronting the 'analog' coherent reception techniques employed in the 1980s, such as the laser linewidth and the frequency offset between the local oscillator and the channel carrier, the phase and clock recovery, and, most importantly, the compensation of the distortion effects due to linear chromatic dispersion as well as nonlinear effects described in previous chapters. It is noted that coherent reception can be either self-coherent detection, in which the signals are beating themselves, or non-self-coherence, indicating the mixing between the signals and a local oscillator to boost the amplitudes of the resultant signals. This chapter and subsequent chapters discuss both of these coherent reception techniques.

These DSP-coherent receivers have now been dominating the long haul optical transmission systems with the a bit rate of 100 Gbps, 400 Gbps, and 1 Tera-bps. It has now been planned to deploy these systems in long haul, metropolitan, and access networks. Thus, this chapter is dedicated to introduce this modern optical communication technique. A number of Simulink® models for these optical digital transmission systems without the digital signal processing parts of the receivers are available for download from CRCPress.com. Readers must contact the publisher for details. It is straightforward for readers to add more DSP models available in several Simulink toll boxes.

11.1 Advanced Photonic Communications and Challenging Issues

11.1.1 Background

Beginning from the first research phase around the early 1970s, fiber-optic communications have progressed tremendously over the last three decades. The first-generation lightwave systems were commercially deployed in 1983 and operated in the first wavelength window

of 800 nm at transmission bit rates of up to 45 Mb/s [1,2]. After the introduction of ITU-G652 Standard Single Mode Fibers (SSMF) in the 1970s [2,3], the second generation of lightwave transmission systems became available in the early 1980s [4,5]. The operating wavelengths were shifted to the second window of 1300 nm, which offered much lower attenuation for the optical fiber compared to the previous 800 nm region. These systems could operate at transmission rates of up to 1.7 Gb/s and have a repeater-less transmission distance of about 50 km [6]. Optical communications then evolved to third-generation transmission systems, which used the lowest attenuation window of 1550 nm wavelength and operated at 2.5 Gb/s bit rate [6,7]. These systems were commercially available in 1990 [6,8] with a repeater spacing of around 60–70 km. At this stage, the generation of optical signals was based mainly on the direct modulation of the semiconductor laser source. Since the invention of the erbium-doped fiber amplifiers (EDFA) in the early 1990s [9,10], lightwave systems have rapidly evolved to wavelength division multiplexing (WDM) and then dense WDM (DWDM) optically amplified transmission systems that are capable of transmitting multiple 10 Gb/s channels. These high-speed and long-haul systems employ external modulation in their optical transmitters. The present fiber-optic transmission systems are considered to be the fifth generation with a transmission capacity of a few Tb/s [6].

Coherent detection was the focus of extensive research and development during the 1980s and early 1990s [11–16] and was the main detection technique in the first three generations of lightwave transmission systems. At that time, the main motivation for the development of coherent optical systems was to improve the receiver sensitivity, commonly by 3–6 dB [12,15]. It was thus possible to extend the repeater-less transmission distance to more than 60 km of SSMF (with 0.2 dB/km attenuation factor). However, coherent optical systems suffer severe performance degradation because of fiber dispersion impairments. In addition, the phase coherence for the lightwave carriers of the laser source and the local laser oscillator was very difficult to maintain. On the contrary, incoherent detection technique minimizes the linewidth obstacles of the laser source as well as the local laser oscillator and relaxes the requirement of phase coherence. Moreover, incoherent detection mitigates the problem of polarization control for the mixing of the transmitted lightwaves and the local laser oscillator at multi-THz optical frequency range. The invention of EDFAs [17] that are capable of producing optical gains of 20 dB and above has also greatly contributed to further progress in incoherent optical transmission systems. Therefore, since the mid 1990s, incoherent detection is the preferred choice for digital photonic transmission systems.

11.1.2 Challenging Issues

In recent years, there has been a huge increase in the demand for broadband communications driven mainly by the rapid growth of multimedia services, peer-to-peer networks, and IP streaming services, in particular IP TV. It is most likely that such tremendous growth will continue in the coming years. This is the main driving force for local and global telecommunication service carriers to develop high-performance and high-capacity next generation optical networks. The overall capacity of WDM or DWDM optical systems can be boosted by either increasing the base transmission bit rate of each optical channel, multiplexing more channels in a DWDM system, or preferably, by combining both of these schemes. While implementing these schemes, optical transmission systems encounter a number of challenging issues that are outlined in the following paragraphs.

The current 10 Gb/s transmission systems employ intensity modulation (IM), also known as on–off keying (OOK) and use the non–return-to-Zero (NRZ) pulse shapes.

The term OOK can be used interchangeably with amplitude shift keying (ASK). It is noted here that the OOK format simply implies the on–off states of the optical light waves where only the manipulation of the intensity is considered. On the other hand, the ASK format takes into account not only the amplitude but also the phase in the constellation diagram. Moving toward high-bit-rate transmission, the performance of OOK photonic systems is severely degraded due to fiber impairments including fiber dispersion and fiber nonlinearities. The fiber dispersion is classified into chromatic dispersion (CD) and polarization mode dispersion (PMD), causing the intersymbol interference (ISI) problem. On the other hand, severe deterioration in the performance as a result of fiber nonlinearities is the result of the high-power spectral components at the carrier and signal frequencies of OOK-modulated optical signals. It is also of concern that existing transmission networks comprise thousands of kilometers of SSMF, which have been in place for approximately two decades. These fibers are not only low-performance fibers compared to the state-of-the-art fibers used in the present laboratory "hero" experiments but have also degraded after many years of use.

The total transmission capacity can also be enlarged by increasing the number of multiplexed DWDM optical channels. This can be carried out by reducing the spacing between these channels, for instance, from 100 GHz down to 50 GHz, or even 25 GHz as has been reported [18,19]. The reduction of the channel spacing also results in narrower bandwidths for the optical multiplexers (muxes) and demultiplexers (demuxes). Passing through these narrowband optical filters, signal waveforms are distorted and optical channels suffer from interchannel cross talks. These narrowband filtering problems are getting more severe especially at high transmission bit rates, for example, 40 Gb/s, thus degrading the system performance significantly.

Together with the demand for boosting the total system capacity, another challenge for the service carriers is to find cost-effective solutions for the upgrading process. These cost-effective solutions should require minimum renovation to the existing photonic and electronic subsystems, that is, the upgrading should take place only at the transmitter and receiver ends of an optical transmission link. In short, although next generation optical networks are required to meet the desired high performance, the cost of upgrading the system should also be considered.

All the problems facing contemporary fiber-optic communications that are described here can be overcome with spectrally efficient transmission schemes. The main motivation of this research is to find effective solutions to upgrade the aggregate transmission capacity while at the same time minimizing the effects of the fiber shortfalls, particularly the dispersion impairments. The enabling technologies presented in this research aim to overcome the challenging issues addressed earlier.

11.2 Enabling Technologies

11.2.1 Digital Modulation Formats

Spectrally efficient transmission schemes can be achieved by utilizing advanced modulation formats. A number of modulation formats have recently been proposed as the alternatives for the OOK format. These include return-to-zero (RZ) pulses in OOK/ASK systems [20–22], differential phase shift keying (DPSK) [18,20–25], and more recently,

minimum-shift keying (MSK) [26–33]. These formats are adopted into photonic communications from the knowledge of wireline and wireless communications.

DPSK has received much attention over the past few years, particularly when it is combined with RZ pulses. The main advantages of this format are (1) 3 dB improvement over OOK on receiver sensitivity by using an optical balanced receiver [21,34,35], and (2) high tolerance to fiber nonlinearities [6,20,34,36] such as intrachannel self phase modulation (SPM) and interchannel cross phase modulation (XPM) effects. Several experimental demonstrations of DPSK long-haul DWDM transmission systems for 10 Gb/s, 40 Gb/s, and higher bit rates have been reported recently [18,23,37–39]. However, there are a few practical experiments addressing the performance of cost-effective 40 G DPSK–10 G OOK hybrid systems on the existing old-vintage SSMF infrastructure [40,41]. In addition, the performance of 40 Gb/s DPSK for use in this hybrid transmission scheme has not been thoroughly studied. Therefore, one of the main contributions of this chapter and others in this book is to present the feasibility of overlaying 40 Gb/s DPSK channels on the existing 10 Gb/s OOK channels for implementing the hybrid systems.

The MSK format offers a spectrally efficient modulation scheme compared to the DPSK counterpart at the same bit rate. As a subset of continuous phase frequency shift keying (CPFSK), MSK possesses spectrally efficient attributes of the CPFSK family. The frequency deviation of MSK is equal to a quarter of the bit rate, and this frequency deviation is also the minimum spacing to maintain the orthogonality between two FSK-modulated frequencies. On the other hand, it can also be considered as a particular case of offset differential quadrature phase shift keying (ODQPSK) [42–46], which enables MSK to be represented by I and Q components on the constellation. The advantageous characteristics of the optical MSK format can be summarized as follows:

- Compact spectrum, which is of particular interest for the spectrally efficient high-speed transmission systems. In addition, this provides robustness to the problem of tight optical filtering.
- High suppression of the side lobes in the optical power spectrum compared to the DPSK. The roll-off factor follows f^{-4} rather than f^{-2} as in the case of DPSK.
- Constant envelop property, which eases the measure of the average optical power.
- No high power spikes in the power spectrum and high energy concentration in the main lobe offer the advantage of lower peak input powers into the fiber, thus reducing the fiber's nonlinear effects.
- Being a subset of CPFSK or ODQPSK, MSK can be detected either incoherently based on the phase or the frequency of the lightwave carrier or coherently based on the popular *I*–*Q* detection structure.

In addition, if MSK can be combined with multilevel modulation schemes, the baud rate would be reduced and the spectral efficiency can be even more effective. This is of great interest for long-haul and metropolitan optical networks and provides the main motivation for investigation of the performance of the proposed dual-level MSK modulation format in this research.

Several studies have been conducted recently [26–29] focusing on the generation and direct detection of externally modulated optical MSK as well as the format's CD tolerance. However, there are little reported/published works investigating the potential of externally modulated MSK format for digital photonic transmission systems, particularly at high bit rates such as 40 Gb/s [26,47,48]. Therefore, another key description of this chapter

is to provide comprehensive studies on the performance of MSK-based modulation formats for long-haul and metropolitan optical transmission systems.

11.2.2 Incoherent Optical Receivers

The modulation formats described in this chapter, the optical DPSK- and MSK-based formats, can be demodulated incoherently by using an optical balanced receiver that employs a Mach–Zehnder delay interferometer (MZDI). In the incoherent detection of optical DPSK, MZDI is used to detect the differentially coded phase information between every two consecutive symbols [6,34,35,49]. This detection is carried out in the photonic domain as it is beyond the speed of the electrical domain, especially at very high Mach–Zehnder bit rates of 40 Gb/s or above. The MZDI balanced receiver is also used for the incoherent detection of optical MSK signals [26,28,29]. However, using the MZDI-based detection scheme, optical MSK does not improve the CD tolerance significantly over its DPSK counterpart [28,30].

To fully exploit the advantages of optical MSK spectral characteristics, MSK-modulated light waves can be incoherently detected based on the principles of optical frequency discrimination. Thus, an optical frequency discrimination receiver (OFDR) is proposed in this research, which employs dual narrowband optical filters and an optical delay line (ODL). This receiver scheme effectively mitigates the CD-induced ISI effects and enables breakthrough CD tolerances for optical MSK transmission systems. These results have been recently reported in my first-author papers [30,31]. The feasibility of this novel optical receiver is based on recent advances in the design of optical filters, in particular the micro-ring resonator filters. Such optical filters have very narrow bandwidths, for example, less than 2 GHz (3 dB bandwidth), and they have been realized commercially by Little Optics [50–53]. This research provides a comprehensive study not only on this OFDR scheme, from the receiver operational principles to the analysis of the receiver design, but also on the performance of OFDR-based optical MSK systems.

In phase modulation techniques, the phase transition between two consecutive bit slots can be either noncontinuous or continuous. In the noncontinuous format, DPSK phase, in particular the RZ DPSK phase, has received considerable attention in research as RZ DPSK displays advantages such as 3 dB improvement on the receiver sensitivity with the use of balanced receivers [5,6] and robustness to fiber nonlinear effects [2,7–9].

Spectral efficiency is a critical requirement for modern high-performance digital photonic transmission systems. The fact that noncontinuous phase modulation schemes, such as DPSK, are not spectrally efficient motivates the exploration of continuous phase modulation (CPM), especially continuous phase frequency shift keying (CPFSK) formats, which are popularly for their compact power spectrums [10,11]. Among CPFSK formats, MSK is most widely used in bandwidth-limited digital wireless and satellite communications. However, the potential of MSK using external modulation techniques in noncoherent optical communications has been studied only in the last few years [12–17]. In MSK, the frequency deviation from the lightwave carrier is equal to a quarter of the bit rate and this is also the minimum spacing required to maintain the orthogonality attributes between the two modulated frequencies. Additionally, MSK is a special case of ODQPSK in which I and Q components are interleaved by one bit period [10,18,19]. The two approaches from CPFSK and ODQPSK enable two possible schemes for generating optical MSK signals.

If a multilevel scheme can be incorporated with the MSK format, the transmission baud rate would be reduced in addition to the spectral efficiency. This effectively mitigates the fiber impairments for optically amplified long-haul and ultra long-haul transmission systems as well as relaxes the requirement for high-speed processing electronics. The aforesaid demand is the principal motivation for exploring the dual-level MSK modulation scheme in fiber-optic communications, which utilizes two binary bits for each modulated symbol. The transmission symbol rate is thus halved compared to the data rate from a bit pattern generator.

The advanced modulation formats described so far can be detected either coherently or incoherently. The incoherent detection is preferred as it overcomes the laser's linewidth obstacles facing homodyne or heterodyne coherent detection systems. Furthermore, the incoherent detection scheme can be easily implemented by using a MZDI. This structure reflects the main advantages of the optical domain over the electrical domain for systems operating at ultra high bit rates, such as 40 Gb/s. This MZDI is normally used in balanced receivers for incoherent detection of both DPSK and MSK optical signals. Additionally, optical MSK signals can also be incoherently detected by using an optical frequency discrimination receiver (OFDR) employing dual optical narrowband filters and an optical delay line (ODL).

This chapter is organized as follows: Section 11.3.1 presents principles for generating several types of RZ optical pulses, with and without the suppression of the lightwave carrier. The modulation process of these RZ pulses can be clearly explained in Section 13.3.2, by using a phasor representation. Section 11.4 then presents optical transmitter and receiver configurations of the DPSK format. In Section 11.5, two MSK optical transmitter schemes are presented. These two schemes are derived from the knowledge that MSK is either a subset of CPFSK or a special case of ODQPSK. Sections 11.5 and 11.6 also describes the incoherent detection techniques for optical MSK systems, which are either a MZDI balanced receiver or an OFDR scheme. In Section 11.6, the novel dual-level MSK modulation format is proposed for optical communications together with its generation and incoherent detection schemes. Finally, Section 11.7 compares key spectral characteristics of all modulation formats under the study before a summary of this chapter is provided.

11.3 Return-to-Zero Optical Pulses

11.3.1 Generation Principles

A conventional RZ OOK optical transmitter comprises two external $LiNbO_3$ optical MZIMs, as shown in Figure 11.1.

The first MZIM serves as a pulse carver to generate a periodic pulse train of a specific RZ pulse shape format, and it is usually implemented with a chirp-free X-cut single-drive MZIM. Different types of RZ pulses can be generated depending on the amplitude of sinusoidal electrical driving voltages and the biasing schemes of MZIM. Suppression of the lightwave carrier can be carried out at this stage to form carrier suppressed-RZ (CS-RZ) pulses. Compared to other RZ types, CS-RZ is found to have interesting attributes for long-haul transmission including the π phase difference between adjacently modulated bits, the suppression of high power carrier, and the narrower spectral width. Another

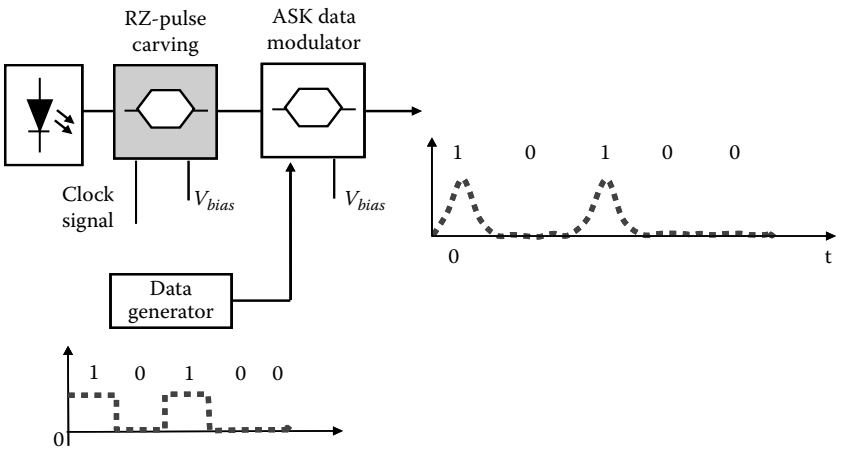

FIGURE 11.1
Conventional structure of an OOK/ASK optical transmitter using two MZIMs.

type of the RZ pulse, RZ33, also has several advantages due to its soliton-like properties. The RZ33 pulse has full-width half maximum (FWHM) positions occupying 33% of the duty circle, whereas CS-RZ has a FWHM of 67%. These optical RZ pulses are represented in the optical field $E(t)$ as follows [20]:

$$E(t)=\begin{cases}\sqrt{\dfrac{E_b}{T}}\sin\left[\dfrac{\pi}{2}\cos\left(\dfrac{\pi t}{T}\right)\right] & \text{67\% duty-ratio RZ pulses or CS-RZ}\\ \sqrt{\dfrac{E_b}{T}}\sin\left[\dfrac{\pi}{2}\left(1+\sin\left(\dfrac{\pi t}{T}\right)\right)\right] & \text{33\% duty-ratio RZ pulses or RZ33}\end{cases} \tag{11.1}$$

where
E_b is the pulse energy per transmitted bit
T is the bit period

The art of generating these two RZ pulse types lies in the biasing position on the transmittance characteristic curve of the MZIM pulse carver and the amplitude of the sinusoidal driving signal. The bias point is situated at a minimum or maximum position of the characteristic curve for the case of CS-RZ or RZ, respectively. The peak-to-peak amplitude of the RF driving signal for these two RZ pulses is similar and equal to $2V_\pi$ where V_π is the required driving voltage to obtain a π phase shift on the lightwave carrier at the output of MZIM. It should be emphasized that the electrical driving signal is operating at only half of the bit rate, and hence, the pulse carver is actually implementing the frequency doubling. Figure 11.2a and b shows all the settings described here as well as the pulse shapes of the generated CS-RZ and RZ33 optical pulse trains.

The pulse carver for generating RZ optical pulses can also utilize a dual-drive MZIM, which is driven by two complementary sinusoidal RF signals. The settings of the biasing scheme and driving signal as well as the modulation process in these dual-drive MZIMs are explained in the next section by using the phasor representation.

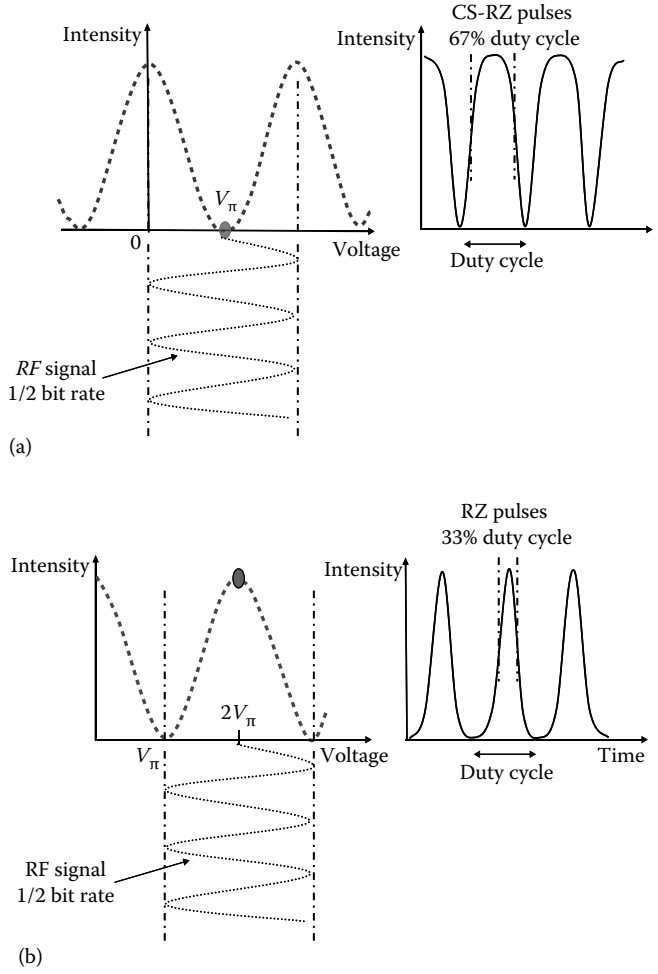

FIGURE 11.2
Bias positions and driving signals for generation of (a) CS-RZ and (b) RZ33 pulses.

11.3.2 Phasor Representation

The output optical field of a dual-drive MZIM is given by

$$E_o = \frac{E_i}{2}\left[e^{j\varphi_1(t)} + e^{j\varphi_2(t)}\right] = \frac{E_i}{2}\left[e^{j\pi V_1(t)/V_\pi} + e^{j\pi V_2(t)/V_\pi}\right] = E_1 + E_2 \tag{11.2}$$

This equation suggests that a phasor diagram (see Figure 11.3) that involves vector addition and simple trigonometric calculus can give a clear view on the superposition of optical fields at the coupling output of dual-drive MZIM. The RF driving signals follow a push–pull configuration, that is, the data $V_1(t)$ and the inverse data (data) $V_2(t)$ ($V_2(t) = -V_1(t)$) are applied into each arm of the MZIM, respectively.

It should be noted that the widths of RZ33 and CS-RZ pulses are measured at FWHM positions that are defined for intensity pulses, whereas the phasor diagram considers optical field vectors. Thus, the normalized output optical field (E_o) has a magnitude value

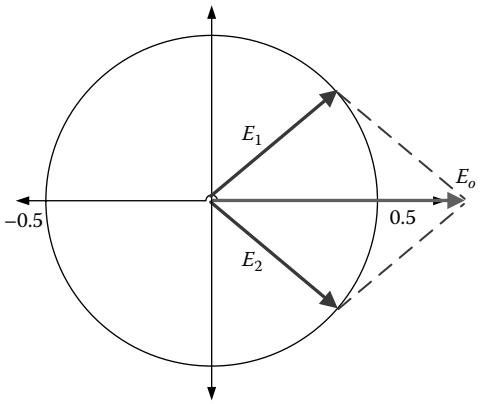

FIGURE 11.3
Phasor representation for generation of optical signals using a dual-drive MZIM.

of $1/\sqrt{2}$ at FWHM positions. In addition, the time interval between these FWHM points defines the time ratios such as 33% or 67%, and they are normalized with respect to the duty cycle.

11.3.2.1 Phasor Representation for CS-RZ Modulation

Figure 11.4a shows key parameters in the generation scheme of CS-RZ pulses, including the biasing voltage V_{bias} and the amplitude of RF driving signals. Accordingly, its initialized phasor representation is demonstrated in Figure 11.4b where the red dot indicates the sum of two initialized field vectors of the two arms.

The values of these key parameters are outlined in the following:

- $V_{bias} = \pm\dfrac{V_\pi}{2}$.
- The RF driving signal on each arm has an amplitude of $V_\pi/2$ (i.e., $V_{p-p} = V_\pi$), swings in opposite directions, and operates at half of the bit rate ($R/2$).
- Considering the generation of 40 Gb/s CS-RZ pulses (R = 40 Gb/s), the modulating frequency is $f_m = R/2$ = 20 GHz.

At FWHM positions of optical intensity pulse, $E_o = \pm 1/\sqrt{2}$ and the field vectors E_1 and E_2 form with the vertical axis a phase of π/4, as shown in Figure 11.5.

The conditions shown in Figure 11.5 lead to

$$\frac{\pi}{2}\sin(2\pi f_m) = \frac{\pi}{4} \Rightarrow \sin 2\pi f_m = \frac{1}{2} \Rightarrow 2\pi f_m = \left(\frac{\pi}{6}, \frac{5\pi}{6}\right) + 2n\pi \tag{11.3}$$

The normalized FWHM (with reference to the duty cycle) of a CS-RZ optical pulse can be obtained as follows:

$$T_{FWHM} = \left(\frac{5\pi}{6} - \frac{\pi}{6}\right)\frac{1}{2\pi R} = \frac{1}{3}\pi \times \frac{1}{R} \Rightarrow \frac{T_{FWHM}}{T} = \frac{1.66\times10^{-4}}{2.5\times10^{-11}} = 66.67\% \tag{11.4}$$

Thus, the generation of CS-RZ pulses is clearly explained via the phasor representation.

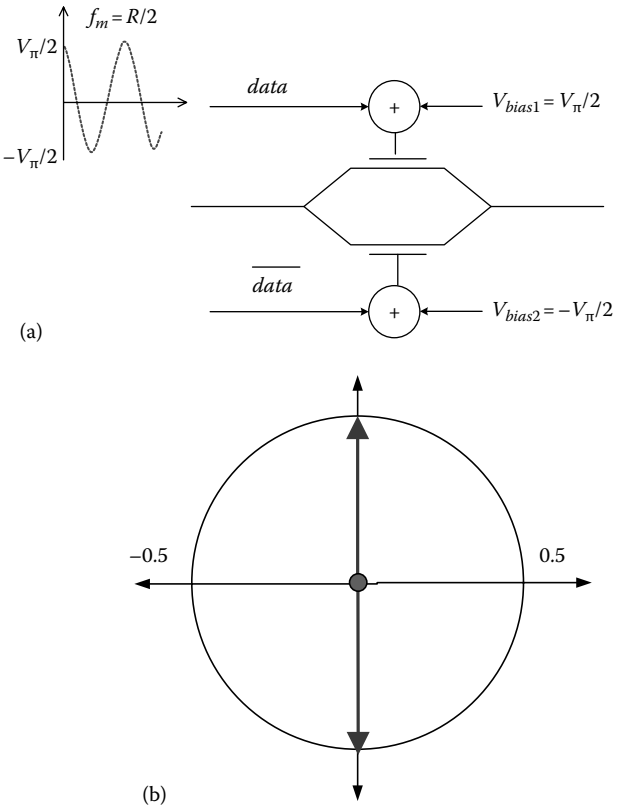

FIGURE 11.4
Initialized stage for generation of CS-RZ optical pulses: (a) RF driving signal and biasing voltages and (b) Initial phasor representation.

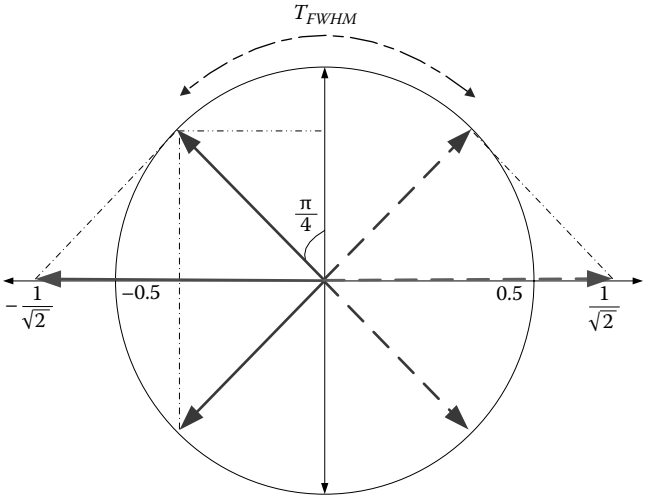

FIGURE 11.5
Phasor representation of CS-RZ generation at FWHM positions using dual-drive MZIM.

11.3.2.2 Phasor Representation for RZ33 Modulation

Key parameters and initial phasor representation for generation of RZ33 pulses are shown in Figure 11.6a and b. The red vector is the sum of two initialized field vectors.

The values of the key parameters are $V_{bias} = V_\pi$ for both arms; the RF driving signal on each arm has an amplitude of $V_\pi/2$ (i.e., $V_{p-p} = V_\pi$), swings in opposite directions, and operates at half of the bit rate ($R/2$); and modulating frequency $f_m = 20$ GHz.

At FWHM positions of the optical intensity pulse, $E_o = \pm 1/\sqrt{2}$ and the field component vectors E_1 and E_2 form with the horizontal axis a phase of $\pi/4$, as displayed in Figure 11.7.

The conditions in Figure 11.7 result in

$$\frac{\pi}{2}\cos(2\pi f_m t) = \frac{\pi}{4}$$
$$\Rightarrow t_1 = \frac{1}{6f_m} \tag{11.5}$$

$$\frac{\pi}{2}\cos(2\pi f_m t) = -\frac{\pi}{4}$$
$$\Rightarrow t_2 = \frac{1}{3f_m} \tag{11.6}$$

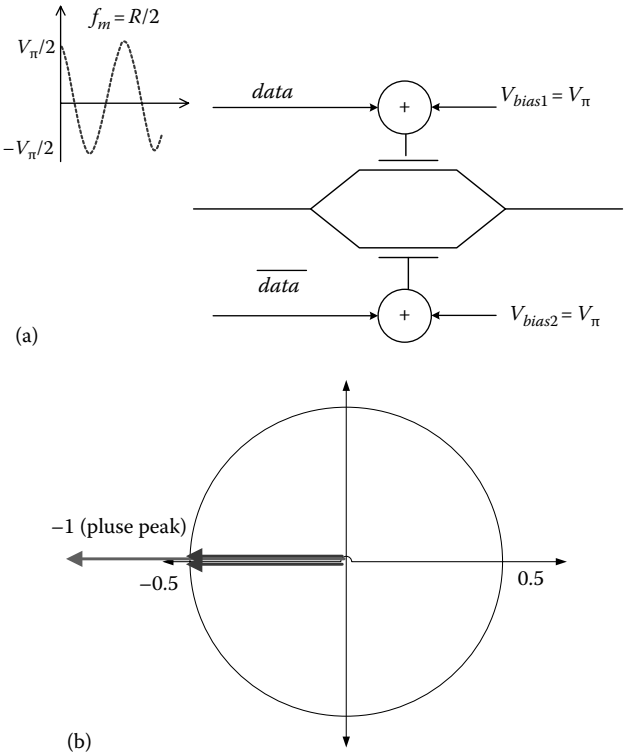

FIGURE 11.6
Initialized stage for generation of RZ33 pulses: (a) RF driving signals and the biasing voltages and (b) initial phasor representation.

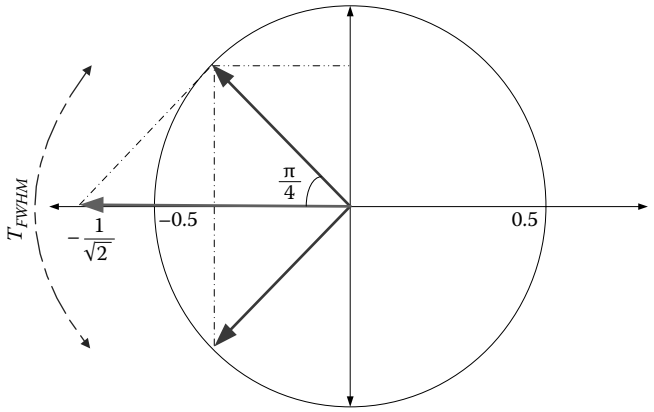

FIGURE 11.7
Phasor representation of RZ33 generation at FWHM positions using dual-drive MZIM.

The normalized FWHM of RZ33 optical pulses can be calculated by

$$T_{FWHM} = \frac{1}{3f_m} - \frac{1}{6f_m} = \frac{1}{6f_m}$$
$$\therefore \frac{T_{FWHM}}{T} = \frac{1/6f_m}{1/2f_m} = 33\% \tag{11.7}$$

This equation clearly verifies the generation of RZ33 optical pulses from the phasor representation.

11.4 Differential Phase Shift Keying (DPSK)

11.4.1 Background

Digital encoding of data information by modulating the phase of the lightwave carrier is referred to as optical phase shift keying (PSK). Optical PSK was extensively researched for coherent photonic transmission systems [21–24]. These systems strictly require the coherence between the phase of the lightwave carrier and the phase of the laser local oscillator. This phase coherence was difficult to maintain because of problems of phase noise, broad linewidth, and chirping effects of the laser source. In contrast, the DPSK format minimizes the aforementioned problems. The detection of DPSK modulated optical signals is conducted incoherently by comparing differentially coded phases between every two consecutive optical pulses. The existing incoherent receiver scheme for optical DPSK format uses the MZDI balanced receiver.

In DPSK, a binary "1" is encoded if the present and the past encoded bits are opposite logics, whereas a binary "0" is encoded if the logics are similar. This operation is equivalent to an XOR logic operation. An XOR gate is employed as a differential precoder. In addition, the XOR gate can be replaced by an NOR gate (see Figure 11.8a). In DPSK, data "1" indicates a π phase change on the optical carrier between consecutive data bits, while

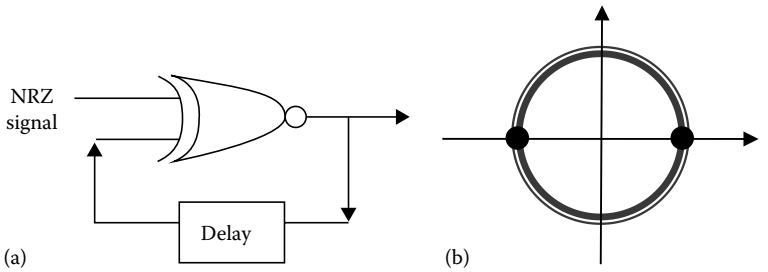

FIGURE 11.8
(a) DPSK precoder and (b) DPSK signal constellation diagram.

binary "0" implies no phase change between them. Thus, two discrete points, which are located exactly at a π phase difference with respect to each other in a signal constellation diagram, are used to represent this encoding scheme (refer to Figure 11.8b). In the case of a continuous phase shift keying format, for example, MSK, signal phase evolves continuously between one state to the other as indicated by the inner bold circle in Figure 11.8b.

11.4.2 Optical DPSK Transmitter

The conventional structure of a DPSK optical transmitter employs two external $LiNbO_3$ optical MZIMs (see Figure 11.9). The first MZIM is an optical pulse carver, which was described in the previous section. Generated RZ optical pulses are then fed into the second MZIM, and these RZ pulses are modulated with precoded binary data to generate RZ DPSK optical signals.

Binary electrical data are differentially encoded in a precoder using an XOR or an NOR operation. Without the pulse carver, the structure shown in Figure 11.9 becomes an NRZ DPSK optical transmitter. In the DPSK data modulation, the second MZIM is biased at the minimum transmission point. The precoded RF driving signal has a peak-to-peak

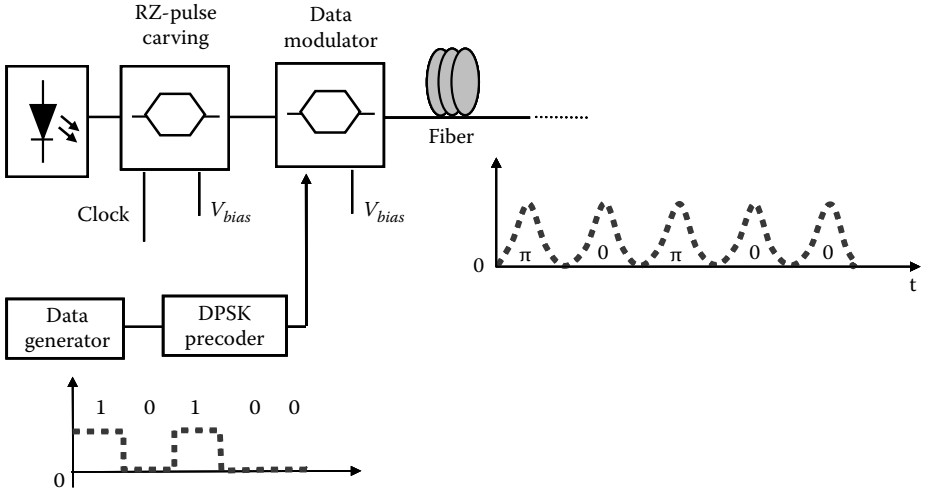

FIGURE 11.9
DPSK optical transmitter with RZ pulse carver.

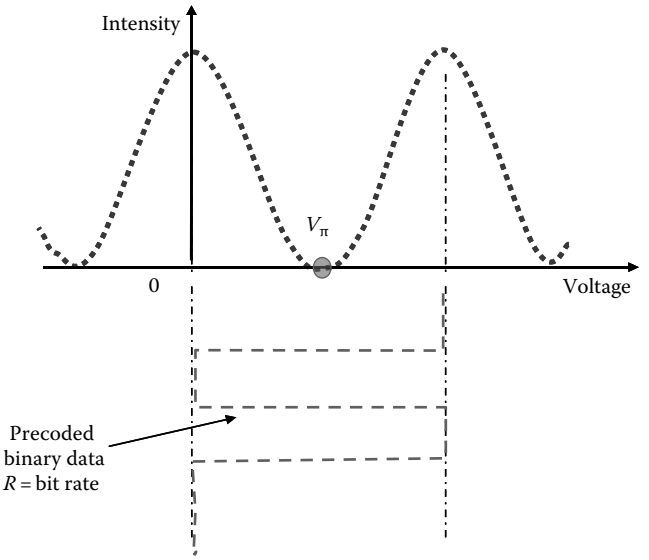

FIGURE 11.10
Bias point and RF driving signal for generation of optical NRZ DPSK signals.

amplitude equal to $2V_\pi$ and operates at the transmission bit rate. The data modulation of NRZ DPSK optical signals is demonstrated in Figure 11.10.

In addition, an electro-optic phase modulation (EOPM) might also be used for the generation of NRZ DPSK optical signals. However, EOPM produces chirps, whereas MZIM, in particular the X-cut type, generates chirp-free optical signals. In practice, a small amount of chirp might be desirable in transmission [25].

11.4.3 Incoherent Detection of Optical DPSK

An optically delayed balanced receiver is well known for the incoherent detection of DPSK-modulated lightwaves. It consists of a photonic MZDI followed by dual photo detectors connected in a balanced structure, as shown in Figure 11.11a [5,6]. At the input

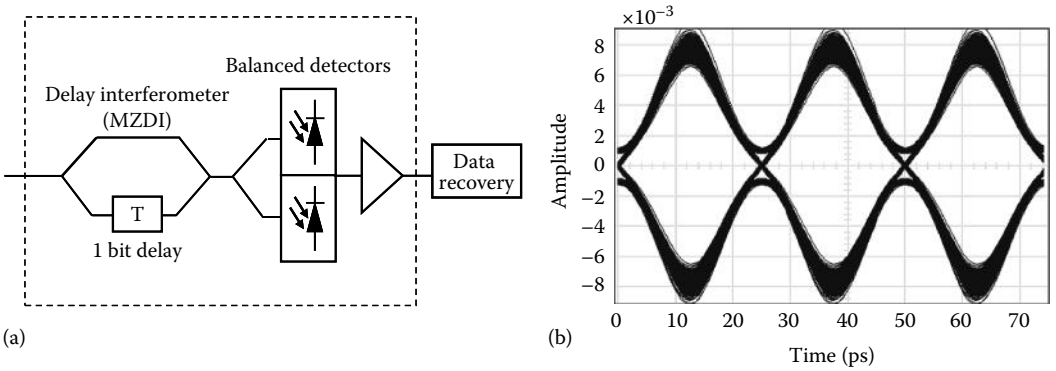

FIGURE 11.11
(a) MZDI balanced receiver for incoherent detection of optical DPSK signals and (b) detected electrical eye diagrams.

of MZDI, the light waves are split into two guided paths and one path is delayed with respect to the other by a physical length that equals a propagation time delay of one bit interval.

MZDI can be effectively seen as an optical self-heterodyne structure, and it performs the differential phase demodulation in the photonic domain. This photonic processing overcomes the bandwidth and speed limitations of the electrical domain. MZDI has constructive and destructive ports, which are inputs to the balanced-structure photo detectors. Hence, a push–pull eye diagram is produced (see Figure 11.11b). This detection scheme offers a 3 dB improvement over the direct detection using a single photo detector [5,6]. In addition, the DPSK MZDI balanced receiver is inherently insensitive to the absolute phase of the lightwave carrier. The received signal current at the output of the push–pull photo detectors are expressed by [26]

$$\begin{aligned} i(t) &= \left|E(t)+E(t-T)\right|^2 - \left|E(t)-E(t-T)\right|^2 \\ &= 4\Re\left\{E(t)E^*(t-T)\right\} = 4\left|E(t)\right|^2\cos\left(\Delta\phi+\varsigma\right) \end{aligned} \tag{11.8}$$

where

$E(t)$ and $E(t - T)$ are the current and the one-bit-delay version of the optical field, respectively

$\Delta\phi$ represents the differential phase

ς indicates the phase noise caused by either the nonlinear phase noise or the imperfection of waveguide path lengths in MZDI

This MZDI imperfection can be overcome by thermally fine-tuning the thin-film heater integrated on the waveguide of MZDI [6,27].

11.5 Minimum Shift Keying

MSK can be formulated from either CPFSK or ODQPSK format [10,19,28]. The signal trajectory of optical MSK signals shown in Figure 11.12 is continuously evolving. This is unlike the discrete DPSK format where encoded bits are located exactly at the "0" and "π" phase positions. Two novel schemes are proposed for generating optical MSK signals.

11.5.1 CPFSK Approach

11.5.1.1 Theoretical Background

In CPFSK modulation, binary data are modulated to either upper side band (USB) frequency f_1 or lower side band (LSB) frequency f_2 such that $f_1 = f_c + f_d$ and $f_2 = f_c - f_d$ where f_c is the lightwave carrier frequency and f_d is the frequency deviation from f_c. In the case of MSK format, $f_d = 1/4T$ and the frequency modulation index, defined as $h = 2f_dT$, is equal to 1/2 ($h = 1/2$). It is emphasized that the phase of the optical MSK carrier is continuous at symbol transitions as MSK meets the condition that the frequency spacing between the USB and LSB must be a multiple of $1/2T$ in order to obtain phase continuity [10,19,28]. In addition, this frequency spacing ($h = 1/2$) is also the minimum value to maintain the

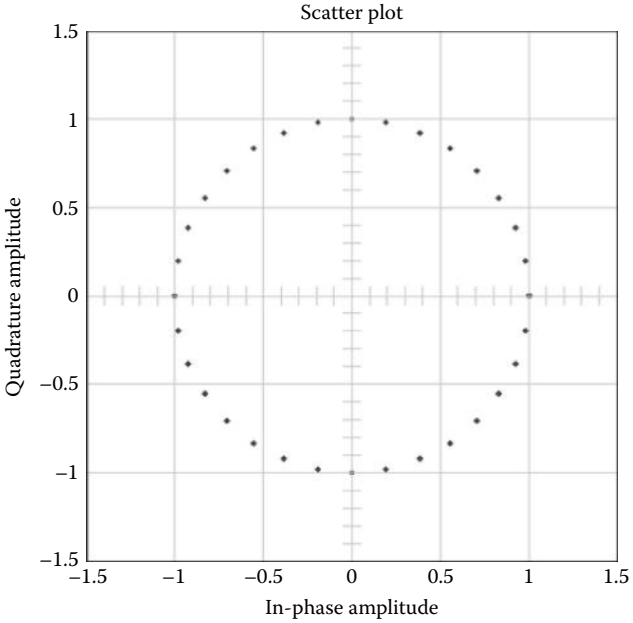

FIGURE 11.12
Signal trajectory of optical MSK signals.

orthogonality between the two frequency modulated signals [10,19,28]. The base-band representation of an optical MSK pulse train $x(t)$ at the nth symbol interval is expressed by [10]

$$x(t) = \sqrt{\frac{E_b}{T}} e^{j\Phi_n(t,a)} nT - T/2 \le t \le nT + T/2 \tag{11.9}$$

where E_b is the bit energy. The phase term, $\Phi_n(t,a)$, is given by

$$\begin{aligned}\Phi_n(t,a) &= \left[\pi/2 \sum_{k=-\infty}^{n-1} a_k\right] + 2\pi f_d(t + T/2 - nT)a_n \\ &= \theta_{n-1}(t,a) + 2\pi f_d(t + T/2 - nT)a_n\end{aligned} \tag{11.10}$$

where $a_n \in \{+1, -1\}$ is the data logics transmitted at the nth interval.

Equation 11.10 shows that the MSK phase evolution follows a linear phase trellis. It increases linearly up to $\pi/2$ within a bit slot with transmitted data "1" and linearly decreases by $\pi/2$ with transmitted data "0" (Figure 11.13).

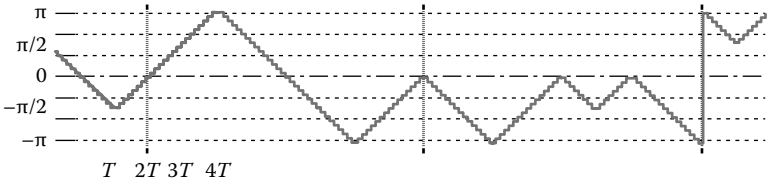

FIGURE 11.13
Phase trellis of MSK signals.

11.5.1.2 Proposed Generation Scheme

MSK optical transmitter employing two external EOPMs can be arranged in a cascaded configuration, as shown in Figure 11.14. The first EOPM enables the frequency modulation of data logics into either USB or LSB frequency. The RF driving voltage $V_d(t)$ requires a periodic ramp signal source with a duty cycle of $4T$. It should be noted that the differential phase precoder and bias voltages are not required in this configuration. This reduces the complexity of this MSK optical transmitter scheme.

The second external EOPM enforces the phase continuity of the lightwave carrier at transitions between every two consecutive symbols. The driving voltage of the second EOPM (V_{prep}) is precomputed to fully compensate transitional phase discrepancy at the output $E_{01}(t)$ of the first EOPM. An electrical phase shifter is usually used to control the synchronization between the EOPMs. The calculation of V_{prep} at the nth instance is given by the following algorithm:

$$V_{prep_n}(t,a) = \frac{V_\pi}{2}\left(\sum_{k=0}^{n-1} a_k - a_n I_n \sum_{k=0}^{n-1} I_k\right) \tag{11.11}$$

where

$a_n = \pm 1$ are the logic levels

$I_n = \pm 1$ represents two stages of a clock pulse $V_c(t)$ whose duty cycle is equal to $4T$

It is emphasized that the values of V_{prep} are either 0 or V_π.

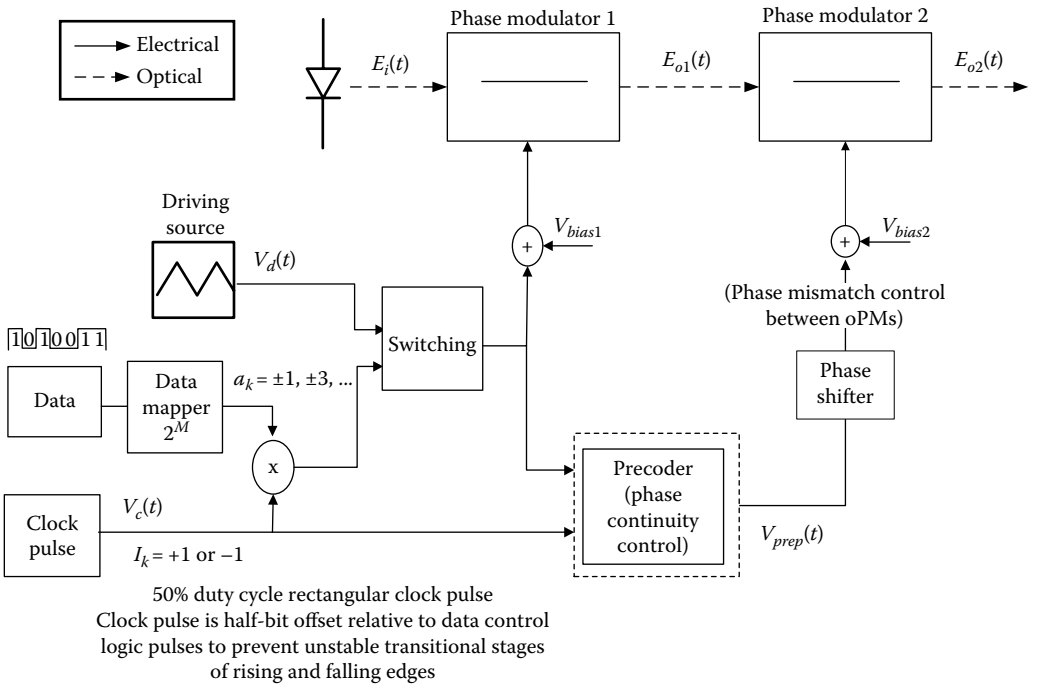

FIGURE 11.14
Block diagram of MSK optical transmitter employing two cascaded external optical phase modulators.

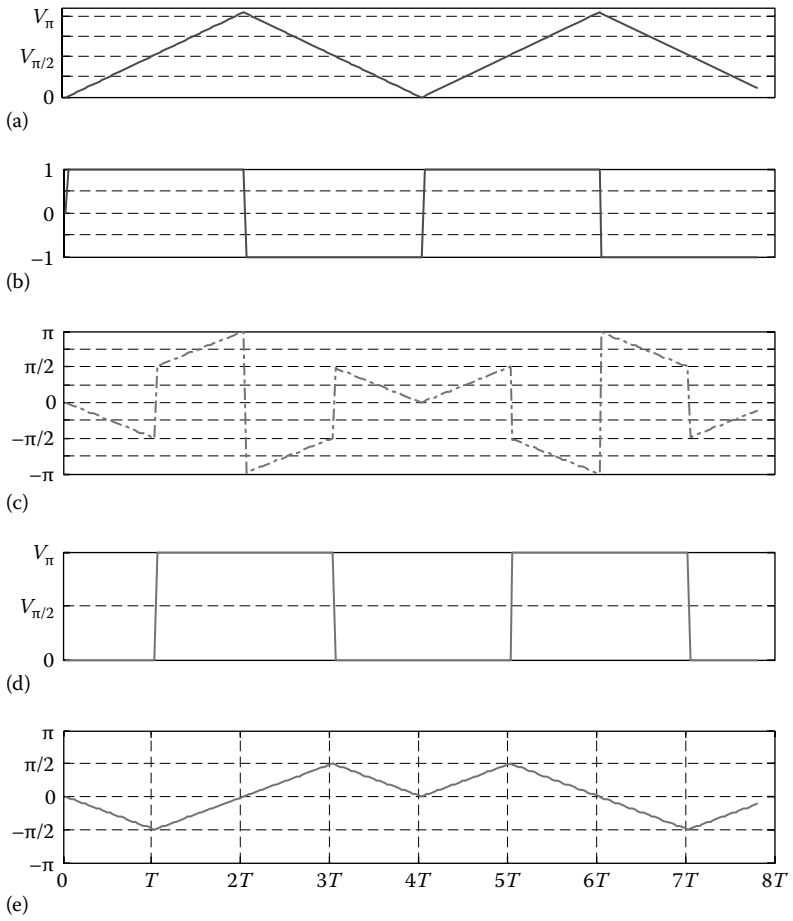

FIGURE 11.15
Evolution of time-domain phase trellis of an optical MSK sequence [–1 1 1 –1 1 –1 –1 1] at different stages of the MSK optical transmitter: (a) $V_d(t)$, (b) $V_c(t)$, (c) $E_{01}(t)$, (d) $V_{prep}(t)$, and (e) $E_{02}(t)$.

The time-domain signal phase evolution during the modulation process for an optical MSK sequence [–1 1 1 –1 1 –1 –1 1] is demonstrated step by step in Figure 11.15. The key points of this figure are as follows:

- Figure 11.15a shows the periodic ramp signal $V_d(t)$ with a duty cycle of $4T$.
- Figure 11.15b illustrates the clock pulse $V_c(t)$ with a duty cycle of $4T$. In order to mitigate the overshooting effect at the rising and falling edges of electronic circuits, the clock pulse $V_c(t)$ is delayed, by $2T$, compared to the driving signal $V_d(t)$.
- Figure 11.15c outlines the phase of the carrier at the output of the first EOPM $E_{01}(t)$. It can be observed that optical signals at this stage are of FSK type, and thus, the phase at transitions of consecutive symbols is not continuous.
- In Figure 11.15d, the transitional phase discrepancy is fully compensated by the precomputed driving signal $V_{prep}(t)$, which is calculated from Equation 11.11.
- Figure 11.15e demonstrates the continuous phase trellis of generated optical MSK sequence [–1 1 1 –1 1 –1 –1 1] at the output of the second EOPM.

The proposed generation scheme is realizable with the advance in the design of EOPM. EOPMs operating up to 40 Gb/s using resonant-type electrodes have been reported in some previous research [29,30]. In addition, high-speed electronic driving circuits evolved with the ASIC technology using 0.1 μm GaAs P-HEMT or InP HEMTs have recently been realized [31]. Furthermore, a simplified version of the proposed optical MSK transmitter can be implemented by alternating the ramp driving signals $V_d(t)$ with a sinusoidal driving source. Finally, this transmitter scheme is also capable of generating *M*-ary FSK optical signals. The next section describes optical transmitter configuration for generating optical MSK signals based on the *I*–*Q* approach of ODQPSK format.

11.5.2 ODQPSK Approach

11.5.2.1 Theoretical Background

MSK format can be formulated in the form of DQPSK by using in-phase *I* and quadrature-phase *Q* components [10,28]:

$$s(t) = \pm\sqrt{\frac{E_b}{T}}\cos\left(\frac{\pi t}{2T}\right)\cos(2\pi f_c t) \pm \sqrt{\frac{E_b}{T}}\sin\left(\frac{\pi t}{2T}\right)\sin(2\pi f_c t) \tag{11.12}$$

The *I* and the *Q* components consist of a half-cycle cosine and sine waveforms, respectively, expressed as

$$s_I(t) = \pm\sqrt{\frac{E_b}{T}}\cos\left(\frac{\pi t}{2T}\right) \quad -T < t < T \tag{11.13}$$

$$s_Q(t) = \pm\sqrt{\frac{E_b}{T}}\sin\left(\frac{\pi t}{2T}\right) \quad 0 < t < 2T \tag{11.14}$$

During even bit intervals, the *I* component consists of positive cosine waveforms for the zero phase and negative cosine waveforms for the π phase. On the other hand, during odd bit intervals, the *Q* component consists of positive sine waveforms with a phase of π/2, and negative sine waveforms with a phase of −π/2. Hence, any of the four states "0", "π/2", "−π/2", and "π" can arise. However, only state 0 or π can occur in any even bit interval, and only state π/2 or −π/2 can occur in any odd bit interval. The output signal is the superposition of *I* and *Q* signal components.

Two important characteristics in generating optical MSK signals using the *I*–*Q* approach of ODQPSK format are the *I* and *Q* driving signals operate at half the bit rate, and they are interleaved by one bit period. Therefore, only either *I* or *Q* component can change at a time, that is, when one is at zero crossing, the other is at maximum peak.

11.5.2.2 Proposed Generation Scheme

The MSK optical transmitter shown in Figure 11.16 consists of two dual-drive MZIMs in parallel, reflecting *I*–*Q* structure. The binary logic data are precoded and de-interleaved into even and odd symbol streams, which are staggered with each other by a one bit duration.

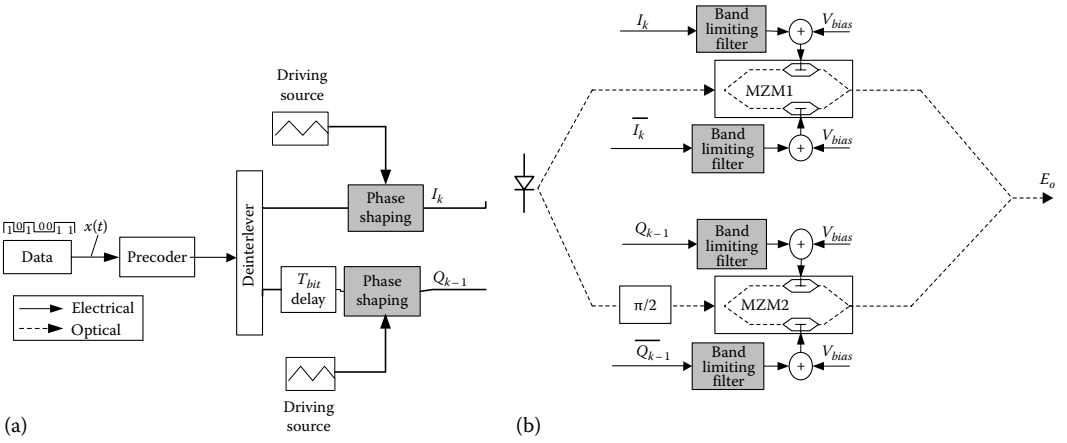

FIGURE 11.16
Block diagram of the *I*–*Q* MSK optical transmitter employing two dual-drive MZIMs: (a) general block structure and (b) device and signals.

These precoded *I* and *Q* data are operating at half the data bit rate. In this generation scheme, phase shaping filters can also be used for reducing the spectral width of driving signals before modulating the dual-drive MZIMs. In addition, two arms of the dual-drive MZIMs are biased at $V_\pi/2$ and $-(V_\pi/2)$ and driven by push–pull driving voltages, that is, *data* and $\overline{data}$.

The phase shaping driving source can be either a periodic ramp source in the case of a linear MSK or, preferably, a sinusoidal source for nonlinear optical MSK. By using sinusoidal waveforms, the hardware complexity for implementing this *I*–*Q* MSK optical transmitter scheme is significantly reduced. This is the main motivation for generating weakly nonlinear and strongly nonlinear types of optical MSK signals. The waveform amplitude of nonlinear MSK optical signals is fluctuating, and this ripple level depends on the magnitude of the electrical sinusoidal driving source. The main properties in the generation of linear and nonlinear optical MSK signals are described in the following text.

Linear MSK

The phase shaping signal to drive the dual-drive MZIMs is a periodic ramp signal with a duty cycle of 4*T*. The *Q* driving path is delayed by one bit period with respect to the I path. Optical MSK signals are obtained at the output of two MZIMs as the superposition of *I* and *Q* modulated signals and generated MSK waveforms clearly display the constant amplitude characteristic of the CPM format. In addition, its signal trajectory is a perfect circle. These characteristics are illustrated in Figure 11.17a.

Weakly Nonlinear MSK

The generation of a weakly nonlinear MSK format requires a sinusoidal driving signal having the amplitude of about $V_\pi/4$ and operating at half the data bit rate. The I phase pulse shaper is a cosine waveform while the *Q* counterpart is a sine waveform. The time-domain variation of the carrier phase is thus nonlinear. As a result, this causes a mismatch between two MZIMs when *I* and *Q* waveforms are superimposed, resulting in the ripples on generated optical MSK waveforms. The signal trajectory is thus not a perfect circle. The magnitude ripples of weakly nonlinear optical MSK waveforms are less than 10% of the push–pull signal levels. All of the aforementioned characteristics are illustrated in Figure 11.17b.

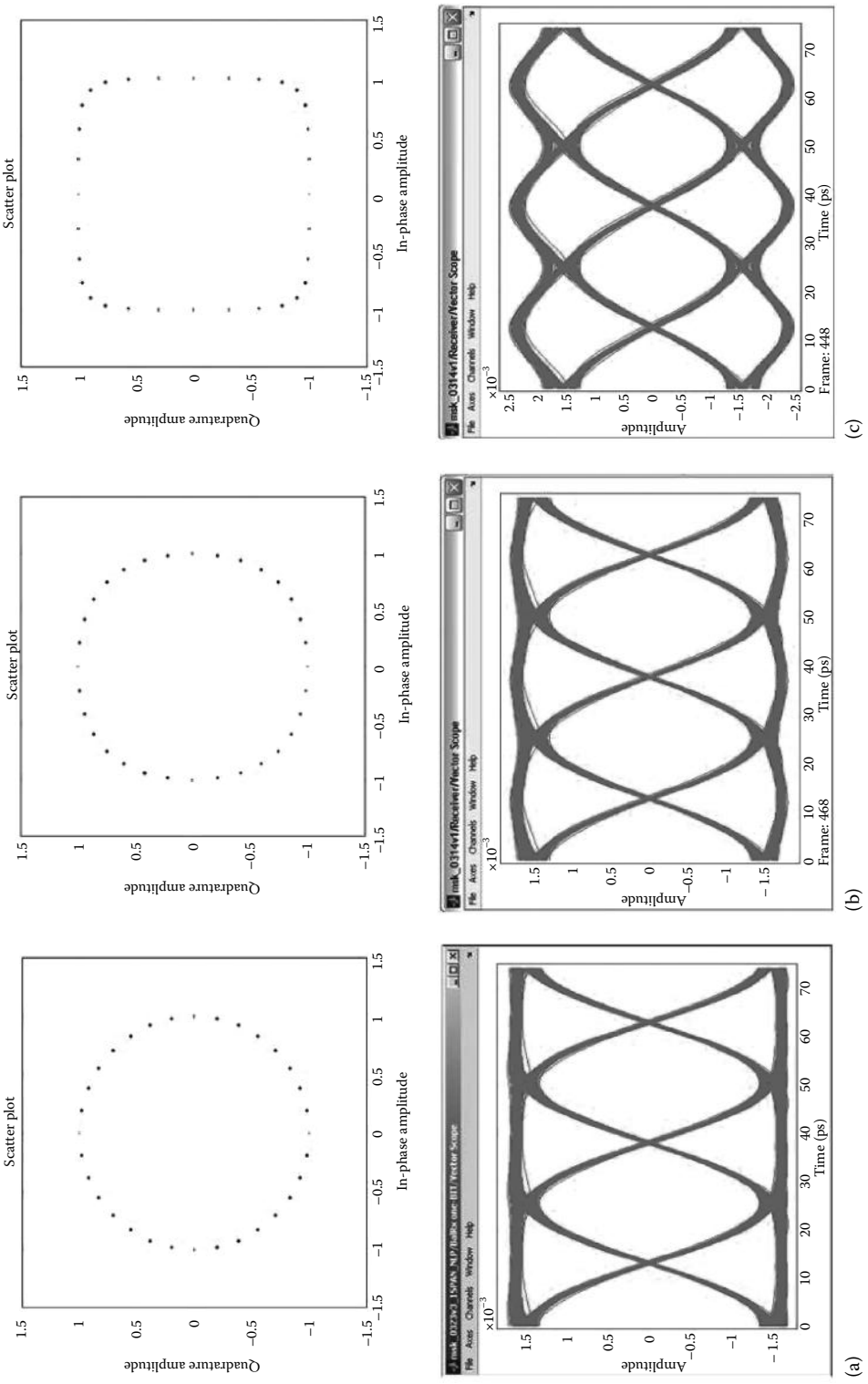

FIGURE 11.17
Signal constellation and eye diagrams of MSK optical signals: (a) linear, (b) weakly nonlinear, and (c) strongly nonlinear types.

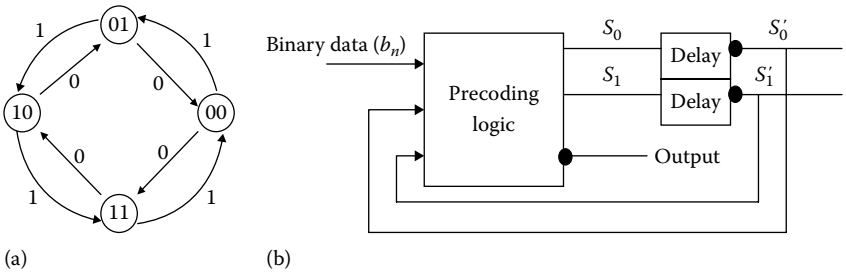

FIGURE 11.18
(a) State diagram for MSK (the arrows indicate continuous increment or decrement of the phase of the carrier), and (b) combinational logic for constructing the truth table of the precoder.

Strongly Nonlinear MSK
Sinusoidal phase shaping waveforms are also used for generating strongly nonlinear MSK optical signals. However, the magnitude of this driving signal is close to V_π compared to $V_\pi/4$ in the case of weakly nonlinear MSK. Strongly nonlinear optical MSK signals have the amplitude ripples of above 10% of the push–pull signal levels. This fluctuation is also caused by the mismatch of the waveforms on two arms at the output of the MZIMs. Figure 11.17c illustrates the signal trajectory and the ripples of strongly nonlinear optical MSK signals.

Precoder
The logic operations of the precoder are constructed based on a state diagram as shown in Figure 11.18a.

It can be observed that the current state of the signal is dependent on the previous state. Therefore, memory is needed to store the previous state. The state diagram in Figure 11.18a is then developed into a logic state diagram demonstrated in Figure 11.18b. In this case, S_0, S_1 and S_0', S_1' represent current states and previous states, respectively. The precoding logic block computes the current state and the output based on the feedback state (previous state) and binary data (b_n) from the bit pattern generator. Hence, a Karnaugh map is constructed to derive the logic gates within the precoding logic block:

$$\begin{aligned} S_0 &= \overline{b_n}\,\overline{S_0'}\,\overline{S_1'} + b_n\overline{S_0'}S_1' + \overline{b_n}S_0'S_1' + b_nS_0'\overline{S_1'} \\ S_1 &= \overline{S_1'} = \overline{b_n}\,\overline{S_1'} + b_n\overline{S_1'} \\ Output &= \overline{S_0} \end{aligned} \tag{11.15}$$

The truth table (Table 11.1) is then constructed. For a positive half cycle cosine wave and a positive half cycle sine wave, the output is "1," whereas for a negative half cycle cosine wave and a negative half cycle sine wave, the output is "0".

11.5.3 Incoherent Detection of Optical MSK

11.5.3.1 MZDI Balanced Receiver

Similar to the optical DPSK, an MZDI balanced receiver is used for the direct detection of MSK-modulated optical signals (see Figure 11.19). However, the main difference in this

TABLE 11.1

Truth Table Based on MSK State Diagram

$b_n S_0' S_1'$	$S_0 S_1$	Output
100	01	1
001	00	1
010	01	1
101	10	0
110	11	0
111	00	1
000	11	0
011	10	0

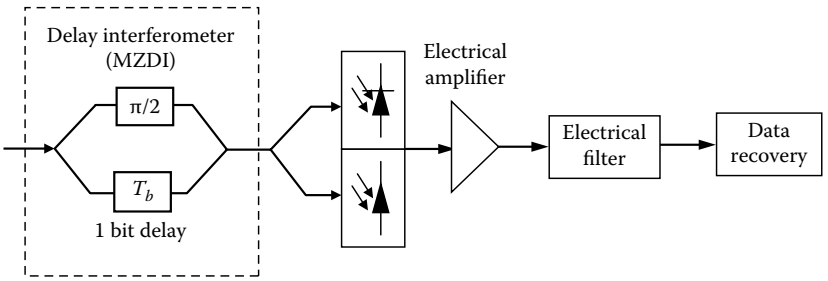

FIGURE 11.19
MZDI balanced receiver for incoherent detection of optical MSK signals.

MZDI configuration compared to that of the DPSK counterpart is an additional π/2 phase shift inserted on one arm of the MZDI [14,17,32,33]. This π/2 phase shift can be located on either arm of the MZDI.

11.5.3.2 Optical Frequency Discrimination Receiver

The detection of optical MSK signals using frequency discrimination principles was studied in the early 1990s, mainly for heterodyne coherent receivers [23,34–37]. The frequency discrimination was conducted in the electrical domain, at the intermediate frequency (IF) range. The noncoherent frequency discrimination in photonic domain for the direct detection of MSK lightwaves could not be effectively implemented at that time because of the unavailability of optical filters with very narrow bandwidths (a fraction of the signal bandwidth).

However, with recent advances in the design and fabrication of optical filters, in particular using micro-ring resonator type, the 3 dB bandwidth of optical filters can be narrowed down to around 2 GHz [38–40]. The availability of such narrowband optical filters thus enables the feasibility of the noncoherent optical frequency discrimination for detecting modulated frequencies of optical MSK signals. An implementable receiver scheme employing dual narrowband optical filters and an optical delay line is proposed in this research for optical MSK transmission systems. Detailed descriptions on the design and performance characteristics of this receiver are provided in Chapter 6.

11.6 Dual-Level MSK

11.6.1 Theoretical Background

Dual-level MSK is a multilevel scheme encoding two data bits into a modulated symbol. One of the information bits is for coding amplitude levels, whereas the other is for the linear phase trellis coding of $\pm\pi/2$ phase change within one symbol period. Therefore, the transmission baud rate is halved compared to the bit rate from the data pattern generator. This clearly offers the transmission bandwidth efficiency as well as significantly reduces the requirement of high-speed electronic processing. Figure 11.20 illustrates the signal constellation of dual-level MSK format.

The mapping scheme of data information a and b in dual-level MSK is shown in Table 11.2.

The dual-level MSK modulation format can be generated from the superposition of two MSK signals having different amplitudes, given by [10]

$$s(t) = A\cos\left(2\pi f_c t + \phi_n(t,a)\right) + B\cos\left(2\pi f_c t + \phi_n(t,b)\right) \tag{11.16}$$

where

f_c is the frequency carrier

A and B are signal amplitude levels

At the transition of the nth symbol interval, these two amplitudes are either in-phase or π-phase shift with each other. The phase terms $\phi_n(t,a)$ and $\phi_n(t,b)$ are defined as

$$\phi_n(t,a) = \pi h\frac{a_n(t-nT)}{T} + \pi h\sum_{k=-\infty}^{n-1} a_k \quad nT \le t \le (n+1)T \tag{11.17}$$

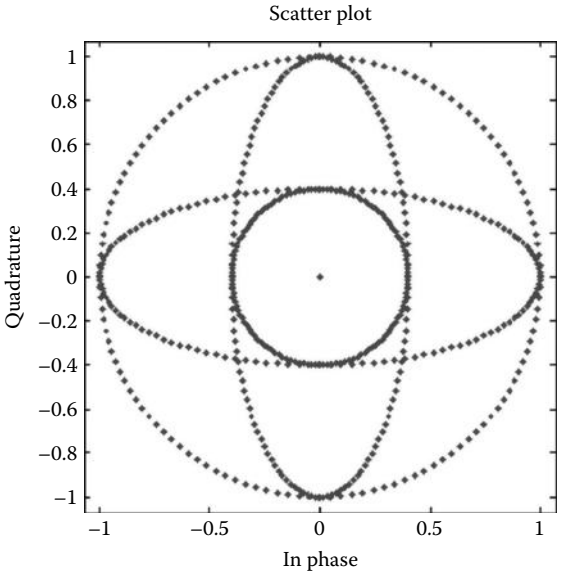

FIGURE 11.20
Signal constellation of dual-level MSK.

TABLE 11.2

Mapping of Data Information in Dual-Level MSK Format

a	*b*	**Remarks on Signal Constellation**
1	1	Amplitude unchanged, phase increased
1	–1	Amplitude unchanged, phase decreased
–1	1	Amplitude changed, phase increased
–1	–1	Amplitude changed, phase decreased

$$\phi_n(t,b) = \pi h \frac{b_n(t-nT)}{T} + \pi h \sum_{k=-\infty}^{n-1} b_k \quad nT \le t \le (n+1)T \tag{11.18}$$

The logic values a_n and b_n are statistically independent and taken from the set of {±1}. The frequency modulation index h of the dual-level MSK is equal to 1/2.

Precoder

A precoder is compulsory for the generation of dual-level MSK signals. At the nth instance, the logic values of a_n and b_n taken from {±1} are precoded from the binary logics d and d' as follows:

$$\begin{aligned} a_n &= 2d_n - 1 \\ b_n &= a_n\left(1 - \frac{d'_n}{h}\right) \end{aligned} \tag{11.19}$$

where the logics d and d' are statistically independent and taken from {0,1}.

11.6.2 Proposed Generation Scheme

Any configuration of MSK optical transmitters presented in Section 11.3.4 or reported in some previous research [12,14,17,32] can be used for the following proposed generation of dual-level MSK optical signals. Figure 11.21 shows the block diagram of a dual-level MSK optical transmitter in which two MSK optical transmitters are arranged in a parallel configuration.

It can be seen from Figure 11.21 as well as from Equations 11.16 that the amplitude levels A and B, which are input into the two MSK optical transmitters, play significant roles in the proposed generation scheme as they determine the amplitude levels of the transmitted

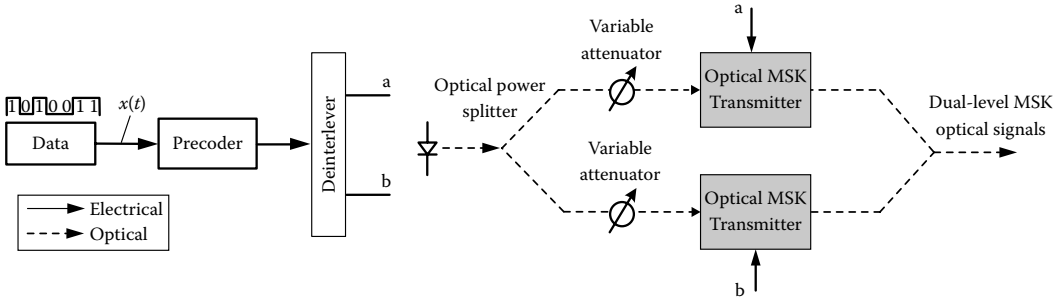

FIGURE 11.21
Block diagram of the proposed dual-level MSK optical transmitter.

dual-level MSK optical signals. In practice, optical components are normally specified by the optical intensity rather than the magnitude of the optical field. Thus, we consider the optical powers input into the two MSK optical transmitters rather than the amplitude levels *A* and *B*. Moreover, the splitting ratio between these two optical powers is more important than their individual values. This intensity-splitting ratio can be obtained by using a high-precision optical power splitter or simply by using a 3 dB or a 50:50 optical power splitter followed by a variable optical attenuator on each path.

11.6.3 Incoherent Detection of Optical Dual-Level MSK

As a combination between optical MSK and multilevel modulation formats, the demodulation of dual-level MSK optical signals requires the incoherent detection of both amplitude and phase components, as shown in Figure 11.22.

Similar to an optical MSK, an MZDI balanced receiver is implemented for the phase detection and an additional π/2 phase shift is also inserted on one arm of MZDI. On the other hand, the lightwave amplitude is detected by a single photo detector. It should be noted that a differential decoder is required to detect the amplitude changes between two consecutive bits (refer to Table 11.2). Detected eye diagrams for the amplitude and phase detections of dual-level MSK received signals are demonstrated in Figure 11.23a and b. In these figures, the dotted line represents the decision threshold voltage.

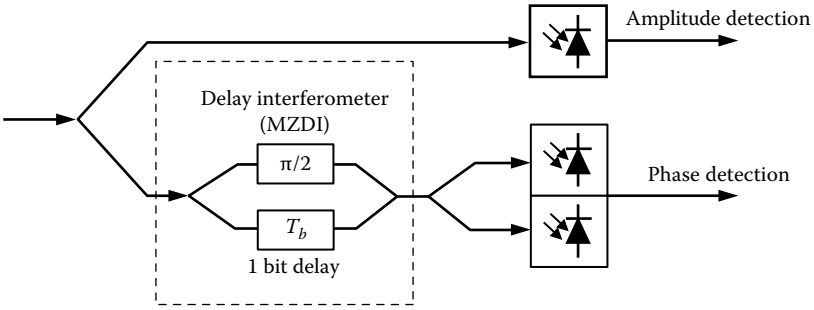

FIGURE 11.22
Incoherent detection for both amplitude and phase of dual-level MSK optical signals.

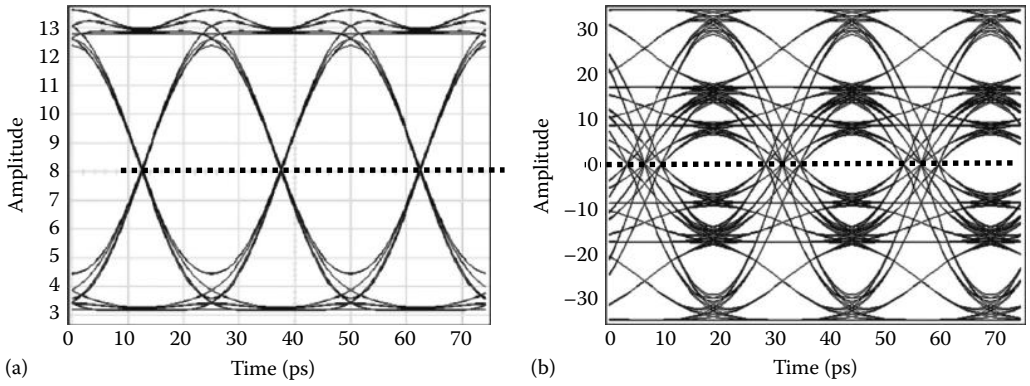

FIGURE 11.23
Eye diagrams for (a) amplitude and (b) phase detection of dual-level MSK received signals. The decision threshold is plotted in broken-line style.

It can be observed that the phase detection of dual-level MSK gives a push–pull eye diagram having multiple levels. However, the interest is only on either the positive or the negative attribute of these levels, which corresponds to either the zero phase or π phase change, respectively. Thus, the threshold level for the phase detection is set at zero level, whereas the amplitude threshold is a nonzero value to distinguish between the two modulated signal levels.

11.7 Spectral Characteristics of Advanced Modulation Formats

Optical power spectra of 40 Gb/s NRZ/RZ33/CS-RZ DPSK and OOK optical signals are shown in Figures 11.24 and 11.25, respectively.

Several main points observed in Figures 11.24 and 11.25 are as follows:

- The optical power spectra of OOK formats have high-power components at the carrier and signal frequencies, thus causing fiber nonlinear effects. On the contrary, DPSK spectra do not contain high power frequency components. Therefore, optical DPSK formats are more resistant to fiber nonlinear effects.
- RZ pulses are more susceptible to fiber CD because of their broader spectra compared to NRZ pulses. In particular, RZ33 type has the broadest spectrum (at 20 dB position down from the peak) and thus, RZ33 is least tolerant to fiber CD.

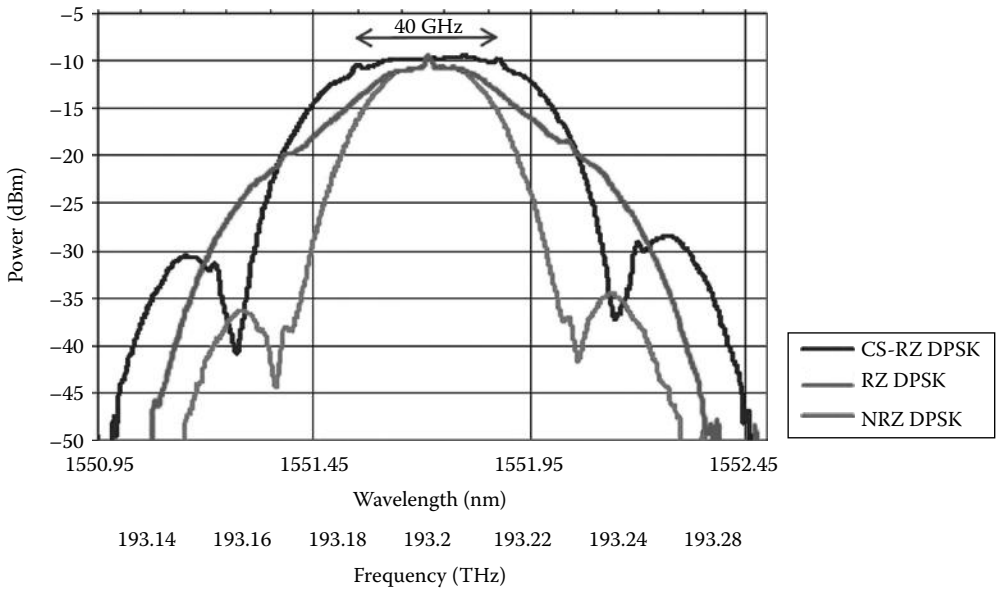

FIGURE 11.24
Spectra of 40 Gb/s CS-RZ/RZ33/NRZ DPSK optical signals.

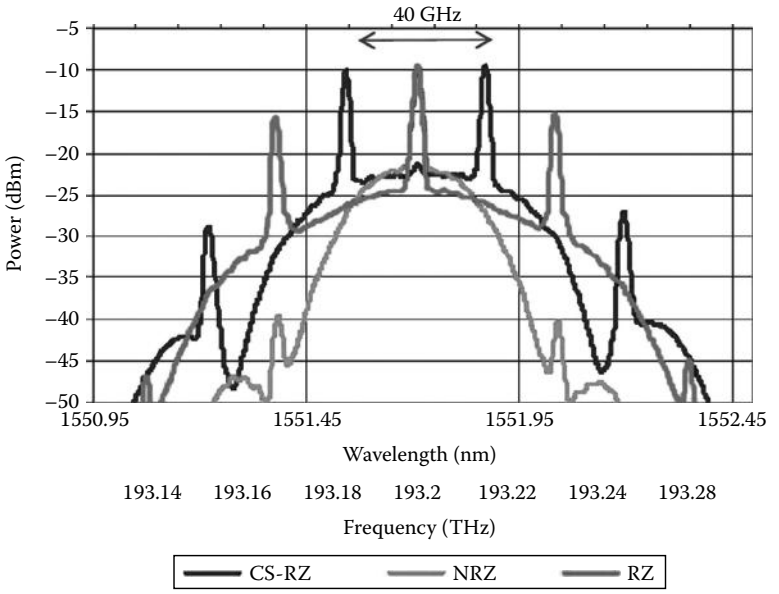

FIGURE 11.25
Spectra of 40 Gb/s CS-RZ/RZ33/NRZ OOK optical signals.

- However, the susceptibility of RZ33 and CS-RZ pulses to fiber CD provides a trade-off in the improvement of the resistance to fiber nonlinearities. This is because time-domain peaks of these fast spreading optical pulses decrease rapidly when propagating along the fiber, hence lowering effects of fiber nonlinearities.

Optical power spectra of 40 Gb/s linear, weakly nonlinear, and strongly nonlinear MSK formats are compared in Figure 11.26. It can be observed that these formats' power spectra are similar, with the exception point that side lobes in the power spectrum of strongly-nonlinear MSK are not highly suppressed as in the case of linear and weakly nonlinear MSKs. All three formats offer better spectral efficiency compared to the DPSK counterpart.

Figure 11.27 compares the power spectra of three modulation formats: 80 Gb/s dual-level MSK, 40 Gb/s linear MSK, and 40 Gb/s NRZ DPSK. The intensity-splitting ratio for the optical dual-level MSK format is set at "0.8/0.2".

A number of key points are observed:

- The signal power spectrum of 80 Gb/s optical dual-level MSK has identical characteristics to that of the 40 Gb/s MSK format. The main lobe spectral widths of these two formats are narrower than that of NRZ DPSK. More specifically, the base width takes a value of approximately ±32 GHz on either side compared to ±40 GHz in the case of DPSK. Hence, it is expected that these MSK-based formats are more tolerant to fiber CD and more robust to tight optical filtering than NRZ DPSK.
- High suppression of side lobes and the confinement of signal energy in the main spectral lobe of 80 Gb/s dual-level MSK and 40 Gb/s MSK optical power spectra significantly mitigate interchannel cross talks between DWDM channels.

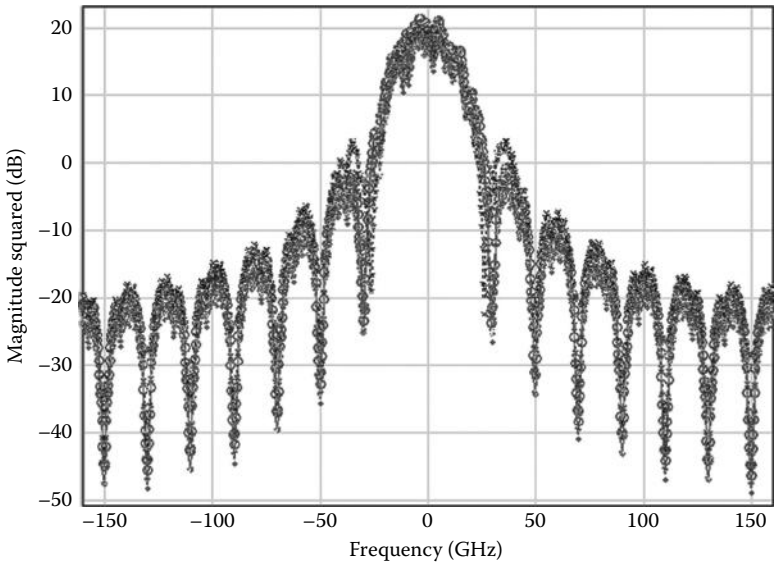

FIGURE 11.26
Optical power spectra of three 40 Gb/s optical MSK formats: linear (light gray), weakly nonlinear (mid gray), and strongly nonlinear (dark gray).

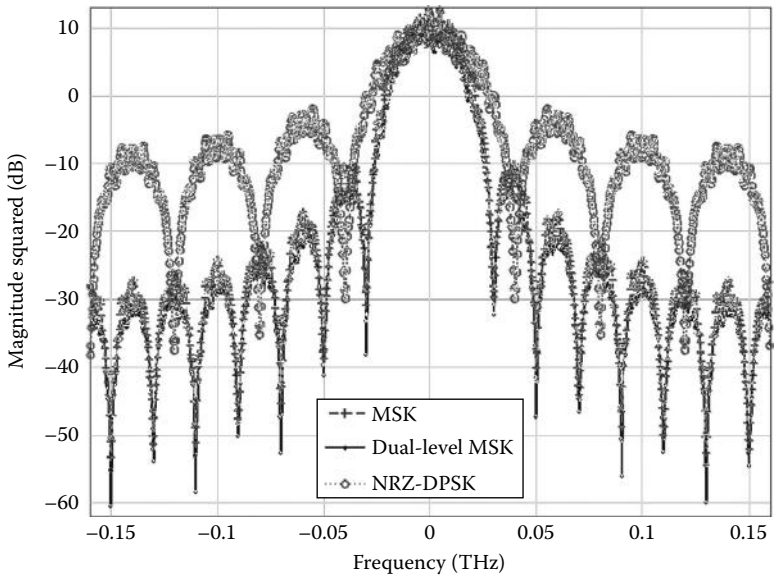

FIGURE 11.27
Spectral properties of three modulation formats: 40 Gb/s MSK (light gray, dash), 80 Gb/s dual-level MSK (dark gray, solid), and 40 Gb/s NRZ DPSK (mid gray, dot).

11.8 Summary

This chapter presents the principles for generating RZ33 and CS-RZ optical pulses. The phasor representation providing a clear explanation of the modulation process was verified mathematically. The generation and detection of optical DPSK signals were also described.

This chapter proposes two novel MSK optical transmitter schemes. The first scheme is based on the CPFSK approach and implements two cascaded electro-optic phase modulators. The second scheme consists of two dual-drive MZIMs, reflecting the *I*–*Q* configuration of the ODQPSK format. These *I* and *Q* driving signals are staggered by one bit period and operate at half the bit rate. This scheme can generate either linear or nonlinear type of optical MSK pulses. Nonlinear optical MSK signals are identified based on the magnitude of the ripple levels of transmitted waveforms. Optical MSK signals with a small ripple of less than 10% of the push–pull amplitude levels are referred to as weakly nonlinear type, whereas ripples of more than 10% of the signal levels are observed on strongly nonlinear optical MSK waveforms. Key differences in the implementations of these MSK optical transmitters are the waveforms and the magnitudes of the phase shaping electrical driving signals. In the case of linear MSK, periodic ramp waveforms are used, whereas sinusoidal waveforms are used for generation of weakly nonlinear and strongly nonlinear MSKs. In order to generate weakly nonlinear MSK optical pulses, sinusoidal waveforms have an amplitude of approximately $V_\pi/4$ compared to a value of close to V_π in the case of strongly nonlinear optical MSK. The precoder for I–Q optical MSK structure was also derived. The incoherent detection of MSK-modulated optical signals is based on the MZDI balanced receiver. The main difference in this MSK, receiver compared to the DPSK is the additional $\pi/2$ phase shift inserted into one arm of the MZDI.

The dual-level MSK format has been proposed for fiber-optic communications. The optical transmitter of this format is constructed from two MSK optical transmitters arranged in a parallel structure while the demodulation requires the noncoherent detection of both amplitude and phase components of the light waves. The phase detection for dual-level MSK format is similar to that of optical MSK, whereas the amplitude detection is simply implemented with a single photo detector.

Finally, spectral properties of optical 80 Gb/s dual-level MSK, 40 Gb/s MSK, and 40 Gb/s NRZ/RZ33/CS-RZ DPSK, and OOK formats were discussed. There is a trade-off between RZ33/CS-RZ and NRZ pulse types. Compared to NRZ pulses, RZ33 and CS-RZ pulses are more resistant to fiber nonlinear effects but less tolerant to fiber CD. The spectral properties of 40 Gb/s MSK and 80 Gb/s dual-level MSK are similar to each other and more advantageous than 40 Gb/s optical DPSK and OOK. These advantages include (1) the spectral efficiency and filtering robustness because of the narrow spectral main lobe and (2) the mitigation of interchannel cross talks because of high suppression of side lobes. Therefore, optical MSK and dual-level MSK formats offer promising potential for high-speed and high-capacity optical long-haul and metropolitan transmission systems.

References

1. I.P. Kaminow and T. Li, *Optical Fiber Communications, Volume IVB*, Elsevier Science, New York, 2002.
2. R.S. Sanferrare, Terrestrial lightwave systems, *AT&T Technology Journal*, 66, 95–107, 1987.
3. C. Lin, H. Kogelnik, and L.G. Cohen, Optical pulse equalization and low dispersion transmission in single-mode fibers in the 1.3–1.7 μm spectral region, *Optics Letters*, 5, 476–478, 1980.

4. A.H. Gnauck, S.K. Korotky, B.L. Kasper, J.C. Campbell, J.R. Talman, J.J. Veselka, and A.R. McCormick, Information bandwidth limited transmission at 8 Gb/s over 68.3 km of single mode optical fiber, in *Proceedings of OFC'86*, Atlanta, GA, paper PDP6, 1986.
5. H. Kogelnik, High-speed lightwave transmission in optical fibers, *Science*, 228, 1043–1048, 1985.
6. G.P. Agrawal, *Fiber-Optic Communication Systems*, 3rd ed.,John Wiley & Sons, New York, 2002.
7. A.R. Chraplyvy, A.H. Gnauck, R.W. Tkach, and R.M. Derosier, 8 × 10 Gb/s transmission through 280 km of dispersion-managed fiber, *IEEE Photonics Technology Letters*, 5, 1233–1235, 1993.
8. H. Kogelnik, High-capacity optical communications: Personal recollections, *IEEE Journal on Selected Topics in Quantum Electronics*, 6(6), 1279–1286, November/December 2000.
9. C.R. Giles and E. Desurvire, Propagation of signal and noise in concatenated erbium-doped fiber amplifiers, *IEEE Journal of Lightwave Technology*, 9(2), 147, 1991.
10. P.C. Becker, N.A. Olsson, and J.R. Simpson, *Erbium-Doped Fiber Amplifiers, Fundamentals and Technology*, Academic Press, San Diego, CA, 1999.
11. T. Okoshi, Heterodyne and coherent optical fiber communications: Recent progress, *IEEE Transactions on Microwave Theory and Techniques*, 82(8), 1138–1149, 1982.
12. T. Okoshi, Recent advances in coherent optical fiber communication systems, *IEEE Journal of Lightwave Technology*, 5(1), 44–52, 1987.
13. J. Salz, Modulation and detection for coherent lightwave communications, *IEEE Communications Magazine*, 24(6), 38–49, 1986.
14. T. Okoshi, Ultimate performance of heterodyne/coherent optical fiber communications, *IEEE Journal of Lightwave Technology*, 4(10), 1556–1562, 1986.
15. P.S. Henry, *Coherent Lightwave Communications*, IEEE Press, New York, 1990.
16. A.F. Elrefaie, R.E. Wagner, D.A. Atlas, and A.D. Daut, Chromatic dispersion limitation in coherent lightwave systems, *IEEE Journal of Lightwave Technology*, 6(5), 704–710, 1988.
17. M.C. Farries, P.R. Morkel, R.I. Laming, T.A. Birks, D.N. Payne, and E.J. Tarbox, Operation of erbium-doped fiber amplifiers and lasers pumped with frequency-doubled Nd:YAG lasers, *IEEE Journal of Lightwave Technology*, 7(10), 1473–1477, 1989.
18. G. Charlet et al., Comparison of system performance at 50, 62.5 and 100 GHz channel spacing over transoceanic distances at 40 Gbit/s channel rate using RZ-DPSK, *Electronics Letters*, 41(3), 145–146, 2005.
19. P.S. Cho, V.S. Grigoryan, Y.A. Godin, A. Salamon, and Y. Achiam, Transmission of 25-Gb/s RZ-DQPSK signals with 25-GHz channel spacing over 1000 km of SMF-28 fiber, *IEEE Photonics Technology Letters*, 15(3), 473–475, 2003.
20. K. Ishida, T. Kobayashi, J. Abe, K. Kinjo, S. Kuroda, and T. Mizuochi, A comparative study of 10 Gb/s RZ-DPSK and RZ-ASK WDM transmission over transoceanic distances, in *Proceedings of OFC'03*, Atlanta, GA, vol. 2, pp. 451–453, 2003.
21. W.A. Atia and R.S. Bondurant, Demonstration of return-to-zero signaling in both OOK and DPSK formats to improve receiver sensitivity in an optically preamplified receiver, in *Proceedings of IEEE LEOS'99*, Enschede, the Netherlands, vol. 1, pp. 226–227, 1999.
22. G. Bosco, A. Carena, V. Curri, R. Gaudino, and P. Poggiolini, On the use of NRZ, RZ, and CSRZ modulation at 40 Gb/s with narrow DWDM channel spacing, *IEEE Journal of Lightwave Technology*, 20(9), 1694–1704, 2002.
23. A.H. Gnauck, G. Raybon, P.G. Bernasconi, J. Leuthold, C.R. Doerr, and L.W. Stulz, 1-Tb/s (6/spl times/170.6 Gb/s) transmission over 2000-km NZDF using OTDM and RZ-DPSK format, *IEEE Photonics Technology Letters*, 15(11), 1618–1620, 2003.
24. B. Zhu, L.E. Nelson, S. Stulz, A.H. Gnauck, C. Doerr, J. Leuthold, L. Gruner-Nielsen, M.O. Pedersen, J. Kim, and R.L. Lingle, Jr., High spectral density long-haul 40-Gb/s transmission using CSRZ-DPSK format, *IEEE Journal of Lightwave Technology*, 22(1), 208–214, 2004.
25. A. Hirano, Y. Miyamoto, and S. Kuwahara, Performances of CSRZ-DPSK and RZ-DPSK in 43-Gbit/s/ch DWDM G.652 single-mode-fiber transmission, in *Proceedings of OFC'03*, Anaheim, CA, vol. 2, pp. 454–456, 2003.

26. L.N. Binh and T.L. Huynh, Linear and nonlinear distortion effects in direct detection 40 Gb/s MSK modulation formats multi-span optically amplified transmission, *Optics Communications*, 237(2), 352–361, May 2007.
27. J. Mo, D. Yi, Y. Wen, S. Takahashi, Y. Wang, and C. Lu, Optical minimum-shift keying modulator for high spectral efficiency WDM systems, in *Proceedings of ECOC'05*, Glasgow, U.K., vol. 4, pp. 781–782, 2005.
28. J. Mo, Y.J. Wen, Y. Dong, Y. Wang, and C. Lu, Optical minimum-shift keying format and its dispersion tolerance, in *Proceedings of OFC'05*, Anaheim, CA, paper JThB12, 2005.
29. M. Ohm and J. Speidel, Optical minimum-shift keying with direct detection (MSK/DD), *Proceedings of SPIE on Optical Transmission, Switching and Systems*, 5281, 150–161, 2004.
30. T.L. Huynh, T. Sivahumaran, L.N. Binh, and K.K. Pang, Narrowband frequency discrimination receiver for high dispersion tolerance optical MSK systems, in *Proceedings of Coin-Acoft'07*, Melbourne, Victoria, Australia, paper TuA1-3, June 2007.
31. T.L. Huynh, T. Sivahumaran, L.N. Binh, and K.K. Pang, Sensitivity improvement with offset filtering in optical MSK narrowband frequency discrimination receiver, in *Proceedings of Coin-Acoft'07*, Melbourne, Victoria, Australia, paper TuA1-5, June 2007.
32. T. Sivahumaran, T.L. Huynh, K.K. Pang, and L.N. Binh, Non-linear equalizers in narrowband filter receiver achieving 950 ps/nm residual dispersion tolerance for 40 Gb/s optical MSK transmission systems, in *Proceedings of OFC'07*, Anaheim, CA, paper OThK3, 2007.
33. T. Sakamoto, T. Kawanishi, and M. Izutsu, Optical minimum-shift keying with external modulation scheme, *Optics Express*, 13, 7741–7747, 2005.
34. A.H. Gnauck and P.J. Winzer, Optical phase-shift-keyed transmission, *IEEE Journal of Lightwave Technology*, 23(1), 115–130, 2005.
35. J.A. Lazaro, W. Idler, R. Dischler, and A. Klekamp, BER depending tolerances of DPSK balanced receiver at 43 Gb/s, in *Proceedings of IEEE/LEOS Workshop on Advanced Modulation Formats 2004*, San Francisco, CA, pp. 15–16, 2004.
36. H. Kim and A.H. Gnauck, Experimental investigation of the performance limitation of DPSK systems due to nonlinear phase noise, *IEEE Photonics Technology Letters*, 15(2), 320–322, 2003.
37. S. Bhandare, D. Sandel, A.F. Abas, B. Milivojevic, A. Hidayat, R. Noe, M. Guy, and M. Lapointe, 2/spl times/40 Gbit/s RZ-DQPSK transmission with tunable chromatic dispersion compensation in 263 km fibre link, *Electronics Letters*, 40(13), 821–822, 2004.
38. T. Mizuochi, K. Ishida, T. Kobayashi, J. Abe, K. Kinjo, K. Motoshima, and K. Kasahara, A comparative study of DPSK and OOK WDM transmission over transoceanic distances and their performance degradations due to nonlinear phase noise, *Journal of Lightwave Technology*, 21(9), 1933–1943, 2003.
39. C. Xu, X. Liu, L.F. Mollenauer, and X. Wei, Comparison of return-to-zero differential phase-shift keying and ON-OFF keying in long-haul dispersion managed transmission, *IEEE Photonics Technology Letters*, 15(4), 617–619, 2003.
40. L.N. Binh and T.L. Huynh, Phase-modulated hybrid 40 Gb/s and 10 Gb/s DPSK DWDM long-haul optical transmission, in *Proceedings of OFC'07*, Anaheim, CA, paper JWA94, 2007.
41. T. Ito, K. Sekiya, and T. Ono, Study of 10 G/40 G hybrid ultra long haul transmission systems with reconfigurable OADM's for efficient wavelength usage, in *Proceedings of ECOC'02*, Copenhagen, Denmark, paper 1.1.4, 2002.
42. K. Iwashita and N. Takachio, Experimental evaluation of chromatic dispersion distortion in optical CPFSK transmission systems, *IEEE Journal of Lightwave Technology*, 7(10), 1484–1487, 1989.
43. J.G. Proakis, *Digital Communications*, 4th ed., McGraw-Hill, New York, 2001.
44. J.G. Proakis and M. Salehi, *Communication Systems Engineering*, 2nd ed., Prentice Hall, Inc., Upper Saddle River, NJ, pp. 522–524, 2002.
45. K.K. Pang, *Digital Transmission*, Mi-Tec Media Pty. Ltd., Melbourne, Victoria, Australia, 2005.
46. K. Iwashita and T. Matsumoto, Modulation and detection characteristics of optical continuous phase FSK transmission system, *IEEE Journal of Lightwave Technology*, 5(4), 452–460, 1987.
47. J. Mo, Y.J. Wen, and Y. Wang, Performance evaluation of externally modulated optical minimum shift keyed data, *Optical Engineering*, 46(3), 35001, 2007.

48. T.L. Huynh, L.N. Binh, and K.K. Pang, Optical MSK long-haul transmission systems, in *Proceedings of SPIE APOC'06*, Gwangju, Korea, paper 6353-86, Thu9a, 2006.
49. A.F. Elrefaie and R.E. Wagner, Chromatic dispersion limitations for FSK and DPSK systems with direct detection receivers, *IEEE Photonics Technology Letters*, 3(1), 71–73, 1991.
50. B.E. Little, Advances in microring resonator, in *Integrated Photonics Research Conference 2003*, Washington, DC, Invited Paper, 2003.
51. V. Van, B.E. Little, S.T. Chu, and J.V. Hryniewicz, Micro-ring resonator filters, in *Proceedings of LEOS'04*, Rio Grande, PR, vol. 2, pp. 571–572, 2004.
52. P.P. Absil, S.T. Chu, D. Gill, J.V. Hryniewicz, F. Johnson, O. King, B.E. Little, F. Seiferth, and V. Van, Very high order integrated optical filters, in *Proceedings of OFC'04*, Anaheim, CA, vol. 1, 2004.
53. B. Little, S. Chu, W. Chen, W. Chen, J. Hryniewicz, D. Gill, O. King et al., Advanced ring resonator based PLCs, lasers and electro-optics society, 2006. LEOS 2006. *19th Annual Meeting of the IEEE*, pp.751–752, October 2006.

12

Design of Optical Communications Systems

12.1 Introduction

12.1.1 Remarks

Chapters 2 through 6 have been dedicated to the study of optical fibers and their operation parameters, optical passive and active components, and the opto-electronic receivers as well as optical transmitters. An optical transmission system combines all these components with appropriate optical powers at the transmitter and at the receiver so as to satisfy the bit error rate (BER) requirement or the optical signal-to-noise ratio (OSNR). Shown in Figure 12.1a is the basic structure of the transmission system of multispan and multiwavelength channels with midspan optical amplifiers in bidirectional arrangement. Figure 12.1b and c also shows the working fiber and protection fiber structures including add/drop mux insertion.

This chapter gives a general approach to the design of optical transmission systems, especially when optical fibers are used as the transmission medium. Both nondispersion compensating fibers and compensating fibers employed in the transmission systems are described.

Readers may consider summarizing the transmission properties of various photonic and optical components that make up the transmission system, in particular, their insertion losses and dispersion factors as well as spectral properties. For example, for optical amplifiers one needs to know the minimum input power level, the optical gain, the saturated output power level, and the noise figure. Naturally, for single-mode optical fibers one needs the dispersion factor and the attenuation factor as well as the nonlinear threshold and factor. We must possess the details of the optical components and their the parameters essential for systems design considerations. Simulink® models are based on the operational principles of each component, which are formed by blocks. These blocks are interconnected together to form a transmission system. The principles of operations of each physical component are very important and must be represented faithfully in Simulink to obtain accurate simulation results.

The next section gives generic outlines of the design strategy for transmission systems, followed by a detailed study of the attenuation and dispersion budget for different optical transmission structures. First, a single-span transmission system is developed followed by multispan optical amplified fiber transmission systems. The techniques for generation of the dispersion and power budget are given for unidirectional and bidirectional

transmissions. Some typical design examples are given (see Figure 12.1a and b) for bidirectional transmission of dense wavelength division multiplexing (DWDM) channels in the same fiber. Bidirectional transmission means that the wavelength channels are transmitted and received from both ends of the fiber link. Some optical components such as optical circulators are required for routing the lightwave channels. Figure 12.1c and d shows the arrangement of bidirectional amplification and transmitter, respectively.

It is noted that only digital systems are described in this chapter using both intensity modulation and direct detection (IM/DD). Advanced, optically amplified transmission systems employing coherent detection or direct detection under external modulation formats, such as differential phase shift keying (DPSK), ASK, and FSK, are also given accompanied by samples of Simulink models, which can be downloaded from the website of CRCPress.com. Readers are asked to contact the publisher for further details.

12.1.2 Structure of DWDM Long-Haul Transmission Systems

As shown in Figure 12.1a, at the transmitting side a number of wavelength transmitters are employed to accept input data channels from different clients. The wavelengths of the optical carriers to transport these data channels are currently assigned to the grids in C-band and L-band if necessary. These grids can be displayed as tabulated in Table 12.2. Currently, flexible grids in the C-band and L-band are under intense discussions so as to accommodate different bandwidth channels carrying ultra-high bit rates such as 400 G and Tbp/s [1–3]. Under current optical networks, the wavelengths of the channels are assigned to a fixed spacing grid of 500 or 100 GHz, which is equivalent at 1550 nm to 0.4 or 0.8 nm, respectively, in the wavelength scale. Note also that the spacing must be specified in the frequency scale, which is unchanged and not in the wavelength scale because the wavelength is changed.

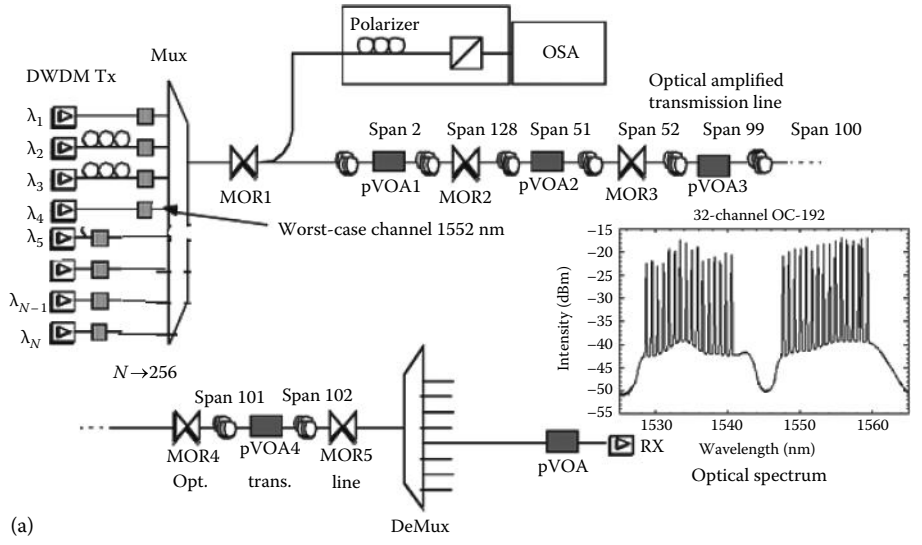

FIGURE 12.1
Optical transmission link with mid-spans and optical amplifiers—bidirectional transmission in fibers and multiwavelength channels, and (a) basic structure for DWDM channels—insert is the spectra of DWDM channels (*Continued*)

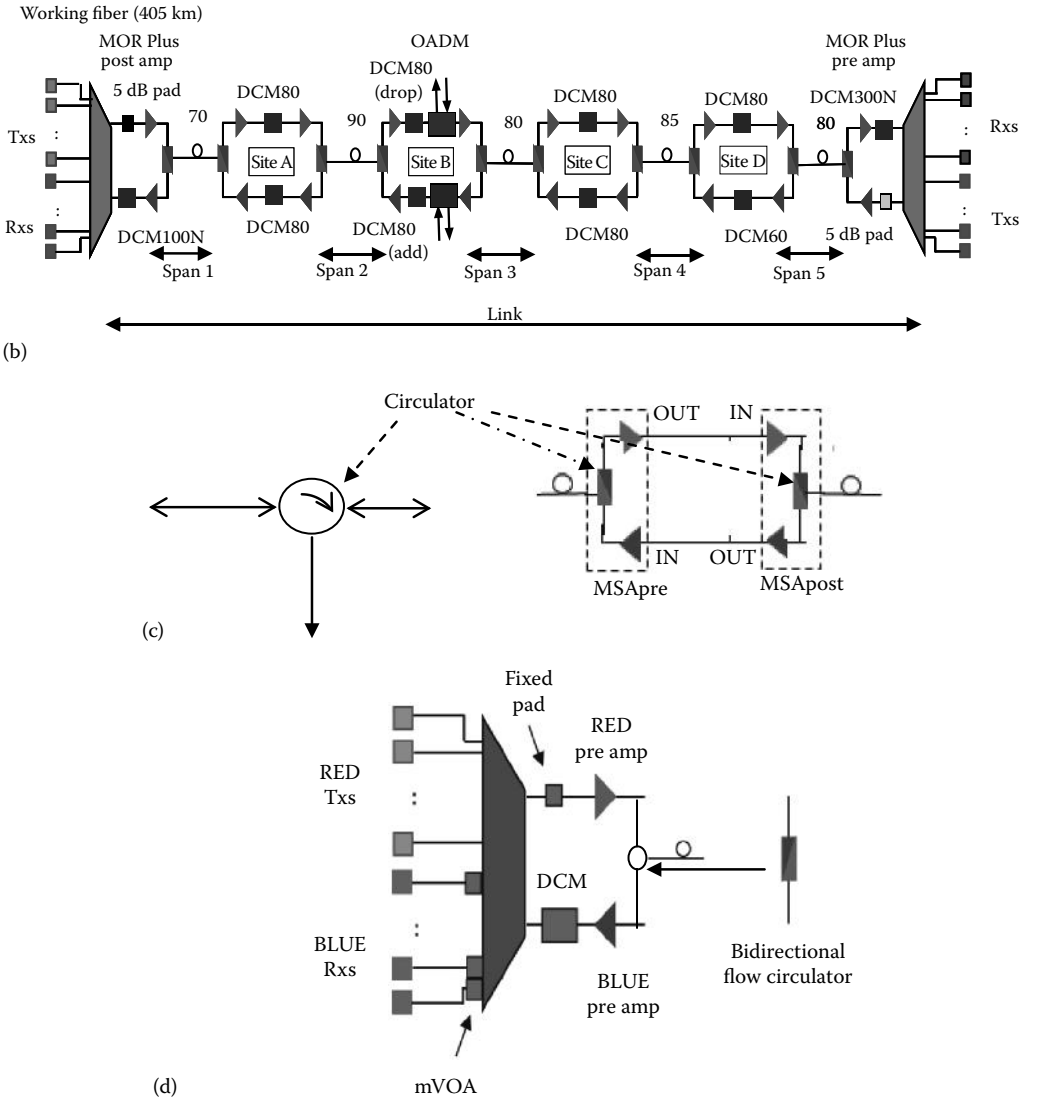

FIGURE 12.1 (*Continued*)
Optical transmission link with mid-spans and optical amplifiers—bidirectional transmission in fibers and multiwavelength channels (b) 405 km fiber structures. MOR = midspan optical repeater, DCM = dispersion compensating modules, DCMxxx = compensating module for xxx km of SSMF, Pad = adjustable optical attenuator. (c) Arrangement of optical amplifiers—mid-span amplifier (MSA) for bidirectional amplification. (d) Details of bidirectional transmitter. MSAPre and MASPost = pre- and postoptical midspan amplification.

The DWDM channels are then combined via an array wavelength grating (AWG) device and then launched into the optical transmission lines after passing through a midspan optical amplifier/regenerator (MOR). The total average optical power of all channels must be below the nonlinear self phase modulation (SPM) threshold of about 10 dBm so that no nonlinear impairments are suffered by the transmitted channels. A fiber coupler would be used at the location of launch to monitor the channel spectrum

and the total power launched into the fiber line. The optical transmission line consists of a number of cascade optical amplified spans. Each span may compose a transmission fiber and a dispersion compensating fiber (DCF) in association with an optical amplifier EDFA at the end of the transmission fiber to compensate for its attenuation and then another optical amplifier to boost up the power to launch into the DCF as shown in Figure 12.1c. The optical power at the output of each span is designed so that it is the same level as at the input so that when cascading to the next span the behavior is the same for all spans, except in different odd spans the design of the optical power may vary. For a two-way transmission or bidirectional transmission, two optical circulators may be used as shown in Figure 12.1c. Figure 12.1b shows the structure of the bidirectional transmission system. An optical circulator works, by accepting the input at one port and sending the output to the next port in clockwise direction. Thus, a three-port optical circulator would in turn accept lightwave input in one port and then circulate to the next port and so on. When bidirectional transmission is structured, then two wavelength bands are assigned, one marked as "red" and the other one marked as "blue" as shown in Figure 12.1d. Furthermore, variable optical attenuators (VOA) are used to ensure that the optical power launched into the fiber or the receiver is at an appropriate level. Sometimes, the attenuation pad or fixed optical attenuators are used to adjust the power level. Along the optical transmission line, there are possibilities that a number of optical channels may be dropped or inserted via the optical add/drop mux (OADM) or reconfigurable OADM (ROADM) as indicated in Figure 12.1b.

In the next section, the design of optically amplified span with and without dispersion compensating module (DCM) is described. DCM is used in association with a number, for example, DCM80 implies that the module dispersion factor is equal to the dispersion of 80 km SSMF or 80 km × 17 ps/(nm · km) or 1360 ps/nm. The length of the fiber in each span is normally 80 km whose attenuation is 20 dB. This attenuation can be equalized by the gain or typical EDFA. The reason for selection of 80 km is also to fit the typical distance of repeater housing in early optical transmission systems of the 1980s for single-mode fiber without optical amplifiers. At that time, the repeater distance was determined at 40 km for IM/DD and bit rate was normally at 155 or 622 Gb/s. There were many repeater sites built for such housing, and hence it is more economical to design the span length of 80 km to take advantage of these housing infrastructures.

Over the last decade of the twentieth century extensive development and demonstrations of transmission systems employing advanced modulation format and self homodyne detection, that is, no local oscillator is used but the channel is split into two paths with one path delayed by one bit period and recombined. These techniques have allowed the transmission of bit rates reaching 80 Gb/s using optical time division multiplexing, and then with DWDM the total capacity may reach several thousand kilometers.

Since the beginning of the twenty-first century, there has been extensive research and development on the coherent techniques, especially the homodyne or intradyne method as described in Chapter 8, in association with the DSP. These DSP techniques allow the compensation of linear and nonlinear impairments as well as recovery of the carrier phase, and hence the clock rates for sampling the pulse sequence for decision and recovery of the original data sequence. Furthermore, forward error coding (FEC) techniques have also been employed to enhance the BER with coding gain (Figure 12.2).

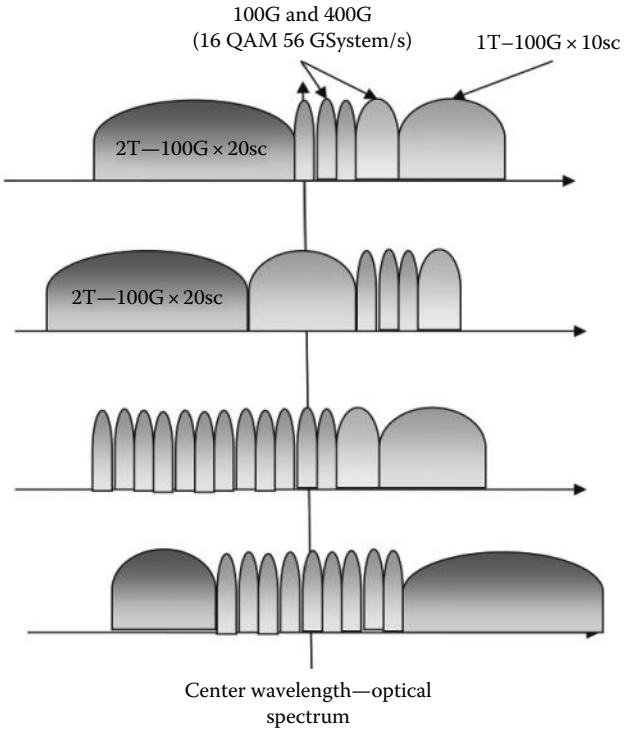

FIGURE 12.2
Flexible grid for superchannels.

12.2 Long-Haul Optical Transmission Systems

A long-haul transmission system by definition is one in which the distance between the transmitter and receiver is an important factor. This means that the maximum transmission between these subcomponents of the systems must be extended without the use of optical–electrical repeaters although optical amplifiers in midspans can be employed. The total distance is normally divided into a number of spans. Each span is connected through to the next one by MOR. Systems transponders are considered briefly here as they are now standard subsystems.

12.2.1 Intensity Modulation Direct Detection Systems

A direct detection optical receiver requires a minimum received signal power to sustain an adequate SNR to satisfy the BER requirement. Since the total fiber attenuation is dependent on the fiber length, there is a maximum path length beyond which the received signal strength will be inadequate to satisfy the SNR requirement of the communication systems.

If in the system design we start with specifications that include the transmitted power and the receiver sensitivity, we can estimate the maximum attenuation allowable for the

transmission medium. This total attenuation includes distributed losses in fibers, coupling losses into and out of the fiber, other coupling losses at the signal monitoring site, OADM or ROADM. In addition to these average losses, a system operating margin is also added to protect against aging components, occasional misalignment of fiber components, or additional repairs of broken fibers by splicing.

Example 12.1

An optical transmission system consists of the following: (i) Optical transmitter: direct intensity modulation output power = −0.5 dBm at the output of the fiber pig tail; (ii) Optical receiver: receiver sensitivity = −41.5 dBm; (iii) Optical fibers: average fiber attenuation and splicing losses: 0.4 dB/km; (iv) Coupling losses at the receiver = 0.5 dB; (v) Operating margin = 3 dB; and (vi) What is the maximum distance between the transmitter and receiver?

Solution

Optical transmitter	−0.5 dBm
Optical receiver	−41.5 dBm
Operating margin	3 dBm
Loss coupling at receiver	0.5 dB
Hence total loss allowable for fibers	41.5 − 3 − 0.5 = 38 dB
Fiber attenuation (average)	0.4 dB/km
Thus, total maximum distance	38/0.4 = 38 × 2.5 km = 95 km

The receiver sensitivity is a critical parameter of the link and can be determined by the acceptable probability of error in the detection and the decision level as described in Chapter 7. We recall the energy b_1 required for a bit "1" received under IM/DD as follows:

$$b_1 = \frac{q}{\Re}\left[\partial^2 G^x + \frac{2\partial i_{Neq} T_b}{qG}\right] \tag{12.1}$$

Hence, the receiver sensitivity RS is given by

$$RS = 10\,\mathrm{Log}_{10}\frac{P_{av}}{P_0}\ \text{in dBm} \quad \text{when } P_0 = 1\,\text{mW} \tag{12.2}$$

where
$P_{av} = b_1/T_b$
P_0 = 1.0 mW (the reference power level for evaluating power in dBm)

The term δ is specified by the BER curve (see Figure 12.3 for pulse amplitude modulation [PAM] modulation scheme) and the statistical property of the distribution of the received "1" and "0". Hence, with a specific BER, the bit period, and the photodetector type, we could estimate the required noise equivalent current at the input of the electronic preamplifier so that the required optical power for the lightwave channel can be detected. This would allow us to decide whether an optical amplifier preamplifier is needed at the front

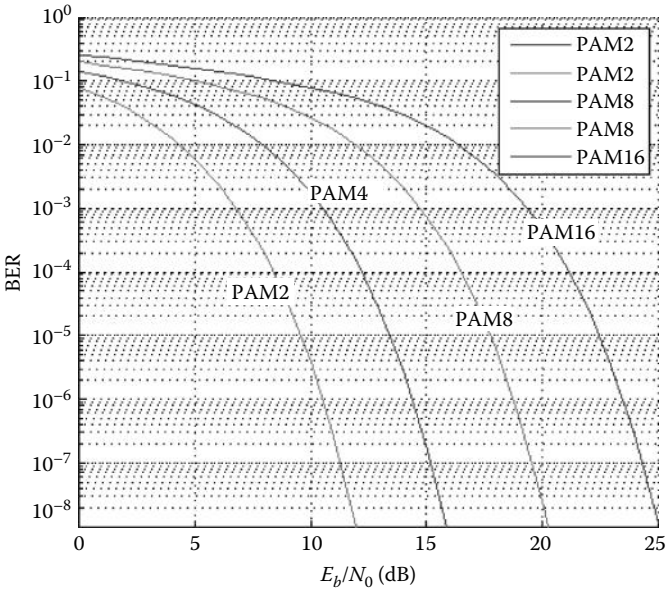

FIGURE 12.3
BER versus OSNR per bit period or PAM 2–16.

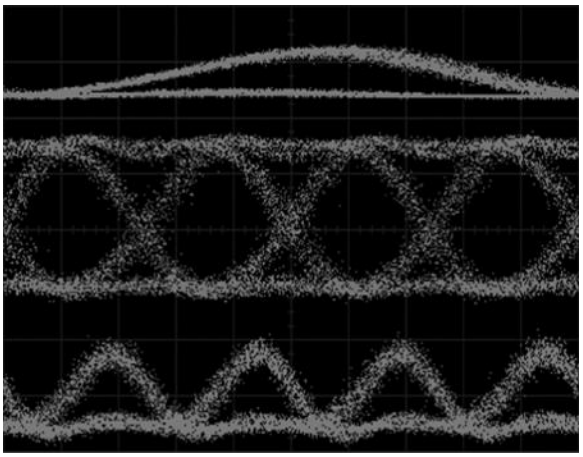

FIGURE 12.4
Typical eye diagrams monitored on a sampling oscilloscope with the optical receiver for different formats (NRZ or RZ) at different bit rates.

end of the optical receiver. The decision threshold does also affect the BER, and this is normally used to set the level. Typical eye diagrams at different bit rates and non-return to zero (NRZ) and return to zero (RZ) modulation formats are shown in Figure 12.4.

We note that the two terms within the bracket of Equation 12.1 represents the number of photons required to overcome the BER and the electronic noise current requirement. This is due to the fact that the term q/R is indeed the photon energy.

Example 12.2

For a 10 Gb/s IM/DD transmission system,

(a) What is the RS of the optical receiver if the following conditions must be met: BER = 1e−9, photodetector (PD) is PIN type with quantum efficiency of 0.8.
(b) What is the equivalent number of photons per bit that must be available at the receiver?
(c) What is the number of photons required to overcome the BER requirement?
(d) What is the number of photons per bit to overcome the electronic noise current?
(e) Repeat (a)–(d) for an avalanche photodetector (APD) with an avalanche gain of 20.

We see that the receiver sensitivity varies with respect to the bit rate. Naturally, the shorter the pulse width, the higher the peak power of the pulse to satisfy the average power required as estimated from the RS.

12.2.2 Loss-Limited Optical Communications Systems

Fiber loss plays an important role in the design and implementation of optical communications systems. Consider an optical transmitter generating an optical power of P_{tr}, and optical signals received with an optical receiver with the ability to detect a minimum optical power of P_r at a bit rate B_R. The maximum transmission distance would then be given by

$$L = \frac{10}{\alpha_F} \mathrm{Log}_{10}\left(\frac{P_{tr}}{P_r}\right) \tag{12.3}$$

where α is the total fiber loss per unit length (in dB/km) including splice and connector losses. The bit rate dependence of L arises from the linear dependence of P_r on the bit rate B_r by $P_r = N_p h\nu B_r$ where N_g is the average number of photons/bit required for the receiver to detect with a certain OSNR.

Exercise 12.1

Given that the fiber loss for the wavelength regions 810, 1300, and 1550 nm are 2.5, 0.4, and 0.15, respectively, plot the maximum transmission distance versus the bit rate when the transmitter average power is 0 dBm and the average number of photons that the receiver can detect is 300.

12.2.3 Dispersion-Limited Optical Communications Systems

We have described the dispersion effect in optical fibers that is very important for optical transmission systems when the loss is no longer a problem if optical amplifiers are employed. When the loss-limited distance is longer than that of the dispersion-limited transmission distance, then they are called dispersion-limited transmission systems. The relationship between the rise and fall and the frequency response of a system (including cable connections) can be found in Annex 4.

The limit for a system with a bit rate of B_r and a total dispersion factor D_T of the fiber is given by

$$B_r L \leq \frac{1}{4|D_T|\sigma_\lambda} \tag{12.4}$$

where σ_λ is the full width half mark (FWHM) in the optical spectral window of the source. Thus, for a standard optical fiber operating at 1550 nm, the total dispersion factor is about –15 ps/nm·km, and for a source FWHM of 1.0 nm, the bit rate distance product is about 166.6 (Gb/s)-km. That is if a 10 Gb/s operating bit rate system would be able to transmit signals for 16.6 km. If a dispersion shifted fiber is used with a typical dispersion factor of about 1–2 ps/(nm·km), then the transmission distance can be increased about 7.5–15 times that of the SSMF or more than 100 km and up to 240 km. When these fibers are employed for extremely long distances, the polarization dispersion becomes significant and the PMD DGD parameters must be taken into account to estimate the total allowable transmission distance, especially for 10 Gb/s operating bit rate.

Several schemes are currently under investigation including the use of fiber gratings, dispersion compensators, optical signal processors/filters, and optical solitons where the nonlinear effects of fibers through self-phase modulation are used to counter the linear effects of chromatic dispersion.

12.2.4 System Preliminary Design

12.2.4.1 Single-Span Optical Transmission System

In practice, the design of an optical communications system would require two principal design requirements: the power budget and the rise time budget, which account for the loss-limited and dispersion-limited systems, respectively.

Specifications for the system would be the system bit rate B_r and the design transmission distance. There are generally two main cases: the point-to-point links and the ultra-long or terrestrial/undersea links. The performance of the optical fiber systems is specified through the BER and the operating wavelength. The cost of operating in the 810 nm window would incur the lowest loss and increases with the wavelength windows 1300 and 1550 nm. Normally, for systems operating in the 100 Mb/s with a distance less than 20 km, a single-mode fiber can be used and this is the case for most LAN and Intranet applications. These systems and networks can be wired to the 810 nm window. For longer transmission systems, the two wavelength windows 1310 and 1550 nm must be used.

12.2.4.2 Power Budget

The power budget of a transmission link can be represented as shown in Figure 12.5. Depending on the availability of the power at the output of the transmitter or the sensitivity of the optical receiver, one can determine the operating conditions of other subsystems or optical components, for example, the fiber distance, the number of spans, the noise of the electronic preamplifiers, and system operating margins. Either a table of the power budget of the transmission link or a graph as shown in Figure 12.5 can be established.

In case there is a saturation level of the electronic preamplifier with a very high transimpedance gain, for example the differential amplifier used as a preamplifier with a transresistance of 4500 Ω. Then one must specify the saturation level and hence the dynamic range of the system as described in Annex 3.

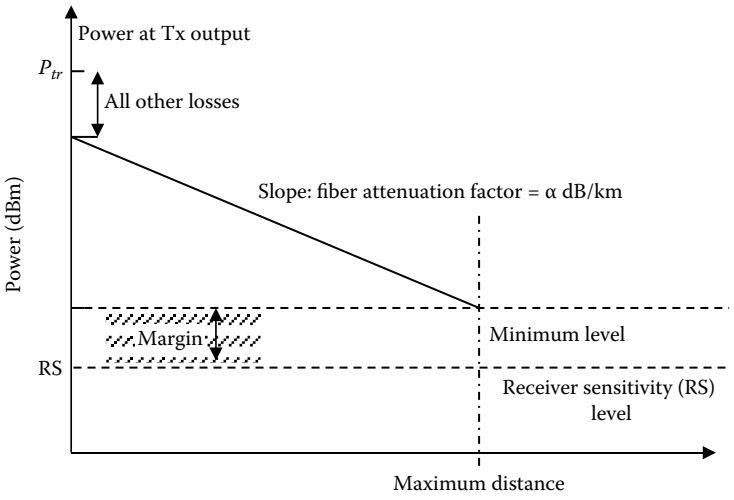

FIGURE 12.5
Power budget by graphical representation for a single transmission distance.

12.2.4.3 Rise Time/Dispersion Budget

We have previously established an approximate relationship between the dispersion, the bit rate, and the bandwidth. For on–off keying (OOK), the bandwidth Δf of the detection system can be about 1/2 the bit rate (pulse repetition rate). The relationship of $B_r L \leq 1/4|D_T|\sigma_\lambda$ can be used, or the bit rate B_R can be approximately written as

$$B_R \frac{1}{4\Delta\tau} = 2\Delta f \tag{12.5}$$

However, when writing the relationship between all components and subsystems of the transmission system, we must have the summation of all the root mean squares (RMS) of all the rise time* and broadening factors must be less than 70% of the bit period (NRZ or RZ bit time). This can be written as

$$\sigma = \sqrt{\sum_{i=1}^{N} \left(t_{ri}^2 + t_{fi}^2 + \Delta\tau_j^2 \right)} \tag{12.6}$$

where

t_{ri} and t_{fi} are the rise and fall time, respectively, of the ith component in the transmission link

$\Delta\tau$ is the pulse broadening of the ith fiber span in the link taken for both sides of a pulse after transmission through an optical fiber of length L

* The rise time is measured from 10% to 90% of the rising edge of a rectangular pulse; this is usually the step function of the subsystem. Thus, the rule of thumb is that the broadening factor is approximately 50% of the rise time. If the bandwidth of the subsystem is measured, then the pulse broadening can be roughly 1/4 (BW).

TABLE 12.1

RMS Pulse Width, σ, and Spectral Width, Δf of Three Typical Pulse Shapes

	h(t)	σ	*H(f)*	BW
Exponential pulse	$\frac{1}{\tau}e^{-\frac{t}{\tau}}$	τ	$\frac{1}{1+j\omega\tau}$	$\frac{0.159}{\sigma}$
Rectangular pulse	$\frac{1}{\tau}-\frac{\tau}{2}\le t\le\frac{\tau}{2}$	$\frac{\tau}{2\sqrt{3}}$	$\frac{\sin(f\tau)}{f\tau}$	$\frac{0.402}{\sigma}$
Gaussian pulse	$\frac{1}{\sqrt{2\pi}\tau}e^{-\frac{t^2}{2\tau^2}}$	τ	$e^{-2(\pi f\tau)^2}$	$\frac{0.133}{\sigma}$

Thus both the rise and fall time must be accounted for. Hence, we must have

$$\sigma=\sqrt{\sum_{i=1}^{N}\left(t_{ri}^2+t_{fi}^2+\Delta\tau_j^2\right)}\le 70\%\frac{1}{B_R} \tag{12.7}$$

That is the total broadening of the pulse must be less than 70% of the bit period. The relationship between the RMS pulse width and the bandwidth of the system specified by the pulse shape can be found as shown in Table 12.1.

The RMS pulse width σ of a pulse shape $h(t)$ can be found by normalizing pulse shape and the RMS definition (see Annex 3) as

$$\int_{-\infty}^{+\infty}h(t)dt=1 \tag{12.8}$$

$$\sigma=\left\langle t^2\right\rangle-\left\langle t\right\rangle^2 \tag{12.9}$$

where

$$\left\langle t\right\rangle=\int_{-\infty}^{+\infty}t\cdot h(t)dt$$

$$\left\langle t\right\rangle^2=\int_{-\infty}^{+\infty}t^2\cdot h(t)dt$$

When a number of cascaded linear systems are involved (e.g., optical fiber spans in cascade), then the overall impulse response can be found by convolving the impulse response of each individual fiber span. The resulting RMS pulse broadening can be found by taking the RMS of all pulse broadening factors. That is

$$\sigma^2=\sigma_1^2+\sigma_2^2+\sigma_3^2+\cdots+\sigma_N^2 \tag{12.10}$$

Example 12.3

The rise time and fall times of the transmitter and the optical detector are 1 and 0.5 ns, respectively. The bandwidth of the optical receiver is 2 GHz. The total pulse broadening of the fiber is 1.5 ns. What is the maximum bit rate of the OOK system?

Solution

Broadening due to optical transmitter	1/2 ns
Broadening due to optical receiver	1/2 × 0.5 ns
Fiber broadening	1.5 ns
Broadening due to electronic amplifiers of the optical receiver	1/(4 × 2 × 1e−9) = 1/8 ns
Total RMS pulse broadening (pulse width)—impulse response	$\sigma = (0.5)^2 + (0.25)^2 + (1.5)^2 + (1/8)^2 = (0.763)^{\wedge 2}$ ns
Thus, the maximum bit rate would be	$B_R = 1/4(\sigma) = 328.8$ MHz

12.2.4.4 Multiple-Span Optical Transmission System

For multispan transmission systems, the power budget should be designed for upgrading an existing installed optical fiber system or a newly to-be-installed system. For the upgrading of a nonamplified single-mode transmission system, DCMs are to be inserted at the end of fiber transmission spans, usually in multiple lengths of 40 km sections. Thus, the span length must be of the order of 80 or 100 km depending on the quality of the single-mode fibers. Two optical amplifiers are to be inserted: one at the end of the transmission fiber (normally standard single-mode optical fibers) and the other at the output of the DCM. The optical power at the output of the first optical amplifier must be less than the nonlinear threshold of the DCM, which should be very low, about 0 dBm in view of the small effective area of the DCF. The optical power at the output of the optical amplifier after the DCM must be sufficiently high that is close to the launched power level in the first span. This optical amplifier must be a booster optical amplifier type. The power distribution of the optical channels along the multispan transmission distance is shown in Figure 12.6.

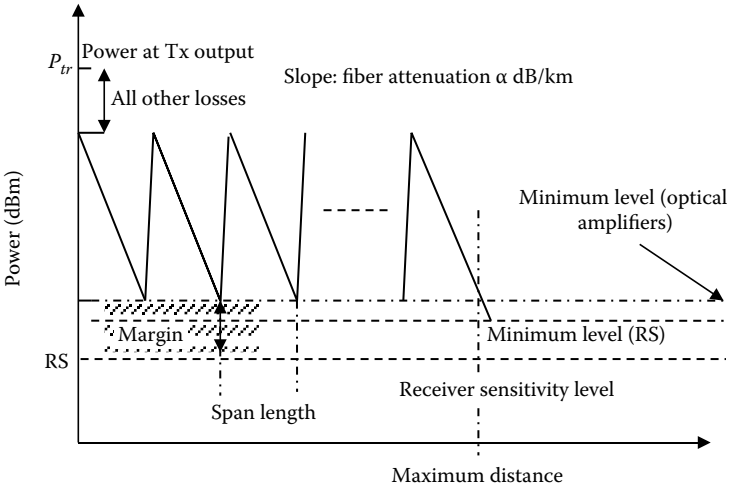

FIGURE 12.6
Power budget by graphical representation for multispan transmission system.

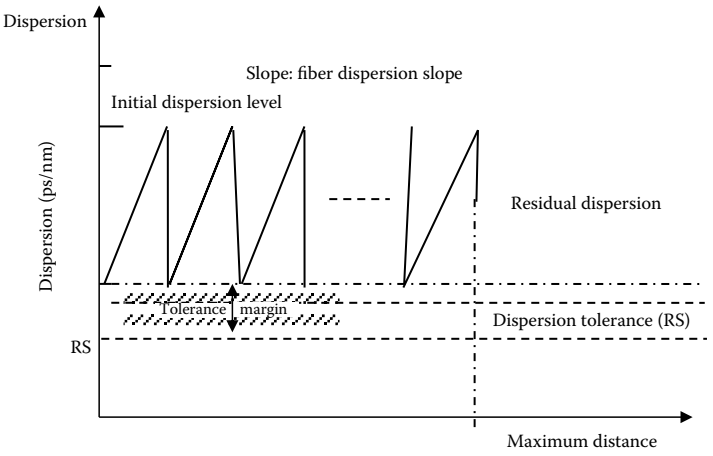

FIGURE 12.7
Dispersion budget by graphical representation for multispan transmission system.

Ideally, the length of each span should be the same and any excess power can be attenuated using attenuation pads. This is preferred for manufacturing of almost identical optical amplifiers in all spans and, hence, minimizes the transmission system management. Shown in the figure also is the minimum level so as to ensure that this meets the minimum power level for optical amplification.

Figure 12.7 shows the dispersion budget for multispan transmission. The minimum dispersion tolerance is to be determined depending on the modulation formats. Initially, there is no dispersion at the output of the transmitter. The dispersion gradually increases as a function of the transmission distance in the first span. If DCM is used at the end of each span, then the dispersion can be fully compensated before the transmission to the next span and so on. This dispersion map varies with respect to the change of the wavelength channel. This change can be estimated using the spectral dependence of the dispersion factor. At the end of the multispan transmission, there is always residual dispersion at each wavelength channel. This residual dispersion can be compensated for each channel at the output of a wavelength demultiplexer before the optical signals are received. Tuneable fiber Bragg gratings (FBG) can be used to tune to match the residual dispersion. Alternatively, this dispersion can be compensated in the electronic domain by digital signal processors (DSPs).

12.2.5 Gaussian Approximation

In many cases of the optical transmitter, the impulse responses of the single-mode optical fiber can be approximated as Gaussian pulse shapes in the far field while it is strongly chirped in the near-field region as shown Figure 12.8. And, when they are in cascade, the overall impulse response of the transmission system can be represented as Gaussian. The impulse response and its Fourier transform to give the frequency response of the system are given by* (see Figures 12.8 and 12.9 and Appendix)

$$h(t) = e^{-\frac{t^2}{2\tau^2}} \rightarrow H(\omega) = e^{-\frac{(\omega\tau)^2}{2}} \tag{12.11}$$

* See Appendix—Chapter 13 impulse responses of single-mode optical fibers.

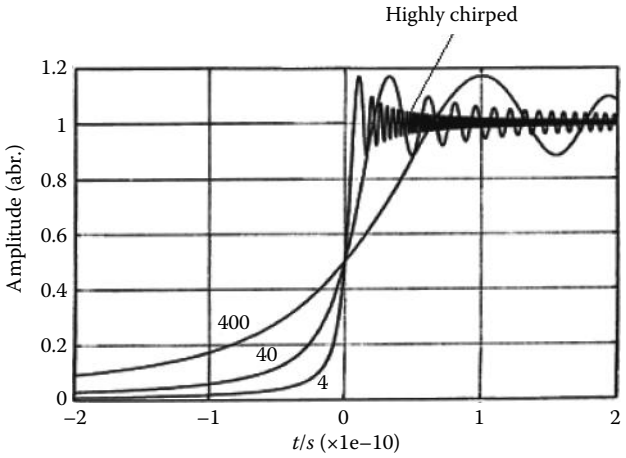

FIGURE 12.8
Fiber step response for single-mode optical fiber of distance 1, 10, and 100 km and chirp effects near the edge.

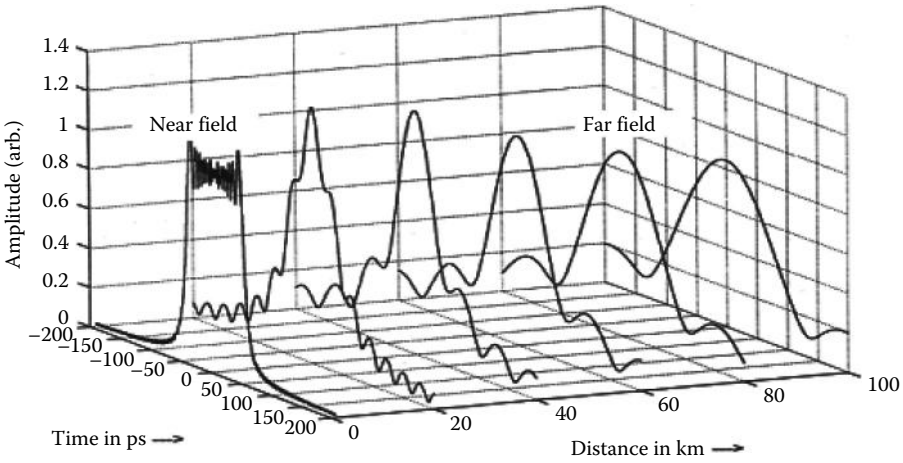

FIGURE 12.9
Gaussian impulse response of single-mode optical fibers—near field and far field.

The bandwidth (BW) of this system can then be found by setting the absolute value of the $H(\omega)$ to $1/\sqrt{2}$ and solving for ω. Then the 3-dB bandwidth and the rise time of the system can be found using the relationship

$$\omega_{3\,\mathrm{dB}} = \frac{0.83}{\tau} \tag{12.12}$$

If the link is made up of N fiber spans of the same dispersion factor, then each fiber length in tandem has a transfer function of

$$H_n(\omega) = e^{-\frac{N(\omega\tau)^2}{2}} \tag{12.13}$$

The dependence of the transfer function as a square of the frequency indicates that whenever the bit rate is doubled, the transmission distance is reduced by a factor of 4. This is the "rule of thumb" for fiber transmission, for setting the dispersion tolerance as a function of the bit rate.

Note that the design described in this section is given as a preliminary design so as to determine the selection of optical systems and electronic property of the receiver and the electrical driving unit of the transmitter.

Power budget and dispersion budget are generally used for the preliminary design. Accurate design details must be conducted by simulation and/or by laboratory demonstration prior to field installation.

12.2.6 System Preliminary Design under Nonlinear Effects

12.2.6.1 Link Budget Measurement

For measuring and estimating the operating margins in a worst-case scenario and also in the end of life (EOL) limit, it is required to ensure that the BER satisfying BER <1e-12 (Figure 12.10).

Figure 12.11 shows the layout of the power budget in which an OSNR in dB of 3.88 accounts for a Q factor of 7 (BER = 1e–12) and makes allowances for aging, corrections of the transmitter and receiver, and distortion as well as the error in power control.

12.2.6.2 System Margin Measurement

The magnitude of any impairment that degrades the system to $Q = 7$ can be used as a metric for a system margin. Any distortion by linear and nonlinear dispersion effects and/or noise contribution to the transmission of lightwave channels must be estimated, and allowance of degradation of the eye diagram must be allocated in the power budget. Figure 12.12 shows various effects that would degrade the eye diagram and the aspects of noise measurement for link budget estimation.

Figure 12.12 shows the effects of the noise margin on the quality factor Q, especially the slope of the BER. The noise is loaded when cascaded optical amplifiers (MOR and MSA)

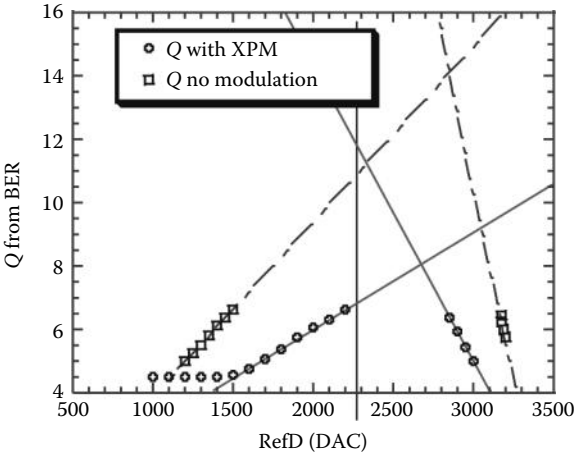

FIGURE 12.10
Details of Q factor as a function of sampling and decision point (voltage) of the eye diagram.

Stressed span loss (dB)	24.95
OSNR margin to $Q = 7$	3.88
Aging allowance	−4.00
w.c Rx/Tx correction	−1.90
w.c. distortion dBQ × 2	−0.60
Power control error	−1.50
Sum degradations (dB)	−8.00
System margin (dB)	−4.12
Guaranteed max. span loss (dB)	20.83

FIGURE 12.11
Table arrangement of loss per span in optical transmission (in dB).

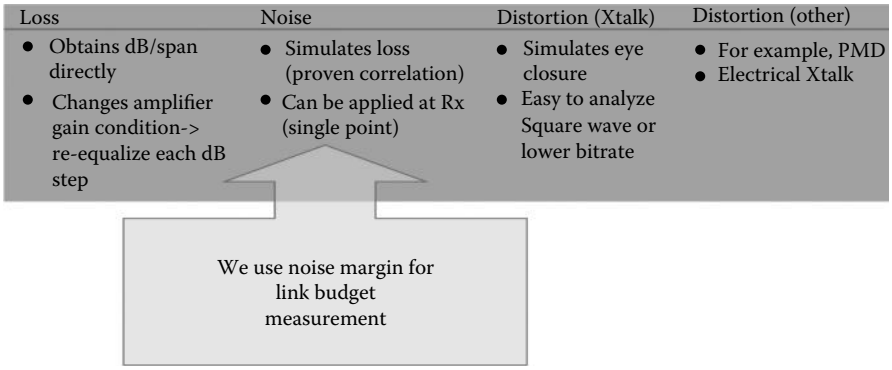

FIGURE 12.12
Budget measurement.

are active. These noises are accumulated along the multispan transmission line and hence superimposed on the received voltage levels. The bandwidth of the amplification spontaneous emission (ASE) noises is very wide, and they are mixed with the optical signals creating noise levels in the detected eye diagram. This would decrease the degree of eye opening, and sometimes, we would measure the degradation by using the term eye-opening penalty (EOP).

12.2.6.2.1 Noise Margin

A noise margin measurement is conducted by using an ASE noise source superimposed on the optical signals as shown in Figure 12.13. Then the BER and Q factor can be determined under unloaded and loaded environments (Figure 12.14).

12.2.6.2.2 Dispersion Map

The dispersion map of the transmission system under noise margin is also important, and an arrangement for such measurement is as shown in Figure 12.15a. A dispersion compensator is inserted after the transmitter whose dispersion factor can be varied so as to determine the dispersion tolerance and the noise margin level at a specific BER. Figure 12.15b

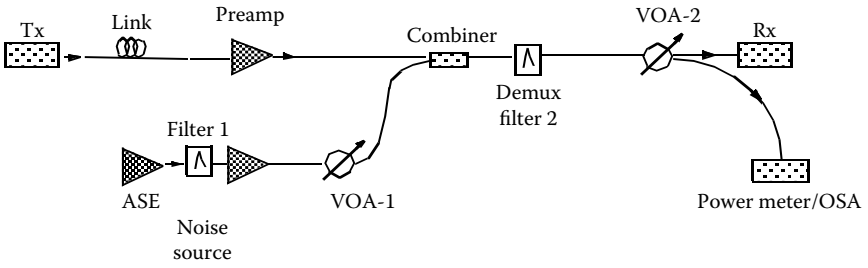

FIGURE 12.13
Arrangement for noise margin measurement—ASE = noise sources, VOA = variable optical attenuator, an, OSA = optical spectrum analyzer.

shows a typical noise margin versus dispersion for a wavelength channel. These measurements are done by simulation. That is why a good and accurate simulation package is important for evaluation of modern optical fiber communication systems.

12.2.6.2.3 Worst-Case Distortion

The worst case (w.c.) includes "inaccessible distortion" for the worst-case model, for example, four wave mixing (FWM), power fluctuation. This worst case is very critical for DWDM in which the wavelength channels are equally spaced, that is, when three waves interact to create the fourth wave located exactly on another channel wavelength. This generates the unwanted cross talk. Two rows of the worst case penalty are inserted in the table of Figure 12.16 to account for these circumstances.

12.2.6.2.4 Guarantee of Maximum Span Loss

Finally, the maximum span loss is determined so as to ensure that the loss of the span during installation is met to achieve quality transmission. This is also proved by checking to see if verification agrees with analysis so that the loss/span is within ±0.5 dB/span (1-sigma), the dispersion window is within ±30 ps/nm (1-sigma), and the provisioned peak power is within ±0.25 dBm (1-sigma). The verifications are reproducible within ±0.3 dB/span, and on average verification is 0.5 dB/span better than analysis (Figure 12.17).

12.2.6.2.5 From Modeled Budget to Installation Budget

Verified modeled budgets are further adjusted to account for equipment behavior and installation and operating procedures, for example, super-decoder penalty and equalization penalty. The verification of the modeled budget and the installed budget is confirmed from the experience of installed transmission systems. The system operating margin can also be reduced from the statistical data obtained from these installed transmission systems.

12.2.7 Some Notes on the Design of Optical Transmission Systems

In modern optical transmission systems, the design procedures depending on specific applications need to (1) employ basic DWDM for Tb/s transmission principles and clarify the DWDM Tb/s modulation for Tx; (2) deal with dispersion and losses in Tb/s transmission system design, advanced fibers; (3) set engineering rules for impacts due to nonlinearity effects; and (4) examine optical amplifiers, distributed and lumped types for system design rules.

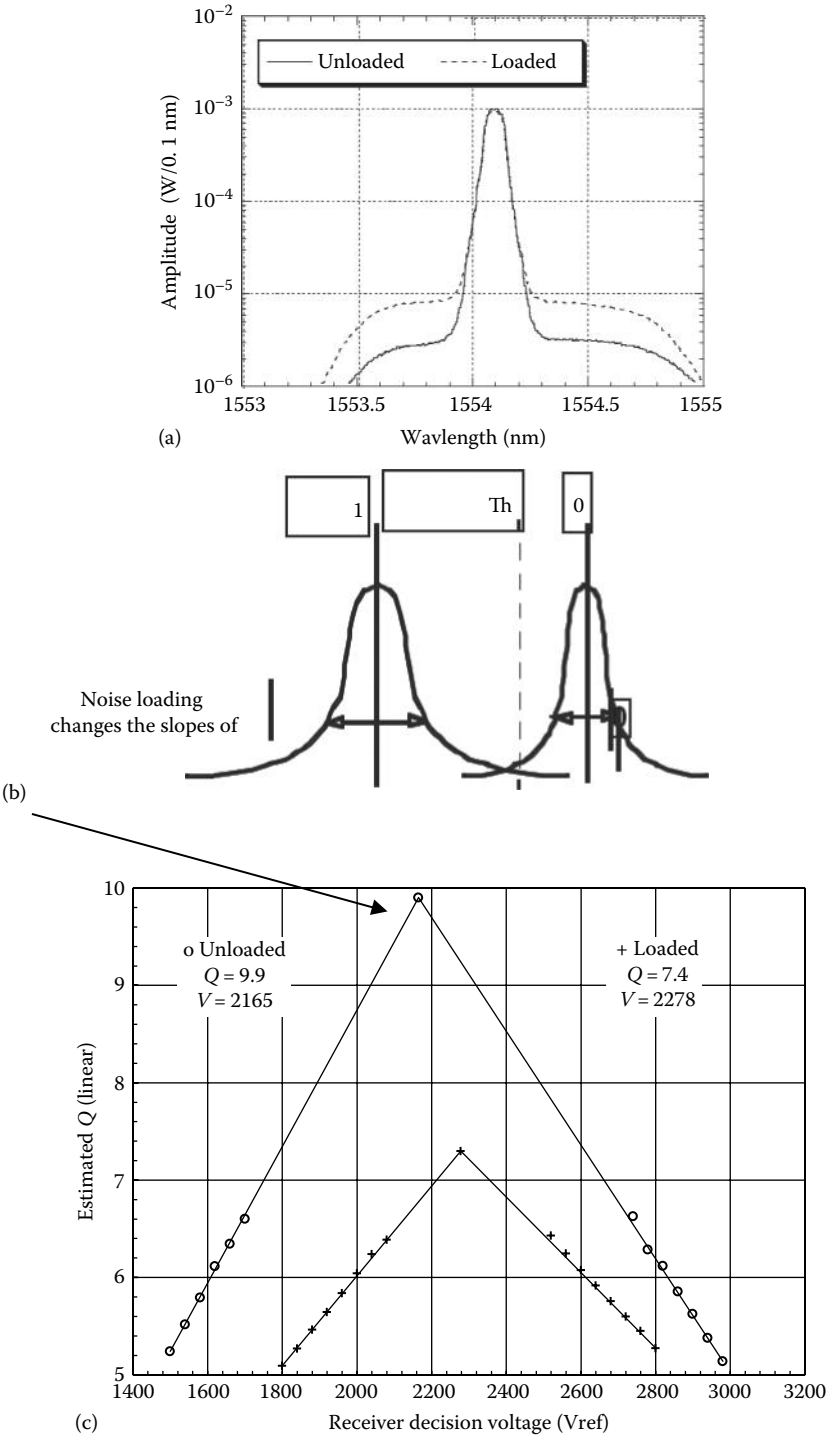

FIGURE 12.14
Noise margin measurement. (a) Noise spectra under unloading and loading conditions, (b) probability distribution, and (c) BER versus decision voltage level.

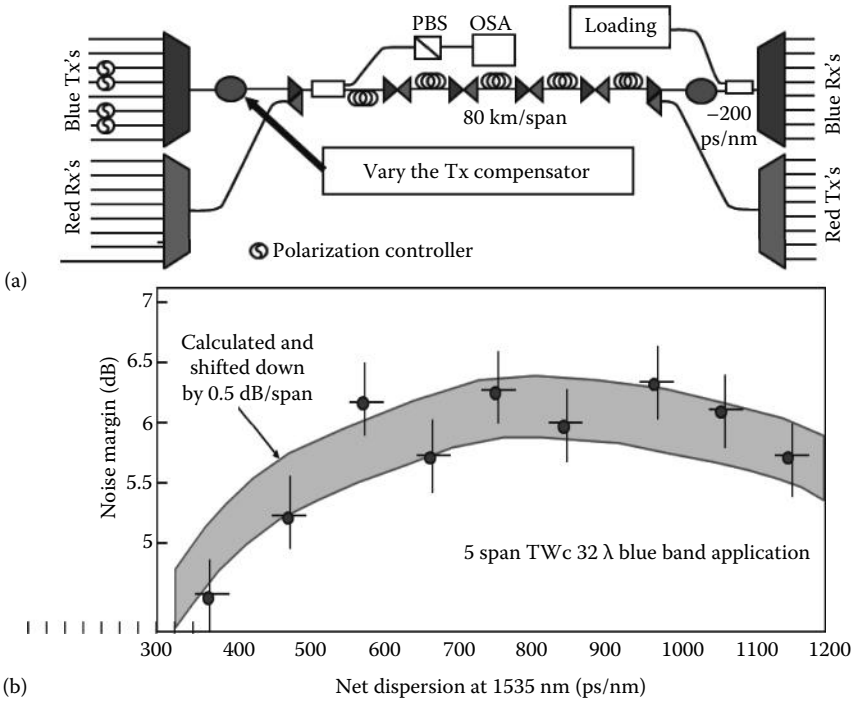

FIGURE 12.15
Dispersion map testing. TWc = total wavelength channels. Blue band = lower spectral region as compared to red band in the C-band. (a) Bidirectional transmission systems for "blue" and "red" channels; and (b) noise margin variation as function of the total net residual dispersion over the whole transmission line.

12.2.7.1 Allocations of Wavelength Channels

The DWDM channel spacing and locations of the frequencies of the channel follow the International Telecommunication Union (ITU) standard. Such locations can be observed from Table 12.2. The frequency grid and channel spacing, that is, the frequency spacing between adjacent channels are estimated by

$$f = \frac{c}{\lambda}$$
$$\Delta f = -\frac{c}{\lambda^2}\Delta\lambda = -\frac{f}{\lambda}\Delta\lambda \tag{12.14}$$

By selecting a reference wavelength, for example, the absorption wavelength of a chemical substance and the frequency of such channel, the frequencies of other wavelength channels can be estimated. Channel spacing of 50 GHz is now the normal standard for 10 and 40 Gb/s bit rate in which 44 channels can be accommodated in the C-band.

The number of WDM channels possible depends on (1) channel spacing, (2) amplifier spectral range, (3) source spectral width, (4) bit rate per optical channel and modulation formats, (5) fiber dispersion, and (6) multiplexer/demultiplexer range.

The number of channels is estimated by $N = 1 + \frac{\lambda_1 - \lambda_2}{\Delta\lambda}$ where $\Delta\lambda$ is the channel spacing, and λ_1 and λ_2 are the two extreme wavelengths of the end channels.

Stressed span loss (dB)	24.95
OSNR margin to $Q = 7$	3.88
Aging allowance	–4.00
w.c Rx/Tx correction	–1.90
w.c. distortion dBQ × 2	–0.60
Power control error	–1.50
Sum degradations (dB)	–8.00
System margin (dB)	–4.12
Guaranteed max. span loss (dB)	20.83

(a)

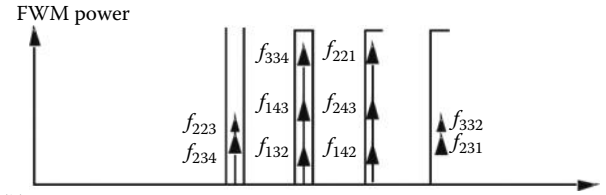

(b)

FIGURE 12.16
Worst-case distortion illustrated (a) table of power budget and (b) FWM and variation of cross talk due to fluctuation of power level.

Stressed span loss (dB)	24.95
OSNR margin to $Q = 7$	3.88
Aging allowance	–4.00
w.c Rx/Tx correction	–1.90
w.c.distortion dBQ × 2	–0.60
Power control error	–1.50
Sum degradations (dB)	–8.00
System margin (dB)	–4.12
Guaranteed max. span loss (dB)	20.83

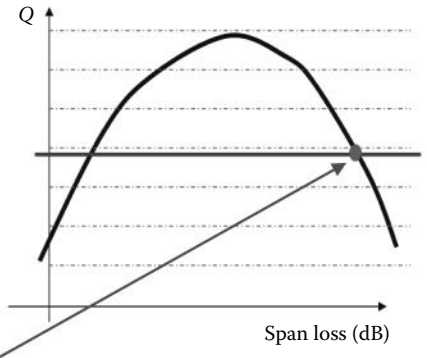

FIGURE 12.17
Guarantee of span loss for quality transmission.

TABLE 12.2

ITU Wavelength Grid for Dense Wavelength Division Multiplexing

	L-Band				C-Band				S-Band			
	100 GHz Grid		50 GHz Offset		100 GHz Grid		50 GHz Offset		100 GHz Grid		50 GHz Offset	
	THz	nm	THz	nm	THz	nm	THz	nm	THz	nm	THz	nm
1	186.00	1611.78	186.05	1611.35	191.00	1569.59	191.05	1569.18	196.00	1529.55	196.05	1529.16
2	186.10	1610.92	186.15	1610.48	191.10	1568.77	191.15	1568.36	196.10	1528.77	196.15	1528.38
3	186.20	1610.05	186.25	1609.62	191.20	1567.95	191.25	1567.54	196.20	1527.99	196.25	1527.60
4	186.30	1609.19	186.35	1608.76	191.30	1567.13	191.35	1566.72	196.30	1527.21	196.35	1526.82
5	186.40	1608.32	186.45	1607.89	191.40	1566.31	191.45	1565.90	196.40	1526.43	196.45	1526.04
6	186.50	1607.46	186.55	1607.03	191.50	1565.49	191.55	1565.08	196.50	1525.66	196.55	1525.27
7	186.60	1606.60	186.65	1606.17	191.60	1564.67	191.65	1564.27	196.60	1524.88	196.65	1524.49
8	186.70	1605.74	186.75	1605.31	191.70	1563.86	191.75	1563.45	196.70	1524.11	196.75	1523.72
9	186.80	1604.88	186.85	1604.45	191.80	1563.04	191.85	1562.63	196.80	1523.33	196.85	1522.94
10	186.90	1604.02	186.95	1603.59	191.90	1562.23	191.95	1561.82	196.90	1522.56	196.95	1522.17
11	187.00	1603.16	187.05	1602.73	192.00	1561.41	192.05	1561.01	197.00	1521.78	197.05	1521.40
12	187.10	1602.31	187.15	1601.88	192.10	1560.60	192.15	1560.20	197.10	1521.01	197.15	1520.63
13	187.20	1601.45	187.25	1601.02	192.20	1559.79	192.25	1559.38	197.20	1520.24	197.25	1519.86
14	187.30	1600.60	187.35	1600.17	192.30	1558.98	192.35	1558.57	197.30	1519.47	197.35	1519.09
15	187.40	1599.74	187.45	1599.31	192.40	1558.17	192.45	1557.76	197.40	1518.70	197.45	1518.32
16	187.50	1598.89	187.55	1598.46	192.50	1557.36	192.55	1556.95	197.50	1517.93	197.55	1517.55
17	187.60	1598.04	187.65	1597.61	192.60	1556.55	192.65	1556.15	197.60	1517.16	197.65	1516.78
18	187.70	1597.18	187.75	1596.76	192.70	1555.74	192.75	1555.34	197.70	1516.40	197.75	1516.01
19	187.80	1596.33	187.85	1595.91	192.80	1554.94	192.85	1554.53	197.80	1515.63	197.85	1515.25
20	187.90	1595.48	187.95	1595.06	192.90	1554.13	192.95	1553.73	197.90	1514.86	197.95	1514.48
21	188.00	1594.64	188.05	1594.21	193.00	1553.32	193.05	1552.92	198.00	1514.10	198.05	1513.72
22	188.10	1593.79	188.15	1593.36	193.10	1552.52	193.15	1552.12	198.10	1513.33	198.15	1512.95
23	188.20	1592.94	188.25	1592.52	193.20	1551.72	193.25	1551.31	198.20	1512.57	198.25	1512.19
24	188.30	1592.10	188.35	1591.67	193.30	1550.91	193.35	1550.51	198.30	1511.81	198.35	1511.43
25	188.40	1591.25	188.45	1590.83	193.40	1550.11	193.45	1549.71	198.40	1511.05	198.45	1510.67
26	188.50	1590.41	188.55	1589.98	193.50	1549.31	193.55	1548.91	198.50	1510.28	198.55	1509.90
27	188.60	1589.56	188.65	1589.14	193.60	1548.51	193.65	1548.11	198.60	1509.52	198.65	1509.14
28	188.70	1588.72	188.75	1588.30	193.70	1547.71	193.75	1547.31	198.70	1508.76	198.75	1508.38
29	188.80	1587.88	188.85	1587.46	193.80	1546.91	193.85	1546.51	198.80	1508.01	198.85	1507.63
30	188.90	1587.04	188.95	1586.62	193.90	1546.11	193.95	1545.72	198.90	1507.25	198.95	1506.87
31	189.00	1586.20	189.05	1585.78	194.00	1545.32	194.05	1544.92	199.00	1506.49	199.05	1506.11
32	189.10	1585.36	189.15	1584.94	194.10	1544.52	194.15	1544.12	199.10	1505.73	199.15	1505.36
33	189.20	1584.52	189.25	1584.10	194.20	1543.73	194.25	1543.33	199.20	1504.98	199.25	1504.60
34	189.30	1583.68	189.35	1583.27	194.30	1542.93	194.35	1542.53	199.30	1504.22	199.35	1503.84
35	189.40	1582.85	189.45	1582.43	194.40	1542.14	194.45	1541.74	199.40	1503.47	199.45	1503.09
36	189.50	1582.01	189.55	1581.60	194.50	1541.34	194.55	1540.95	199.50	1502.71	199.55	1502.34
37	189.60	1581.18	189.65	1580.76	194.60	1540.55	194.65	1540.16	199.60	1501.96	199.65	1501.59
38	189.70	1580.35	189.75	1579.93	194.70	1539.76	194.75	1539.37	199.70	1501.21	199.75	1500.83
39	189.80	1579.51	189.85	1579.10	194.80	1538.97	194.85	1538.58	199.80	1500.46	199.85	1500.08
40	189.90	1578.68	189.95	1578.27	194.90	1538.18	194.95	1537.79	199.90	1499.71	199.95	1499.33
41	190.00	1577.85	190.05	1577.43	195.00	1537.39	195.05	1537.00	200.00	1498.96	200.05	1498.58
42	190.10	1577.02	190.15	1576.61	195.10	1536.60	195.15	1536.21	200.10	1498.21	200.15	1497.83

(*Continued*)

TABLE 12.2 (*Continued*)

ITU Wavelength Grid for Dense Wavelength Division Multiplexing

	L-Band				C-Band				S-Band			
	100 GHz Grid		50 GHz Offset		100 GHz Grid		50 GHz Offset		100 GHz Grid		50 GHz Offset	
	THz	nm	THz	nm	THz	nm	THz	nm	THz	nm	THz	nm
43	190.20	1576.19	190.25	1575.78	195.20	1535.82	195.25	1535.42	200.20	1497.46	200.25	1497.09
44	190.30	1575.36	190.35	1574.95	195.30	1535.03	195.35	1534.64	200.30	1496.71	200.35	1496.34
45	190.40	1574.54	190.45	1574.12	195.40	1534.25	195.45	1533.85	200.40	1495.97	200.45	1495.59
46	190.50	1573.71	190.55	1573.30	195.50	1533.46	195.55	1533.07	200.50	1495.22	200.55	1494.85
47	190.60	1572.88	190.65	1572.47	195.60	1532.68	195.65	1532.28	200.60	1494.47	200.65	1494.10
48	190.70	1572.06	190.75	1571.65	195.70	1531.89	195.75	1531.50	200.70	1493.73	200.75	1493.36
49	190.80	1571.23	190.85	1570.82	195.80	1531.11	195.85	1530.72	200.80	1492.99	200.85	1492.61
50	190.90	1570.41	190.95	1570.00	195.90	1530.33	195.95	1529.94	200.90	1492.24	200.95	1491.87

Note: The International Telecommunication Union established the following grid for Dense Wavelength Division Multiplexing systems. ITU recommends the 100 GHz (0.8 nm) spacing for DWDM operation. The 50 GHz offset (0.4 nm spacing) offers twice the bandwidth. The grid is centered at 193.10 THz (1552.52 nm).

Example: λ_1, λ_2 = 1540,1560 nm and a channel spacing of 1.6 nm (200 GHz), N = 12.5 channels. Similarly, for λ_1, λ_2 = 1535 and 1565 nm and a channel spacing of 50 GHz, $N \sim 44$.

12.2.7.2 Link Design Process

- Chose an application means; know your line rate and fiber type, whether it is a currently installed fiber system requiring upgrading or a newly installed transmission system.
- Determine what amplifier configuration meets the requirements.
- Check to see if the application is supported, for example, if link budgets and optical ADD/DROP Multiplexer (OADM) rules are available.
- Remember in span loss calculations to consider the minimum span loss: if you have to pad (fixed attenuator) to reach the minimum span loss, the value after padding is used in all calculations.

Choosing an application means to (1) know your line rate and fiber type, (2) determine what amplifier configuration meets the requirements, and (3) check to see if the application is supported by link budgets and if OADM rules are available.

12.2.7.3 Link Budget Considerations

12.2.7.3.1 Forward Error Coding

FEC is normally used at the transmitter to increase the chance of detection without error. In this process, a number of redundant bits are used and coded in the data sequence:

- FEC adds dB/span and reduces BER.
- FEC benefits are system dependent and may vary from application to application.
- If FEC is to be used, check standards for specific information.
- FEC Reed-Solomon codes are 42.7 Gb/s for 40 Gb/s base rate; 10.7 Gb/s for 9.953 Gb/s.

12.2.7.3.2 Excess Loss: Operating Margin

- Calculating the excess loss (EL) (in dB)
  L = actual span loss; L_{total} = sum of actual losses (including fixed pads if any); n = number of spans; $L_{\max}$ = link budget max. dB/span (with/without FEC)

$$EL = \sum_{L_{\max} < L < L_{\max+2}} L - L_{\max} \tag{12.15}$$

Then the EL rules can be stated as

- $L < L_{\max} + 2$
- $L_{total} < n \cdot L_{\max}$
- If $EL > 4$ dB is not supported, then FEC may be used to improve the SNR and thus increase the operating margin by

$$\text{If } 2 < EL < 4 \Rightarrow L_{total} < n\left(L_{\max} - 1\right) \tag{12.16}$$

12.2.7.3.3 Basic Steps in Design Transmission Systems

The following are the basic steps to be considered in the design of an optical transmission system. Select the types of the transmission fibers and if required the dispersion compensating fibers for each span of the transmission line.

Define system's span losses and lengths: (1) What budgets and windows are available for this application? (2) What extra margin (if any) must be added to the span losses? (3) What BER is required? (4) Is FEC an option or requirement? (5) Where should the regenerator be placed? To eliminate mixed fiber links where possible: (1) Check the length windows to ensure that there are DCM solutions available. (2) Check the losses using the excess loss rules, attenuation pad span losses to be kept to a minimum.

If there is an OADM site, (1) check all sublinks for DCM windows and check midspan-access losses. This may place a limit on sites and the number of add/drop wavelengths supported. (2) Determine the DCMs required and their locations. (3) Take into account special OADM placement rules.

DCMs may be required at the Add Tx or Drop Rx: (1) Add Tx's may be required to have a specific chirp. (2) Use a MidSpan-Opt-Regen Plus (MOR Plus) if DCMs are required at a line amp site.

Calculate the MOR losses and add fixed pads where required.

Find the transmitter fixed pad information, and note the fixed pad attenuator upgrade strategy.

Corning LEAF and enhanced LEAF (ELEAF) perform differently. (1) Using LEAF budgets provides a conservative but safe estimate for ELEAF links; however, DCMs and pads will be different. (2) TrueWave Classic, TrueWave-RS, TrueWave+, and TrueWave− are not equivalent. (3) Treat them as completely separate fiber types as both link budgets and DCMs will vary between these different fiber types.

Note: Use for link designs for 100 or 50 GHz, but do not apply to 200 GHz as DWDM filter specifications are different. Use array waveguide gratings (AWG)—bidirectional filters, multiplexing, and demultiplexing.

12.2.8 Link Budget Calculations under Linear and Nonlinear Impairments

Under nonlinear effects, the transmission performance needs to take into account (1) distortion versus noise, (2) high optical power: distortion of the signal, and (3) low power: low signal-to-noise ratio (SNR).

Figure 12.18 shows the variation of the *Q* factor as a function of the launched power. When the launched power reaches the nonlinear threshold, the distortion happens and the system performance is degraded. Figure 12.19 shows the effects of the decision level on the *Q* factor. Gaussian distribution of the amplitude and noise levels are assumed. Optimum performance is achieved when the probability of error for detection of "1" and "0" is the same.

12.2.8.1 Power Budget

When designing the transmission, we must keep in mind the following:

- Link budgets are evaluated and verified for the system at (1) the worst case, (2) EOL, and (3) reference equalization (RefEQ).
- Budget guarantees include the worst-case equalization at EOL.
- Based on the worst case, implementation and power control errors over life.

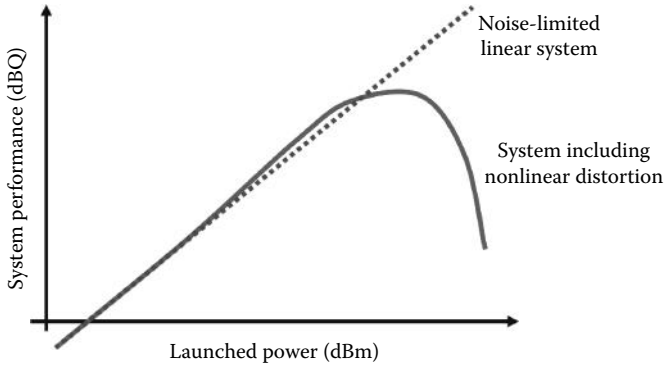

FIGURE 12.18
Variation of system performance as a function of the launched power—note the linear and nonlinear regions.

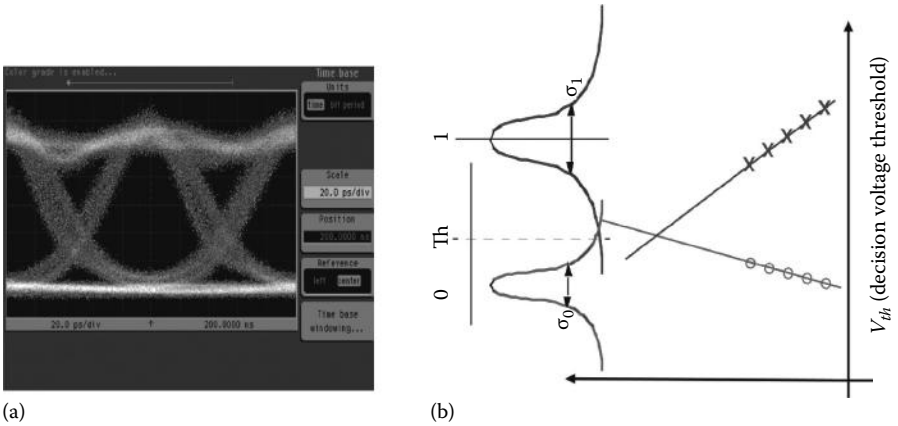

(a) (b)

FIGURE 12.19
Eye diagram and extrapolation of *Q* factor: (a) received eye diagram and (b) extrapolation of *Q* factor.

- The worst case incorporates (1) *Transmitter*: waveform, chirp, power, wavelength, noise, and jitter; (2) *Receiver*: complex transfer function, power, noise, jitter, and sampling; (3) *Fiber*: dispersion, DGD, and loss; (4) *Amplifiers*: noise figure, gain ripple and tilt, and output power; (5) *System*: net dispersion, dispersion map, channel separation, and polarization.

12.2.8.2 System Impairments

The impairments fall into two groups: distortion impairments and noise impairments.

1. *Distortion impairments*
   Any bounded reduction of the inner part of the eye diagram within the sample window including (1) Rx distortions, transfer function related; (2) Tx distortions, driving technique related, extinction ratio effect; (3) Optical path distortions, dispersion, SPM, FWM, and XPM <5 channels; and (4) PMD, cross talk, multipath interference (MPI) may be because of reflection from attenuators.
2. *Noise impairments*
   Any unbounded stochastic reduction of the inner eye within the sample window including (1) Receiver noise, (2) Tx noise, (3) Optical amplifier noise, (4) Modulation instability noise, and (5) FWM and XPM >4 channels.
3. *Signal-dependent noise contribution to the* δ *factor as a function of distortion*
   Noise and distortion can be separated for budgeting purposes.

12.2.8.3 Power and Time Eyes

The BER must include both the amplitude or power eye and the time eye, which may be a result of the jittering of the waveform at the sampling instant for evaluation of the system performance. This is illustrated in Figure 12.20. Figure 12.21 shows the eye diagram at both the transmitter and its degradation at the end of the transmission link.

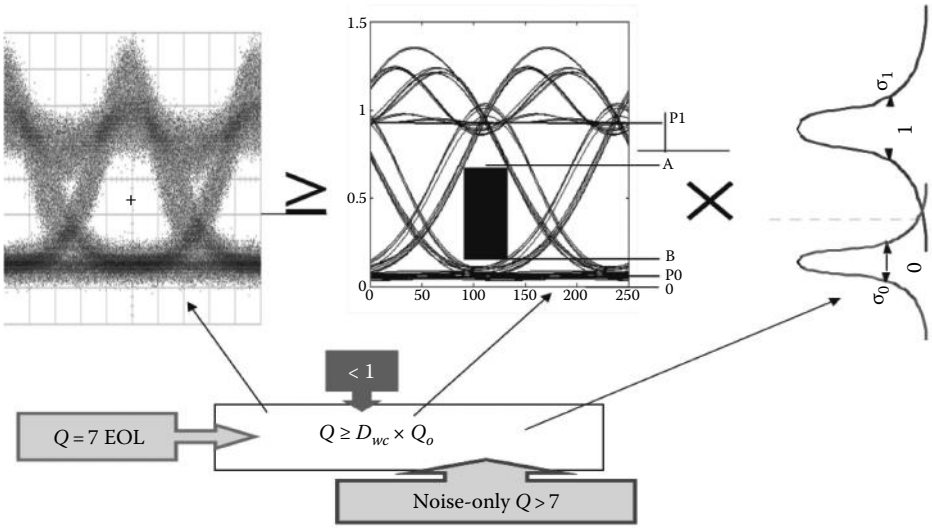

FIGURE 12.20
Illustrations of the eye diagram expected at the EOF with the original *Q* factor and effects of jittering—or time *Q* without using FEC.

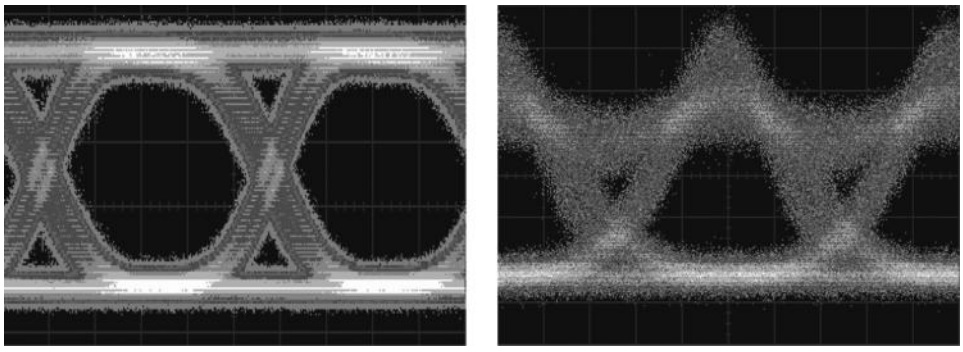

(a) (b)

FIGURE 12.21
Eye at the transmitter output (a) and at the end (b) of the transmission link.

12.2.8.4 Dispersion Tolerance Because of Wavelength Channels and Nonlinear Effects

We must note that (1) distortion depends on net dispersion and hence on wavelength and bundled wavelength groups, (2) self phase modulation makes distortion curves power dependent, (3) budgets are guaranteed over a net dispersion window meaning that the dispersion windows are reduced by any errors in link dispersion values.

12.2.8.4.1 Dependence on Wavelength Channels and Launched Power

Figure 12.22 shows examples of the dispersion tolerance in terms of the variation of eye opening penalty as a function of wavelength and launched power. It is expected that the worst performance must be targeted for the design that is the worst-case scenario.

The quality factor Q may also vary with respect to the total span length, that is, the optical amplification would contribute to the ASE noises, and hence, degradation of the quality of the system. This is illustrated in Figure 12.23. Thus, the design of optical amplifiers is very important to achieve optimum performance of the transmission systems.

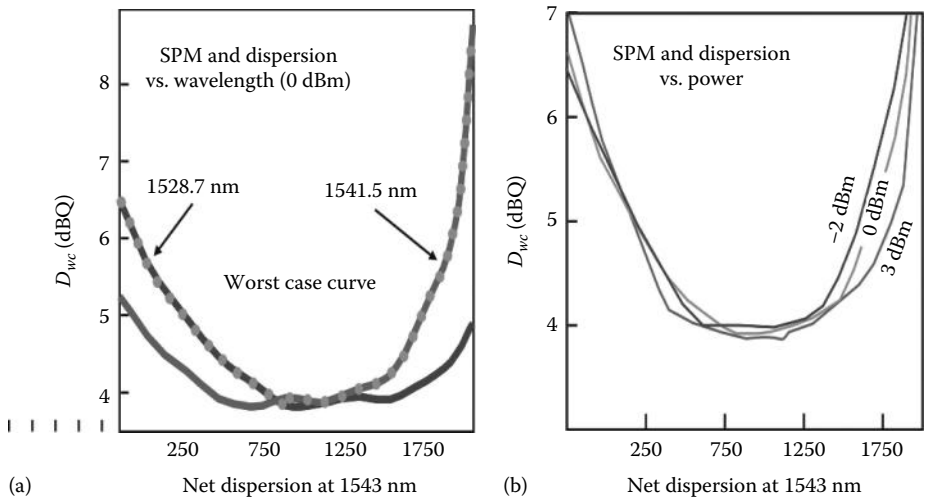

(a) (b)

FIGURE 12.22
Eye opening penalty versus dispersion as a function of (a) wavelength and (b) launched power.

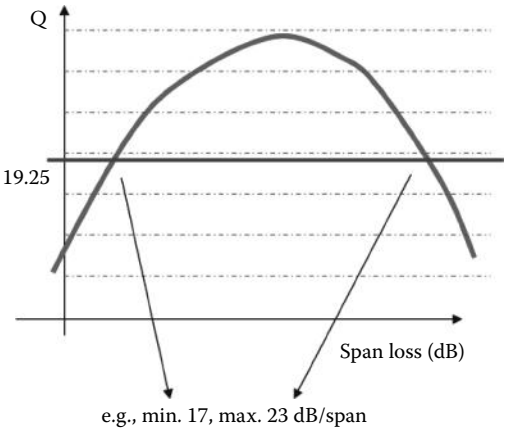

FIGURE 12.23
Variation of the quality factor *Q* with respect to the total span loss.

12.2.8.4.2 Design Cases

Example 12.4

Six-span optically amplified link—upgrading of existing transmission system with standard single-mode optical fibers.
A Transmission System requires

- Six-span non dispersion shifted fiber (NDSF), 16 wavelength channels at 200 GHz spacing or 32 wavelength channels at 100 GHz spacing, OC192 × 476 km total length
- Bidirectional transmission using one fiber only
- 1.4 dB of margin added to each calculated span loss
- Fiber attenuation is 0.22 dB/km—single optical fiber
- Not using 1625 nm as reserved for online continuity monitoring

Two options A and B of the transmission systems are given in the following:

- Compare options A and B.
- Choose an application type.
- Find dispersion compensation modules (DCM), fixed pad (attenuator), provisioning information for the final link design, and then select the cheapest possible solution (minimizing the number of MORs as much as possible).
- Bidirectional transmission and compensation require optical circulators that would then allow the dispersion compensation for wavelength channels of different spectral regions (reds and blues) (Figures 12.24 and 12.25).
- Midspan amplification for DCM60 loss of 7.3 dB, 11 − 7.3 = 3.7; therefore, use 4 dB attenuation pad. DCM80 = 9.3; therefore, use 2 dB attenuation pad.
- Attenuation pads are required for minimum span loss requirements as well. For example, 16.4 requires 2 dB attenuation pads.

Suggest a solution when provisioning is required to further extend the link by one extra span of the transmission link shown in Figure 12.26.

Example 12.5

Sixteen wavelength channel five-span NDSF MOR bidirectional optical transmission.

With the same transmission distance as the previous example but with only five spans. Readers should inspect the following design and check to see whether they can confirm the design (Figure 12.27):

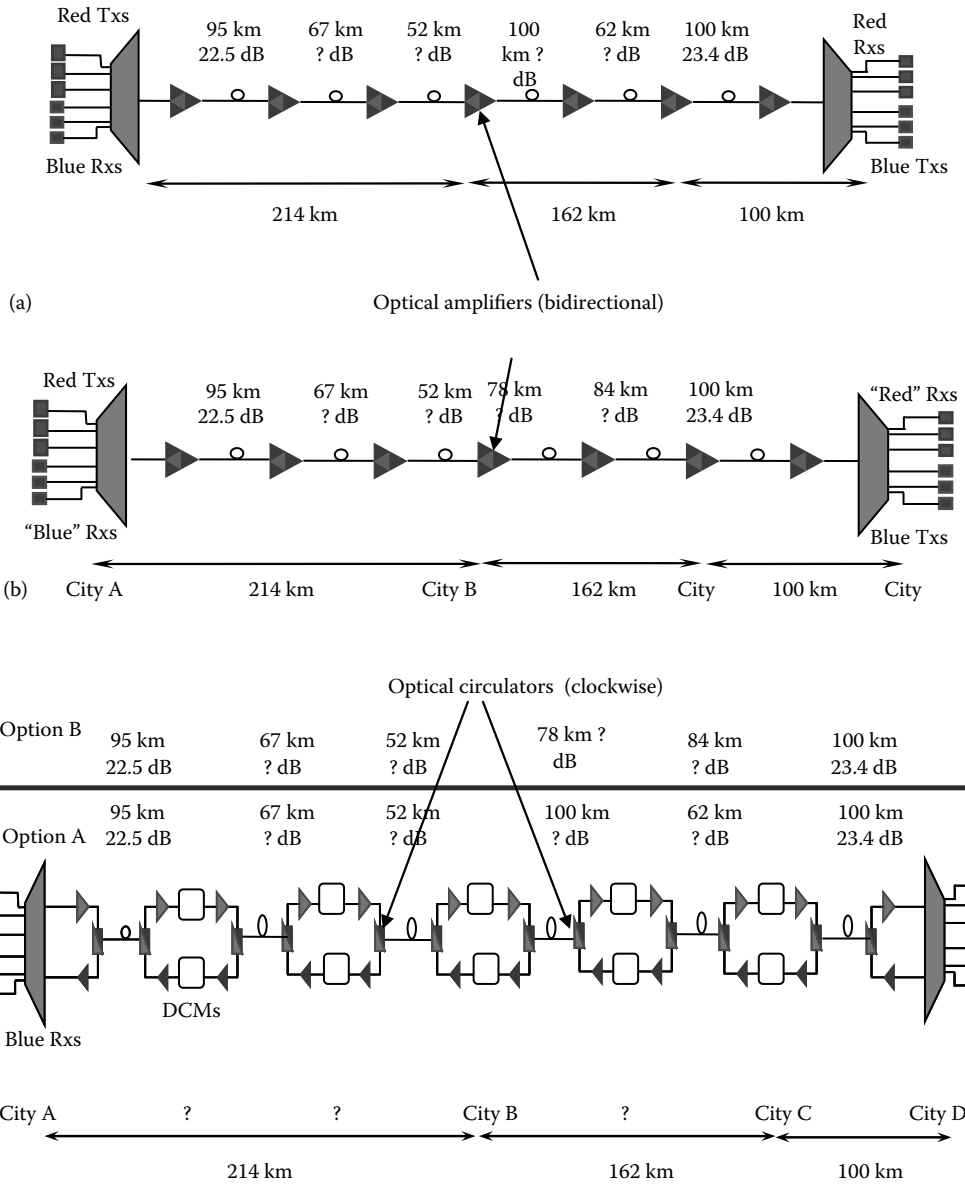

FIGURE 12.24
Design structures of multispan link using bidirectional techniques: (a) option A, (b) option B, and (c) detailed arrangement.

- Site A is the site closest to the line amplifier site, to the RED transmitter (Tx).
- In each case, the chirp on the add/drop wavelengths must be positive (to compensate for the large negative DCMs within the add/drop sublink).
- Two-span windows must be 154–166 km in length (155 km).
- Three-span windows must be 231–249 km in length (245 km).
- Rules apply for FEC with a BER of 10^{-12}.

Option B	95 km 22.5 dB	67 km 18 dB	52 km 18 dB	78 km 18.8 dB	84 km 20.1 dB	100 km 23.4 dB
Option A	95 km 22.5 dB	67 km 18 dB	52 km 18 dB	100 km 23.7 dB	62 km 18 dB	100 km 23.4 dB

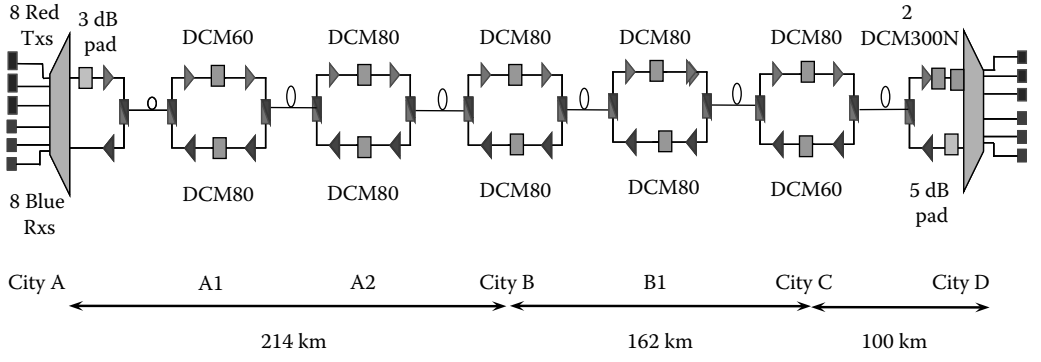

FIGURE 12.25
Solution of six-span link for 405 km distance via three cities.

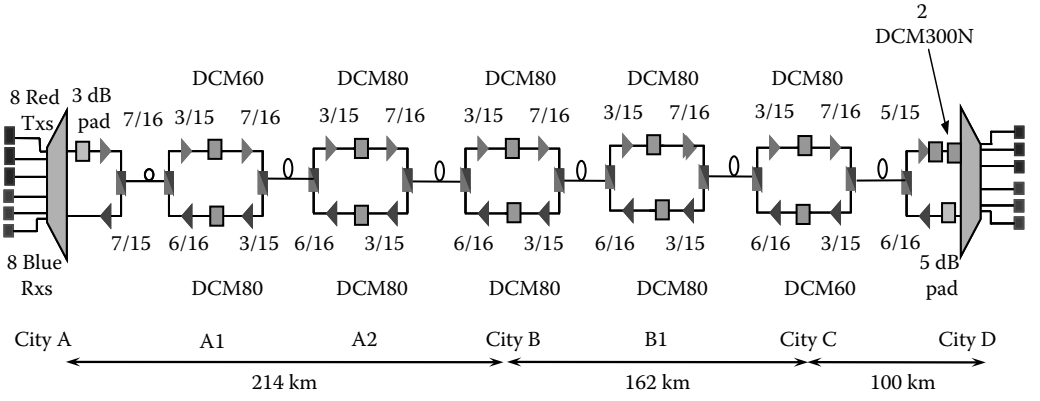

FIGURE 12.26
Transmission system solution with provisioning.

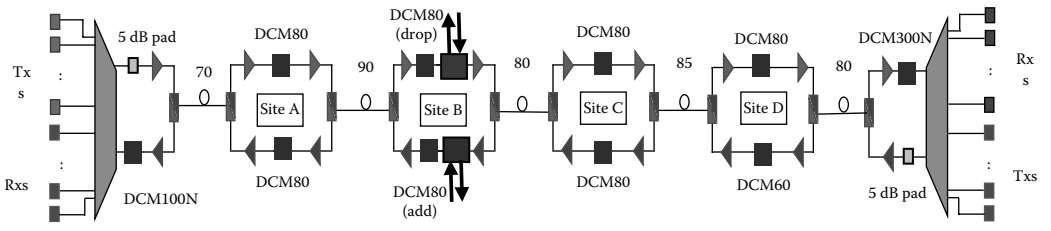

FIGURE 12.27
Transmission with provisioning for OADM insertion.

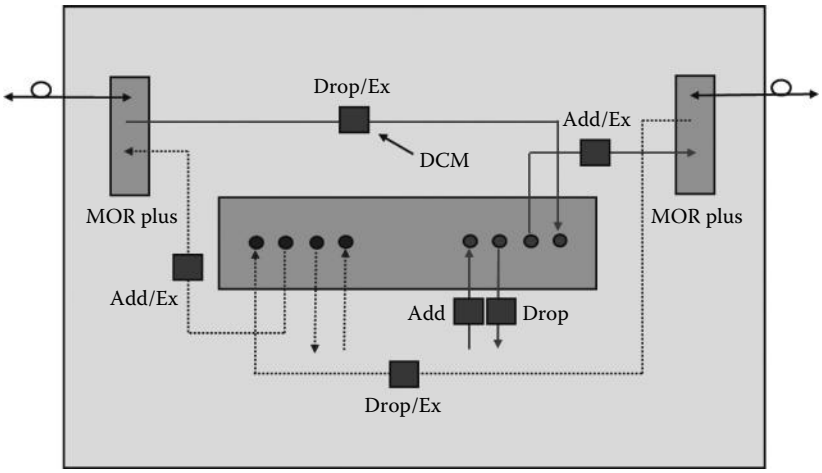

FIGURE 12.28
Structure of an OADM. MOR, midspan optical regenerator.

12.2.9 Engineering an OADM Transmission Link

The structure of an OADM is shown in Figure 12.28. Selected wavelength channels of the incoming muxed channels dropped or wavelength channels added to the transmission system can be observed from this diagram. The details of the optical components such as optical filters and circulators are not shown in this section but observed from the system point of view.

Knowing the fiber and amplifier type and the number of wavelength channels, we can determine the express compensation rules for the link. MSA loss now includes DCMs and OADM couplers (attenuation pad up if required). Furthermore, provisioning of powers of sites, which changed the amplifier type as a result of the OADM, should also be made. Then determine the OADM compensation rules (in both power budget and dispersion) for the link. One should also apply these rules for both the working and protection fiber transmission paths.

12.3 Appendix: Power Budget

Power budget is the counterpart of the rise time budget (see Section 12.2.3) to ensure that the signals entering the reception subsystem have sufficient energy for detection that satisfies a certain criteria for error-free reception. The two scenarios of distinct reception sensitivities of a communication receiver are whether FEC is employed or not. If no FEC is employed then for a Gaussian pdf, the BER is required to reach 10^{-9} or the amplitude ratio of the average levels between the "1" and "0" must be at least six times the total standard deviation of the noise levels of the "1" and "0". With FEC then this BER can be lowered to about 10^{-3} or thereabouts depending on the error coding method.

The following steps are employed to determine the power budget:

- Identifying the modulation format of the signals and hence the Euclidean distance between the states. Then the required ratio between the energy level and the noise power for a specified BER can be determined.
- Identify the probability density function of the transmission and detection processes, hence, the noises. Then identify the noise sources contributed to the modulated and transmitted signals or signal levels.
- Obtain the attenuation factor, for example, dB/km in fiber and any noise sources superimposing on the signals during transmission, for example, the ASE noises of inline optical amplifiers.
- Then determine the required receiver sensitivity of the reception systems, which is defined as the minimum power level required for the signals to be available at the input of the receiver at a specified BER.
- Work back, using a linear log scale diagram to estimate the required signal power to be launched at the output of the transmitter to achieve this reception receiving sensitivity.

These steps can be done in our head without resorting to top computing devices, not even a simple calculator. This can be done by converting all power and attenuation in log scale or in dB level, then all estimations are just additions and subtractions.

12.3.1 Power Budget Estimation: An Example

As an example consider the transmission system given in Figure 12.29. The modulation is assumed to be binary OOK, the transmission link is a multispan SSMF optically amplified type, and the reception system is based on direct detection technique with a PD and followed by trans-impedance amplifier (TIA) and automatic gain control (AGC) if required.

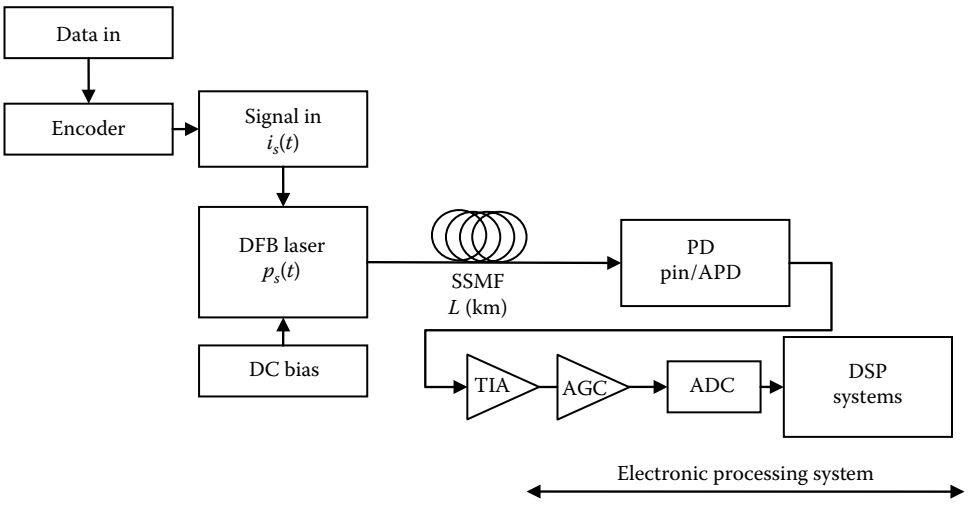

FIGURE 12.29
Intensity modulation direct detection transmission scheme.

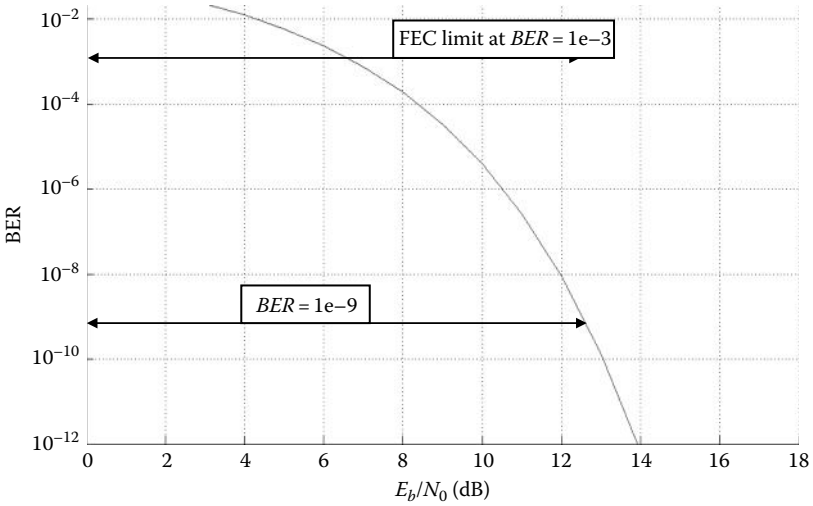

FIGURE 12.30
Theoretical estimation for BER versus SNR for binary OOK of Gaussian noisy system.

Under binary OOK modulation scheme, we estimate that an SNR of 6 is required for a BER of 1e−9. With some uncertainty in the transmission system, a *BER* of 1e−12 is used leading to an SNR of 7 (the *Q* factor in linear scale). Figure 12.30 depicts the required SNR for BER values over ten decades, that is, the *Q*-factor increase by one unit required for a decade of BER for a Gaussian pdf detection process. Thus, corresponding to *Q* of 6 and 7 the OSNR can be determined to be $10\text{Log}_{10}6$~15 dB.

So, for an optical receiver how do we determine the noise power at its input port, that is, at the front of the PD. This implies that we have to estimate all noise equivalent power at the input port of the receiver, or alternatively we find all equivalent noise currents referred to the input port of the receiver as shown in Figure 12.31 in which we identify that (1) i_s^2 represents average input current as converted by the photodetection process of the input signal; (2) total equivalent noise current i_{Neq}^2 as referred to the input of the electronic preamplifier following the PD*; and (3) total noise equivalent, i_{sq}^2, generated during the opto-electronic conversion such as the quantum shot noise by the signal input and the dark current noise of the PD.

It is noted that under direct detection the amplifier noise current normally dominates over the quantum shot noises, while this is opposite in the case of coherent detection in which the quantum shot noises are because of the high average power of the coherent sources.

Now reverting back to the optical fiber transmission link, we have for direct modulation and bias at current $I_b = 5I_{th}$ with a magnitude of $4.5I_{th}$ the average optical power at the

* Commercial amplifiers normally specify the noise characteristics as the total equivalent noise spectral density referred to the input in units of A/√Hz. This parameter is normally measured by connecting the output of the amplifier to a spectrum analyzer with no signals input. The output is integrated over the bandwidth of the amplifier to obtain the total noise voltage at the output. In case of a TIA, this output voltage noise is then transferred back to the input by a simple division. Hence, we can get the total equivalent noise current referred to the input. This noise current referred to the input can be converted to equivalent optical power by using the responsivity of the PD. From this value and the OSNR it can be determined if the transmission link operates to give the required BER.

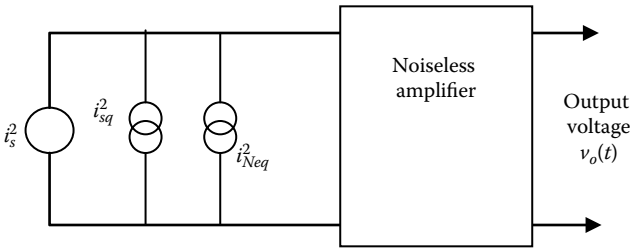

FIGURE 12.31
Equivalent current model referred to the input of the optical receiver, average signal current, and equivalent noise current of the electronic preamplifier as seen from its input port.

output of the distributed feedback (DFB) can reach 10 dBm. But for the "0" we would have to drive with a magnitude of about $1.5I_{th}$. So, we expect noisy signals at the base level, a "high" level, and we expect a distinction ratio of more than 20 dB. Under this driving condition, let us assume that the average power of 0 dBm is obtained at the output of the DFB laser.

The attenuation and power requirements for each subsystem of the link can now be estimated as follows:

The fiber loss for 80 and 100 km SSMF would be about 20–25 dB.

Using the pin or APD (avalanched gain of 10) PD and a differential TIA (Inphi model 3250A) with a noise spectral density referred to the input of $\left(di_N^2/df\right)^{1/2} = 20 - 40\ \text{pA}/\sqrt{\text{Hz}}$, we would be −7 and −17 dBm, respectively, for a required OSNR of 15 dB and BER of 1e−9–1e−12 (δ or Q factor of 6 or 7 under the assumption of a Gaussian pdf).

This indicates that an APD is preferred as the PD so that the use of an optical amplifier is avoided. The projection in the variation of transmission distance with respect to the launched power at the output of the transmitter is shown in Figure 12.32.

With the *p–i–n* PD, we expect to transmit 25G NRZ channel over only 40 km with a launched power of 4 dBm. However, with the APD of a gain of 10, the transmission distance limited by the power budget can reach over 80 km on condition that the pulse sequence is equalized at the DSP-based receiver or an SSB modulation scheme such as the duo-binary modulation format is employed.

12.3.2 Signal to Noise Ratio (SNR) and Optical SNR

Referring to Figure 12.31 that represents the total noises as referred to the input and the generated signal current from the input optical signals, it must be noted that superimposing on the signals are other noises, commonly known as the quantum shot noises, that are signal dependent and dependent on the signal average current whose spectral density is given by

$$\begin{aligned} &S_{NQ} = 2q\langle i_S \rangle \text{ in A}^2/\text{Hz} \\ &\rightarrow i_{NQ} \text{ by\_integrating\_over\_BW and sqrt} \end{aligned} \tag{12.17}$$

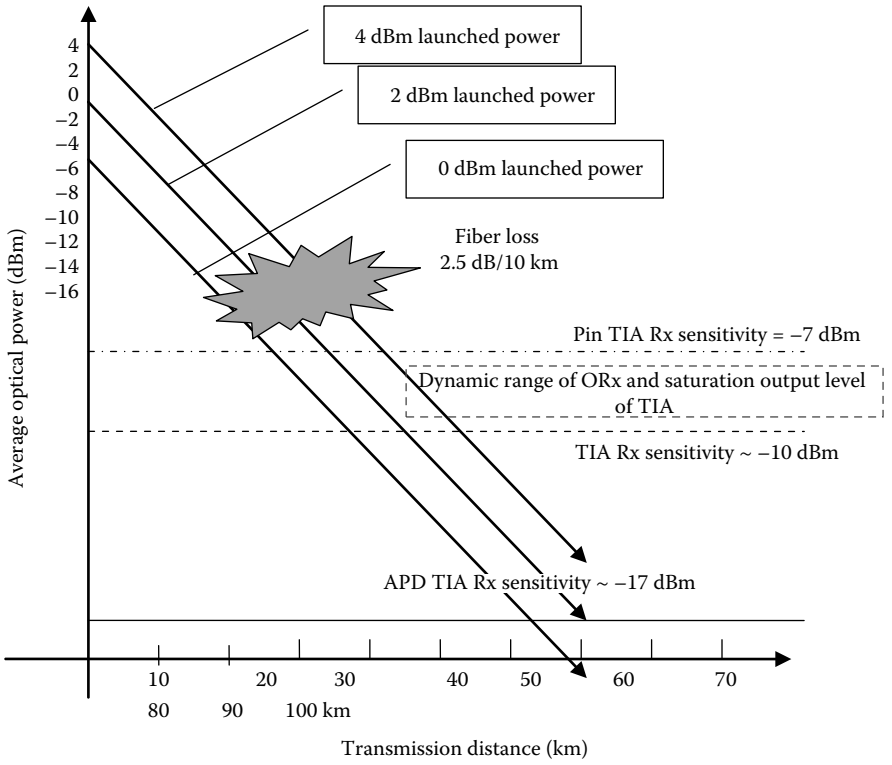

FIGURE 12.32
Power budget with an average launched power of 0, 2, and 4 dBm with receiver sensitivity of –7 and –17 dBm and fiber loss of 2.5 dB/10 km (see also Annex 3).

Furthermore, there are noise currents coming from the dark current of the PD i_{Nd}, that is, the electronic current in the semiconductor junction at a temperature above the absolute reference temperature. So, let the total noise current referred to the input of an optical receiver be written as

$$i_{NT} = i_{NA} + i_{NQ} + i_{Nd} \tag{12.18}$$

Thus, the SNR, in terms of power, is formed as

$$SNR = \frac{\left\langle i_S^2 \right\rangle}{i_{NT}^2} \tag{12.19}$$

The BER can be estimated for ASK or PAM. If under a different modulation format, one can refer to Figure 12.3 or use betoll.m of MATLAB® to obtain the energy per bit then the ratio of the amplitude of the signal and the noise. Then for binary signals PAM-2 and under Gaussian noise assumptions, we obtain

$$BER = \frac{1}{2} ercf\left(\frac{Q}{\sqrt{2}}\right) \quad \text{where } Q = \frac{I_1 - I_0}{\sigma_1 - \sigma_0} \tag{12.20}$$

with I_1, I_0 as the average current detected by the PD for "1" and "0," respectively, and σ_1, σ_0 are the standard deviation of the noises levels due to "1" and "0," respectively. If the modulation format is quadrature amplitude modulation (QAM), then the errors of detection can be considered as the summation of the two orthogonal "binary" signals, the complex and real components. The BER can be estimated for both directions as given in (12.20). If there are cross talks between adjacent channels or between channels traveling in opposite directions, then these are taken into account as additional noise contributions.

Thus, we see that by estimating the total current noise referred to the input of the electronic preamplifier, normally a TIA, and the dark current, and the signal-dependent signal current noise with a typical average optical power at the input, we obtain a rough estimate of the SNR and the OSNR. Note that the estimation of the noises should be considered for the dominating noise term.

Naturally, the electronic current at the output of the preamplifier of the receiver would not be sufficient for the ADC and signal processor, so a voltage gain amplifier with or without an automatic gain control stage (see Figure 12.29) would commonly be employed to boost the signal level up. The noise at the input of this voltage gain stage as referred to the input of the optical receiver is normally much smaller than that of the preamplifier, so it can be ignored.

Other modulation can be derived using the principles of superposition of probability of errors contributed to the considered constellation point by neighboring points.

12.3.3 TIA: Differential and Nondifferential Types

TIA is the critical amplifying device, which is to be connected in cascade with a high-speed PD to provide the preamplification of the current produced in the PD to the voltage output whose level would be appropriate for an analog to digital conversion so that digitized signals can then be processed in the digital domain by a DSP. The total equivalent noises referred to the input port of this amplifier are very critical to the impact of the SNR of the optical receiver. The method for calculations of noise processes and noise currents as well as the total equivalent noises referred to the input is given in Annex 3.

Traditionally, single input or nondifferential input TIA has been extensively exploited over the years [4]. However, currently differential TIAs (DTIAs) offer wider bandwidth and high differential trans-impedance gain of around 3000–5000 Ω over the 30–40 GHz bandwidth by Si-Ge technology, and the hose transition frequency f_T can reach 280 GHz* [5,6]. However, these DTIAs [7] are limited in their dynamic range, and normally an automatic gain control stage is required. A typical setup of a PD pair and a DTIA is shown in Figure 12.33. Typical circuit diagrams of the DTIA employing Si-Ge and InP are shown in Figure 12.34a and b, respectively, in which there is the main differential long-tail pair followed by two common collector stages connected to the differential output of this long tail pair. The outputs of these stages are then fed back by a shunt feedback to obtain the highest transfer-impedance and wideband property. The outputs are fed back to the

* The transition frequency f_T is defined as the frequency at which the short-circuit current gain of a transistor equals unity.

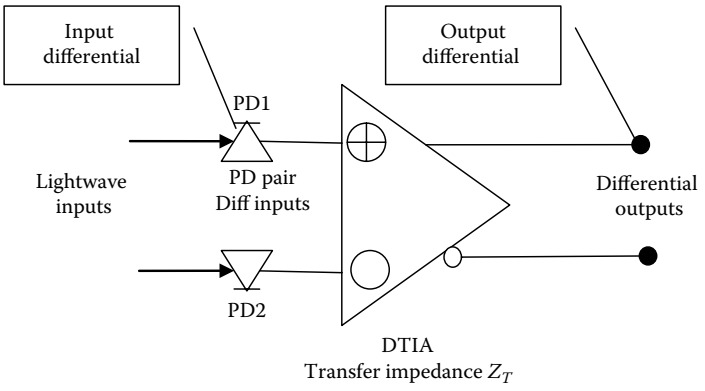

FIGURE 12.33
DTIA and PD pair.

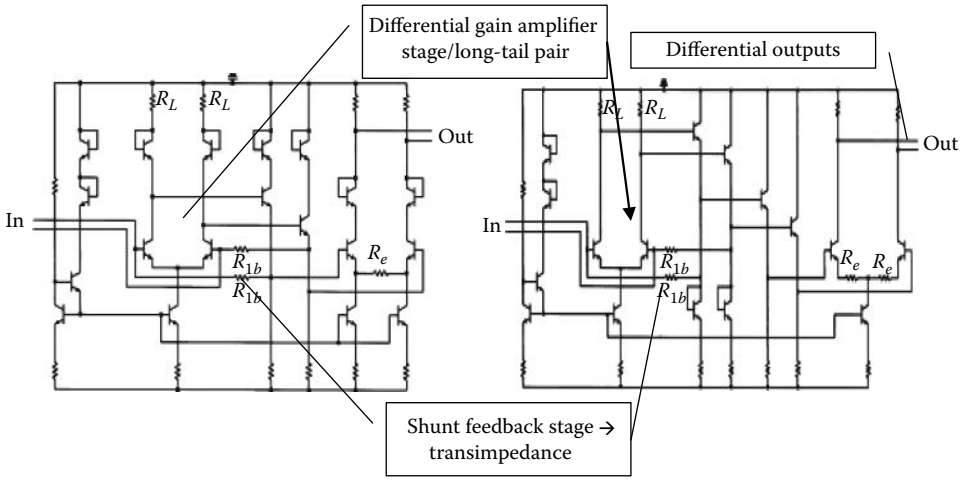

FIGURE 12.34
Typical circuit topologies of DTIA by Si-Ge and InP technology. (Extracted with permission from Ref. [7].)

differential input. These differential ports are then fed into a further differential voltage gain stage (without any feedback stage).

The DTIA can offer a transfer impedance of 4000–5000 Ω. Thus, with an optical signal average power input of 0 dBm (or 1 mW) and a responsivity of the PD of 0.9~1.0 A/W, a current of 1 mA is produced and fed into the DTIA. This in turn produces a differential voltage of 4–5 V signals at the output. Unfortunately, this level saturates the outputs of the DTIA. So normally, an automatic gain control stage is employed to increase the dynamic range of the optical receiver. The parameters of the DTIA with the input-referred current noise of the InP TIA are approximately $25\,\text{pA}/\sqrt{\text{Hz}}$ on average for a bandwidth of 40 GHz.

Problems

12.1 The distance between the transmitter and the receiver in an optical fiber transmission link using direct detection, intensity modulation is 100 km. The fiber link is made by splicing similar fibers of 22 km length each. The splicing loss is 0.15 dB per splice. The fiber attenuation is 0.4 dB/km.

(a) How many splices are required for 100 km link? Hence, estimate the total splice loss.

(b) The coupling loss is 1.5 dB in total at the transmitter and the receiver.

If the optical receiver has a receiver sensitivity of −30 dBm, what is the required power at the output of the optical transmitter if a power operating margin of 5 dB is used?

12.2 An optical fiber transmission system over 1500 km distance is to be designed with a span length of 100 km. The following components are to be selected from websites of jdsuniphase.com, corning.com, and avenex.com. The following parameters of the systems are specified as

- Bit rate = 10 Gb/s with *BER* = 1e–12
- Modulation format: OOK or DPSK, DQPSK or MSK or Star QAM
- The number of wavelength channels in the C-band must be at least 40 with 50 GHz spacing between channels and DWDM transmission
- Operating margin 3 dB

Fiber: single-mode type either standard or nonzero dispersion shifted fiber.

(a) Select appropriate optical subsystems: optical transmitters including laser and an external optical modulator. Give reasons why an external modulation must be used. Use the 3 dB bandwidth of the modulator to estimate the pulse broadening factor of the transmitter.

(b) Select an integrated optical receiver and state the rise and fall time of the receiver and hence, estimate the broadening factor of the receiver. State the total equivalent noise current at the input of the receiver.

(c) Select either SMF-28 or LEAF or any other fibers that you can find. Corning Vascade fibers should be used for undersea routes. Hence, select DCF modules to match the dispersion of the transmission fiber per 100 km span.

(d) Specify the wavelength grid of the channels and the dispersion factor at the wavelength position of the channels. Hence, calculate the residual dispersion of the channels at the extreme wavelength locations.

(e) Select optical amplifiers such as EDFAs. State their minimum and maximum input optical powers, maximum optical power at the output, the optical gain, and noise figure. Hence, what is the power level that would drive the amplifier into saturation?

(f) Establish the structure of the transmission systems including spans, optical transmitters, and receivers. Make sure that details of the optical transmission spans are specified.

(g) Establish the rise time budget table. Sketch the dispersion/broadening of the pulse over each span. Make sure that the broadening satisfies the 70% bit period criteria for all channels.

(h) Establish an attenuation budget table. Make sure that receiver sensitivity can be employed to recover the signals.

12.3 Mini–Project Design: Optical Communications System Design

Network distribution	Australian ultra-wideband optical fiber backbone networks
Transmission link distance	Melbourne–Sydney; Melbourne–Hobart; Melbourne–Adelaide
Transmission techniques	Dense wavelength division multiplexing techniques with synchronous digital hierarchy technology STM-64, bit rate = 9953 Mb/s or 40 Gb/s return-to-zero format or Ethernet 100 Gb/s
Modulation formats	ASK, DPSK, DQPSK, and MSK with pulse shaping NRZ or RZ to be considered
BER	$<10^{-12}$—to be confirmed with numerical simulation
Network configuration	SDH ring—suggestion: for example, double ring with optical cross connect near Canberra
Total capacity	40 Gb/s × 32 wavelength channels or 80 Gb/s × 16 wavelength channels
Wavelength regions	Suggested C-, L-, or S-bands 1485–1625 nm
Optical channel frequency spacing	50 or 100 GHz spacing between channels
Transmission medium	SMF-28 (G.652 ITU standard) with dispersion compensating techniques (fiber or chirped transmitters) or NZDSF, for example, LEAF and TrueWave
Fault monitoring systems	Optical time domain reflectometry (OTDR) and wavelength channel fault identification—specify OTDR management system
Optical amplifiers	Erbium-doped fiber amplifiers and/or Raman fiber amplifiers
Photonic components	DWDM multiplexers/demultiplexers, couplers, and so on available from websites or Laboratory of Optical Communications (Monash)
Operating margin	3.5 dB
Transmitters and receivers	Refer to commercial products at websites of manufacturers, for example, www.nel.co.jp, www.jds-uniphase.com, www.lucent.com, and www.fujitsu.com

Suggestions

- Build a technical case for the optical fiber transmission systems and networks
- Build a business case for a rollout of a new network linking the capital cities in Australia. You should consider the following: (a) base the case on carrying bulk data (IP over SDH—synchronous digital hierarchy to remove cost of provision of an ATM layer) and (b) assume the incumbent is currently operating on 2.5 Gb/s equipment over fibers up to 15-year old.
- On the basis of the technical design of the network, present a business case requesting funding from a venture capitalist to build the network.

12.4 A long-haul optically amplified fiber transmission system operating at a wavelength of 1550 nm is envisaged to use EDFAs spaced at intervals of 100 km. Alternating +D and −D single-mode optical fibers are used. The mode spot size of these fibers is the same. The power launched into the link at the transmitter is 0 dBm. The fiber attenuation is 0.22 dB/km. In addition, there are slice losses that average out at 0.03/km.

An optical SNR of 17 dB is required at the receiver to provide a BER of 1e–9 at an operating bit rate of 10 Gb/s. Assuming that the system bandwidth is equal to that of the bit rate and the noise figure of the amplifier NF = 3 dB for an optical gain of 20 dB. Estimate the maximum transmission length of the system such that satisfactory performance can be maintained.

12.5 1. Sketch the structure of an optical transmission consisting of
   a. An optical transmitter that can multiplex all optical channels allocated in the C-band with 50 GHz spacing between the channels
   b. Optical demultiplexers and receivers for each wavelength channel
   c. The transmission distance is 200 km with a span length of 100 km on average—dispersion compensators as optical fibers can be installed along the transmission path
   d. Optical amplifiers are required in each span

2. Design the transmitters, optical receivers, and the fiber spans with optical amplifiers with the following parameters:
   a. Fiber nonlinear threshold for SMF-28 is 5–10 dBm for the total average power of all channels.
   b. The diameter of the spot size of the DCF is about 30% of the SMF-28, and its dispersion factor is −68 ps/nm/km. The attenuation of this DCF is about 0.35 dB/km.
   c. Optical amplifiers can have two types: Type 1: gain = 25 dB, saturation output power = 15 dBm. Minimum input power = –25 dBm and maximum input is 0 dBm. Type 2: gain = 20 dB, saturation output power = 10 dBm. Minimum input power = –25 dBm and maximum input is 0 dBm.
   d. Optical receiver sensitivity is –28 dBm, and an optical SNR of 15 dB is required for the bit rate of 10 Gb/s.
   e. Excess loss of multiplexer and demultiplexer is about 1 dB.

It is suggested that you should conduct the following:

- Following the example in Question 1, estimate the maximum transmission distance.
- Obtain a power budget and distribution along all spans of the transmission system.
- Obtain the dispersion map of the system along all spans.

12.6 For the system bit rates of 10 Gb/s and ASK NRZ transmission format with a BER of 1e–12 and the photonic and optoelectronic components specified and given, respectively, in Question 2 and any other necessary optical components, design an optical transmission system for a section of the network, which has a total transmission distance of 1000 km. In case you cannot obtain the receiver sensitivity of Part (b), it is possible to assume that the electronic preamplifier is adjusted so that the receiver sensitivity is –20 dBm, the rise and fall time remains the same.

Optical transmitters using distributed feedback lasers with typical laser linewidth of 0.001 nm and an external modulator. The average optical power of –10 to 2 dBm at the output of the fiber pigtail of the modulator is normally available for such transmission systems. The transmitter would have a total rise and fall time of not higher than 2 ps.

Optical fibers can be selected from Corning fiber products SMF-28 or LEAF, that is, the dispersion factor at 1550 nm is 17ps/(nm·km) and 4 ps/nm·km, respectively. The nonlinear SPM coefficient for silica is about 2.3×10^{-20} m^2/W, and attenuation of the fibers is 0.2 dB/km. The spot sizes are about 4 μm for SMF-28 and 5 μm for LEAF.

Now, if a number of optical channels with wavelength spacing of 50 GHz over the entire C-band 1525–1560 nm carrying NRZ data at 40 Gb/s are multiplexed into the same fiber, taking the fiber nonlinearity into considerations, describe details of considerations for any change in the design of Part (a).

12.7 An undersea optical transmission is to be designed. The undersea distance is 220 km. The bit rate is 40 Gb/s, and optical receiver with a sensitivity of –20 dBm is available. Optical amplifiers EDFA and ROA are considered with the following parameters: fiber types, SSMF and DCF (–85 ps/nm/km and effective area of 17 μm^2); EDFA: Gain 20 dB, *NF* = 5 dB output power, saturated output power = 15 dBm for booster amplifier type and +10 dBm for optical preamplification type. Raman optical amplifiers: pump power of 500 mW, gain in SSMF is 12 dB over 20 km distributed distance of the fiber and *NF* = 3 dB, for both co- and contra-directional pump:

(a) Sketch a proposed structure of the transmission link.

(b) Obtain a diagram of the signal power or power budget over the link.

(c) Obtain the dispersion budget over the link.

References

1. *OIF Workshop—Challenges for Next Generation 400G Electrical Links*, San Jose, CA, 2014, http://www.oiforum.com/public/OIF_PLL_Workshop2014_reg.html. Accessed March, 2014.
2. B. Collings, FlexGrid Technologies, *ECOC 2012, WS08 Beyond 100G—Technology Options*, Amsterdam, the Netherlands, September 16, 2012.
3. L.N. Binh, *Digital Optical Communications*, 2nd ed., CRC Press, Boca Raton, FL, 2014.
4. T. van Muoi, Receiver design for high speed optical fiber systems, *IEEE Journal of Lightwave Technology*, LT-2(3), 243–266, 1984.
5. P. Kempf and M. Racanelli, Silicon germanium BiCMOS technology, in *IEEE GaAs IC Symposium Digital*, pp. 3–6, Monterey CA, 20–23 October 2002.
6. B. Jagannathan, M. Khater, F. Pagette, J.-S. Rieh, D. Angell, H. Chen, J. Florkey et al., Self-aligned site NPN transistors with 285 GHz f_{max} and 207 GHz f_T in a manufacturable technology, *IEEE Electron Device Letters*, 23, 258–260, May 2002.
7. J.S. Weiner, A. Leven, V. Houtsma, Y. Baeyens, Y.-K. Chen, P. Paschke, Y. Yang et al., SiGe differential transimpedance amplifier with 50-GHz bandwidth, *IEEE Journal of Solid-State Circuits*, 38(9), 1512–1517, September 2003.

13

Self-Coherent Optically Amplified Digital Transmission Systems: Techniques and Simulink® Models

This chapter gives examples and simulation models in MATLAB® Simulink® of a number of optically amplified transmission systems employing advanced modulation formats amplitude shift keying (ASK), differential phase shift keying (DPSK), differential quadrature phase shift keying (DQPSK), minimum shift keying (MSK), and Star–quadrature amplitude modulation (QAM) with optically amplified spans using either Er:doped fiber amplifiers (EDFAs) or distributed ROAs. In the Appendix, we give guidance for the uses of these models whose MATLAB Simulink codes can also be downloaded from CRC Press website. The Appendix gives some guidelines for using and modeling with MATLAB Simulink.

13.1 ASK Modulation Formats Transmission Models

Advanced optical fiber communications have been attracting tremendous interests in recent years because of urgent demands on the upgrading of the fiber backbone transmission systems and networks [1]. In these modern optical transmission systems, modulation techniques employing amplitude, phase, and/or frequency shift keying (SK) modulation schemes are considered to be the keys for reducing the signal and carrier spectral properties. Together with these schemes, the formats of the pulse sequence such as return-to-zero (RZ), non–return-to-zero (NRZ), carrier-suppressed RZ (CSRZ), or duo-binary or bi-phase shaping of the pulse sequence are considered to optimize the transmission energy contents of the transmitted sequence, and hence, enhancement of the total transmission distance without violating the nonlinear/linear limit of the transmission or dispersion compensating fibers.

This section outlines the modeling of the amplitude SK in association with the pulse shaping modes of RZ, NRZ, and CSRZ and duo-binary formats so that the simulated results can be corroborated. The modeling platform is based on MATLAB Simulink as this mathematical and graphical modeling package offers sufficient signal representations and processing blocksets that allow the generation, modulation, and processing of light waves and signals schemes at optical frequencies in the passband and baseband domains. Furthermore, it offers a range of equipment that could be employed to inspect signals in the temporal and spectral domains to study the impacts of the modulation spectra on the transmitted data sequence.

Models have been developed for ASK for all formats and their transmissions; especially, the dispersion tolerance over standard SMF fibers is demonstrated. Further, the duo-binary modulation scheme with the alternating phase property is also demonstrated. The developed models have been proved effective in transmission and in receiving by interferometric

delay schemes for differential detection and recovery of the precoded sequence. The optical modulation employing external modulators such as the electro-absorption (EA) and electro-optic (EO) ones is very important for modulation schemes using both amplitude and phase. These are exploited in our study with the EA and $LiNbO_3$ type modulators. We note that the models representing photonic components such as the modulators, interferometric delay balanced receiver, are operating in the photonic domain. That is the interaction between guided optical waves and traveling wave electrical signals represent exactly the real EO operation. No mathematical representation is used. This contrasts the modeling of several packages developed for optical communications systems in which the mathematical language has been used. The Simulink models are described wherever appropriate to prove these findings.

13.1.1 Introductory Remarks

Owing to the tremendous growing demand for high-capacity transmission over the Internet, a high data rate of 40 Gb/s per channel has become an attractive feature in the next generation of lightwave communication systems. Under the current 10 Gb/s dense wavelength division multiplexing (DWDM) optical system, overlaying 40 Gb/s on the existing network can be considered to be the most cost-effective method for upgrading purpose. However, there are a number of technical difficulties involving interoperability that confront communications engineers—requiring 40 Gb/s line system to have signal optical bandwidth, tolerance to chromatic dispersion, resistance to nonlinear crosstalk, and susceptibility to accumulated noise over multispan of optical amplifier to be similar to the 10 Gb/s system.

In view of this, advanced modulation formats have been demonstrated as an effective scheme to overcome 40 Gb/s system impairments. DPSK modulation format has attracted extensive studies over the conventional ASK or on–off keying (OOK)* signaling format, including 3 dB lower optical signal-to-noise ratio (OSNR) at a given BER, because it is more robust to narrow-band optical filtering, more resilient to some nonlinear effects such as cross-phase modulation and self-phase modulation (SPM). Moreover, spectral efficiencies can be improved by using multilevel signaling. On top of that, coherent detection is not critical as differential detection requires comparison of two consecutive pulses; hence, the source coherence is required only over 1-bit period.

Nevertheless, DPSK format involves rapid phase change causing intensity ripples as a result of chromatic dispersion that induce the pattern-dependent SPM-GVD (group velocity dispersion) effect. Therefore, the RZ pulse can be employed in conjunction with DPSK to generate more tolerance to the data pattern-dependent SPM-GVD effect. In addition, RZ improves dispersion tolerance and nonlinear effects particularly in long-haul networks at high data rate. Specific RZ formats, such as CSRZ, help to reduce the inherent larger spectral bandwidth.

At 40 Gb/s, generation of RZ pulse is not feasible as it is at 10 Gb/s because of the large bandwidth requirement. Thus, 40 Gb/s RZ signals are produced optically in the "pulse carver" by driving the modulator with 20 GHz RF signal. With the remarkable advancement in the external modulator, especially the Mach–Zehnder interferometric modulator (MZIM), this is easily achieved by using the microwave optical transfer characteristic of MZIM.

* The term ASK is preferred rather than OOK as it reflects the quasi coherence of the detection scheme in which the amplitude and phase of the carriers do contribute to the sensitivity of the receiving system.

In this chapter, we present the viability of RZ–ASK modulation formats for the next generation of lightwave communication system, especially for ultra-high-capacity and ultra-long-haul link. Simulation models have been described based on the MATLAB Simulink platform. A user-friendly environment Simulink provides fast design and modeling tools to simulate components and essential devices such as MZIM. System performances, optical signal bandwidth, eye diagram, and error probabilities can be evaluated instantaneously by changing design parameters. In high-cost and expensive long-haul optical transmission systems, these simulation results are important for communication engineers to design network configurations prior to experiment and installation.

This section is organized as follows: In Section 13.1.2, a general optical communication system comprising essential photonic components in single-channel and multichannel structures is described. In Section 13.1.3, the basic principles of the components in photonic transmitters such as laser source and optical modulators are discussed. Section 13.1.4 briefly describes the principal propagation phenomena and its constants and its second- and third-order parameters that would severely distort the carrier modulated data sequence. Section 13.1.5 gives details of the model.

The principles of generation by using the Mach–Zehnder interferometric structures based on biasing voltage and voltage swing of the modulating signals and characteristics such as signal spectra of different modulation formats are depicted in Section 13.6. The receiver structures and working principles based on single-ended and balanced detection are explained in Section 13.7.

In Section 13.8, the modeling design process of the optical source, MZIM, fiber propagation, receiver, and BER evaluation are described. In particular, the results of RZ-DPSK are illustrated to prove the interconnection and working of each module. In Section 13.9, system performances such as dispersion tolerance of different modulation formats, the advantages of balanced detection over single-ended detection, and the penalty of mismatch in MZDI are presented. Analysis is included to discuss the strengths and limitations of the developed models. Finally, concluding remarks about novelties of the developed models and future works on improving the simulator are given.

13.1.2 Components Revisited for Advanced Optical Communication System

Although in previous chapters (Chapters 4 through 7) we have described in detail a number of photonic components, this section revisits and iterates a number of important parameters that affect the performance of the transmission system, rather than recalling the parameters from those chapters, even though we would suggest readers revise the important parameters of the optical components given therein. Further, the polarization division multiplexed (PDM) and QAM formats are briefly described, again as the standard 100G in current ultra-high-capacity long-haul backbone (lineside) transmission. The 100G deployment into metro and access optical networks is introduced. We will also witness the introduction of 400G and Tera-bit per second into the optical networks in the near future.

The transmitter consists of a modulator, which is responsible for converting data in the electrical domain to the optical domain either directly or externally using electro-optic or electro-absorption modulator. The modulated optical signal is then transmitted through a single-mode optical fiber using compensating fibers. In the long-haul link, propagation loss is considered to be significant and requires an optical amplifier to boost the optical signal power in the span of 80–120 km at regeneration point. At the receiver, the optical signal is detected using the typical PIN photodiode or avalanche photodiode with gain

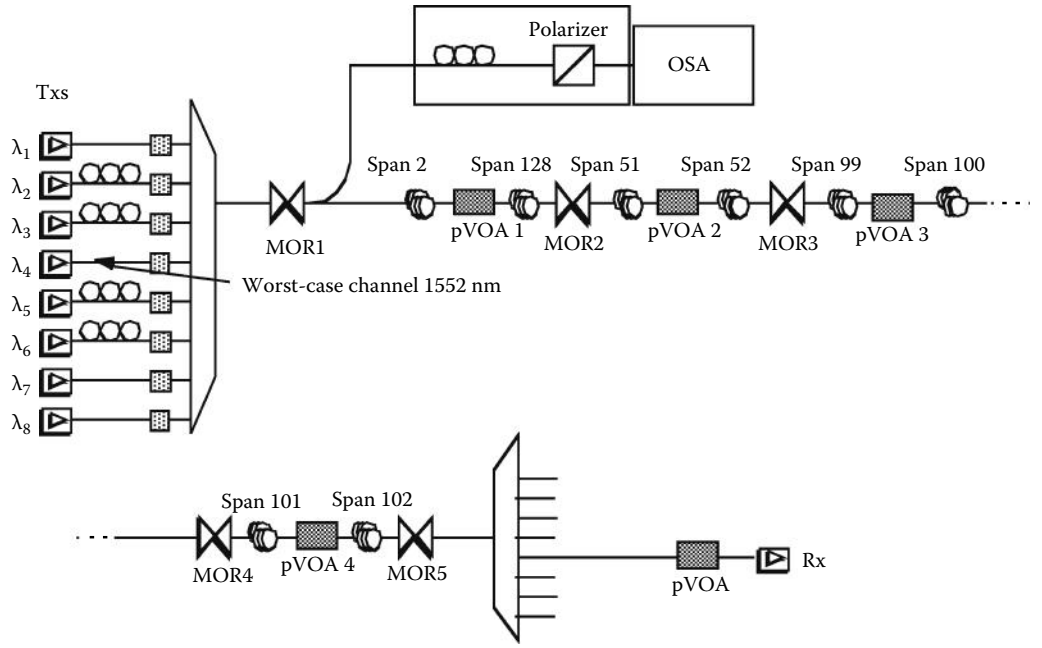

FIGURE 13.1
Typical long-haul DWDM multispans optical fiber transmission system with eight channels of different carrier wavelengths, MOR = midspan optical regenerator, VOA = variable optical attenuator, OSA = optical spectrum analyzer, Tx = transmitter, Rx = receiver, and VOA = variable optical attenuator (a more complex system is given in Figure 12.1).

equalization, chromatic compensation. The signal is decoded and regenerated in the electrical domain for user output.

The next level of complexity in optical transmission system involves addition of multiple wavelengths of light on a single fiber to make full use of the costly bandwidth efficiently. Each channel consists of a wavelength of light, which is a distinct "color" that can be combined with multiplexer for transmission and separated at receiver with demultiplexer. This technique is called wavelength-division-multiplexing (WDM), and a typical WDM system is illustrated in Figure 13.1.

As the exponentially growing internet traffic puts higher data rate on extreme high demand, DWDM system is realized by multiplexing more channels within a band window with approximately 100 GHz spacing. With the advent of EDFAs, DWDM is made practical and economical by allowing a multitude of wavelengths in the fiber to be boosted simultaneously.

In recent optical transmission systems for 100 Gb/s and multiplexed wavelength channels, PDM, and 4-QAM (QPAK) modulation formats are employed with 28–32 GB, hence the term 100G PDM QPSK is used. The extra bits are used for coding to achieve gains in OSNR and BER. The BER of 2e−4 or 1e−3 can be used when 7%–20% extra redundant bits are used for coding.

The optical transmission systems for such 100G are shown in Figure 13.2 in which the transmitters composed of two sets of the *I*- and *Q*-components of polarized MZIM accept the in-phase and quadrature-phase signal sequences and transfer them into their corresponding optical domains. The PDM QPSK channels are transmitted through *n* spans of optically amplified and nondispersion compensating links, then enter a polarization

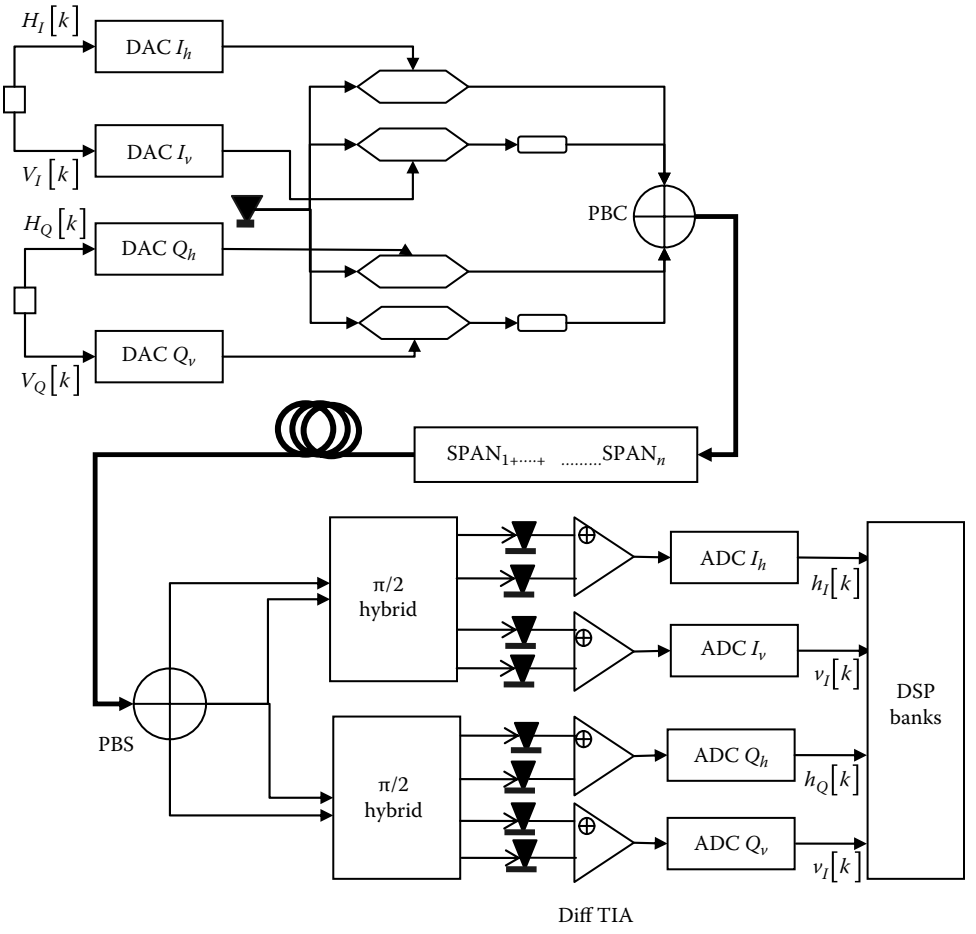

FIGURE 13.2
Schematic of PDM QAM optical transmission systems.

splitter in which the two polarized channels are then fed into π/2 hybrid couplers as described in Chapter 8. Then both the in-phase and quadrature components are recovered in the electronic domain via balanced receivers and differential trans impedance amplifier (DTIA). The electrical signals are then sampled by 4× ADCs and then into a system of digital processors in which processing algorithms are stored to recover the original sequences.

13.1.3 Optical Sources

In this book, the laser sources such as distributed feedback lasers (DFB) are used throughout because of their superior performance and characteristics in long-haul communication links. DFB lasers have narrow linewidths typically about 100 MHz or even narrower (~100 KHz or 100 Hz) by incorporating an external cavity. Linewidth refers to the spectral range of the carrier variation and is used to indicate the coherence quality of real sources. Narrower linewidth is attributed to less sensitivity to temperature variation than other laser sources. The wavelength shifts are under 0.1 nm/°C owing to stabilization by the

grating. For this reason, in this section, DFB lasers can be characterized using a single frequency sine wave function provided in MATLAB Simulink that we assume to be nearly monochromatic. The frequency of these optical sources is very high, of the order of a few hundred THz. If sampling is used, then the sampling rate is extremely high and no computing resources can meet this demand. Thus, complex amplitudes are used. That means that the phase of the optical carrier (OC) is represented as the resultant angle between the real and complex parts of the sampled amplitude.

13.1.4 Optical Modulators

As presented in Chapter 5, it is important to note that the laser diode presents problems to optical modulation because it has a threshold current. Because threshold current is age and temperature dependent, degradation will result in an L-I curve. (L-I curve is a representation of relationship between the output light signal and the direct current of the laser diode). Generally, external modulators consist of electro-absorption modulators and EO modulators. The common operating principle is based on an electro-optic effect (the change of refractive index in the material is proportional to the applied electric field). This is extremely useful in high-speed operations because the refractive index changes quickly with respect to the applied electric field.

Electro-absorption modulators are monolithic semiconductor planar waveguides. They operate on either the Fraz-Keldysh effect (FKE) or quantum stark effect by forming multiple quantum wells that consist of multiple *p*-type and *n*-type layers. The advantages of using these modulators are chirp relaxation (even though there is some inherent chirp), high-input impedance and monolithically integrated on the same semiconductor chip with the laser diode [4]. This offers greater advantage over EO modulators since insertion loss can be reduced. The modulators are diodes that operate in reverse bias. When there is no bias voltage, electro-absorption modulators are transparent to incoming optical signal. On the other hand, the applied voltage can generate a photocurrent that increases waveguide attenuation and signal losses. In other words, output power from electro-absorption modulators is the highest with no applied bias voltage and decreases as the bias voltage increases as shown in Figure 13.3b. It is noted that the optical modulation index of EA modulators does not reach unity, so there is some residual optical power level and this may cause an increase in the zero level and hence, lower the quality *Q*-factor or the BER of the transmission system. For this reason, the MZIM, which has been described in

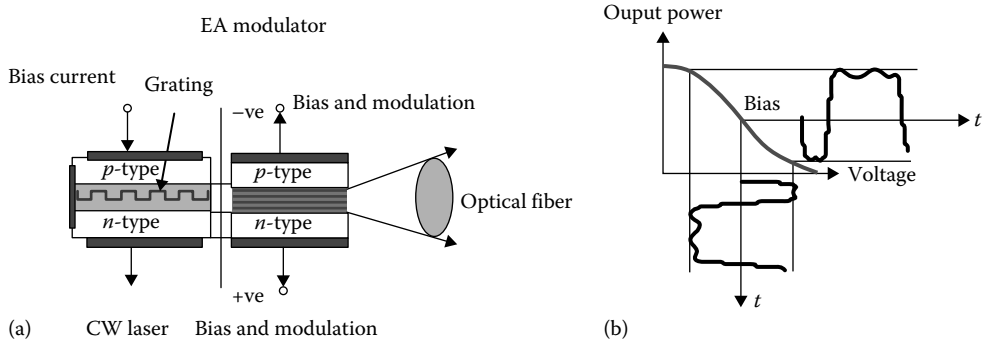

FIGURE 13.3
(a) Structure of EA modulator coupled with a DFB laser and (b) optical–electrical transfer characteristics of the EA modulator.

Chapter 5 and briefly revisited in the next section, is preferred. These EA modulators are commonly integrated in cascade with a DFB laser to form electro-absorption modulated laser (EML) modules [2,3].

13.1.5 Mach–Zehnder (MZ) Intensity Modulators Revisited

For 10 or 40 Gb/s DWDM application, EO modulators are the technology of choice because of better performance in terms of chirp, extinction ratio (higher), and modulation speed compared to electro-absorption devices. Over the years, lithium niobate ($LiNbO_3$) is the most popular material for EO modulators owing to its properties of enabling low loss waveguide and high EO effect. The most popular $LiNbO_3$ EO modulators employed nowadays, particularly in high-performance long-haul optical transmission systems, are based on MZ interferometric optical waveguide structure. The MZ modulators have two pairs of electrodes deposited along the interferometer arms, one for DC bias voltage and the other for modulating signals. Meanwhile, the numbers of the DC bias voltage categorizes the operation of MZ modulators as single drives and dual drives.

13.1.5.1 Single-Drive MZIM

In an MZ modulator, the incoming light is split equally into two paths like a Y branch (3 dB splitter) and travels along the upper and lower wave electrodes. An electric field is applied across the optical waveguide by the electrode that generates a change in the refractive index of the EO waveguide material via the EO effect. The change in the refractive index profile causes the speed of the light wave in the waveguide to change according to c/n_{eff}, and a phase shift occurs. When the guided light waves from the upper and lower waveguides recombine at the output Y branch, either a constructive or a destructive interference is generated depending on the relative phase shift of the two branches. If the light waves from the two arms are in phase "ON" state or logic 1 is inferred because of constructive interference. The output is interpreted as "OFF" state or logic 0 if the light waves are π (or 180°) out of phase derived from destructive interference. If a coupler is placed at the Y junction, then naturally the constructive and destructive interference outputs can be obtained. These two outputs are then detected by a back-to-back (BtB) connected photodetectors acting as push–pull receivers (Figure 13.4).

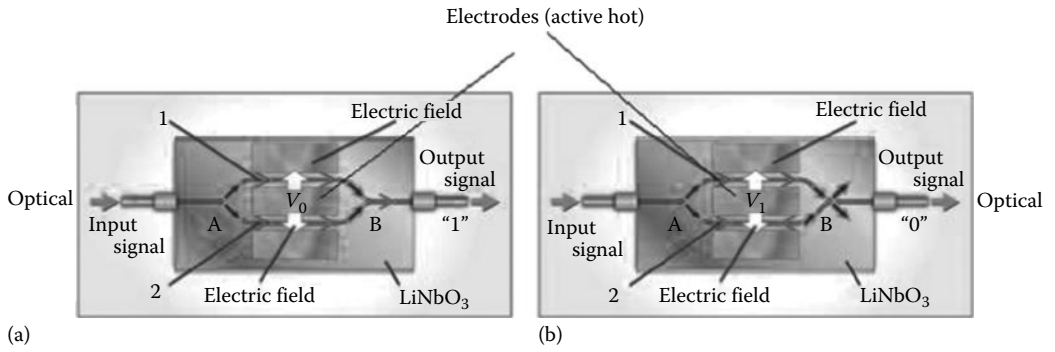

FIGURE 13.4
Illustration of the (a) constructive and (b) destructive interference occurring through a single-/dual-drive MZ modulator.

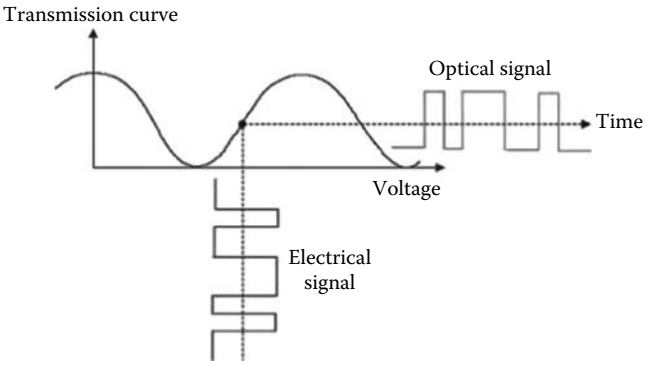

FIGURE 13.5
The transmission curve of MZIM forms the periodic waveform as a function of applied biasing voltage. Note: The transfer curve is based on the intensity or power and not the field of the optical waves.

The combined optical wave at the output of the Y branch is described by

$$E_o = \frac{E_i}{2}\left[1 + e^{j\pi\frac{V(t)}{V_\pi}}\right] = E_i \cos\left(\frac{\pi}{2}\frac{V(t)}{V_\pi}\right) e^{j\pi\frac{V(t)}{V_\pi}} \tag{13.1}$$

To express this in terms of optical intensity and derive the input–output transfer characteristic of MZIM

$$E_o^2 = E_i^2 \cos^2\left(\frac{\pi}{2}\frac{V(t)}{V_\pi}\right) \tag{13.2}$$

where
E_o and E_i are the output and input electric fields of the light waves
$V(t)$ is the driving voltage or applied voltage at traveling each electrode
V_π is the voltage required to cause π phase shift of the guided optical wave

Although the equations are given here, it is strongly recommended that the operational mechanism of the modulators should be understood from the first principles of splitting and interference via the effects of the phase modulation on the optical path of the interferometers. The techniques based on the construction of the phasor diagram can be well understood as the derivations come from the first principles of optics.

As the electrical–optical power transfer characteristic is $\cos^2$ shaped, the modulator can be biased in a different region and the modulating signal is superimposed onto the bias voltage (Figure 13.5). The nonlinear transfer function has been used to generate NRZ, RZ pulses with various duty cycles, and DPSK signals.

13.1.5.2 Dual-Drive MZIM

MZIM can also be driven with dual electrode structure, commonly referred to as push–pull modulator. In this section, we are considering chirp-free driving by using two driving voltages with π phase difference (i.e., $u_1(t) = -u_2(t)$, $\delta = \pi$) with $u_1(t)$ and $u_2(t)$ representing

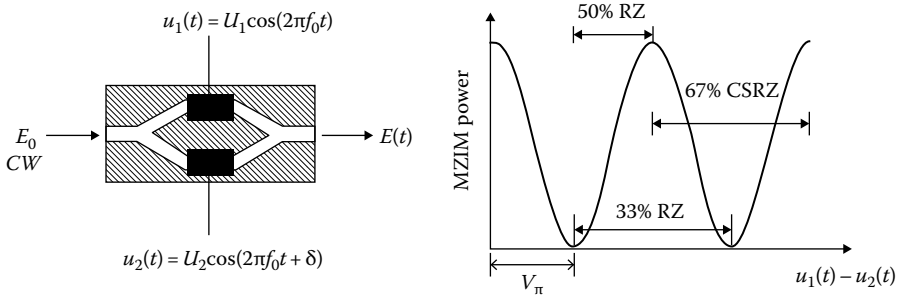

FIGURE 13.6
Schematic and intensity transmission curve of a dual-drive MZIM.

the time-dependent signals applied to the electrodes of the modulator. The operational principle is similar to the single-drive MZIM but with voltage applied to both arms to phase modulate the OC via EO effect. The interference at the output of the Y branch produces phase modulation. If the phase modulation is exactly equal in each path but opposite in sign, by combining the two optical signals, the phase modulation is converted into intensity modulation. As a consequence, dual-drive MZIM has an attractive feature; it can be driven as phase modulator (PM) or intensity modulator by changing its driving voltage (Figure 13.6). The phasor representation of the dual-driven optical modulators is also described in Section 13.3.3. The phasor diagrams given for the RZ33, RZ67, and CSRZ in Chapter 6 have illustrated the generation of these pulse formats.

13.2 Transmission Loss and Dispersion Revisited

In an optical transmission system, optical fibers serve as the medium to transport optical signals from source to destination. Because of low attenuation and ultra wide transmission bandwidth, optical fibers can transmit signals over long distances at high speed without amplification. Fiber losses impose a severe limitation on optical transmission because the signal power is greatly attenuated when reaching the receiver. With the advent of optical amplifiers, long-haul transmission exceeding several thousand kilometers is achieved by compensating accumulated losses. However, the loss profile is necessary to determine spacing between the amplifiers. The fiber loss is expressed in units of dB/km, and dispersion characteristics have been described in Chapters 2 and 3.

13.2.1 Nonlinear Effects

Nonlinear effects contribute to pulse distortion when optical power exceeds several mW in a single-channel optical transmission system as a result of their proportional relationship with the intensity of the EM field of propagating optical signals. In spite of negative impacts such as signal crosstalk, optical signal power attenuation, and signal distortion, nonlinear effects can be exploited in curbing chromatic dispersion. Nonlinear effects can be categorized according to nonlinear refractive index or nonlinear optical signal scattering. The effects related to nonlinear refractive index are those on SPM, cross-phase modulation (XPM), and four-wave mixing (FWM). On the other hand, stimulated Raman

scattering (SRS) and stimulated Brillouin scattering (SBS) are affected by nonlinear optical signal scattering caused by interaction between light and the material. The nonlinear effects and their penalty on system performance are given in Chapter 12. These effects are also included in the nonlinear Schrödinger equation (NLSE) which can be revisited in the next section with reference to the Simulink model and MATLAB m-files for representation of the optical wave propagation.

13.2.2 Signal Propagation Model

13.2.2.1 Nonlinear Schrodinger Propagation Equation

Signal propagation in optical fibers is the most important issue to be addressed in lightwave transmission systems. Optical pulses are subjected to linearities and nonlinearities in the fibers. Linear degrading effects comprise optical loss and GVD while nonlinearities include SPM, FWM, SRS, and SBS effects. Interaction between these effects, including linear and nonlinear effects can cause temporal and spectral properties of the optical pulse to change significantly. A mathematical model commonly used to describe the slowly-varying envelope of the optical field is the NLSE. The detailed derivations are not discussed in this section but can be found in Ref. [4]. The general form of NLSE can be expressed by

$$\frac{\partial A}{\partial z} = -\frac{j}{2}\beta_2 \frac{\partial^2 A}{\partial T^2} + \frac{1}{6}\beta_3 \frac{\partial^2 A}{\partial T^3} + \frac{j}{24}\beta_4 \frac{\partial^4 A}{\partial T^4} - \frac{1}{2}\alpha A + j\gamma |A|^2 A - a_1 \frac{\partial}{\partial T}\left(|A|^2 A\right) - j\alpha_2 \frac{\partial}{\partial T}\left(|A|^2\right) \tag{13.3}$$

where

$A = A(z, t)$ is slowly varying *complex* envelope of the optical signal
α is the fiber loss
β_2 and β_3 are second- and third-order dispersion coefficients, respectively
γ is the nonlinearity coefficient of the fiber

When the pulses have duration over 1 ps, the NLSE can be simplified to

$$\frac{\partial A}{\partial z} = -\frac{j}{2}\beta_2 \frac{\partial^2 A}{\partial T^2} - \frac{1}{2}\alpha A + j\gamma |A|^2 A \tag{13.4}$$

For the system to transmit at 10 Gb/s and above, the effects of the third-order dispersion have to be taken into consideration. By contrast, for systems operating below 10 Gb/s, if the channel is not at λ_D, the third-order dispersion can be neglected. The MATLAB m-file [`ssprop _ matlabfunction _ modified(input)`] was given and described in Chapter 3 and is included in all models related to optical systems employing ASK, DPSK, Star-QAM, and others.

13.2.2.2 Low-Pass Equivalent Model: Linear Operating Region

In developing a low-pass equivalent model of signal propagation in optical fibers, first, we have to assume that linear and nonlinear terms do not interact with each other. This is achieved by setting the power under a certain threshold to prevent the interaction taking place.

Hence, we can set $\gamma = 0$. The simplified model is solved directly in the frequency domain to obtain

$$A(z,\omega) = \exp\left(-\frac{\alpha z}{2} - j\frac{\beta_2 \omega^3 z}{2}\right) A(0,\omega) \tag{13.5}$$

Since $A(z, \omega)$ is the Fourier transform of $A(z, t)$, the low-pass equivalent model for single-mode fiber transfer function is given by (see Chapter 3)

$$H(f) = \exp(-j\phi(f)) = \exp(-j\alpha f^2) = \exp\left(-j\left[\alpha B^2\left(\frac{f}{B}\right)\right]^2\right) \tag{13.6}$$

where

$$\alpha = \pi D(\lambda)\frac{\lambda^2}{c}L$$

$$f = \upsilon - \upsilon_c$$

B is the data rate
f is the frequency
α is the attenuation constant
$D(\lambda)$ is the total chromatic dispersion factor
λ is the operating wavelength
c is the speed of light

Hence, the fiber is effectively a linear filter with attenuation and phase shift dependent on the transmission length. This transfer function is used whenever the nonlinear effects are not large to minimize the computation time.

13.3 Modulation Formats

Optimal modulation formats play an essential role to combat linear and nonlinear impairments, particularly in ultra-long-haul lightwave transmission systems. An optimal modulation format is required to carry the maximum bit rate with a narrow optical spectrum to enable closer channel spacing in DWDM system. Further, a high tolerance to the chromatic dispersion effect and robustness to nonlinearities such as SPM, XPM, and FWM are major properties to pursue. The format should also be compatible with the detection scheme to minimize receiver renovation and thus increase cost effectiveness.

In this section, the modulation formats covered were NRZ or NRZ–ASK, RZ or RZ–ASK, NRZ–DPSK, RZ–DPSK (including CSRZ–DPSK), and duo binary. Although NRZ and RZ are not advanced modulation formats, they have been used explicitly in conjunction with DPSK formats to develop a generic photonic transmitter based on the fundamental

optical principles. In this section, the basic generation principles and characteristics of these five modulation formats are discussed, whereas their applications in developing the simulator are described in Section 13.3.1.

13.3.1 NRZ or NRZ–ASK

For simplicity, we use NRZ to refer to NRZ–ASK also as they are fundamentally similar. NRZ has been the dominant modulation format in the last two decades because it is simple to generate, detect, and has a compact spectra. On top of all this, it can attain high sensitivity with EDFAs. Although the demand for higher bit rates has taxed the limit of NRZ signaling and new schemes are being deployed to replace NRZ, it served as a good reference for the purpose of comparison.

NRZ data are encoded by the following logic. A "zero" is a low logic level and "one" is a high logic level. Figures 13.7 and 13.8 show the NRZ signals corresponding to the logic levels .

A continuous wave (CW) laser is injected from the DFB laser source into the MZ modulator. The modulator is biased at a linear region and driven with V_π. The modulator acts as an intensity modulator to convert NRZ electrical signal with data rate B_R into an ASK optical signal at the same rate. Because of the nonlinear characteristics of the modulator, the NRZ optical signal usually has a better Q factor than the electrical signal. The optical spectrum of the B data rate NRZ signal will have a signal bandwidth of $B(Hz)$ (Figure 13.9).

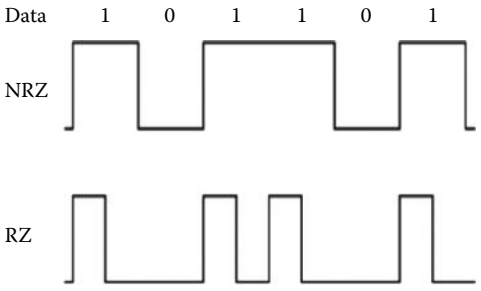

FIGURE 13.7
NRZ and RZ line codings for 101101 data sequence.

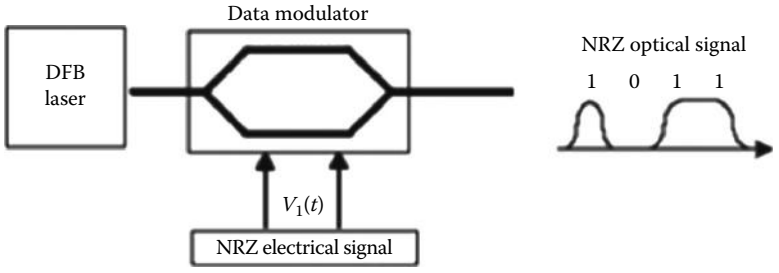

FIGURE 13.8
Block diagram of NRZ photonic transmitter.

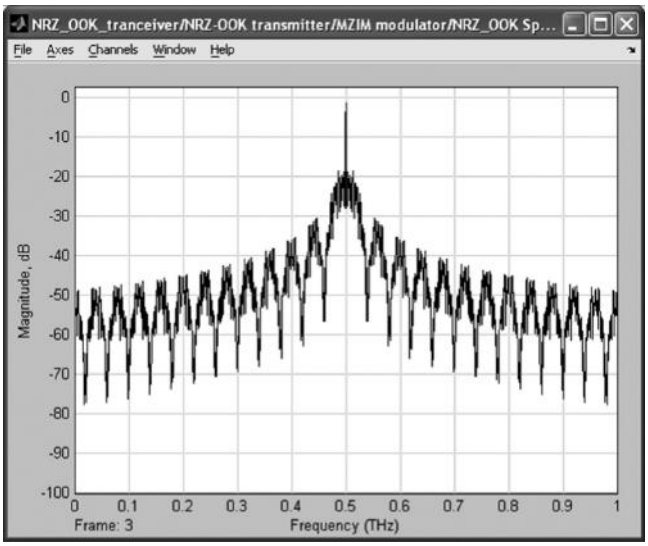

FIGURE 13.9
Optical spectrum of NRZ at carrier of 500 GHz.

13.3.2 RZ (or RZ–ASK)

RZ–ASKs, also known as RZ pulses, have several advantages over the NRZ signals. The advantages are attributed to how RZ handles the optical power. As illustrated in Figure 13.10, the power level of RZ pulses always return to zero even when successive logic "1" bits occur.

First, to generate optical RZ pulses, an MZ modulator commonly known as *pulse carver* is fed with sinusoidal electrical signal to "carve" pulses from the optical CW carrier wave. The optical RZ pulse train is then fed into another MZ modulator known as intensity modulator to modulate the electrical data on the RZ pulses. There are a number of variations in the RZ format based on the biasing point in the transmission curve shown in Table 6.1.

The RZ pulse sequence has a wider spectrum than the NRZ because of its narrower pulse width, but CSRZ has eliminated this inherent disadvantage. CSRZ has an optical phase difference of π in adjacent bits, removes the OC component in the optical spectrum, and reduces the spectral width (Figure 13.11).

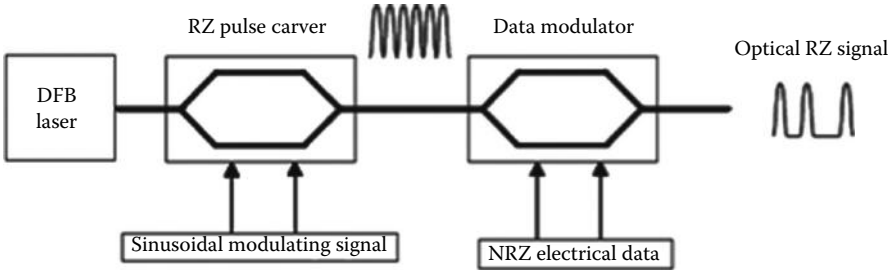

FIGURE 13.10
Block diagram of RZ photonics transmitter.

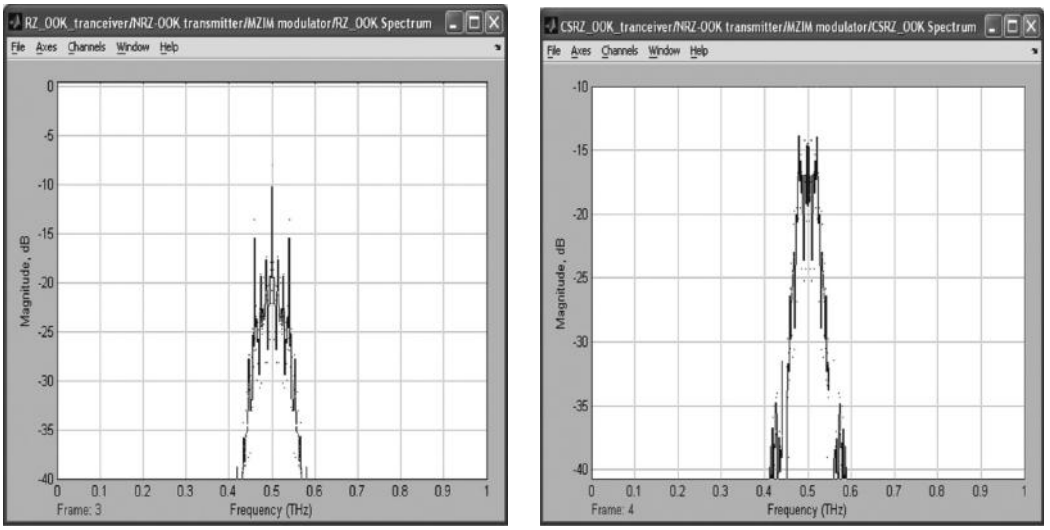

(a) (b)

FIGURE 13.11
Optical spectra of (a) RZ and (b) CSRZ at an artificial carrier of 500 GHz.

The Simulink model for the pulse carver is shown in Figure 13.12. Figure 13.13 shows another Simulink model of the pulse carver using the principles of operations of an intensity modulator, the MZIM. We can observe that the two arms of the modulator have been modeled as phase shifters that are also biased in the opposite sign. This is essential for the operation as a dual-drive interferometric modulation device. The driving signals are also complementary with respect to each other so that the phase shift of the two optical arms act in a push–pull manner. The phasor diagram representing the pulse carver operation is described in the next section. Readers can modify the model to accommodate the generation of these RZ pulses.

13.3.3 Return-to-Zero Optical Pulses

13.3.3.1 Generation

Figure 13.14 shows the conventional structure of a RZ–ASK transmitter in which two external $LiNbO_3$ MZIMs can be used. The MZIM shown in this transmitter can be either a single- or dual-drive (push–pull) type. The operational principles of the MZIM were presented in Section 12.2.2. The optical OOK transmitter would normally consist of a narrow linewidth laser source to generate light waves whose wavelength satisfies the ITU grid standard.

The first MZIM, commonly known as the pulse carver, is used to generate the periodic pulse trains with a required RZ format. The suppression of the lightwave carrier can also be carried out at this stage if necessary, commonly known as the CSRZ. Compared to other RZ types, CSRZ pulse shape is found to have attractive attributes for long-haul WDM transmissions including the π phase difference of adjacent modulated bits, suppression of the OC component in the optical spectrum, and narrower spectral width.

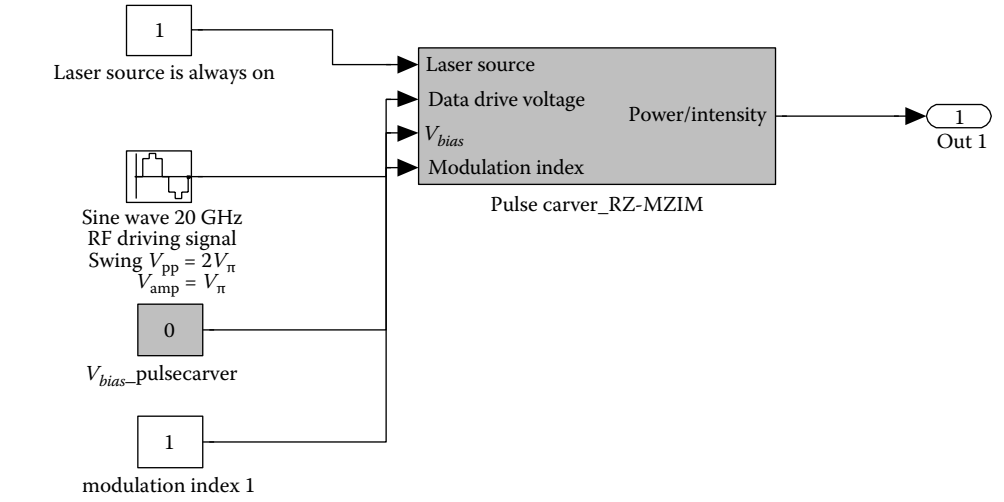

(a)

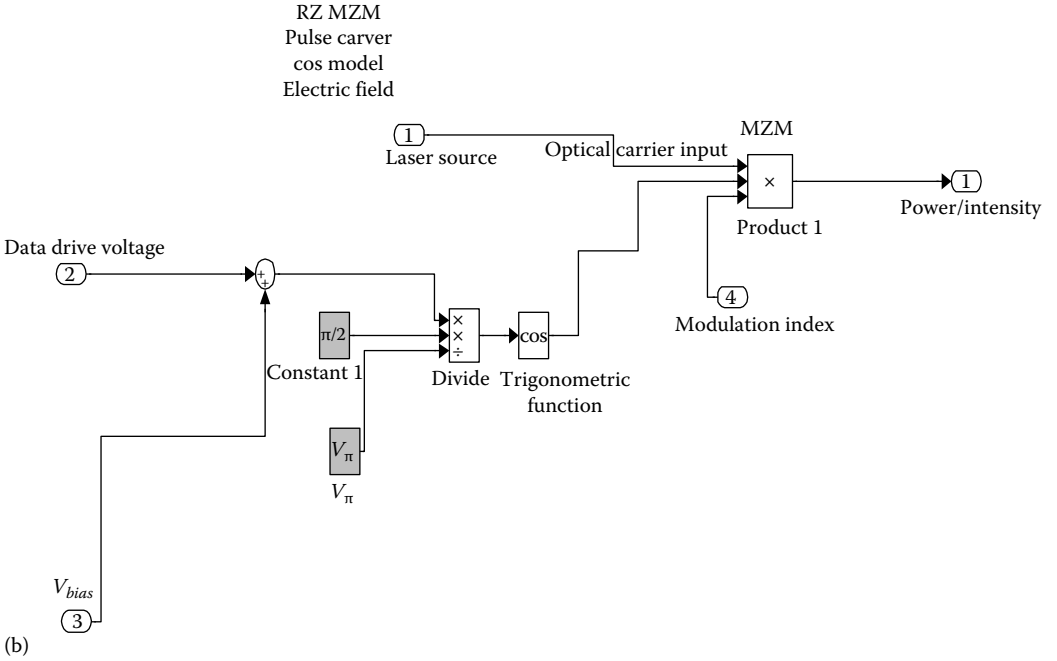

(b)

FIGURE 13.12
Simulink® model of an optical pulse carver using a mathematical model: (a) general block model and (b) inside the pulse carver.

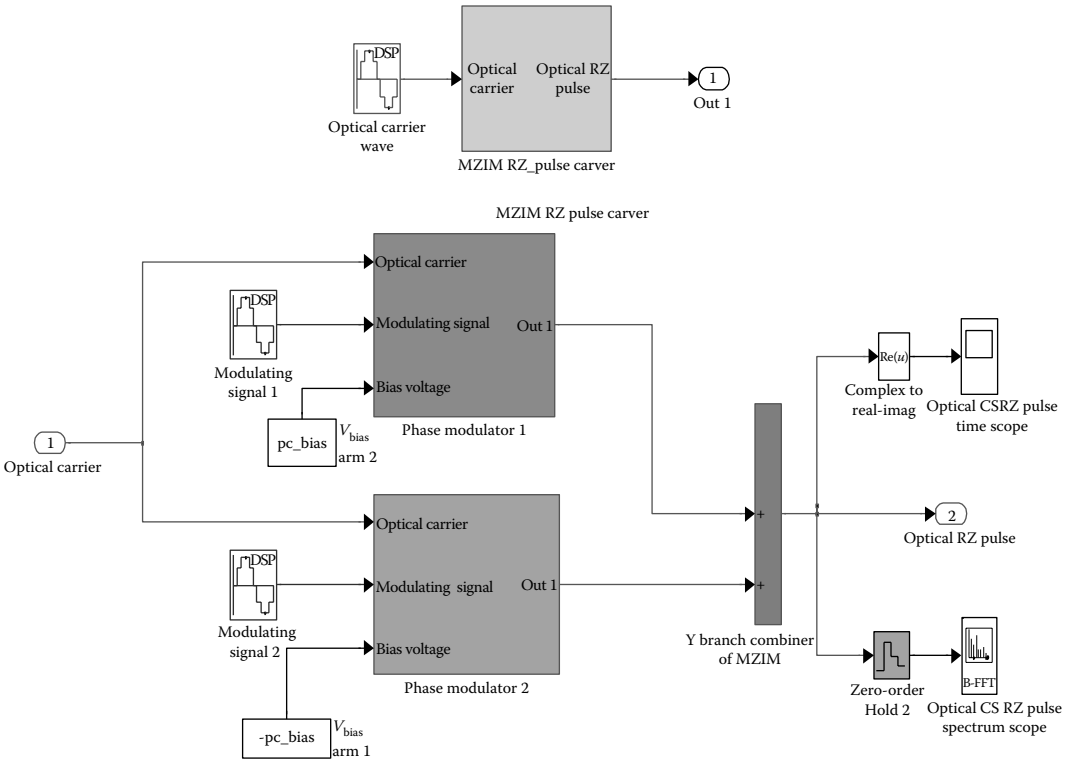

FIGURE 13.13
Simulink® model of an optical pulse carver modeled using the principles of operation of MZIM.

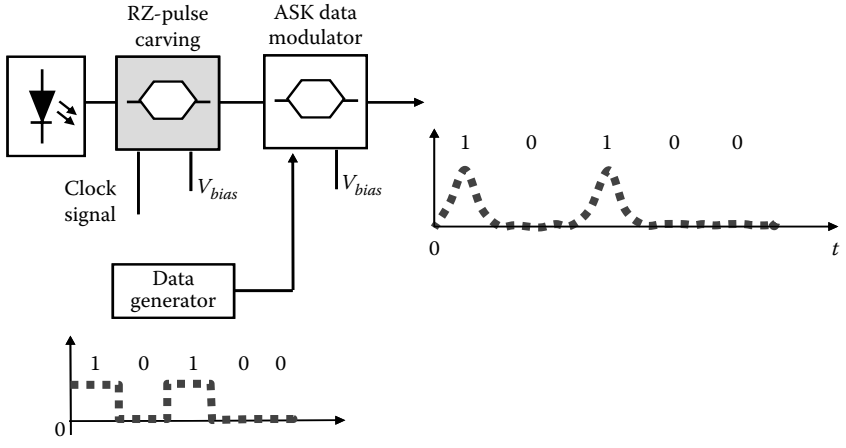

FIGURE 13.14
Conventional structure of an OOK optical transmitter using two MZIMs.

Different types of RZ pulses can be generated depending on the driving amplitude of the RF voltage and the biasing schemes of the MZIM. The equations governing the RZ pulses electric field waveforms are

$$E(t)=\begin{cases}\sqrt{\dfrac{E_b}{T}}\sin\left[\dfrac{\pi}{2}\cos\left(\dfrac{\pi t}{T}\right)\right] & \text{67\% duty-ratio RZ pulses or CSRZ}\\ \sqrt{\dfrac{E_b}{T}}\sin\left[\dfrac{\pi}{2}\left(1+\sin\left(\dfrac{\pi t}{T}\right)\right)\right] & \text{33\% duty-ratio RZ pulses or RZ33}\end{cases} \tag{13.7}$$

where

E_b is the pulse energy per a transmitted bit
T is 1-bit period

The 33% duty ratio RZ pulse is denoted as RZ33 pulse, whereas the 67% duty cycle RZ pulse is known as the CSRZ type. The art of generating these two RZ pulse types is in the difference of the biasing point on the transfer curve of an MZIM.

The bias voltage conditions and the pulse shape of these two RZ types, the carrier suppression, and nonsuppression of the maximum carrier can be implemented with the biasing points at the minimum and maximum transmission points of the transmittance characteristics of the MZIM, respectively. The peak-to-peak amplitude of the RF driving voltage is $2V_\pi$, where V_π is the required driving voltage to obtain a π phase shift of the lightwave carrier. Another important point is that the RF signal is operating at only half the transmission bit rate. Hence, pulse carving is actually doubling the frequency. The generation of the RZ33 and CSRZ pulse trains is demonstrated in Figure 13.15a and b.

The pulse carver can also utilize a dual-drive MZIM that is driven by two complementary sinusoidal RF signals. This pulse carver is biased at $-V_{\pi/2}$ and $+V_{\pi/2}$ with the peak-to-peak amplitude of $V_{\pi/2}$. Thus, a π phase shift is created between the states of "1" and "0" of the pulse sequence and hence, the RZ with alternating phase 0 and π. If carrier suppression is required, then the two electrodes are applied with voltages V_π and swing voltage amplitude of V_π.

Although RZ modulation offers improved performance, RZ optical systems usually require more complex transmitters than those in the NRZ ones. Compared to only one stage for modulating data on the NRZ optical signals, two modulation stages are required for generation of RZ optical pulses.

13.3.3.2 Phasor Representation

Recalling (13.1) we have

$$E_o=\frac{E_i}{2}\left[e^{j\varphi_1(t)}+e^{j\varphi_2(t)}\right]=\frac{E_i}{2}\left[e^{j\pi v_1(t)/V_\pi}+e^{j\pi v_2(t)/V_\pi}\right] \tag{13.8}$$

It can be seen that the modulating process for generation of RZ pulses can be represented by a phasor diagram as shown in Figure 13.16. This technique gives a clear understanding of the superposition of the fields at the coupling output of the two arms of the MZIM. Here, a dual-drive MZIM is used, that is, the data-driving signals [$V_1(t)$] and inverse data ($\overline{data}: V_2(t) = -V_1(t)$) are applied into each arm of the MZIM, respectively, and the RF voltages swing in inverse directions. Applying the phasor representation, vector addition, and simple trigonometric calculus, the process of generation of RZ33 and CSRZ is explained in detail and verified.

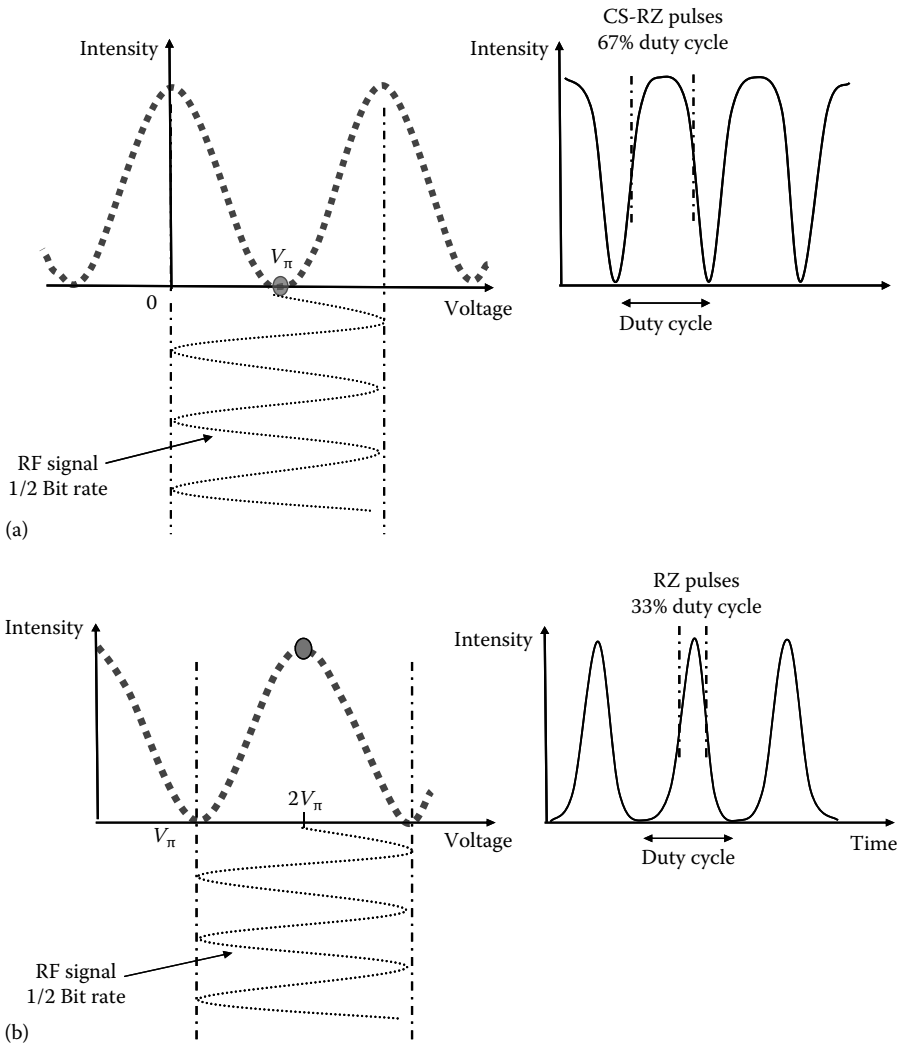

FIGURE 13.15
Bias point and RF driving signals for generation of (a) CSRZ and (b) RZ33 pulses.

The width of these pulses is commonly measured at the position of full-width half maximum (FWHM). It is noted that the measured pulses are intensity pulses whereas we are considering the addition of the fields in the MZIM. Thus, the normalized E_o field vector has the value of $\pm 1/\sqrt{2}$ at the FWHM intensity pulse positions, and the time interval between these points gives the FWHM values.

13.3.3.2.1 Phasor Representation of CSRZ Pulses

The key parameters including the V_{bias}, the amplitude of the RF driving signal, are shown in Figure 13.17a. Accordingly, its initialized phasor representation is demonstrated in Figure 13.17b.

The values of the key parameters are outlined as follows: (1) V_{bias} is $\pm V_\pi/2$; (2) Swing voltage of driving RF signal on each arm has the amplitude of $V_\pi/2$ (i.e., $V_{p-p} = V_\pi$); (3) RF signal

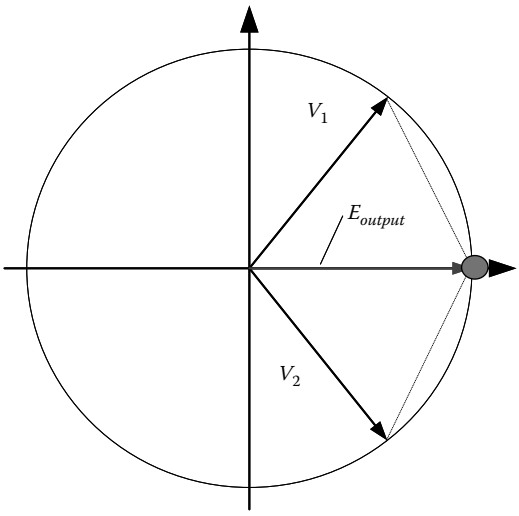

FIGURE 13.16
Phasor representation for generation of output field in dual-drive MZIM.

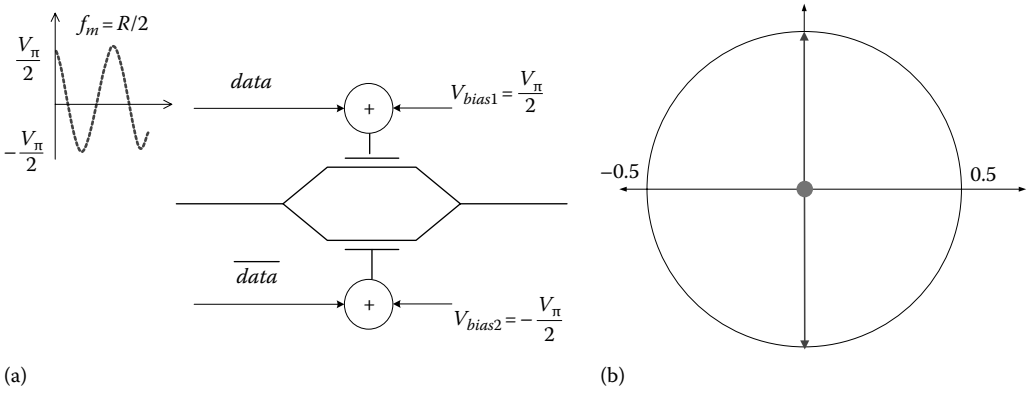

FIGURE 13.17
Initialized stage for generation of CSRZ pulse: (a) RF driving signal and the bias voltages and (b) initial phasor representation.

operates at half the bit rate ($B_R/2$); and (4) At the FWHM position of the optical pulse, the $E_{out} = \pm 1/\sqrt{2}$ and the component vectors V_1 and V_2 form a phase of π/4 with the vertical axis as shown in Figure 13.18.

Considering the case for generation of 40 Gb/s CSRZ optical signal, the modulating frequency is f_m (f_m = 20 GHz = $B_R/2$). At the FWHM positions of the optical pulse, the phase is given by the following expressions:

$$\frac{\pi}{2}\sin(2\pi f_m) = \frac{\pi}{4} \Rightarrow \sin 2\pi f_m = \frac{1}{2} \Rightarrow 2\pi f_m = \left(\frac{\pi}{6}, \frac{5\pi}{6}\right) + 2n\pi \tag{13.9}$$

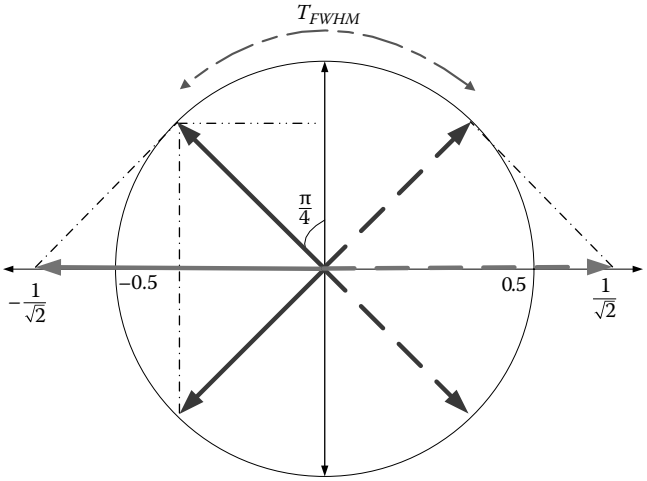

FIGURE 13.18
Phasor representation of CSRZ pulse generation using dual-drive MZIM.

Thus, the calculation of TFWHM can be carried out and hence, the duty cycle of the RZ optical pulse can be obtained as given in the following expressions:

$$T_{FWHM} = \left(\frac{5\pi}{6} - \frac{\pi}{6}\right)\frac{1}{R2\pi} = \frac{1}{3}\pi \times \frac{1}{R} \Rightarrow \frac{T_{FWHM}}{T_{BIT}} = \frac{1.66 \times 10^{-4}}{2.5 \times 10^{-11}} = 66.67\% \tag{13.10}$$

The result obtained in (13.10) clearly verifies the generation of CSRZ optical pulses from the phasor representation.

13.3.3.2.2 Phasor Representation of RZ33 Pulses

The key parameters including the V_{bias}, the amplitude of driving voltage, and its correspondent initialized phasor representation are shown in Figure 13.19a and b, respectively.

The values of the key parameters are (1) V_{bias} is V_π for both arms; (2) Swing voltage of driving RF signal on each arm has the amplitude of $V_\pi/2$ (i.e., $V_{p-p} = V_\pi$); and (3) RF signal operates at half the bit rate ($B_R/2$).

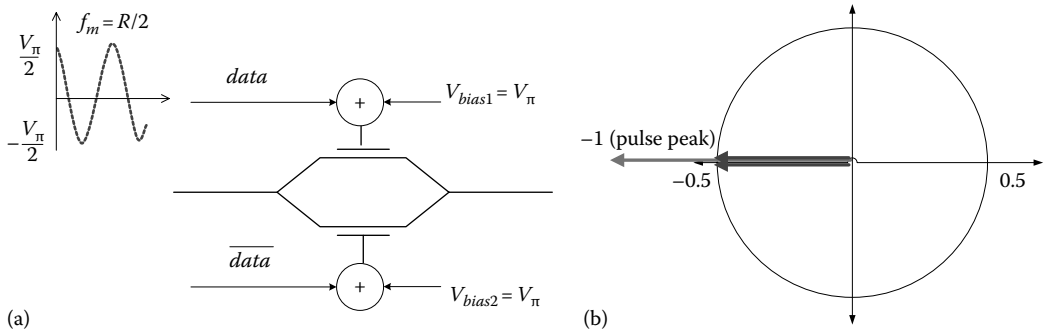

FIGURE 13.19
Initialized stage for generation of RZ33 pulse: (a) RF driving signal and the bias voltage and (b) initial phasor representation.

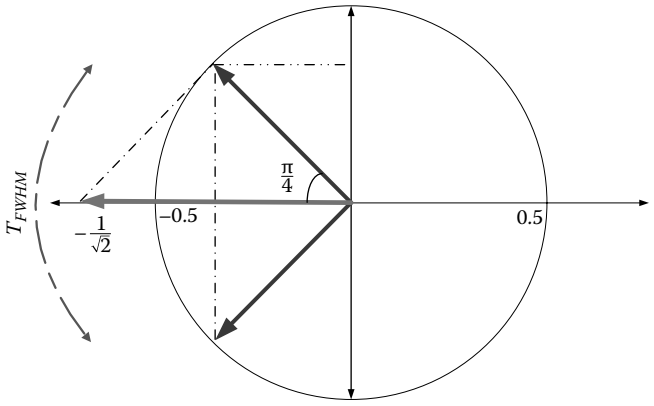

FIGURE 13.20
Phasor representation of RZ33 pulse generation using dual-drive MZIM.

At the FWHM position of the optical pulse, the $E_{output} = \pm 1/\sqrt{2}$ and the component vectors V_1 and V_2 form a phase of $\pi/4$ with the horizontal axis as shown in Figure 13.20.

Considering the scenario for generation of 40 Gb/s CSRZ optical signal, the modulating frequency is f_m (f_m = 20 GHz = $B_R/2$). At the FWHM positions of the optical pulse, the phase is given by the following expressions:

$$\frac{\pi}{2}\cos(2\pi f_m t) = \frac{\pi}{4} \Rightarrow t_1 = \frac{1}{6f_m} \tag{13.11}$$

$$\frac{\pi}{2}\cos(2\pi f_m t) = -\frac{\pi}{4} \Rightarrow t_2 = \frac{1}{3f_m} \tag{13.12}$$

Thus, the calculation of TFWHM can be carried out and hence, the duty cycle of the RZ optical pulse can be obtained as given in the following expressions:

$$T_{FWHM} = \frac{1}{3f_m} - \frac{1}{6f_m} = \frac{1}{6f_m} \quad \therefore \frac{T_{FWHM}}{T_b} = \frac{1/6f_m}{1/2f_m} = 33\% \tag{13.13}$$

The result obtained in (13.8) clearly verifies the generation of RZ33 optical pulses from the phasor representation.

13.4 Differential Phase Shift Keying (DPSK)

Information encoded in the phase of an OC is commonly referred to as optical phase SK. In early days, phase shift keying (PSK) required precise alignment of the transmitter and demodulator center frequencies. Hence, PSK system is not widely deployed. With the DPSK scheme introduced, coherent detection is not critical since DPSK detection only requires source coherence over 1-bit period by comparison of two consecutive pulses.

A binary 1 is encoded if the present input bit and the past encoded bit are of opposite logic and a binary 0 is encoded if the logic is similar. This operation is equivalent to XOR

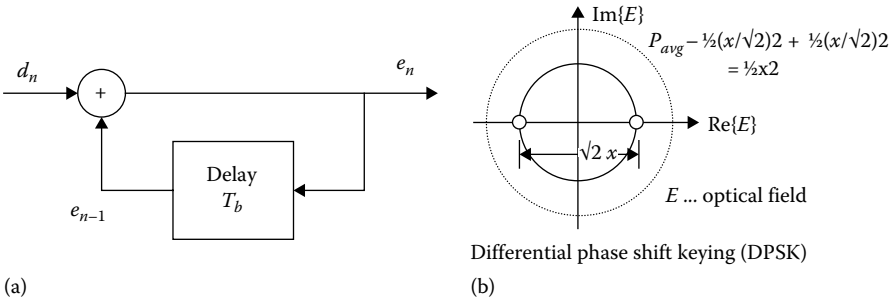

FIGURE 13.21
(a) The encoded differential data are generated by $e_n = d_n \oplus e_{n-1}$. (b) Signal constellation diagram of DPSK.

(exclusive OR) logic operation. Hence, an XOR gate is usually employed in differential encoder. NOR (not OR) can also be used to replace XOR operation in differential encoding.

In optical application, electrical data "1" is represented by a π phase change between the consecutive data bits in the OC, while state "0" is encoded with no phase change between the consecutive data bits. Hence, this encoding scheme gives rise to two points located exactly at π phase difference with respect to each other in the signal constellation diagram (Figure 13.21).

13.4.1 NRZ–DPSK

Figure 13.22 shows the block diagram of a typical NRZ–DPSK transmitter. The differential precoder transforms the binary electrical data sequence into the DPSK format. This is implemented using the logic described in Section 13.4. In phase modulation of an OC, MZ modulator known as data PM is biased at minimum point and driven by a data swing of $2V_\pi$. The modulator showed excellent behavior in that the phase of the OC is altered by exactly π when the signal transits the minimum point of the transfer characteristic.

13.4.2 RZ–DPSK

Setup of RZ–DPSK transmitter is essentially similar to RZ–ASK with the data intensity modulator replaced by the data PM (Figure 13.23). The difference between them is the biasing point and the electrical voltage swing. Different RZ formats can also be generated according to Table 6.1.

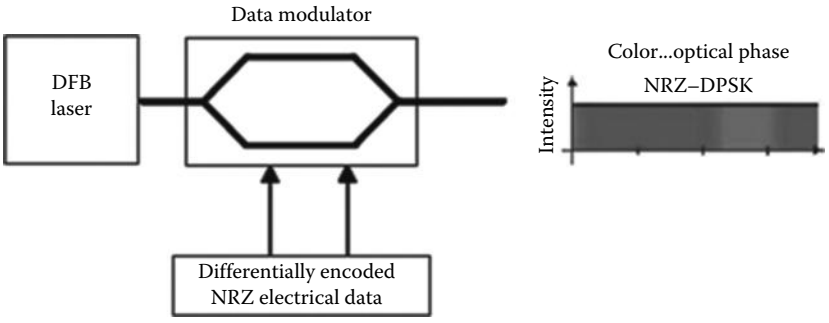

FIGURE 13.22
Block diagram of NRZ-DPSK photonic transmitter.

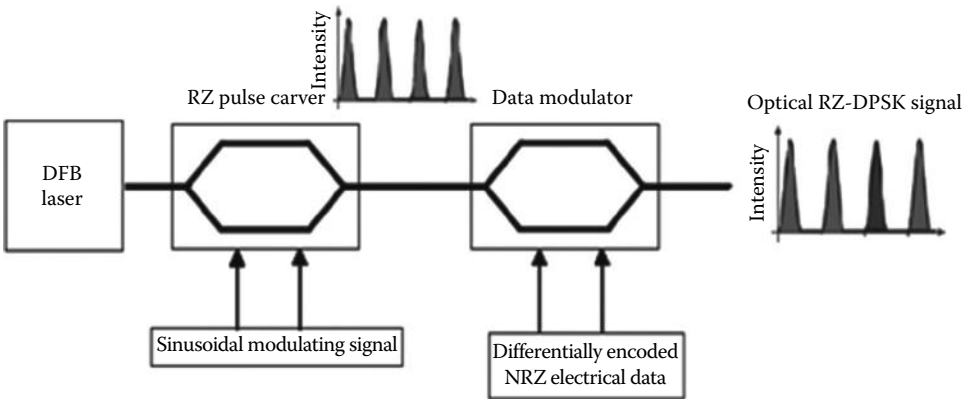

FIGURE 13.23
Block diagram of RZ-DPSK photonic transmitter.

13.4.3 Receiver

The receiver structure is dependent on the modulation format imposed on the OC. If ASK and the duo-binary formats are used, single photodiode direct detection receiver is usually employed to convert the optical signal power into electrical signals using the photodiode. The single photodiode direct detection scheme is depicted in Figure 13.24.

DPSK receiver requires an optical preprocessing stage to accomplish demodulation. The optical signal is first passed through an MZ delay interferometer (MZDI) which has a differential delay equal to a bit period. The delay is achieved by extending the second path of the MZ arm approximately λ_{bit} as shown in Figure 13.25. Since in practice, the exact delay is too difficult to construct, a heating element is applied on the interferometer arm to fine tune the differential phase delay.

When there is no phase change between adjacent bits, maximum power appears at the constructive port. When the phase in adjacent bit differs by π, maximum power exists at the destructive port. Hence, the preceding bit serves as a phase reference for demodulating the current bit. As a result, the bit coherency is only required for two bit periods.

FIGURE 13.24
Single photodiode direct detection receiver after optical filtering for limiting noise effects.

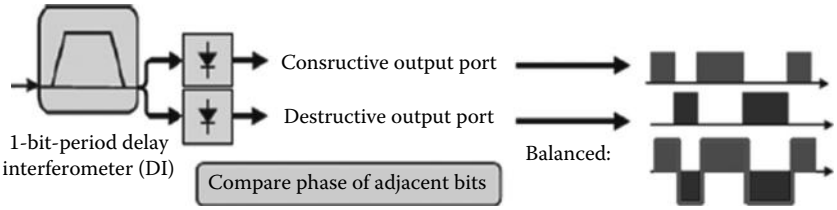

FIGURE 13.25
Balanced detection with delay demodulation using two-photodiode direct detection.

Under DPSK modulation and demodulation scheme, both the constructive port and the destructive port carry similar but logically inverted data streams. Therefore, they can be either detected by themselves (single-ended detection) or balanced. Single-ended detection simply uses a photodiode to convert the optical signal power at either port to an electrical signal. Balanced detection is completed by connecting two photodiodes and processing digitally.

13.4.4 Simulink® Models

An analytical engineering approach to identify optimization of parameters, especially in long-haul communication systems, may impose limitations on the number of optical channels as well as distances. Since the interaction of these parameters may give hundreds of even thousands of combinations, a computer-aided engineering approach provides assistance in terms of accuracy and speed from a precise engineering point of view. There are a number of computer-based programs and simulation tools available to achieve optical system design modeling. These packages offer various benefits depending on the applications and situations investigated. However, some of them provide a click-and-drop interface and some of them are closed to the user's intervention.

MATLAB Simulink is one of the most user-friendly software platforms that can write the simulation software using different building blocks and tools. Simulink provides a set of libraries that contain digital signal processing blocksets, communication blocksets, mathematical fundamentals, and electronic modules. Hence, it is open for optical module modeling, which is critical in the modeling of optical components from the physical to the system level. The flexibility of the simulation by appropriate sampling techniques enhances the integration of the optical module modeled with a physical operating principle such as an optical modulator with a mathematical model that is required to solve fiber propagation equations.

The design processes depicted in Figure 13.26 illustrate how a 40 Gb/s photonic transmitter can be designed and tested. First, a pseudorandom bit generator can be easily modeled using the Bernoulli binary generator provided in the Simulink communication blockset. The optical CW carrier, which was assumed to be a DFB laser as explained earlier is modeled readily by the sine wave in the signal processing blockset. Three circled processes in Figure 13.26 form a circular procedure that requires constant testing and feedback from outcome results and analysis. Often, the design on an MZ modulator had to be adapted, modified, and implemented both with a mathematical model and physical operating principles. The modulator model would have to be confirmed with the modulation format as well as the receiver to demodulate the signal. When modulation formats were compatible with BtB receivers, a propagation model was developed to test the system performance with a BER model. This process can consume a lot of time as the system growing in complexity because a slight change in the model would alter the result significantly. During the design process, results are collected to gain information and feedback on necessary model alteration and confirmation. The rest of this section discusses the modeling process and presents the results from time to time to demonstrate the working principles of the model. Although the developed model can generate different modulation formats, only RZ–DPSK results including eye diagrams, time scope, and spectrum scope are shown for demonstration purpose.

13.4.4.1 Bernoulli Binary Generator (Figures 3.27 and 3.28)

The pseudo random bit pattern can be set by using a Bernoulli binary generator of MATLAB Simulink as shown in Figure 13.27. Figure 13.28 shows the generated pulse sequence at the output of this block as monitored by a scope of Simulink.

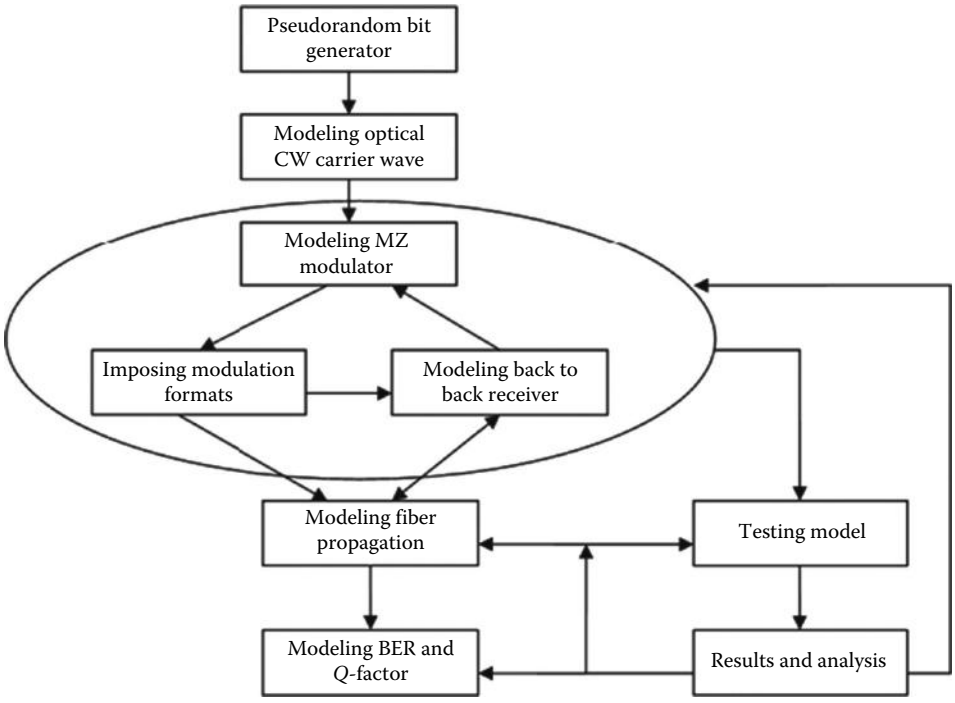

FIGURE 13.26
Flow diagram of simulator design processes.

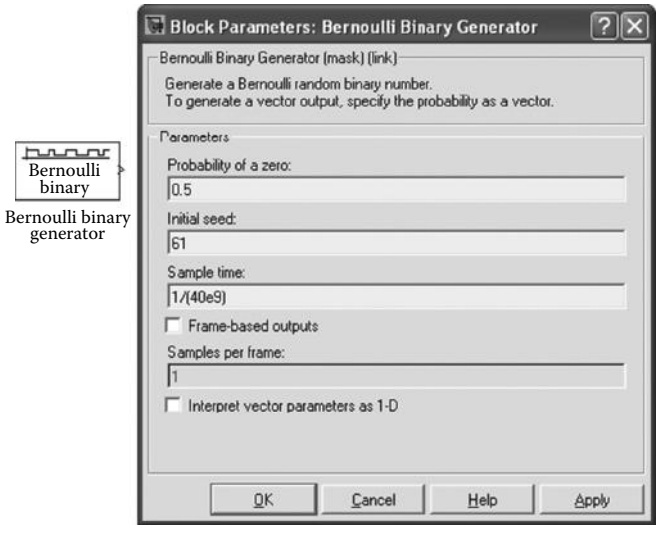

FIGURE 13.27
Block parameters setup and block diagram of Bernoulli Binary Generator in Simulink®. Probability of a zero is set to 0.5, and sample time is set to 25 ps to output 40 Gb/s data sequence.

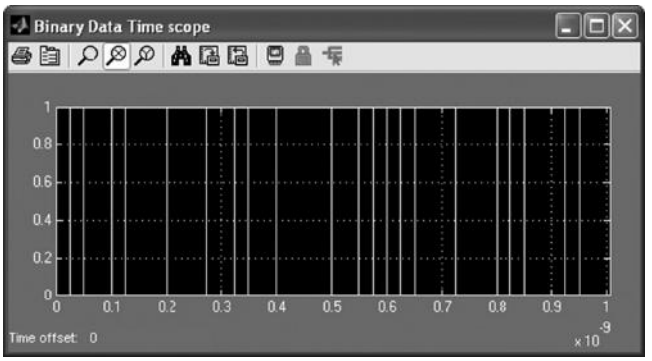

FIGURE 13.28
Binary data in 1 ns generated by Bernoulli Binary Generator.

13.4.4.2 DFB Laser

The OC frequency in this case is set at 2.048 THz. It is different from 193 THz (1550 nm) because $2^n \times$ data rate of OC will simplify calculation in setting up eye diagram parameters since we can compute exactly the number of cycles of the sinusoidal sine wave in a bit period. The sample mode was set to discrete for the same reason stated earlier. The sample time was relatively subject to how accurate we the OC was required to be; typically, 200 samples in a frame is substantial to produce a clean and nice wave (Figures 13.29 and 13.30).

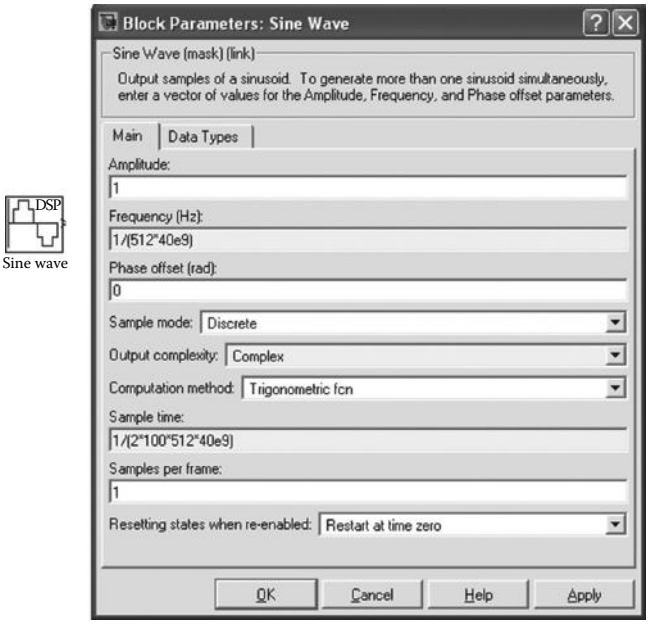

FIGURE 13.29
Block parameters setup and block diagram of DFB laser in Simulink®.

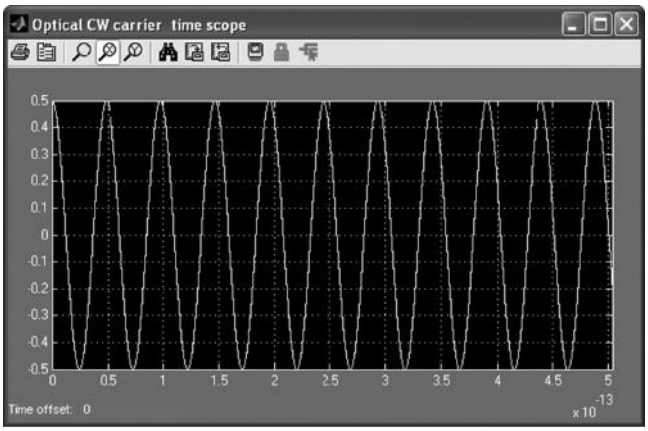

FIGURE 13.30
Optical CW carrier wave at 2.048 THz shown in 0.5 ps time span.

13.4.4.3 Mach–Zehnder Interferometric Modulator

MZIM model was developed based on the principle explained in 0. Implementation can be divided into the intensity modulator and the PM depending on the biasing voltage and voltage swing. Hence, the model was developed based on the pulse carver applications.

13.4.4.4 Pulse Carver

Because optical phase distortions (such as chirp) will affect DPSK receiver performance, dual drive MZIM pulse carver was required to operate in a perfect push–pull operation. In other words, the sinusoidal electrical signals amplitude has to be similar and of exactly opposite phase. This requirement is difficult to achieve in practice but fairly straightforward in a simulation environment. Assuming the extinction ratio is large, the optical field exiting a dual-drive MZIM is described mathematically by

$$E(t) = \frac{E_o}{2}\left\{\exp\left[j\pi\frac{u_1(t)}{V_\pi}\right] + \exp\left[j\pi\frac{u_2(t)}{V_\pi}\right]\right\} \approx E_o \exp\left[j\pi\frac{u_1(t)+u_2(t)}{2V_\pi}\right] \times \cos\left[\pi\frac{u_1(t)-u_2(t)}{2V_\pi} + \phi\right] \tag{13.14}$$

where

E_o is magnitude of input optical field
V_π is the electrical voltage to produce π phase shift in either of modulator's two arms
ϕ is the relative optical phase between two arms without electrical drive signals
$u_1(t) = U_1\cos(2\pi f_m t)$
$u_2(t) = U_1\cos(2\pi f_m t + \theta)$
f_m is the electrical signal frequency

Since chirp-free driving condition required $u_1(t) = -u_2(t)$, Equation 13.3 can be reduced to

$$E(t) \approx E_o \cos\left[\pi\frac{u_1(t)-u_2(t)}{2V_\pi} + \phi\right] \tag{13.15}$$

Let $\phi = \frac{\phi_1 - \phi_2}{2}$ where $\phi_1 = \pi \frac{V_{DC1}}{V_\pi}$; $\phi_2 = \pi \frac{V_{DC2}}{V_\pi}$. By incorporating the OC frequency into (13.16), the optical field exiting the dual-drive MZIM can be re-expressed as

$$E(t) = E_o \left\{ \cos\left[2\pi f_c t + \alpha\pi \cos(2\pi f_m t) + \phi_1 \right] + \cos\left[2\pi f_c t + \alpha\pi \cos(2\pi f_m t + \theta) + \phi_2 \right] \right\} \quad (13.16)$$

where

f_c is the OC frequency

$\alpha = \pi \frac{U_{1,2}}{V_\pi}$ (assigned as the modulation index)

The mathematical analysis shows that the biasing voltage, V_π is reduced by half with respect to single-drive MZIM, and with driving voltage as well, an advantage in using the balanced modulator structure (Figure 13.31).

The MZIM has two arms biased at voltage set by "pc_bias" and modulated by two modulating signals with exactly π difference between them to create push–pull configuration. The output of each arm was combined using the sum that acts like a coupler so that they can interfere constructively and destructively. The output was monitored using a time scope and spectrum scope (Figure 13.32).

Figure 13.33 shows the equally split OC signal enter one of MZIM paths. Biasing voltage is fed to create a relative phase reference for the electrical modulating signal. The electrical signal was used to modulate the OC signal with phase relative to the biasing voltage phase. Table 13.1 shows the level of signal amplitudes and the biasing points for generating the RZ optical clock pulses for uses under three formats, linear region, CSRZ (biased at minimum transmission point), and maximum biasing RZ. This model is essentially represented by one of the two cosine terms in Equation 13.16. Hence, if MZ interferometric structure is discarded, this model alone acts like a PM (Figure 13.34).

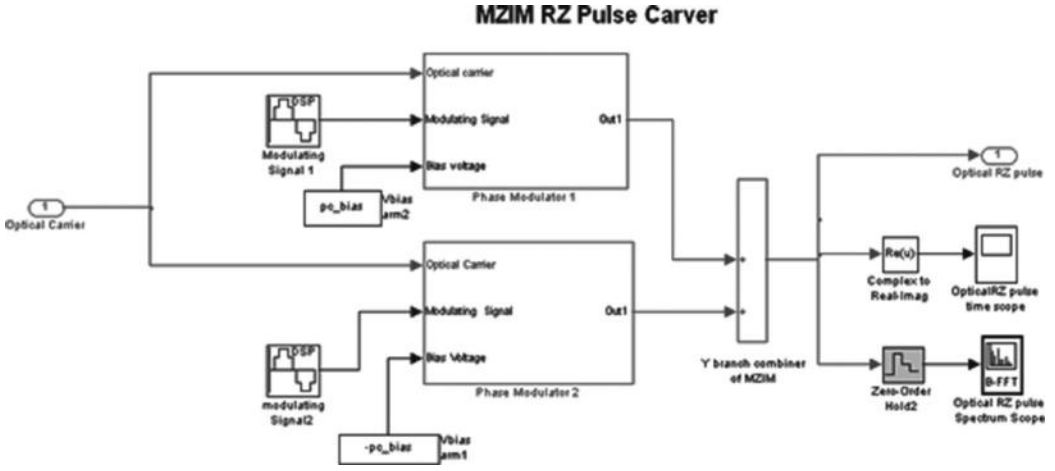

FIGURE 13.31
MATLAB Simulink model of a dual-drive MZIM pulse carver.

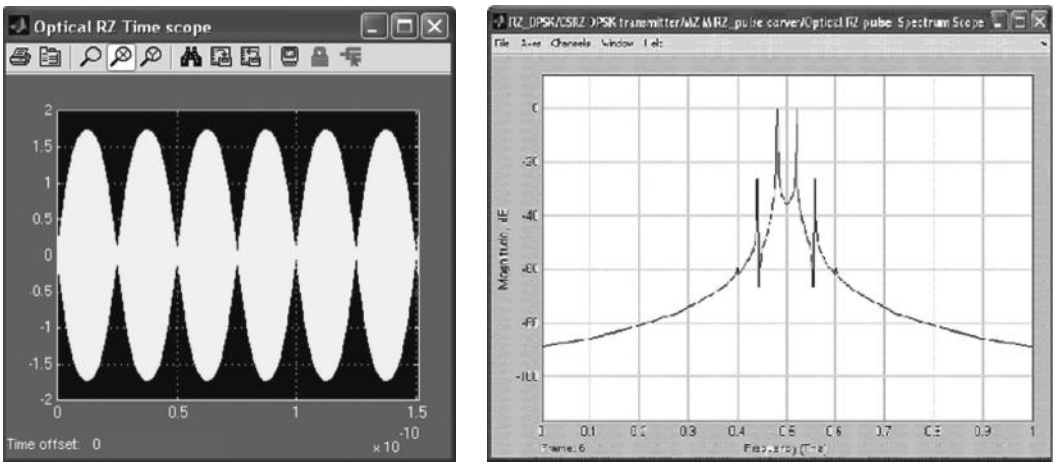

(a) (b)

FIGURE 13.32
(a) CSRZ pulse in time domain. The pulse is 25 ps wide with the carrier residing in the pulse at 2.048 THz. (b) Spectral characteristics of CSRZ pulse. The carrier was shown clearly being eliminated at 500 GHz.

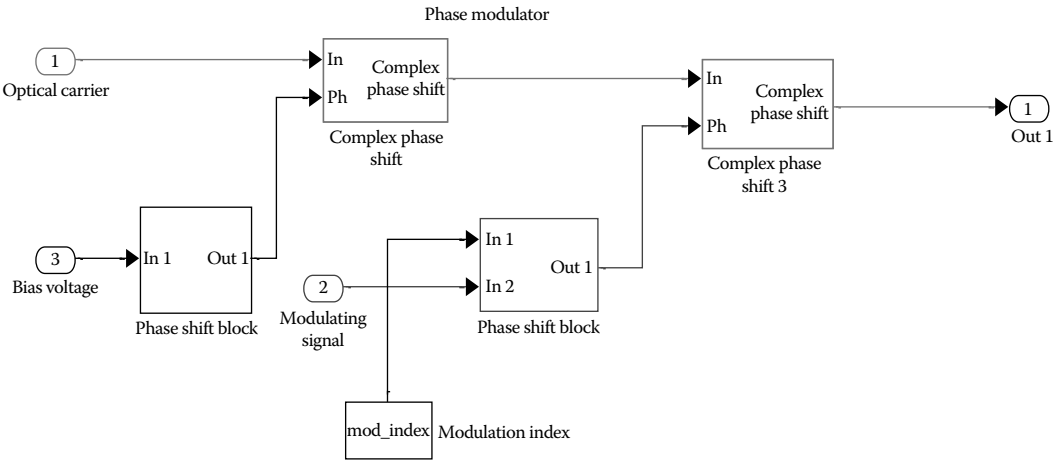

FIGURE 13.33
Phase modulation implemented in Simulink®. One of the PM arms in Figure 13.31.

13.4.4.5 Data Modulator

The data modulator based on the MZIM structure employed a similar model as in pulse carver. However, when the MZIM model was driven as a PSK data modulator, the biasing voltage was always $V_{\pi/2}$ and $V_{\pi/2}$ the data voltage swing. The phase modulation is limited to 0 and π, equivalent to the signal constellation diagram with two points at 0 and π and doubling in the frequency of driving data. If modulation formats other than PSK are used, then the biasing voltage and data voltage swing will be different as explained in Section 13.3.

Before feeding into the PMs, there is a data-type conversion to convert data in Boolean form generated by the Bernoulli generator to double type to be processed by the PM model.

TABLE 13.1

Parameters Setting for Three Formats of RZ Pulses

Biasing Point	Parameters Setting	
	Arm 1	**Arm 2**
Linear	Modulation index: $\pi/4$	Modulation index: $\pi/4$
	Signal frequency: 40 GHz	Signal frequency: 40 GHz
	Biasing voltage: $V_{\pi/4}$	Biasing voltage: $-V_{\pi/4}$
	Phase offset: $\pi/2$	Phase offset: $\pi + \pi/2$
Minimum (CSRZ)	Modulation index: $\pi/3$	Modulation index: $\pi/3$
	Signal frequency: 20 GHz	Signal frequency: 20 GHz
	Biasing voltage: $V_{\pi/2}$	Biasing voltage: $-V_{\pi/2}$
	Phase offset: 0	Phase offset: π
Maximum	Modulation index: $\pi/2$	Modulation index: $\pi/2$
	Signal frequency: 20 GHz	Signal frequency: 20 GHz
	Biasing voltage: V_{π}	Biasing voltage: $-V_{\pi}$
	Phase offset: $\pi/2$	Phase offset: $\pi/2$

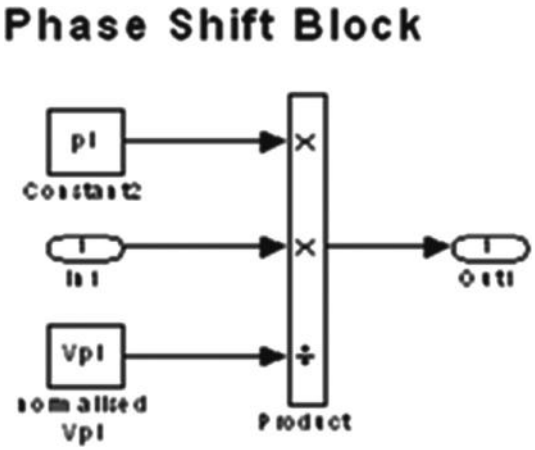

FIGURE 13.34
Structure of the phase shift block given in Figure 13.33, which represents a direct mathematical model derived for phase implementation.

The PM is similar to that shown in Figure 13.35. Logically, they are similar, but the phase shift block is slightly altered to assemble the data modulation principle in this model (Figures 13.36 and 13.37).

13.4.4.6 Differential Data Encoder

Differential data encoder was implemented using differential encoding logic described in 13.4. Bernoulli binary generator was driven at 20 Gb/s and sampled at the same frame rate to XOR with the past encoded bit. This model consists of two NRZ DPSK data output that complement each other, and which are necessary to operate the dual-drive MZIM (Figures 13.38 through 13.40).

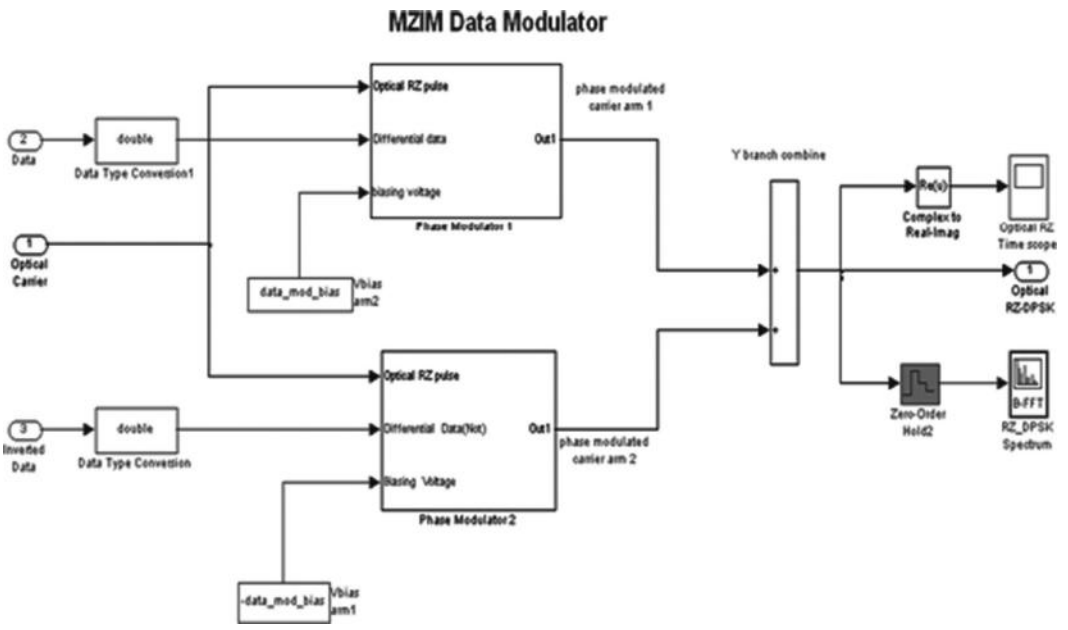

FIGURE 13.35
Simulink model of a data modulator based on dual-drive Mach–Zehnder interferometric structure driven by data and inverted data.

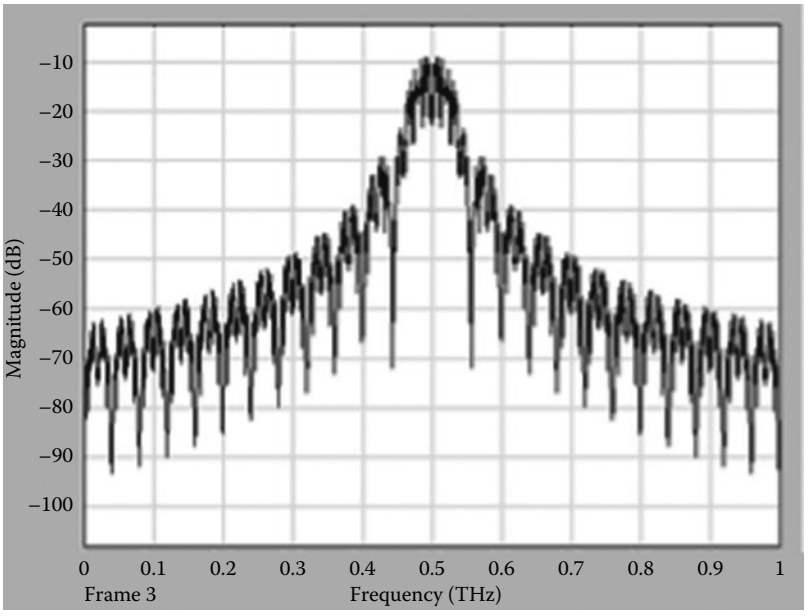

FIGURE 13.36
Spectrum scope of monitored after data modulator using CSRZ–DPSK modulation format with a carrier of 500 GHz.

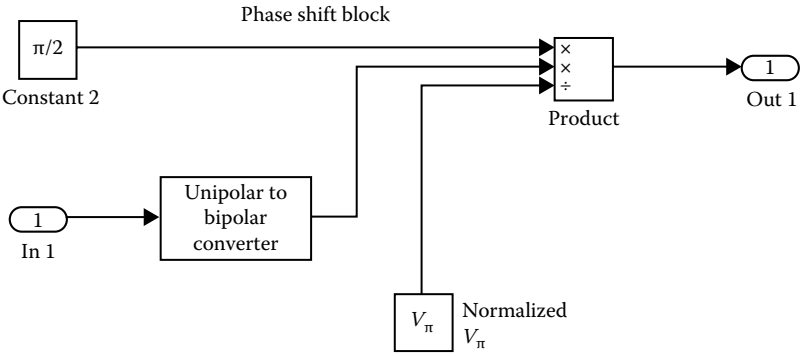

FIGURE 13.37
Second phase shift block in one of the PM arms in Figure 13.35.

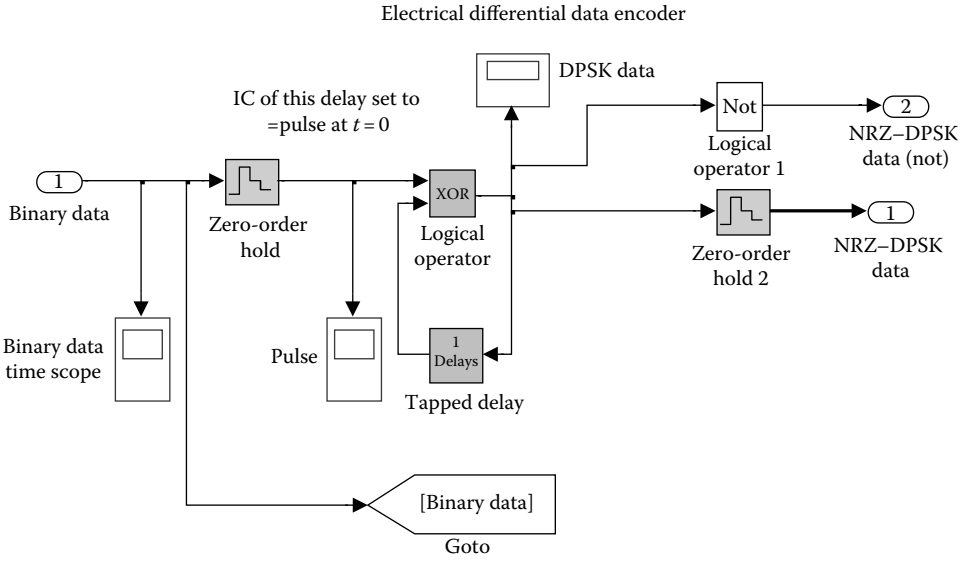

FIGURE 13.38
Electrical differential data encoder.

13.4.4.7 Back-to-Back Receiver

The balanced receiver was constituted by an MZDI model, 2 photodiode models, and a comparator with time scopes and eye diagrams to evaluate performance. MZDI was implemented by the delay block provided in Simulink library. Because the OC wave was calculated in discrete sizes of $2^n \times 40e^9$, it was simple to calculate the exact number of samples required to delay a bit period. For instance, in this case, $2^n = 512$, therefore, 512 samples were required to delay the bit period (Figures 13.41 and 13.42).

Constructive and destructive interferences of received signal and a-bit-delay signal were implemented by addition and subtraction, respectively. When there is no phase change between adjacent bits, addition will constructively superpose two signals. Conversely, subtraction will superpose two signals with π phase shift. Because the photodiode converts optical power to an electrical signal, it could be modeled as the square of the magnitude.

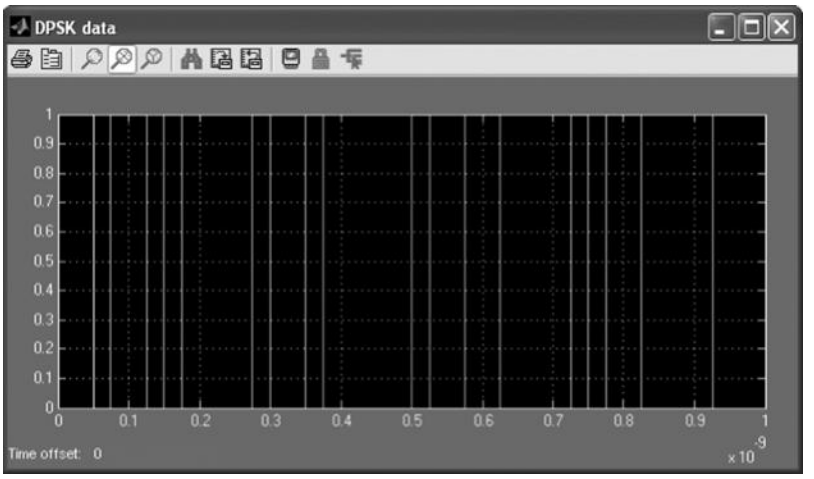

FIGURE 13.39
Differential encoded binary data in Figure 13.38.

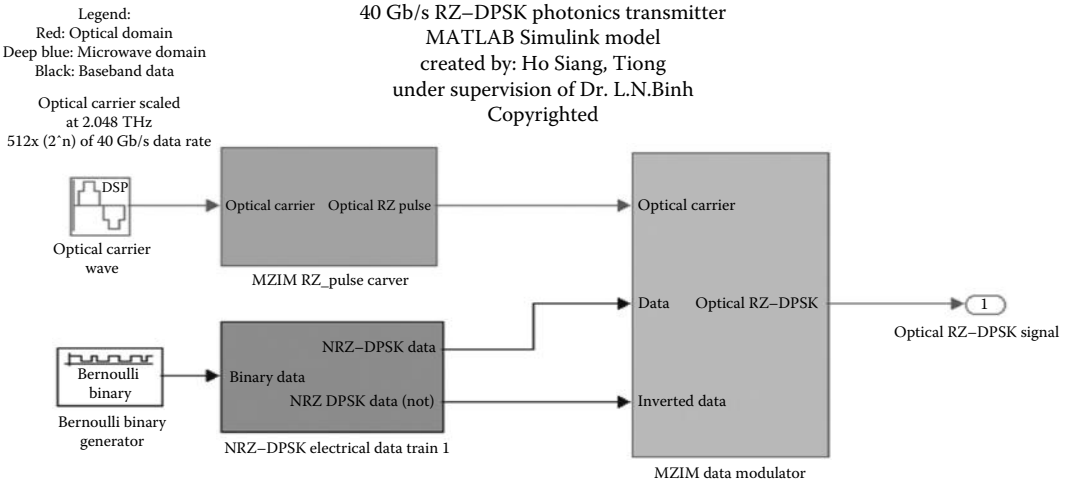

FIGURE 13.40
A complete Simulink® model of the photonic transmitter.

Single-ended detection would require either of one of the ports to be detected by the eye diagram block. On the other hand, balanced detection would require subtraction (logically) between two outputs before being detected by eye diagram (Figure 13.43).

13.4.4.8 Eye Diagram

Samples per symbol can be set by carrier frequency × bit period. As shown in Figure 13.44, 2*eye_diagram implies that the eye diagram displays two-bit periods. Hence, it can be adjusted accordingly to view the number of bit periods.

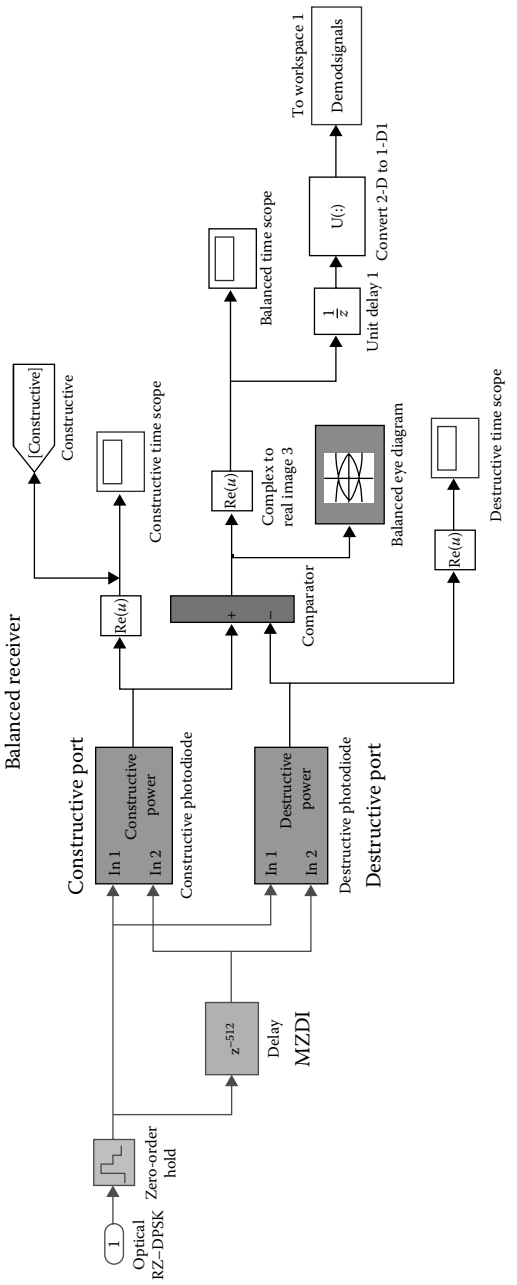

FIGURE 13.41
Simulink® model of a balanced receiver.

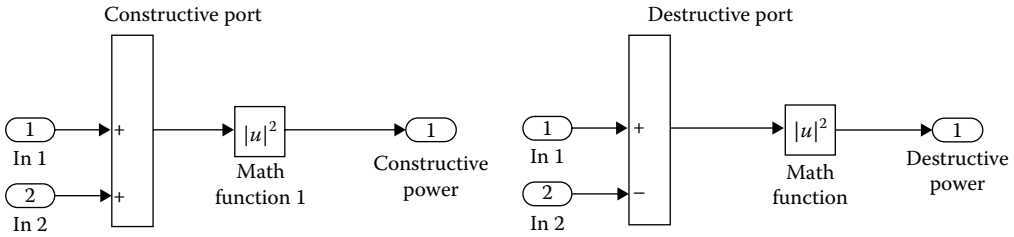

FIGURE 13.42
Constructive and destructive port in balanced receiver. Math function magnitude ^ 2 represents the photodiode.

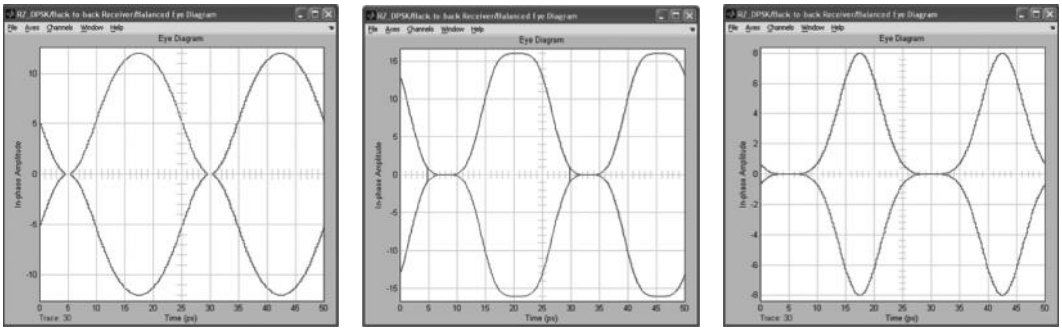

(a) (b) (c)

FIGURE 13.43
Eye diagrams of three different RZ modulation formats detected by BtB balanced receiver. From left to right: (a) CSRZ, (b) 50% RZ, and (c) 33% RZ.

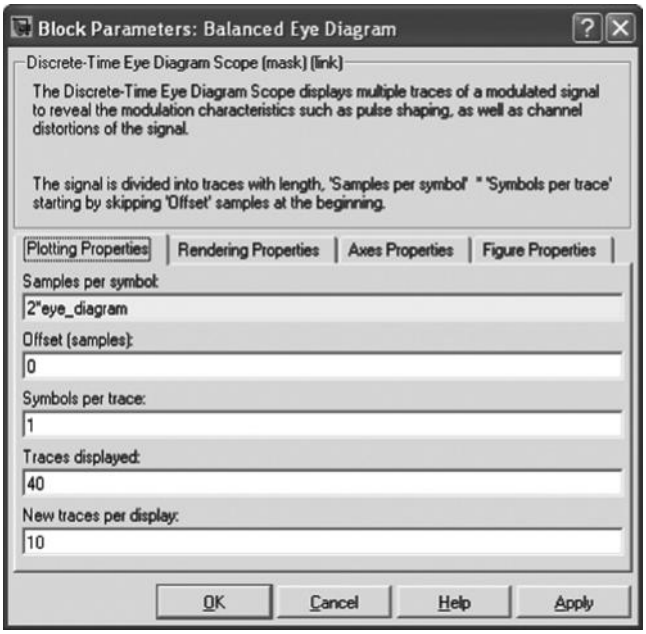

FIGURE 13.44
Parameter settings for eye diagram.

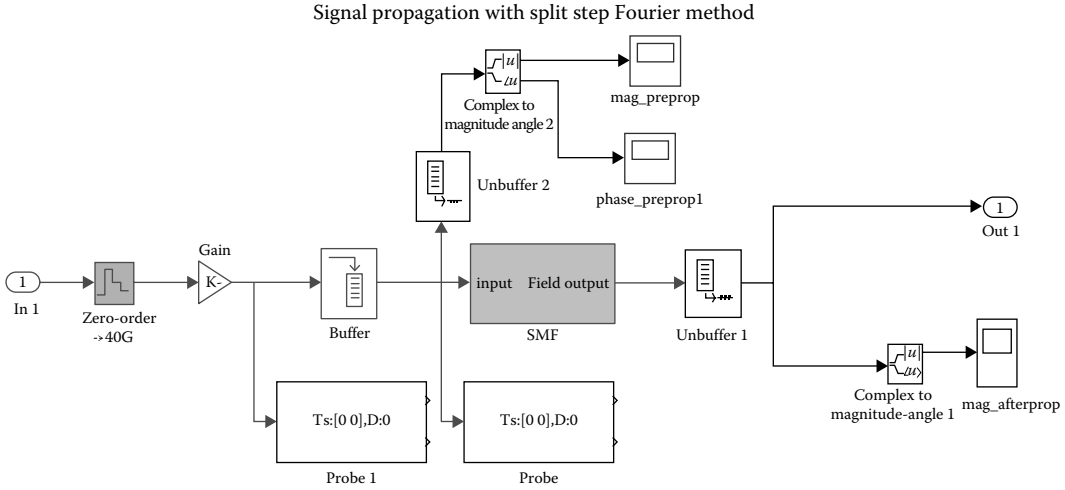

FIGURE 13.45
Simulink® model of signal propagation in fiber.

13.4.4.9 Signal Propagation

The zero-order hold (sampler in green color) is used to obtain a pulse envelope of the optically modulated signal. The signal propagation model can only deal with the pulse envelope because it was developed using the split-step Fourier method (SSFM) to solve the NLSE equation, assuming the signal has a slow-varying time envelope as explained in Section 3.7. The gain acted like an attenuator to control the power input to the fiber. The buffer was not used in actual practice, but it was necessary to specify the number of bit samples in a particular fast Fourier transform (FFT) window. The buffered signal was the input to the SMF block to be processed by a MATLAB function ssprop_matlabfunction_modified.m (Figures 13.45 and 13.46).

In the SMF block, the signal was concatenated by parameters such as the number of FFT, time step, step size, number of steps, fiber loss constant, propagation constants, and nonlinear coefficients. The signal was processed by MATLAB function ssprop_matlabfunction_modified.m which implemented the SSFM algorithm.

13.4.4.10 Bit Error Rate (BER)

The BER of the obtained eye diagram of Figure 13.47 can be calculated by using MATLAB programs listed in the Appendix. The histogram was first computed using histogram.m and a sample result of the histogram after 2 km fiber span is illustrated in Figure 13.48. The Q factor and BER were calculated using BER_GaussianQ.m by assuming the signal distortion due to fiber propagation was Gaussian distributed. This m-file is also listed in the Appendix.

13.5 DQPSK Modulation Formats Transmission Models

The required bandwidth availability to support modern day optical fiber communication systems is now extended into the terabit per second region. Many system designs focusing on multi wavelength DWDM implementation have been proposed, allowing increased

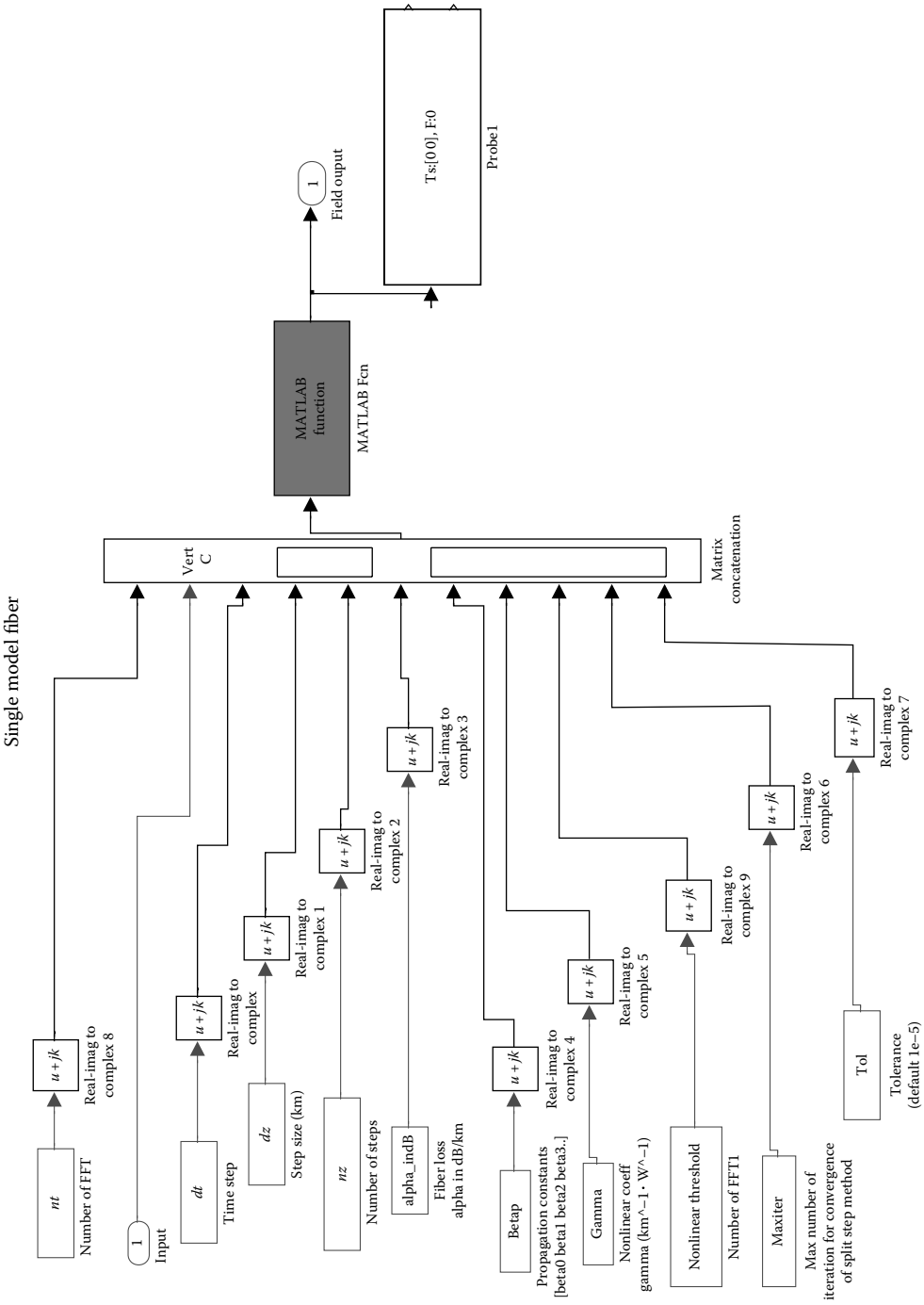

FIGURE 13.46
Parameters setting in SMF block.

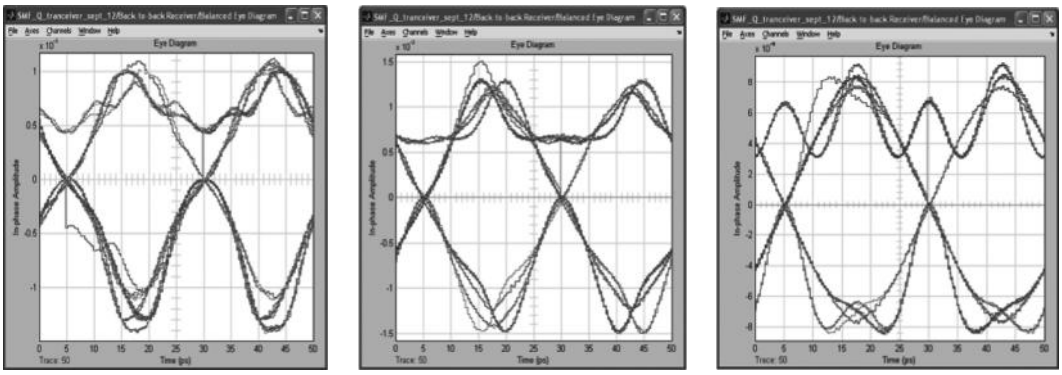

(a) (b) (c)

FIGURE 13.47
Eye diagrams of three different RZ modulation formats after 2 km fiber propagation using balanced receiver. From left to right: (a) CSRZ–DPSK, (b) 50% RZ_DPSK, and (c) 33% RZ–DPSK.

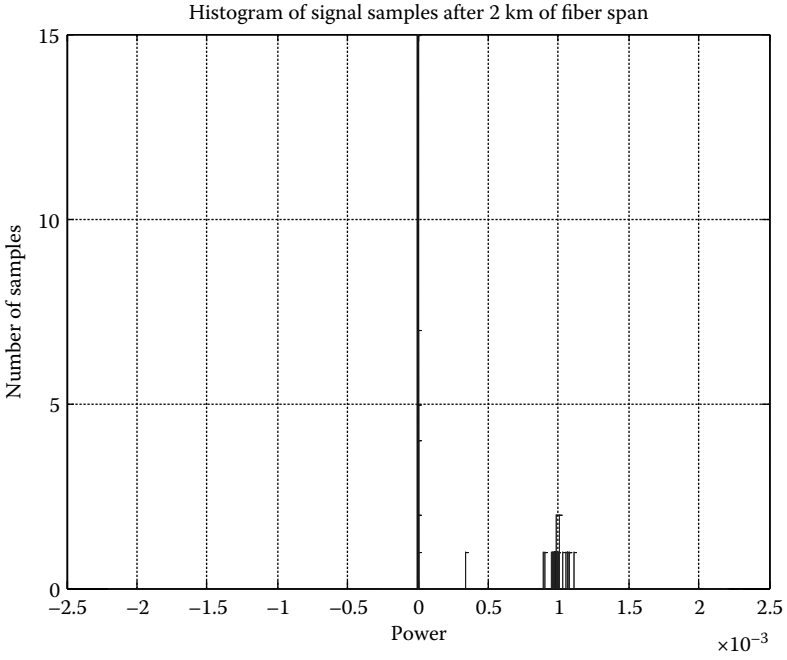

FIGURE 13.48
Histogram of signal samples after 2 km of fiber span detected at constructive port using CSRZ-DPSK modulation format.

channel capacity using existing available hardware. Some modulation formats that were implemented only in the electrical domain in the past are now being transposed to the optical domain, allowing for increased transmission capacity. An example of such a modulation format is the DQPSK format [5]. This format is also important for the bit rate reaching 100 Gb/s. At this rate, electronic detection is not possible and lowering the rate to the symbol rate plus polarization multiplexing may bring the detection speed down to 25 or 28 Gsymbols/s.

A high capacity 20 Gb/s (2 × 10 Gb/s) single-channel optical DQPSK simulator can be developed, which is capable of doubling the bit rate compared to conventional OOK signaling techniques. The simulator has been developed in the MATLAB Simulink. The versatile nature of the simulator is capable of showing the effects of incorrect dispersion management in fiber links and generates data that can be easily analyzed with the support of MATLAB. Optical components included in the model can be user defined, enhanced, or removed as desired.

This chapter outlines the necessary theoretical background for the design of the optical DQPSK system. It also explains the detailed operation and purpose of each component model and its representation in Simulink. Each model developed in the simulator focuses on theoretical and practical design principles. As a result, the fundamental operation of each component in the system has been understood together with their impairments. This document also outlines the future extension of this simulator to support DWDM operations to allow Terabit per sec. (Tb/s), $N \times 40$ Gb/s systems to be simulated accurately before any physical implementation is performed.

13.5.1 DQPSK Optical System Components

Given what we now know of the general configuration of a DWDM system channel, we focus on the key optical components used in the transmitter (Tx), fiber and receiver (Rx) of a single-channel RZ–DQPSK fiber link. We begin by considering the transmitter components first, we then present some optical fiber characteristics, and lastly we consider the receiver components.

13.5.1.1 DQPSK Transmitter

We present a brief description of the key optical components that comprise the transmission system. Simulink models of these components are given in later sections.

13.5.1.1.1 Mach–Zehnder Modulator (MZM)

The MZMs are the most widely used optical devices for external modulation. Although several types of MZMs exist, in this chapter we consider the well-known Lithium niobate ($LiNbO_3$) single-electrode modulator based on its common use in 10 Gb/s PSK systems. Its role in most DWDM systems, and in this chapter, is to externally modulate the phase of the OC and is thus usually placed in cascade with the DFB laser. The MZM consists of a Y splitter (3 dB), two waveguide arms, and a Y combiner as described in Chapter 5.

The physics behind the operation of this device is the EO effect. We only mention the core details here to gain an understanding of its operation. The EO effect allows the refractive index of the material to change as a response to an applied voltage $u_2(t)$ ($u_1(t) = 0$ in single-electrode MZM, also known as the modulating data stream. The phase of the signal as it passes through this region of applied voltage (binary or sinusoidal varying) is changed. At the input, the power of the incident carrier is ideally split equally, one carrier wave experiences a phase change (assumed to be 0 or π rad in this chapter), while the other passes through unchanged, and two waves emerge at the output. It should be noted that the OC that has experienced the 0 or π phase shift (in the lower arm of MZM) is of great importance since the differential phase of this waveform will represent the first encoded bit of the two bits (di-bit) to be transmitted. The driving voltage to power (P–V) is characteristic of the MZM. To best simulate the MZM in this system design, we will assume that

one of the MZMs is biased at the minimum transmission point with biasing voltage, V_{π} (~3.5 V in practice, with $2V_{\pi p-p}$ non–return to zero driving voltage swing) and $V_{\pi/2}$ for the second MZM (with $V_{\pi p-p}$ sinusoidal [approximately RZ] driving voltage swing).

The MZM is also a useful device in its response to certain high-bit-rate pulse shapes (e.g., NRZ, RZ), which are outlined later. They are normally used in replacement of a normal PM biased to a π phase shift. Other PMs simulated in this section that operate under the same physical principles as the MZM, however, are assumed to be biased to produce a π/2 phase shift in the OC.

13.5.1.1.2 Chirp

The role of chirp α and, in particular, its influence on the performance of modern fiber optic systems are to be considered. Chirp, in particular, transmitter chirp, is known to be a main contributor to spectral broadening, also limiting transmission to short distances (for $\alpha > 0$).* Thus, to minimize the effects of chirp, we have considered the sources of this effect. In this chapter, as outlined later, we simulate the Mach–Zehnder external modulator (MZM) behavior. This EO device is integral to the design of the DQPSK transmitter and is used in many DWDM systems. The MZM is chosen as it provides superior signal integrity and normally has smaller chirping effects. Frequency chirp is common in most optical transmitters; however, in the context of this chapter, we have also considered phase chirping effects.

13.5.2 DQPSK Receiver

In this section, we consider the operation and theory of the optical components that are integral to allowing for the demodulation and detection of the DQPSK transmitted signal.

13.5.2.1 Mach–Zehnder Delay Interferometer (MZDI)

The principle operation of this device is to convert phase-coded information, such as that generated by the DQPSK transmitter, into an intensity signal that can be detected by the photodiode circuitry at the output of the DI arms. The intensity of the signal at the output of the DI arms is dependent on the phase difference between the adjacent bit $\Delta\phi_{mod}$ of the OC in both the upper and lower arms, the relationship between phase and intensity is expressed as

$$I(\Delta\phi) = 0.5\cos\left(\Delta\phi_{mod} \pm \frac{\pi}{4} + \delta\phi_{DI}\right) + 0.5 \tag{13.17}$$

where $\delta\phi_{DI}$ is a phase offset. Note that this is an MZ device and thus operates on the principles of interference between the two arms, which is dependent on the phase difference. For the applications of DQPSK demodulation, the delay T is 1 bit in length (100 ps for 10 Gb/s operation) to allow for proper interference between two adjacent bits. Effectively the delayed signal acts as a phase reference for the incoming symbol. The extra phase delay (phase = ±π/4) is normally implemented in practice for DQPSK systems only using integrated thermal heaters.

The phase to intensity characteristic of the MZDI is shown in Figure 13.49 along with the expected eye diagram that will allow for performance measurements to be made.

* For $\alpha < 0$ (negative chirp), the transmission distance by compressing the pulse can actually increase; this technique is known as pre-chirp compensation.

This optical eye diagram is then detected by a photodetector. These optical devices have been shown to operate in a stable manner using either fiber-based or planar-lightwave-circuit (PLC) technologies. The current waveform shape at the output of the photodiode owing to the response of the incident power on the photodiode has *cos*-like form. This pulse shape has been approximated by the *cos*-like I_{pulse} variable in our simulations.

13.5.2.2 Photodiode

To detect the optical intensity signal at the output of the MZDI shown in Figure 13.49 and to display this signal for later BER analysis, a photodiode diode or a pair of balanced diodes connected back to back is required. The types most commonly used are the PIN and the avalanching photodiode (APD). The primary objective of the photodiode is to produce a conversion from optical photonic energy to an electrical (electron flow) current. In this chapter, we are considering the PIN photodetector type. In practice, these PIN diodes (reverse biased) are placed at the output arms of the MZDI (Figure 13.50). It is common practice to use either the single or balanced diode detection at the receiver; however, in practice, the balanced receiver configuration has shown higher sensitivity for DQPSK and other PSK modulation formats. In this chapter, we consider the single-diode detection model for the sake of simplicity; however, we suggest that balanced detection be investigated at some stage in the future.

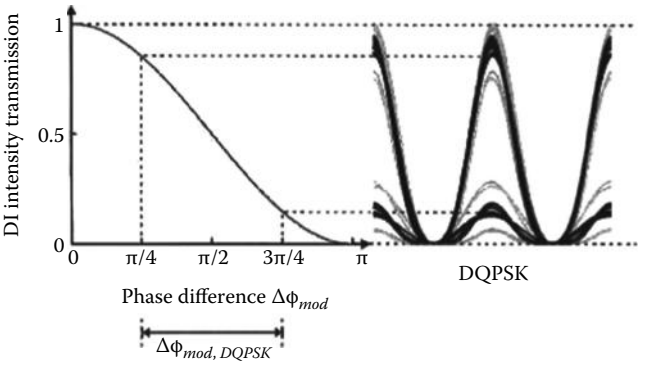

FIGURE 13.49
The phase to intensity characteristic of the MZDI and the expected eye diagram generated at the output of the MZDI based on the phase difference between the two arms; the lighter eye pattern is due to phase offset, $\delta\phi_{DI}$, from heater.

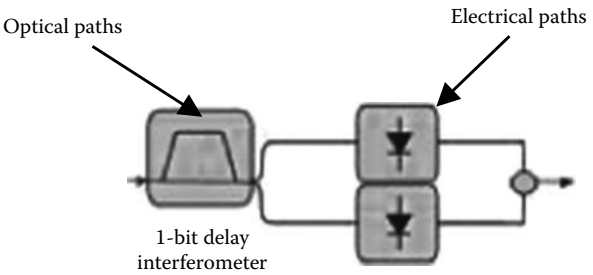

FIGURE 13.50
Balanced photodiode detection, diode placed at output of each MZDI arm.

13.5.2.3 Noise Sources

In order to best simulate a true optical transmission system, we have considered various noise factors within the link, particularly at the receiver end. The noise sources implemented into the simulations include: (1) MZDI phase offset $\delta\phi_{DI}$, (2) photodiode noise effects (i.e., quantum shot noise, photodiode dark current, and thermal noise), and (3) receiver electronic amplifier noise.

13.5.2.4 Digital Data Sampling

Most of the data supported by the blocksets can only support discrete data sources/values. It is, therefore, necessary to find a way to convert continuous waveforms to discrete values. Signaling theory states that a continuous signal $s(t)$ can be represented by a set of samples taken at a sampling frequency (f_S). This sampling frequency must be at least twice that of the highest frequency contained in the signal waveform, B. This is represented mathematically by $f_S \geq 2B$ samples/second; $f_S = 2B$ is referred to as the Nyquist rate. All samples made during the simulation are made at the Nyquist rate to ensure synchronization between data samples and to minimize sampling errors.

13.5.2.5 Pulse Shapes

We mentioned earlier the concept of pulse shapes in the application to the MZIM. We consider now the RZ digital signal, the pulse shape used in the final design of this chapter. This pulse shape has a duration of half the bit period ($T_b/2$) and thus has a 50% duty cycle. In most modern optical systems, this RZ pulse shape is often approximated by a sinusoid having frequency $1/T_b$ Hz. The brief nature of the pulse makes the RZ pulse shape more tolerable to intersymbol interference (ISI) compared to the NRZ pulse shape; however, its power spectra occupy a larger bandwidth. In this chapter, we consider the RZ pulse shape as it is more compatible with the simulation development [6].

The NRZ pulse shape has a data rate of $1/T_b$ b/s; however, its duration is now T_b seconds. The power spectrum is also reduced to half that of the RZ pulse spectrum. When digitizing data for transmission across many hundreds of kilometers, many digital modulation formats have been proposed and investigated. This chapter investigates the DQPSK modulation format. This modulation scheme, although in existence for quite some time, has only been implemented in the electrical domain. Its application to optical systems proved difficult in the past as constant phase shifts in OCs were required to be maintained. However, with the improvement in optical technology and alternative transmitter design setup, these difficulties have been eliminated.

One of the main attractive features of the DQPSK modulation format is that it offers both twice as much bandwidth and increased spectral efficiency compared to OOK. As an example, comparisons between 8 × 80 Gb/s DQPSK systems and 8 × 40 Gb/s OOK systems show that DQPSK modulation offers superior performance (i.e., spectral efficiency). The very nature of the signaling process also allows noncoherent detection at a receiver to be possible, thus reducing the overall cost of the system design.

As the name suggests, the idea behind DQPSK modulation format is to apply a differential form of phase shift modulation to the OC which encodes the data. DQPSK is an extension to the simpler DPSK format. Rather than having two possible symbol phase states (0 or π phase shift) between adjacent symbols, DQPSK is a four-symbol equivalent $\{0, \pi/2, \pi, \text{or } 3\pi/2\}$. Depending on the desired di-bit combination to be encoded, the difference in phase, $\Delta\phi_{mod}$, between the two adjacent symbols (OC pulses)

TABLE 13.2

DQPSK Modulation Phase Shifts

Di-Bit	Phase Difference $\Delta\phi = \phi_2 - \phi_1$ (Degrees)
00	0
01	90
10	180
11	270

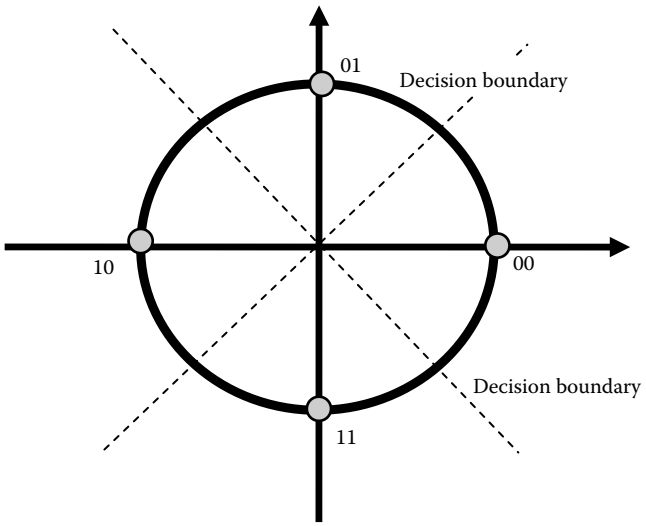

FIGURE 13.51
DQPSK signal constellation and decision boundaries for different states at $\pi/4$.

is varied systematically. Table 13.2 outlines this phase transfer, where ϕ_1 and ϕ_2 are the phases of consecutive symbols.

Table 13.2 can also be represented in the form commonly known as a "constellation diagram" (see Figure 13.51), which graphically explains the signal state in both amplitude and phase.

Ideally, we would maintain constant amplitude and alter the phase of the signal during transitions; however, because of the characteristics of the optical equipment (i.e., MZM), some form of optical intensity modulation should also be observed in practice. This effect was investigated but not implemented in the final simulator because of data pulse representation inaccuracies.

13.5.2.6 MATLAB® Simulink® Simulator

With adequate knowledge of the optical components required for the design of a single-channel 10 Gb/s DQPSK transmission link, we can now consider the development process of the optical simulator. This simulator considers only one channel implementing the DQPSK signaling technique (total 20 GBaud/s baud rate); multiple-channel configurations (DWDM) have been considered for future work. The primary design of a single-channel operating efficiently was considered critical. We have developed this simulator

package in three main steps, each relating to the three main components in the transmission link. These include the transmitter, fiber, and receiver models. As this section focuses on an optical signaling technique (DQPSK) not attempted earlier, a significant amount of research into how this signaling technique is implemented in the optical domain using optical hardware was essential. The work done used a previously developed simulator, developed in Simulink, implementing the OOK format as a guide for initial development.

The transmitter performing the DQPSK transmission format was developed first and proved to be the most time consuming as this digital signaling technique can be implemented several ways using different hardware. Given that the concept of modeling in the Simulink environment was also a new experience resulting in additional time being allocated to familiarize

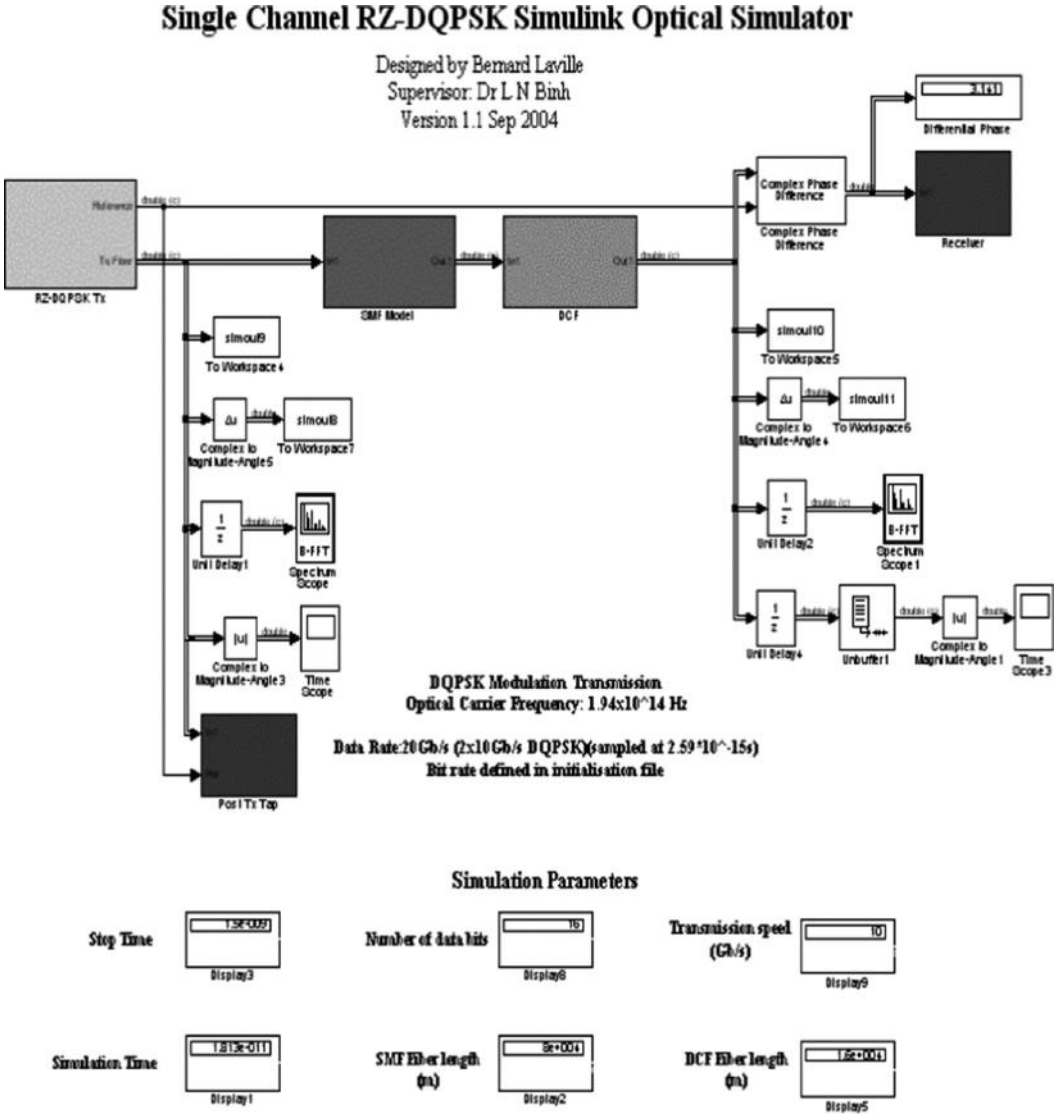

FIGURE 13.52
Simulink® optical simulator of single channel RZ-DQPSK transmission.

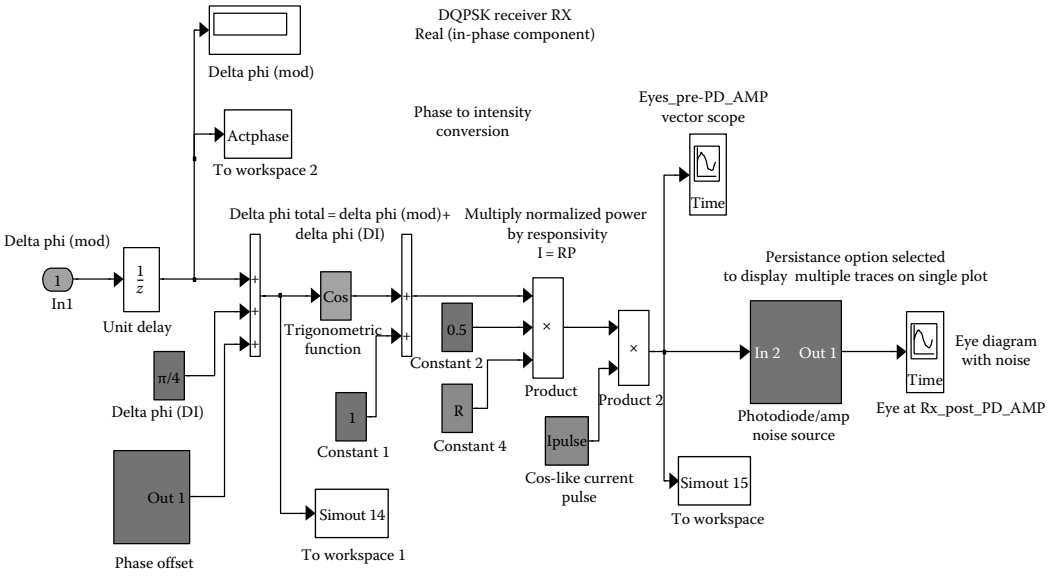

FIGURE 13.53
Structure of DQPSK receiver.

ourselves with the Simulink package. The final technique chosen proved to be the simplest to design and simulate using conventional data processing blocks in Simulink. The configuration of this transmission system is based on the research and development work performed in the field of DQPSK signaling transmission [6,7] and other available literature.

Figure 13.52 shows the top level of the single-channel optical DQPSK Simulink model developed. This model can be later altered, and new blocks added to optimize the system to individual requirements.

The final results displayed during simulations include the di-bit NRZ electrical bit stream (2 × 10 Gb/s), which modulates the OC via the MZM and PM, the spectrum of the transmitted OC, the RZ time-domain pulse generated, and finally the eye diagrams both prior to and after fiber propagation to allow for BER testing and other system performance measurements. We now consider each block shown in Figure 13.52 and present the development of the simulator model (Figure 13.53).

13.6 PDM-QAM

13.6.1 PDM-QPSK

13.6.1.1 System Configuration

The structure of the PDM transmitter is shown in Figure 13.2 and arranged for the test BtB as in Figure 13.54. The transmitter (Tx) is selected with a lightwave source whose wavelength falls into one of the standard grid lines tabulated in Chapter 5. The light wave is modulated with PDM-QPSK formats and launched directly into the fiber of the optical receiver via the wavelength demultiplexer. An optical amplifier unit (OAU) is used

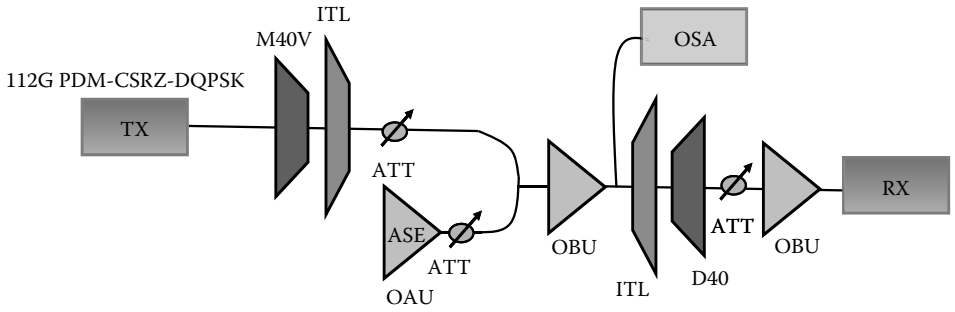

FIGURE 13.54
B2B test system configuration.

in the free running without any input signals as the optical amplifier noise (ASE) source to inject noises for evaluation of the OSNR. The balanced receiver operating in coherent mode (Agilent type) is used in this test.

Test procedure: (1) Connect the commercial laser modulated Tx with the instruments as in Figure 13.54; (2) Observe the eye diagram after QPSK modulation of every polarization and align the data input and clock; (3) Directly connect the Tx and the Rx, and sample two sets of data, and process using DSP algorithms to obtain the PRBS sequence under an error free condition; (4) Connect the system as shown in Figure 13.54; (5) Keep the signal power constant, vary the attenuation after the ASE source to obtain different values of the OSNR, and keep the received signal power constant; (6) Sample three sets of data at every OSNR value; and (7) Process the data to deduce the BER.

A bit pattern generator-type SHF12100* is used to generate electrical data streams as required for modulating the LiNbO3 *I-Q* modulator (see Figure 13.2). The QPSK eye diagram was first obtained and displayed on the sampling scope, where the eye diagram of one polarization is normal and the other is in a mess just like the eye diagram of the NRZ signal integrated in a sampling oscilloscope (optical port) by direct detection as depicted in Figure 13.55. This shows the three-level amplitude owing to the magnitude of the four states

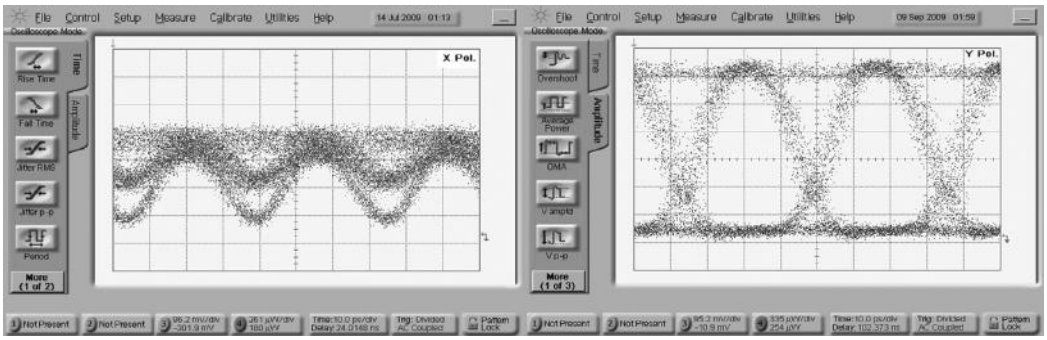

(a) (b)

FIGURE 13.55
Eye diagram of the two polarized channels after QPSK modulation: (a) X-polarized channel (correct eye) and (b) Y-polarized channel (incorrect eye).

* SHF GmbH, http://www.shf.de/.

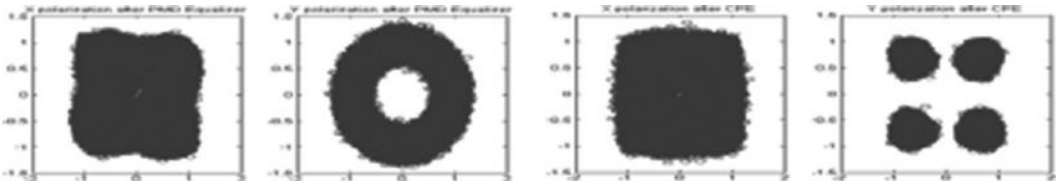

(a) (b)

FIGURE 13.56
(a) Constellation of the QPSK modulated sequence detected after PMD (polarization dispersion) module and (b) after carrier phase estimation (CPE) module.

"00, 01, 11, and 10" of the QPSK or in other words the amplitude difference is in the ratio of $\sqrt{2}$. So, the square of the amplitude and then the conversion of this direct detection via the photodetector give a ratio of 1/2 as seen in Figure 13.55, and this cannot be optimized by adjusting the bias of the QPSK and the 90° phase shift embedded in the *I*–*Q* modulator.

The direct connection between the Tx and Rx is carried out with the sampled data obtained from the sampling oscilloscope, which are processed off-line. The signal constellations for both the X- and Y-polarized channels are obtained as shown in Figure 13.56.

From Figures 13.55 and 13.56, it can be concluded that one polarization does not function properly as is also confirmed by the eye diagram shown in Figure 13.55. The other polarized channel performs well. It is noted that the single-ended electronic amplifier is used in the Agilent coherent receiver instead of the balanced optoelectronic structure. Correction of the polarization by using a polarization controller is made before launching the lightwave source into the *I*–*Q* modulator to ensure the functioning of the two polarized channels. Both polarized channels are subject to the variation of the polarization rotation via a polarization mode dispersion (PMD) module and the off-tuning of the carrier frequency (between the local oscillator and the modulated carrier) so as to gauge the recovery of the receiver using the carrier phase estimation (CPE) (carrier phase recovery algorithm).

The BtB OSNR is then tested with the working polarized channel. The OSNR requirement at the BER of 2e−3 is about 16.5 dB. However, this result was obtained as shown in Figure 13.57, without the 90° monitoring and control, but locked by the algorithm itself when PRBS 31 was used. There may be a 90° phase deviation during the test when PRBS 15 is used.

The experimental setup is used to test the performance of the PDM-QPSK under back-to-back transmission before launching into the multispan cascaded optical transmission line without incorporating the dispersion compensating fiber (DCF) length (DCM—dispersion compensating module).

Coherent detection would offer both advantages in terms of sensitivity and complex amplitude signals recovered for digital signal processing. A typical optical transmission employing PDM-QPSK is depicted in Figure 13.58.

In coherent detection, there is a mixing between the LO laser and the modulated signals whose carrier frequency is very close to that of the LO. It is important to estimate the difference in frequency between these two sinusoidal waves whose frequency is in the THz region. This is called LOFO or frequency offset of the local oscillator with respect to that of the carrier. In coherent receivers, the optical signals are demodulated in terms of polarization and QPSK in the optical domain and then opto-electronically recovered in the electronic domain. In the digital electronic domain, the phases are processed via ADC and DSP systems as given in Figure 13.2. Hence, any offset of the frequencies between the LO and the light waves is critical for the phase estimation in the digital domain, and the absolute phase of the carrier may be altered by this offset.

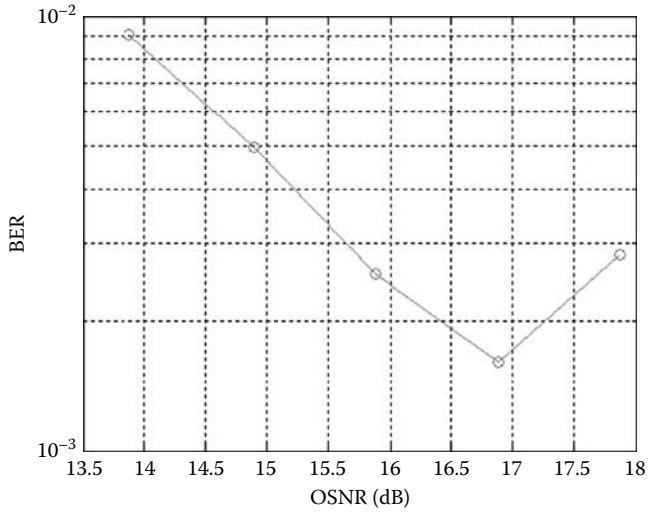

FIGURE 13.57
OSNR versus BER curve of the PDM–QPSK transmitter of the functioning polarized channel.

It is thus critical that any offset must be identified and estimated so that the DSP algorithms can be validated. This report outlines briefly, in terms of an engineering report, the measurement techniques, experimental setup, and estimation results of the offset. The lasers used as LO, transmitter, and LO in built-in receivers are measured.

13.6.1.2 Measurement Setup for LOFO

As shown in Figure 13.59, the two lasers are mixed in the hybrid coupler with their orthogonal polarizations demultiplexed and detected by analog optical receivers and then digitally processed off-line. If the sampling oscilloscope or analog oscilloscope is available, then it is quite simple to observe the beating signals. The two lasers are manually tuned to the right point at which they are nearly identical.

When there is a frequency difference between the two lasers, then we would observe a high peak power in the spectrum. This comes from the high-power laser, in this case, the local oscillator as shown in Figure 13.60. The phase difference of the two laser light waves are monitored and expected to circulate around the QPSK constellation as shown in Figure 13.61. It is obvious that the remaining power of the local oscillator laser is displayed at the center of the spectrum, and the two sidebands of single frequency represent the frequency difference of the two lasers. This indicates an amplitude modulation of the light waves whose frequency is equal to half the sum of the two frequencies of the laser. We can observe that the modulating signals vary with respect to time, and there is a time variant frequency offset between the two lasers as depicted in Figure 13.62.

Test procedure: (1) Connect the system as in Figure 13.59; (2) Store the received data in the realtime sampling scope with the maximum storage length of 250M points (stored by Tektronix sampling scope directly) or 25M points by Agilent software installed in the realtime sampling oscilloscope; (3) Do the FFT to evaluate the frequency offset from the beginning of the data to the end of the data block by block to see the LOFO variation and to ensure that the length of every block is equal to the length of FFT size; and (4) evaluate the LOFO variation speed (Figure 13.63).

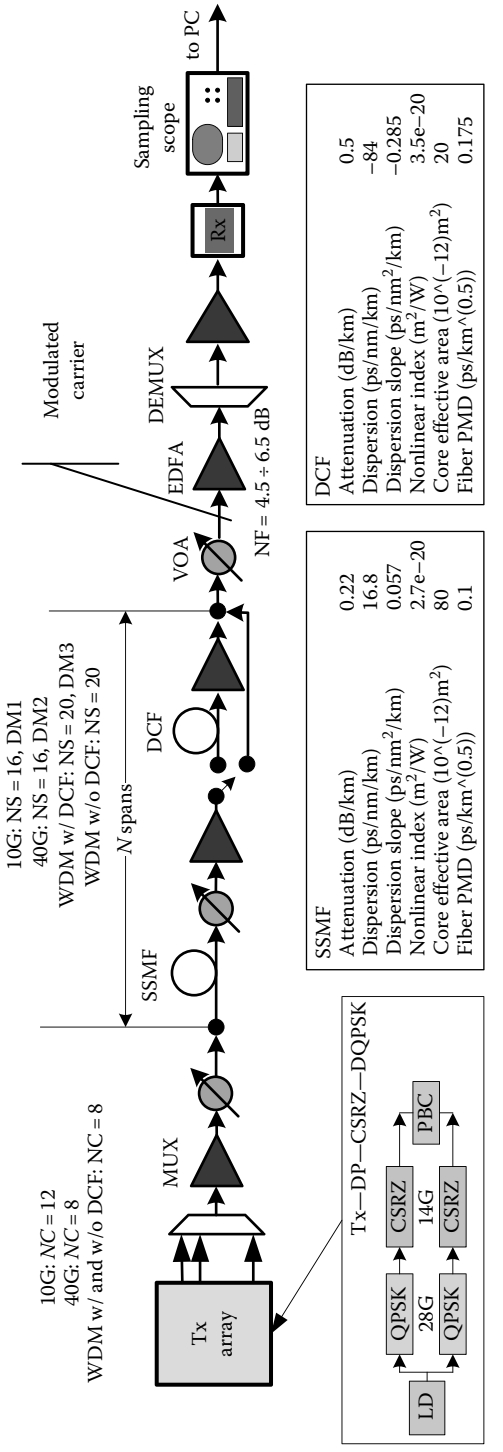

FIGURE 13.58
Experimental measurement setup; NS: number of spans, NC: number of channels, and DM: dispersion map.

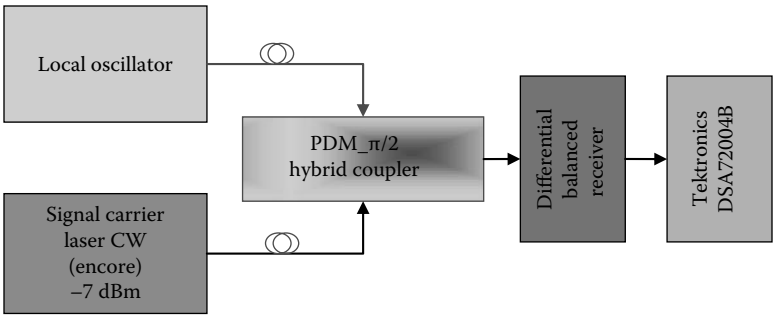

FIGURE 13.59
Test setup for measuring the frequency offset between LO and carrier laser.

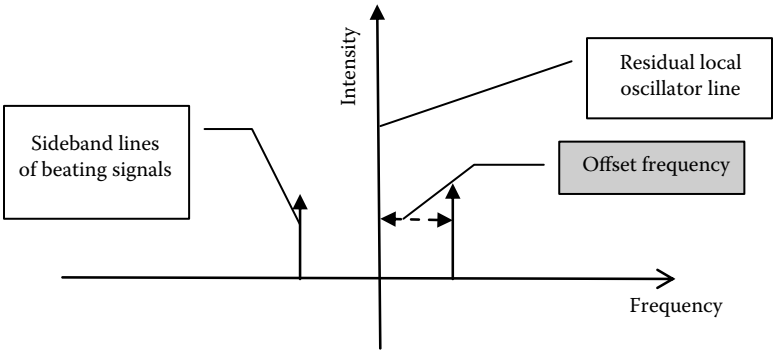

FIGURE 13.60
Spectrum of the beating signals.

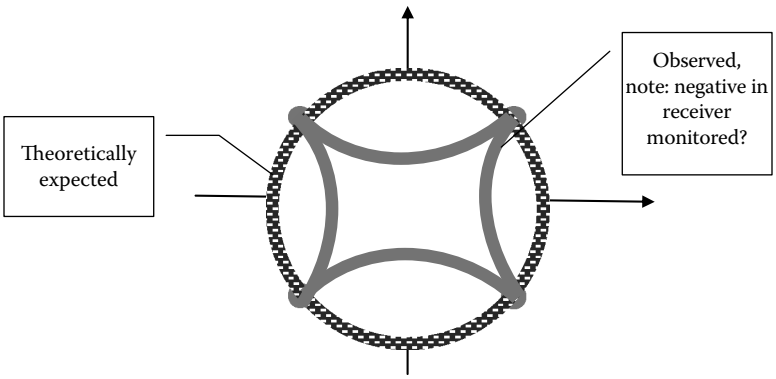

FIGURE 13.61
QPSK beating signal constellation as detected after the π/2 polarization diversity hybrid coupler. Phase rotation owing to the unlocking of the absolute phase of the two lasers.

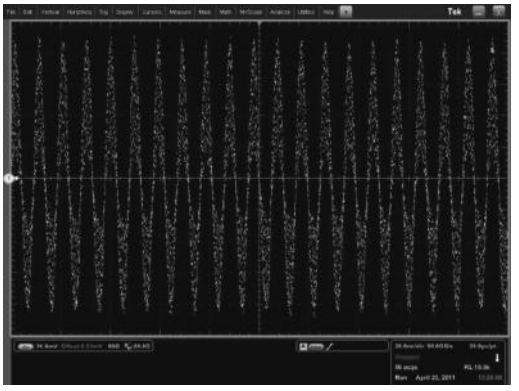
(a)

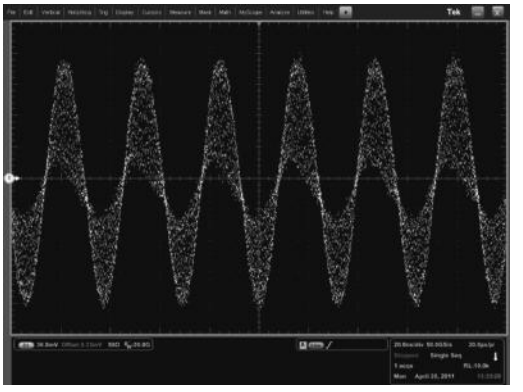
(b)

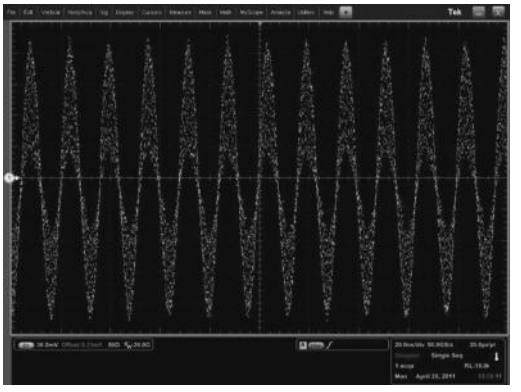
(c)

FIGURE 13.62
Beating signals of the two mixed lasers as observed by realtime sampling oscilloscope recorded at different time intervals (a), (b), and (c).

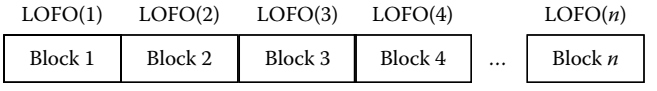

FIGURE 13.63
LOFO estimation by FFT of the sampled dataset.

Test parameters of the two lasers are as follows:

1. Commercial CW laser as the LO, and C02 CW laser as the signal
   Parameters:
   Laser type: Encore TTX1994(LO and signal)
   LO power: 13 dBm
   Signal power: –7.5 dBm
   Sample rate: 50 GS/s
   Data length: 250 M points

2. Agilent LO, and Tx CW laser as signal

   Parameters:

   Laser type: LO—Agilent, signal—Encore TTX1994

   LO power: 14 dBm

   Signal power: –7.5 dBm

   Sample rate: 50 GSa/s

   Data length: 25M points

Test results are conducted using a commercial CW external laser as the LO, and the Agilent CW laser as the signal with FFT size of 2^15. It is noted that only one channel of the *I*- or *Q*-channel is employed for the measurement of the offset frequency between the two lasers. The frequency shift, analyzed with respect to time, is depicted in Figures 13.64 and 13.65.

Figure 13.65 shows the beating signals observed in the time domain, or in fact, the Doppler signals of the two laser sources, the LO and the carrier laser. Figure 13.64 shows

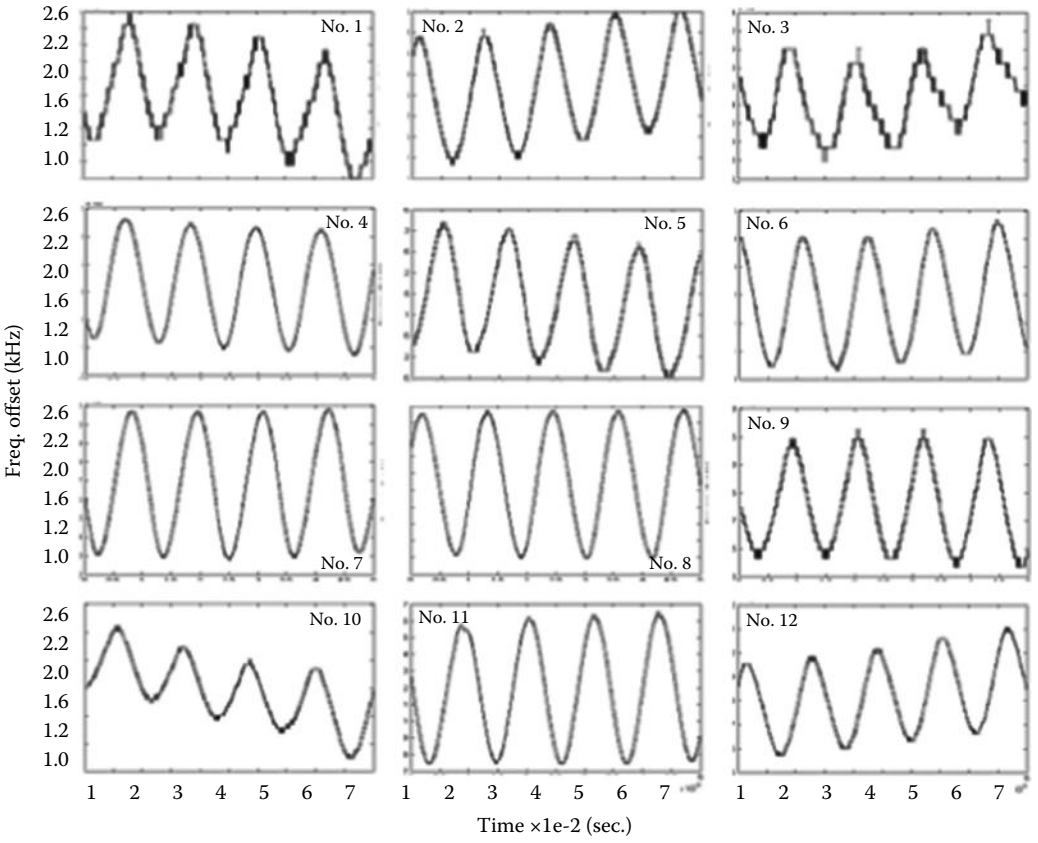

FIGURE 13.64
LOFO variation curves for 12 sets of data (dark gray: original curve of LOFO variation with time; light gray: filtered curve with sliding average window with the length of 2^7).

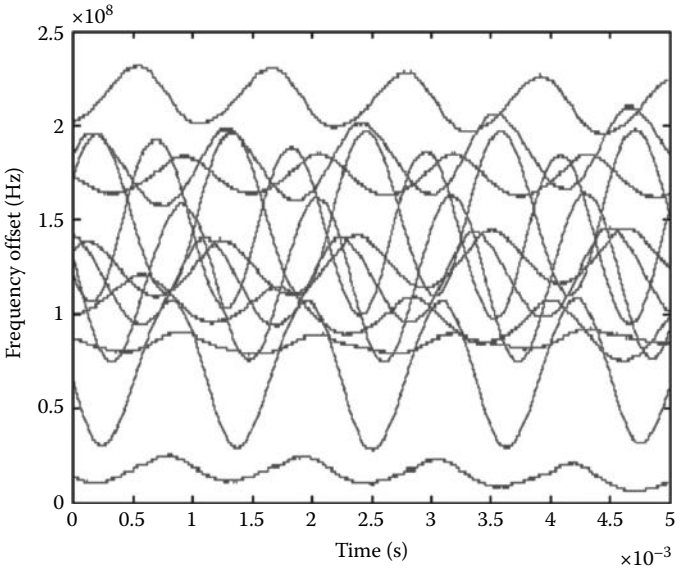

FIGURE 13.65
LOFO variation with respect to time of 12 datasets given in Figure 13.64.

the variation of LOFO of the 12 sets of data extracted from the time-dependent signals monitored in Figure 13.62. LOFO variations are estimated by using a sliding window of 2^7 whose smoothing versions are also displayed

We can observe the following:

- The frequency shift is oscillating at a frequency of 880 Hz. This is explained by inspecting the external cavity of the laser as shown in Figure 13.66. The back mirror is attached to a piezoelectric device which vibrates with a controlled driving electrical signal and is generated from the microcontroller.

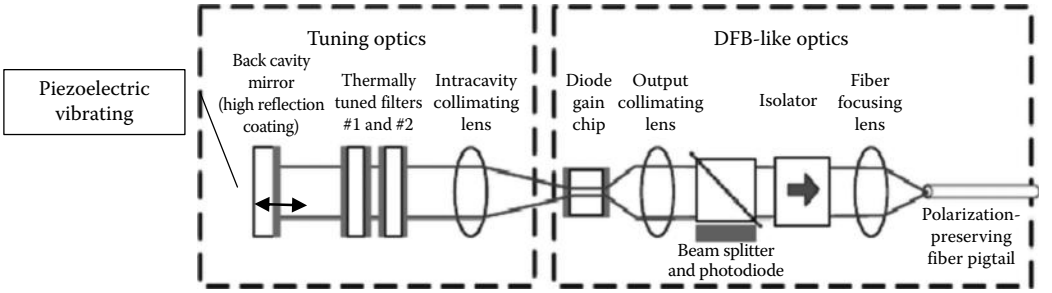

Note: The tunable laser consists of backside external cavity tuning optics and DFB-like optics. The diode gain device is coated with antireflection coating on the cavity-side facet so as to transmit light into the external laser cavity.

FIGURE 13.66
External cavity structure of the laser.

- The frequency shift varies with respect to time that is also observed in the time domain beating signal as reported earlier.
- The frequency offset reaches 80–250 MHz in less than 1.0 ms (one oscillating period of the external cavity).

From the tests presented here, it is clear that we must pay attention to the stability and any oscillation in the frequency of the local oscillator or that of the carrier, and compensate such LOFO to ensure that the performance is not severely affected.

Simulation results are presented in Figure 13.67. NLE canceller (NLEC) offers no gain for the case of 10G hybrid, and therefore, is not discussed here. In the scenario of 100G WDM w/o DCM, the SBP was not effective, while the NPCC offers a slightly improved performance. The main improvement comes from the quaternary MLSE. More details can be found in Chapter 15. The overall Q improvement varies from 0.7 to 1.7 dB depending on the launch power. The optimum optical power was shifted by 1 dBm. In the scenario of 100G WDM w/DCF, the combination of SBP and NPCC was inferior to MLSE. By the use of all algorithms, improvements from 0.8 to 1.8 dB (Q-factor) were achieved.

Although in previous two transmission scenarios the MLSE was always superior to SBP and NPCC, in a 40G hybrid transmission at high optical power, the combination of SBP and NPCC outperformed the MLSE by almost 0.3 dB in Q-factor. Overall, they together allow similar Q-gain as in previous scenarios. It is noted that at lower optical power in 40G hybrid transmissions, the total performance of all NLECs is worse by approximately 0.2 dB in the Q-factor. On the other hand, in pure 100G transmission (WDM), the gain is achieved at both low and high optical powers.

13.6.2 PDM-16 QAM Transmission Systems

Figure 13.68 depicts the wavelength division multiplexed (WDM) system of dual-carrier PDM-16 QAM. In the receiver, two subcarriers are filtered out by DEMUX, and then a local laser with frequency fixed at the center of the two carriers beats the received optical signal to down-convert them to baseband. PDs and ADCs are used to convert the optical signal to a digital one. And then, DSP not only plays the role of equalizer and synchronizer but also separates the subcarriers. Note that since the bandwidth of the signal are doubled, it requires the bandwidth of PDs and the sampling rate of the ADCs to be doubled correspondingly.

Figure 13.69 illustrates the structure of the receiver DSP (see also Chapter 14). FFT is used to compensate CD and separate the subcarriers. As the carrier's frequency offset would introduce interchannel interference (ICI), FFT shift is used to avoid it. Figure 13.70 illustrates the FFT-based subcarrier separation. In the output of $2 \times N$ points FFT, the leftward N points in this figure belong to the first subcarrier and likewise the rightward N points belonging to the other subcarrier. So, two N-point IFFTs follow the $2 \times N$-points FFT to recover the time-domain signal of each subcarrier. CD is calculated using the frequency-domain signal of the first subcarrier. And then, it is used for both subcarriers' compensation. 2×2 Multiple-input multiple-output (MIMO) filters is used for residual CD and PMD compensation. Similar with CD compensation, the coefficients of MIMO filters are calculated only using the time-domain signal of the first subcarrier. But, the slight difference is that the coefficients are multiplied with a constant factor first before being used for the filtering of second subcarrier. The said constant factor converges initially at the beginning of the DSP work.

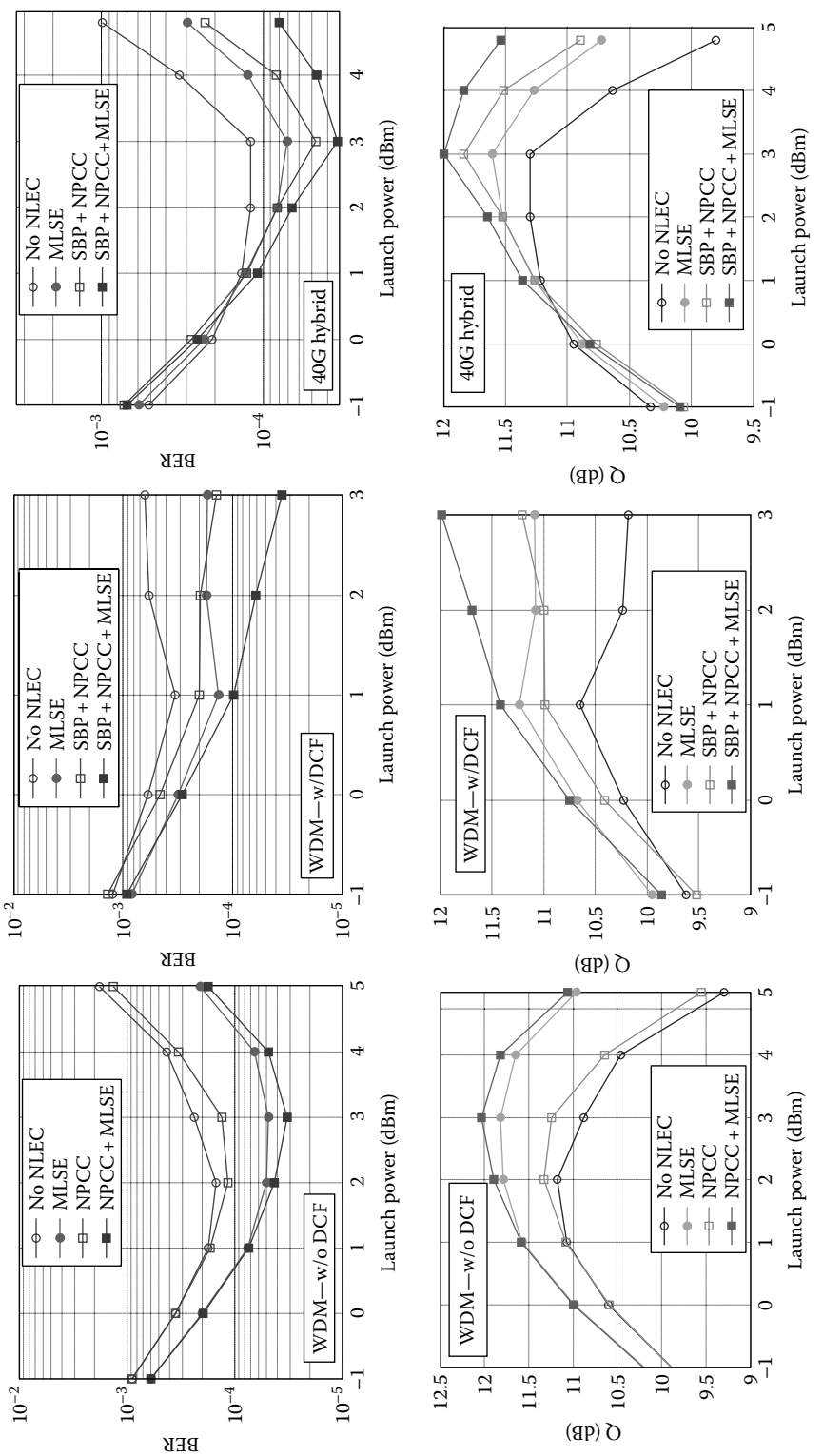

FIGURE 13.67
DSP results: PDM–QPSK BER and *Q*-factor versus optical power.

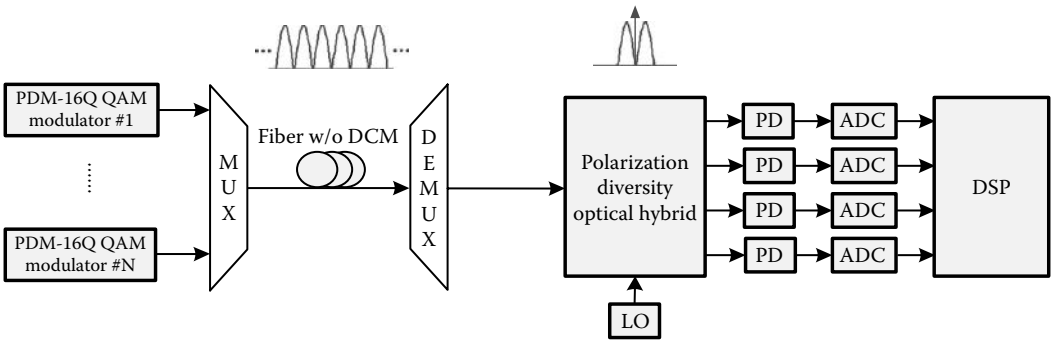

FIGURE 13.68
Architecture of 2sc-PDM-16 QAM with SLD (see also Figure 13.2).

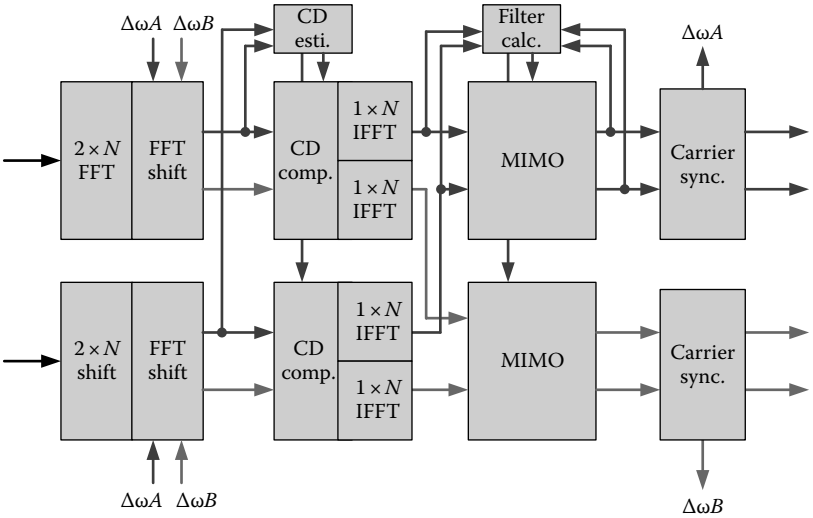

FIGURE 13.69
Block diagram of DSP.

The dual-carrier 32 GBaud/s NRZ PDM-16 QAM in 100 GHz channel is simulated. In the transmitter, each subcarrier is passed over a 40 GHz filter to reduce the out-of-band noise and then coupled together. Five such 100 GHz channels are combined together with MUX. In the receiver, the most central channel is filtered out with 75 GHz Gaussian optical filter, and then they are beaten with a local laser, whose frequency is fixed at the central frequency of the dual subcarrier signal. PDs with a bandwidth of 48 GHz and ADCs of 128 GHz sampling rate are used. The line width of all lasers is configured as 100 kHz. The fiber link is DCM free, each span has 80 km, the span loss is 22 dB, and the noise figure of EDFA is 5.5 dB.

In the receiver DSP, CD is estimated in the frequency-domain with the method presented in Ref. [8]. Subcarriers are separated as detailed in Section 13.2. For the MIMO filter, its coefficients converge with the constant modulus algorithm (CMA) [9], and the DD-least mean square (DD-LMS) algorithm is used to track the channel variety. For carrier synchronization, the signal of the outer and inner circles in 16 QAM constellation is picked out to estimate the frequency offset with the differential Viterbi and Viterbi algorithm [10] (see Chapter 15 for

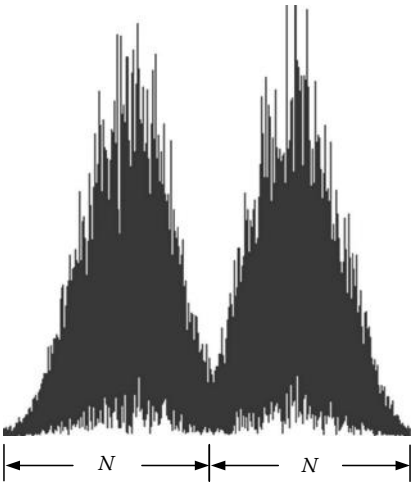

FIGURE 13.70
Illustration of FFT-based subcarrier separation.

more details). Blind phase search algorithm is applied to deal with the phase error [11], and 1/128 training bit sequence helps to effectively avoid cycle slips or the misalignment of the clock sampling time and that of the corresponding sequence (Figure 13.71).

Figure 13.72 shows the constellations of both the subcarriers after DSP recovery. The simulation result of the BER performance is shown in Figure 13.73. SC-B filtered with shared coefficients of SC-A has a BER that is a little worse than SC-A both in BtB scenario and 10-span transmitted scenario. It is within our expectation because the coefficients only approach the best mean square error for SC-A but not for SC-B with the help of CMA and DD-LMS. But for both subcarriers of the 400G system, after averaging the BER, the penalty of the *Q*-factor is less than 0.3 dB after transmission over 10 spans. Experimental results of such modulation schemes over 10 spans are shown in Figure 13.73.

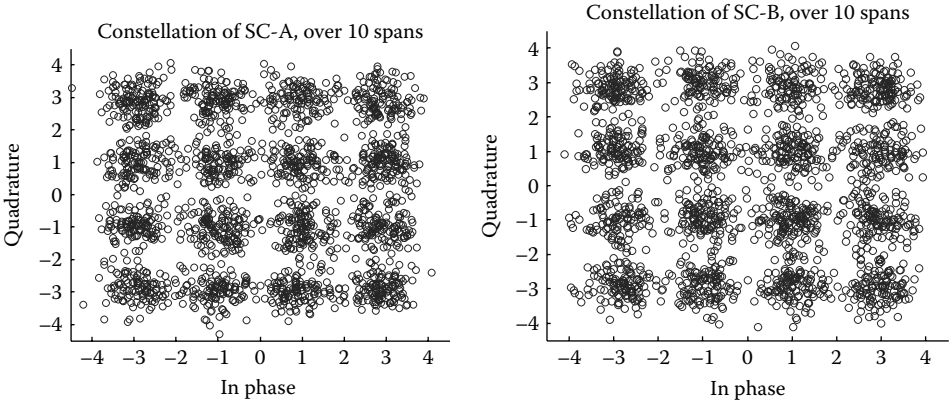

FIGURE 13.71
Constellation of the two subcarriers; MIMO filter calculated with CMA and DD-LMS applied to the leftward subcarrier designated as SC-A; the rightward subcarrier designated as SC-B is filtered with coefficients shared by SC-A.

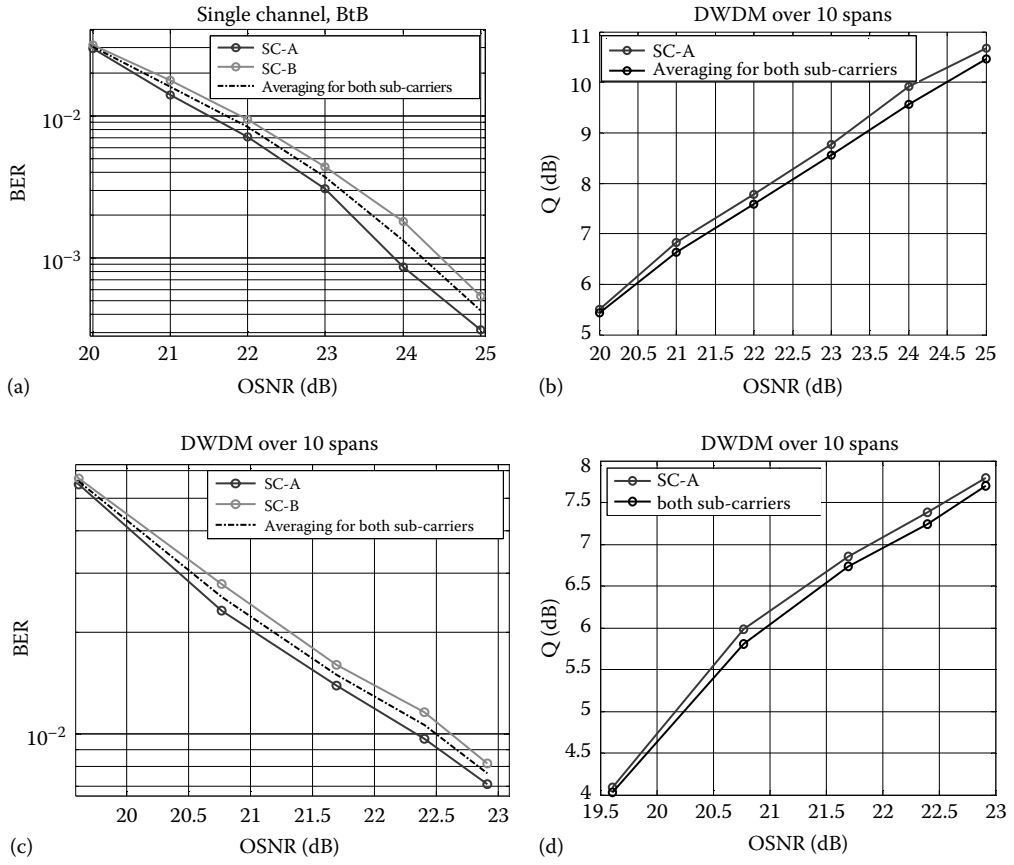

FIGURE 13.72
BER and *Q*-factor versus OSNR for single channel and multiplexed channels: (a) single carrier, (b) multiplexed 10 channels, (c) two sub carriers per channel, and (d) one single subcarrier only under 10 multiplexed channels.

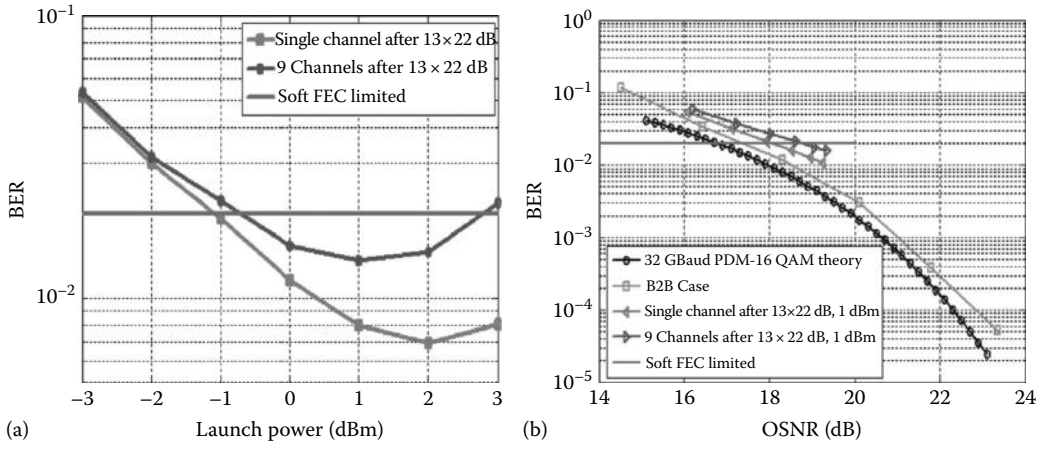

FIGURE 13.73
Experimental demonstration of 16 QAM: launch power and OSNR versus BER performance after DWDM transmission over 800 km (10 optically amplified spans without using DCM): (a) single channel and (b) multiplexed channel.

13.7 MSK Transmission Model

13.7.1 Introductory Remarks

The generation of MSK requires a linear variation of the phase, hence a constant frequency of the OC [1,12–15]. However, the generation of the optical phase may be preferred by driving an optical modulator using the sinusoidal signal for practical implementation. Thus, there is a nonlinear variation of the carrier phase, and hence some distortion effects are produced. In this chapter, we investigate the use of linear and nonlinear phase shaping filtering and their impacts on MSK-modulated optical signal transmission over optically amplified long-haul communication systems [16]. The evolution of the phasor of the in-phase and quadrature components is illustrated for lightwave-modulated signal transmission. The distinct features of three different MSK modulation formats—linear MSK, weakly nonlinear MSK, and strongly nonlinear MSK—and their transmission are simulated. The transmission performance obtained indicates the resilience of the MSK signals in transmission over multi-optically amplified multispans.

Recent years have witnessed intense interest in the use of advanced modulation formats to explore their advantages and performance in high-density and long-haul transmission systems [14,17]. RZ and NRZ with or without carrier suppression (CS-RZ) formats can be associated with SK modulation schemes such as ASK, PSK, and DPSK and DQPSK [18]. Differential detection offers the best technological implementation in view of the nonrequirement of coherent sources and the avoidance of polarization control of the mixing of the signals and a local oscillator at multi-THz frequency range. Continuous phase modulation (CPM) is also another form of PSK in which the phase of the OC evolves continuously from one phase state to the other. For MSK, the phase change is limited to $\pi/2$. Although MSK is a well-known modulation format in radio frequency digital communications, it has been attracting interest in optical system research only in the last few years. The phase continuous evolution of the MSK has many interesting features: the main lobe of the power spectrum is wider than that of quadrature phase-shift keying (QPSK) and DPSK and the side lobes of the MSK signal spectrum are much lower allowing the ease of optical filtering and hence less distortion because of dispersion effects. In addition, higher signal energy is concentrated in the main lobe of the MSK spectrum rather than its side lobes leading to better SNR at the receiver.

Advanced modulation formats for 40 Gb/s and higher bit rate long-haul optical transmission systems have recently attracted intensive research including various amplitude and discrete differential phase modulation and pulse shape formats (ASK-NRZ/RZ/CSRZ, DPSK, and DQPSK–NRZ/RZ/CSRZ). However, there are only a few reports on optical CPM schemes using external electro-optical modulators. Compared to discrete phase modulation, CPM signals have very interesting and attractive characteristics including high spectral efficiency, higher energy concentration in the signal bands, and more robustness to interchannel crosstalk in DWDM as a result of greater suppression of the side lobes, which has recently come up as a critical issue in DWDM optical systems.

In bandwidth-limited digital communication including wireless and satellite digital transmission, MSK has been proven as a very efficient modulation format because of its prominent spectral efficiency, high sideband suppression, constant envelop, and high energy concentration in the main spectral lobe. In modern high-capacity and high-performance optical systems, we have witnessed the acceleration of the transmission bit rate approaching 40 Gb/s and even 160 Gb/s [19]. At these ultra-high bit transmission

speeds, the essence of efficient modulation formats for long-haul transmission is critical. There are several technical published works on advanced modulation techniques for optical transmission, which mostly focus on discrete phase modulation including binary DPSK and DQPSK with various pulse carving formats including NRZ and CS-RZ. However, there are only a limited number of published papers on MSK modulation format. The features of MSK comparing to other modulation formats have prompted researchers to investigate its suitability for high capacity long-haul transmission. The side lobes of MSK power spectrum are greatly suppressed giving it good dispersion tolerance and avoiding interchannel cross talks. Thus, this modulation is of interest for further investigation.

Two different proposals of transmitter configurations for generation of linear and nonlinear phase optical MSK modulation were reported in a paper in this conference. A brief description of the operation of these two transmitter configurations are presented in Section 13.2 whereas the direct detection techniques for both linear and nonlinear optical MSK signals are stated in Section 13.3. Our simulation models for the modulation and system transmission are based on MATLAB Simulink platform with detailed discussions in Section 13.4. In this chapter, we have also proven that the optical MSK signal is capable of propagating over an optically amplified and fully dispersion-compensated system. Not only the performance of the conventional MSK format but also the weakly and strongly nonlinear optical MSK sequences can be evaluated.

The MSK format exhibits dual alternating frequencies and offers orthogonal property of the two consecutive bit periods. More interestingly, MSK can be considered as either a special case of continuous phase frequency shift keying (CPFSK) or a staggered/offset QPSK in which the *I*- and *Q*-components are interleaved with each other. These characteristics are greatly advantageous to optically amplified long-haul transmissions because such a compact spectrum potentially gives a good dispersion tolerance, making MSK a suitable candidate for DWDM systems.

This section investigates a number of novel structures of photonic transmitters for the generation of optical MSK signals. The theoretical background for MSK modulation formats discussed in two different approaches is presented in Section 13.2. Section 13.3 proposes two configurations of the optical MSK transmitters which employ (1) two cascaded EO phase modulators (E-OPMs) and (2) parallel dual-drive MZMs. Different types of linear and nonlinear phase shaped optical MSK sequences can be generated. The precoder for the *I*–*Q* optical MSK structure is also derived in this section. We present in Section 13.4, a simple noncoherent configuration for detection of the MSK and nonlinear MSK modulated sequences. The optical detection of MSK and nonlinear MSK signals employs a $\pi/2$ phase shift in one arm of the Mach–Zehnder interferometric MZIM delay balanced receiver. New techniques in the measurement of the BERs with the probability density function (pdf) of received signals after the decision sampling are to be computed with the superposition of a number of weighted Gaussian pdfs. The following performance results and observations are obtained in Section 13.5: (1) spectral characteristics of linear and nonlinear MSK-modulated signals, and (2) improvement on dispersion tolerance of MSK and nonlinear MSK over ASK and DPSK counterparts.

Advanced modulation formats have attracted intensive research in recent times for long-haul optical transmission systems including various amplitude and discrete differential phase modulation and pulse shape formats (ASK–NRZ/RZ/CSRZ, DPSK, and DQPSK–NRZ/RZ/CSRZ). For the case of phase modulation, the phases of the OC are discretely coded with "0", "π" (DPSK) or "0", "π" and "$\pi/2$", "$-\pi/2$" (DQPSK). Although the differential phase modulation techniques offer better spectral properties, higher energy concentration in the signal bands, and more robustness to combat the nonlinearity impairments as

compared to the amplitude modulation formats, phase continuity would offer even better spectral efficiency and would be at least 20 dB better in the suppression of the side lobes. MSK, exhibiting a dual alternating frequency between the two consecutive bit periods, is believed to offer the best scheme as this offers the orthogonal property of f_1 and f_2, the two frequencies of FSK of the carriers which carry the consecutive bits. Further, it offers the simplest form for implementation in the photonic domain.

This section investigates a number of novel structures of photonic transmitters and differential noncoherent balanced receivers for generation and detection of MSK optical signals as follows:

1. Cascaded E-OPMs MSK transmitter: This structure employs two cascaded optical phase modulators (OPMs). The first OPM plays the role of modulating the binary data logic into two carrier frequencies deviating from the OC of the laser source by a quarter of the bit rate. The second OPM enforces the phase continuity of the lightwave carrier at the transitional time of every bit. The driving voltage of this second OPM is precoded in such a way that the phase discrepancy owing to the frequency modulation of the first OPM will be compensated, thereby preserving the phase continuity characteristic of the MSK signal.

   Using this double-phase modulation configuration, different types of linear and nonlinear CPM phase shaping signals including MSK, weakly MSK, and linear-sinusoidal MSK can be generated. The optical spectra of the modulation scheme obtained confirm the bandwidth efficiency of this novel optical MSK transmitter.
2. Parallel dual-drive MZ modulators optical MSK transmitter: In this second configuration, MSK signals with small ripples of approximately 5% signal amplitude level are generated. The optical spectrum demonstrated is equivalent to the configuration of (1). This configuration can be implemented using commercially available dual drive intensity interferometric EO modulators.

   We also describe a simple noncoherent configuration for detection of the MSK- and nonlinear MSK-modulated sequences. The optical detection of MSK and nonlinear MSK signals employs a $\pi/2$ OPM followed by the MZIM delay balanced receiver.

The following performance results and observations are obtained:

1. The modeling platform based on MATLAB Simulink developed for transmission systems.
2. Spectral characteristics of linear and nonlinear MSK modulated signals.
3. Improvement on dispersion tolerance of MSK and nonlinear MSK over ASK and DPSK.
4. New techniques in the measurement of the BERs with the pdf of received signals after the decision sampling are to be computed with superposition of a number of weighted Gaussian pdfs. This technique has been proven to be effective, convenient, and accurate for estimating the non-Gaussian pdf for the case of continuous phase modulation and its transmission over long-haul optically amplified systems.

The MSK format has been demonstrated via modeling as a promising candidate in the selection of advanced modulation formats for DWDM long-haul optical transmission system.

13.7.2 Generation of Optical MSK-Modulated Signals

The two optical MSK transmitter configurations can be described briefly here.

13.7.2.1 Optical MSK Transmitter Using Two Cascaded EO Phase Modulators

E-OPMs and interferometers operating at high frequency using resonant-type electrodes can be used to reduce the driving power at microwave frequency. In addition, high-speed electronic driving circuits, which evolved with the ASIC technology using 0.1 μm GaAs P-HEMT or InP HEMTs, enable the realization of the proposed optical MSK transmitter structure. The base-band equivalent optical MSK signal is represented in Equation 13.4.

The second E-OPM enforces the phase continuity of the lightwave carrier at every bit transition. The delay control between the E-OPMs is usually implemented by the phase shifter shown in Figure 13.74. The driving voltage of the second E-OPM is precoded to fully compensate the transitional phase jump at the output $E_{01}(t)$ of the first E-OPM. Phase continuity characteristic of the optical MSK signals is determined by the algorithm as

$$\Phi(t,k) = \frac{\pi}{2}\left(\sum_{j=0}^{k-1} a_j - a_k I_k \sum_{j=0}^{k-1} I_j\right) \tag{13.18}$$

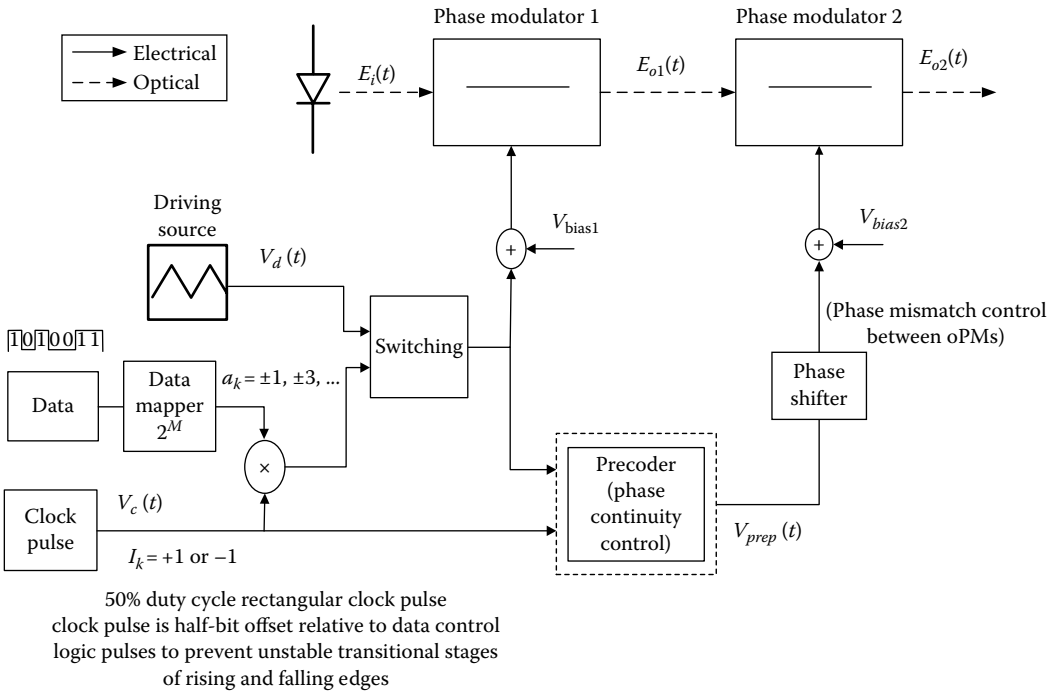

FIGURE 13.74
Block diagram of optical MSK transmitter employing two cascaded OPMs.

where

$a_k = \pm 1$ are the logic levels

$I_k = \pm 1$ are clock pulses whose duty cycle is equal to the period of the driving signal $V_d(t)$

f_d is the frequency deviation from the OC frequency

$h = 2f_dT$ is previously defined as the frequency modulation index

In case of optical MSK, $h = 1/2$ or $f_d = 1/(4T)$. The phase evolution of the continuous phase optical MSK signals is shown with detailed discussion in Figure 13.75. To mitigate the effects of the unstable stages of rising and falling edges of the electronic circuits, the clock pulse $V_c(t)$ is offset with the driving voltage $V_d(t)$.

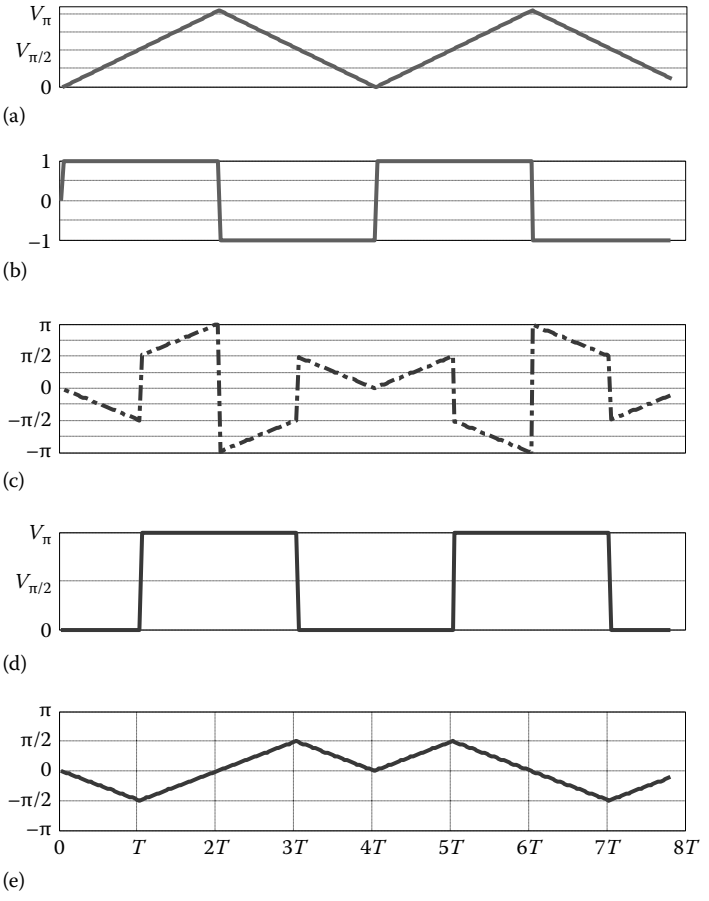

FIGURE 13.75

Evolution of time-domain phase trellis of optical MSK signal sequence [−1 1 1 −1 1 −1 1 1] as inputs and outputs at different stages of the optical MSK transmitter The notation is denoted in Figure 13.81 accordingly; (a) $V_d(t)$: periodic triangular driving signal for optical MSK signals with duty cycle of 4 bit period, (b) $V_c(t)$: the clock pulse with duty cycle of 4*T*, (c) $E_{01}(t)$: phase output of oPM1, (d) $V_{prep}(t)$: precomputed phase compensation driving voltage of oPM2, and (e) $E_{02}(t)$: phase trellis of transmitted optical MSK sequences at output of oPM2.

13.7.2.2 Generating Optical M-Ary CPFSK Format (Figure 13.76)

$$\tilde{s}(t) = A\exp j\left\{a_k I_k f_d \frac{2\pi t}{T} + \Phi(t,k)\right\} kT \le t \le (k+1)T \quad a_k = \pm 1, \pm 3\ldots \tag{13.19}$$

13.7.2.3 Detection of M-Ary CPFSK-Modulated Optical Signal

The detection of linear and nonlinear optical *M*-ary CPFSK uses the well-known structure MZDI balanced receiver. The addition of π/2 phase on one arm of MZDI is also

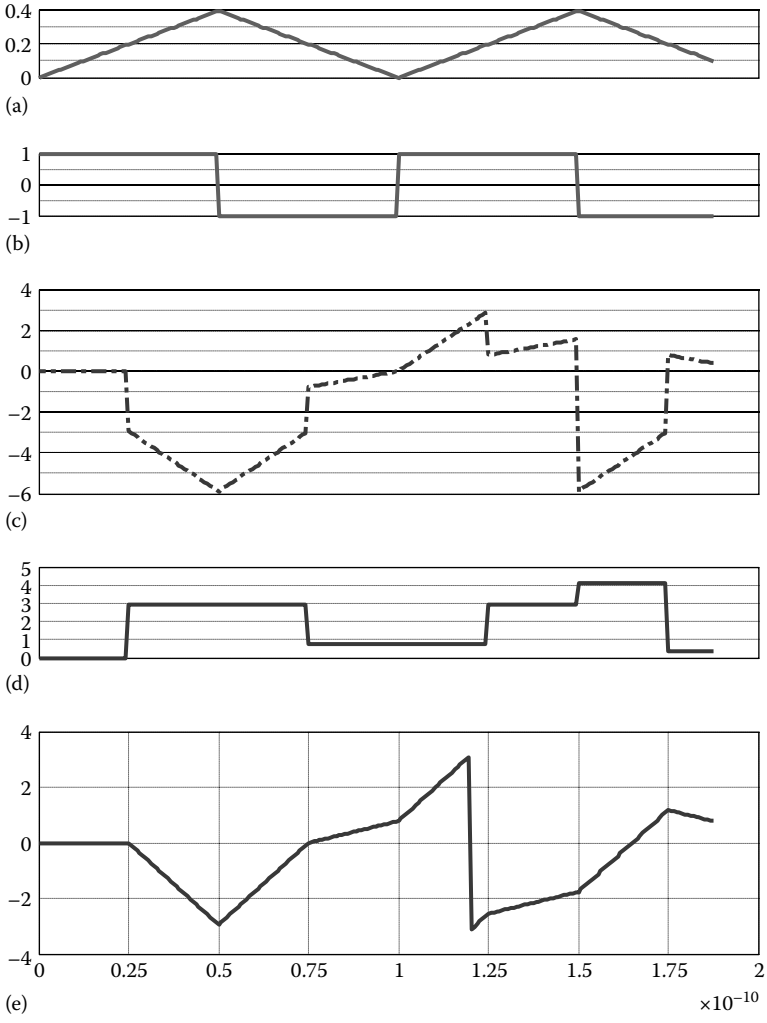

FIGURE 13.76
Demonstration of phase compensation for enforcement of phase continuity at bit transitions, (a) shows the periodic triangular driving signal whose peak voltage is $V_\pi/8$ and duty cycle is a 4-bit period, (b) shows the clock pulse corresponding to the driving signal, (c) shows frequency switching with h = ±1/8, ±7/8, (d) shows the computed phase compensation, and (e) shows the phase trellis of an optical quaternary CPFSK.

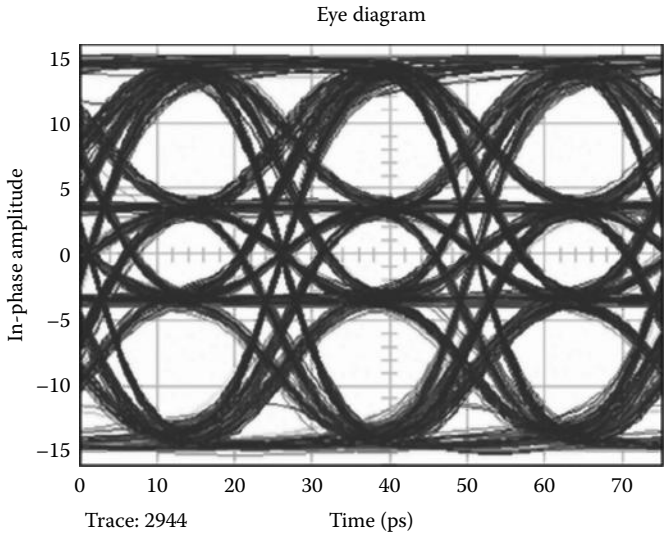

FIGURE 13.77
Eye phase trellis detection of optical *M*-ary CPFSK-modulated signal.

introduced. The time delay being a fraction of a bit period enables the phase trellis detection of optical *M*-ary CPFSK. The detected phase trellis using the proposed technique is shown in Figure 13.77. An optimized ratio of switching frequencies results in the maximum eye open. The detection of optical *M*-ary CPFSK with delay of $T_b/2$ at $t = (k + 1)T_b/2$ is expressed in (13.19) as

$$\sin(\Delta\Phi) = \sin\left[a_{k+1} \frac{2\pi f_s (k+1) T_b/2}{T_b} - a_k \frac{2\pi f_s (k) T_b/2}{T_b} \right] \tag{13.20}$$

On the same slope in the phase trellis, the differential phase and hence, the modulated frequency levels can be mapped to detected amplitude levels via (13.20):

$$\sin(\Delta\Phi) = \sin(a_{k+1} \pi f_d) \tag{13.21}$$

13.7.2.4 Optical MSK Transmitter Using Parallel Mach–Zehnder Intensity Modulators (I–Q Approach)

The conceptual block diagram of optical MSK transmitter is shown in Figure 13.78. The transmitter consists of two dual-drive EO MZIMs generating chirpless *I*- and *Q*-components of MSK-modulated signals, which is considered as a special case of staggered or offset QPSK. The binary logic data are precoded and de-interleaved into even and odd bit streams that are interleaved with each other by 1-bit duration offset. Figure 13.78 shows a general block diagram configuration of band-limited phase shaped optical MSK and (Figure 13.78b) the detailed structure of the optical modulator in which the *I*- and *Q*-components are generated with continuous phase variation between the states.

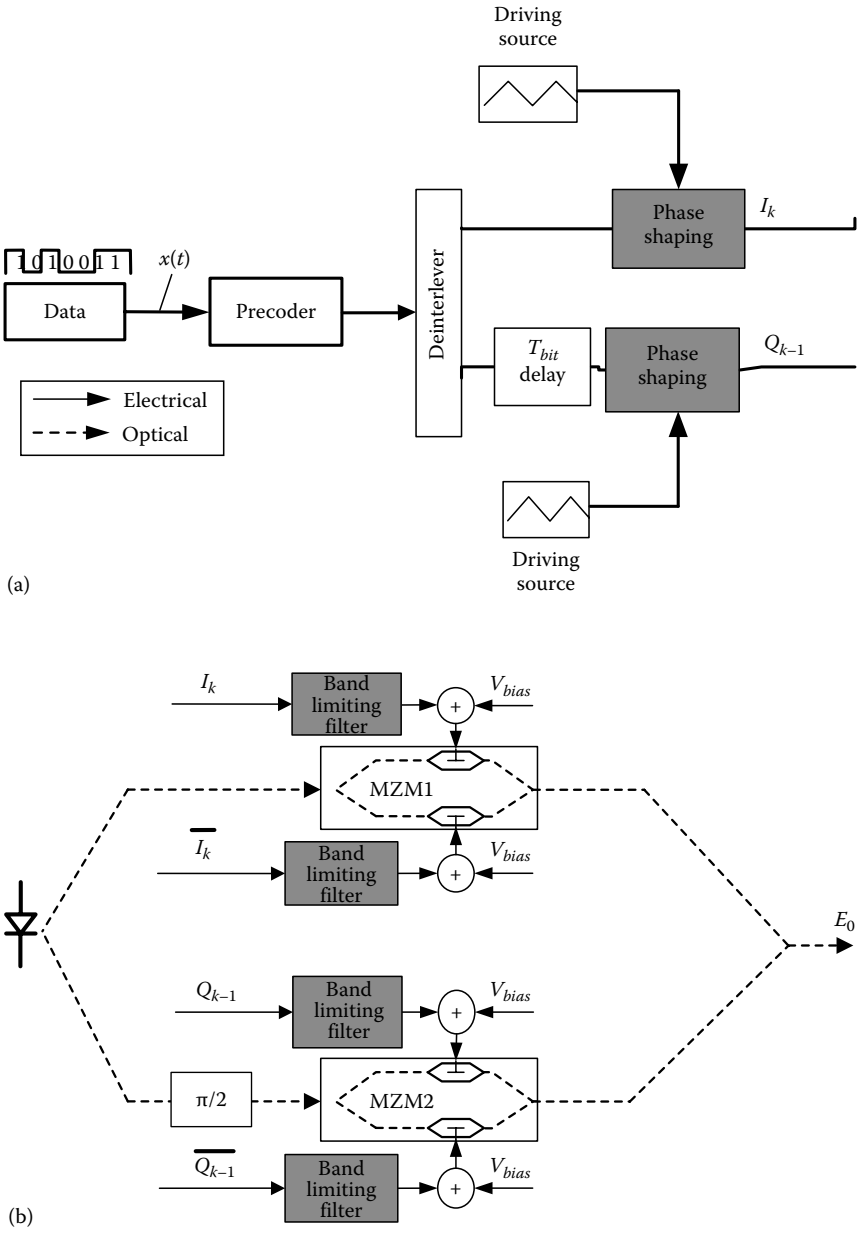

FIGURE 13.78
Block diagram configuration of band-limited phase shaped optical MSK: (a) general structure and (b) details of the optical modulators.

The two arms of the dual-drive MZM modulator are biased at $V_{\pi/2}$ and $-V_{\pi/2}$ and driven with *data* and $\overline{data}$. Phase shaping driving sources can be a periodic triangular voltage source in the case of linear MSK generation or simply a sinusoidal source for generating a nonlinear MSK-like signal, which also obtains a linear phase trellis property but with small ripples introduced in the magnitude. The magnitude fluctuation level depends on the

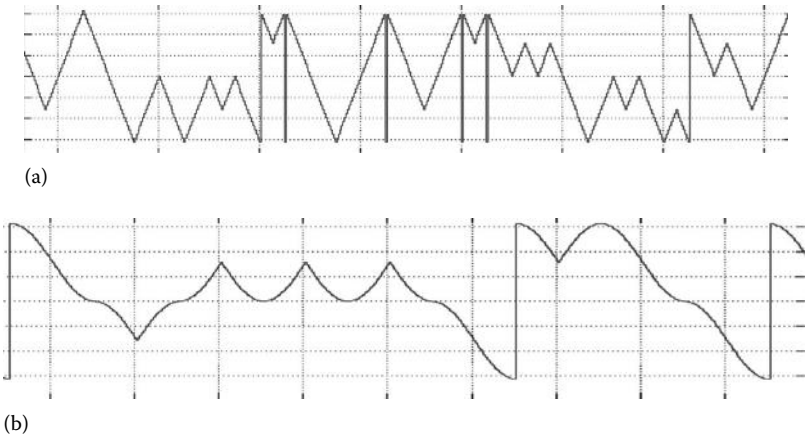

FIGURE 13.79
Phase trellis of (a) linear and (b) nonlinear MSK transmitted signals.

magnitude of the phase shaping driving source. High spectral efficiency can be achieved with tight filtering of the driving signals before modulating the EO MZMs. Three types of pulse shaping filters are investigated including Gaussian, raised-cosine, and squared-root raised-cosine filters. The OC phase trellis of linear and nonlinear optical MSK signals is shown in Figure 13.79.

The generation of linear and nonlinear optical MSK sequences is briefly discussed in the following text.

13.7.2.4.1 Linear MSK

The pulse shaping waveform for linear MSK is a triangular waveform with a duty cycle of $4 \times T_b$. The triangular waveform for the quadrature path is delayed by 1-bit period with respect to the in-phase path; hence, they are interleaved with each other. The optical MSK signal is the superposition of both even and odd waveforms from the MZIMs. The amplitude of the signal is perfectly constant, clearly displaying the constant amplitude characteristic of continuous phase modulation. The phase trellis is perfectly linear, and the phase transition is continuous as shown in Figure 13.79a. The signal constellation is a perfect circle.

13.7.2.4.2 Weakly Nonlinear MSK

The pulse shaping waveform for weakly nonlinear MSK is a sinusoidal waveform with an amplitude of $1/4V_{\pi}$, and its symbol period is equal to a two-bit period (symbol rate of 20 Gb/s). The in-phase pulse shaper is a cosine waveform while the quadrature pulse shaper is a sine waveform. There is ripple of approximately 5%. Because of the sinusoidal pulse shaper, the variation of phase with time, which is represented by the phase trellis is nonlinear. Therefore, the rate of frequency change is not constant. This causes a mismatch of MZIM when the modulated waveforms are added up, resulting in the ripple.

13.7.2.4.3 Strongly Nonlinear MSK

The pulse shaping waveform for strongly nonlinear MSK is the sinusoidal waveform, the same as for the weakly nonlinear. However, the amplitude of pulse shaper is $V_{\pi/2}$. The waveforms

are interleaved with each other. The optical MSK signal has a ripple of approximately 26%. This ripple is also caused by the mismatch of MZIM as the modulating waveform is strongly nonlinear. The effect of nonlinearity is obvious in the phase trellis in Figure 13.79b.

The signal state constellations and eye diagrams of optical MSK sequences are shown in Figure 13.80a through c for both of linear and nonlinear schemes, respectively. In case of nonlinear configuration, MSK signals with small ripples of approximately 5% signal amplitude level are generated. This configuration can be implemented using commercially available dual-drive intensity interferometric EO modulators.

The conceptual block diagram of optical MSK transmitter is shown in Figure 13.74. The transmitter consists of two dual-drive electro-optical MZIMs generating chirpless *I*- and *Q*-components of MSK-modulated signals, which is considered as a special case of staggered or offset QPSK. The binary logic data are precoded and de-interleaved into even and odd bit streams, which are interleaved with each other by 1-bit duration offset.

Two arms of the dual-drive MZM modulator are biased at $V_{\pi/2}$ and $-V_{\pi/2}$ and driven with *data* and $\overline{data}$. Phase shaping driving sources can be a periodic triangular voltage source in the case of linear MSK generation or simply a sinusoidal source for generating a nonlinear MSK-like signal which also obtains linear phase trellis property but with small ripples introduced in the magnitude. The magnitude fluctuation level depends on the magnitude of the phase shaping driving source. High spectral efficiency can be achieved with tight filtering of the driving signals before modulating the EO MZMs. Three types of pulse shaping filters are investigated including Gaussian, raised-cosine, and squared-root-raised cosine filters. Narrow spectral width and high suppression of the side lobes can be achieved.

The logic gates in the precoder are constructed based on the state diagram as this approach eases the implementation of the precoder. As seen from the state diagram, the current state of the signal is dependent on the previous state, since the state of the signal advances corresponds to the binary data from the previous state. Therefore, memory is

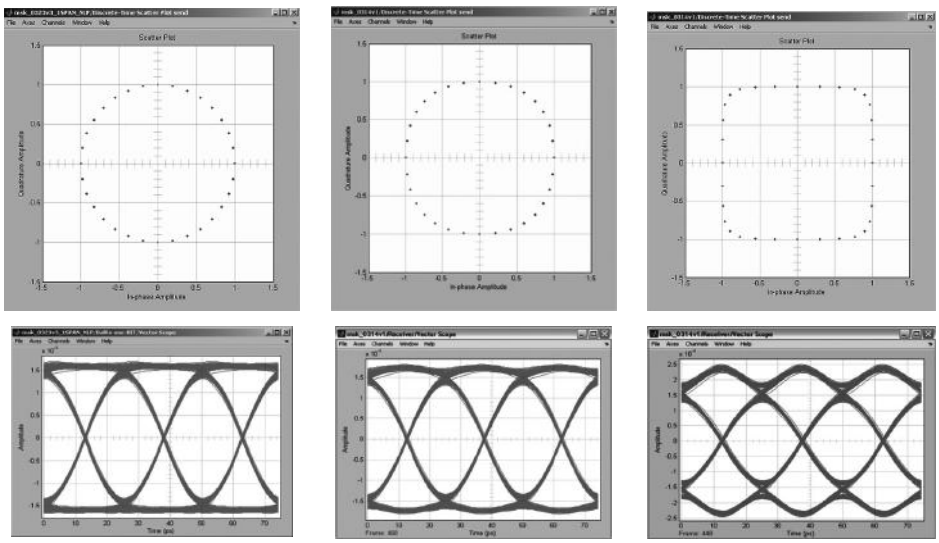

(a) (b) (c)

FIGURE 13.80
Constellation diagrams and eye diagrams of optical MSK-transmitted signals: (a) linear, (b) weakly nonlinear, and (c) strongly nonlinear transmission.

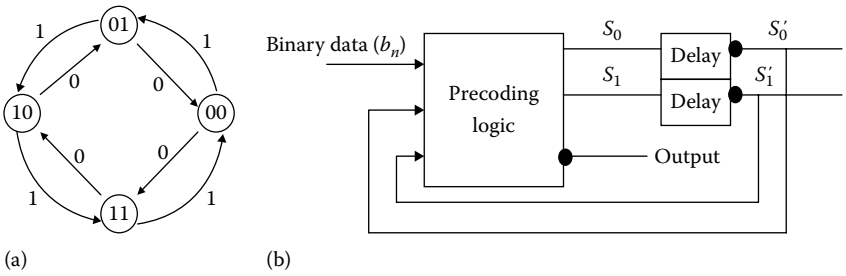

FIGURE 13.81
(a) State diagram for MSK. The arrows indicate continuous increment or decrement of the phase of the carrier; (b) combinational logic, the basis of the logic for constructing the truth table of the precoder.

needed to store the previous state. The state diagram in Figure 13.81a is developed into a logic state diagram in Figure 13.81b to enable the construction of truth table. $S_0S_1 = 00$ or $S_0'S_1' = 00$ corresponds to state 0, $S_0S_1 = 01$ or $S_0'S_1' = 01$ corresponds to state $\pi/2$ and $S_0S_1 = 10$ or $S_0^1S_1' = 10$ corresponds to state π, while $S_0S_1 = 11$ or $S_0'S_1' = 11$ corresponds to state $-\pi/2$, with S_0S_1 as the current state and $S_0^1S_1'$ as previous state.

Two delay units in Figure 13.81b function as memory by delaying the current state and feedback into the precoding logic block as the previous state. The precoding logic block which consists of logic gates would compute the current state and output based on the feedback state (previous state) and binary data from the Bernoulli binary generator.

The truth table can be constructed based on the logic state diagram and combinational logic diagram earlier. For positive half cycle cosine wave and positive half cycle sine wave, the output is 1; for negative half cycle cosine wave and negative half cycle sine wave, the output is 0. Then, the Karnaugh maps can be constructed to derive the logic gates within the precoding logic block, based on the truth table. The following three precoding logic equations are derived as

$$S_0 = \overline{b}_n\overline{S}_0'\overline{S}_1' + \overline{b}_n\overline{S}_0'S_1' + \overline{b}_nS_0'S_1' + b_nS_0'S_1' \tag{13.22}$$

$$S_1 = \overline{S}_1' = \overline{b}_n\overline{S}_1' + \overline{b}_n\overline{S}_1' \tag{13.23}$$

$$Output = \overline{S}_0 \tag{13.24}$$

The final logic gates construction for the precoder is as shown in Table 13.3

13.7.2.4.4 Optical MSK Receivers

The optical detection of MSK and nonlinear MSK signals employs a $\pi/2$ OPM followed by an optical phase comparator, an MZDI, and then a balanced receiver (BalRx). This detection for optical MSK and nonlinear MSK signals, similar to the well-known structure employing one arm of MZDI, is introduced to detect $\pm\pi/2$ phase difference of two adjacent bits due to the nature of MSK modulation.

A new technique for evaluation of the BERs is implemented. The pdf of noise-corrupted received signals after decision sampling are computed with superposition of a number of weighted Gaussian pdfs. The technique implements the expected maximization (EM) theorem and has shown its effectiveness in determining arbitrary distributions.

TABLE 13.3
Truth Table Based on MSK State Diagram

$b_n S_0' S_1'$	$S_1 S_0$	Output
100	01	1
001	00	1
010	01	1
101	10	0
110	11	0
111	00	1
000	11	0
011	10	0

13.7.3 Optical Binary-Amplitude MSK Format

13.7.3.1 Generation

The optical MSK transmitters are integrated in the proposed generation of optical M-ary MSK (MAMSK) signals. However, in this section, we propose a new simple-in-implementation optical MSK transmitter configuration employing high-speed cascaded E-OPMs as shown in Figure 13.82. E-OPMs and interferometers operating at high frequency using resonant-type electrodes have been studied and proposed in [6]. In addition, high-speed electronic driving circuits, which evolved with the ASIC technology using 0.1 μm GaAs P-HEMT or InP HEMTs, enable the realization of the proposed optical MSK transmitter structure. The base-band equivalent optical MSK signal is represented in Equation 13.23:

$$\tilde{s}(t) = A\exp\left\{j\left[a_k I_k 2\pi f_d t + \Phi(t,k)\right]\right\},$$

$$kT \le t \le (k+1)T = A\exp\left\{j\left[a_k I_k \frac{\pi t}{2T} + \Phi(t,k)\right]\right\} \tag{13.25}$$

where

$a_k = \pm 1$ are the logic levels
$I_k = \pm 1$ is a clock pulse whose duty cycle is equal to the period of the driving signal $V_d(t)$
f_d is the frequency deviation from the OC frequency
$h = 2f_d T$ is defined in Equations 13.19 and 13.20 as the frequency modulation index

In the case of optical MSK, $h = 1/2$ or $f_d = 1/(4T)$.

The first E-OPM enables the frequency modulation of data logics into the upper side bands (USBs) and lower side bands (LSBs) of the OC with frequency deviation of f_d. Differential phase precoding is not necessary in this configuration because of the nature of the continuity of the differential phase trellis. By alternating the driving sources $V_d(t)$ to sinusoidal waveforms or combination of sinusoidal and periodic ramp signals, different schemes of linear and nonlinear phase shaping MSK transmitted sequences can be generated. The second E-OPM enforces the phase continuity of the lightwave carrier at every bit transition. The delay control between the E-OPMs is usually implemented by the phase shifter shown in Figure 13.82. The driving voltage of the second E-OPM is precoded to fully compensate the transitional phase jump at the output $E_{01}(t)$ of the first

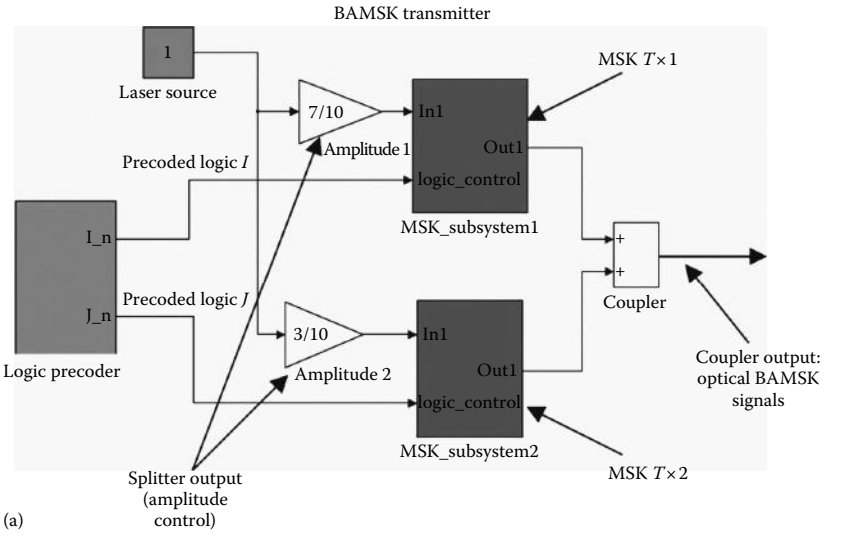

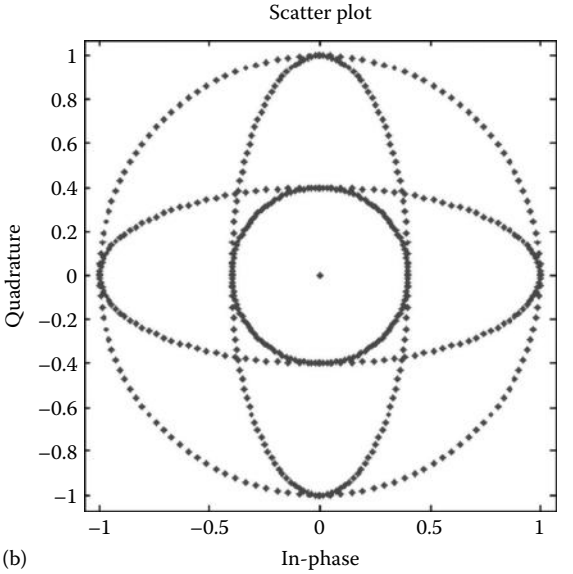

FIGURE 13.82
(a) Block diagram of optical BAMSK transmitter, and (b) signal trajectories of optical BAMSK transmitted signals.

E-OPM. Phase continuity characteristic of the optical MSK signals is determined by the algorithm in Equation 13.25. In order to mitigate the effects of unstable stages of rising and falling edges of the electronic circuits, the clock pulse $V_c(t)$ is offset with the driving voltages $V_d(t)$:

$$\Phi(t,k) = \frac{\pi}{2}\left(\sum_{j=0}^{k-1} a_j - a_k I_k \sum_{j=0}^{k-1} I_j\right) \tag{13.26}$$

Binary-amplitude minimum shift keying (BAMSK) modulation format is proposed for optical communications. This section describes numerical results of 80 Gb/s two-bit-per-symbol BAMSK optical system on spectral characteristics and residual dispersion tolerance to different types of fibers. BER of 1e−23 is obtained for 80 Gb/s optical BAMSK transmission over 900 km Vascade-fiber systems enabling the feasibility of long-haul transmission for the modulation format.

MSK that is well known in radio frequency and wireless communications has recently been adapted into optical communications. For optically amplified communications systems, if multilevel concepts can be incorporated in those reported schemes, the symbol rate would be reduced and hence the bandwidth efficiency can be achieved. This is the principal motivation for the proposed modulation scheme. BAMSK is a special case of *M*-ary CPM format which enables binary-level (PAM- or QAM-like) transmission scheme while the bandwidth efficiency because of transitional phase continuity properties between two consecutive symbols (CPM-like signals) are preserved. The generation of *M*-ary CPM sequences can be expressed in Equations 13.26 through 13.28 as

$$s(t) = A_n \cos\left(\omega_C t + \phi_n(t,a)\right) + \sum_{m=1}^{N-1} B_n \cos\left(\omega_C t + \phi_m(t,b_m)\right) \tag{13.27}$$

where

$$\phi_n(t,a) = \pi h a_n q\left(t - nT\right) + \pi h \sum_{k=-\infty}^{n-1} a_k \quad \text{with } nT < t < (n+1)T \tag{13.28}$$

$$\phi_m(t,b_m) = \pi a_n \left(h + \frac{b_{mn}+1}{2}\right) q\left(t - mT\right) + \pi \sum_{k=-\infty}^{n-1} a_k \left(h + \frac{b_{mn}+1}{2}\right) \quad \text{with } mT < t < (m+1)T \tag{13.29}$$

In a generalized *M*-ary CPM transmitter, values of an and b_{mn} are statistically independent and taken from the set of {±1, ±3, …}. a_n and b_m are the signal state amplitude levels, which are either in phase or π phase shift with the largest level component at the end of nth symbol interval; $q(t)$ is the pulse shaping function, and h is the frequency modulation index. In the case of BAMSK, Equations 13.19 and 13.20 which show the constraints of ϕ_m to maintain the phase continuity characteristic of CPM sequences are simplified to Equations 13.21 and 13.22, respectively, where $h = 1/2$ and the phase shaping function $q(t - nT)$ is a periodic ramp signal with duty cycle of 4*T*:

$$\phi_n(t,a) = \pi h a_n \frac{t - nT}{T} + \pi h \sum_{k=-\infty}^{n-1} a_k \quad \text{with } nT < t < (n+1)T \tag{13.30}$$

$$\phi_m(t,b_m) = \pi a_n \left(h + \frac{b_{mn}+1}{2}\right) \frac{t - mT}{T} + \pi \sum_{k=-\infty}^{n-1} a_k \left(h + \frac{b_{mn}+1}{2}\right) \quad \text{with } mT < t < (m+1)T \tag{13.31}$$

Any configuration of the reported optical MSK transmitters in [20,21] can be used in the proposed generation scheme of optical BAMSK signals. Figure 13.82a shows the block

structure of the optical BAMSK transmitter in which two optical MSK transmitters are integrated in parallel configuration. The amplitude levels are determined from Equations 13.26 through 13.28 and 13.30 by the splitting ratio at the output of a high-precision power splitter. The logic sequences {±1,…} of a_n and b_n are precoded from the binary logic {0,1} of d_n as $a_n = d_n - 1$ and $b_n = a_n(1 - d_n - 1/h)$. The signal-space trajectories of BAMSK signals are shown in Figure 13.81b.

A simple non coherent configuration for detection of the optical BAMSK sequences consists of phase and amplitude detections. In the case of BAMSK, that is $n = 2$, the system effectively implements 2 bits per symbol with two amplitude levels. Phase detection is enabled with employment of the well-known integrated optic phase comparator MZDI balanced receiver with 1-bit time delay on one arm of the MZDI. An additional $\pi/2$ phase shift is introduced. Figure 13.83a and b shows the eye diagrams of the amplitudes and phases of the optical BAMSK signals, respectively. In phase detection, the decision threshold, which is plotted in broken-line style is at zero level whereas amplitude levels are determined by different thresholds. The new technique in the calculation of BER for dispersive and noise-corrupted received signals, which exploits the EM theorem, is implemented with the superposition of a number of weighted Gaussian probability distribution functions.

13.7.3.2 Detection

A simple noncoherent configuration for detection of a linear and nonlinear optical M-ary MSK sequences consists of phase and amplitude detections, which are very well known in the discrete phase SK schemes such as DPSK or quadrature DPSK. Phase detection can be enabled by employing the well-known integrated optic phase comparator MZDI balanced receiver with 1-bit time delay on one arm of the MZDI. An additional $\pi/2$ phase shift can be introduced to detect the differential $\pi/2$ phase shift difference of two adjacent optical MSK pulses. Figure 13.83a and b shows the eye diagrams of the amplitudes and phases of the optical B-AMSK detected signals, respectively. In case of $N = 2$ and $N = 3$, the system effectively implements 2 bits-per-symbol scheme and 3 bits-per-symbol scheme with two and four amplitude levels, respectively. In phase detection, the decision threshold, which is plotted in broken-line style, is at zero level because only in-phase and π differential phase are of interest.

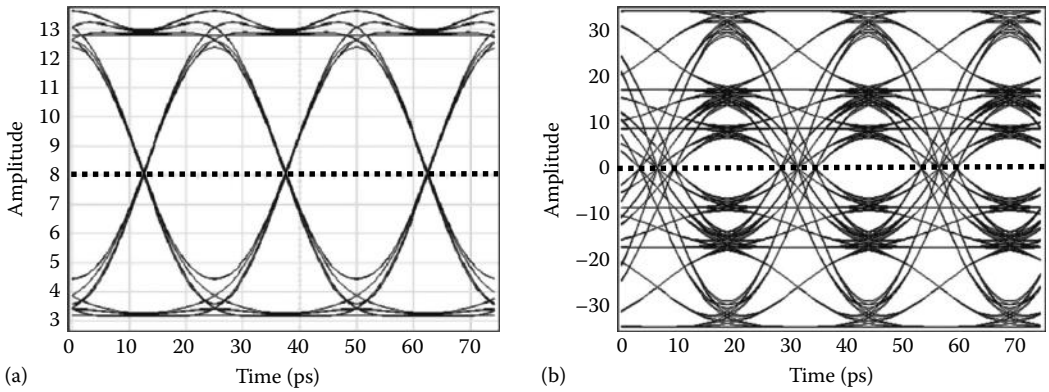

FIGURE 13.83
Eye diagrams of (a) amplitude and (b) phase detection of optical BAMSK received signals with normalized amplitude ratio of 0.285/0.715. The decision threshold is plotted in broken-line style.

13.7.3.3 Typical Simulation Results: Transmission Performance of Linear and Nonlinear Optical MSK Systems

The block diagram of the simulation setup is shown in Figure 13.84. The dispersion tolerances of linear, weakly nonlinear, and strongly nonlinear optical MSK signals are numerically investigated and the results are shown in Figure 13.84. Among the three types, linear MSK is most tolerant to residual dispersion with 1 dB eye open penalty at 72 ps/nm/km. Strongly nonlinear MSK suffers a severe penalty when residual dispersion exceeds 85 ps/nm/km, or equivalently, 5 km standard single mode fiber (SSMF).

Figure 13.85 shows the typical performance of three types of optical MSK-modulated signals versus OSNR in transmission over 540 km Vascade fibers of optically amplified and fully compensated multispan links (6 spans × 90 km/span). The receiver sensitivity of the differential phase comparison balanced receiver is –24.6 dBm. In Vascade fibers, the dispersion factors of the dispersion compensating fiber are negatively opposite to that of the transmission fiber, a standard single-mode fiber, of +17.5 ps/nm/km at 1550 nm wavelength. In addition, the dispersion slopes of these fibers are also matched. Optical amplifiers of EDFA types are placed one at the end of the transmission fiber and one after the DCF so that it would boost the optical power to the right level, which is equal to that of the launched power. The EDFA optical gain of 19 dB and a 5 dB ASE noise figure is used. The noise margin reduces severely after the propagation over 6 × 90 km spans. Effects of positive and negative dispersion mismatch and mid-link nonlinearity on phase evolution are shown in Figure 13.86.

The tolerance of these MSK modulations using transmission models to nonlinear effects is also studied, and simulation results are shown in Figure 13.87. The input power into the fiber span is increasing whereas the length of transmission link is constant at 180 km. At BER = 1e–9, linear MSK can tolerate an increase in the input-launched power up to 10.5 dBm, weakly nonlinear can tolerate up to 10.2 dBm compared to 9.2 dBm in the case of strongly nonlinear MSK. The nonlinear phase shift is proportional to the input power; therefore, increasing the input power would increase nonlinear phase shift as well. This nonlinear phase shift is observed through the asymmetries in the eye diagram and through the scatter plot, which shows that the phases of the in-phase and quadrature components have shifted from the x and y axes. The maximum phase shift that could be tolerated is approximately 15°.

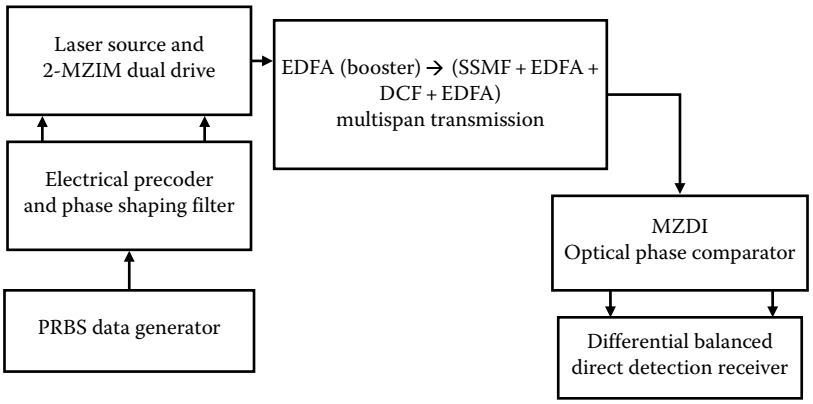

FIGURE 13.84
Schematic diagram of an optically amplified optical transmission system.

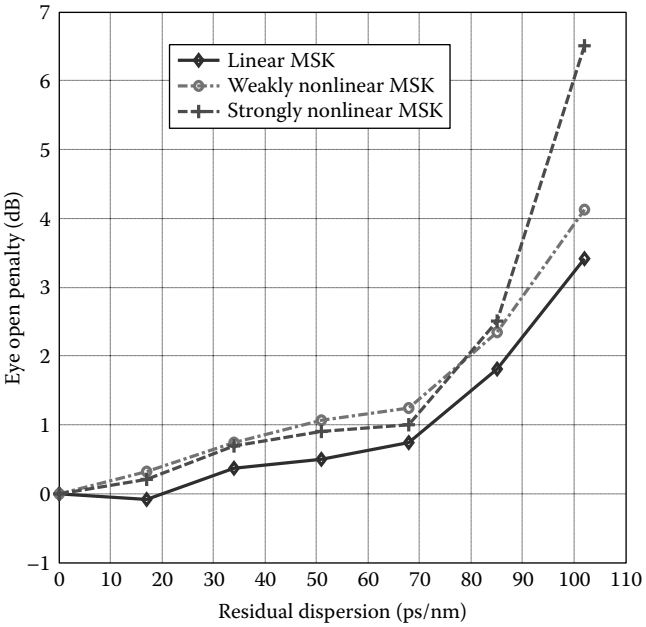

FIGURE 13.85
Dispersion tolerance of 40 Gb/s linear MSK, weakly nonlinear MSK, and strongly nonlinear MSK optical signals.

Although increasing input power increases the noise margin of the eye diagram, it is paid off by the large distortion at sampling time causing the signal-to-noise ratio (SNR) to decrease. Typical eye diagrams for full compensation and after transmission over 540 km Vascade fibers of optically amplified and fully compensated multispan links (6 spans × 90 km/span) are shown in Figures 13.88 and 13.89. We note that if the sampling is conducted at the center of the bit period, then the error is at its minimum as the ripples of the eyes fall on this position. This is the principal reasons why the MSK signals can suffer minimum pulse spreading because of residual and nonlinear phase dispersion.

Linear, weakly nonlinear, and strongly nonlinear MSK phase shaping functions are investigated. It has been proven that optical MSK is a very efficient modulation that offers excellent performance. With OSNR of about 17 dB, BER is obtained to be 1e−9 and reaches 1e−17 for an optical SNR of 19 dB under linear MSK modulation. The modulation formats of linear and nonlinear phase shaping MSK are also highly resilient to nonlinear effects. Nonlinear distortion appears when the total average power reaches about 9 dBm, that is, about 3–4 dB above that of NRZ ASK format over a 50 μm diameter SSMF fiber.

At this point, we must point out that the self-homodyne detection is a complex detection; so, if a local oscillator is used to mix with the signal to boost the resulting beating signals, a significant improvement in the receiver sensitivity is achieved. Further, ADC and DSP are employed after the electronic preamplifier to compensate for the residual dispersion of the optical transmission line, and hence, extend the reach of the transmission systems.

The nonlinear phase shaping filters offer better implementation structures in the electronic domain for driving the dual-drive MZIMs than the linear type but suffer some power penalty; however, they are still better than those candidates with other amplitude or phase or differential phase modulation formats. Weakly nonlinear MSK

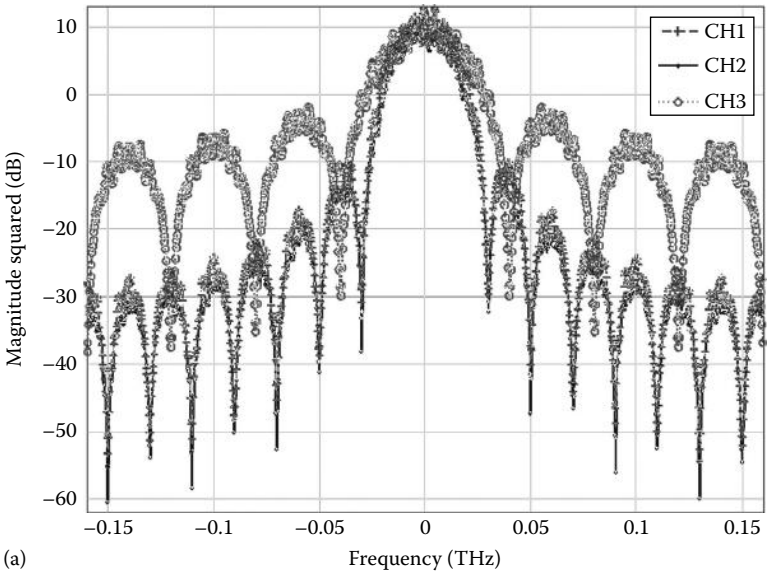

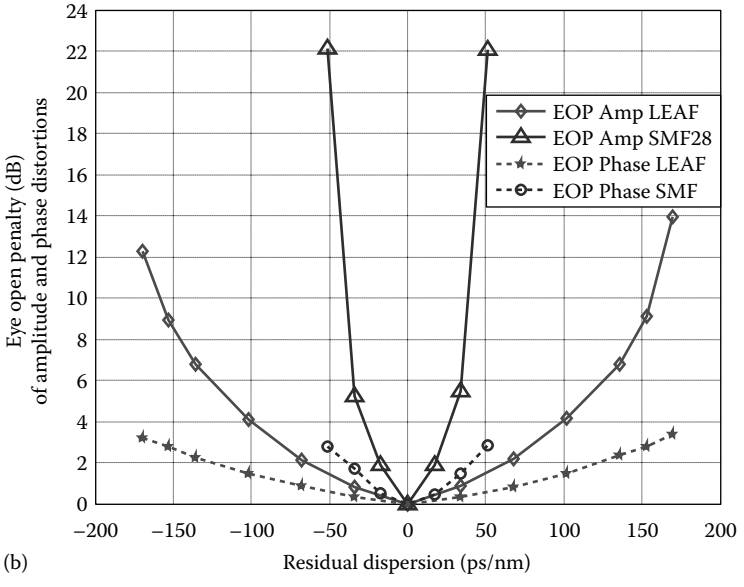

FIGURE 13.86
(a) Comparison of spectra of 80 Gb/s optical BAMSK, 40 Gb/s optical MSK, and 40 Gb/s optical binary DPSK signals; (b) numerical results on residual dispersion tolerance of 80 Gb/s optical BAMSK systems (effectively 40 Gb/s symbol rate) with normalized amplitude ratio of 0.285/0.715 in both amplitude and phase detection.

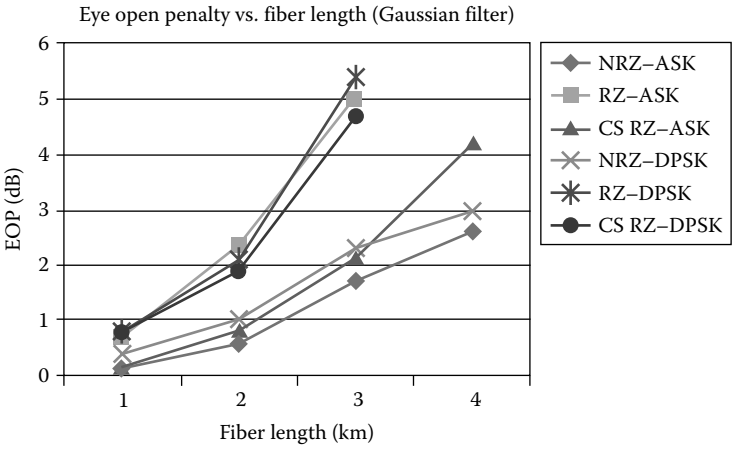

FIGURE 13.87
Simulation of EOP versus transmission distance 1–4 km of SSMF.

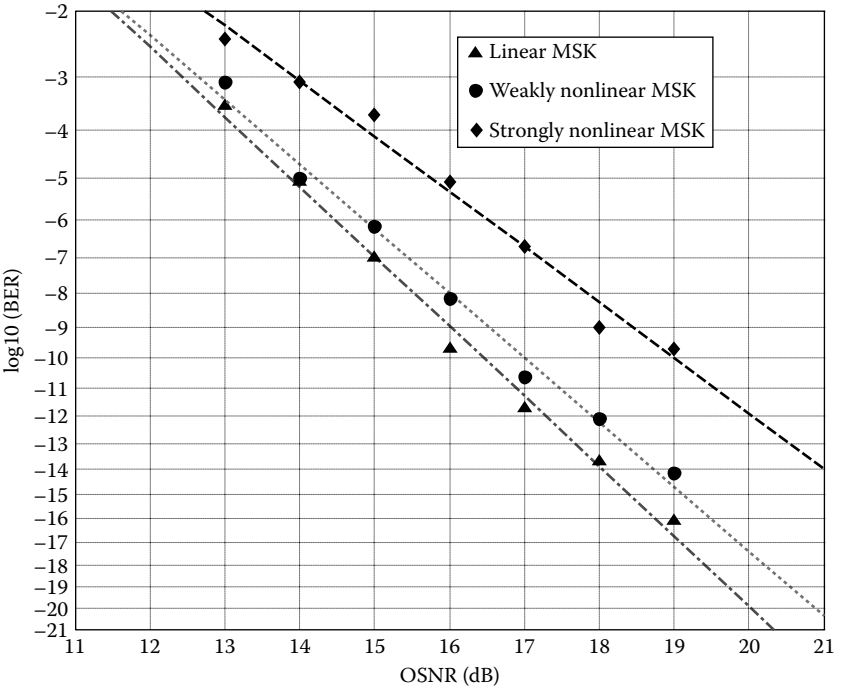

FIGURE 13.88
BER versus optical SNR for transmission of three types of modulated optical MSK signals over 540 km Vascade fibers of optically amplified and fully compensated multispan links (6 spans × 90 km/span).

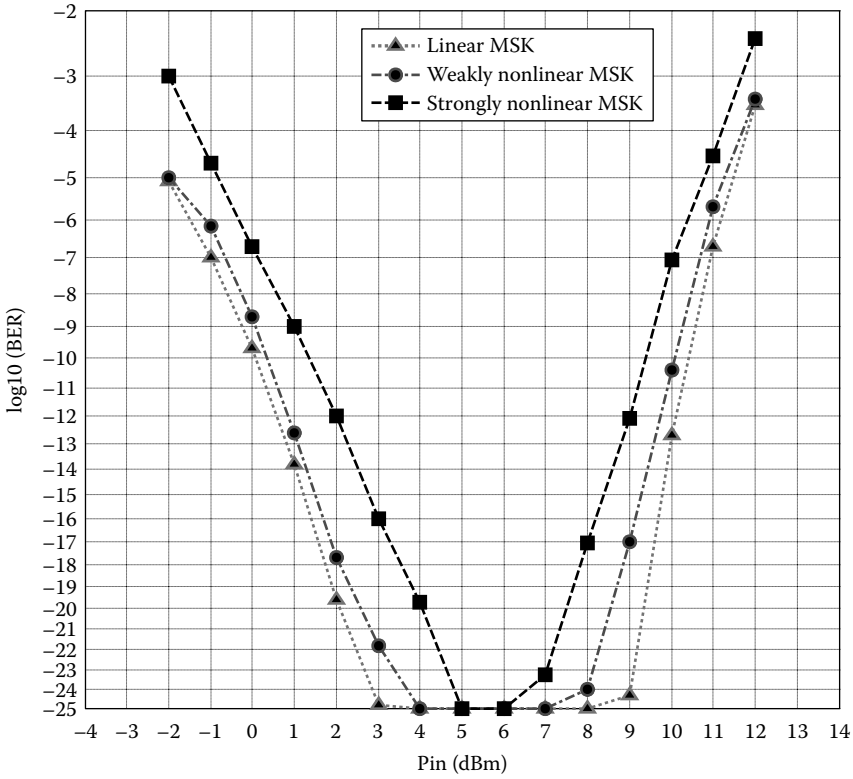

FIGURE 13.89
BER versus input power showing robustness to nonlinearity of linear, weakly nonlinear, and strongly nonlinear optical MSK signals with transmission over 180 km Vascade fibers of two optically amplified and fully compensated span links.

offers much lower power penalty and ease of implementation for precoders and phase shaping filters; it is the preferred MSK format for long-haul transmission over optically amplified multispan systems. At *BER* = 1e–12, linear MSK is 0.3 and 1.2 dB more resilient to nonlinear phase effects than weakly nonlinear MSK and strongly nonlinear MSK, respectively.

Shown in Figure 13.90 is the transmission performance of 80 Gb/s optical BAMSK over 900 km Vascade fiber systems in two cases of normalized amplitude ratios: 0.25/0.75 (round markers and solid line) and 0.285/0.715 (diamond markers and dashed line.

13.8 Star-QAM Transmission Systems for 100 Gb/s Capacity

This section presents the simulation of the transmission performances of optical transmission systems over 10 spans of dispersion-compensated and optically amplified fiber transmission systems with a bit rate of 100 Gb/s, an effective symbol rate of 25 Gsymbols/s, and two amplitude levels, and eight phase states per amplitude level.

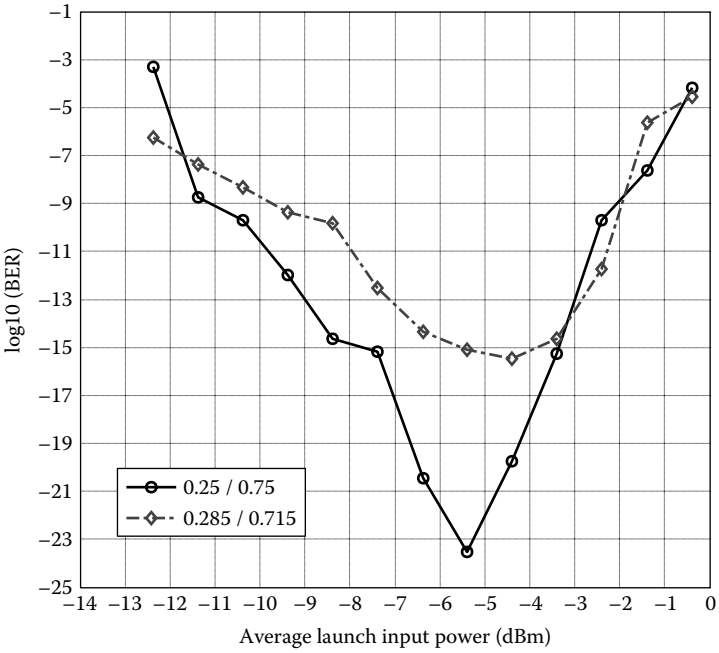

FIGURE 13.90
Transmission performance of 80 Gb/s optical BAMSK over 900 km Vascade fiber systems in two cases of normalized amplitude ratios: 0.25/0.75 (round markers and solid line) and 0.285/0.715 (diamond markers and dashed line).

The modulation format employs the Star 16-QAM with two-level and eight-phase state constellation. Different QAM structures are given to determine the dual-level and the eight-phase SK rings. Optical transmitters and coherent receivers are proposed with the transmitter using only two MZIM optical modulators. The transmitted lightwave signals are coherently demodulated and detected. Simulation results have shown that it is possible to transmit and detect the data symbols for 107 Gb/s without much difficulty. The OSNR with 0.1 nm optical filters is achieved with 18 and 23 dB for BtB and long-haul transmission cases with a dispersion tolerance of 300 ps/nm. The multilevel modulation scheme with eight phases and two amplitude levels at a bit rate of 100 Gb/s effectively uses 4 bits per one symbol for transmission, in which the first 3 bits are for coding phase information while the coding of the amplitude levels is implemented with the 4th bit. As a result, the transmission baud rate is equivalently a quarter of the bit rate from the bit pattern generator. The detection of this scheme is pseudocoherent detection in which the amplitude detection is directly detected and the phase detection is conducted via an *M*-ary phase SK coherent demodulator that estimates the phase state of the received symbol. Monte Carlo simulation is performed, and a receiver sensitivity of –15 dBm is achieved for a BER of 10^{-5} after 1100 km of dispersion-compensated and optically amplified transmission of 100 km fiber spans.

13.8.1 Introduction

To increase the channel capacity and bandwidth efficiency in optical transmissions, the multilevel modulation formats such as the QAM formats are of interest, especially when 100 Gb/s is expected to be the basic transmission rate for 10 Gb/s Ethernet in the near future. In digital

transmission with multilevel (*M*-levels) modulation, m-bits are collected and mapped onto a complex symbol from an alphabet with $M = 2$ m possibilities on the transmitter side.

The symbol duration is $T_s = m \cdot T_B$ with T_B as the bit duration, and the symbol rate is $f_S = f_B/m$ with $f_B = 1/T_B$ as the bit rate. This shows that for a given bit rate the symbol rate decreases if the modulation level increases. That means higher bandwidth efficiency can be achieved by a higher-order modulation format. For 16-QAM format, $m = 4$ bits are collected and mapped to one symbol from an alphabet with $M = 16$ possibilities. In comparison to the case of binary modulation format, only the $m = 1$ bit is mapped to one symbol from an alphabet with $M = 2$ possibilities. With the 16-QAM format and a data source with a bit rate of $f_B = 40$ Gb/s, only a symbol rate of $f_s = 10$ GBaud is necessary. From a commercial point of view, it means that a 40 Gb/s data rate can be transmitted with 10 Gb/s transmission devices. In the case of binary transmission, the transmitter needs a symbol rate of $f_s = 40$ GBaud. This implies that the 16-QAM transmission requires four times slower transmission devices than that for the binary transmission. It is noted here that a 10.7 Gsymbols/s is used as the symbol rate so as to compare the simulation results with the well-known 10.7 Gb/s modulation schemes such as DPSK, CSRZ, and DPSK. For a 107 Gb/s bit rate the transmission performance, that is, the sensitivity and OSNR can be scaled accordingly without any difficulty.

This section gives a general approach regarding the design and simulation of Star 16-QAM using coherent and pseudo coherent detection techniques. Section 13.2 gives the design of the QAM and Star-QAM with two rings and non–interleaved eight phases per ring to determine an optimum ring ratio. The simulation of the transmission performances of a modulation Star-QAM scheme is demonstrated for effectiveness at 100 Gb/s bit rate. The transmission format is discussed with theoretical estimates and simulation results to determine the transmission performance. The optimum Euclidean distance is defined for the design of Star 16-QAM and further analytically determined and studied with an optimum ratio of the amplitudes of the two rings of the 16-Star-QAM. Then in the second section, the coherent and pseudo coherent detection schemes for Star-QAM constellations are demonstrated. Alternatively, Section 13.3 investigates an eight-phase state and two amplitude levels denoted as 8-DPSK_2-ASK, effectively uses 4 bits per one symbol for transmission, in which the first 3 bits are for coding phase information while the coding of the amplitude levels is implemented with the 4th bit. Only one MZIM is used.

13.8.2 Design of 16-QAM Signal Constellation

There are many possibilities to design 16-QAM signal constellation. The three most popular constellations are introduced. For 16-QAM, the modulation schemes are (1) Star 16-QAM, (2) Square 16-QAM, and (3) Shifted-square 16-QAM. The first two of these constellations are in use. However, only the Star 16-QAM with two amplitude levels and eight phase states per amplitude level is employed as the preferred constellation in this work.

13.8.3 Star 16-QAM

13.8.3.1 Signal Constellation

The signal constellation for Star 16-QAM with Gray coding is shown in Figure 13.91a. The binary presentation of the symbols (4 bits per symbol) can be mapped onto the constellation points of circular Star-QAM [22,23], which can be compared to that of a Square-QAM shown in Figure 13.91b. As can be seen from the figure, the symbols are evenly distributed

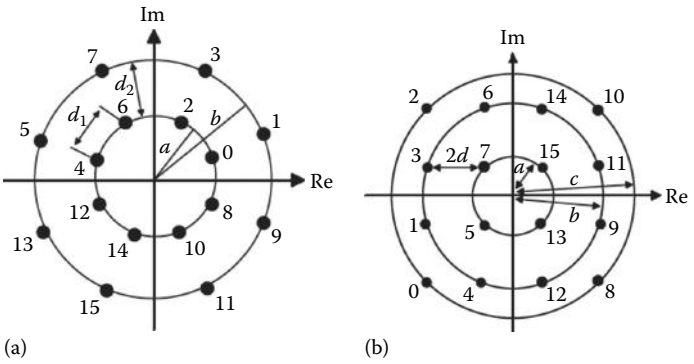

FIGURE 13.91
Theoretical arrangement of the modulation constellation for (a) Star 16-QAM and (b) square QAM.

on two rings and the phase difference between the neighboring symbols on the same ring are equal (π/4). To detect a received symbol, its phase and amplitude must be determined. In other words, between two amplitude levels of the rings and among eight phase possibilities, there are a number of ways to form this constellation.

The ring ratio (RR) for this constellation is defined as $RR = b/a$, where a and b are the ring radii as shown in Figure 13.81. The RR can be set to different values to optimize the transmission performance.

13.8.3.2 Optimum Ring Ratio for Star Constellation

From Figure 13.91, it can be seen that there are many options to choose the RR for the Star 16-QAM constellation. Theoretically, the best RR is defined to minimize the error probability in an AWGN channel by maximizing the minimum distance $d_{\min}$ between the neighboring symbols [24]. The results for AWGN channel can be used approximately for optically amplified fiber transmission systems. For Star 16-QAM the minimum distance $d_{\min}$ is maximized, when

$$d_1 = d_2 = b - a = d_{\min} \tag{13.32}$$

With some geometrical manipulations, it can be shown that

$$d_{\min} = 2a \cdot \sin\frac{\pi}{8} \tag{13.33}$$

which leads to an optimal ring ratio RR_{opt} of

$$RR_{opt} = \frac{b}{a} = \frac{d_{\min} + a}{a} = \frac{2a \cdot \sin\frac{\pi}{8} + a}{a} = 1.77 \tag{13.34}$$

Under the condition of no noises, the average power of the Star 16-QAM constellation is then determined as

$$P_0 = \frac{a^2 + b^2}{2} \tag{13.35}$$

We have the relationship between the average optical power and the minimum distance between the two rings at the two amplitude levels as

$$d_{\min} = 0.53P_0^{1/2} \tag{13.36}$$

The obtained RR_{opt} = 1.77 does not depend on P_0 and is constant for each P_0 value. For an average power of 5 dBm (3.16 mW), $d_{\min} = 2.98\times10^{-2}\sqrt{W}$, $a = 3.98\times10^{-2}\sqrt{W}$, and $b = 6.87\times10^{-2}\sqrt{W}$.

13.8.4 Square 16-QAM

The signal constellation of the square 16-QAM with Gray coding is shown in Figure 13.91b. In the constellation of the square 16-QAM, the 16 symbols are equidistant from their immediate neighbors and have totally 12 different phases [25], that is, three phases per quarter, distributed on three rings. The phase differences between neighboring symbols on the inner and outer rings are equal (π/2) but the phase differences between neighboring symbols on the middle ring are different (37° or 53°). If the distance between direct neighbors in the square 16-QAM is noted as 2*d*, the average symbol power (P_0) of the constellation is

$$P_0 = 10d_2 \tag{13.37}$$

For an average power of 5 dBm (3.16 mW), $d = 1.77\times10^{-2}\sqrt{W}$ and $a = 2.5\times10^{-2}\sqrt{W}$, $b = 5.6\times10^{-2}\sqrt{W}$ and $c = 7.5\times10^{-2}\sqrt{W}$. In comparison with square 16-QAM, in this case the distance between the middle ring and the outer ring is much smaller. It means, to achieve the same BER, square 16-QAM needs a higher average power than Star 16-QAM. The decision method for the square 16-QAM is more complicated than that for Star 16-QAM.

13.8.5 Offset-Square 16-QAM

To optimize the phase detection of the middle ring, the phase differences between neighboring symbols on the middle ring in square 16-QAM should be equal. Thus, the shifted-square 16-QAM is introduced by shifting (rotation) symbols on the middle ring to obtain equal phase differences between all neighboring symbols. After shifting the symbols on the middle ring, the distances between all direct neighbors are not necessarily equal. In comparison to square 16-QAM, this constellation may offer more robust detection against phase distortions according to our amplitude and phase detection method introduced in a later section.

13.9 8-DPSK_2-ASK 16-Star QAM

We have examined the Star-QAM and the determination of the ring ratio between the inner and outer rings of the constellation. This part investigates a multilevel modulation scheme of Figure 13.91a that has eight phases per ring and two amplitude levels, with non–interleaved phase angles between the rings. This scheme, which is named in short as 8-DPSK_2-ASK, effectively uses 4 bits per one symbol for transmission, in which the first

3 bits are for coding phase information while the coding of the amplitude levels is implemented with the 4th bit. As a result, the transmission baud rate is equivalent to a quarter of the bit rate from the bit pattern generator. This section is organized as follows: Section 13.9.1 presents a detailed description of the optical transmitter for generating 8-DPSK_2-ASK signals. In Section 13.9.2, the detailed configuration of the receiver is provided. Section 13.9.3 provides a study of the dispersion tolerance and transmission performance of the 8-DPSK_2-ASK scheme.

13.9.1 Configuration of 8-DPSK_2-ASK Optical Transmitter

There have been several different configurations of an optical transmitter for generating multiphase/level optical signals with the use of amplitude or PMs arranged in either serial or parallel configurations. However, the optical transmitters reported in Refs. [2–4] require a precoder with high complexity. On the contrary, the configuration uses the Gray mapping technique to differentially encode the phase information, and this significantly reduces the complexity of the optical transmitter. In addition, as elaborated in more detail in Section 13.9.3, this precoding technique enables the detection scheme using the *I*–*Q* demodulation techniques, as equivalent in coherent transmission systems.

The optical transmitter of the 8-DPSK_2-ASK scheme employs the differential coding and *I*–*Q* modulation technique with two MZIM in parallel and a π/2 OPM, as shown in Figure 13.92.

At each *k*th instant, the absolute phase of transmitted light waves θ_k is expressed as $\theta_k = \theta_{k-1} + \Delta\theta_k$, where θ_{k-1} is the phase at the $(k-1)$th instant and $\Delta\theta_k$ is the differentially coded phase information. The encoding of this $\Delta\theta_k$ for generating 8-DPSK_2-ASK modulated optical signals (4 bits per one transmitted symbol) follows the well-known Gray mapping rules. This Gray mapping phasor diagram is shown in Figure 13.93. The phasor can be normalized with the maximum energy on each branch, that is, $E_1/2$.

The amplitude levels are optimized so that the Euclidean distances d_1, d_2, and d_3 are equal, that is, $d_1 = d_2 = d_3$. After a simple derivation, we obtain $r_1 = 0.5664$. The *I* and *Q* field vector corresponding to Gray mapping rules from the M-ADPSK precoder (Figure 13.93) are provided in Table 13.4.

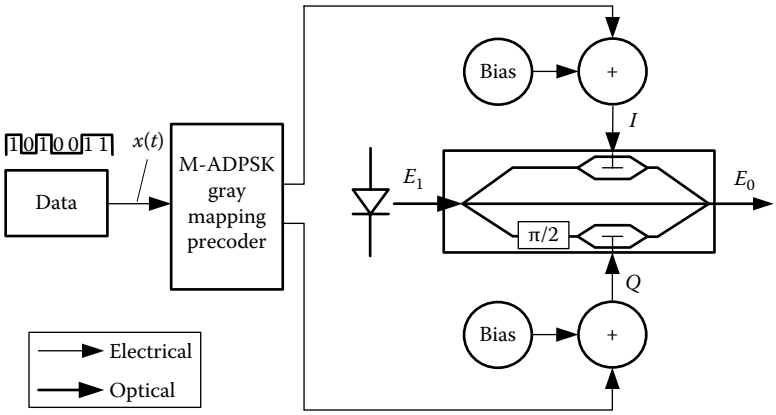

FIGURE 13.92
Optical transmitter configuration of the 8-DPSK_2-ASK modulation scheme.

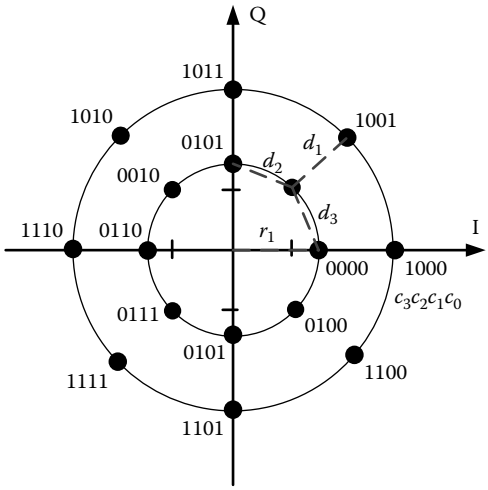

FIGURE 13.93
Gray mapping for optimal 8-DPSK_2-ASK modulation scheme.

TABLE 13.4

I and *Q* Field Vectors in 8-DPSK_2-ASK Modulation Scheme Using Two MZIMs in Parallel

Binary Sequence	($\Delta\theta_k$, Amplitude)	I_k	Q_k
1000	(0, 1)	1	0
1001	($\pi/4$, 1)	$\sqrt{2}/2$	$\sqrt{2}/2$
1011	($\pi/2$, 1)	0	1
1010	($3\pi/4$, 1)	$-\sqrt{2}/2$	$\sqrt{2}/2$
1110	(π, 1)	−1	0
1111	($-3\pi/4$, 1)	$-\sqrt{2}/2$	$-\sqrt{2}/2$
1101	($-\pi/2$, 1)	0	−1
1100	($-\pi/4$, 1)	$\sqrt{2}/2$	$-\sqrt{2}/2$
0000	(0, 0.5664)	1×0.5664	0
0001	($\pi/4$, 0.5664)	$\sqrt{2}/2 \times 0.5664$	$\sqrt{2}/2 \times 0.5664$
0011	($\pi/2$, 0.5664)	0	1×0.5664
0010	($3\pi/4$, 0.5664)	$-\sqrt{2}/2 \times 0.5664$	$\sqrt{2}/2 \times 0.5664$
0110	(π, 0.5664)	-1×0.5664	0
0111	($-3\pi/4$, 0.5664)	$-\sqrt{2}/2 \times 0.5664$	$-\sqrt{2}/2 \times 0.5664$
0101	($-\pi/2$, 0.5664)	0	-1×0.5664
0100	($-\pi/4$, 0.5664)	$\sqrt{2}/2 \times 0.5664$	$-\sqrt{2}/2 \times 0.5664$

The transmitter configuration described here can be replaced with a dual-drive MZIM. The explanation and derivation for generating 8-DPSK_2-ASK optical signals are also based on the phasor diagram of Figure 13.93. In this case, the output field vector is the summation of two component field vectors, each of which is not only determined by the amplitude but also by initially biased phases.

13.9.2 Configuration of 8-DPSK_2-ASK Detection Scheme

The detection of 8-DPSK_2-ASK optical signals is implemented with the use of two MZDI balanced receivers (see Figure 13.94).

Several key notes in this detection structure are as follows: (1) The MZDI introducing a delay corresponding to the baud rate. (2) One arm of MZDI has a π/4 optical phase shifter while the other arm has an optical phase shift of − π/4. (3) The outputs from the two balanced receivers, which are superimposed positively and negatively, lead to *I* and *Q* detected signals, respectively. The *I* and *Q* detected components are expressed as $I = \mathrm{Re}\left\{E_k E_{k-1}^*\right\}$ and $Q = \mathrm{Im}\left\{E_k E_{k-1}^*\right\}$, respectively. (4) The *I*–*Q* detected components which are demodulated using the popular *I*–*Q* demodulator. The detected signals (after sampler) are represented in the signal constellation.

13.9.3 Transmission Performance of 100 Gb/s 8-DPSK_2-ASK Scheme

The performance characteristics of the 8-DPSK_2-ASK scheme operating at 100 Gb/s bit rate are studied in terms of receiver sensitivity, dispersion tolerance, and the feasibility for long-haul transmission. The BERs are the pre–forward error correct (FEC) BERs and the pre-FEC limit is conventionally referenced at 2e–3. In addition, the BERs are evaluated by the Monte Carlo method.

13.9.4 Power Spectrum

The power spectrum of 8-DPSK_2-ASK optical signals is shown in Figure 13.95. It can be observed that the main lobe spectral width is about 25 GHz as the symbol baud rate of this modulation scheme is equal to a quarter of the bit rate from the bit patter generator. The harmonics are not highly suppressed, thus requiring the bandwidth of the optical filter to be necessarily large so as to not distort signals severely.

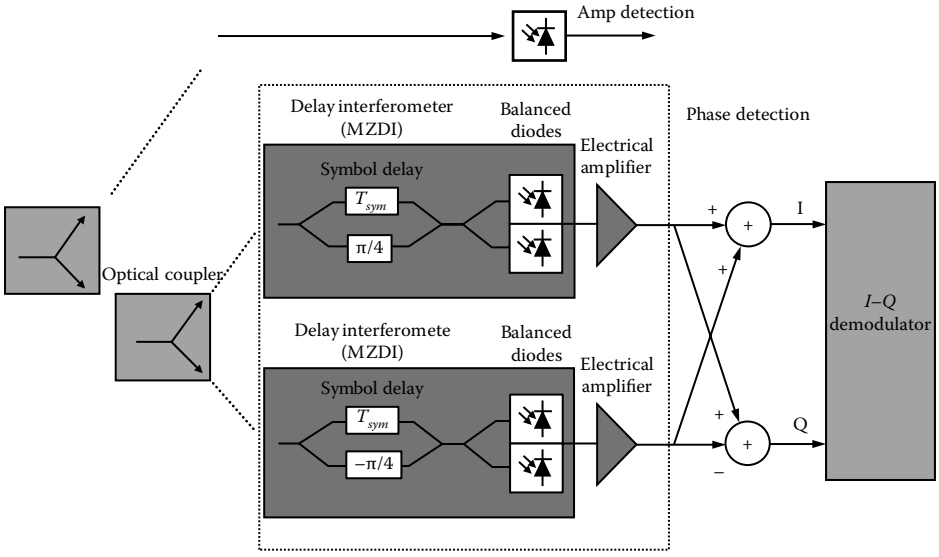

FIGURE 13.94
Detection configuration for the 8-DPSK_2-ASK modulation scheme.

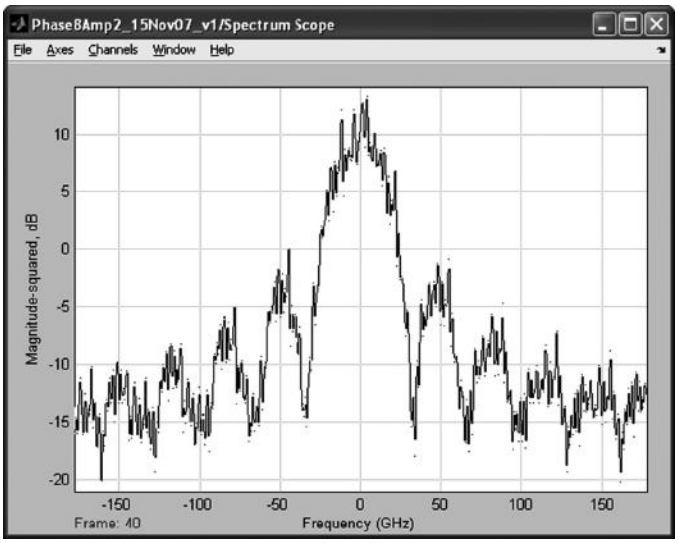

FIGURE 13.95
Power spectrum of 8-DPSK_2-ASK signals as observed by the spectrum scope of Simulink®.

13.9.5 Receiver Sensitivity and Dispersion Tolerance

The receiver sensitivity is studied by connecting the optical transmitter of the 8-DPSK_2-ASK scheme directly to the receiver to make a BtB setup (see Figure 13.96). On the other hand, the dispersion tolerance is studied by varying the length of SSMF from 0 to 5 km ($|D|$ = 17 ps/(nm · km)). The received powers are varied by using an optical attenuator. The optical Gaussian filter has BT = 3 (B is approximately 75 GHz). The modeling of receiver noise sources comprises shot noise, equivalent noise current density of 20 pA/$\sqrt{\text{Hz}}$ at the input of the trans impedance electrical amplifier, and dark current of 10 nA for each of the two photodiodes in the balanced structure. A fifth-order Bessel electrical filter with a bandwidth of BT = 0.8 is used.

The numerical BER curves of the receiver sensitivity for cases of 0–5 km SSMF are shown in Figure 13.97. The receiver sensitivity of the 8-DPSK_2-ASK scheme is approximately –18.5 dBm at BER = 1e–4. The receiver sensitivity at BER = 1e–9 can be obtained by extrapolating the BER curve in the 0 km case.

The power penalty versus residual dispersion results are then obtained and plotted in Figure 13.98. It is realized that the 2 dB penalty occurs for the residual dispersion of approximately 60 ps/nm, the equivalent of 3.5 km SSMF.

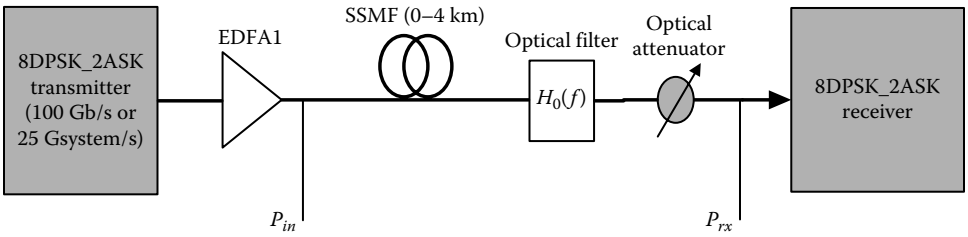

FIGURE 13.96
Setup for the study of receiver sensitivity (BtB) and dispersion tolerance (0–4 km SSMF) for the 8-DPSK_2-ASK modulation scheme.

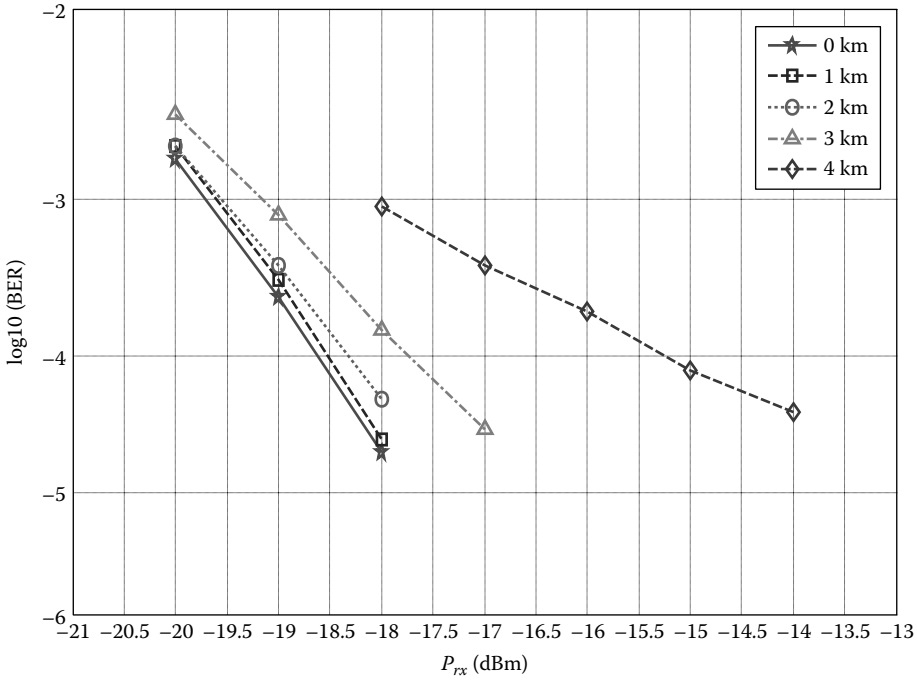

FIGURE 13.97
Receiver sensitivity (BtB) and dispersion tolerance (0–4 km SSMF) for the 8-DPSK_2-ASK modulation scheme.

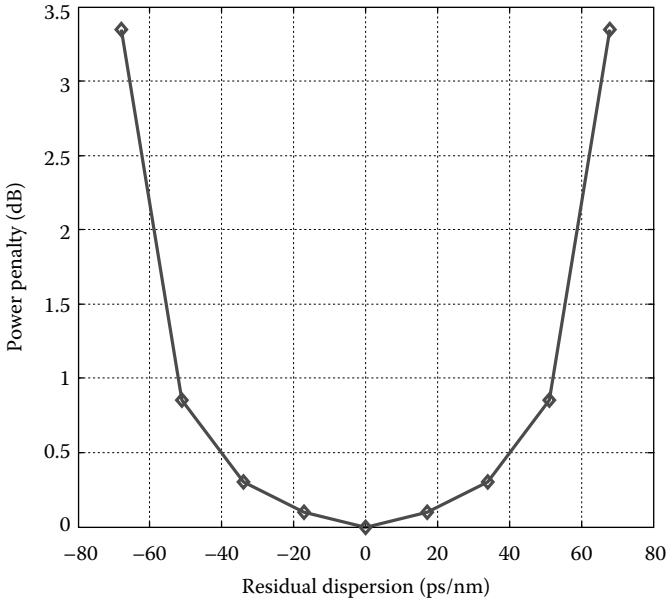

FIGURE 13.98
Power penalty due to residual dispersions for the 8-DPSK_2-ASK modulation scheme.

13.9.6 Long-Haul Transmission

The long-haul transmission performance of this modulation format is conducted over 10 optically amplified and fully compensated spans, and each span is composed of 100 km SSMF and 10 km DCF100 (Sumitomo fiber). As a result, the length of the transmission fiber link is 1100 km. This long-haul range is selected to reflect the distance between Melbourne and Sydney of Australia. The wavelength of interest is 1550 nm, and the dispersion at the end of the transmission link is fully compensation. The simulation setup is shown in Figure 13.99. Additionally, the fiber attenuation owing to SSMF and DCF is also fully

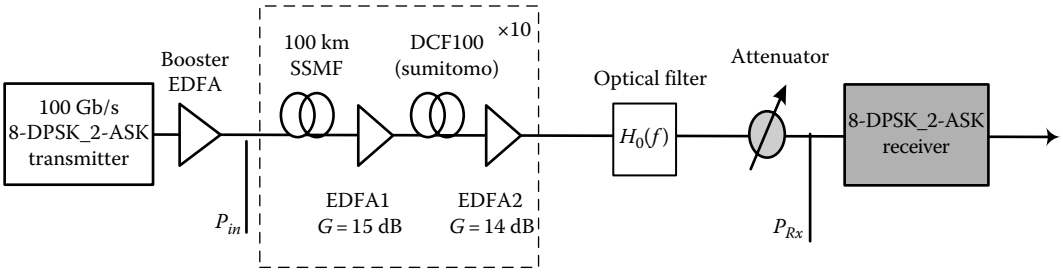

FIGURE 13.99
Transmission setup of 1100 km optically amplified and fully compensated fiber link.

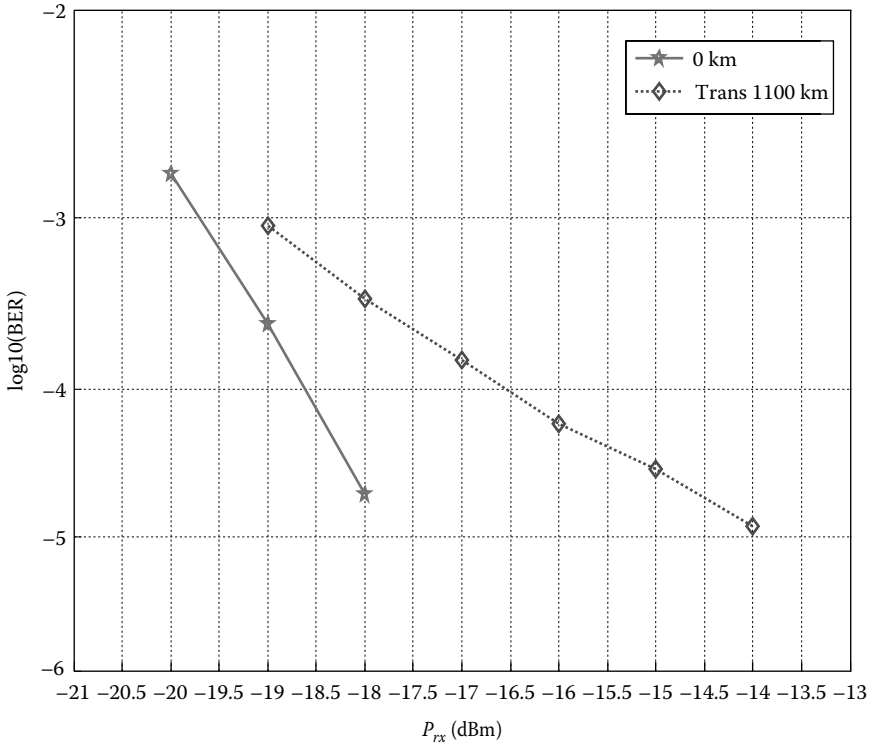

FIGURE 13.100
BER versus receiver sensitivity for 8-DPSK_2-ASK modulation format transmission.

compensated by using two EDFAs with optical gains as depicted in Figure 13.99. These EDFAs have noise figure (NF) set at 5 dB.

Numerical transmission BERs are plotted against received powers in Figure 13.100 and compared to the BtB BER curve. It can be observed that the BER curve of 1100 km follows a linear trend and reaches 1e–9 if extrapolated as shown in Figure 13.100. It should be noted that this transmission performance can be significantly improved with the use of high-performance FEC scheme.

This section has presented in detail the transmitter and receiver configurations and associate Simulink models for generating 8-DPSK_2-ASK optical signals. In addition, performance characteristics of this modulation format at 100 Gb/s (equivalently 25 Gsymbols/s) has also been investigated in terms of the receiver sensitivity and dispersion tolerance in the long-haul transmission performance. The simulation results show that 8-DPSK_2-ASK is a promising modulation for 100 Gb/s Ethernet and long-haul optical communications.

13.10 Appendix: Simulink® and Simulation Guidelines

This section gives a brief introduction to MATLAB Simulink and guidelines for simulation of optically amplified fiber transmission employing modulation formats ASK, PSK, and FSK.

13.10.1 MATLAB® Simulink®

MATLAB Simulink is a package integrated in MATLAB (from MATLAB 7.0 onward). Simulink is a simulation platform based on blocks of functions for users to structure their mathematical development and algorithm. That means that a number of MATLAB.m extension files have been transformed into blocks.

Thus MATLAB Simulink platform is shown in Figure 13.101 in which there is a section on Simulink (Figure 13.102) which consists of several blocksets including basic Simulink blocksets, communication blocksets, and signal processing blocksets. The basic Simulink blocksets consist of commonly used blocksets for manipulation of mathematical operations, discrete and continuous blocks for sampling and operations in the continuous and discrete domain, sources and sink blocks, which are used for monitoring equipment and generation of signals. A user-defined function can be used to integrate MATLAB.m files into a block for integration in the Simulink block diagram.

Thus Simulink can be employed as a computer development for testing and simulation of communication transmission systems. With the availability of communication blocksets and signal processing blocksets, manipulation, modulation, and receiving of optical signals can be implemented without much difficulty.

To develop a Simulink model, one needs to open a file in Simulink and then drag blocks that are required to implement an algorithm. It is noted that the advantage of Simulink is that the principles of operations of systems are important and mathematical analysis skill is minimized. Thus, developing Simulink is like setting up experiments on a computer, MATLAB platform without writing any .m file codes.

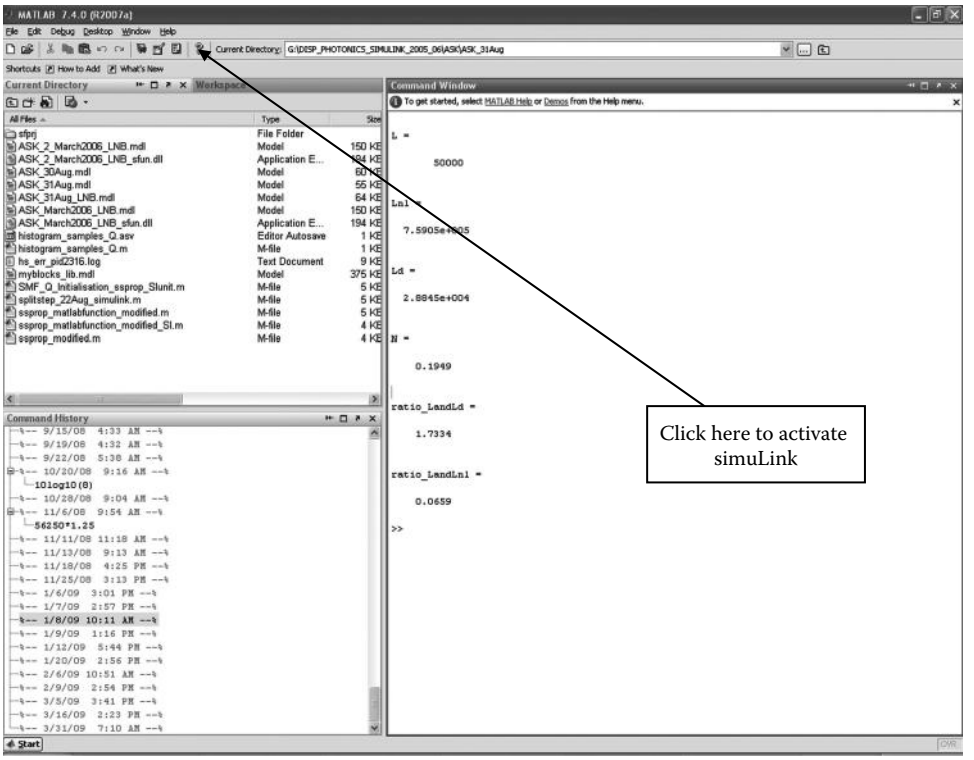

FIGURE 13.101
MATLAB® platform and where to click to activate Simulink®.

13.10.2 Guide for Use of Simulink® Models

This section outlines a number of models that can be used to simulate the transmission of optical signals over the optically amplified fiber multispan systems.

A transmission system would normally consist of the following:

- System parameters as are defined and specified in the next section.
- A general block model given in Figure 13.103 which consists of the optical transmitters, the fiber and optical amplifier spans, and the optical receivers and the evaluation of BERs. There are also a number of blocks for monitoring signals at various points in the transmission systems.
- Optical transmitters, which accept electrical signals, data bit sequence of arbitrary distribution. That is the "0" and "1" are randomly distributed in the data sequence. This random binary sequence is essential for obtaining the eye diagram at the output of the transmitter and the optical receiver so as to evaluate the BER of the transmission system. The transmitter module is available and indicated in the model. Figure 13.103 shows the Simulink model for the generation of ASK modulation signals. The Bernoulli arbitrary signal generator is used to generate arbitrary binary data bits.
- Modules of fiber spans which consist of a length of single-mode optical fiber for transmission and that of dispersion compensation fiber plus optical amplifiers

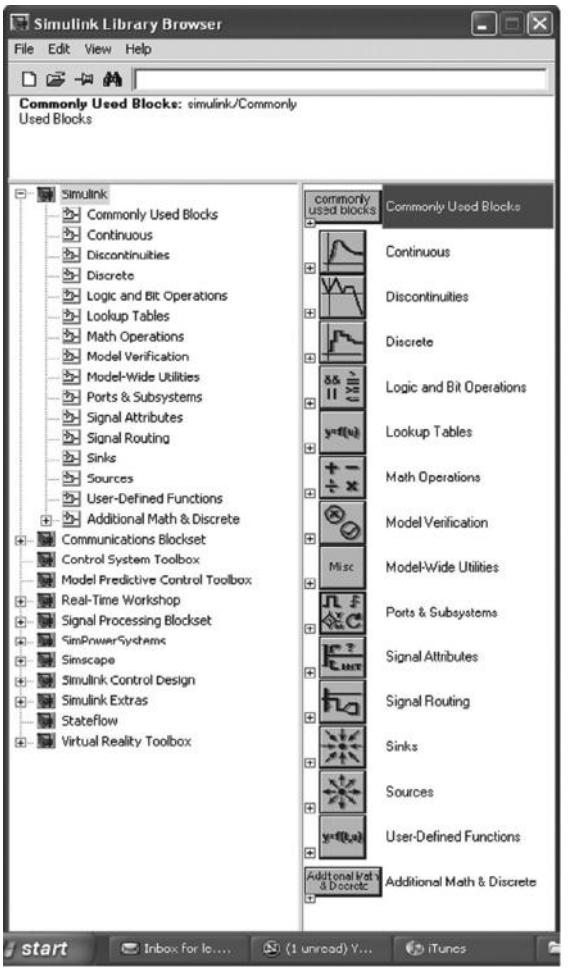

FIGURE 13.102
Blocksets of Simulink®.

(Figures 13.104 and 13.105). The propagation of optical signals can be represented by the NLSE (only SPM is included) given by

$$\frac{\partial u}{\partial z} + j\frac{\beta_2}{2}\frac{\partial^2 u}{\partial T^2} - \frac{\beta_3}{6}\frac{\partial^3 u}{\partial T^3} + \frac{\alpha}{2}u = j\gamma|u|^2 u$$

where the parameter u represents the normalized amplitude of the signal. Note that because of the extremely high value of the frequency of the OC, ultra-high sampling is required, and the optical signals take complex amplitudes. That means that the amplitude is the envelope of the signals and the complex parts of the amplitude represents the phase of the OCs. The coefficient α is the attenuation factor, T is the normalized time variable, and g is the nonlinear self-phase modulation coefficient. The .m file for solving this propagation is given in the Appendix. This program must be included in the "call back" of the "model property" of the Simulink model.

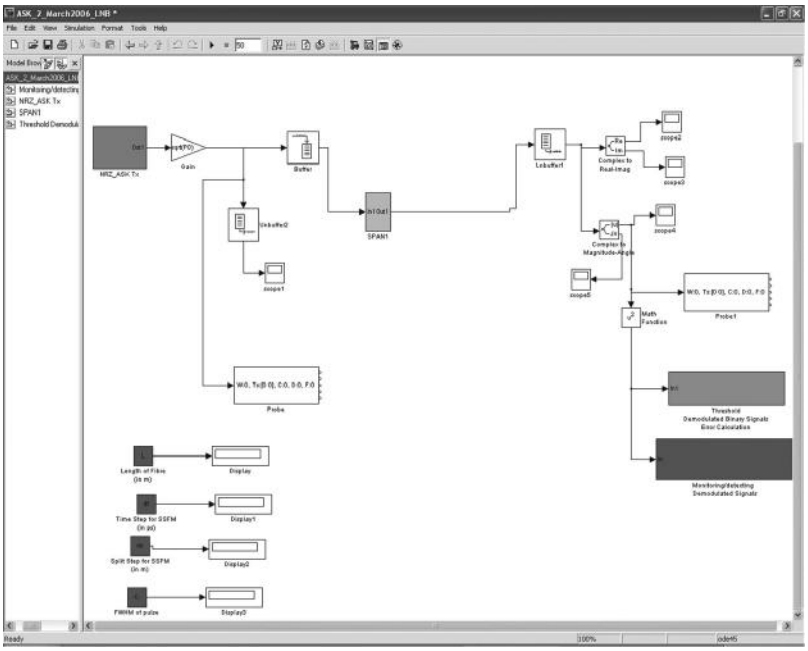

FIGURE 13.103
General structure of an ASK-modulated optically amplified transmission systems.

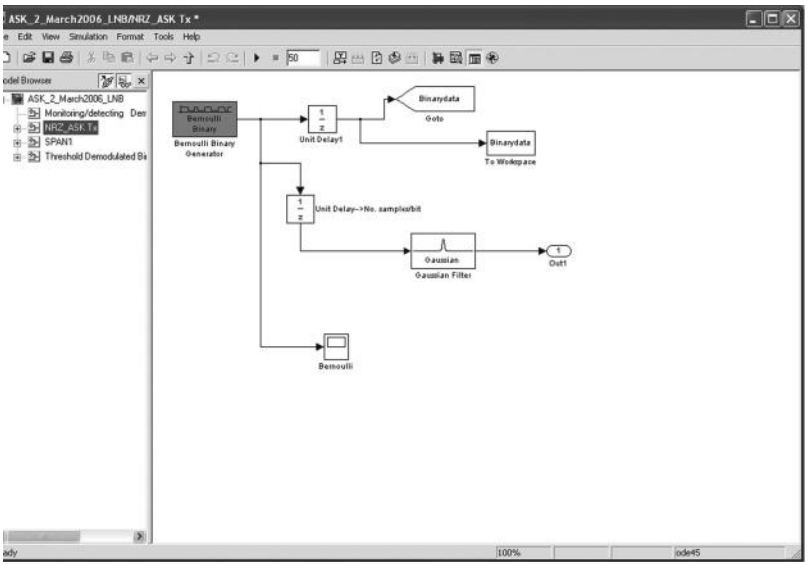

FIGURE 13.104
Optical transmitter employing ASK modulation format.

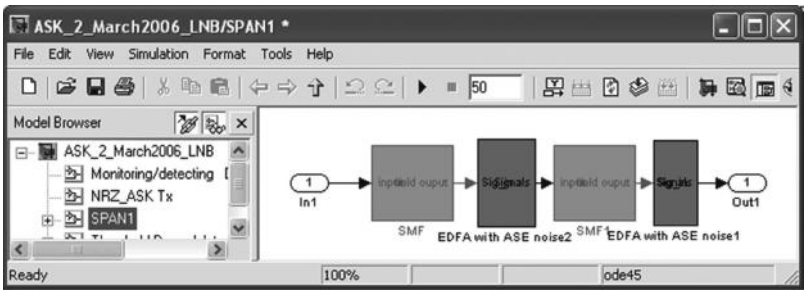

(a)

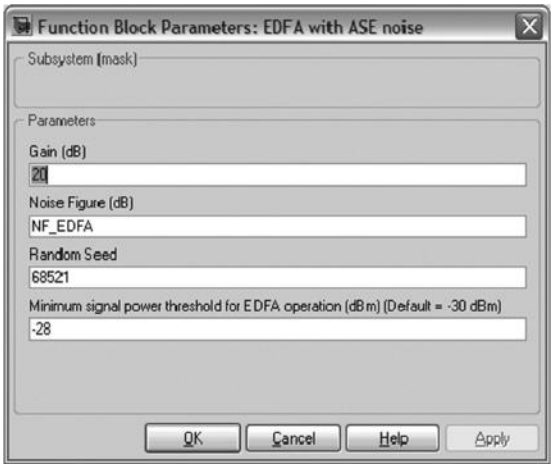

(b)

FIGURE 13.105
An optically amplified span consisting of a section of a single-mode optical fiber, a section of dispersion compensating fiber and two optical amplifiers (a) EDFA in transmission span (b) under mask of EDFA.

A block diagram for representing the fiber propagation is shown in Figure 13.106. The structures of the subsystems are given in the following text:

- Dispersion compensating fiber can be structured by estimating the dispersion factor which is opposite in sign to the transmission fiber so as to reverse the phase effects of the transmission length. This can be implemented by using the model given in Figure 13.106, but the beta parameters must have a negative sign for equal dispersion factor. For different dispersion factors between the fibers, the appropriate lengths of the fibers must be modified by taking the difference in the number of small sections *nz* and *dz*, which are also specified in the initialization file given in the Appendix.
- Optical amplifiers are inserted after the SMF transmission fiber and the dispersion compensation fiber. The specification of the gain and NF of the amplifiers can be altered by clicking the block and entering the parameters. The under mask model of the amplifier is shown in Figure 13.107b, and its integration into a transmission span is shown in Figure 13.107a.

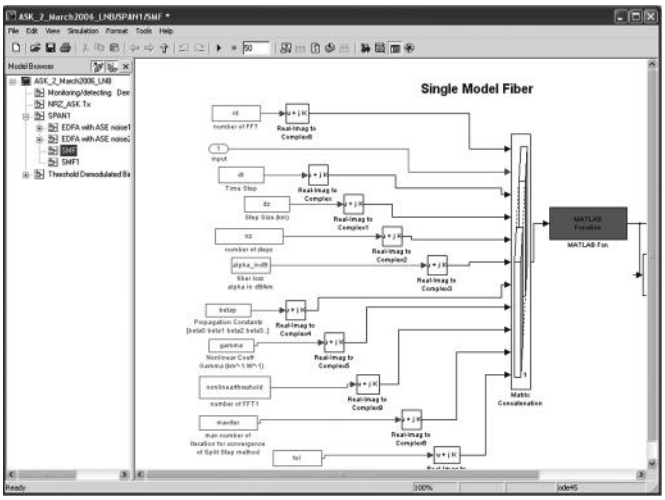

(a)

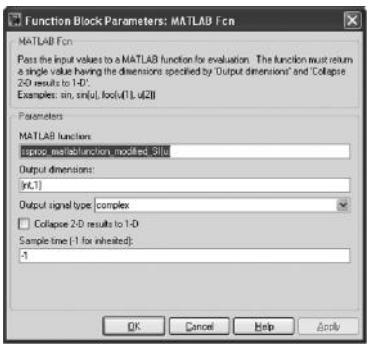

(b)

FIGURE 13.106
Simulink® model of the propagation of optical signals through a section of optical fibers (a) model with input parameters and signals (b) under mask of block "MATLAB® functions" which contains the m-file too calculate the propagation effects on signals by the dispersive property of the single-mode fiber.

- The optical receiver is represented by square-law detection, that is, taking the absolute value of the amplitude and the square. This is the photo detection process. That means that the photodetector absorbs the optical power and then converts it into electronic current, which is then further amplified in the electronic domain and then displayed on an oscilloscope. At this point, the eye diagram is achieved and the BER can be evaluated by getting the raw data generated from the Simulink model and calculating in Excel or m-files. An error detection and calculation of BER is given in the models for DPSK modulation format transmission system. Monitoring of the data received and the output of the receiver are required to obtain the raw data for evaluation of the BER (Figure 13.108).

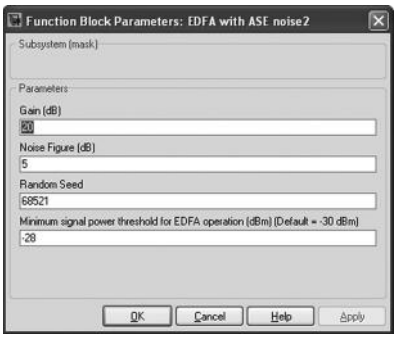

(a)

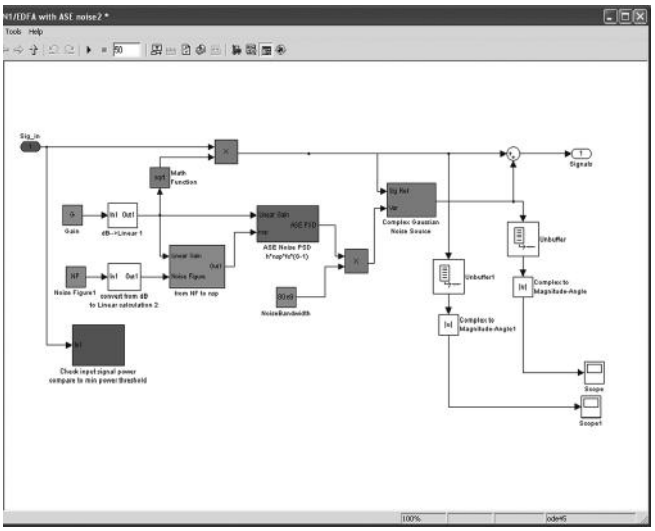

(b)

FIGURE 13.107
Optical amplifier (a) parameters for specification of the optical amplifier, gain and noise figure (NF) and (b) model under mask of the amplifier.

13.10.3 MATLAB® Files

13.10.3.1 Initialization File

```
% This file solves NLSE for
% pulse propagation in an optical fiber using the split-step
% Fourier method as given in: GP. Agrawal,"Nonlinear Fiber Optics", 2nd ed.
% AP, 1995, Chapter 2
%
% The following effects are included in the model: group
% velocity dispersion (GVD), GVD-slope / third-order
% dispersion, loss, and self-phase modulation (n2).  The core
% routine is implementing the split-step propagation
```

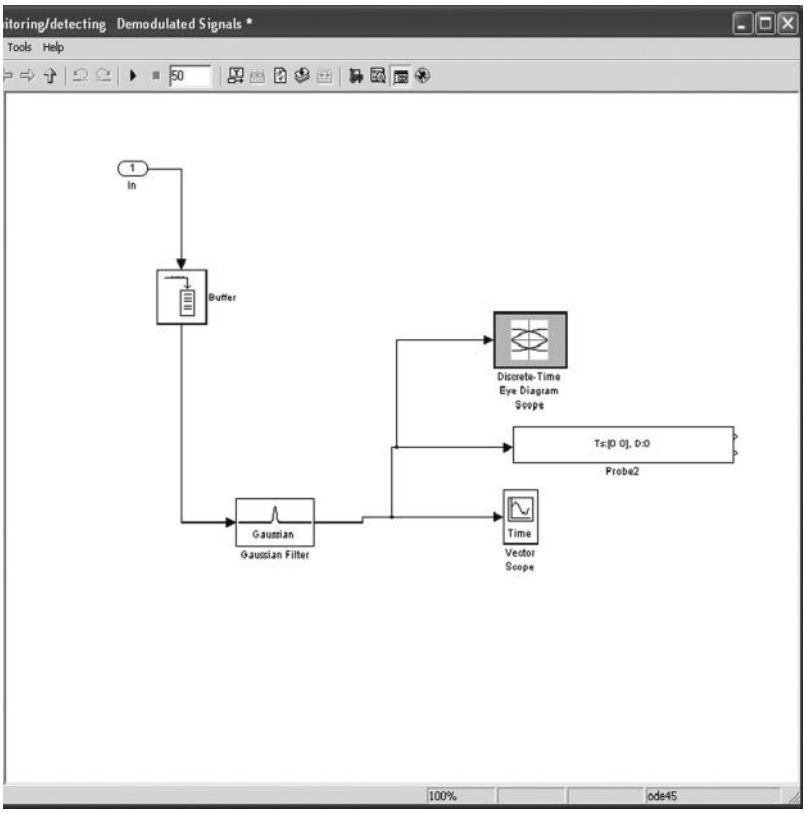

FIGURE 13.108
Block diagram of optical receiver and eye diagram monitor.

```
close all
clear all

% CONSTANTS
c = 3e8;                        % speed of light (m/s)

% NUMERICAL PARAMETERS
numbitspersymbol = 1;
P0 = 0.001;                     % peak power (W)
FWHM = 25e-12;                  % pulse width FWHM (ps)
FWHMps = 25e-12;
%halfwidth = FWHM/1.6651        % for Gaussian pulse
halfwidth = FWHM;               % for square pulse

bitrate = 1/halfwidth;          % THz
bitrateG = 1/FWHMps;
baudrate = bitrate/numbitspersymbol;
signalbandwidth = baudrate;
%%%%%%%%%%%%%%%%%%%%%%%%%%%%%%%

%%%%%%%%%%%%%%%%%%%%%%%%%%%%%%%
```

```
PRBSlength = 2^8;

% Make sure : FFT time window (=nt*dt) = PRBSlength * FWHM...
% FFTlength nt = PRBSlength/block * numbersamples/bit = PRBSlength *
(FWHM/dt)
% num_samplesperbit = FWHM/dt should be about 8 - 16 samples/bit

num_samplesperbit = 32;              % should be 2^n
dt = FWHMps/num_samplesperbit ;      % sampling time(ps);%time step(ps)
nt = PRBSlength*num_samplesperbit;   % FFT length

dz = 500;                            % distance stepsize (m)
nz = 100;                            % number of z-steps
maxiter = 20;                        % max # of iterations
tol = 1e-5;                          % error tolerance

% OPTICAL PARAMETERS

nonlinearthreshold = 0.005; % 5mW -- % Nonlinear Threshold Peak Power for
silica core fiber

lambda = 1550e-9;
% lambda_carrier = 14648.4375;  % wavelength (nm)with
                                % Level 4 group the carrier freq is scaled
down to 500G or 200 GHz
optical_carrier = c/lambda;     %carrier freq
num_samplesperperiod = 8;
sampling_fac = 16;

carrier_freq = num_samplesperperiod*num_samplesperbit*bitrateG;
% artificial freq

%dt = FWHM/(num_samplesperbit*num_samplesperperiod*sampling_fac) ;
% sampling time(ps);  % time step (ps)
%nt = PRBSlength*num_samplesperbit*num_samplesperperiod*sampling_fac ;
% FFT length
%dBperkm = 0.2;       % loss (dB/km)
alpha_indB = 0.2;     % loss (dB/km)
D = 17e-6;            % NZDSF GVD (s/m^2); if anomalous dispersion (for
                      compensation),D is negative
%D = 17;              % SSMF GVD (ps/nm.km); if anomalous dispersion (for
                      compensation),D is negative

ng = 1.46;      % group index
n2 = 2.6e-20;   % nonlinear index (m^2/W)
Aeff = 80e-12;  % effective area (um^2)

% CALCULATED QUANTITIES

T = nt*dt;    % FFT window size in sec. (ps) -Agrawal: should be about
10-20 times of the pulse width
alpha_loss = log(10)*alpha_indB/10^4;  % alpha (1/m)
beta2 = D*lambda^2/(2*π*c);            % beta2 (s^2/m);
```

```
beta3 = 0.3e-39;                          % GVD slope (s^3/m)
%beta2 =0;
%-------------------------------------------------------------------
% beta 3 can be calculated from the Slope Dispersion (S) as follows:]
% Slope Dispersion S = 0.092;     % ps/(nm^2.km)
% beta31 = (S - (4*π*c./lambda.^3))./(2*π*c./lambda.^2)
%-------------------------------------------------------------------
gamma = 2*π*n2/(lambda*Aeff);     % nonlinearity coef (m^-1.W^-1)

% STARTING FIELD

L = nz*dz

Lnl = 1/(P0*gamma)              % nonlinear length (m)
Ld = halfwidth^2/abs(beta2)     % dispersion length (m)
N = sqrt(abs(Ld./Lnl))          % governing the which one is dominating:
dispersion or Non-linearities
ratio_LandLd = L/Ld             % if L << Ld --> NO Dispersion Effect
ratio_LandLnl = L/Lnl           % if L << Lnl --> NO Nonlinear Effect

% Monitor the broadening of the pulse with relative the Dispersion Length
% Calculate the expected pulsewidth of the output pulse
% Eq 3.2.10 in Agrawal "Nonlinear Fiber Optics" 2001 pp67

FWHM_new = FWHM*sqrt(1+(L/Ld)^2);

% N<<1 --> GVD ; N >>1 ---> SPM
Leff = (1-exp(-alpha_loss*L))/alpha_loss;
expected_normPout = exp(-alpha_loss*2*L);
NlnPhaseshiftmax = gamma*P0*Leff ;

betap = [0 0 beta2 beta3]';

% Constants for ASE of EDFA
% PSD of ASE: N(at carrier freq) = 2*h*fc*nsp*(G-1) with nsp = Noise
% Figure/2 (assume saturated gain)
%***************** Standard Constant ******************************
h = 6.626068e-34;   %Plank's Constant
%****************************************
```

13.10.3.2 Propagation of Optical Signals over a Single-Mode Optical Fiber—SSMF

```
function output = ssprop_matlabfunction_modified(input)
nt = input(1);
u0 = input(2:nt+1);
dt = input(nt+2);
dz = input(nt+3);
nz = input(nt+4);
alpha_indB = input(nt+5);
betap = input(nt+6:nt+9);
gamma = input(nt+10);
P_non_thres = input(nt+11)
```

```
maxiter = input(nt+12);
tol = input(nt+13);

tic;
%tmp = cputime;

% %-------------------------------------------------------------
% This function solves the nonlinear Schrodinger equation for
% pulse propagation in an optical fiber using the split-step
% Fourier method described in:
% Agrawal, Govind. Nonlinear Fiber Optics, 2nd ed.  Academic
% Press, 1995, Chapter 2
%
% The following effects are included in the model: group velocity
% dispersion (GVD), higher order dispersion, loss, and self-phase
% modulation (gamma).
%
% USAGE
%
% u1 = ssprop(u0,dt,dz,nz,alpha,betap,gamma);
% u1 = ssprop(u0,dt,dz,nz,alpha,betap,gamma,maxiter);
% u1 = ssprop(u0,dt,dz,nz,alpha,betap,gamma,maxiter,tol);
%
% INPUT
%
% u0 - starting field amplitude (vector)
% dt - time step - [in ps]
% dz - propagation stepsize - [in km]
% nz - number of steps to take, ie, ztotal = dz*nz
% alpha - power loss coefficient [in dB/km], need to convert to linear to
  have P=P0*exp(-alpha*z)
% betap - dispersion polynomial coefs, [beta_0 ... beta_m] [in ps^(m-1)/km]
% gamma - nonlinearity coefficient [in (km^-1.W^-1)]
% maxiter - max number of iterations (default = 4)
% tol - convergence tolerance (default = 1e-5)
%
% OUTPUT
%
% u1 - field at the output
%---------------
% Convert alpha_indB to alpha in linear domain
%---------------
alpha = 1e-3*log(10)*alpha_indB/10;     % alpha (1/km) - see Agrawal p57
%---------------

ntt = length(u0);

w = 2*π*[(0:ntt/2-1),(-ntt/2:-1)]'/(dt*nt);
%w = 2*π*[(ntt/2:ntt-1),(1:ntt/2)]'/(dt*ntt);

clear halfstep

halfstep = -alpha/2;
```

```
for ii = 0:length(betap)-1;
       halfstep = halfstep - j*betap(ii+1)*(w.^ii)/factorial(ii);
end

clear LinearOperator
% Linear Operator in Split Step method
LinearOperator = halfstep;
% pause
halfstep = exp(halfstep*dz/2);

u1 = u0;
ufft = fft(u0);

% Nonlinear operator will be added if the peak power is greater than the
% Nonlinear threshold
iz = 0;
while (iz < nz) & (max((abs(u1).^2 + abs(u0).^2)) > P_non_thres)
  iz = iz+1;

  uhalf = ifft(halfstep.*ufft);

  for ii = 1:maxiter,
    uv = uhalf .* exp(-j*gamma*(abs(u1).^2 + abs(u0).^2)*dz/2);
    ufft = halfstep.*fft(uv);
    uv = ifft(ufft);

    fprintf('You are using SSFM\n');

    if (max(uv-u1)/max(u1) < tol)
        u1 = uv;
        break;
    else
        u1 = uv;
    end
  end
  if (ii == maxiter)
    warning(sprintf('Failed to converge to %f in %d iterations',...
        tol,maxiter));

  end

  u0 = u1;
end
if (iz < nz) & (max((abs(u1).^2 + abs(u0).^2)) < P_non_thres)

% u1 = u1.*rectwin(ntt);

  ufft == fft(u1);
  ufft = ufft.*exp(LinearOperator*(nz-iz)*dz);
  u1 = ifft(ufft);
  fprintf('Implementing Linear Transfer Function of the Fiber
Propagation');
end
```

```
toc;
%*****************
% OUTPUT
%*****************
% u1 = u1(1:16);
%  angle_ifft_test = angle(u1)
%  pause
 output = u1;
```

13.10.3.3 BER Evaluation

```
clear Q_Gaussian BER_simple varied_threshold index_bit1 index_bit0 ...
       mean_bit1 mean_bit0 std_bit1 std_bit0;
%-----------------------------------------
Q_Gaussian = 0; % Initialise Q value
% Simple Q-factor calculation with assumption:
% Gaussian Noise distribution
%-----------------------------------------
%*************************************************
%*************************************************
% Assign variables from SimuLink to Matlab variables
%*************************************************
  delay = 32;

  % To determine received "1"
  index1_temp = find(Bernoulli==0);
  tmp1 = find(index1_temp > length(demodsignal)- delay);

  index1 = index1_temp(2:tmp1(1)-1);

  for i = 1 : length(index1)
    var_1(i) = demodsignal(delay+index1(i));
  end

  % To determine received "0"
  index0_temp = find(Bernoulli==1);
  tmp0 = find(index0_temp > length(demodsignal)-delay);

  index0 = index0_temp(2:tmp0(1)-1);

  for ii = 1 : length(index0)
    var_0(ii) = demodsignal(delay+index0(ii));
  end
% End
%*****************
Thres_Volt = 0;
%*****************

% % BER
% % Assume bit 1 and 0 have a Gaussian normal distribution
%   mean_bit1 = mean(var_1); % I1
%   std_bit1 = std (var_1) ; % sigma1
%
```

```
% mean_bit0 = mean(var_0); % I0
% std_bit0 =  std(var_0) ; % sigma2
% % Q-factor
% Q = (mean_bit1 - mean_bit0) / (std_bit1 + std_bit0) ;
%
% BER = 1/2 * (erfc(Q/sqrt(2))) ;

% Determine BER
% Determine Mean value of samples for bit 1
mean_bit1 = mean(var_1);
std_bit1 = std(var_1);

% Determine Mean value of samples for bit 0
mean_bit0 = mean(var_0);
std_bit0 = std(var_0);

% Calculation of Q-factor and BER
% Assumption: Gaussian approximation for the distributions of samples of
% bit 1 and bit 0
% Pe = P0*E(1/2 of erfc((S-X0)/sqrt(2)*sigma0) + P1*E(1/2 of ...
% erfc((S-X1)/sqrt(2)*sigma0)
```

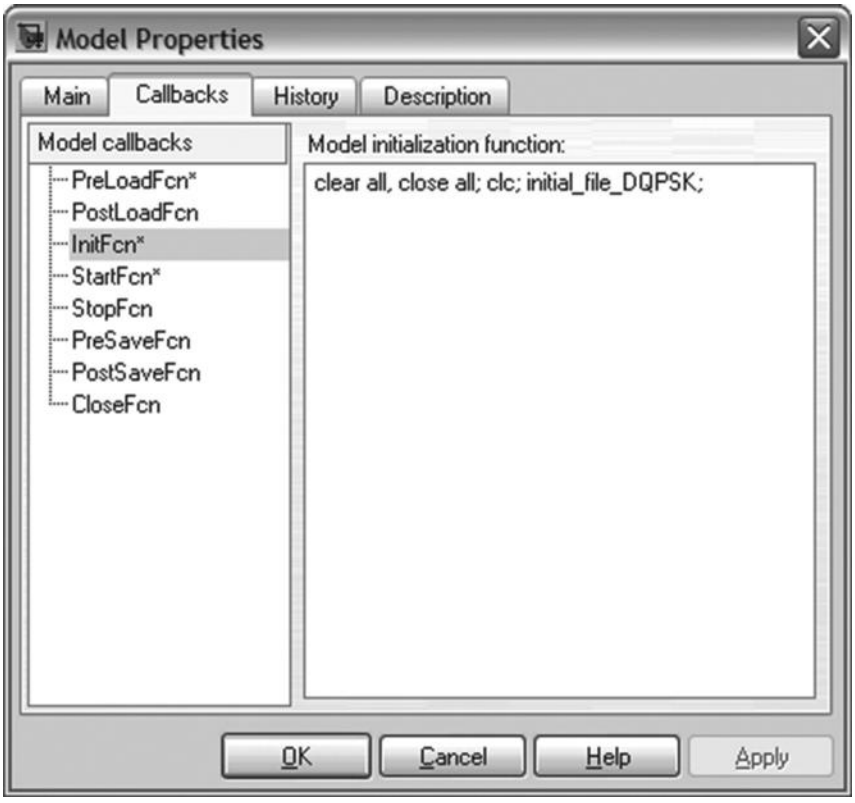

FIGURE 13.109
Model property and related .m files for model parameters.

```
BER_Gaussian = length(var_0)/length(Bernoulli(delay+1:le
ngth(Bernoulli)))* mean(1/2.*erfc(abs(Thres_Volt - var_0)./
(sqrt(2)*std_bit0))) + ...

length(var_1)/length(Bernoulli(delay+1:length(Bernoulli)))*
mean(1/2.*erfc(abs(var_1 - Thres_Volt)./(sqrt(2)*std_bit1)));

% clc
mean_bit1
mean_bit0
std_bit1
std_bit0
Q_Gaussian = sqrt(2)*erfcinv(BER_Gaussian*2)
BER_Gaussian
 BER_Gaussian_Agrawal = 1/2*(erfc(Q_Gaussian/sqrt(2)))
 Q_Gaussian = abs(mean_bit1 - mean_bit0)/(std_bit1 + std_bit0)
```

13.10.3.4 Linking Initialization File and Other Related Files Such as ssprop_matlab_modified.m with the Model

The initialization file is required to pass on the values of the parameters to the Simulink model by inserting these file names in the section "call back" of "model property" of Simulink model as shown in Figure 13.109. The fiber propagation .m file "ssprop_matlab-function_modified.m" must be included in the folder that contains the Simulink model for the model to call this function for execution.

References

1. T. Hoshida, O. Vassilieva, K. Yamada, S. Choudhary, R. Pecqueur, and H. Kuwahara, Optimal 40 Gb/s modulation formats for spectrally efficient long haul DWDM systems, *IEEE Journal of Lightwave Technology*, 20, 1989–1996, 2002.
2. T. Yagisawa and T. Ikeuchi, Compact 40-Gb/s EML module using broadband FPC connection technique, in *Proceedings of the Optical Fiber Communication Conference*, San Diego, CA, paper OthC3, March 21–25, 2010.
3. T. Tatsumi, K. Tanaka, S. Sawada, H. Fujita, and T. Abe, 1.3 μm, 56-Gbit/s EML module target to 400 GbE, in *Proceedings of the Optical Fiber Communication Conference*, Los Angeles, CA, paper OTh3F.4, March 4–8, 2012.
4. G.P. Agrawal, *Nonlinear Fiber Optics (Optics and Photonics)*, 4th ed., Elsevier, Burlington, VT, 2006.
5. Y. Zhu, K. Cordina, N. Jolley, R. Feced, H. Kee, R. Rickard, and A. Hadjifotiou, 1.6 bit/s/Hz orthogonally polarized CSRZ—DQPSK transmission of 8 × 40 Gbit/s over 320 km NDSF, in *Proceedings of OFC'04*, Los Angeles, CA, Tu-F1, 2004.
6. C. Wree, J. Leibrich, J. Eick, W. Rosenkranz, and D. Mohr, Experimental investigation of receiver sensitivity of RZ-DQPSK modulation using balanced detection, in *Proceedings of OFC'03*, Oklahoma City, OK, vol. 2, pp. 456–457, 2003.
7. C. Wree, RZ-DQPSK format with high spectral efficiency and high robustness towards fiber nonlinearities, University of Kiel, Kiel, Germany, 2002.
8. F.N. Hauske, Z. Zhang, C. Li, C. Xie, and Q. Xiong, Precise, robust and least complexity CD estimation, in *Proceedings of OFC'10*, San Diego, CA, paper JThA11, 2010.

9. D.N. Goddard, Self-recovering equalization and carrier tracking in two dimensional data communication systems, *IEEE Transactions on Communications*, 28, 1867–1875, November 1980.
10. A.J. Viterbi and A.M. Viterbi, Nonlinear estimation of PSK-modulated carrier phase with application to burst digital transmissions, *IEEE Transactions on Information Theory*, IT-29, 543–551, July 1983.
11. J.G. Proakis, *Digital Communications*, McGraw-Hill, New York, Chapter 6, p. 348, 2000.
12. J.G. Proakis, *Digital Communications*, 4th ed., McGraw-Hill, New York, Ch. 4, pp. 199–202, 2001.
13. T. Sakamoto, T. Kawanishi, and M. Izutsu, Initial phase control method for high-speed external modulation in optical minimum-shift keying format, in *Proceedings of ECOC'05*, Glasgow, U.K., vol. 4, pp. 853–854, 2005.
14. M. Ohm and J. Spiedel, Optical minimum shift keying with direct detection, *Proceedings of SPIE on Optical Transmission, Switching and Systems*, 5281, 150–161, 2004.
15. T.L. Huynh, L.N. Binh, and K.K. Pang, Optical MSK long-haul transmission systems, in *SPIE Proceedings of APOC'06*, Gwangju, South Korea, paper 6353-86, Thu9a, 2006.
16. T.L. Huynh, L.N. Binh, and K.K. Pang, Linear and weakly nonlinear optical continuous phase modulation formats for high performance DWDM long-haul transmission, in *Proceedings of ECOC'06*, Cannes, France, 2006.
17. J. Mo, D. Yi, Y. Wen, S. Takahashi, Y. Wang, and C. Lu, Optical minimum-shift keying modulator for high spectral efficiency WDM systems, in *Proceedings of ECOC'05*, Milan, Italy, vol. 4, pp. 781–782, 2005.
18. T.L. Huynh, L.N. Binh, K. K. Pang, and L. Chan, Photonic MSK transmitter models using linear and non-linear phase shaping for non-coherent long-haul optical transmission, in *SPIE Proceedings of APOC'06*, Gwangju, South Korea, paper 6353-85, 2006.
19. J.G. Proakis, *Digital Communications*, 4th ed., McGraw-Hill, New York, pp. 185–213, 2001.
20. L.N. Binh and T.L. Huynh, Linear and nonlinear distortion effects in direct detection 40 Gb/s MSK modulation formats multi-span optically amplified transmission, *Optics Communications*, 273, 352–361, 2007.
21. L.N. Binh, T.L. Huynh, and K.K. Pang, Direct detection frequency discrimination optical receiver for minimum shift keying format transmission, *IEEE Journal of Lightwave Technology*, 26(18), 3234–3247, September 15, 2008.
22. I.B. Djordjevic and B. Vasic, Multilevel coding in M-ary DPSK/differential QAM high-speed optical transmission with direct detection, *IEEE Journal of Lightwave Technology*, 24, 420–428, 2006.
23. M. Serbay, C. Wree, and W. Rosenkranz, Implementation of different precoder for high-speed optical DQPSK transmission, *Electronics Letters*, 40, 1–3, September 2004.
24. M. Seimetz, M. Noelle, and E. Patzak, Optical systems with high-order DPSK and star QAM modulation based on interferometric direct detection, *IEEE Journal of Lightwave Technology*, 25, 1515–1530, 2007.
25. H. Yoon, D. Lee, and N. Park, Performance comparison of optical 8-ary differential phase-shift keying systems with different electrical decision schemes, *Optic Express*, 13, 371–376, 2005.

14

Tbps Optical Transmission Systems: Digital Processing–Based Coherent Reception

14.1 Introduction

The demand for ultra-high capacity transmission networks led to intensive development and research on Tere-bits/s (Tb/s) transmission over long distance that would occupy minimum aggregate bandwidth. Thus, there is a need for (1) modulated channels that have a minimum bandwidth and are optimum in ISI with the maximum possible symbol rate reaching the limits of electronic processing and optical technology, and (2) multiple channels whose lightwave carriers are commonly generated and synchronized with the original laser source, the comb-generated laser lines.

The comb-generated carriers that can be used are

- 100 Gb/s × 10 comb generated carriers with 4 × 25 GS/s for 100 Gb/s by 2 polarization multiplexed channels with each modulated by QSPK at 25 GS/s, that is 2 pol. × 2 bits/symbol × 25 Gb/s to give 100 Gb/s. In practice instead of 25 GS/s, forward error coding (FEC) would be used; so, 28 GS/s may be used with 12% extra-bits.
- 200 Gb/s × 5 comb-generated carriers with 56 GS/s instead of 28 GS/s.
- 400 Gb/s × 5 to give 2 Tb/s with 56 GS/s and 16 QAM (4 bits/symbols).

Note that the number of comb generated carriers can reach 10, 20, and even near 100 over the whole C-band as reported in Ref. [1]. Further, pulse shaping can be implemented by employing Nyquist theoretical techniques so that any intersymbol interference (ISI) would be eliminated at the sampling time at the center of the eyes. This can be implemented using digital processors. The receivers are the coherent type incorporating analog to digital convertor (ADC) and digital signal processing (DSP) subsystems as described in Chapter 8. The transmitters for these Tb/s are described in Chapter 6 with two *I*–*Q* optical modulators based on $LiNbO_3$ multiplexed via a polarization combiner to generate polarization division multiplexed–quadrature phase-shift keying (PDM-QPSK) or PDM-QAM channels.

A generic flowchart of the digital signal process shown in Figure 14.1 is now introduced here with the clock/timing recovered signals are fed back into the sampling unit of the ADC so as to obtain the best timing for sampling the incoming data sequence to generate digitalized samples for processing in the DSP. Any errors made at this stage of timing would result in high deviation of the bit error rate (BER) in the symbol decoder shown in Figure 14.1. It is also noted that the Vertical polarized (V-pol.) and Horizontal polarized (H-pol.) channels are detected and their in-phase (*I*-) and quadrature (*Q*-)

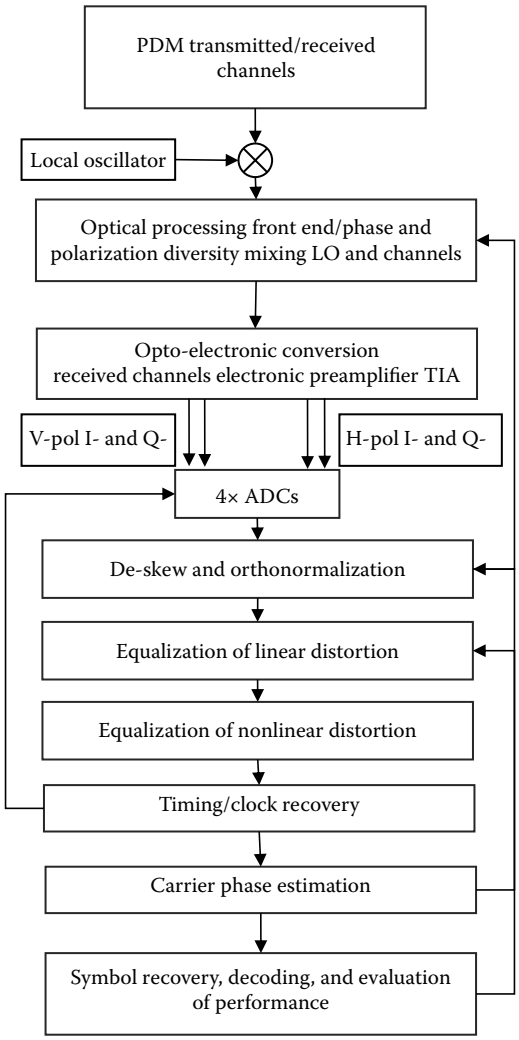

FIGURE 14.1
Flow of functionalities of DSP processing in a coherent optical receiver of a coherent transmission system. A modified diagram from Figure 6.1 with feedback path diverted to ADC.

components are produced in the electrical domain with signal voltage conditioned for the conversion to the digital domain by the ADC.

The processing of a sampled sequence from the received optical data and photo-detected electronic signals passing through the ADC relies on the timing of the recovery from the sampled events of the sequence. The flowing stages of the blocks given in Figure 14.1 may be changed or altered depending on the modulation formats and pulse shaping, for example, the Nyquist pulse shapes in Nyquist superchannel transmission systems.

This chapter attempts to illustrate the performance of the processing algorithms in optical transmission systems employing coherent reception techniques over the highly dispersive optical transmission line, especially the multispan optically amplified non-DCM long-haul distance. First, the QPSK homodyne scheme and then the 16 QAM incorporating both polarized channels multiplexed in the optical domain are examined; hence, the

terms PDM-QPSK or PDM-16 QAM. We then expand, in Section 14.3, the study for the superchannel transmission systems in which several subchannels are closely spaced in the spectral region so as to increase the spectral efficiency so that the total effective bit rate can reach at least 1 Tb/s. Because of the overlapping of adjacent channels, there are cross talks and modifications of the processing algorithms have to be made.

Further, the nonlinearity impairments on transmitted subchannels would degrade the system performance. Combining the two by linear and nonlinear equalization schemes in a back-propagation technique effectively combats these impairments. Algorithms useful for processing of received signals distorted by linear and nonlinear impairments are given briefly in Chapter 8. Further details on DSP algorithms can be found in Ref. [2].

14.2 Quadrature Phase Shift Keying Systems

14.2.1 Carrier Phase Recovery

Homodyne coherent reception requires a perfect match of the frequency of the signal carrier and the local oscillator (LO). Any frequency difference between these leads to phase noise of the detected signals. This was the largest hurdle for the first optical coherent system initiated in the mid-1980s. In DSP-based coherent reception systems, the recovery of the carrier phases, and hence the frequency, is critical to achieve the most sensitive reception with maximum performance in the BER or evaluation of the probability of error. This section illustrates the recovery of carrier phase for QPSK and 16 QAM optical transmission systems whose constellations feature a single circle or multilevel circular distribution. How would the DSP algorithms perform under the effects of the physical impairment to the recovery of the phase of the carrier?

14.2.2 112G QPSK Coherent Transmission Systems

Currently, several equipment manufacturers are striving to provide commercially advanced optical transmission systems at 100 Gb/s employing coherent detection techniques for long-haul backbone networks and metro networks as well. Since the 1980s, it is well known that single-mode optical fibers can support such transmissions because of the preservation of the guided modes and the polarized modes of the weakly guiding linearly polarized (LP) electromagnetic waves [3]. Naturally, both transmitters and receivers must satisfy the coherency conditions of narrow linewidth sources and coherent mixing with a local oscillator, an external cavity laser (ECL), to recover both the phase and amplitude of the detected lightwaves. Both polarized modes of the LP can be stable over long distances to provide the PDM channels, even with polarization mode dispersion (PMD) effects. All linear distortion due to PMD and chromatic dispersion (CD) can be equalized in the DSP domain employing algorithms in realtime processors.

It is thus very important to ensure that these subsystems perform the coherent detection and transmitting functions. This section thus presents a summary of the tests conducted with a back-to-back (B2B) transmission of QPSK PDM channels. The symbol rate of the transmission system is 28 Gsymbols/s (GS/s) under the modulation format PDM-CSRZ-QPSK. It is noted that the differential QPSK (DQPSK) encoder and the bit pattern generator are provided.

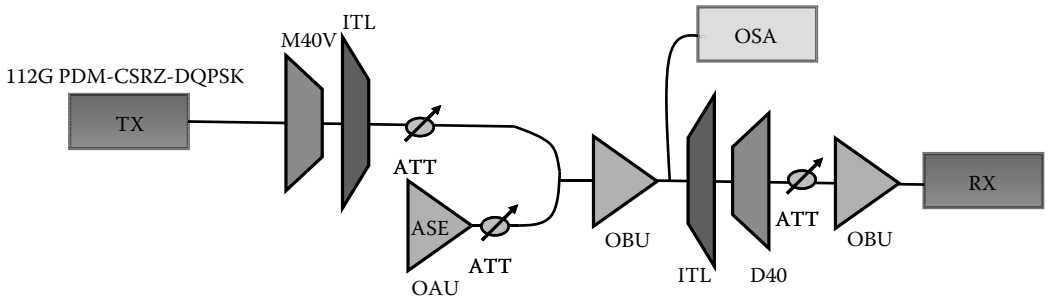

FIGURE 14.2
Setup of the PDM QPSK optical transmission system.

The transmission system is arranged as shown in Figure 14.2. The carrier suppressed return to zero (CSRZ) QPSK transmitter consists of a CSRZ optical modulator, which is biased at the minimum transmission point of the transfer characteristics of the MZIM, driven by sinusoidal signals whose frequency is half the symbol rate or 14 GHz for 28 GS/s. A wavelength-division multiplexed (WDM) mux (multiplexer) is employed to multiplex other wavelength channels located within the C-band (1530–1565 nm). An optical amplifier (EDFA [erbium doped fiber amplifier] type) is employed at the front end of the receiver so that noises can be superimposed on the optical signals to obtain the optical signal-to-noise ratio (OSNR). The DSP-processed signals in the digital domain are carried out off-line, and the BER is obtained.

The transmitter consists of an ECL, an encore type, a polarization splitter coupled with a 45° aligned ECL beam, two separate CS-RZ external $LiNbO_3$ modulators and then two *I*–*Q* optical modulators. The linewidth of the ECL is specified at about 100 kHz, and with external modulators we can see that the spectrum of the output modulated light waves is dominated by the spectrum of the baseband modulation signals. However, we observed that the laser frequency is oscillating about 300 MHz as a result of the integration of a vibrating grating so as to achieve stability of the optical frequency.

The receivers employed in this system are two types. One is a commercialized type, Agilent N4391 in association with an Agilent external local oscillator (LO), the other one is a transimpedance amplifier (TIA) type including a photodetector pair connected back-to-back in a push–pull manner and a broadband TIA. In addition to the electronic reception part, a $\pi/2$ hybrid coupler including a polarization splitter, $\pi/2$ phase shift and polarization combiner that mixes the signal-polarized beams and those of the LO (an ECL type identical to the one used in the transmitter) is employed as the optical mixing subsystem at the front end of the receiver. The mixed polarized beams (*I*–*Q* signals in the optical domain) are then detected by balanced receivers. *I*–*Q* signals in the electrical domain are sampled and stored in the realtime oscilloscope (Tektronix 7200). The sampled *I*–*Q* signals are then processed off-line using the algorithms provided in the scope or self-developed algorithms such as the evaluation of EVM described earlier for the *Q* factor and the BER.

Both the transmitter and receivers function with the required OSNR for a back-to-back (B2B) of about 15 dB at a BER of 2e−3. It is noted that the estimation of the amplitude and phase of the received constellation is quite close to the received signal power and the noise contributed by the balanced receiver with a small difference, because of the quantum shot noise contributed by the power of the LO. The estimation technique was described in Chapter 4. Figure 14.3 shows the BER versus OSNR for B2B QPSK PDM channels. As shown in Figure 14.4 the variation of BER as a function of the signal energy

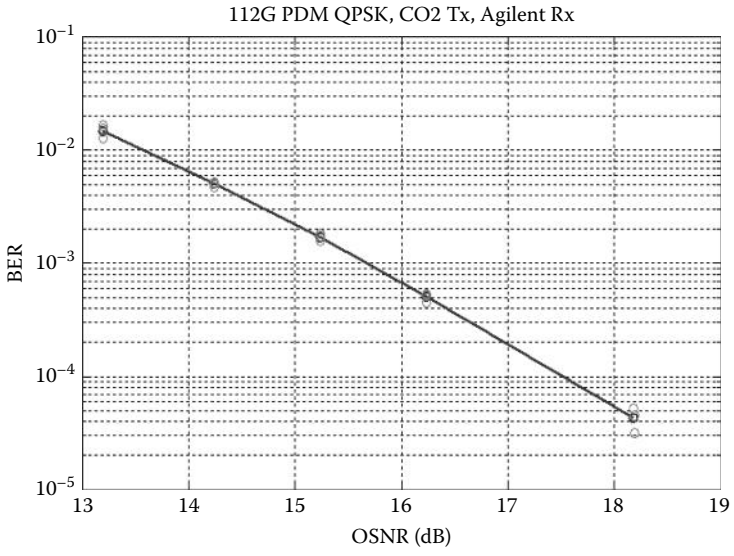

FIGURE 14.3
B2B OSNR versus BER performance with Agilent Rx in 112Gb/s PDM-CSRZ-DQPSK system.

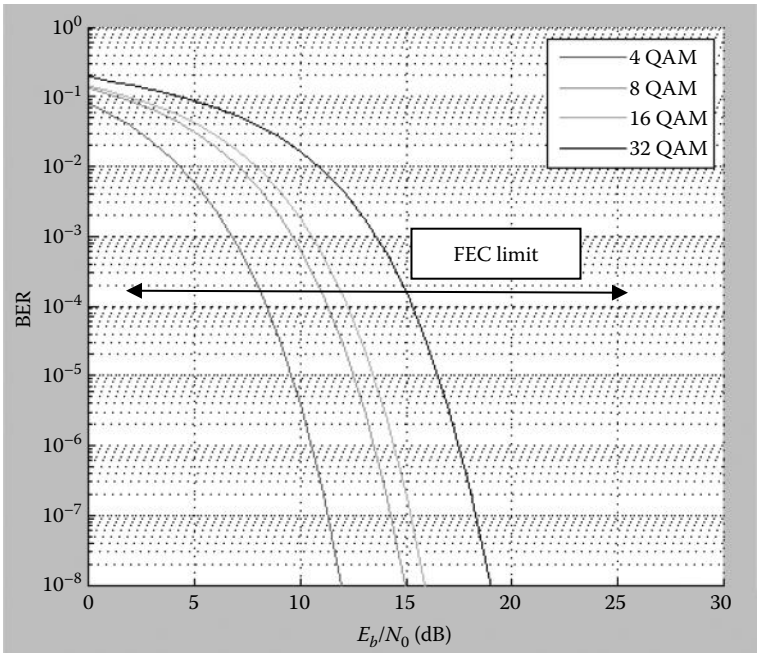

FIGURE 14.4
Theoretical BER versus SNR for different level QAM scheme obtained by bertool.m of MATLAB®.

over noise for arbitrary white Gaussian noise (AWGN) noise, for 4-QAM or QPSK coherent then the SNR is expected to be at about 8 dB for BER of 1e−3. Experimental processing of such schemes in B2B configuration shows an OSNR of about 15.6 dB. This is due to the 3 dB split by the polarized channels and additional noises contributed by the receiver; hence, about 15.6 dB OSNR is required. The FEC is set at 1e−3. The receiver is the Agilent type as mentioned earlier.

A brief analysis of the noises at the receiver gives the following results. The noise is dominated by the quantum shot noise generated by the power of the LO which is about at least 10 times greater than that of the signals. Thus, the quantum shot noises generated at the output of the photodetector are

$$
\begin{aligned}
&i_{N-LO}^2 = 2qI_{LO}B \\
&I_{LO} = 1.8 \text{ mA at } 0.9 - PD\_\text{quantum}\_\text{efficiency} \\
&B = 31 \text{ GHz} - BW\_U^2t\_\text{Agilennt}\_\text{Rx} \\
&i_{N-LO}^2 = 2\times10^{-19}\times1.8\times10^{-3}\times30\times10^{9} \\
&\qquad = 10.8\times10^{-12} \\
&\longrightarrow i_{N-LO} = 3.286 \text{ μA}
\end{aligned}
$$

The bandwidth of the electronic preamplifier of 31 GHz is taken into account. This shot noise current is due to the LO imposed on the PD pair and is compatible with that of the electronic noise of the electronic receiver given that the noise spectral density equivalent at the input of the electronic amplifier of the U^2t balanced receiver is specified at 80 pA/$\sqrt{\text{Hz}}$, that is,

$$\left(80\times10^{-12}\right)^2\times30.10^9 = 19.2\times10^{-12}A^2 \xrightarrow[\text{noise\_current}]{} i_{Neq.} = 4.38 \text{ μA}$$

Any variation in the LO would affect this shot noise in the receiver. It is thus noted that with the transimpedance of the electronic preamplifier estimated at 150 Ω, a dBm difference in the LO would contribute to a change in the voltage noise level of about 0.9 mV in the signal constellation obtained at the output of the ADC. A further note is that the noise contributed by the electronic front end of the ADC has not been taken into account. We note that differential TIA offers at least 10 times higher transimpedance of around 3000 Ω over 30 GHz midband. These TIAs offer much higher sensitivities as compared to single-input TIA type [4,5].

14.2.3 *I–Q* Imbalance Estimation Results

There are imbalances resulting from the propagation of the polarized channels and the *I*- and *Q*-components. They must be compensated to minimize the error. The *I–Q* imbalance of the Agilent BalRx and U^2t BalRx is less than 2 degrees, which might be negligible for the system as shown in Figure 14.5. This imbalance must be compensated for in the DSP domain.

14.2.4 Skew Estimation

In addition to the imbalance of the *I*- and *Q*-components because of optical coupling and electronic propagation in high-frequency cables, there are propagation delays—time

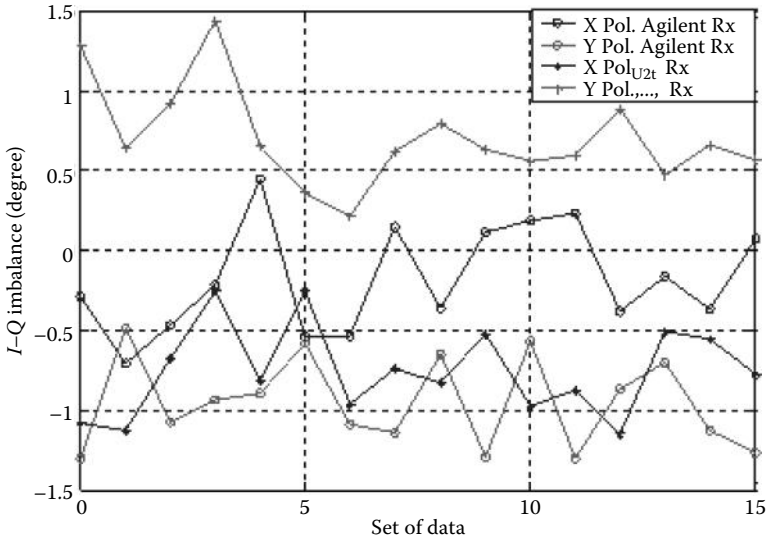

FIGURE 14.5
I–Q imbalance estimation results for both Rx. Note maximum imbalance phase of $\pm 1.5^0$.

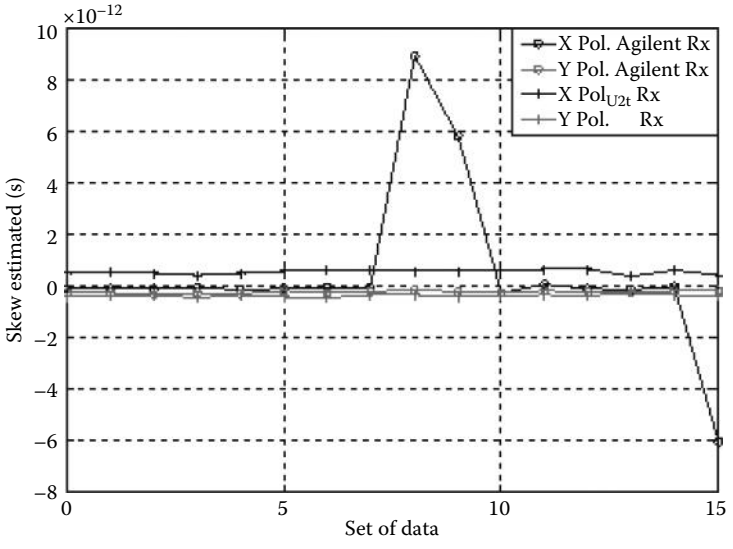

FIGURE 14.6
Skew estimation results for both types of Rx.

difference between these components—that must be compensated. The skew estimation shown in Figure 14.6 is obtained over a number of datasets.

Abnormal skew variation from time to time was also observed, which should not happen if there is no modification of the hardware. Consider the skew variation in the Agilent receiver, which has a very short RF cable and a tight connection. There is a high probability that the skew occurred inside the Tektronix oscilloscope rather than at the optical or electrical connection outside.

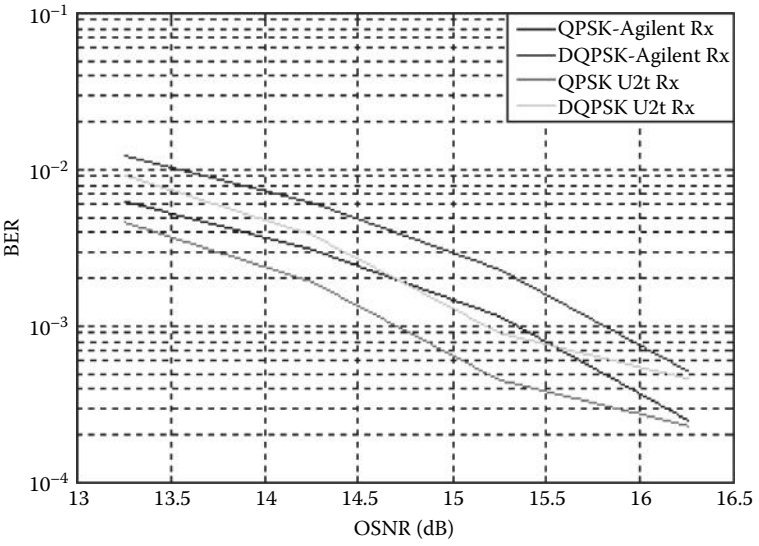

FIGURE 14.7
OSNR versus BER for two types of integrated coherent receiver after compensating *I*–*Q* imbalance and skew.

Figure 14.7 shows the BER versus the OSNR when the skew and the imbalance between *I*- and *Q*-components of the QPSK transmitter are compensated. The OSNR of DQPSK is improved by about 0.3–0.4 dB at 1e−3 BER compared to the result without *I*–*Q* imbalance and skew compensation. In the time domain, comparing with the result that we obtained in 2009, the required OSNR of DQPSK at a BER of 1e−3 is about 14.7 dB, that is, improved by 0.1 dB. The required OSNR at 1e−3 BER of QPSK is about 14.7 dB, which is around the standard performance of the state of the art for QPSK. For a *BER* = 1e−3, an imbalanced CMRR = −10 dB would create a penalty of 0.2 dB in the OSNR for the Agilent receiver and an improvement of 0.7 dB for a commercial balanced receiver employed in the Rx subsystems (Figure 14.8).

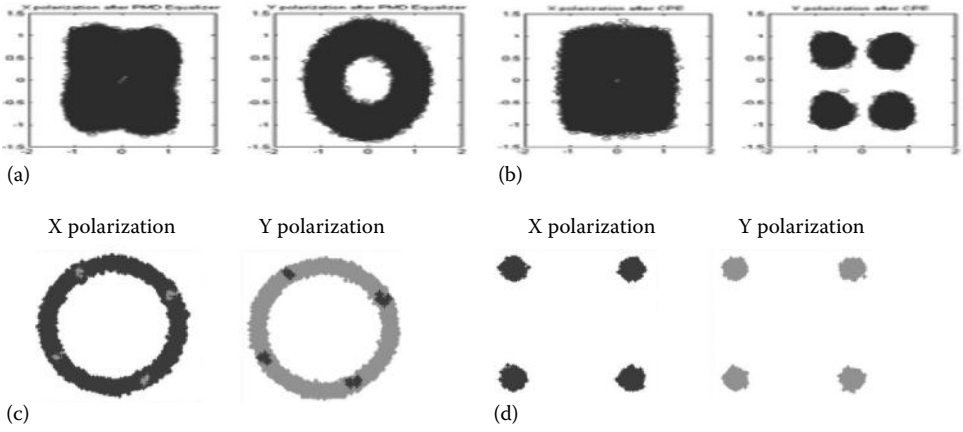

FIGURE 14.8
Constellation after PMD module (a) and after applying CPE algorithm module (b) and low noise scenarios at the receiver (c) XX_Y polarized channels before and after (d) compensation. Scale on the real and imaginary axes is the same but arbitrary.

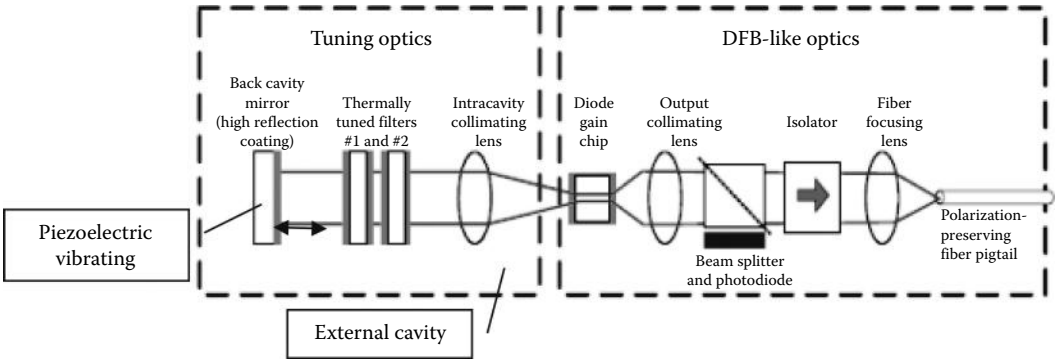

FIGURE 14.9
External cavity structure of the laser with the back mirror vibration in the external cavity structure.

Figure 14.9 shows the structure of the ECL incorporating a reflecting mirror, which is vibrating at a low frequency of around 300 MHz. A control circuit is included to indicate the electronic control of the vibration and cooling of the laser so as to achieve stability and to eliminate the stimulated Brillouin scattering (SBS) effects.

14.2.5 Fractionally Spaced Equalization of CD and PMD

Ip and Kahn [6] have employed the fractional spaced equalization scheme with mean square error (MSE) to evaluate the effectiveness of PDM amplitude shift keying (ASK) with nonreturn to zero (NRZ) or return to zero (RZ) pulse shaping transmission systems. Their simulation results are displayed in Figure 14.10 for the maximum allowable CD (normalized in ratio with respect to the dispersion parameter of the single-mode fiber as defined in Chapter 2) versus the number of equalizer taps N for a 2 dB power penalty launched at an OSNR of 20 dB per symbol for ASK RZ and NRZ pulse shapes, with sampling rate $1/T = M/KT_s$; T_s = symbol_period, with M/K as the fractional ratio, as shown in Figure 14.10 for a fractional ratio of (a) $M/K = 1$, (b) 1.5, and (c) 2 using a Bessel antialiasing filter, and (d through f, with M/K of 1, 1.5 and 2 correspondingly) using a Butterworth antialiasing filter. The sampling antialiasing filter is employed to ensure that artificial fold back to the spectrum is avoided. The filter structures of Bessel and Butterworth exhibit similar performance for fractional spaced equalizers but less tap for the Bessel filtering cases when equally spaced equalizers are used (see Figure 14.10a and d).

14.2.6 Linear, Nonlinear Equalization and Back-Propagation Compensation of Linear and Nonlinear Phase Distortion

Ip and Kahn [7] first developed and applied back propagation as given in Chapter 2 to equalize the distortion resulting from nonlinear impairment of optical channels in transmission through the single-mode optical fibers. The back-propagation algorithm is simply a reverse phase rotation at the end of each span of the multispan link. The rotating phase is the equivalent of the phase exerted on the signals in the frequency domain with a dependence on the square of the frequency. Thus, this back propagation is efficient in that the

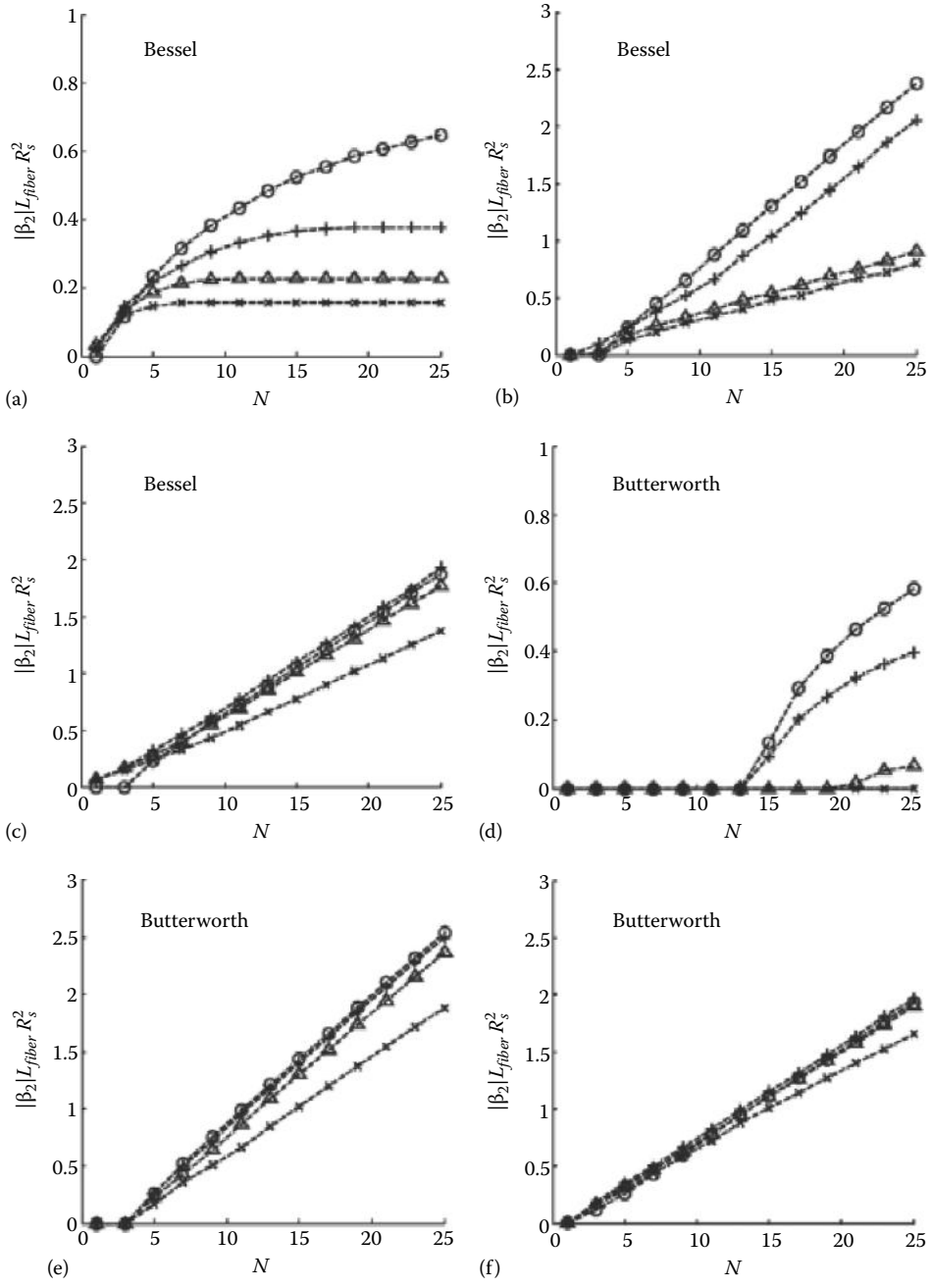

FIGURE 14.10
Maximum allowable CD versus the number of equalizer taps N for a 2 dB power penalty at an input SNR of 20 dB per symbol for RZ and NRZ pulse shapes, using a Bessel antialiasing filter. "o" denotes transmission using NRZ pulses, "x" denotes 33% RZ, "Δ" denotes 50% RZ, and "+" denotes 67% RZ, by fractional spaced equalizer (FSE) and sampling rate R_s $1/T = M/KT_s$; T_s = symbol_period. M/K is the fractional ratio: (a) $M/K = 1$, (b) 1.5 and (c) 2, (d–f) using a Butterworth antialiasing filter. The modulation scheme is ASK with NRZ and RZ pulse shaping. N = number of taps of the equalizer. (After Ip, E. and Kahn, J.M., *IEEE J. Lightwave Tech.*, 25(8), 2033, August 2007. With permission.)

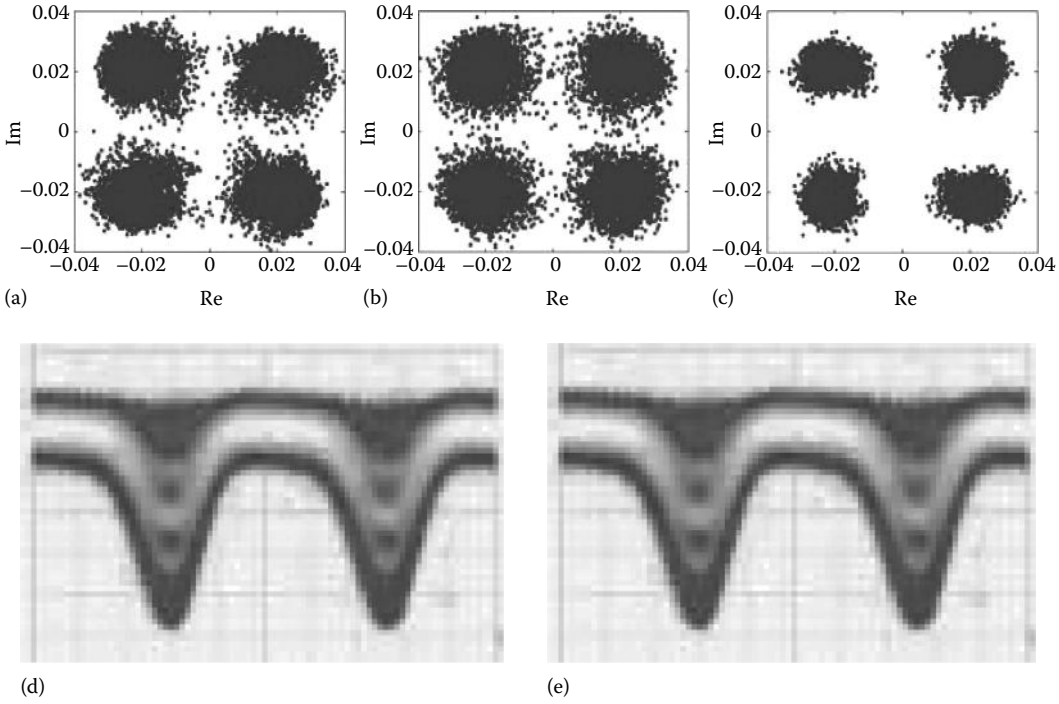

FIGURE 14.11
Constellation of QPSK scheme as monitored at (a) with linear CD equalization only, (b) nonlinear phase noise compensation, and (c) after back-propagation processing combining with linear equalization. (d and e) Experimental observation of two polarized channels by a sampling oscilloscope—direct detection optical ports. (From Weiner, J.S. et al., *IEEE J. Solid-State Circ.*, 38(9), 1512, 2003.)

whole span can be compensated so as to minimize the numerical processes, thereby reducing processing time and the central processing unit time of the digital signal processor.

Figure 14.11 shows the equalized constellations of a 21.4 Gsystems/s QPSK modulation scheme system after transmission through 25 × 80 km non-DCF spans under the equalization using (a) linear compensation only, (b) nonlinear equalization, and (c) using combined back-propagation and linear equalization. Obviously, the back propagation contributes to the improvement of the performance of the system. The eye diagrams of both polarized channels obtained by direct detection via a sampling oscilloscope optical port are shown in Figure 14.11d and e, which confirm the right modulation formats of QPSK.

Figure 14.12 shows the phase errors of the constellation states at the receiver versus the launched power of 25 × 80 km multispan QPSK 21.4 Gsystems/s transmission system. The results extracted from Ref. [5] shows the performance of back-propagation phase rotation per span for 21.4 Gb/s 50% RZ-QPSK transmitted over 25 × 80 km spans of SMF with five reconfigurable optical add-drop module (ROADMs), with 10% CD under-compensated. The algorithm is processed off-line of received sampled data after 25 × 80 km SSMF propagation by using the nonlinear Schrodinger equation (NLSE) and coherent reception technique described in Chapter 4. It is desired that the higher the launched power the better the OSNR that can be employed for longer-distance transmission. Fractional space ratios of 3 and 4 offer higher launched power and are, therefore, the preferred equalization schemes as compared with equal space or sampling rates equal to that of the symbol rate.

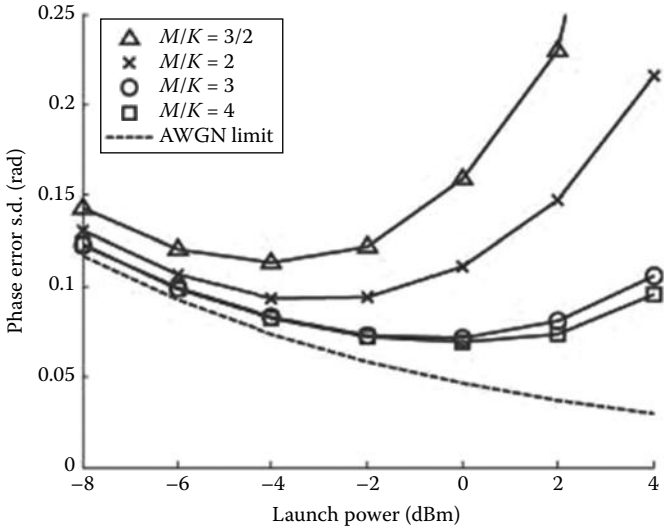

FIGURE 14.12
Phase errors at the receiver versus launched power or 25 × 80 km multispan QPSK at 21.4 Gsystems/s. Performance of back-propagation phase rotation per span for 21.4 Gb/s 50% RZ-QPSK transmitted over 25 × 80 km spans of SMF with five ROADMs, with 10% CD under-compensation using fractionally spaced equalizer with M/K factor of 1.5–4. (From Weiner, J.S. et al., *IEEE J. Solid-State Circ.*, 38(9), 1512, 2003. With permission.)

The ROADM is used to equalize the power of the channel under consideration as compared with other DWDM channels.

14.3 16 QAM Systems

Consider the 16-QAM received symbol signal whose phase Φ denoting the phase offset. The symbol d_k denotes the magnitude of the QAM symbols and n_k as the noises superimposed on the symbol at the sampled instant. The received symbols can be written as

$$r_k = d_k e^{j\phi} + n_k; \quad k = 1, 2, \ldots, L \tag{14.1}$$

Using the maximum likelihood sequence estimator (MLSE), the phase of the symbol can be estimated as

$$l(\phi) = \sum_{k=1}^{L} \ln \left\{ \sum_{d} e^{-\frac{1}{2\sigma^2}\left|r_k - de^{j\phi}\right|^2} \right\} \tag{14.2}$$

or effectively one would take the summation of the contribution of all states of the 16-QAM on the considered symbol measured as the geometrical distance in the natural logarithmic scale with the noise contribution of a standard deviation σ.

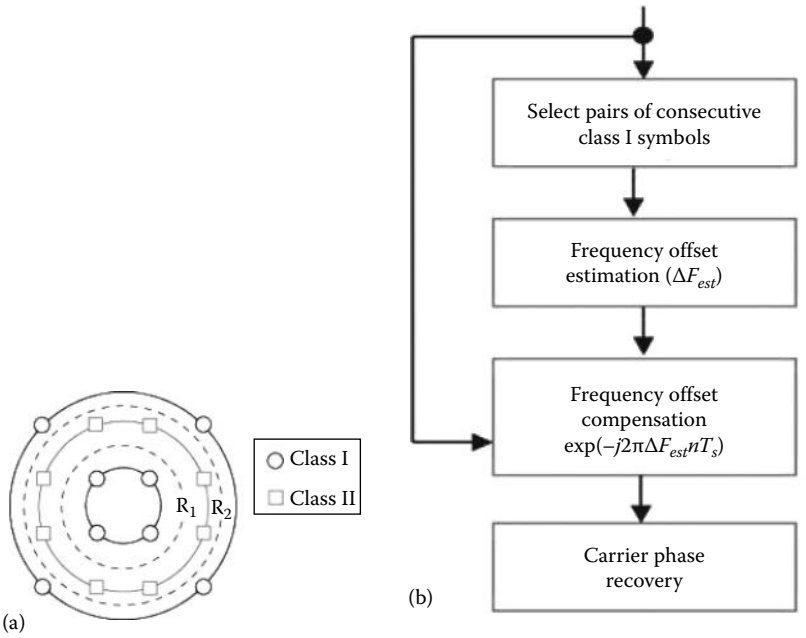

FIGURE 14.13
Processing of 16 QAM for carrier phase estimation. (a) Constellation of 16-QAM. (b) Processing for carrier phase recovery with classes I and II of circulator subconstellation. (From Fatadin, I. and Savory, S.J., *IEEE Photon. Tech. Lett.*, 23(17), 1246, 2001.)

The frequency offset estimation for 16-QAM can be conducted by partitioning the 16 QAM constellations into a number of basic QPSK constellations as shown in Figure 14.13. There are two QPSK constellations in the 16 QAM whose symbols can be extracted from the received sampled dataset. They are then employed to estimate the phase of the carrier as described in the previous section on carrier phase estimation for QPSK-modulated transmission systems. At first, a selection from the innermost QPSK constellation is taken, classified as Class I symbols, and then an estimation of the frequency offset of the 16 QAM transmitted symbols is made. An FO compensation algorithm is then processed. The phase recovery of all 16 QAM symbols is thus derived. Further confirmation of the difference in carrier phase recovery or estimation can be obtained with the constellation of Class I as indicated in Figure 14.13a.

Carrier phase recovery based on the Viterbi–Viterbi algorithm on the Class I QPSK subconstellation of the 16 QAM may not be sufficient, so a modified scheme has been reported by Fatadin et al. [9]. This estimation of the carrier phase for 16 QAM by partitioning and rotating is further refined so as to match certain symbol points to those of the Class I constellation of the 16 QAM. The procedures are as shown in the flow diagram of Figure 14.14.

Classifying the carrier phase into different classes of constellations and then rotate the Class 2 symbols in either the clockwise or anticlockwise direction by an angle of $\pm\theta_{rot} = \pi/4 - \tan^{-1}(1/3)$. To avoid rotation in a direction opposite to the real direction, the estimation of the error in the rate of change of the phase variation or frequency estimation can be

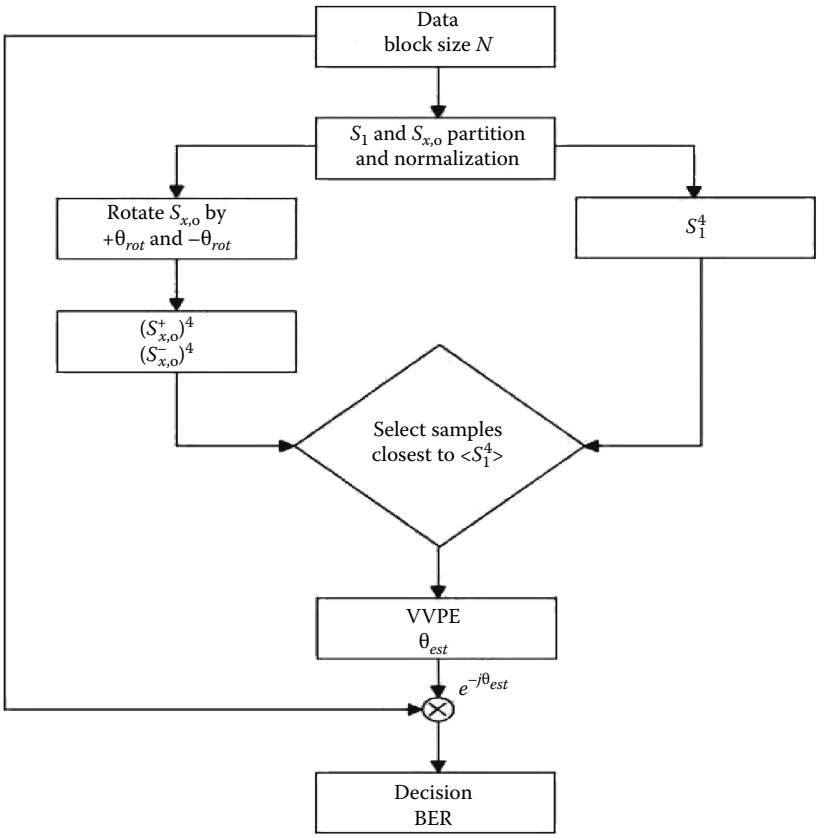

FIGURE 14.14
Refined carrier phase recovery of 16 QAM by rotation of class I and class II subconstellations.

found by the use the fourth power of the argument of the angles between two consecutive symbols, given by

$$\Delta F_{est.} = \frac{1}{8\pi T_s} \arg\left(\sum_{k=0}^{N} S_{k+1} S_k \right)^4 \tag{14.3}$$

Check their quadratic mean, then select the closer symbol, then apply the standard Viterbi–Viterbi procedure. Louchet et al. [10] also employed a similar method and confirmed the effectiveness of such a scheme. The effects on the constellation of the 16 QAM because of the different physical phenomena are shown in Figure 14.15. Clearly, the FO would generate the phase noises in (a) and influence both the *I*- and *Q*-components by the CD of a small amount (so as to see the constellation noises) and the delay of the polarized components on the *I*- and *Q*-components. These distortions of the constellation allow practical engineers to assess the validity of algorithms that are normally separate and independent and are implemented in serial mode. This is in contrast to the constellations illustrated for QPSK as shown in Figure 14.8. Figure 14.16 also shows the real-time signals that result from the beating of the two sinusoidal waves of FO beating in a real-time oscilloscope.

Noe et al. [11] have simulated the carrier phase recovery for QPSK with polarization multiplexed (PDM) channels under constant modulus algorithm (CMA) and

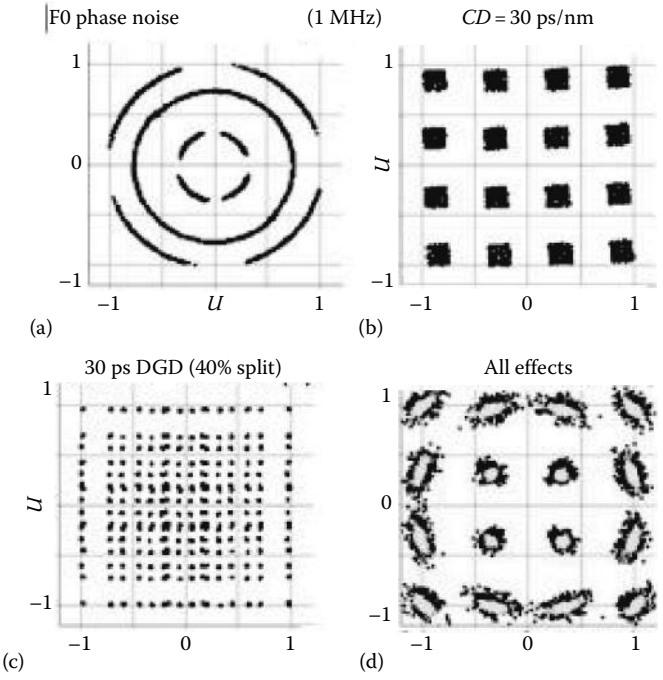

FIGURE 14.15
16 QAM constellation under the influence of (a) phase rotation due to FO of 1 MHz and no amplitude distortion, (b) residual CD impairment, (c) DGD of PMD effect, and (d) total phase noises effect. (Adapted from Ip, E. and Kahn, J.M., *IEEE J. Lightwave Tech*., 25(8), 2033, August 2007.)

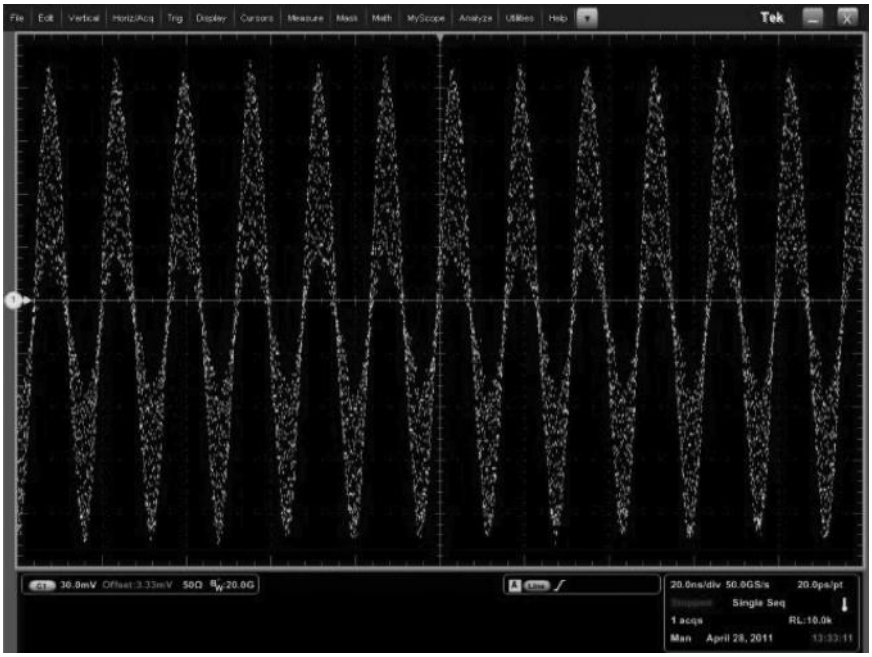

FIGURE 14.16
Beating signals of the two mixed lasers as observed by realtime sampling oscilloscope.

decision directed (DD) with and without modification in which the error detected at each stage is updated. The transmission system under consideration is B2B with superimposition of white Gaussian noises and phase noises on the signals. For an OSNR of 11 dB, the CMA with modification offers a BER of 1e–3 while it is 4e–2 for CMA without modification. This indicates that the updating of the matrix coefficients is very critical to recover the original data sequence. The modified CMA was also recognized to be valid for 16 QAM.

14.4 Tb/s Superchannel Transmission Systems

14.4.1 Overview

PDM-QPSK has been exploited as the 100 Gb/s long-haul transmission commercial system; the optimum technology for 400 GE/1TE transmission for next generation optical networking is now attracting significant interest for deploying ultra-high capacity information over the global internet backbone networks. Further intense research on Tbps transmission systems has also attracted several research groups as the logical rate to increase from 100 Gb/s. The development of hardware platforms for 1–*N* Tb/s is critical for proving the design concept. The Tbps can be considered as a superchannel that is defined as an optical channel comprising a number of subrate subchannels whose spectra would be the narrowest allowable. To achieve efficient spectral efficiency, phase shaping is required and one of the most efficient techniques is Nyquist pulse shaping. Nyquist QPSK can be considered as the most effective format for delivery of high spectral efficiency and is effective in coherent transmission and reception as well as equalization at both the transmitting and reception ends.

In this section, we describe in detail a design and experimental platform for delivery of Tbps using Nyquist-QPSK at a symbol rate of 28–32 GSa/s and 10 subcarriers. The generation of subcarriers has been demonstrated using either recirculating frequency shifting (RFS) or nonlinear driving of an *IQ* modulator to create five subcarriers per main carrier, and hence requiring two main carriers. Nyquist pulse shaping is used to effectively pack multiplexed channels whose carriers are generated by the comb generation technique. A digital to analog converter (DAC) with sampling rate varying from 56G to 64 GS/s is used for generating the Nyquist pulse shape including the equalization of the transfer functions of the DAC and optical modulators.

14.4.2 Nyquist Pulse and Spectra

The raised-cosine filter is an implementation of a low-pass Nyquist filter, that is, one that has the property of vestigial symmetry. This means that its spectrum exhibits odd symmetry about $1/2T_s$, where T_s is the symbol period. Its frequency domain representation is the "brick-wall-like" function, given by

$$H(f)=\begin{cases} T_s & |f|\le \dfrac{1-\beta}{2T_s} \\ \dfrac{T_s}{2}\left[1+\cos\left(\dfrac{\pi T_s}{\beta}\left\{|f|-\dfrac{1-\beta}{2T_s}\right\}\right)\right] & \dfrac{1-\beta}{2T_s}<|f|\le\dfrac{1+\beta}{2T_s} \\ 0 & \text{otherwise} \end{cases} \tag{14.4}$$

with $0\le\beta\le 1$

This frequency response is characterized by two values: β, the *roll-off factor* (ROF), and T_s, the reciprocal of the symbol rate in Sym/s, that is, $1/2T_s$ is the half bandwidth of the filter. The *impulse response* of such a filter can be obtained by analytically taking the inverse Fourier transformation of (14.4), in terms of the normalized *sinc* hyperbolic function, as

$$h(t) = \sin c\left(\frac{t}{T_s}\right)\frac{\cos\left(\frac{\pi\beta t}{T_s}\right)}{1-\left(2\frac{\pi\beta t}{T_s}\right)^2} \tag{14.5}$$

where the ROF, β, is a measure of the *excess bandwidth* of the filter, that is, the bandwidth occupied beyond the Nyquist bandwidth as from the amplitude at $1/2T$. Figure 14.17 depicts the frequency spectra of raised cosine pulse with various ROFs. Their corresponding time domain pulse shapes are given in Figure 14.18.

When used to filter a symbol stream, a Nyquist filter has the property of eliminating ISI, as its impulse response is zero at all nT (where n is an integer), except when $n = 0$. Therefore, if the transmitted waveform is correctly sampled at the receiver, the original symbol values can be recovered completely. However, in many practical communication systems, a matched filter is used at the receiver, so as to minimize the effects of noises.

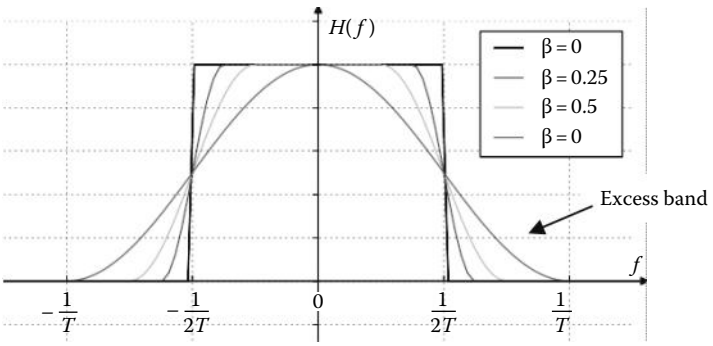

FIGURE 14.17
Frequency response of raised-cosine filter with various values of the ROF β.

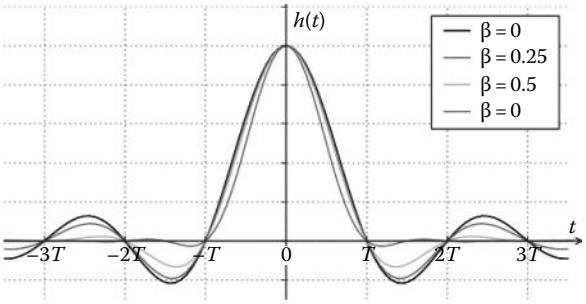

FIGURE 14.18
Impulse response of raised-cosine filter with the ROF β as a parameter.

For zero ISI, the net response of the product of the transmitting and receiving filters must equate to $H(f)$, thus we can write

$$H_R(f)H_T(f) = H(f) \tag{14.6}$$

Or alternatively, we can rewrite that

$$|H_R(f)| = |H_T(f)| = \sqrt{|H(f)|} \tag{14.7}$$

The filters which can satisfy the conditions of (14.7) are the root-raised-cosine (RRC) filters. The main problem with RRC filters is that they occupy a larger frequency band than that of the Nyquist *sinc* pulse sequence. Thus, for the transmission system, we can split the overall raised cosine filter with RRC filter at both the transmitting and receiving ends, provided the system is linear. This linearity is to be specified accordingly. An optical fiber transmission system can be considered to be linear if the total power of all channels is under the nonlinear self phase modulation (SPM) threshold limit. When it is over this threshold, a weakly linear approximation can be used (Figure 14.19).

The design of a Nyquist filter influences the performance of the overall transmission system. Oversampling factor, selection of ROF for different modulation formats, and finite impulse response (FIR) Nyquist filter design are key parameters to be determined. If the transfer functions of the overall transmission channel including fiber, wavelength selective switch (WSS), and the cascade of the transfer functions of all O/E components are taken into account, the total channel transfer function is more Gaussian like. To compensate this effect in the Tx-DSP, one would thus need a special Nyquist filter to achieve the overall frequency response equivalent to that of the rectangular or raised cosine with ROF shown in Figure 14.20.

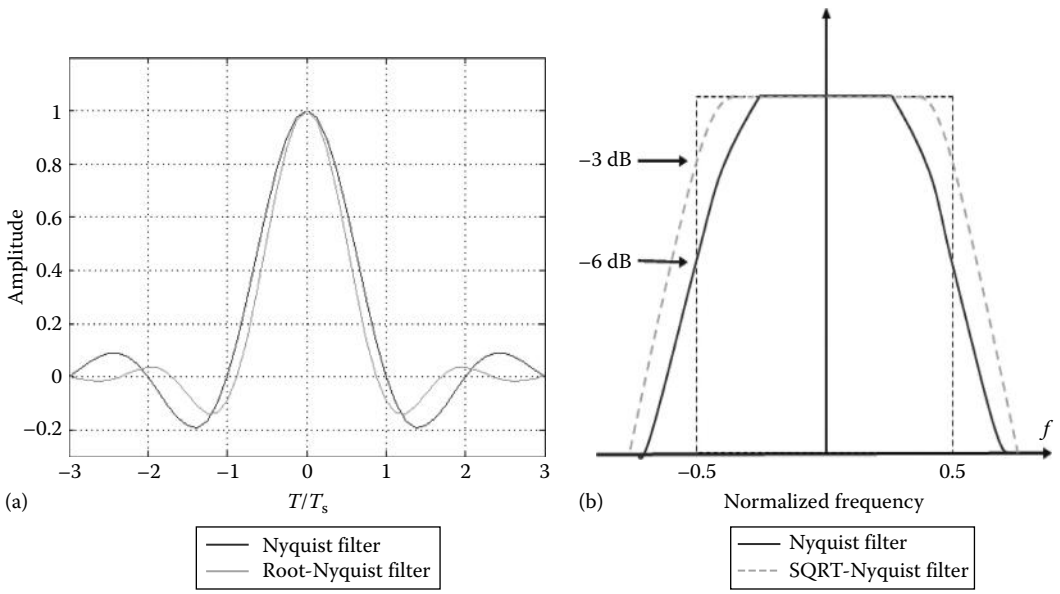

FIGURE 14.19
(a) Impulse and (b) corresponding frequency response of *sinc* Nyquist pulse shape or RRC Nyquist filters.

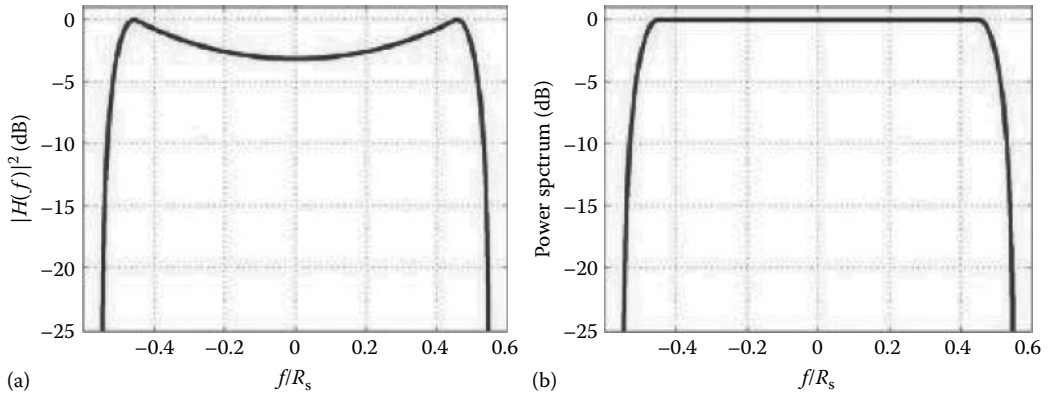

FIGURE 14.20
(a) Desired Nyquist filter for spectral equalization and (b) output spectrum of the Nyquist filtered QPSK signal.

14.4.3 Superchannel System Requirements

Transmission distance: As the backbone of the next generation of transport, the transmission distance should be comparable to the previous generation, namely 100 Gb/s transmission system. As the most important requirement, we require the 1 Tb/s transmission for long haul should be 1500–2000 km, for metro application ~300 km.

CD tolerance: As SSMF fiber CD factor/coefficient 16.8 ps/nm is the largest among the current deployed fibers, CD tolerance should be up to 30,000 ps/nm at the central channel whose wavelength is approximated at 1550 nm. At the edge of C-band, this factor is expected to increase by about 0.092 ps/(nm^2·km) or about 32,760 ps/nm at 1,560 nm and 26,400 ps/nm at 1,530 nm [12].

PMD tolerance: The worse case of deployed fiber with 2000 km would have a differential group delay (DGD) of 75 ps or about a three symbol periods for 25 Gsystems/s per subchannel. So, the PMD (mean all-order DGD) tolerance is 25 ps.

SOP rotation speed: According to the 100 Gb/s experiments, SOP rotation can be up to 10 kHz; we take the same spec as for the 100 G system.

Modulation format: PDM-QPSK for long-haul transmission; PDM-16 QAM for metro application.

Spectral efficiency: Compared to 100G system with an increasing of factor 2, both Nyquist-WDM and coherent orthogonal frequency division multiplexing (CO-OFDM) can fulfill this. However, the technological and economical requirements would determine the suitability of the technology for optical network deployment.

Table 14.1 tabulates the system specifications of various transmission structures with parameters of subsystems, especially when the comb generators are employed using either recirculating or nonlinear generation techniques. The DSP reception and off-line digital signal processing are integrated in these systems.

14.4.4 System Structure

14.4.4.1 DSP-Based Coherent Receiver

A possible structure of a superchannel transmission system can be depicted in Figure 14.21. At the transmitter, the data inputs can be inserted into the pulse shaping and individual data streams can be formed. A DAC can be used to shape the pulse with Nyquist equivalent shape, the raised cosine form whose spectra also follow a raised cosine with the

TABLE 14.1

1 Tb/s Off-Line System Specifications

Parameter Technique	Superchannel: RCFS Comb Gen.	Superchannel: Nonlinear Comb Gen.	Some Specs	Remarks
Bit rate	1, 2, …, N Tbps (whole C-band)	1 Tb/s, 2, …, N Tbps	~1.28 Tb/s at 28–32 GB	20% OH for OTN, FEC.
Number of ECLs	1	$N \times 2$		
Nyquist roll-off α	0.1 or less	0.1 or less		DAC pre-equalization is required.
Baud rate (GBauds)	28–32	28–32	28, 30, or 31.5 GBaud	Pending on FEC coding allowance.
Transmission distance	2500	2500	1200 (16 span) ~ 2000 km (25 spans) 2500 km (30 spans)	20% FEC req. for long-haul application.
			500 km	Metro application.
Modulation format	QPSK/16 QAM	QPSK/16 QAM	Multicarrier Nyquist WDM PDM-DQPSK/QAM	For long haul.
				For long haul.
			Multi-carrier Nyquist WDM PDM-16 QAM	For metro.
Channel spacing			4 × 50 GHz	For long haul.
			2 × 50 GHz	For long haul.
Launch power	≪0 dBm if 20 Tb/s is used		~ −3 to 1 dBm lower if $N > 2$	Depending on QPSK/16 QAM and long haul/metro can be different.
B2B ROSNR at 2e−2 (BOL) (dB)	14.5	14.5	15 dB for DQPSK	1 dB hardware penalty.
			22 dB for 16 QAM	1 dB narrow filtering penalty.
Fiber type	SSMF G.652 or (G.655)	SSMF G.652 (or 655)	G.652 SSMF	
Span loss	22	22	22 dB (80 km)	
Amplifier	EDFA ($G > 22$ dB); $NF < 5$ dB		EDFA (OAU or OBU)	
BER	2e−3	2e−3	Pre-FEC 2e−2 (20%) or 1e−3 classic FEC (7%)	
CD penalty (dB)			0 dB at ±3000 ps/nm <0.3 dB at ±30,000 ps/nm	16.8 ps/nm/km and 0.092 ps/(nm^2·km).
PMD penalty (DGD)			0.5 dB at 75 ps, 2.5 symbol periods	
SOP rotation speed	10 kHz	10 kHz	10 kHz	OPLL may be required due to oscillation of the LO carrier.
Filters cascaded penalty			<1 dB at 12 ps WSS	
Driver linearity	Required	Required	THD < 3%	16 QAM even more strict.

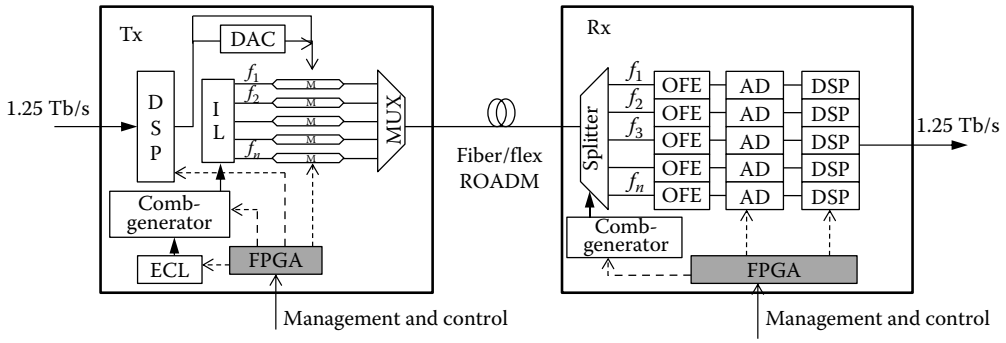

FIGURE 14.21
A possible structure of superchannel Tbps transmission system.

roll-off factor β varying from 0.1 to 0.5. If this off factor takes the value of 0.1, the spectra would follow the shape of a rectangle approximately. A comb generator can be used to generate equally spaced subcarriers for the superchannel from a single-carrier laser source, generally an ECL of very narrow band of linewidth of about 100 kHz. These comb-generated subcarriers (see Figure 14.22) are then demultiplexed into subcarriers and fed into a bank of *I*–*Q* optical modulators as described in Chapter 3 and Nyquist-pulse shape pulse sequences, as output of the DAC, are then employed to modulate these subcarriers to form the superchannels at the output of an optical multiplexer shown in the block at the left side of Figure 14.21. More details of the transmitter for superchannels are shown in Figure 14.23. It is to be noted that the generation of a comb source can be recirculation of the shifting of the original carrier around the closed loop. The frequency shift is the spacing frequency between the subcarriers. So, the *N*th subcarrier would be the *N*th time circulation of the original carrier. There would be superimposing of noises due to the ASE incorporated in the loop; this would be minimized by inserting into the loop an optical filter whose band width would be the same or wider than that of the superchannel.

The fiber transmission line is an optically amplified optical fiber multispan without incorporating any dispersion compensating fibers. Thus, the transmission is very dispersive. The broadening of a 40 ps width pulse would be spread across at least 80–100 symbol periods after propagating over 3000 km of SSMF. One can assume that the pulse launched into the fiber of the first span would be considered to be an impulse as compared to that after 3000 km SSMF propagation.

After the propagation over the multispan non-DCF line, the transmitted subchannels are demuxed via a wavelength splitter into individual subchannels, with minimum crosstalk. Each subchannel is then coherently mixed with an LO which is generated from another comb source incorporating an OPLL to lock the comb into that of the subcarriers of the superchannel. Thus, a comb generator is indicated on the right side, the reception system of Figure 14.21. The coherently mixed subchannels are then detected by a balanced receiver (as described in Chapter 4 and Section 14.2), then electronically amplified and fed into the sampler and ADC. The digital signals are then processed in the DSP of each subchannel systems or parallel and interconnected DSP system. In these DSPs, the sequence of processing algorithms is employed to recover the carrier phase and hence, the clock recovery, compensating for the linear and nonlinear dispersions, and the evaluation of the BER versus different parameters such as OSNR. Figure 14.24 shows the modulated spectra of five channels whose subcarriers are selected from the multiple-subcarrier source of Figure 14.22. The modulation is QPSK with Nyquist pulse shaping.

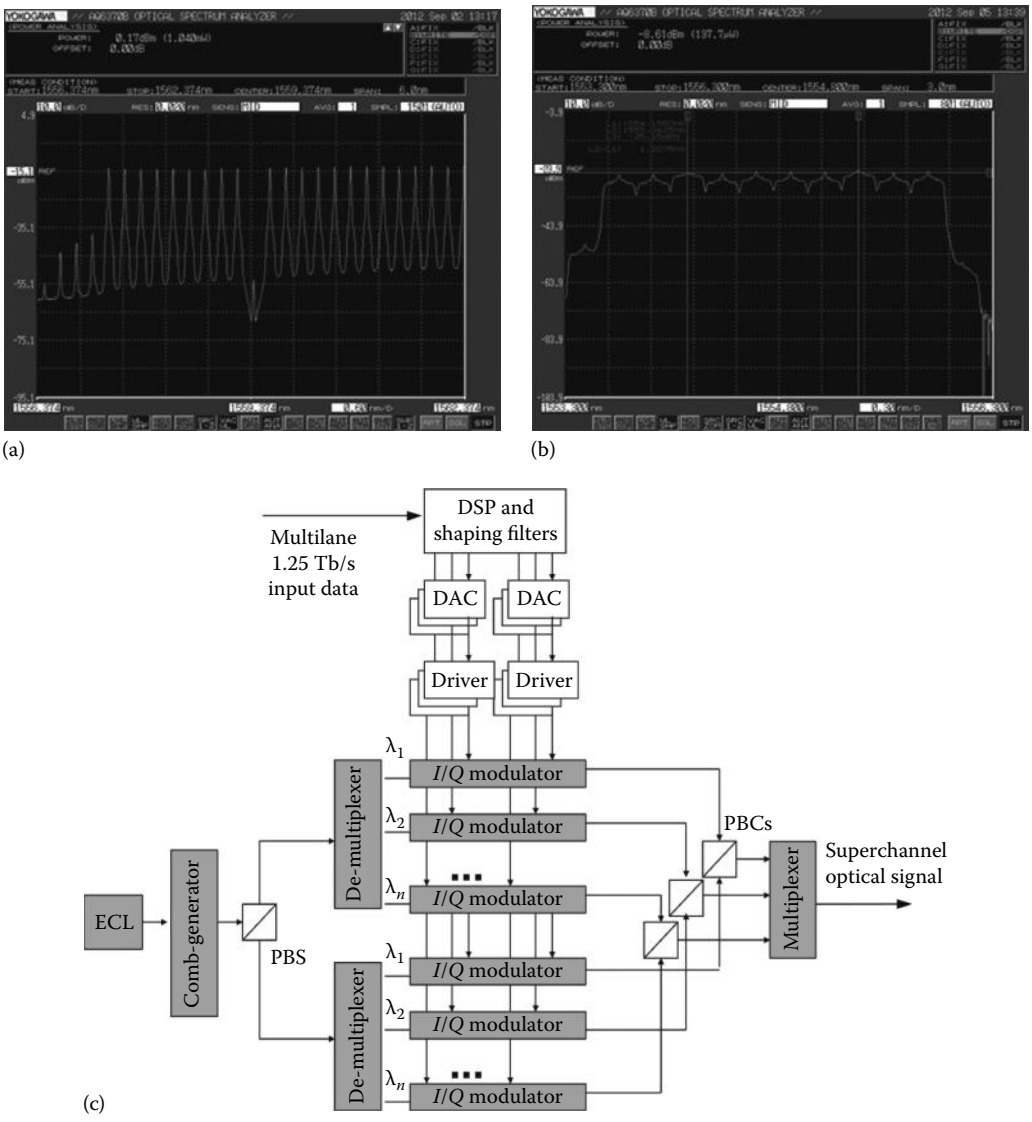

FIGURE 14.22
Block diagram of a recirculating frequency-shifting comb generator (a), a typical generated spectrum of the comb generator (b) with 28 GHz spacing between channels over more than 5 nm in spectral region and about 30 dB carrier-to-noise ratio (CNR), and (c) digital circuit diagram of the optical transmitter using optical comb generation sources.

14.4.4.2 Optical Fourier Transform–Based Structure

Superchannel transmission systems can also be structured using optical fast Fourier transform (OFFT) as demonstrated in Ref. [13] and shown in Figure 14.25 in which MZDI components (see Figure 14.25a) act as the spectral filter and splitter (see Figure 14.25b), the optical FFT. The outputs of these MZDI are then fed into coherent receivers and processed digitally as in Figure 14.25c with the electro-absorption modulator (EAM) performing the switching function so as to adjust the demultiplexing time, the ultra-fat signal speed, to lower speed sequence so that the detection system can decode and convert to the digital domain for further processing.

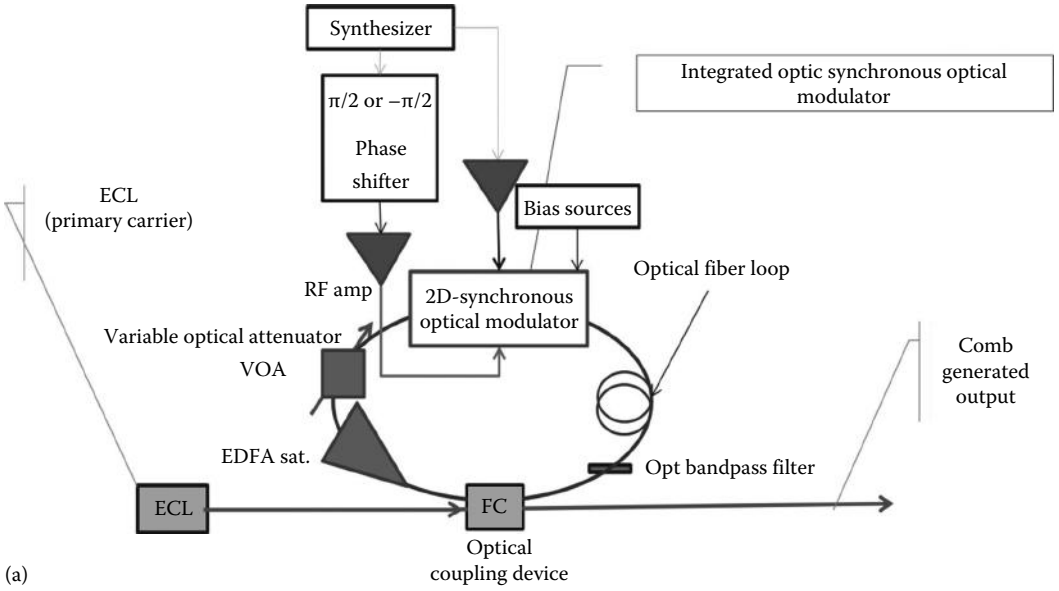

(a)

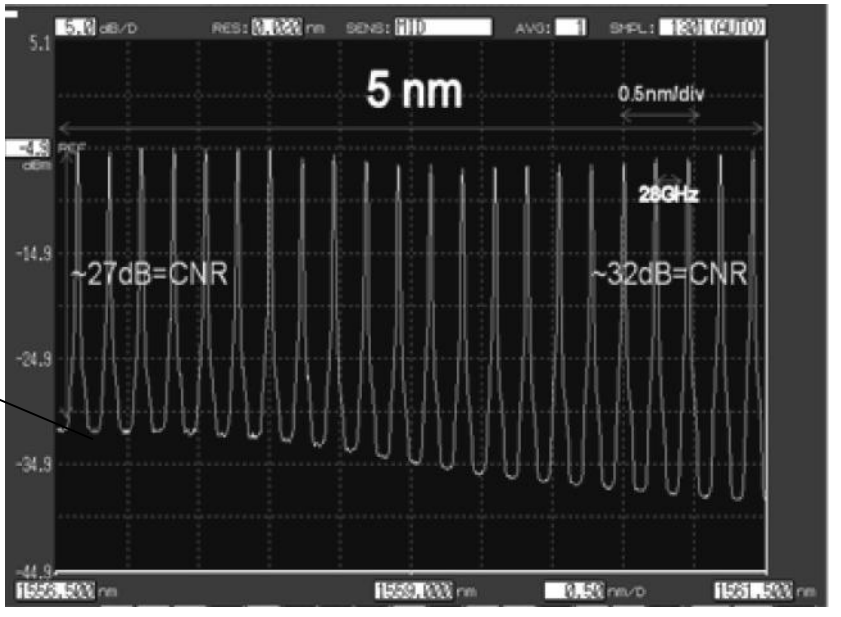

(b)

FIGURE 14.23
Generic detailed architecture of a superchannel transmitter, (a) schematic of the comb generator, and (b) spectrum of comb generator at output. PBC, polarization beam combiner; PBS, polarization beam splitter; *I*/*Q*, in-phase–quadrature phase; DAC, digital to analog convertor; ECL, external cavity laser.

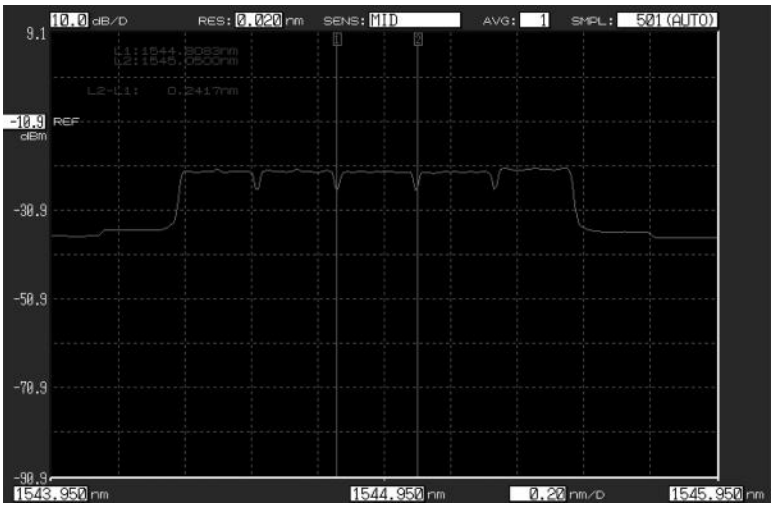

FIGURE 14.24
Selected five subcarriers with modulation.

The spectra of superchannels at different positions in the transmission system can be seen in Figure 14.26a through c. It is noted that the pulse shape is Nyquist and the subchannels are placed close and satisfying the orthogonal condition, thus the name optical orthogonal frequency division multiplexing (OFDM) is used to indicate this superchannel arrangement.

14.4.4.3 Processing

The processing of superchannels can be considered as similar to the digital processing of individual subchannels except when there may be cross talk between subchannels because of overlapping of certain spectral regions between the considered channel and its adjacent channels.

For the Nyquist QPSK subchannel, the DSP processing would be much the same as for QPSK DWDM for 112G described earlier taking care of the overlapping either at the transmitter or at the receiver. The error vector magnitude is a parameter that indicates the scattering of the vector formed by the *I*- and *Q*-components departing from the center of the constellation point. The variance of this EVM in the constellation plane is used to evaluate the noises of the detected states, from which the *Q* factor can be evaluated with ease as also the BER by using the probability density function and the magnitude of the vector of a state on the constellation plane. The BER of the subchannels of the OFDM superchannel is shown in Figure 14.27b and c [9] for different percentage overloading due to FEC. The loading factor is important as this will increase the speed or symbol rate of the subchannel one has to offer. The higher this percentage, the higher the increase in the symbol rate and hence, requiring high-speed devices and components.

In the receiver of the optical OFDM superchannel system of Ref. [9], to judge the effectiveness of the optical FFT receiver, three alternative receiver concepts were tested for a QPSK signal. A QPSK signal was chosen because it was not possible to receive a 16 QAM signal with the alternative receivers owing to their inferior performance [9]. First, a subcarrier with a narrow bandpass filter was used to extract a subchannel. The filter passband is adjusted for the best performance of the received signal (Figures 14.26a and 14.27). The selected filter

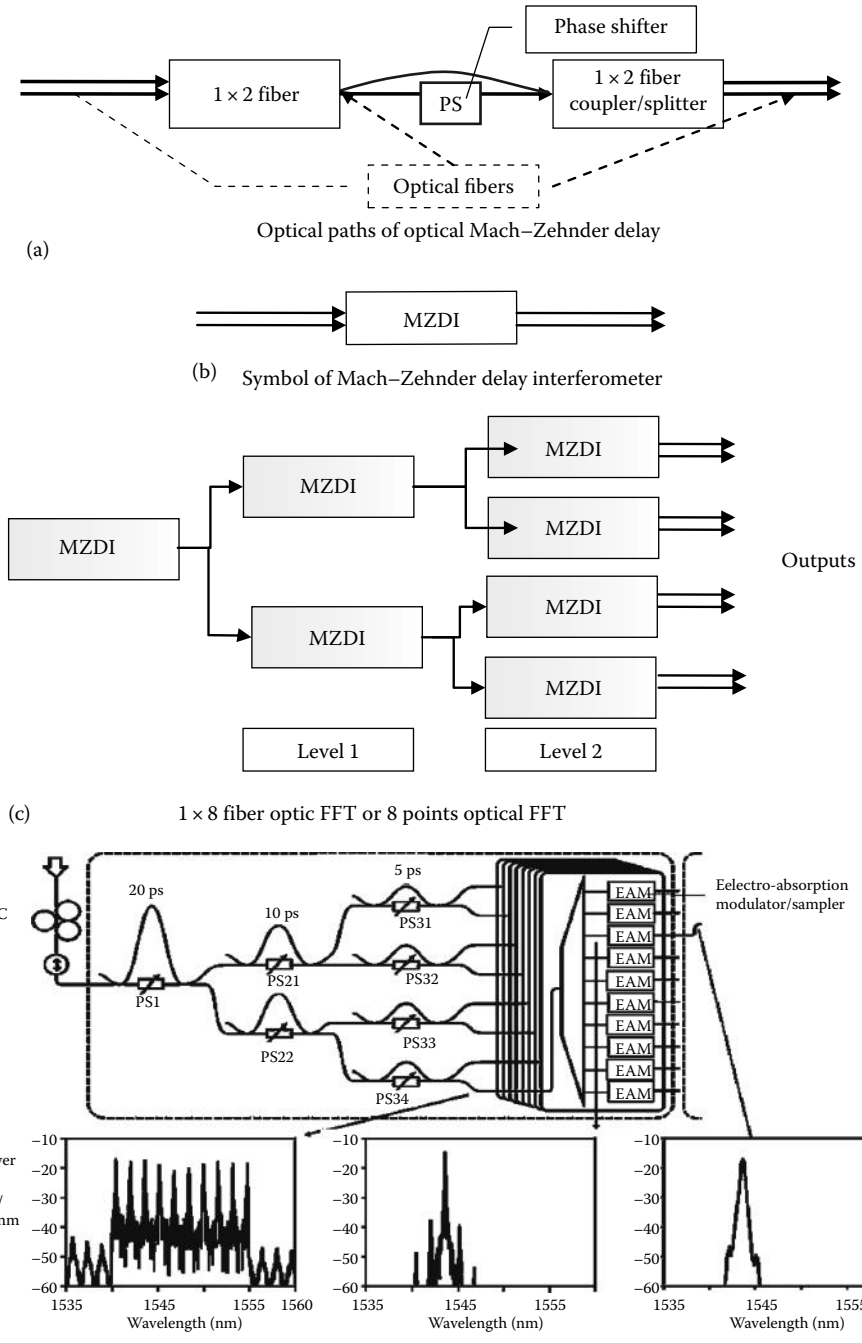

FIGURE 14.25

Operations by guided wave components using fiber optics (a) guided wave optical path of a Mach–Zehnder delay interferometer or asymmetric interferometer with phase delay tuneable by thermal or electro-optic effects, (b) block diagram representation, (c) implementation of optical FFT using cascade stages of fiber optical MZDI structure, and (d) optical spectra monitored at different position of the optical FFT. EAM = electro-absorption modulator used for demultiplexing in time domain. Note also phase shifters employed in MZDIs between stages. Inserts are spectra of optical signals at different stages as indicated by the optical FFT (serial type). EAM = electro-absorption modulator; PC = polarization controller. (Extracted from [14].)

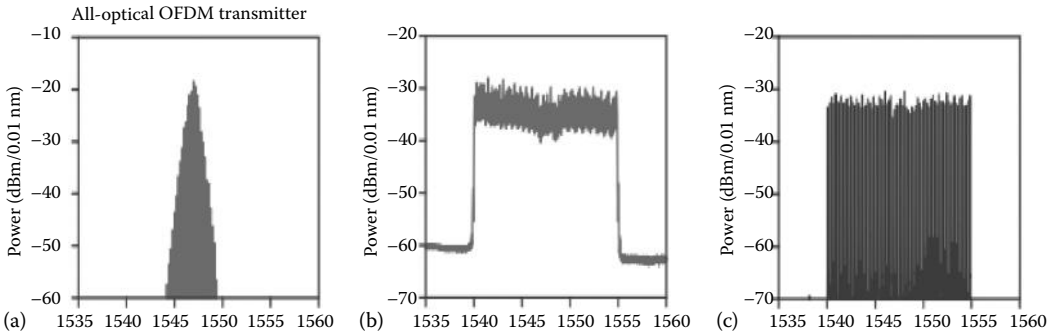

FIGURE 14.26
Spectrum of superchannels and demuxed channels. All subchannels are orthogonal and thus the name OFDM. (a) At output of transmitter, (b) after fiber propagation, and (c) after polarization demux. (Extracted from Fatadin, I. et al., *IEEE Photon. Tech. Lett*., 22(9), 631, 2010. With permission.)

bandwidth is 25 GHz. The constellation diagram showed severe distortion. When using narrow optical filtering, one has to accept a compromise between cross talk from neighboring channels (as modulated OFDM subcarriers necessarily overlap) and ISI owing to the increasing length of the impulse response when narrow filters are used. Narrow filters can be used, however, if the ringing from ISI is mitigated by additional time gating. The reception of a subcarrier using a coherent receiver is then performed. In the coherent receiver, the signal is down converted in a hybrid coupler as described in Chapter 5, and detected using balanced detectors and sampled in a real-time oscilloscope. Using a combination of error low-pass filtering due to the limited electrical bandwidth of the oscilloscope and digital signal processing, the subcarrier is extracted from the received signal. This receiver performs better than the filtering approach, but a larger electrical bandwidth and sampling rate of the ADC and additional DSP would be needed to eliminate the cross talk from other subcarriers to achieve a performance similar to that of the optical FFT.

Thus, optical OFDM may offer significant advantages for the superchannel, but additional processing time would be required, whereas Nyquist QPSK superchannels allow better performance and less complexity in the receiver DSP subsystem structure.

14.4.5 Timing Recovery in Nyquist QAM Channel

Nyquist pulse shaping is one of the efficient methods to pack adjacent subchannels into superchannel. The timing recovery of such Nyquist subchannel is critical for sampling the data received and improving the transmission performance. Timing recovery can be done either before or after the PMD compensator. The phase detector scheme is shown in Figure 14.28, a Godard type [15] which is a first-order linear scheme. After CD compensation (CD^{-1} blocks), the signal is sent to a state-of-polarization (SOP) modifier to improve the clock extraction. The clock performance of NRZ QPSK signal in the presence of a first-order PMD characterized by a DGD and azimuth is presented in Figure 14.3. The azimuth of 45° and DGD of a half symbol/unit interval (UI) completely destroy the clock tone. Therefore, the SOP modifier is required to enable the clock extraction. In practical systems, a raised cosine filter is used to generate Nyquist pulses. A filter pulse response is defined by two parameters, the ROF β, and the symbol period T_s and described by taking the inverse Fourier transform of Equation 14.4. The Godard phase detector cannot recover the carrier phase even with small β; thus, the channel spectra are close to rectangular. A higher-order phase detector must be used to effectively recover the timing clock period

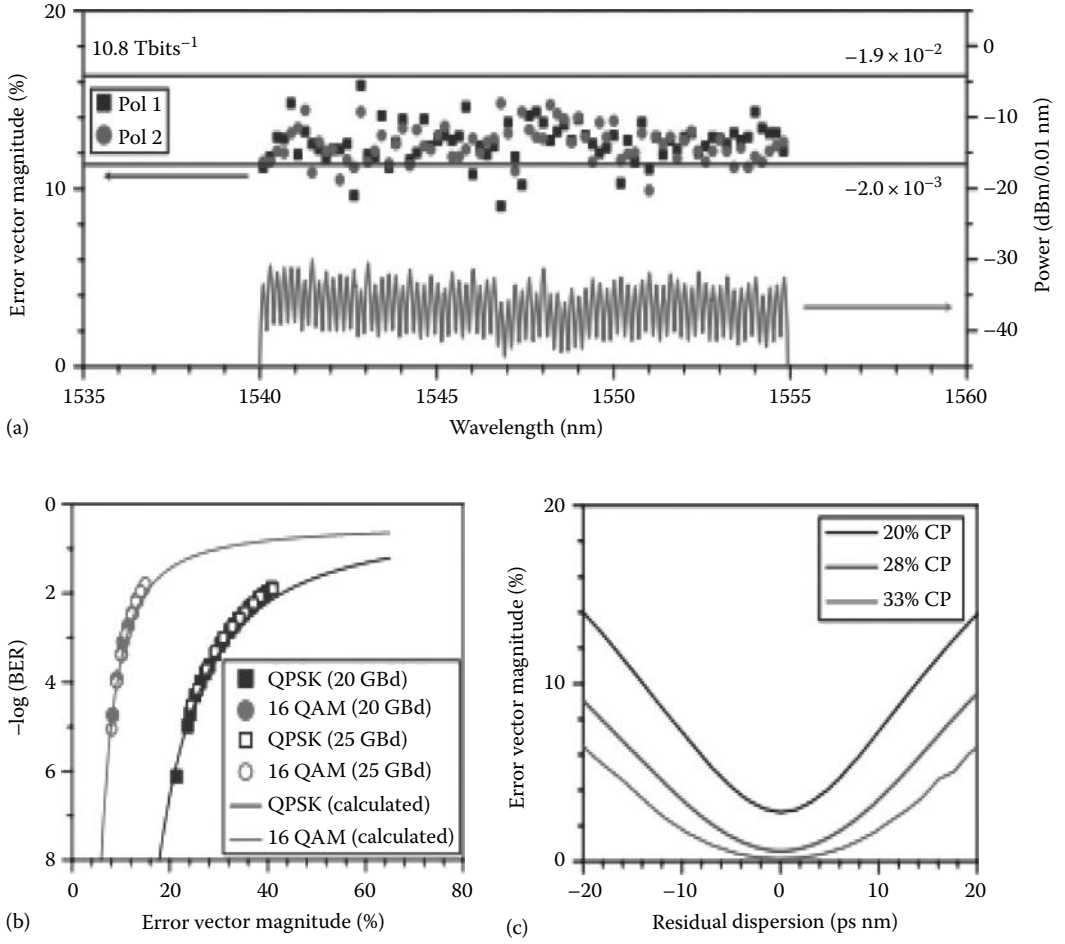

FIGURE 14.27
All-optical 10.8 Tbit/s OFDM results. (a) Measured error vector magnitude (EVM) for both polarizations (symbols) and for all subcarriers of the OFDM signal decoded with the all-optical FFT. The estimated BER for all subcarriers is below the third-generation FEC limit of 1.9e–2. The optical spectrum far left trace is drawn beneath. (b) Relationship between BER and EVM. Measured points (symbols) and calculation of BER as a function of EVM for QPSK and 16 QAM. (c) Tolerance toward residual CD of the implemented system decoded with the eight-point FFT for a cyclic prefix of 20%, 28%, and 33%. (Extracted from Fatadin, I. et al., *IEEE Photon. Tech. Lett.*, 22(9), 631, 2010. With permission.)

as shown in Ref. [16]. A fourth-power law PD (4PPD) with prefiltering presented in Ref. [17] as shown in Figure 14.28b can deal with small β values.

The 4PPD operates by first splitting and forming the combination of these components *X*- and *Y*-polarized channels, then conducting the frequency-domain detection, and regenerating the frequency shift required for the ADC through the voltage control oscillator (VCO) to ensure that the sampling timing is correct with the received sample for processing.

The use of such a phase detector in coherent optical receivers requires large hardware effort. Because of PMD effects the direct implementation of this method before PMD compensation is almost impossible. Therefore, the 4PPD implementation in the frequency domain after the PMD compensation has been proven to be most effective, performing well even in the most extreme case with ROF equal to zero.

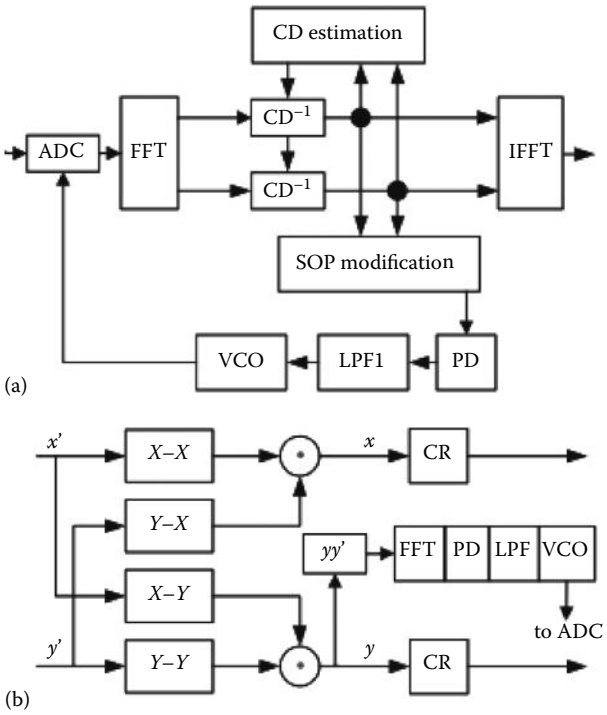

FIGURE 14.28
(a) Godard phase detector algorithm. (b) Fourth-order 4PPD. VCO, voltage control oscillator; FFT, fast Fourier transform; IFFT, inverse FFT; CD, chromatic dispersion; SOP, state of polarization.

14.4.6 128 Gb/s 16 QAM Superchannel Transmission

An experimental setup was used by Dong et al. [18] for the generation and transmission of six channels each carrying 128-Gb/s under PDM-16 QAM modulation format and polarization multiplexing. The two 16-GBaud electrical 16 QAM signals are generated from the two arbitrary waveform generators. Laser sources at 1550.10 nm and the second source with a frequency spacing of 0.384 nm (48 GHz) are generated from two ECLs, each with the line width less than 100 kHz and the output power of 14.5 dBm, respectively. Two *I*/*Q* modulators are used to modulate the two optical carriers with *I*- and *Q*-components of the 64-Gb/s (16-GBaud) electrical 16-QAM signals after power boosting using four broadband electrical amplifiers/drivers. Two phase shifters with a bandwidth of 5k–22.5 GHz provide 2-symbol extra delay to de-correlate the identical patterns. For the operation to generate 16 QAM, the two parallel Mach–Zehnder modulators (MZMs) for *I*/*Q* modulation are both biased at the null point and driven at full swing to achieve zero-chirp and phase modulation. The phase difference between the upper and the lower branches of *I*/*Q* MZIM is also controlled at the null point. The data input is shaped so that about 0.99 roll-off factor of raised cosine pulse shape could be generated.

The power of the signal is boosted using polarization-maintaining EDFAs. The transmitted optical channels are mixed with an LO and polarization demultiplexed via a $\pi/2$ hybrid coupler, then *I*- and *Q*-components are detected by four pairs of balanced photodetector pair (PDP). They are then transimpedance amplified and re-sampled.

The sampled data are then processed in the following sequence, CD compensation, clock recovery, then re-sampling, and passing through classical CMA, a three-stage CMA,

frequency offset compensation, a feed-forward phase equalization, least-mean-square equalizer (LMSE), and then differentially detected to avoid cycle slip effects.

Further, the detailed processing [18] for the electrical polarization recovery is achieved using a three-stage blind equalization scheme: (1) First, the clock is extracted using the "square and filter" method, and then the digital signal is re-sampled at twice the baud rate based on the recovery clock. (2) Second, a $T/2$-spaced time domain FIR filter is used for the compensation of CD, where the filter coefficients are calculated from the known fiber CD transfer function using the frequency domain truncation method. (3) Third, adaptive filters employing two complex-valued, 13 tap coefficients and partial $T/2$ space are employed to retrieve the modulus of the 16 QAM signal.

The two adaptive FIR filters are based on the classic CMA and followed by a three-stage CMA, to realize multimodulus recovery and polarization demultiplexing. The carrier recovery is performed in the subsequent step, where the fourth power is used to estimate the frequency offset between the LO and the received optical signal. The phase recovery is obtained by feed-forward and the least-mean-square (LMS) algorithms for local oscillator frequency offset (LOFO) compensation. Finally, differential decoding is used for BER calculation after the decision.

The spectra of the six Nyquist channels under B2B and 1200 km SSMF transmission are shown in Figure 14.29. It is noted that even with a 0.01 roll-off of Nyquist channels, we do not observe the flatness of individual channels in the diagram. The constellation as expected would require significant amount of equalization and processing.

On average, the achieved BER of 2e–3 with a launched power of –1 dBm over 1200 km SSMF nondispersion compensation link was demonstrated by the authors of Ref. [17]. The link is determined by a recirculating loop consisting of four spans with each span length of 80 km SSMF and an inline EDFA. WSS is employed wherever necessary to equalize the average power of the subchannels. The optimum launched power is about –1 dBm for the six subchannel superchannel transmission.

14.4.7 450 Gb/s 32 QAM Nyquist Transmission Systems

Further spectral packing of subchannels in a superchannel can be done with a Nyquist pulse shaping and predistortion or pre-equalization at the transmitting side.

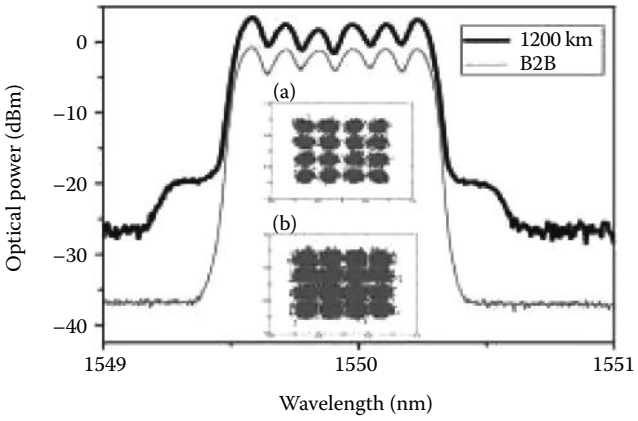

FIGURE 14.29
Spectra of Nyquist channels, 6 × 128G PDM-16QAM back-to-back (B2B) and 1200 km transmission. 16QAM constellation under B2B transmission: (a) back-to-back and (b) after 1200 km.

Zhou et al. [19] have recently demonstrated the generation and transmission of 450 Gb/s WDM channels over the standard 50 GHz ITU-T grid optical network at a net spectral efficiency of 8.4 b/s/Hz. This result is accomplished by the use of Nyquist-shaped, PDM 32-QAM, or 5 bits/symbol × 2 (polarized modes) × 45 Gsystems/s to give 450 Gb/s. Both pre- and posttransmission digital equalization techniques are employed to overcome the limitation of the DAC bandwidth. A nearly ideal Nyquist pulse-shaping with ROF of 0.01 allows guard bands of only 200 MHz between subcarriers. To mitigate the narrow optical filtering effects from the 50 GHz–grid ROADM, a broadband optical pulse-shaping method is employed. By combining electrical and optical shaping techniques, the transmission of 5 × 450 Gb/s PDM-Nyquist 32 QAM on the 50 GHz–grid over 800 km and one 50 GHz–grid ROADM was proven with soft DSP equalization and processing. The symbol rate is set at 28 Gsystem/s.

It is noted that the transmission SSMF length is limited to 800 km due to the reduced Euclidean geometrical distance between constellation points of 32 QAM and by avoiding the accumulated ASE noises contributed by EDFA in each span, Raman optical amplifiers with distributed gain are used in a recirculating loop of 100 km ultra-large area fibers. The BER performance for all five subchannels is shown in Figure 14.30a with insertion of the spectra of all subchannels. Note the near flat spectrum of each subchannel that indicates the near Nyquist pulse shaping. Figure 14.30b and c show the spectra of a single subchannel before and after the WSS with and without optical filtering that performs as spectra shaping. Further to this published work, Zhou et al. have also time multiplexed 64 QAM and transmitted over 1200 km [20], that is, three circulations around the ring of 400 km of 100 km span incorporating Raman pumped amplification. About 5 dB penalty between 32 QAM and 64 QAM in receiver sensitivity at the same FEC BER of 6e−3 is obtained. Note that electrical time division multiplexing of digital sequences from the arbitrary waveform generators was implemented by interleaving so that higher symbol rate can be achieved. Furthermore, 20% soft decision FEC using quasicyclic low-density parity-check (LDPC) code is employed to achieve BER threshold 2.4e−2; thus, the 20% extra overhead is required in the symbol rate.

Simulated results by Bosco et al. [21] without using soft FEC also show the variation of the maximum reach distance with a BER of 2e−3 for capacity in the C-band (bottom axis) and spectral efficiency for PDM-BPSK, PDM-QPSK, PDM-8 QAM, and PDM-16 QAM as shown in Figure 14.31 for SSMF non-DCF optical transmission lines as well as nonzero dispersion shifted fibers (NZ-DSF) indicated by the dashed lines. The design of the NZ-DSF types was described in Chapter 3.

14.5 Non-DCF 1 and 2 Tb/s Superchannel Transmission Performance

14.5.1 Transmission Platform

The schematic structure of the transmission system is shown in Figure 14.32 consisting of an optically amplified multi-SSMF span fiber transmission incorporating variable optical attenuators, and optical transmitters and coherent optical receiver with off-line DSP. Optical bandpass filter (OBPF) is employed using either the D-40 demux or Yenista sharp roll-off (500 dB/nm) to extract the subchannel of the superchannel whose performance is to be measured, normally in terms of BER versus OSNR. The multispan optically amplified fiber transmission line consists of two main parts: the fiber spools and banks of

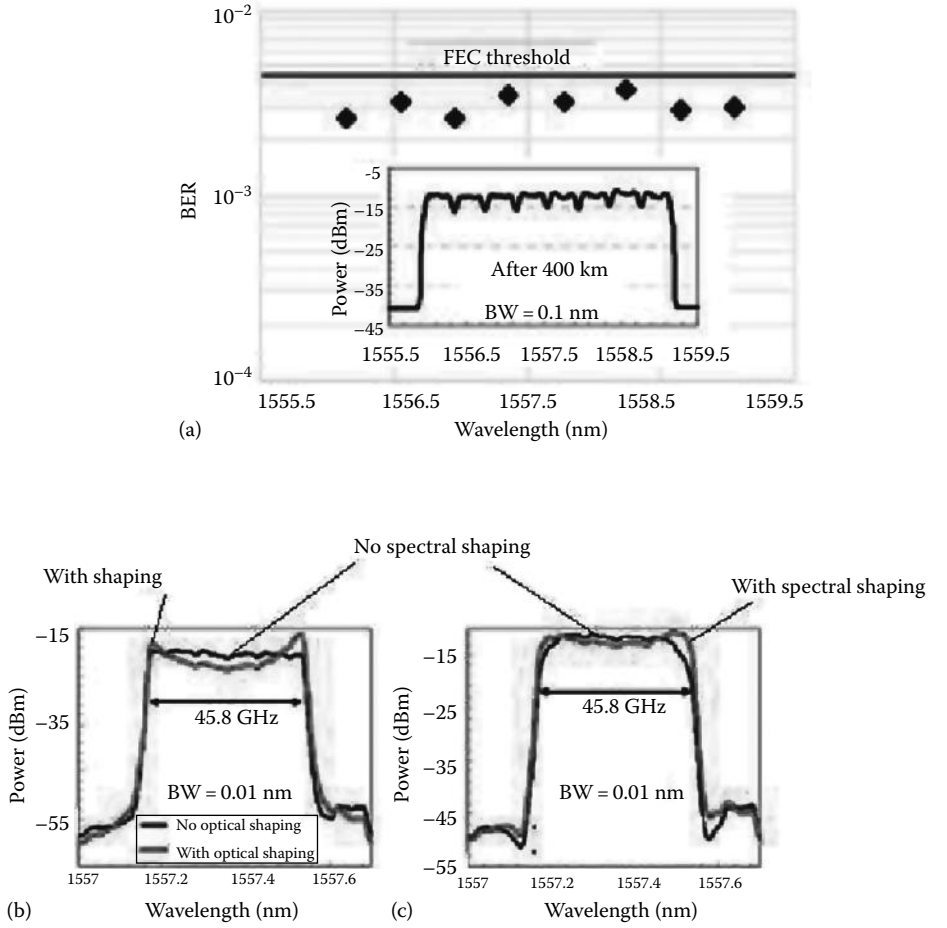

FIGURE 14.30
(a) Spectra of five subchannels of 450 Gb/s channel, that is, 5 × 450 Gb/s superchannels after 400 km (one loop circulating) of 5 × 80 km plus Raman amplification. BER versus wavelength and FEC threshold at 2.3e–3; (b) spectrum of a single subchannel before and (c) after WSS with and without optical shaping by optical filters. *Note*: Dark line for original spectra and light line for spectra after spectral shaping. (Adopted from Dong, Z. et al., *IEEE J. Lightwave Tech*., 30(24), 4000, December 15, 2012. With permission.)

optical amplifiers and VOA as shown in Figure 14.2. The launch power to the first span is adjusted and then at the VOA and at the amplifiers of each span as the saturation level of EDFA varies with respect to the total launched power. To achieve the same launch power into each span, the remote control is employed to adjust the launched power span by span, especially when the launched power is varied to obtain different OSNRs. B2B is measured by inserting noises at different levels to the signal power monitoring port. A D-40 demultiplexer is also available and incorporated into the 19″ rack so that a subchannel of the superchannel can be extracted for measuring the transmission or B2B performance.

The transmitter employs Nyquist QPSK, as described in a previous section, where the channel spacing and baud rate can be varied and the DAC optimized. The optical receiver is a coherent type with an external LO whose wavelength is tuned to the right wavelength location of the subchannel whose performance is to be measured. In practice, this LO must be remotely/automatically locked to the wavelength of the subchannel [22].

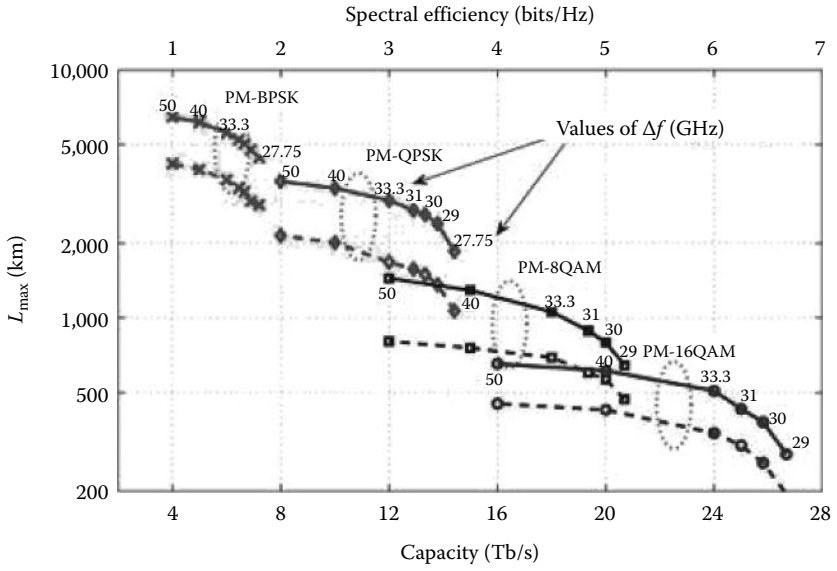

FIGURE 14.31
Transmission reach distance variation with respect to spectral efficiency and total capacity of superchannels. Different QAM schemes are indicated, PM = polarization multiplexing. The numbers are for bandwidth of the subchannel. (Extracted from Zhou, X. et al., *IEEE J. Lightwave Tech*., 30(4), 553, February 15, 2012. With permission.)

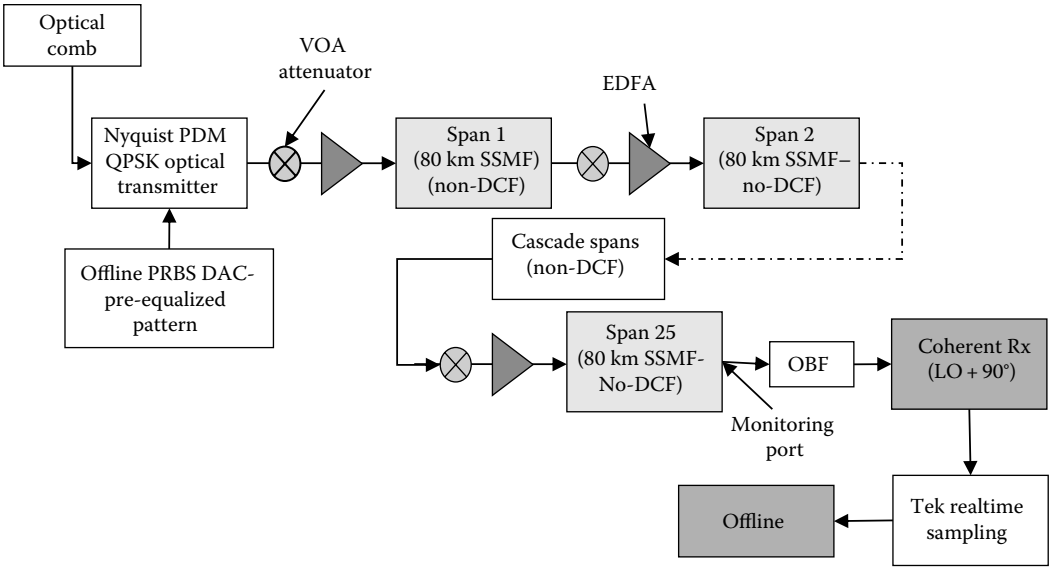

FIGURE 14.32
Schematic structure of the Nyquist QPSK PDM optically amplified multispan transmission line.

14.5.2 Performance

14.5.2.1 Tb/s Pretransmission Test Using Three Adjacent Subchannels

During the initial phase of the development of the Tbps transmission system, we considered a test of transmission of three channels for transmission over 2000 km optically amplified multispan, as described in the previous section, to ensure that the signal quality can be achieved using the Nyquist QPSK criteria with the interference of linear cross talk because of overlapping of subchannels packed close to each other. So, we set up the generation of three subchannels by using an ECL source split 50:50 into two branches, one fed though a CSRZ optical modulator driven with a sinusoidal signal source of frequency equal to the subchannel spacing, and the other branch modulated with Nyquist QPSK format combined with the two CSRZ carriers, also modulated by Nyquist QPSK but with a different random pattern. We then have three subchannels, which are de-correlated, and hence, the BER versus OSNR can be obtained to ensure that the effects of overlapping can be justified. The schematic of this arrangement is shown in Figure 14.33. The transmission performance measured with BER against launched power and subchannel spacing of 28 and 30 GHz with 28 GBaud Nyquist QPSK transmitted over 1600 km line is shown in Figure 14.34.

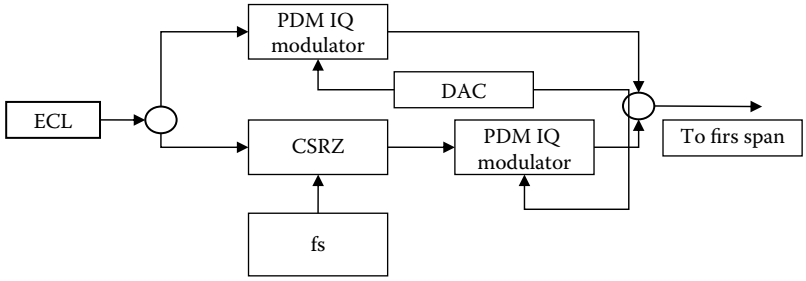

FIGURE 14.33
Schematic of generation of three-subcarrier channel transmitter for test transmission in the initial phase for Tbps transmission system.

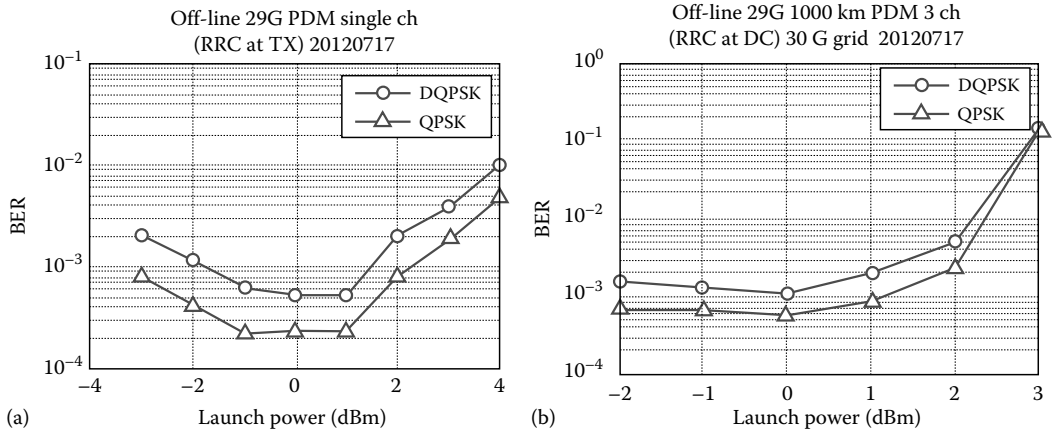

FIGURE 14.34
BER versus launched power (dBm) using three channels with central channel as probe channel over transmission distance of 1600 km non-DCF, 20 optically amplified 80 km SSMF spans with VOA inserted in front of EDFA. 28 GBaud PDM-Nyquist QPSK (a) single channel and (b) three channels.

The BER is optimum at a launched power of –1 to 0 dBm for both the single channel and probe channel, which is the central one of the three channels. This proves that the Nyquist pulse shaping can offer the same performance close to that of a single-channel transmission over 1600 km optically amplified multispan and nondispersion compensating fiber line (Figures 14.35 and 14.36). These performance results provided confidence

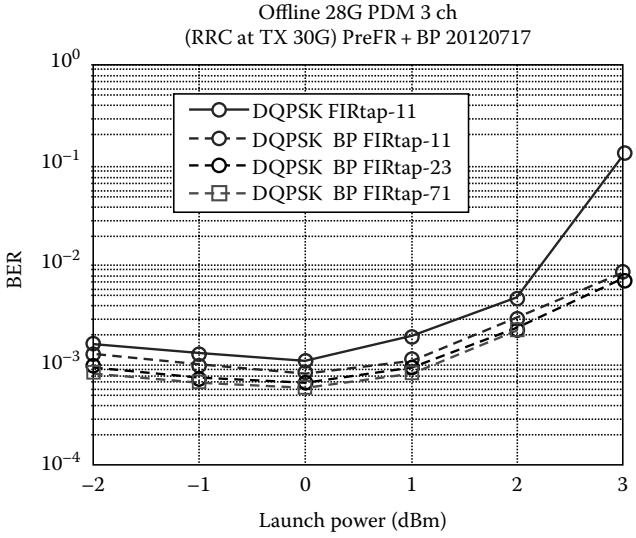

FIGURE 14.35
BER versus launched power for the transmission over 1600 km transmission employing Nyquist QPSK processed with FIR 11–23 taps: BER versus OSNR. The number of subchannels is three, generated and modulated as shown in Figure 14.34.

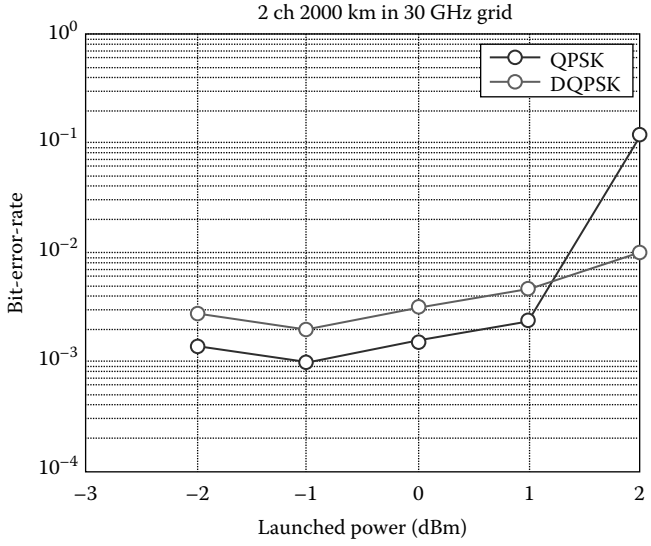

FIGURE 14.36
BER versus launched power for the case of three adjacent channels with central channel as probe over 2000 km transmission by simulation of the 31.8 GHz channel spacing 28 GBaud QPSK with processing QPSK and DPQSK (to optimize for cycle slippage).

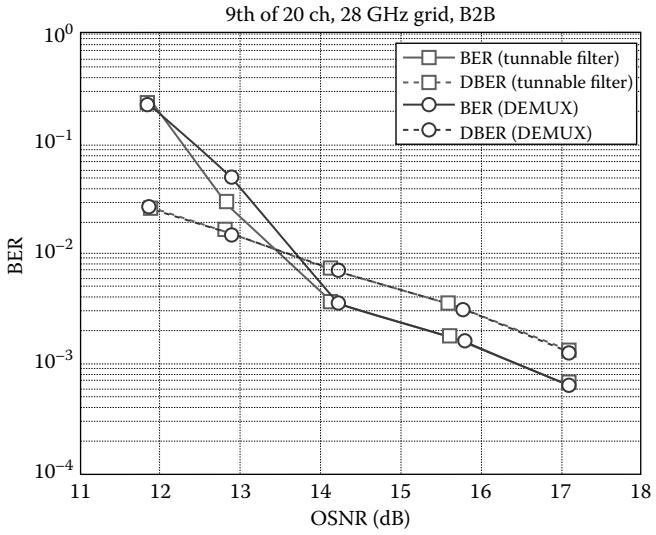

FIGURE 14.37
Performance of channel 9 of the superchannel transmission over 2000 km with D-40 demux or a sharp narrow band pass filter.

in the pulse shaping and helped proceed to superchannel 1 and 2 Tb/s over a single dual polarized mono-mode fiber.

Further, we also used optical filter at the receiver, that is, an optical filter that can be a demux D-40 or a sharp roll-off bandpass optical filter with 500 dB/nm, before feeding into the hybrid coupler to extract the probe channel. The transmission performance for a five-channel superchannel is shown in Figure 14.37. In general, the sharp roll-off filter would offer 1 dB improvement over the wavelength demux unit which commonly has a parabola-like roll-off filtering characteristic.

14.5.2.2 1, 2, or N Tb/s Transmission

We can now extend the transmission of Nyquist pulse-shaped subchannels with the total capacity of all channels of 1 Tb/s and thence 2 Tb/s. For 1 Tb/s, we use nine subchannels plus one probe channel, which are all modulated and pulse shaped satisfying the Nyquist criteria with raised cosine filter and pre-equalization. Thus, we have 10 channels generated either using RCFS or nonlinear comb generation. Then one channel is suppressed by using band stop filter of a WSS and then combined with another Nyquist-shaped QPSK channel independently driven by a de-correlated sequence generated from DAC ports. This inserted channel acts as the probe channel, to measure the performance of transmission for any sub-channel of the superchannel as required, instead of all independently driven subchannels in view of the limitation of independent sequencing from one DAC subsystem. Figure 14.38 shows the generic scheme for generating such probe channels within the superchannel. We can select whichever channel spectral location to insert the probe channel by tuning the source wavelength and the WSS depending on whether the RCFS or nonlinear comb generator is employed. Figure 14.39 shows the B2B performance of 10 subchannels (2×5 by nonlinear driving modulator described earlier) under Nyquist pulse shaping and PDM QPSK modulation format. Individual in-phase and quadrature phase components are also processed to see the effects of one component on other channels. The total BER of QPSK

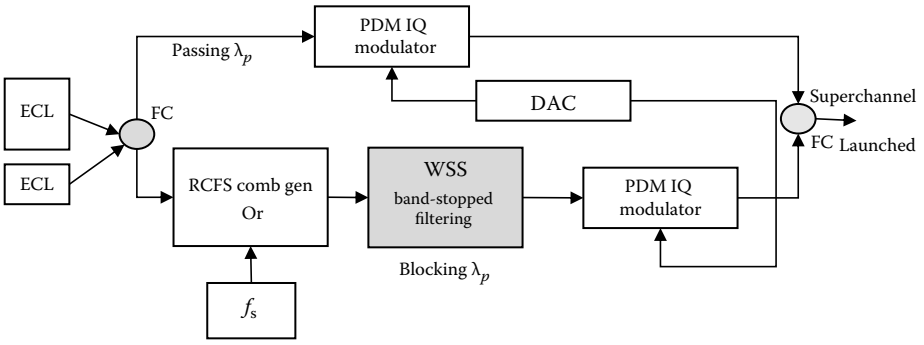

FIGURE 14.38
Generation of $(N-1)$ subcarrier dummy channels and plus-one probe channel for Tbps superchannel transmission systems.

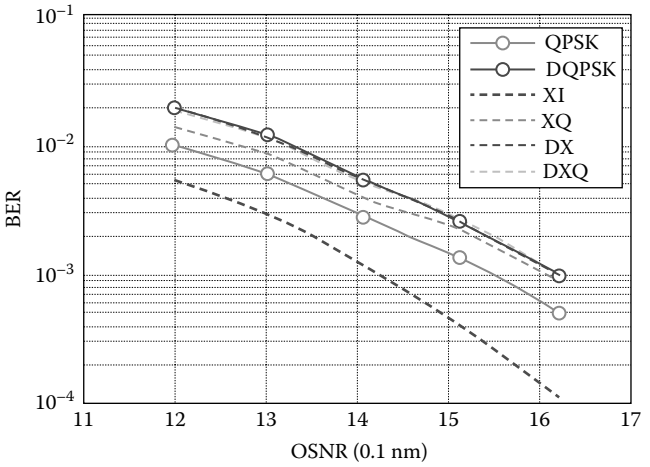

FIGURE 14.39
Ten subchannels of 112 Gb/s 28 GBauds Nyquist QPSK superchannel generation and transmission using nonlinear driven comb generator. 28 GBauds, 30G grid subchannel spacing, and 10 subchannels with one probe channel.

is thus the sum of all these individual components. DQPSK processing offers 1 dB better in OSNR for the same BER, and BER of 1e−3 is achieved for OSNR of 15.2 and 16 dB for QPSK and DQPSK, respectively. The main reasons for evaluating all individual in-phase and quadrature received signals are to ensure that the DAC-generated signals are at the ports $(V_I^+, V_Q^+)(H_I^+, H_Q^+)$ and $(V_I^-, V_Q^-)(H_I^-, H_Q^-)$ enforcing no penalties on the coherent detected signals. With this scheme for generation of 1 and 2 Tb/s, it is not difficult to extend to N Tp/s provided that the RCFS comb generator is used or one has to employ $N/5$ ECLs if the nonlinear comb generation technique is resorted to. The principal problems that we would face in this case would be the nonlinear distortion effects that are described in the next section.

Using nonlinear comb generator, 10 subchannels are generated, and then one channel is eliminated by passing through the WSS set by band-stopped filtering. These subcarriers are then modulated and combined with the probe channel then amplified and launched into the first span. The B2B performance is shown in Figure 14.39. The channel spacing is 30 GHz with 28 GBauds as the symbol rate, the BER obtained is 1e−3 at 14.5 dB. The transmission

performance of the 10 subchannel superchannel over 200 km of optically amplified non-DCF SSMF multispan transmission line is shown in Figures 14.39 and 14.40 in which B2B with four in-phase and quadrature components of the PDM-28G Nyquist QPSK is analyzed with their BER plotted against OSNR at the initial phase prior to transmission and then over the complete link. The attenuation per span is 22 dB, and the EDFA stages are optimized so that the launched power into each span is kept the same at each span. The optimum launched power is –1 to 0 dBm with a BER of 2e–3 with 11 taps FIR filter and back propagation to moderately compensate for fiber nonlinearity (Figures 14.41 through 14.43).

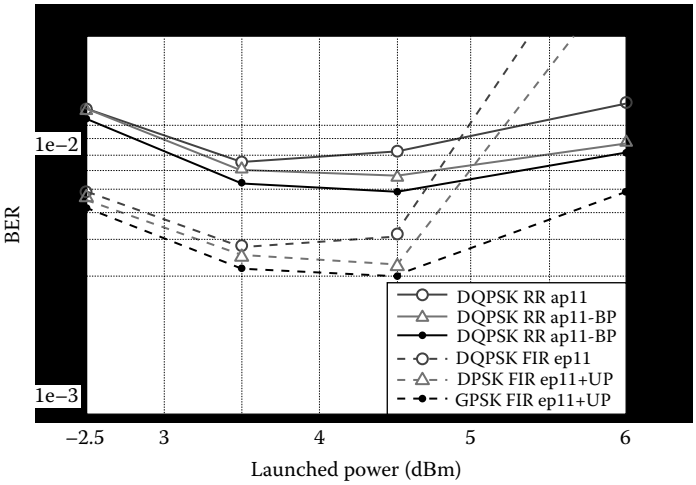

FIGURE 14.40
BER versus launched power (–2 dBm to 1.5 dB with 0.5 dBm per division in horizontal scale) 28 GBauds Nyquist QPSK with 30 GHz spacing with and without back-propagation additional processing and 11 tap FIR and 2000 km transmission Non-DCF fiber multispan line probe channel selected using D40 demux.

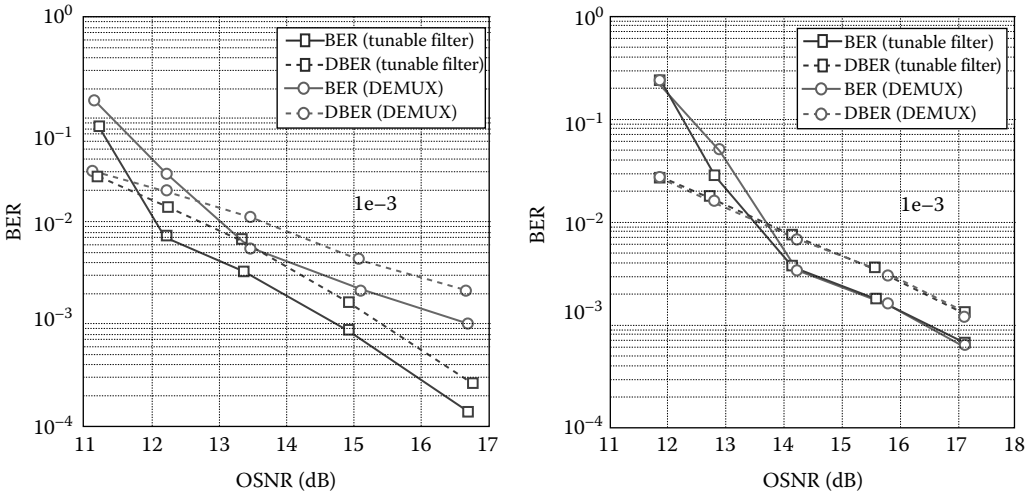

FIGURE 14.41
Transmission performance of channel 9 and channel 20 of the >2 Tb/s superchannel with channel spacing of 30 GHz and 28 GBauds Nyquist QPSK roll-off factor 0.1 using D-40 demux and Yenistar sharp roll-off filter (500 dB/nm).

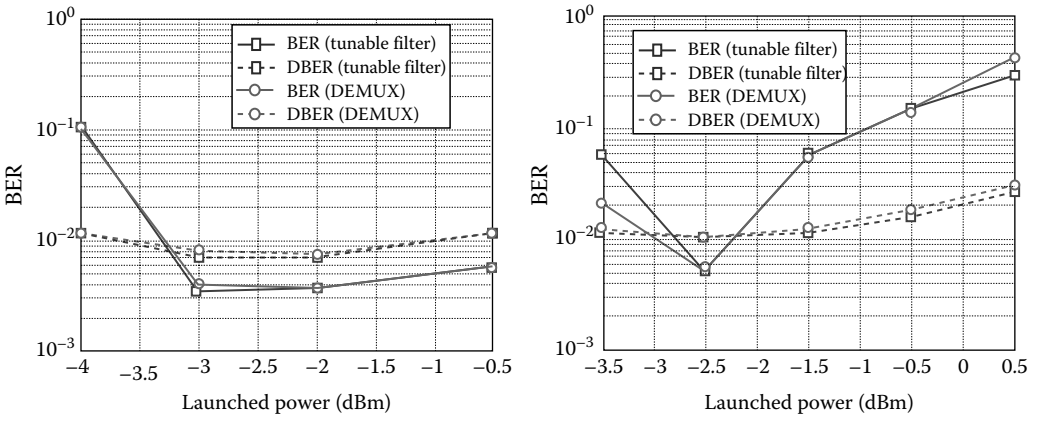

FIGURE 14.42
BER versus launched power of superchannel and probe channels are channels 9 and 20, transmission distance 2000 km on a multispan optically amplified non-DCF line.

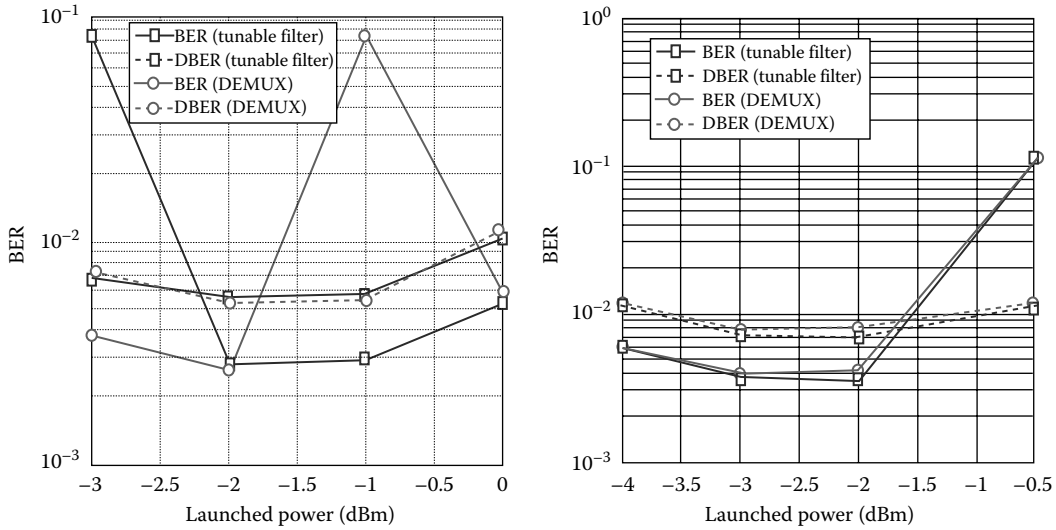

FIGURE 14.43
Five channels nonlinear comb gen subcarriers transmission over 2000 km: BER versus OSNR using wavelength AWG demux or sharp roll-off optical filter (Yenistar).

The back propagation is conducted by propagating the received sampled signals at the receiver, then converted to the optical domain level, and then propagated through span by span with the nonlinear coefficient equal and in opposite sign with those of the SSMF. The back-propagation distance per span is about 22 km as the effective length of the fiber under nonlinear SPM effects.

14.5.2.3 Tbps Transmission Incorporating FEC at Coherent DSP Receiver (Figures 14.44 through 14.48)

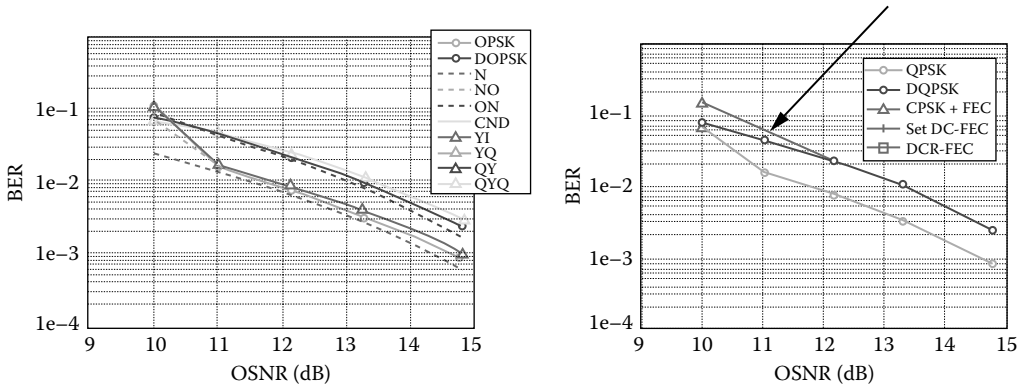

FIGURE 14.44
Soft differential FEC processing for Nyquist QPSK, BER versus OSNR. 28 GBauds with individual components of QPSK, that is, real and imaginary parts (in-phase and quadrature phase components), B2B setup.

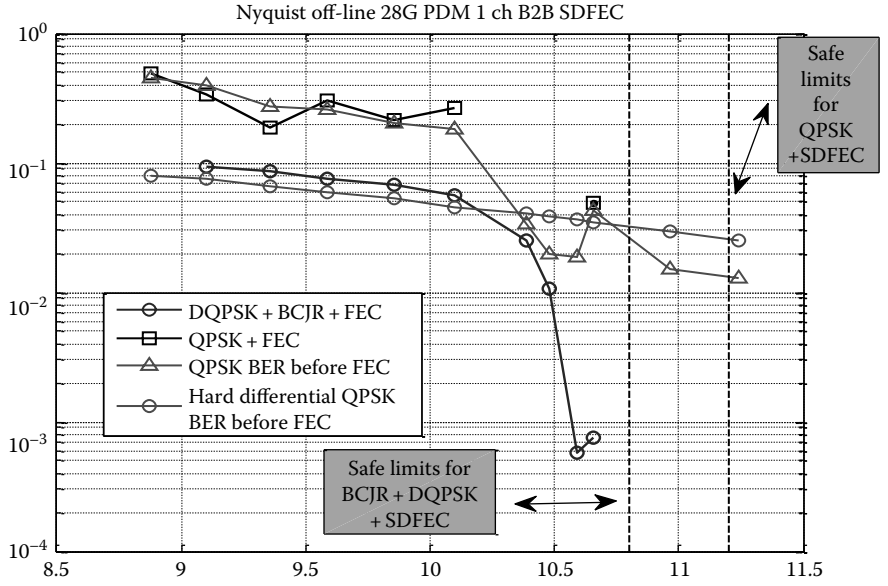

FIGURE 14.45
FEC improvement BER versus OPSNR for Nyquist QPSK with BCJR and without FEC.

14.5.2.4 Coding Gain of FEC and Transmission Simulation

Simulations are conducted to estimate the gain and BER against OSNR with error coding and noncoding so as to assist with the experimental performance. The simulation proves the coding gain for Nyquist QPSK of 0.1 roll-off factor as shown in Figure 14.49. Under coding, we could see that the OSNR requirement for a BER of 1e−3 may be reduced down to 11 dB. An extra margin of 4 dB gain can be provided to allow an extra 500 km extension

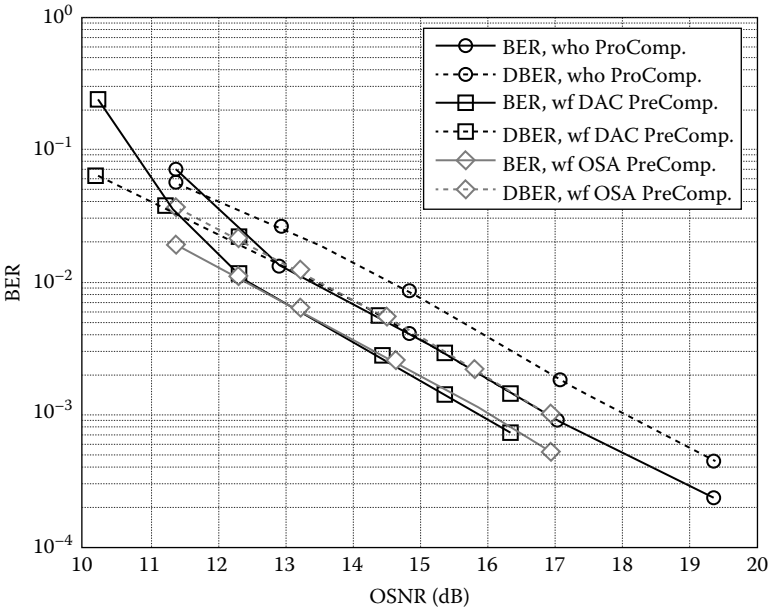

FIGURE 14.46
32 GBauds PDM Nyquist QPSK transmission, BER versus OSNR with and without electronic compensation in DAC, B2B scenario.

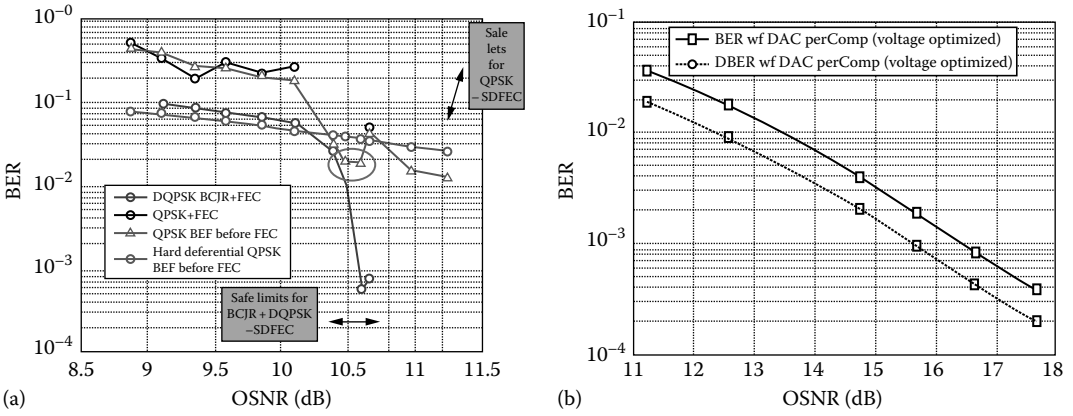

FIGURE 14.47
Performance of transmission systems under optimization and nonoptimized DAC generation of random sequence at 28G and 32 GBauds, B2B scenario, and modulation format Nyquist QPSK. (a) DAC without optimization and (b) DAC optimized.

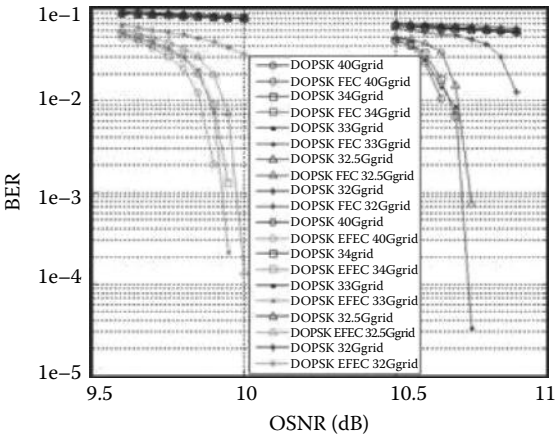

FIGURE 14.48
32 GB Nyquist QPSK roll-off = 0.1 with subchannel spacing as parameter and transmission over 2000 km non-DCF optically amplified spans under scenarios of with and without FEC 20%, far left and far right of the graph, respectively.

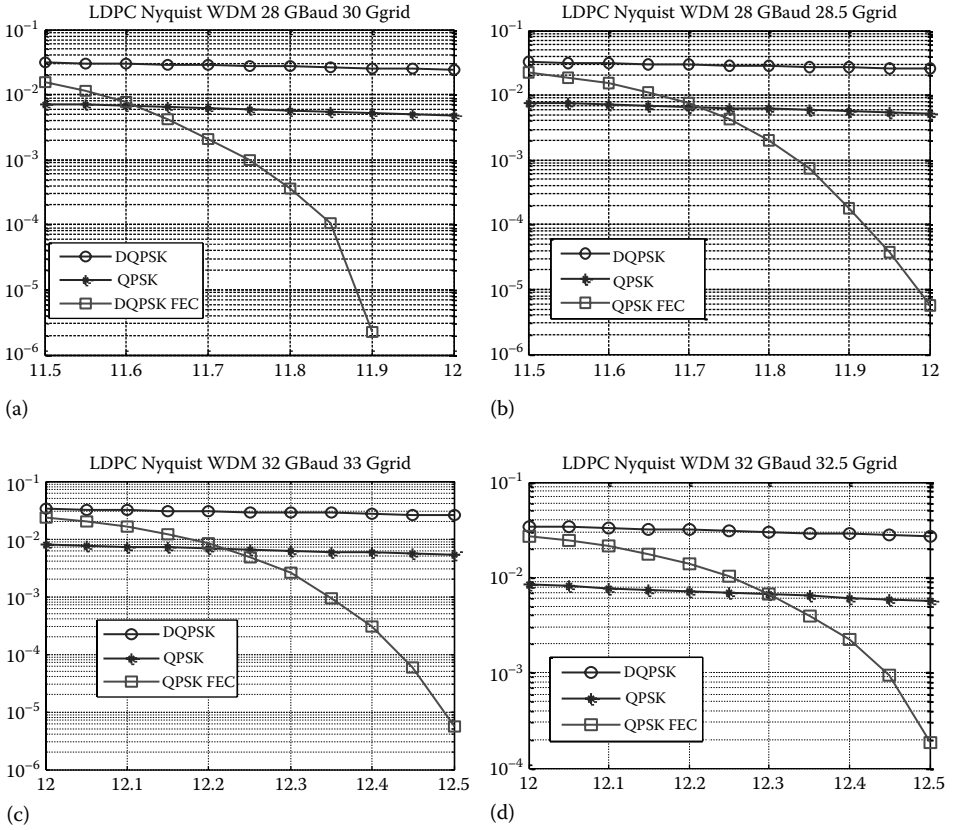

FIGURE 14.49
Simulation of Nyquist QPSK with and without error coding gain (a and b) LDPC coding and gain at 28 GHz grid; (c and d) LDPC Nyquist QPSK with 33 GHz grid; (*Continued*)

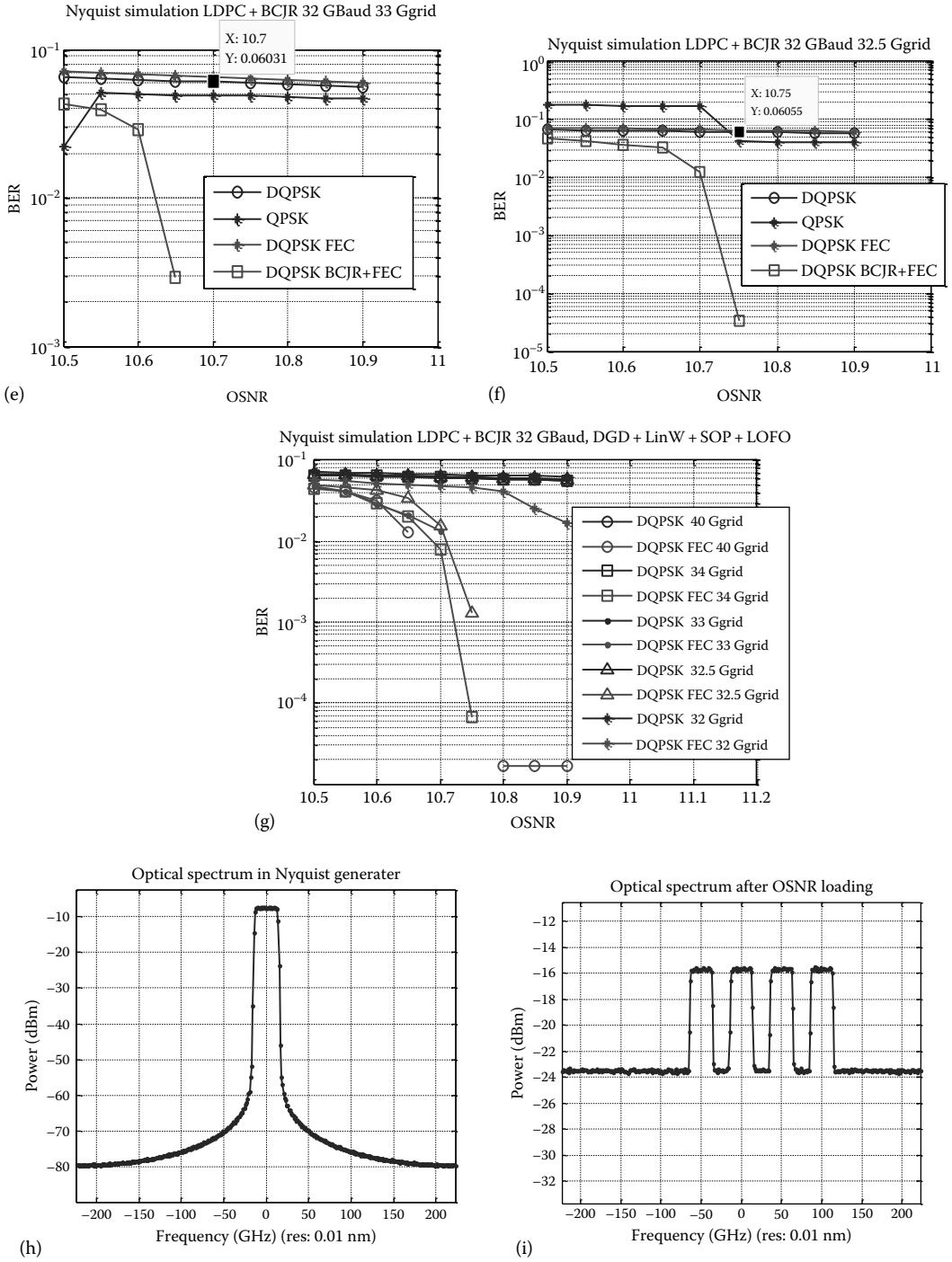

FIGURE 14.49 (*Continued*)
Simulation of Nyquist QPSK with and without error coding gain (e and f) BCJR + LDPC and 3 GHz grid (g) Nyquist QPSK with and without coding gain with grid-frequency spacing as parameters (32–40 GHz) as summary of (a–f); (h and i) Spectra of channels before and after ASE noise loading.

of the transmission reach of Nyquist QPSK. Figure 14.49a and b shows the effects of 30 and 28.5 GHz subchannel spacing on the BER of the Nyquist QPSK with LDPC and significant improvement of FEC on their performance. So is the case for Figure 14.49c and d related to 33 and 32.5 subchannel spacing with 32 GBauds. Figure 14.49e and f then provides the improvement when BCJR (Bahl-Cocke-Jelinek-Raviv) additional coding is superimposed to obtain further coding gain. Figure 15.49g displays all gain curves in one graph, and Figure 14.49h and i shows the spectra of subchannels, the odd channels only.

14.6 Multicarrier Scheme Comparison

A preliminary comparison of Nyquist QPSK transmission and CO-OFDM and electrical OFDM (eOFDM) scheme for superchannel Tbps transmission over long haul and in metropolitan optical networks is shown in Table 14.2.

The following text gives briefly the contrast between complexity and spectral efficiency of the schemes.

Hardware complexity: At the transmitter side, all schemes require a comb generator, which can be either by using one ECL, then employing RCFS technique to generate N subcarriers of locked phase and frequency or a multiple factor of five subcarriers per ECL using nonlinear driving method. Furthermore, a set of parallel PDM I/Q modulators and DAC with eight ports of positive and complementary signals, an optical subchannel DeMux, and a Mux would be necessary for generating independent sets of in-phase and quadrature signals for modulating the PDM-IQ modulators. At the receiver side, a standard coherent receiving system can be used and the insertion of a sharp optical filter at the front end of the optical hybrid coupler is required to separate the subchannels. This may require a set of optical filters, one for each subchannel. Thus, a technical solution should be provided to avoid this complex and expensive solution. This is the setback in the Nyquist WDM technique.

TABLE 14.2

Comparisons of Tbps Transmission Schemes

	Nyquist-WDM	**CO-OFDM**	**eOFDM**
Hardware complexity	Tx: similar	Tx: similar	Tx: similar
	Rx: multi-OFE	Rx: need OFFT	Rx: multi-OFE
DSP complexity	More complex, possibly due to compensation—but no higher degree of complexity, possibly more processing time required for CPU	Normal	Normal
SE (theoretically)	Similar	Similar	Similar
Tx-DSP + DAC	Essential	Possibly not	Essential
ADC sampling rate	1.2 × Baud	2 × Baud	2 × Bandwidth
Bandwidth requirement on O/E components	Depending on subchannel spacing	Depending on subchannel spacing	Depending on subchannel spacing
Special requirements	DSP for sequence estimation (MAP, MLSE)	Orthogonal channel separation	Cyclic prefix and guard band for OFDM symbols
Flexibility	Medium	Medium	High

DSP complexity: For Nyquist-WDM, because the Nyquist filtering results in ISI, at the receiver side one needs sequence estimation algorithms such as MAP and MLSE. For Nyquist QPSK and different comb-generated subcarriers and subchannels, FIR with lesser number of taps would be suitable, so that the complexity can be acceptable.

ECLs: For recirculating frequency shifting (RCFS) comb generation, only one ECL source is necessary but additional modulators and optic components are required, whereas for nonlinear driving comb generation, the number of ECLs is increased accordingly. To cover the whole C-band with superchannels of 30 GHz spacing, there would be around 12 ECLs. This number may be high especially when they are to be packaged in the same line card.

Spectral efficiency: All Nyquist pulse shaping schemes can enhance the spectral efficiency (SE) by a factor of about 2; the overlapping between subchannels would create minimum cross talk if the roll-off factor is less than 0.1 and the third-order harmonics of the subchannels and comb-generated subcarriers is more than 30 dB below the primary carrier.

Tx-DSP and DAC: Ideally, CO-OFDM may not need DSP; but for compensation of components and transmission impairments, it is preferable to use Tx-DSP. The other two schemes must use Tx-DSP and DAC to shape the pulse or generate the designed signal.

ADC sampling rate: This depends on channel spacing, ideally a factor of 2× the single-sided signal bandwidth. As Nyquist-WDM narrows filters, the two-sided signal bandwidth is reduced to only 1.3 of the baud rate, and for the same baud rate it requires the lowest sampling rate of ADC. The 56–64 GS/s ADC and DAC are available from Fujitsu Co. Ltd., which allow the generation of a random sequence for 28–32 GB/s.

Bandwidth requirements on O/E components: Similar to the sampling rate, Nyquist-WDM needs the lowest bandwidth assuming the same baud rate. The other two schemes are similar.

Flexibility: All three schemes have flexibility in a number of subchannels, modulation formats, and bandwidth of subchannels; whilst the OFDM can adjust some parameters in the electrical domain by means of Tx-DSP, it has more flexibility than the other two schemes.

14.7 Remarks and Challenges

The total information capacity transmitted over a single single-mode-fiber has been increased tremendously as a result of the spectral packing of subchannels by pulse shaping techniques and DSP processing algorithms as well the soft FEC so as to allow a higher order of modulation QAM to be realized. Thus, digital processing in realtime and digitally based coherent optical transmission systems have been proven to be the most modern transmission systems for the global internet in the near future. The principal challenges are now dependent on the realization of application-specific integrated circuits (ASIC) using microelectronics technology or ultra-fast field programmable gate array (FPGA)–based systems. The concepts of processing in the digital domain have been proven in off-line systems, and thus, more efficient algorithms are required for realtime systems. These remain topical research topics and engineering issues. Higher symbol rates may be possible when wider bandwidth optical modulators and DAC and ADC systems are available, for example, grapheme plasmonic silicon modulators [23] and their integration with microelectronic DAC and ADC, and DSP systems.

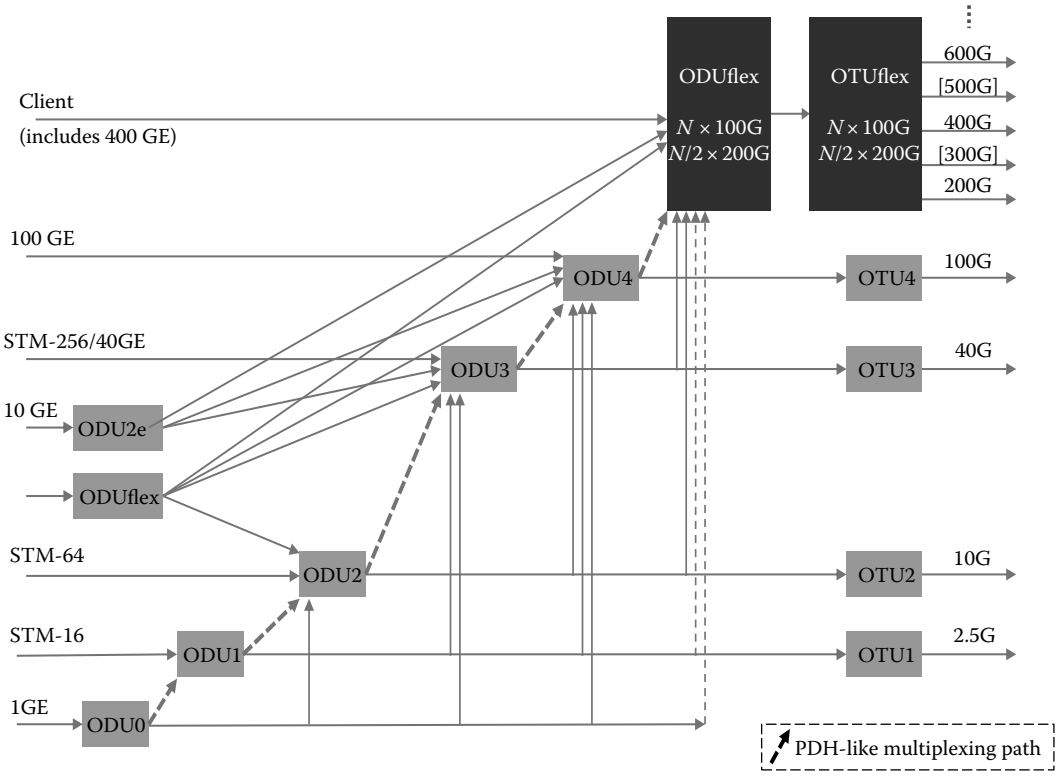

FIGURE 14.50
Flexible hierarchy beyond 100G to Tb/s.

The processing algorithms for QAM vary from level to level, but essentially they are based on the number of circles existing in multilevel QAM as compared to a mono-cycle constellation of the QPSK scheme. The algorithms developed for QPSK can be extended and modified for higher-level circular constellation.

The digital hierarchy of the optical transport networks is to be developed and standardized for deployment as shown in Figure 14.50 in which the synchronous digital hierarchy (SDH) levels are evolving to adapt the 100G, 400G, and then multi-Tbps. Both the Ethernet 100G and SDH levels can be integrated into a flexible grid optical networking. For flexible grid technology, the wavelength grid need not be uniform to accommodate different capacities, and hence, the bandwidth demanded by clients and nodes of networks. The challenges to introducing Tbps transmission technology into modern optical networks are enormous.

References

1. L.N. Binh et al., Synchronous modulator incorporated re-circulating comb laser sources for Tbps superchannel transmission, in *OSA Congress Proc. Conference on Advanced Solid State Lasers*, Paris, France, paper JTh2A.13-1, November 2013.
2. L.N. Binh, *Digital Processing: Optical Transmission and Coherent Receiving Techniques*, CRC Press/Taylor & Francis Group, Boca Raton, FL, 2013.

3. T.E. Bell, Communications: Coherent optical communication shows promise, the FCC continues on its path of deregulation, and satellite communications go high-frequency, *IEEE Spectrum*, 23(1), 49–52, 1986.
4. Linear Circuits Inc., Single ended to different input trans-impedance amplifier, http://circuits.linear.com/267. Accessed October, 2013.
5. J.S. Weiner et al., SiGe differential transimpedance amplifier with 50-GHz bandwidth, *IEEE Journal of Solid-State Circuits*, 38(9), 1512–1517, 2003.
6. E. Ip and J.M. Kahn, Digital equalization of chromatic dispersion and polarization mode dispersion, *IEEE Journal of Lightwave Technology*, 25(8), 2033, August 2007.
7. E. Ip and J.M. Kahn, Compensation of dispersion and nonlinear impairments using digital back propagation, *IEEE Journal of Lightwave Technology*, 26(20), 3416, October 15, 2008.
8. I. Fatadin and S.J. Savory, Compensation of frequency offset for 16-QAM optical coherent systems using QPSK partitioning, *IEEE Photonics Technology Letters*, 23(17), 1246–1248, 2001.
9. I. Fatadin, D. Ives, and S.J. Savory, Laser linewidth tolerance for 16-QAM coherent optical systems using QPSK partitioning, *IEEE Photonics Technology Letters*, 22(9), 631–633, 2010.
10. H. Louchet, K. Kuzmin, and A. Richter, Improved DSP algorithms for coherent 16-QAM transmission, in *Proceedings of ECOC'08*, Brussels, Belgium, paper Tu.1.E6, September 2008.
11. R. Noe, T. Pfau, M. El-Darawy, and S. Hoffmann, Electronic polarization control algorithms for coherent optical transmission, *IEEE Journal of Selected Topics in Quantum Electronics*, 16(5), 1193–1199, September 2010.
12. Technical specification of Corning fiber G.652 SSMF given in L.N. Binh, *Digital Optical Communications*, CRC Press, Boca Raton, FL, 2010, Chapter 3, Appendix.
13. D. Hillerkuss et al., 26 Tbit/s line-rate super-channel transmission utilizing all-optical fast Fourier transform processing, *Nature Photonics*, 5, 364, June 2011.
14. D. Hillerkuss, M. Winter, M. Teschke, A. Marculescu, J. Li, G. Sigurdsson, K. Worms et al., Simple all-optical FFT scheme enabling Tbit/s real-time signal processing, *Optics Express*, 18(9), 9324–9340, April 26, 2010.
15. N. Godard, Pass and timing recovery in an all-digital modem receiver, *IEEE Transactions on Communications*, 26, 517–523, May 1978.
16. N. Stojanovic, N. G. Gonzalez, C. Xie, Y. Zhao, B. Mao, J. Qi, and L.N. Binh, Timing recovery in Nyquist coherent optical systems, in *International Conference Telecommunications Systems*, Belgrade, Serbia, 2012.
17. T.T. Fang and C.F. Liu, Fourth-power law clock recovery with pre-filtering, in *Proceedings of ICC*, Geneva, Switzerland, vol. 2, pp. 811–815, May 1993.
18. Z. Dong, X. Li, J. Yu, and N. Chi, 6 × 128-Gb/s Nyquist-WDM PDM-16 QAM generation and transmission over 1200-km SMF-28 with SE of 7.47 b/s/Hz, *IEEE Journal of Lightwave Technology*, 30(24), 4000–4006, December 15, 2012.
19. X. Zhou, L.E. Nelson, P. Magill, R. Isaac, B. Zhu, D.W. Peckham, P. I. Borel, and K. Carlson, PDM-Nyquist-32 QAM for 450-Gb/s per-channel WDM transmission on the 50 GHz ITU-T Grid, *IEEE Journal of Lightwave Technology*, 30(4), 553, February 15, 2012.
20. X. Zhou, L.E. Nelson, R. Isaac, P. Magill, B. Zhu, D.W. Peckham, P. Borel, and K. Carlson, 1200 km transmission of 50 GHz spaced, 5 × 504-Gb/s PDM-32-64 hybrid QAM using electrical and optical spectral shaping, in *Proceedings of OFC 2012*, Los Angeles, CA, 2012.
21. G. Bosco, V. Curri, A. Carena, P. Poggiolini, and F. Forghieri, On the performance of Nyquist-WDM terabit superchannels based on PM-BPSK, PM-QPSK, PM-8 QAM or PM-16 QAM subcarriers *IEEE Journal of Lightwave Technology*, 29(1), 53, January 2011.
22. L.N. Binh et al., Optical PLL super combed carrier cloning: Circuit and methodology for locking superchannel coherent receivers, patent under submission, October 2013.
23. M. Liu and X. Zhang, Graphene-based optical modulators, in *Proceedings of OFC 2012*, Los Angeles, CA, paper OTu1I.7, 2012.

15

Digital Signal Processing for Optical Transmission Systems

15.1 Introduction

Digital signal processing (DSP) is the principal functionality of modern optical communications systems at both the coherent optical receivers and the transmitter. At the transmitter, the DSP is employed for shaping the pulse at the output of optical modulators and for compensation of the limited bandwidth of the digital to analog converter (DAC) as well as that of the transfer characteristics of the electro-optic external modulators and de-skewing of the electrical path differences between the in-phase and quadrature-phase signals, which occur often in ultra-high-speed systems. It is noted that the mixing of the received signals and the local oscillator (LO) laser happens in the photo-detection stage.

Because of the square law process in the optoelectronic conversion, this mixing gives a number of terms, two square terms related to the intensity of the optical signal and the intensity of the LO laser, and two product terms that result from the beating between the optical signal beam and that of the LO. Only the resultant product between these two optical-frequency field components gives the signal frequency detected at the coherent reception subsystem. When the optical frequencies of the optical signal field and that of the oscillator are the same, then the reception is termed as homodyne coherent detection. Thus, provided that perfect homodyne mixing is achieved in the photo detection device, the detected signals, now in the electrical domain, are in the baseband superimposed by noises of the detection process. After electronic preamplification, the signals are converted by the analog to digital converter (ADC) to the discrete domain and thus processed by digital signal processors, which can be considered to be similar to processing in wireless communications systems. The main difference lies in the physical processes of distortion, dispersion, nonlinear distortion, and clock recovery, and broadband properties of optical modulated signals transmitted over long-haul optical fibers or short reach scenarios.

On the other hand, at the receiver end, DSP follows the ADC with the digitalized symbols and processes the noisy and distorted signals with algorithms to compensate for linear distortion impairments such as chromatic dispersion (CD), polarization mode dispersion (PMD), nonlinear self phase modulation effects (SPM), clock recovery, LO frequency offset (FO) with respect to the relieved channel carrier, and so on. A possible flow of sequences in DSP is illustrated in Figure 15.1 for the modulated channel with the in-phase and quadrature components and polarization multiplexing as recovered in the electronic domain after the optical processing at the front end as shown in the beginning, the input boxes. There are two pairs of electrical signals output from the two polarized channels and two for the in-phase and quadrature components. Interprocessing of these pairs of signals can

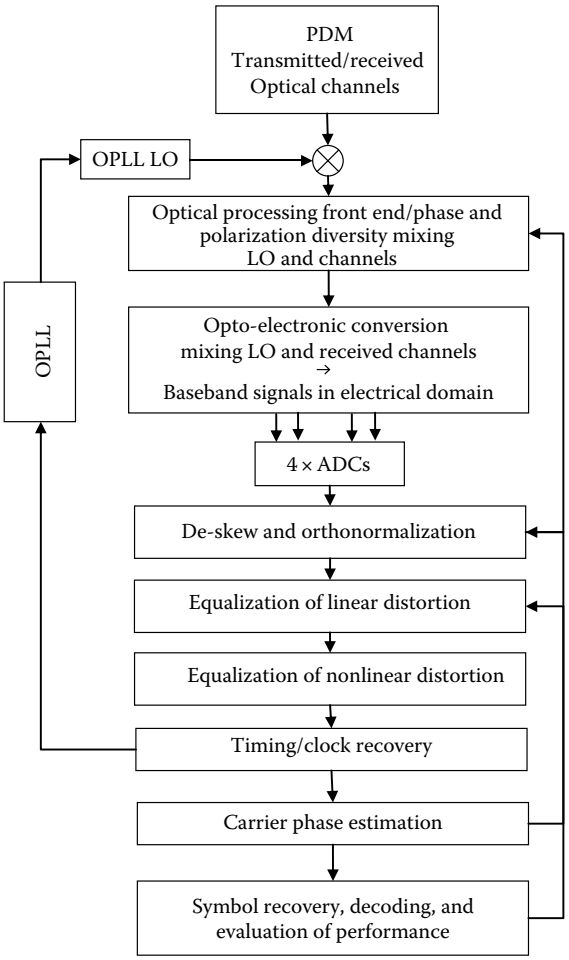

FIGURE 15.1
Flow of functionalities of DSP processing in a QAM coherent optical receiver with possible feedback control.

be implemented using 2 × 2 multiple input multiple outputs (MIMO) techniques, which are well known in the digital processing of wireless communications signals [1].

After the opto-electronic detection of the mixed optical signals, the electronic currents of the PDM channels are then amplified with a linear transimpedance amplifier and a further amplification at the main stage if required to boost the electric signals to the level at which the ADC can digitalize the signals into their equivalent discrete states. Once the digitalized signals are obtained, the first task would be to ensure that any delay difference between the channels and the in-phase and quadrature components in the electronic and digitalization processes are eliminated by de-skewing. All the equalization processing can then be carried out to compensate for any distortion on the signals resulting from the propagation through the optical transmission line. Further nonlinear distortion effects on the signals can also be superimposed at this stage. Then the clock recovery and carrier phase detection can be implemented. Hence, the processes of symbol recovery, decoding, and evaluation of performance can be implemented.

On the other hand, for incoherent reception only one component current generated from the absorption of the direct modulated light waves is generated and amplified via the front

end transimpedance amplifier (TIA). Hence, there is only one set of digitalized data to be processed, implying a lesser degree of freedom as compared to the complex digitalized sequence for the coherent case. However, the algorithms are still valid for DSP of the incoherent system. Only one ADC is needed to sample the analog signals at the output of the TIA. This digitalized sequence is then fetched into the DSP for compensation, equalization, clock recovery, decoding, and performance evaluation. All these actions are to be implemented in realtime.

Regarding noises in the optical detection, if it is coherent detection then the noises are mainly dominated by the shot noises generated by the LO power. However, if it is direct detection, then the quantum shot noises of the signal power also contribute, and hence, it becomes signal dependent. These noises will contribute to the convergence of algorithms.

This chapter is organized as follows. Section 15.2 gives a basic background to equalization using transversal filtering and zero-forcing (ZF) with and without feedback in the linear sense, the linear equalizer (LE). Then when a decision, in a nonlinear sense, is employed under some criteria to provide feedback to the input sequence, the equalization is nonlinear and the equalizer is classified as nonlinear equalizer (NLE) or decision-directed (DD) equalizer. Tolerance to noises is also given, and the simple quality factor of the system's performance is deduced.

Clock recovery is important for recovery of the timing for sampling of the received sequence, and that technique is also briefly given. Determining the reference phase for coherent reception is also critical so as to evaluate several quadrature-modulated transmitted signals. Thus, carrier phase recovery technique is also described using DSP technique, especially in the case when there is significant offset between the LO and the light waves carrying the signals. This is described in Section 15.5.

When the maximum likelihood sequence estimation (MLSE) is used in the NLE, the equalization can be considered optimum but consuming substantial memory. We dedicated Section 15.3 to this algorithm and illustrated with an example of this MLSE to demonstrate the effectiveness of MLSE in minimum shift keying (MSK) self-homodyne coherent reception transmission systems under the influence of linear distortion effects with the modulation scheme is a MSK. This is given in Section 15.6.

We can see that DSP algorithms are most critical in modern DSP-based optical receivers or transponders. This chapter thus introduces the fundamental aspects of these algorithms for optical transmission systems over dispersive channels whether under linear or nonlinear distortion physical effects.

The functionalities of each processing block of Figure 15.1 can be categorized as shown in Table 15.1 [2].

TABLE 15.1

Functionalities of Subsystem Processing in a DSP-Based Coherent Receiver

De-skewing	Alignment of in-phase and quadrature components or polarized channel components temporarily or any different propagation time due to electrical connections
Orthogonalization	Ensuring independence or decorrelation between channels
Normalization	Standardization of amplitude of components to maximum value of unity
Equalization	Compensation of impairments due to physical effects or imperfections of subsystems
Interpolation	Correction of timing error
Carrier phase estimation	Compensation of phase errors of the carrier
FO	Correction of the offset frequency between LO and carrier frequencies
OPLL	Optical phase locked loop to ensure matching between channel lightwave carrier and that of the local oscillator carrier (see locking mechanism given in Chapter 5)

15.2 General Algorithms for Optical Communications Systems

Indeed, in coherent optical communication systems incorporating DSP the reception of the transmitted signals by mixing them with an LO whose frequency is identical or close to equality, the homodyne or intradyne technique, can convert the optical signals back to the baseband whose phase and amplitude can be distorted but complex valued as they are at the input of the transmitter in the electrical domain. One can thus apply a number of processing algorithms developed for high-speed modems [3] or algorithms for wireless communication systems [4].

Naturally, a number of steps of conversions from optical to electrical and vice versa at the receiver and transmitter are involved with further optical amplifier noises and electronic noises accumulated along the optical transmission line.

In this chapter, we assume that the signal level is quite high compared with the electronic noise level at the output of the electronic preamplifier which follows the photodetector. Hence, the processing algorithms are conducted in the baseband electrical digital domain after the ADC stage.

15.2.1 Linear Equalization

Coherent optical communications systems can be considered as synchronous serial systems. In transmitting optical signals over uncompensated optical fiber spans across long-haul multispan link or uncompensated metropolitan networks at very high bit rates, now in the second decade of the twenty-first century, at 25 Gsystems/s or 28–32 Gsystems/s including forward error coding overloading, the received signals are distorted because of linear and nonlinear dispersive effects, hence leading to intersymbol interference (ISI) in the baseband after the coherent homodyne detection at the receiver. In Chapters 7 and 8, we have described in detail the processes of incoherent and coherent receptions, especially homodyne, self-homodyne, and direct detection of optical signals including noise processes. Over the nondispersion compensating multispan fiber links, the most important signal distortion is the linear chromatic dispersion and polarization mode dispersion, especially when PDM is employed with two polarization orthogonal channels being simultaneously transmitted. The ISI naturally occurs as a result of the band limiting of the signals over the limited bandwidth of the long fiber link as described in Chapter 3 on the transfer function of optical fibers. Other nonlinear distortion effects have also been included in their transfer function indicating the uneven or nonflatness of the passband of the transfer function of the fiber. These ISI effects will degrade the performance of the optical communications and need to be tackled with the equalization processes treated in this chapter.

The optical coherent detection processes and DSP of sampled digital signals may be classified into two separate groups.

The first of these, the received sampled digital signals are fed through an equalizer that corrects the distortion introduced by the chromatic dispersion and PMD effects and restores the received signals into a copy of the transmitted signals in the electrical domain. The received signals are then detected in the conventional manner as applicable to any serial digital signal in the absence of ISI. In other words, the equalizer acts as the inverse of the channel so that the equalizer and the channel together introduce no signal distortion,

and each data symbol is detected as it arrives, independent of one another. The equalizers can be either linear or nonlinear.

In the second group of detection processes, the decision process is modified to take into account the signal distortion that has been introduced by the channel and no attempt needs, in fact, to be made here to reduce signal distortion prior to the actual decision process. Although no equalizer is now required, the decision process may be considerably complex, and hence, complex algorithms are necessary to deal with this type of decision processing.

In addition to these two decision groups, there are additional issues to resolve involving the synchronization of the sampling at the receivers, the clock recovery, and carrier phase estimation so that a reference clocking instant can be established and the reference phase of the carrier can be used to detect the phase states of the received samples. Concurrently, any skew or delay differences between the *I*- and *Q*-components (for coherent detection) as well as the polarized multiplexed channels must be detected and de-skewed so that the synchronous processes can be preserved in the coherent detection processes.

Further, any delay difference as a result of the different propagation time of the polarized channels or electrical connection lines, the de-skewing process is conducted to eliminate this effect as indicated in Figure 15.1.

In this section the linear equalization (LE) process is introduced.

15.2.1.1 Basic Assumptions

In general, a simplified block diagram of the coherent optical communication system can be represented in the baseband, that is, after optical field mixing and detection by optoelectronic receivers and E/O conversion at the transmitter, as shown in Figure 15.2. The input to the transmitter is a sequence of regularly spaced impulses, assuming that the pulse width is much shorter than that of the symbol period, which can be represented

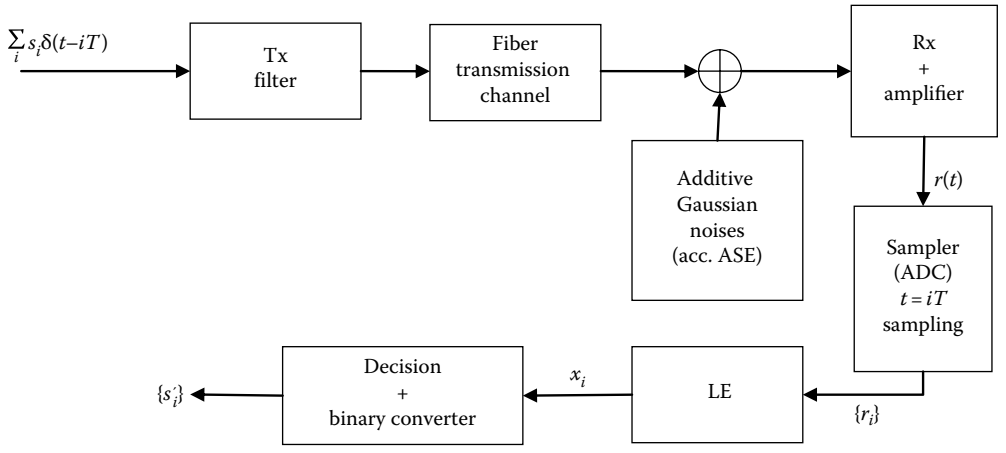

FIGURE 15.2
Simplified schematic of coherent optical communication system. Note equivalent baseband transmission systems due to baseband recovery of amplitude and phase of optically modulated signals.

by $\sum_i s_i \delta(t - iT)$ with s_i of binary states taking both positive and negative values as the amplitude of the input signal sequence. Thus, we can write

$$s_i = \pm k; \quad k > 0 \tag{15.1}$$

The impulse sequence is a binary polar type. This type of signal representation is advantageous in practice as it can be employed to modulate the optical modulators, especially the Mach–Zehnder interferometric modulator (MZIM) or *I*–*Q* modulator as described in Chapter 3 so that the phase of the carrier under the modulated envelop can take positive or negative phase angles, which can be represented on the phasor diagram. In practice, naturally, the impulse can be replaced by a rectangular or rounded or Gaussian waveform by modifying the transmitter filter, which can be a Nyquist-raised cosine type to tailor the transmitting pulse shape.

It is further noted that the phase of the optical waves and the amplitude modulated by the *I*- and *Q*-MZIM in the two paths of the *I*–*Q* modulator ensure the negative and positive positions of the *I*- and *Q*-components on the real and imaginary axes of the constellation as shown in Figure 3.21 (4-ASK-1 and 4-ASK-2). Under coherent reception, these negative and positive amplitudes are recovered as they are in the transmitter and with superimposed noises. We can see that the synchronization of the modulation signals fed to the two MZIM is very critical to avoid degradation of the sampling instant due to skew.

15.2.1.2 Zero-Forcing Linear Equalization (ZF-LE)

Consider a transmission system and receiver subsystem as shown in Figure 15.3 in which the transmitter transfer function can be represented by $H_{Tx}(f)$, the transfer function of the channel in the linear domain $H_C(f)$, and the transfer function of the equalizer or filter $H_{Eq}(f)$, which must meet the condition for an overall transfer function of all subsystems equating to unity

$$H(f) = H_{Tx}(f)H_C(f)H_{Eq}(f)e^{j\omega t_0} \tag{15.2}$$

Thus, from (15.2) we can obtain, if the desired overall transfer response follows that of a Nyquist raised-cosine filter, the equalizer frequency response as

$$H_{Eq}(f) = \frac{T \text{ raise cos}\left(\dfrac{f}{1/T}, \rho\right)}{H_{Tx}(f)H_C(f)} e^{j\omega t_0} \tag{15.3}$$

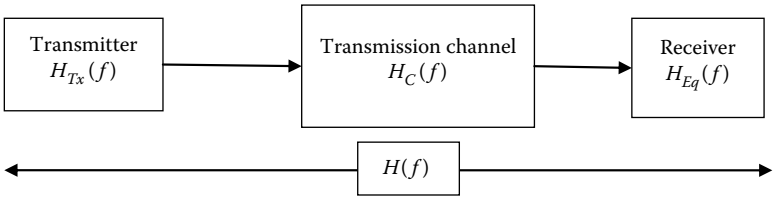

FIGURE 15.3
Schematic diagram of a transmission system including a ZF equalizer/filter.

With the raised-cosine function defined with β as the roll-off factor as the frequency response of the equalizer

$$H_{Eq}(f) = \text{raise\_cos}\left(\frac{f}{1/T}, \beta\right) = \begin{cases} 1 & 0 \le |x| \le \dfrac{1-\beta}{2} \\ \cos^2\left(\dfrac{\pi}{2}\dfrac{|x| - \dfrac{1-\beta}{2}}{\beta}\right) & \dfrac{1-\beta}{2} \le |x| \le \dfrac{1+\beta}{2} \\ 0 & |x| > \dfrac{1+\beta}{2} \end{cases} \tag{15.4}$$

Implying that the filter is a Nyquist filter of the raised-cosine shape; ω is the signal baseband frequency, and t_0 is the time at the observable instant. When two channels are observed simultaneously, then the right-hand side of (15.2) is a unity matrix and the unitary condition must be satisfied, that is, the conservation of energy.

From (15.3), the magnitude and phase response of the equalizer can be derived. This condition guarantees a suppression of the ISI; the equalizer can be renamed linear equalizer zero-forcing (LE-ZF) filter.

15.2.1.3 ZF-LE for Fiber as Transmission Channel

The ideal ZF equalizer is simply the inverse of the channel transfer function given in (15.2). Thus, the required equalizer transfer function $H_{Eq}(f)$ is given by

$$H_{Eq}(f) = H_{SSMF}^{-1}(f) = e^{j\alpha\omega^2} \tag{15.5}$$

where ω is the radial frequency of the signal envelope, and α is the parameter dependent on dispersion, wavelength, and the velocity of light in vacuum as described in Chapter 4. However, this transfer function does not maintain the conjugate symmetry, that is

$$H_{Eq}(f) = e^{j\alpha\omega^2} \neq H_{Eq}^{-1}(f) \tag{15.6}$$

This is due to the square law dependence of the dispersion parameter of the fiber on frequency.

Thus, the impulse response of the equalizing filter is complex. Consequently, this filter cannot be realized by a baseband equalizer using only one baseband received signal that explains the limited capability of LEs employed in direct-detection receivers to mitigate the chromatic dispersion. On the other hand, it also explains why fractionally spaced LEs that are used within a coherent receiver can potentially extend the system reach to distances that are only limited by the number of equalizer taps [5]. Under coherent detection and particularly the quadrature amplitude modulation (QAM), both the real and imaginary parts are extracted separately and processed digitally. The schematic of a fractionally spaced finite impulse response (FIR) filter is shown in Figure 15.4 in which the delay time between taps is only a fraction of the bit period. The weighting coefficients $W_0(n)$ … $W_{N-1}(n)$ are determined and then multiplied with the signal paths $S(n)$ at the outputs of the taps. These outputs are then summed up and subtracted by the expected filter coefficients $d(n)$ to obtain the errors of the estimation. This process is then iteratively operated till the final output sequence $Y(n)$ is closed to the desired response.

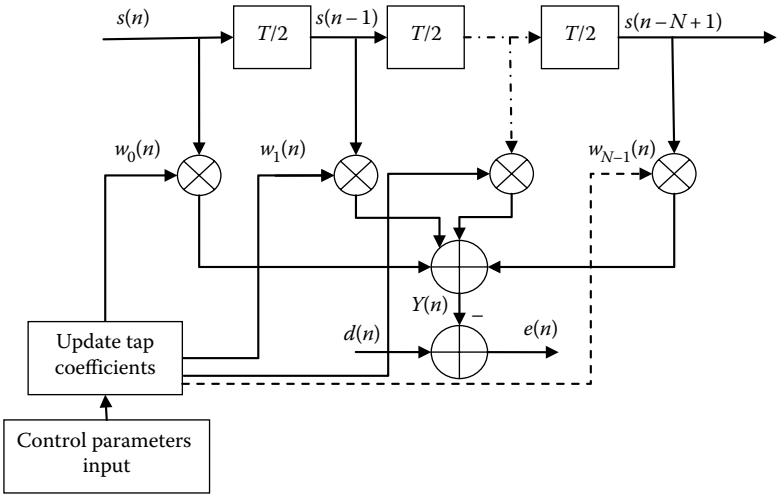

FIGURE 15.4
Schematic of a fractionally spaced FIR filter.

Under ZFE at the sampling instant, the noise may have been increased due to errors in the delay of the zero crossing point of adjacent pulses, hence ISI effects. Thus, the signal to noise ratio (SNR) may not be optimum.

The number of taps must cover the whole length of the dispersive pulses, for example, for a 1000 km SSMF transmission line and BW channel it is is 25 GHz (or ~0.2 nm at 1550 nm) and the total pulse spreading of the pulse is 17 ps/nm/km × 1000 km × 0.2 nm equals to about 3400 ps. The sampling rate would be 50 GSa/s (2 samples per period at 25 Gb/s assuming modulation that results in the BW equal to symbol rate) then one would have 3400/40 period or ~85 periods or taps with 170 samples altogether.

15.2.1.4 Feedback Transversal Filter

Transversal equalizers are considered as linear feedforward (FFE) transversal filters employed in practice over several decades since the invention of digital communications. Alternatively, equalization may be achieved by the feedback transversal filter, provided that certain conditions are met by the channel responses, in this case, the linear transfer function of the fiber transmission line.

Let the z-transform of the sampled impulse response of the channel, the fiber field propagation, and coherent detection be

$$Y(z) = y_0 + y_1 z^{-1} + y_2 z^{-2} + \cdots + y_g z^{-g} \tag{15.7}$$

where $y_0 \neq 0$. Let $V(z)$ be the z-transform derived from the scaling of $Y(z)$ so that the first term becomes unity. Thus, we have

$$V(z) = \frac{1}{y_0} Y(z) = 1 + \frac{y_1}{y_0} z^{-1} + \frac{y_2}{y_0} z^{-2} + \cdots + \frac{y_g}{y_0} z^{-g} \tag{15.8}$$

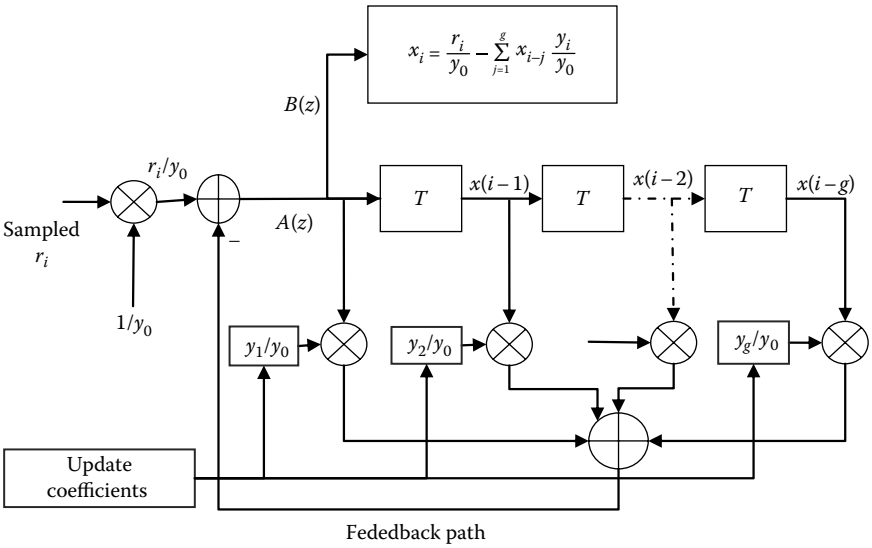

FIGURE 15.5
Schematic structure of a linear feedback transversal equalizer for a channel whose impulse response in *z-transform* of $Y(z)$.

or written in the cascade factorized form

$$V(z) = \left(1 + \beta_1 z^{-1}\right)\left(1 + \beta_2 z^{-1}\right)\ldots\left(1 + \beta_g z^{-1}\right) \tag{15.9}$$

where β_i can be real or complex valued. The feedback transversal filter can then be configured as shown in Figure 15.5 following the operation just described. Obviously, the received sequence is multiplied with a factor $1/y_0$ to normalize the sequence and delayed by one period with a multiplication ratio, then summed up, and feedback is subtracted from the normalized incoming received sequence. The output is taped from the feedback path as shown in the diagram, at the point where the transversal operation is started.

15.2.1.5 Tolerance to Additive Gaussian Noises

Consider a linear FFE with $(m + 1)$ taps as shown in Figure 15.6. Assume that the equalizer has equalized the input signals in the baseband so that the output of the equalizer is given by

$$x_{i+h} \simeq s_i + u_{i+h}$$
$$\text{with} \begin{cases} s_i = \pm k; \text{binary level signal amplitude} \\ u_{i+h} = \text{noise-component} \end{cases} \tag{15.10}$$

Note that noise always add to the signal level so that for positive k the noise u_{i+h} follows the same sign and vice versa for negative value.

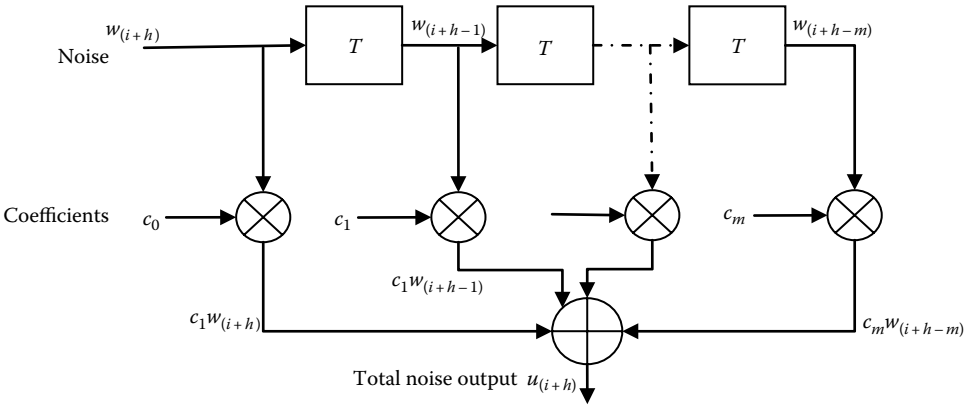

FIGURE 15.6
Noisy signals in a $(m + 1)$-tap linear FFE.

The output noise signals of the FFE can be written as

$$u_{i+h} = \sum_{j=0}^{m} w_{i+h-j} c_j \tag{15.11}$$

The noise components $\{w_i\}$ are statistically independent Gaussian random variables with the mean as zero and variance σ^2 so that the total accumulated noise output given by (15.11) is also the uncorrelated Gaussian random variable with zero mean and variance

$$\eta^2 = \sum_{j=0}^{m} \sigma^2 c_j^2 = \sigma^2 C C^T = \sigma^2 |C|^2 \tag{15.12}$$

where $|C|$ is the Euclidean length of the $(m + 1)$ component vector $[C] = [c_0 \quad c_1 \quad \ldots \quad c_m]$, the sampled channel impulse response. Thus, η^2 is the mean square noise of the process and is also the mean square error of the output sample values x_{i+h}.

The probability noise density function of this Gaussian noise is given by

$$p(u) = \frac{1}{\sqrt{2\pi\eta^2}} e^{-\frac{u^2}{2\eta^2}} \tag{15.13}$$

With the average value of the magnitude of the received signal value, k (equalized without any distortion), the probability of error of the noisy detection process is given by

$$P_e = Q\left(\frac{k}{\eta}\right) = Q\left(\frac{k}{\sigma|C|}\right) \tag{15.14}$$

And, the electrical SNR is given by

$$SNR = 20\text{Log}_{10}\left(k/\sigma\right) \text{dB} \tag{15.15}$$

with $Q(x)$ as the quality function of x, that is, the complementary error function as commonly defined. In practice, this SNR can be measured by the standard deviation of the constellation point and the geometrical distance from the center of the constellation to the central point of the constellation. We see in the next section that the equalized constellation would offer much higher SNR as compared with that of the nonequalized constellation. Thus, under the Gaussian random distribution, the noises contributed to the equalization process are also Gaussian and the probability density function would follow the Euclidean distance of the channel impulse response.

15.2.1.6 Equalization with Minimizing MSE in Equalized Signals

It has been recognized that a linear transversal filter that equalizes and minimizes the mean square error in its output signals [6–8] generally gives a more effective degree of equalization than an equalizer that minimizes the peak distortion. Thus, an equalizer that minimizes the mean square difference between the actual and ideal sampled sequence at its output for a given number of taps would be advantageous when noises are present.

Now revisiting the transmission given in the sampled impulse response of the channel, the sampled impulse response of $(m + 1)$ tap linear FFE and the combined sampled impulse response of channel and the equalizer, the matrices [**Y**], [**C**], and [**E**], respectively, are given by

$$\begin{aligned}[\mathbf{Y}] &= \begin{bmatrix} y_0 & y_1 & \cdots & y_g \end{bmatrix} \\ [\mathbf{C}] &= \begin{bmatrix} c_0 & c_1 & \cdots & c_m \end{bmatrix} \\ [\mathbf{E}] &= \begin{bmatrix} e_0 & e_1 & \cdots & e_{m+g} \end{bmatrix}\end{aligned} \tag{15.16}$$

Under the condition that for the combined impulse response of the channel and the equalizer the recovered output sequence is only a pure delay of h periods of the sampling period, the input sampled sequence we have

$$x_{h+i} \approx s_i + u_{h+i} \tag{15.17}$$

Or it is a pure delay superimposed by the Gaussian noises of the transmission line. In the case of optical transmission lines, these can then be the accumulated amplified spontaneous emissions (ASEs) over many spans of the dispersive optically amplified transmission spans. Thus, the resultant *ideal* vector at the output of the equalizer can be written as

$$[\mathbf{E}] = \left[\underbrace{0 \quad \cdots \quad 0}_{h} \quad 1 \quad 0 \quad 0 \quad 0 \quad \cdots \quad 0 \right]; \quad h = \text{interger} \tag{15.18}$$

But in fact, the equalized output sequence would be (as seen from [15.16])

$$x_{h+i} \approx \sum_{j=0}^{m+g} s_{i+h} - je_j + u_{h+i}; \quad j = 0, 1, \ldots, (m+g) \tag{15.19}$$

The input sampled values are statistically independent and have equal probability of taking values of $\pm k$, indicating that the expected value (denoted by symbol $\xi[.]$) is given by

$$\xi\left[s_{i+h-j}s_{i+h-l}\right]=0;\quad \forall j\neq l \text{ and } \xi\left[s_{i+h-j}^2\right]=k^2 \tag{15.20}$$

The noises superimposed on the sampled values are also statistically independent of the sampled signals with zero mean, and thus the sampled signals and noises are orthogonal and we have the expected value $\xi[s_{i+h-j}u_{i+h}] = 0$.

Thus, an LE that minimizes the mean square error in its output signals would also minimize the mean square value of $[x_{i+h}-s_i]$ which can be written as

$$\xi\left[\left(x_{i+h}-s_i\right)^2\right]=\begin{cases}\xi\left[\left(\sum_{j=0}^{m+g}s_{i+h-j}e_j+u_{i+h}-s_i\right)^2\right]\\ \quad=k^2\left|E-E_h\right|^2+\sigma^2\left|C\right|^2\end{cases} \tag{15.21}$$

$$\text{with } \left|E-E_h\right|^2=\sum_{\substack{j=0\\ j\neq h}}^{m+g}e_j^2+k^2\left(e_h-1\right)^2$$

where $|E - E_h|$ and $|C|$ are the Euclidean distances of the vectors $[\mathbf{E} - \mathbf{E}_h]$ and $\mathbf{C} = [\mathbf{C}]$, respectively. We can now observe that the first and second terms of (15.21) are the mean square error in x_{i+h} due to ISI and the mean square error due to Gaussian noises. Thus, we can see that the MSE process minimizes not only the distortion in terms of the mean square error due to ISI but also minimizes that of the superimposing noises.

15.2.1.7 Constant Modulus Algorithm for Blind Equalization and Carrier Phase Recovery

15.2.1.7.1 Constant Modulus Algorithm (CMA)

Consider the ISI, additive noise, and carrier FO. Then a received signal, $x(k)$, can be written before processing as

$$x(k)=\sum_{i=0}^{M-1}h(i)a(k-i)e^{j\phi(k)}+n(k) \tag{15.22}$$

where $h(k)$ is the overall complex baseband equivalent impulse response of the overall transfer function including the transmitter, unknown channel, and receiver filter. Note that all E/O and O/E with coherent reception steps are removed and assume only noises contribute but there is no distortion in both phase and amplitude. $n(k)$ are the total accumulated noises assumed to be Gaussian and mainly contributed by the ASE noises over cascaded amplifiers. The input data sequence $a(k - i)$ is assumed to be independent and identically distributed, and $\phi(k)$ is the carrier phase difference between the signal carrier and the LO laser.

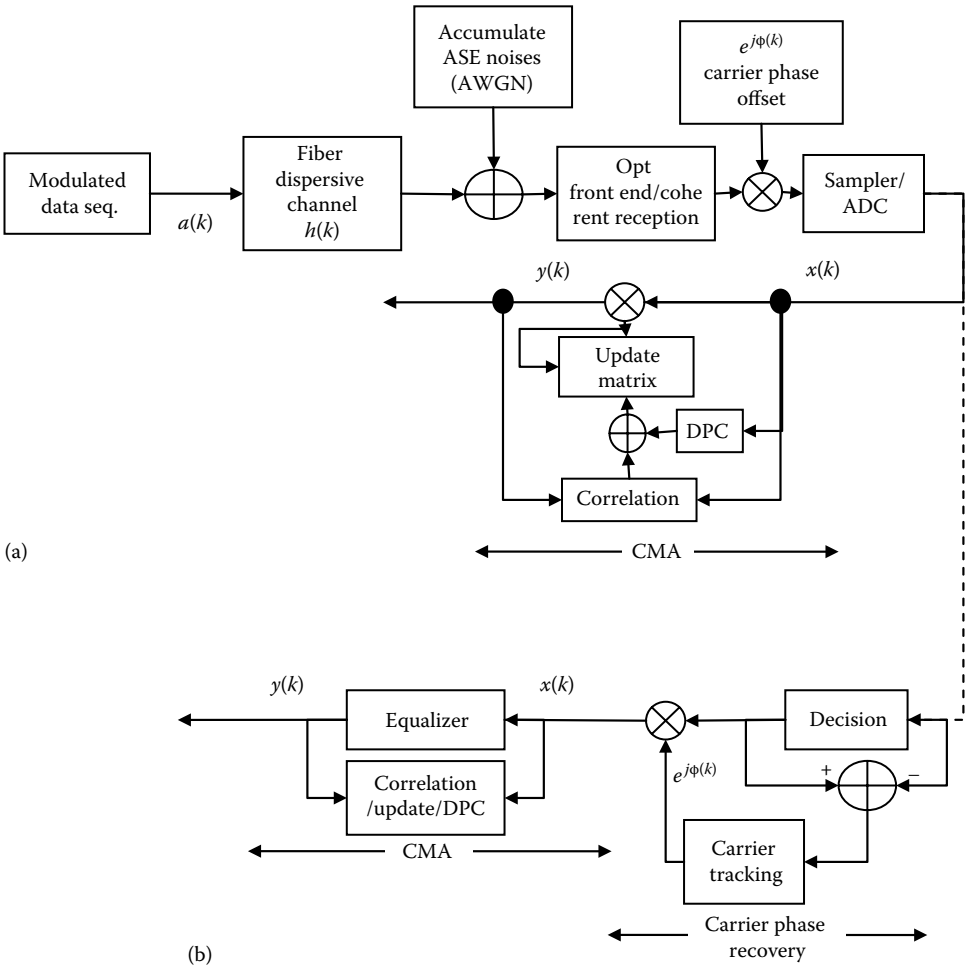

FIGURE 15.7
Equivalent model for baseband equalization: (a) blind CMA and (b) modified CMA by cascading CMA with carrier phase recovery. Signal inputs come from the digitalized received samples after coherent reception. DPC = differential phase compensation.

Now, let the impulse response of the equalizer be $\mathbf{W}(k)$ as denoted in the schematic given in Figure 15.7, then the output of the equalized signals can be obtained by

$$y(k) = \mathbf{X}^T(k)\mathbf{W}(k) \tag{15.23}$$

where

$\mathbf{W}(k) = [w_0, w_1, \ldots, w_k]^T$ is the tap weight vector of the equalizer as described in the earlier sections of this chapter

$\mathbf{X}(k) = [x(k), x(k-11), \ldots, x(k-N+1)]^T$ is the vector input to the equalizer with N, the length of the weight vector

In the fiber transmission, there is a pure phase distortion as a result of the chromatic dispersion effects in the linear region and the constellation rotating in the phase plane. In addition, the carrier phase also creates additional spinning rotation of the constellation as observable in (15.22). To equalize the linear phase rotation effects, one must cancel the pinning effects due to this carrier phase difference created by the mixing between the LO and the signal carrier. Thus, we can see that the CMA must be associated with the carrier phase recovery so that an additional phase rotation in reverse can be superimposed on the phase rotation because of channel phase distortion to fully equalize the constellation.

The constant modulus (CM) criterion may be expressed by the nonnegative cost function $J_{cma,p,q}$ parameterized by positive integers p and q such that

$$J_{cma,p,q} = \frac{1}{pq} E\left\{\left|\left|y_n\right|^p - \gamma\right|^q\right\}; \quad \text{with } \gamma = \text{constant} \tag{15.24}$$

where $E(.)$ indicates the expected statistical value. The CM criterion is usually implemented as CMA where $p, q = 2$. Using this cost function, the weight vectors can be updated by writing

$$\begin{aligned}\mathbf{W}(k+1) &= \mathbf{W}(k) - \mu \cdot \nabla \mathbf{J}(k) \\ &= \mathbf{W}(k) - \mu \cdot \left(y(k)\left|y(k)\right|^p \left|y(k)\right|^{p-2}\left(\left|y(k)\right|^p - R_p\right)\right) \cdot \mathbf{X}^*(k)\end{aligned} \tag{15.25}$$

with R_p as the constant depending on the type of constellation. Since the final output of the equalizer system would converge to the original input state, one can rewrite (15.25) as

$$\left(a(k)\left|y(k)\right|^p \left|a(k)\right|^{p-2}\left(\left|a(k)\right|^p - R_p\right)\right) = 0 \tag{15.26}$$

Assuming that the in-phase and quadrature-phase components of $a(k)$ to be decorrelated with each other and using the convolution of the input sequence $a(k)$ and the convolution with the impulse response of the channel $h(k)$, we have $x(k) = h(k)^* a(k)$, and the constant R_p can be determined as

$$R_p = \frac{E\left[\left|a(k)\right|^{2p}\right]}{E\left[\left|a(k)\right|^p\right]} \tag{15.27}$$

The flow of update procedure for the weight coefficients of the filter of the equalizer is shown in Figure 15.8.

15.2.1.7.2 Modified CMA: Carrier Phase Recovery Plus CMA

As we know from the cost function (15.24) used in the CMA, since the cost function is phase blind, the CMA can converge even in the presence of phase error. Although it is a merit of the CMA, at convergence the equalizer output will have a constant phase rotation. This phase rotation is generally a result of the difference between the frequency

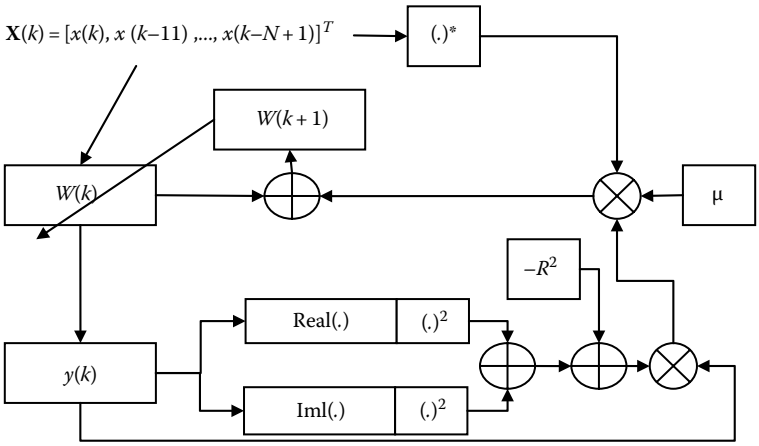

FIGURE 15.8
Block diagram of tap update with CMA cost function.

of the LO and the carrier or LO frequency offset (LOFO). Further, the constellation will be spinning at the carrier FO rate (considered as the phasor rotation) because of the lack of carrier frequency locking. While this phase-blind nature of the CMA is not a serious problem for the constant phase rotation, for some parameters such as the random polarization mode dispersion and the fluctuation of the phase of the carrier, for example, the 100 MHz oscillation of the feedback mirror in the external cavity of the LO, the performance of the CMA is severely degraded by randomly rotating phase distortion. Thus, the carrier phase recovery is essential to determine the LOFO, the offset of the LO and the carrier of the signal channel. The block diagram of combined CMA blind equalization and carrier tracking and locking is illustrated in Figure 15.7. The carrier recovery (CR) loop uses the error between the output of the equalizer and the corresponding decision. The phase updating rule is given by $\phi(k + 1) = \phi(k) - \mu_\phi \, \mathrm{I}[z(k)e^*(k)]$ where μ_ϕ is the step-size parameter, $e(k)$ is the error signal, given by $e(k) = z(k) - \hat{a}(k)$ with $z(k) = y(k)e^{-j\phi(k)}$ is the equalized output with phase error correction and $\hat{a}(k)$ is the estimation of $z(k)$ by a decision device. The carrier tracking loop described earlier gives the estimate of the phase error as shown in Figure 15.7b. Then a differential phase compensation (DPC) can be implemented.

The modified CMA is implemented by cascading the carrier phase recovery first and then cascaded with the standard CMA. Typical CMA operation with carrier phase recovery is shown in Figure 15.9 for 16-QAM constellation with optical coherent transmission and reception described in Chapter 4 in which 100 MHz oscillation of the LO laser is observed. We can observe that the constellation of the nonequalized processing is noisy and certainly cannot be used to determine the bit error rate (BER) of the transmission system. However, in Figure 15.9b, if only the CMA is employed, then the phase rotation is a result of the phase offset between the LO and the signal channel carrier. When carrier phase recovery is applied, the constellation can then be recovered as shown in Figure 15.9c and d with and without DD processing stage which offers similar constellations. The DD processing will be described in the section dealing with NLEs or decision feedback equalizers (DFE) of this chapter.

Noe et al. [9] have reported simulation of coherent receivers under polarization multiplexed quadrature phase shift keying (QPSK) employing CMA algorithms under standard

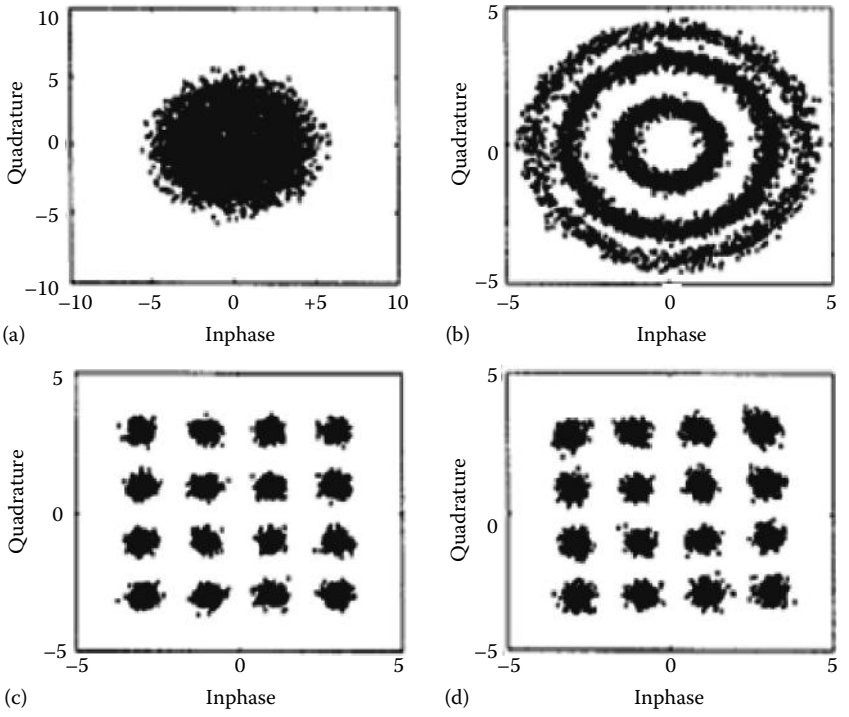

FIGURE 15.9
Constellations of 16-QAM-modulated signals with a carrier FO with respect to that of the local oscillator laser. (a) Unequalized output; (b) output equalized by CMA; (c) output by joint CMA and carrier phase DD recovery; and (d) output by modified CMA, carrier phase recovery, and CMA is cascade.

and modified as well as original and modified DD algorithms under the effects of finite linewidth of the laser (carrier source). There are certain penalties within 0.5 dB on the receiver sensitivity under coherent detection and DSP-based processing in the electronic domain with a 1e−3 FEC level for the linewidth—symbol rate product of 1e−4–1e−3.

15.2.2 Nonlinear Equalizer (NLE) or Decision Feedback Equalizers (DFE)

15.2.2.1 Decision Directed Cancellation of ISI

It has been demonstrated in both wireless and optical communications systems over recent years that nonlinear (decision feedback) equalizers achieve better performance than their linear counterparts. The method of operation of these DD equalizers for cancellation of ISI is as follows.

Consider the transmission systems given in Figure 15.10a which is also similar to Figure 15.2 except that the LE is replaced with the nonlinear one. The linear feedforward (FF) equalizer or transversal filter in this NLE is given in Figure 15.10c. The arrow directing from the decision block across the FF transversal filter indicates the updating of coefficients of the filter.

Similar to the LE case, the input sampled data sequence also follows the notations given in Section 15.2 of this chapter. Multilevel data symbol can be treated in the same way without unduly affecting any of the important results in this analysis.

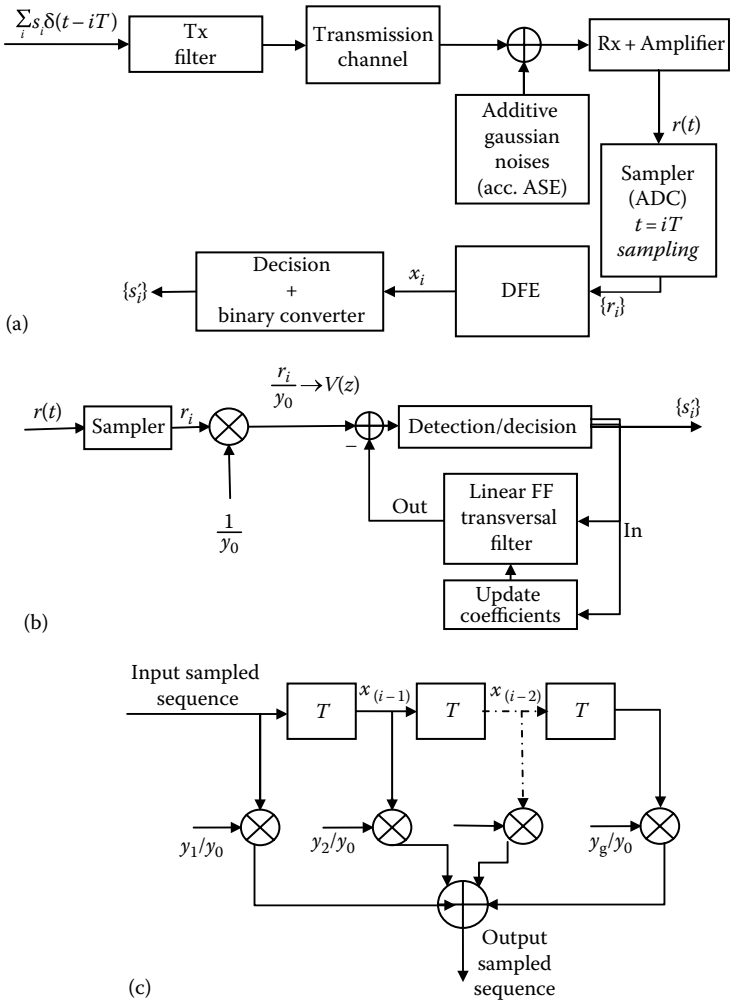

FIGURE 15.10
(a) Simplified schematic of coherent optical communication system incorporating an NLE. Note equivalent baseband transmission systems due to baseband recovery of amplitude and phase of optically modulated signals. (b) Structure of the DFE employing linear FFE and a decision device. (c) Structure of the FF transversal filter.

The pure NLE uses the detected data symbols $\{s_i'\}$ to synthesize the ISI component in a received signal $\{r_i\}$, and then it removes the ISI by subtraction. This is the process of DD cancellation of ISI.

Mathematically, following the notation used in Equation 15.10 for the section just before the decision/detection block of Figure 15.10a or the sampled sequence at the input of Figure 15.10b, the signals entering the detector at the instant $t = iT$ are given by

$$x_i = \frac{r_i}{y_0} - \sum_{j=1}^{g} s'_{i-j} v_j = s_i + \sum_{j=1}^{g} s'_{i-j} v_j + \frac{w_i}{y_0} - \sum_{j=1}^{g} s'_{i-j} v_j \tag{15.28}$$

With corrected detection of each sampled value s_{i-j} such that

$$s'_{i-j} = s_{i-j} \quad \text{for } j = 1, 2, \ldots, g \rightarrow x_i = s_i + \frac{w_i}{y_0} \tag{15.29}$$

In the correct detection and equalization, we have recovered the sampled sequence $\{x_i\}$. It is clear that so long as the data symbols $\{s_i\}$ are correctly detected, their ISI is removed from the equalized signals followed by the NLE, and the channel continues to be accurately equalized.

The tolerance of this pure NLE operating with a channel sampled impulse response whose z-transform is given by $\{Y(z)\}$ as defined in Equation 15.5. The equalized sampled signals at the detector input is given by

$$\begin{aligned} x_i &= s_i + \frac{w_i}{y_0} \\ s_i &= \pm k; \quad \text{binary amplitude of input-seq.} \end{aligned} \tag{15.30}$$

As it is assumed that the sampled sequence is detected as $+k$ or $-k$ depending on whether x_i takes negative or positive value, error would occur if the noise levels corrupt the magnitude, that is, the noise magnitude is greater than k. As in the previous section related to the Gaussian noise (Section 15.2.1.5), we can obtain the probability density function of the random variable noise, w, as

$$p(w) = \frac{1}{\sqrt{2\pi y_0^{-2}\sigma^2}} e^{-\frac{w^2}{2y_0^{-2}\sigma^2}} \tag{15.31}$$

The probability of error can be found as

$$P_e = \int_k^\infty p(w)dw = \int_k^\infty \frac{1}{\sqrt{2\pi y_0^{-2}\sigma^2}} e^{-\frac{w^2}{2y_0^{-2}\sigma^2}} dw = \int_{k\frac{|y_0|}{\sigma}}^\infty \frac{1}{\sqrt{2\pi}} e^{-\frac{w^2}{2}} dw = Q\left(k\frac{|y_0|}{\sigma}\right) \tag{15.32}$$

The most important difference between the nonlinear and LEs is that the NLE can handle the equalization process when there are poles on the unit circle of the *z-plane* of the *z-transform* impulse response of the transmission channel.

A relative comparison of the LE and NLE shows the following: (1) when all zeroes of the channel transfer function in the *z-plane* lie inside the unit circle in the *z-plane*, the NLE with samples including the initial instant would gain an advantage in the tolerance of the Gaussian additive noise over that of LE. The NLE would now be preferred in contrast to LE as the number of taps of the NLE would be smaller than that required for LE; (2) when the transmission is purely phase distortion, which means that the poles lie outside the unit circle of the z-plane and the zeroes are reciprocally conjugates of the poles (inside the unit circles), then the LE is a matched filter and offers a better performance than that by NLE and is closer to a maximum likelihood (ML) detector. The complexity of NLE and LE is nearly the same in terms of taps and noise tolerances. (3) Sometimes, there would be about 2–3 dB better performance between NLE and LE processing.

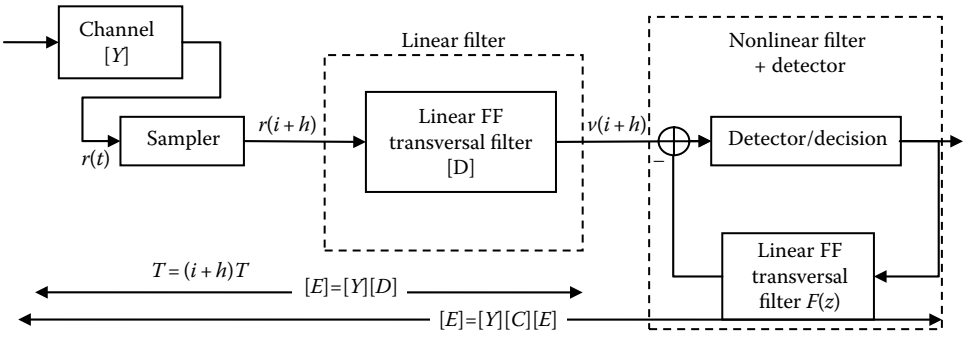

FIGURE 15.11
DFE incorporating a linear and nonlinear filter with overall transfer impulse responses.

15.2.2.2 Zero-Forcing Nonlinear Equalization (ZF-NLE)

When an NLE is used in lieu of the LE of the ZE-FE illustrated in Figure 15.3, then the equalizer is called ZF-NLE as illustrated in the transmission system shown in Figure 15.11 that consists of a linear feedforward transversal filter and a NLE with a linear feedback transversal filter and a decision/detector operation.

The DFE performs the equalization by ZF which is similar as in the case of ZF-LE with ZF described in Section 15.2.1.2. The operational principles for this type of NLE are as follows:

- The linear filter of Figure 15.11 partially equalizes the channel by setting as zero all components of the channel sampled impulse response preceding that of the largest magnitude, without affecting the relative values of the remaining components.
- The NLE section then completes the equalization process by the operations exactly as have been described in Section 15.2.2.1.

Similar to the use of the notations assigned for the input sequence, the channel impulse response of g-sampling instants in the z-transform $Y(z)$ given in Equations 15.10 through 15.12, we can set that the required equalizer impulse response in the z-domain $C(z)$ of m-tap as

$$Y(z)C(z) \simeq z^{-h} \quad \text{with } 0 < h < m + g \tag{15.33}$$

where h is an integer in the range of 0 to $(m + g)$ with

$$\begin{aligned} &[\mathbf{Y}] = [\,y_0 \quad y_1 \quad \ldots \quad y_g\,]; \quad \text{Channel impulse reponse} \\ &[\mathbf{C}] = [\,c_0 \quad c_1 \quad \ldots \quad c_m\,]; \quad \text{LE impulse response} \\ &\text{so that} \\ &Y(z) = y_0 + y_1 z^{-1} + \cdots + y_g z^{-g}; \text{ and } C(z) = c_0 + c_1 z^{-1} + + c_m z^{-m} \end{aligned} \tag{15.34}$$

Let the LE having [**D**] as an $(n+1)$-*tap* gain filter with the impulse response $D(z)$ of $(n+1)$-*tap* be expressed as

$$[\mathbf{D}] = \begin{bmatrix} d_0 & d_1 & \cdots & d_n \end{bmatrix};$$

$$\text{impulse response linear} \rightarrow D(z) = c_0 + c_1 z^{-1} + \cdots + c_m z^{-m} \tag{15.35}$$

transversal filter

Thus, the overall transfer function of the channel and the equalizer can be written, when setting [**D**] = [**C**][**E**], as

$$Y(z)C(z)E(z) \simeq z^{-h}E(z) \quad \text{with } n = m + g - l \tag{15.36}$$

with [**E**] as the required sampled impulse response so that the NLE that can equalize the input pulse sequence, that is, to satisfy the condition that the product of the two transfer functions must be unitary, or

$$[\mathbf{E}] = \begin{bmatrix} 1 & \dfrac{y_{l+1}}{y_l} & \dfrac{y_{l+2}}{y_l} & \dfrac{y_g}{y_l} \end{bmatrix} \rightarrow$$

z-transform impulse response (15.37)

$$E(z) = 1 + \frac{y_{l+1}}{y_l} z^{-1} + \frac{y_{l+2}}{y_l} z^{-2} + \cdots + \frac{y_g}{y_l} z^{-g+l}$$

where y_l is the largest component of the channel sampled impulse response. When this condition is satisfied, then the nonlinear filter ZF-NLE acts now the same as ZF-LE but with the tap gain order reduced to $(g–l)$ taps whose coefficients are $\frac{y_{l+1}}{y_l}, \frac{y_{l+2}}{y_l}, \ldots, \frac{y_g}{y_l}$ instead of g-taps with gains $v_1, v_2, \ldots, v_g$. The probability of error can be evaluated in a similar manner as described earlier for additive noises of a Gaussian distribution of the probability density function with mean zero and a standard deviation σ, to give

$$P_e = Q\left(\frac{k}{\sigma|D|}\right); \quad |D| = \text{Euclidean length of impulse response } [D] \tag{15.38}$$

15.2.2.3 Linear and Nonlinear Equalizations of Factorized Channel Response

In the normal case, the z-domain transfer function of the channel $Y(z)$ can be factorized into a cascade of two subchannels given by

$$Y(z) = Y_1(z)Y_2(z) \tag{15.39}$$

so that we can employ the first LE to equalize the subchannel $Y_1(z)$ and the NLE to tackle the second subchannel $Y_2(z)$. The procedure is a combined cascading of the two processing stages which have been described earlier.

15.2.2.4 Equalization with Minimizing MSE in Equalized Signals

As we have seen the equalization using NLEs described in the previous section, the decision or detection will enhance the SNR performance of the system. However, under what criteria can the NLE make the decision block so that an optimum performance can be achieved. The mean square error can be employed as described earlier to minimize the errors in the decision stage of the NLE.

15.3 Maximum Likelihood Sequence Detection (MLSD) and Viterbi

Consider the detection of the first data symbol s_0 of the sequence $\{s_i\}$; $i = 0 \ldots m$ by an arrangement by which the delay of the *h-sampling* intervals increased to $m + g + 1$ such that all signals $\{v_i\}$ at the output of the filter *D*, that are dependent on any of the *m* received data symbols $\{s_0 \quad s_1 \quad \ldots \quad s_{m-1}\}$ (see also Figure 15.11), are involved in the detection process at once. Since s_0 is the first detected value of the sequence of data symbols, no DD cancellation of the ISI can be carried out and the detection process operates on the $m + g$ signals $\{v_0 \quad v_1 \quad \ldots \quad v_{m+g-1}\}$. The detected value s_0' of the initial data symbol is, therefore, taken as its possible value for which

$$\sum_{i=0}^{m+g=1}\left(v_i - \sum_{j=0}^{g} s'_{i-j}e_j\right)^2 \rightarrow \text{minimum} \quad \text{for } \forall \text{ combinations} \tag{15.40}$$

of all possible values of $\{s_0' \quad s_1' \quad \ldots \quad s_{m-1}'\}$ with the note that $s_i' = s_i = 0$; for $-i, 0$ and $i > m-1$. This detection process is the maximum likelihood detection (MLSD) or MLSE (estimation) when the estimation is used in place of detection, of the data symbols $\{s_0 \quad s_1 \quad \ldots \quad s_{m-1}\}$ from the corresponding received sequence of signals $\{v_0 \quad v_1 \quad \ldots \quad v_{m+g-1}\}$ at the output of the filter *D*.

Under the assumed conditions, the detection process minimizes the probability of error in the detection of the complete sequence of data symbols. Thus, all the data symbols are detected simultaneously in a single detection process that is optimum. Unfortunately, when *m* is large, especially in DSPs operating at ultra high speed the processing speed would not allow such an operation. Thus, successive processing of the data symbols is necessary, and hence, a requirement for memory storage so that the detection process can be considered to be equivalent to the simultaneous process. This sequential detection can be implemented using the Viterbi algorithm detector [10].

The Viterbi algorithm operates as follows. Consider the data transmission as shown in Figure 15.11 in which the detector (by thresholding) and the transversal filter *F* are replaced by a more complex subsystem. Assuming that the *l-level* data symbols $\{s_i\}$ are transmitted, after the optical to electronic detection and preamplification, the received signals are sampled and stored as components of l^g $h + 1$ component vectors of sequences $\{Q_{i-1}\}$ where

$$Q_{i-1} = \begin{bmatrix} x_{i-h-1} & x_{i-h} & x_{i-1} \end{bmatrix} \tag{15.41}$$

The symbol x_j for any j in the range of $\{0 \ldots m-1\}$ may take on any possible values of s_j and $h > g$. Each vector Q_{i-1} is formed by the last $(h + 1)$ components of the corresponding

i-component vector $X_{i-1} = \begin{bmatrix} x_0 & x_1 & \dots & x_{i-1} \end{bmatrix}$ which represents a possible received sequence of data symbols $\{s_j\}$. Associated with each stored vector $\{Q_{i-1}\}$ is its cost

$$c_{i-1} = \sum_{j=0}^{i-1} \left(v_j - z_j\right)^2; \quad \text{with } v_j = z_j + u'_j \quad z_j = \sum_{k=0}^{g} x_{j-k} e_k$$
$$x_j = 0 \quad \text{for } j < 0 \text{ and } j > m-1 \tag{15.42}$$

The symbol z_j takes the value of v_j, which is received in the absence of noises. The cost c_{i-1} is the Euclidean distance between vectors $V_{i-1} = \begin{bmatrix} v_0 & v_1 & \dots & v_{i-1} \end{bmatrix}$ and $Z_{i-1} = \begin{bmatrix} z_0 & z_1 & \dots & z_{i-1} \end{bmatrix}$. Since Z_{i-1} is the sequence up to the time instant $t = (i-1)T$ resulting from the transmitted sequence X_{i-1} in the absence of noises, the cost c_{i-1} is the measure of the probability that this sequence is correct. The smaller the value of this cost the more likely that the corresponding sequence X_{i-1} is correct.

In summary, in an MLSE, the decision is performed by calculating the transmitted bit stream with the highest probability. This means that the probability of all bit combinations for the whole sequence is taken into account and the combination of the highest probability is assumed as the transmitted bit sequence.

15.3.1 Nonlinear MLSE

MLSE is a well-known technique in communications for equalization and detection of the transmitted digital signals. The concept of MLSE is discussed in brief. An MLSE receiver determines a sequence b as the most likely transmitted sequence when the conditional probability Pr(**y** | **b**) is maximized where *y* is the received output sequence. If the received signal **y** is corrupted by a noise vector **n,** which is modeled as a Gaussian source (i.e., **y = b + n**), it is shown that the above maximization operation can be equivalent to the process of minimization of the Euclidean distance *d* [11]:

$$d = \sum_{k} |\, \mathbf{y}_k - \mathbf{b}_k \,|^2 \tag{15.43}$$

MLSE can be carried out effectively with the implementation of the Viterbi algorithm based on state trellis structure.

15.3.1.1 Trellis Structure and Viterbi Algorithm

15.3.1.1.1 Trellis Structure

Information signal *b* is mapped to a state trellis structure by a finite state machine (FSM) giving the mapping output signal *c* as shown in Figure 15.12. The FSM can be a convolutional encoder, a trellis-based detector, or, as presented in more detail later on, the fiber medium for optical communications.

A state trellis structure created by the FSM is illustrated in Figure 15.13. At the *n*th epoch, the current state B has two possible output branches connecting to states E and F. In this case, these two branches correspond to the two possible transmitted symbols of "0" or "1," respectively. This predefined state trellis applies to the 1 bit-per-symbol modulation formats such as binary ASK or DPSK formats. In cases of multibit modulation per symbol, the

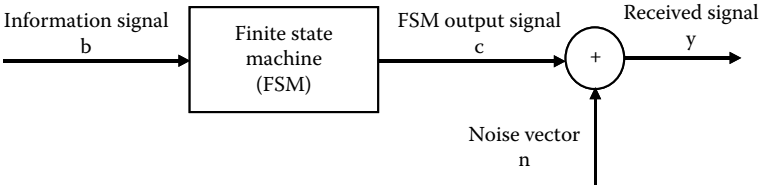

FIGURE 15.12
Schematic of the MLSE equalizer as a FSM.

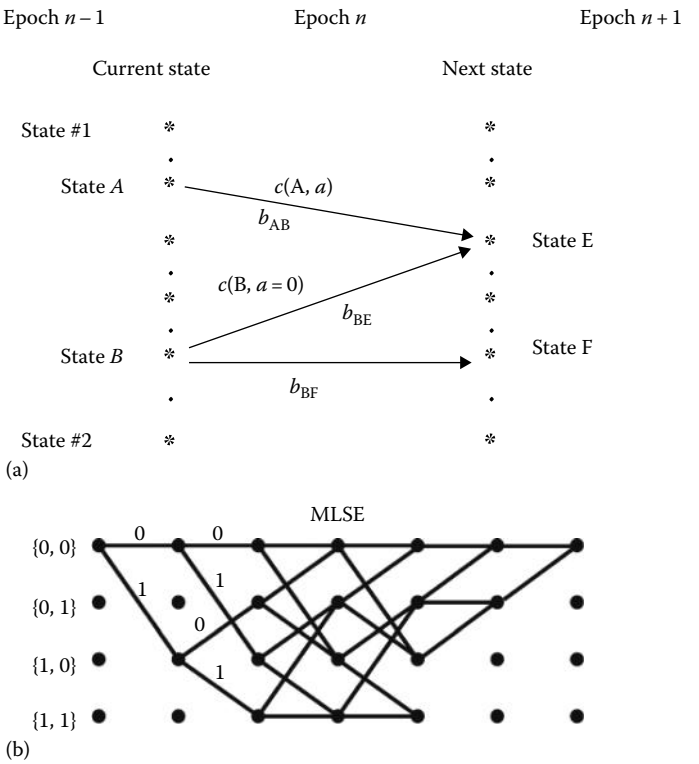

FIGURE 15.13
State trellis of a FSM (a) trellis path (b) tracing of possible ML estimation with assigned bit pattern.

phase trellis has to be modified. For example, in the case of QPSK, there are four possible branches leaving the current state B and connecting the next states, corresponding to the possible input symbols of "00", "01", "10," and "11."

Further, for a simplified explanation, several assumptions are made. These assumptions and the corresponding notations can be described as follows: (1) Current state B is the starting state of only two branches, which connects to states E and F, denoted as b_{BE} and b_{BF}. In general, b_{B*} represents all the possible branches in the trellis which starts from state B. In this case, these two branches correspond to the possible binary transmitted information symbols of "0" or "1," respectively. The notation $c(B, a = 0)$ represents the encoded symbol (at the FSM output) for the branch BE, b_{BE} that starts from

state B and corresponds to a transmitted symbol $a = 0$. Similar conventions are applied for the case of branch BF, b_{BF}, that is $c(B, a = 1)$ and all the branches in the trellis. (2) There are only two possible output branches ending at state E (from state A and state B). They are denoted as b_{AE} and b_{BF}. In general, b_{*E} represents all the possible branches in the trellis that end at state E. The number of states 2^{δ} in the trellis structure is determined by the number of memory bits, δ , also known as the constraint length. Figure 15.13b also shows a possible trace of the trellis with the assigned states of the bit pattern.

15.3.1.1.2 Viterbi Algorithm

In principle, the Viterbi algorithm follows two main phases:

1. *Phase 1: Calculation of state and branch metrics*:
   At a sampling index n, epoch n, a *branch metric* is calculated for each of the branches in the trellis. For example, considering the connecting branch between the current state B and the next state E, which corresponds to the case when the "0" symbol is transmitted, the *branch metric* is calculated as

$$BM_{BE}(n) = |\,\mathbf{y}_{(n)} - \mathbf{c}_{BE}\,|^2 \tag{15.44}$$

   The state metric $SM_E(n)$ of the state E is calculated as the sum between the metric of the previous state, that is state B and the branch metric obtained earlier. The calculation of state metrics $SM_E(n)$ of state E is given by

$$SM_E(n) = \min_{\forall B \to E} \left\{ SM_B(n-1) + BM_{BE}(n) \right\} \tag{15.45}$$

   The branch giving the minimum state metric $SM_E(n)$ for state E is called the preferred path.
2. *Phase 2: Trace-back process*
   The process of calculating state and branch metrics continues along the state trellis before terminating at epoch N_{trace}, which is usually referred to as the trace-back length. A rule of thumb as referred in Refs. [11,12] is that the value of N_{trace} is normally taken to be five times the sequence length. This value comes from the results showing that the solution for the Viterbi algorithm converges giving a unique path from epoch 1 to epoch N_{trace} for the MLSE detection. (1) At N_{trace}, the terminating state with the minimum state metric and its connecting preferred path are identified. (2) The previous state is then identified as well as its previous preferred path. (3) The trace-back process continues until reaching epoch 1.

15.3.1.2 Optical Fiber as a Finite State Machine

The structure of the FSM shown in Figure 15.13 is now replaced with the optical channel based on optical fiber. It is important to understand how the state trellis structure is formed for an optical transmission system. In this case, the optical fiber involves all the ISI sources causing the waveform distortion of the optical signals, which includes CD, PMD, and filtering effects. Thus, the optical fiber FSM excludes the signal corruption by noise as well as the random-process nonlinearities. The ISI is caused by dispersion effects and nonlinear phase and ASE and nonlinear effects [13].

15.3.1.3 Construction of State Trellis Structure

At epoch n, it is assumed that the effect of ISI on an output symbol of the FSM, c_n is caused by both executive δ pre-cursor and δ post-cursor symbols on each side. In this case, c_n is the middle symbol of a sequence which can be represented as

$$c = (c_{n-\delta}, \ldots, c_n, \ldots, c_{n+\delta}) \quad b \in \{0,1\}; n > 2\delta + 1 \tag{15.46}$$

Unlike the conventional FSM used in wireless communications, the output symbol c_n of the optical fiber FSM is selected as the middle symbol of the sequence c. This is because the middle symbol gives the most reliable picture about the effects of ISI in an optical fiber channel.

A state trellis is defined with a total number of $2^{2\delta}$ possible data sequences. At epoch n, the current state B is determined by the data sequence

$$(b_{n-2\delta+1}, \ldots, b_{n-\delta}, \ldots, b_n) \quad b \in \{0,1\}; n \geq 2\delta + 1 \tag{15.47}$$

where b_n is the current input symbol of the optical fiber FSM. Therefore, the state trellis structure is constructed from the optical fiber FSM and is ready to be integrated with the Viterbi algorithm, especially for the calculation of a branch metric.

The MLSE NLE can effectively combat all the above ISI effects, and it is expected that the tolerance to both CD and PMD of optical MSK systems with optical frequency discrimination receiver (OFDR) receiver can be improved significantly.

15.3.2 Shared Equalization between Transmitter and Receivers

Figure 15.14a and b depicts the arrangement of equalizers at the transmitter only and combined at both transmitter and receiver side, respectively. There are advantages when equalization is conducted at both sides of the transmitter and receiver, in the digital domain. At the transmitter the equalizer performs the pre-direction to compensate for the chromatic dispersion by chirping the phase. However, the dispersion can never be determined exactly, and so it is always necessary to have an equalizer at the reception subsystem so that residual CD effects by others such as PMD and nonlinear impairment can be equalized.

15.3.2.1 Equalizers at the Transmitter

Consider the arrangement so that the equalizer acting as a pre-distortion and placed at the transmitter as shown in Figure 15.14a. An ultra-high-speed analog to digital converter (DAC) would be best and flexible in generating pre-emphasis digital signals for compensation of the linear CD distortion effects. The NLE in this case converts the sequence of data symbols $\{s_i\}$ into a nonlinear channel $\{f_i\}$ at the output of the transmitter, normally an optical modulator driven by the output of the nonlinear electrical equalizer as shown in Figure 15.14b and re-modeled as shown in Figure 15.15. These symbols are sampled and transmitted as sampled impulses $\{f_i\delta(t - iT)\}$. The SNR in this case is given by $E[f_i^2]/\sigma^2$ with the energy as the expected average energy of the predistorted signal sequence and must be equal to k^2.

A NLE is necessary at the output before the final recovery of the system. This processor performs a modulo-m operation on the received sequence x[modulo] $- m = x - jm$

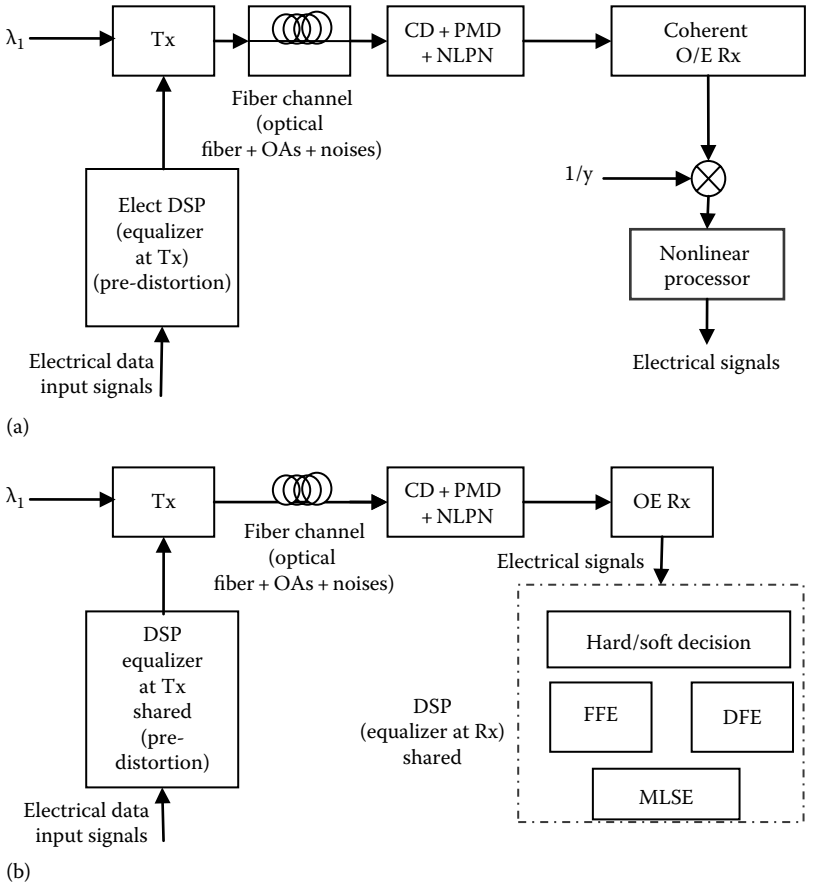

FIGURE 15.14
Arrangement of electronic DSP for equalization in optical transmission systems. Electronic DSP for pre-distortion, electronic DSP at the Rx is for post-equalization, and shared pre-distortion and post-equalization at the Tx and Rx (a) equalization at the transmitter side, (b) equalization at the receive side, and equalization shared between Tx and Rx sides.

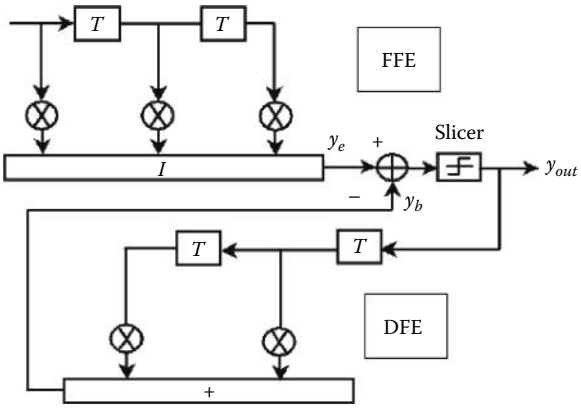

FIGURE 15.15
Schematic of a nonlinear feedback equalizer at the transmitter.

with j an appropriate integer. The z-transform $F(z)$ at the output of the nonlinear distortion equalizer is given by

$$F(z) = M\left[S(z) - F(z)y_0^{-1}Y(z) - 1\right] \tag{15.48}$$

where
$S(z)$ is the z-transform of the sampled input signals
$Y(z)$ is the z-transform of the channel transfer function

Then the z-transform at the output of the nonlinear processor at the receiver can be written as

$$\begin{aligned} &X(z) = M\left[F(z)Y(z) + W(z)\right] = M\left[F(z)y_0^{-1}Y(z) - y_0^{-1}W(z)\right] \\ &\text{or } X(z) = M\left[S(z) - y_0^{-1}W(z)\right] \\ &\text{that is} \\ &x_i = M\left[y_0^{-1}r_i\right] = M\left[s_i + y_0^{-1}w_i\right] \end{aligned} \tag{15.49}$$

with x_i denoting the signal at the output of the nonlinear processor. Clearly, all ISI has been eliminated except the noise contribution. The nonlinear processor M operates as a modulo-m as

$$\begin{aligned} M\left[q\right] &= \left[(q + 2k)\text{modulo} - 4k\right] - 2k = q - 4jk \\ -2k &\le M\left[q\right] \le 2k \end{aligned} \tag{15.50}$$

Thus an error would happen when

$$(4j-3)k \le y_0^{-1}w_i \le (4j-1)k \quad \forall j \tag{15.51}$$

The probability of error is then given as

$$P_e = 2\int_k^\infty \frac{1}{\sqrt{2\pi y_0^{-2}\sigma^2}} e^{-\frac{w^2}{2y_0^2\sigma^2}} dw = 2Q\left(\frac{k|y_0|}{\sigma}\right) \tag{15.52}$$

15.3.2.2 Shared Equalization

Long-haul transmission requires the equalization so that the extension of the transmission is as long as possible. Equalization at the receiver can be supplemented with that at the transmitter to further increase the reach.

The equalizer at the transmitter of the previous section can be optimized by inserting another filter at the receiver as shown in Figure 15.14c. Consider the channel transfer function $Y(z)$ that can be written as a cascade of two linear transfer functions $Y_1(z)$ and $Y_2(z)$ as

$$\begin{aligned} &Y(z) = Y_1(z)Y_2(z) \\ &\text{with} \begin{cases} Y_1(z) = 1 + p_1 z^{-1} + \cdots + p_{g-f} z^{-g+f} \\ Y_2(z) = q_0 + q_1 z^{-1} + \cdots + q_f z^{-f} \end{cases} \end{aligned} \tag{15.53}$$

$Y_1(z)$ has all the zero inside the unit circle and $Y_2(z)$ has all outside the unit circle. Then we can find a third system with a transfer function that has all the coefficients in reverse of those of $Y_2(z)$ given as

$$Y_3(z) = q_f + q_{f-1}z^{-1} + \cdots + q_0 z^{-f} \tag{15.54}$$

With the reverse coefficients, the zeroes of the $Y_3(z)$ now lie inside the unit circle.

The linear FFE filter D of the nonlinear filter formed by cascading an FFE and a DFE as shown earlier can minimize the length of the vector D and minimizing e_0 can be satisfied provided that

$$D(z) = z^{-h}Y_2^{-1}(z)Y_3(z) \tag{15.55}$$

which represents an orthogonal transformation without attenuation or gain. The LE with a z-transform $Y_2(z)Y_3^{-1}(z)$ is an all pass pure phase distortion.

This transfer function of the all pass pure phase distortion is indeed a cascade of optical interferometers, known as half-band filters [14,15]. This function can also be implemented in the electronic domain. The equalizer can then be followed by an electronic DFE. Hence, the feedback linear filter $F(z)$ in Figure 15.16 can be written as

$$F(z) = Y_1(z)Y_3(z) \tag{15.56}$$

The probability of error can be similarly evaluated and given by

$$P_e = \int_k^\infty \frac{1}{\sqrt{2\pi y_0^{-2}\sigma^2}} e^{-\frac{w^2}{2y_0^2\sigma^2}} dw = Q\left(\frac{k|q_f|}{\sigma}\right) \tag{15.57}$$

with q_f taken as the first coefficient of $Y_3(z)$.

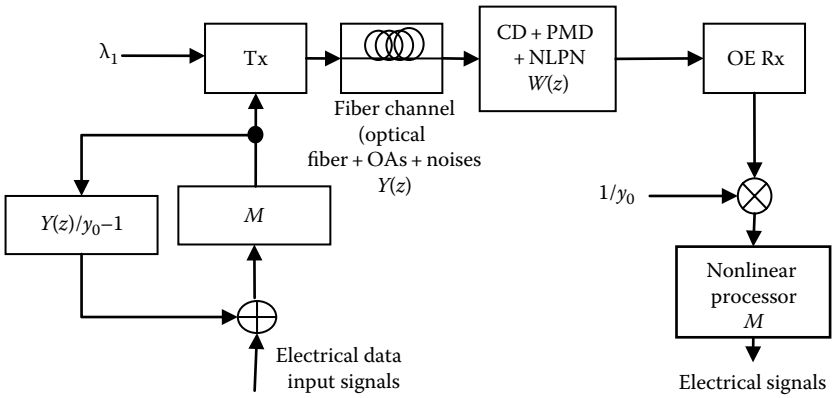

FIGURE 15.16
Schematic of a nonlinear feedback equalizer following an optical receiver combined FFE and DFE equalization slicer or decision/detector is the data decision.

15.4 Maximum a Posteriori (MAP) Technique for Phase Estimation

15.4.1 Method

Assume that we want to estimate an unobserved population parameter θ on the basis of an observed variable x. Let f be the sampling distribution of x, so that $f\left(x|\theta\right)$ is the probability of x when the underlying population parameter is θ. Then the function that transforms $\theta \to f\left(x|\theta\right)$ is known as the likelihood function, and the estimate $\hat{\theta}_{ML}(x) = \max_{\theta} f\left(x|\theta\right)$ is the ML estimate of θ.

Now assume that a prior distribution g over θ exists. This allows us to treat θ as a random variable as in Bayesian statistics. Then the posterior distribution of θ can be determined as

$$\theta \to f\left(\theta|x\right) = \frac{f\left(x|\theta\right)g(\theta)}{\int_{\nu\in\Theta} f\left(x|\nu\right)g(\nu)d\nu} \tag{15.58}$$

where
g is the density function of θ
Θ is the domain of g

This is a straightforward application of Bayes' theorem. The method of MAP estimation then estimates θ as the mode of the posterior distribution of this random variable

$$\hat{\theta}_{MAP} = \arg\_\max \frac{f\left(x|\theta\right)g(\theta)}{\int_{\nu} f\left(x|\nu\right)g(\nu)d\nu} = \arg\_\max_{\theta} f\left(x|\theta\right)g(\theta) \tag{15.59}$$

The denominator of the posterior distribution (so-called partition function) does not depend on θ and therefore plays no role in the optimization. Observe that the MAP estimate of θ coincides with the ML estimate when the prior g is uniform (i.e., a constant function). The MAP estimate is a limit of Bayes' estimators under a sequence of 0–1 loss functions, but generally not a Bayes' estimator per se, unless θ is discrete.

15.4.2 Estimates

MAP estimates can be computed in several ways:

1. Analytically the mode(s) of the posterior distribution can be obtained in closed form. This is the case when the conjugate priors are used.
2. By numerical optimization such as the conjugate gradient method or by Newton's method, which may usually require first or second derivative, the modes are to be evaluated analytically or numerically.
3. By a modification of an expectation–maximization algorithm, the modes can be calculated. This does not require derivatives of the posterior density.

One of the possible processing algorithm can be the *ML* phase estimation for coherent optical communications [16]. The differential QPSK (DQPSK) optical system can be considered as an example. In this system, as described in Chapter 5, the phase-diversity

coherent reception technique, with a mixing of an LO, can be employed to recover the in-phase (I) and quadrature-phase (Q) components of the signals. Such a receiver comprises a 90° optical hybrid coupler to mix the incoming signal with the four quadruple states associated with the LO inputs in the complex-field space. A $\pi/2$ phase shifter can be used to extract the quadrature components in the optical domain. The optical hybrid can then provide four lightwave signals to two pairs of balanced photodetectors to reconstruct I and Q information of the transmitted signal. In case the LO is the signal itself, then the reception is equivalent to a self-homodyne detection. For this type of reception subsystem, the balanced receiver would integrate a one-bit delay optical interferometer so as to compare the optical phases of two consecutive bits. We can assume a complete matching of the polarization between the signal and the LO fields so that only the impact of phase noise is considered. Indeed, the ML algorithm is the modern MLSE technique [17].

The output signal reconstructed from the photocurrents can be represented by

$$r(k) = E_0 \exp[j(\theta_s(k) + \theta_n(k))] + \tilde{n}(k) \tag{15.60}$$

where

k denotes kth sample over time interval $\left[kT, (k+1)T\right]$ (T is the symbol period)

$$E_0 = \Re\sqrt{P_{LO} p_s}$$

$\Re$ is the photodiode responsivity

P_{LO} and p_s are the power of LO and received signal, respectively

$\theta_s(k) \in \{0, \pi/2, \pi, -\pi/2\}$ is the modulated phase, the phase difference carrying the data information

$\theta_n(k)$ is the phase noise during the transmission

$\{\tilde{n}(k)\}$ is complex white Gaussian random variables with $E[\tilde{n}(k)] = 0$ land $E\left[\left|\tilde{n}(k)\right|^2\right] = N_0$

To retrieve information from the phase modulation $\theta_s(k)$ at time $t = kT$, the carrier phase noise $\theta_n(k)$ is estimated based on the received signal over the immediate past L symbol intervals, that is, based on $\{r(l),\ k - L \le l \le k - 1\}$. In the decision-feedback strategy, a complex phase reference vector $\mathbf{v}(k)$ is computed by the correlation of L received signal samples $r(l)$ and decisions on L symbols $\{\hat{m}(l), k - L \le l \le k - 1\}$, where $\hat{m}(l)$ is the receiver's decision on $\exp(j\theta_s(l))$:

$$\mathbf{v}(k) = \sum_{l=k-L}^{k-1} r(l)\hat{m}^*(l) \tag{15.61}$$

Here, * denotes the complex conjugation. An initial L-symbol long-known data sequence is sent to initiate the processor/receiver. Alternatively, the ML decision processor can be trained prior to the transmission of the data sequence. It is important to note that not only can the $\pi/4$-rad phase ambiguity be resolved but also the decision-aided method is now totally linear and efficient to implement based on (15.61). To some extent, the reference $v(k)$ assists the receiver to acquire the channel characteristic. With the assumption that $\theta_n(k)$ varies slowly compared to the symbol rate, the computed complex

reference $v(k)$ from the past L symbols forms a good approximation to the phase noise phasor $\exp(j\theta_n(k))$ at time $t = kT$.

Using the phase reference $\mathbf{v}(k)$ from (15.61), the decision statistic of the *ML* receiving processor is given as

$$q_i(k) = \mathbf{r}(k)C_i^* \bullet \mathbf{v}(k), \quad i = 0, 1, 2, 3 \tag{15.62}$$

where

$C_i \in \{\pm 1, \pm j\}$ is the DQPSK signal constellation

• denotes inner product of two vectors

The detector declares the decision $\hat{m}(k) = C_k$ if $q_k = \max q_i$. This receiver/processor has been shown to achieve coherent detection performance if the carrier phase is a constant and the reference length L is sufficiently long.

The performance of *ML*, the receiving processor, can be evaluated by simulation using Monte Carlo simulations in two cases: a linear phase noise system and a nonlinear phase noise system. For comparison, the *M*th power phase estimator and differential demodulation can also be employed.

Nonlinearity in an optical fiber can be ignored when the launch optical power is below the threshold, so the fiber optic can be modeled as a linear channel. The phase noise difference in two adjacent symbol intervals, that is, $\theta_n(k) - \theta_n(k-1)$, obeys a Gaussian distribution with the variance σ^2 determined by the linewidth of the transmitter laser and the LO, given by the Lorentzian linewidth formula $\sigma^2 = 2\pi\Delta vT$, where Δv is the total linewidth of the transmitter laser and the LO [18]. In the simulations, σ can be set to 0.05, corresponding to the overall linewidth $\Delta v = 8$ MHz when the baud rate is 40 symbols/s.

As observed in Figure 15.17, the *ML* processor outperforms the phase estimator and differential demodulation by about 0.25 and 1 dB, respectively. Although the performance gap between the *ML* processor and *M*th power phase estimation is not very large in the case of the multiple phase shift keying (M-PSK) system, the *M*th power phase estimator requires more nonlinear computations, such as an arctan(·), which incurs a large latency in the system and leads to phase ambiguity in estimating the block phase noise. On the contrary, the *ML* processor is a linear and efficient algorithm, and there is no need to deal with the $\pi/4$-rad phase ambiguity, making it more feasible for on-line processing for the real systems. We also extend our *ML* phase estimation technique to the QAM system. The conventional *M*th-power phase estimation scheme suffers from the performance degradation in QAM systems, since only a subgroup of symbols with phase modulation $\pi/4 + n \cdot \pi/2$ ($n = 0, 1, 2, 3$) can be used to estimate the phase reference. The maximum tolerance of linewidth per laser in *Square*_16 QAM can be improved 10 times compared to the *M*th-power phase estimator scheme.

Let us now consider the case with nonlinear phase noise. In a multispan optical communication system with erbium-doped fiber amplifiers (*EDFAs*), the performance of optical *DQPSK* is severely limited by the nonlinear phase noise converted by amplified ASE noise through the fiber nonlinearity [19]. The laser linewidth is excluded to only consider the impact of the nonlinear phase noise on the receiver. The transmission system can comprise a single-channel *DQPSK* modulated optical signal transmitted at 10–40 Gsymbols/s over N 100 km equally spaced amplified spans, which are fully compensated for chromatic dispersion and gain-equalized optical power along the fiber as shown in Figure 15.18. The following parameters are assumed for the transmission system: $N = 20$, fiber nonlinear coefficient $\gamma = 2$ W/km, fiber loss $\alpha = 0.2$ dB/km, the amplifier gain $G = 20$ dB with an *NF* of

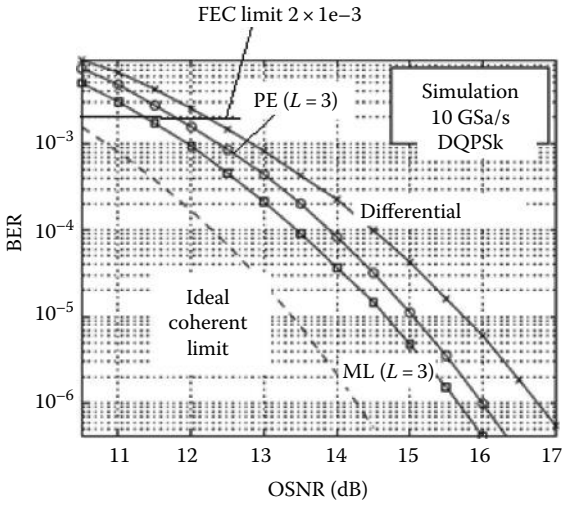

FIGURE 15.17
Simulated BER performances of a 10-Gsymbols/s DQPSK signal in linear optical channel with laser linewidth 2 MHz (σ = 0.05) and decision-aided length $L = 3$. (Modified from Zhang, S. et al., A comparison of phase estimation in coherent optical PSK system, in *Photonics Global'08*, Singapore, paper C3-4A-03, December 2008.) The FEC limit can be set at 2 × 1e−3 to determine the required OSNR.

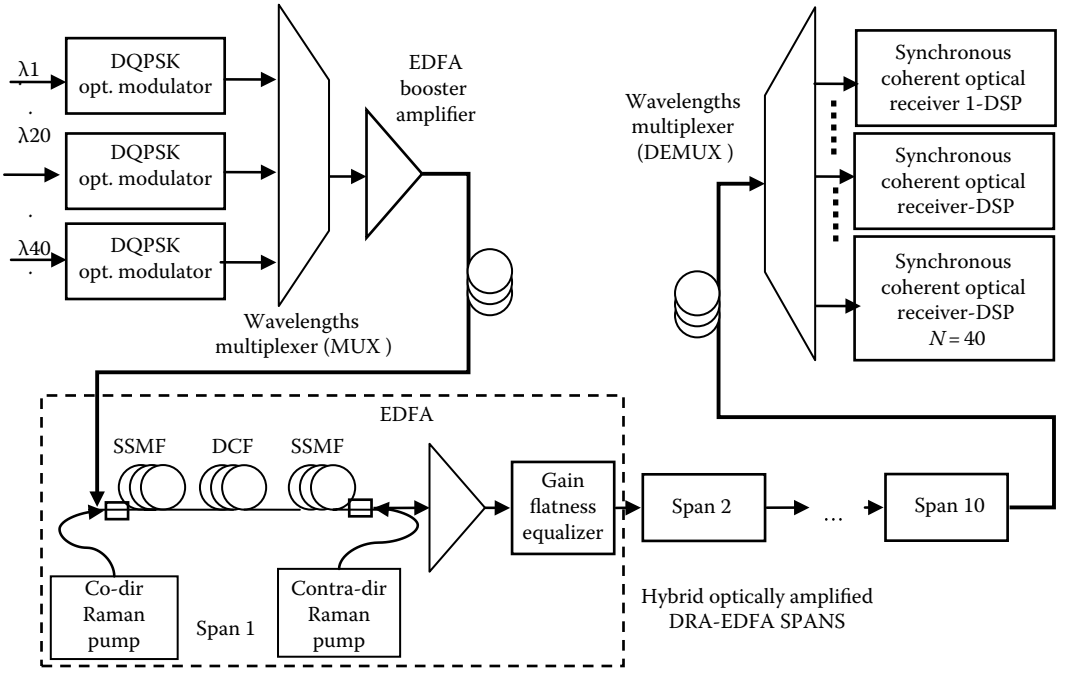

FIGURE 15.18
DWDM Optical DQPSK system with N-span dispersion-compensated optic fiber transmission link using synchronous self-homodyne coherent receiver to compensate nonlinear phase noise under both Raman amplification and EDF amplification.

6 dB, the optical wavelength $\lambda = 1553$ nm, the bandwidth of optical filter and electrical filter of $\Delta\lambda = 0.1$ nm and 7 GHz, respectively. The *optical signal to noise ratio (OSNR)* is defined at the location just in front of the optical receiver as the ratio between the signal power and the noise power in two polarization states contained within a 0.1 nm spectral width region. As shown in Figure 15.19a, the receiver sensitivity of the *ML* processor has improved by about 0.5 dB and 3 dB over phase estimation and differential demodulation, respectively, at the *BER* level of 10^{-4}. Besides, it is noteworthy that differential demodulation has exhibited an error floor as a result of severe nonlinear phase noise with high launch optical power at the transmitter.

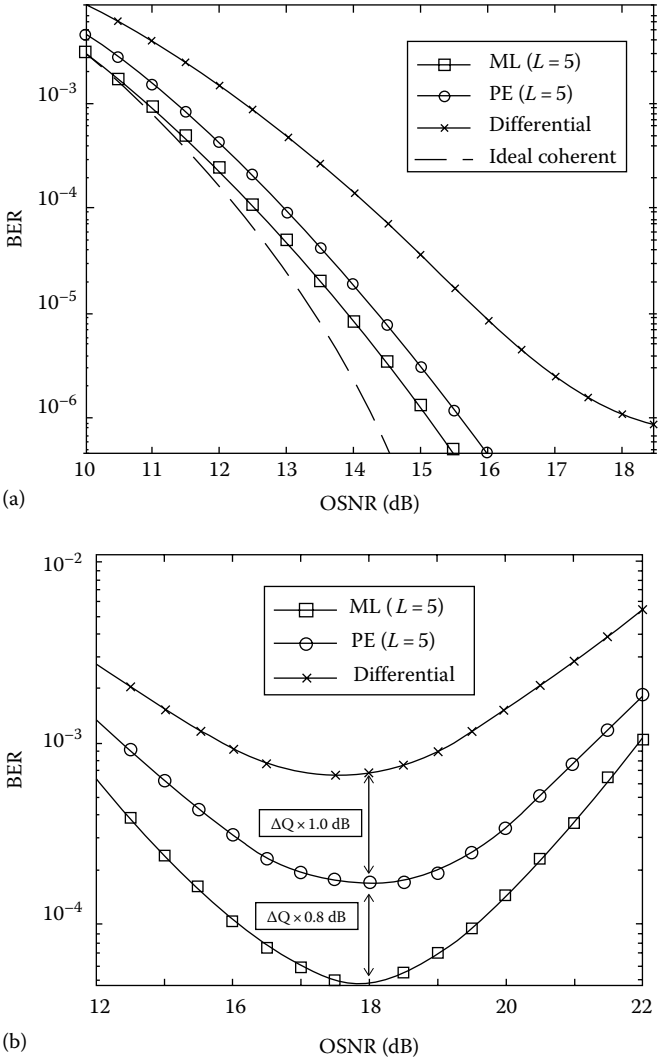

FIGURE 15.19
Monte Carlo–simulated BER of a 10-Gsymbol/s DQPSK signal in an *N*-span optical fiber system with template length $L = 5$: (a) $N = 20$ and (b) $N = 30$ under different detection schemes of ML estimator, phase estimator, differential demodulation, and ideal coherent detection. ML = maximum likelihood, PE = phase estimation. (Extracted from Zhang, S. et al., A comparison of phase estimation in coherent optical PSK system, in *Photonics Global'08*, Singapore, paper C3-4A-03, December 2008. With permission.)

To obtain the impact of the nonlinear phase on the demodulation methods and the noise loading effects, the number of amplifiers can be increased to $N = 30$. The *Q-factor* is used to show a numerical improvement of the *ML* processor/receiver. As shown in Figure 15.19b, with the increase in launch power, the *ML* receiver/processor approximates the optimum performance because of the reducing variance of the phase noise. At the optimum point, the *ML* receiver/processor outperforms the *M*th power phase estimator by about 0.8 dB while having about 1.8 dB receiver sensitivity improvement compared to differential detection. It is also found that the optimum performance occurs at an OSNR of 16 dB when the nonlinear phase shift is almost 1 rad. With the launch power exceeding the optimum level, nonlinear phase noise becomes severe again. Only the *ML* phase estimator can offer BER beyond 10^{-4}, while both the *M*th power phase estimator and differential detection exhibit error floor before BER reaches 10^{-4}. From the numerical results, the *ML* processor carrier phase estimation shows a significant better receiver sensitivity improvement than the *M*th power phase estimator and conventional differential demodulation for optical DQPSK signals in systems dominated by nonlinear phase noise. Again, we want to emphasize that the *ML* estimator is a linear and efficient algorithm, and there is no need to deal with the $\pi/4$-rad phase ambiguity, thus, it is feasible for on-line processing for real systems.

In summary, the performance of synchronous coherent detection with the *ML* processor carrier phase estimation may offer a linear phase noise system and a nonlinear optical noise system separately. The *ML* DSP phase estimation can replace the optical phase locked loop (PLL), and the receiver sensitivity is improved compared to conventional differential detection and *M*th power phase estimator. The receiver sensitivity is improved by approximately 1 and 3 dB in these two channels (20 spans for the nonlinear channel), respectively, compared to differential detection. For the 30-span nonlinear channel, only the *ML* processor can offer BER beyond 10^{-4} (using Monte Carlo simulation) while both the *M*th power phase estimator and differential detection exhibit error floor before BER reaching 10^{-4}. At the optimum point of the power, the *Q*-factor of the *ML* receiver/processor outperforms the *M*th power phase estimation by about 0.8 dB. In addition, an important feature is the linear and efficient computation of the *ML* phase estimation algorithm, which enables the possibility real-time on-line DSP processing.

15.5 Carrier Phase Estimation

15.5.1 Remarks

Under the homodyne reception or intradyne reception, the matching between the LO laser and that of the signal carrier is very critical to minimize the deviation of the reception performance, and hence enhancement of the receiver sensitivity so as to maximize the transmission system performance. This difficulty remains a considerable obstacle for the first generation of coherent systems developed in the mid-1980s employing analog or complete hardware circuitry.

The first few parts of this chapter deal with the recovery of the carrier phase. Then later part involves some advanced processing algorithm to deal with the carrier phase recovery under the scenario that the frequency of the LO laser is oscillating, an operational condition to get the stabilization of an external cavity laser which is essential for homodyne reception with high sensitivity.

In DSP-based optical reception subsystems, this hurdle can be overcome by processing algorithms which are installed in a realtime memory processing system, the application-specific integrated circuit (ASIC), which may consist of an ADC and a digital signal processor and high-speed fetch memory.

The FO between the LO and the signal lightwave carrier is commonly due to the oscillation of the LO and is used as an external cavity incorporating an external grating, which is oscillating by a low frequency of about 300 MHz so as to stabilize the feedback of the reflected specific frequency line to the laser cavity. This oscillation, however, degrades the sensitivity of the homodyne reception systems. The later part of this section illustrates the application of DSP algorithms described in the earlier sections of this chapter to demonstrate the effectiveness of these algorithms in real-time experimental setup.

It is noted that the carrier phase recovery must be implemented before any equalization process can be implemented as explained in Sections 15.2.1 and 15.2.2.

It is noted here that the optical phase locking (OPL) technique presented in Chapter 5 is another way to reduce the FO between the LO and the signal carrier with operation in the optical domain while the technique described in this section is at the receiver output in the digital processing domain.

15.5.2 Correction of Phase Noise and Nonlinear Effects

Kikuchi's group [20] at the University of Tokyo uses electronic signal processing based on the *M*th power phase estimation to estimate the carrier phase. However, DSP circuits for the *M*th power phase estimator need nonlinear computations, thus impeding the potential possibility of real-time processing in the future. Further, the *M*th power phase estimation method requires dealing with the $\pi/4$-rad phase ambiguity when estimating the phase noise in adjacent symbol blocks. While the electronic DSP is based on the *ML* processing for carrier phase estimation to approximate the ideal synchronous coherent detection in the optical phase modulation system, which requires only linear computations, it eliminates the optical PLL and is more feasible for on-line processing for the real systems. Some initial simulation results show that the *ML* receiver/processor outperforms the *M*th power phase estimator especially when the nonlinear phase noise is dominant, thus significantly improving the receiver sensitivity and tolerance to the nonlinear phase noise.

Liu's group [21,22] at Alcatel-Lucent Bell Labs uses optical delay differential detection with DSP to detect differential BPSK (DPSK) and DQPSK signals. Since direct detection only detects the intensity of the light, the improvement of DSP is limited after the direct detection. While after the synchronous coherent detection of our technique, the DSP such as electronic equalization of CD and PMD offers better performance since the phase information is retrieved. And, as the level of phase modulation increases, it becomes more and more difficult to apply the optical delay differential detection because of the rather complex implementation of the receiver and the degraded SNR of the demodulated signal, while the *ML* estimator/processor can still demodulate other advanced modulation formats such as 8-PSK, 16-PSK, 16-QAM, and so on.

15.5.3 Forward Phase Estimation QPSK Optical Coherent Receivers

Recent progress in DSP [23,24] with the availability of ultra-high sampling rate allows the possibility of DSP-based phase estimation and polarization management techniques that

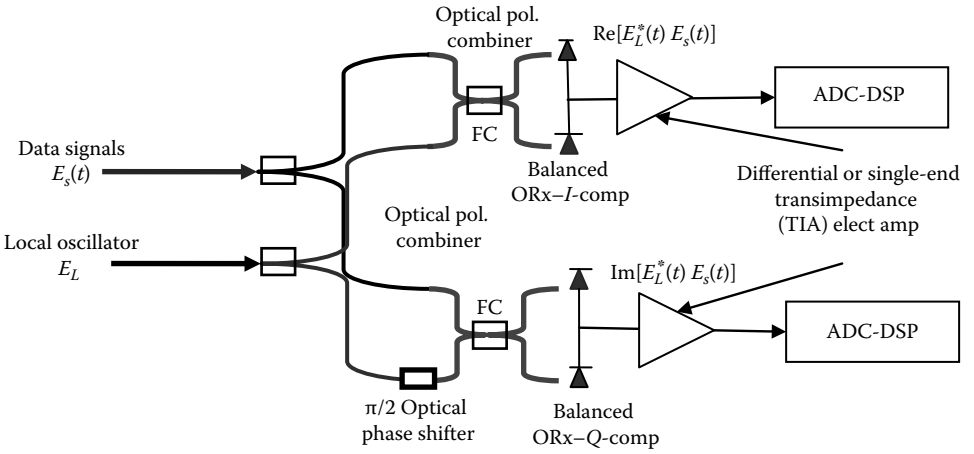

FIGURE 15.20
Schematic of a coherent receiver using balanced detection technique for I–Q component phase and amplitude recovery, incorporating DSP and ADC.

make the coherent robust and practical. This section is dedicated to the new emerging technology which will significantly influence the optical transmission and detection of optical signals at ultra high speed.

Recalling the schematic of a coherent receiver of Figure 15.20, it shows a coherent detection scheme for QPSK optical signals in which they are mixed with the LO field. In the case of modulation format QPSK or DQPSK, a π/2 optical phase shifter is needed to extract the quadrature component, thus the real and imaginary parts of a phase shift keyed signal can be deduced at the output of a balanced receiver from a pair of identical photodiodes connected back to back. Note that for a balanced receiver, the quantum shot noise contributed by the photodetectors is double as noise is always represented by the noise power and no current direction must be applied.

When the received signal is raised to the quadratic power, the phases of the signal disappear because $e^{j4\theta_S(t)} = 1$ for DQPSK whose states are 0, π/2, π, 3π/2, and 2π. The data phase is excluded, and the carrier phase can be recovered with its fluctuation with time. This estimation is computed using DSP algorithm. The estimated carrier phase is then subtracted with the detected phase of the signal to give only the phase states of the signals as indicated in the diagram. This is a FF phase estimation and most suitable for DSP implementation either offline or real time (Figure 15.21).

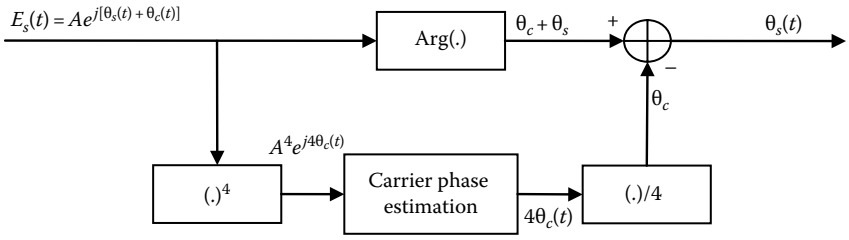

FIGURE 15.21
Schematic of a QPSK coherent receiver.

15.5.4 Carrier Recovery in Polarization Division Multiplexed Receivers: A Case Study

Advanced modulation formats in combination with coherent receivers incorporating digital signal processing subsystems enable high capacity and spectral efficiency [25,26]. PDM, QAM, and coherent detection are dominating the next generation high-capacity optical networks, since they allow information encoding in all the available degrees of freedom [27] with the same requirement of OSNR. The coherent technique is homodyne or intradyne mixing of the signal carrier and the LO. However, as just mentioned, a major problem in homodyne coherent receiver is the CR so that matching between the channel carrier and the LO can be achieved to maximize the signal amplitude and phase strength, hence the SNR in both the amplitude and phase plane. This section illustrates an experimental demonstration of the CR of a PDM–QPSK, PDM–QPSK, transmission scheme carrying 100 Gb/s per wavelength channel including two polarized modes (H [horizontal] and V [vertical] polarized modes) of the linear polarized mode in standard single-mode optical fiber (SSMF), that is 28 Gsystems/s × 2 (2 bits/symbol) × 2 (polarized channels) using some advanced DSP algorithms, especially the Viterbi–Viterbi (V-V) algorithm with MLSE nonlinear decision feedback procedures [28].

Feedforward carrier phase estimation (FFCPE) [29] has been commonly considered as the solution for this problem. The fundamental operation principle is to assuming a time invariant of the phase offset between the carrier and local laser during N ($N > 1$) consecutive symbol periods.

In coherent optical systems using tunable lasers, the maximum absolute FO can vary by 5 GHz. To accommodate such a large FO, a coarse digital frequency estimation (FDE) and recovery (FDR) techniques [30,31] can be employed to limit the FO to within allowable range so that phase recovery can be implemented/managed using FFCPE and feedforward carrier phase recovery (FFCPR) techniques [32]. The algorithm presented in Ref. [21], the so-called Differential Viterbi (DiffV), estimates the phase difference between two successive complex symbols. This method enables the estimation of large FO of MPSK-modulated signal up to $\pm f_s/(2M)$, where f_s stands for the symbol rate frequency. Larger FO is possible to estimate by the technique presented in Ref. [6], which generates insignificant estimation error that can be handled by the FFCPE and FFCPR. However, the FFCPE or "Viterbi and Viterbi" (V-V) would not perform well when the absolute residual FO at the input of the estimation circuit is larger than $\pm f_s/(2MN)$. This problem becomes more serious when the laser frequency oscillates and the coarse feedforward equalization (FFE) can be realized with a low-speed processor to decrease the complexity of integrated digital electronic circuits to release valuable processing time for processing the signals at ultra-high sampling rates, which is a very important factor in the cost and power consumption in ultra-high-speed coherent DSP-based optical receivers.

An algorithm for coupling carrier phase estimations in PDM systems is presented in Ref. [33]. The algorithm requires two loop filters, and the coupling factor should be carefully selected. In this section we describe an enhanced carrier recovery concept covering large frequency offset and enabling almost zero residual frequency offset for the V-V CPE. Also, a novel polarization coupling algorithm with reduced complexity is extracted from the work in Ref. [16].

15.5.4.1 FO Oscillations and Q-Penalties

Figure 15.22 shows the typical digital signal processing of medium complexity for coherent PDM optical transmission system. CD and polarization effects are compensated in CD and MIMO blocks, respectively. The DV FE is realized in the μ*c*. Several

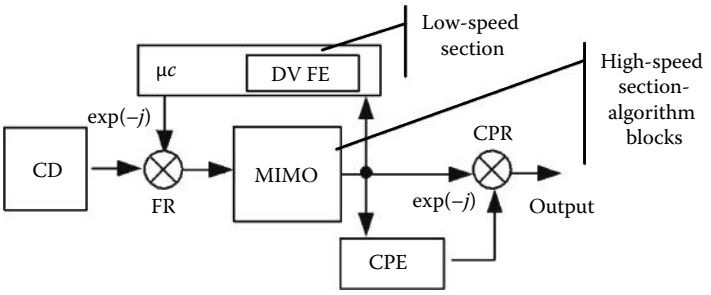

FIGURE 15.22
Typical digital signal process structure in PDM coherent receivers including a low-speed processor and high-speed digital signal processing system. CPE, carrier phase estimation; MIMO, multiple input multiple output; CPR, carrier phase recovery; FR, frequency recovery; CD, chromatic dispersion.

thousands of data are periodically loaded to the micro controller that calculates FO. A small bandwidth of the estimation loop delivers only averaged FO value to the CMOS ASIC part. However, long-time experimental tests with commercially available lasers, for example, the EMCORE laser, show that laser frequency oscillations are sinusoidal with frequency of 888 Hz in order to stabilize its central frequency by the use of feedback control and amplitude of more than 40 MHz (see Figure 15.23 for measured oscillation of the Emcore external cavity laser as LO). This oscillation is created by the vibration of the external reflector—a grating surface, so that the cavity can be stabilized. The mean offset is close to 300 MHz. So, the DiffV enables the averaging of the FO of 300 MHz while the residual offset of ±50 MHz can be compensated by the V-V algorithm.

Penalties caused by the residual offset of 50 MHz have been investigated for the case of V-V CPE. Figure 15.24 shows the simulation values of the *Q* penalties versus V-V averaging window length (WL) for two scenarios under off-line data processing. In the first case, we multiplexed 112G PDM–QPSK channel with twelve 10G on–off keying (OOK) neighbors

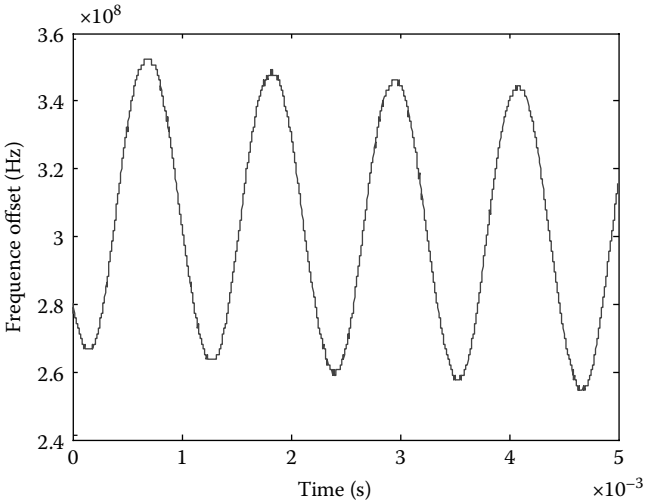

FIGURE 15.23
Laser frequency oscillation of EMCORE external cavity laser as measured from an external cavity laser.

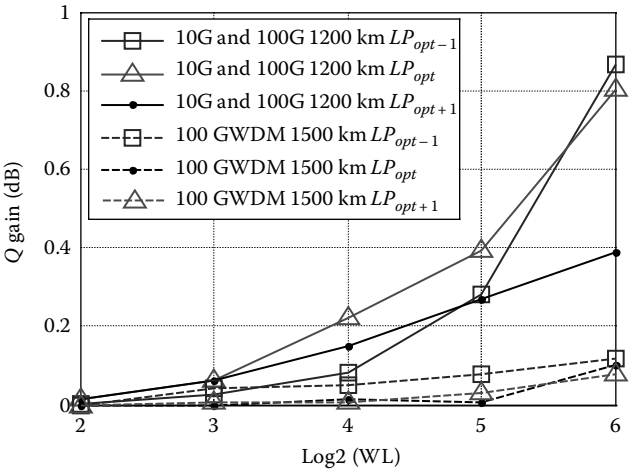

FIGURE 15.24
Penalties of V&V CPR with residual FO of 50 MHz.

(10 G and 100 G over 1200 km link) while the second scenario included the transmission of eight 112 G PDM–QPSK channels (100 G WDM—1500 km link). Channel spacing was 50 GHz (ITU-grid). The FO was partly compensated with the residual offset of 50 MHz to check the V&V CPR performance. Three values of launch power have been checked: optimum launched power (LP_{opt}), LP_{opt} – 1 dB (slightly linear regime), and LP_{opt} + 1 dB (slightly nonlinear regime). Maximum Q penalties of 0.9 dB can be observed that strongly depend on the averaging window length parameter WL.

15.5.4.2 Algorithm and Demonstration of Carrier Phase Recovery

A robust FFCPE and FFCPR with polarization coupling circuit are shown in Figure 15.25. The FFCFE and FFCPR are developed for the recourses of the V-V, and by simple recourses reallocation an enhanced CR is obtained. The proposed method is designed to maximize

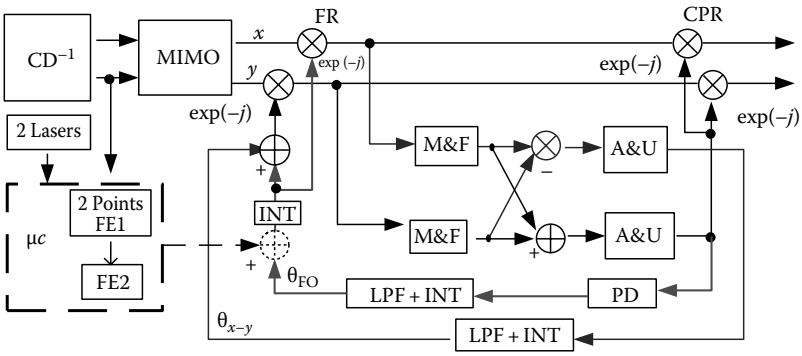

FIGURE 15.25
Modified structure of algorithms for CR. *Legend*: M&F—*M*th power operation and averaging filter; A&U—arctan and unwrapping; PD—phase difference calculation; LPF—low-pass filter; INT—integrator. (Extracted from Zhang, S. et al., A comparison of phase estimation in coherent optical PSK system, in *Photonics Global'08*, Singapore, paper C3-4A-03, December 2008. With permission.)

CR performance with a moderate realization complexity. The method consists of four main parts: coarse carrier frequency estimation by processing in low-speed DSP subsystems (indicated by μc) and recovery (CCFE-R), feedback carrier frequency estimation and recovery (FBCFE-R, red line in Figure 15.4), XY phase offset estimation and compensation (H-V (or XY)-POE-C, gray line in Figure 15.25), and joint H-V feedforward carrier phase estimation and recovery (JFF-CPE-R).

The M-F block conducts the *M*th power operation and averaging for the case of the M-PSK modulation format [6]. For K-QAM signal, the *M* constellation points on the ring with specific radius may be selected and used in the *M*th power block. More rings can be selected to improve the estimation procedure (e.g., inner and outer rings in 16-QAM can be used). So, the use of the method is not limited to PSK schemes.

Large FO (FO > $\pm f_s/(2MN)$) can be estimated by the method presented in Ref. [31] (denoted by FE1 in Figure 15.25) that can estimate FO within ±10 GHz FO (linear curve in case of 112 G PDM–QPSK). A small amount of data are transferred into the μc for calculating the coarse range of the FO. Depending on FO estimation sign, one can superimpose certain FOs (e.g., 4 GHz) of opposite sign. Using a linear interpolation (FE2), the current FO can be estimated to an error within a few hundreds of MHz. Similarly depending on available electrical bandwidth and the receiver structure, the compensation of such a large FO can be conducted either in CMOS ASIC or by controlling the frequency of the LO, generally an external cavity laser.

The residual FO after CCFE and CCFER may have values of several hundred MHz plus 50 MHz generated by low processing speed and laser frequency oscillations. The FBCFE estimates the residual frequency that is compensated by the CFR feedback loop. The frequency estimation is in the range of FBCFE&R is $\pm f_s/(2MN)$ due to its implementation based on the DiffV algorithm.

The FBCFE&R compensates almost the total FO. The residual FO and finite laser linewidth influence can be compensated by the JFF-CPE&R. This operation can be supported by ideal coupling of the carrier estimations from both polarizations. Prior to the coupling of estimations, both X and Y constellations are aligned using the XY-POE&C, and the phase difference between adjacent outputs of the lower unwrapping block can then be used for the alignment. It is sufficient to rotate the Y polarization for the constellation angle mismatch.

The algorithm employing MIMO and V-V CPE is compared with the CR as presented in Figure 15.24 in which the uncompensated FO after the MIMO block is set to 50 MHz to simulate a realistic scenario. The measured FO after the MIMO is around 300 MHz. All data processing algorithms are done block-wise with parallelization of 64 symbols per block, and a realistic processing delay is added [16].

Figure 15.26 shows the gain in the quality factor *Q* for the two measurement cases. Since the FO is recovered by the feedback CR, the penalties shown in Figure 15.24 are completely compensated, with an additional gain coming from the estimations of coupling.

The 10G and 100G hybrid off-line optical transmission with homodyne coherent reception experiments is used to demonstrate the convergence of the feedback loops of the modified algorithm shown in Figure 15.25. As shown in Figure 15.27, the FO of 327 MHz can be acquired after 3.4 μs or 1500 blocks of processing [16], the steady state of the plateau region. The XY constellation offset is acquired after 3000 blocks due to the demand for correct FO compensation. The estimated XY phase offset is 0.8 rad. The CR can cope with a laser frequency oscillation of 36 kHz. Acquisition and tracking times are shown in Figure 15.28. The CR is able to track the laser frequency changes after 100 ms.

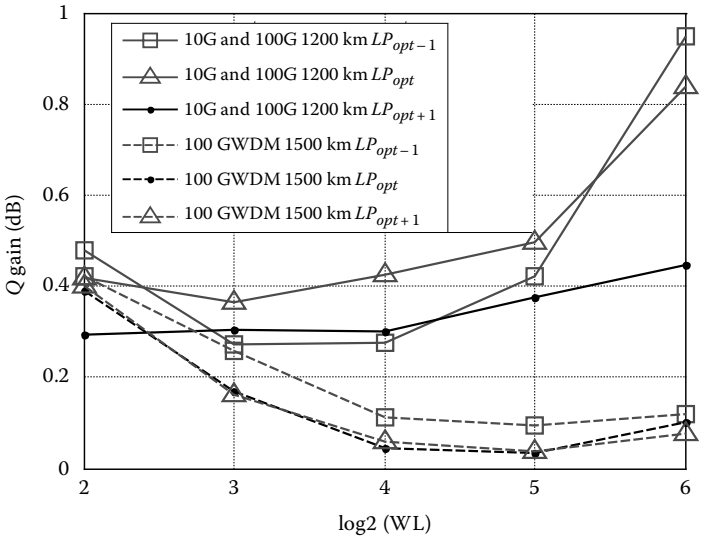

FIGURE 15.26
CR *Q* gain.

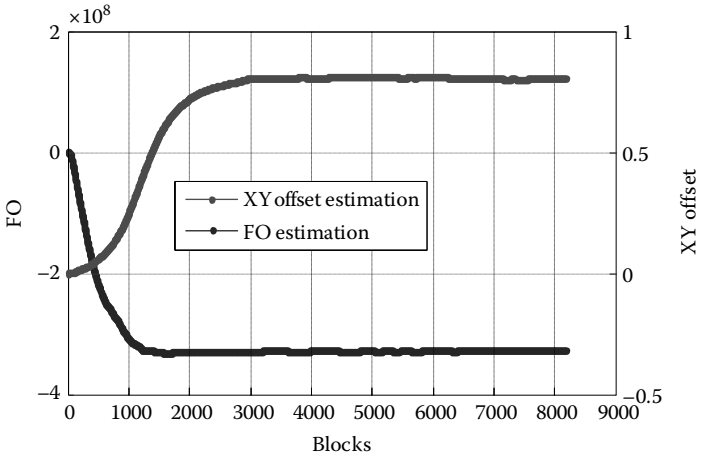

FIGURE 15.27
10G hybrid off-line experiments LOFO and XY phase offset estimation by FO variation with respect to the number of blocks. FO = frequency offset—vertical axis.

Note that a feedback loop can cause delay between real oscillations and estimation (delay between two lines in Figure 15.28), hence resulting in some penalties.

The high-precision CR is achieved by the use of the V-V circuits under appropriate allocation and connections. Using feedback and feedforward CR, significant improvements can be achieved. Laser FO can be compensated by complex circuit design and appropriate parameters selection. The ideal coupling of estimations coming from two polarizations further enhances CR performance with less complexity.

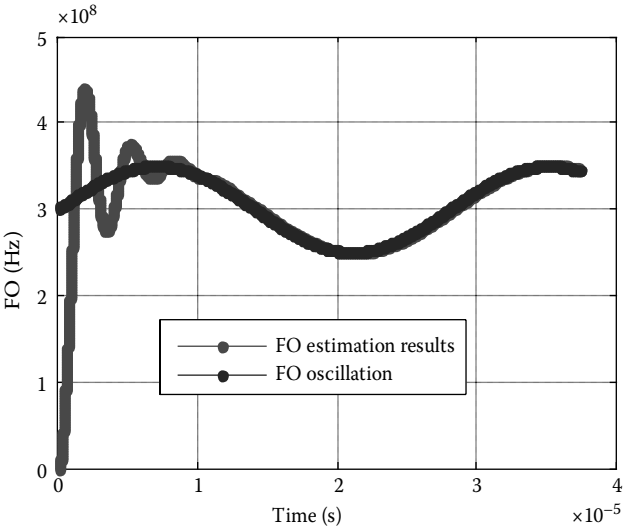

FIGURE 15.28
36 kHz oscillation variation of the laser frequency.

15.6 Systems Performance of MLSE Equalizer-MSK Optical Transmission Systems

15.6.1 MLSE Equalizer for Optical MSK Systems

15.6.1.1 Configuration of MLSE Equalizer in Optical Frequency Discrimination Receiver (OFDR)

Figure 15.29 shows the block diagram of narrowband filter receiver integrated with NLEs for the detection of 40 Gb/s optical MSK signals. The MSK transmitter is described in Chapter 3 on modulation technique, the 2 bits/symbol modulation as in the case of QPSK, except that the phase change from one state to the other is continuous rather than a discrete

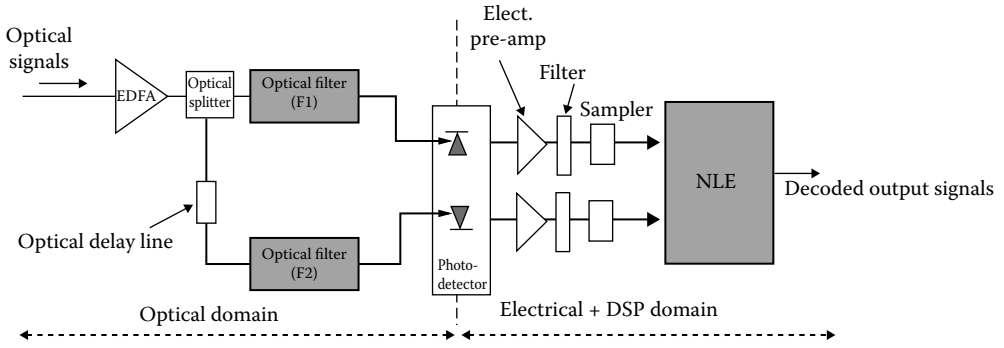

FIGURE 15.29
Block diagram of narrowband filter receiver integrated with NLEs for the detection of 40 Gb/s optical MSK signals.

step change. Continuous phase change implies frequency step change. So, when the frequency difference between states equals a quarter of the bit rate, the minimum distance between them, so that the channel states can be recovered with minimum ISI, is when the two frequency states are orthogonal and then the modulation is termed as minimum shift keying or MSK.

In the reception of MSK channels, two narrowband filters can be used to discriminate the upper sideband (USB) channel and the lower sideband (LSB) channel frequencies that correspond to logic "1" and "0" transmitted symbols, respectively. A constant optical delay line which is easily implemented in integrated optics is introduced on one branch to compensate any differential group delay $t_d = 2\pi f_d \beta_2 L$ between f_1 and f_2 where $f_d = f_1 - f_2 = R/2$, β_2 represents the group velocity delay (GVD) parameter of the fiber and L is the fiber length as described in Chapter 2. Alternatively, de-skewing can be implemented in the digital domain to compensate for this delay difference. If the differential group delay is fully compensated, the optical light waves in the two paths arrive at the photodiodes simultaneously. The outputs of the filters are then converted to the electrical domain through the photodiodes. These two separately detected electrical signals are sampled before being fed as the inputs to the NLE.

It is noted here that the MSK reception system described here can be a self-homodyne detection or a coherent system with the signal channel employed as the LO. Alternatively, the reception subsystem is coherent one where the LO has a power level at that of the average power of the signal.

15.6.1.2 MLSE Equalizer with Viterbi Algorithm

At epoch k, it is assumed that the effect of ISI on an output symbol of the FSM c_k is caused by both executive δ pre-cursor and δ post-cursor symbols on each side. First, a state trellis is constructed with 2δ states for both detection branches of the OFDR. A lookup table per branch corresponding to symbols "0" and "1" transmitted and containing all the possible $2^{2\delta}$ states of all 11 symbol-length possible sequences is constructed by sending all the training sequences incremented from 1 to $2^{2\delta}$.

The output sequence $\boldsymbol{c}(k) = f(b_k, b_{k-1}, \ldots, b_{k-2\delta-1}) = (c_1, c_2, \ldots, c_2\delta)$ is the nonlinear function representing the ISI caused by the δ adjacent pre-cursor and post-cursor symbols of the optical fiber FSM. This sequence is obtained by selecting the middle symbols c_k of 2δ possible sequences with length of 2δ + 1 symbol intervals.

The samples of the two filter outputs at epoch k y_k^i, $i = 1, 2$ can be represented as $\mathbf{y}^i(k) = \mathbf{c}^i(k) + \mathbf{n}_{ASE}^i(k) + \mathbf{n}_{Elec}^i(k)$, $i = 1, 2$. Here, $\mathbf{n}_{ASE}^i$ and $\mathbf{n}_{Elec}^i$ represent the ASE noise and the electrical noise, respectively.

In linear transmission of an optical system, the received sequence $\mathbf{y}_n$ is corrupted by ASE noise of the optical amplifiers, $\mathbf{n}_{ASE}$ and the electronic noise of the receiver, $\mathbf{n}_E$. It has been proven that the calculation of the branch metric, and hence, the state metric is optimum when the distribution of noise follows the normal/Gaussian distribution, that is, the ASE accumulated noise and the electronic noise of the reception subsystem, are collectively modeled as samples from Gaussian distributions. If noise distribution departs from the Gaussian distribution, the minimization process is suboptimum.

The Viterbi algorithm subsystem is implemented on each detection branch of the OFDR. However, the MLSE with the Viterbi algorithm may be too computationally complex to be implemented at 40 Gb/s with the current integration technology. However, there have been commercial products available for 10 Gb/s optical systems. Thus, a second MLSE equalizer using the technique of reduced-state template matching is presented in the next section.

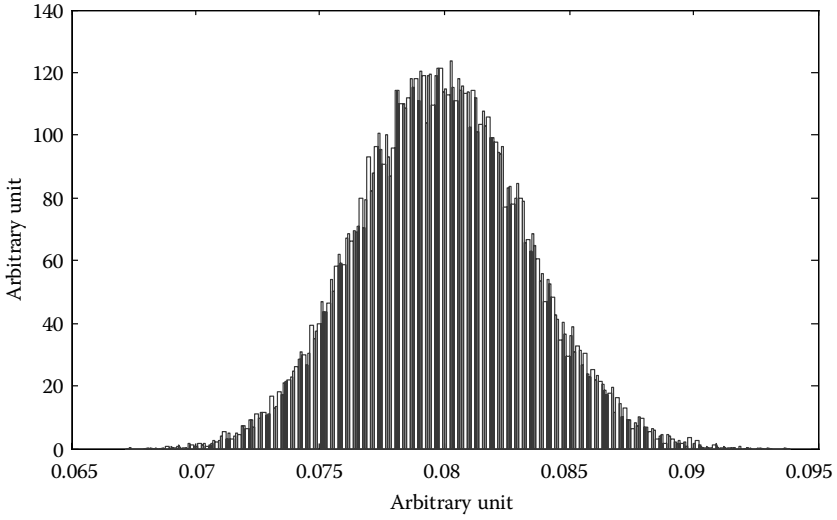

FIGURE 15.30
Noise distribution following Gaussian shape due to narrowband optical filtering.

In an optical MSK transmission system, narrowband optical filtering plays the main role in shaping the noise distribution back to the Gaussian profile. The Gaussian profile noise distribution is verified in Figure 15.30. Thus, branch metric calculation in the Viterbi algorithm, which is based on the minimum Euclidean distance over the trellis, can achieve the optimum performance. Also, the computational effort is less complex than ASK or DPSK systems due to the issue of non-Gaussian noise distribution.

15.6.1.3 MLSE Equalizer with Reduced-State Template Matching

The modified MLSE is a single-shot template matching algorithm. First, a table of $2^{2\delta+1}$ templates, $\mathbf{g}^k$, $k = 1, 2,\ldots, 2^{2\delta+1}$ corresponding to the $2^{2\delta+1}$ possible information sequences, $\mathbf{I}^k$ of length $2\delta + 1$ is constructed. Each template is also a vector of size $2\delta + 1$ which is obtained by transmitting the corresponding information sequence through the optical channel and obtaining the $2\delta + 1$ consecutive received samples. At each symbol period, n the sequence, $\hat{\mathbf{I}}_n$ with the minimum metric is selected as $\mathbf{c}(k) = \arg\min_{\mathbf{b}(k)}\{m(\mathbf{b}(k), \mathbf{y}(k))\}$. The middle element of the selected information sequence is then output as the nth decision, $\hat{\mathbf{I}}_n$, that is, $\hat{\mathbf{I}}_n = \hat{\mathbf{I}}_n(\delta+1)$. The minimization is performed over the information sequences, $\mathbf{I}^k$ which satisfy the condition that the δ-2 elements are equal to the previously decoded symbols $\hat{\mathbf{I}}_{n-\delta}, \hat{\mathbf{I}}_{n-(\delta-1)},\ldots,\hat{\mathbf{I}}_{n-2}$ and the metric, $m(\mathbf{I}^k,\mathbf{r}_n)$ is given by $m(\mathbf{I}^k, \mathbf{r}_n) = \left\{\mathbf{w}\bullet\left(\mathbf{g}^k - \mathbf{r}_n\right)\right\}^T \left\{\mathbf{w}\bullet\left(\mathbf{g}^k - \mathbf{r}_n\right)\right\}$ where $\mathbf{w}$ is a weighting vector which is chosen carefully to improve the reliability of the metric. The weighting vector is selected so that when the template is compared with the received samples, less weighting is given to the samples further away from the middle sample. For example, we found through numerical results that a weighting vector with elements $\mathbf{w}(i) = 2^{-|i-(\delta+1)|}$, $i = 1, 2,\ldots, 2\delta + 1$ gives good results. Here, • represents the Hadamard multiplication of two vectors, $(.)^T$ represents transpose of a vector and $|.|$ is the modulus operation.

15.6.2 MLSE Scheme Performance

15.6.2.1 Performance of MLSE Schemes in 40 Gb/s Transmission Systems

Figure 15.31 shows the simulation system configuration used for the investigation of the performance of both the schemes mentioned earlier when used with the narrowband optical Gaussian filter receiver for the detection of noncoherent 40 Gb/s optical MSK systems. The input power into fiber (P_0) is −3 dBm, which is much lower than the nonlinear threshold power. The EDFA2 provides 23 dB gain to maintain the receiver sensitivity of −23.2 dBm at $BER = 10^{-9}$. As shown in Figure 15.31, the optical received power (P_{Rx}) is measured at the input of the narrowband MSK receiver and the OSNR is monitored to obtain the BER curves for different fiber lengths. Length of SSMF varies from 48 to 60 km in a step of 4 km to investigate the performance of the equalizers to the degradation caused by fiber cumulative dispersion. The narrowband Gaussian filter with the time bandwidth product of 0.13 is used for the detection filters.

Electronic noise of the receiver can be modeled with equivalent noise current density of the electrical amplifier of 20 pA/$\sqrt{\text{Hz}}$ and dark current of 10 nA. The key parameters of the transmission system are given in Table 15.2.

The Viterbi algorithm used with the MLSE equalizer has a constraint length of 6 (i.e., 2^5 number of states) and a trace back length of 30. Figure 15.32 shows the BER performance of both NLEs plotted against the required OSNR. The BER performance of the optical MSK receiver without any equalizers for 25 km SSMF transmission is also shown in Figure 15.32 for quantitative comparison. The numerical results are obtained via

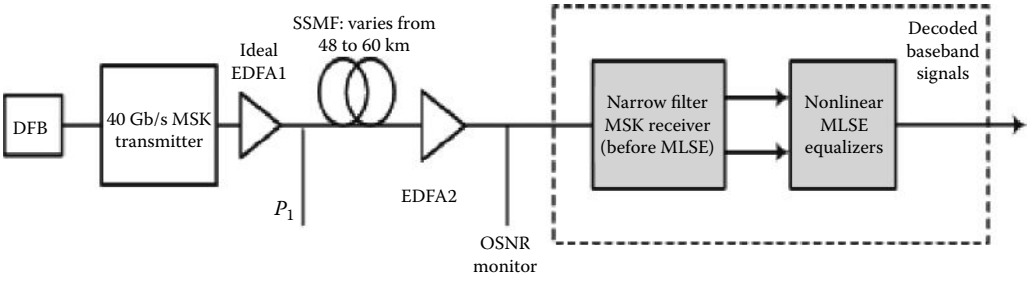

FIGURE 15.31
Simulation setup for performance evaluation of MLSE and modified MLSE schemes for detection of 40 Gb/s optical MSK systems.

TABLE 15.2

Key Simulation Parameters Used in the MLSE MSK Modulation Format

Input power: $P_0 = -3$ dBm	*Narrowband Gaussian filter: B* = 5.2 GHz *or* $BT = 0.13$
Operating wavelength: $\lambda = 1550$ nm	*Constant delay:* $t_d = \lvert 2\pi f_D \beta_2 L \rvert$
Bit rate: $R = 40$ Gb/s	*Pre-amp EDFA of the OFDR: G = 15 dB and NF = 5 dB*
SSMF fiber: $\lvert\beta_2\rvert = 2.68\text{e}{-26}$ or $\lvert D \rvert = 17$ ps/nm/km	$i_d = 10$ *nA*
Attenuation: $\alpha = 0.2$ dB/km	$N_{eq} = 20$ pA/(Hz)$^{1/2}$

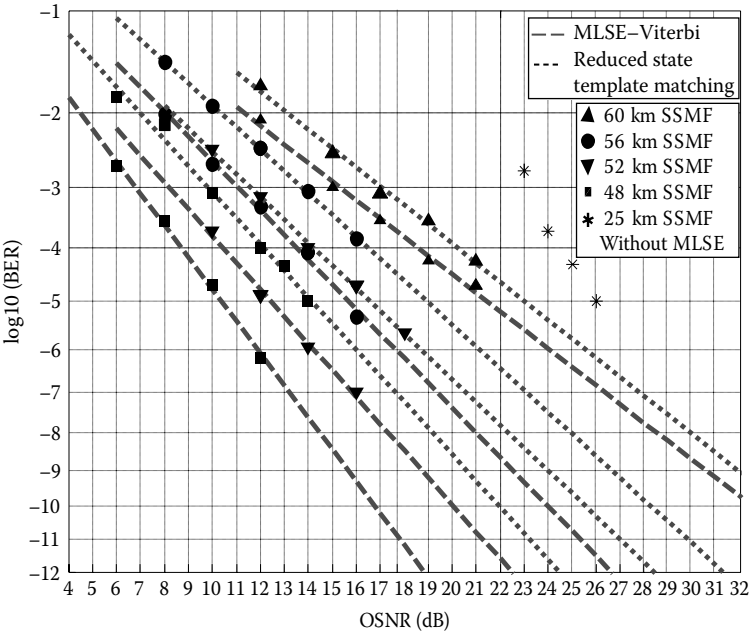

FIGURE 15.32
Performance of modified Viterbi-MLSE and template matching schemes, BER versus OSNR.

Monte Carlo simulation (triangular markers as shown in Figure 15.32) with the low BER tail of the curve linearly extrapolated. The OSNR penalty (at $BER = 10^{-9}$) versus residual dispersion corresponding to 48, 52, 56, and 60 km SSMF are presented in Figure 15.33. The MLSE scheme outperforms the modified MLSE schemes especially at low OSNR. In the case of 60 km SSMF, the improvement at $BER = 10^{-9}$ is approximately 1 dB and in the case of 48 km SSMF, the improvement is about 5 dB. In the case of transmission of 52 and 56 km SSMF, MLSE with the Viterbi algorithm has 4 dB gain in OSNR compared to the modified scheme. With residual dispersion at 816, 884, 952, and 1020 ps/nm, at BER of 10^{-9}, the MLSE scheme requires 12, 16, 19, and 26 dB OSNR penalty, respectively, while the modified scheme requires 17, 20, 23, and 27 dB OSNR, respectively.

15.6.2.2 Transmission of 10 Gb/s Optical MSK Signals over 1472 km SSMF Uncompensated Optical Link

Figure 15.34 shows the simulation setup for 10 Gb/s transmission of optical MSK signals over 1472 km SSMF. The receiver employs an optical narrowband frequency discrimination receiver integrated with a 1024-state Viterbi-MLSE post-equalizer. The input power into fiber (P_0) is –3 dBm lower than the fiber nonlinear threshold power. The optical amplifier EDFA1 provides an optical gain to compensate the attenuation of each span completely. The EDFA2 is used as a noise loading source to vary the required OSNR. The receiver electronic noise is modeled with equivalent noise current density of the electrical amplifier of 20 $\text{pA}/\sqrt{\text{Hz}}$ and dark current of 10 nA for each photodiode. A narrowband optical Gaussian filter with two-sided bandwidth of 2.6 GHz (one-sided $BT = 0.13$) is optimized for detection. A back-to-back $OSNR = 8$ dB is required for BER at 10^{-3} for each branch. The corresponding received power is –25 dBm. This low OSNR is possible due to large

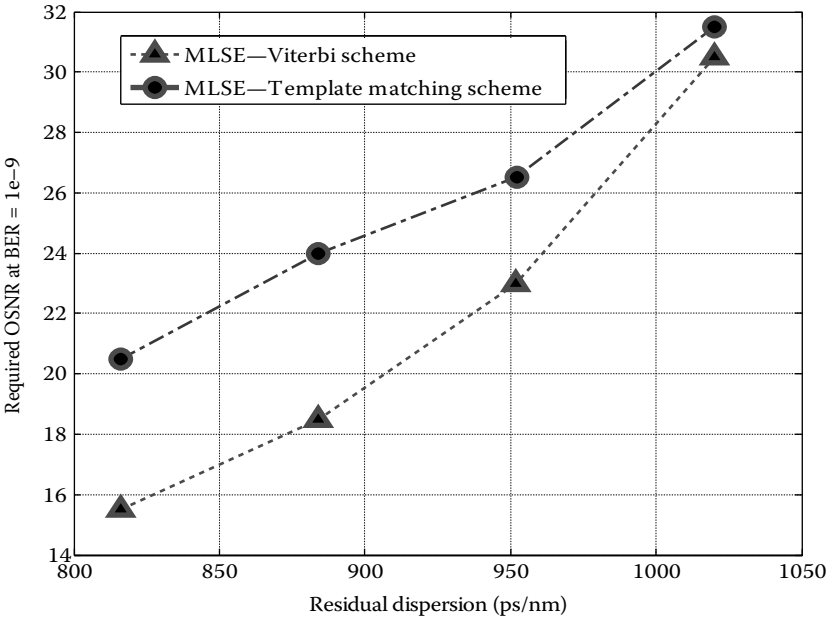

FIGURE 15.33
Required OSNR (at *BER* = 1e–9) versus residual dispersion in Viterbi-MLSE and template-matching MLSE schemes.

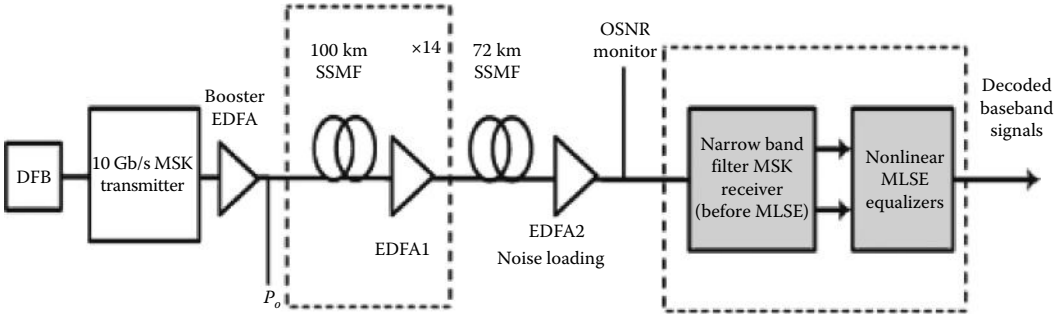

FIGURE 15.34
Simulation setup for transmission of 10 Gb/s optical MSK signals over 1472 km SSMF with MLSE-Viterbi equalizer integrated with the narrowband optical filter receiver.

suppression of noise after being filtered by narrowband optical filters. A trace-back length of 70 is used in the Viterbi algorithm. Figure 15.34 shows the simulation results of BER versus the required OSNR for 10 Gb/s optical MSK transmission over 1472 and 1520 km SSMF uncompensated optical links with 1, 2, and 4 samples per bit, respectively. The 1520 km SSMF with one sample per bit is seen as the limit for 1024-state Viterbi algorithm due to the slow roll-off and the error floor. However, 2 and 4 samples per bit can obtain error values lower than the FEC limit of 10^{-3}.

Thus, 1520 km SSMF transmission of 10 Gb/s optical MSK signals can reach the error-free detection with use of a high-performance FEC. In the case of 1472 km SSFM transmission,

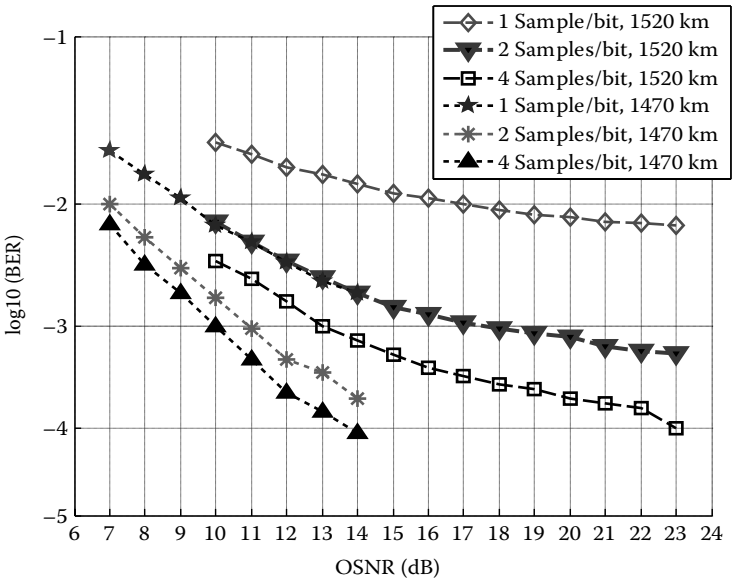

FIGURE 15.35
BER versus required OSNR for transmission of 10 Gb/s optical MSK signals over 1472 and 1520 km SSMF uncompensated optical link.

the error events follow a linear trend without a sign of error floor, and therefore, error-free detection can be comfortably accomplished.

Figure 15.35 also shows the significant improvement in OSNR of 2 and 4 samples per bit over 1 sample per bit counterpart with values of approximately 5 dB and 6 dB, respectively. In terms of OSNR penalty at BER of 1e−3 from back-to-back setup, 4 samples per bit for 1472 and 1520 km transmission distance suffers 2 and 5 dB penalty, respectively.

15.6.2.3 Performance Limits of Viterbi-MLSE Equalizers

The performance limits of the Viterbi-MLSE equalizer to combat ISI effects are investigated against various SSMF lengths of the optical link. The number of states used in the equalizer is incremented accordingly to this increase and varied from 2^6 to 2^{10}. This range was chosen as reflecting the current feasibility and the future advance of electronic technologies which can support high-speed processing of the Viterbi algorithm in the MLSE equalizer. In addition, these numbers of states also provide feasible time for simulation.

In addition, one possible solution to ease the requirement of improving the performance of the equalizer without increasing much of the complexity is by multisampling within one bit period. This technique can be done by interleaving the samplers at different time. Although, a greater number of electronic samplers are required, they only need to operate at the same bit rate as the received MSK electrical signals. Moreover, it will be shown later on that there is no noticeable improvement with more than two samples per bit period. Hence, the complexity of the MLSE equalizer can be affordable while improving the performance significantly.

Figure 15.36 shows the simulation setup for 10 Gb/s optical MSK transmission systems with lengths of uncompensated optical links varying up to 1472 km SSMF. In this setup, the input power into fiber (P_0) is set to be −3 dBm, thus avoiding the effects of fiber

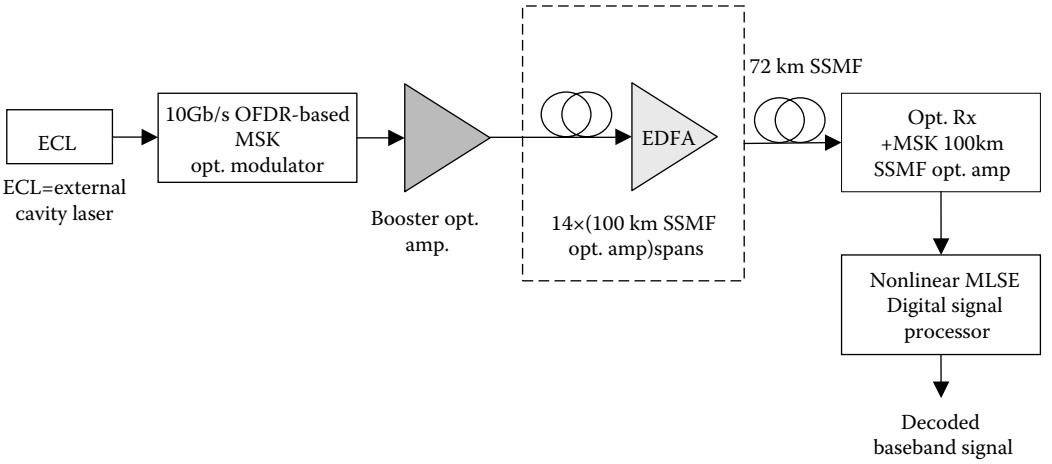

FIGURE 15.36
Simulation setup of OFDR-based 10 Gb/s MSK optical transmission for study of performance limits of MLSE-Viterbi equalizer.

nonlinearities. The optical amplifier EDFA1 provides an optical gain to compensate the attenuation of each span completely. The EDFA2 is used as a noise loading source to vary the required OSNR values. Moreover, a Gaussian filter with two-sided 3 dB bandwidth of 9 GHz (one-sided $BT = 0.45$) is utilized as the optical discrimination filter because this BT product gives the maximized detection eye openings. The receiver electronic noise is modeled with equivalent noise current density of the electrical amplifier of 20 $\text{pA}/\sqrt{\text{Hz}}$ and a dark current of 10 nA for each photodiode. A back-to-back OSNR = 15 dB is required for a BER of 10^{-4} on each branch, and the correspondent receiver sensitivity is –25 dBm. A trace-back length of 70 is used for the Viterbi algorithm in the MLSE equalizer. Figures 15.36 through 15.38 show the BER performance curves of 10 Gb/s OFDR-based MSK optical transmission systems over 928, 960, 1280, and 1470 km SSMF uncompensated optical links for different number of states used in the Viterbi-MLSE equalizer. In these figures, the performance of Viterbi-MLSE equalizers is given by the plot of the BER versus the required OSNR for several detection configurations: balanced receiver (without incorporating the equalizer), the conventional single sample per bit sampling technique and the multisample per bit sampling techniques (2 and 4 samples per a bit slot). The simulation results are obtained by the Monte-Carlo method.

The significance of multisamples per bit slot in improving the performance for MLSE equalizer in cases of uncompensated long distances is shown. It is found that the tolerance limits to the ISI effects induced from the residual CD of a 10 Gb/s MLSE equalizer using 2^6, 2^8, and 2^{10} states are approximately equivalent to lengths of 928, 1280, and 1440 km SSMF, respectively. The equivalent numerical figures in the case of 40 Gb/s transmission are corresponding to lengths of 62, 80, and 90 km SSMF, respectively.

In the case of 64 states over 960 km SSMF uncompensated optical link, the BER curve encounters an error floor which cannot be overcome even by using high-performance FEC schemes. However, at 928 km, the linear BER curve indicates the possibility of recovering the transmitted data with the use of high-performance FEC. Thus, for 10 Gb/s OFDR-based MSK optical systems, a length of 928 km SSMF can be considered as the transmission limit for the 64-state Viterbi-MLSE equalizer. Results shown in Figures 15.37 and 15.38 suggest that the length of 1280 km SSMF uncompensated optical link is the transmission

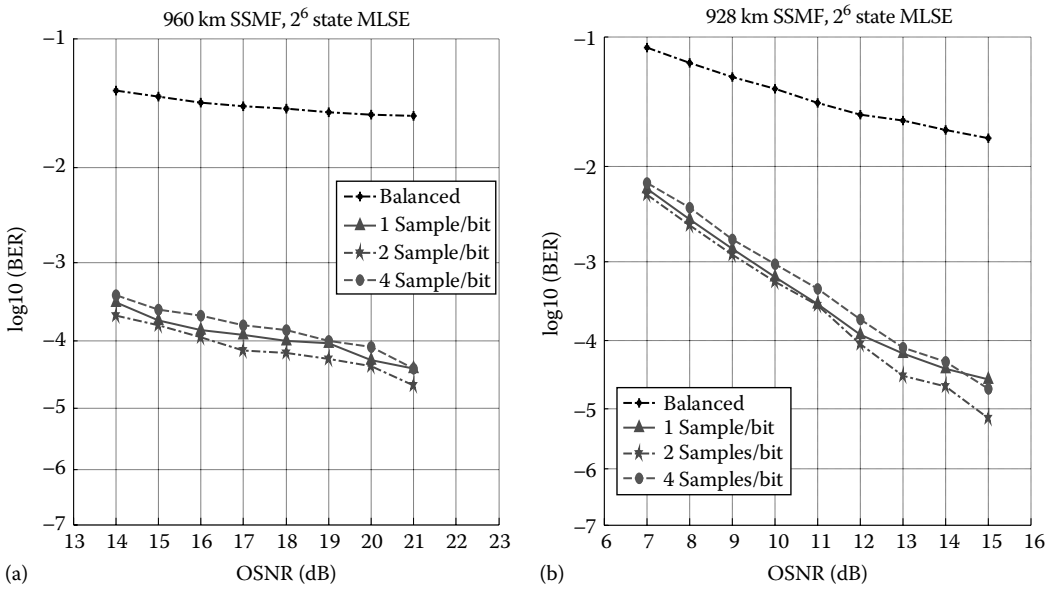

FIGURE 15.37
Performance of 64-state Viterbi-MLSE equalizers for 10 Gb/s OFDR-based MSK optical systems over (a) 960 km and (b) 928 km SSMF uncompensated link.

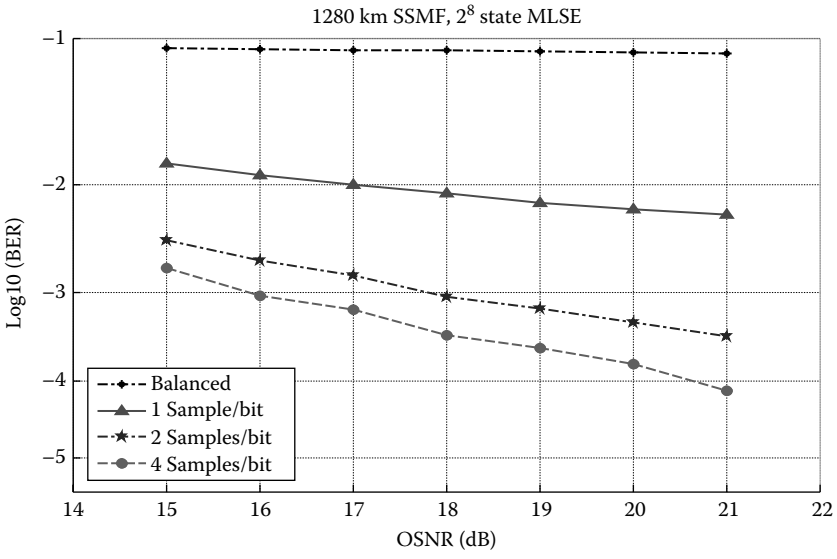

FIGURE 15.38
Performance of 256-state Viterbi-MLSE equalizer for 10 Gb/s OFDR-based MSK optical systems over 1280 km SSMF uncompensated link.

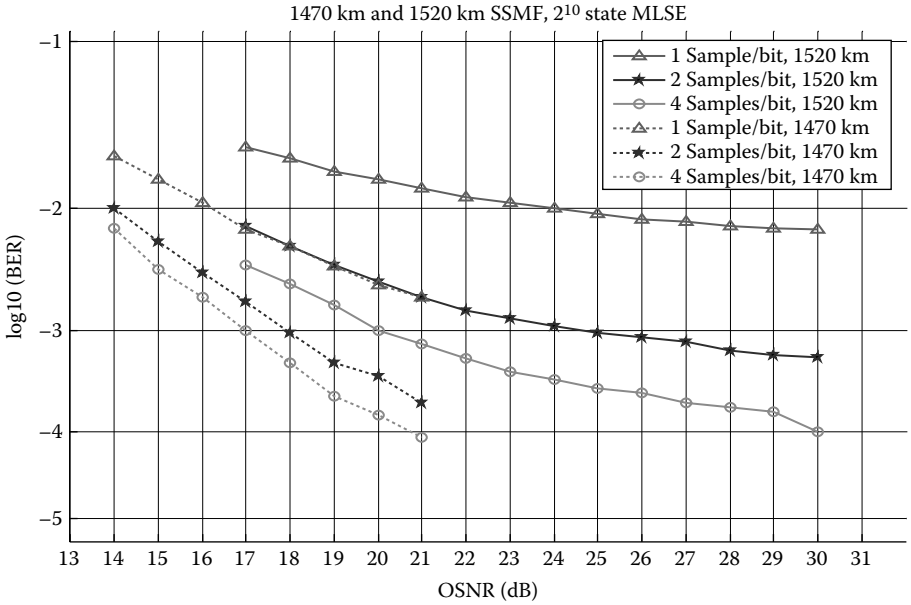

FIGURE 15.39
Performance of 1024-state MLSE equalizer for 10 Gb/s optical MSK signals versus required OSNR over 1472 and 1520 km SSMF uncompensated optical link.

limit for the 256-state Viterbi-MLSE equalizer when incorporating with OFDR optical front end. It should be noted that this is achieved when using the multisample per bit sampling schemes.

It is observed from Figure 15.39 that the transmission length of 1520 km SSMF with one sample per bit is seen as the limit for 1024-state Viterbi algorithm due to the slow roll-off and the error floor. However, 2 and 4 samples per bit can obtain error values lower than the FEC limit of 10^{-3}. Thus, 1520 km SSMF transmission of 10 Gb/s optical MSK signals can reach error-free detection with use of a high-performance FEC. In the case of 1472 km SSFM transmission, the error events follow a linear trend without any sign of error floor, and therefore, error-free detection can be achieved. Figure 15.39 also shows the significant OSNR improvement of the sampling techniques with 2 and 4 samples per bit compared to the single sample per bit counterpart. In terms of OSNR penalty at BER of 1e−3 from back-to-back setup, 4 samples per bit for 1472 and 1520 km transmission distance suffers 2 and 5 dB penalty, respectively.

It is found that for incoherent detection of optical MSK signal based on the OFDR, MLSE equalizer using 2^4 states does not offer better performance than the balanced configuration of the OFDR itself, that is, the uncompensated distance is not over 35 km SSMF for 40 Gb/s or 560 km SSMF for 10 Gb/s transmission systems, respectively. It is most likely that in this case, the severe ISI effect caused by the optical fiber channel has spread beyond the time window of 5 bit slots (2 pre-cursor and 2 post-cursor bits), the window that the 16-state MLSE equalizer can handle. Thus, it is necessary that the number of taps or states of MLSE covers the full length of the dispersive pulse.

The trace-back length used in the investigation is chosen to be 70 which guarantees the convergence of the Viterbi algorithm. The longer the trace-back length, the larger memory

is required. With state-of-the-art technology for high storage capacity nowadays, the memory is no longer a big issue. Very fast processing speed at 40 Gb/s operations hinders the implementation of 40 Gb/s Viterbi-MLSE equalizers at the mean time. Multisample sampling schemes offer an exciting solution for implementing fast signal processing process. This challenge may also be overcome in the near future together with the advance in the semiconductor industry. At present, the realization of Viterbi-MLSE equalizers operating at 10 Gb/s has been commercially demonstrated [34].

15.6.2.4 Viterbi-MLSE Equalizers for PMD Mitigation

Figure 15.40 shows the simulation test bed for the investigation of MLSE equalization of the PMD effect. The transmission link consists of a number of spans which are comprised of 100 km SSMF (with D = +17 ps/nm·km, α = 0.2 dB/km) and 10 km DCF (with D = –170 ps/nm·km, α = 0.9 dB/km). Power launched into each span (P_0) is –3 dBm. The $EDFA_1$ has a gain of 19 dB, hence providing input power into the DCF to be –4 dBm, which is lower than the nonlinear threshold of the DCF. The 10 dB gain of $EDFA_2$ guarantees the input power into the next span unchanged with an average power of –3 dBm. An OSNR of 10 dB is required for receiver sensitivity at BER of 10^{-4} in the case of back-to-back configuration. Considering the practical aspect and complexity a Viterbi-MLSE equalizer for PMD equalization, a small number of 4-state bits or effectively 16 states were chosen for the Viterbi algorithm in the simulation study.

The performance of MLSE against the PMD dynamics of optical fiber is investigated. BER versus required OSNR for different values of normalized average differential group delay (DGD) <Δt> are shown in Figure 15.41. The mean DGD factor is normalized over one bit period of 100 and 25 ps for 10 and 40 Gb/s bit rate, respectively. The numerical studies are conducted for a range of values from 0 to 1 of normalized DGD <Δt> which equivalently corresponds to the instant delays of up to 25 or 100 ps in terms of 40 and 10 Gb/s transmission bit rate, respectively.

The advantages of using multiple samples per bit over the conventional single sample per bit in MLSE equalizer are also numerically studied, and the Monte Carlo results for normalized DGD values of 0.38 and 0.56 are shown in Figures 15.42 and 15.43. However, the increase from 2 to 4 samples per bit does not offer any gain in the performance of the Viterbi-MLSE equalizer. Thus, 2 samples per symbol are preferred to reduce the complexity of the equalizer. Here and for the rest of this chapter, multisamples per bit implies the implementation of 2 samples per symbol. Performance of MLSE equalizer for different

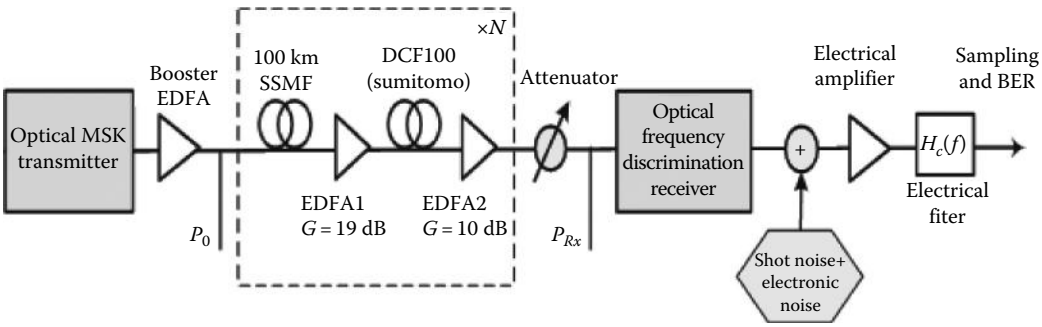

FIGURE 15.40
Simulation test bed for investigation of effectiveness of MLSE equalizer to PMD.

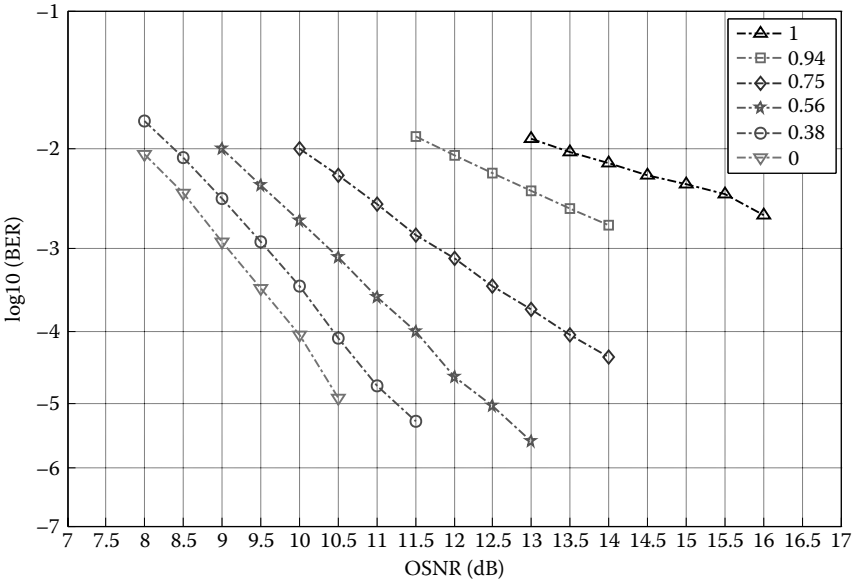

FIGURE 15.41
Performance of MLSE equalizer versus normalized <Δτ> values for 1 sample per bit.

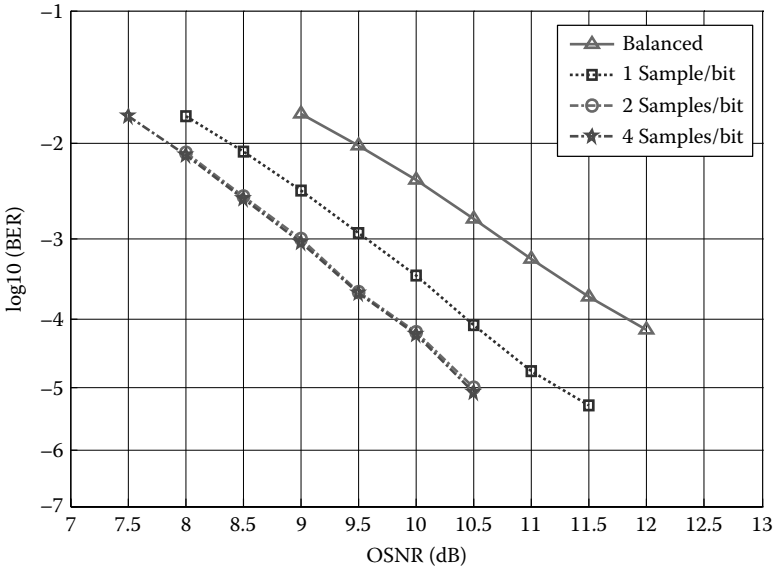

FIGURE 15.42
Comparison of MLSE performance for configurations of 1, 2, and 4 samples per bit with normalized <Δτ> value of 0.38.

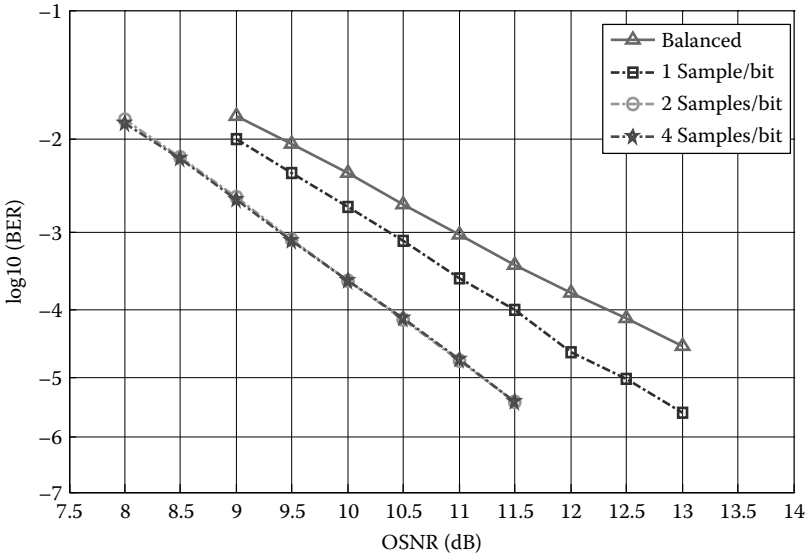

FIGURE 15.43
Performance of Viterbi–MLSE equalizer for configurations of 1, 2, and 4 samples per bit with a normalized <Δ*t*> value of 0.56.

normalized DGD values with 2 samples per bit is shown in Figure 15.44. From Figure 15.44, the important remark is that 16-state MLSE equalizer implementing 2 samples per symbol enables the optical MSK transmission systems achieving a PMD tolerance of up to one bit period at $BER = 10^{-4}$ with a required OSNR of 8 dB. This delay value starts introducing a BER floor indicating the limit of the 16-state MLSE equalizer. This problem can be overcome with a high-performance FEC. However, the DGD mean value of 0.94 can be considered as the limit for an acceptable performance of the proposed MLSE equalizer without the aid of high-performance FEC. Figure 15.45 shows the required OSNR for MLSE performance at 10^{-4} versus normalized <Δ*t*> values in configurations of balanced receiver, 1 sampler per bit and 2 samples per bit.

A balanced receiver with no MLSE equalizer incorporated requires an $OSNR = 5$ dB to obtain a $BER = 10^{-4}$ when there is no effect of the PMD compared to the required OSNR of 3 and 1 dB in cases of 1 sample per bit and 2 samples per bit, respectively. The OSNR penalty for various normalized <Δ*t*> values of the aforesaid three transmission system configurations are shown in Figure 15.46.

It can be observed that the OSNR penalties (back to back) of approximately 3 and 1 dB apply to the cases of balanced receiver and 1 sample per bit, respectively, with reference to the 2 samples per bit configuration. Another important remark is that 16-state Viterbi-MLSE equalizer that implements 2 samples per bit enables the optical MSK transmission systems to achieve a PMD tolerance of up to one bit period at a BER of 10^{-4} with a power penalty of about 6 dB. Moreover, the best 2 dB penalty occurs at 0.75 for the value of normalized <Δ*t*>. This result shows that the combination of OFDR-based MSK optical systems and Viterbi-MLSE equalizers, particularly with the use of multisample sampling schemes was found to be highly effective in combating the fiber PMD dynamic impairment and better than recently reported PMD performance for OOK and DPSK modulation formats [35].

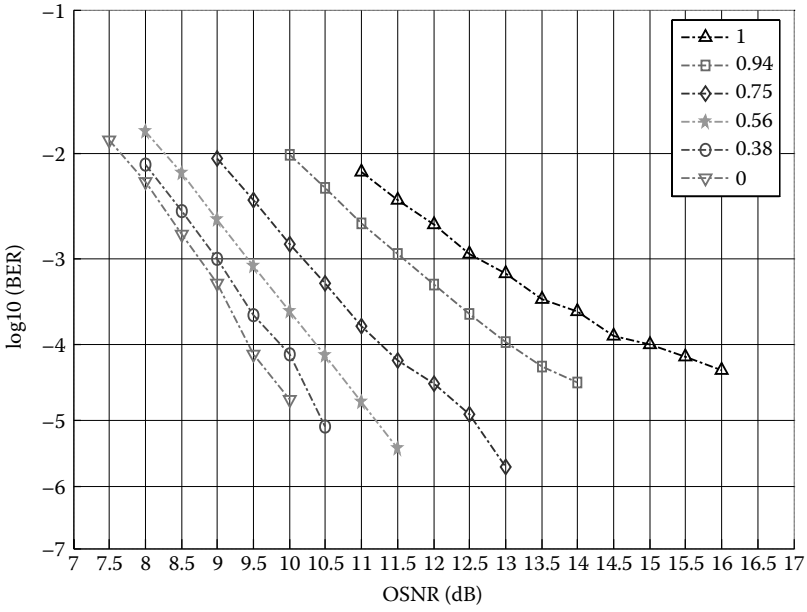

FIGURE 15.44
Performance of Viterbi–MLSE equalizer for different normalized <Δ*t*> values with 2 and 4 samples per bit.

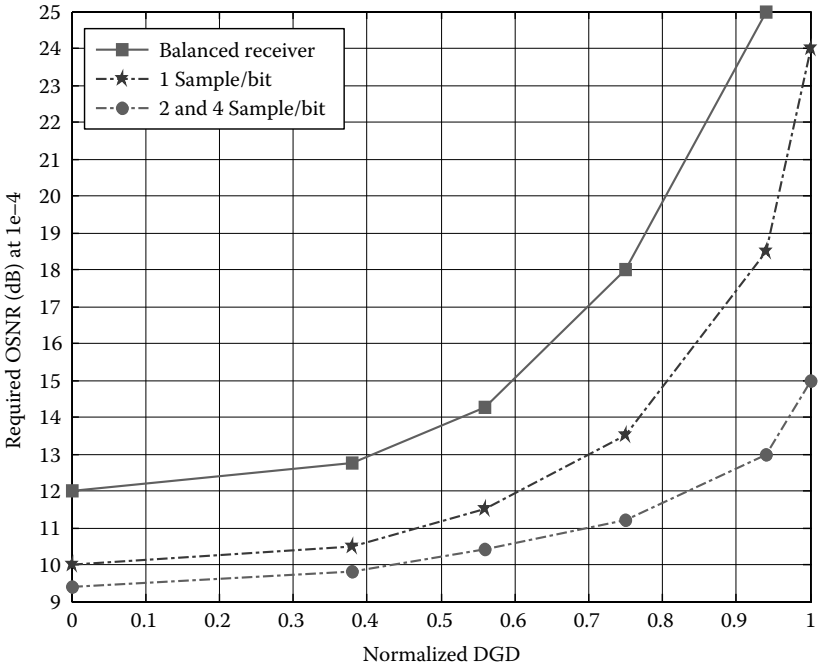

FIGURE 15.45
Required OSNR for MLSE performance at 10^{-4} versus normalized <Δ*t*> values in configurations of balanced receiver and 1 and 2 samples per bit.

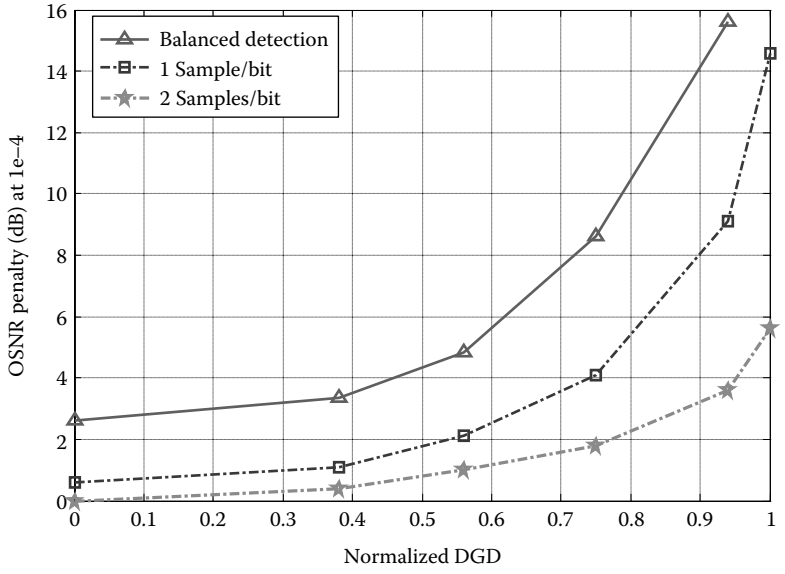

FIGURE 15.46
OSNR penalties of MLSE performance at 10^{-4} for various normalized $<\Delta t>$ values in configurations of balanced receiver, single sample, and two samples per bit sampling schemes.

15.6.2.5 On the Uncertainty and Transmission Limitation of Equalization Process

The fundamental limitations of a quadratic phase media on the transmission speed are formulated in signal space for significant applications in signal equalization. These limitations are quantitatively derived for both coherent and incoherent optical systems. This section investigates the dispersive effect of optical fiber on the transmission speed of the media. The main effect of dispersion is pulse broadening (and frequency chirping) as the signal pulses propagate through the quadratic phase media. This causes ISI and thereby limits the speed of transmission. There are various ways of mitigating the harmful effect of ISI. One way is to use optical fiber with antidispersive property to equalize the dispersion. In practice, this optical scheme reduces signal level and thus requires amplification. The amplifier introduces noise, which in turn limits the channel speed (Shannon's information capacity theorem). Another way of combating ISI is by digital electronic equalization, means such as MLSE, which is applicable for both coherent and incoherent detection schemes [35–39]. These reported results show clearly that there is a fundamental limit on the achievable transmission speed for a given fiber length.

This section studies the limitation of quadratic phase channel, the single-mode optical fiber, in terms of signal space. The signal space is chosen so that it consists of binary signals in 8-bit block code. As the 8-bit symbols propagate down the quadratic phase channel, naturally the waveform patterns of the symbols become less and less distinctive, making it more and more difficult to discriminate between symbols. How do we quantify the detrimental effect of the quadratic phase channel? Although it is obvious that the more information we have at hand the more accurate one would be able to obtain the BER, this system performance is approached entirely from digital communication perspective, and the results so derived are the fundamental limits imposed by the quadratic phase channel (pure phase distortion but quadratic or square dependence of frequency by the linear dispersion).

It is virtually independent of the detection scheme used. Two mechanisms that limit the transmission speed are explained. One is brought about by the finite time window available for detection. In all practical schemes, the decoder must decode each symbol within a finite time. This requires an algorithm as least complex as possible. The other is brought about by not using the phase information for detection. Depending on the complexity of the detection scheme chosen, quite often the phase information may be lost inadvertently when the optical signal is converted into an electrical signal. Another issue is the power consumption of the ASIC for implementation of digital algorithm for real-time applications. The more complex the algorithms the higher the number of digital circuits and hence the higher the power consumption. It is expected that all ASIC must consume less than 70 W in realtime processing.

15.7 MIMO Equalization

15.7.1 Generic MIMO Equalization Process

MIMO stands for multiple inputs multiple out puts technique in which the systems under considerations would have N input port and N or M output ports. The use of MIMO allows the processing of signals with much higher possibilities of recovering the original signals due to higher degree of processing. In the case of optical transmission over a single-mode fiber, the two polarization modes are of the LP_{01} mode over which two QAM channels are transmitted. Each polarized channel can be considered as an input, and thus we do have 2×2 MIMO systems for PDM–QPSK or PDM–QAM transmission systems. Due to the cross coupling of the polarized modes via the PMD as described in Chapter 5, the cross coupling leads to disturbances and distortion of signals propagating through such fibers. Thus, the development of algorithms for eliminating these impairments would be of much interest. This section is thus dedicated to this MIMO processing technique and gives a brief introduction to some experimental work applying this MIMO technique.

The filter structure incorporated into the DSP processing is shown in Figure 15.47. Because of whitening noise effects in the optical amplification stages in the link, the root-raised cosine filter is used at the receiver for match filtering. That is the complete filtering process in the link forms a complete Nyquist filter and satisfies the Nyquist shaping criteria. Following the Rx imperfections compensation and CD compensation, a complex butterfly FIR structure is applied to compensate for PMD. Each of four complex FIR filters is realized by a butterfly structure of corresponding real FIR filters. The recursive CMA LMS algorithm continuously updates the filter taps, which guarantee the initial convergence and tracking of time-variant channel distortions. In the steady state, the complex butterfly structure is a digital, real representation of the inverse impulse response determined by the tap coefficients.

The output signals from the FIR equalization stage (x' and y') at time instant k are related to the input signal vectors (x and y) containing samples $k - L + 1$ to k by

$$\begin{bmatrix} x'(k) \\ y'(k) \end{bmatrix} = \begin{bmatrix} \mathbf{h}_{xx} & \mathbf{h}_{yx} \\ \mathbf{h}_{xy} & \mathbf{h}_{yy} \end{bmatrix} \bullet \begin{bmatrix} \mathbf{x}(k) \\ \mathbf{y}(k) \end{bmatrix} \tag{15.63}$$

where $\mathbf{h}_{xx}$, $\mathbf{h}_{xy}$, $\mathbf{h}_{yy}$, and $\mathbf{h}_{yx}$ are the $T/2$ spaced tap impulse response functional vectors (T is symbol period), for the FIR filter, and the dot "$\bullet$" denoting the vector dot product. $\mathbf{h}_{xx}$ and $\mathbf{h}_{yy}$

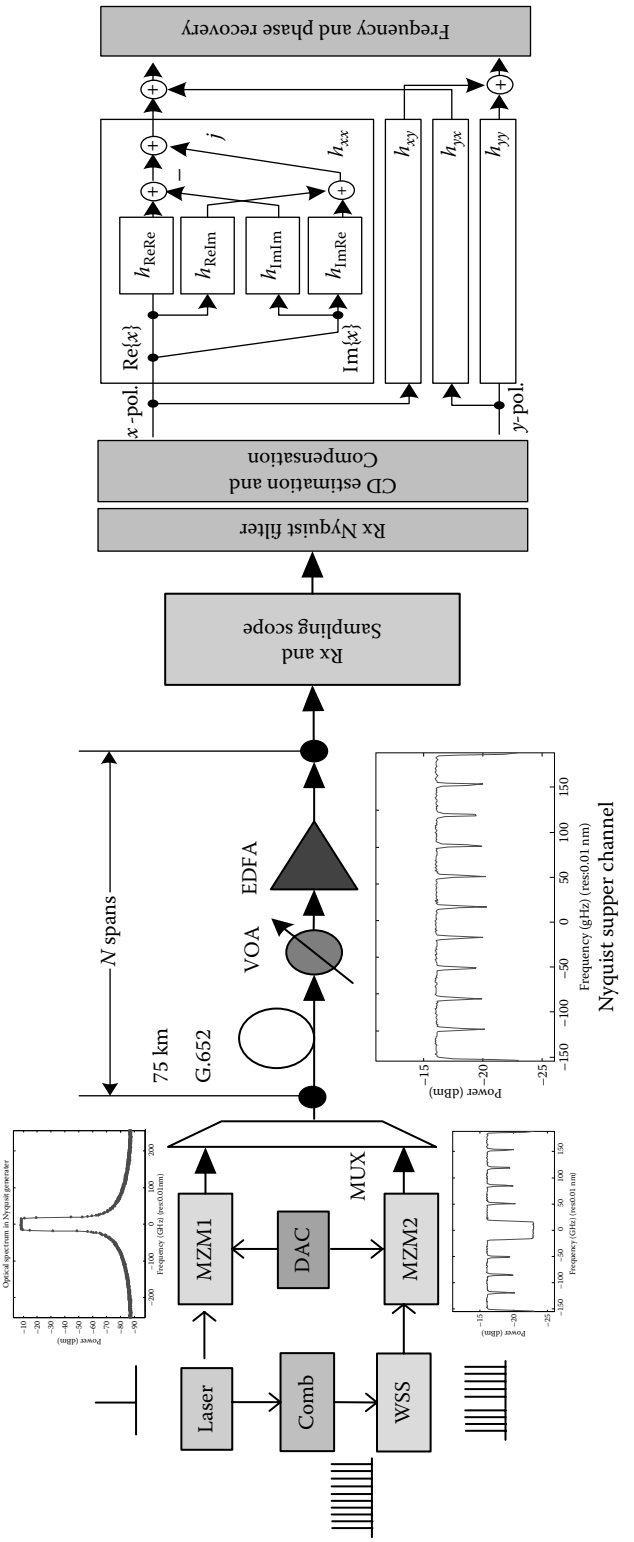

FIGURE 15.47
Nyquist superchannel experimental setup and receiver structure; each of four complex MIMO filters consists of four real FIR filters.

can be considered as the autocorrelation vector matrices of the propagation medium obtained with the input as an impulse sampled vectors, and $\mathbf{h}_{xy}$ and $\mathbf{h}_{yx}$ are the cross-coupling correlation matrices indicating the cross coupling between the two polarized propagation directions. The length L of the tap vector is equal to the impulse response of the distorted transmission medium to be compensated. Initial equalizer acquisition is performed on the first several thousand symbols depending on the "learning/training" process. These symbols are subsequently discarded in error counting. The equalizer tap vectors are then updated continuously throughout the processing of the dataset to track channel changes.

The impulse responses of the overall transmission systems when under perturbation due to linear impairments can be obtained by convolving the impulse responses of each subsystem in cascade. The input signals can be a vector representing the sampled sequence. Thus, there are two possibilities. One is conducting the equalization blindly and second by using a training sequence. The training sequence, for example, constant amplitude zero autocorrelation (CAZAC) [40] sequence can be employed [41]. The main aim of the training sequence is to identify the disturbance of the propagation medium, for example, due to CD and PMD by finding the cross-coupling matrices $\mathbf{h}_{xy}$ and $\mathbf{h}_{yx}$. The processes of equalization for MIMO systems can be summarized as shown in Figure 15.48.

In the case when there is no polarization rotation, then the cross correlation matrices are null. Thus, the autocorrelation becomes orthogonal. Both $\mathbf{h}_{xy}$ and $\mathbf{h}_{yx}$are complex conjugates of each other when the total energy is conserved. When there are polarization-dependent losses (PDL), then no energy conservation is held and these two matrix vectors are not conjugated to each other.

Another point to clarify is the energy conservation in the auto- and cross-coupling matrices. The Wronskian [42] of the matrices must be zero, that is,

$$\det\begin{bmatrix}\mathbf{h}_{xx} & \mathbf{h}_{yx}\\ \mathbf{h}_{xy} & \mathbf{h}_{yy}\end{bmatrix} = 0 \Rightarrow \mathbf{h}_{xx}\mathbf{h}_{yy} - \mathbf{h}_{yx}\mathbf{h}_{xy} = 0 \tag{15.64}$$

So, when the polarization division loss is significant, this relationship is not held and so the coefficients of the equalizer must be corrected. In the case the energy is conserved then

$$\mathbf{h}_{yx} = \mathbf{h}_{xy}^{*} \tag{15.65}$$

Thus in practice, the obtained matrices can be checked to see if the PDL is significant before designing the coefficients of an equalizer. In practice, it is generally expected that these two matrices are not mutually complex conjugates due to several practical problems, and hence, an approximation should be made.

The MIMO filter length in the commercial 100G receivers without tailoring for Nyquist transmission is usually set between 7 and 11 as a trade-off between complexity and the requirements, since the measured mean DGD in real long-haul optical links is around 25 ps. Further increasing the FIR complexity would enhance the gain in the case of a longer pulse response to be employed due to the limited transfer function of the transmission system. This is verified in our experimental platform with the BER against OSNR, the launched power and number of taps as depicted in Figure 15.49a through c. It is noted that the tap number higher than 9 does not offer any gain improvement in performance as depicted in Figure 15.49, The MIMO filter tap length extending effects in commercial WDM optical transmission experiments (a) back-to-back (B2B) performance, L stands for the filter tap length; (b) 1500 km transmission line; (c) 2000 km transmission line; and

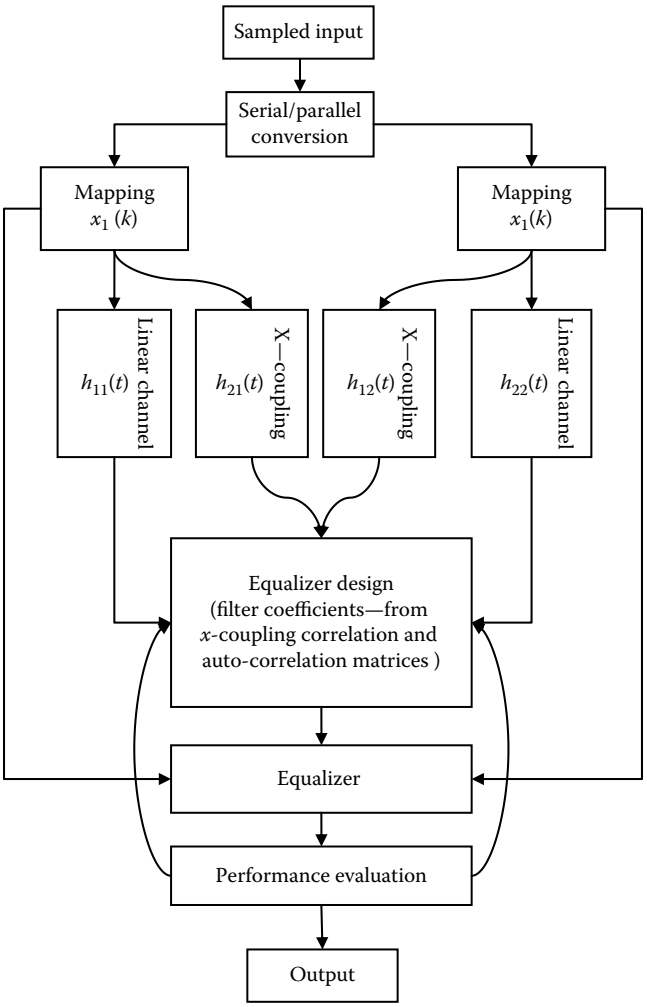

FIGURE 15.48
Equalization process and equalizer design using 2 × 2 MIMO.

(d) MIMO filter with tap length of 23 convergence results. $\mathbf{h}_{xx}$ for the inphase real part of $\mathbf{h}_{xx}$ and $\mathbf{h}_{xx}$ for the quadrature imaginary part of $\mathbf{h}_{xx}$ vector $\mathbf{h}_{xx}$.

In the Nyquist experimental platform, the pulse sequence shaped by a Nyquist square root filter (SRF) of a roll-off factor of 0.1 generating by a time-domain FIR filter with 65 taps. Simulation results do not show any penalty caused by our FIR tap settings. However, hardware imperfections likely require filter pulse response of more FIR taps to achieve the best performance. Further, the convergence of the CMA algorithm would fail for FIR with longer tap length as shown in Figure 15.50. With 7 taps, we are able to acquire the channel while we can acquire the FIR filter and no convergence with 23 and 43. Therefore, the conventional CMA method is used and the performance is shown in Figure 15.50. The coarse step applies fast learning via larger values of a weighting factor μ_1 and a forgetting factor α_1. The fine step uses smaller values of these two parameters and improves the final performance.

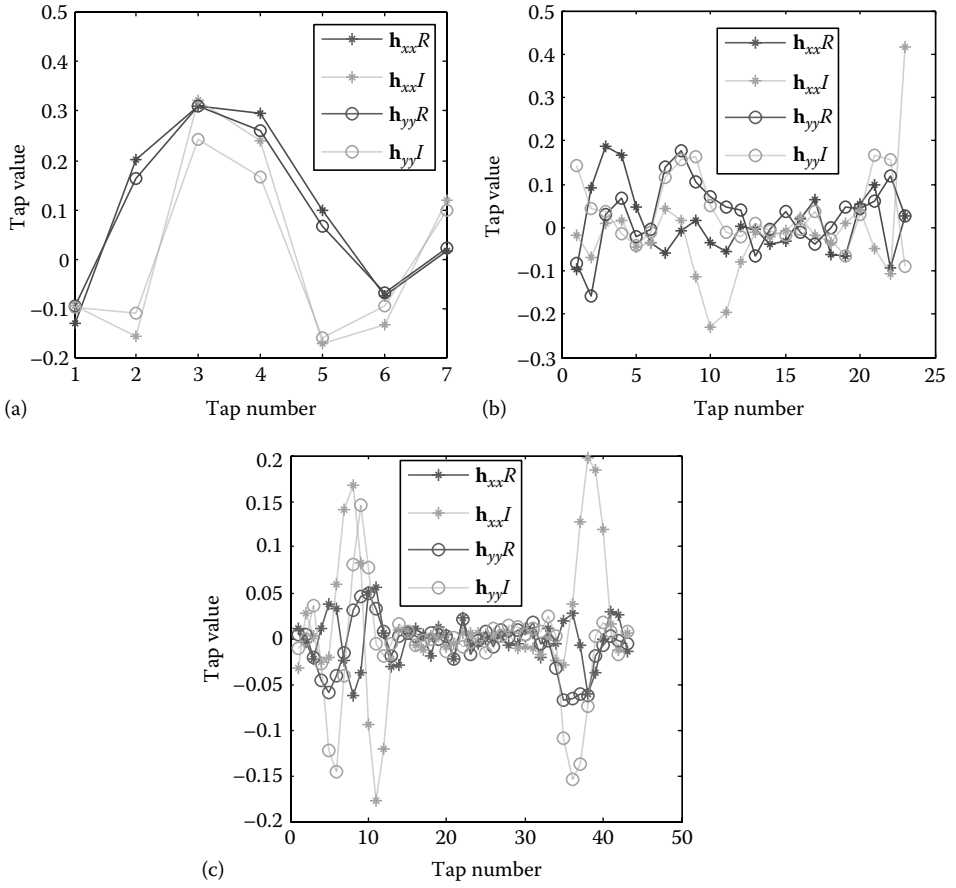

FIGURE 15.49
MIMO filter tap length extending effects in Nyquist WDM optical transmission experimental results. (a) Tap length 7, (b) tap length 23, (c) tap length 43, $\mathbf{h}_{xx}R$ for the real part of $\mathbf{h}_{xx}$, and $\mathbf{h}_{xx}I$ for the imaginary part of $\mathbf{h}_{xx}$.

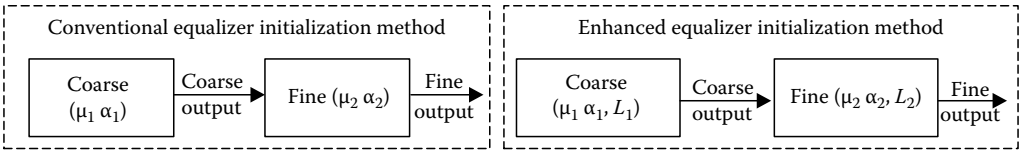

FIGURE 15.50
Conventional and enhanced MIMO filter tap convergence algorithm.

To resolve the convergence problem, we perform the acquisition procedure in two steps, with smaller and larger FIR filter lengths. First, a shorter FIR filter with a smaller number of taps L_1 for example less than 9, and larger μ_1 and α_1 can be used in the initial step to find the main values of the starting taps. After the pre-convergence phase, the filter is extended with the reiterative tap values obtained in the first procedure while the extended taps are set to null in association with smaller values of μ_2 and α_2. This method assures the filter convergence.

Using this new algorithm, the B2B performance can be improved by up to 0.7 dB at BER of 10^{-3} with a tap extension from 7 to 23 as shown in Figure 15.51a. The performance of the

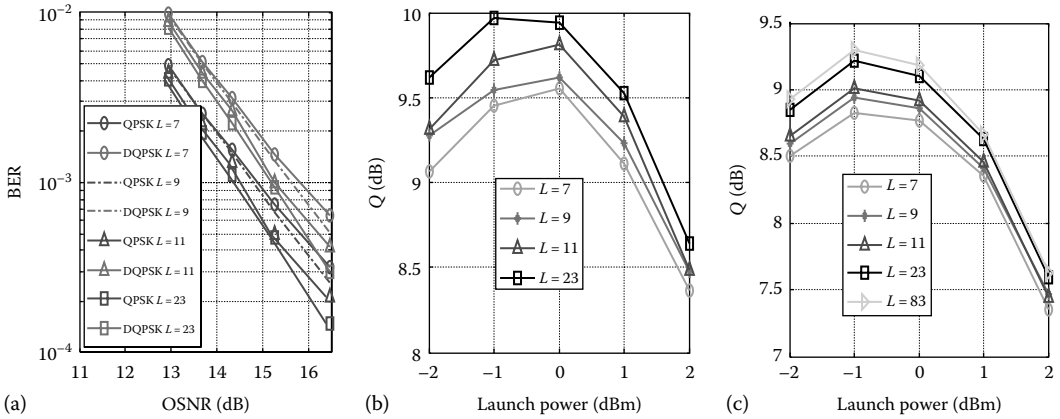

FIGURE 15.51
Enhanced MIMO filter tap length extending performance (BER vs. OSNR) in Nyquist WDM optical transmission experiments. (a) B2B, (b) 1500 km transmission results, and (c) 2000 km transmission.

new algorithm is further verified over the transmission in 1500 and 2000 km links. The tap extension from 7 to 23 enables a Q gain of almost 0.5 dB at two optimum launch power of –1 and 0 dBm. To test the MIMO filter performance improvement by extending the filter length, we checked the filter of length 83. The improvement could only be about 0.1 dB indicating that further increasing the complexity brings only a negligible gain. Thus, a filter length of 23 is the FIR filter limit.

15.7.2 Training-Based MIMO Equalization

Performance of the signal equalization and OPM is based on a 28 GBaud PDM system with 16-QAM leading to a transmission rate of 224 Gb/s. Simulations of the linear channel include residual CD, all-order PMD, polarization rotation angle α, and polarization phase ϕ. At the receiver, white Gaussian noise is loaded onto the signal, followed by an optical Gaussian bandpass filter (second order, double sided 35 GHz), the polarization diverse 90° hybrid and an electrical fifth-order Bessel filter of bandwidth of 19 GHz. An ADC stage digitalizes the received signal at two samples per symbol. The channel is estimated with the aid of the received and transmitted training sequences spectra. Averaging over channel estimations following the scheme illustrated in Figure 15.2 is applied prior to filter update. The received signal is equalized by a $2 \times N$-tap FDE employing a minimum mean square error (MMSE) filter whereas OPM is based on a ZF filter both updated after 20 channel estimation averages.

For each OSNR value (ranging between 15 and 30 dB), 100 random channels have been generated with parameters randomly chosen from the distributions specified in Table 15.3.

TABLE 15.3
Parameter Range and Distribution for Channel Simulations

Impairment	Distribution	Value Range
PMD (all order)	Maxwellian	25 ps mean
Residual CD	Uniform	[−400:400]
Polarization rotation angle α	Uniform	[0,2π]
Polarization phase angle ϕ	Uniform	[0,2π]

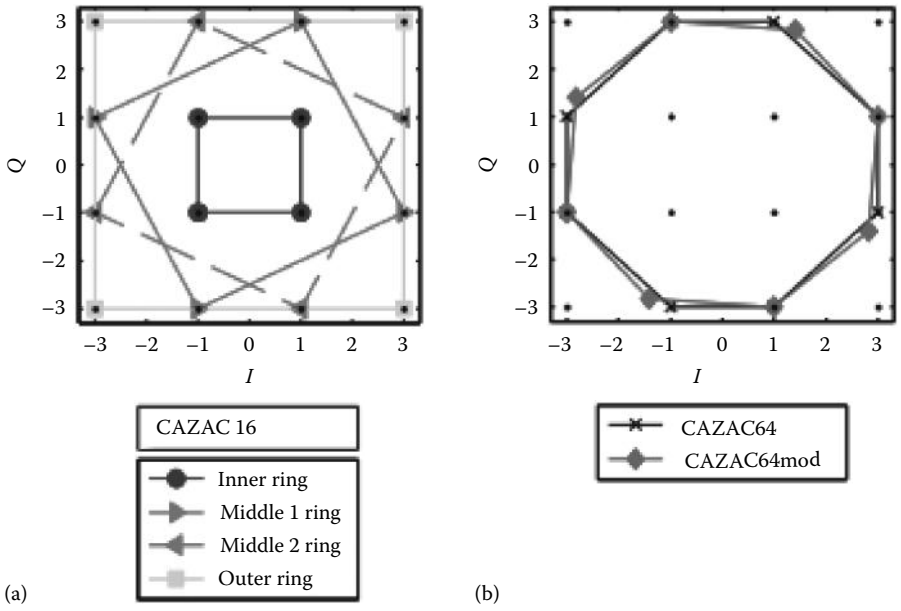

FIGURE 15.52
Mapping short-length CAZAC sequences with low-order modulation format on a 16-QAM constellation diagram: (a) 16-symbol QPSK-CAZAC sequences and (b) 64-symbol 8PSK-CAZAC sequences. (After from Binh, L.N., *Digital Optical Communications*, CRC Press/Taylor & Francis Group, Boca Raton, FL, 2009. With permission.)

As shown in Figure 15.54, estimating the channel by using 16-symbol QPSK-CAZAC sequences (Figure 15.52), the required OSNR at *BER* = 1e−3 is 21.37 dB if the sequences are mapped in the outer ring of the 16-QAM constellation diagram, 22.78 dB if mapped in one of the middle rings, and 24.75 dB if mapped in the inner ring. For channel estimations based on 64-symbol 8PSK-CAZAC sequences, the required OSNR at BER of 1e−3 is 22.71 dB and by alternating the CAZAC properties to make the sequence fit with the eight points of the middle ring of the 16-QAM plot one gets an OSNR penalty of 0.1 dB (Figure 15.53). The better estimation quality of CAZAC sequences mapped in

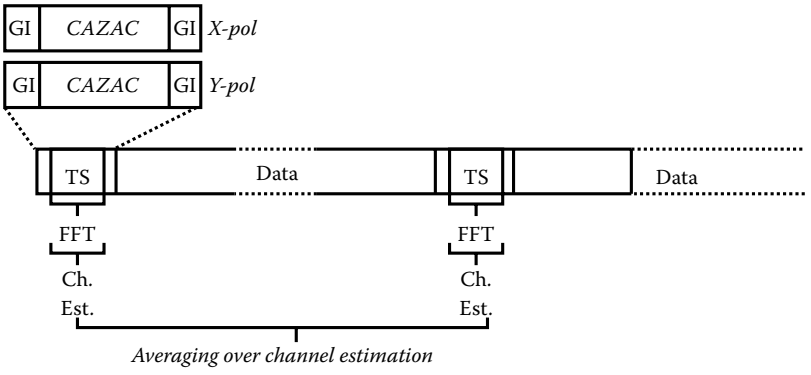

FIGURE 15.53
Training sequence transmission for channel identification. (Adapted from Pittalà, F. et al., Trainingbased channel estimation for signal equalization and OPM in 16-QAM optical transmission systems, in *Proceedings of ECOC 2012*, Amsterdam, the Netherlands, Technical Digest, paper P3.16.pdf, 2012.)

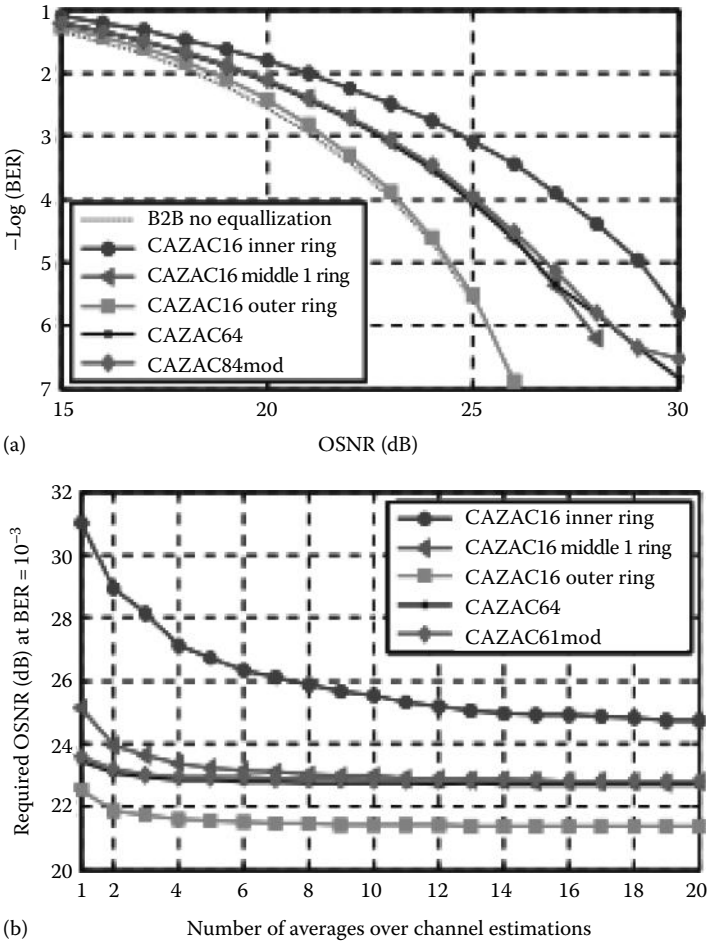

FIGURE 15.54
Signal equalization performance: BER versus OSNR for different CAZAC mappings on the 16-QAM (a) constellation and required OSNR at *BER* = 1e−3 and (b) for different channel estimation averages.

the outer ring is a result of the higher SNR that these points have. In addition, as illustrated in Figure 15.54b, the channel estimation averaging converges faster for training sequences mapped on the outer ring than for sequences mapped in the internal rings (inner/middle ring). The curves of Figure 15.54b do not converge to a single point because of a channel estimation error that cannot be reduced by simply averaging the channel estimations. The BER performance of a single 64-symbol CAZAC sequence equals that obtained by averaging four 16-symbol sequences mapped on the middle ring. This is true as far as the time windowing used to extract the CIR in the channel estimation is 8 symbols long. In this case, both sequences have same tolerance to channel impairments. On the other hand, if the time windowing is set to $N/2$ symbols, CAZAC sequences of 64 symbols would have four times larger tolerance to channel impairments than 16-symbol sequences, but for the same number of channel estimation averages the two sequences would have same BER performance.

15.8 Remarks on References

The major contents of this chapter have also been published in the book of the same author *Digital Processing: Optical Transmission an Coherent Receiving Techniques*, by CRC Press, 2013.

References

1. N. Benuveto and G. Cheubini, *Algorithms for Communications Systems and Their Applications*, John Wiley & Sons, Chichester, U.K., 2004.
2. S. Savoy, Digital coherent optical receivers, *IEEE Journal of Selected Topics in Quantum Electronics*, 16(5), 1164–1178, 2010.
3. A.P. Clark, *Equalizers for High Speed Modem*, Pentech Press, London, U.K., 1985.
4. L. Hanzo, S.X. Ng, T. Keller, and W. Webb, *Quadrature Amplitude Modulation: From Basics to Adaptive Trellis Coded, Turbo-Equalized and Space-Time Coded OFDM CDMA and MC-CDMA Systems*, 2nd ed., John Wiley & Sons, Chichester, U.K., 2004.
5. J. Winters, Equalization in coherent lightwave systems using a fractionally spaced equalizer, *IEEE Journal of Lightwave Technology*, 8(10), 1487–1491, October 1990.
6. R.W. Lucky, J. Salz, and E.J. Weldon, *Principles of Data Communications*, McGraw-Hill, New York, pp. 93–165, 1968.
7. A. Papoulis, *Probability, Random Variables and Stochastic Processes*, McGraw-Hill, New York, 1965.
8. S. Bennetto and E. Biglieri, *Principles of Digital Transmission with Wireless Applications*, Kluwer Academic, New York, 1999.
9. R. Noe, T. Pfau, M. El-Darawy, and S. Hoffmann, Electronic polarization control algorithms for coherent optical transmission, *IEEE Journal of Selected Topics in Quantum Electronics*, 16(5), 1193–1199, September 2010.
10. A.P. Clark, Pseudobinary Viterbi detector, *IEE Proceedings F*, 131, 208–218, 1984.
11. J.G. Proakis and M. Salehi, *Communication Systems Engineering*, 2nd ed., Prentice Hall, Inc., Upper Saddle River, NJ, 2002.
12. J.G. Proakis, *Digital Communications*, 4th ed., McGraw-Hill, New York, pp. 185–213, 2001.
13. L.N. Binh, *Digital Optical Communications*, CRC Press, Boca Raton, FL, 2009, Chapter 5.
14. K. Jinguji and M. Oguma, Optical half-band filters, *IEEE Journal of Lightwave Technology*, 18(2), 252–259, February 2000.
15. L. Binh and V.A.T. Tran, Design of photonic half-band filters using multirate DSP technique, Technical report MECSE-27, 2004, http://www.ds.eng.monash.edu.au/techrep/reports/2004/MECSE-27-2004.pdf.
16. S. Zhang, P.Y. Kam, J. Chen, and C. Yu, A comparison of phase estimation in coherent optical PSK system, in *Photonics Global'08*, Singapore, paper C3-4A-03, December 2008.
17. A.P. Clark, *Equalizers for Digital Modem*, Pentec Press, London, U.K., 1985.
18. G. Nicholson, Probability of error for optical heterodyne DPSK system with quantum phase noise, *Electronic Letters*, 20(24), 1005–1007, November 1984.
19. J.P. Gordon and L.F. Mollenauer, Phase noise in photonic communications systems using linear amplifiers, *Optics Letters*, 15, 1351–1353, 1990.
20. D.-S. Ly-Gagnon, S. Tsukamoto, K. Katoh, and K. Kikuchi, Coherent detection of optical quadrature phase-shift keying signals with carrier phase estimation, *Journal of Lightwave Technology*, 24, 12–21, 2006.
21. X. Liu, X. Wei, R.E. Slusher, and C.J. McKinstrie, Improving transmission performance in differential phase-shift-keyed systems by use of lumped nonlinear phase-shift compensation, *Optics Letters*, 27(18), 1351–1353, September 2002.

22. X. Wei, X. Liu, and C. Xu, Numerical simulation of the SPM penalty in a 10-Gb/s RZ-DPSK system, *IEEE Photonics Technology Letters*, 15(11), 1636–1638, November 2003.
23. E. Ip and J.M. Kahn, Digital equalization of chromatic dispersion and polarization mode dispersion, *IEEE Journal of Lightwave Technology*, 25, 2033–2043, 2007.
24. R. Noe', PLL-free synchronous QPSK polarization multiplex/diversity receiver concept with digital I&Q baseband processing, *IEEE Photonics Technology Letters*, 17, 887–889, 2005.
25. L.N. Binh, *Digital Optical Communications*, CRC Press/Taylor & Francis Group, Boca Raton, FL, 2009.
26. J.G. Proakis, *Digital Communications*, 4th ed., McGraw-Hill, New York, 2001.
27. Y. Han and G. Li, Coherent optical communication using polarization multiple-input-multiple output, *Optics Express*, 13, 7527–7534, 2005.
28. N. Stojanovic, Y. Zhao, B. Mao, C. Xie, F.N. Hauske, and M. Chen, Robust carrier recovery in polarization division multiplexed receivers, in *Proceedings of OFC 2013*, Anaheim, CA, March 2013.
29. H. Meyr et al., *Digital Communication Receivers*, John Wiley & Sons, New York, 1998.
30. A. Leven et al., Frequency estimation in intradyne reception, *IEEE Photonics Technology Letters*, 19, 366–368, 2007.
31. Z. Tao et al., Simple, robust, and wide-range frequency offset monitor for automatic frequency control in digital coherent receivers, in *Proceedings of ECOC 2007*, Berlin, Germany, paper Tu3.5.4, 2007.
32. A.J. Viterbi and A.M. Viterbi, Nonlinear estimation of PSK-modulated carrier phase with application to burst digital transmission, *IEEE Transactions on Information Theory*, 29, 543–551, 1983.
33. M. Kuschnerov et al., DSP for coherent single-carrier receivers, *Journal of Lightwave Technology*, 27, 3614–3622, 2009.
34. CoreOptics Inc. http://www.coreoptics.com/product/prod_ic.php, March 2010.
35. T. Sivahumaran, T.L. Huynh, K. K. Pang, and L.N. Binh, Non-linear equalizers in narrowband filter receiver achieving 950 ps/nm residual dispersion tolerance for 40Gb/s optical MSK transmission systems, in *Proceedings of OFC'07*, Anaheim, CA, paper OThK3, 2007.
36. P. Poggiolini, G. Bosco, M. Visintin, S.J. Savory, Y. Benlachtar, P. Bayvel, and R.I. Killey, MLSE-EDC versus optical dispersion compensation in a single-channel SPM-limited 800 km link at 10 Gbit/s, in *Proceedings of ECOC 2007*, Berlin, Germany, paper 1.3, 2007.
37. N. Alic, G.C. Papen, and Y. Fainman, Performance of maximum likelihood sequence estimation with different modulation formats, in *Proceedings of LEOS'04*, Puerto Rico, Spain, pp. 49–50, 2004.
38. V. Curri, R. Gaudino, A. Napoli, and P. Poggiolini, Electronic equalization for advanced modulation formats in dispersion-limited systems, *Photonics Technology Letters*, 16(11), 2556–2558, 2004.
39. G. Katz, D. Sadot, and J. Tabrikian, Electrical dispersion compensation equalizers in optical long-haul coherent-detection system, in *Proceedings of ICTON'05*, Barcelona, Spain, paper We.C1.5, 2005.
40. Y. Wen, W. Huang, and Z. Zhang, CAZAC sequence and its application in LTE random access, in *Proceedings of 2006 IEEE Information Theory Workshop (ITW'06)*, Chengdu, China, 2006.
41. F. Pittalà, F.N. Hauske, Y. Ye, I.T. Monroy, and J.A. Nossek, Trainingbased channel estimation for signal equalization and OPM in 16-QAM optical transmission systems, in *Proceedings of ECOC 2012*, Amsterdam, the Netherlands, Technical Digest, paper P3.16.pdf, 2012.
42. N.Kh. Rozov, Wronskian, in M. Hazewinkel (Ed.), *Encyclopedia of Mathematics*, Springer, Berlin, Germany, 2001.

Appendix A: Technical Data of Single-Mode Optical Fibers

A.1 Standard Single-Mode Optical Fibers

A.1.1 Corning® SMF-28™ Optical Fiber

Product Information

PI-1036

Issued: April 2001

Supercedes: March 2001

ISO 9001 Registered

A.1.2 Corning® Single-Mode Optical Fiber

A.1.2.1 The Standard for Performance

Corning® SMF-2S™ single-mode optical fiber has set the standard for value and performance for telephony, cable television, submarine, and utility network applications. Being widely used in the transmission of voice, data, and/or video services, SMF-28 fiber is manufactured with the most demanding specifications in the industry. SMF-28 fiber meets or exceeds ITU-T recommendation CI.6S2, TIA/EIA-492CAAA, IEC Publication 60793-2, and GR-20-CORE requirements.

Taking advantage of today's high-capacity, low-cost transmission components developed for the 1310 nm window, SMF-28 fiber features low dispersion and is optimized for use in the 1310 nm wavelength region. SMF-28 fiber can also be used effectively with time-division multiplexing (TDM) and wavelength-division multiplexing (WDM) systems operating in the 1550 nm wavelength region.

A.1.2.2 Features and Benefits

- Versatility in 1310 and 1550 nm applications
- Outstanding geometrical properties for low splice loss and high splice yields
- OVD manufacturing reliability and product consistency
- Optimized for use in loose tube, ribbon, and other common cable designs

A.1.2.3 Sales Leader

Corning SMF-28 fiber is the world's best-selling fiber. In 2000, SMF-28 fiber was deployed in over 45 countries around the world. All types of network providers count on this fiber to support network expansion into the twenty-first century.

A.1.2.4 Protection and Versatility

SMF-28 fiber is protected for long-term performance and reliability by the CPC™ coating system. Corning's enhanced, dual acrylate CPC coatings provide excellent fiber protection and are easy to work with. CPC coatings are designed to be mechanically stripped and have an outside diameter of 245 μm. They are optimized for use in many single- and multifiber cable designs including loose tube, ribbon, slotted core, and tight buffer cables.

A.1.2.5 Patented Quality Process

SMF-28 fiber is manufactured using the outside vapor deposition (OVD) process, which produces a totally synthetic ultrapure fiber. As a result, Corning SMF-28 fiber has consistent geometric properties, high strength, and low attenuation. Corning SMF-28 fiber can be counted on to deliver excellent performance and high reliability, reel after reel. Measurement methods comply with ITU recommendations G.650, IEC 60793-1, and Bellcore GR-20-CORE.

A.1.2.6 Optical Specifications

Attenuation

Standard Attenuation Cells

	Attenuation Cells (dB/km)	
Wavelength (nm)	**Premium[a]**	**Standard**
1310	≤0.35	≤0.40
1550	≤0.25	≤0.30

[a] Lower attenuation available in limited quantities.

Point of discontinuity

No point of discontinuity greater than 0.10 dB at either 1310 or 1550 nm

Attenuation at the water peak

Attenuation at 1383 ± 3 nm shall not exceed 2.1 dB/km

Attenuation vs. Wavelength

Range (nm)	Ref. λ (nm)	Max. α Difference (dB/km)
1285–1330	1310	0.05
1525–1575	1550	0.05

The attenuation in a given wavelength range does not exceed the attenuation of the reference wavelength (λ) by more than the value α.

Attenuation with Bending

Mandrel Diameter (mm)	Number of Turns	Wavelength (nm)	Induced Attenuation[a] (dB)
32	1	1550	≤0.50
50	100	1310	≤0.05
50	100	1550	≤0.10

[a] The induced attenuation due to fiber wrapped around a mandrel of a specified diameter.

Cable Cutoff Wavelength (λ_{eff})

$$\lambda_{eff} \leq 1260 \text{ nm}$$

Mode-field diameter
9.2 ± 0.4 μm at 1310 nm
10.4 ± 0.8 μm at 1550 nm

Dispersion
Zero-dispersion wavelength (λ_0)
1302 nm ≤ λ_0 ≤ 1322 nm
Zero-dispersion slope (S_0):
≤0.092 ps/(nm^2 · km)

$$\text{Dispersion} = D(\lambda) :\approx \frac{S_0}{4}\left[\lambda - \frac{\lambda_0^4}{\lambda^3}\right] \text{ps/(nm} \cdot \text{km)}, \quad \text{for } 1200 \text{ nm} \leq \lambda \leq 1600 \text{ nm}$$

$$\lambda = \text{Operating wavelength}$$

Polarization mode dispersion

Fiber Polarization Mode Dispersion (PMD)

	Value (ps/$\sqrt{\text{km}}$)
PMD link value	≤0.1[a]
Maximum individual fiber	≤0.2

[a] Compiles with IEC SC 86A/WGI, Method I, September 1997.

The PMD link value is a term used to describe the PMD of concatenated lengths of fiber (also known as the link quadrature average). This value is used to determine a statistical upper limit for system PMD performance.

Individual PMD values may change when cabled. Corning's fiber specification supports network design requirements for a 0.5 ps/$\sqrt{\text{km}}$ maximum PMD.

Environmental Specifications

	Induced Attenuation (dB/km)	
Environmental Test Condition	**1310 nm**	**1550 nm**
Temperature dependence −60°C to + 85°C[a]	≤0.05	≤0.05
Temperature-humidity cycling −10°C to +85°C[a], up to 98% RH	≤0.05	≤0.05
Water immersion, 23° ± 2°C[a]	≤0.05	≤0.05
Heat aging, 85° ± 2°C[a]	≤0.05	≤0.05

[a] Reference temperature = +23°C.

Operating Temperature Range
−60°C to +85°C

A.1.2.7 Dimensional Specifications

Standard length (km/reel): 2.2–50.4*

Glass geometry
Fiber curl: ≥4.0 m radius of curvature
Cladding diameter: 125.0 ± 1.0 μm
Core-clad concentricity: ≤0.5 μm
Cladding noncircularity: ≤1.0%

$$\text{Defined as: } \left[1 - \frac{\text{Min. cladding diameter}}{\text{Max. cladding diameter}}\right] \times 100$$

Coating geometry
Coating diameter: 245 ± 5 μm
Coating-cladding concentricity: <12 μm

A.1.2.8 Mechanical Specifications

Proof test
The entire fiber length is subjected to a tensile proof stress ≥100 kpsi (0.7 GN/m^2)†

A.1.2.9 Performance Characterizations

Characterized parameters are typical values.

Core diameter: 8.2 μm

Numerical aperture: 0.14
NA is measured at the 1% power level of a 1D far-field scan at 1310 nm.

Zero-dispersion wavelength (λ_0): 1313 nm

Zero-dispersion slope (S_0): 0.086 ps/(nm$^2 \cdot$ km)

Refractive index difference: 0.36%

Effective group index of refraction

(N_{eff} @) nominal MFD):
1.4677 at 1310 nm
1.4682 at 1550 nm

Fatigue resistance parameter (n_d): 20

Coating strip force
Dry: 0.6 lbs. (3N)
Wet, 14-day room temperature: 0.6 lbs. (3N)

Rayleigh backscatter coefficient (for 1 ns pulse width)
1310 nm: –77 dB
1550 nm: –82 dB

* Longer spliced lengths available at a premium.
† Higher proof test levels available at a premium.

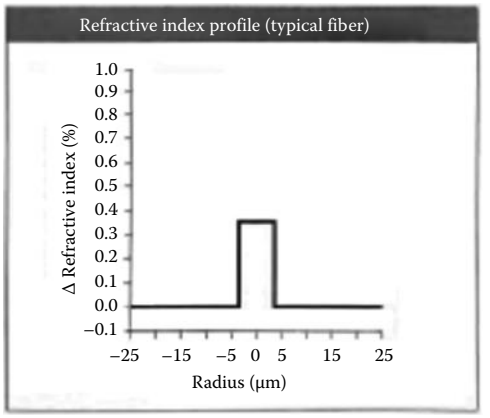

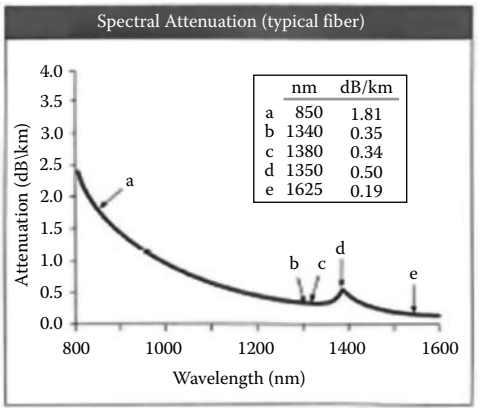

A.2 Enhanced Standard Single-Mode Optical Fibers

A.2.1 Corning® SMF-28™ Optical Fiber

Product Information

PI-1344

Issued: April 2001

ISO 9001 Registered

A.2.2 Corning® Single-Mode Optical Fiber

A.2.2.1 Introducing SMF-28e™ Optical Fiber

Corning SMF-28e single-mode optical fiber continues Corning's long history and performance as a premium fiber supplier. While allowing low water peak attenuation for system installers seeking a low water peak fiber, it meets all the requirements for standard single-mode fiber.

A.2.2.2 Reduced Attenuation

SMF-28e fiber is designed with low water peak attenuation and complies with the requirements of the newly adopted US standard, TIA/EIA 492-CAAB, and the international standard, ITU G.6523.C. These requirements define standard single-mode fibers for use across a broad wavelength range including the extended band (1360–1460 nm).

SMF-28e fiber provides superior attenuation performance throughout the 1260–1625 nm wavelength range including a specified attenuation at 1383 nm $\leq$ 0.31 dB/km.

A.2.2.3 Impact of Low Water Peak

Typical optical fiber displays an attenuation increase at or about 1383 nm. This "water peak" region (1375–1400 nm) is where light is strongly absorbed by hydroxyl (–OH) ions that are present in the glass core leading to increased attenuation over this wavelength

range. SMF-28e fiber has had these ions removed during manufacture, thus reducing the attenuation and leading to a smooth curve across the extended band.

SMF-28e fiber boasts superior low water peak performance, providing excellent first-day attenuation as well as unparalleled lifetime performance.

A.2.2.4 Features and Benefits

- Versatility in the 1310, 1383, and 1550 nm windows
- Low attenuation throughout the extended band
- Characterized out to 1625 nm
- Longer transmission distance
- Enables emerging technologies like CWDM and SOA
- More options for network management
- Lengths up to 50.4 km/spool

A.2.2.5 Optical Specifications

Premium Attenuation

Wavelength (nm)	Attenuation (dB/km)
1310	≤0.35
1383	≤0.31[a]
1550	≤0.25

[a] Attenuation increases due to hydrogen aging at this wavelength will be ≤ 0.01 dB/km and evaluated in accordance with the IEC 60793-2 test procedure.

Point of Discontinuity

No point of discontinuity greater than 0.10 dB at either 1310 or 1550 nm

Attenuation vs. Wavelength

Range (nm)	Ref λ (nm)	Max α Difference (dB/km)
1285–1330	1310	0.05
1525–1575	1550	0.05

The attenuation in a given wavelength range does not exceed the attenuation of the reference wavelength (λ) by more than the value α.

Attenuation with Bending

Mandrel Diameter (nm)	Number of Turns	Wavelength (nm)	Induced Attenuation (dB)[a]
32	1	1550	≤0.50
50	100	1310	≤0.05
50	100	1550	≤0.10
75	100	1625	≤0.50

[a] The induced attenuation due to fiber wrapped around a mandrel of a specified diameter.

Cable Cutoff Wavelength (λ_{eff})

$$\lambda_{eff} \leq 1260 \text{ nm}$$

Mode-Field Diameter
9.2 ± 0.4 μm at 1310 nm
10.4 ± 0.5 μm at 1550 nm

Dispersion
Zero-Dispersion Wavelength (λ_0): 1302 nm ≤ λ_0 ≤ 1322 nm
Zero-Dispersion Slope (S_0): ≤ 0.092 ps/(nm²·km)

$$\text{Dispersion} = D(\lambda) :\approx \frac{S_0}{4}\left[\lambda - \frac{\lambda_0^4}{\lambda^3}\right] \text{ps/(nm·km)}, \quad \text{for } 1200 \text{ nm} \leq \lambda \leq 1600 \text{ nm}$$

λ = Operating wavelength

Polarization Mode Dispersion

Fiber Polarization Mode Dispersion (PMD)

	Value $\left(\text{ps}/\sqrt{\text{km}}\right)$
PMD link value	≤0.1[a]
Maximum individual fiber	≤0.2

[a] Compiles with IEC SC 86A/WGI, Method I, September 1997.

The PMD link value is a term used to describe the PMD of concatenated lengths of fiber (also known as the link quadrature average). This value is used to determine a statistical upper limit for system PMD performance.

Individual PMD values may change when cabled. Corning's fiber specification supports network design requirements for a 0.5 $\text{ps}/\sqrt{\text{km}}$ maximum PMD.

Environmental Specifications

	Induced Attenuation (dB/km)	
Environmental Test Condition	**1310 nm**	**1550 nm**
Temperature dependence −60°C to + 85°C[a]	≤0.05	≤0.05
Temperature-humidity cycling −10°C to +85°C[a], up to 98% RH	≤0.05	≤0.05
Water immersion, 23°± 2°C[a]	≤0.05	≤0.05
Heat aging, 85°± 2°C[a]	≤0.05	≤0.05

[a] Reference temperature = +23°C.

Operating Temperature Range
−60°C to +85°C

A.2.2.6 Dimensional Specifications

Standard Length (km/spool): 2.2–50.4*

Glass Geometry
Fiber curl: ≥4.0 m radius of curvature
Cladding diameter: 125.0 ± 1.0 μm
Core-clad concentricity: ≤0.5 μm
Cladding noncircularity: ≤1.0%

$$\text{Defined as: } \left[1 - \frac{\text{Min. cladding diameter}}{\text{Max. cladding diameter}}\right] \times 100$$

Coating Geometry
Coating diameter: 245 ± 5 μm
Coating-cladding concentricity: <12 μm

A.2.2.7 Mechanical Specifications

Proof Test
The entire fiber length is subjected to a tensile proof stress ≥ 100 kpsi (0.7 GN/m^2).†

A.2.2.8 Performance Characterizations

Characterized parameters are typical values.

Core Diameter: 8.2 μm

Numerical Aperture: 0.14
NA is measured at 1% power level of a 1D far-field scan at 1310 nm.

Zero-Dispersion Wavelength (λ_0): 1313 nm

Zero-Dispersion Slope (S_0): 0.086 ps/(nm^2·km)

Refractive Index Difference: 0.36%

Effective Group Index of Refraction (N_{eff} @) nominal MFD):
1.4677 at 1310 nm
1.4682 at 1550 nm

Fatigue Resistance Parameter (n_d):
20

Coating Strip Force
Dry: 0.6 lbs. (3N)
Wet, 14-day room temperature: 0.6 lbs. (3N)

* Longer spliced lengths available at a premium.
† Higher proof test levels available at a premium.

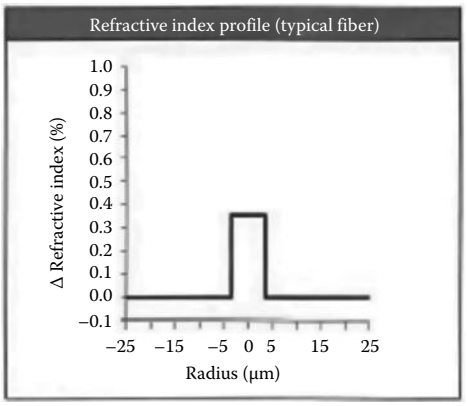

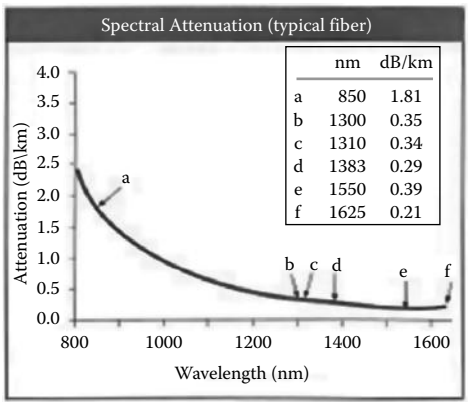

A.3 Large Effective Area Fiber

A.3.1 Corning® LEAF™ Optical Fiber

Product Information

PI-1107

Issued: April 2001

Supercedes: April 2001

ISO 9001 Registered

A.3.1.1 Backbone by LEAF Fiber: What a Powerful Network Needs

With the ever-accelerating race for bandwidth, network designers are challenged to build a network for the present that will also maximize future technologies. It deploys the fiber that revolutionized network technology and gives you room to move and it breaks the bandwidth barrier with a fiber so technologically advanced it gives you the optical backbone you need for today's and tomorrow's networks—Corning LEAF™ optical fiber.

Find out what the world's most powerful networks have in common: backbone by LEAF fiber.

A.3.1.2 Large Effective Area Advantage

LEAF fiber's large effective area (A_{eff}) offers higher power-handling capability, improved optical signal-to-noise ratio, longer amplifier spacing, and maximum dense wavelength-division multiplexing (DWDM) channel plan flexibility compared with other nonzero dispersion-shifted fibers (NZ-DSFs). A fiber with a large A_{eff} also provides a critical performance advantage—the ability to uniformly reduce all nonlinear effects (Figure A.1). Nonlinear effects represent the greatest performance limitations in today's multichannel DWDM systems.

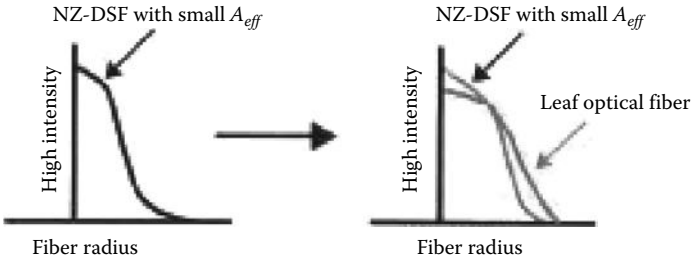

FIGURE A.1
LEAF fiber's larger A_{eff} increases the area where the light can propagate, thereby reducing nonlinear effects.

A.3.1.3 Next Generation

In addition to outperforming other NS-DSFs in the conventional band (C-band: 1530–1564 nm), LEAF fiber facilitates the next technological development in fiber-optic networks—the migration to the long band (L-band: 1565–1625 nm). In both C-band and L-band operations, LEAF fiber has demonstrated greater ability to handle more channels by reducing nonlinear effects such as four-wave mixing, self-phase modulation, and cross-phase modulation in multichannel DWDM transmission.

A.3.1.4 Reduce Network Costs

With its increased optical reach advantage, LEAF fiber requires fewer amplifiers and regenerators and therefore provides immediate and long-term cost savings. LEAF fiber is also compatible with installed base fibers and photonic components. In fact, LEAF fiber's slightly larger mode-field diameter improves its splicing performance, especially when connecting to standard single-mode fiber such as Corning SMF-28 fiber. And, as with all Corning optical fibers, LEAF fiber's geometry package is the cost in the industry. With LEAF fiber, it is easy and economical to increase the information-carrying capacity of your network.

A.3.1.5 Fiber for Today and Tomorrow

While LEAF fiber is exceptionally suited to operate with already-installed 2.5 Gbps systems, it is techno-economically optimized for today's high-channel-count 10 Gbps systems and provides the ability to upgrade in the future to tomorrow's high bit systems. Additionally, LEAF fiber's unparalleled specifications on PMD allow fiber installed today to operate at data rates higher than 10 Gbps. The combination of LEAF fiber's large A_{eff} and its demonstrated Raman upgradeability allows transmission engineers to design and build networks advantaged over other fiber plants.

A.3.1.6 LEAF™ Fiber—All About Value

With LEAF fiber's proven large A_{eff} advantage, the industry's best geometry package, and inherent future-proof design, LEAF fiber continues to be the fiber of choice for today's high-capacity and tomorrow's all-optical networks. Network providers on the cutting edge have embraced large A_{eff} technology as the fiber "backbone" for high-data-rate networks now and in the future.

A.3.1.7 Technology Awards

Corning Incorporated has received multiple industry awards for its patented LEAF optical fiber. Independent panels of experts have chosen LEAF fiber based on its technical merits for the following awards:

"Annual Technology Award" from *Fiberoptic Product News*

"Commercial Technology Achievement Award for Fiber-Optics" from *Laser Focus World Magazine*

"Circle of Excellence Award" from *Photonics Spectra Magazine*

"R&D 100 Award" from *R&D Magazine*

A.3.1.8 Coating

Corning fiber is protected for long-term performance and reliability by the CPC coating system.

A.3.1.9 Optical Specifications

Attenuation
≤0.25 dB/km at 1550 nm
≤0.25 dB/km at 1625 nm
No point of discontinuity greater than 0.10 dB at 1550 nm
Attenuation at 1383 ± 3 nm shall not exceed 1.0 dB/km

Attenuation vs. Wavelength

Range (nm)	Ref. λ (nm)	Max Increase α (dB/km)
1525–1575	1550	0.05
1625	1550	0.05

The attenuation in a given wavelength range does not exceed the attenuation of the reference wavelength (λ) by more than the value α. In all cases, a maximum attenuation of ≤0.25 dB/km applies at 1550 and 1625 nm.

Attenuation with Bending

Mandrel Diameter (mm)	Number of Turns	Wavelength (nm)	Induced Attenuation (dB)
32	1	1550 and 1625	≤0.50
75	100	1550 and 1625	≤0.05

The induced attenuation due to fiber wrapped around a mandrel of a specified diameter.

Mode-Field Diameter
9.20–10.00 μm at 1550 nm

Dispersion
Total Dispersion: 2.0–6.0 ps/(nm·km) over the range 1530–1565 nm
4.5–11.2 ps/(nm·km) over the range of 1565–1625 nm

Fiber Polarization Mode Dispersion (PMD)

	Value (ps/$\sqrt{\text{km}}$)
PMD link value	≤0.4[a]
Maximum individual fiber	≤0.2

[a] Complies with IEC SC 86A/WG1, Method 1, September 1997 (n-24, Q-0.1%).

The PMD link design value is a term used to describe the PMD of concatenated lengths of fiber (also known as PMDQ). This value represents a statistical upper limit for total link PMD.

PMD values may change when fiber is cabled. Corning's fiber specification supports emerging network design requirements for high-data-range systems operating at 10 Gbps (TDM) rates and higher.

Environmental Specifications

	Induced Attenuation (dB/km)
Environmental Test Condition	**1550 nm**
Temperature dependence −60°C to + 85°C[a]	≤0.05
Temperature-humidity cycling −10°C to +85°C[a], up to 98% RH	≤0.05
Water immersion, 23°± 2°C[a]	≤0.05
Heat aging, 85°± 2°C[a]	≤0.05

[a] *Reference temperature* = +23°C.

Operating temperature range
−60°C to +85°C

A.3.1.10 Dimensional Specifications

Standard Length (km/reel): 4.4–25.2*

Glass Geometry
Fiber curl: ≥4.0 m radius of curvature
Cladding diameter: 125.0 ± 1.0 μm
Core-clad concentricity: ≤0.5 μm
Cladding noncircularity: ≤1.0%

Defined as

$$\left[1-\frac{\text{Min. cladding diameter}}{\text{Max. cladding diameter}}\right]\times 100$$

Coating Geometry
Coating diameter: 245 ± 5 μm
Coating-cladding concentricity: <12 μm

* Longer spliced lengths available at a premium.

A.3.1.11 Mechanical Specifications

Proof Test
The entire fiber length is subjected to a tensile proof stress ≥ 100 kpsi (0.7 GN/m^2).*

A.3.1.12 Performance Characterizations

Characterized parameters are typical values.

Effective Area (A_{eff})
72 μm^2

Effective Group Index of Refraction (N_{eff})
1.469 at 1550 nm

Fatigue Resistance Parameter (n_d)
20

Coating Strip Force
Dry: 2.8 N (0.6 lbs)
Wet, 14-day room temperature: 2.7 N (0.6 lbs)

A.3.1.13 Consistency with Global Standards

The values in this product information sheet demonstrate Corning LEAF fiber's conformity with ITU-T recommendation G.655, IEC 60793-2 for B4 class fibers, and Belcore/ Telcordia GR-20-CORE.

A.3.1.14 Dispersion Calculation

$$\text{Dispersion} = D(\lambda) = \left(\frac{D(1565\ \text{nm}) - D(1530\ \text{nm})}{35} * (\lambda - 1565) \right) + (1565\ \text{nm})$$

λ = Operating wavelength upto 1565

$$\text{Dispersion} = D(\lambda) = \left(\frac{D(1625\ \text{nm}) - D(1565\ \text{nm})}{60} * (\lambda - 1625) \right) + (D1625\ \text{nm})$$

λ = Operating wavelength upto 1565 – 1625

Special selections of LEAF fiber attributes are available upon request.

* Higher proof test levels available at a premium.

Appendix B: RMS Definition and Power Measurement

B.1 Definitions and Mathematical Representation

In mathematics, the root mean square (abbreviated RMS or rms), also known as the quadratic mean, is a statistical measure of the magnitude of a varying quantity. It is especially useful when the variates are positive and negative, for example, sinusoids. RMS is used in various fields, including electrical engineering and optical technology, especially in the measurement of optical power for evaluating the optical signal-to-noise ratio (OSNR) in optical transmission systems.

It can be calculated for a series of discrete values or for a continuously varying function. Its name comes from its definition as the square root of the mean of the squares of the values. It is a special case of the generalized mean with the exponent $p = 2$.

The RMS value of a set of values (or a continuous-time waveform) is the square root of the arithmetic mean (average) of the squares of the original values (or the square of the function that defines the continuous waveform).

In the case of a set of n values $\{x_1, x_2,\ldots,x_n\}$, the RMS value can be mathematically written as

$$x_{rms}\sqrt{\frac{1}{n}\left(x_1^2 + x_2^2 + \cdots + x_n^2\right)}. \tag{B.1}$$

The corresponding formula for a continuous function (or waveform) $f(t)$ defined over the interval $T_1 \le t \le T_2$ is

$$f_{rms}\sqrt{\frac{1}{T_2 - T_1}\int_{T_1}^{T_2}\left[f\left(t\right)\right]^2 dt}, \tag{B.2}$$

and the RMS for a function over all time is

$$f_{rms} = \lim_{T\to\infty}\sqrt{\frac{1}{T}\int_{0}^{T}\left[f\left(t\right)\right]^2 dt}. \tag{B.3}$$

Thus, the RMS over all time of a periodic function is equal to the RMS of one period of the function. The RMS value of a continuous function or signal can be approximated by taking the RMS of a series of equally spaced samples. Additionally, the RMS value of various waveforms can also be determined without calculus. In the case of the RMS statistic of a random process, the expected value is used instead of the mean and the square of the RMS

of the random noise term is the sum of the square of the means plus the standard deviation of the random function, for example, Gaussian noise.

$$x_{rms}^2 = \bar{x}^2 + \sigma_x^2. \tag{B.4}$$

Thus, the RMS value is always greater than the mean value.

B.2 RMS of Common Functions

The mathematical representations of a sinusoidal function and for a number of common functions are tabulated in Table B.1 and illustrated in Figures B.1 and B.2, respectively. For optical waves, the term V can be replaced with the electric field of the optical waves. Thus, a measurement of the optical power is indeed the measurement of the square of the RMS value of the optical waves. Hence, in the case that the optical waves are modulated by a sequence of the square wave sequence of a modulated light wave, then the RMS value of this modulated sequence equals to the product of the RMS value of sinusoidal wave function of the optical carrier (assumed normalized peak value) multiplied by the RMS value of the square function, thus equal to $\frac{1}{\sqrt{2}} a\sqrt{D}$ with a as the amplitude of the pulse sequence and D as the duty cycle of the pulse sequence that can be derived without difficulty from the return-to-zero or non-return-to-zero pulse shaping.

TABLE B.1

Waveform and RMS Values

Waveform	Equation	RMS
DC, constant	$y = a$	A
Sine wave	$y = a\sin(2\pi ft)$	$\frac{a}{\sqrt{2}}$
Square wave	$y = \begin{cases} a & \{ft\} < 0.5 \\ -a & \{ft\} > 0.5 \end{cases}$	A
DC-shifted square wave	$y = \begin{cases} a + DC & \{ft\} < 0.5 \\ -a + DC & \{ft\} > 0.5 \end{cases}$	$\sqrt{a^2 + DC^2}$
Modified square wave	$y = \begin{cases} 0 & \{ft\} < 0.25 \\ a & 0.25 < \{ft\} < 0.5 \\ 0 & 0.5 < \{ft\} < 0.75 \\ -a & \{ft\} > 0.75 \end{cases}$	$\frac{a}{\sqrt{2}}$
Triangle wave	$y = \lvert 2a\{ft\} - a \rvert$	$\frac{a}{\sqrt{3}}$
Sawtooth wave	$y = 2a\{ft\} - a$	$\frac{a}{\sqrt{3}}$
Pulse sequence	$y = \begin{cases} a & \{ft\} < D \\ 0 & \{ft\} > D \end{cases}$	$a\sqrt{D}$

Notes: t is the time; f is the frequency; a is the amplitude (peak value); D is the duty cycle or the percent (%) spent high of the period $(1/f)$; $\{r\}$ is the fractional part of r.

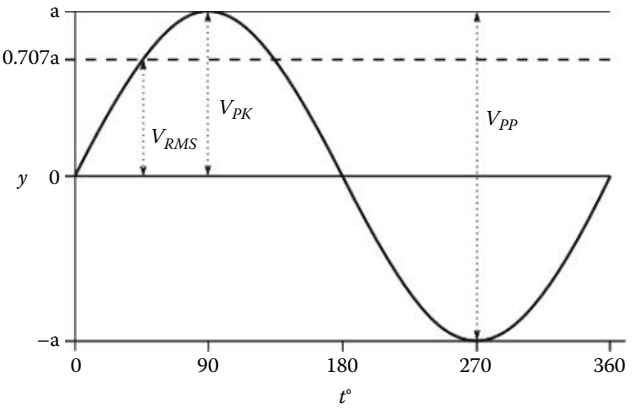

FIGURE B.1
Generic feature of the RMS value of a periodic sinus function versus the time. *V* can be replaced by the field *E* of the optical waves.

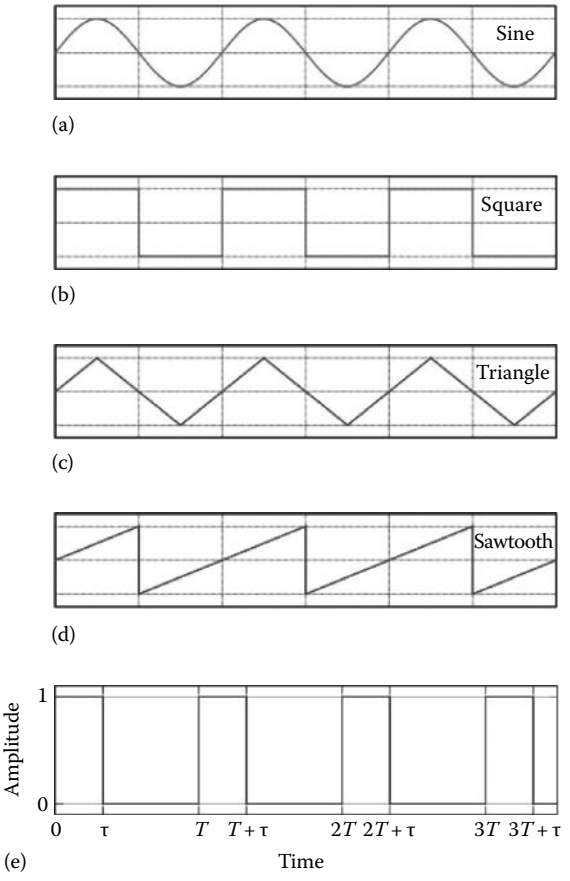

FIGURE B.2
Typical periodic waveforms: (a) sinusoidal, (b) square, (c) triangular, and (d) sawtooth, and (e) pulse sequence with duty cycle of $\tau/T = D$.

Appendix C: Power Budget

C.1 Overview

Power budget is the counterpart of the rise-time budget to ensure that the signals entering the reception subsystem have sufficient energy for detection that satisfies certain criteria for an error-free reception. The two scenarios of distinct reception sensitivities of a communication receiver are when FEC is employed or not. If no forward error coding (FEC) is employed, then for a Gaussian probability density function (pdf), the bit error rate (BER) is required to reach 10^{-9}, or the amplitude ratio of the average levels between "1" and "0" must be at least 6 times the total standard deviation of the noise levels of "1" and "0." If FEC is employed, then this BER can be lowered to about 10^{-3}, depending on the error coding method.

Thus, the following steps must be employed to determine the power budget:

- Identifying the modulation format of the signals and hence the Euclidean distance between the states. Thence, the required ratio between the energy level and the noise power for a specified BER can be determined.
- Identifying the pdf of the transmission and detection processes, hence the noises. Thence, identify the noise sources contributing to the modulated and transmitted signals or signal levels.
- Obtaining the attenuation factor, for example, dB/km in fiber and any noise sources superimposing on the signals during transmission, for example, the amplification spontaneous emission (ASE) noises of inline optical amplifiers.
- Thence, detemining the required receiver sensitivity of the reception systems, which is defined as the minimum power level required of the signals to be available at the input of the receiver at a specified BER.
- Working back, using a linear log-scale diagram to estimate the required signal power to be launched at the output of the transmitter in order to achieve the reception receiving sensitivity.

The earlier steps can be done in our head without resorting to top computing devices, not even a simple calculator. This can be done by converting all power and attenuation in a log scale or in dB level; thence, all estimations are just additions and subtractions.

C.2 Power Budget Estimation Example

As an example, consider the transmission system given in Figure C.1. The modulation is assumed to be binary on-off keying (OOK), the transmission link can be an optically amplified multispan standard single mode fiber (SSMF) type, and the reception system is based on the direct detection technique with a photodetector (PD) and followed by a transimpedance amplifier (TIA) and automatic gain control (AGC) if required.

Under the binary OOK modulation scheme, we can estimate the required signal/noise ratio (SNR) of 6 for a BER of 1e−9. With some uncertainty in the transmission system, *BER* = 1e−12 can be used leading to the required SNR of 7 (the *Q* factor in the linear scale). Figure C.2 depicts the required SNR for BER values over ten decades. That is, the *Q* factor increases by one unit as required for a decade of BER for a Gaussian pdf detection process. Thus, corresponding to *Q* of 6 and 7, the optical SNR (OSNR) can be determined to be $10\text{Log}_{10}6 \sim 15$ dB.

So for an optical receiver, how do we determine the noise power at its input port, that is, at the front of the PD? This means that we have to estimate all noise-equivalent power to the input port of the receiver, or alternatively, we have to find all equivalent noise currents referred to the input port of the receiver as shown in Figure C.3 in which we can identify the following: (1) $\langle i_s^2 \rangle$ represents the average input current as converted by the photodetection process of the input signal; (2) the total equivalent noise current i_{Neq}^2 as referred to the input of the electronic preamplifier following the PD*; and (3) the total noise equivalent, i_{sq}^2,

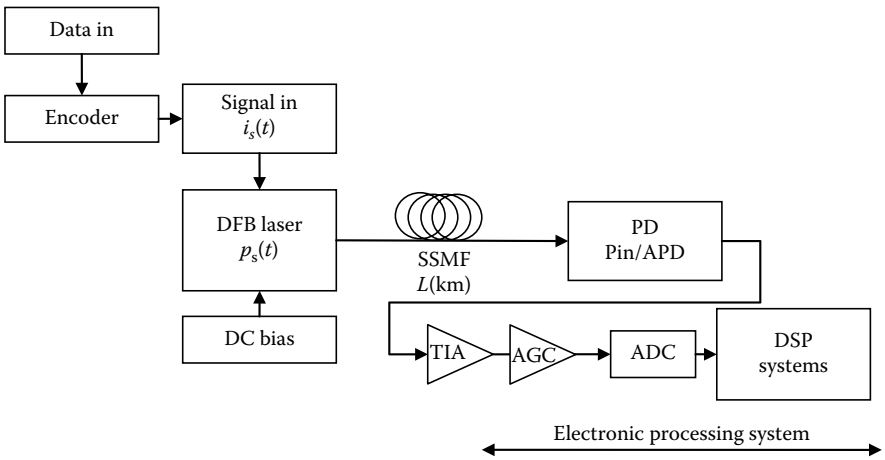

FIGURE C.1
Intensity modulation direct detection transmission scheme.

* Commercial amplifiers normally specified the noise characteristics as the total equivalent noise spectral density referred to the input in units of $A/\sqrt{Hz}$. This parameter is normally measured by connecting the output of the amplifier to a spectrum analyzer with no signal input. The output is integrated over the bandwidth of the amplifier to obtain the total noise voltage at the output. In case of a TIA, this output voltage noise is then transferred back to the input by a simple division. Hence, we can get the total equivalent noise current referred to the input. This noise current referred to the input can be converted to the equivalent optical power by using the responsivity of the photodetector. From this value and the OSNR, we can justify whether the transmission link would operate to give the required BER.

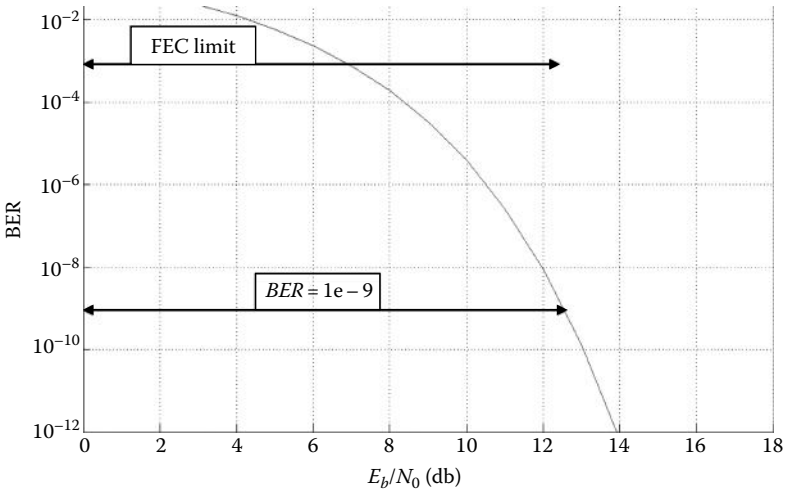

FIGURE C.2
Theoretical estimation for BER versus SNR for binary OOK of a Gaussian noise system.

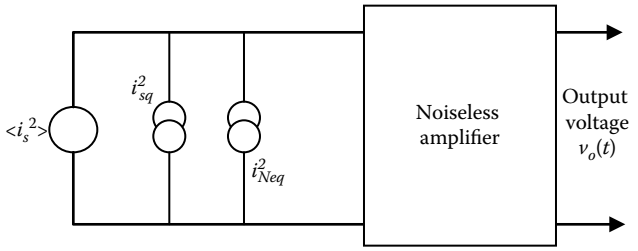

FIGURE C.3
Equivalent current model referred to the input of the optical receiver: average signal current and equivalent noise current of the electronic preamplifier as seen from its input port.

generated during the optoelectronic conversion such as the quantum shot noise by the signal input and the dark current noise of the PD.

It is noted that under direct detection, the amplifier noise current normally dominates over the quantum shot noises, while this is opposite in the case of coherent detection in which the quantum shot noises are due to the high average power of the coherent sources.

Now reverting back to the optical fiber transmission link, if we have the direct modulation and bias at current $I_b = 5I_{th}$ with a magnitude of $4.5I_{th}$, then an average optical power at the output of the distributed feedback laser (DFB) can reach 10 dBm. But for "0," we would have to drive with a magnitude of about $1.5I_{th}$. So we expect noisy signals at the base level, which is at a "high" level, and we expect a distinction ratio of more than 20 dB. Under this driving condition, let us assume that the average power of 0 dBm can be obtained at the output of the DFB laser.

The attenuation and power requirements for each subsystem of the link can now be estimated:

- The fiber loss for 80 and 100 km SSMF would be about 20–25 dB.
- Using the pin or avalanche photodetector (APD) (avalanched gain of 10) PD and a differential transimpedance amplifier (DTIA) (Inphi model 3250A with a noise spectral density referred to the input of $\left(\frac{di_N^2}{df}\right)^{1/2} = 20 - 40\ \text{pA}/\sqrt{\text{Hz}}$), we would get –7 and –17 dBm, respectively, for a required OSNR of 15 dB and BER of 1e–9–1e–12 (δ or *Q* factor of 6 or 7 under the Gaussian pdf).
- This indicates that an APD is preferred as the PD so that we can avoid the use of an optical amplifier. The projection variation of transmission distance with respect to the launched power at the output of the transmitter is shown in Figure C.4.
- With the *p–i–n* PD, we expect to transmit a 25G NRZ channel over only 40 km with a launched power of 4 dBm. However, with the APD gain of 10, the transmission distance limited by the power budget can reach over 80 km on the condition that the pulse sequence is equalized at the DSP-based receiver or an SSB modulation scheme is employed such as the duo binary modulation format.

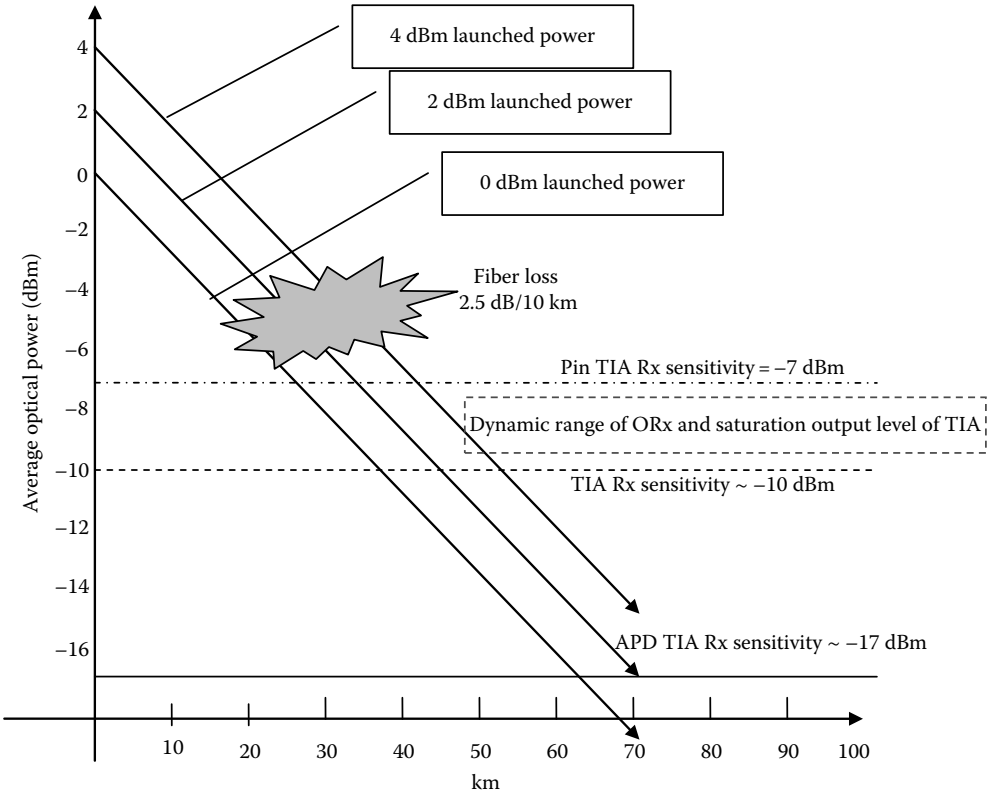

FIGURE C.4
Power budget with an average launched power of 0, 2, and 4 dBm with receiver sensitivity of –7 and –17 dBm and fiber loss of 2.5 dB/10 km.

C.3 Signal to Noise Ratio and Optical Signal to Noise Ratio

Refer to Figure C.3 for the total noise as referred to the input and the generated signal current from the input optical signals. It must be noted that superimposing on the signals, there are also noises commonly known as the quantum shot noise, which is signal dependent and is dependent on the signal average current whose spectral density is given by

$$\begin{aligned} &S_{NQ} = 2q\langle i_S \rangle \text{ in A}^2/\text{Hz} \\ &\rightarrow i_{NQ} \text{ by integrating over BW and sqrt} \end{aligned} \tag{C.1}$$

Furthermore, there are noise currents coming from the dark current of the PD i_{Nd}, that is, the electronic current in the semiconductor junction at a temperature above the absolute reference temperature. So, the total noise current referred to the input of an optical receiver can be written as

$$i_{NT} = i_{NA} + i_{NQ} + i_{Nd} \tag{C.2}$$

Thus, the SNR, in terms of power, can be formed as

$$SNR = \frac{\langle i_S^2 \rangle}{i_{NT}^2} \tag{C.3}$$

The BER can be estimated for amplitude shift keying (ASK) binary signals under Gaussian noise assumptions as

$$BER = \frac{1}{2} ercf\left(\frac{Q}{\sqrt{2}}\right) \quad \text{where } Q = \frac{I_1 - I_0}{\sigma_1 - \sigma_0} \tag{C.4}$$

where

I_1, I_0 is the average current detected by the PD for "1" and "0," respectively
σ_1, σ_0 are the standard deviations of the noise levels due to "1" and "0," respectively

If the modulation format is quadrature amplitude modulation (QAM), then the errors of detection can be considered as the summation of the two orthogonal "binary" signals, the complex and real components. The BER can be estimated for both directions as given in (C.4).

Thus, we could see that by estimating the total current noise referred to the input of the electronic preamplifier, normally a TIA, and then the dark current and the signal-dependent current noise with a typical average optical power at the input, we can obtain a rough estimate of the SNR and the OSNR. Note that the estimation of the noises should be considered for the dominating noise term.

Naturally, the electronic current at the output of the preamplifier of the receiver would not normally be sufficient for the analog to digital converter (ADC) and signal processor, so a voltage gain amplifier with or without an AGC stage (see Figure C.1) would be commonly employed to boost the signal level up. The noise referred to the input of this voltage gain stage as referred to the input of the optical receiver is normally much smaller than that of the preamplifier, so it can be ignored.

Other modulations can be derived using the principles of superposition of probability of errors contributed by the considered neighboring constellation points.

C.4 Transimpedance Amplifier: Differential and Nondifferential Types

TIA is the critical amplifying device that is to be connected in cascade with a high-speed PD to provide the preamplification of the current produced in the PD to the voltage output whose level would be appropriate for an analog to digital conversion so that digitized signals can then be processed in the digital domain by a digital signal processor (DSP). The total equivalent noises referred to the input port of this amplifier are very critical for estimating the impact of the SNR on the optical receiver. The method for calculating noise processes and noise currents and the total equivalent noises referred to the input are given in Chapter 7 (Section 7.5.4.2.2).

Traditionally, single input or nondifferential input TIA has been extensively exploited over the years [1]. However, currently, DTIAs offer a wider bandwidth and high differential transimpedance gain of around 3000–5000 Ω over a 30–40 GHz bandwidth by Si–Ge technology whose transition frequency f_T can reach 280 GHz* [2,3]. However, these DTIAs [4] are limited in their dynamic range and normally an AGC stage would be required. A typical setup of a PD pair and a DTIA is shown in Figure C.5. Typical circuit diagrams of the DTIA employing Si–Ge and InP are shown in Figure C.6a and b, respectively, in which there is a main differential long-tail pair followed by two common collector stages connected to its differential output. The outputs of these stages are then fed back by a shunt feedback to obtain the highest transfer impedance and wideband property. The outputs are fed back to the differential input. These differential ports are then fed into a further differential voltage gain stage (without any feedback stage).

The DTIA can offer a transfer impedance of 4000–5000 Ω. Thus, with an optical signal average power input of 0 dBm (or 1 mW) and a responsivity of the PD of 0.9–1.0 A/W, a

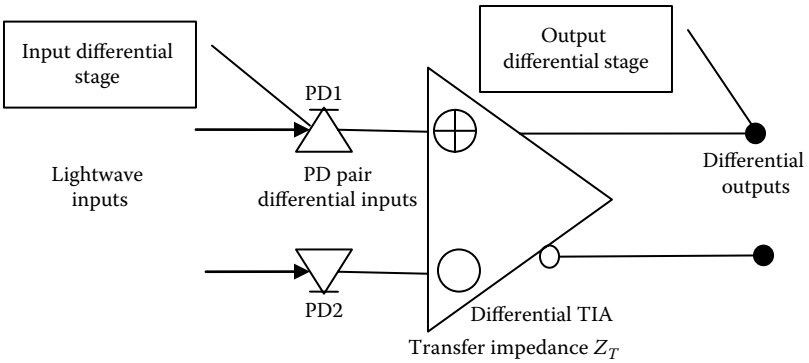

FIGURE C.5
DTIA and PD pair.

* The transition frequency f_T is defined as the frequency at which the short-circuit current gain of a transistor equals to unity.

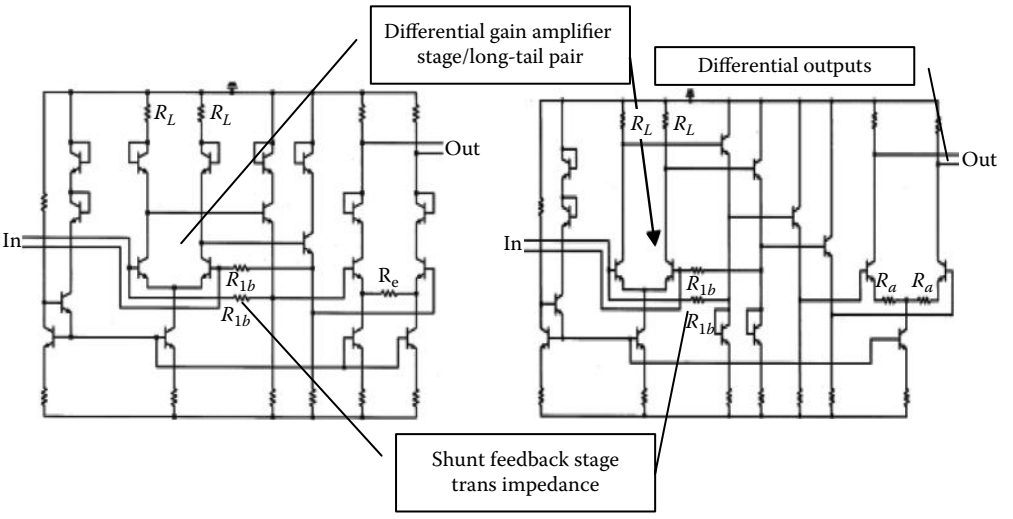

FIGURE C.6
Typical circuit topologies of DTIA by Si–Ge and InP technology. (Extracted from Joseph, S. et al., *IEEE J. Solid-State Circ.*, 38(9), 1512, September 2003.)

current of 1 mA is produced and fed into the DTIA. This in turn produces a differential voltage at the output of 4–5 V signals. Unfortunately, this level will saturate the outputs of the DTIA. So normally an AGC stage would be employed to increase the dynamic range of the optical receiver. The parameters of DTIA can be with the input-referred current noise of the InP TIA, which is approximately 25 $\text{pA}/\sqrt{\text{Hz}}$ on average to a bandwidth of 40 GHz.

References

1. T. van Muoi, Receiver design for high speed optical fiber systems, *IEEE Journal of Lightwave Technology*, LT-2(3), 243–266, 1984.
2. P. Kempf and M. Racanelli, Silicon germanium BiCMOS technology, in *IEEE GaAs IC Symposium Digital*, Monterey, CA, pp. 3–6, October 2002.
3. B. Jagannathan et al., Self-aligned site NPN transistors with 285 GHz $f_{\max}$ and 207 GHz f_T in a manufacturable technology, *IEEE Electron Device Letters*, 23, 258–260, May 2002.
4. S. Joseph et al., SiGe differential trans-impedance amplifier with 50-GHz bandwidth, *IEEE Journal of Solid-State Circuits*, 38(9), 1512, September 2003.

Appendix D: How to Relate the Rise/Fall Time with the Frequency Response of Network and Power Budget Analyses for Optical Link Design and in Experimental Platforms

Summary

One of the main problems that one would commonly face in any experimental platform is the monitoring and observation of time-domain signals or output sequences of transmission systems, regardless of whether they are electrical or optical systems. In optical systems, the optical sequences are converted back to the electrical domain via an optical detector/receiver. After passing through both optical and electrical subsystems, the signals are broadened and captured in a sampled formed via an analog to digital converter (ADC) and memory storage.

Estimation of the rise time and power available at the front end of an optical receiver of an optical link is very critical to ensure the high probability of successful simulation and experimental implementation. The parameters available from the specifications of individual components that form the link would be employed for this estimation.

This book thus outlines the methods for estimation of the rise time and power budget. The rise time for electrical networks under the influence of optical fiber dispersion and optical to electrical conversion and vice versa is defined. Networks with a single dominating time constant or isolated pole and two poles of complex conjugates are given. Considerations for selecting a band-limited oscilloscope for the observation of time-domain sampled signals are provided, and the expected anti-aliasing effects are especially outlined so that readers would not be surprised when using a digital sampling oscilloscope (DSO).

Noises and noise processes of optical receivers and a brief method for the estimation of the required optical power available at the front end of an optical receiver are given. A technique for transforming the noise components of an electrical network to an equivalent noise referred to the input port is also provided in Appendix 3.

In general in any linear systems, there always exists a combination of the natural responses and transient responses of the circuits or networks. The natural responses are due to the energy storage elements of a system that correspond to energy accumulation or discharging processes. The transient responses due to the responses of the system when transferring from a state to the others that depending on the storing or releasing of the energy in the systems and how fast these dynamic responses are depending on their storage/discharging capacity. Furthermore, the initial conditions of the storage elements would also determine the initial state of the transient response. Hence, transient responses are dependent on the initial conditions of the systems. In the frequency domain,

for example, the steady state, the locations of the poles and zeroes, which are defined as the frequencies at which the denominator and numerator are nullified, respectively, determine whether they are isolated or interacting with each other, hence their relationship with the time response behavior.

Thence by observing the time responses at the output of a system, one can estimate its frequency response, and thus, the possible contributions of different elements/components of the system to its output waveforms correspond to an excitation input.

Abbreviations

BW	bandwidth
f_{hC}	"high-frequency cutoff" (–3 dB point) of the analyzed system, measured in Hz
f_{lC}	"low-frequency cutoff" (–3 dB point) of the analyzed system, measured in Hz
FFT	fast Fourier transform
FT	Fourier transform
$h(t)$	the impulse response of the analyzed system in the time domain
$H(\omega)$	the frequency response of the analyzed system in the frequency domain
PD	photodetector
RC network	electrical circuit network consisting of only R and C elements
t_r	"rise time" of the analyzed system, measured in seconds

D.1 Overview

In electronic and telecommunication systems, when describing a voltage or current step function, the "rise time" is the time taken by a signal to change from a specified low value to a specified high value. Our main concern is how to estimate the output pulse or pulse sequence at the output of the receiver given a set of input pulses, the fiber dispersive characteristics, and the frequency responses of each subsystem. Evaluating the overall transfer function of the systems by either time domain or frequency domain requires either a short optical pulse generator whose width is much shorter than that of a period of the wave whose frequency is near the corner frequency of the system or a sinusoidal signal generator whose frequency band is larger than that of the system passband. These techniques face severe difficulties. So, a step function can normally be used as well as the measurement of the rise and fall time and/or the time constant.

It is noted that in the case that the pole of the system is isolated from other poles, or they are far apart by at least one decade of frequency, then a clear exponential growth can be observed and a time constant can be obtained. On the other hand, when the poles of the overall system are not far away from each other or when they are within a decade of frequency, then their corresponding responses interact with each other in the time domain and so there seems to have no distinct time constant or distinct exponential growth or descending. Thus, the rise-time method is to be used.

The rise time can be estimated by measuring the time difference between the instant at which 10% and 90% of the step height at a steady-state flattop are reached. In general, the rise time can be defined as "the time required for the response to rise from x% to y% of its final value," with 0%–100% rise time common for underdamped second-order systems, 5%–95% for critically damped, and 10%–90% for overdamped [1]. The final time is determined as the level at which the response reaches its saturation level. The output signal of a system is characterized also by the fall time: both parameters depend on the rise and fall times of the input signal and on the characteristics of the system.

D.1.1 Definitions of Some Parameters

The aim of this section is to calculate the rise time of the step response for some simple systems: all notations and assumptions required for the following analysis are listed here:

- t_r is the "rise time" of the analyzed system, measured in seconds.
- f_{lC} is the "low-frequency cutoff" (–3 dB point) of the analyzed system, measured in Hz.
- f_{hC} is "high-frequency cutoff" (–3 dB point) of the analyzed system, measured in Hz.
- $h(t)$ is the impulse response of the analyzed system in the time domain.
- $H(\omega)$ is the frequency response of the analyzed system in the frequency domain.
- The bandwidth (BW) or the midband* range is defined as

$$BW = f_{hC} - f_{lC} \tag{D.1}$$

  and since the low-frequency cutoff f_{lC} is usually several decades lower than the high-frequency cutoff f_{lC},

$$BW \cong f_{hC} \tag{D.2}$$

- All systems analyzed here have a frequency response that extends to 0 (low-pass systems); thus,

$$BW = f_{hC} \tag{D.3}$$

- All systems analyzed are thought as electrical networks and all the signals are thought as voltages for the sake of simplicity: The input is a step function of V_0 volts, or in the optical system, the optical modulator is driven with a sharp step function, and the BW of the optical modulator is much wider than that of the system under consideration.

* The midband is defined as the frequency range over which the gain or attenuation is constant or varied within a certain small range, for example, ±0.5 dB.

D.1.2 Gaussian-Response System

A system is said to have a Gaussian response if it is characterized by the following frequency response:

$$H(\omega) = e^{-\frac{\omega^2}{\sigma^2}} \tag{D.4}$$

where $\sigma > 0$ is a constant, related to the high-frequency cutoff as

$$f_{hC} = \frac{\sigma}{2\pi}\sqrt{\frac{3}{10\log e}} = 0.0935\sigma \tag{D.5}$$

Then the corresponding impulse response can be calculated using the inverse Fourier transform of the shown frequency response:

$$h(t) = \Im^{-1}\left(H(\omega)\right) = \frac{1}{2\pi}\int_{-\infty}^{\infty} e^{-j\omega t} e^{\frac{\omega^2}{\sigma^2}} d\omega = \frac{\sigma}{2\pi^{0.5}} e^{-0.25\sigma^2 t^2} \tag{D.6}$$

So applying directly the definition of step response,

$$v(t) = V_0 u(t) * h(t) = \frac{V_0}{2\pi}\int_{-\infty}^{\frac{\sigma t}{2}} e^{-\tau^2} d\tau = \frac{V_0}{2\pi}\left[1 + e^{\frac{\sigma t}{2}}\right] \tag{D.7}$$

with V_0 as the high amplitude of the step function $u(t)$.

Solving for t, utilizing the two following equations by using known properties of the error function, and thence evaluating the time instants at which the amplitude equals to 0.1 and 0.9 (10% and 90%), the rise time can be estimated as the difference of these temporal instants:

$$t_r = \frac{4}{\sigma} erf^{-1}(0.8) \simeq \frac{0.3394}{f_{hC}} \rightarrow f_{hC} = BW = \frac{0.34}{t_r} \tag{D.8}$$

D.1.3 System Evaluation

D.1.3.1 One-Stage Low-Pass RC Network

For a simple, one-stage low-pass RC network, only one energy storage element, the rise time, is proportional to the network time constant τ*, which can be derived by using the

* The term "time constant" is employed instead of the rise time is due to the fact that there is only one storage element and thus only one "pole" in the frequency response and only one natural response. This dominates the time response and the time constant is the inverse of the radial frequency. While the rise time would be best employed when there are more than one pole which are close and interacting with others, there is no dominating/isolated pole. An isolated pole is defined when it is at least one decade of frequency from the other poles of the network.

output response of the network to a unit step function input signal of V_0 amplitude, and its step response can be written as

$$v(t) = V_0(t); \quad v(t) = V_0\left(1 - e^{-t/\tau}\right) \tag{D.9}$$

With τ = time constant, which is related to the rise time by evaluating this impulse response at 10% and 90% amplitude and the corresponding time instants, we have

$$t_r = 2.2\tau \tag{D.10}$$

In practice and experimental works, the time constant can be measured by sketching the tangential to the step response of the RC network till the steady-state level at which the time constant can be obtained as the difference of this point and the time at which the tangential starts. The time constant and the rise time can be related to the BW by Equation D.8. This formula implies that if the BW of an oscilloscope is 350 MHz, its 10%–90% rise time is 1.0 ns, which is similar for the sampling oscilloscope.

D.1.3.2 Rise Time of Cascaded Systems

Consider a system composed by N-cascaded noninteracting blocks, each having a rise time t_{ri} and overshoot in their response; suppose also that the input signal of the first block has a rise time whose value is t_{rS} (Figure D.1). Then its output signal has a rise time t_{rO} equal to

$$t_{rO} = \sqrt{t_{rS}^2 + t_{r1}^2 + \cdots + t_{rN}^2} \tag{D.11}$$

This analytical expression can be derived from the central limit theorem, as reported in Wallman [1,2] in 1950 and Nise [3]. Note that in such cascaded system, the time constant or rise time may be difficult to obtain especially in cases where the poles of individual networks are close to each other.

The rise-time constants of linear circuits are primarily due to the stray capacitance and inductance in the circuit. Because every circuit exhibits not only the resistance but also the capacitance and inductance, a delay in the voltage and/or current at the load is apparent until the steady state is reached. In a pure RC circuit or a first-order RC circuit, the output rise time (10%–90%), as shown earlier, is approximately equal to 2.2 RC.

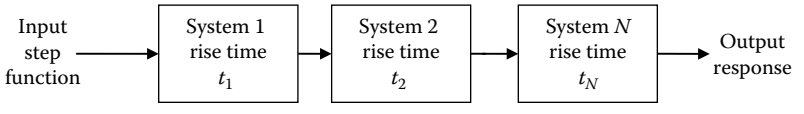

FIGURE D.1
Cascade of subsystems and their rise-time parameters.

D.1.4 Fall Time

In electronics, the fall time (pulse decay time) t_f is the time taken for the amplitude of a pulse to decrease (fall) from a specified value (usually 90% of the peak value exclusive of overshoot or undershoot) to another specified value (usually 10% of the maximum value exclusive of overshoot or undershoot).

Limits on undershoot and oscillation (also known as ringing and hunting) are sometimes additionally stated when specifying fall-time limits. The fall time can be affected by the lower-frequency pole positions in a network/system.

D.1.5 Frequency Responses

The frequency response is the quantitative measure of the output spectrum of a system or device in response to a stimulus and is used to characterize the dynamics of the system. It is a measure of the magnitude and phase of the output as a function of frequency, in comparison to the input. In simplest terms, if a sine wave is injected into a system at a given frequency, a linear system will respond at that same frequency with a certain magnitude and a certain phase angle relative to the input. In addition, if the system is time invariant, then the frequency response also will not vary with time. Usually, the excitation or stimulus function is a sinusoidal function generator that can be scanned with variable frequency.

Commonly defined by the numerator and denominator, the frequency response can be represented by the locations of the "poles" and "zeroes," respectively, as the complex values of the zeroes as shown in Figure D.2. Notations and explanations are given for real poles, real zeroes, and complex pole pairs, which can lead to oscillation with damping and nondamping (pure oscillation) and nonphysical oscillation. Thus, one must design a system or network that would give all the poles located in the left half plane of the *s*-plane. The *s*-plane is defined as the plane that represents the frequency response of the Laplace-transform frequency response with $s = \sigma + j\omega$ with σ as the real part that leads to damping and ω as the radial frequency.

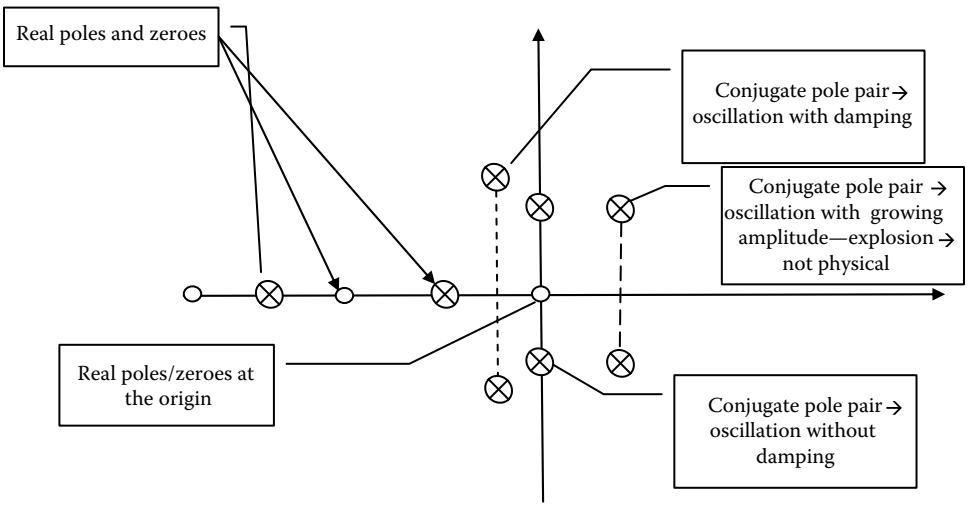

FIGURE D.2
Complex frequency plane for positioning poles and zeroes of physical networks/system frequency responses.

Instead of the frequency response, system performance may be specified in terms of parameters describing the time dependence of the response. The step response can be described by the following quantities related to its time behavior:

- Overshoot
- Rise time
- Settling time
- Ringing

In the case of linear dynamic systems, much can be inferred about the system from these characteristics. Later, the step response of a simple two-pole amplifier is presented, and some of these terms are illustrated.

D.1.6 General Principles of Poles, Zeroes, and Time Response

In general, in any physical systems in which energy conservation is satisfied, for the *N*th-order energy storage element, there must be N poles and hence N zeroes in the system transfer function written as

$$H(s) = A\frac{(s-z_0)(s-z_1)\ldots(s-z_N)}{(s-p_0)(s-p_1)\ldots(s-p_N)}; \quad s = \sigma + j\omega \tag{D.12}$$

where s is the Laplace parameter indicating the frequency and the attenuation or associated loss. The poles and zeroes of the cascaded subsystems are given by $z_0, z_1,\ldots,z_N$ and $p_0, p_1,\ldots,p_N$.* This indicates that when there are no finite poles or zeroes in the expression (D.12), they can be located at infinitive. Thus, there would be N time constants contributed to the step response of the system corresponding to the frequency components represented by the locations of the poles.

Corresponding to (D.12), if the network is composed of parallel subsystems, then using a decomposition technique, one can obtain the transfer function as

$$H(s) = A_0\frac{(s-z_{p0})}{(s-p_0)} + A_1\frac{(s-z_{p1})}{(s-p_{p1})} + \cdots + A_N\frac{(s-z_{pN})}{(s-p_{pN})} \tag{D.13}$$

where $A_0, A_1,\ldots, A_N$ are the constants dependent on the gain of attenuation of each subsystem connected in parallel. One can decompose Equation D.12 to obtain the other from Equation D.13 using the common decomposition method.

* For readers who are not familiar with "zeroes" and "poles" of networks, the definition of a zero of a network is the frequency value at which the transfer function becomes nullified. On the other hand, a pole is the frequency position at which the transfer function magnitude goes to infinitive. From a circuit point of view, the pole occurs when the circuit is at resonance. From an optical circuit point of view, a zero is equivalent to the destructive interference. On the other hand, a pole is equivalent to a resonance, for example, resonance in a ring laser.

D.1.7 Rise Time in Overdamped System

In a preemphasis transmission system, normally a second-order circuit filter is cascaded with a band-limited transfer function subsystem whose passband frequency is above the corner frequency of the system. This second-order transfer function indicates that there are two energy storage elements in the circuit, which can be two charging or two discharging energy elements, or one charging element corresponding to one discharging amount of energy. In the latter case, there would be competition for getting access to the energy for storing or discharging. If such discharging and charging energy mechanism overlaps, then some instability may occur. The roll-off of this band-pass filter matched with the right-side roll-down of the system so that equalization can be achieved. In this case, the response of the overall cascade system is equivalent to that of overdamped systems; the rise time is then commonly defined as the time for a waveform to go from 10% to 90% or 5% to 95% of its final value.

The quadratic approximation for normalized "rise time" for a second-order system, step response, and no zeroes is

$$t_r\omega_0 = 2.230\zeta^2 - 0.078\zeta + 1.12 \tag{D.14}$$

where
ζ is the damping ratio
ω_0 is the natural frequency of the network

However, the proper calculation for the rise time from 0% to 100% of an underdamped second-order system is

$$t_r\omega_0 = \frac{1}{\sqrt{1-\zeta^2}}\left(\pi - \tan^{-1}\frac{\sqrt{1-\zeta^2}}{\zeta}\right) \tag{D.15}$$

where
ζ is the damping ratio
ω_0 is the natural frequency of the network (Figure D.3)

The step response of a system in a given initial state consists of the time evolution of its outputs when its control inputs are Heaviside step functions. In electronic engineering and control theory, the step response is the time behavior of the outputs of a general system when its inputs change from zero to one in a very short time. The concept can be extended to the abstract mathematical notion of a dynamical system using an evolution parameter.

From a practical standpoint, knowing how the system responds to a sudden input is important because large and possibly fast deviations from the long-term steady state may have extreme effects on the component itself and on other portions of the overall system dependent on this component. In addition, the overall system cannot act until the component's output settles down to some vicinity of its final state, delaying the overall system response. Formally, knowing the step response of a dynamical system gives information on the stability of such a system and on its ability to reach one stationary state when starting from another.

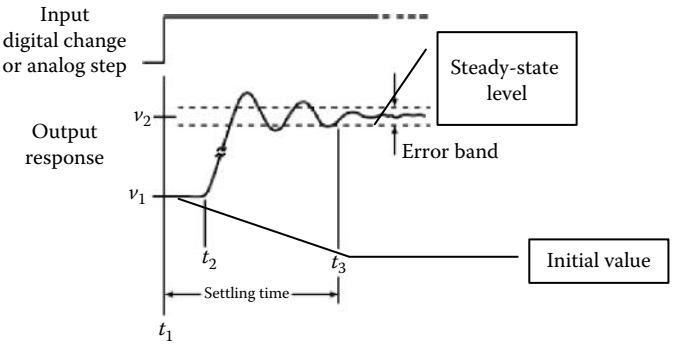

FIGURE D.3
A typical step response for a second-order system, illustrating "overshoot," followed by "ringing," all subsiding within a "settling time," for example, a reached steady-state level. This indicates that there is a complex pole pair with a certain damping coefficient, or nonzero real constant.

A useful application of the overshooting is to preemphasize or predistort the input signals so that the system under consideration would act as an equalizer. The preemphasis subsystem has a band-pass filtering characteristic whose complex pole pair results in a passband with its center frequency located above the corner frequency of the low pass of the system. The arrangement of the preemphasized system is shown in Figure D.4a. The eye diagram and the time sequence of the output and input of the preemphasis circuits are illustrated in (b) and (c), respectively. The time-domain sequence and its appearance in the eye diagram are monitored when the distorted subsystem is moved. Figure D.4d and e depicts the eye diagram of the distorted signal sequence without and with preemphasis, respectively. Readers can refer to the poles located in the *s*-plane for the preemphasis circuit and low-pass pole location (real and noncomplex pole) as depicted in Figure D.5 [4]. The systems are assumed to be linear and time invariant.

D.1.8 Estimation and Plotting

Estimating the frequency response for a physical system generally involves exciting the system with an input signal, measuring both input and output time histories, and comparing the two through a process such as the fast Fourier transform (FFT). One thing to keep in mind for the analysis is that the frequency content of the input signal must cover the frequency range of interest or the results will not be valid for the portion of the frequency range not covered (Figure D.6).

The frequency response of a system can be measured by applying a "test signal," for example

- Applying an impulse to the system and measuring its response (see impulse response)
- Sweeping a constant-amplitude pure tone through the BW of interest and measuring the output level and phase shift relative to the input
- Applying a signal with a wide frequency spectrum (e.g., digitally generated maximum length sequence noise, or analog filtered white noise equivalent, like pink noise) and calculating the impulse response by deconvolution of this input signal and the output signal of the system

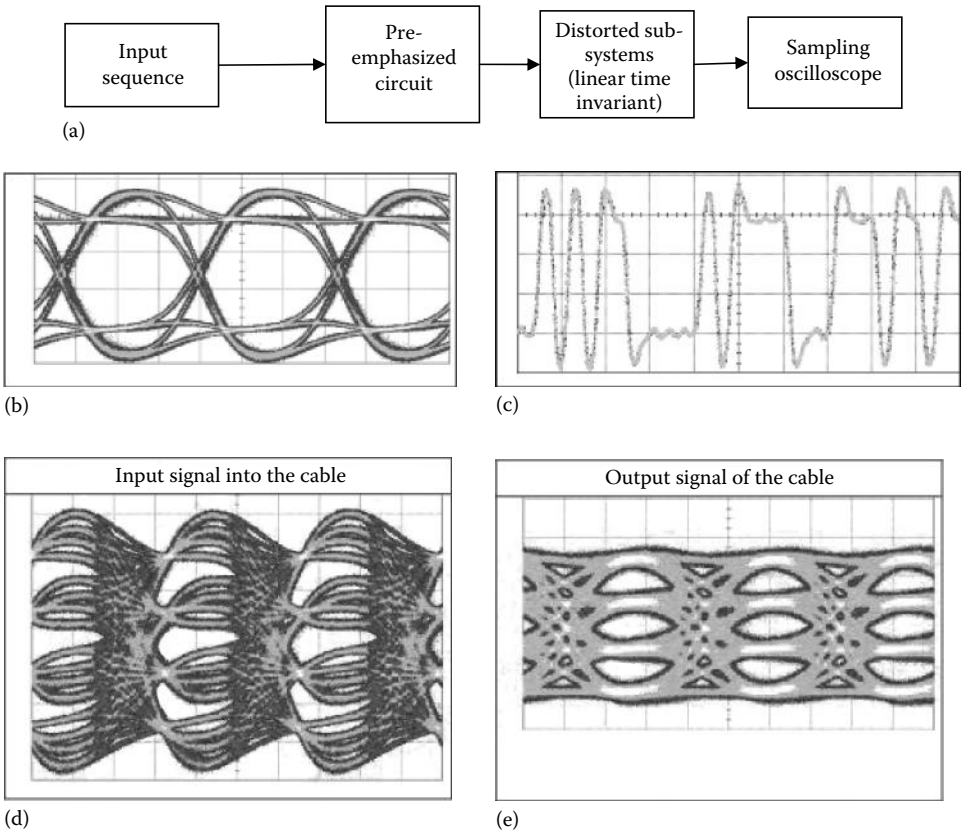

FIGURE D.4
Preemphasized signals seen as (a) a preemphasis circuit in a distorted subsystem, (b) eye diagram and (c) time-domain sequence, (d) in a distorted sequence without and (e) with a preemphasis circuit. (Courtesy of SHF Communications Technologies AG, Berlin, Germany.)

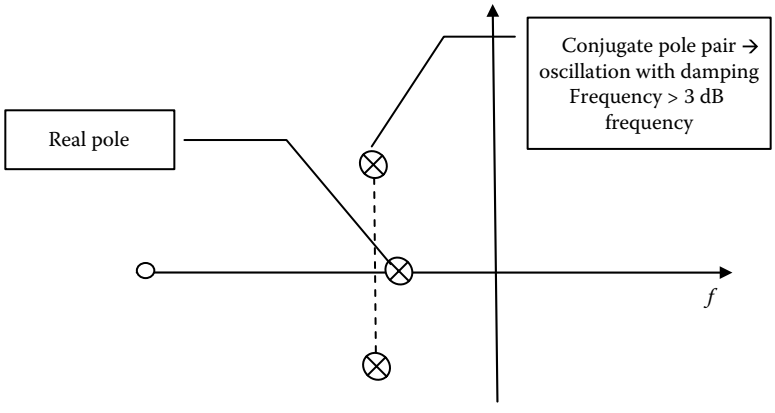

FIGURE D.5
Poles of real 3 dB rolling-off and complex conjugates for peaking for preemphasis.

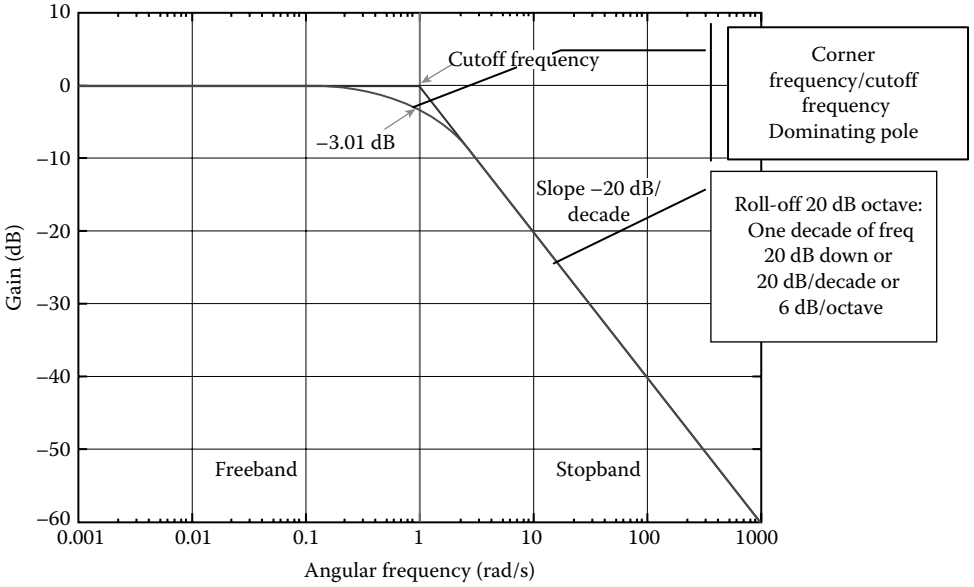

FIGURE D.6
Frequency response of a low-pass filter with 6 dB per octave or 20 dB per decade, an isolated pole.

The frequency response is characterized by the magnitude of the system's response, typically measured in decibels (dB) or as a decimal, and the phase, measured in radians or degrees, versus frequency in radians/second or Hz.

These response measurements can be plotted in three ways: by plotting the magnitude and phase measurements on two rectangular plots as functions of frequency to obtain a Bode plot, by plotting the magnitude and phase angle on a single polar plot with frequency as a parameter to obtain a Nyquist plot, or by plotting the magnitude and phase on a single rectangular plot with frequency as a parameter to obtain a Nichols plot.

For audio systems with nearly uniform time delay at all frequencies, the magnitude versus frequency portion of the Bode plot may be all that is of interest. For the design of control systems, any of the three types of plots (Bode, Nyquist, and Nichols) can be used to infer closed-loop stability and stability margins (gain and phase margins) from the open-loop frequency response, provided that for the Bode analysis, the phase-versus-frequency plot is included.

D.1.9 Example of a Second-Order System: Shunt Feedback Amplifier

This section describes the step response of a simple "negative feedback amplifier" such as a transimpedance amplifier or a voltage feedback amplifier shown in Figure D.7. The feedback amplifier consists of a main open-loop amplifier of gain A_{0L} and a feedback loop governed by a feedback factor β. This feedback amplifier is analyzed to determine how its step response depends upon the time constants governing the response of the main amplifier and upon the amount of feedback used.

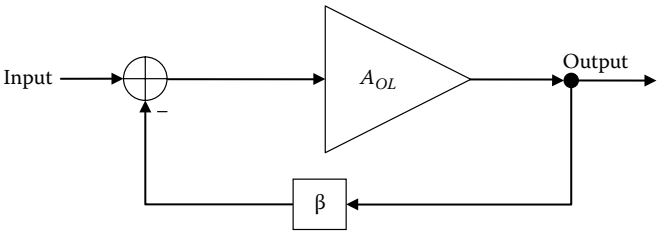

FIGURE D.7
Ideal negative feedback model; open-loop gain is A_{OL} and a feedback factor β is Z_F.

D.1.9.1 Analysis

A negative feedback amplifier has gain given by (see negative feedback amplifier)

$$A_{FB} = \frac{A_{OL}}{1+\beta A_{OL}} \tag{D.16}$$

where
A_{OL} is the open-loop gain
A_{FB} is the closed-loop gain (the gain with negative feedback present)
β is the feedback factor

The step response of such an amplifier is easily handled in the case that the open-loop gain has two poles (two time constants (τ_1, τ_2)), that is, the open-loop gain is given by

$$A_{OL} = \frac{A_0}{(1+j\omega\tau_1)(1+j\omega\tau_2)} \tag{D.17}$$

with zero-frequency gain A_0 and angular frequency $\omega = 2\pi f$, which leads to the closed-loop gain:

$$A_{FB}(j\omega) = \frac{A_0}{1+\beta A_0}\frac{1}{1+j\omega\dfrac{\tau_1+\tau_2}{1+\beta A_0}-\omega^2\dfrac{\tau_1\tau_2}{1+\beta A_0}} \tag{D.18}$$

The time dependence of the amplifier is easy to discover by substituting $s = j\omega$, for example, the Laplace equivalent form, whereupon the gain becomes

$$A_{FB}(s) = \frac{A_0}{\tau_1\tau_2}\frac{1}{s^2+s\left(\dfrac{1}{\tau_1}+\dfrac{1}{\tau_2}\right)+\dfrac{1+\beta A_0}{\tau_1\tau_2}} \tag{D.19}$$

The poles of this expression (i.e., the zeros of the denominator) occur at

$$s^2 + s\left(\frac{1}{\tau_1} + \frac{1}{\tau_2}\right) + \frac{1+\beta A_0}{\tau_1\tau_2} = 0 \rightarrow 2s = -\left(\frac{1}{\tau_1} + \frac{1}{\tau_2}\right) \pm \sqrt{\left(\frac{1}{\tau_1} - \frac{1}{\tau_2}\right)^2 - \frac{4\beta A_0}{\tau_1\tau_2}} \tag{D.20}$$

which shows for large enough values of βA_0 that the square root becomes the square root of a negative number, that is, the square root becomes imaginary, and the pole positions are complex conjugate numbers, either s_+ or s_- (see Figure D.2):

$$s_\pm = -\rho \pm j\mu \tag{D.21}$$

with

$$\rho = \frac{1}{2}\left(\frac{1}{\tau_1} + \frac{1}{\tau_2}\right) \tag{D.22}$$

and

$$\mu = \frac{1}{2}\sqrt{\frac{4\beta A_0}{\tau_1\tau_2} - \left(\frac{1}{\tau_1} - \frac{1}{\tau_2}\right)^2} \tag{D.23}$$

Using polar coordinates with the magnitude of the radius to the roots given by $|s|$ (Figure D.8),

$$|s| = |s_\pm| = \sqrt{\rho^2 + \mu^2} \tag{D.24}$$

and the angular coordinate ϕ is given by

$$\cos\phi = \frac{\rho}{|s|}; \quad \sin\phi = \frac{\mu}{|s|} \tag{D.25}$$

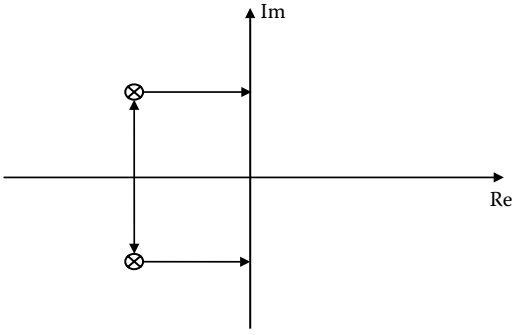

FIGURE D.8
Conjugate pole locations for a two-pole feedback amplifier; Re(*s*) = real axis and Im(*s*) = imaginary axis.

Tables of Laplace transforms show that the time response of such a system is composed of combinations of the two functions:

$$e^{-\rho t}\sin\mu t; \quad e^{-\rho t}\cos\mu t \tag{D.26}$$

which is to say, the solutions are damped oscillations in time. In particular, the unit step response of the system can be found to be [5]

$$S(t) = \frac{A_{0L}}{1+\beta A_{0L}}\left[1 - e^{-\rho t}\frac{\sin(\mu t+\phi)}{\sin\phi}\right] \tag{D.27}$$

which simplifies to

$$S(t) = 1 - e^{-\rho t}\frac{\sin(\mu t+\phi)}{\sin\phi} \tag{D.28}$$

When $A_{OL} \to \infty$ and $\beta \to 1$, for example, the feedback factor reaches unity.

Notice that the damping of the response is set by ρ, that is, by the time constants of the open-loop amplifier. In contrast, the frequency of oscillation is set by μ, that is, by the feedback parameter through βA_0. Because ρ is the sum of reciprocals of time constants, it is interesting to note that ρ is dominated by the "shorter" of the two.

D.1.9.2 Step Responses

Figure D.9 shows the time response to a unit step input for three values of the parameter μ. It can be seen that the frequency of oscillation increases with μ, but the oscillations are contained between the two asymptotes set by the exponentials $1 - e^{-\rho t}$ and $1 + e^{-\rho t}$.

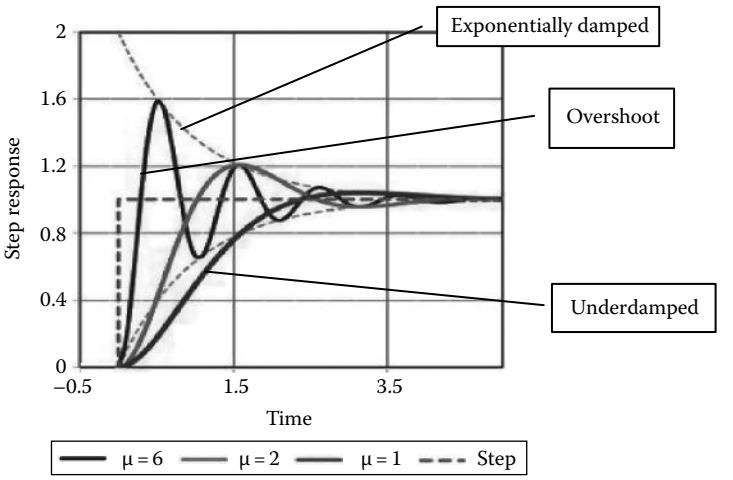

FIGURE D.9
Step response of a linear two-pole feedback amplifier; time is in units of 1/ρ, that is, in terms of the time constants of A_{OL}; curves are plotted for three values of μ, which is controlled by β.

These asymptotes are determined by ρ and therefore by the time constants of the open-loop amplifier, independent of the feedback. This is the exponentially decayed coefficient as indicated in Figure D.9.

The phenomena of oscillation about the final value are called ringing. The overshoot is the maximum swing above the final value and clearly increases with μ. Likewise, the undershoot is the minimum swing below the final value, again increasing with μ. The settling time (or steady state) is the time of departure from the final value to sink below some specified level, say 10% of the final value.

The dependence of settling time upon μ is not obvious, and the approximation of a two-pole system probably is not accurate enough to make any real-world conclusions about the feedback dependence of the settling time. However, the asymptotes $1–e^{-\rho t}$ and $1 + e^{-\rho t}$ clearly impact the settling time, and they are controlled by the time constants of the open-loop amplifier, particularly the shorter of the two time constants. This suggests that a specification on the settling time must be met by an appropriate design of the open-loop amplifier.

The two major conclusions from this analysis are as follows:

1. Feedback controls the amplitude of oscillation about the final value for a given open-loop amplifier and given values of open-loop time constants, τ_1 and τ_2.
2. The open-loop amplifier decides the settling time. It sets the time scale of Figure D.8, and the faster the open-loop amplifier, the faster the time scale.

As an aside, it may be noted that real-world departures from this linear two-pole model occur due to two major complications: First, real amplifiers have more than two poles as well as zeros, and second, real amplifiers are nonlinear, so their step response changes with signal amplitude.

D.1.9.3 Control of Overshoot

How an overshoot can be controlled by appropriate parameter choices is discussed next. Using the equations earlier (D.16 through D.28), the amount of overshoot can be found by differentiating the step response and finding its maximum value. The result for the maximum step response S_{max} is [6]

$$S_{max} = 1 + e^{-\pi\frac{\rho}{\mu}} \tag{D.29}$$

The final value of the step response is 1, so the exponential is the actual overshoot itself. It is clear that the overshoot is zero if μ = 0, which is the condition

$$\frac{4\beta A_0}{\tau_1\tau_2} = \left(\frac{1}{\tau_1} - \frac{1}{\tau_2}\right)^2 \tag{D.30}$$

This quadratic is solved for the ratio of time constants by setting $x = (\tau_1/\tau_2)^{1/2}$ leading to

$$x = \sqrt{\beta A_0} + \sqrt{1 + \beta A_0} \tag{D.31}$$

Because $\beta A_0 \gg 1$, the 1 in the square root can be dropped, and thence

$$\frac{\tau_1}{\tau_2} = 4\beta A_0 \tag{D.32}$$

In other words, the first time constant must be much larger than the second. To be more adventurous than a design allowing for no overshoot, we can introduce a factor α in the previous relation:

$$\frac{\tau_1}{\tau_2} = \alpha\beta A_0 \tag{D.33}$$

and let α be set by the amount of overshoot that is acceptable.

Figure D.9 illustrates the procedure. Comparing the top figure of Figure D.10 (α = 4) with the lower one (α = 0.5) shows lower values for α, increasing the rate of response but enhancing the overshoot. The case α = 2 (center figure) is the maximally flat design that shows no

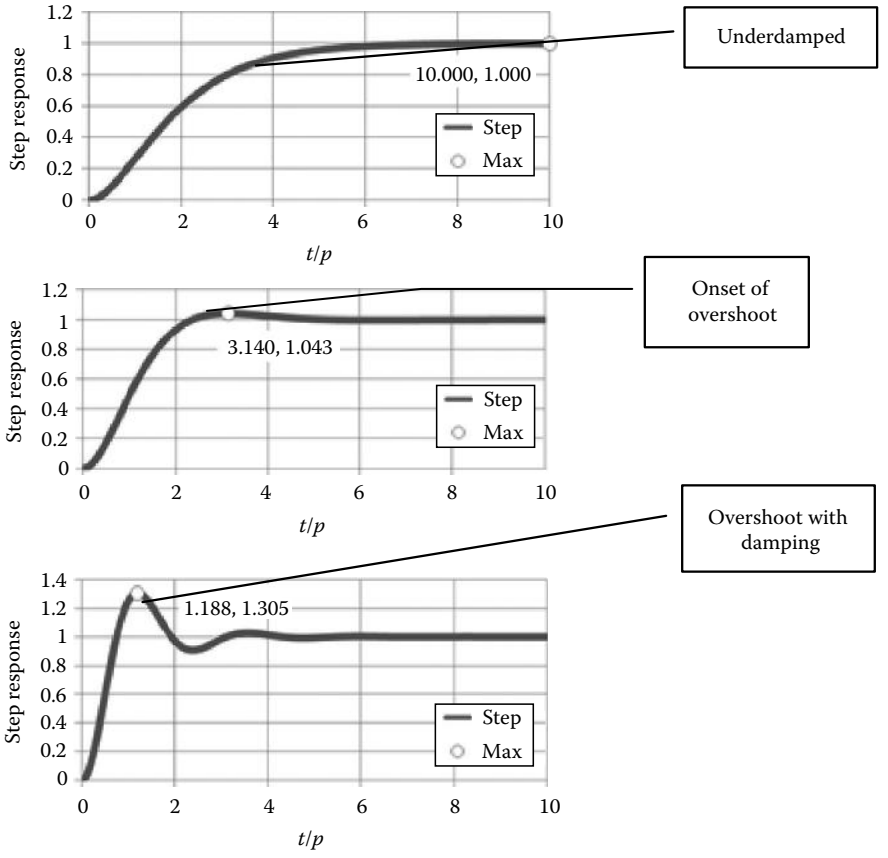

FIGURE D.10
The step response for three values of α. (Top) α = 4 underdamped; (center) α = 2 at the onset of overshooting; (bottom) α = 0.5 overshooting with damping. *Note*: As α is reduced, the pole separation reduces, and the overshoot increases.

peaking in the plot of Bode gain versus frequency. As a rule of thumb, the design has to have a built-in safety margin to deal with nonideal realities like multiple poles (or zeros), nonlinearity (signal amplitude dependence), and manufacturing variations, any of which can lead to too much overshoot. The adjustment of the pole separation (i.e., setting α) is the subject of frequency compensation, and one such method is pole splitting.

A number of circuit topologies that can exhibit different poles and zeroes are given in Appendix 1. The resistors and capacitors represent energy dissipating elements and storage elements in networks that can be electrical or optical as far as the energy storage and the dissipation of energy are concerned. For optical systems, the energy storage can be an optical ring resonator with the total gain close to unity, and thus, the optical waves can circulate around the loop without losing its energy.

With these circuit topologies, one can measure the step responses at the designated point (A or B) under the excitation of a step waveform by monitoring the output waveforms on an oscilloscope and measuring the initial points, the final points, the slope at the initial starting point, and the time constants of the transitional region. Then the network can be configured to confirm the behavior of the topology circuits.

D.1.9.4 Control of Settling Time

The amplitude of ringing in the step response in Figure D.8 is governed by the damping factor $e^{-\rho t}$. Thus, if we specify some acceptable step response deviation from the final value, say Δ, that is,

$$S(t) \leq 1 + \Delta \tag{D.34}$$

this condition is satisfied regardless of the value of βA_{OL} provided the time is longer than the settling time, say t_S given by*

$$\Delta = e^{-\rho t_S} \rightarrow t_S = \frac{\ln(1/\Delta)}{\rho} = \tau_2 \frac{2\ln(1/\Delta)}{\rho} \simeq 2\tau_2 \ln(1/\Delta) \tag{D.35}$$

where the approximation $\tau_1 \gg \tau_2$ is applicable because of the overshoot control condition, which makes $\tau_1 = \alpha\beta A_{OL}\tau_2$. Often the settling time condition is referred to by saying the settling period is inversely proportional to the unity gain BW, because $1/(2\pi\tau_2)$ is close to this BW for an amplifier with a typical dominant pole compensation. However, this result is more precise than this rule of thumb. As an example of this formula, if $\Delta = e^{-4} = 1.8\%$, the settling time condition is $t_S = 8\tau_2$.

In general, the control of overshoot sets the time constant ratio, and the settling time t_S then sets τ_2 [7,8].†

Next, the choice of the pole ratio τ_1/τ_2 is related to the phase margin of the feedback amplifier.‡ The procedure outlined in the "Bode plot" article follows. Figure D.11 is the Bode gain

---

* This estimate is a bit conservative (long) because the factor 1/sin(φ) in the overshoot contribution to $S(t)$ has been replaced by $1/\sin(\varphi) \approx 1$.

† According to Johns and Martin, *op. cit.*, settling time is significant in switched-capacitor circuits, for example, where an op amp settling time must be less than half a clock period for sufficiently rapid charge transfer.

‡ The gain margin of the amplifier cannot be found using a two-pole model, because the gain margin requires determination of the frequency f_{180} where the gain flips sign, and this never happens in a two-pole system. If we know f_{180} for the amplifier at hand, the gain margin can be found approximately, but f_{180} then depends on the third and higher pole positions, as does the gain margin, unlike the estimate of the phase margin, which is a two-pole estimate.

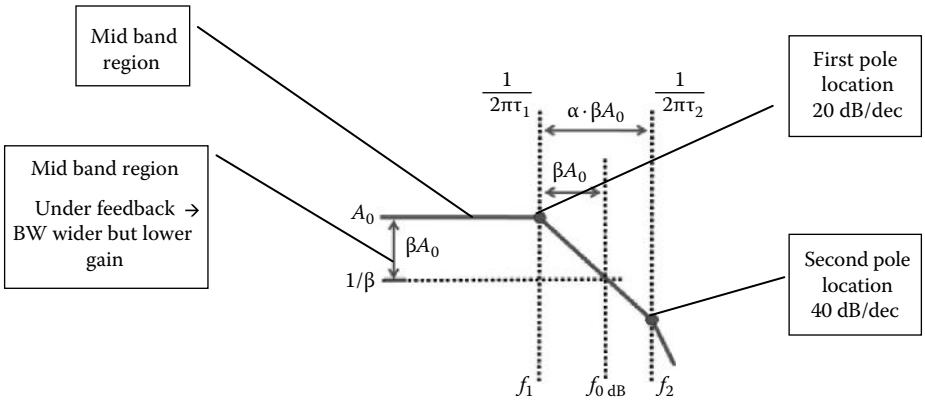

FIGURE D.11
Plot of gain versus frequency in a log–log scale. Bode gain plot to find the phase margin; scales are logarithmic, so labeled separations are multiplicative factors. For example, $f_{0\,\mathrm{dB}} = \beta A_0 \times f_1$. Note the locations of the two frequencies f_1 and f_2; their distance would determine the oscillation and damping of the time response.

plot for the two-pole amplifier in the range of frequencies up to the second pole position. The assumption behind Figure D.5 is that the frequency $f_{0\,\mathrm{dB}}$ lies between the lowest pole at $f_1 = 1/2\pi\tau_1$ and the second pole at $f_2 = 1/2\pi\tau_2$. As indicated in Figure D.11, this condition is satisfied for values of $\alpha \geq 1$. Using Figure D.11, the frequency (denoted by $f_{0\,\mathrm{dB}}$) can be found where the loop gain βA_0 satisfies the unity gain or 0 dB condition, as defined by

$$\left|\beta A_{OL}(f_{0\,\mathrm{dB}})\right| = 1 \tag{D.36}$$

The slope of the downward leg of the gain plot is 20 dB/decade*, meaning that for every factor of 10, an increasing amount in terms of frequency, the gain drops by the same factor:

$$f_{0\,\mathrm{dB}} = \beta A_{OL} f_1 \tag{D.37}$$

The phase margin is the departure of the phase at $f_{0\,\mathrm{dB}}$ from –180°. Thus, the margin is

$$\phi_m = \pi - \tan^{-1}\frac{f_{0\,\mathrm{dB}}}{f_1} - \tan^{-1}\frac{f_{0\,\mathrm{dB}}}{f_2} \tag{D.38}$$

Because $f_{0\,\mathrm{dB}}/f_1 = \beta A_0 >> 1$, the term in f_1 is 90°. That makes the phase margin:

$$\phi_m = \pi/2 - \tan^{-1}\frac{f_{0\,\mathrm{dB}}}{f_2} \rightarrow \pi/2 - \tan^{-1}\frac{\beta A_0 f_1}{\alpha\beta A_0 f_1} = \pi/2 - \tan^{-1}\alpha \tag{D.39}$$

In particular, for case $\alpha = 1$, $\phi_m = 45°$, and for $\alpha = 2$, $\phi_m = 63.4°$. Sansen [9] recommends $\alpha = 3$, $\phi_m = 71.6°$ as a starting point.

If α is increased by a shortening time τ_2, the settling time t_S also is shortened. If α is increased by a lengthening time τ_1, the settling time t_S is minimally altered. More

* 20 dB/decade means that when the frequency is changed by one decade (e.g., 100–1000 Hz), then the attenuation or gain changes by 20 dB. Thus, plotting a transfer function in a log–log paper, one can identify the number of poles or zeroes of a transfer function of a network.

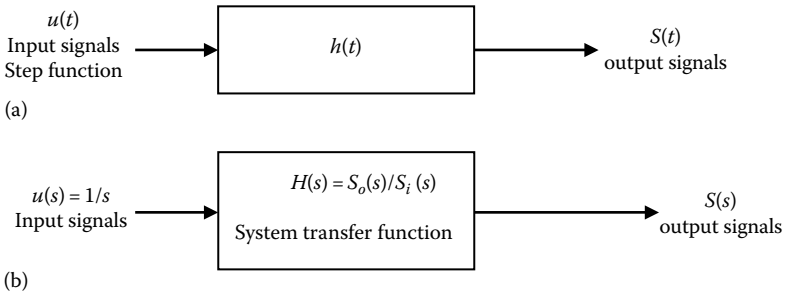

FIGURE D.12
Black box representation of a dynamical system, its input, and its step response: (a) time-domain model and (b) Laplace-domain representation.

commonly, both τ_1 and τ_2 change, for example, if the technique of pole splitting is used. As an aside, for an amplifier with more than two poles, the diagram in Figure D.5 still may be made to fit the Bode plots by making f_2 a fitting parameter, referred to as an "equivalent second pole" position [10].

D.1.9.5 Relationship between Rise Time and Bandwidth

This section provides a formal mathematical definition of step response in terms of the abstract mathematical concept of a dynamical system $H(s)$, $u(t)$, which are the step response transfer function and the step response output. All notations and assumptions are required for the following descriptions: (1) $t \in T$ is the evolution parameter of the system, called "time" for the sake of simplicity; (2) $S(t)$ is the system response output due to a step input signal $u(t)$ at time t, called "output" for the sake of simplicity; (3) $h(t)$ is the impulse response of the system with $H(s)$ ($H(s)$ is the system response in the Laplace domain); and (4) $u(t)$ is the step function (Figure D.12).

D.1.9.6 Nonlinear Dynamical System

For a general dynamical system, the step response is defined as the evolution function when the control inputs (or source term, or forcing inputs) are a step function. The notation emphasizes this concept showing $u(t)$ as a step function commonly defined in the circuit theory [11]. For a linear time-invariant black box, the step response can be obtained by a convolution of the step function and the impulse response $h(t)$ of the system itself:

$$a(t) = h(t) * u(t) = \int_{-\infty}^{+\infty} h(\tau)u(t-\tau)\,d\tau = \int_{-\infty}^{t} h(\tau)\,d\tau \tag{D.40}$$

D.2 Relationship between the Bandwidth and the Rise Time

Problem
If one wishes to digitize a square signal with a specific rise time he/she must be sure what the recommended BW would be and what devices could achieve it

Solution

To satisfy the Nyquist theorem, we need to sample at least twice as fast as the maximum BW of the signal (or about 10 times) to have a proper shape. This statement has been seen in other documents (see related links for more information), but square signals have sharp edges and therefore, the total BW of the signal is not straightforward to calculate. The following is a general equation relating BW and rise time as given in (D.8). For example, if we need to measure a square signal with 100 ns rise time, our BW will be about 3.5 MHz (0.35/100e−9). Therefore, we should choose a digitizer that can sample at least twice as fast or, for shape purposes, 10 times faster: ~35 MS/s (samples per second). For example, the NI 5112 or NI 5122 is a good choice because they have a sampling rate of 100 MS/s. Additionally, be sure that the anti-alias and noise filters on our digitizer are not enabled, as these can reduce the measurable BW.

D.3 How Is Bandwidth Related to Rise Time in an Oscilloscope System?

Historically, the oscilloscope frequency response tended to approximately follow the rule: the product (BW × rise time) is ~ 0.35. This corresponds to a 1- or 2-pole filter roll-off in the frequency domain. Today, at the high end, most real-time digital oscilloscopes more closely follow this rule:

$$BW \text{ (rise time)} = 0.45 \tag{D.41}$$

This corresponds to a much steeper frequency roll-off above the specified BW. The steeper the roll-off, the better is the frequency response of digital oscilloscopes that oversample by four or three times or even less because it prevents aliasing by eliminating any signal above the Nyquist frequency, which equates to 1/2 the sample rate—the minimum sample rate required for accurate signal representation.

D.4 Scope Bandwidth, Rise Time, and the "Rule of 5"

One might easily think that a 500 MHz oscilloscope would be good for measuring sine waves up to 500 MHz. However, this is not the case. There are at least two approaches one can take to make sure that they get the right scope BW for the application.

First, if one has a maximum sinusoidal frequency in mind, one can work with the BW specification of the scope. However, one would need to account for the roll-off of the scope. Figure D.13 shows a roll-off curve for a 1 GHz oscilloscope. We can notice that at one-fifth of the BW, or 200 MHz, the response of the scope is within 2% of the flat gain curve. So, a 1 GHz BW scope is recommended for sine frequencies up to 200 MHz for accurate measurement of the amplitude. This generic roll-off characteristic is at the root of the "rule of 5" for selecting the scope BW. Choose a scope with five times the BW of the highest-frequency component of the signal to be measured. One can then be confident that the scope will accurately represent the amplitude of the measured signal (Figure D.13).

Second, if we are looking at nonsinusoidal signals, such as digital pulses, the highest frequency in our signals will be a multiple of the highest repetition rate. We will need to use

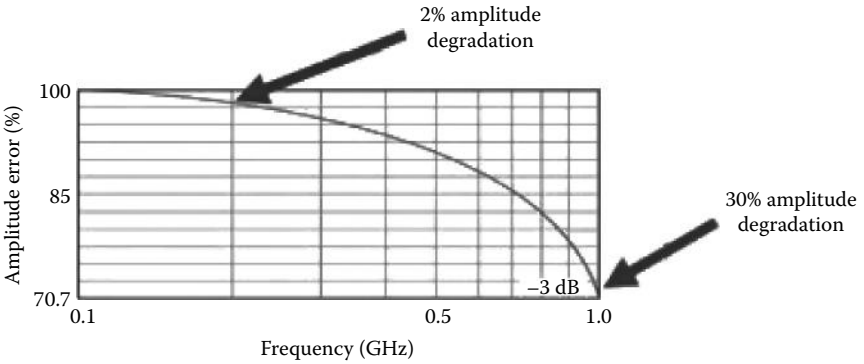

FIGURE D.13
Frequency response of a typical oscilloscope.

a scope BW much more than five times the repetition rate to account for harmonics. If we are working on digital systems, it is often easier to consider the rise-time specifications for scopes. The rise-time spec, like BW, characterizes the frequency response of the scope's front end, but the rise time may be easier to apply. Applying the rise-time spec properly also involves a rule of 5 to account for roll-off. In this case, the scope rise time should be no more than one-fifth the rise time of the pulses of interest. If we want to see the rise times of 10 ps, for example, we should choose a scope with a rise time of 2 ps or less. Using the rule of 5 will help specify a scope that will accurately show the desired signal's amplitude. However, when the BW of our signals is very wide, such as 28 GHz, then there would be no oscilloscope that can offer a BW of 5 × 28 GHz, so some calculation must be implemented to eliminate the effects of the oscilloscope rise time.

D.5 Rise Time versus Bandwidth and Applications

A simple, practical mathematical model allows one to relate the signal rise time to the available BW of a measurement instrument. In measurement instruments such as oscilloscopes and spectrum analyzers, the maximum rise time, t_r, that can be measured with reasonable amplitude accuracy is directly related to the instrument's −3 dB BW (B). The rise time is commonly specified as the transition time for a signal to go from the 10% to the 90% level of the steady maximum value (see Figure D.14). However, the BW describes the range of frequencies over which the majority of the energy of a signal is contained. Specifically, it is defined as the frequency range over which the frequency response of a signal degrades by 3 dB, assuming a single-pole high-pass frequency response as shown in Figure D.15.

In an engineering environment, it is common to hear people using both terminologies (rise time and BW) interchangeably, depending upon which instrument they are using. The relationships usually included in most oscilloscope catalogs and technical discussion handbooks are based on the following equation (see Section D.1):

$$t_r = \frac{0.35}{BW} \tag{D.42}$$

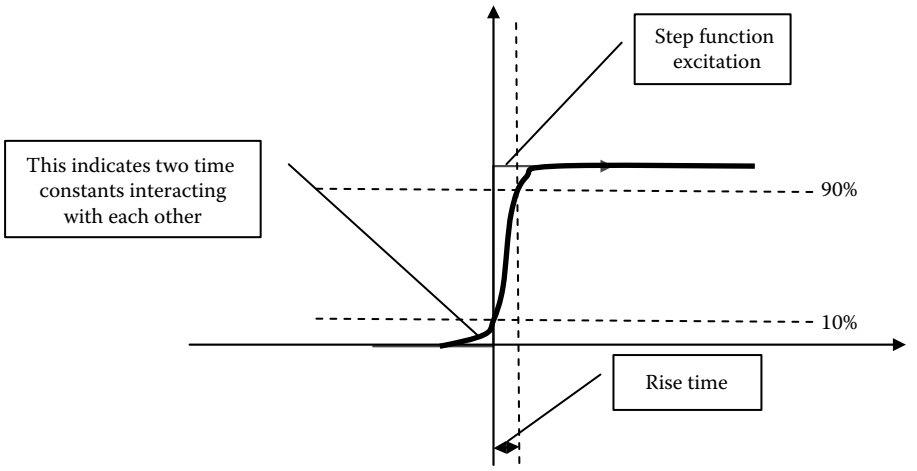

FIGURE D.14
Time-domain response of an impulse input. Note the two-slope rise times, one slow and one fast with their large ratio so that they do not interfere with one another.

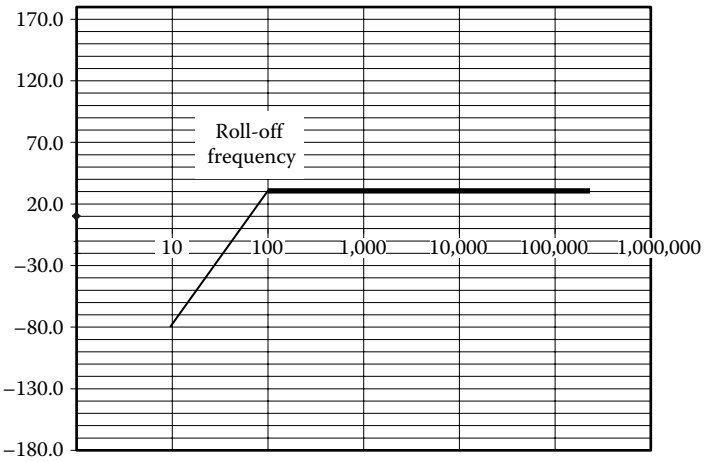

FIGURE D.15
Frequency-domain response of a dominant pole circuit with scanned frequency sinusoidal input. An 80 dB roll-off per decade indicating four identical poles at the same location. Vertical axis is linear ìn unit of dB, and horizontal axis is the frequency in the log scale.

where BW is the 3 dB BW. The most frequently asked question is: Exactly what is the relationship between the time-domain (rise time) and frequency-domain (BW) components of the equation? Or what is the basis of the constant "0.35" for that matter? Or precisely how is this expression derived?

D.5.1 How Does the Relationship Arise?

The best approach to understanding the origin of Equation D.42 is to consider an electrical passive filter. This approach provides an exact value. Other methods of analysis

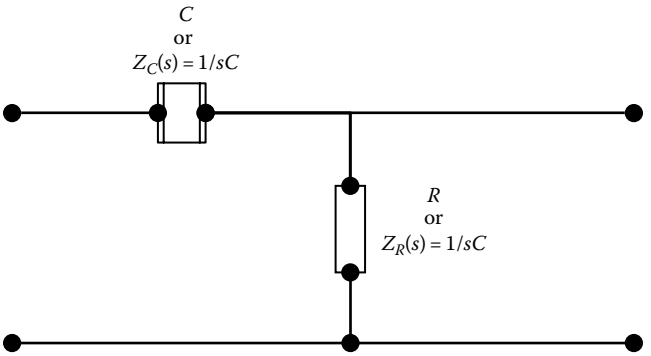

FIGURE D.16
A simple *R-C* circuit schematic representing the time domain and Laplace frequency domain. In the frequency domain, the resistors and capacitors are represented by their corresponding impedances, $Z_R(s)$,$Z_C(s)$, respectively, which are in the Laplace plane. See also circuit topologies given in Appendix 1 for more than one energy storage elements.

could be used instead such as the Gaussian distribution or Fourier expansion, but they give rise to errors of 2.9% and 8.6%, respectively.

To examine this relationship, we make use of a simple first-order system of a low pass, high pass, or band pass. Its topology need not be of any particular structure. It can be in parallel or in series, and its network configuration can also be in any form, such as *R-C*, *R-L*, and *R-L-C*. For the purpose of demonstrating why the t_r in Equation D.1 is accurate, think of a simple *R-C* schematic as shown in Figure D.3, in both the time and frequency domains.

D.5.2 Circuit Analysis

Using the fundamentals of linear circuit analysis and the concepts of Kirchhoff theorems, mesh and nodal procedures will be used to investigate the time-domain and frequency-domain behavior of a capacitor and a resistor connected as shown in Figure D.16. This circuit can be approximated for a network with dominant C and R.

D.5.3 Time-Domain Analysis

We can approach this analysis by writing the respective output equations of the previous circuit topology. Applying the Kirchhoff voltage law to the mesh, we can obtain a differential equation of the first order. This is the natural response of a circuit containing only one storage element. However, the common rule is that for a network having *N* storage element, there would be *N* time constants correspondent to *N* poles whose frequencies are determined by shorting all voltage sources and opening the circuits in all capacitors and short-circuiting all inductors and then finding the total equivalent input resistance between the two points under consideration. So for an energy storage element, there will be one natural response. If there are *N* energy storage elements, then we will have an *N*th-order differential system of equations and hence *N* natural frequency responses. Depending on the distance between these frequencies, the roll-off and hence the corresponding rise time of the step response would be influenced. If two frequencies are close to each other, for example, the distance is less than one decade, then there would be interactions between these frequency locations and hence interaction in the time-domain transitional region.

Working through the first-order differential equation, we can arrive at

$$v_R(t) = v_i(t)\left[1 - e^{\frac{t}{RC}}\right] \tag{D.43}$$

Now assuming an input voltage of a unit step function, one can easily determine the speed of response by solving for *t*. Thence solving for t and replacing $RC = \tau$, we get

$$\frac{v_R(t)}{v_i(t)} = 1 - e^{-t/\tau} \longrightarrow t = -\tau \ln\left(1 - \frac{v_R(t)}{v_i(t)}\right) \tag{D.44}$$

With this equation, we can now calculate the transitory points of time of the response curve. Widely used measurement points are 10%–90% levels of the swing:

$$\begin{aligned} t_{10\%} &= -\tau \ln(0.9) \\ t_{90\%} &= -\tau \ln(0.1) \end{aligned} \tag{D.45}$$

Having established that the rise time is dependent on τ, an analysis in the frequency-domain point of view can also be carried out to confirm these time constants.

D.5.4 Frequency-Domain Analysis

Using a voltage divider approach, we then consider the "half-power" frequency, usually termed as the (–3 dB) BW. As the terminology would imply, half of the power in the input signal is absorbed by the reactive element of the filter, and the other half is transferred to the output. The 3 dB frequency can be found to be

$$\omega_{3\,\mathrm{dB}} = \frac{1}{RC} \tag{D.46}$$

Note that the imaginary (j) can be removed by taking the absolute value because the phase has no relevance in this analysis. Where *f* is the –3 dB cutoff frequency or the BW or *B* (Hz) and *RC* is the time constant (τ), leading to

$$\tau = \frac{1}{\omega} = \frac{1}{2\pi BW} \tag{D.47}$$

Going back to our last time-domain equation (D.10) and substituting τ with (D.17), we obtain the most sought-after equation on the rise time and the BW as

$$t_r = \frac{1}{2\pi BW} = \frac{0.35}{BW} \tag{D.48}$$

Alternatively, the earlier analysis could easily be achieved through an intuitive investigation. Use the half-power BW or cutoff frequency (–3 dB) as mentioned previously where

the output power is 50% of the input power at the operating frequency with $Z_C = Z_R$ of an electrical filter. Since $Z_C = 1/2\pi fC$, we can then say that at $f_{-3\ dB}$, $Z_C = Z_R$, so $R = 1/2\pi f_{-3\ dB}C$. This result leads us straight to $2\pi f_{-3\ dB} = 1/RC = 1/\tau$.

Example

A signal to be analyzed has a rise time of 10 ns. What should the minimum BW of an oscilloscope or the minimum resolution bandwidth (RBW) of a spectrum analyzer be?

Substituting the numbers into (D.48) results in

$$t_r = \frac{1}{2\pi BW} = \frac{0.35}{BW} \longrightarrow BW = 0.35 \times 1/10 \text{ ns} \tag{D.49}$$

What this result implies is that if the BW of an oscilloscope, or the RBW of a spectrum analyzer, is 35 MHz, then the fastest signal rise time that the instrument can display on its screen—without the displayed amplitude being significantly attenuated—would have a rise time no shorter than 10 ns. Similarly, if one wished to measure the amplitude of a 1 ns rise-time signal with reasonable accuracy, the oscilloscope or spectrum analyzer would require a –3 dB BW (or RBW) of at least 350 MHz [12,13].

D.5.5 Remarks

A systematic approach has been proposed for understanding the basics of the equation that relates the signal rise time to the –3 dB BW of a system by using both a time-domain and a frequency-domain analysis of a simple lumped-element filter circuit. This simple but practical mathematical model allows one to relate the signal rise time to the available BW of a measurement instrument. Because of the reciprocal nature of the two variables, the wider the BW of the measuring instrument, the faster is its response time. A further implication of this result is that for the measurement system to display a reasonably accurate representation of an impulse input signal, indicating that its –3 dB BW (B) must be set to a minimum of (D.49).

D.6 Relating Wideband DSO Rise Time to Bandwidth: Lose the 0.35 Factor! [14]

Traditionally, oscilloscopes have exhibited a Gaussian frequency response. A Gaussian response results from the combination of many circuit elements of the scope design that have similar frequency responses. Analog oscilloscopes achieve their frequency response in this manner, thanks to chains of amplifiers from the input to the display. (Analog oscilloscopes used the input signal to directly deflect the electron beam in a CRT. This architecture required amplifying the input signal by three orders of magnitude and driving the large capacitive load that the CRT deflection plates presented.) The properties of Gaussian-response oscilloscopes are fairly well taught and well understood throughout the industry.

The flat responses become nowadays a very common feature in modern, high-BW DSOs. A DSO has a shorter chain of analog amplifiers to contribute to a Gaussian response and can use DSP techniques to optimize the accuracy of its response. More importantly, a DSO is subject to sampling-alias errors, which have no counterpart in analog scopes.

Sampling-alias errors occur when a signal contains frequencies greater than half the sample rate. Half the sample rate is called the Nyquist frequency. Compared with a Gaussian response, a flat response reduces these errors, thus satisfying an important requirement in the design and operation of digital oscilloscopes.

D.6.1 Gaussian-Response Oscilloscopes

Figure D.17 shows a typical Gaussian frequency response for a 1 GHz oscilloscope. A Gaussian response offers good pulse response without overshoot, regardless of the input signal's speed. Figure D.18 shows the response to a fast step input of a 1 GHz Gaussian-response oscilloscope.

In a Gaussian-response oscilloscope, the oscilloscope's rise time is related to the oscilloscope's BW by the familiar and commonly used formula:

$$t_r = \frac{0.35}{BW} \tag{D.50}$$

BW is defined as the frequency at which the response is down 3 dB relative to dc. The theoretical relationship for a Gaussian system is rise time = 0.339/BW, but the industry has settled on 0.35/BW as a practical formula.

Another commonly used property of Gaussian systems is the overall system BW, which is the RMS. value of the individual BWs. We can calculate it using the familiar relationship, system BW:

$$\text{Observed system BW} = \frac{1}{\sqrt{\left(\frac{1}{BW_{probe}^2} + \frac{1}{BW_{OSC}^2}\right)}} \tag{D.51}$$

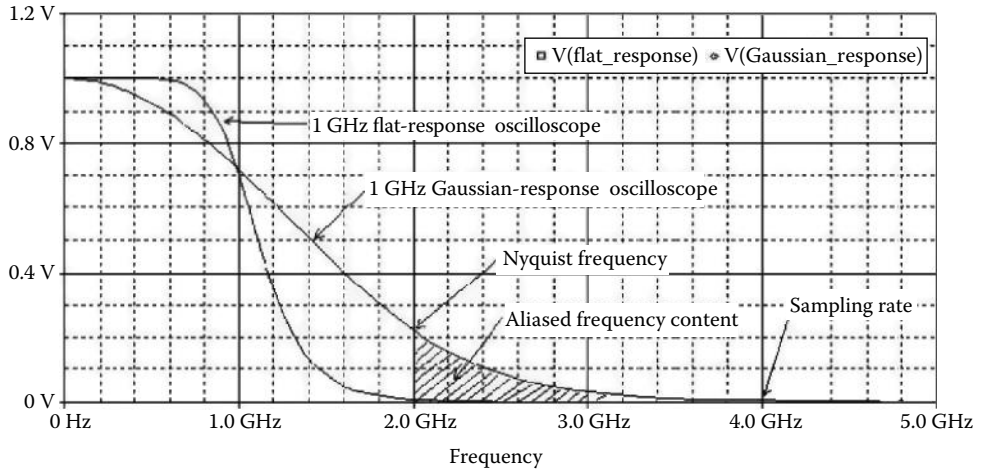

Although these Gaussian- and flat-response scopes have equal 1 GHz –3 dB, points, the flat-response unit attenuates high-frequency components just below the –3 dB point much less and components just above the –3 dB point much more

FIGURE D.17
Frequency response: amplitude measured in the frequency domain.

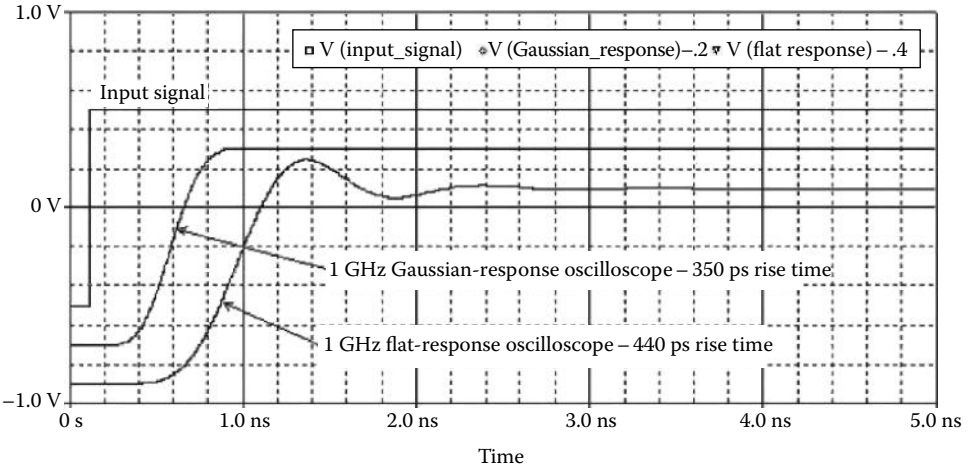

Unlike a Gaussian-response scope, a 1 GHz bandwidth flat-response scope responds to a step input by displaying some ripple

FIGURE D.18
Step response of a system as observed at the output of an oscilloscope.

The term "system bandwidth" refers to the BW that one measures as observed in the oscilloscope. That is, the signal is affected by a combination of an oscilloscope probe and oscilloscope.

Oscilloscope probes are often designed to have sufficiently higher BW than the oscilloscope BW, so the previous formula is unnecessary for derating the system BW.

Inversely, the measured rise time is commonly related to the system and signal rise time:

$$\text{Measured rise time} = \sqrt{Rt_{sig}^2 + Rt_{sys}^2} \tag{D.52}$$

One can use this relationship to estimate the actual signal rise time when the oscilloscope's system rise time is not sufficiently faster than the signal's rise time.

It is noted here that when a coaxial cable of high-frequency characteristics is used to connect a probe point to the DSO, then the contribution of the cable capacitance and resistance must be taken into account. The capacitance per unit length is 80–90 pF/m and an equivalent of 50 Ω. Then if a meter of this cable is used, a low-frequency pole would be located at around 1 GHz, which will contribute to a long time constant in the eye diagram observed and captured by the DSO. A penalty of around 0.5 dB would be expected.

D.6.2 Flat-Response Oscilloscopes

Figure D.17 depicts a flat response with a Gaussian response in the time domain. Note that the flat response is much flatter below the –3 dB BW but then rapidly drops off above the –3 dB BW. Commonly, one can refer to this response shape as a maximally flat, or brick-wall, response or a raised cosine. A flat response presents a number of advantages. First, the frequency contents of the signal below –3 dB BW are less attenuated; thus, we can measure more accurately. Second, the steeper roll-off helps reduce the sampling-alias errors.

In the time domain, applying a fast step input to a system that exhibits a flat frequency response produces a pulse response with overshoot and ringing (Figure D.18). Oscilloscope

users often perceive overshoot and ringing as undesirable effects. However, ringing occurs only if the signal rise time is significantly faster than the fastest rise time that the oscilloscope can accurately measure. In such cases, we need a higher BW oscilloscope.

Unlike Gaussian systems, the RMS value of the subsystem parts does not determine the system BW of a flat-response oscilloscope. The commonly used BW and rise-time formulas for Gaussian-response oscilloscope systems do "not" apply to flat-response oscilloscope systems. Instead, we should rely on the oscilloscope vendor to specify the BW of an oscilloscope/probe combination.

In the case of a flat-response oscilloscope, the rise time is related to the BW as rise time = N/BW, where N = 0.4–0.5. The larger the value of N the steeper the "brick wall" frequency response becomes. Oscilloscope specifications sometimes include this relationship, which can indicate the type of response the oscilloscope exhibits.

D.6.3 Measurement Accuracy

To determine which type of frequency response offers the best measurement accuracy, we need to consider the maximum signal frequency and the oscilloscope's sampling-alias errors. The example in Figure D.17 shows that a flat response offers less signal attenuation below the –3 dB BW (1 GHz in the example) than does a Gaussian response. It stands to reason, then, that for signals with frequencies primarily below the –3 dB BW, a flat-response oscilloscope offers better measurement accuracy than a Gaussian-response oscilloscope. This statement implies that the phase response in the passband must be linear. For example, by comparing the measurement of the rise time of a digital signal with a 700 ps rise time using scopes that have both types of response, one can determine the signal's maximum frequency component from the rise time as follows: maximum signal frequency = 0.5/rise time.

The maximum signal frequency is defined so that any system (including an oscilloscope) that can accurately measure the components at frequencies up to and including the maximum signal frequency accurately reproduces the signal [15].

Using this relationship, a signal with a 700 ps rise time primarily contains frequencies of less than 714 MHz. From Figure D.17, we can see that at less than 714 MHz, a flat-response scope attenuates less than does a unit with a Gaussian response. Indeed, a flat-response oscilloscope measures the rise time of this 700 ps edge more accurately than does a Gaussian-response oscilloscope shown in Figure D.19. The flat-response oscilloscope measures the rise time with 3% error, whereas a Gaussian-response oscilloscope exhibits a 9% error.

As the signal rise time decreases (faster edges), a Gaussian-response system eventually surpasses a flat-response system's rise-time measurement accuracy. This situation occurs because as the rise time decreases, the frequency content of the signal increases above the –3 dB BW. In this region, the flat-response oscilloscope has less sensitivity in amplitude response than does the Gaussian-response oscilloscope.

Figure D.19 illustrates the 1 GHz BW oscilloscope's rise-time measurement error for various signal rise times. Note that the rise-time measurement error is already 15% at the point at which the Gaussian-oscilloscope measurement becomes more accurate than the flat-response oscilloscope. Thus, for less than 15% error measurements of signal rise times, a flat-response oscilloscope is superior to a Gaussian-response oscilloscope of equal BW. This result is counterintuitive, given that, with an ideal (fast) step input, a Gaussian-response oscilloscope has a faster rise time than does a flat-response oscilloscope. Remember, though, that a scope's rise-time specification does not by itself

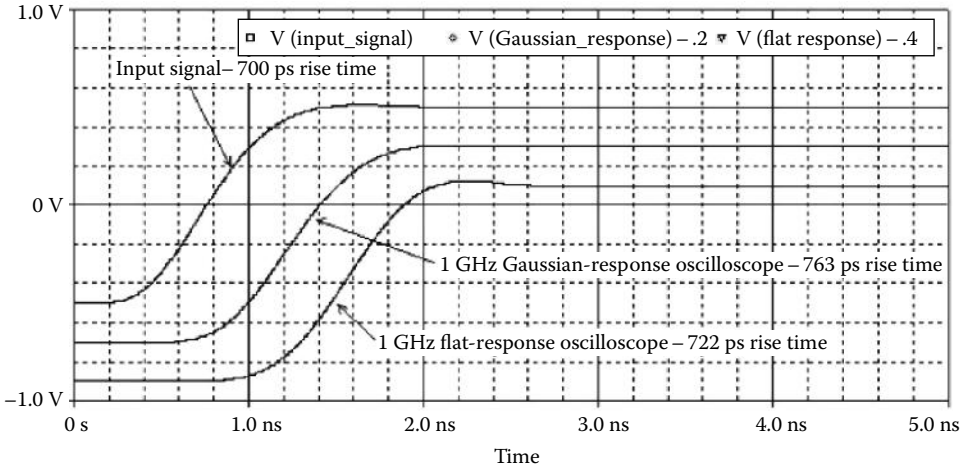

A flat-response oscilloscope measures the rise time of this 700 psec edge more accurately than does a Gaussian-response oscilloscope

FIGURE D.19
Typical step response of a Gaussian-response oscilloscope.

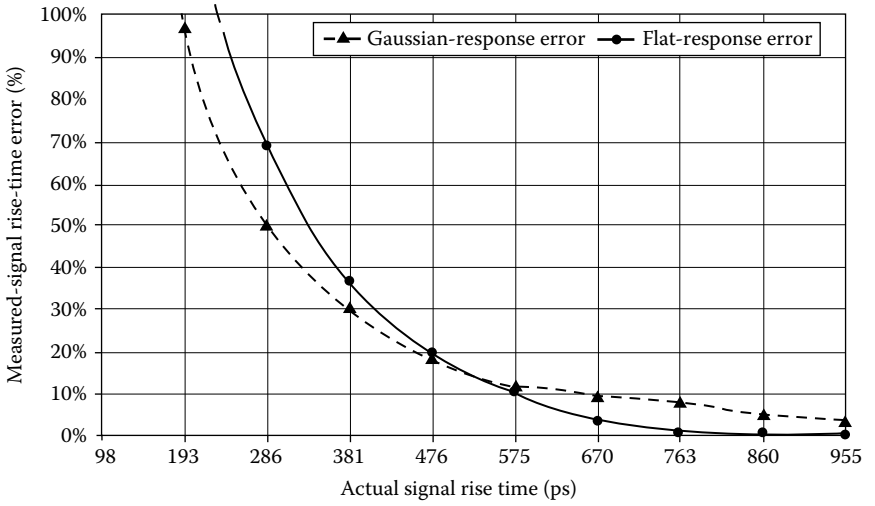

FIGURE D.20
Measurement error of the rise time as a function of Gaussian- and flat-response oscilloscope.

indicate how accurately the scope can measure the rise times; we must also consider the character of the scope's response (Figure D.20).

D.6.4 Sampling-Alias Errors

Digital oscilloscopes use repetitive and real-time sampling methods. A repetitive-sampling oscilloscope samples the signal over many repetitions of the signal and is not subject to sampling-alias errors. A real-time oscilloscope samples and captures the signal in one pass, or occurrence. This discussion applies to the more common real-time sampling oscilloscopes, which offer many benefits over repetitive-sampling oscilloscopes.

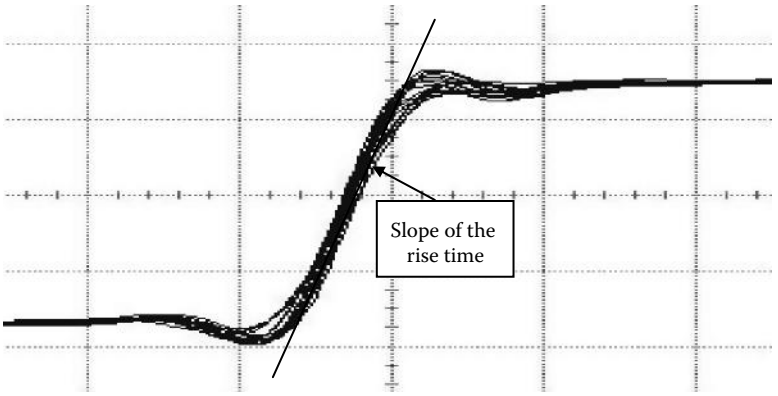

By creating components that are absent from the original data, sampling-alias errors cause wobble to appear in the displayed waveform, even though no such wobble is present in the real signal.

FIGURE D.21
Time-domain responses indicating sampling-alias errors with additional frequency components nonexistent in the original signal.

For a digital real-time oscilloscope to accurately measure a signal, the signal must not have significant frequency content above the Nyquist frequency, which is half the sampling frequency. Frequency content above the Nyquist frequency folds back into the frequency-domain region below the Nyquist frequency. In the time domain, this error manifests itself as a pulse response with "wobbling" edges (see Figure D.21). These wobbling edges result in inconsistent rise times and time-delay measurements.

For the example in Figure D.17, the sample rate is 4 GHz, so the Nyquist frequency is 2 GHz. A Gaussian-response oscilloscope allows the sampling of significant frequency content beyond 2 GHz and produces sampling-alias errors for signals with significant frequency content above 2 GHz. A flat-response oscilloscope, however, significantly attenuates all frequency content above 2 GHz, essentially eliminating alias errors.

To avoid alias errors, the oscilloscope must have a sufficient sample rate. A Gaussian-response oscilloscope may need a sample rate as much as six times the oscilloscope's BW, though four times is more typical. On the other hand, a flat-response oscilloscope with a sharp filter may need to sample only 2.5 times the oscilloscope's BW to avoid alias errors.

D.6.5 How Wide Is the Required Bandwidth?

Table D.1 lists the steps to estimate the necessary oscilloscope BW to make accurate measurements. We first determine the maximum signal frequency, F_{max}, based on the signal's rise time. (Depending on the application, additional BW may be necessary to reproduce noise or jitter beyond the maximum signal frequency.) Next, we determine whether the scope has a Gaussian or a flat response. Then, based on the accuracy we need, we then multiply F_{max} by the appropriate multiplier to determine the required oscilloscope BW. Finally, ensure that the oscilloscope has a sufficient sample rate to achieve the required BW without introducing alias errors.

TABLE D.1

Oscilloscope Bandwidth and Accuracy

	0.5/singal rise time (10 to 90%) or	
Determine maximum signal frequency (F_{MAX})	0.4/signal rise time (20 to 80%)	
Determine oscilloscope-response type	Gaussian response	Flat response
Rise-time/bandwidth relationship	0.35/bandwidth	(0.4 to 0.5)/bandwidth
Rise-time measurement error	Oscilloscope bandwidth	
20%	1 F_{MAX}	1 F_{MAX}
10%	1.3 F_{MAX}	1.2 F_{MAX}
3%	1.9 F_{MAX}	1.4 F_{MAX}
Minimum sample rate[a]	4 × bandwidth	2.5 × bandwidth

[a] Typical values; values vary with oscilloscope model; refer to the oscilloscope's specifications.

For example, measuring a 100 ps rise time (20%–80%) signal with a flat-response oscilloscope to an accuracy of 10% requires a (0.4/100 ps)·1.2 = 4.8 GHz BW and a minimum sample rate of 4.8 GHz·2.5 = 12 Gsamples/s.

This procedure is only a tool to estimate the necessary BW. It is prudent to verify actual rise-time accuracy with measurements, because frequency response varies among oscilloscope models.

The signal rise time, not its repetition rate, can primarily determine the necessary oscilloscope BW. For accurate measurements, pick an oscilloscope that has the flattest possible frequency response up to the maximum signal frequency, determined by 0.5/rise time (10%–90%). In the case of a modern flat-response oscilloscope, an oscilloscope BW that is 1.4 times the maximum signal frequency usually suffices for accurate rise-time measurements.

D.7 Concluding Remarks

In summary, a link design that would offer the most likely chance of working in practice without resorting to complex simulation would require the following:

- A detailed consideration for the rise time and dispersion budget. This can be done without using any simple calculator using the technique given in Section D.2.
- Thence a power budget analysis can be carried out to determine whether the power supplied by the lightwave sources and the sensitivity of the receiver can meet the demands for launched power and reception without any error. These parameters must be extracted from the technical specifications of the components of the systems.
- All these steps can be calculated in one's head without using calculators.

Besides these points and off-the-head calculations, one can use the presented principles in this document to observe the monitored eye diagram on a DSO and decide whether the waveform or eyes would be reasonable as expected. For example, if the eye diagram gives a rise

time shorter than expected, then it is highly possible that the signals are clipped due to overshooting of the signals over the allowable voltage level. In addition, the noise voltage level, as observed on the oscilloscope, can be used to confirm the correctness of the test setup.

D.8 Appendix 1: Circuit Topologies of Different Corner Frequencies and Their Relationship with Rise and Fall Time

This appendix gives a number of electrical circuit topologies that consist of capacitors and resistors. No inductors are used so that the frequency responses of the circuit would consist only of real poles and zeroes, hence no complex pole pairs.

In optical circuit equivalence, a resistor would represent a loss optical path and a capacity would represent an optical energy storage element such as a ring resonator. For the sake of simplicity, the topologies of capacitors and resistors are given here. The number of corner frequencies is the number of energy storage element. Thus, a circuit with N capacitors would have N poles or N frequencies at which the amplitude would go to affect the amplitude of the system response, hence the corner frequencies. Explanations for the dynamic behavior of the circuit given by Topology I are given as an example. The readers will find out the dynamic responses of the other topologies, without much difficulty. An input resistor can also be considered as the equivalent impedance looking into the output port of an oscilloscope operating at high frequency, 50 Ω indeed.

D.8.1 Topology

In these topological circuits, there are two capacitors or energy storage elements, one energy supplier, and two resistive elements. Thus, there are two "poles" or "corner frequencies" that are located at

$$\begin{aligned} \omega_1 &= R_1 C_1 \\ C_1 &= 0.022\ \text{nF} \\ R_1 &= 22\ \text{k}//5.6\ \text{k} \end{aligned} \tag{D.53}$$

Due to 0.022 nF (the left side of the circuit), this capacitor is about the same as the other capacitor. When this is charging, the other would also charge, depending on what loads these capacitors are seen, and their charging time would be different and hence the corner frequencies. When considering the load for the capacity, we short-circuit the voltage source. The other capacitor of the same value as this cap is also charging and hence can be shorted. Thus, the resistive load of this cap is parallel to 22 k and 5.6 k resistors.

Similarly, due to other 0.022 nF capacitor, the frequency and loads are

$$\begin{aligned} \omega_2 &= R_2 C_2 \\ C_2 &= 0.022\ \text{nF} \\ R_2 &= 5.6\ \text{k} \end{aligned} \tag{D.54}$$

The resistive load is due to 5.6k only as the other resistor is shorted by the other cap and the voltage source. Hence by inspecting (D.53) and (D.54), we could see that the corner frequency due to capacitor C_1 is slightly smaller than that due to the other cap. These poles are not far apart and hence they interact so that we can see that the time constant or the rise time of the transient response would be overlapping in this circuit. The initial value is dependent on at which point A or B we tap the signals. For example, at A, initial voltage $v_A(0)= 0$ if capacitor C_1 is uncharged. At time $t = 0^-$, capacitor C_1 looks like an open circuit, and when $t = 0^+$, the capacitor starts charging and this capacitor looks like shorted, thence the voltage $v_A(0^+) = V_1$, where V_1 is the high-voltage level of the rectangular sequence applied to the input port. Thus, we can observe a "step" jumping from the value 0 V to V_{DC} at the start of an applied step voltage to the circuit. The final value at point A of Figure D.22a would be 0 V as the capacitors are fully charged and look like an open circuit, with no connection to the supply source.

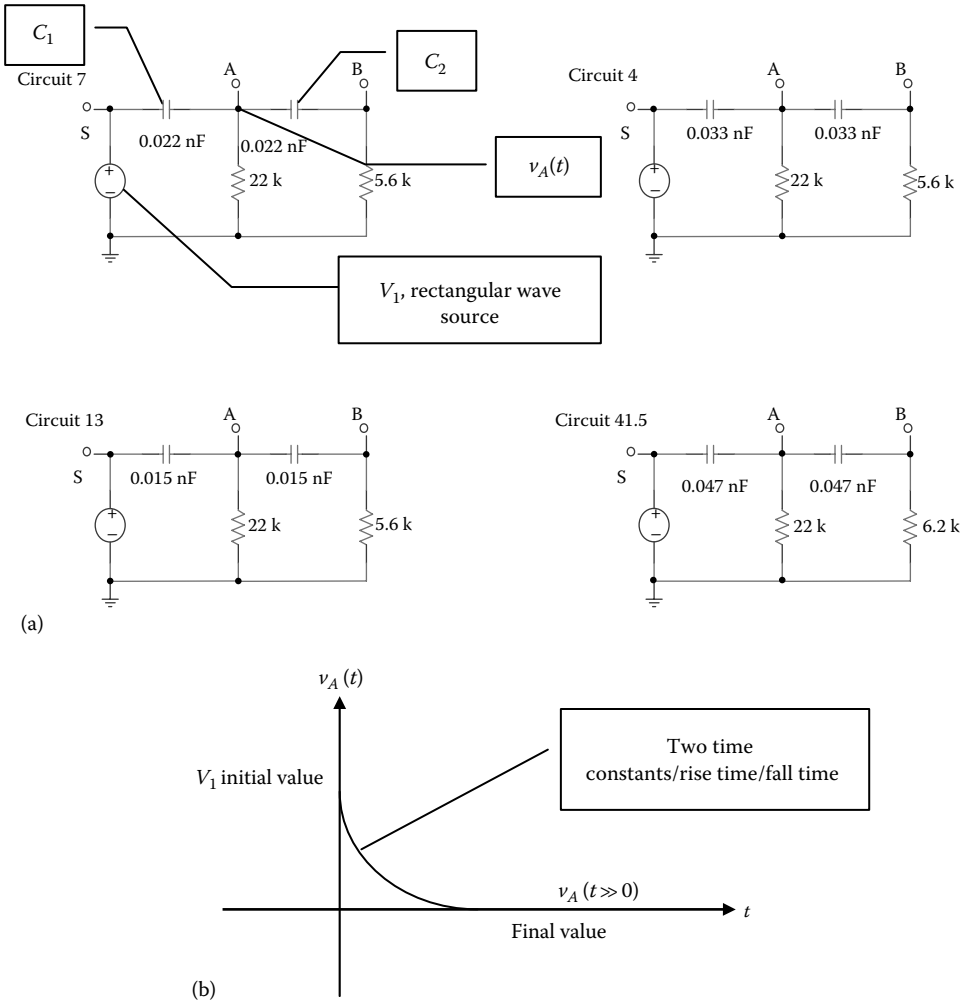

FIGURE D.22
Topology I: (a) circuit diagrams and (b) typical response in the time domain.

Note that in all topologies, the source can generate a rectangular sequence whose rise time is much shorter than that of the responses of the circuit so the square wave or rectangular wave can be considered ideal.

D.8.2 Topology II

This topology also consists of two capacitors and resistors and a voltage supply source. Cap C_1 is about 10 times larger than C_2. The loads for these two capacitors are 22k/5.6k and 5.6k/5.6k, respectively. So, the corner frequencies due to these caps are more than 10 times apart (or wider than one decade in terms of frequency). Thus, they are isolated from one another. Hence, there are two distinct time constants (hence the rise time) in the transient responses from one state to another (Figure D.23).

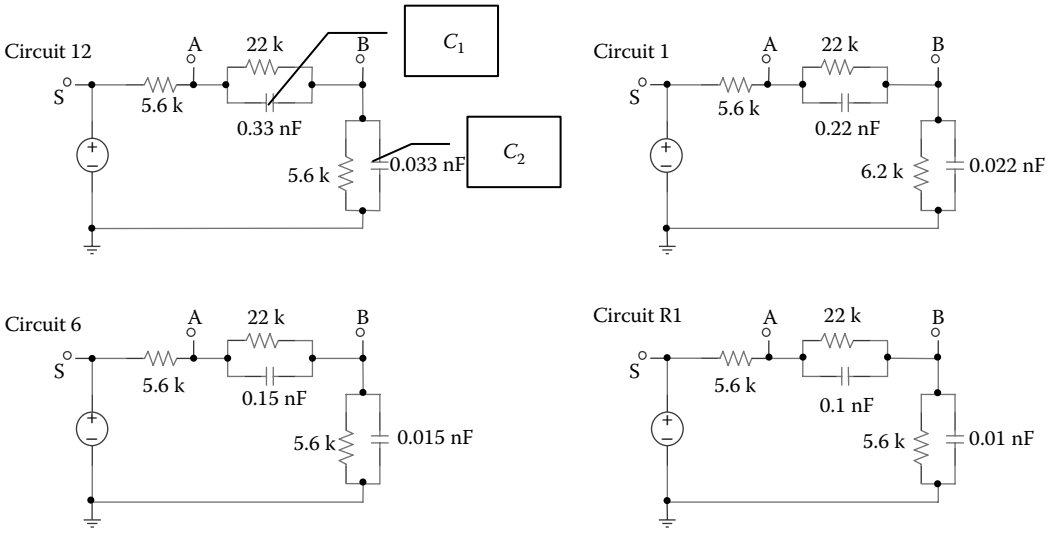

FIGURE D.23
Topology II with two capacitors that are loaded with a resistor in parallel so that the initial value would be finite. The ratio of the values of these capacitors is at least 10 times so that their time constant or corner frequencies can be isolated from one another.

D.8.3 Topology III (Figure D.24)

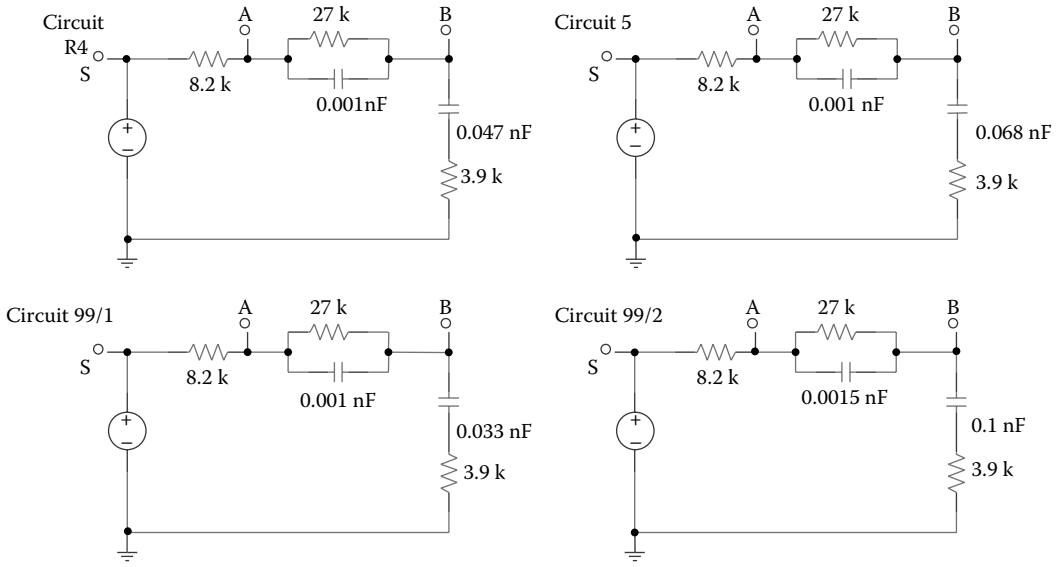

FIGURE D.24
Topology III with two capacitors and different loaded resistors.

D.8.4 Topology IV (Figure D.25)

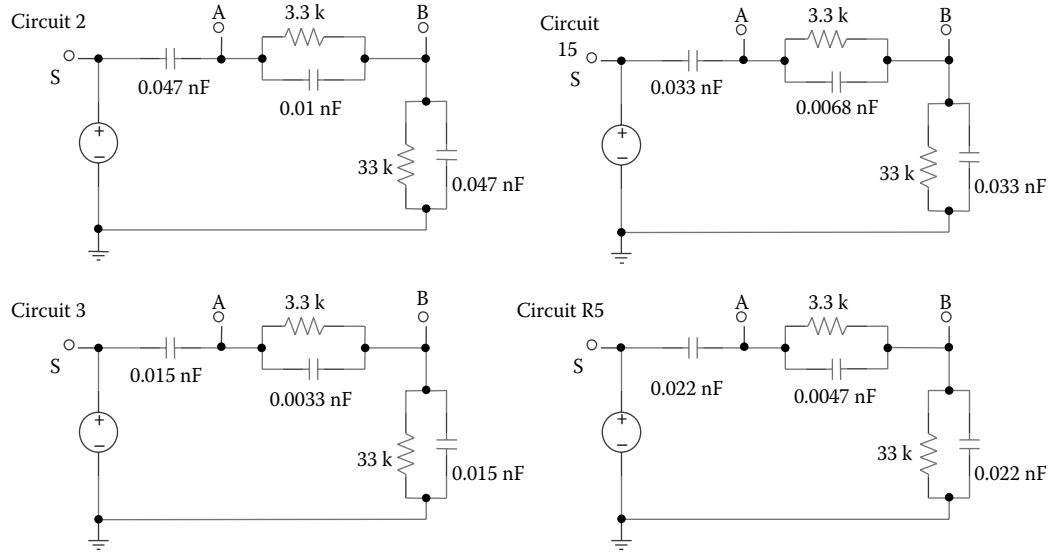

FIGURE D.25
Topology IV with three capacitors and loading resistors.

D.8.5 Topology V (Figure D.26)

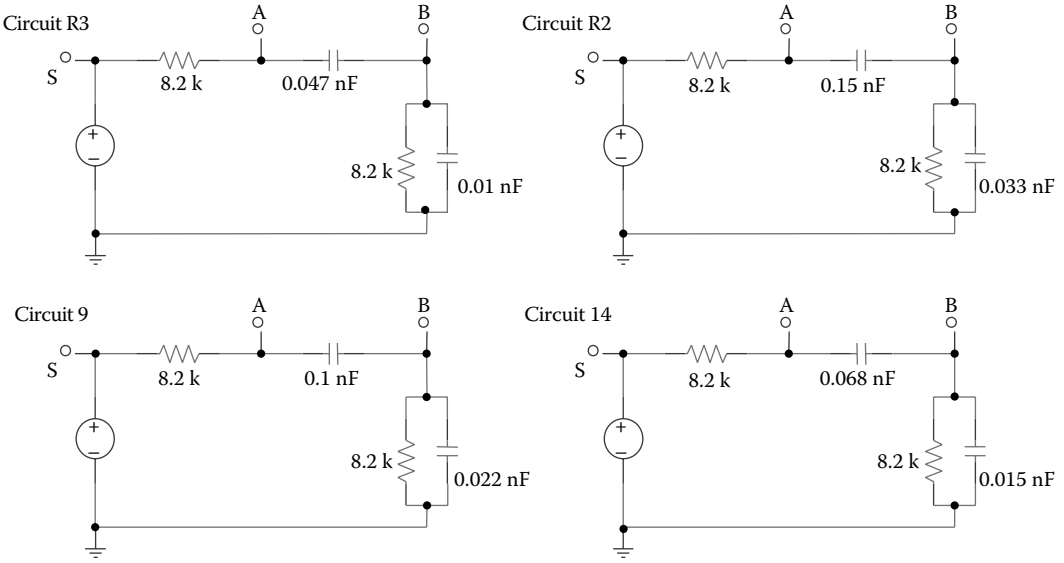

FIGURE D.26
Topology V with two capacitors whose values are four times with respect to one another.

D.8.6 Topology VI (Figure D.27)

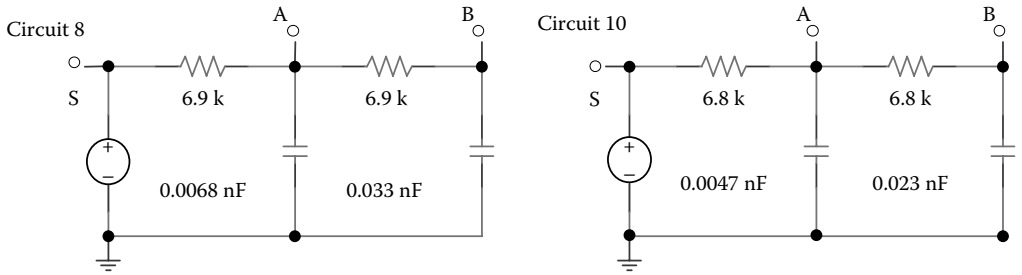

FIGURE D.27
Topology VI with two capacitors connected in typical filtering circuitry.

D.9 Appendix 2: Receiver Noises

As mentioned in Section D.7 about the power budget, the estimation of noises is very critical for the determination of receiver sensitivity. This appendix outlines the definitions and techniques for calculating the noises generated in the PD and the preamplifier front end.

Readers can in fact consider investigating the system calculation and returning back to the noise calculation provided that they are taking either the total equivalent noise spectral density at the input of the detector or its noise (Figure D.28). This section describes all noise mechanisms related to the photodetection process including the electronic noise associated with the receiver.

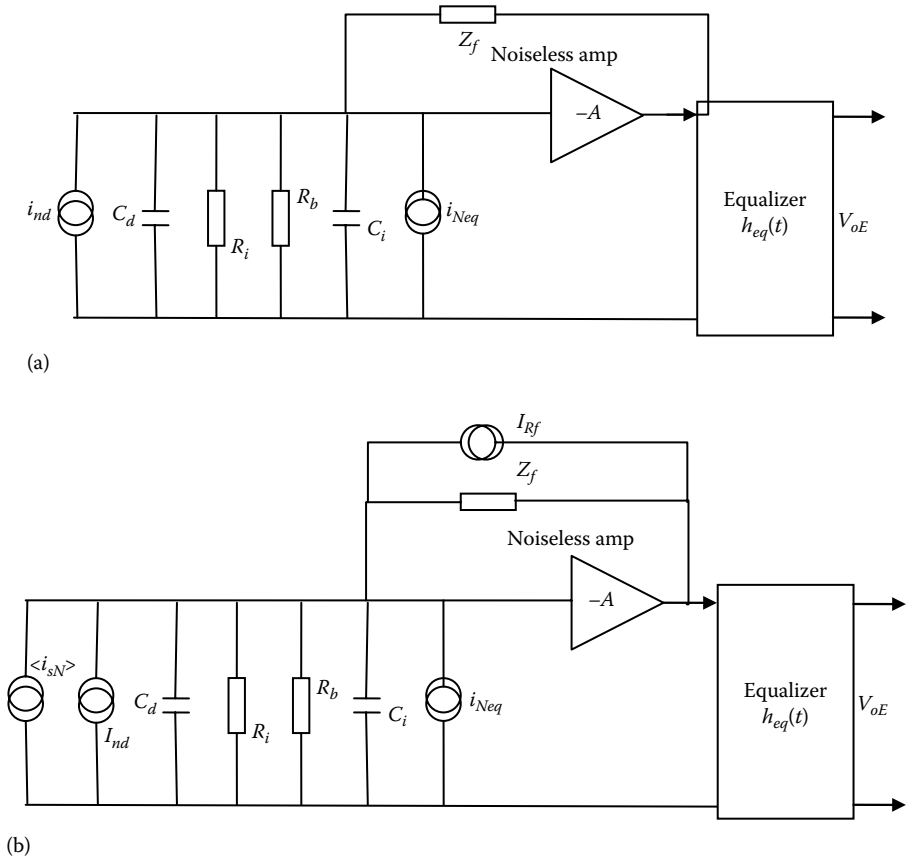

FIGURE D.28
Optical receiver small-signal model and associate noise sources: (a) without and (b) with noise source of shunt feedback impedance.

Shot noises and thermal noises are the two most significant noises in optical detection systems. Shot noises are generated by either the quantum process or electronic biasing. The noises are specified in noise spectral density that is the square of the noise current per unit frequency (in Hz). Thus, the noise spectral power density (by squaring the noise spectral density) is to be integrated over the total amplifier BW to obtain the equivalent noise currents.

For a transimpedance by taking the square root, this total equivalent noise square (referred to its input port) gives an equivalent noise current referred to the input. Then multiply this current by the transresistance (the value of the transimpedance at the mid-band frequency region) to obtain the total noise voltage as referred to the output port, which is normally observed on a sampling oscilloscope. Although a further gain amplifier may be needed, the noise contributed in this stage is commonly neglected as when referring to the input port, this is much smaller than that of the transimpedance amplifier (TIA).

D.9.1 Shot Noises

Electrical shot noises are generated by the random generation of streams of electrons (current). In optical detection, shot noises are generated by (1) biasing currents in electronic devices and (2) photocurrents generated by the photodiode.

For a bias current I, the randomness of electron movement would generate uncertainty in its current; thus, the spectral current noise density S_I can be defined as

$$S_I = \frac{d(i_{NI}^2)}{df} = 2qI \text{ in A}^2/\text{Hz} \tag{D.55}$$

where q is the electronic charge. The current i_{NI}^2 represents the noise current due to the biasing current I.

D.9.2 Quantum Shot Noise

The term "quantum" is referred to the quantum generation process under absorption of lightwaves by a semiconductor medium and then collection via a *pn* junction under reversed bias. The average current $\langle i_s^2 \rangle$ generated by the PD by an optical signal with an average optical power P_{in} is given by

$$S_Q = \frac{d\langle i_s^2 \rangle}{df} = 2q\langle i_s^2 \rangle \text{ in A}^2/\text{Hz} \tag{D.56a}$$

In the case that the APD is used, the noise spectral density is given by

$$S_Q = \frac{d\langle i_s^2 \rangle}{df} = 2q\langle i_s^2 \rangle \langle G_n^2 \rangle \text{ in A}^2/\text{Hz} \tag{D.56b}$$

with $\langle G_n^2 \rangle$ as the average avalanche gain of the detector. It is noted here again that the dark currents generated by the PD must be included to the total equivalent noise current at the input after it is evaluated. These currents are generated even in the absence of the optical signal. The dark currents can be eliminated by cooling the PD to at least below the temperature of liquid nitrogen (77 K).

D.9.3 Thermal Noise

At a certain temperature, the conductivity of a conductor varies randomly. This random movement of electrons generates a fluctuating current even in the absence of an applied voltage. The thermal noise of a resistor R is given by

$$S_R = \frac{d\left(i_R^2\right)}{df} = \frac{2k_BT}{R} \text{ in A}^2/\text{Hz} \tag{D.57}$$

where

k_B is Boltzmann's constant
T is the absolute temperature (in K)
R is the resistance (in Ω)
i_R denotes the noise current due to the random generation of a current passing a resistor R

D.9.4 Noise Calculations

In this part, the design of a receiver for use in a digital communication system and the methods for noise calculations are described. Binary and multilevel operations are also given. The schematic of an optical preamplifier of the receiver and an electronic analog equalizer for the detection of optical digital modulated signals is shown in Figure D.28. An equalizer is considered in order to extend the BW of the receiver to the range of several GHz for ultra-high-speed operations of these digital optical receivers. This is similar to earlier design considerations of optical receivers when multimode fibers were used in first-generation optical fiber communication systems [16–18]. The noise sources and small amplification circuit model can be simplified as shown in Figure D.29 in which all the noise sources of the electronic amplifier and the PD are presented and grouped into total noise current sources at the input and output of the amplifier. These sources are then transferred to a total equivalent current source as seen in the input of the amplifier. Thus, it is very straightforward to find out the signal to noise ratio and contribution of noises from the electronic amplification process and the quantum shot noise process in the detection of optical signals.

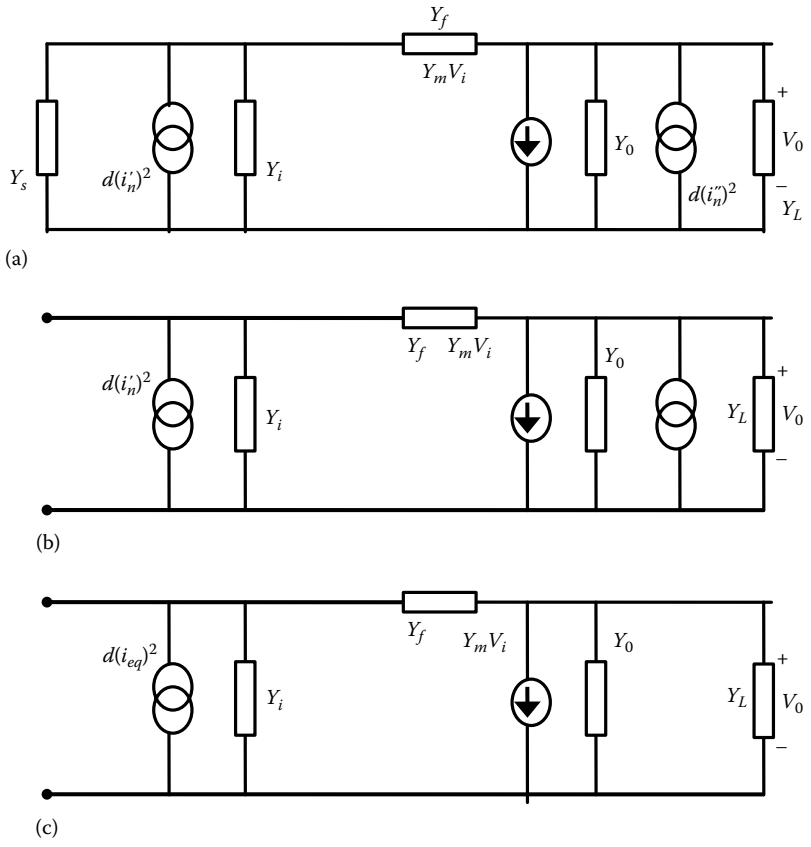

FIGURE D.29
Small equivalent circuits including noise sources: (a) a *Y*-parameter model representing the ideal current model and all current noise sources at the input and output ports, (b) with noise sources at these ports, and (c) with a total equivalent noise source at the input.

Our goal is to obtain an analytical expression of the noise spectral density equivalent to a source looking into the electronic amplifier including the quantum shot noises of the PD. A general method for deriving the equivalent noise current at the input is by representing the electronic device by a *Y*-equivalent linear network as shown in Figure D.29. The two current noise sources $d\left(i_N'^2\right)$ and $d\left(i_N''^2\right)$ represent the summation of all noise currents at the input and at the output of the *Y*-network. This can be transformed into a *Y*-circuit with the noise current at the input as follows.

The output voltages V_0 of Figure D.29a can be written as

$$V_0 = \frac{i_N'(Y_f - Y_m) + i_N''(Y_i + Y_f)}{Y_f(Y_m + Y_i + Y_o + Y_L) + Y_i(Y_o + Y_L)} \tag{D.58a}$$

and for Figure D.29b,

$$V_0 = \frac{(i_N')_{eq}(Y_f - Y_m)}{Y_f(Y_m + Y_i + Y_o + Y_L) + Y_i(Y_o + Y_L)} \tag{D.58b}$$

Thus, comparing these two equations we can deduce the equivalent noise current at the input of the detector as*

$$i_{Neq} = i_N' + i_N'' \frac{Y_i + Y_f}{Y_f - Y_m} \tag{D.59a}$$

Then reverting the mean square generators for a noise source, we have the total equivalent noise spectral density as referred to the input as

$$d(i_{Neq})^2 = d(i_N')^2 + d(i_N'')^2 \left| \frac{Y_i + Y_f}{Y_f - Y_m} \right|^2 \tag{D.59b}$$

It is therefore expected that if the *Y*-matrix of the front-end low-noise amplifier is known, the equivalent noise at the input of the amplifier can be obtained using (D.59b). This parameter is commonly prescribed by manufacturers of TIA, for example, 20 $\text{pA}/\sqrt{\text{Hz}}$. Thus, this amount is to be squared and integrated over the BW of the amplifier to give the total equivalent referred to the input of the TIA.

Thus, once the total equivalent input noise spectral density of the electronic preamplifier can be found, the receiver model can be simplified, in the small-signal sense, as shown in

* Note that quite a number of companies around the world have misled readers and users with the term "thermal noise," which is completely wrong, for example, VPIsystems or RSoft. So be aware that noises can be specified in terms of the noise temperature, noise resistance, total equivalent noise voltage or currents, and noise spectral density. The noise density is much better to use as it is independent with the bandwidth, so just a simple integration over the bandwidth and the square of the term, we can get the total noise current (taking the square root of the square of the current).

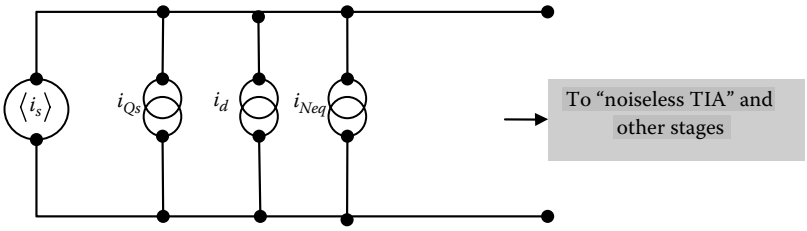

FIGURE D.30
Final equivalent noises and signals at the input of the electronic receiving subsystem.

Figure D.30 in which the signal average current source $\langle i_s \rangle$ represents the average signal current generated by the PD when the optical signal is received; i_{Qs} represents the quantum shot noises generated in the PD due to this signal current and any DC generated by the CW optical source such as the residual local oscillator in coherent detection; and i_d is the dark current noise of the PD. Thus, the electrical power signal to noise ratio can be written as

$$SNR = \frac{\langle i_s \rangle^2}{i_{Neq}^2 + i_{Qs}^2 + i_d^2} \tag{D.60}$$

Note that the symbol for the noise sources shown in Figure D.30 indicates that there are no positive or negative directions of the noise current source as they always superimpose an additional amount on the signal current. The quantum shot noise can be found by taking the average optical power multiplied by the responsivity of the PD to give the magnitude of the current and then using the definition of the quantum shot noise spectral density given by (D.56). Thus, by taking the integration of these noise sources over the 3 dB BW, one can estimate the total noise current and its power to be employed in (D.60).

Once this signal-to-noise ratio (SNR) of (D.60) is found, then with the responsivity of the PD, we can estimate the required average optical power of the signal sequence. The bit error rate (BER) can then be derived using the probability density function (pdf) and the constellation of the received signals together with the noise estimated. Thus, with the noise estimation technique described here, we can estimate the BER without much difficulty for any modulated signal sequence.

As an example, let us consider pulse amplitude modulation (PAM2), and then under Gaussian pdf, 13 dB in SNR is required for *BER* = 1e−9, or about 10 dB in amplitude SNR or a ratio of about 6 for BER. Thus, for a noise of 20 $\text{pA}/\sqrt{\text{Hz}}$ as the total equivalent referred to the input as the dominating noise, then with a BW of 30 GHz TIA, we would expect a noise current of $(20\text{pA}/\sqrt{\text{Hz}})^2 * 30\text{e}^9\text{A}^2 \approx 1.2\text{e}-11\ \text{A}^2$ or 3.46e−6 A at the output of TIA without taking the transimpedance Z_T into account. Now assuming a TIA with a transimpedance of 150 Ω, the output noise average voltage would be about 0.52 mV at the output of the TIA and Z_T, and we can estimate the required output voltage level of the signal. Thus to obtain the BER of e−9, we need a signal average level of about 6.4 mV. From this value, we can estimate the PD current required and hence the optical power of the optical sequence to be received depending on the modulation as given in Figure D.31.

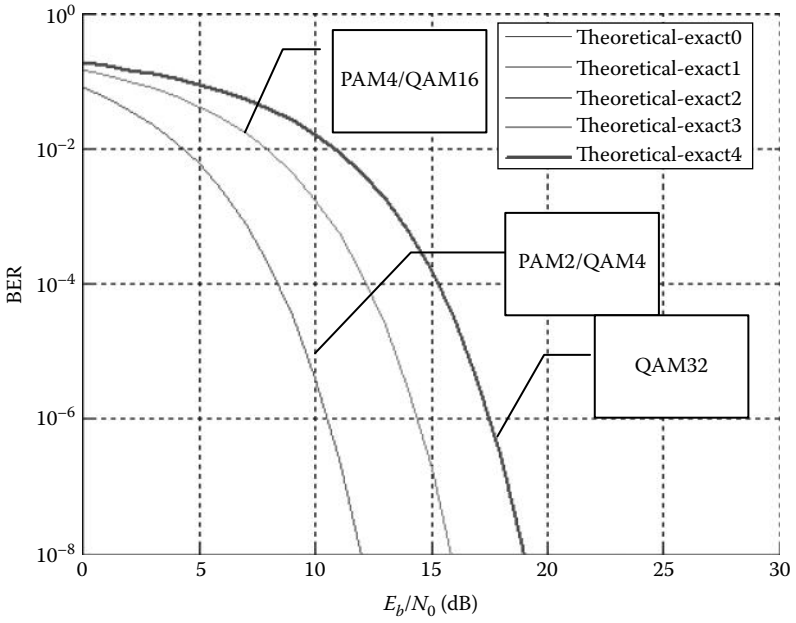

FIGURE D.31
Theoretical curve of BER versus E_b/N_0 or SNR in terms of power for different modulation formats—employing bertool.m.

References

1. H. Wallman, Transient response and the central limit theorem of probability, *Proceedings of Symposia in Applied Mathematics* 2, 91, 1950.
2. G.E. Valley, Jr. and H. Wallman, *Vacuum Tube Amplifiers*, MIT Radiation Laboratory Series 18, McGraw-Hill, New York, pp. xvii+743, Paragraph 2 of chapter 2 and paragraphs 1 to 7 of chapter 7, 1948.
3. N.S. Nise, *Control Systems Engineering*, 5th ed., John Wiley & Sons, Hoboken, NJ, p. xvii+880, 2008.
4. SHF Communication Technologies AG, Application Note: 4 Level generation including pre-emphasis, Berlin, Germany, V001, August 21, 2013.
5. B.C. Kuo and F. Golnaraghi, *Automatic Control Systems*, 8th ed., John Wiley & Sons, New York, p. 253, 2003.
6. B.C. Kuo and F. Golnaraghi, *Automatic Control Systems*, 8th ed., John Wiley & Sons, New York, p. 259, 2003.
7. D.A. Johns and K.W. Martin, *Analog Integrated Circuit Design*, John Wiley & Sons, New York, pp. 234–235,1997.
8. M.C. Sansen, *Analog Design Essentials*, Springer, Dordrecht, the Netherlands, p. §0528, 163, 2006.
9. M.C. Sansen, *Analog Design Essentials*, Springer, Dordrecht, the Netherlands, p. §0526, 162, 2006.
10. G. Palumbo and S. Pennisi, *Feedback Amplifiers: Theory and Design*, Kluwer Academic Press, Boston, MA, pp. §4.4, 97–98, 2002.
11. K.C. Kuo and C.A. Desoer, *Basic Circuit Theory*, McGraw-Hill, New York, 1972.
12. Hewlett Packard Company, Test & measurement catalog 1999, Santa Clara, CA, p.111, December, 1998.

13. Fluke Corporation, *ABC's of Oscilloscopes*, Everett, WA, pp. 94–36, 8 and 35, 1994.
14. http://www.edn.com/design/test-and-measurement/4340453/Relating-wideband-DSO-rise-time-to-bandwidth-Lose-the-0-35. Accessed October, 2013.
15. http://www.edn.com/design/test-and-measurement/4340453/Relating-wideband-DSO-rise-time-to-bandwidth-Lose-the-0-35-#. Accessed October, 2013.
16. S.D. Personick, Receiver design for digital fiber optic communication systems, *Bell System Technical Journal*, 52, 843–886, 1973.
17. S.D. Personick, Optical detectors and receivers, *IEEE Journal of Lightwave Technology*, 26(9), 1005–1020, 2008.
18. J.L. Hullet and T.V. Muoi, A feedback receive amplifier for optical transmission systems, *IEEE Transactions on Communications*, 24(10), 1180–1185, 1976.

Appendix E: Problems on Optical Fiber Communication Systems

E.1 Problem Set on Lightwave Technology

Question 1

(i) What are the frequencies of lightwaves with wavelengths of 1300 and 1550 nm in vacuum?

(ii) What are the *frequencies* and *wavelengths* of these lightwaves if they are propagating in optical fibers with a refractive index of 1.448 at 1330 nm and 1.446 at 1550 nm? You may assume single-mode operation of the lightwaves at these wavelengths.

(iii) What is the frequency difference between these two lightwaves?

(iv) What is the frequency difference between lightwaves of 1530 and 1560 nm? If we now divide this wavelength ranges into grid of 50 GHz spacing. Tabulate your wavelength grid and corresponding spectral table.

(v) What are the colors of the lightwaves of parts (i) and (iv)?

NOTE: Velocity of light in vacuum is c = 299,792,458 m/s. Can you state the reasons why this velocity must be very accurate?

Question 2

(i) What are the colors of the following lightwaves: wavelengths of 210, 418, 514, 633, 670, 810, 1310, and 1550 nm? What are their frequencies in vacuum?

(ii) If the lightwaves in (i) are propagating in a glass medium with varied refractive index with respect to the wavelength as given in Chapter 2, would their frequencies or wavelength change? Give reasons.

(iii) What is the color of the lasers commonly used in CDs or DVDs. What do people mean by Blue-ray discs?

E.2 Problem Set on Optical Fibers for Optical Communications Systems and Networks

Problem 1

An optical fiber with a step-index profile, a core diameter of 65 μm, and a numerical aperture of 0.2 with a wavelength of 1300 nm is used for signal distribution and transmission in a local area network.

(a) What is the V parameter of this optical fiber? Is the fiber operating in single-mode or multimode region at 1310 nm operating wavelength?
(b) Approximately how many guided modes would it support? Comment on this number regarding the velocities of lightwaves.
(c) What is the typical cladding diameter for this fiber? Give reasons.
(d) * Find the maximum acceptance angle of this fiber. Hence, estimate the coupling loss of a laser source with a uniform radiation cone of 30°.

Problem 2

An optical fiber has the following parameters: index profile = step-like, core diameter = 9.0 μm, numerical aperture = 0.11, and cladding refractive index = 1.4468.

(a) Find the normalized frequency of the fiber at 1550 nm wavelength.
(b) Is the fiber operating in single-mode or multimode region at 1550 nm? If it is in the single-mode region, estimate its mode-field diameter (MFD) and its spot size. Sketch its field and intensity distributions across the fiber cross section.
(c) Find the cutoff wavelength of the fiber. If lightwaves with wavelength smaller than this cutoff wavelength are launched into the fiber, will the fiber still operate in single-mode region?

Problem 3

A single-mode step-index optical fiber has the following parameters: core diameter = 8.0 μm, cladding diameter = 0.125 mm, core refractive index = 1.460, and relative index difference = 0.2% at 1550 nm.

(a) Confirm that the fiber can be operated in the single-mode regime at 1550 nm wavelength.
(b) Find the fiber cutoff wavelength.
(c) What is the fiber MFD if it is operating at 1550 nm wavelength region?

Problem 4a

For the optical fiber in Problem 1, if the refractive index profile is parabolic ($\alpha = 2$) or triangular ($\alpha = 1$) with the given numerical aperture at the central axis, repeat (a) through (c).

Problem 4b

Single-mode optical fibers produced by Corning Inc. such as SMF-28 have typical characteristics as per the technical data sheet distributed in lectures.

(a) Using the fiber physical characteristics and technical data on its MFD confirms the value of its numerical aperture and the fiber functional characteristics such as the cutoff wavelength range.

(b) * If this fiber is launched with an 850 nm laser, how many modes would it support? Sketch the mode fields for LP_{01} and LP_{11} modes. Would you recommend operation of the fiber in this wavelength region for ultra-broadband operations? Give reasons.

(c) If lightwaves at 1310 nm travel over 10 km of this fiber, calculate the travel time of these waves.

Problem 5

(a) The Corning SMF-28 optical fiber is used in an optical fiber transmission system with a laser source operating at 1550 nm and a linewidth of 100 MHz. The output power of 1.0 mW is monitored at the output of the fiber pigtail. The fiber length is 200 km. An optical receiver can detect an average optical power of 0.1 μW. Is it possible to detect the optical power at the end of the fiber length due to this loss? You must use the attenuation coefficient of the fiber as specified by Corning fibers—typical value is 0.19 dB/km and slightly higher in specification.

(b) Assuming the rise time and fall time of the transmitter and receiver are negligible compared with that of the fiber, estimate the total pulse broadening and hence find the maximum bit rate that can be used for transmission through this fiber length.

(c) If the source has an optical linewidth of 0.2 nm, estimate the pulse broadening as in (b).

Problem 6

A step-index optical fiber is used for an optical communication system that operates at 1310 nm and has a core radius of 25 μm, core refractive index of 1.460, and cladding refractive index of 1.4550.

(a) What is the numerical aperture of the fiber?

(b) Estimate the number of guided modes.

Problem 7

(a) Show that for a graded-index fiber having a core refractive index $n^2(r) = n_2^2\left[1 + 2\Delta s\left(\frac{r}{a}\right)\right]$ with $s(r/a) = 1-(r/a)^{\alpha}$, the acceptance angle $NA(r)$ is given by $\sin NA(r) = \left[n^2(r) - n_2^2\right]^{1/2}$

(b) If the optical fiber has a parabolic profile shape, show that $\sin\alpha(r) = NA_0\sqrt{1-\left(\frac{r}{a}\right)^{1/2}}$ where $NA_0 = n_2(2\Delta)^{1/2}(1 + \Delta)$ evaluated at the center of the core.

(c) A parabolic graded-index silica optical fiber has a cladding refractive index of 1.460 and a relative index difference at the core axis of 1%. Find the maximum acceptance angle at the core axis of the fiber. Plot $\sin\alpha(r)$ as a function of r. What is the acceptance angle of the fiber at the core and cladding interface? Comment on the launch of a laser source into this fiber.

Problem 8*

(a) For a single-mode optical fiber having a graded-index central dip, that is, $s(r/a) = 1 - (1 - r/a)^{\alpha}$, the equivalent step index (ESI) parameters of V and radius are given by

$$\frac{V_e}{V} = \left[1 - \frac{2\gamma}{(\alpha+1)(\alpha+2)}\right]^{1/2} \quad \text{and} \quad \frac{a_e}{a} = \frac{(\alpha+1)(\alpha+2)(\alpha+3) - 6\gamma}{(\alpha+1)(\alpha+2)(\alpha+3) - 2\gamma}$$

where $V = ka(2\Delta)^{1/2}$

(b) The fiber has a physical core radius of 8.2 μm, a maximum relative index difference of 0.3%, and a cladding refractive index of 1.460. Find its ESI parameters for the normalized frequency and radius at 1550 nm wavelength. Find also its ESI cutoff wavelength and its MFD at this wavelength.

Problem 9

What is the spectral range of infrared light, ultraviolet light, and far-infrared light? What are the approximate wavelengths of the colors in the color band of resistors? Are they corresponding to the color of the rainbow?

What is the exact value of the speed of light in vacuum? What is the optical frequency of lightwaves with wavelength 1553.8 nm? What is the wavelength spacing between lightwaves at 1550 nm with frequency spacing of 200 GHz?

Give the wavelength range for optical channels in the C-, L-, and S-bands in the 1550 nm wavelength window.

Problem 10

For the GeO_2-doped silica-based Corning SMF-28 optical fiber using the information sheet:

(a) Estimate the refractive index of the fiber core and the refractive index difference at 1550 nm operating wavelength.

(b) Can you estimate the V parameters of the fiber at 1550 nm wavelength?

(c) What is the spot size of the fiber at 1550 nm operating wavelength?

(d) What is the estimate loss of this fiber at this wavelength? What are the minimum and maximum attenuation factors of the C-, L-, and S-bands of the 1550 nm silica fiber window? How can these attenuation factors be estimated?

(e) What are the total dispersion factors at 1520 and 1620 nm?

(f) This fiber is to be used in optical systems with bit rates of 10 Gb/s. What is the maximum fiber length that the signal can transmit without suffering the allowable signal degradation? You can assume 1000 ps tolerance.

Problem 11a

(a) Give a brief account of the pros and cons of optical fiber communications systems operating at 810, 1300, and 1550 nm wavelength regions.

(b) Why silica optical fiber becomes very lossy at 1380–1400 nm wavelength regions? What is the attenuation of the Corning SMF-28e fiber?

(c) What are the typical optical fiber losses at the given wavelength regions? Give typical cable losses.

Problem 11b

(a) Show that the material dispersion factor is zero at the wavelength given by $\lambda^4 = -\frac{3c_3}{c_2}$, where the coefficients c_1–c_3 are defined in the lecture notes.

(b) The coefficients c_1, c_2, and c_3 for pure and GeO_2-doped silica fibers are given as follows:

Coefficients c's	Pure Silica	7.9% GeO_2-Doped Silica
c_1	1.45084	1.46286
c_2 in μm^{-2}	–0.00334	–0.00331
c_3 in μm^2	0.00292	0.00320

Find the zero-dispersion wavelengths due to the material of these fibers.

(c) Hence, estimate the material dispersion factor for silica fiber at 1550 nm wavelength.

(d) Using the approximate expression for the normalized propagation constant b as a function of V, state the waveguide dispersion factor due to the waveguide as a function of b and V.

(e) Design a nonzero dispersion-shifted single-mode optical fiber at 1550 nm where its dispersion factor is +2 ps/nm/km or –2 ps/(nm · km) at this wavelength.

Problem 12

Figures 1.1 through 1.3 show the output optical power spectra of a laser diode, an LED, and a super radiant diode, respectively. These diodes are used in an optical communication trunk route using a single-mode fiber of Ge-doped silica.

Calculate the total material dispersion per unit length at their peak operating wavelength.

Problem 13 on ESI

A silica optical fiber has the following characteristics:

1. Refractive index profile: linear with $\Delta n_o = n_o - n_2 = 0.2\%$ at 1.3 μm.
2. Core radius: $a = 4$ μm.
   (a) Find the equivalent step-index parameters of this fiber.
   (b) Calculate its waveguide dispersion factor using both the ESI parameters approach and the spot-size dependence relationship.
   (c) This fiber is launched with optical sources whose characteristics are given in Problem 1. Calculate the total dispersion at the center wavelength of the source optical power spectra.
   (d) Calculate the splicing loss for this fiber when a splicing machine with a 0.5 μm misalignment is used.

Problem 14

An optical fiber with a step-index profile, a core diameter of 62.5 μm, and a numerical aperture of 0.2 with a wavelength of 1300 nm is used for signal distribution and transmission in a local area network.

(a) What is the V parameter of this optical fiber?
(b) How many guided modes would it support? Comment on this number regarding the velocities of lightwaves.
(c) Select a cladding diameter. Give reasons for your selection.
(d) Find the maximum acceptance angle of this fiber. Hence, estimate the coupling loss of a laser source with a uniform radiation cone of 30°.

Problem 15a
An optical fiber has the following parameters: index profile = step-like, core diameter = 9.0 μm, numerical aperture = 0.11, and cladding refractive index = 1.48.

(a) Find the normalized frequency of the fiber at 1550 nm wavelength.
(b) Is the fiber operating in single-mode or multimode region at 1550 nm? If it is in the single-mode region, estimate its MFD and its spot size. Sketch its field and intensity distributions across the fiber cross section.
(c) Find the cutoff wavelength of the fiber. If lightwaves with wavelength smaller than this cutoff wavelength are launched into the fiber, will the fiber still operate in single-mode region?

Problem 15b
A single-mode step-index optical fiber has the following parameters: core diameter = 8.0 μm, cladding diameter = 0.125 mm, core refractive index = 1.460, and relative index difference = 0.25% at 1550 nm.

(a) Confirm that the fiber can be operated in the single-mode regime at 1550 nm wavelength.
(b) Find the fiber cutoff wavelength.
(c) What is the fiber MFD if it is operating at 1550 nm wavelength?

Problem 16
For the optical fiber in Problem 15, if the refractive index profile is parabolic ($\alpha = 2$) or triangular ($\alpha = 1$) with the given numerical aperture at the central axis, repeat (a) through (c).

Problem 17
Single-mode optical fibers produced by Corning have typical characteristics as per the technical data sheet attached at the end of Chapter 2.

(a) Using the fiber physical characteristics and technical data on its numerical aperture confirms the fiber functional characteristics such as the cutoff wavelength range.
(b) If this fiber is launched with an 850 nm laser, how many modes would it support? Sketch the mode fields for LP_{01} and LP_{11} modes.
(c) If lightwaves at 1300 nm travel over 10 km of this fiber, calculate the travel time of these waves.
(d) Estimate the fiber core diameter at 1300 nm wavelength.
(e) If the same spot size of (d) is required for the fiber to operate at 1550 nm, can you advise the manufacturer on any changes of the fiber physical parameters?

Problem 18

(a) The optical fiber in Problem 1.3 is used in an optical fiber transmission system with a laser source operating at 1310 nm having an output power of 1.0 mW. The fiber length is 50 km. An optical receiver can detect an average optical power of 0.1 μW. Is it possible to detect the optical power at the end of the fiber length?

(b) Referring to the technical data of the standard optical fiber, estimate the spreading of optical pulse after transmitting through the 50 km length fiber if the source has an optical linewidth of 2.0 nm.

Problem 19

A step-index optical fiber is used for an optical communication system that operates at 1310 nm and has a core radius of 25 μm, core refractive index of 1.460, and cladding refractive index of 1.4550.

(a) What is the numerical aperture of the fiber?

(b) Estimate the number of guided modes.

Problem 20

(a) Show that for a graded-index fiber having a core refractive index $n^2(r) = n_2^2\left[1 + 2\Delta s\left(\frac{r}{a}\right)\right]$ with $s(r/a) = 1 - (r/a)^{\alpha}$, the acceptance angle $\alpha(r)$ is given by

$$\sin\alpha(r) = \left[n^2(r) - n_2^2\right]^{1/2}$$

(b) If the optical fiber has a parabolic profile shape, show that $\sin\alpha(r) = NA\sqrt{1 - \left(\frac{r}{a}\right)^{1/2}}$, where $NA = n_2(2\Delta)^{1/2}(1 + \Delta)$.

(c) A parabolic graded-index silica optical fiber has a cladding refractive index of 1.460 and a relative index difference at the core axis of 1%. Find the maximum acceptance angle at the core axis of the fiber. Plot sin $\alpha(r)$ as a function of r. What is the acceptance angle of the fiber at the core and cladding interface? Comment on the launch of a laser source into this fiber.

E.3 Questions on Optical Fibers for Optical Communications Systems and Networks: Corning Technical Lectures

General fiber structures and manufacturing

1. Give an account on how optical fibers guide lightwaves. In particular, make a clear distinction between the lightwave guiding mechanism in multimode and single-mode fiber types. You can use a diagram to illustrate your answers.
2. Sketch light rays of both radiation and guided types, as they are propagating or radiating in step-index and graded-index optical fibers.

3. Is it possible to repeat (2) for single-mode optical fibers?
4. What are the typical diameters of the core and cladding regions of single-mode and multimode fibers? Give some specific dimensions for Corning SMF-28 and Corning multimode silica fibers.
5. What is the range of the relative refractive index difference between the core and cladding regions of Corning SMF-28? Give reasons why this is very small.
6. Give an account of the weakly guiding phenomena for lightwaves in single-mode optical fibers.
7. Give an account of the fabrication and manufacturing of silica-based glass fibers by the chemical vapor deposition (CVD) process.
8. Sketch the refractive index profile of single-mode optical fibers having matched cladding and depressed cladding regions.
9. What is the typical length bandwidth product of a multimode fiber?

Single-mode fiber performance characteristics

1. What are the typical ranges of the attenuation of silica-based single-mode fiber in the first, second, and third windows?
2. Give an account of the intermodal dispersion, intramodal dispersion, and material and waveguide chromatic dispersion factors.
3. Why material dispersion is almost zero in the regions around 1310 nm for various doped silica fibers?
4. Could you design an optical fiber that would have a total dispersion factor close to zero at 1550 nm and describe its design?
5. What is the MFD of a single-mode optical fiber? Explain why the MFD is larger than that of the core of the fiber.
6. What is cutoff wavelength? What is the region of the cutoff wavelength of Corning SMF-28? Why a region of wavelength and not a specific wavelength specifies the cutoff wavelength? Hence, give an account of the effective cutoff wavelength of an optical fiber. Make sure that you distinguish between the cutoff wavelength of fiber cables and noncabled bare fibers.
7. What are mechanical and fusion splices and their typical (acceptable) attenuation coefficient?

(see also the self-test section of the article "Corning fiber-optic technology tutorial," http://www.iec.org.)

E.4 Question Set on Polarization Mode Dispersion

1. What does it mean by "linearly polarized" guided mode in a single-mode optical fiber?
2. Under the condition that there is nonuniformity of the fiber core due to installation stress, fabrication, microbending, etc., give an account of the propagation of the modes of the linearly polarized mode propagating through a "single-mode" fiber. Hence, give a statement about the polarization mode dispersion (PMD).

3. What is the differential group delay (DGD)?
4. Describe the statistical property of PMD (to the first-order effect). What is the unit of the PMD?
5. Consider a digital optical fiber transmission link that is limited due to the PMD effect only. The transmission bit rates are 2.5 and 10 Gb/s. The rule of thumb for determination of the limited distance is that the total broadening of the pulse must not exceed 70% of its width. Assume that the system is operating at 1550 nm wavelength.
   a. For a single-mode fiber used in the link with an averaged PMD coefficient of $0.5\,\text{ps}/\sqrt{(\text{km})}$, estimate the link limited distance.
   b. Repeat (a) for PMD coefficient varying from 0.01 to 10 $\text{ps/km}^{1/2}$.
   c. Repeat (b) for the transmission bit rate of 40 Gb/s.
   d. Repeat (b) and (c) for the case that the total chromatic dispersion is that of the Corning LEAF fiber (technical data are available in the Appendix).
6. Examine Equation (2) of the technical paper *System PMD Requirements for Multichannel Analog and Digital Operation on Non-Zero Dispersion Shifted Optical Fiber* and obtain the allowable dispersion and PMD of optical amplifiers and the dispersion compensating module as a function of operating bit rate.

E.5 Question Set on Next-Generation Multimode Fibers for 10 Gb Ethernet

1. What is the length bandwidth product of Corning next-generation multimode fibers? Hence, determine the maximum transmission distance for 10 Gb/s Ethernet.
2. Comment on the performance of such multimode fiber and other transmission technologies.

E.6 Question Set on Advanced Optical Fiber for Long-Distance Telecommunications Networks

1. Outline the XS-, S-, C-, and L-bands for the 1485–1625 nm wavelength transmission regions in optical fibers.
2. Give typical dispersion factors for the following Corning fibers: SMF-28 and non-zero dispersion-shifted fiber (NZ-DSF). Hence, give a comparison between these types of single-mode fibers.
3. What is the optical frequency of lightwaves emitted at 1550 nm wavelength? What is the frequency spacing between lightwaves separated by 1.0 nm in the region of 1550 nm wavelength? If two lightwaves are separated by 100 GHz in the frequency domain, what is their separating wavelength if one of the wavelength channels is emitted at 1550 nm?
4. What are the transmission bit rates of OC-192 (optical communications level) or STM-48 (synchronous transfer mode), as well as for OC-786 and STM-192?

5. Compare the dispersion performance of standard single-mode fiber and NZ-DSF.
6. Give a brief account of wavelength division multiplexing (WDM) techniques for optical communication systems.
7. Briefly give an account of optical amplifiers using in-line Erbium-doped fiber type.
8. Give a brief account of Raman amplification process and its advantages and disadvantages for wavelength division multiplexed optical communications systems.
9. Give a reason why G.653 dispersion-shifted fiber has fallen out of favor compared to 0.655 NZ-DSF.

E.7 Question Set on Optical Transmitters and Receivers for Optical Communications Systems and Networks

1. Digital transmission capacity is measured as (a) bandwidth in MHz, (b) rise time in microseconds, (c) number of bits transmitted per second, (d) frequency of 3 dB cutoff point.
2. If the rise time of the transmitter is 1 ns, what is its theoretical bandwidth? (a) 1 Gbps, (b) 100 MHz, (c) 350 MHz
3. Which of the following is not found in a direct optical fiber transmitter? (a) electronic drive circuitry, (b) photodiode to sense the output power, (c) temperature sensor, (d) He–Ne gas laser.
4. What provides feedback to help in stabilizing laser intensity in an optical transmitter? (a) output from the rear face of the laser monitored by a photodiode, (b) a signal relayed from the receiver, (c) change in input impedance, (d) light scattered from the optical interface with the output fiber.
5. What is the usual modulation method for fiber-optic transmitter? (a) intensity modulation, (b) frequency modulation, (c) wavelength modulation, (d) voltage modulation.
6. What does TDM do? (a) interleaves several digital signals into a single stream of bits, (b) encrypts signals for secure transmission, (c) shifts the frequencies of several analog signals to combine them into a single output.
7. What is the total data rate of a WDM system carrying 2.5 Gbps signals at 1550, 1552, 1554, 1556, 1558, 1560, 1562, and 1564 nm? (a) 10 Gbps, (b) 15 Gbps, (c) 20 Gbps, (d) 40 Gbps.
8. In an external modulation transmitter, the laser is (a) directly modulated with the data stream, (b) turned on continuously and the lightwaves are modulated by an optical modulator, (c) simultaneously modulated together with the external modulator.
9. What is the typical total optical insertion loss of an electro-optic modulator? (a) 10 dB, (b) 25 dB, (c) 2.5 dB, (d) 40 dB.
10. What is the typical optical bandwidth of a distributed feedback (DFB) laser? (a) 1 MHZ, (b) 10 GHz, (c) 100 MHz, (d) 40 GHz.
11. What is the typical linewidth of a Fabry–Perot (FP) laser? (a) 10 nm, (b) 15 nm, (c) 1.5 nm, (d) 40 nm.

12. In transmission 2.5 Gbps data streams through a length of SMF-28 fiber, a transmitter using directly modulated DFB laser would be more dispersive than that of the transmitter employing FB laser. (a) false, (b) true.
13. In direct modulation, it is necessary to set the zero level of the input pulses near the threshold of the power-current characteristics in order to avoid (a) turn-off switching effect, (b) sinusoidal oscillation, (c) turn-on delay effects.
14. What is the typical maximum bit rate that a transmitter can be modulated by direct switching on and off the injection current into the lasing cavity? (a) 10 Gbps, (b) 40 Gbps.
15. In broadband optical communications systems and networks, the structures of optical receivers can be both purely electronic and optical preamplification plus electronic preamplifier. (a) true, (b) false.
16. What is the function of the photodiode at the front end of the optical receiver? (a) direct converting the optical pulse intensity into electronic current, (b) direct converting the optical pulse intensity into voltage.
17. What are the noises generated at the electronic preamplifier of an optical receiver? (a) optical quantum shot noises dependent on the signals, (b) electronic shot noises due to bias currents, (c) electronic thermal noises, (d) all of the above.
18. The two types of an optical receiver are (a) high impedance and transimpedance and (b) open circuit and distributed detection circuit.
19. The transimpedance amplifier would provide wider bandwidth than that of a high-impedance electronic preamplifier. (a) true, (b) false.

E.8 Problem/Question Set on Photonic Components for Optical Communications Systems and Networks

Question 1
You have a 1 × 16 coupler that divides an input signal equally among the 16 output ports, assuming that it has no excess loss. If the input signal average power is –10 dBm, what is the output power at any port? Note: 0 dBm = equivalent to 1 mW, 10 dBm = 10 mW, –10 dBm = 0.1 mW. (a) –12 dBm, (b) –20 dBm, (c) –22 dBm, (d) –30 dBm.

Question 2
If you have a 1 × 20 coupler with an input signal of –10 dBm and an output signal of –30 dBm at each output port, what is the excess loss? (a) 2 dB, (b) 1 dB, (c) 0 dB, (d) 4.2 dB, (e) 7.2 dB.

Question 3
A WDM system delivers an input power of –20 dBm at each of the four wavelengths to a wavelength demultiplexer. Assuming no excess loss, what is the output power at each of the four ports? (a) –26 dBm, (b) –30 dBm, (c) –20 dBm.

Question 4
A coupler splits an input signal between two ports with 90:10 intensity splitting ratio. If the input signal is 0 dBm and the coupler has no excess loss, what is the output optical power at the port of 10%? (a) –10 dBm, (b) –20 dBm, (c) –1 dBm.

Question 5
Which type of coupler would be the best choice for distributing identical signals to 20 different points? (a) 1 × N splitter, (b) free space 1 × 2 beam splitter, (c) free space 1 × 2 splitter, (d) NxM splitter.

Question 6
Which of the following technologies can be used in wavelength selective couplers? (a) micro-optics, (b) fused fibers, (c) array waveguide grating (AWG), (d) fiber gratings.

Question 7
Which of the following technologies can be best suited for dense WDM? (a) none of the below, (b) bulk optics, (c) AWGs.

Question 8
At the optical receiver end of your fiber optical communication system, *a* −5 dBm signal enters a 1 × 10 tree coupler that divides the signal equally. The receiver at each port can accept a maximum signal of −18 dBm before saturation. What attenuator do you need to insert in front of the receiver to avoid saturation? (a) 13 dB, (b) 10 dB, (c) 5 dB.

Question 9
Which of the following are advantages of direct modulation over external modulation? (a) simple, (b) can handle higher power, (c) less signal distortion, (d) no wavelength chirp, (e) can operate at high frequencies (up to 40 GHz).

Question 10
Which of the following are advantages of external modulation over direct modulation? (a) simple, (b) can handle higher power, (c) less signal distortion, (d) no wavelength chirp, (e) can operate at high frequencies (up to 40 GHz).

Question 11
How does the interferometric waveguide modulator (usually called Mach–Zehnder intensity modulator [MZIM]) work? (a) a phase delay causes lightwaves to be absorbed, (b) a phase delay between two waveguide branches causes interference "on–off," (c) they rotate polarization so a polarize blocks light, (d) they become opaque as voltage increases

Question 12
What phase shift do you need to cause destructive interference between two coherent lightwaves? (a) 360°, (b) 90°, (c) 180°.

Question 13
Where do you want to use the microelectromechanical sensors (MEMS)? (a) to rearrange connections in a building patch panel, (b) for protection routing to alternate cable in case of cable failure, (c) to switch large blocks of traffic at multiple wavelengths.

Question 14
An MEMS (a) mechanically moves an electronic switch to redirect optical signals, (b) uses light to mechanically throw an electrical switch, (c) uses light to mechanically throw an optical switch, (d) none of the above.

Question 15
Integrated optical circuits consist of (a) planar waveguides and optical elements on semiconductor substrates, (b) planar waveguides and optical elements on lithium niobate electro-optic substrates, (c) optical fibers fused together, (d) a and b.

E.9 Problem Set on Digital Optical Receiver for Optical Communications Systems and Networks

Problem 1

(a) Suppose that we have an ideal photodetector that produces no dark current, that is, no electron hole pairs are generated in the absence of an optical pulse and that an optical pulse of an energy b_1 falls on the photodetector in an interval T. It can be interpreted by the receiver as a "0" pulse if no electron-hole pairs are generated with the pulse present. Show that if the probability of this pulse being interpreted as a "0" is 10^{-9}, then $b_1 = 21\ h\upsilon/\eta$, where η is the quantum efficiency of the photodetector.

(b) Assume that the average power detected $p(t)$ with this photodetector is b_1/T, where T is the system bit period and that equal number of "1" and "0" is randomly received. Show that if the quantum efficiency is 1.0, calculate the minimum optical power (in mW and dBm) required at a bit error rate (BER) of 10^{-10} for a bit rate of 10 Gbps at an operating wavelength of 1550 nm.

Problem 2

A 1550 nm digital optical receiver for an STM-16 synchronous digital hierarchy (SDH) network is operating at 2.5 Gbps and has an effective noise bandwidth of 15 GHz. The PIN photodiode of the receiver has a negligible dark current and a quantum efficiency of 90%. The electronic preamplifier has an equivalent input resistance of 100 Ω and an equivalent noise current of 0.5 pA/(Hz)$^{1/2}$. Calculate the receiver sensitivity corresponding to a BER of 10^{-12}. How much does it change if the receiver is designed to operate reliably up to a BER of 10^{-15}?

Problem 3

Consider an optical receiver operating at 10 Gbps in SDH transmission STM-64 systems. It has an avalanche photodiode (APD) with an x-factor of 0.8 and a responsivity of 0.7 A/W. Its avalanche gain depends on the bias reverse voltage and is set at a value of 20. An electronic amplifier that follows the photodetector has an equivalent noise current density of 1.0 pA/(Hz)$^{1/2}$ and a 3 dB bandwidth of 20 GHz. For a system BER of 10^{-10}, calculate the receiver sensitivity.

Problem 4

A digital optical receiver consists of a PIN photodiode or an APD followed by an electronic amplifier with the following characteristics:

PIN-PD

- InGaAs type with a quantum efficiency of 0.8 average over the wavelength region of 1.2–1.7 μm,
- Dark current noise of 2.0 pA
- Total rise time and fall time of 1.0 ps
- Diode capacitance at a typical reverse bias of 0.5 pF.

APD

- Ge type with an x-factor of 0.9
- An average avalanche gain of 30 over the wavelength range of 1200–1700 nm

- Total dark current of 7.0 pA
- Total rise and fall time of 1.0 ps

Electronic Amplifier
Low input impedance type front end followed by a main amplifier and equalizer with a total equivalent noise spectral density of 1.0 pA/$(Hz)^{1/2}$ and an overall bandwidth of 20.0 GHz.

(a) For an STM-64 system bit rate of 10 Gbps and a BER of 10^{-10}, find the energy of the "1" pulse required at the input of the photodetector. You may assume that the probability density distribution of receiving "1" and "0" is Gaussian and equal. Hence, deduce the receiver sensitivity in dBm.

(b) The aforementioned receiver is to be considered for a new receiver configuration that is to be specified for two optical communications links with the following requirements:

(b1) Link 1: Optical communications between two supercomputers operating at a bit rate of 20 Gbps.

(b2) Link 2: STM-64 10 Gbps optical communications transmission systems using a single-mode optical fiber (Corning SMF-28) for the SDH ring of 400 km perimeter. Bidirectional transmission via a pair of optical fiber at 1550 nm wavelength regions is employed.

A number of optoelectronic components such as photodetectors and sources by Fujitsu, NTT Electronics, www.nel.co.jp, or other manufacturers are available from their websites. Select appropriate components and design the link.

Problem 5
An optical fiber communications link has the following components:

- Optical transmitter: InGaAsP laser diode operating in the region about 1550 nm with a spectral width of 0.1 nm.
- The laser power at the output of the fiber pigtail is 1.0 mW.
- The transmission fiber is Corning SMF-28.
- The receiver consisting of an InGaAs PIN photodiode that has a sensitivity of –28 dBm.

For a bit rate of 10 Gbps, plot the attenuation-limited transmission distance including a 0.1 dB connector loss at each end and a 5.0 dB system operating margin.

If EDF optical amplifiers of 30 dB gain and 5 dB noise figure are used, plot the optical power (dBm) as a function of distance—make sure that the distance between optical amplifiers is determined.

E.10 Problem/Question Set on OTDR for Optical Communications Systems and Networks

1. OTDR stands for
   (a) Optical tunable domain reflection
   (b) Optical transfer domain reflector
   (c) Optical time-domain reflectometer

2. Give an account on the main principle of the OTDR.
3. What is Rayleigh scattering? Show how this phenomenon in an optical fiber is measured using the OTDR technique. Sketch a typical trace of the OTDR showing this scattering loss in a single-mode optical fiber using the 1550 nm wavelength source in the OTDR.
4. Is Rayleigh scattering an intrinsic loss mechanism by lightwaves propagating through glass fibers or an extrinsic loss process?
5. What are the extrinsic losses in single-mode optical fiber communication systems?
6. What is the order of wavelength dependence of Rayleigh scattering?
7. Indicate the dead zone in the OTDR trace.
8. Sketch a typical OTDR trace indicating the loss of a mechanical connector.
9. Sketch the loss curves obtained by OTDR for optical fiber SMF-28 with and without 2 FC/PC connectors and 5 splices over 30 km length.
10. Sketch a typical OTDR trace of a sharp bend.
11. Indicate a typical trace of the reflection from the end of an optical fiber length? What if the end of the fiber is terminated with an index matching fluid?
12. What is the low-coherence time-domain reflectometer? (* = optional)
13. What is the OFDR? Explain how it works. (* optional)
14. What are typical sensitivity, dynamic range, resolution, etc., of the OFDR? (* = optional)
15. What is photon-counting OTDR? Explain how it works. (* optional)
16. What are typical sensitivity, dynamic range, resolution, etc., of the photon-counting OTDR?*
17. Sketch the OTDR trace of two spliced fibers together when one fiber has an MFD of 8.8 μm and the other 9.6 μm. What would this OTDR trace look like when measured from other directions? Using this knowledge, show how should an OTDR be used to measure the actual attenuation of a length of SMF.

E.11 Problem Set on Practical Optical Fibers

Question 1

(i) What are the attenuation of lightwaves of 1300 and 1550 nm wavelength when propagating through silica-based glass fibers?

(ii) What is the peak attenuation within this spectral range. Give reasons why Corning Inc. has spent time and money to develop SMF-28 for metropolitan optical networks.

(iii) Could you obtain a relationship between the loss or attenuation as a function of wavelength?

(iv) Examine the Corning single-mode fibers SMF-28 and SMF-28e which are available on email request and spot the differences between them. Give reasons why Corning spends time and money to develop SMF-28e for metropolitan optical networks.

(v) Write down the frequency responses of a standard single-mode optical fiber, including the phase and amplitude frequency responses.

Question 2

(i) Examine the Corning standard single-mode fiber SMF-28 and write down the principal parameters related to
   a. The geometrical aspects of the fiber
   b. The refractive index distribution
   c. The operation of the fibers when modulated lightwaves are propagating
   d. The impairments that may cause signal distortion

(ii) Repeat (i) for Corning LEAF fibers.

(iii) Repeat (i) for Corning dispersion compensating fibers, which are available on several websites, for example, avenex.com, jdsu.com, and corning.com (registration required).

(iv) Examine the dispersion factors given in these fibers. Why are there differences between them? Calculate the temporal broadening of lightwave pulse sequence of 10 Gb/s bit rate with lightwave carrier wavelength at 1550 nm and similarly at 1560 nm.

Question 3
If the wavelength channels in Question 2 part (iv) are used as optical carriers for optical transmission systems that are modulated with a data rate of 10 Gb/s using on–off keying non-return-to-zero (NRZ) format,

(a) Sketch the frequency spectrum of a single optical channel whose carrier wavelength is in the region of 1550 nm.

(b) Sketch the spectrum of all possible consecutive multiplexed optical channels in the spectral region of 1530–1565 nm.

(c) Repeat (b) for a data rate of 100 Gb/s. Comment on the spectrum of this part.

NOTE: You should refer to the materials on Digital Communications delivered in the last semester. You may also refer to the table of Fourier transform accompanying this problem set.

Question 4: Optical fibers
Refer to the technical data of the following fibers:

(i) Corning SMF-28, SMF-28e, LEAF, extract the following information:
   - Geometrical parameters: core diameter, cladding diameter, relative refractive index difference, attenuation versus wavelength, core eccentricity, and International Telecommunication Union (ITU) standard of the fibers
   - Operational parameters: MFD, effective area, cutoff wavelength or wavelength range (why range?), dispersion factor and its variation as a function of wavelength, dispersion slope thence deriving the values for beta 2 and beta 3, nonlinear coefficient, and PMD factor

(ii) Compare the parameters of these different fibers and give some applications in optical transmission systems and give reasons. Especially state why a large effective area LEAF fiber is preferred for long-haul transmission system.

(iii) Consider the dispersion factor of LEAF fiber and explain why the fiber is designed so that its zero dispersion is outside the operational spectrum of C- or S-band.

E.12 Question Set on Optical Filters, Muxes, Demuxes, and Fiber Nonlinear Impairment

(Problems marked with an asterisk (*) are for high distinction and those who wish to conduct further study/research in the field of optical communications.)

E.12.1 Optical Filters, Muxes, and Demuxes

Question 1
The WDM technique is a common method for increasing the total transmission capacity over a single-strand optical fiber. It is now widely employed in long-haul high-speed optical transmission systems throughout the world.

(i) Briefly explain the WDM techniques and state the typical wavelength or frequency spacing between the channels so that it can be named dense wavelength division multiplexing (DWDM) optical transmission systems.

(ii) What are the ***frequencies*** and ***wavelengths*** of these lightwaves so that they can be transmitted with minimum loss. You may consider the spectral regions called S-, C-, and L-bands of a silica-based single-mode optical fiber.

(iii) Sketch the structure of a long-haul optical transmission system using multiple spans with optical fibers, optical amplifiers, dispersion compensating fibers, optical filters as multiplexers and demultiplexers, and optical transmitters and receivers.

(iv) *Search the Internet and find at least one array waveguide multiplexer that would be able to satisfy your DWDM optical transmission system.

NOTE: Velocity of light in vacuum is c = 299,792,458 m/s. Can you state the reasons why this velocity must be very accurate?

Question 2: Optical filter using Mach–Zehnder interferometers

(i) Sketch the basic structure of a symmetric and an asymmetric Mach–Zehnder interferometer.

(ii) Obtain the optical intensity transmittance between an input port and the other two output ports, for example, T_{11} and T_{12}. Hence, show that a complete power transfer can be achieved with a total phase difference of π. You may select to state the relationship of the transmittance or derive the equations.

You could use the z-transform to obtain the transmittance of the filter and thence the continuous transmittance with an appropriate substitution of the z-variable. Hence, determine the zeroes and poles of the transmittance. Sketch the poles and zeroes on the z-plane.

*How close the zeroes of the transfer function to the unit circle should be so that the filter passband can provide the highest filtering property? Determine the frequency of the cutoff band (–20 dB from the 3 dB roll-off). Sketch the filter passband. Explain the physical meaning of the zeroes and poles of the transfer function.

(iii) Now with and without using the equations, can you explain the mechanism of coupling and filtering of optical waves?

(iv) Now consider silica-on-silicon interferometric filters of the previous parts. The effective refractive index of the single-mode waveguide of the filter is assumed to be 1.4465 at 1550 nm. Estimate the propagation constant β of the guided wave. Hence, estimate the difference length of an asymmetric interferometer so that a complete filtered channel can be achieved at the cross output port.

(v) If there are some fabrication errors of the path difference, then could you suggest a method so that the filter can be tuned to the exact filtering property?

(vi) If the delay difference path is now set to be 1-bit long for a 10 Gb/s phase modulation system, suggest a function of this interferometer. Now suppose two consecutive bits of a data sequence of 10 Gb/s whose optical carrier are "0" and "π" phase or "π" and "π" phase or "0" and "0" phase. Work out the intensity of the outputs of the interferometer under these receiving conditions.

(vii) Determine the length of the delay path of the interferometer so that a 1-bit delay can be achieved for part (vi).

Question 3: Ring resonator filter

(i) Refer to the ring resonator given in lecture set 6. State the power transfer function $H_{11}(z)$ or $H_{11}(\omega)$ including the frequency responses of its power amplitude, its phase, and its group delay and dispersion. Use MATLAB to plot these frequency responses. What is the resonant frequency and the 3 dB bandwidth of the filter, hence its Q-factor? If the resonant frequency is to be set at the equivalent vacuum frequency with wavelength of 1550 nm, what is the length of the ring resonator? The effective refractive index of a guided wave at 1550 nm of the ring resonator is 1.448.

(ii) Thence, by cascading at least two ring resonators, obtain the frequency responses for the power amplitude and phase. This part is best achieved by using the $H_{11}(z)$, that is, the transfer function would have multiple identical poles. Hence, obtain its corresponding group delay and dispersion at the resonant wavelength.

(iii) * How close the poles of the transfer function to the unit circle should be so that the filter passband can provide the highest filtering property? Determine the frequency of the cutoff band (–20 dB from the 3 dB roll-off). Sketch the filter passband. Explain the physical meaning of the poles of the transfer function.

(iv) * If there are losses of lightwaves propagating in the ring, how would you correct this loss so that the poles of the resonator can be set close to the unit circle?

(v) Now that the frequency of the input lightwaves can be shifted to the right or to the left of the resonant peak frequency, obtain the dispersion factor at these edges of the filter passband.

(vi) If the ring resonator is used as a dispersion compensator of a 100 km standard single-mode optical fiber (about +17 ps/nm/km depending on the wavelength), determine the wavelength at which the resonator should be operating so that a complete compensation can be achieved.

(vii) Comment on the stability of the optical ring resonator and that of the interferometric filter of Problem 2.

Question 4
Referring to the lecture notes on optical filters (Section 6), the frequency response of the power transmittance of an FP optical filter is given by

$$G_{PF} = \frac{1}{1+\left[\frac{2\sqrt{R}}{1-R}\sin\left(\frac{2\pi nL}{c}f\right)\right]^2}$$

(a) Sketch the structure of the FP filter and indicate all the parameters of the equation in this diagram.

(b) State the assumptions and approximations for the derivation of this transfer function.

(c) Determine the frequencies or wavelengths of the resonant peaks. Hence, the free-spectral range as a function of n, L, and R. Hence, sketch the frequency response of the power transfer between the input and output ports of the filter.

(d) Determine the 3 dB bandwidth of the filter as a function of n, L, and R, thence the Q-factor of the filter and its finesse. Determine the cutoff frequency of the filter passband at which the power is –20 dB from the 3 dB roll-off point.

(e) Tunable filter. The center frequency of the FP filter can be tuned so that it can be matched with the center wavelength of a received data channel. What parameter can be changed so that the center passband of the filter can be tuned?

(f) If the FP filter is used for filtering noises of the optical amplifier, the amplified spontaneous emission (ASE) noise, determine the finesse of the filter for ASE noise reduction at a center wavelength of 1565 nm and a bandwidth of 0.1 nm.

Question 5: AWGs

(i) Based on the information provided in the lecture notes and the manufacturer's website (e.g., www.avenex.com, www.jdsu.com), sketch the structure of an integrated optic AWG. State the physical mechanism of the filtering property of the AWG. You may note the path length difference between waveguide channels, hence the interference effects.

(ii) Provide the operation parameters such as center wavelength or frequency spacing, number of channels, insertion loss, and passband cutoff wavelength for an AWG, which can be used either as a multiplexer or as a demultiplexer in a 50 GHz spacing DWDM optical transmission system.

(iii) If the average power at the output pigtail of an optical modulator of an optical transmitter is –10 dBm. The output lightwave is launched into the AWG multiplexer of (ii) and a total average power into the transmission fiber is 10 dBm for 44 optical channels is required, find out whether there needs of optical amplification. If it does, then what is the required gain of the optical amplifier?

Question 6: Fiber Bragg grating (FBG) as an optical filter and a dispersion compensating device
Consider the passband reflectance and its group delay characteristics of an FBG as shown in Figure E.1.

(i) What are the center wavelength of the passband and the 3 dB bandwidth (passband) of the filter? Note that the transfer characteristic is plotted in linear scale.

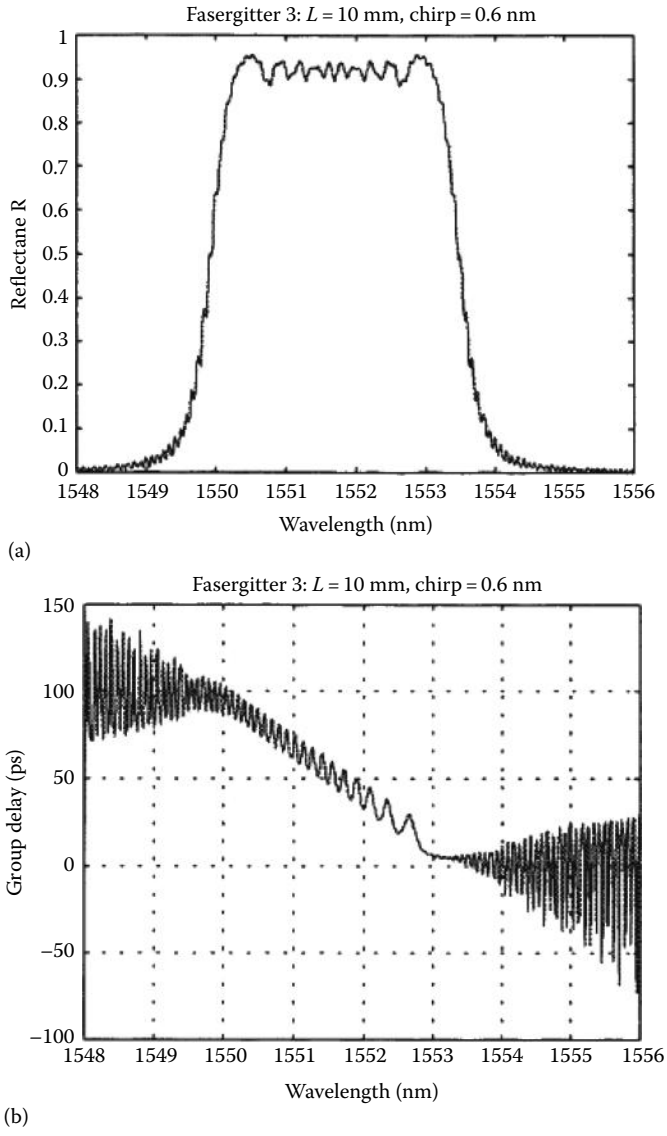

FIGURE E.1
Frequency responses of an FBG filter: (a) Frequency response—power versus wavelength, (b) group delay response.

(ii) The group delay is measured using a tunable laser source launched into one end of the FBG. Determine the average dispersion factor of the FBG in ps/nm. Note the sign of the dispersion factor. If you want to reverse the sign of the dispersion, suggest what could you do to the FBG to achieve this? Give your reasons.

(iii) If this FBG is used for compensating a length of standard single-mode fiber, determine the length of the fiber.

(iv) Comment on the ripple of the group delay and its effects on the total dispersion characteristics when it is used for dispersion compensation.

(v) Obtain the transmittance of the FBG.

(vi) Show how you can connect the FBG to an in-line optical system to compensate for any residual dispersion of the fiber transmission line. You are suggested to use the FBG together with an optical circulator.

Question 7: Optical coupler

A 2 × 2 coupler has an intensity coupling coefficient of 0.5. This is called a 3 dB coupler.

(i) Write down the transmittance matrix of the coupler.

(ii) Write down the relationship between the output optical fields and the input fields for the coupler.

(iii) Sketch the signal flow model of the coupler.

Question 8

Consider a Mach–Zehnder interferometric filter as shown in the following.

(i) Write down the transmittance matrices for the two couplers and the middle section.

(ii) Write down its relationship with the input and output fields at the input ports 1,2 and the output ports 1,2.

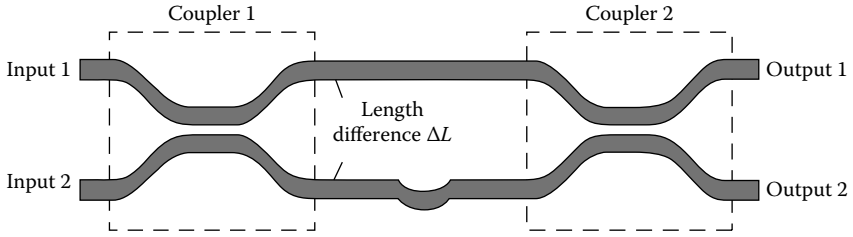

(iii) Sketch the signal flow graph of the filter and thence show that for a delay length ΔL, which is equivalent to the traveling time of a bit period, the output field E_{01} and E_{02} and its input field E_{i1} can be written as

$$E_{01}(z) = H_{11}(z)E_{i1}(z) = \left(1 + z^{-1}\right)E_{i1}(z) = z^{-\frac{1}{2}}\left[z^{+\frac{1}{2}} + z^{-\frac{1}{2}}\right]E_{i1}(z)$$

where $z = e^{j\beta L} = e^{j\omega t}$ is the "unit sampled delay." Plot the zeroes and poles of the transfer function on the z-plane and hence the transmittance frequency responses of the filter.

E.12.2 Optical DWDM Network Elements

E.12.2.1 Optical Components: Add/Drop Muxes

Question 1

WDM and DWDM networks are now installed throughout the global communication backbone networks.

(i) Define the wavelength or frequency spacing between channels for dense and coarse WDM systems and networks.

(ii) Give reasons why Corning fibers SMF-28e and SMF-28 (ITU G.652 standard) are usually selected for CWDM and DWDM in metropolitan networks. What is the main difference between these types of fibers?

(iii) What are the typical wavelengths that can be used for CWDM? Give reasons. Hint: consider downloading and uploading speed and refer to pages 7–14 of the lecture notes.

(iv) Refer to the Chapter 3 and specify the spectral regions for the S-, C-, and L-bands for silica-based optical fibers.

(v) For the transpacific transmission systems with a total capacity of 1806 Gb/s in 2006 and a 10 Gb/s wavelength channel, how many wavelength carriers are required to carry this capacity? If they are to be transmitted in the C-band, then determine the frequency spacing between the channels.

(vi) Sketch a DWDM optical transmission system with optical transmitters, multiplexers, amplifiers, dispersion compensators, and demultiplexers and receivers. Indicate in your system whether the signals are in the optical or electronic domain.

Question 2

(i) What are DXC and ADM and LTE in an optical network? You may explain with a sketch of the structure of an optical network.

(ii) Sketch the structure of a cascade of Mach–Zehnder interferometers that would form a 2-channel and 4-channel wavelength demultiplexers. If the wavelength channels are separated by 50 GHz, determine the delay length L.

NOTE: The reference BH. Verbeeck et al., "Integrated four-channel Mach-Zehnder Multi/Demultiplexer fabricated with Phosphorous Doped SiO_2 Waveguide on silicon," *IEEE J. Lightwwave Tech*. The condition for splitting the wavelength channels l and 2 to the two output ports is given as

$$2\pi n_{eff}\Delta L\left(\frac{1}{\lambda_1}-\frac{1}{\lambda_2}\right)=\pi$$

where n_{eff} is the effective guided refractive index of guided mode and λ_1, λ_2 are the wavelengths of two consecutive channels.

Question 3

(i) Sketch a possible structure of the open systems interconnection (OSI) layer model.

(ii) Give a structure of the super-high frequency (SHF) model and how data channel can be integrated from STM-1 to STM-16, likewise for synchronous optical network (SONET).

(iii) Show clearly how the data formats of SHF or SONET can be integrated into optical transmission system.

Question 4: Optical switching

(i) Sketch a structure of an 8 × 8 switching matrix for Benes strict-sense nonblocking and rearrangeable nonblocking architectures. Comment on the advantages and disadvantages of these structures.

(ii) What is the typical switching speed of the optical switches of part (i)? Compare their speed with that of the electromechanical switches.

Question 5

A wavelength router can be designed using a wavelength converter and an optical demultiplexer. A wavelength converter is usually formed in a semiconductor optical amplifier (SOA).

(i) Sketch the structure of this wavelength router.

(ii) Refer to pages 7–21 of the lecture notes and sketch the structure of a wavelength "add/drop" multiplexer.

(iii) Use the wavelength router of part (i) in the design of the wavelength add/drop of part (II).

Question 6: Interchannel and intrachannel cross-talk penalty

(i) Consider an optical add/drop multiplexer as shown in the following figure.

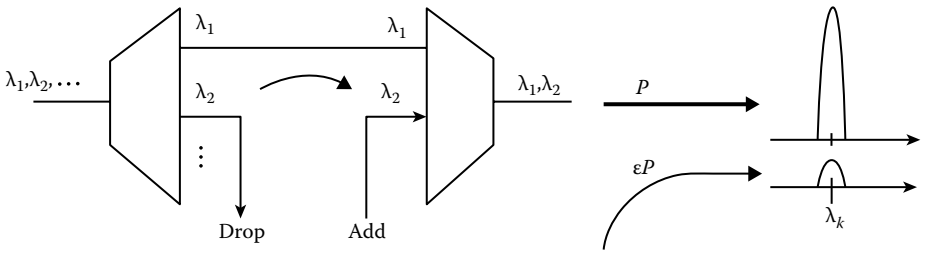

(i) If a –20 dBm optical power of the channel of wavelength next to the channel exists in the channel, estimate the penalty of the eye diagram due to this interchannel cross talk. The average power of the channel is –10 dBm.

(ii) Now if the same amount of optical power of the optical channel on the left of the operating channel is residual in this channel, reestimate the eye penalty.

(iii) A DWDM transmission system has an interchannel spacing of 50 GHz and an average optical power of each channel is –10 dBm. The C-band has been filled with all channels. Estimate the number of channels that are contained in the C-band 1530–1565 nm. The data bit rate is 40 Gb/s and the modulation is return-to-zero (RZ) amplitude-shift keying (ASK).

(iv) An optical filter is now used to extract the channel of wavelength 1552.93 nm, which has a characteristic center wavelength of 1552.93, an optical bandwidth of 40 GHz (3 dB), and a roll-off of –12 dB per decade.

a. Sketch the spectral distribution of all data channels.

b. Sketch the filter frequency response.

c. Estimate the power residual of the other wavelength channel onto this channel and hence estimate the eye penalty due to this cross talk. What kind of cross talk is this, interchannel or intrachannel? You may assume the pulse shape of the data bits being of perfect rectangular or Gaussian.

d. What can you propose to reduce the power penalty to the eye opening?

HINT: You may refer to the theoretical analyses given in pages 7–6 of the lecture notes or page 303 in the textbook by R. Ramaswami, K. N. Sivarajan, "Optical Networks."

Question 7: Self-phase modulation effects
The nonlinear coefficient due to the intensity of lightwave propagating in a silica fiber is given by $n_2 = 2.5 \times 10^{-20}$ m^2/W. A Gaussian-guided mode lightwave is propagating through a length L of standard single-mode optical fiber. Its average optical power is 10 dBm.

(i) What is the effective area of the standard single-mode fiber, that is, the ITU Standard G.652?

(ii) What is the intensity imposed on the cross section of the standard single-mode fiber?

(iii) The change in the refractive index of the silica fiber can be given by $\Delta n_{NL} = n_2 I$. Estimate this change in the refractive index of the fiber due to the propagation of this guided mode.

(iv) Obtain the change in the phase of the lightwave carrier at 1550 nm after propagating through a length L (km). Hence, estimate the fiber length so that the nonlinear phase change is less than or equal to 0.1 rad.

(v) *Refer to the lecture notes, write down the Schrödinger wave equation in which the nonlinear effects such as the self-phase modulation are included. Make sure that you state clearly the meaning of all variables and notation of this equation. Refer to pages 7–9 of the lecture notes. By using a diagram, explain the split-step Fourier method that can be used to represent and model the propagation of the complex envelope of the lightwave through an optical-guided fiber/waveguide.

E.12.3 Fiber Impairments

Question 8: Nonlinear four-wave mixing (FWM)

(i) Give a brief account of FWM. Indicate clearly the mixing of the waves and the generated wavelength channel.

(ii) Give a condition of the fiber dispersion so that there are significant impacts of FWM on transmission systems. Sketch the generated waves that interfere with other DWDM channels.

(iii) Refer to pages 7–13 of the lecture notes. Sketch the maximum transmitted power per channel versus fiber distance and specify the average power per channel that must be satisfied so that the transmitted channels would not be affected by the FWM.

E.13 Problem Set on Advanced Modulation Formats for Long-Haul Transmission Systems

Question 1
A bit pattern "1 1 0 1 0 0 1 1 0 1" with a bit rate of 10 Gb/s is input into two separate modulators to generate ASK and binary differential phase-shift keying (BDPSK) modulation formats.

(a) Sketch the modulated bit pattern including the carrier that can be drawn with two or three periods within the duration of a bit period. Hence plot the phase distribution or the scatter diagram of the modulated sequence.

* This part is for high distinction–level students

(b) An MZIM is used as an optical modulator; its $V\pi$ is 5 V. Show how the data sequence can be conditioned to feed into the electrode port of the modulator so that ASK or BDPSK signals can be generated. Make sure that you show the biasing voltage.

(c) Repeat (b) in case of a dual-drive type of optical modulator.

(d) Give a structure of a precoder for DPSK modulation. That is the precoder that would generate the differential codes that are then used to drive the optical modulator with signal conditioning to appropriate levels for driving the electrodes.

Question 2: Optical modulator and phasor diagram

Sketch the schematic diagram of an intensity optical modulator which consists of an optical waveguide as the input light guide. This waveguide is then split into two parallel paths whose refractive indices would be modulated by an electrode, hence a phase modulation of the lightwaves that pass through these waveguides. This type of optical modulator can be termed as an interferometric intensity modulator.

(a) For a single-drive modulator, only one path of the lightwave is modulated. What is the total phase change exerted on the lightwaves if the following parameters are employed for the optical modulation: electro-optic coefficient: $r = 10^{-11}$ m/V……., electrode length = 10 mm, separation between active electrode and earth electrode = 5 μm?

   i. Estimate the change in the refractive index due to the applied voltage via the electro-optic effect.

   ii. Estimate the change in the velocity of the lightwave.

   iii. Estimate the total phase change over the electrode length, noting that a phase change of 2π is equivalent to the slowing down of one wavelength.

   You may confirm that the phase change can be given by $\Delta\phi = \frac{c\Delta n}{n^2} L \frac{2\pi}{\lambda}$

(b) Estimate the voltage required for applying to the electrode so that a π phase change occurs on the lightwave carrier passing through it.

(c) Write down an expression that represents the lightwave at the input. Thence those for the split waves propagating in the two parallel lightpaths of the interferometer. Represent their phasors in a plane.

(d) Then find the sum of the two phasors and hence project this total phasor vector on the real axis and obtain the equation of the lightwave at the output of the modulator as a function of the applied voltage *V*.

Question 3b:

The following figure shows the pulse sequence and its optical modulated spectrum for NRZ and RZ formats.

(i) What is the bit rate of the sequence?

(ii) Examine the spectra and identify their principal features such as the lightwave carrier and its power, and the 3 dB bandwidth of the passband spectrum. Thence, compare the 3 dB of RZ and NRZ modulation formats. What modulation schemes can we derive from the spectra?

NRZ modulation with cosine edge pulses

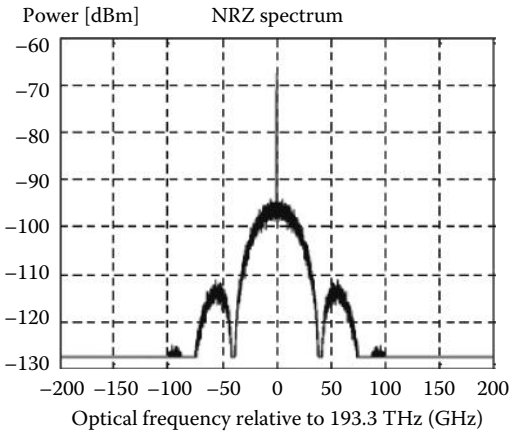

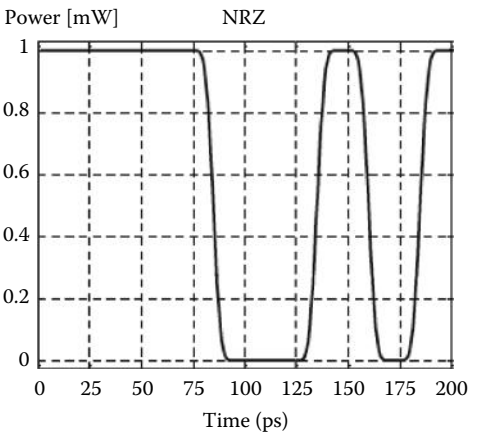

RZ modulation with 50% duty cycle

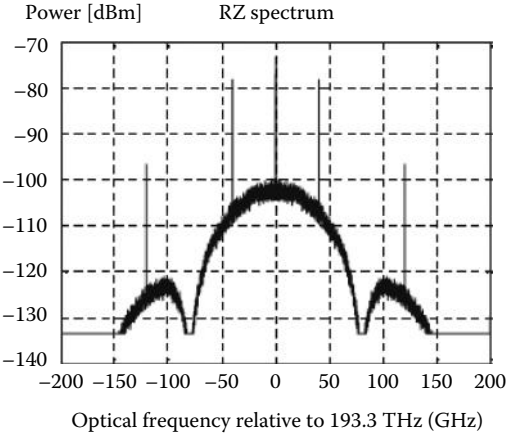

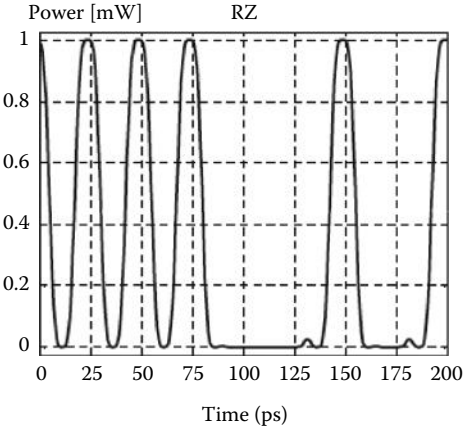

NOTE: Vertical scale should be from 10 dBm and the 10 dB per division.

Question 3c

A "carrier-suppressed RZ" optical transmitter is shown here.

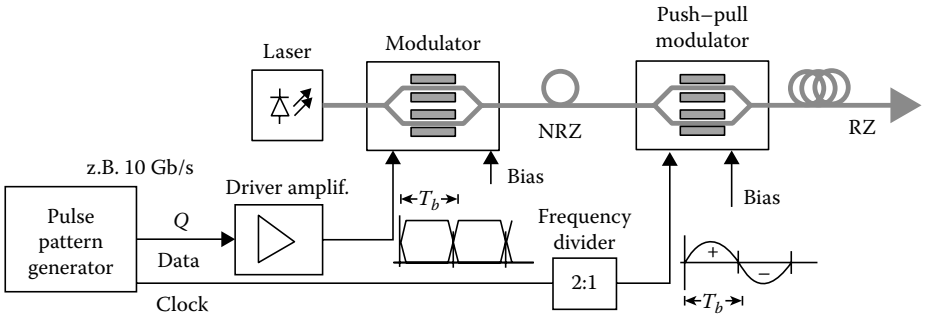

(i) Sketch the time-domain pulse sequence over a 10-bit period for a bit rate of 40 Gb/s at the output of the pulse pattern generator.

(ii) Give a brief description of the principles of the suppression of the carrier. Which component of the transmitter would implement the suppression?

(iii) What are the functions of the laser, the modulator, and the push–pull modulator? If the V_π for the two modulators is 5 V, sketch the transfer characteristics of the modulators—that is, the output power versus the input driving voltage. Make sure that you set appropriate biasing voltages for the modulators. The output power of the laser is 10 dBm and the total insertion loss for each modulator is 4 dB. For the pulse pattern generator, the output power at the output port data is 10 dBm and that at the clock output port is 2 Vp-p. All line impedances are 50 Ω.

(iv) Is it necessary to use a booster optical amplifier to increase the total average power launching into an optical fiber for transmission? If it does, then what is the gain and noise of the optical amplifier? Note that the nonlinear limit of a standard single-mode fiber is around 5 dBm.

(v) Sketch the spectra at the outputs of the laser, the modulator, and the push–pull modulator.

Question 4: Optical modulator and phasor diagram—dual-drive MZM.

(a) Repeat Question 3 with a bias voltage of $V_b = V_\pi/2_\pi$ and $V_b = V_\pi$ and a time-varying signal of $v_s(t) = \frac{V_\pi}{2}\cos 2\pi f_s t$ with $f_s = 20$ GHz.

(b) Now the modulator is a dual-drive MZM, repeat Question 1 with a bias voltage of $V_b = V_\pi/2$ and $V_b = V_\pi$ and a time-varying signal of $v_s(t) = \frac{V_\pi}{4}\cos 2\pi f_s t$ with $f_s = 20$ GHz.

Question 5

An optical fiber communication system consists of the following:

- An optical transmitter using a 1550 nm DFB laser with a linewidth of 10 pm (picometers), an external optical modulator whose bandwidth is 20 GHz, and a total insertion loss of 5 dB.
- The modulator is driven with a bit pattern signal generator with a 10 dBm electrical power output into a 50 Ω line. A microwave amplifier is used to boost the electrical data pulse to an appropriate level for driving the optical modulator. The data bit rate is 10 Gb/s and its format is NRZ.
- An 80 km standard single-mode fiber is used for the transmission of the modulated signals.

(i) Sketch the block diagram of the transmission system. You may refer to pages 8–2 of the lecture notes.

(ii) If the V_π of the external modulator is 5 V, what is the gain of the microwave amplifier so that an extension ratio of 20 dB can be achieved for the output pulses of "1" and "0" at the output of the modulator? Make sure that you sketch the amplitude and power output of the modulator versus the driving voltage into the modulator. What type of connector that you would use for connecting the microwave amplifier to the modulator and that to the bit pattern generator.

(iii) If the DFB laser emits 0 dBm optical power at its pigtail output, then what is the average optical power contained in the signal spectrum? You may assume that the pulse sequence generated at the output of the bit pattern generator is a perfect rectangular shape.

(iv) What is the effective 3 dB bandwidth of the signal power spectrum? Estimate the total pulse broadening of the pulse sequence at the end of the 80 km fiber length. Similarly, estimate the pulse sequence if the bit rate is 40 Gb/s.

(v) Now if a dispersion compensating fiber of 20 km is used to compensate for the signal distortion in the 80 km fiber, what is the required dispersion factor of this fiber so that there would be no distortion? If the loss of the dispersion compensating fiber is 1.0 dB/km at 1550 nm, estimate the average optical power of the signal at the output of the dispersion compensating fiber.

(vi) Based on the dispersion limit given in the following, plot the dispersion length as a function of the bit rate for NRZ format.

NOTE: The dispersion limit, under linear regime operation, can be estimated in the following equation (Ref. Forgheti et al.* 1997):

$$L_D = \frac{c}{\lambda} \frac{\rho}{B_R{}^2 D}$$

where
B_R is the bit rate
D is the dispersion factor (s/m^2)
ρ is the duty cycle ratio, that is, the ratio between the "on" and "off" in a bit period
L_D is in meters

Question 6
Repeat Question 1 for RZ format and ASK modulation. Sketch the structure of the optical transmitter. Note that an extra optical modulator must be used and coupled with the data modulator of Question 1, the optical pulse carver. Give details of the pulse carver including driving voltage, driving signal, and synchronization with the data generator.

Question 7: Spectral efficiency

(a) A DWDM optical transmission system can transmit optical channels whose channel spacing is 100 GHz. What is the spectral efficiency if the bit rate of each channel is 40 Gb/s and the modulation is NRZ-ASK?

(b) Repeat (a) for RZ-ASK modulation format.

(c) Repeat (a) and (b) for the channel spacing of 50 GHz.

* Forghieri et al., RZ versus NRZ in nonlinear WDM systems, *IEEE Photonics Technology Letters*, vol. 9, No.7, July 1997, pp 1035–1037.

Question 8

(a) Give a structure of an optical transmitter for generation of RZ-ASK modulation format. Make sure that you assign the optical power of lightwaves generated from the light source and at the output of the optical modulators so that a maximum of 10 dBm optical power is launched into the standard single-mode fiber so that it is below the nonlinear SPM effect limit.

(b) Describe the operation of the optical modulator, the pulse carver, so that it can generate a periodic pulse sequence before feeding into the data generator. Make sure that you provide the amplitude and intensity levels versus the driving signal voltage levels, which are used to drive the optical modulators.

Question 9: Nonlinear SPM effect

The nonlinear refractive index coefficient of silica-based standard single-mode fiber is $n_2 = 2.5 \times 10^{-20}$ m^2/W.

(a) What is the effective area of the standard single-mode fiber? You can refer to the technical specification of the Corning SMF-28 and its MFD to estimate this area.

(b) Estimate the change in the refractive index as a function of the average optical power. Hence, estimate the total phase change due to this nonlinear effect after propagating through a length L (in km) of this fiber.

(c) Estimate the maximum length L of the standard single-mode fiber that the lightwaves can travel so that no greater than 0.1 rad of the phase change on this lightwave carrier would be suffered.

(d) Show how you can generate a format that would have an RZ format and a suppression of the lightwave carrier. Show that the width of the RZ pulse on this case is 67% of the bit period. Hint: you may represent the lightwaves in the path of the optical modulator with an optical interferometer by using phasors. First, sketch the phasor of the input lightwave, those of the two paths, and then the phase applied onto these paths. Then sum up to give the resultant output. For the pulse width, you can estimate the width over which the amplitude falls to $1/\sqrt{2}$ of its maximum.

(e) Now show how you can generate RZ pulse sequence with 50% and 33% pulse width of the bit period.

Question 10: Balanced Receiver

(a) Sketch the schematic diagram of an optical balanced receiver—a balanced receiver would consist of a delay interferometer and a back-to-back connected pair of photodetector with its output connected to the input of an optical preamplifier.

   i. What is the functionality of the delay interferometer? What is the temporal length of the delay unit?

   ii. What are the roles of the two optical couplers and their ideal coupling coefficients?

   iii. What is the relationship between the two output ports of the delay interferometer?

(b) Suppose that a sequence of 4 bits of a DPSK 10 Gb/s data channel is presented at the input of a balanced receiver. The phases of the lightwave carrier contained within these four bits are [π, π, 0, π] at the transition of the bit period.

i. Sketch the carrier wave and the pulse envelope. The lightwave has a wavelength of 1550 nm; however, to illustrate the wave, you are expected to sketch only a few periods of the waves contained within the bit period at the input of the receiver.

ii. Sketch the electrical signal at the output of the electronic preamplifier not including noises.

iii. Now assuming that an optical amplifier is used as an optical preamplifier placed at the input of the balanced receive that would give an optical signal power of –10 dBm for the DPSK sequence. The responsibility of the photodetector is 0.9 and the electronic preamplifier has a transimpedance of 150 Ω and a total equivalent noise current spectral density of 2 pA/(Hz)$^{1/2}$ and a bandwidth of 15 GHz. Sketch the signal waveform at the output of the electronic preamplifier.

Question 11: Duobinary modulation format

(i) Design a block diagram of a precoder that would generate trilevel modified duobinary format signals. Make sure that the coefficients of the filters are specified. Hence, derive the spectrum of the signals after the precoder of the modified duobinary.

(ii) If possible, obtain the precoders for alternate mark inversion (AMI), duobinary, and their frequency responses. Compare the frequency responses of the three modulation schemes.

(iii) Sketch the structure of the trilevel duobinary precoder with its output of –1, 0, +1.

(iv) Then show how to use the coded signals to drive a dual-drive MZIM to generate optical duobinary signals.

Question 12: Duobinary modulation format

Duobinary is a modulation format that would allow the detection of the modulated signals, which is a special case of partial response coding (see lecture notes on digital communications).

- Give a brief account of the principles of operation of this line code.
- A duobinary coder using delay and add coding structures are shown in the following. If a three-level duobinary-coded signal is required, design the precoder for this type of modulation.

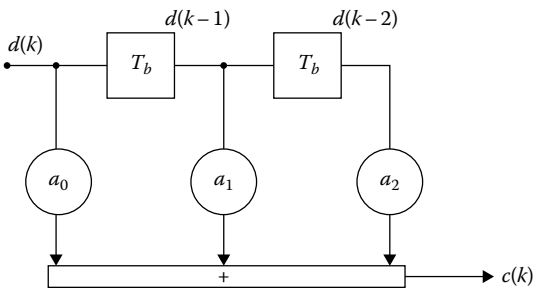

- Now if setting the delay time Tb is that of a bit period, transform the structure into the z-transform diagram and hence obtain the transfer function of the coder in the z-domain, thence the frequency response of this coder. Plot the frequency response of the transfer function of the filter in continuous domain.
- Find the impulse response of the coder, hence the term partial response.
- Sketch a block diagram that shows the functionality of precoding, coding, trilevel conversion (offset), and decoding.
- A binary sequence $d(k) = \{0\ 0\ 1\ 1\ 0\ 1\ 0\ 0\ 1\}$ is applied to the input of the duobinary coder. Determine the data sequences $b(k)$, $c(k)$, and $c'(k)$ in the electrical domain, which can be used to modulate an optical modulator.
- Assuming that there is no dispersion in the transmission of the duobinary data sequence, find the output pulse sequence at the output of the decoder. What is the physical realization of the decoder? Thence, sketch the sequence at the output of a decision circuit.

Now the electrical signals are applied to a microwave amplifier that would condition the signals to appropriate signal levels so as to modulate the optical modulator. The measured spectra are recorded as shown in the following diagrams.

Determine where in the block diagram (Figure E.2) that each of the spectrum belongs to the points of the diagram of the transmission system.

Question 13: Differential quadrature phase-shift keying (DQPSK)
DQPSK is a 2-bit per symbol modulation, that is, 2 bits/symbol; thus, the scheme is spectral efficient.

(i) Give a brief account of the modulation schemes DPSK and DQPSK.
(ii) Give a structure of a precoder for DPSK, which gives a differential phase modulation as the codes for "1" and "0."
(iii) Now extend this precoder and the phase quadrature modulation technique for the structure of a DQPSK optical transmitter.

Question 14: Single-sideband (SSB) and double-sideband (DSB) modulations
Referring to Figure E.2a through c for generation of optical signals with SSB,

(a) State the functionality of the Hilbert transformer. Hence, could you deduce a general principle for suppression of a sideband to generate SSB signals?
(b) What is the role of the phase shifter $\pi/2$?
(c) Explain the operation of the optical SSB transmitter, in both time and frequency domain. Confirm that the spectrum is correct.

Question 15: Coherent optical communication systems
Sketch a structure of an optical coherent receiver. Give a brief description of the roles of each component in your system.

What is the typical modern linewidth of the laser that acts as the local oscillator?

Give a distinction between the homodyne and heterodyne coherent system.

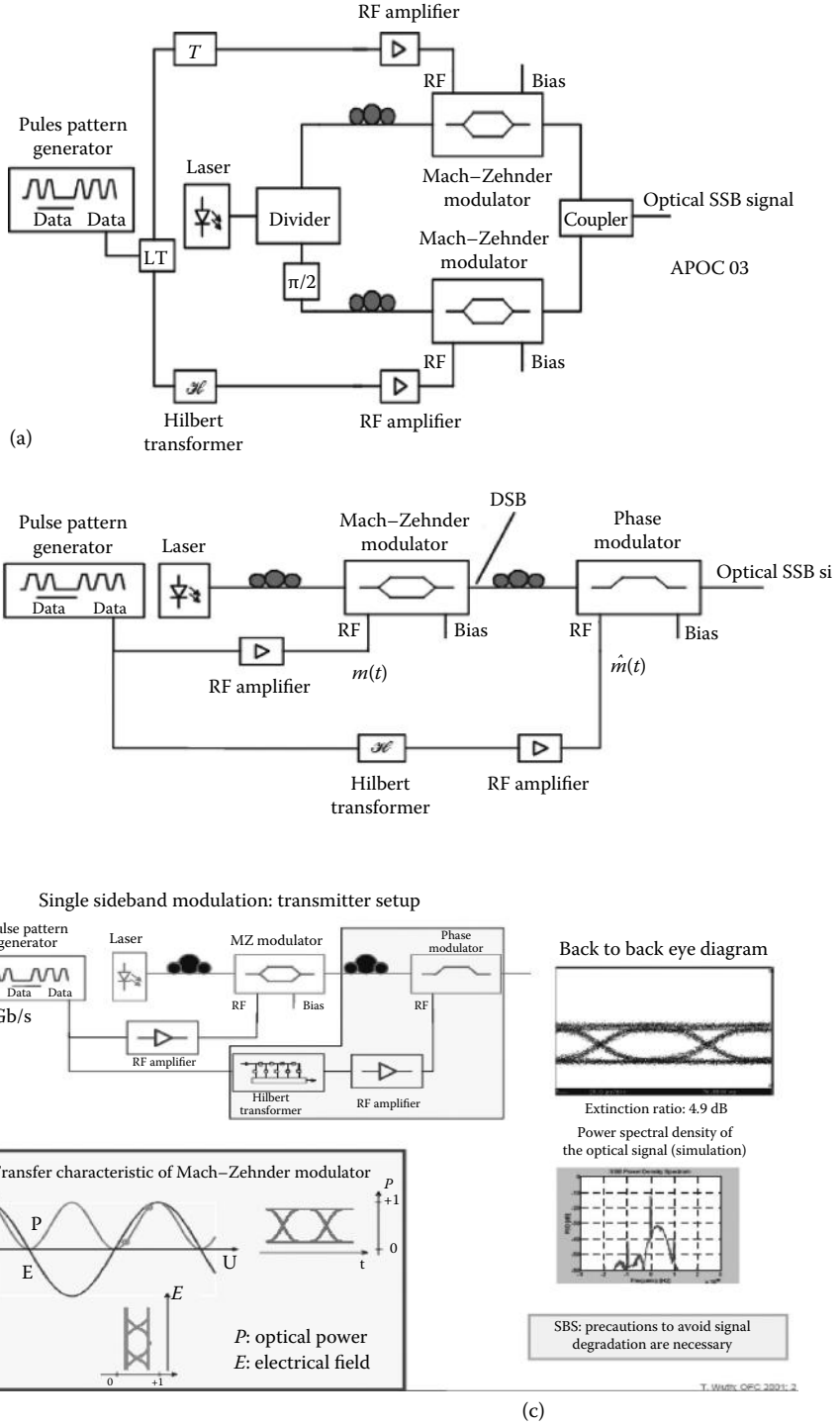

FIGURE E.2
SSB modulation and generation using (a) transform in optical domain, (b) transform in electrical domain, and (c) realization of an SSB optical transmitter.

A homodyne optical receiver has the following parameters:

a. A photodetector with a responsibility of 0.9 is followed by an electronic preamplifier whose total equivalent noise spectral density is 5 pA/(Hz)$^{1/2}$ and an electrical bandwidth of 15 GHz. The transmission bit rate is 10 Gb/s.
b. The local oscillator is a tunable laser source with a linewidth of 100 MHz. The wavelength in vacuum of both the signals and the local oscillator is 1550.92 nm. The average optical power of the local oscillator coupled to the photodetector is 0 dBm.

Sketch the structure of the receiver and then its equivalent small-signal circuit, which includes the generated electronic signal current at the output of the photodetector and the total noise currents looking from the input of the electronic preamplifier. What is the dominant noise source in this receiver?

For an optical signal with an average power of –20 dBm, estimate the signal-to-noise ratio (SNR) at the output of the photodetector.

Recalculate the SNR of the receiver if the frequency of the local oscillator is 20 GHz away from that of the signal carrier frequency.

E.14 Problems on Digital Optical Receiver for Optical Communications Systems and Networks

E.14.1 Optical Communications Systems Design: Mini Project

Network Distribution	Australian Ultra-Wideband Optical Fiber Backbone Networks
Transmission link distance	Melbourne–Sydney (air km x 1.25); Sydney–Brisbane; Brisbane Alice Springs (NT)–Port Headland (WA); Port Headland–Perth; Perth–Kalgoorlie–Port Augusta–Adelaide; Adelaide–Melbourne; and Melbourne–Hobart. Hanoi–HCM City–Can Tho (underseas or terrestrial routes)
Transmission techniques	DWDM techniques with SDH technology STM-64 9953 Mb/s NRZ format
BER	$<10^{-12}$—to be confirmed with numerical simulation
Network configuration	SDH ring (suggestion: double ring with optical cross connect near Canberra)
Total capacity	10 Gbps × 32 wavelength channels or 10 Gbps × 16 wavelength channels
Wavelength regions	Suggested C-, L-, or S-bands 1485–1625 nm
Optical channel frequency spacing	50 GHz, 100 GHz, or 200 GHz or narrower (25 GHz spacing between channels) if possible
Transmission medium	SMF-28 (G.652 ITU standard) with dispersion compensating techniques (fiber or chirped transmitters) or NZ-DSF, e.g., LEAF, TrueWave
Fault monitoring systems	OTDR and wavelength channel fault identification—specify OTDR management system
Optical amplifiers	Erbium-doped fiber amplifiers and/or Raman fiber amplifiers
Photonic components	DWDM multiplexers/demultiplexers, couplers, etc., available from websites or laboratory of optical communications
Transmitters and receivers	Refer to commercial products at manufacturers' website, e.g., www.nel.co.jp, www.jds-uniphase.com, www.nortelnetworks.com, www.lucent.com, www.fujitsu.com

Suggestions:

- Build a technical case for the optical fiber transmission systems and networks
- Build a business case for a rollout of a new network linking the capital cities in Australia. You should consider the following: (a) Base the case on carrying bulk data (IP over SDH to remove cost of provision of an ATM layer). (b) Assume that the incumbent is currently operating on 2.5 Gb/s equipment over fibers up to 15 years old.
- Based on the technical design of the network, present a business case requesting funding from a venture capitalist to build the network.

Design groups: Suggestion—groups of 3–6 engineers to design sections of a terrestrial Australian ultra-broadband ring network or Vietnam undersea or terrestrial transmission routes

E.14.2 Transform Pairs

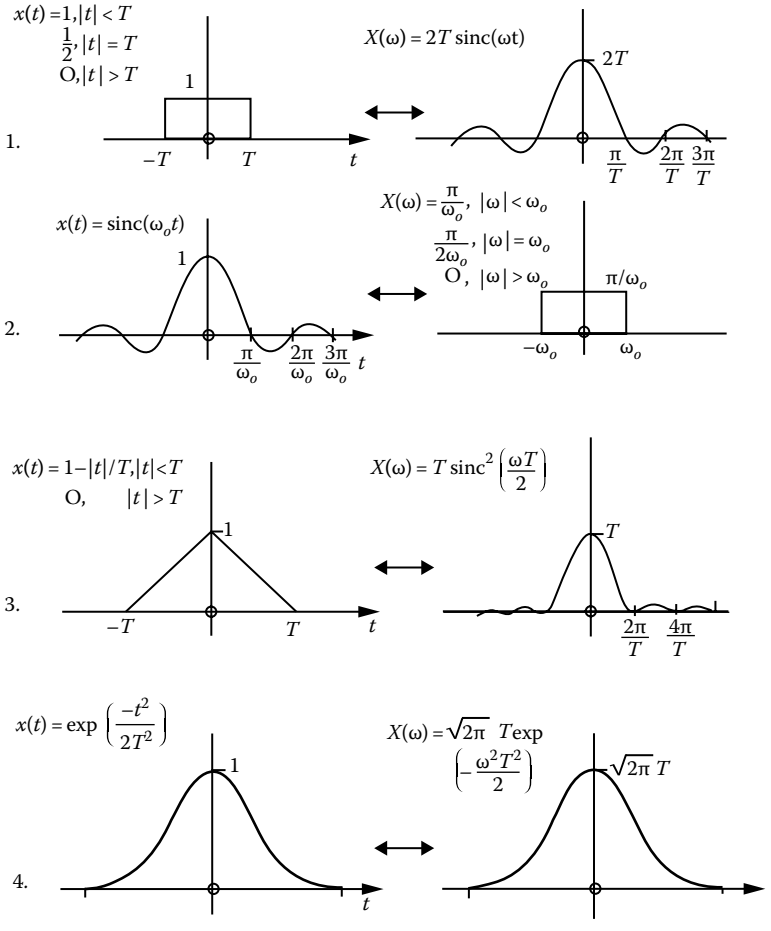

Table of Fourier Transform Pairs

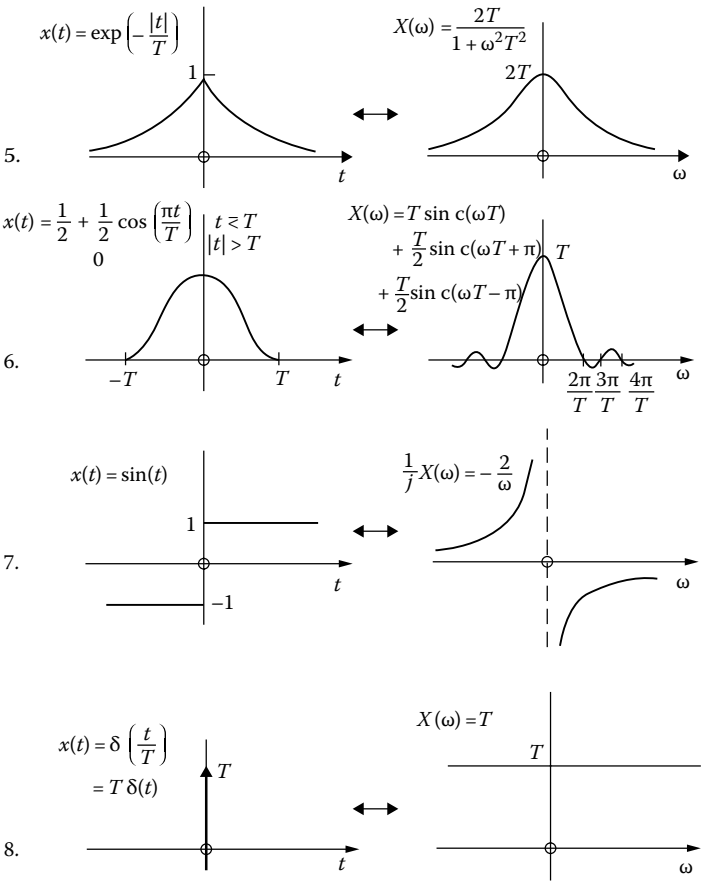

E.14.3 Problems on Optical Transmitters

Question 1: Direct modulation

(a) Sketch a diagram on how to connect the laser source and the electrical data generator for direct modulation.

(b) A laser has a threshold current of 10 mA and output power of 10 mW at a driving current of 40 mA. Data sequence is assuming a perfect square wave. Sketch the laser P-I relationship and then a diagram on how to drive the laser using the time-amplitude scale of the input current. Make sure that there would be no turn-on delay.

(c) If the rise time of the laser is 10 ps and the data bit rate is 10 Gb/s, sketch the output optical pulse sequence.

Question 2: Direct modulation

(a) State the advantages and disadvantages of FP lasers and DFB lasers in terms of optical linewidth, output power, spectrum under modulation, and bias conditions.

(b) Give reasons why direction modulation of lasers cannot work for bit rates greater than 8 Gb/s.

Question 3: External modulation
A bit pattern "1 1 0 1 0 0 1 1 0 1" with a bit rate of 10 Gb/s is input into two separate modulators to generate ASK and BDPSK modulation format.

(a) Sketch the modulated bit pattern including the carrier which can be drawn with two or three periods within the duration of a bit period. Hence the phase distribution or the scatter diagram of the modulated sequence.
(b) An MZIM is used as an optical modulator, its V_π is 5 V. Show how the data sequence can be conditioned to feed into the electrode port of the modulator so that ASK or BDPSK signals can be generated. Make sure that you show the biasing voltage.
(c) Repeat (b) for the case that the modulator is a dual-drive type of optical modulator.
(d) Give a structure of a precoder for DPSK modulation, that is, the precoder that would generate the differential codes which are then used to drive the optical modulator with signal conditioning to appropriate level for driving the electrodes.

Question 4a: Optical modulator and phasor diagram

(a) Sketch the schematic diagram of an intensity optical modulator which consists of an optical waveguide as the input light guide which is then split into two parallel paths whose refractive indices would be modulated by an electrode, hence a phase modulation of the lightwaves that pass through these waveguides. This type of optical modulator can be termed as an interferometric intensity modulator.
(b) For a single-drive modulator, only one path of the lightwave is modulated. What is the total phase change exerted on the lightwaves if the following parameters are employed for the optical modulation: electro-optic coefficient: $r = 10^{-11}$ m/V, electrode length = 10 mm. Separation between active electrode and earth electrode = 5 μm.
(c) Estimate the change in the refractive index due to the applied voltage via the electro-optic effect, then
(d) The change in the velocity of the lightwave.
(e) The total phase change over the electrode length, note that a phase change of 2π is equivalent to the slowing down of one wavelength. You may confirm that the phase change can be given by $\Delta\phi = \frac{c\Delta n}{n^2} L \frac{2\pi}{\lambda}$.
(f) Estimate the voltage required for applying to the electrode so that a π phase change occurs on the lightwave carrier passing through it.
(g) Write down an expression that represents the lightwave at the input. Thence those for the split waves propagating in the two parallel lightpaths of the interferometer. Represent their phasors in a plane.
(h) Then find the sum of the two phasors and hence project this total phasor vector on the real axis and obtain the equation of the lightwave at the output of the modulator as a function of the applied voltage V.

Question 5
Optical modulator and phasor diagram—dual-drive MZM.

(a) Repeat Question 3 with a bias voltage of $V_b = V_{\pi/2}$ and V_π and a time-varying signal of $v_s(t) = V_{\pi/2} \cos\omega_s t$ with $\omega_s = 2\pi f_s$ and $f_s = 20$ GHz.

(b) Now the modulator is a dual-drive MZM, repeat Question 1 with a bias voltage of $V_b = V_{\pi/2}$ and V_π and a time-varying signal of $v_s(t) = V_{\pi/2} \cos\omega_s t$ with $\omega_s = 2\pi f_s$ and $f_s = 20$ GHz.

Question 6a
An optical fiber communication system consists of an optical transmitter using a 1550 nm DFB laser with a linewidth of 10 pm (pico-meters), an external optical modulator whose bandwidth is 20 GHz, and a total insertion loss of 5 dB. The modulator is driven with a bit-pattern-signal generator with a 10 dBm electrical power output into a 50 Ω line. A microwave amplifier is used to boost the electrical data pulse to an appropriate level for driving the optical modulator. The data bit rate is 10 Gb/s and its format is NRZ. An 80 km standard single-mode fiber is used for the transmission of the modulated signals.

(a) Sketch the block diagram of the transmission system.

(b) If the V_π of the external modulator is 5 V, what is the gain of the microwave amplifier so that an extension ratio of 20 dB can be achieved for the output pulses of "1" and "0" at the output of the modulator. Make sure that you sketch the amplitude and power output of the modulator versus the driving voltage into the modulator. What type of connector that you would use for connecting the microwave amplifier to the modulator and that to the bit pattern generator.

(c) If the DFB laser emits 0 dBm optical power at its pigtail output then what is the average of optical power contained in the signal spectrum. You may assume that the pulse sequence generated at the output of the bit pattern generator is a perfect rectangular shape.

(d) What is the effective 3 dB bandwidth of the signal power spectrum. Thence estimate the total pulse broadening of the pulse sequence at the end of the 80 km fiber length. Similarly, estimate the pulse sequence if the bit rate is 40 Gb/s.

(e) Now if a dispersion compensating fiber of 20 km is used to compensate for the signal distortion in the 80 km fiber, what is the required dispersion factor of this fiber so that there would be no distortion. If the loss of the dispersion compensating fiber is 1.0 dB/km at 1550 nm, estimate the average optical power of the signal at the output of the dispersion compensating fiber.

(f) Based on the dispersion limit given in the following, plot the dispersion length as a function of the bit rate for NRZ format.

NOTE: The dispersion limit, under linear regime operation, can be estimated in the following equation (Ref. Forgheti et al.* 1997):

$$L_D = \frac{c}{\lambda} \frac{\rho}{B_R^2 D}$$

* Forghieri et al., RZ versus NRZ in nonlinear WDM systems, *IEEE Photonics Technology Letters*, vol. 9, No.7, July 1997, pp 1035–1037.

where
B_R is the bit rate
D is the dispersion factor (s/m^2)
ρ is the duty cycle ratio, that is, the ratio between the "ON" and "OFF" in a bit period
L_D is in meters.

Question 6b
Repeat Question 6 for return-to-zero (RZ) format and ASK modulation. Sketch the structure of the RZ optical transmitter, note that an extra optical modulator must be used and coupled with the data modulator of Question 1, the optical pulse carver. Give details of the pulse carver including driving voltage, driving signal, and synchronization with the data generator.

Question 6c: Spectral efficiency

(a) A DWDM optical transmission system that can transmit optical channels whose channel spacing is 100 GHz. What is the spectral efficiency if the bit rate of each channel is 40 Gb/s and the modulation is NRZ-ASK.
(b) Repeat (a) for RZ-ASK modulation format.
(c) Repeat (a) and (b) for the channel spacing of 50 GHz.

Question 7

(a) Give a structure of an optical transmitter for generation of RZ-ASK modulation format. Make sure that you assign the optical power of lightwaves generated from the light source and that at the output of the optical modulators so that a maximum of 10 dBm of optical power is launched into the standard single-mode fiber so that it is below the nonlinear SPM effect limit.
(b) Describe the operation of the optical modulator, the pulse carver, so that it can generate periodic pulse sequence before feeding into the data generator. Make sure that you provide the amplitude and intensity levels versus the driving signal voltage levels which are used to drive the optical modulators.

Question 8: Nonlinear SPM effect
The nonlinear refractive index coefficient of silica-based standard single-mode fiber is $n_2 = 2.5 \times 10^{-20}$ m^2/W.

(a) What is the effective area of the standard single-mode fiber—you can refer to the technical specification of the Corning SMF-28 and its MFD to estimate this area.
(b) Estimate the change in the refractive index as a function of the average optical power. Hence, estimate the total phase change due to this nonlinear effect after propagating through a length L (in km) of this fiber.
(c) Hence, estimate the maximum length L of the standard single-mode fiber that the lightwaves can travel so that not higher than 0.1 rad of the phase change on this lightwave carrier would be suffered.
(d) Show how you can generate a format that would have an RZ format and a suppression of the lightwave carrier. Show that the width of the RZ pulse on this case is 67% of the bit period. Hint: you may represent the lightwaves in the path of the optical modulator, an optical interferometer by using phasors. First sketch the

phasor of the input lightwave. Then those of the two paths and then the phase applied onto these paths. Then sum up at the output to give the resultant output. For the pulse width you can estimate the width over which the amplitude fall to $1/\sqrt{(2)}$ of its maximum.

(e) Now show you can generate RZ pulse sequence with 50% and 33% pulse width of the bit period.

Question 9: Balanced Receiver

(a) Sketch the schematic diagram of an optical balanced receiver—a balanced receiver would consist of a delay interferometer and a back-to-back connected pair of photodetector with its output connected to the input of an optical preamplifier.

(b) What is the functionality of the delay interferometer. What is the temporal length of the delay unit?

(c) What are the roles of the two optical couplers and their ideal coupling coefficients?

(d) What is the relationship between the two output ports of the delay interferometer?

(e) Suppose that a sequence of 4 bits of a DPSK 10 Gb/s data channel is presented at the input of a balanced receiver. The phases of the lightwave carrier contained within these four bits are π π o π at the transition of the bit period.

(f) Sketch the carrier wave and the pulse envelope. The lightwave has a wavelength of 1550 nm—however to illustrate the wave you are expected to sketch only a few periods of the waves contained within the bit period at the input of the receiver.

(g) Sketch the electrical signal at the output of the electronic preamplifier not including noises.

(h) Now assuming that an optical amplifier is used as an optical preamplifier is placed at the input of the balanced receiver that would give an optical signal power of –10 dBm for the "0" and "1" of the DPSK sequence. The responsibility of the photodetector is 0.9 and the electronic preamplifier has a trans impedance of 150 Ω and a total equivalent noise current spectral density of 2 pA/(Hz)$^{1/2}$ and a bandwidth of 15 GHz. Sketch the signal waveform at the output of the electronic preamplifier.

Question 10: Duobinary modulation format

(a) Design a block diagram of a precoder that would generate tri-level modified duobinary format signals. Make sure that the coefficients of the filters are specified. Hint: you may refer to pages 8–11 of the lecture notes. Hence, derive the spectrum of the signals after the precoder of the modified duobinary.

(b) If possible obtain the precoders for AMI and duobinary and their frequency responses. Compare the frequency responses of the three modulation schemes.

(c) Sketch the structure of the tri-level duobinary precoder with its output of –1, 0, +1.

(d) Now then show how to use the coded signals to drive a dual-drive MZIM to generate optical duobinary signals.

Question 11: Duobinary modulation format

(a) A modulation format that would allow the detection of the modulated signals is duobinary which is a special case of partial response coding (see Chapter on modeling and optical transmitters).

(b) Give a brief account of the principles of operation of this line code.

(c) A duobinary coder using a delay and add coding structures is shown in the following. If a three-level duobinary-coded signals are required, design the precoder for this type of modulation.

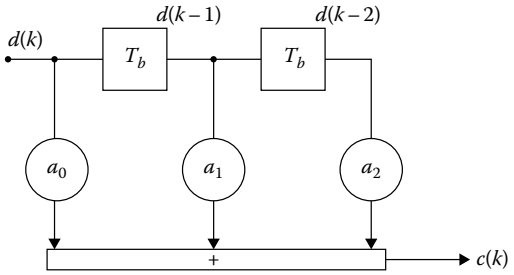

(d) Now if setting the delay time Tb is that of a bit period, transform the structure into the z-transform diagram and hence obtain the transfer function of the coder in the z-domain, thence the frequency response of this coder. Plot the frequency response of the transfer function of the filter in continuous domain.

(e) Find the impulse response of the coder, and hence the term partial response.

(f) Sketch a block diagram that shows the functionality of precoding, coding, tri-level conversion (offset) and decoding.

(g) A binary sequence $d(k)$ = {0 0 1 1 0 1 0 0 1} is applied to the input of the duobinary coder. Determine the data sequences $b(K)$, $c(k)$, and c'(k) in the electrical domain which can be used to modulate an optical modulator.

(h) Assuming that there is no dispersion in the transmission of the duobinary data sequence find the output pulse sequence at the output of the decoder. What is the physical realization of the decoder? Thence sketch the sequence at the output of a decision circuit.

(i) Now the electrical signals are applied to a microwave amplifier that would condition the signals to appropriate signal levels so as to modulate the optical modulator. The measured spectra are recorded as shown in Figure E.3(c).

(j) Determine where in the block diagram (as per attached diagram) that each of the spectrum belongs to the points of the diagram of the transmission system.

Question 12: DQPSK

DQPSK is a 2-bit per symbol modulation, that is, 2 bits/symbol, thus the scheme is spectral efficient.

(a) Give a brief account of the modulation schemes DPSK and DQPSK.

(b) Give a structure of a precoder for DPSSK—that gives a differential modulation with phase as the codes for "1" and "0."

(c) Now extend this precoder and the phase quadrature modulation technique for the structure of a DQPSK optical transmitter.

Question 13: SSB and DSB Modulation
Referring to Figure E.3a through c for generation of optical signals with SSB,

(a) State the functionality of the Hilbert transformer. Hence, could you deduce a general principle for suppression of a sideband to generate single sideband signals?
(b) What is the role of the phase shifter π/2?
(c) Explain the operation of the optical SSB transmitter, in both the time and frequency domain. Confirm that the spectrum is correct.

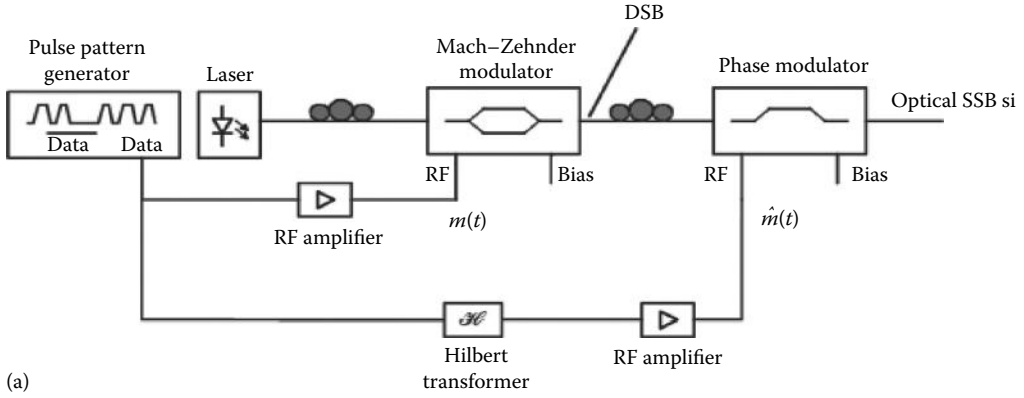

(a)

Single sideband modulation: transmitter setup

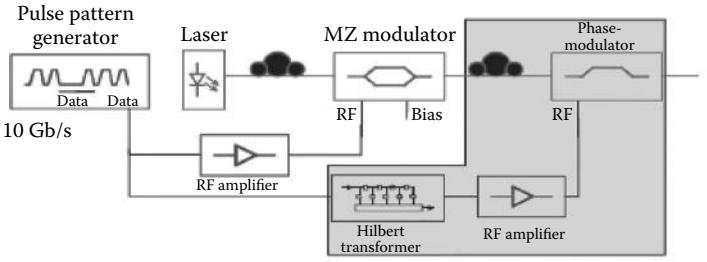

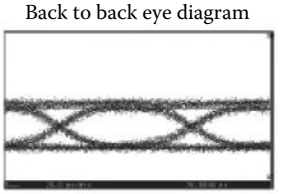

Back to back eye diagram

Extinction ratio: 4.9 dB

Power spectral density of the optical signal (simulation)

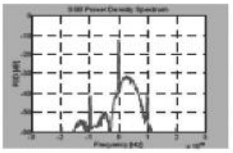

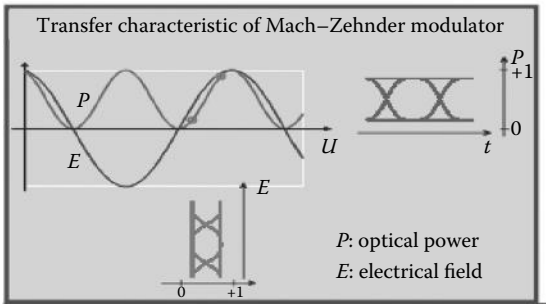

SBS: precautions to avoid signal degradation are necessary

T. Wuth: OFC 2001: 2

(b) (c)

FIGURE E.3
SSB modulation and generation using (a) transform in optical domain, (b) transform in electrical domain, (c) realization of an SSB optical transmitter.

Question 14: Coherent Optical Communication Systems

(a) Sketch a structure of an optical coherent receiver. Give a brief description of the roles of each component in your system.
(b) What is the typical modern linewidth of the laser that acts as the local oscillator?
(c) Give a distinction between the homodyne and heterodyne coherent system.
(d) A homodyne optical receiver has the following parameters:

FLD150F3CJ — **InGaAsP/InP LASER DIODE MODULE**

Absolute maximum ratings (T_C = 25°C)

Parameter	Symbol	Condition	Ratings	Unit
Storage temperature	T_{stg}		−40 to +70	°C
Operating case temperature	T_{op}		−20 to +65	°C
Optical output power	P_f	CW	8	mW
Forward current	I_F	CW	150	mA
Reverse voltage	V_R		2	V
Photodiode reverse voltage	V_{DR}		20	V

Optical and Electrical characteristics (T_L = 25°C, T_L : Laser temperature)

			Limits			
Parameter	Symbol	Test Condition	Min.	Typ.	Max.	Unit
Threshold current	I_{th}	CW	—	20	30	mA
Forward voltage	V_F	CW, I_F = 30 mA	—	1.1	1.5	V
Optical output power	P_f	CW	4	—	—	mW
Threshold optical output power	P_{th}	CW, $I_F = I_{th}$	—	30	120	μW
Slope efficiency	η	CW, P_f = 4 mw	0.07	0.09	—	mW/mA
Monitor Current	I_m	CW, P_f = 4 mw V_{DR} = 5 V	0.05	0.08	—	mA
Peak wavelength	λ_P	CW, P_f = 4 mw	1530	1550	1570	nm
Side-mode suppression ratio	S_r		30	33	—	dB
Rise time	t_r	P_{peak} = 4 mW, $I_{bias} = I_{th}$	—	0.2	0.5	ns
Fall time	t_f		—	0.4	0.5	ns
Photodiode dark current	I_D	V_{DR} = 5 V	—	1	100	nA
Photodiode capacitance	C_t	V_{DR} = 5 V, f = 1 MHz	—	12	—	pF
Tracking error	TE	T_C = −20 to +65°C T_L = 25°C, P_f = 4 mW at T_C = 25°C APC with monitor PD	—	±5	—	%
Cooling capacity	ΔT	CW, P_f = 4 mw	40	—	—	°C
Cooler current	I_C	ΔT = 40°C P_f = 4 mW	—	0.5	1	A
Cooler voltage	V_C		—	1.2	2.1	V
Thermistor resistance	R_{th}		9.5	10	10.5	KΩ
Thermistor B constant	B		3500	3900	4300	°K

FIGURE E.4
Technical data of a semiconductor laser diode.

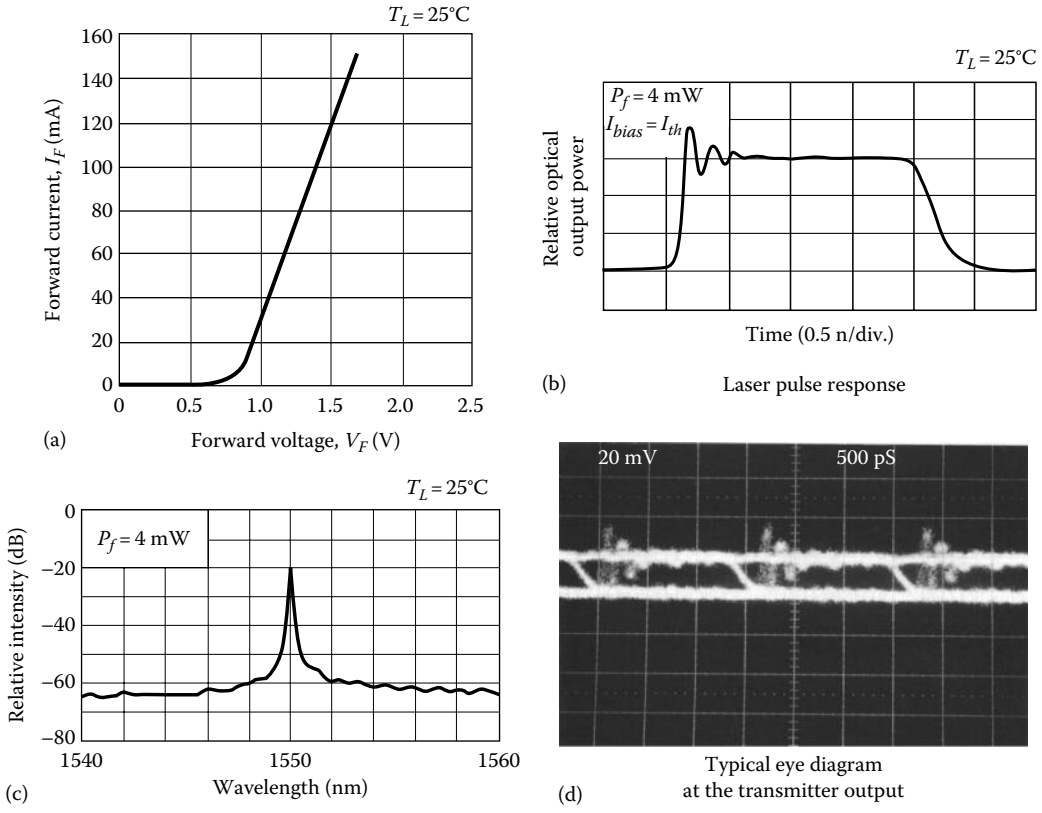

FIGURE E.5
Laser *P–I* characteristics and output pulses and eye diagram. (a) Forward current versus forward voltage. (b) Pulse response. (c) Lasing spectrum. (d) Eye diagram generated from modulated laser.

(e) A photodetector with a responsibility of 0.9 which is followed by an electronic preamplifier whose total equivalent noise spectral density is 5 pA/(Hz)$^{1/2}$ and an electrical bandwidth of 15 GHz. The transmission bit rate is 10 Gb/s.

(f) The local oscillator is a tunable laser source with a linewidth of 100 MHz. The wavelength in vacuum of both the signals and the local oscillator is 1550.92 The average optical power of the local oscillator coupled to the photodetector is 0 dBm.

(g) Sketch the structure of the receiver and then its equivalent small-signal circuit which includes the generated electronic signal current at the output of the photodetector, the total noise currents looking from the input of the electronic preamplifier. What is the dominant noise source in this receiver?

(h) For an optical signal with an average power of –20 dBm, estimate the signal to noise ratio at the output of the photodetector.

(i) Re-calculate the SNR of the receiver if the frequency of the local oscillator is 20 GHz away from that of the signal carrier frequency (Figures E.4 and E.5).

SECOND EDITION

Optical Fiber Communication Systems with MATLAB® and Simulink® Models

Carefully structured to instill practical knowledge of fundamental issues, **Optical Fiber Communication Systems with MATLAB® and Simulink® Models** describes the modeling of optically amplified fiber communications systems using MATLAB® and Simulink®. This lecture-based book focuses on concepts and interpretation, mathematical procedures, and engineering applications, shedding light on device behavior and dynamics through computer modeling.

Supplying a deeper understanding of the current and future state of optical systems and networks, this **Second Edition**:

- Reflects the latest developments in optical fiber communications technology
- Includes new and updated case studies, examples, end-of-chapter problems, and MATLAB® and Simulink® models
- Emphasizes DSP-based coherent reception techniques essential to advancement in short- and long-term optical transmission networks

Solutions manual available with qualifying course adoption

Optical Fiber Communication Systems with MATLAB® and Simulink® Models, Second Edition is intended for use in university and professional training courses in the specialized field of optical communications. This text should also appeal to students of engineering and science who have already taken courses in electromagnetic theory, signal processing, and digital communications, as well as to optical engineers, designers, and practitioners in industry.

CRC Press
Taylor & Francis Group
an informa business
www.crcpress.com

6000 Broken Sound Parkway, NW
Suite 300, Boca Raton, FL 33487
711 Third Avenue
New York, NY 10017
2 Park Square, Milton Park
Abingdon, Oxon OX14 4RN, UK

K22108

ISBN: 978-1-4822-1751-3
90000
9 781482 217513